Nanoscale Organo-Rare-Earth-Metal Clusters

DISSERTATION

der Mathematisch-Naturwissenschaftlichen Fakultät
der Eberhard Karls Universität Tübingen
zur Erlangung des Grades eines
Doktors der Naturwissenschaften
(Dr. rer. nat.)

vorgelegt von
M. Sc. Dennis Alexander Buschmann
aus Nürtingen

Tübingen
2022

Gedruckt mit Genehmigung der Mathematisch-Naturwissenschaftlichen Fakultät der Eberhard Karls Universität Tübingen.

Tag der mündlichen Qualifikation:	21.07.2022
Dekan:	Prof. Dr. Thilo Stehle
1. Berichterstatter:	Prof. Dr. Reiner Anwander
2. Berichterstatter:	Prof. Dr. Andreas Schnepf

Nanoscale Organo-Rare-Earth-Metal Clusters

Dennis Alexander Buschmann

Preface

The following PhD thesis consists of a review on synthesis strategies toward high-nuclearity rare-earth-metal clusters as well as their physicochemical properties and applications, a summary of the main results, and original scientific papers. The work has been carried out at the Institute of Inorganic Chemistry of the Eberhard Karls Universität Tübingen, Germany, over the period from March 2018 to June 2022 under the supervision of Prof. Dr. Reiner Anwander. Funding has been gratefully received from the Deutsche Forschungsgemeinschaft (DFG).

Parts of this thesis have been presented at international and national conferences as poster contributions and oral presentations.

Acknowledgements

First and foremost, I want to thank my supervisor Prof. Dr. Reiner Anwander. Thank you for allowing me to join your laboratory throughout my academic carrer as a Bachelor, Master and PhD student, and your help and support with any research related topic. Thank you for letting me follow my interest in rare-earth-metal and cluster chemistry, as well as for the opportunity to attend and present my work at national and international conferences. I am thankful for initiating the possibility to visit the laboratory of Prof. Kazushi Mashima during my Master studies.

I am deeply grateful to Prof. Dr. Kazushi Mashima and Prof. Dr. Hayato Tsurugi for the time I was allowed to spend at Osaka University. Thank you for accepting me as short-term scholar in your laboratory and for providing me with an interesting research topic. I want to thank all members of the Mashima laboratory for the warm response, friendly atmosphere and interesting discussions. Special thanks go to Dr. Haruki Nagae, Hideaki Ikeda, Mariko Inoue, Koichi Shinohara and Satoru Shirase for their helpful support in any situation. My time in Japan has been one of the most precious and valuable experiences of my life.

Furthermore, I would like to thank our collaboration partners Prof. Dr. Richard Layfield, Prof. Dr. Michael Seitz, Dr. James Durrant and Dr. Wolfgang Leis for their invaluable contribution to my work.

I want to especially thank Dr. Cäcilia Maichle-Mössmer for the introduction into X-ray crystallography, her help with structure determination, and interesting and helpful discussions. Further thanks go to Dr. David Schneider for providing the basis of my interesting research topic.

I would like to thank Dr. Klaus Eichele, Dr. Markus Kramer, Dominik Brzecki, Kristina Heß and Priska Kolb for their expertise and help regarding NMR spectroscopy and the measuring of various samples. Additional thanks go to Wolfgang Bock and Mohammad Ghani for conducting elemental analyses, as well as Elke Nadler for recording EDX spectra.

My thanks go to Elke Nique and Heinz-Jürgen Kolb for taking care of chemical orderings and keeping the lab running. Additionally, I want to thank Tobias Wolf for the maintenance of lab equipment and help with IT related problems, and Sabine Ehrlich for her help with administrative work.

I want to thank my current and fomer coworkers of the Anwander group Dr. Uwe Bayer, Dr. Verena Bayer, Dr. Lorenz Bock, Dr. Martin Bonath, Dr. Dominic Diether, Dr. Jochen Friedrich, Dr. Jochen Glaser, Dr. Lars Hirneise, Dr. Christoph Hollfelder, Dr. Yucang Liang, Dr. Leilei Luo, Dr. Manfred Manßen, Dr. Dorothea Schädle, Dr. Christoph Stuhl, Dr. Daniel Werner, Dr. Benjamin Wolf, Dr. Yanzhong Zhen, Damir Barisic, Tassilo Berger, Denis Burghardt, Adrian Jenner, Markus Katzenmayer, Felix Kracht, Jakob Lebon, Simon Matt, Olga Mironova, Eric Moinet, Xin Ning, Jitpisut Poolwong, Jonas Riedmaier, Theresa Rieser, Georgios Spiridopoulos, Andrea Sonström, Simon Trzmiel, Yali Yang and Gernot Zug for the friendly working atmosphere and support as well as interesting discussions, with special thanks to my

“mentor” Damir Barisic for introducing me to the world of rare-earth-metal chemistry and Dr. Dorothea Schädle for proofreading this thesis.

Further thanks go to my Bachelor and pratical students Jan Beitlberger, Lion Schumacher, and Hannah Wittmann. Thank you for your diligence and your valuable contribution to my work.

Der wichtigste Dank gebührt meiner Familie. Meinen Eltern Heinz und Heidi, meinen Geschwistern Svenja und Sebastian, sowie meinen Großeltern bin ich zutiefst dankbar für ihre uneingeschränkte Hilfe und Unterstützung in allen Lebenslagen, während meines Studiums und während meiner Doktorarbeit. Ihr habt einen unermesslichen Anteil daran, und ohne euch wäre das alles nicht möglich gewesen.

Contents

Abbreviations

AC	Alternating Current	EDX	Energy-dispersive X-ray spectroscopy
*t*Bu	*tert*-Butyl	*e.g.*	*exempli gratia*
ca.	circa	Em.	Emission
Cp	Cyclopentadienyl	Et	Ethyl
Cp*	C_5Me_5	*et al.*	*et alii* or *et aliae*
Cp'	$C_5H_4SiMe_3$	Exc.	Excitation
Cp*'	$C_5Me_4SiMe_3$	h	Hour
d	Day	Hal	Halide (Cl, Br, I)
DC	Direct Current	IR	Infrared
dipp	2,4-*iso*propylpentadienyl	Ln	Rare-earth metals (Sc, Y, La – Lu)
dmp	2,4-methylpentadienyl	Me	Methyl
do	Donor	NMR	Nuclear Magnetic Resonance
dtbp	2,4-*tert*butylpentadienyl	*i*Pr	*iso*-Propyl
DRIFT	Diffuse Reflectance Infrared Fourier Transform	*n*-Pr	*n*-Propyl
EA	Elemental Analysis	rt	ambient temperature

SQUID	Superconducting Quantum Interference Device
THF	Tetrahydrofuran
THP	Tetrahydropyran
THT	Tetrahydrothiophene
UV-Vis	Ultraviolet–Visible
VT	Variable temperature
X	Halide (Cl, Br, I)

Abstract

Although rare-earth-metal clusters serve as established model systems for distinct reaction patterns, the formation process of metal clusters is rather complex and often not well understood.

Primarily, the process of formation of high-nuclear lanthanide clusters was scrutinized. The halfsandwich tetramethylaluminate complexes $Cp^{R}Ln(AlMe_4)_2$ (R = Me_3Si (Cp'), Me_5 (Cp*)) were treated with different halidogenido-transfer reagents (Me_3SiI, Me_3GeBr, Me_3GeCl) to afford multinuclear Ln clusters. By applying modular changes to the synthesis protocol, effects of various parameters on the cluster formation could be revealed. The sterically less demanding Cp' ligand enabled cluster enlargement to the dodecametallic lanthanum clusters $[Cp'LaX_2]_{12}$ (X = I, Br) and characterization by NMR spectroscopy in contrast to the Cp* ligand, yielding the nonanuclear cluster $[Cp^*LaI_2]_9$. Similarly, the larger iodido and bromido ligands afforded the larger coordination clusters $[Cp'LaX_2]_{12}$ (X = I, Br) compared to the smaller chlorido ligand, where the decametallic cluster $[Cp'LaCl_2]_{10}$ was isolated. Changing the rare-earth-metal center from lanthanum to marginally smaller cerium or praseodymium metal centers revealed a size effect for the metal center by the isolation of structurally diverse clusters, e.g. the hexadecanuclear lanthanide nanowheel $[Cp'_4Ln_4I_8]_4$ (Ln = Ce, Pr). Lastly, establishing a kinetically controlled reaction pathway via a diffusion synthesis protocol enabled the isolation of lanthanide clusters with distinct structural motifs that can be exclusively obtained by this route, such as the desilylated octanuclear lanthanum cluster $[(\mu\text{-}Cp)_2Cp'_8Ce_8I_{14}]$. Further mechanistic studies by NMR spectroscopy were conducted on the trinuclear model cluster $[Cp^*_3Y_3(\mu_2\text{-}Me)_3(\mu_3\text{-}CH_2)(\mu_3\text{-}H)(thf)_3]$, featuring a rare mixed methyl/methylidene/hydrido derivative, which gave detailed insight on the process of formation of simple lanthanide clusters.

Additionally, the physicochemical properties of the complexes were investigated. The cerium precursor complexes and clusters both showed interesting photoluminescence behavior, which can be precisely tuned by changing the ligand system. Furthermore, clusters showing single-molecule magnet (SMM) behavior were targeted by using ferromagnetic lanthanides as metal centers. The obtained tetranuclear dysprosium cluster $[Cp^*DyI_2]_4$ then displayed single-molecule magnetism properties, hence establishement of a straightforward synthesis route toward potential SMM clusters was feasible.

Zusammenfassung

Seltenerdmetallcluster dienen als etablierte Modellsysteme für spezifische Reaktionswege. Dennoch ist der Bildungsprozess von Clustern hochgradig komplex und häufig auch nur unzureichend charakterisiert.

Im Wesentlichen wurde der Bildungsprozess von Seltenerdmetallclustern genauer untersucht. Die Halbsandwich-Tetramethylaluminatkomplexe $Cp^{R}Ln(AlMe_4)_2$ (R = Me_3Si (Cp'), Me_5 (Cp*)) wurden mit den Halogenido-Transferreagenzien (Me_3SiI, Me_3GeBr, Me_3GeCl) umgesetzt um mehrkernige Seltenerdmetallcluster zu erhalten. Durch gezielte Änderungen im Syntheseprotokoll wurden die Auswirkungen verschiedener Faktoren auf die Clusterbildung untersucht. Der sterisch weniger anspruchsvolle Cp'-Ligand ermöglichte die Synthese der größeren zwölfkernigen Cluster $[Cp'LaX_2]_{12}$ (X = I, Br) sowie eine NMR-spektroskopische Charakterisierung im Gengensatz zum Cp*-Liganden, der den neunkernigen Cluster $[Cp^*LaI_2]_9$ als Produkt lieferte. Gleichermaßen ergaben die größeren Iodido- und Bromido-Liganden die größeren Cluster $[Cp'LaX_2]_{12}$ (X = I, Br) im Gegensatz zum kleineren Chlorido-Liganden, mit dem der zehnkernige Cluster $[Cp'LaCl_2]_{10}$ isoliert werden konnte. Ein Wechsel des Metallzentrums hin zu den geringfügig kleineren Cer- oder Praseodym-Metallzentren zeigte einen Größeneffekt auf, welcher durch die Isolierung strukturell vielfältiger Cluster, wie beispielsweise dem sechzehnkernigen Nanorad $[Cp'_4Ln_4I_8]_4$, belegt werden konnte. Zuletzt konnte durch eine Diffusions-Reaktionstechnik eine Methode etabliert werden, welche die Synthese von Clustern durch einen kinetisch kontrollierten Mechanismus ermöglichte. Dadurch konnten Cluster isoliert werden, welche ausschließlich über diese Route zugänglich sind, wie der achtkernige, desilylierte Lanthan-Cluster $[(\mu\text{-}Cp)_2Cp'_8Ce_8I_{14}]$. Weitere mechanistische Untersuchungen mittels NMR Spektroskopie wurden am dreikernigen Modellcluster $[Cp^*_3Y_3(\mu_2\text{-}Me)_3(\mu_3\text{-}CH_2)(\mu_3\text{-}H)(thf)_3]$ durchgeführt, welcher eine sehr seltene Methyl/Methyliden/Hydrid-Verbindung darstellt, und detaillierte Einblicke in den Bildungsprozess einfacher Seltenerdmetallcluster ermöglichte.

Außerdem wurden die physikochemischen Eigenschaften der Komplexe untersucht. Sowohl die Cer-Vorstufen als auch die Cer-Cluster zeigten interessante Photolumineszenzeigenschaften, welche durch die Wahl des Ligandensystems angepasst werden konnten. Zusätzlich sollten durch den Einbau ferromagnetischer Seltenerdmetallzentren potenzielle Einzelmolekülmagnet-Cluster synthetisiert werden, was für den vierkernigen

Dysprosiumcluster $[Cp^*DyI_2]_4$ möglich war. Hierdurch konnte eine einfache Syntheseroute für Einzelmolekülmagnet-Seltenerdmetallcluster etabliert werden.

Publications

Publications incorporated into this thesis

Paper I Nanoscale Organolanthanum Clusters: Nuclearity-Directing Role of Cyclopentadienyl and Halogenido Ligands
D. A. Buschmann, H. M. Dietrich, D. Schneider, V. M. Birkelbach, C. Stuhl, K. W. Törnroos, C. Maichle-Mössmer, R. Anwander
Chem. Eur. J. **2020**, *26*, 10834-10840.
https://doi.org/10.1002/chem.202001482

Paper II Half-Sandwich Complexes $[Cp'_4Ln_4I_8]_4$ (Ln = Ce, Pr): Emergence of Donor-Free Organolanthanide Nanowheels
D. A. Buschmann, D. Schneider, C. Maichle-Mössmer, R. Anwander
Eur. J. Inorg. Chem. **2022**, e202100862
https://doi.org/10.1002/ejic.202100862

Paper III Cerium Fluorenyl Complexes Including CC Coupling Reactions
L. Hirneise, D. A. Buschmann, C. Maichle-Mössmer, R. Anwander
Organometallics, **2022**, *41*, 962-976.
https://doi.org/10.1021/acs.organomet.2c00029

Paper IV Rare-earth-metal half-sandwich complexes incorporating methyl, methylidene, and hydrido ligands
D. A. Buschmann, L. Schumacher, R. Anwander
Chem. Commun. **2022**, *58*, 9132-9135.

Paper V Half-Sandwich Rare-Earth-Metal Clusters – Synthesis, Characterization, and Magnetic Properties
D. A. Buschmann, J. Durrant, C. Maichle-Mössmer, R. A. Layfield, R. Anwander
Manuscript

Publications with minor contributions

Paper VI Rare-Earth-Metal Pentadienyl Half-Sandwich and Sandwich Tetramethylaluminates – Synthesis, Structure, Reactivity, and Performance in Isoprene Polymerization
D. Barisic, D. A. Buschmann, D. Schneider, C. Maichle-Mössmer, R. Anwander
Chem. Eur. J. **2019**, *25*, 4821-4832.
https://doi.org/10.1002/chem.201900108

Poster presentations

Poster I Homometallic Monocyclopentadienyl Rare-Eart Metal Halogenido Clusters: Synthesis and Characterization
D. A. Buschmann, D. Schneider, C. Maichle-Mössmer, R. Anwander
6th International Workshop on Transition Metal Clusters IWTMC, Tübingen, Germany, *September 5-7*, **2018**.

Poster II Highly Symmetrical Monocyclopentadienyl Rare-Earth-Metal Halogenido Clusters from Alkyl Precursors
D. A. Buschmann, D. Schneider, C. Maichle-Mössmer, R. Anwander
19. Vortragstagung für Anorganische Chemie der Fachgruppen der Wöhler-Vereinigung und Festkörperchemie und Materialforschung, Regensburg, Germany, *September 24-27*, **2018**.

Oral presentations

Presentation I Effect of Synthesis and Crystallization Technique on the Formation of Organolanthanum Clusters
D. A. Buschmann, D. Schneider, C. Maichle-Mössmer, R. Anwander
XXIX. Tage der Seltenen Erden Terrae Rarae 2019, Stockholm/Helsinki, Sweden/Finland, *May 30 - June 1*, **2019**.

Presentation II Tunable Luminescence of Cerium Cyclopentadienyl Complexes
D. A. Buschmann, J. Beitlberger, W. Leis, C. Maichle-Mössmer, M. Seitz, R. Anwander
Pacifichem, The International Chemical Congress of Pacific Basin Societies 2021, Honolulu, United States of America, *December 16-21*, **2021**.

Personal Contribution

Paper I:

All reactions and analyses described involving Cp' compounds were planned and conducted by myself, based on a modified synthesis protocol by Dr. David Schneider. Analyses include NMR spectroscopy (^{1}H, $^{13}C\{^{1}H\}$), DRIFT spectroscopy, and EDX analyses. The synthesis and analyses of [Cp*$LaI_2(thf)_3$] and [$Cp^*_6La_6I_8(AlMe_4)_4$] were planned and performed by Dr. Verena M. Birkelbach. The synthesis and analyses of [$Cp^*LaI_2]_9$ were planned and performed by Dr. H. Martin Dietrich. Manuscript writing was done by myself.

Elemental analyses were performed by Wolfgang Bock. The structural analyses by single-crystal X-ray diffraction were performed by Dr. Cäcilia Maichle-Mössmer, Prof. Dr. Karl W. Törnroos, and Dr. Christoph Stuhl. EDX spectra were recorded by Elke Nadler.

Paper II:

All reactions and analyses described were planned and conducted by myself. Analyses include ^{1}H NMR spectroscopy and IR spectroscopy. The synthesis and analyses of [Cp'$Ce(AlMe_4)_2$] and [$Cp'CeCl_2]_{12}$ were planned and performed by Dr. David Schneider and me. Manuscript writing was done by myself.

Elemental analyses were performed by Mohammad Ghani. The structural analyses by single-crystal X-ray diffraction were performed by Dr. Cäcilia Maichle-Mössmer, Dr. David Schneider, and myself. Photoluminescence measurements were performed by Dr. Wolfgang Leis.

Paper III:

Syntheses and analyses of cerium complexes and $LiFlu(thf)_3$ (Flu = fluorenyl) were planned and performed by Lars Hirneise. Analyses include ^{1}H NMR spectroscopy and IR spectroscopy. Syntheses and analyses of $FluLaCl_2(thf)_3$, $FluNdCl_2(thf)_3$, and $Cp^*CeCl_2(thf)_3$ were planned and conducted by myself. Analyses include NMR spectroscopy (^{1}H, $^{13}C\{^{1}H\}$) and IR spectroscopy. Coupling reactions were performed by Lars Hirneise and me. Manuscript writing was done by Lars Hirneise and myself.

Elemental analyses were conducted by Wolfgang Bock and Mohammad Ghani. The structural analyses by single-crystal X-ray diffraction were performed by Dr. Cäcilia Maichle-Mössmer and myself. VT-NMR spectra were recorded by Felix Kracht, and EPR spectra by Dominik Brzecki.

Paper IV:

All reactions described were planned by myself. The synthesis and analyses of [Cp*$_3$Ln$_3$(μ_2-Me)$_3$(μ_3-CH$_2$)(μ_3-H)(thf)$_3$] (Ln = Y, Dy) were conducted by Lion Schumacher, during his Bachelor thesis, under my supervision. Analyses include NMR spectroscopy (^{1}H, ^{13}C{^{1}H}) and DRIFT spectroscopy. ^{1}H NMR experiments were performed by Lion Schumacher and me. Manuscript writing was done by myself.

Elemental analyses were conducted by Wolfgang Bock. The structural analyses by single-crystal X-ray diffraction were performed by myself.

Paper V:

All reactions and analyses described were planned and conducted by myself. Analyses include NMR spectroscopy (^{1}H, ^{13}C{^{1}H}), DRIFT spectroscopy, and EDX analyses. Manuscript writing was done by myself, Dr. James Durrant and Prof. Dr. Richard Layfield.

Elemental analyses were conducted by Wolfgang Bock. The structural analyses by single-crystal X-ray diffraction were performed by Dr. Cäcilia Maichle-Mössmer and myself. Magnetic measurements and theoretical calculations were performed by Dr. James Durrant and Prof. Dr. Richard Layfield. EDX spectra were recorded by Elke Nadler.

Paper VI:

All reactions and analyses described were planned and conducted by Damir Barisic. Analyses include NMR spectroscopy (^{1}H, ^{13}C{^{1}H}) and DRIFT spectroscopy. Synthesis and analyses of K(2,4-dipp) and [(2,4-dipp)La(AlMe$_4$)$_2$] were done by myself. Analyses include NMR spectroscopy (^{1}H, ^{13}C{^{1}H}) and DRIFT spectroscopy. Polymerization reactions and analyses were performed by Damir Barisic. Manuscript writing was done by Damir Barisic.

Elemental analyses were conducted by Wolfgang Bock. The structural analyses by single-crystal X-ray diffraction were performed by Dr. Cäcilia Maichle-Mössmer and Dr. David Schneider.

Objective of this Thesis

The main objective of this thesis is to gain insight in the agglomeration process of high-nuclearity anhydrous metalorganic rare-earth-metal clusters and modify the developed synthesis protocols, and examine the physicochemical properties like molecular magnetism or photoluminescence behavior.

Chapter A gives a review on rare-earth-metal alkylaluminate complexes and their derivatization as well as synthesis strategies, properties and applications of donor-free rare-earth-metal clusters.

Chapter B consists of a summary of the main results of this thesis.

The unpublished results, which are neither part of a publication nor a manuscript, are presented in **Chapter C**. This section contains cyclopentadienyl-supported complexes, investigations on their photoluminescence properties, and redox chemistry.

Publications are compiled in **Chapter E**.

A

Cyclopentadienyl-Supported Rare-Earth-Metal Clusters

1 Introduction

Metal cluster compounds represent the intermediate state between the molecular level and the solid-state. As such, metal clusters serve as model systems for studying reactivities and exhibit unique structural motifs.[1-4] Despite numerous examples of metal clusters and synthesis routes, the formation procedure of metal clusters is still barely understood, and often involves complex self-assembly processes.[5-7] Therefore, the development of synthesis strategies toward controlled cluster formation represents a popular target worth striving for.

Over the past decades, rare-earth-metal clusters gained significant scientific interest due to important possible areas of applications, including magnetic cooling,[8-14] single-molecule magnetism,[15-22] and optical applications.[21, 23-26] The formation process of polynuclear rare-earth-metal complexes is highly influenced by a multitude of parameters, though the key factor is undoubtedly the choice of the synthesis medium. Large Ln^{III} clusters are usually synthesized by self-assembly processes in donor media via hydro- or solvothermal synthesis,[7, 11, 27-29] and often feature the incorporation of transition metal heteroatoms within the cluster core.[12, 14, 30] Switching the reaction medium to a non-coordinating solvent is accompanied with a significant decrease in cluster nuclearity,[31] with the so far largest structurally characterized donor-free rare-earth-metal cluster $[Cp^{12}Sm^{12}Cl_{24}]$ by TEUBEN.[32] The applied synthesis protocol of dechlorosilylation of the activated rare-earth-metal salt $SmCl_3(thf)_3$ by Me_3SiCp with subsequent removal of coordinated THF under reflux hints at the necessity of distinct and precisely controlled reaction mechanisms for the synthesis of lanthanide clusters.

This overview will cover the synthesis and possible applications of rare-earth-metal coordination clusters. Special consideration is given to different ligand systems as well as the applied synthesis protocol. Since a broad variety of lanthanide clusters exists, the focus will be placed on donor-free compounds. The first part focuses on the synthesis and reactivity of rare-earth-metal tetramethylaluminates. Part 2 firstly deals with the synthesis and derivatization of discrete rare-earth-metal halide complexes, before covering different types of lanthanide coordination clusters and their respective synthesis routes. The last part gives an overview of current applications of organo-rare-earth-metal clusters, focusing on the two major aspects of optical and magnetic properties.

2 Rare-Earth-Metal Tetramethylaluminates

The first homoleptic rare-earth-metal tetramethylaluminate complexes $Ln(AlMe_4)_3$ (**1**^{Ln} Ln = Y, La, Nd) were synthesized by EVANS via a two-step reaction protocol.[33] Treatment of the respective rare-earth-metal trichlorides with $LiNMe_2$ resulted in the formation of $Ln(NMe_2)_3(LiCl)_3$, which was subsequently reacted with excess trimethylaluminum to generate the rare-earth-metal tris(tetramethylaluminate) complexes. Even though known for two and a half decades now, the series of homoleptic rare-earth-metal tetramethylaluminates – except for Pm – was only recently completed by ANWANDER *et al.* with the isolation of the respective $Sc(AlMe_4)_3$ (**1**^{Sc}) compound.[34] In contrast to other rare-earth-metal tris(tetramethylaluminate) complexes,[33, 35-39] the successful synthesis of **1**^{Sc} requires a low-temperature synthesis protocol, treating the scandium ate complex $[Li_3ScMe_6(thf)_{1.2}]$ with $AlMe_3$ and subsequent workup steps between -40 °C and -15 °C.

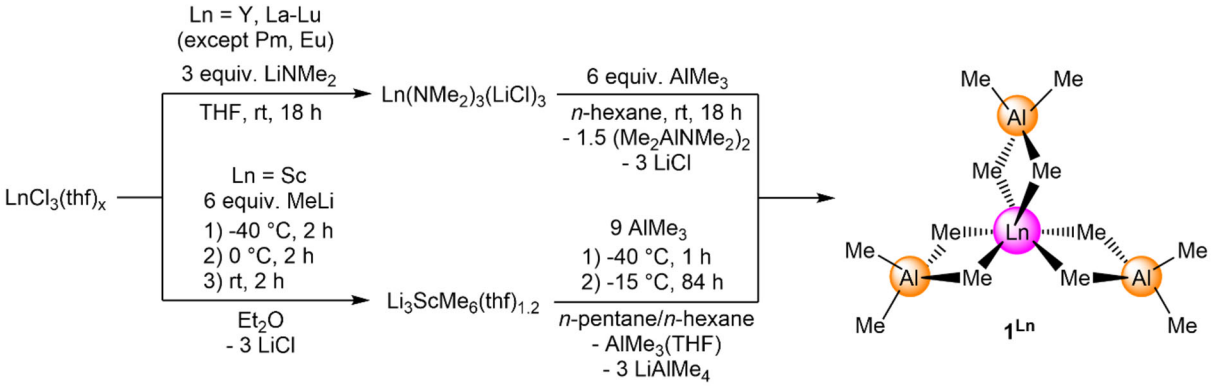

Scheme A1. Conventional synthesis routes toward homoleptic rare-earth-metal tris(tetramethylaluminate) complexes $Ln(AlMe_4)_3$.[33-39] For scandium, single-crystalline $Sc(AlMe_4)_3$ was isolable only with 0.5 molecules of co-crystallized Al_2Me_6.

Depending mainly on the metal size, homoleptic rare-earth-metal tetramethylaluminates show similar reactivities. The donor-induced cleavage with a stoichiometric amount of diethylether (Et_2O) allows the conversion into the respective trimethylated rare-earth-metal compounds.[34, 40] Furthermore, this conversion can be reversed by again adding a stoichiometric amount of trimethylaluminum, re-generating the tris(tetramethylaluminate) complexes again.

Moreover, complexes $Ln(AlMe_4)_3$ (**1**^{Ln}) are efficient precursors for the synthesis of halfsandwich-type lanthanide bis(tetramethylaluminate) compounds. Providing several advantageous features like variable steric demand and excellent stabilizing properties,[41] the cyclopentadienyl ligand or its derivatives are commonly used for the syntheses of this type of

complexes. ANWANDER *et al.* reported on the first halfsandwich lanthanide bis(tetramethylaluminate) complexes (C_5Me_5)Ln($AlMe_4$)$_2$ (**2^{Ln}**, C_5Me_5 = Cp*) accessible by treatment of the halfsandwich silylamide complexes ($C_5Me_4^R$)Ln[N($SiHMe_2$)$_2$]$_2$ (Ln = Y, Lu; R = H, Me, $SiHMe_2$, $SiMe_3$, $SiHPh_2$) with 4 equivalents of trimethylaluminum, forming the respective mono-pentamethylcyclopentadienyl rare-earth-metal bis(tetramethylaluminate) compounds (Cp*)Ln($AlMe_4$)$_2$ (**2^{Ln}**).[42] Further advances in the synthesis of halfsandwich derivatives involve syntheses via protonolysis or salt metathesis of the respective homoleptic rare-earth-metal tris(tetramethylaluminates) with cyclopentadiene derivatives[43] or the corresponding alkali metal salts.[44] Meanwhile, a plethora of variously substituted cyclopentadienyl rare-earth-metal bis(tetramethylaluminates) was isolated.[45-50] Similar to the respective homoleptic complexes,[51] halfsandwich-type lanthanide bis(tetramethylaluminate) complexes serve as efficient catalysts for the polymerization of conjugated dienes.[45, 46, 49, 52]

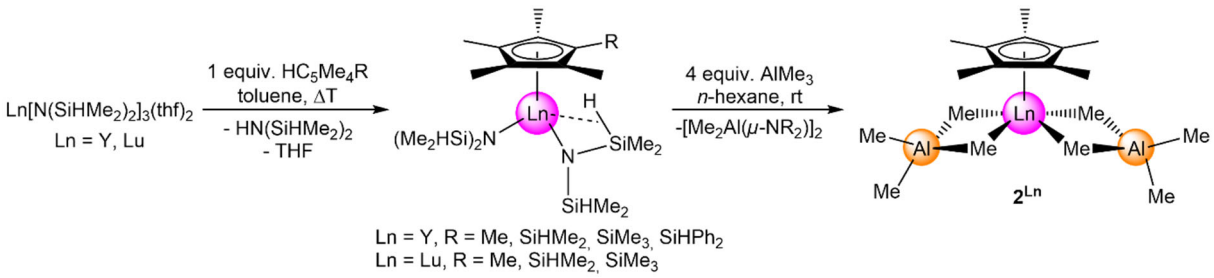

Scheme A2. Synthesis of halfsandwich pentamethylcyclopentadienyl (Cp*) bis(tetramethylaluminate) lanthanide complex Cp*Ln($AlMe_4$)$_2$ (**2^{Ln}**).[42]

In general, three different coordination modes for rare-earth-metal tetramethylaluminates **1^{Ln}** were determined in the solid state. Depending on the steric demand of the ligand, tetramethylaluminato ligands can either adopt a η^1- (high steric saturation of the metal center)[53] or a η^3-coordination mode (low steric saturation of the metal center),[54] though the most common one is the η^2-coordination motif, that complexes **1^{Ln}** and **2^{Ln}** display in the crystal structure. The respective halfsandwich complexes **2^{Ln}** revealed two different structural motifs, a planar and a bent coordination of the η^2-tetramethylaluminato ligand.[42]

Halfsandwich bis(tetramethylaluminate) rare-earth-metal complexes engage in selective derivatization reactions. Homoleptic rare-earth-metal methyl complexes of the general composition [$LnMe_3$] (**3^{Ln}**, Ln = Sc, Y, Ho, Lu)[34, 40, 55] are feasible via donor-induced tetramethylaluminate cleavage. Similar to homoleptic complexes **1^{Ln}**,[40] methylation of the respective halfsandwich complexes is achieved by $AlMe_3$ displacement (Scheme A3). Addition of two equivalents of Et_2O to an *n*-hexane solution of **2^{Ln}** (Ln = Y, Lu) leads to the formation

of trimeric halfsandwich rare-earth-metal dimethyl complexes [Cp*LnMe$_2$]$_3$ (**4^{Ln}**),[43] whereas treatment of a toluene/*n*-hexane solution of **2^{Y}** with one equivalent of diethyl ether resulted in the formation of the yttrium-aluminum-methine cluster [Cp*$_4$Y$_4$(μ_2-CH$_3$)$_2${(CH$_3$)Al(μ_2-CH$_3$)$_2$}$_4$-(μ_4-CH)$_2$] (**5**).[56]

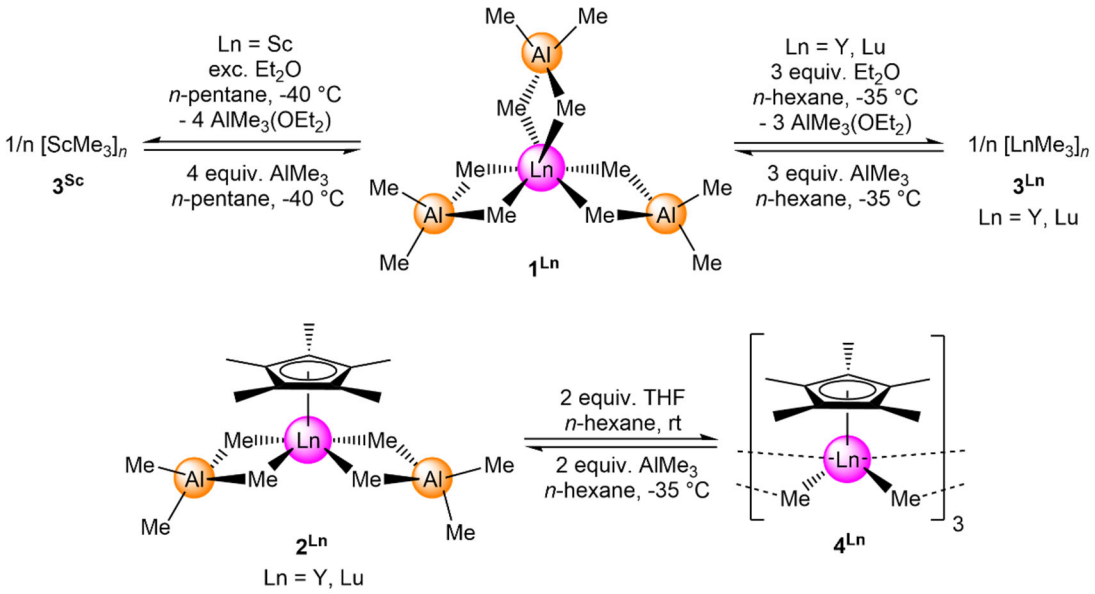

Scheme A3. Synthesis of homoleptic (**3^{Ln}**) and halfsandwich (**4^{Ln}**) rare-earth-metal methyl complexes via donor-induced cleavage of tetramethylaluminato ligands.[34, 40, 43]

Diethyl ether plays a key role in the synthesis of rare-earth-metal alkylgallate complexes as well. The homoleptic and halfsandwich tetramethylgallate compounds La(GaMe$_4$)$_3$ (**6**) and Cp*La(GaMe$_4$)$_2$ (**7**) are accessible via the addition of 3 equivalents of neat GaMe$_3$ and 4 equivalents of the diethyl ether adduct GaMe$_3$·OEt$_2$ to an *n*-hexane solution of either La(AlMe$_4$)$_3$ or Cp*La(AlMe$_4$)$_2$ (Scheme A4),[57] respectively, allowing the reverse reaction of the previously reported gallate/aluminate exchange reaction.[47] Accordingly, halfsandwich bis(tetramethylgallate) complexes are accessible via the protonolysis of La(GaMe$_4$)$_3$ (**6**) with stoichiometric amounts of HCp* or by employing the donor-assisted Al/Ga exchange (Scheme A4). Whereas the reaction of **6** can be performed at ambient temperature to give the corresponding lanthanum sandwich complex Cp*$_2$La(GaMe$_4$) (**8^{La}**), the respective conversions to yttrium complexes **1^{Y}** and **2^{Y}** with HCp* require elevated temperatures of 130 °C to afford the yttrocene Cp*$_2$Y(GaMe$_4$) (**8^{Y}**).[47]

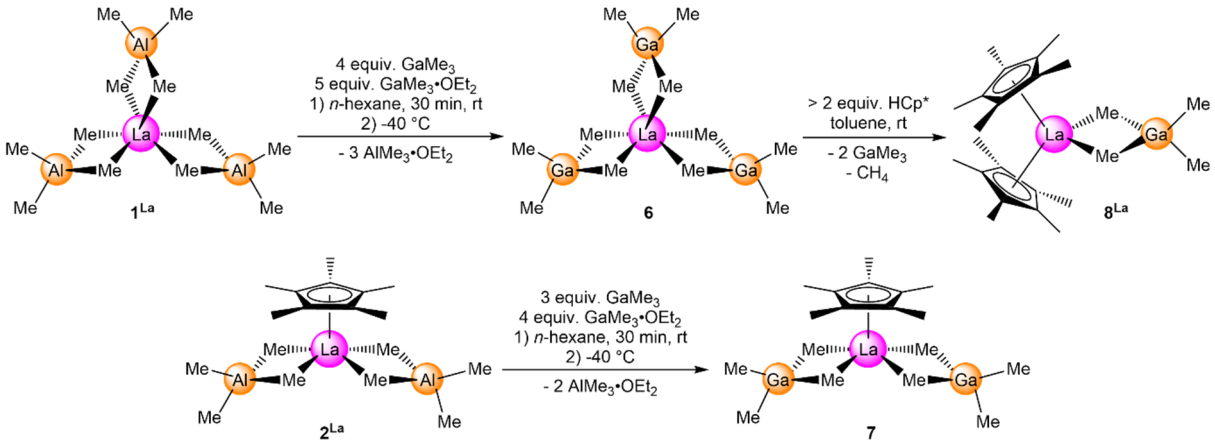

Scheme A4. Synthesis of lanthanum tetramethylgallate complexes via Al/Ga exchange.[47, 57]

The variation of the steric demand of the ancillary ligand system by substitution with pentadienyl ligands[58] allows for new reactivities of rare-earth-metal halfsandwich bis(tetramethylaluminate) complexes. Such "open" halfsandwich derivatives are only accessible via a salt metathesis reaction protocol,[59] in contrast to the established protonolysis synthesis route for cyclopentadienyl-based halfsandwich complexes. The addition of an *n*-hexane or toluene solution of $\mathbf{1^{Ln}}$ (Ln = La, Ce, Pr, Nd) to a suspension of a pentadienyl potassium salt K(2,4-R) (R = dimethylpentadienyl (dmp), diisopropylpentadienyl (dipp), di-*tert*-butylpentadienyl (dtbp)) leads to the formation of the respective pentadienyl-supported rare-earth-metal halfsandwich compounds (2,4-R)Ln($AlMe_4$)$_2$ ($\mathbf{11^{La}}$, R = dmp; $\mathbf{12^{La}}$, R = dipp; $\mathbf{13^{Ln}}$, R = dtbp) (Figure A1). In contrast to the larger lanthanides, smaller rare-earth metals tend to form sandwich complexes instead. As such, the reaction of $\mathbf{1^{Ln}}$ (Ln = Y, Lu) with one equivalent of K(2,4-dmp) afforded the "open" sandwich complex (2,4-dmp)$_2$Ln($AlMe_4$) ($\mathbf{14^{Ln}}$).

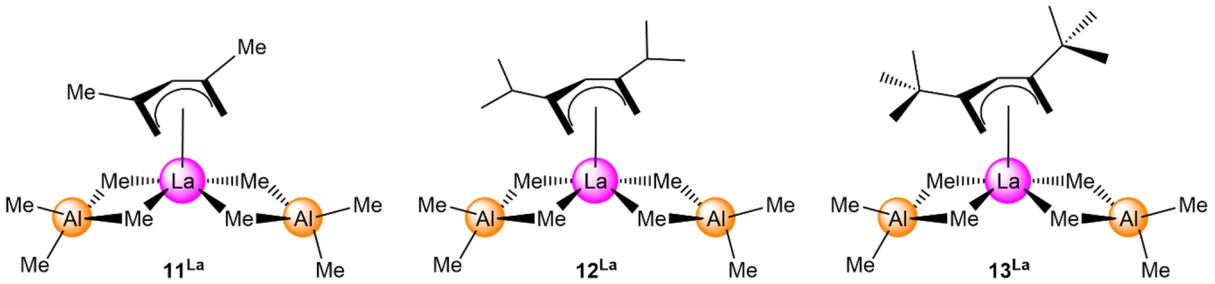

Figure A1. Halfsandwich lanthanum pentadienyl complexes (2,4-R)La($AlMe_4$)$_2$ $\mathbf{11^{La}}$, $\mathbf{12^{La}}$ and $\mathbf{13^{La}}$.[59]

Subsequent derivatization reactions include aluminate/gallate exchange and cationization reactions with different perfluorinated borates or perfluorinated borane.[59] Surprisingly, in the latter case a different reactivity can be observed. While treatment of $\mathbf{13^{La}}$ with the perfluorinated borates [Ph_3C][$B(C_6F_5)_4$] or [$PhNMe_2H$][$B(C_6F_5)_4$] affords a product mixture of the cationized

species $[La(AlMe_4)_2]^+$ (**15**) and (2,4-dtbp)$La(AlMe_4)^+$ (**16**) – both with $[B(C_6F_5)_4]^-$ as respective counterion – the reaction with the perfluorinated borane gave access to the dimeric complex $[\{(2,4\text{-dtbp})La(\mu\text{-}Me)_2AlMe(C_6F_5)\}\{Me_2Al(C_6F_5)_2\}]_2$ (**17**) exclusively (Scheme A5).

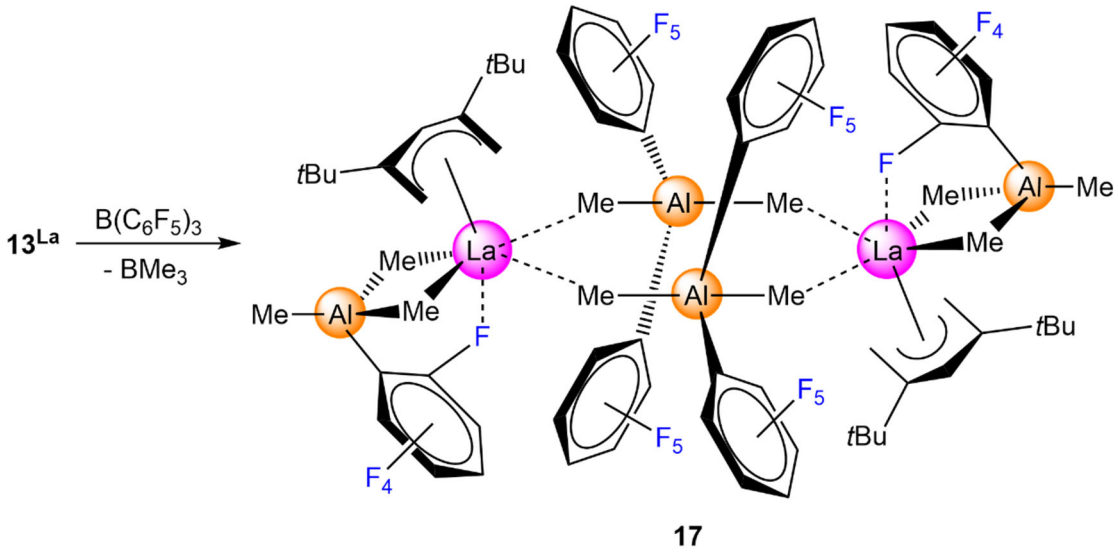

Scheme A5. Synthesis of $[(C_6F_5)_2AlMe_2]$-bridged complex **17**.[59]

The corresponding cyclopentadienyl-based rare-earth-metal halfsandwich complexes undergo similar cationization reactions as the aforementioned pentadienyl compounds.[60] Reacting $\mathbf{3^{Ln}}$ (Ln = Y, La, Nd) with perfluorinated borates afforded the cationic species $[Cp^*Ln(AlMe_4)]^+$ ($\mathbf{18^{Ln}}$) with the counterion $[B(C_6F_5)_4]^-$, though the formation of a product mixture was not observed. Accordingly, the reaction of $\mathbf{3^{La}}$ with two equivalents of $B(C_6F_5)_3$ results in the formation of dimeric $[\{Cp^*La(\mu\text{-}Me)_2AlMe(C_6F_5)\}\{Me_2Al(C_6F_5)_2\}]_2$ (**19**). Like the cyclopentadienyl-supported compounds, the cationic complexes bearing ancillary pentadienyl ligands serve as potential pre-catalysts in the polymerization of dienes.[59]

Other reactivities of rare-earth-metal halfsandwich bis(tetramethylaluminate) compounds include the derivatization with amido or imido ligands,[61, 62] C–H bond activation,[49, 52] or tetramethylaluminato/halogenido exchange reactions.[46, 63, 64] Depending on the steric demand of the ancillary ligand, the halogenido ion size as well as the stoichiometry of halogenido-transfer reagent, a multitude of structural motifs are accessible, ranging from dimeric halogenido-bridged complexes to polynuclear cluster compounds.

3 Cyclopentadienyl-Supported Rare-Earth-Metal Clusters

3.1 Cyclopentadienyl-Supported Rare-Earth-Metal Halide Complexes

The first halfsandwich rare-earth-metal halide complexes bearing ancillary cyclopentadienyl derivatives with the general formula $CpLnCl_2$ (Ln = Sm, Eu, Gd, Dy, Ho, Er, Lu) were isolated by DUBECK *et al*. as the respective THF adducts via three different synthesis routes.[65]. Addition of a stoichiometric amount of sodium cyclopentadienide to a THF suspension of rare-earth-metal trichlorides $LnCl_3$ (Ln = Sm, Eu, Gd, Dy, Ho, Er, Lu) led to the formation of the corresponding halfsandwich rare-earth-metal dichlorido THF adducts $CpLnCl_2(thf)_3$ (**20^{Ln}**). Alternative synthesis routes include the reaction of the homoleptic tris(cyclopentadienyl) erbium Cp_3Er with two equivalents of the respective erbium trichloride $ErCl_3$ in THF, affording the cyclopentadienyl erbium dichloride $CpErCl_2(thf)_3$ (**20Er**). Similarly, the addition of one equivalent of hydrogen chloride to di(cyclopentadienyl)ytterbium chloride Cp_2YbCl in THF gave the cyclopentadienyl ytterbium dichloride $CpYbCl_2(thf)_3$ (**20^{Yb}**). Accordingly, the sandwich complexes $(C_5H_4R)_2LnCl$ (**21^{Ln}**, R = H; **22^{Ln}**, R = Me; Ln = Sm, Gd, Dy Ho, Er, Yb, Lu) were prepared via salt metathesis by treatment of the lanthanide trichloride with two equivalents of sodium cyclopentadienide in THF.[66] Subsequent removal of coordinated THF was achieved by sublimation of the respective sandwich complexes.

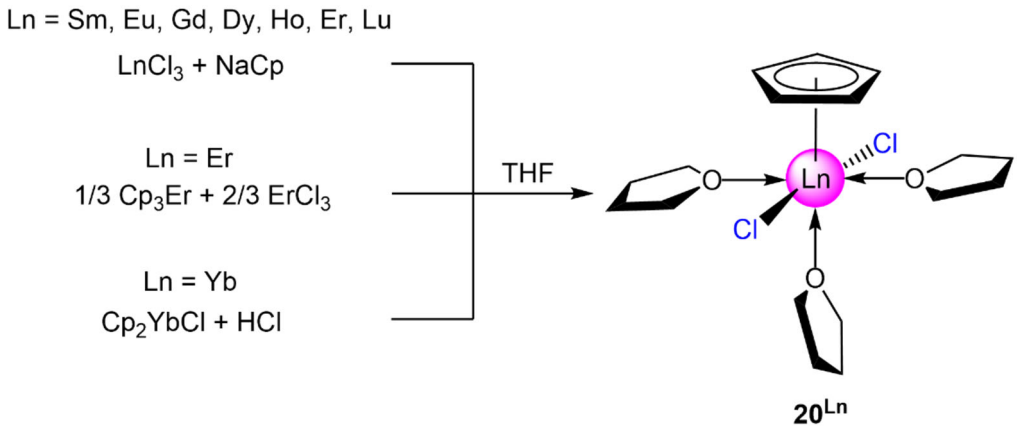

Scheme A6. Synthesis of rare-earth-metal halfsandwich dichloride complexes $CpLnCl_2(thf)_3$ (**20^{Ln}**, co-products are not shown).[65]

Despite being established compounds in organolanthanide chemistry,[67-72] the "major drawback" of these THF adducts is the blocking of coordination sites at the rare-earth-metal center, preventing the aggregation of larger complexes. In order to remove coordinated donor molecules, refluxing the respective donor adduct **20^{Ln}** in toluene with simultaneous removal of solvent has proven to be efficient for organometallic halfsandwich complexes $CpLnCl_2$.[73] An

alternative route was demonstrated by the group of SCHAVERIEN.[74] Removal of coordinated THF in the halfsandwich diiodide complex $Cp^*LaI_2(thf)_3$ is feasible via the reaction with Me_3SiI, affording the THF-free polyiodide complex $[Cp^*LaI_2]_n$.

Depending on the steric demand of the ancillary cyclopentadienyl ligand, different structural motifs have been observed. In 1981, HUNTER *et al.* reported on the synthesis of chlorido-bridged lanthanide ate-complexes with different donors.[75] Using the rare-earth-metal trichloride $LnCl_3$ (Ln = Sc, Y, La, Ce, Pr, Nd, Yb) as starting material, the reaction with different lithium salts (e.g. $LiCp^{(SiMe_3)_2}$ = LiCp", $LiOC_6H_2tBu_2$-2,6-Me-4) in either equimolar or 1:2 ratio afforded the corresponding chlorido-bridged lithium ate-complexes $[Cp^R{}_2Ln(\mu\text{-}Cl)_2Li(thf)_2]$. Accordingly, treatment of $NdCl_3$ with two equivalents of LiCp" in THF afforded the neodymium ate-complex $[Cp"_2Nd(\mu\text{-}Cl)_2Li(thf)_2]$ (**23**).

Whereas rare-earth-metal complexes bearing cyclopentadienyl ligands with a high steric demand (e.g., Cp*, Cp") tend to form dimeric complexes,[76-81] smaller rare-earth-metal centers, especially in combination with small bridging ligands (such as hydrido or fluorido), are susceptible to the formation of ring-like structures[82-85] (Figure A2) or even oligomers.[86]

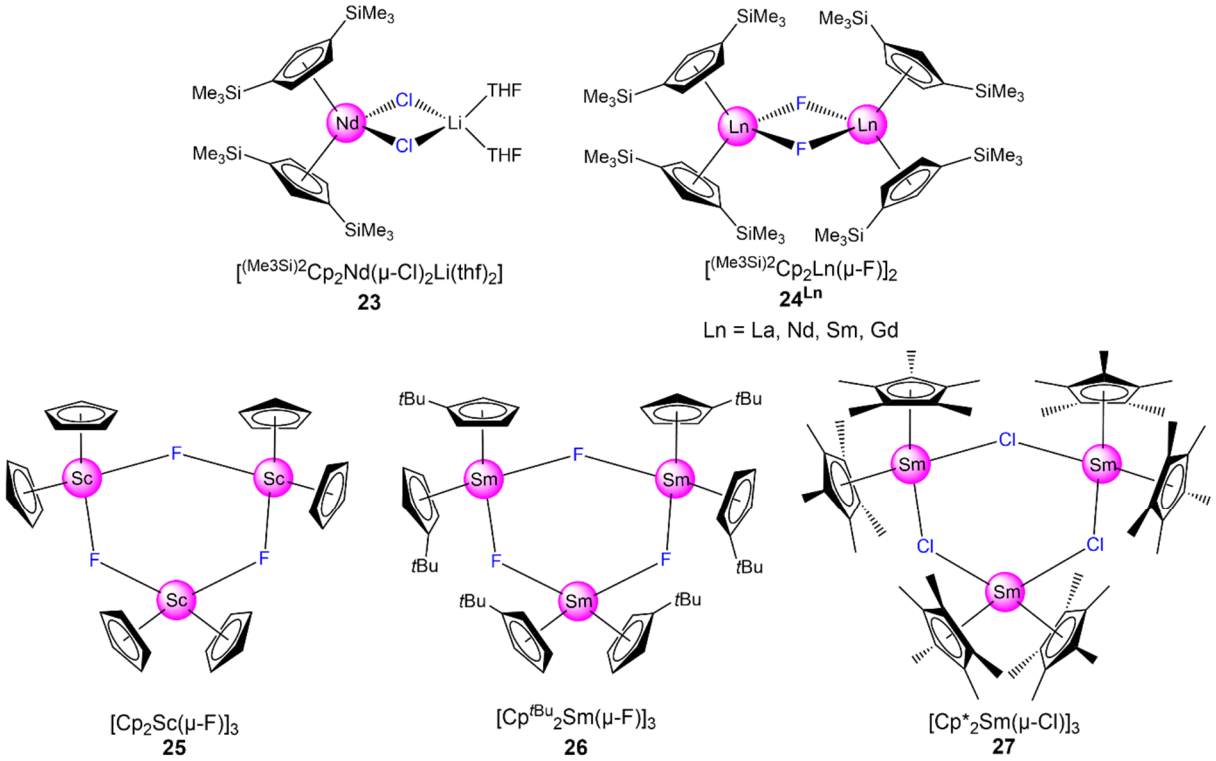

Figure A2. Halogenido-bridged sandwich-type rare-earth-metal complexes bearing different ancillary Cp derivatives.[75, 79, 82, 84, 87]

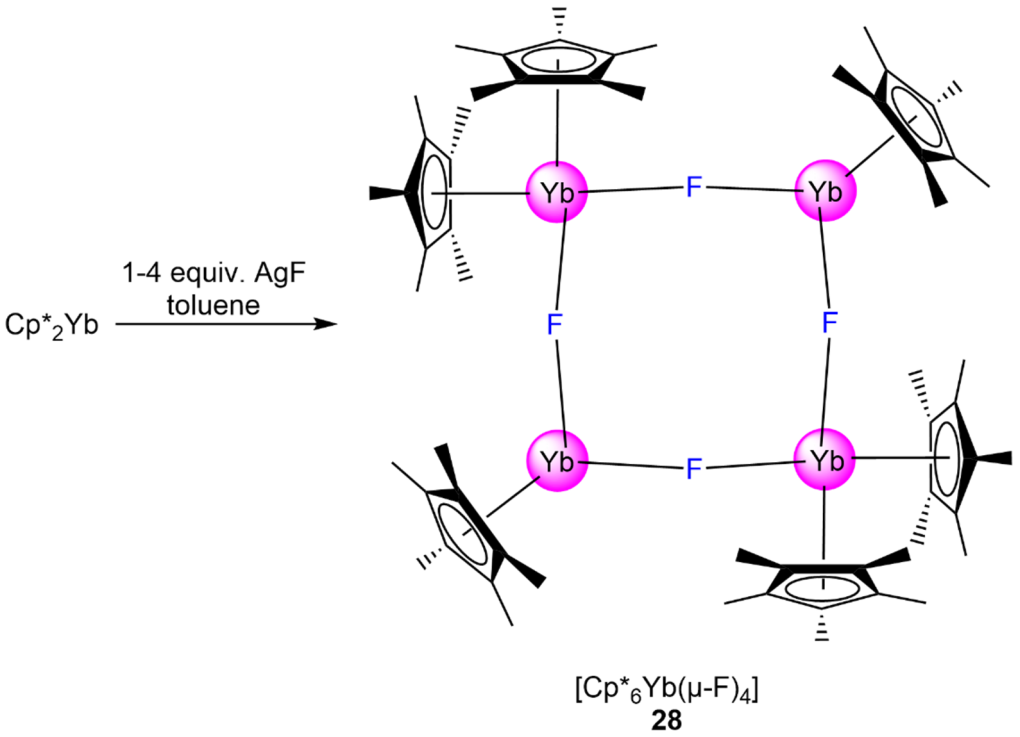

Scheme A7. Synthesis of mixed-valent tetranuclear ytterbium complex **28**.[83]

The tetranuclear fluorido-bridged complex [Cp*$_6$Yb$_4$(μ-F)$_4$] (**28**) by ANDERSEN *et al.* was prepared by the addition of 1 up to 4 equivalents of silver fluoride to a toluene solution of the divalent ytterbium sandwich complex Cp*$_2$Yb (Scheme A7).[83] The mixed-valent complex showed a planar arrangement of the ytterbium metal centers, despite the relatively high steric demand of the ancillary Cp* ligands. General synthesis routes toward complexes of this type involve the removal of donor molecules and subsequent aggregation under reflux,[84] salt-metathesis with alkali-metal cyclopentadienides,[82, 85] or oxidation reactions[87]. Overall, the formation of ring-like structural motifs is a common phenomenon for cyclopentadienyl-based rare-earth-metal halide compounds.[31]

In order to facilitate the formation of higher-aggregated rare-earth-metal compounds or clusters, a switch to halfsandwich precursors is indicated due to the lower steric saturation at the rare-earth-metal center.

3.2 Cyclopentadienyl-Supported Rare-Earth-Metal Clusters

In 1966, COTTON defined clusters as chemical compounds bearing at least two metal atoms and interaction between the metal atoms.[1] This definition was further specified by SCHNÖCKEL, more precisely, the distinct classification is given by the average oxidation number (n_{av}) of the metal atoms: "naked" metal clusters ($n_{av} = 0$), metalloid clusters ($0 < n_{av} < n_{salt}$), and salt-like clusters ($n_{av} = |n_{salt}|$).[3, 88] Due to the highly polarized bonding situation in rare-earth-metal clusters,[89] exclusively salt-like clusters have been isolated so far. Furthermore, a three-dimensional arrangement for the metal centers is expected, precluding the previously described ring-like complexes from being defined as "clusters" as well.

The first donor-free rare-earth-metal halide cluster was isolated by the group of WATSON in 1990.[90] Removal of coordinated diethyl ether from the ytterbocene complex $Cp^*_2Yb(Et_2O)$ in toluene was achieved by the stoichiometric addition of perfluoro-2,4-dimethyl-3-ethylpent-2-ene (C_9F_{18}) (Scheme A8). Red crystals of pentanuclear ytterbium cluster $[Cp^*_6Yb_5(\mu_4\text{-}F)(\mu_3\text{-}F)_2(\mu_2\text{-}F)_6]$ (**29**) were isolated, consisting of a $Cp^*_4Yb_4F_7$ unit and a bridging $Cp^*_2Yb(\mu_2\text{-}F)_2$ unit in the apical position. The identical structural motif was later detected by EVANS by the isolation of the pentanuclear cluster $[Cp^*_6Sm_5(\mu_4\text{-}Cl)(\mu_3\text{-}Cl)_2(\mu_2\text{-}Cl)_6]$ (**30**) as a side product in the synthesis of $[Cp^*_2Sm(\mu\text{-}Me)_2AlMe_2]_n$ (Figure A3).[91]

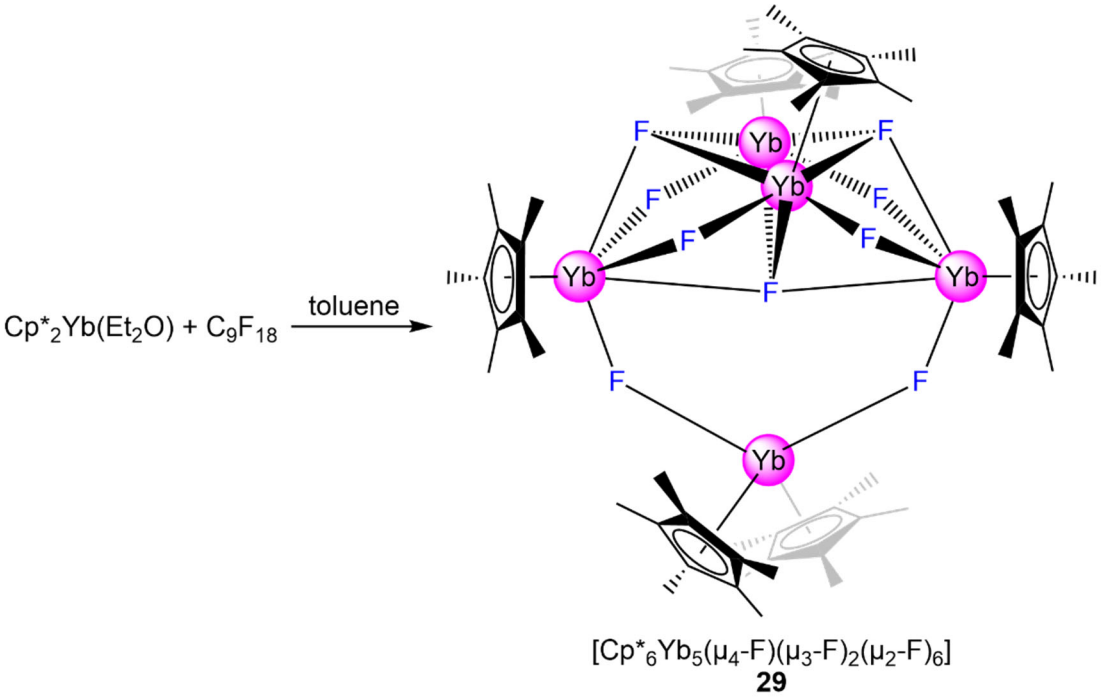

Scheme A8. Synthesis of fluorido-bridged ytterbium cluster **29**.[90]

A simple salt-metathesis protocol, the treatment of ytterbium(II) iodide YbI_2 with an equimolar amount of lithium (*tert*-butyl-dimethylsilyl)tetramethyl cyclopentadienide $LiCp^{Me_4(SiMe_2tBu)}$ ($LiCp^s$) in THF, led to the formation of the hexanuclear anionic ytterbium cluster $[Cp^s{}_6Yb_6I_8]^{2-}$ (**31**) with two molecules of $[Li(thf)_4]^+$ as counterions.[92]

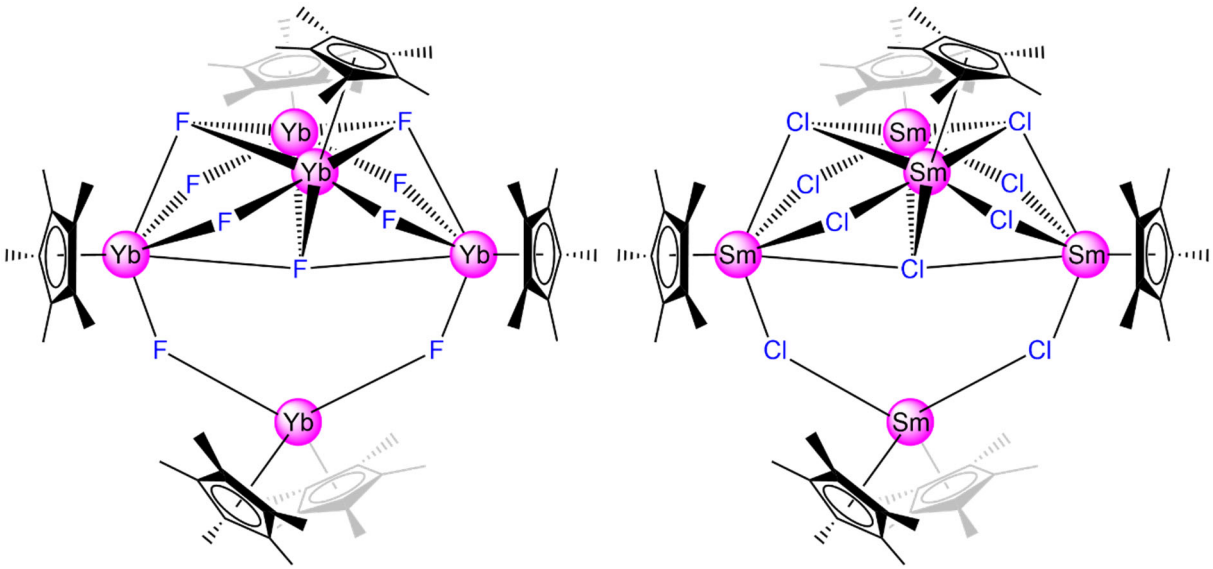

$[Cp^*{}_6Yb_5(\mu_4\text{-}F)(\mu_3\text{-}F)_2(\mu_2\text{-}F)_6]$ **29**

$[Cp^*{}_6Sm_5(\mu_4\text{-}Cl)(\mu_3\text{-}Cl)_2(\mu_2\text{-}Cl)_6]$ **30**

Figure A3. Pentanuclear clusters $[Cp^*{}_6Yb_5(\mu_4\text{-}F)(\mu_3\text{-}F)_2(\mu_2\text{-}F)_6]$ (**29**) and $[Cp^*{}_6Sm_5(\mu_4\text{-}Cl)(\mu_3\text{-}Cl)_2(\mu_2\text{-}Cl)_6]$ (**30**).[90, 91]

In cluster **31**, the ytterbium metal centers are in a highly symmetric octahedral arrangement, and the cluster core is supported by sterically demanding Cp ligands. Furthermore, this cluster represents the first example of a lanthanide cluster consisting exclusively of divalent rare-earth-metal centers. A similar octahedral arrangement of lanthanide metal centers was established by KUBICKI *et al.* in borohydrido-bridged cluster $[Cp^{*n\text{-}Pr}Ln(BH_4)_2]_6$ (**32^{Ln}**, Ln = Nd, Sm; $Cp^{*n\text{-}Pr}$ = $C_5Me_4n\text{-}Pr$),[93] as well as the isostructural Cp*-coordinated neodymium cluster $[Cp^*Nd(BH_4)_2]_6$ (**33**) by ARNOLD *et al* (see Figure A4, left).[94]

The dodecanuclear chlorido-bridged samarium cluster $[CpSmCl_2]_{12}$ (**34**) reported by the group of TEUBEN has remained unmatched in nuclearity.[32] Cluster **34** was synthesized by refluxing a toluene suspension of the halfsandwich samarium chloride $CpSmCl_2(thf)_3$ with simultaneous removal of the solvent by distillation. In contrast, reflux of a toluene suspension of $YbCl_3(thf)_3$ with 0.9 equivalents of trimethylsilyl cyclopentadiene for 24 h did not result in complete removal of coordinated THF, but produced a separated ion pair of clusters, the trinuclear cationic ytterbium cluster $[Cp_3Yb_3Cl_5(thf)_3]^+$ (**35**), and the anionic hexanuclear ytterbium cluster $[Cp_6Yb_6Cl_{13}]^-$ (**36**), featuring a central chlorido ligand located inside the cluster core. In

cluster **34**, the samarium atoms adopt an icosahedral symmetry, with the faces of the icosahedron capped by 20 chlorido ligands, which are in a dodecahedral arrangement. Additionally, four chlorido ligands are located inside the cluster core in a tetrahedral geometry. Similar to clusters **31**, **32^{Ln}** and **33**, the ytterbium metal centers in **36** show an octahedral arrangement, in this particular case with a central μ_4-bridging chlorido ligand in the cluster core.

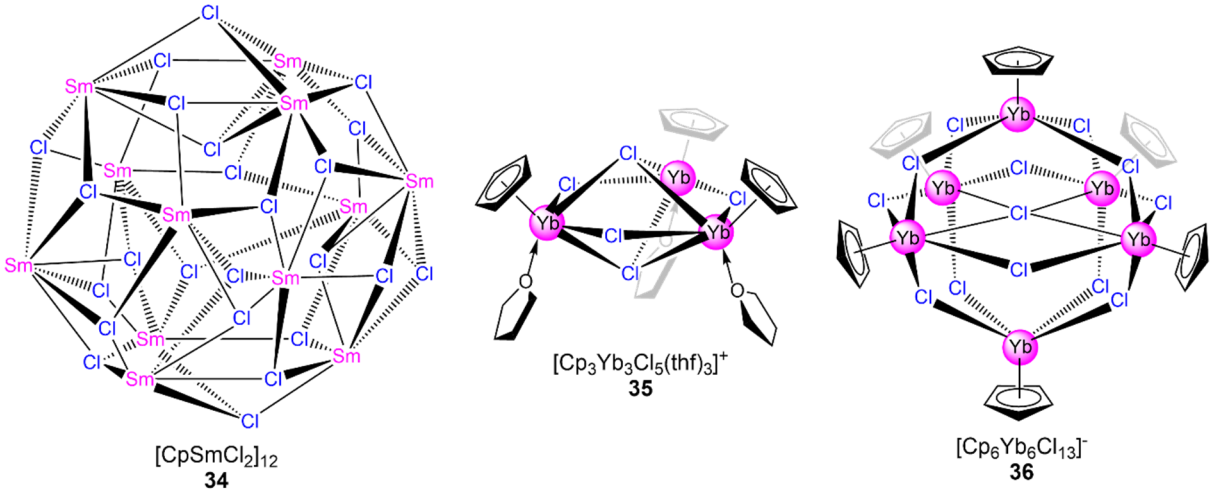

Figure A4. Dodecanuclear cluster [CpSmCl$_2$]12 (**34**, Cp ligands omitted for clarity), trinuclear cluster [Cp$_3$Yb$_3$Cl$_5$(thf)$_3$]$^+$ (**35**) and hexanuclear cluster [Cp$_6$Yb$_6$Cl$_{13}$]$^-$ (**36**).[32]

The recurrent formation of distinct structural motifs in rare-earth-metal cluster chemistry provides evidence for the exceptional stability of such cluster compounds. Clusters feature structural motifs which are reminiscent of LnX$_3$ in the solid state and molecular complexes, hence lanthanide halide coordination modes established by the solid-state structure are regularly present in cluster compounds as well.[3, 95-99] Clusters **29**, **30** and **34** display the structural subunit Ln$_4$X$_7$, featured by several solid-state modifications of rare-earth-metal halides.[100-102] Depending on factors like rare-earth-metal ion size, the ion size of the bridging ligands, or the steric demand of the ancillary cyclopentadienyl ligand, multinuclear Ln clusters preferably adopt this highly stable subunit.[63, 64, 103-105]

Halogenido-bridged lanthanide coordination clusters are also accessible using halfsandwich compounds Cp^{R}Ln(AlMe$_4$)$_2$ as starting materials, though the exclusion of donor solvents accounts for the necessity of carefully monitored reaction conditions. Depending on the rare-earth-metal center ion size, treatment of an *n*-hexane solution of **2^{Ln}** (Ln = Y, La, Nd) with dimethylaluminum chloride Me$_2$AlCl (Y: 0.5-0.9 equiv. Me$_2$AlCl, Nd: 0.9-1.7 equiv. Me$_2$AlCl, La: 0.5-1.3 equiv. Me$_2$AlCl) at low temperatures afforded heterobimetallic complexes with different nuclearities. The reaction with the yttrium halfsandwich bis(tetramethylaluminate)

produced the dimeric yttrium complex [{Cp*Y[(μ-Me)$_2$AlMe$_2$](μ-Cl)}$_2$] (**37**), bridged by two chlorido ligands, and two additional terminal tetramethylaluminato ligands.

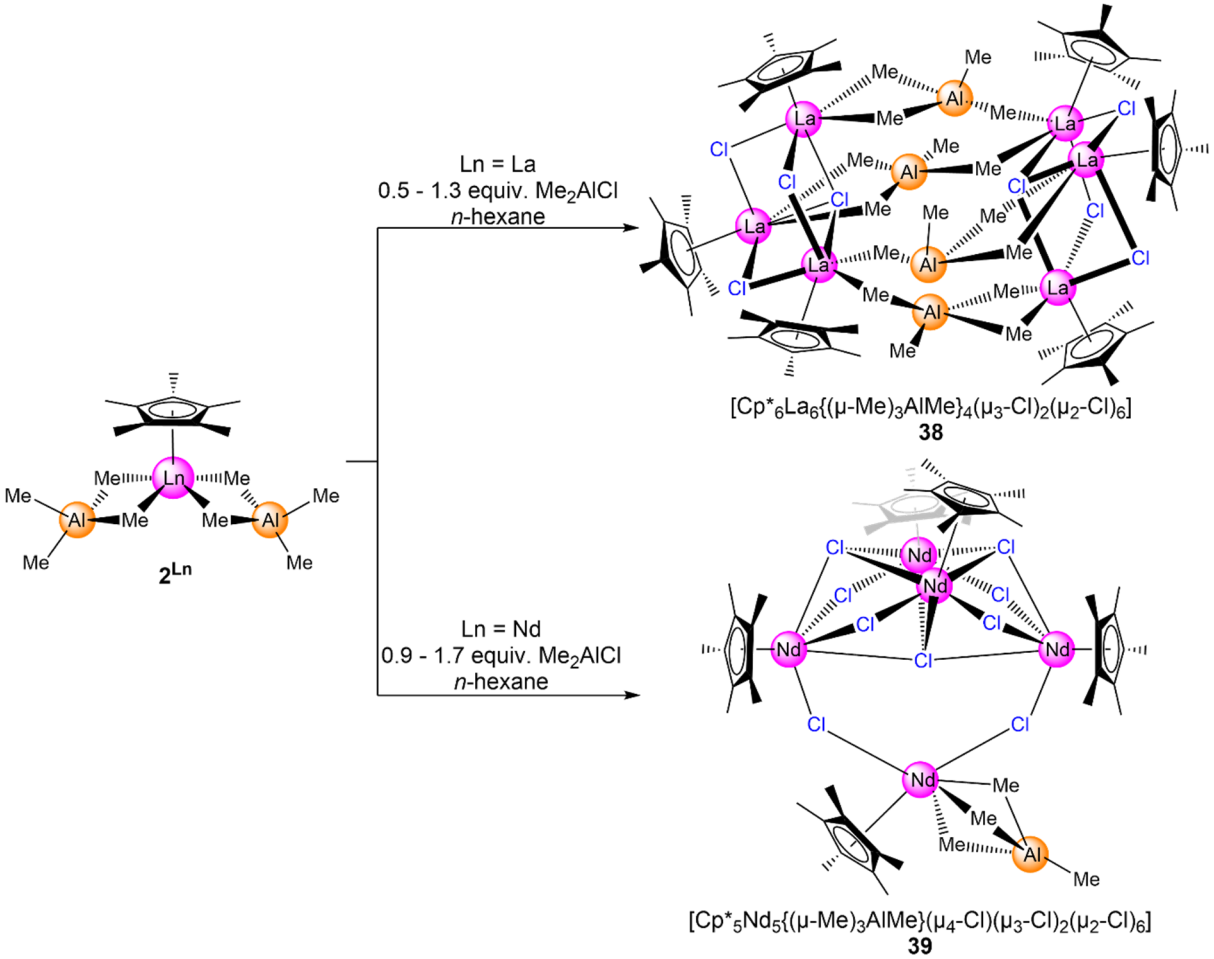

Scheme A9. Synthesis of heterobimetallic clusters [Cp*$_6$La$_6${(μ-Me)$_3$AlMe}$_4$(μ_3-Cl)$_2$(μ_2-Cl)$_6$] (**38**) and [Cp*$_5$Nd$_5${(μ-Me)$_3$AlMe}(μ_4-Cl)(μ_3-Cl)$_2$(μ_2-Cl)$_6$] (**39**) via a partial tetramethylaluminato/halogenido exchange reaction.[63]

Using the lanthanum halfsandwich bis(tetramethylaluminate) as precursor, the addition of Me$_2$AlCl led to the formation of the hexanuclear lanthanum cluster [Cp*$_6$La$_6${(μ-Me)$_3$AlMe}$_4$(μ_3-Cl)$_2$(μ_2-Cl)$_6$] (**38**) (Scheme A9, top). This cluster consists of two La$_3$Cl$_4$ subunits resembling a cuboid structure with a cut-off corner, which are bridged via for tetramethylaluminato ligands. In contrast, treatment of the respective neodymium halfsandwich bis(tetramethylaluminate) with Me$_2$AlCl afforded a completely different type of cluster. The pentanuclear complex [Cp*$_5$Nd$_5${(μ-Me)$_3$AlMe}(μ_4-Cl)(μ_3-Cl)$_2$(μ_2-Cl)$_6$] (**39**) consists of a distinct Nd$_4$Cl$_7$ subunit, with the vertices bridged via a (μ_2-Cl)$_2$Nd unit, bearing one ancillary Cp* and one terminal (μ-Me)$_3$AlMe ligand (Scheme A9, bottom). For complexes **37**-**39**, shielding of the Ln metal center is achieved by the ancillary Cp* ligands.

The steric demand of the ancillary carbocyclic ligand is a crucial factor for the formation of rare-earth-metal clusters, as evidenced by ANWANDER *et al.* in 2017.[106] Using the bulky 1-(trimethylsilyl)fluorenyl ($C_{13}H_9SiMe_3$ = Flu^{Si}) halfsandwich yttrium bis(tetramethylaluminate) $(Flu^{Si})Y(AlMe_4)_2$ (**40**) as a precursor, the alkyl/chlorido exchange with Me_2AlCl afforded either complex **41** or **42** (Scheme A10). While the stoichiometric reaction resulted in incomplete tetramethylaluminato/halogenido exchange and the formation of the dimeric chlorido-bridged complex $[Flu^{Si}Y(AlMe_4)(\mu\text{-}Cl]_2$ (**41**), complete exchange was achieved for the reaction with 1.7 equivalents of Me_2AlCl, giving access to the chlorido-bridged hexanuclear yttrium coordination cluster $[Flu^{Si}{}_6Y_6Cl_{12}]$ (**42**). Cluster **42** consists of the trinuclear subunits $[(\mu\text{-}Cl)_3(\mu_3\text{-}Cl)Y_3]$ and $[(\mu\text{-}Cl)_3(\mu_3\text{-}Cl)_2Y_3]$, which are interlinked via three bridging chlorido ligands, resulting in a cluster core resembling a highly symmetric ellipsoid.

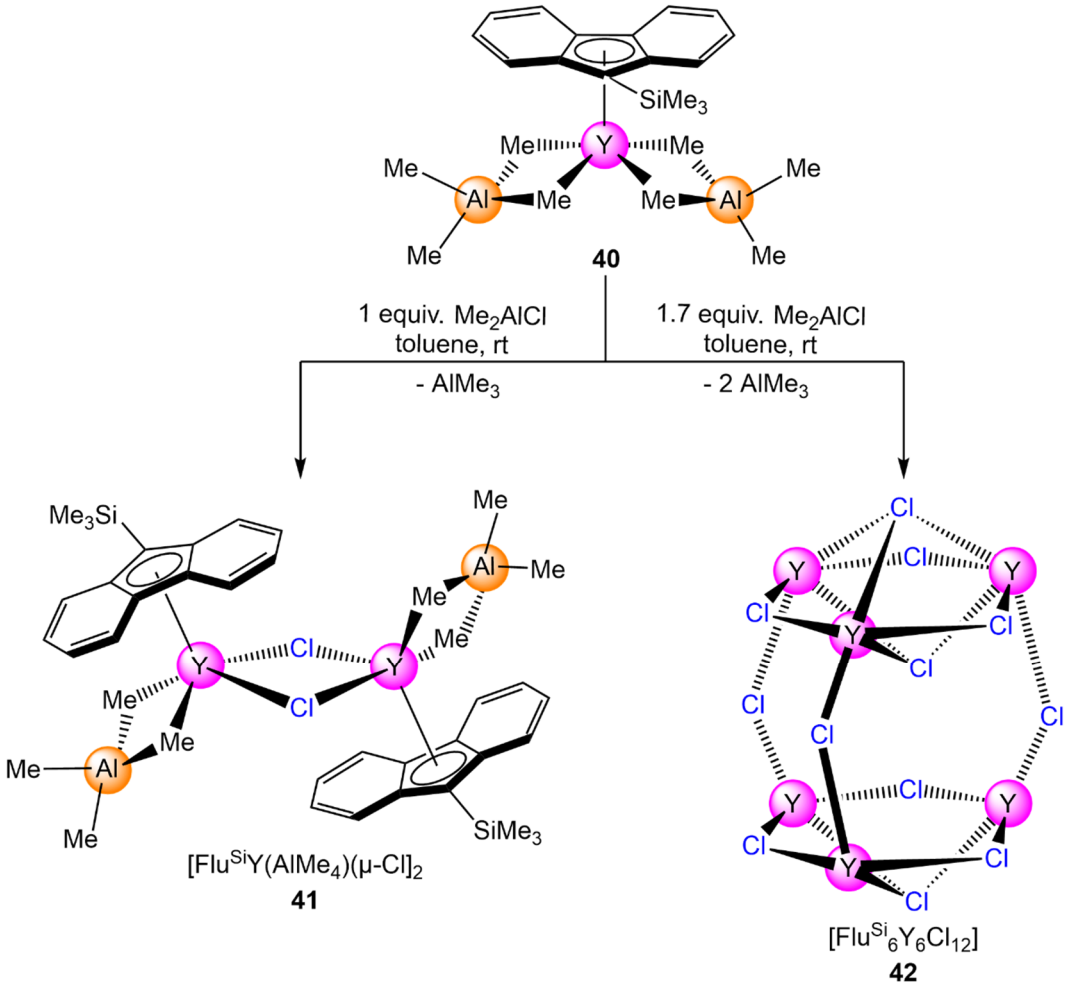

Scheme A10. Synthesis of dimeric halfsandwich complex **41** and chlorido-bridged cluster **42** (FluSi ligands omitted for clarity).[106]

Unlike previously reported clusters of this type, **42** marked the first example of a donor-free rare-earth-metal cluster with trinuclear subunits linked through halogenidos. Other complexes of this type usually consist of two [(μ-X)$_3$(μ_3-X)$_2$Ln$_3$] (X = Hal, BH$_4$) subunits, with one coordination site of the trinuclear subunit blocked by coordination of a donor atom, leading to a sheared ellipsoidal overstructure.[93, 107-109] Our group synthesized a holmium congener of this type via derivatization of the amino-functionalized halfsandwich bis(allyl) rare-earth-metal complex Cp^{NMe_2}Ln(η^3-C$_3$H$_5$)$_2$ (**43^{Ln}**, Ln = Y, Ho; Cp^{NMe_2} = 1-[2-(*N*,*N*-dimethylamino)ethyl]-2,3,4,5-tetramethylcyclopentadienyl) with diethylaluminum chloride.[109] The respective precursor **43^{Ln}** was synthesized in a two-step reaction by treatment of rare-earth-metal trichloride LnCl$_3$(thf)$_x$ with the amino-functionalized LiCp^{NMe_2} and a subsequent Grignard reaction with allylmagnesium chloride C$_3$H$_5$MgCl. The reaction of complex **43^{Ln}** with two equivalents of Et$_2$AlCl in [D$_6$]benzene led to the formation of chlorido-bridged hexanuclear clusters [{(Cp^{NMe_2AlEt_3})$_2$(Cp ^{NMe_2})Ln$_3$(μ_2-Cl)$_3$(μ_3-Cl)$_2$}(μ_2-Cl)]$_2$ (**44^{Ln}**, Ln = Y, Ho) (Scheme A11). Cluster **44^{Ln}** consists of two [(Cp^{NMe_2AlEt_3})$_2$(Cp ^{NMe_2})Ln$_3$(μ_2-Cl)$_3$(μ_3-Cl)$_2$] subunits linked by bridging chlorido ligands. Please note that in the subunit two equivalent triethylaluminum are coordinated by amino groups, while the usually observed N-dimethylamino-sidearm-coordination to the Ln metal center is detected for one Cp^{NMe_2} ligand.

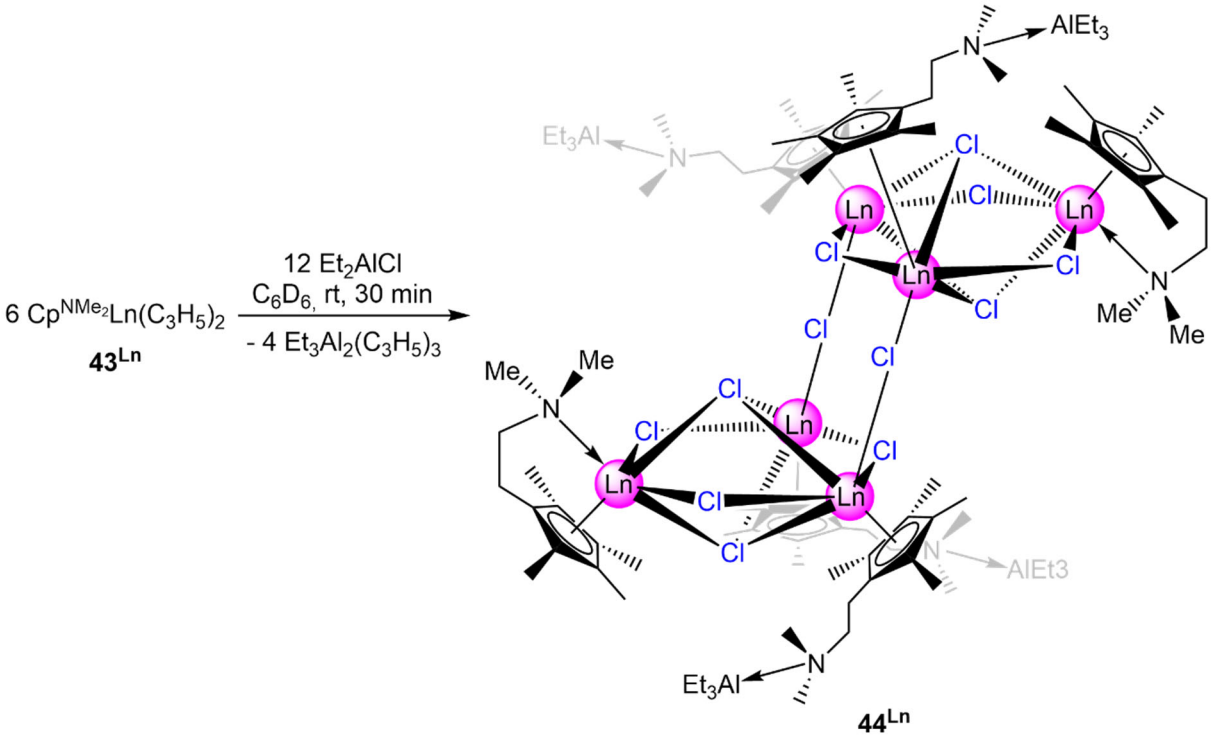

Scheme A11. Synthesis of hexanuclear chloride cluster **44^{Ln}** stabilized by amino-functionalized Cp ligands.[109]

As already mentioned in Chapter A3.2, organo-rare-earth-metal compounds are prone to the formation of ring-like structural motifs. Surprisingly, this accounts for halfsandwich-based rare-earth-metal halogenido complexes as well, despite the reduced steric demand in comparison to sandwich-type complexes. Consequently, the nuclearity of these ring-cluster-hybrids did not exceed four rare-earth-metal centers so far.[91, 108, 110-112]

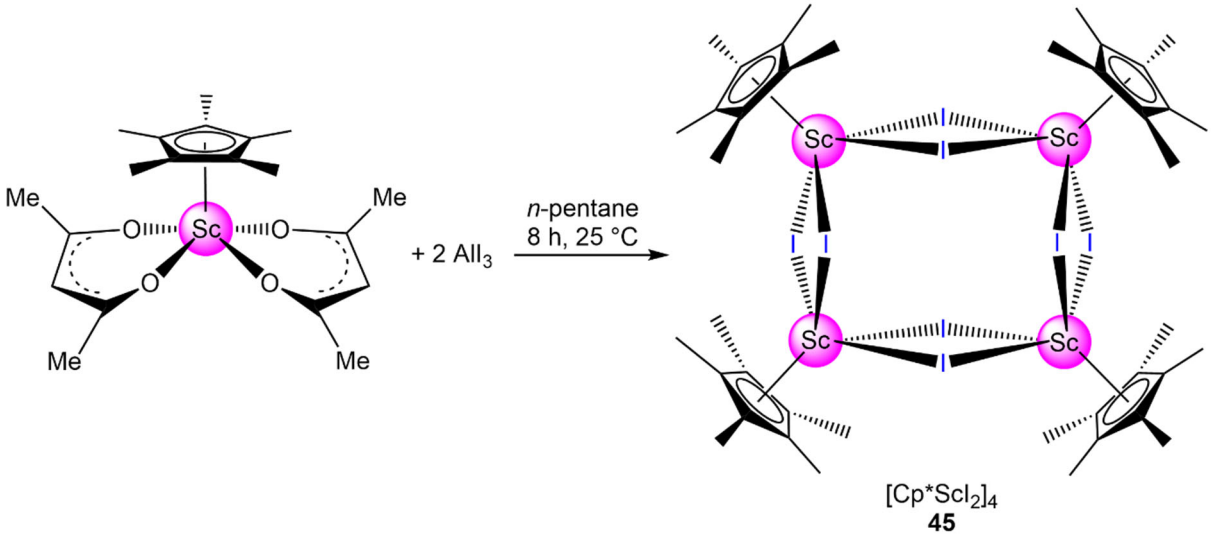

Scheme A12. Synthesis of tetranuclear ring-cluster-hybrid **45**.[110]

The tetranuclear halfsandwich scandium diiodide complex $[Cp^*ScI_2]_4$ (**45**) by TILLEY *et al.* was synthesized by treatment of halfsandwich scandium acetylacetonate (acac) $Cp^*Sc(acac)_2$ with two equivalents of aluminum iodide AlI_3 in *n*-pentane (Scheme A12, Figure A5, top).[110] Rather unexpected, dysprosium forms a trinuclear ring,[91] considering the larger ionic radius of the dysprosium metal center (CN 6: Sc^{3+} = 0.745 Å, Dy^{3+} = 0.912 Å).[113] Cluster $[Cp^*DyI_2]_3$ (**46**) is accessible as co-product by the reaction of dysprosium(II)iodide DyI_2 and LiCp* in diethyl ether (Figure A5, top). Additionally, the formation of anionic ring-like complexes led to the incorporation of a central halogenido ligand inside the ring structure (Figure A5, bottom).[108, 111] So far, only two examples of these anionic rings have been reported, the first one being the tetranuclear cluster $[Cp^*_4Nd_4Cl_9]^-$ (**47**) by EISEN *et al* in 2007.[108] Treatment of $Cp^*_2NdCl(LiCl)_2$ in THF with a slight excess of catecholborane in toluene at elevated temperatures (110 °C) afforded cluster **47**, which crystallizes with LiO_2+/Li_2O/O_2 as counterion. The similar tetranuclear yttrium cluster $[Cp^{*\prime}_4Y_4Cl_9]^-$ (**48**, Cp*' = $C_5Me_4SiMe_3$) by HORACEK *et al*., which was isolated by the salt metathesis reaction of $YCl_3(thf)_{3.5}$ and LiCp*' at ambient temperature.[111]

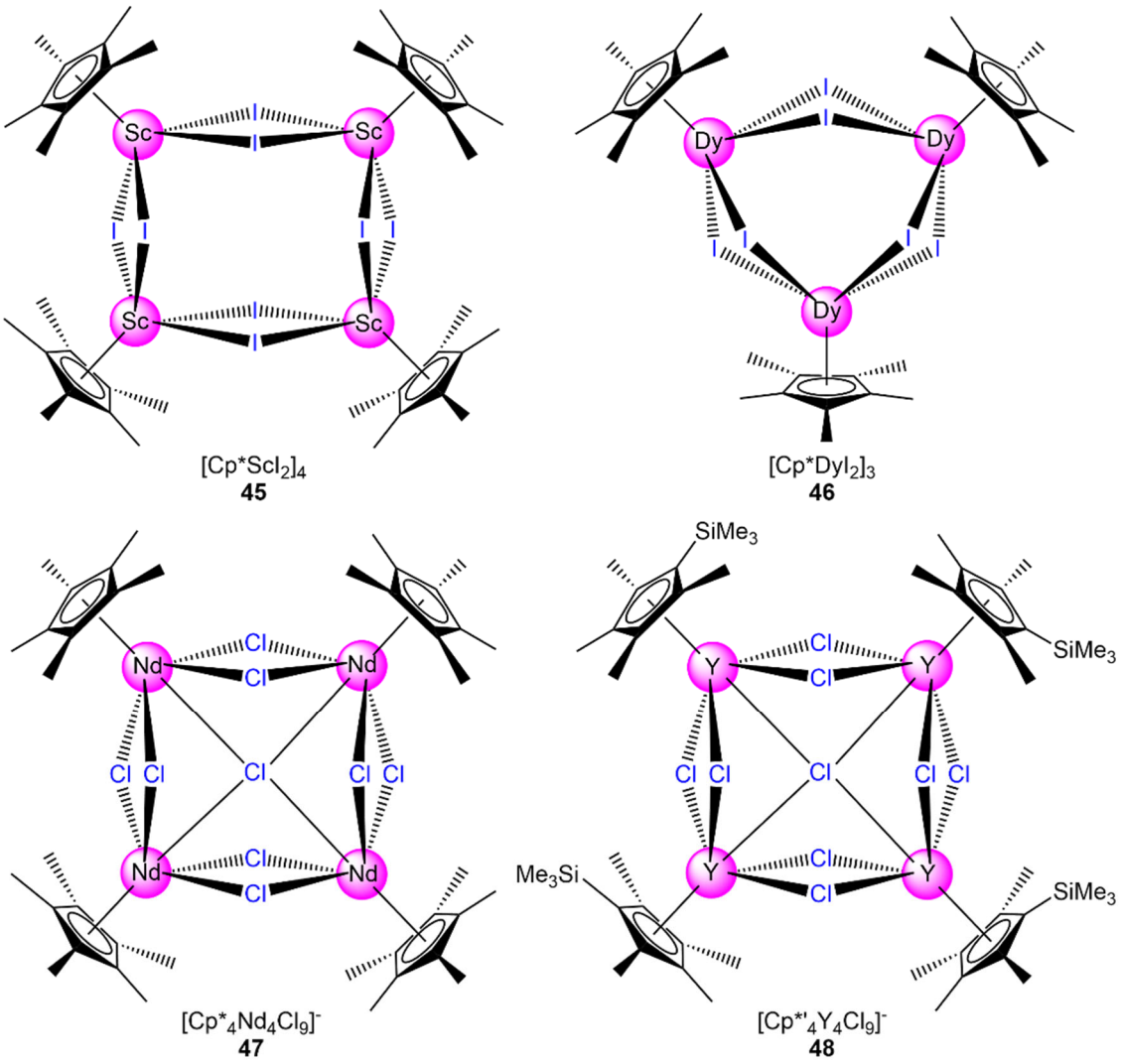

Figure A5. Structurally characterized halfsandwich rare-earth-metal ring-cluster-hybrids.[91, 108, 110, 111]

Even though donor coordination hampers the aggregation of rare-earth-metal clusters (as previously mentioned in Chapter A3.1), removal of persistent donor ligands enabled the subsequent self-assembly of coordination clusters, as evidenced by our group.[114] The reaction of samarium(II)iodide $SmI_2(thf)_2$ with plumbocene Cp^*_2Pb and partial removal of THF gave access to tri-, tetra- and pentanuclear clusters, dependent on the amount of coordinated THF.

The addition of 0.5 equivalents of Cp^*_2Pb to an *n*-hexane solution of $[Cp^*SmI_2(thf)_2]$ and crystallization from toluene afforded the trinuclear complex $[Cp^*_3Sm_3I(\mu_2\text{-}I)_3(\mu_3\text{-}I)_2(thf)_2]$ (**49**) as a ring-cluster hybrid (Scheme A13).

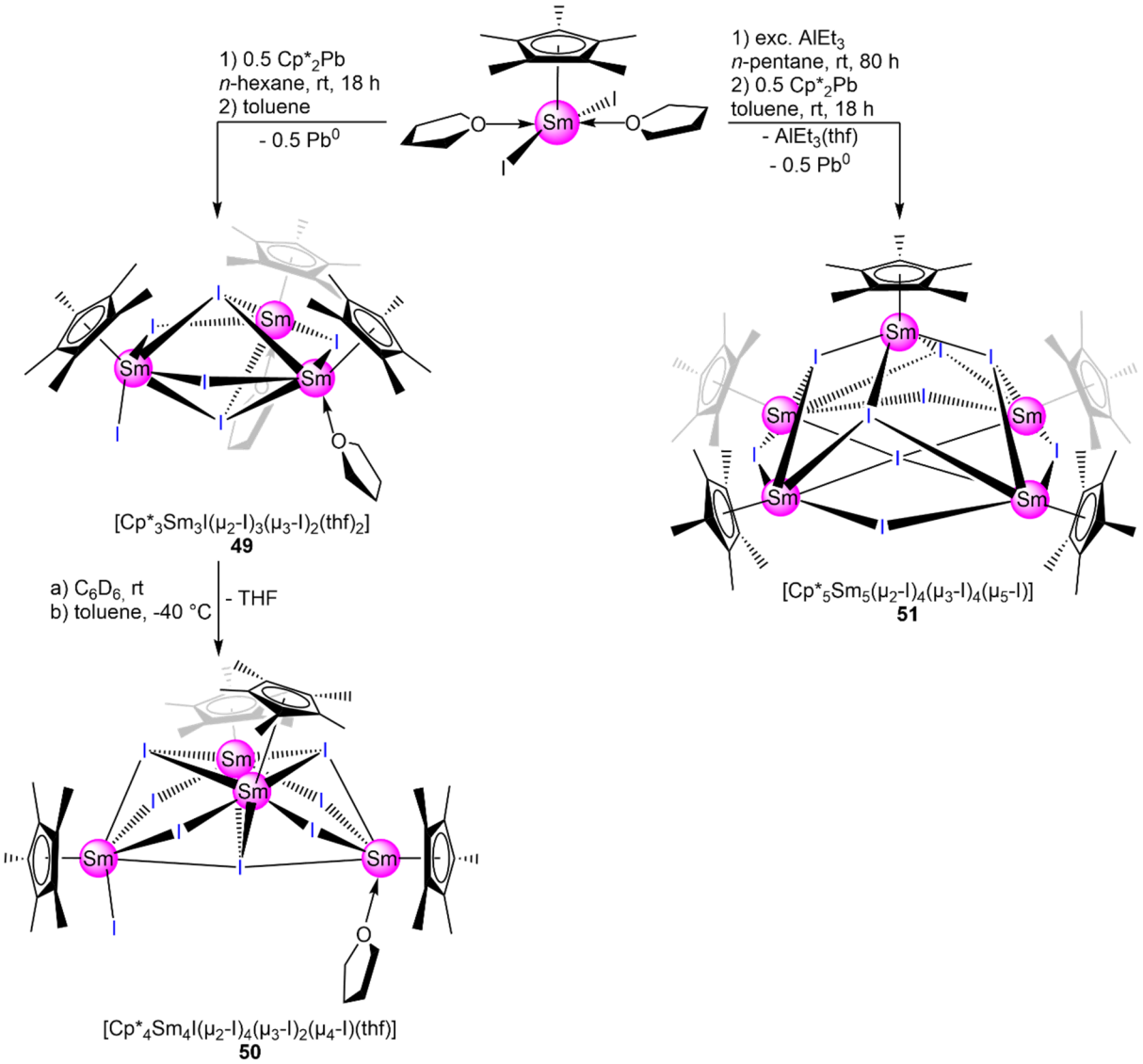

Scheme A13. Synthesis of tri-, tetra- and pentanuclear clusters **49**, **50** and **51**.[114]

In **49** the samarium metal centers bear one ancillary Cp* ligand, two metal centers are coordinated by one molecule of THF each, while the other metal center shows coordination of a terminal iodido ligand. Recrystallization of **49** from either deuterated benzene C_6D_6 at ambient temperature or toluene at -40 °C led to the displacement of one molecule of coordinated THF and conversion into the tetranuclear cluster [Cp*$_4$Sm$_4$I(μ_2-I)$_4$(μ_3-I)$_2$(μ_4-I)(thf)] (**50**) (Scheme A11). Cluster **50** shows the characteristic Ln_4X_7 structural motif, while the apical samarium metal centers show coordination by either THF or a terminal iodido ligand. Complete removal of THF from [Cp*SmI$_2$(thf)$_2$] was feasible via a two-step synthesis protocol. Initial treatment of [Cp*SmI$_2$(thf)$_2$] with excess AlEt$_3$ in *n*-pentane, and the addition of 0.5 equivalents of Cp*$_2$Pb in toluene, led to the formation of the pentanuclear cluster [Cp*$_5$Sm$_5$(μ_2-I)$_4$(μ_3-I)$_4$(μ_5-I)] (**51**). The five samarium metal centers show a highly symmetric square pyramidal arrangement, and each metal center is six-coordinate in a distorted octahedral geometry.

Moreover, cluster **51** resembles the hexanuclear cluster $[Cp_6Yb_6Cl_{13}]^-$ (**36**) with a central halogenido ligand inside the cluster core, though without the Cp^*LnX_4 unit in the apical position (see Figures A4 and A9).[32] Otherwise, the coordination motif of **51** is commonly found in rare-earth-metal alkoxide clusters.[115-119]

Analogously to rare-earth-metal halogenido clusters, other monoanionic ligands are suitable for the formation of clusters as well. As such, rare-earth-metal polyhydride clusters are established compounds in organo rare-earth-metal chemistry.[104, 105, 120-126] The first donor-free hydride-bridged lanthanide clusters were isolated in the early 2000s by the group of HOU. The reaction of mixed alkyl/hydride complex $[Cp^*'Lu(CH_2SiMe_3)(\mu_2\text{-}H)(thf)]_2$ with two equivalents of phenyl silane $PhSiH_3$ afforded the tetranuclear lutetium polyhydride cluster $[Cp^*'Lu(\mu_2\text{-}H)_2]_4$ (**52**) (Scheme A14).[120] Alternatively, this cluster can be obtained with one additional molecule of coordinated THF by dissolving the donor-free cluster in THF, or by treatment of complex $[Cp^*'Lu(CH_2SiMe_3)(\mu_2\text{-}H)(thf)]_2$ with hydrogen in THF.

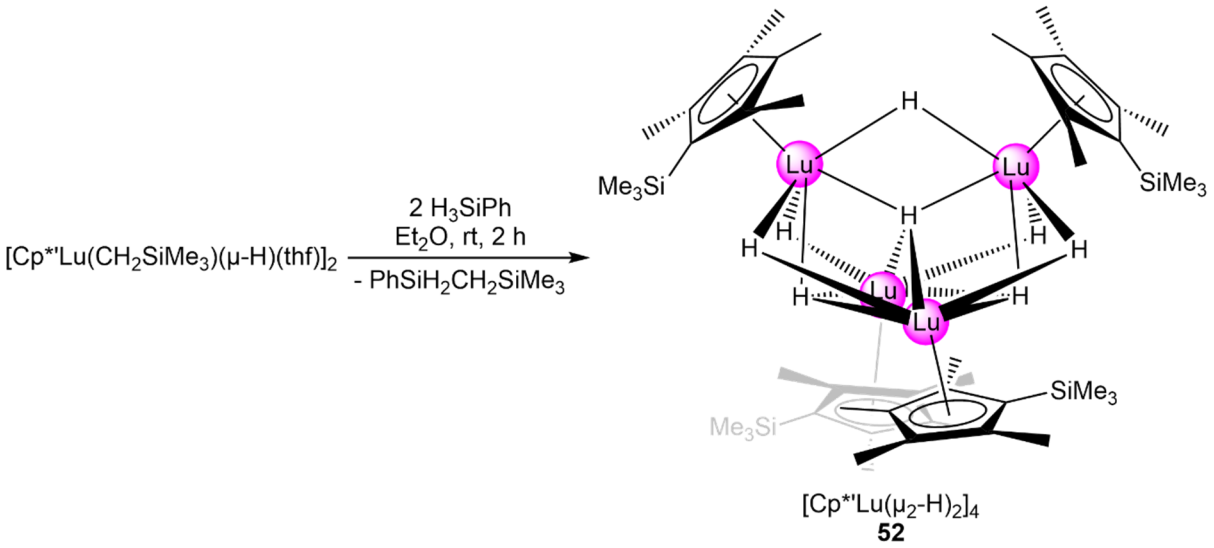

Scheme A14. Synthesis of halfsandwich lutetium dihydride cluster $[Cp^*'Lu(\mu_2\text{-}H)_2]_4$ (**52**).[120]

Likely due to the relatively small ionic radius of the bridging hydrido ligands, the nuclearity of rare-earth-metal hydrido clusters typically ranges from tetra- to hexanuclear clusters for (partially) donor-free clusters, while the most common synthesis route is the direct application of H_2 pressure to organometallic precursors.[104, 105, 121, 124, 126, 127]

This strategy was established for the entire lanthanide series, as reported by HOU *et al.*[105] The reaction of the halfsandwich rare-earth-metal dialkyl complex [Cp*'Ln(CH_2SiMe_3)$_2$(thf)] (Ln = Sm, Y, La-Lu, except Pm, Eu, Yb) in toluene with H_2 pressure gave access to the respective dihydride clusters [(Cp*'LnH$_2$)$_4$(thf)$_x$)] (**53^{Ln}**) with different amounts of coordinated THF. The isolation of a donor-free cluster was only feasible for scandium, however, clusters **53^{Ln}** show the identical tetranuclear core structure (see Scheme A15). Additionally, the formation of the trinuclear ring-cluster-hybrid [Cp*'$_2$Lu$_2$(μ-H)$_5$Lu(μ-$CH_2SiMe_2C_5Me_4$)(thf)$_2$] (**54**) was observed exclusively for lutetium due to activation of one $SiMe_3$ group, followed by coordination to one lutetium metal center. Typically, halfsandwich rare-earth-metal hydride clusters [Cp^{R}LnH$_2$]$_x$ engage in polymerization catalysis[121, 123] or small molecule activation.[104]

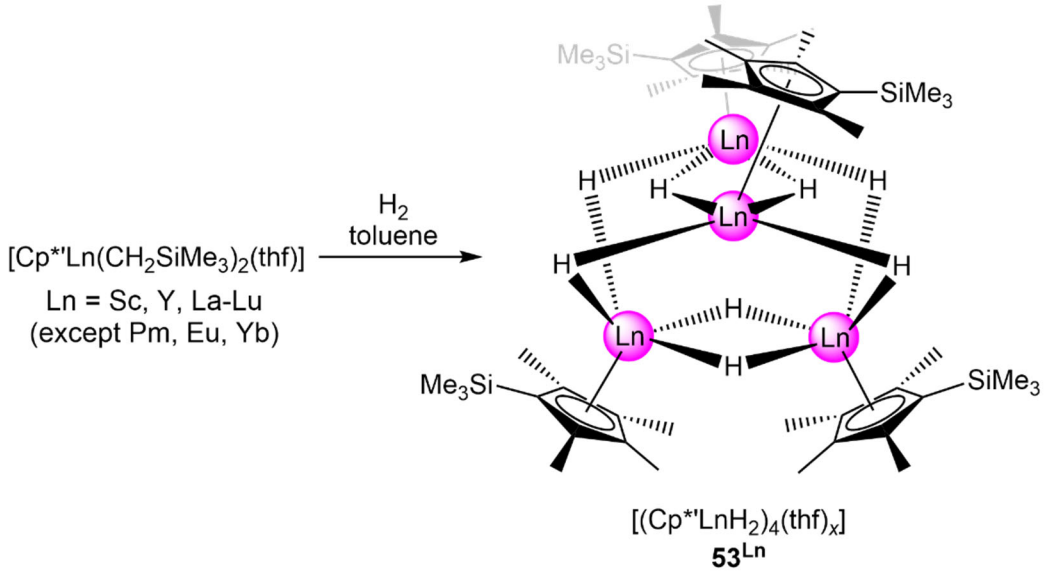

Scheme A15. Synthesis of halfsandwich rare-earth-metal dihydride cluster **53^{Ln}** (coordinated THF not shown).[105]

Furthermore, the selective incorporation of transition metals into rare-earth-metal hydrido clusters is possible via the transformation of polyhydride clusters.[128, 129] The reaction of [(Cp*'YH$_2$)$_4$(thf)$_x$] (**53^{Y}**, x = 1) with one equivalent of the group 6 pentahydride complex [Cp*M(PMe_3)H$_5$] (M = Mo, W) afforded the mixed Y$_4$/M undecahydride complexes [{(Cp*'Y)$_4$(μ-H)$_7$}(μ-H)$_4$MCp*(PMe_3)] (**55^{M}**, M = Mo, W) upon release of dihydrogen.

Similar to halogenido complexes (**24**-**27**), the switch to sandwich-type precursors is in accord with a decrease in cluster nuclearity. Consequently, rare-earth-metal sandwich hydride compounds are limited to trinuclear complexes, which display a planar or quasi-planar structural motif.[73, 130-132]

The formation of rare-earth-metal clusters can be achieved by bridging methyl ligands as well, as demonstrated by our group in 2006.[56] As previously mentioned in Chapter A2, ether cleavage of halfsandwich **2**^{Y} with THF led to the formation of the trinuclear yttrium polymethyl ring-cluster-hybrid **4**^{Y}, or complete tetramethylaluminate cleavage is feasible with excess Et_2O (> 2 equivalents) as well. In contrast, the equimolar reaction with diethyl ether resulted in incomplete $AlMe_4$ cleavage and aggregation of the heterobimetallic methyl/methine cluster $[Cp^*_4Y_4(\mu_2\text{-}CH_3)_2\{(CH_3)Al(\mu_2\text{-}CH_3)_2\}_4(\mu_4\text{-}CH)_2]$ (**56**) (Scheme A16). Cluster **56** consists of two $[Cp^*_2Y_2\{(CH_3)Al(\mu_2\text{-}CH_3)_2\}_2(\mu_4\text{-}CH)]$ subunits which are linked by two bridging methyl groups. Furthermore, **56** represents the first example of the implementation of a bridging methine group in rare-earth-metal cluster chemistry.

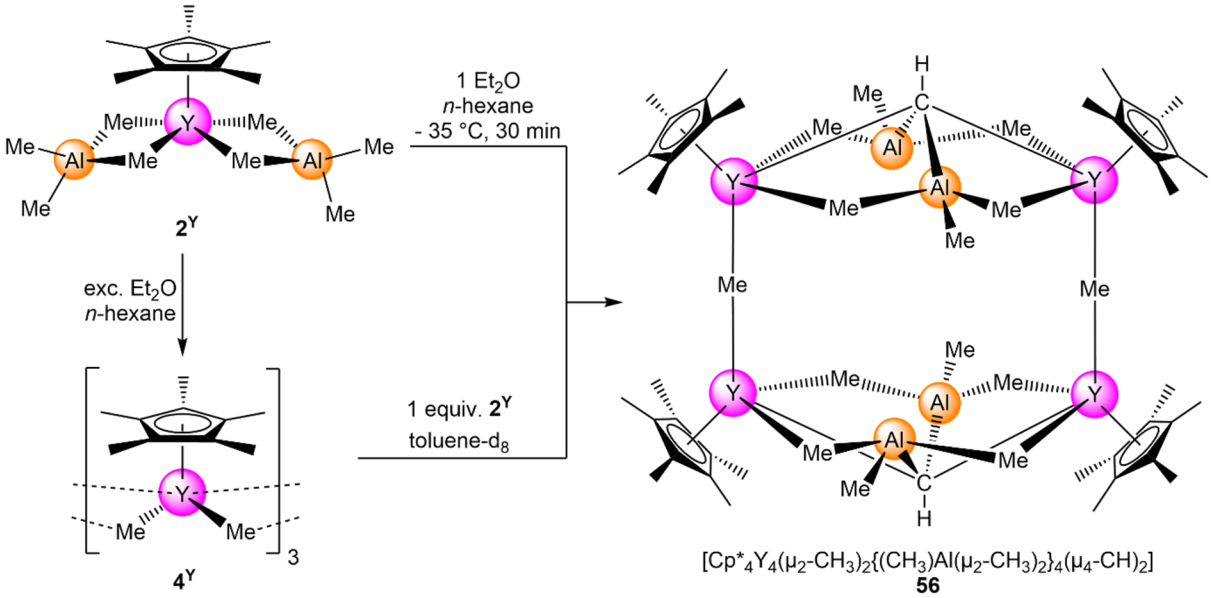

Scheme A16. Synthesis of heterobimetallic cluster **56** via donor-induced tetramethylaluminate cleavage.[56]

The isolation of cluster **56** provided evidence that trinuclear rare-earth-metal polymethyl complexes **4**^{Ln} are valuable precursor compounds for the synthesis of larger rare-earth-metal clusters.

Aiming at methylidene functionalization, the first lanthanide methylidene cluster was isolated by HOU *et al*. in 2011 by heating a benzene solution of the lanthanide polymethyl complex $[Cp^*Ln(\mu_2\text{-}CH_3)_2]_3$ (**57**^{Ln}, Ln = Tm, Lu) with simultaneous elimination of methane, producing the Ln_4 polymethylidene cubane cluster $[Cp^*Ln(\mu_3\text{-}CH_2)]_4$ (**58**^{Ln}, Ln = Tm, Lu).[133]

The isolation of the intermediate trinuclear mixed methyl/methylidene thulium complex [Cp*'$_3$Tm$_3$(μ_2-Me)(μ_3-Me)(μ_3-CH$_2$)] (**59**) is feasible by elimination of methane in [Cp*'Tm(μ_2-CH$_3$)$_2$]$_3$ (**57^{Ln}**) at ambient temperature (see Scheme A17). **58^{Lu}** is then prone to further hydrogenolysis. Whereas protonation of [Cp*'Lu(μ_3-CH$_2$)]$_4$ with [PhMe$_2$NH][B(C$_6$F$_5$)$_4$] affords the cationic cubane cluster [Cp*'Lu(μ_3-CH$_2$)$_3$(μ_3-Me)]$^+$ with [B(C$_6$F$_5$)$_4$]$^-$ (**60**) as counterion, the hydrogenolysis with 1 atm H$_2$ pressure gave access to the tetrametallic monohydride heptamethyl complex [Cp*'$_4$Lu$_4$(μ_4-H)(μ_3-Me)(μ_2-Me)$_6$] (**61**).[134]

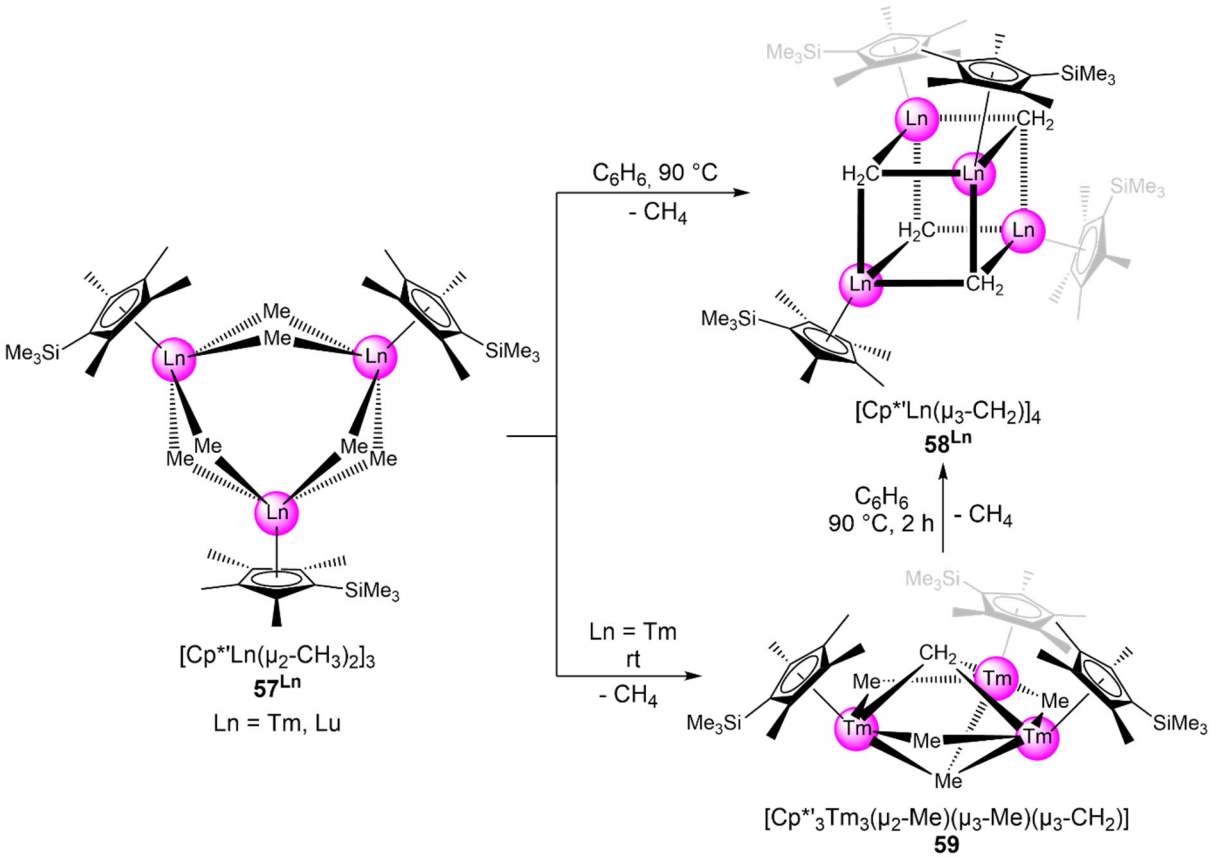

Scheme A17. Synthesis of polymethylidene cluster **58^{Ln}** and mixed methyl/methylidene thulium complex **59**.[133]

Although the first rare-earth-metal complex coordinated exclusively by methylidenes was synthesized by our group in 2006, the respective trinuclear mixed methyl/chlorido bridged cluster [Cp*$_3$Ln$_3$(μ-Cl)$_3$(μ_3-Cl)(μ_3-CH$_2$)(thf)$_3$] (**62**) is rather considered as ring-cluster-hybrid.[135] Complex **62** was synthesized by donor-induced aluminate cleavage of the mixed tetramethylaluminato/chlorido halfsandwich lanthanide complex [Cp*Ln(AlMe$_4$)$_x$(Cl)$_y$]$_2$ (Ln = Y: z = 2, y = x; Ln = La: z = 6, y = 2x) in a toluene/THF mixture and concomitant C–H bond activation, which led to structural rearrangement and formation of trinuclear **62** (Scheme A18).

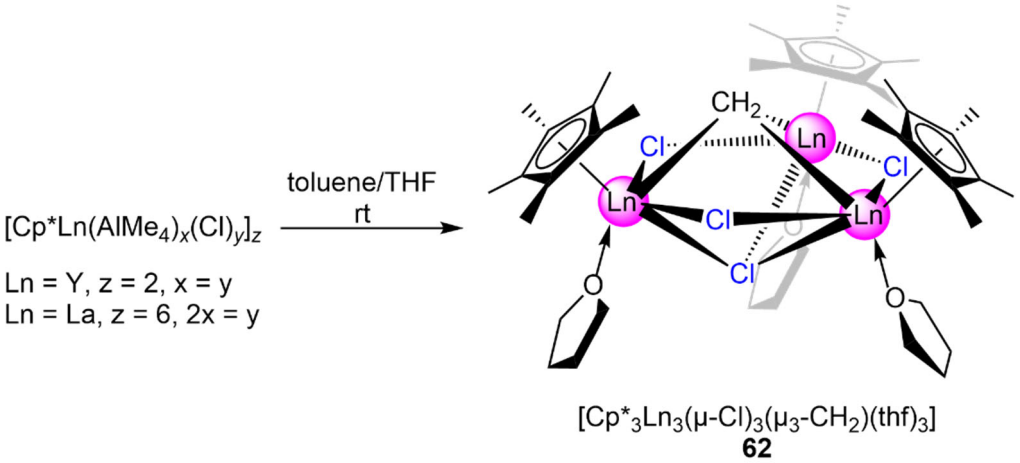

Scheme A18. Synthesis of methylidene/chlorido-bridged lanthanide complex **62**.[135]

The trinuclear arrangement of the lanthanide metal centers is a recurrent structural motif in rare-earth organo-rare-earth-metal chemistry and is often accompanied by donor coordination or the incorporation of donor atoms,[34, 50, 133, 135-137] although such complexes are considered as ring-cluster-hybrids. Exceptional performance in methylidene transfer is observed for trinuclear rare-earth-metal methylidene complexes acting as Schrock-type nucleophilic carbenes,[55, 137] with conversion rates similar to the benchmark systems by SCHROCK and TEBBE.[138-140] Noteworthy, a trinuclear lanthanum-chlorido complex capped by a pyrene trianion was isolated by the group of THIELE.[141] Treatment of the lanthanum ate-complex [Cp*LaCl(μ-Cl)$_2$Li(thf)$_2$] with pyrene and potassium resulted in the formation of the trimetallic lanthanum pyrene complex [Cp*$_3$La$_3$Cl$_3$(C$_{16}$H$_{10}$)(thf)] (**63**), representing the first rare-earth-metal complex with a pyrene trianion (Scheme A19).

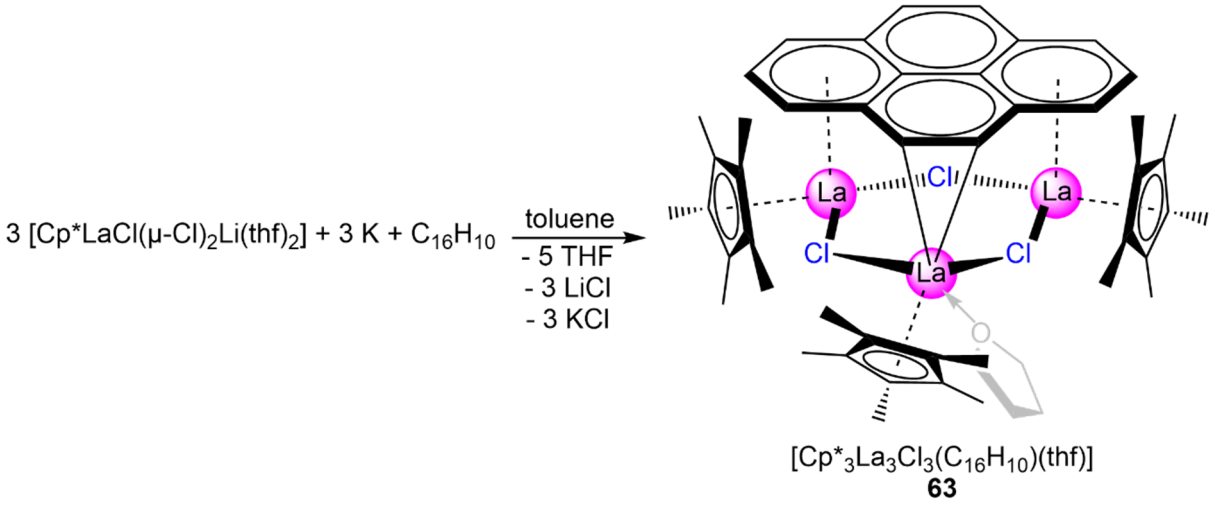

Scheme A19. Synthesis of trimetallic lanthanum pyrene complex **63**.[141]

Similar decomposition reactions of the trinuclear polymethyl yttrium complex $\mathbf{4^{Y}}$ were investigated by our group.[136] The transformation into the mixed methyl/methylidene complex [Cp*$_3$Y$_3$(μ_2-Me)(μ_3-Me)(μ_3-CH$_2$)(thf)$_2$] (**64**) occurred rather rapidly by donor (THF) addition to $\mathbf{4^{Y}}$ at -35 °C, while the conversion into the hexanuclear mixed methyl/methylidene cluster [Cp*$_6$Y$_6$Me$_4$(CH$_2$)$_4$] (**65**) was observed at elevated temperature in deuterated benzene after 12 h upon the release of methane. Further self assembly of clusters from polymethyl precursors was observed employing $\mathbf{4^{Gd}}$ and $\mathbf{4^{Tb}}$.[52] Interestingly, the aggregation in *n*-hexane led to the pentanuclear clusters [(Cp*Ln)$_5$(CH$_2$)(Me)$_8$] (**66^{Ln}**, Ln = Gd, Tb), bridged by eight methyl groups and only one methylidene group.

Rare-earth-metal alkoxide clusters were first reported by the group of EVANS.[115, 142, 143] The pentanuclear yttrium cluster [Cp*$_5$Y$_5$(μ-OCH$_3$)$_4$(μ_3-OCH$_3$)$_4$(μ_5-O)] (**67**) was obtained from the reaction of Cp*$_2$YCl with 1.4 equivalents of KOCH$_3$·CH$_3$OH in THF, and features a square pyramidal arrangement of the yttrium metal centers (Scheme A20).[115] Bridging in this cluster is achieved via μ_2- and μ_3-methoxy ligands as well as one central μ_5-oxo ligand.

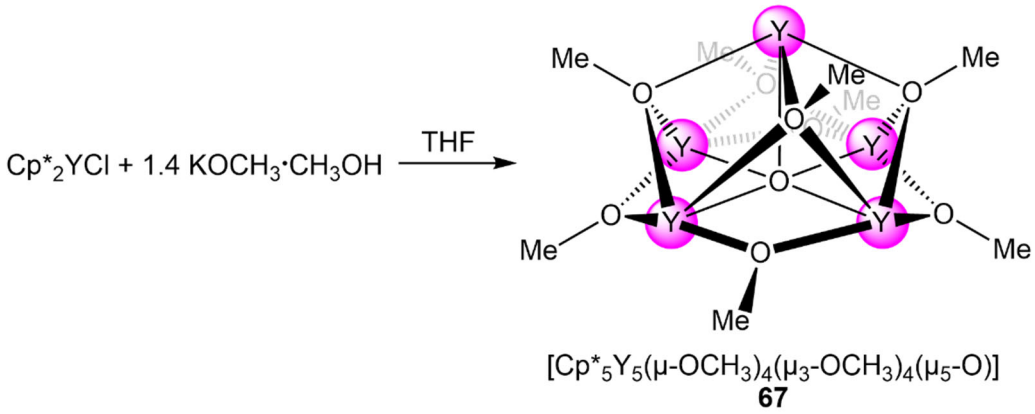

Scheme A20. Synthesis of pentametallic yttrium methoxide cluster **67**.[115]

Other structural motifs of lanthanide alkoxide clusters include dimeric complexes, trinuclear ring-cluster hybrids and complexes with the distinct Ln$_4$X$_7$ (X = Hal, –OCH$_3$) substructure.

4 Applications of Rare-Earth-Metal Clusters

4.1 Luminescence

Lanthanide(III) ions (electron configuration [Xe]4f^n, n = 0-14) can adopt a wide range of electronic levels, which are given by the formula 14!/*n*!(14-*n*)!. Photoluminescence properties of lanthanide(III) ions are determined by f-f transitions between spectroscopic states, moreover, parity allowed 4f-5d excitation and 5d-4f emission transitions or metal-ligand charge transfer with large energies of up to >50000 cm^{-1}.[144-146] In combination with stabilizing or electron-rich ligand systems such as cyclopentadienyl derivatives[103, 147] or hydrido(tris)pyrazolylborato ligands,[148] an intense emission can be observed. Consequently, lanthanide-based coordination clusters exhibit complex structural arrangements, often paired with a bright photoluminescence.[103, 149-157]. Here, the choice of the ligand system is crucial, enabling precise tuning of the emission wavelengths.[103, 158, 159] Especially for cerium(III), adjusting the emission wavelength is facile due to only two ground state energy levels ($^2F_{5/2}$, $^2F_{7/2}$), combined with exclusively d-f transitions for the emission process. The energy of the excited ^{2}D levels is then strongly determined by the ligand and metal to ligand charge transfer processes.[160]

As such, previous studies on the luminescence properties of Cp-substituted cerium complexes by the group of BRUNO revealed the effects of the ligand system (e.g. alkyl, Hal) on their photophysical behavior.[72, 159] The dimeric cerium chlorido complex [(Cp$^{t\mathrm{Bu2}}$)$_2$Ce(μ-Cl)]$_2$ (**68**) by EDELMANN *et al*. exhibits a bright yellow emission with a very high quantum yield of 61%,[147] which is comparable to prominent Ce^{3+}-doped LED phosphors.[161-164] This complex is accessible via a salt-metathesis reaction protocol, treating the homoleptic cerium chloride CeCl3 with 2 equivalents of KCp$^{t\mathrm{Bu2}}$. Another example of a molecular organo-rare-earth-metal emitter is the europocene complex [Eu(Cp$^{\mathrm{BIG}}$)$_2$] (**69**, Cp$^{\mathrm{BIG}}$ = C$_5$(4-*n*Bu-C$_6$H$_4$)$_5$) by the group

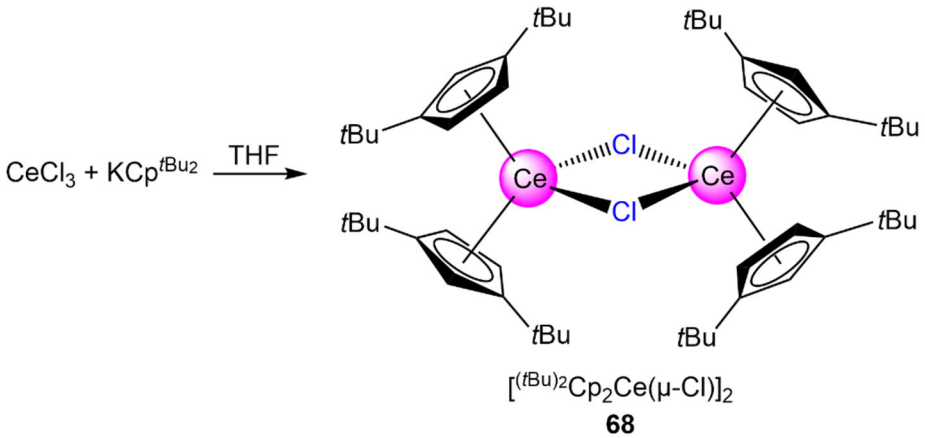

Scheme A21. Synthesis of sandwich cerium chlorido complex **68**.[147]

of HARDER,[165] which in contrast displays orange emission, with a slightly lesser quantum yield (45%) though.

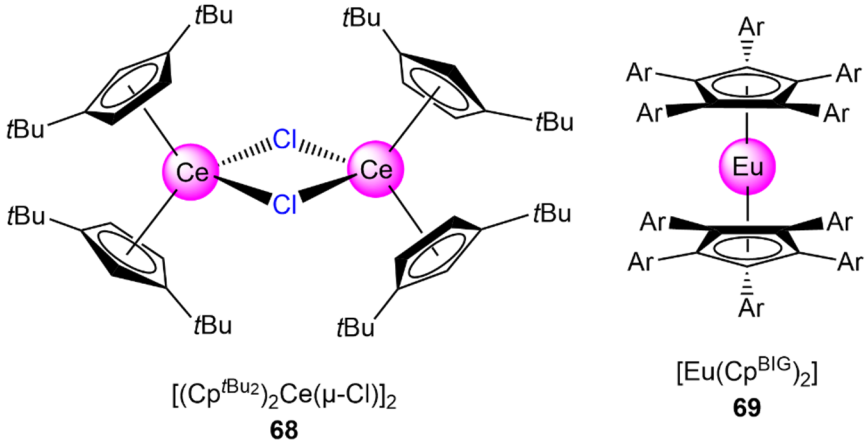

Figure A6. Molecular organometallic photoluminescence emitters **68** and **69**.[147, 165]

As for lanthanide clusters, the avoidance of donor ligands significantly limits structural diversity and cluster nuclearity.[103, 105] Hence, the synthesis of luminescent lanthanide clusters often involves hydro- or solvothermal synthesis protocols[150, 153, 154, 156] and derivatization of rare-earth-metal salts with donor ligands.[155, 157] Photoluminescent clusters have a wide range of possible applications, ranging from chemical sensors[153, 154, 156] over near-infrared (NIR) emitters for bioimaging,[155] model systems for upconversion processes,[166] to optical barcoding.[157]

Prominent examples of NIR emitters are the molecular wheels of the general formula $[Ln_{42}(L)_{14}(OH)_{28}(OAc)_{84}]$ (**70^{Ln}**, Ln = La, Nd, Sm, Yb; L = 2-hydroxy-3-methoxybenzaldehyde).[25, 153, 154] The homoleptic lanthanide acetates $Ln(OAc)_3$ were used as starting materials, and dissolved in EtOH at ambient temperature with addition of a substoichiometric amount of 2-hydroxy-3-methoxybenzaldehyde (0.75 equiv.) as well as excess triethylamine (2.5 equiv.), followed by heating under reflux conditions for 30 minutes. Subsequently, the reaction mixture was cooled to ambient temperature and filtered. Diffusion of diethyl ether into the solution then led to the formation of the crystalline product (yield: La = 42%, Nd = 37%, Sm = 37%, Yb = 40%), which shows emission in the visible spectrum as well as in the NIR region.

Control of the reaction stoichiometry enables modular changes to the luminescence properties of rare-earth-metal coordination clusters, as recently shown by MURUGESU and coworkers.[26] The respective homometallic cluster aggregates of the general composition

$[Ln_{20}(chp)_{30}(CO_3)_{12}(NO_3)_6(H_2O)_6]$ (**71^{Ln}**, Ln = Sm, Eu, Gd, Tb; chp^- = deprotonated 6-chloro-2-pyridinol) are synthesized by reacting the lanthanide nitrates $Ln(NO_3)_3{\cdot}6H_2O$ in a stoichiometric reaction with chp and triethylamine in a 1:1 mixture of methanol and acetonitrile. After 12 h reaction time, the reaction mixture was filtered, and evaporation of the solvent at ambient temperature led to the crystallization of the respective cluster complexes (yield: 25-35%). By precisely controlling the stoichiometric ratio of the lanthanide nitrates, the emission wavelength observed in the UV/VIS spectra of the corresponding clusters ranges from blue to red, and white emission was achieved for the composition $\{Eu_3Gd_5Tb_{12}\}$. Both homo- and heterometallic clusters show decent to high quantum yields, ranging from 9 to 56%.

4.2 Molecular Magnetism

Compounds exhibiting single-molecule magnetism (SMM) gained significant importance recently due to their possible application in data storage.[167-169] The first reported example of a SMM was the manganese-acetate cluster $\{Mn_{12}\}$ by SESSOLI *et al.* in 1993.[170] Continous efforts in the last three decades then produced a broad variety of mixed transition metal and lanthanide SMM complexes.[171-181] Recent studies revealed that the most powerful examples of SMMs are lanthanide-based, given their advantageous combination of a large number of unpaired f-electrons with their large single-ion magnetic anisotropy. Although the highest anisotropy barriers and blocking temperatures are achieved for cyclopentadienyl-substituted sandwich complexes with magnetic hysteresis up to 80 K,[182-185] recent examples of polynuclear lanthanide complexes are efficient single-molecule magnets as well.[22, 169, 186, 187] Similar to mononuclear examples, cyclopentadienyl derivatives prevail for lanthanide clusters with SMM behavior.[188] The increase in cluster nuclearity has major impact on the single-molecule magnetism by interference of the respective magnetic anisotropy axes rather than desired magnetic interactions between 4f metal centers, inevitably leading to a decrease in both blocking temperature as well as the effective energy barrier.[180, 181, 189, 190]

So far, the hexanuclear dysprosium halide cluster $[(Cp^*Dy)_6K_4Cl_{16}(thf)_6]$ (**72**) by MEYER *et al.* displays the highest energy barrier (561 K) for organolanthanide cluster compounds.[22] This cluster is accessible via a simple salt metathesis reaction protocol, treating dysprosium trichloride with potassium cyclopentadienide in tetrahydrofuran. In this particular case, all magnetic anisotropy axes are oriented in the same directing, leading to an overall improvement in the magnetic performance.

Beside this hexanuclear cluster, a variety of ring-cluster hybrid systems are known, ranging from mixed-metal compounds such as $[(\eta^5\text{-}Cp^{Me}{}_2Dy)\mu\text{-}SeMes]_3$ (U_{eff} = 252(4)cm^{-1}) (**73**, Mes = mesityl)[191] or $[(Cp^{Me})_2Dy(\kappa{:}\eta^5\text{-}C_5H_4)FeCp]_2$ (**74**)[192] to organometallic complexes bridged via heterocyclic ligand systems $[Yb_4(bpzch)_2(fod)_{10}]$ (**75**, bpzch = 3,6-dipyrazin-2-yl-1,2,4,5-tetrazine; fod$^-$ = 6,6,7,7,8,8,8-heptafluoro-2,2-dimethyl-3,5-octadionate)[187] and $[(Cp^*{}_2Ln)_4(tz^{\bullet})_4]\cdot 3(C_6H_6)$ (**76^{Ln}**, Ln = Gd, Dy; tz = 1,2,4,5-tetrazine).[186]

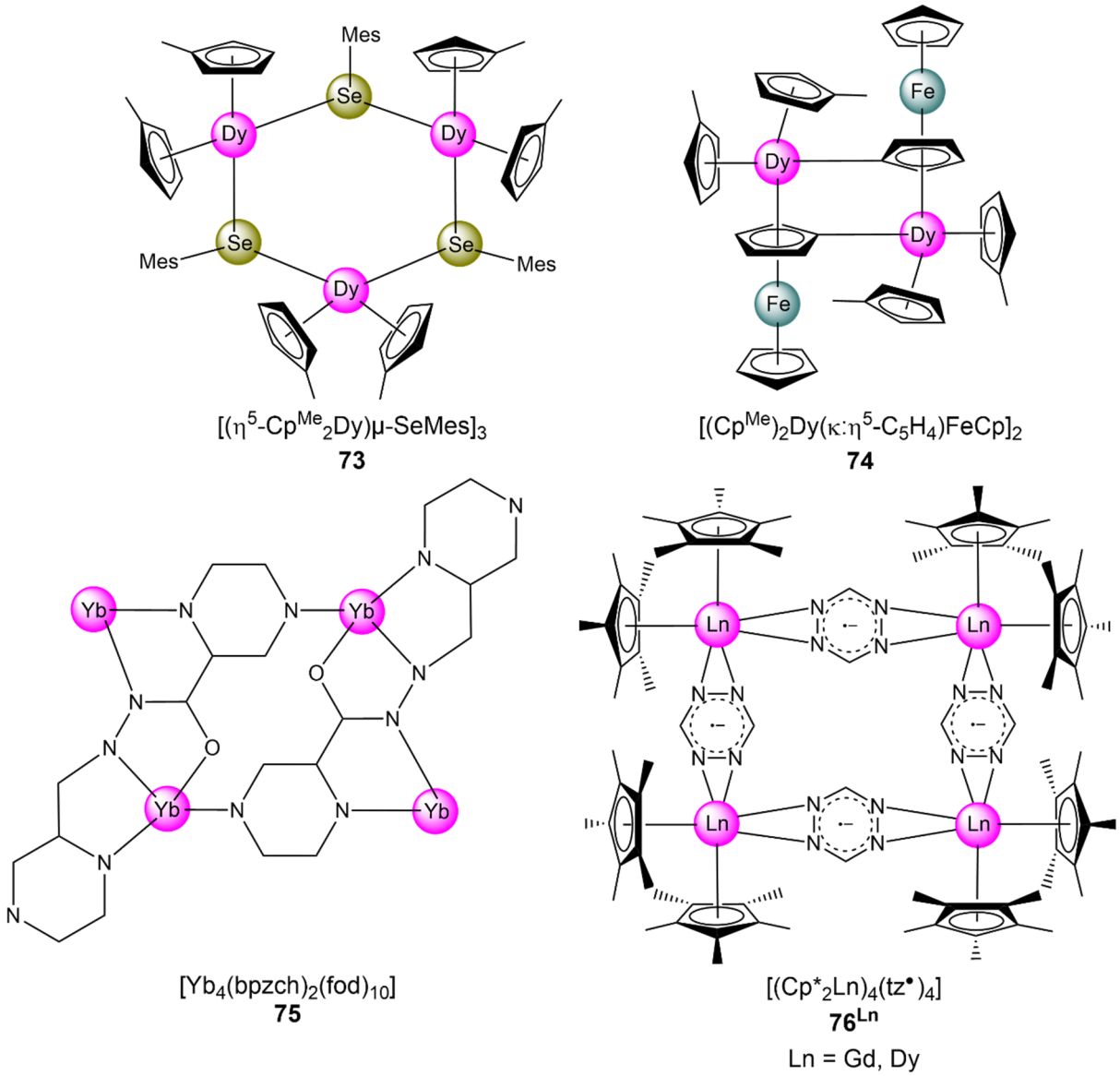

Figure A7. Lanthanide-based complexes exhibiting molecular magnetism (fod^--ligands of **75** omitted for improved visualization).[186, 187, 191, 192]

Especially the tetranuclear tetrazine-bridged compounds **76^{Ln}** by MURUGESU *et al.* display impressive magnetic properties.[186] The respective complexes were synthesized in a stoichiometric reaction by addition of a benzene solution of tetrazine and KC_8 in a 1:1 ratio to a benzene solution of [Cp*$_2$Ln][(μ-Ph$_2$)BPh$_2$] (Ln = Gd, Dy) (1 equiv., Scheme A22). Single-crystal X-ray diffraction revealed a planar structural arrangement between the lanthanide metal centers and the bridging tetrazine ligands. Surprisingly, both complexes show only one spin center, rather than a combination of individual spin centers for the different metal centers, which could be attributed to strong coupling between the tetrazine radicals and the metal centers. As such, these tetranuclear compounds show extremely large coercive fields of approximately 30 kOe.

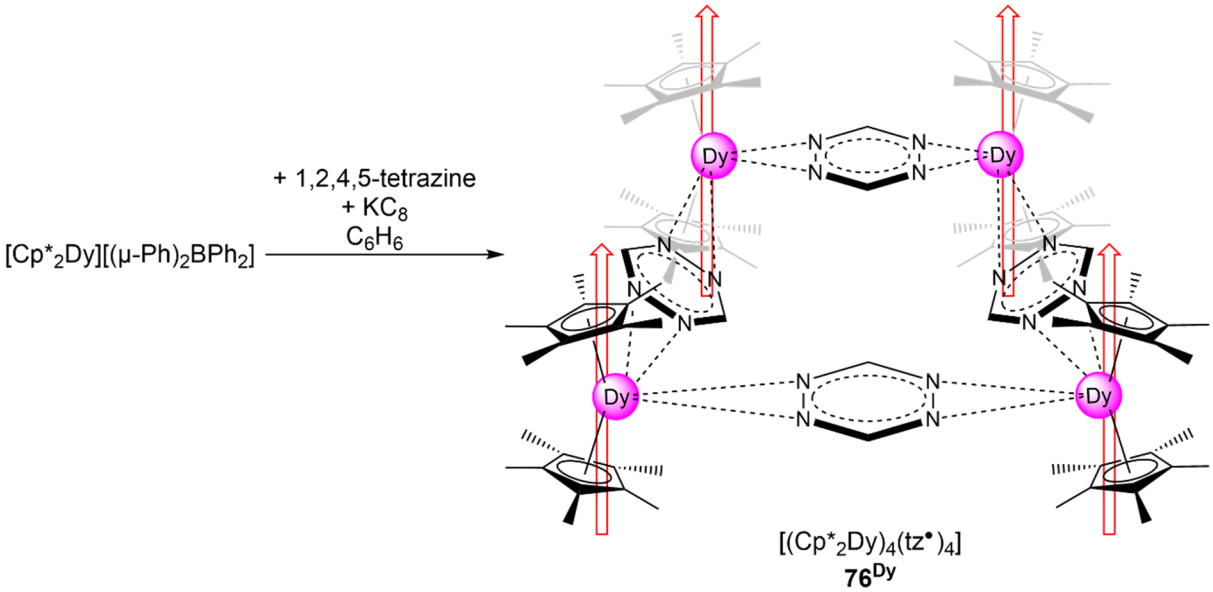

Scheme A22. Synthesis of tetrazine-bridged dysprosium complex $\mathbf{76^{Dy}}$. The orientation of the magnetic anisotropy axes is indicated with a red arrow.

B

Summary of the Main Results

1 $[Cp^RLnX_2]_n$: Effect of Cp^R Steric Demand

The donor-free synthesis of rare-earth-metal clusters in non-aqueous media like aromatic or aliphatic solvents requires controlled shielding by ancillary ligands. Particularly, the cyclopentadienyl ligand and its derivatives have emerged as invaluable in rare-earth-metal cluster chemistry.[31, 32, 193-196] In spite of several straightforward synthesis routes toward rare-earth-metal clusters, including salt-metathesis[93, 194, 196, 197] or serendipitous hydrolysis pathways,[195, 198] the highest nuclearity achieved for donor-free lanthanide clusters so far remained at $\{Ln_{12}\}$ for the dodecanuclear samarium cluster $[CpSmCl_2]_{12}$ by TEUBEN.[32] The cluster itself was synthesized by refluxing $SmCl_3(thf)_3$ with Me_3SiCp, leading to the formation of the intermediate $CpSmCl_2$ fragment, followed by self-assembly to the dodecanuclear structure. This reaction pathway emphasizes the suitability of halfsandwich precursors for the synthesis of large rare-earth-metal coordination clusters.

Aiming at the synthesis of a similar, stable halfsandwich precursor of the general composition Cp^RLnX_2, the trimethylsilyl cyclopentadienyl lanthanum bis(tetramethylaluminate) complex [Cp'La($AlMe_4$)$_2$] (**A**, $C_5H_4SiMe_3$ = Cp') was selected, implying two advantageous properties: Firstly, **A** shows a reduced steric demand to other Cp derivatives like Cp* or Cp*' which were employed in previous syntheses of lanthanide clusters (see Chapter A3.2). Secondly, the tetramethyl aluminate ligand can be easily replaced via donor-cleavage or halogenido exchange reactions for monoanionic ligands (e.g. Me, X = Hal)[34, 40, 56, 63, 135, 137] that are prone to the formation of coordination clusters.

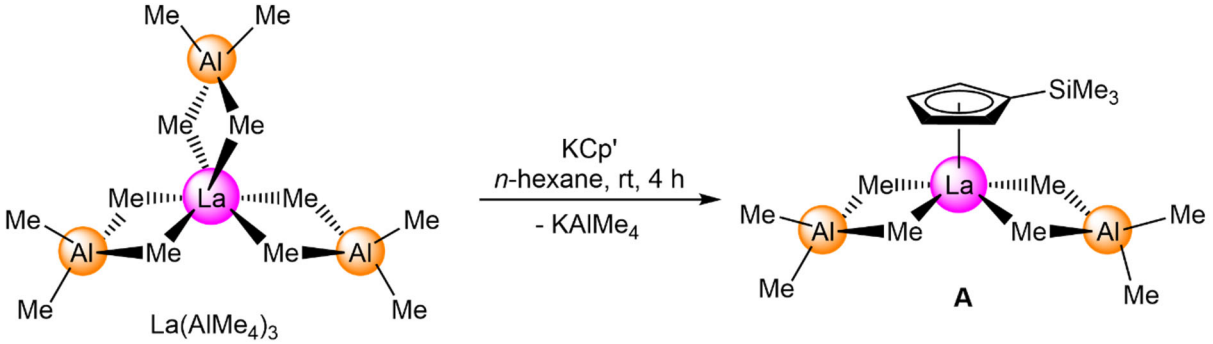

Scheme B1. Synthesis of halfsandwich complex **A** by salt-metathesis.

Following a salt-metathesis protocol, homoleptic lanthanum tris(tetramethylaluminate)[35] was treated with KCp', affording the desired halfsandwich complex **A** in high crystalline yield (92%) after recrystallization from a saturated *n*-hexane solution.

In order to compare the effect of the cyclopentadienyl steric demand on cluster formation, the Cp*-substituted congener [Cp*La(AlMe$_4$)$_2$] (**B**) was selected as reference.[43] Whereas the stoichiometric iodination reaction of **A** and **B** with Me$_3$SiI gave access to the isostructural heterobimetallic clusters [Cp$^R_6$La$_6$I$_8$(AlMe$_4$)$_4$] (**C^A**, R = SiMe$_3$; **C^B**, R = Me$_5$), the reaction with excess (2.5 equiv.) Me$_3$SiI led to the formation of different crystalline products. While the reaction of **B** with iodination reagent yielded the nonametallic halfsandwich lanthanum diiodide cluster [Cp*LaI$_2$]$_9$ (**D**, 56% cryst.), the similar reaction of **A** afforded the larger dodecametallic cluster [Cp'LaI$_2$]$_{12}$ (**E**, 48% cryst.), providing evidence for the benefit of a reduced steric demand of the ancillary ligand on effective cluster enlargement. The molecular structure of clusters **C^A**, **C^B**, **D** and **E** were unambiguously revealed via single-crystal XRD analyses (Figure B1). The increased solubility given by the Cp' ligand allowed the unambiguous assignment in ^{1}H and ^{13}C{^{1}H} NMR spectroscopic investigations of complexes **A**, **C^A** and **E**, indicating a rearrangement of **C^A** in solution into the presumably more stable **E** and **A**.

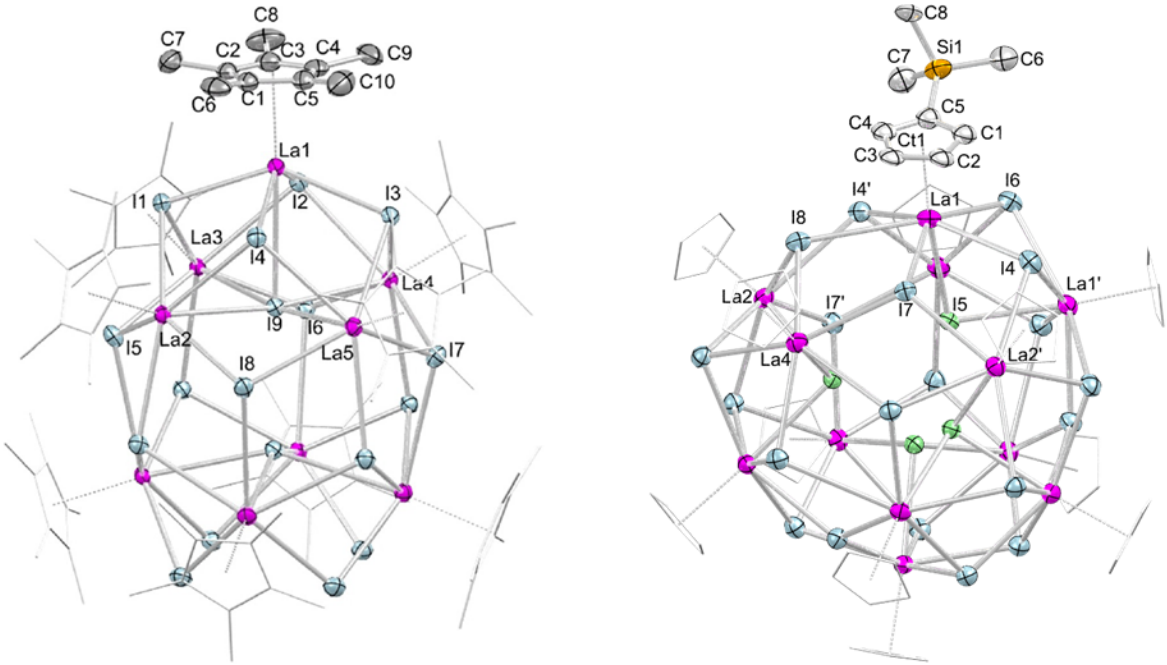

Figure B1. Crystal structures of **D** (left) and **E** (right, **Paper I**).

2 $[Cp^RLnX_2]_n$: Effect of Halogenido Ion Size X

Even though halogenido ions are established ligands in rare-earth-metal cluster chemistry (see Chapter A3.2), there is a lack of comparative studies regarding the effect of the halogenido ion size, despite a relatively large difference of almost 1 Å in the ionic radii between the different halogenido ions (CN 6, Hal ionic radii [Å]: I = 2.20, Br = 1.96, Cl = 1.81, F = 1.33).[113] Consequently, the formation of different structural motifs is expected under otherwise identical reaction conditions.

Whereas Me_2AlCl already proved to be a potential halogenido transfer reagent in the synthesis of the heterobimetallic cluster $[Cp^*_6La_6Cl_8(AlMe_4)_4]$,[63] the reaction conditions at low temperatures and the hard halogenido-transfer reagent impede a targeted, controlled reaction process. Hence, the mild halogenido-transfer reagents Me_3SiX/Me_3GeX (X = I, Br, Cl) were selected as reactants. As already mentioned in the previous section, the addition of excess Me_3SiI to a stirred solution of **A** resulted in the formation of dodecanuclear cluster **E**.

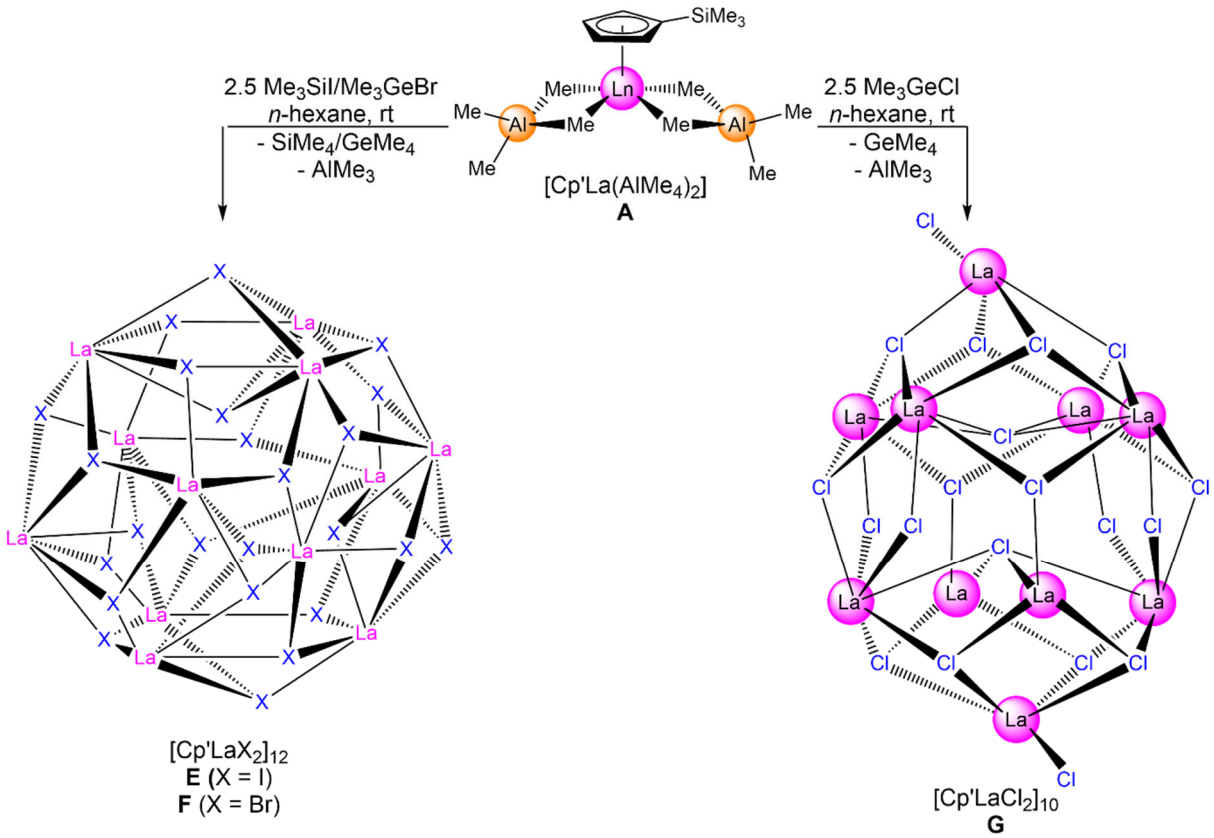

Scheme B2. Reactivity of **A** toward mild halogenido transfer reagents Me_3SiI and Me_3GeX (X = Br, Cl, **Paper I**, Cp' ligands are omitted for clarity).

The isostructural bromido-bridged cluster $[Cp'LaBr_2]_{12}$ (**F**) was obtained under the same reaction conditions (47% cryst. yield), utilizing Me_3GeBr as halogenido-transfer reagent. In contrast, the reaction of **A** with 2.5 equivalents of Me_3GeCl afforded the ellipsoidal decanuclear cluster $[Cp'LaCl_2]_{10}$ (**G**) instead of a spherical cluster like **E** and **F**. While the crystal structure of **E** and **F** was determined via precise single-crystal XRD analysis, only a connectivity was established for **G**. Even more surprisingly, whereas the equimolar reaction of **A** with Me_3GeBr produced the heterobimetallic cluster $[Cp'_6La_6Br_8(AlMe_4)_4]$ (**H**, isostructural to $\mathbf{C^A}$), the respective reaction with Me_3GeCl led to the formation of **G**. Both examples indicate the effect of minor differences in the ionic radii (Br^- vs. Cl^- = 0.15 Å) on the potential formation of coordination clusters. All investigated clusters were further characterized NMR spectroscopically to scrutinize their solution behavior, and complex purity was confirmed by elemental analyses as well as EDX measurements.

Further impact of the bridging halogenido ligand on the cluster properties is indicated by the luminescence of dodecametallic cerium clusters $[Cp'CeX_2]_{12}$ ($\mathbf{I^X}$, X = I, Br, Cl). Previous examples of cerium cyclopentadienyl complexes displayed interesting photoluminescence behavior,[72, 147, 158, 159] hence similar investigations were conducted for $\mathbf{I^X}$. Interestingly, clusters $\mathbf{I^X}$ adopt identical structural motifs, however, the absorption and emission properties change notably. UV-VIS characterization showed a shift toward higher wavelengths in accord with increasing halogenido ion size for both excitation and emission maxima as well as an increase in luminescence lifetime (see Table B1).

Table B1. Photoluminescence properties of clusters $\mathbf{I^X}$.

	$\mathbf{I^{Cl}}$	$\mathbf{I^{Br}}$	$\mathbf{I^{I}}$
Exc. Max. [nm]	287 / **352**	291 / **370**	286 / **420**
Em. Max. [nm]	**459** / 500	**473** / 514	**489** / 533
Lifetime [ns]	77 / 111	115	93 / 147

While the first maxima in the absorption spectrum is assigned to solvent effects, the absorption maxima shift by approximately 70 nm, and emission maxima as well as shoulders in the emission spectrum by ca. 30 nm (see Figure B2). For $\mathbf{I^{Cl}}$ and $\mathbf{I^{I}}$, a biexponential fit was adopted, whereas the fit of $\mathbf{I^{Br}}$ is single exponential.

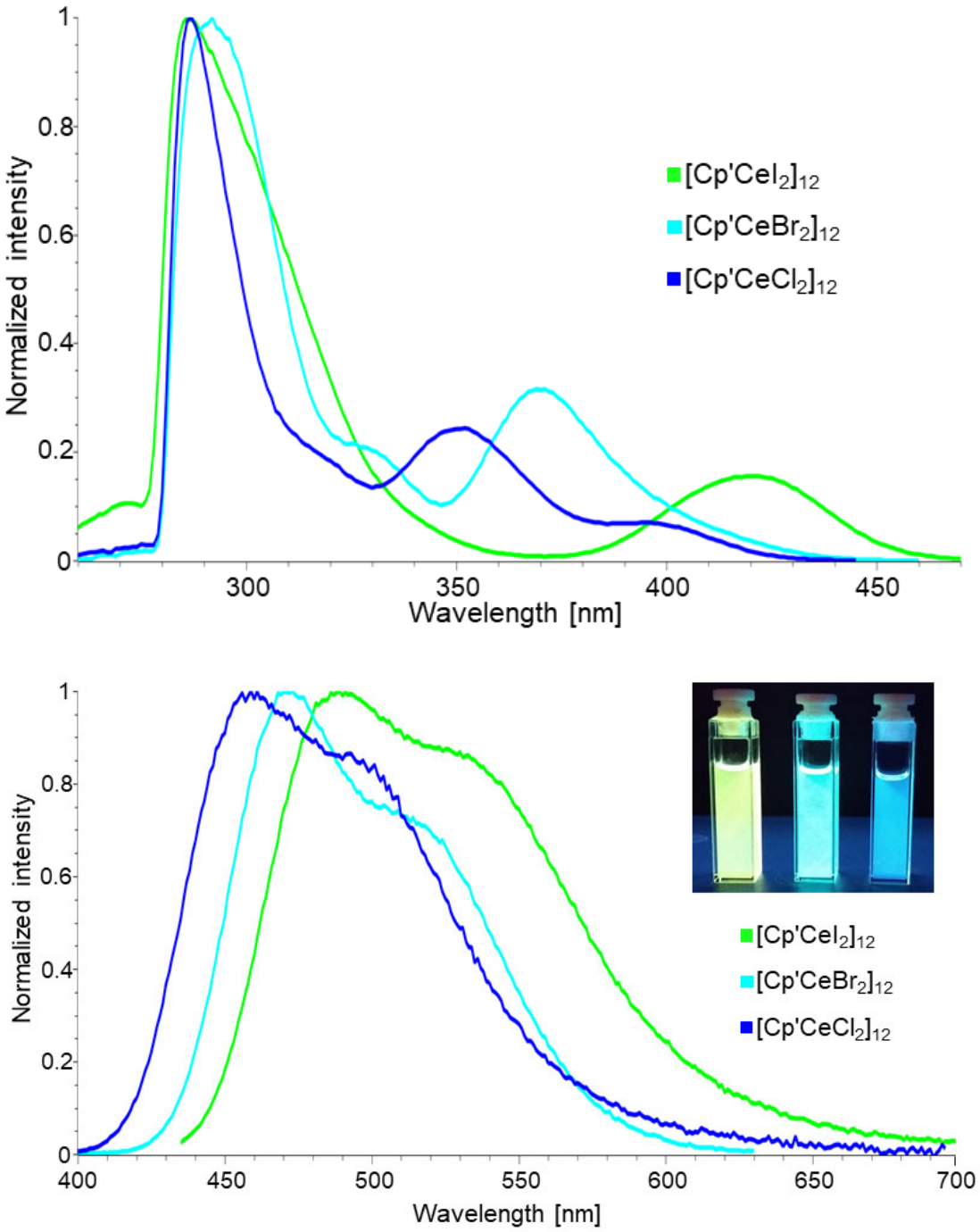

Figure B2. Normalized excitation (top) and emission (bottom) spectra of clusters $\mathbf{I}^{Cl}$, $\mathbf{I}^{Br}$ and $\mathbf{I}^{I}$ and photoluminescence under UV-light (302nm, **Paper II**).

3 $[Cp^RLnX_2]_n$: Effect of Rare-Earth-Metal Center Ln

Even though potential size effects of rare-earth-metal centers have been discussed previously, reliable data have remained scarce, often due to incoherence of the study (e.g. choice of metal centers with large difference in ionic radii, different reaction conditions etc.).[63, 91] Nevertheless, the size can be effect significant, given the wide range of ionic radii for rare-earth-metal centers (CN 6, Ln^{III} ionic radii [Å]: min. = Sc = 0.745; max. = La = 1.032).[113]

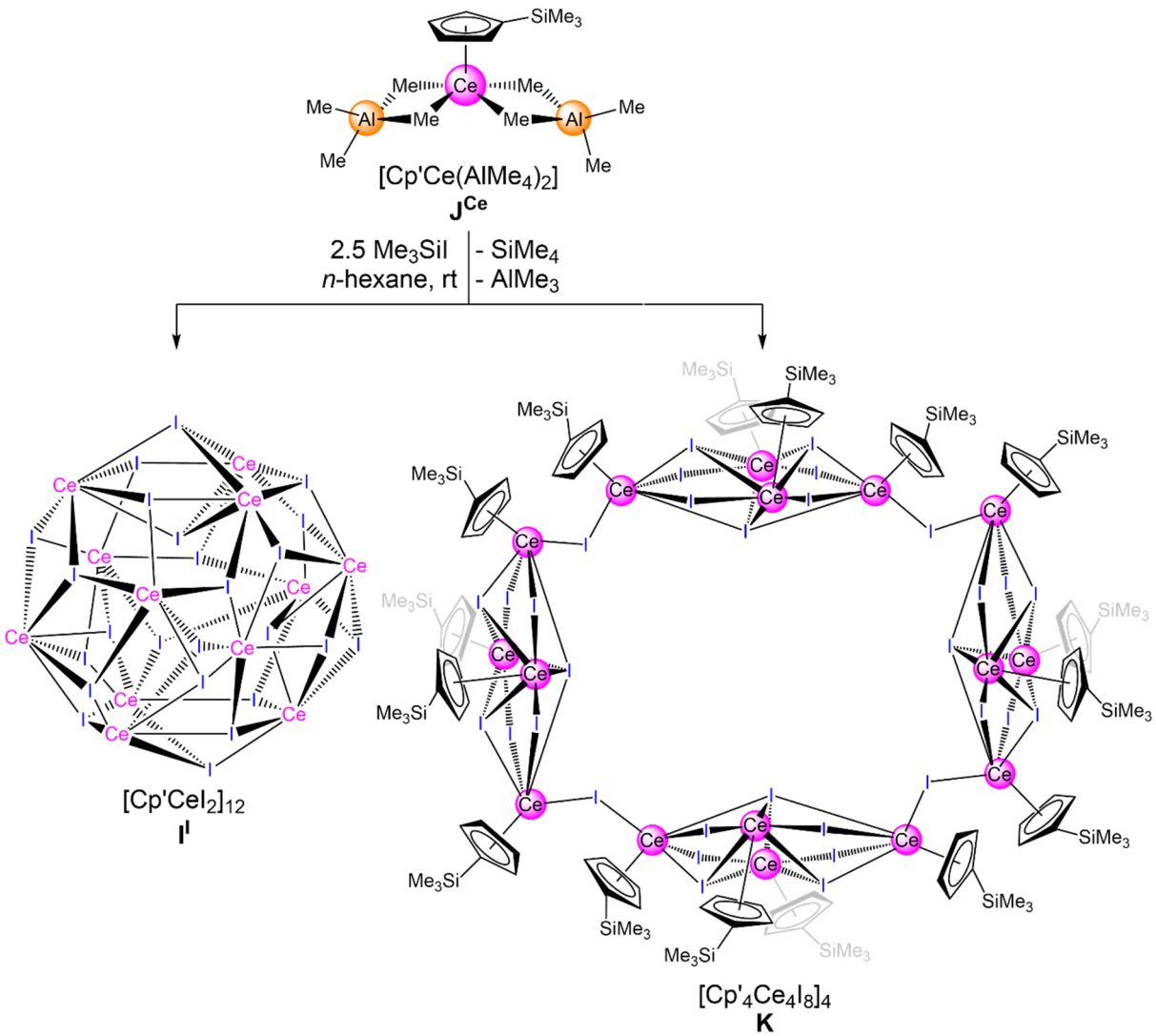

Scheme B3. Reactivity of $\mathbf{J^{Ce}}$ toward iodination reagent Me_3SiI (**Paper II**).

For comparison, previously established reactions with the corresponding lanthanum precursor were performed for the marginally smaller lanthanide metal centers cerium and praseodymium. The respective precursor complexes [Cp'Ln(AlMe4)2] ($\mathbf{J^{Ln}}$, Ln = Ce, Pr) were synthesized as yellow or green oils in excellent yields (> 90%), respectively, by treatment of the homoleptic complexes Ln(AlMe4)3 with equimolar amounts of KCp'.

Employing alkyl complexes Cp'Ln(AlMe$_4$)$_2$ (**J^{Ln}**) revealed potential size effects between the lanthanide metal centers La, Ce and Pr, as evidenced by the isolation of coordination clusters with different structural motifs depending on the metal center ion size (Figure B3). While dodecametallic iodido clusters **E** and **I^{I}** were obtained for lanthanum and cerium, synthesis of putative [Cp'PrI$_2$]$_{12}$ was not feasible. The respective iodination of **J^{Ce}** simultaneously afforded the {Ce$_{16}$} nanowheel [Cp'$_4$Ce$_4$I$_8$]$_4$ (**K**), and single-crystal XRD analysis revealed a coordination of four [Cp'$_4$Ce$_4$I$_7$] subunits interlinked via bridging iodido ligands.

In contrast, AlMe$_4$/Br exchange reactions with excess Me$_3$GeBr gave reproducibly access to dodecametallic bromido clusters [Cp'LnBr$_2$]$_{12}$ (**L^{Ln}**, Ln = La, Ce, Pr) in high crystalline yields (48-65%). Similar to iodido derivatives, size effects were found for chlorido-bridged clusters as well. As previously discussed, decametallic **G** was obtained by chlorination of **A** with Me$_3$GeCl. The related cerium cluster [Cp'$_5$Ce$_5$Cl$_9$(Cl$_2$AlMe$_2$)]$_2$ (**M**) and dodecametallic co-product [Cp'CeCl$_2$]$_{12}$ (**I^{Cl}**) were formed in the reaction of **J^{Ce}** with trimethylgermanium chloride. Unlike [Cp'LaCl$_2$]$_{10}$ (**G**), cluster **M** features two terminal [Cl$_2$AlMe$_2$] units instead of chlorido ligands in the crystal structure. In the praseodymium reaction, the dodecametallic cluster [Cp'PrCl$_2$]$_{12}$ (**N**) was obtained exclusively.

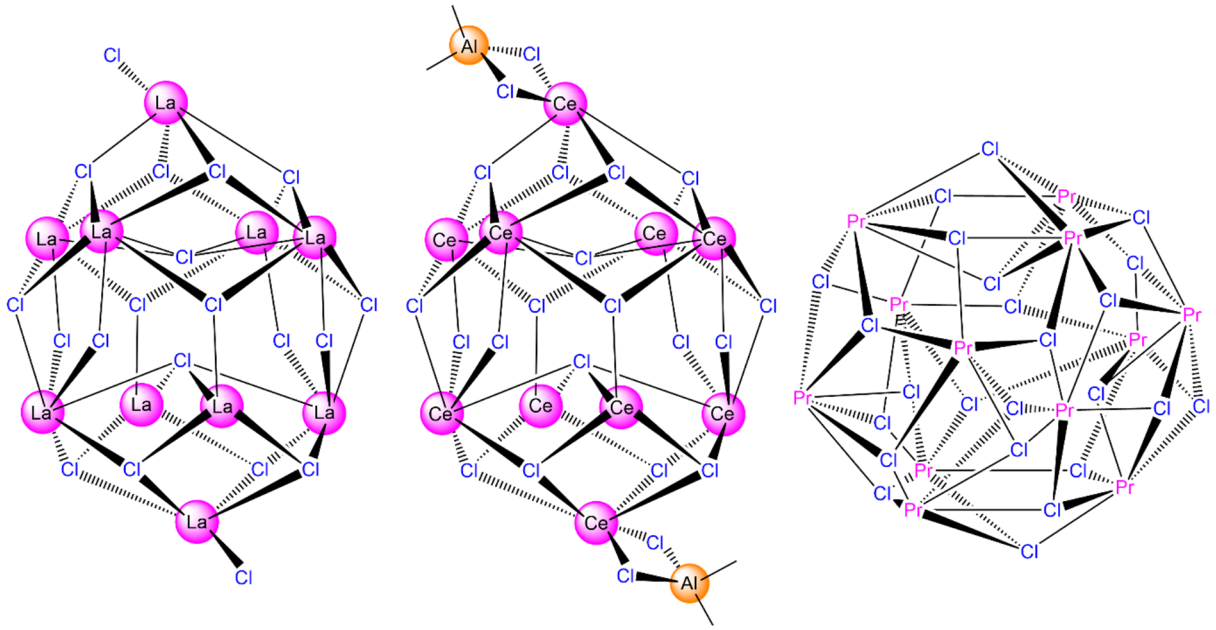

Figure B3. Structural diversity of rare-earth-metal chloride clusters **G** (left), **M** (center) and **N** (right) (Cp' ligands omitted for improved visualization).

4 $[Cp^RLnX_2]_n$: Effect of Crystallization Technique

The mechanistic details of cluster formation are highly complex, and dependent on a multitude of factors such as the choice of solvent, stoichiometry or the synthesis pathway.[4, 6, 7, 199-201] Surprisingly, the effect of the crystallization technique on cluster synthesis has been neglected in previous studies. Consequently, structurally characterized clusters mainly represent the thermodynamically most stable reaction product.

In order to investigate into possible kinetic effects on the formation of lanthanide clusters, a novel synthesis protocol was implemented. By diffusion of the aforementioned halogenido-transfer reagents Me_3SiI and Me_3GeX (X = Br, Cl) into a solution of halfsandwich complex $Cp^RLn(AlMe_4)_2$, a reduced reaction speed, and thus an increased kinetic control of the reaction is feasible. In initial experiments, the iodination of **A** resulted in the formation of the octanuclear cluster $[(\mu\text{-Cp})_2Cp'_8La_8I_{14}]$ (**O**, see Scheme B4). Single-crystal XRD analysis of cluster **O** revealed two La_4I_7 subunits interconnected via desilylated Cp ligands. The desilylation of the Cp' ligands was evidenced by ^1H NMR spectroscopy, indicating the presence of hexamethyldisilane in the residual reaction solution after crystallization. Monitoring by NMR spectroscopy revealed structural rearrangement into cluster **E** in solution, which presumably represents the thermodynamically more stable species.

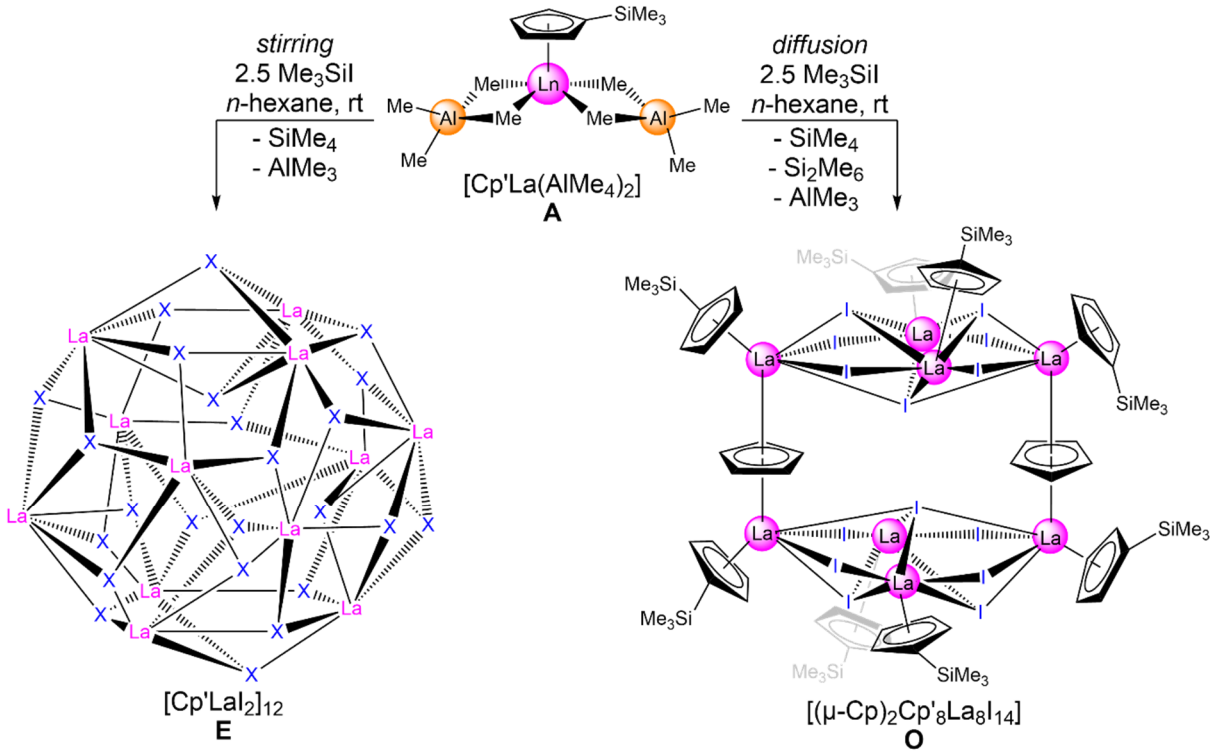

Scheme B4. Reactivity of **A** toward Me_3SiI according to different synthesis methods. In **E**, the Cp' ligands are omitted for clarity.

The respective diffusion reaction of **A** with Me_3GeBr afforded the heteroaluminate cluster $[Cp'_5La_5Br_9(Br_2AlMe_2)]_2$ (**P**). For comparison, the stirred reaction gave dodecametallic $[Cp'LaBr_2]_{12}$ (**F**). Surprisingly, single-crystal XRD analysis of **P** showed the same structural motif like the decametallic cerium cluster **M**, which was obtained by a stirred reaction though. Similar to the previously discussed iodido cluster **O**, cluster **P** undergoes transformation into cluster **F** in solution, which was evidenced by ^1H NMR spectroscopy. Unlike the iodido and bromido derivatives, chlorination of **A** with Me_3GeCl did not afford a structurally different cluster, and instead gave decametallic cluster **G** again.

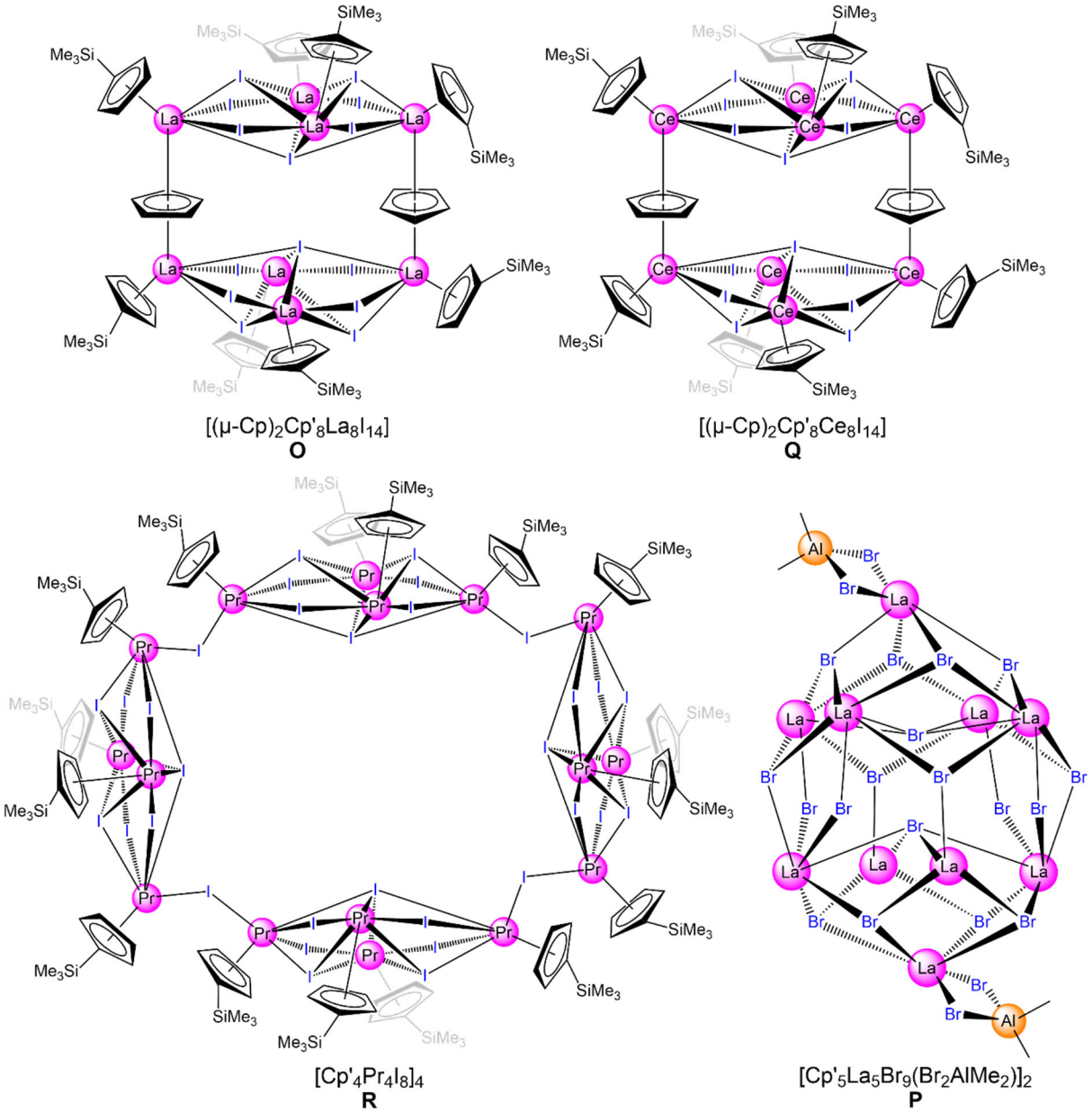

Figure B4. Molecular drawings of clusters exclusively accessible via the diffusion synthesis route (Cp' ligands omitted for **P** for clarity).

Accordingly, the diffusion method was applied for the cerium and praseodymium complexes [Cp'Ln(AlMe$_4$)$_2$] (**J^{Ln}**, Ln = Ce, Pr) as well, though exclusively for the iodination reaction with excess Me$_3$SiI. The reaction of halfsandwich cerium complex **J^{Ce}** gave access to two different clusters, the octanuclear [(μ-Cp)$_2$Cp'$_8$Ce$_8$I$_{14}$] (**Q**) – isostructural to the corresponding lanthanum cluster **O** – and {Ce$_{16}$} nanowheel **K**. Formation of dodecanuclear cluster **I^{I}** was not observed for the diffusion method.

While previous attempts of iodination of **J^{Pr}** via a stirred reaction failed or resulted in precipitation of insoluble white solid, respectively, application of the diffusion protocol led to the exclusive formation of the praseodymium nanowheel [Cp'$_4$Pr$_4$I$_8$]$_4$ (**R**), isostructural to cerium congener **K**. Overall, clusters obtained via the diffusion method represent the kinetically favored products, and some of them are exclusively obtained by this protocol (see Figure B4).

C

Unpublished Results

5 Synthesis of Cerium Halfsandwich and Sandwich Complexes and Photoluminescence Behavior

Introduction

Research efforts on luminescent cerium complexes are spurred by a wide range of potential applications, such as photosensitizers or photocatalysis, lighting, or bioimaging.[144, 202-207] Here, the effective photoluminescence properties of Ce(III) is greatly affected by the ligand environment. As such, the excitation and emission properties can be effectively tuned.[144, 146] While the abovementioned cerium clusters displayed intriguing photoluminescence behavior, we aimed at a systematic study of luminescent Cp*-based cerium complexes, with special consideration given to the electronic properties of the ligand systems. Major aspects include the Cp/$AlMe_4$ ratio, different Cp derivatives, and substitution with halogenido ligands, as previous results already showed interesting photoluminescence behavior for these types of complexes.[72, 147, 158]

Results and Discussion

In order to investigate on the effect of the Cp/$AlMe_4$ ratio, we selected the electron-rich pentamethylcyclopentadienyl ligand as substituent. The respective halfsandwich and sandwich cerium tetramethylaluminate complexes [Cp*Ce($AlMe_4$)$_2$] (**AA**) and [Cp*$_2$Ce($AlMe_4$)] (**BB**) were synthesized by treatment of the homoleptic cerium tris(tetramethylaluminate) Ce($AlMe_4$)$_3$ with KCp*. Whereas Ce($AlMe_4$)$_3$ is a colorless solid, **AA** has a bright yellow color, which changes to bright orange-red for **BB**. This color change is mirrored in the excitation and emission spectra as well (Figure C1). The excitation maxima range is 366 nm for Ce($AlMe_4$)$_3$, 431 nm for **AA** and 505 nm for sandwich complex **BB**. Likewise, a shift toward higher wavelengths is observed in the emission spectra as well, going from 452 nm for Ce($AlMe_4$)$_3$ over 489 nm with a shoulder at 530 nm for **AA** to 563 nm with a shoulder at 635 nm for **BB**. Consequently, the emission color under UV-light is fundamentally different for the three complexes: a dark blue color is observed for Ce($AlMe_4$)$_3$, an intense light blue color for **AA**, and a bright yellow color for **BB**. Additional effects were found for the luminescence lifetime, which significantly increases from 45 ns for Ce($AlMe_4$)$_3$ to 128 ns (**AA**) and 140 ns (**BB**), respectively. Similarly, the luminescence quantum yield can be enhanced from 18% for Ce($AlMe_4$)$_3$ to 56% for **BB**.

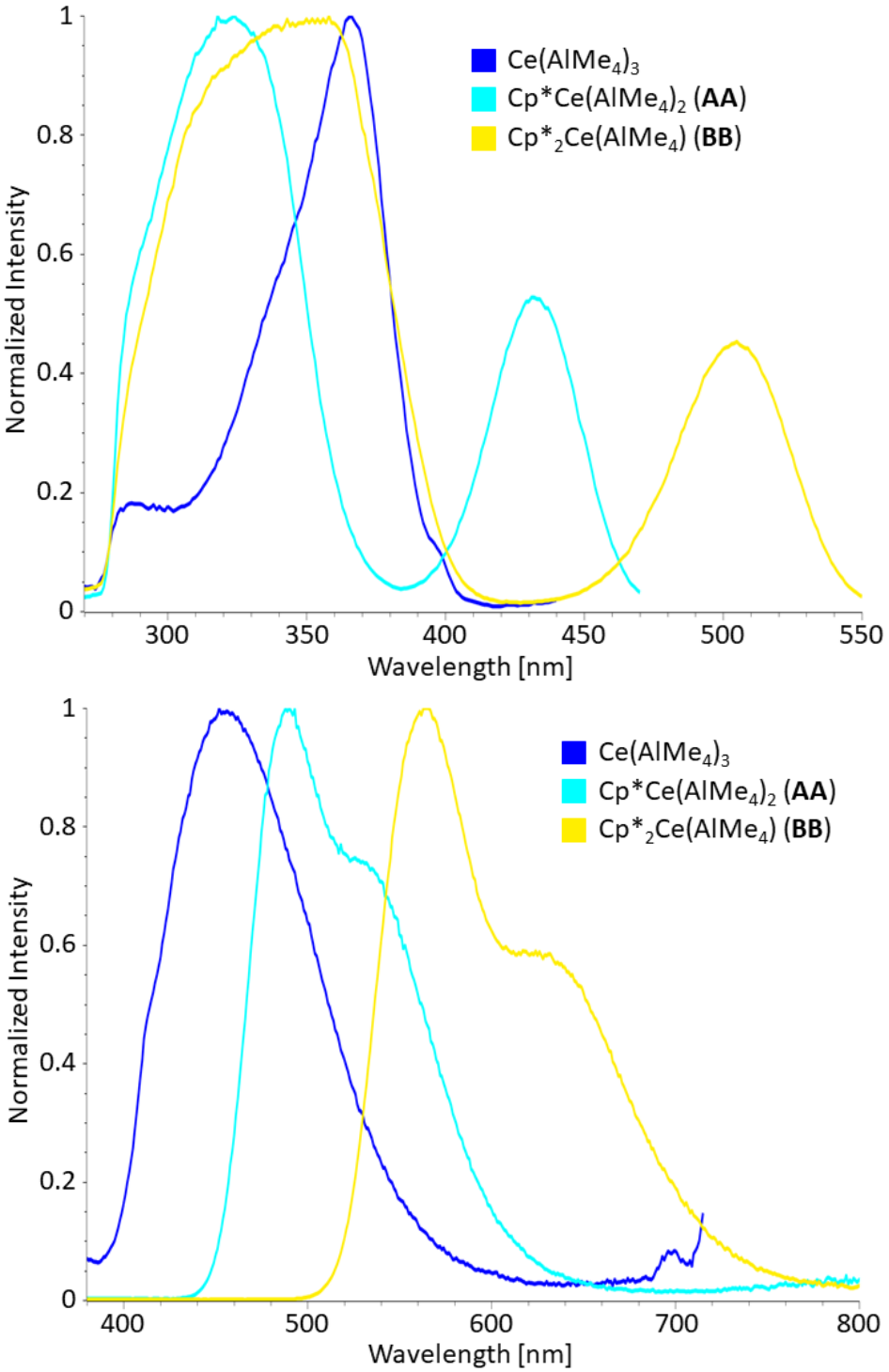

Figure C1. Normalized excitation (top) and emission spectra (bottom) of $Ce(AlMe_4)_3$, **AA**, and **BB**.

In a next step, we focused on the effect of differently substituted cyclopentadienyl ligands. For this purpose, we examined the halfsandwich complexes with unsubstituted cylopentadienyl [$CpCe(AlMe_4)_2$] (**CC**) in comparison to trimethylsilyl (Cp') and pentamethyl (Cp*) substituted derivatives $\mathbf{J}^{Ce}$ and **AA**.

While the complexes with Cp and Cp* substitution show similar spectra with small shifts in excitation and emission maxima for the Cp* compound, the Cp' complex shows two maxima (409 and 471 nm) in the excitation spectrum as well as a broadened emission maximum (Figure C2).

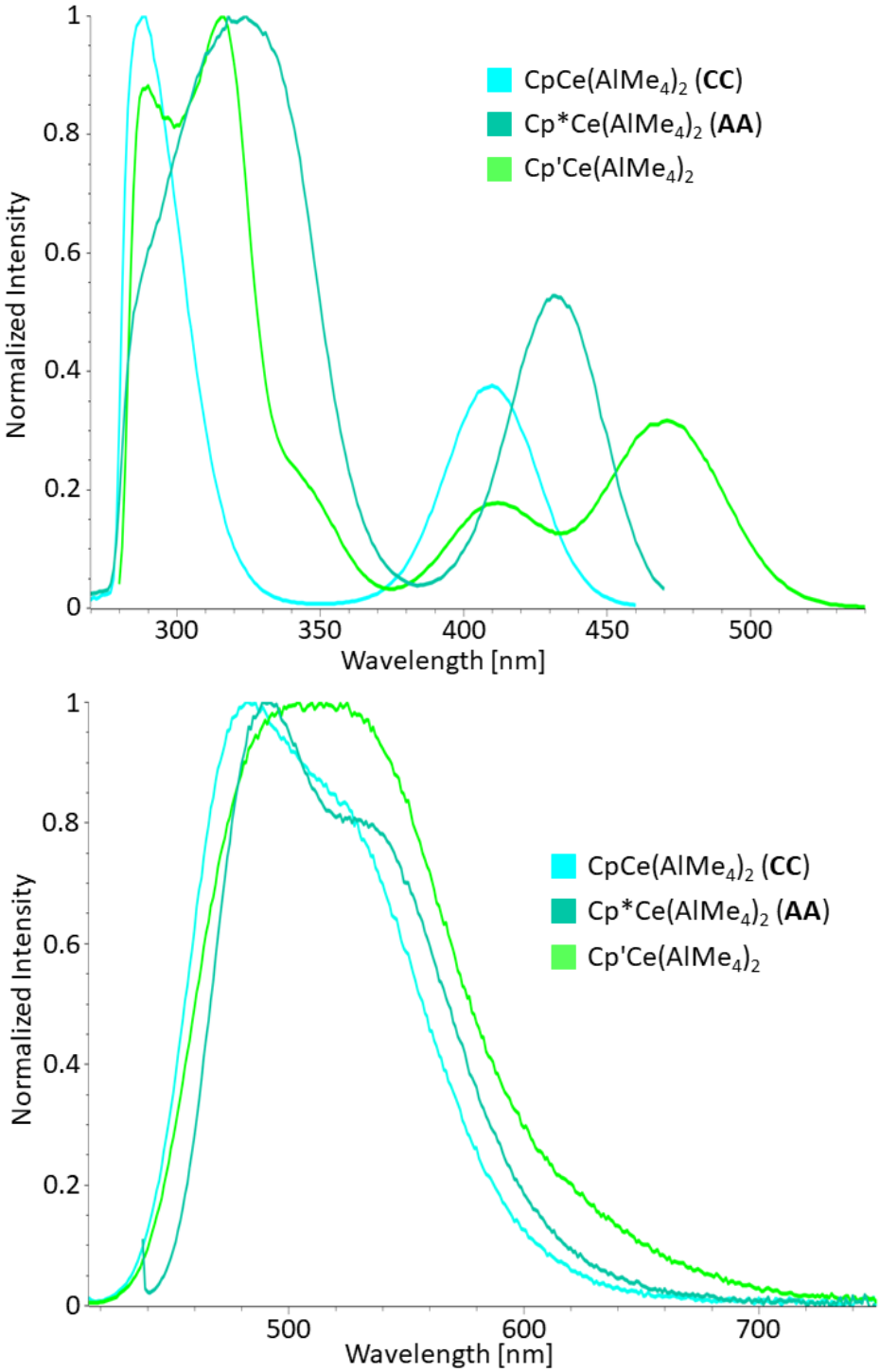

Figure C2. Normalized excitation (top) and emission spectra (bottom) of halfsandwich complexes **CC**, **AA**, and Cp'Ce(AlMe4)2.

Notably, the luminescence lifetime changes slightly from 113 ns for **CC** to 128 ns for [Cp*Ce(AlMe$_4$)$_2$], and increases further in Cp'Ce(AlMe$_4$)$_2$ to 128 and 153 ns with a contribution of 50 :50, again likely to a monomer-dimer equilibrium.

Since halfsandwich rare-earth-metal complexes showed to be suitable precursors for the synthesis of halide THF-adducts,[64] **AA** and **BB** were treated with halogenido transfer reagents Me$_3$SiI or Me$_3$GeX (X = Br, Cl) to achieve complete AlMe$_4$/halogenido exchange (see Scheme C1).

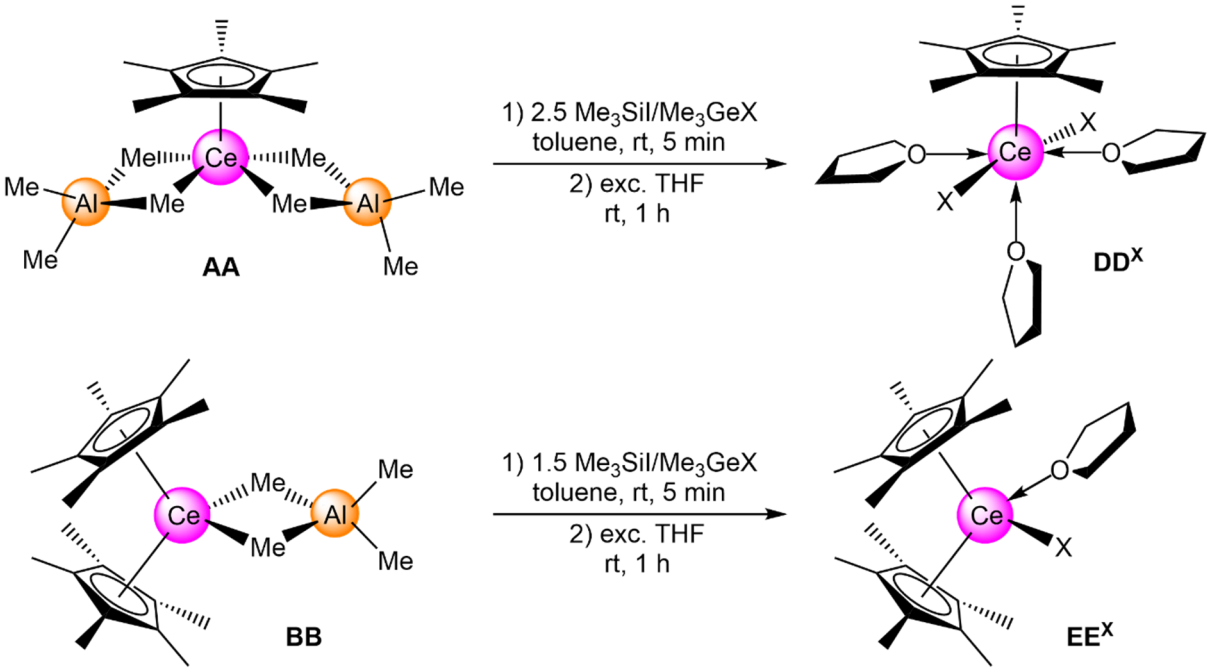

Scheme C1. General synthesis route toward cerium cyclopentadienyl halide complexes **DD^X** and **EE^X** (X = Hal).

Upon addition of excess THF, the formation of the corresponding THF adducts was feasible. As such, the complexes Cp*CeX$_2$(thf)$_3$ (**DD^X**, X = I, Br, Cl) and Cp*$_2$CeX(thf) (**EE^X**, X = I, Br, Cl) were isolated in moderate to excellent yields (29-92%). While **DD^I** was previously reported by BRUNO *et al.*,[72] we were able to isolate the identical compound via a AlMe$_4$/iodide exchange reaction protocol as well.

Other than that, the bromido congener **DD^{Br}** is isostructural to iodide complex **DD^I**, and due to the good solubility in THF, chloride complex **DD^{Cl}** was obtained as a light yellow powder in good yield (76%), while NMR spectroscopic characterization corroborates the formation of the isostructural chloride species Cp*CeCl$_2$(thf)$_3$.

The ^{1}H NMR spectrum of **DD^{Cl}** shows the expected three signals, with resonances assignable to coordinated THF at 3.60 ppm and 1.77 ppm, respectively, as well as a broadened singlet generated by the Cp* methyl groups (3.38 ppm).

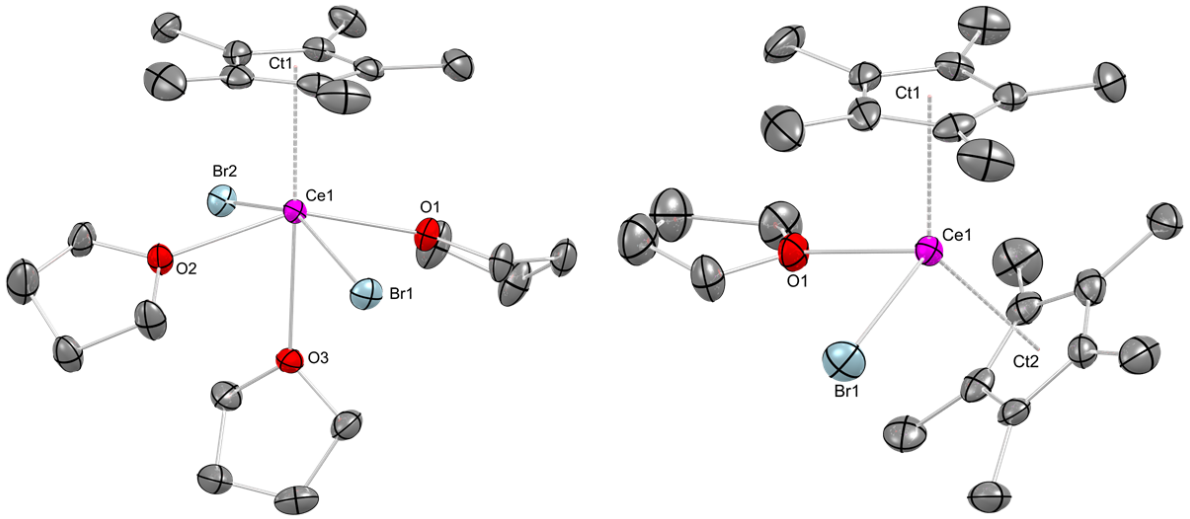

Figure C3. Crystal structures of **DD^{Br}** (left) and **EE^{Br}** (right).

Elemental analysis of **DD^{Cl}** on the other hand proved difficult, due to removal of coordinated THF both under vacuum and by washing the product with *n*-hexane. Upon addition of the halogenido-transfer reagent, the color change was similar for all tested halides I, Br and Cl, going from fluorescent yellow to an even more intense fluorescent light yellow color. In contrast, the toluene solution of sandwich **BB** displayed an intense dark orange fluorescence, which changed marginally upon addition of Me_3SiI, but showed a striking transition to a fluorescent pink color when treated with Me_3GeX (X = Br, Cl), generating **EE^{I}**, **EE^{Br}**, and **EE^{Cl}**, respectively.

Experimental Section

General Considerations. All manipulations were performed under rigorous exclusion of air and moisture, using standard Schlenk and glovebox techniques (MBraun MB200B; <0.1 ppm O_2, <0.1 ppm H_2O, argon atmosphere). The solvents *n*-hexane, toluene and THF were purified using Grubbs-type columns (MBraun SPS, solvent purification system). [D_8]THF (99.5%, Sigma-Aldrich) was dried and stored over molecular sieves prior to filtration. All solvents were stored inside a glovebox. Pentamethylcyclopentadiene (HCp*, 98%) was obtained from abcr and used as received. Potassium pentamethylcyclopentadienide was prepared according to standard procedures by treatment of the proligand with potassium. Iodotrimethylsilane (97%, stabilized with copper), bromotrimethylgermane (98%), and chlorotrimethylgermane (98%) were purchased from abcr and used without further purification. Homoleptic [$Ce(AlMe_4)_3$] was synthesized according to literature procedures.[36] NMR spectra of air and moisture sensitive compounds were recorded using J.Young valve NMR tubes at ambient temperature on a Bruker AVII+400 (^{1}H: 400.11 MHz; ^{13}C: 100.61 MHz) spectrometer. NMR chemical shifts are referenced to internal solvent resonances and reported in parts per million relative to tetramethylsilane. Coupling constants are given in Hertz. Elemental analyses were performed on an Elementar Vario Micro Cube. IR spectra were recorded either on a NICOLET 6700 FTIR spectrometer with a DRIFT cell (KBr window, Kubelka-Munk conversion) or on a Vertex70 IR spectrometer (Nujol, CsI window).

[Cp*Ce($AlMe_4$)$_2$] (AA). Homoleptic [$Ce(AlMe_4)_3$] (200.57 mg, 0.50 mmol) was dissolved in toluene (5 mL) and added to a stirred toluene suspension (10 mL) of KCp* (87.17 mg, 0.50 mmol). After stirring the reaction mixture for 16 h, the solution was centrifuged, the supernatant was filtered, and the solvent was completely removed under vacuum to obtain the crude product as a yellow solid. Single-crystals were obtained by recrystallization from a saturated *n*-hexane/toluene solution at -40 °C (218.1 mg, 0.49 mmol, 97%). ^{1}H NMR (400.1 MHz, [D_6]benzene, 26 °C): δ = 3.83 (s, 15H, C_5*Me*$_5$), -0.61 (bs, 24H, Al*Me*$_4$) ppm. IR(DRIFT): $\tilde{\nu}$ = 2925 (m), 2884 (m), 2790 (w), 2731 (vw), 2142 (vw), 1477 (w), 1458 (w), 1441 (w), 1430 (w), 1390 (w), 1381 (w), 1195 (s), 1120 (vw) 1102 (vw), 1023 (m), 899 (w), 892 (w), 720 (vs), 577 (s), 548 (s), 531 (s), 517 (s), 478 (m) cm^{-1}. Elemental analysis (%) calcd for $C_{18}H_{39}CeAl_2$ (449.59 g/mol) C 48.09, H 8.74; found: C 47.70, H 8.86.

[Cp*$_2$Ce(AlMe$_4$)] (BB). Homoleptic [Ce(AlMe$_4$)$_3$] (200.57 mg, 0.5 mmol) was dissolved in toluene (5 mL) and added to a stirred toluene suspension (10 mL) of KCp* (191.80 mg, 1.10 mmol). After stirring the reaction mixture for 16 h, the solution was centrifuged, the supernatant was filtered, and the solvent was completely removed under vacuum to obtain the crude product as a bright red solid. Single-crystals were obtained by recrystallization from a saturated toluene solution at -40 °C (193.7 mg, 0.39 mmol, 78%). ^{1}H NMR (400.1 MHz, [D$_6$]benzene, 26 °C): δ = 4.17 (bs, C$_5$*Me$_5$*), -1.51 (bs, Al*Me$_4$*) ppm. IR(DRIFT): $\tilde{\nu}$ = 2962 (w), 2913 (s), 2859 (m), 2730 (vw), 2122 (vw), 1487 (w), 1439 (w), 1385 (w), 1178 (m), 1066 (w), 1019 (w), 955 (vs), 799 (m), 773 (m), 737 (s), 676 (s), 619 (s), 566 (s), 542 (vs) cm^{-1}. Elemental analysis (%) calcd for C$_{48}$H$_{84}$Ce$_2$Al$_2$ (995.35 g/mol) C 57.92, H 8.51; found: C 57.81, H 8.14.

[CpCe(AlMe$_4$)$_2$] (CC). Homoleptic [Ce(AlMe$_4$)$_3$] (50.00 mg, 0.125 mmol) was dissolved in toluene (5 mL) and added to a stirred toluene solution (10 mL) of NaCp (12.33 mg, 0.14 mmol). After stirring the reaction mixture for 16 h, the solution was centrifuged, the supernatant was filtered, and the solvent was completely removed under vacuum to obtain the crude product as a yellow solid (32.1 mg, 0.09 mmol, 68%). ^{1}H NMR (400.1 MHz, [D$_6$]benzene, 26 °C): δ = 5.36 (bs, 5H, C$_5$*H$_5$*), 3.63 (bs, 5H, C$_5$*H$_5$*), 1.15 (bs, 24H, Al*Me$_4$*) ppm.

[Cp*CeI$_2$(thf)$_3$] (DD^I). [Cp*Ce(AlMe$_4$)$_2$] (100.00 mg, 0.22 mmol) was dissolved in *n*-hexane (5 mL), and Me$_3$SiI (112.06 mg, 0.56 mmol) was added under vigorous stirring. A color change from intense to light yellow was observed. After stirring the reaction mixture for 30 minutes, 2 mL of THF were added. After stirring the reaction mixture for another 10 minutes, the solvent was removed under vacuum, and the crude product was washed extensively with *n*-hexane to remove residual AlMe$_3$/THF adduct. The crude product was obtained as yellow powder, of which single-crystals were obtained as yellow blocks from a saturated THF solution at -40 °C (47.52 mg, 0.064 mmol, 29%). ^{1}H NMR (400 MHz, [D$_8$]THF, 26 °C): δ = 5.56 (s, 15H, Cp*Me$_5$*), 3.61 (m, coord. C$_4$*H$_8$*O), 1.77 (m, coord. C$_4$*H$_8$*O) ppm. Elemental analysis (%) calcd for C$_{22}$H$_{39}$CeI$_2$O$_3$ (745.48 g/mol) C 35.45, H 5.27; found: C 28.23, H 3.58. The deviation between theoretical and experimental values can be attributed to removal of coordinated THF under vacuum and by washing the product with *n*-hexane. The loss of two THF molecules per cerium would afford calcd C 27.97, H 3.86.

[Cp*CeBr$_2$(thf)$_3$] (DD^{Br}). [Cp*Ce(AlMe$_4$)$_2$] (100.00 mg, 0.22 mmol) was dissolved in *n*-hexane (5 mL), and Me$_3$GeBr (110.68 mg, 0.56 mmol) was added under vigorous stirring. A color change from intense to pale yellow was observed. After stirring the reaction mixture for 30 minutes, 2 mL of THF were added. After stirring the reaction mixture for another 10 minutes, the solvent was removed under vacuum, and the crude product was washed extensively with *n*-hexane to remove residual AlMe$_3$/THF adduct. The product was obtained as a light yellow powder, of which single-crystals were obtained as yellow blocks from a saturated THF solution at -40 °C (146.52 mg, 0.2 mmol, 92%). $C_{22}H_{39}CeBr_2O_3$ (651.48 g/mol) C 40.56, H 6.03; found: C 27.26, H 4.35. The deviation between theoretical and experimental values can be attributed to removal of coordinated THF under vacuum and by washing the product with *n*-hexane. The loss of three THF molecules per cerium would afford calcd C 27.60, H 3.47. Although these results are then outside the range viewed as establishing analytical purity (H: + 0.88), they are provided to illustrate the best values obtained to date.

[Cp*CeCl$_2$(thf)$_3$] (DD^{Cl}). [Cp*Ce(AlMe$_4$)$_2$] (100.00 mg, 0.22 mmol) was dissolved in *n*-hexane (5 mL), and Me$_3$GeCl (85.20 mg, 0.56 mmol) was added under vigorous stirring. A color change from intense to pale yellow was observed. After stirring the reaction mixture for 30 minutes, 2 mL of THF were added. After stirring the reaction mixture for another 10 minutes, the solvent was removed under vacuum, and the crude product was washed extensively with *n*-hexane to remove residual AlMe$_3$/THF adduct. The product was obtained as a light yellow powder (94.50 mg, 76%). ^{1}H NMR (400.1 MHz, [D$_8$]THF, 26 °C): δ = 3.60 (m, coord. THF), 3.38 (bs, 15H, C$_5$*Me$_5$*), 1.77 (m, coord. THF) ppm. IR: $\tilde{\nu}$ = 2954 (Cp, Nujol), 2924 (Cp, Nujol), 2853 (Cp, Nujol), 2725 (w), 2669 (w), 2168 (vw), 1712 (vw), 1626 (vw), 1461 (Nujol), 1377 (Nujol), 1297 (w), 1243 (w), 1194 (w), 1069 (w), 1018 (vs), 913 (w), 865 (vs), 722 (vs), 692 (s), 671 (m), 580 (vw) cm^{-1}. Elemental analysis (%) calcd for $C_{22}H_{39}CeCl_2O_3$ (562.57 g/mol) C 46.97, H 6.99; found: C 40.91, H 5.98. The deviation between theoretical and experimental values can be attributed to removal of coordinated THF under vacuum and by washing the product with *n*-hexane. The loss of two THF molecules per cerium would afford calcd C 40.19, H 5.54.

[Cp*$_2$CeI(thf)] (EE^{I}). [Cp*$_2$Ce(AlMe$_4$)] (100.00 mg, 0.22 mmol) was dissolved in toluene (5 mL), and Me$_3$SiI (55.00 mg, 0.28 mmol) was added under vigorous stirring. A color change from bright to light orange was observed. After stirring the reaction mixture for 30 minutes, 2

mL of THF were added, leading to color change into dark yellow. After stirring the reaction mixture for another 10 minutes, the solvent was removed under vacuum, and the crude product was washed extensively with *n*-hexane to remove residual $AlMe_3$/THF adduct. The crude product was obtained as a yellow powder, of which single-crystals were obtained as orange columns from a saturated THF solution at -40 °C (90.20 mg, 0.15 mmol, 67%). Elemental analysis (%) calcd for $C_{24}H_{38}CeIO$ (745.48 g/mol) C 47.29, H 6.28; found: C 44.88, H 5.15. The deviation between theoretical and experimental values can be attributed to removal of coordinated THF under vacuum and by washing the product with *n*-hexane. The loss of one THF molecule per cerium would afford calcd C 44.69, H 5.63.

[Cp*$_2$CeBr(thf)] (EE^{Br}). [Cp*$_2$Ce(AlMe$_4$)] (100.00 mg, 0.22 mmol) was dissolved in toluene (5 mL), and Me_3GeBr (54.35 mg, 0.28 mmol) was added under vigorous stirring. A color change from bright orange to bright pink was observed. After stirring the reaction mixture for 30 minutes, 2 mL of THF were added, leading to color change into yellow. After stirring the reaction mixture for another 10 minutes, the solvent was removed under vacuum, and the crude product was washed extensively with *n*-hexane to remove residual $AlMe_3$/THF adduct. The crude product was obtained as a yellow powder, of which single-crystals were obtained as light orange needles from a saturated THF solution at -40 °C. Further characterization was hampered by the formation of a product mixture.

[Cp*$_2$CeCl(thf)] (EE^{Cl}). Cp*$_2$Ce(AlMe$_4$) (100.00 mg, 0.22 mmol) was dissolved in toluene (5 mL), and Me_3GeCl (42.89 mg, 0.28 mmol) was added under vigorous stirring. A color change from bright orange to bright pink was observed. After stirring the reaction mixture for 30 minutes, 2 mL of THF were added, leading to color change into dark yellow. After stirring the reaction mixture for another 10 minutes, the solvent was removed under vacuum, and the crude product was washed extensively with *n*-hexane to remove residual $AlMe_3$/THF adduct. The crude product was obtained as a yellow powder, of which single-crystals were obtained as yellow needles from a saturated THF solution at -40 °C (63.25 mg, 0.12 mmol, 55%).

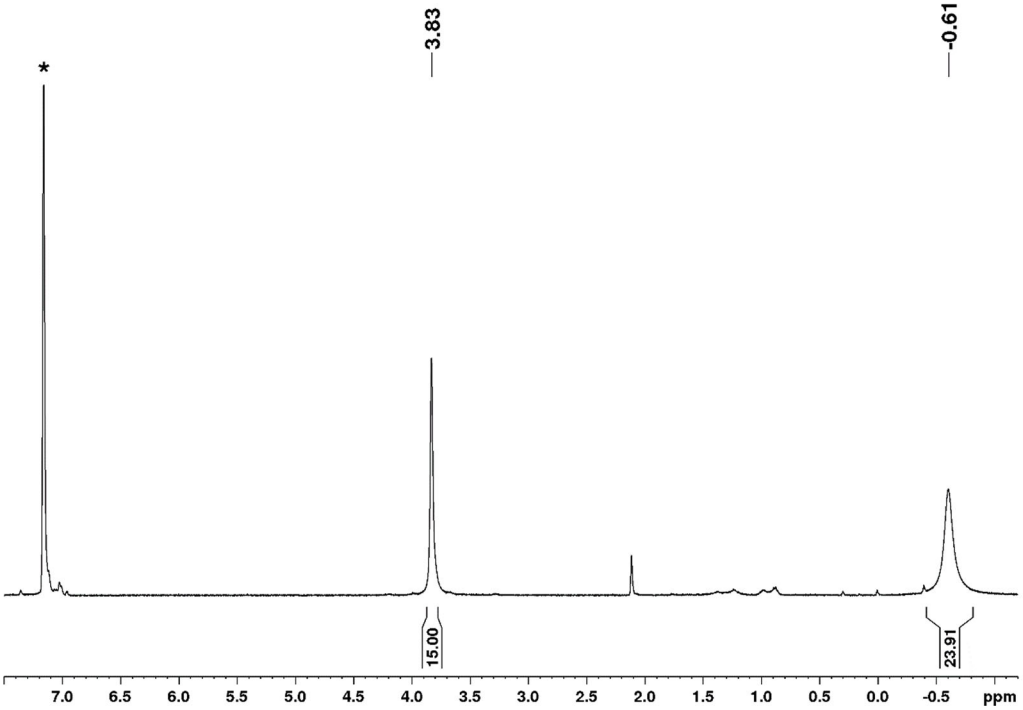

Figure C4. ^{1}H NMR spectrum (400 MHz) of [Cp*Ce(AlMe$_4$)$_2$] (**AA**) in [D$_6$]benzene at 26 °C. The solvent residual signal is marked with an asterisk.

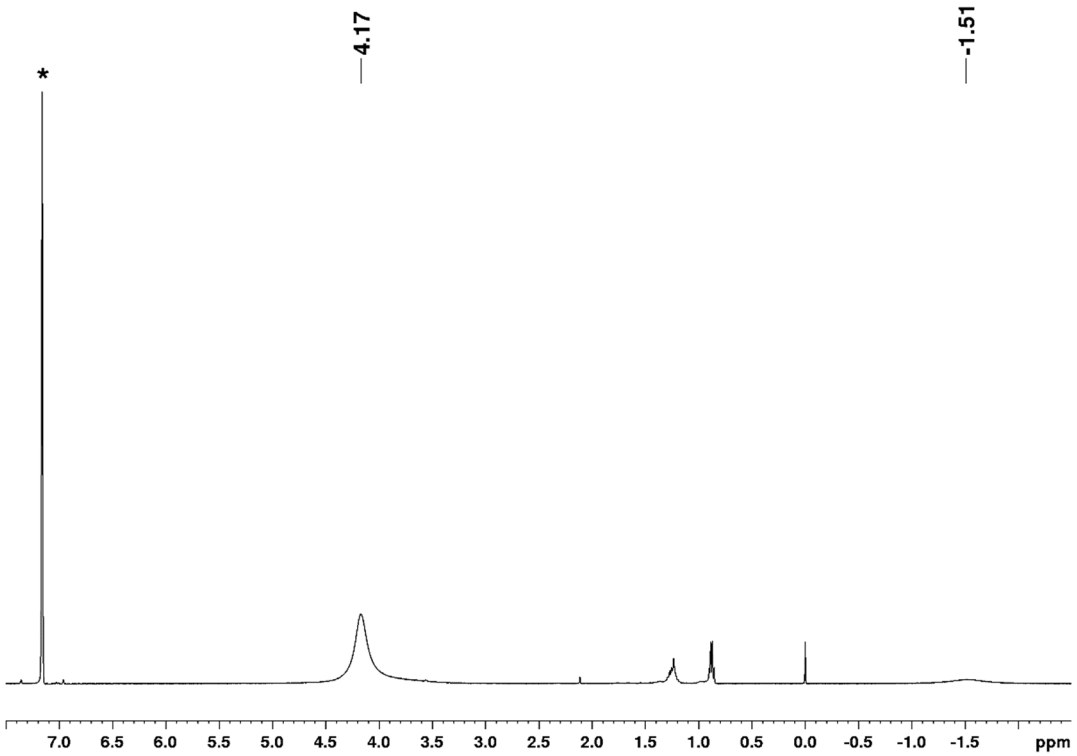

Figure C5. ^{1}H NMR spectrum (400 MHz) of [Cp*$_2$Ce(AlMe$_4$)] (**BB**) in [D$_6$]benzene at 26 °C. The solvent residual signal is marked with an asterisk.

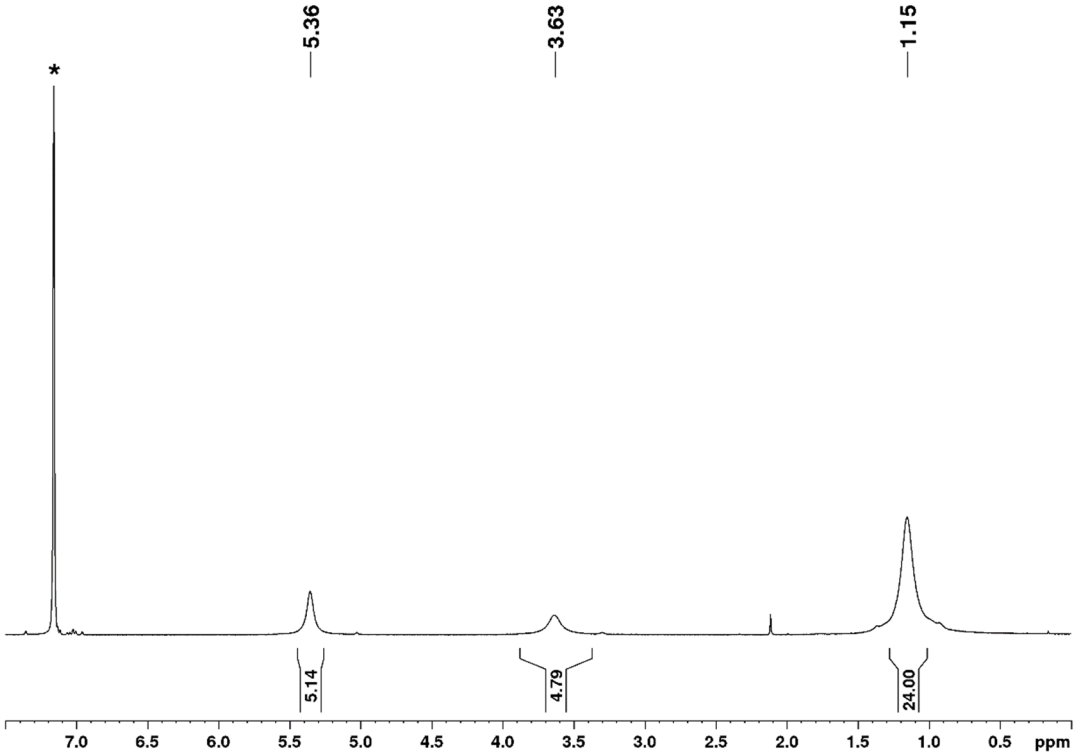

Figure C6. ^{1}H NMR spectrum (400 MHz) of [CpCe(AlMe$_4$)$_2$] (**CC**) in [D$_6$]benzene at 26 °C. The solvent residual signal is marked with an asterisk.

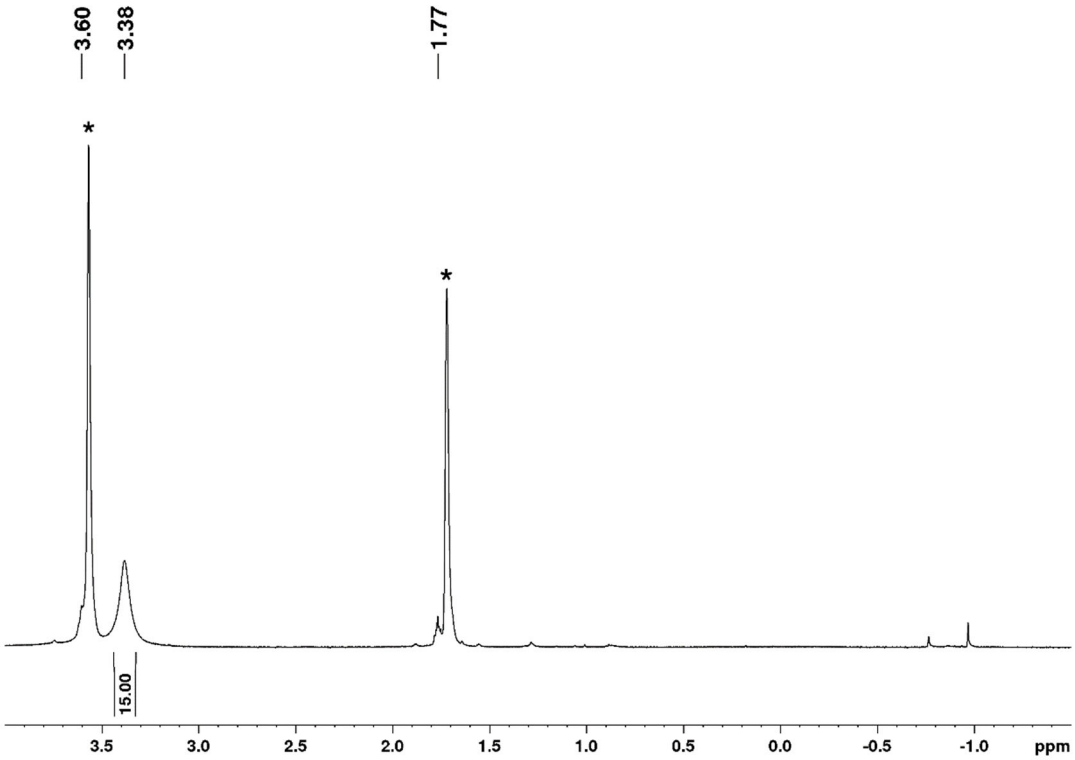

Figure C7. ^{1}H NMR spectrum (400 MHz) of [Cp*CeCl$_2$(thf)$_3$] (**DD^{Cl}**) in [D$_8$]THF at 26 °C. The solvent residual signal is marked with an asterisk.

Table C1. Crystallographic data for compounds **AA**, **BB**, and **DD^{I}**

	AA	**BB**	**DD^{I}**
formula	$C_{18}H_{39}CeAl_2$	$C_{48}H_{84}Ce_2Al_2$	$C_{26}H_{47}CeI_2O_4$
M_r [g/mol]	449.57	995.35	817.55
color/shape	yellow/plate	red/block	yellow/block
crystal dimensions [mm]	0.173 x 0.138 x 0.036	0.090 x 0.058 x 0.034	0.085 x 0.083 x 0.065
crystal system	orthorhombic	monoclinic	trigonal
space group	*Pbca*	*C*2/*m*	$R\bar{3}$
a [Å]	17.0906(7)	17.198(6)	41.996(3)
b [Å]	14.5729(6)	17.325(6)	41.996(3)
c [Å]	17.9317(8)	10.409(4)	9.1258(7)
α [°]	90	90	90
β [°]	90	124.847(3)	90
γ [°]	90	90	120
V [Å^3]	4466.1(3)	2545.2(15)	13938(2)
Z	8	2	18
T [K]	100(2)	100(2)	100(2)
λ [Å]	0.71073	0.71073	0.71073
ρ_{calcd} [g/cm^3]	1.337	1.299	1.753
μ [mm^{-1}]	2.112	1.828	3.489
F (000)	1848	1028	7182
θ range [°]	2.159 – 30.608	2.351 – 23.286	1.680 – 23.265
independent reflections	6863	1786	4432
reflections collected	69527	3222	26246
R1/*w*R2 (I > 2σ)	0.0231/0.0519	0.0429/0.0873	0.0403/0.0899
R1/*w*R2 (all data)	0.0308/0.0564	0.0591/0.0949	0.0564/0.0994
GOF	1.039	1.025	1.027

Table C1. Crystallographic data for compounds **DD^{Br}**, **EE^{I}**, and **EE^{Br}**

	DD^{Br}	**EE^{I}**	**EE^{Br}**
formula	$C_{26}H_{47}CeBr_2O_4$	$C_{24}H_{38}CeIO$	$C_{24}H_{38}CeBrO$
M_r [g/mol]	723.57	609.56	562.57
color/shape	yellow/block	orange/column	orange/needle
crystal dimensions [mm]	0.160 x 0.141 x 0.103	0.228 x 0.154 x 0.142	0.150 x 0.074 x 0.030
crystal system	monoclinic	triclinic	triclinic
space group	$P2_1/c$	$P\bar{1}$	$P\bar{1}$
a [Å]	12.4338(9)	8.7095(5)	8.5794(14)
b [Å]	11.9174(8)	17.4248(11)	17.298(3)
c [Å]	20.5223(14)	18.4250(11)	18.508(3)
α [°]	90	62.1970(10)	62.235(3)
β [°]	104.5600(10)	87.061(2)	88.487(4)
γ [°]	90	84.275(2)	86.168(4)
V [Å³]	2943.3(4)	2461.0(3)	2425.0(7)
Z	4	4	4
T [K]	100(2)	100(2)	100(2)
λ [Å]	0.71073	0.71073	0.71073
ρ_{calcd} [g/cm³]	1.633	1.645	1.541
μ [mm^{-1}]	4.289	3.115	3.535
F (000)	1452	1204	1132
θ range [°]	1.692 – 26.392	1.249 – 30.552	1.680 – 23.265
independent reflections	6025	14958	10039
reflections collected	37379	84942	50612
R1/*w*R2 (I > 2σ)	0.0263/0.0604	0.0234/0.0531	0.0453/0.0996
R1/*w*R2 (all data)	0.0386/0.0654	0.0255/0.0540	0.0701/0.1127
GOF	1.033	1.111	1.027

Table C1 (continued). Crystallographic data for compound **EE^{Cl}**

	EE^{Cl}
formula	$C_{24}H_{38}CeClO$
M_r [g/mol]	518.11
color/shape	yellow/block
crystal dimensions [mm]	0.120 x 0.080 x 0.052
crystal system	triclinic
space group	$P\bar{1}$
a [Å]	8.4870(5)
b [Å]	17.0107(10)
c [Å]	184765(11)
α [°]	62.617(2)
β [°]	89.586(2)
γ [°]	87.168(2)
V [Å³]	2365.3(2)
Z	4
T [K]	100(2)
λ [Å]	0.71073
ρ_{calcd} [g/cm³]	1.455
μ [mm^{-1}]	2.048
F (000)	1060
θ range [°]	1.241 – 26.421
independent reflections	9719
reflections collected	54558
R1/*w*R2 (I > 2σ)	0.0343/0.0707
R1/*w*R2 (all data)	0.0521/0.0779
GOF	1.015

6 Donor-Induced Formation of Separated Ion Pairs and Rare-Earth-Metal Redox Chemistry

Introduction

The equimolar reaction of $Cp^*_2Ce(AlMe_4)$ (**BB^{Ce}**) with Me_3GeBr unexpectedly led to the concomitant formation of $Cp^*_2CeBr(thf)$ (**EE^{Br}**) and the separated ion pair complex $[Cp^*_2CeBr_2]^-[(thf)_2AlMe_2]^+$ (**FF^{Ce}**). While separated ion pairs consisting of anionic sandwich-type rare-earth-metal halide compounds are not entirely new,[107, 208-212] we targeted the controlled synthesis by various donor ligands. The obtained anionic species are then prone to oxidation reactions.

Results and Discussion

Complex **FF^{Ce}** was selectively obtained by treatment of **BB^{Ce}** with excess (≥ 3 equiv.) Me_3GeBr and subsequent addition of excess THF (see Scheme C2), corroborating the particular stability of the separated ion pair. The ^{1}H NMR spectrum of **FF^{Ce}** in [D$_8$]THF shows four signals that can be attributed to the complex. The Cp* methyl groups resonate at 4.73 ppm, and the methyl groups of cationic $[(thf)_2AlMe_2]^+$ at -0.67 ppm, respectively. Coordinated THF shows signals at 3.60 ppm and 1.77 ppm. Furthermore, the ^{27}Al NMR resonance was referenced against precursor complexes $Ce(AlMe_4)_3$ as well as sandwich **BB^{Ce}**. The aluminum metal center of **FF^{Ce}** resonates at 163 ppm in the ^{27}Al NMR spectrum (Figure C8), the other signal is caused by the NMR tube (aluminum silicate).

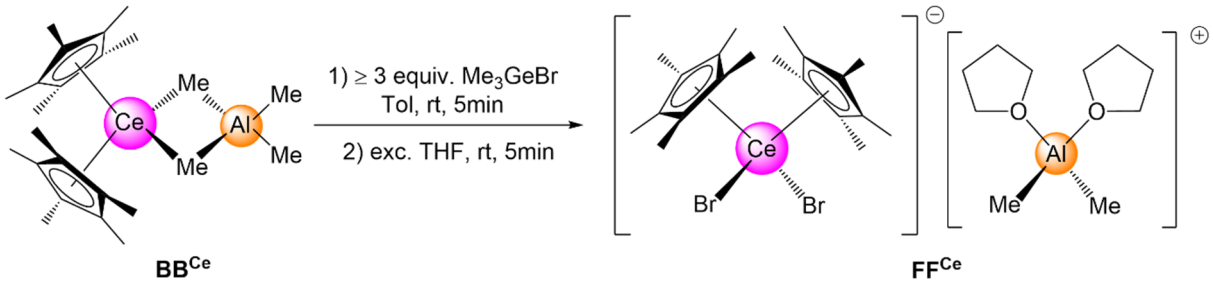

Scheme C2. Synthesis of separated ion pair **FF^{Ce}**.

In comparison to the homoleptic cerium aluminate, the aluminum signal is shifted significantly toward higher field, whereas the resonance of **FF^{Ce}** is located between the two aluminum signals of **BB^{Ce}** (194 ppm and 154 ppm, see Figure C8). Single-crystals were obtained by

dropwise addition of THF to the crude product until crystallization occurred (cryst. yield: 78%), and single-crystal XRD analysis revealed the molecular structure of **FF^{Ce}** (Figure C10), consisting of anionic $[Cp^*_2CeBr_2]^-$ and the cationic counterion $[(thf)_2AlMe_2]^+$. Surprisingly, the formation of a separated ion pair was only observed when excess Me_3GeBr was added and did not occur in the analogous halogenation reactions with Me_3SiI or Me_3GeCl.

Attempts to oxidize **FF^{Ce}** to form putative $[Cp^*_2CeBr_2]$ were taken with $TeBr_4$ to avoid possible ligand scrambling and simultaneously stabilize the bromido ligands. As such, the equimolar addition of $TeBr_4$ resulted in immediate decolorization of the previously intense yellow solution and simultaneous precipitation of Te^0. After stirring the reaction mixture for 1 h, elemental Te was filtered off, leaving a pale yellow solution, indicating incomplete oxidation of the cerium species. Addition of another equivalent of $TeBr_4$ under stirring led to further darkening of the reaction mixture, turning into a dark purple color over night. Excess Te^0 was filtered off again, affording a dark purple solution. The solvent was removed completely under vacuum to afford a purple solid.

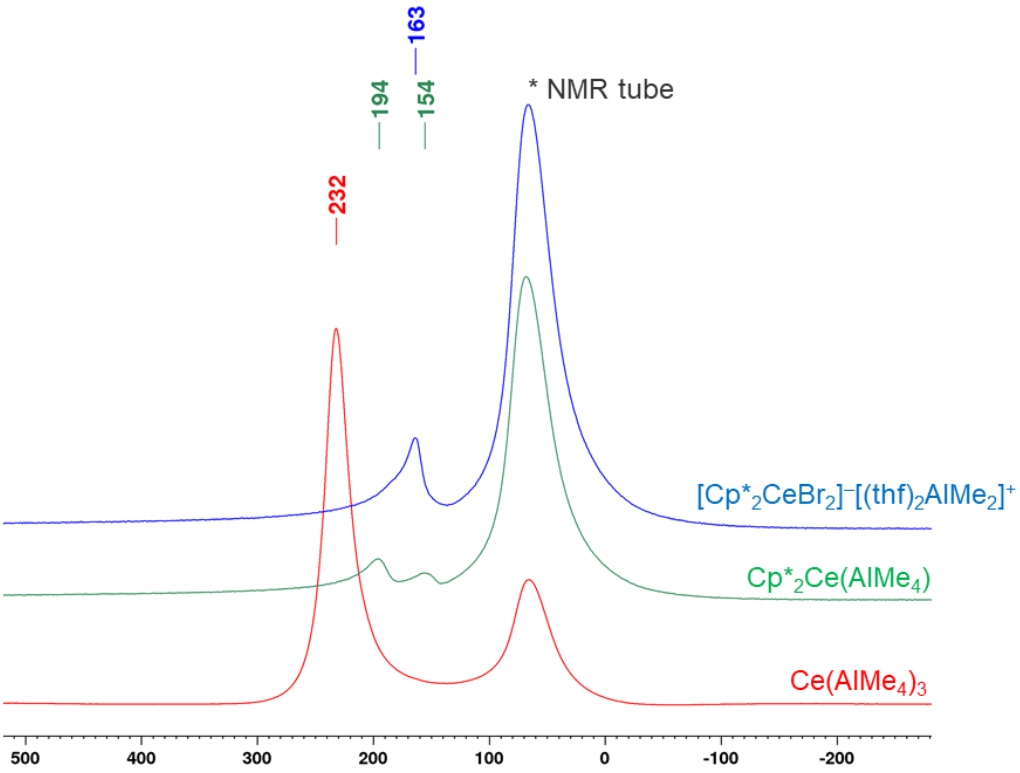

Figure C8. Stacked ^{27}Al NMR spectra (130 MHz, 26 °C) of homoleptic $Ce(AlMe_4)_3$ ([D8]toluene), **BB** ([D8]toluene) and **FF^{Ce}** ([D8]THF).

The relatively sharp ^1H NMR resonances at 3.71 ppm and 3.04 ppm, respectively, indicate a complete oxidation to a diamagnetic Ce(IV) species, and show an integral ratio of 2:1 (Figure

C9). Removal of the solvent under vacuum simultaneously afforded colorless crystals, which were analyzed via single-crystal X-ray diffraction, revealing the formation of the trivalent salt $CeBr_3(thf)_4$.[213] Apparently, coordination of THF led to reduction and formation of the presumably more stable trivalent cerium bromide.

Since oxidation toward a tetravelent species at least in solution seemed feasible, oxidation of the respective praseodymium and neodymium complexes $\mathbf{FF^{Ln}}$ (Ln = Pr, Nd) was attempted. Complexes $\mathbf{FF^{Ln}}$ were obtained by the analogous synthesis route as $\mathbf{FF^{Ce}}$ from the sandwich complexes $Cp^*_2Ln(AlMe_4)$ ($\mathbf{BB^{Ln}}$, Ln = Pr, Nd) in excellent crystalline yields ($\mathbf{FF^{Pr}}$: 90%, $\mathbf{FF^{Nd}}$: 94%). Following the procedure for $\mathbf{FF^{Ce}}$, treatment of $\mathbf{FF^{Pr}}$ gave a dark green solution, whereas for $\mathbf{FF^{Nd}}$ a dark blue solution was obtained. Again, concentrating the respective solutions led to the formation of colorless crystals (putative $LnBr_3(thf)_4$), proving THF as detrimental for the stabilization of any tetravalent species.

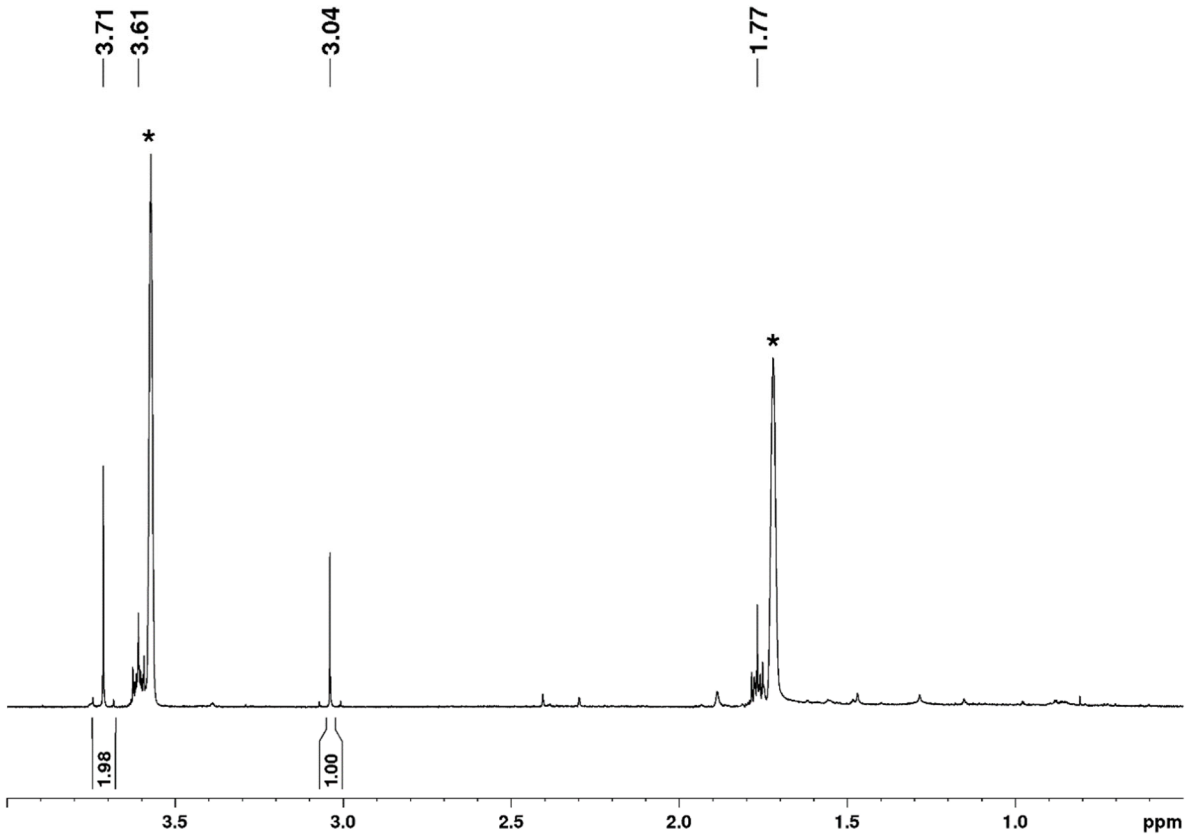

Figure C9. ^{1}H NMR spectrum (400 MHz, 26 °C, $[D_8]$THF) of the purple solid obtained via oxidation of $\mathbf{FF^{Ce}}$ with $TeBr_4$.

As a reduced donor strength was expected for tetrahydrothiophene (THT) in comparison to THF, the synthesis of possible precursor complex $[Cp^*_2LnBr_2]^-[(tht)_2AlMe_2]^+$ (Ln = Ce, Pr,

Nd) was targeted. While the respective reactions showed similar color transitions as the THF reaction, isolation of the corresponding THT species was unsuccessful. Nevertheless, oxidation with $TeBr_4$ was attempted following similar procedures. Surprisingly, the oxidation reactions resulted in a deep red solution, regardless of the metal center, though any isolation of a reaction product was not possible.

Similarly, precursor synthesis with tetrahydropyrane (THP) as donor led to the formation of the respective separated ion pairs $[Cp^*_2LnBr_2]^-[(thp)_2AlMe_2]^+$ (**GG^{Ln}**, Ln = Ce, Nd), again in excellent crystalline yield (**GG^{Ce}**: 93%, **GGNd**: 96%) (Figure C10). In contrast, the reaction with precursor **FF^{Pr}** did not afford the isostructural separated ion pair, but potassium ate-complex $[Cp^*_2PrBr_2K(thp)_4]$ (**HH**), revealing potassium impurities in sandwich **FF^{Pr}** from treatment with KCp*. Hence, the similar formation of $[Cp^*_2PrBr_2]^-[(thp)_2AlMe_2]^+$ is expected after purification of **FF^{Pr}**.

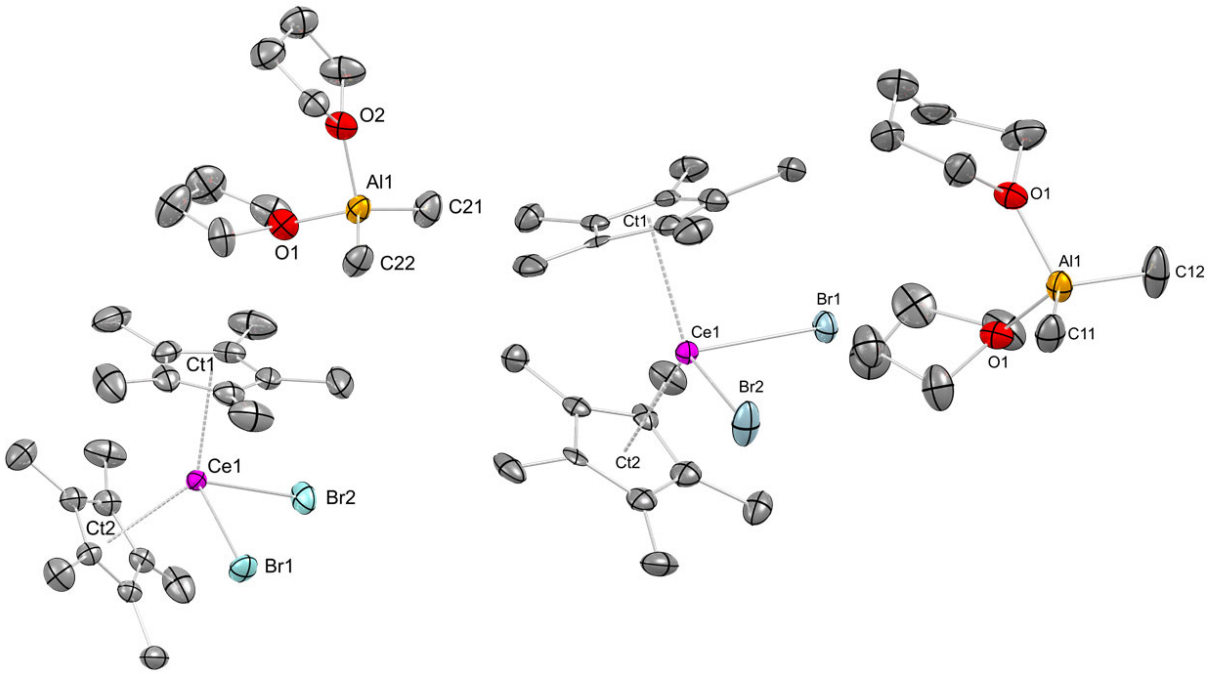

Figure C10. Crystal structures of **FF^{Ce}** (left) and **GG^{Ce}** (right).

The oxidation of complexes **GG^{Ln}** with $TeBr_4$ resulted both in identical color transitions into purple (**GG^{Ce}**) and dark blue (**GGNd**) solutions, and crystallization of the presumable THP salt $LnBr_3(thp)_4$ (Ln = Ce, Nd), disqualifying THP for further reaction studies as well.

Lastly, the synthesis was performed with diethyl ether as a donor due to the expected weak donor strength. While all complexes presumably form the respective separated ion pairs $[Cp^*_2LnBr_2]^-[(Et_2O)_2AlMe_2]^+$ (**II^{Ln}**, Ln = Ce, Pr, Nd) according to identical color change as

FF^{Ln}, isolation was not possible due to likely removal of Et_2O under vacuum (color change back from yellow to pink for **II^{Ce}**). Therefore, all following synthesis steps have been performed *in situ* until a stable product was obtained. Stepwise oxidation with $TeBr_4$ resulted in dark colored solutions similar as in the procedure with THF, hence complete oxidation to the stable tetravalent species [Cp*$_2$LnBr$_2$] was assumed.

As cerium alkoxides have shown better stabilization of tetravalent cerium complexes, *in situ* synthesized sandwich complexes **II^{Ln}** were treated with excess NaO*t*Bu,[214] aiming at substitution of the bromido ligands. Upon addition of NaO*t*Bu to **II^{Ln}**, all reaction mixtures showed a similar color change to an orange solution. As the ^{1}H NMR spectrum in [D$_6$]benzene

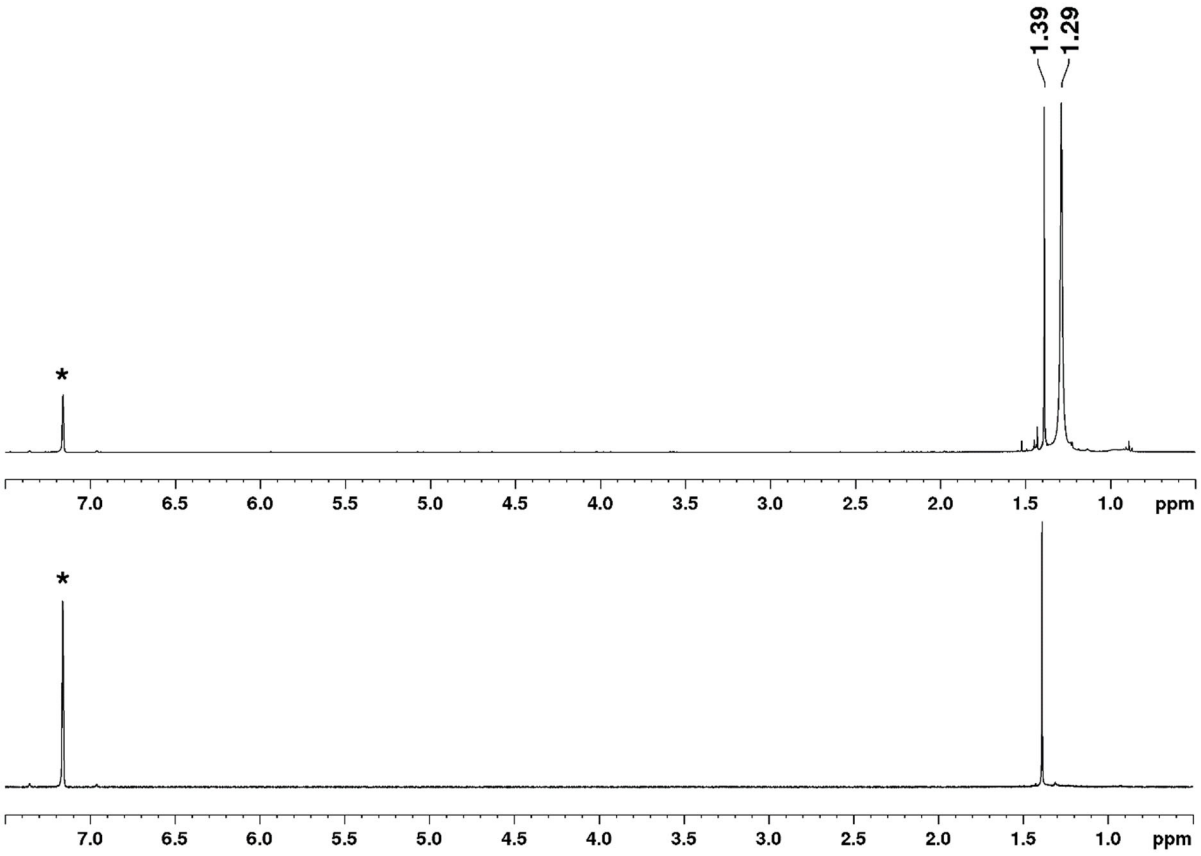

Figure C11. ^{1}H NMR spectrum (400 MHz, [D$_6$]benzene, 26 °C) of [Cp*$_2$CeBr$_2$]$^-$ [(Et$_2$O)$_2$AlMe$_2$]$^+$ (**II^{Ce}**) after the addition of NaO*t*Bu (top) and after the addition of an additional stoichiometric ammount of $TeBr_4$ (bottom).

(Figure C11) for the cerium reaction indicated both tri- and tetravalent species of the homoleptic alkoxide complexes, another equivalent of $TeBr_4$ was added, inducing the disappearance of the broad signal of the paramagnetic species, thus likely affording a tetravalent species exclusively.

Recrystallization from a saturated toluene solution gave access to the unprecedented molecular clathrate cluster [(O*t*Bu)$_{12}$Te/CeNa$_{14}$O$_3$] (**JJ^{Ce}**). Cluster **JJ^{Ce}** consists of a Na$_{14}$ octadecahedron as well as a O$_{12}$ icosahedron of the *tert*-butoxy ligands. Additionally, three faces of this icosahedron are capped by oxy ligands. The non-coordinated tetravalent metal ion is located in the center of **JJ^{Ce}**, although further analysis needs to performed to elucidate the type of element. The isostructural neodymium cluster **JJNd** was obtained by following the identical reaction procedure using the sandwich complex Cp*$_2$Nd(AlMe$_4$) as precursor. Similarly, further analysis to determine the element type of the central metal ion is necessary.

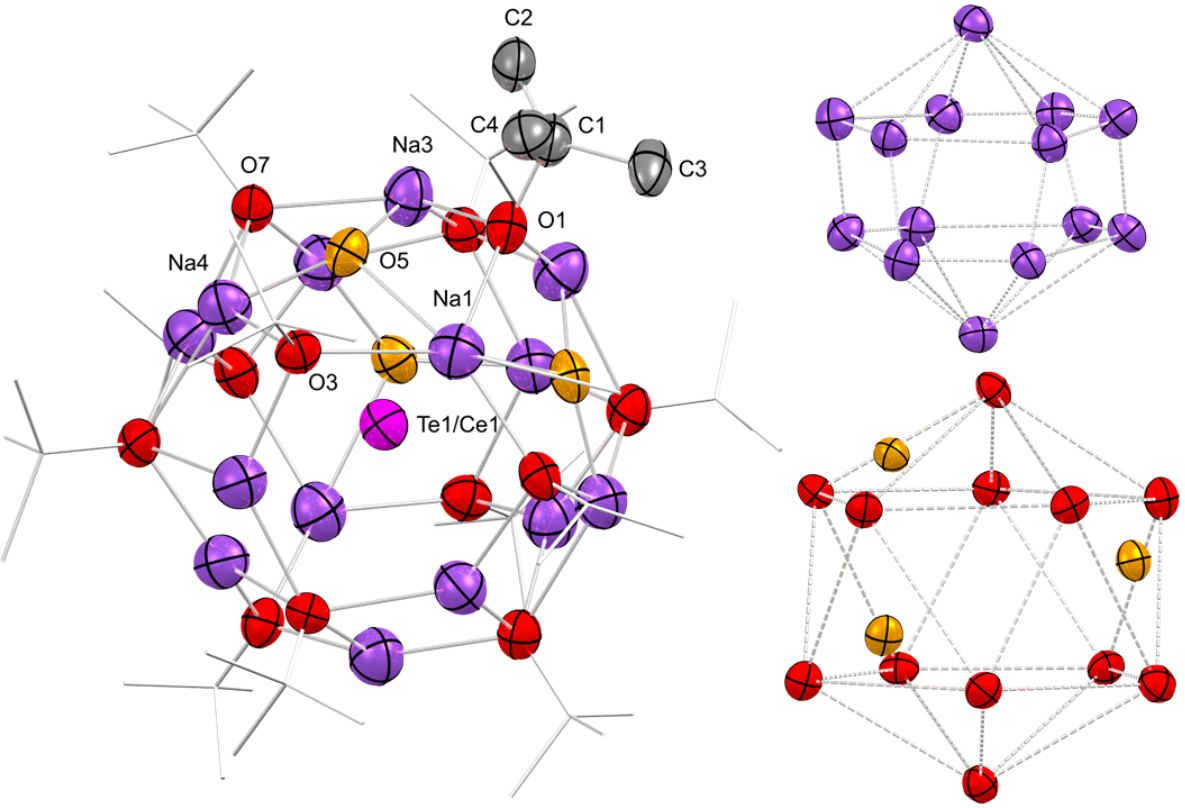

Figure C12. Connectivity of **JJ^{Ce}** (left) with cluster substructures Na$_{14}$ octadecahedron (top right) and O$_{12}$ icosahedron (red, bottom right). Face-capping oxide ligands are colored in orange for improved visualization. Hydrogen atoms are omitted for clarity. *t*Bu groups (except for one) are represented by a wireframe model for improved visualization.

Experimental Section

General Considerations. All manipulations were performed under rigorous exclusion of air and moisture, using standard Schlenk and glovebox techniques (MBraun MB200B; <0.1 ppm O_2, <0.1 ppm H_2O, argon atmosphere). The solvents *n*-hexane, toluene, THF, and diethyl ether were purified using Grubbs-type columns (MBraun SPS, solvent purification system). [D_6]benzene (99.6%, Sigma-Aldrich) and [D_8]toluene (99.6%, Sigma-Aldrich) were dried over Na/K-alloy for at least 24 h prior to filtration. [D_8]THF (99.5%, Sigma-Aldrich) was dried and stored over molecular sieves, prior to filtration. All solvents were stored inside a glovebox. Pentamethylcyclopentadiene (HCp*, 98%) was obtained from abcr and used as received. Potassium pentamethylcyclopentadienide and sodium *tert*-butoxide were prepared according to standard procedures by treatment of the proligand with the respective alkali metal. Tetrahydropyran (THP) and tetrahydrothiophene (THP) were obtained from abcr, degassed, and stored inside a glovebox. Bromotrimethylgermane was purchased from abcr and used without further purification. Tellurium bromide ($TeBr_4$) was purchased from Alfa Aesar and used as recieved. Homoleptic [$Ln(AlMe_4)_3$] (Ln = Ce, Pr, Nd) was synthesized according to literature procedures.[33, 35, 36] NMR spectra of air and moisture sensitive compounds were recorded using J.Young valve NMR tubes at ambient temperature on a Bruker AVII+400 (^{1}H: 400.11 MHz; ^{13}C: 100.61 MHz) or a Bruker AVII+500 (^{1}H: 500.13 MHz, ^{27}Al: 130.32 MHz) spectrometer. NMR chemical shifts are referenced to internal solvent resonances and reported in parts per million relative to tetramethylsilane or aluminum nitrate. Coupling constants are given in Hertz. Elemental analyses were performed on an Elementar Vario Micro Cube. IR spectra were recorded on a Vertex70 IR spectrometer (Nujol, CsI window).

General procedure for the synthesis of [$Cp^*_2Ln(AlMe_4)$] (BB^{Ln}, Ln = Pr, Nd). A toluene solution (3 mL) of homoleptic $Ln(AlMe_4)_3$ was added to a stirred suspension of KCp* (2.2 equiv.) in toluene (3 mL). The reaction mixture was stirred for 18 h at ambient temperature, subsequently centrifuged, filtered, and the solvent was completely removed under vacuum to obtain the crude product.

[$Cp^*_2Pr(AlMe_4)$] (BB^{Pr}). Following the above mentioned procedure, $Pr(AlMe_4)_3$ (200 mg, 0.5 mmol) and KCp* (191.76 mg, 1.1 mmol) afforded BB^{Pr} as light green powder (224.1 mg, 0.45 mmol, 90%). Single-crystals were obtained as light yellow blocks from a saturated *n*-hexane solution at -40 °C. The ^{1}H NMR spectrum of the non-crystalline residue was inconclusive.

[Cp*$_2$Nd(AlMe$_4$)] (BBNd). Following the above mentioned procedure, Nd(AlMe$_4$)$_3$ (101.4 mg, 0.25 mmol) and KCp* (95.88 mg, 0.55 mmol) afforded **BBNd** as blue powder (111.9 mg, 0.22 mmol, 89%). The ^{1}H NMR spectrum of the non-crystalline residue was inconclusive.

General procedure for the synthesis of [Cp*$_2$LnBr$_2$]$^-$[(do)$_2$AlMe$_2$]$^+$ (Ln = Ce, Pr, Nd; do = THF, THP, Et$_2$O). A solution of Me$_3$GeBr (3 equiv.) in toluene (1 mL) was added to a toluene solution (3 mL) of Cp*$_2$Ln(AlMe$_4$) under vigorous stirring. After 5 min, a stoichiometric amount (2 equiv.) of donor compound was added, and the reaction mixture was stirred for another 30 min. Unless otherwise stated, crystals suitable for single-crystal XRD analysis were grown by complete removal of the solvent under vacuum and subsequent, dropwise addition of the respective donor compound.

[Cp*$_2$CeBr$_2$]$^-$[(thf)$_2$AlMe$_2$]$^+$ (FF^{Ce}). Following the procedure described above, Cp*$_2$Ce(AlMe$_4$) (19.90 mg, 0.04 mmol) and Me$_3$GeBr (23.70 mg, 0.12 mmol) afforded **FF^{Ce}** as yellow crystals (24.1 mg, 0.031 mmol, 78%). ^{1}H NMR (400.11 MHz, [D$_8$]THF, 26 °C): δ = 4.73 (bs, 30H, C$_5$*Me$_5$*), 3.60 (m, coord. THF), 1.77 (m, coord. THF), -0.67 (s, 6H, Al*Me$_2$*) ppm. ^{27}Al (130.32 MHz, [D$_8$]THF, 26 °C): δ = 163 ppm.

[Cp*$_2$PrBr$_2$]$^-$[(thf)$_2$AlMe$_2$]$^+$ (FF^{Pr}). Following the procedure described above, Cp*$_2$Pr(AlMe$_4$) (20.10 mg, 0.04 mmol) and Me$_3$GeBr (23.7 mg, 0.12 mmol) afforded **FF^{Pr}** as light yellow crystals (27.9 mg, 0.036 mmol, 90%). The ^{1}H NMR spectrum of the non-crystalline residue was inconclusive.

[Cp*$_2$NdBr$_2$]$^-$[(thf)$_2$AlMe$_2$]$^+$ (FFNd). Following the procedure described above, Cp*$_2$Nd(AlMe$_4$) (20.2 mg, 0.04 mmol) and Me$_3$GeBr (23.7 mg, 0.12 mmol) afforded **FFNd** as light blue crystals (29. mg, 0.037 mmol, 94%). The ^{1}H NMR spectrum of the non-crystalline residue was inconclusive.

[Cp*$_2$CeBr$_2$]$^-$[(thp)$_2$AlMe$_2$]$^+$ (GG^{Ce}). Following the procedure described above, Cp*$_2$Ce(AlMe$_4$) (35.0 mg, 0.07 mmol) and Me$_3$GeBr (41.7 mg, 0.21 mmol) afforded **GG^{Ce}** as yellow crystals (52.4 mg, 0.066 mmol, 93%). The ^{1}H NMR spectrum was inconclusive. IR (Nujol, CsI-window): $\tilde{\nu}$ = 2949 (Cp, Nujol), 2922 (Cp, Nujol), 2854 (Cp, Nujol), 2724 (vw), 2668 (vw), 2615 (vw), 2122 (vw), 1459 (Nujol), 1377 (Nujol), 1311 (w), 1277 (vw), 1262 (vw), 1196 (m), 1157 (vw), 1073 (vw), 1011 (s), 959 (m), 887 (vw), 860 (m), 802 (m), 721 (vs), 693 (vs), 578 (w), 469 (vw) cm^{-1}.

$[Cp^*_2NdBr_2]^-[(thp)_2AlMe_2]^+$ (GG^{Nd}). Following the procedure described above, $Cp^*_2Nd(AlMe_4)$ (25.0 mg, 0.05 mmol) and Me_3GeBr (29.5 mg, 0.15 mmol) afforded **GG^{Nd}** as light blue crystals (38.5 mg, 0.048 mmol, 96%). IR (Nujol, CsI-window): $\tilde{\nu}$ = 2954 (Cp, Nujol), 2924 (Cp, Nujol), 2854 (Cp, Nujol), 2724 (w), 2668 (w), 2624 (w), 1460 (Nujol), 1377 (Nujol), 1311 (m), 1279 (w), 1260 (w), 1196 (m), 1156 (w), 1073 (vw), 1015 (m), 993 (m), 948 (m), 887 (w), 857 (m), 801 (w), 793 (w), 721 (vs), 691 (s), 676 (m), 608 (w), 582 (w), 468 (vw) cm^{-1}.

$[Cp^*_2PrBr_2K(thp)_4]$ (HH). A solution of Me_3GeBr (29.5 mg, 0.15 mmol) in toluene (1 mL) was added to a stirred solution of **BB^{Pr}** (27.08 mg, 0.05 mmol). After stirring the reaction mixture at ambient temperature for 5 min, a stoichiometric amount of THP (2 equiv.) was added. After stirring for another 30 min, the solvent was completely removed under vacuum, and the obtained crude product was recrystallized from a saturated THP solution at -40 °C. Single-crystals of **HH** were obtained as colorless blocks in low yield. The ^1H NMR spectrum of the non-crystalline residue was inconclusive.

$[Cp^*_2CeBr_2]^-[(Et_2O)_2AlMe_2]^+$ (II^{Ce}). Following the procedure described above, $Cp^*_2Ce(AlMe_4)$ (19.9 mg, 0.04 mmol) and Me_3GeBr (23.7 mg, 0.12 mmol) afforded **II^{Ce}** as yellow solution. Recrystallization was impeded by presumable removal of Et_2O and resulting formation of the neutral trivalent sandwich complex $[Cp^*_2CeBr]$ under vacuum.

$[Cp^*_2PrBr_2]^-[(Et_2O)_2AlMe_2]^+$ (II^{Pr}). Following the procedure described above, $Cp^*_2Pr(AlMe_4)$ (20.1 mg, 0.04 mmol) and Me_3GeBr (23.7 mg, 0.12 mmol) afforded **II^{Pr}** as light green solution. Recrystallization was impeded by presumable removal of Et_2O and resulting formation of the neutral trivalent sandwich complex $[Cp^*_2PrBr]$ under vacuum.

$[Cp^*_2NdBr_2]^-[(Et_2O)_2AlMe_2]^+$ (II^{Nd}). Following the procedure described above, $Cp^*_2Nd(AlMe_4)$ (20.2 mg, 0.04 mmol) and Me_3GeBr (23.7 mg, 0.12 mmol) afforded **II^{Nd}** as blue-green solution. Recrystallization was impeded by presumable removal of Et_2O and resulting formation of the neutral trivalent sandwich complex $[Cp^*_2NdBr]$ under vacuum.

General procedure for the synthesis of $[(O\mathit{t}Bu)_{12}Te/LnNa_{14}O_3]$ (JJ^{Ln}, Ln = Ce, Nd). To a stirred solution of the diethyl ether separated ion pair **II^{Ln}**, a stoichiometric amount of $TeBr_4$ (1 equiv.) in toluene was added. Upon addition of tellurium bromide, the solution immediately became pale, and precipitation of a dark solid (Te^0) was observed. Elemental tellurium was

filtered off, and another stoichiometric amount of $TeBr_4$ (1 equiv.) in toluene was added. After stirring the solution over night, the solution showed an intense dark color, hence complete oxidation was assumed. The solvent was removed under vacuum, and the residual dark solid was resuspended in toluene. Under vigorous stirring, a stoichiometric amount of NaO*t*Bu (4 equiv.) was added, resulting in an immediate color change of the solution to orange and precipitation of a colorless solid. After stirring the reaction mixture for 1 h, the suspension was centrifuged, filtered, and the solvent was removed completely under vacuum. If the ^{1}H NMR spectrum in [D_6]benzene showed signals of a trivalent species, an additional stoichiometric amount of $TeBr_4$ (1 equiv.) was added, the solution stirred for 2 h, and filtered again. Colorless crystals of $\mathbf{JJ^{Ln}}$ were obtained from a saturated toluene solution. ^{1}H NMR $\mathbf{JJ^{Ce}}$ (400.11 MHz, [D_6]benzene, 26 °C): δ = 1.39 (s, *tBu*) ppm.

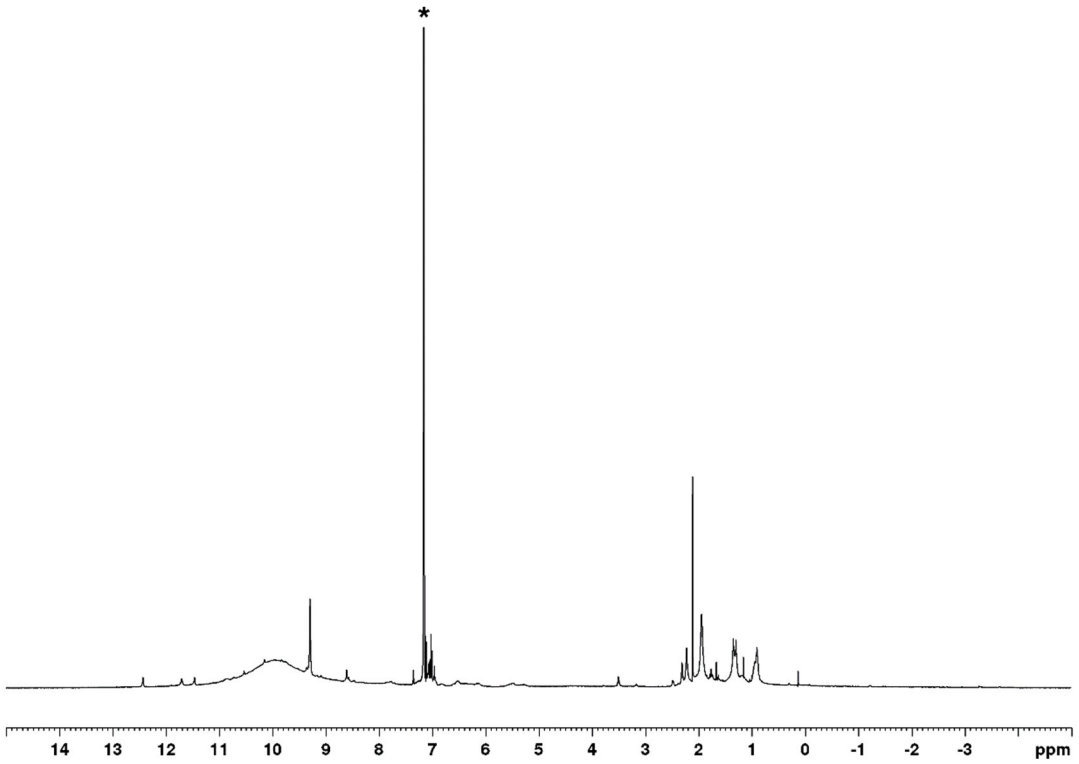

Figure C13. ^{1}H NMR spectrum (400 MHz, [D$_6$]benzene, 26 °C) of [Cp*$_2$Pr(AlMe$_4$)$_2$] (**BB^{Pr}**). Solvent residual signals are marked with an asterisk.

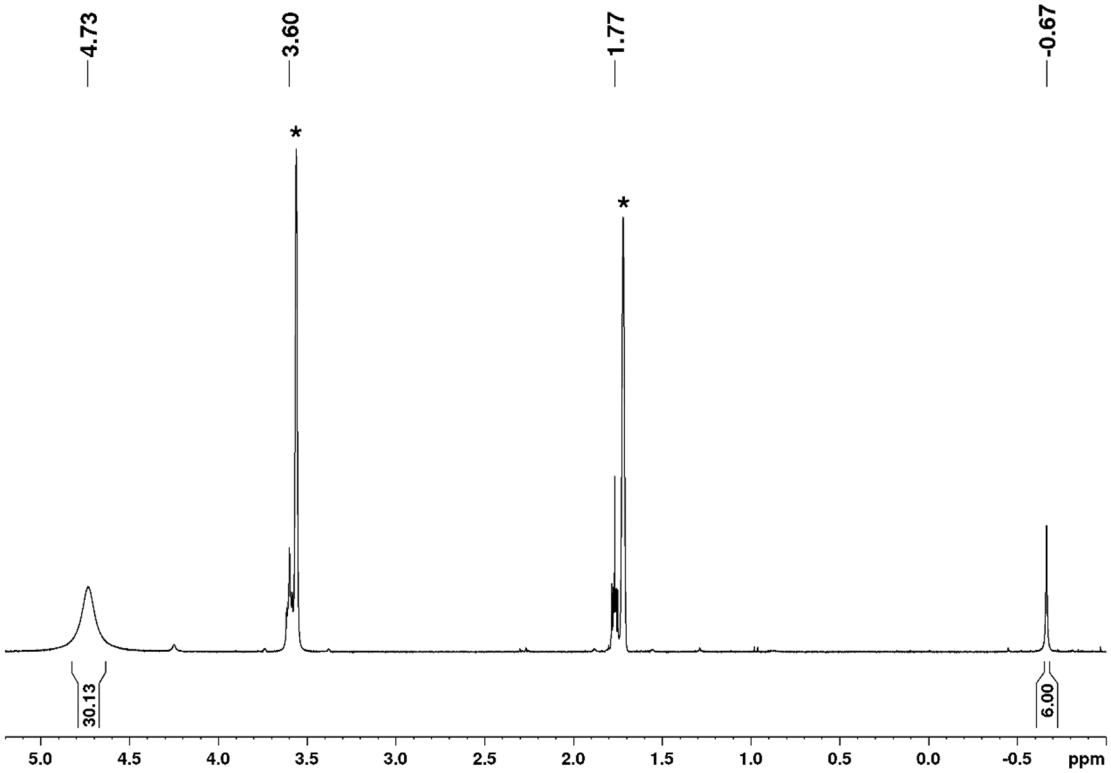

Figure C14. ^{1}H NMR spectrum (400 MHz, [D$_8$]THF, 26 °C) of [Cp*$_2$CeBr$_2$]$^-$[(thf)$_2$AlMe$_2$]$^+$ (**FF^{Ce}**). Solvent residual signals are marked with an asterisk.

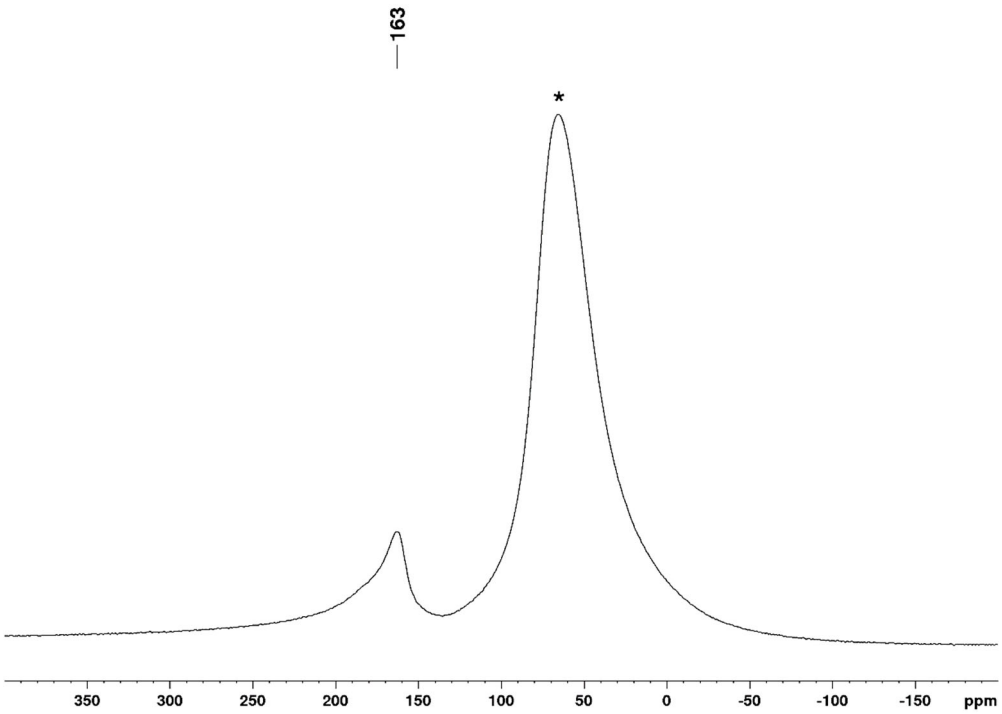

Figure C15. ^{27}Al NMR spectrum (130 MHz, [D$_8$]THF, 26 °C) of [Cp*$_2$CeBr$_2$]$^-$[(thf)$_2$AlMe$_2$]$^+$ (**FF^{Ce}**). The signal of the aluminum silicate NMR tube is marked with an asterisk.

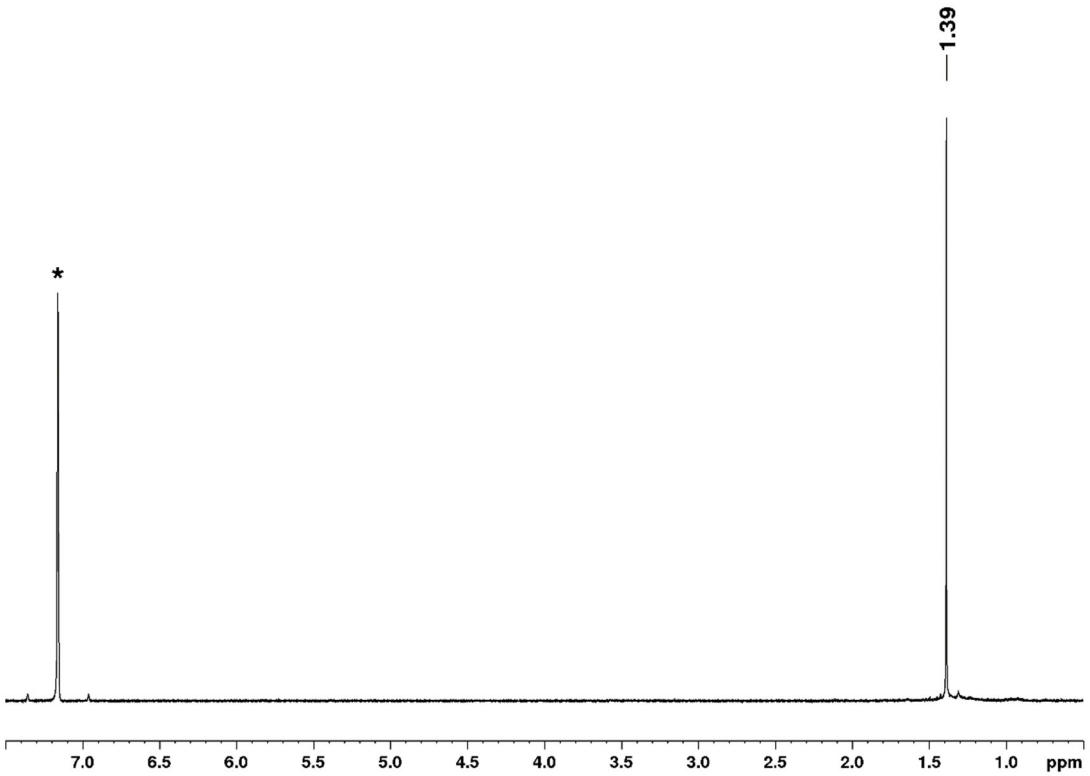

Figure C16. ^{1}H NMR spectrum (400 MHz, [D6]benzene, 26 °C) of [(O*t*Bu)$_{12}$Te/CeNa$_{14}$O$_3$] (**JJ^{Ce}**).

Table C2. Crystallographic data for compounds **EE^{Ce}**, **EE^{Pr}**, and **EENd**

	EE^{Ce}	**EE^{Pr}**	**EENd**
formula	$C_{30}H_{52}AlCeBr_2O_2$	$C_{30}H_{52}AlPrBr_2O_2$	$C_{30}H_{52}AlNdBr_2O_2$
M_r [g/mol]	771.63	772.42	775.75
color/shape	yellow/block	light yellow/block	light blue/block
crystal dimensions [mm]	0.156 x 0.153 x 0.145	0.231 x 0.171 x 0.146	0.139 x 0.106 x 0.104
crystal system	orthorhombic	orthorhombic	orthorhombic
space group	*Pca*2$_1$	*Pca*2$_1$	*Cmc*2$_1$
a [Å]	16.032(3)	16.0167(7)	15.147(4)
b [Å]	15.319(3)	15.1869(7)	16.028(4)
c [Å]	13.737(3)	13.7292(6)	13.728(3)
α [°]	90	90	90
β [°]	90	90	90
γ [°]	90	90	90
V [Å^3]	3373.6(11)	3339.5(3)	3332.6(14)
Z	4	4	4
T [K]	100(2)	100(2)	100(2)
λ [Å]	0.71073	0.71073	0.71073
ρ_{calcd} [g/cm^3]	1.519	1.536	1.546
μ [mm^{-1}]	3.767	3.901	4.005
F (000)	1556	1560	1564
θ range [°]	2.362 – 30.560	2.370 – 30.509	1.850 – 30.499
independent reflections	10144	10189	5250
reflections collected	45595	74803	37933
R1/*w*R2 (I > 2σ)	0.0316/0.0655	0.0230/0.0521	0.0234/0.0512
R1/*w*R2 (all data)	0.0526/0.0728	0.0296/0.0545	0.0252/0.0521
GOF	1.007	1.049	1.038

Table C2 (continued). Crystallographic data for compounds **BB^{Pr}**, **GG^{Ce}**, and **GGNd**

	BB^{Pr}•C$_6$H$_{14}$	**GG^{Ce}**	**GGNd**
formula	$C_{27}H_{49}AlPr$	$C_{32}H_{56}AlCeBr_2O_2$	$C_{32}H_{56}AlNdBr_2O_2$
M_r [g/mol]	541.55	799.68	803.80
color/shape	light yellow/block	yellow/needle	blue/needle
crystal dimensions [mm]	0.253 x 0.235 x 0.123	0.092 x 0.048 x 0.046	0.143 x 0.054 x 0.039
crystal system	triclinic	orthorhombic	orthorhombic
space group	$P\bar{1}$	$Cmc2_1$	$Cmc2_1$
a [Å]	10.7146(7)	15.8059(9)	15.7584(11)
b [Å]	11.5937(8)	16.2400(9)	16.2452(11)
c [Å]	12.5422(9)	13.6597(9)	13.6445(9)
α [°]	71.897(2)	90	90
β [°]	74.032(2)	90	90
γ [°]	88.446(2)	90	90
V [Å^3]	1420.85(17)	3506.3(4)	3493.0(4)
Z	2	4	4
T [K]	100(2)	100(2)	100(2)
λ [Å]	0.71073	0.71073	0.71073
ρ_{calcd} [g/cm^3]	1.266	1.515	1.528
μ [mm^{-1}]	1.755	3.627	3.824
F (000)	566	1620	1628
θ range [°]	1.981 – 28.285	1.798 – 24.729	1.800 – 26.392
independent reflections	6983	3114	3696
reflections collected	32698	21315	21966
R1/*w*R2 (I > 2σ)	0.0269/0.0647	0.0343/0.0630	0.0334/0.0645
R1/*w*R2 (all data)	0.0293/0.0663	0.0427/0.0666	0.0429/0.0685
GOF	1.076	1.045	1.032

Table C2 (continued). Crystallographic data for compounds **HH**, **JJ^{Ce}**, and **JJNd**

	HH•$C_5H_{10}O$	**JJ^{Ce}**	**JJNd**
formula	$C_{45}H_{80}PrBr_2O_5K$	$C_{48}H_{108}CeNa_{14}O_{15}$	$C_{32}H_{56}AlNdBr_2O_2$
M_r [g/mol]	1040.92	1387.32	803.80
color/shape	colorless/block	colorless/block	blue/needle
crystal dimensions [mm]	0.760 x 0.120 x 0.074	0.167 x 0.097 x 0.093	0.143 x 0.054 x 0.039
crystal system	orthorhombic	triclinic	orthorhombic
space group	*Pca*2$_1$	$P\bar{1}$	*Cmc*2$_1$
a [Å]	19.2350(19)	19.354(11)	15.7584(11)
b [Å]	13.7700(13)	19.371(12)	16.2452(11)
c [Å]	18.7750(19)	19.375(11)	13.6445(9)
α [°]	90	90.00(2)	90
β [°]	90	89.96(2)	90
γ [°]	90	90.03(2)	90
V [Å^3]	4972.9(8)	7264(7)	3493.0(4)
Z	4	4	4
T [K]	100(2)	100(2)	100(2)
λ [Å]	0.71073	0.71073	0.71073
ρ_{calcd} [g/cm^3]	1.390	1.269	
μ [mm^{-1}]	2.709	0.762	
F (000)	2152	2912	
θ range [°]	1.479 – 26.388	1.486 – 22.079	
independent reflections	10176	31969	
reflections collected	59272	65242	
R1/*w*R2 (I > 2σ)	0.0703/0.1616	0.1494/0.3688	
R1/*w*R2 (all data)	0.0724/0.1625	0.2900/0.4202	
GOF	1.250	1.852	

D

Bibliography

[1] F. Cotton, *Q. Rev. Chem. Soc.* **1966**, *20*, 389-401.

[2] G. Schmid, *Chem. Rev.* **1992**, *92*, 1709-1727.

[3] A. Schnepf, H. Schnöckel, *Angew. Chem. Int. Ed.* **2002**, *41*, 3532-3554.

[4] G. Schmid, *Clusters and colloids: from theory to applications*, John Wiley & Sons, **2008**.

[5] J.-C. G. Bünzli, C. Piguet, *Chem. Rev.* **2002**, *102*, 1897-1928.

[6] S. Dehnen, J. Corrigan, *Clusters-contemporary insight in structure and bonding, Vol. 174*, Springer, **2017**.

[7] X.-Y. Zheng, J. Xie, X.-J. Kong, L.-S. Long, L.-S. Zheng, *Coord. Chem. Rev.* **2019**, *378*, 222-236.

[8] G. Karotsis, M. Evangelisti, S. J. Dalgarno, E. K. Brechin, *Angew. Chem. Int. Ed.* **2009**, *48*, 9928-9931.

[9] Y.-Z. Zheng, M. Evangelisti, R. E. P. Winpenny, *Angew. Chem. Int. Ed.* **2011**, *50*, 3692-3695.

[10] L.-X. Chang, G. Xiong, L. Wang, P. Cheng, B. Zhao, *Chem. Commun.* **2013**, *49*, 1055-1057.

[11] J.-B. Peng, X.-J. Kong, Q.-C. Zhang, M. Orendáč, J. Prokleška, Y.-P. Ren, L.-S. Long, Z. Zheng, L.-S. Zheng, *J. Am. Chem. Soc.* **2014**, *136*, 17938-17941.

[12] W.-P. Chen, P.-Q. Liao, Y. Yu, Z. Zheng, X.-M. Chen, Y.-Z. Zheng, *Angew. Chem. Int. Ed.* **2016**, *55*, 9375-9379.

[13] X.-Y. Zheng, X.-J. Kong, Z. Zheng, L.-S. Long, L.-S. Zheng, *Acc. Chem. Res.* **2018**, *51*, 517-525.

[14] W.-P. Chen, P.-Q. Liao, P.-B. Jin, L. Zhang, B.-K. Ling, S.-C. Wang, Y.-T. Chan, X.-M. Chen, Y.-Z. Zheng, *J. Am. Chem. Soc.* **2020**, *142*, 4663-4670.

[15] R. Sessoli, A. K. Powell, *Coord. Chem. Rev.* **2009**, *253*, 2328-2341.

[16] D. N. Woodruff, F. Tuna, M. Bodensteiner, R. E. Winpenny, R. A. Layfield, *Organometallics* **2013**, *32*, 1224-1229.

[17] D. N. Woodruff, R. E. Winpenny, R. A. Layfield, *Chem. Rev.* **2013**, *113*, 5110-5148.

[18] P. Zhang, Y.-N. Guo, J. Tang, *Coord. Chem. Rev.* **2013**, *257*, 1728-1763.

[19] K. R. Vignesh, A. Soncini, S. K. Langley, W. Wernsdorfer, K. S. Murray, G. Rajaraman, *Nat. Commun.* **2017**, *8*, 1-12.

[20] G. Fernandez Garcia, D. Guettas, V. Montigaud, P. Larini, R. Sessoli, F. Totti, O. Cador, G. Pilet, B. Le Guennic, *Angew. Chem. Int. Ed.* **2018**, *57*, 17089-17093.

[21] W.-M. Wang, L. Zhang, X.-Z. Li, L.-Y. He, X.-X. Wang, Y. Shi, J. Wang, J. Dong, Z.-L. Wu, *New J. Chem.* **2019**, *43*, 12941-12949.

[22] J. Wu, S. Demeshko, S. Dechert, F. Meyer, *Chem. Commun.* **2020**, *56*, 3887-3890.

[23] D. T. Thielemann, A. T. Wagner, E. Rösch, D. K. Kölmel, J. G. Heck, B. Rudat, M. Neumaier, C. Feldmann, U. Schepers, S. Bräse, P. W. Roesky, *J. Am. Chem. Soc.* **2013**, *135*, 7454-7457.

[24] D. A. Gálico, J. S. Ovens, M. Murugesu, *Nanoscale* **2020**, *12*, 11435-11439.

[25] D. Shi, X. Yang, Z. Xiao, X. Liu, H. Chen, Y. Ma, D. Schipper, R. A. Jones, *Nanoscale* **2020**, *12*, 1384-1388.

[26] D. A. Gálico, A. A. Kitos, J. S. Ovens, F. A. Sigoli, M. Murugesu, *Angew. Chem. Int. Ed.* **2021**, *60*, 6130-6136.

[27] X.-Y. Li, H.-F. Su, Q.-W. Li, R. Feng, H.-Y. Bai, H.-Y. Chen, J. Xu, X.-H. Bu, *Angew. Chem. Int. Ed.* **2019**, *58*, 10184-10188.

[28] X.-Y. Zheng, Y.-H. Jiang, G.-L. Zhuang, D.-P. Liu, H.-G. Liao, X.-J. Kong, L.-S. Long, L.-S. Zheng, *J. Am. Chem. Soc.* **2017**, *139*, 18178-18181.

[29] L. Qin, G.-J. Zhou, Y.-Z. Yu, H. Nojiri, C. Schröder, R. E. P. Winpenny, Y.-Z. Zheng, *J. Am. Chem. Soc.* **2017**, *139*, 16405-16411.

[30] X.-J. Kong, L.-S. Long, R.-B. Huang, L.-S. Zheng, T. D. Harris, Z. Zheng, *Chem. Commun.* **2009**, 4354-4356.

[31] R. Anwander, *Angew. Chem. Int. Ed.* **1998**, *37*, 599-602.

[32] W. P. Kretschmer, J. H. Teuben, S. I. Troyanov, *Angew. Chem. Int. Ed.* **1998**, *37*, 88-90.

[33] W. J. Evans, R. Anwander, J. W. Ziller, *Organometallics* **1995**, *14*, 1107-1109.

[34] D. Barisic, D. Diether, C. c. Maichle-Mössmer, R. Anwander, *J. Am. Chem. Soc.* **2019**, *141*, 13931-13940.

[35] M. Zimmermann, N. Å. Frøystein, A. Fischbach, P. Sirsch, H. M. Dietrich, K. W. Törnroos, E. Herdtweck, R. Anwander, *Chem. Eur. J.* **2007**, *13*, 8784-8800.

[36] G. Occhipinti, C. Meermann, H. M. Dietrich, R. Litlabø, F. Auras, K. W. Törnroos, C. Maichle-Mössmer, V. R. Jensen, R. Anwander, *J. Am. Chem. Soc.* **2011**, *133*, 6323-6337.

[37] S. N. König, N. F. Chilton, C. Maichle-Mössmer, E. M. Pineda, T. Pugh, R. Anwander, R. A. Layfield, *Dalton Trans.* **2014**, *43*, 3035-3038.

[38] A. Nieland, A. Mix, B. Neumann, H.-G. Stammler, N. W. Mitzel, *Eur. J. Inorg. Chem.* **2014**, *2014*, 51-57.

[39] C. O. Hollfelder, L. N. Jende, D. Diether, T. Zelger, R. Stauder, C. Maichle-Mössmer, R. Anwander, *Catalysts* **2018**, *8*, 61.

[40] H. M. Dietrich, G. Raudaschl-Sieber, R. Anwander, *Angew. Chem. Int. Ed.* **2005**, *44*, 5303-5306.

[41] H. Schumann, J. A. Meese-Marktscheffel, L. Esser, *Chem. Rev.* **1995**, *95*, 865-986.

[42] R. Anwander, M. G. Klimpel, H. Martin Dietrich, D. J. Shorokhov, W. Scherer, *Chem. Commun.* **2003**, 1008-1009.

[43] H. M. Dietrich, C. Zapilko, E. Herdtweck, R. Anwander, *Organometallics* **2005**, *24*, 5767-5771.

[44] E. Le Roux, F. Nief, F. Jaroschik, K. W. Törnroos, R. Anwander, *Dalton Trans.* **2007**, 4866-4870.

[45] D. Robert, T. P. Spaniol, J. Okuda, *Eur. J. Inorg. Chem.* **2008**, *2008*, 2801-2809.

[46] M. Zimmermann, K. W. Törnroos, H. Sitzmann, R. Anwander, *Chem. Eur. J.* **2008**, *14*, 7266-7277.

[47] H. M. Dietrich, K. W. Tornroos, E. Herdtweck, R. Anwander, *Organometallics* **2009**, *28*, 6739-6749.

[48] M. Zimmermann, J. Volbeda, K. W. Törnroos, R. Anwander, *C. R. Chim.* **2010**, *13*, 651-660.

[49] L. N. Jende, C. Maichle-Mössmer, R. Anwander, *Chem. Eur. J.* **2013**, *19*, 16321-16333.

[50] A. M. Bienfait, B. M. Wolf, K. W. Tornroos, R. Anwander, *Organometallics* **2015**, *34*, 5734-5744.

[51] A. Fischbach, M. G. Klimpel, M. Widenmeyer, E. Herdtweck, W. Scherer, R. Anwander, *Angew. Chem. Int. Ed.* **2004**, *43*, 2234-2239.

[52] C. O. Hollfelder, M. Meermann-Zimmermann, G. Spiridopoulos, D. Werner, K. W. Törnroos, C. Maichle-Mössmer, R. Anwander, *Molecules* **2019**, *24*, 3703.

[53] M. Zimmermann, K. W. Törnroos, R. Anwander, *Angew. Chem. Int. Ed.* **2007**, *46*, 3126-3130.

[54] A. Fischbach, R. Anwander, in *Neodymium Based Ziegler Catalysts – Fundamental Chemistry* (Ed.: O. Nuyken), Springer Berlin Heidelberg, Berlin, Heidelberg, **2006**, pp. 155-281.

[55] M. Zimmermann, D. Rauschmaier, K. Eichele, K. W. Törnroos, R. Anwander, *Chem. Commun.* **2010**, *46*, 5346-5348.

[56] H. M. Dietrich, H. Grove, K. W. Törnroos, R. Anwander, *J. Am. Chem. Soc.* **2006**, *128*, 1458-1459.

[57] H. M. Dietrich, C. Maichle-Mössmer, R. Anwander, *Dalton Trans.* **2010**, *39*, 5783-5785.

[58] J. E. Mahler, R. Pettit, *J. Am. Chem. Soc.* **1962**, *84*, 1511-1512.

[59] D. Barisic, D. A. Buschmann, D. Schneider, C. Maichle-Mössmer, R. Anwander, *Chem. Eur. J.* **2019**, *25*, 4821-4832.

[60] M. Zimmermann, K. W. Törnroos, R. Anwander, *Angew. Chem. Int. Ed.* **2008**, *47*, 775-778.

[61] D. Schädle, M. Enders, C. Schädle, C. Maichle-Mössmer, K. W. Törnroos, R. Anwander, *New J. Chem.* **2015**, *39*, 7640-7648.

[62] R. Thim, D. Schädle, C. Maichle-Mössmer, R. Anwander, *Chem. Eur. J.* **2019**, *25*, 507-511.

[63] H. M. Dietrich, O. Schuster, K. W. Törnroos, R. Anwander, *Angew. Chem. Int. Ed.* **2006**, *45*, 4858-4863.

[64] D. A. Buschmann, H. M. Dietrich, D. Schneider, V. M. Birkelbach, C. Stuhl, K. W. Törnroos, C. Maichle-Mössmer, R. Anwander, *Chem. Eur. J.* **2020**, *26*, 10834-10840.

[65] S. Manastyrskyj, R. Maginn, M. Dubeck, *Inorg. Chem.* **1963**, *2*, 904-905.

[66] R.-E. Maginn, S. Manastyrskyj, M. Dubeck, *J. Am. Chem. Soc.* **1963**, *85*, 672-676.

[67] J. D. Jamerson, A. P. Masino, J. Takats, *J. Organomet. Chem.* **1974**, *65*, C33-C36.

[68] C. S. Day, V. W. Day, R. D. Ernst, S. H. Vollmer, *Organometallics* **1982**, *1*, 998-1003.

[69] H. Schumann, *Angew. Chem. Int. Ed. Engl.* **1984**, *23*, 474-493.

[70] G. B. Deacon, G. D. Fallon, D. L. Wilkinson, *J. Organomet. Chem.* **1985**, *293*, 45-50.

[71] W. J. Evans, J. W. Grate, H. W. Choi, I. Bloom, W. E. Hunter, J. L. Atwood, *J. Am. Chem. Soc.* **1985**, *107*, 941-946.

[72] P. N. Hazin, J. C. Huffman, J. W. Bruno, *Organometallics* **1987**, *6*, 23-27.

[73] C. J. Burns, R. A. Andersen, *J. Organomet. Chem.* **1987**, *325*, 31-37.

[74] H. Van der Heijden, C. J. Schaverien, A. G. Orpen, *Organometallics* **1989**, *8*, 255-258.

[75] M. F. Lappert, A. Singh, J. L. Atwood, W. E. Hunter, *J. Chem. Soc., Chem. Commun.* **1981**, 1191-1193.

[76] M. F. Lappert, A. Singh, J. L. Atwood, W. E. Hunter, *J. Chem. Soc., Chem. Commun.* **1981**, 1190-1191.

[77] W. J. Evans, S. E. Foster, *J. Organomet. Chem.* **1992**, *433*, 79-94.

[78] S. Song, Q. Shen, S. Jin, J. Guan, Y. Lin, *Polyhedron* **1992**, *11*, 2857-2861.

[79] Z. Xie, K. Chui, Q. Yang, T. C. W. Mak, J. Sun, *Organometallics* **1998**, *17*, 3937-3944.

[80] Z. Xie, Z. Liu, Z.-Y. Zhou, T. C. Mak, *J. Chem. Soc., Dalton Trans.* **1998**, 3367-3372.

[81] F. Ortu, J. Liu, M. Burton, J. M. Fowler, A. Formanuik, M.-E. Boulon, N. F. Chilton, D. P. Mills, *Inorg. Chem.* **2017**, *56*, 2496-2505.

[82] F. Bottomley, D. E. Paez, P. S. White, *J. Organomet. Chem.* **1985**, *291*, 35-41.

[83] C. J. Burns, D. J. Berg, R. A. Andersen, *J. Chem. Soc., Chem. Commun.* **1987**, 272-273.

[84] W. J. Evans, D. K. Drummond, J. W. Grate, H. Zhang, J. L. Atwood, *J. Am. Chem. Soc.* **1987**, *109*, 3928-3936.

[85] W. J. Evans, D. K. Drummond, T. P. Hanusa, R. J. Doedens, *Organometallics* **1987**, *6*, 2279-2285.

[86] S. A. Sulway, R. A. Layfield, F. Tuna, W. Wernsdorfer, R. E. P. Winpenny, *Chem. Commun.* **2012**, *48*, 1508-1510.

[87] H. Schumann, M. R. Keitsch, J. Winterfeld, J. Demtschuk, *J. Organomet. Chem.* **1996**, *525*, 279-281.

[88] H. Schnöckel, *Chem. Rev.* **2010**, *110*, 4125-4163.

[89] K. N. Raymond, C. W. Eigenbrot Jr, *Acc. Chem. Res.* **1980**, *13*, 276-283.

[90] P. L. Watson, T. H. Tulip, I. Williams, *Organometallics* **1990**, *9*, 1999-2009.

[91] W. J. Evans, T. M. Champagne, B. L. Davis, N. T. Allen, G. W. Nyce, M. A. Johnston, Y.-C. Lin, A. Khvostov, J. W. Ziller, *J. Coord. Chem.* **2006**, *59*, 1069-1087.

[92] S. P. Constantine, G. M. De Lima, P. B. Hitchcock, J. M. Keates, G. A. Lawless, *Chem. Commun.* **1996**, 2421-2422.

[93] F. Bonnet, M. Visseaux, D. Barbier-Baudry, A. Hafid, E. Vigier, M. M. Kubicki, *Inorg. Chem.* **2004**, *43*, 3682-3690.

[94] F. Bonnet, C. E. Jones, S. Semlali, M. Bria, P. Roussel, M. Visseaux, P. L. Arnold, *Dalton Transactions* **2013**, *42*, 790-801.

[95] J. Li, X. Li, H.-J. Zhai, L.-S. Wang, *Science* **2003**, *299*, 864-867.

[96] S. Kenzler, C. Schrenk, A. Schnepf, *Angew. Chem. Int. Ed.* **2017**, *56*, 393-396.

[97] R. J. Wilson, N. Lichtenberger, B. Weinert, S. Dehnen, *Chem. Rev.* **2019**, *119*, 8506-8554.

[98] M. Diecke, C. Schrenk, A. Schnepf, *Angew. Chem. Int. Ed.* **2020**, *59*, 14418-14422.

[99] S. Hasegawa, S. Takano, K. Harano, T. Tsukuda, *JACS Au* **2021**, *1*, 660-668.

[100] W. Zachariasen, *Acta Crystallogr.* **1948**, *1*, 265-268.

[101] H. Bärnighausen, H. Pätow, H. Beck, *Z. Anorg. Allg. Chem.* **1974**, *403*, 45-55.

[102] D. Hake, W. Urland, *Z. Anorg. Allg. Chem.* **1990**, *586*, 99-105.

[103] D. A. Buschmann, D. Schneider, C. Maichle-Mössmer, R. Anwander, *Eur. J. Inorg. Chem.***2022**, e202100862.

[104] D. Cui, O. Tardif, Z. Hou, *J. Am. Chem. Soc.* **2004**, *126*, 1312-1313.

[105] M. Nishiura, J. Baldamus, T. Shima, K. Mori, Z. Hou, *Chem. Eur. J.* **2011**, *17*, 5033-5044.

[106] D. Diether, K. Tyulyunov, C. Maichle-Mössmer, R. Anwander, *Organometallics* **2017**, *36*, 4649-4659.

[107] M. E. Burin, M. V. Smirnova, G. K. Fukin, E. V. Baranov, M. N. Bochkarev, *Eur. J. Inorg. Chem.* **2006**, *2006*, 351-356.

[108] E. Barnea, C. Averbuj, M. Kapon, M. Botoshansky, M. S. Eisen, *Eur. J. Inorg. Chem.* **2007**, *2007*, 4535-4540.

[109] L. N. Jende, C. O. Hollfelder, C. Maichle-Mössmer, R. Anwander, *Organometallics* **2015**, *34*, 32-41.

[110] K. A. Tupper, T. D. Tilley, *J. Organomet. Chem.* **2005**, *690*, 1689-1698.

[111] A. Fridrichová, V. Varga, J. Pinkas, M. Lamač, A. Růžička, M. Horáček, *Eur. J. Inorg. Chem.* **2016**, *2016*, 3713-3721.

[112] A. Fridrichová, A. Růžička, M. Lamač, M. Horáček, *Inorg. Chem. Commun.* **2017**, *76*, 62-66.

[113] R. Shannon, *Acta Crystallogr. Sect. A* **1976**, *32*, 751-767.

[114] A. M. Bienfait, B. M. Wolf, K. W. Törnroos, R. Anwander, *Organometallics* **2016**, *35*, 3743-3750.

[115] W. J. Evans, M. S. Sollberger, *J. Am. Chem. Soc.* **1986**, *108*, 6095-6096.

[116] M. Kritikos, M. Moustiakimov, M. Wijk, G. Westin, *J. Chem. Soc., Dalton Trans.* **2001**, 1931-1938.

[117] J. Gromada, A. Mortreux, T. Chenal, J. W. Ziller, F. Leising, J. F. Carpentier, *Chem. Eur. J.* **2002**, *8*, 3773-3788.

[118] G. Westin, M. Moustiakimov, M. Kritikos, *Inorg. Chem.* **2002**, *41*, 3249-3258.

[119] R. J. Blagg, F. Tuna, E. J. McInnes, R. E. Winpenny, *Chem. Commun.* **2011**, *47*, 10587-10589.

[120] O. Tardif, M. Nishiura, Z. Hou, *Organometallics* **2003**, *22*, 1171-1173.

[121] D. Cui, M. Nishiura, Z. Hou, *Macromolecules* **2005**, *38*, 4089-4095.

[122] Y. Luo, J. Baldamus, O. Tardif, Z. Hou, *Organometallics* **2005**, *24*, 4362-4366.

[123] X. Li, J. Baldamus, M. Nishiura, O. Tardif, Z. Hou, *Angew. Chem. Int. Ed.* **2006**, *45*, 8184-8188.

[124] M. Yousufuddin, M. J. Gutmann, J. Baldamus, O. Tardif, Z. Hou, S. A. Mason, G. J. McIntyre, R. Bau, *J. Am. Chem. Soc.* **2008**, *130*, 3888-3891.

[125] M. Nishiura, Z. Hou, *Nat. Chem.* **2010**, *2*, 257-268.

[126] T. Shima, M. Nishiura, Z. Hou, *Organometallics* **2011**, *30*, 2513-2524.

[127] T. Stewart, M. Nishiura, Y. Konno, Z. Hou, G. J. McIntyre, R. Bau, *Inorg. Chim. Acta* **2010**, *363*, 562-566.

[128] T. Shima, Y. Luo, T. Stewart, R. Bau, G. J. McIntyre, S. A. Mason, Z. Hou, *Nat. Chem.* **2011**, *3*, 814-820.

[129] T. Shima, Z. Hou, *Chem. Eur. J.l* **2013**, *19*, 3458-3466.

[130] W. J. Evans, J. H. Meadows, A. L. Wayda, W. E. Hunter, J. L. Atwood, *J. Am. Chem. Soc.* **1982**, *104*, 2015-2017.

[131] S. Y. Knjazhanskij, B. M. Bulychev, O. K. Kireeva, V. K. Belsky, G. L. Soloveichik, *J. Organomet. Chem.* **1991**, *414*, 11-22.

[132] M. T. Dumas, G. P. Chen, J. Y. Hu, M. A. Nascimento, J. M. Rawson, J. W. Ziller, F. Furche, W. J. Evans, *J. Organomet. Chem.* **2017**, *849-850*, 38-47.

[133] W.-X. Zhang, Z. Wang, M. Nishiura, Z. Xi, Z. Hou, *J. Am. Chem. Soc.* **2011**, *133*, 5712-5715.

[134] T. Li, M. Nishiura, J. Cheng, W. Zhang, Y. Li, Z. Hou, *Organometallics* **2013**, *32*, 4142-4148.

[135] H. M. Dietrich, K. W. Törnroos, R. Anwander, *J. Am. Chem. Soc.* **2006**, *128*, 9298-9299.

[136] C. O. Hollfelder, L. N. Jende, H. M. Dietrich, K. Eichele, C. Maichle-Mössmer, R. Anwander, *Chem. Eur. J.* **2019**, *25*, 7298-7302.

[137] V. M. Birkelbach, F. Kracht, H. M. Dietrich, C. Stuhl, C. c. Maichle-Mössmer, R. Anwander, *Organometallics* **2020**, *39*, 3490-3504.

[138] L. J. Guggenberger, R. R. Schrock, *J. Am. Chem. Soc.* **1975**, *97*, 6578-6579.

[139] F. N. Tebbe, G. W. Parshall, G. S. Reddy, *J. Am. Chem. Soc.* **1978**, *100*, 3611-3613.

[140] R. R. Schrock, *Acc. Chem. Res.* **1979**, *12*, 98-104.

[141] K. H. Thiele, S. Bambirra, J. Sieler, S. Yelonek, *Angew. Chem. Int. Ed.* **1998**, *37*, 2886-2888.

[142] W. J. Evans, M. S. Sollberger, T. P. Hanusa, *J. Am. Chem. Soc.* **1988**, *110*, 1841-1850.

[143] W. J. Evans, M. S. Sollberger, J. L. Shreeve, J. M. Olofson, J. H. Hain, J. W. Ziller, *Inorg. Chem.* **1992**, *31*, 2492-2501.

[144] S. V. Eliseeva, J.-C. G. Bünzli, *Chem. Soc. Rev.* **2010**, *39*, 189-227.

[145] J.-C. G. Bünzli, S. V. Eliseeva, *Chem. Sci.* **2013**, *4*, 1939-1949.

[146] Z. Xia, A. Meijerink, *Chem. Soc. Rev.* **2017**, *46*, 275-299.

[147] M. Suta, N. Harmgarth, M. Kühling, P. Liebing, F. T. Edelmann, C. Wickleder, *Chem. Asian J.* **2018**, *13*, 1038-1044.

[148] M. Kühling, C. Wickleder, M. J. Ferguson, C. G. Hrib, R. McDonald, M. Suta, L. Hilfert, J. Takats, F. T. Edelmann, *New J. Chem.* **2015**, *39*, 7617-7625.

[149] D. T. Thielemann, A. T. Wagner, E. Rösch, D. K. Kölmel, J. G. Heck, B. Rudat, M. Neumaier, C. Feldmann, U. Schepers, S. Bräse, *J. Am. Chem. Soc.* **2013**, *135*, 7454-7457.

[150] F. Le Natur, G. Calvez, J.-P. Guégan, L. Le Polles, X. Trivelli, K. Bernot, C. Daiguebonne, C. Neaime, K. Costuas, F. Grasset, *Inorg. Chem.* **2015**, *54*, 6043-6054.

[151] I. Mylonas-Margaritis, A. A. Kitos, C. C. Panteli, K. Skordi, A. J. Tasiopoulos, V. Bekiari, A. Escuer, S. P. Perlepes, *Inorg. Chem. Commun.* **2017**, *83*, 118-122.

[152] H. Yao, G. Calvez, C. Daiguebonne, K. Bernot, Y. Suffren, M. Puget, C. Lescop, O. Guillou, *Inorg. Chem.* **2017**, *56*, 14632-14642.

[153] D. Shi, X. Yang, H. Chen, D. Jiang, J. Liu, Y. Ma, D. Schipper, R. A. Jones, *Chem. Commun.* **2019**, *55*, 13116-13119.

[154] D. Shi, X. Yang, H. Chen, Y. Ma, D. Schipper, R. A. Jones, *J. Mater. Chem. C* **2019**, *7*, 13425-13431.

[155] D. A. Gálico, J. S. Ovens, M. Murugesu, *Nanoscale* **2020**, *12*, 11435-11439.

[156] D. Shi, X. Yang, Z. Xiao, X. Liu, H. Chen, Y. Ma, D. Schipper, R. A. Jones, *Nanoscale* **2020**, *12*, 1384-1388.

[157] D. A. Gálico, A. A. Kitos, J. S. Ovens, F. A. Sigoli, M. Murugesu, *Angew. Chem. Int. Ed.* **2021**, *60*, 6130-6136.

[158] M. D. Rausch, K. J. Moriarty, J. L. Atwood, J. A. Weeks, W. E. Hunter, H. G. Brittain, *Organometallics* **1986**, *5*, 1281-1283.

[159] P. N. Hazin, C. Lakshminarayan, L. S. Brinen, J. L. Knee, J. W. Bruno, W. E. Streib, K. Folting, *Inorg. Chem.* **1988**, *27*, 1393-1400.

[160] Y. Qiao, D.-C. Sergentu, H. Yin, A. V. Zabula, T. Cheisson, A. McSkimming, B. C. Manor, P. J. Carroll, J. M. Anna, J. Autschbach, *J. Am. Chem. Soc.* **2018**, *140*, 4588-4595.

[161] G. Blasse, A. Bril, *J. Chem. Phys.* **1967**, *47*, 5139-5145.

[162] J. Gracia, L. Seijo, Z. Barandiarán, D. Curulla, H. Niemansverdriet, W. van Gennip, *J. Lumin.* **2008**, *128*, 1248-1254.

[163] R. Valiente, F. Rodríguez, J. González, H. U. Güdel, R. Martín-Rodríguez, L. Nataf, M. N. Sanz-Ortiz, K. Krämer, *Chem. Phys. Lett.* **2009**, *481*, 149-151.

[164] J. He, X. Guo, Y. Chen, R. Shi, Y. Huang, J. Zhang, Y. Wang, Z.-Q. Liu, *Chem. Eur. J.* **2018**, *24*, 1287-1294.

[165] S. Harder, D. Naglav, C. Ruspic, C. Wickleder, M. Adlung, W. Hermes, M. Eul, R. Pöttgen, D. B. Rego, F. Poineau, K. R. Czerwinski, R. H. Herber, I. Nowik, *Chem. Eur. J.* **2013**, *19*, 12272-12280.

[166] D. A. Gálico, J. S. Ovens, F. A. Sigoli, M. Murugesu, *ACS Nano* **2021**, *15*, 5580-5585.

[167] R. A. Layfield, *Organometallics* **2014**, *33*, 1084-1099.

[168] R. A. Layfield, M. Murugesu, *Lanthanides and actinides in molecular magnetism*, John Wiley & Sons, **2015**.

[169] R. Marin, G. Brunet, M. Murugesu, *Angew. Chem. Int. Ed.* **2021**, *60*, 1728-1746.

[170] R. Sessoli, D. Gatteschi, A. Caneschi, M. A. Novak, *Nature* **1993**, *365*, 141-143.

[171] C. Aronica, G. Pilet, G. Chastanet, W. Wernsdorfer, J.-F. Jacquot, D. Luneau, *Angew. Chem. Int. Ed.* **2006**, *45*, 4659-4662.

[172] V. Mereacre, A. M. Ako, R. Clérac, W. Wernsdorfer, I. J. Hewitt, C. E. Anson, A. K. Powell, *Chem. Eur. J.* **2008**, *14*, 3577-3584.

[173] G. Abbas, Y. Lan, V. Mereacre, W. Wernsdorfer, R. Clérac, G. Buth, M. T. Sougrati, F. Grandjean, G. J. Long, C. E. Anson, A. K. Powell, *Inorg. Chem.* **2009**, *48*, 9345-9355.

[174] M. Li, Y. Lan, A. M. Ako, W. Wernsdorfer, C. E. Anson, G. Buth, A. K. Powell, Z. Wang, S. Gao, *Inorg. Chem.* **2010**, *49*, 11587-11594.

[175] D. Schray, G. Abbas, Y. Lan, V. Mereacre, A. Sundt, J. Dreiser, O. Waldmann, G. E. Kostakis, C. E. Anson, A. K. Powell, *Angew. Chem. Int. Ed.* **2010**, *49*, 5185-5188.

[176] K. C. Mondal, A. Sundt, Y. Lan, G. E. Kostakis, O. Waldmann, L. Ungur, L. F. Chibotaru, C. E. Anson, A. K. Powell, *Angew. Chem. Int. Ed.* **2012**, *51*, 7550-7554.

[177] J.-B. Peng, Q.-C. Zhang, X.-J. Kong, Y.-Z. Zheng, Y.-P. Ren, L.-S. Long, R.-B. Huang, L.-S. Zheng, Z. Zheng, *J. Am. Chem. Soc.* **2012**, *134*, 3314-3317.

[178] K. Xiong, X. Wang, F. Jiang, Y. Gai, W. Xu, K. Su, X. Li, D. Yuan, M. Hong, *Chem. Commun.* **2012**, *48*, 7456-7458.

[179] S. K. Langley, D. P. Wielechowski, V. Vieru, N. F. Chilton, B. Moubaraki, B. F. Abrahams, L. F. Chibotaru, K. S. Murray, *Angew. Chem. Int. Ed.* **2013**, *52*, 12014-12019.

[180] L. Ungur, J. J. Le Roy, I. Korobkov, M. Murugesu, L. F. Chibotaru, *Angew. Chem. Int. Ed.* **2014**, *53*, 4413-4417.

[181] Y.-S. Meng, Y.-Q. Zhang, Z.-M. Wang, B.-W. Wang, S. Gao, *Chem. Eur. J.* **2016**, *22*, 12724-12731.

[182] C. A. Goodwin, F. Ortu, D. Reta, N. F. Chilton, D. P. Mills, *Nature* **2017**, *548*, 439-442.

[183] F.-S. Guo, B. M. Day, Y.-C. Chen, M.-L. Tong, A. Mansikkamäki, R. A. Layfield, *Angew. Chem. Int. Ed.* **2017**, *56*, 11445-11449.

[184] F.-S. Guo, B. M. Day, Y.-C. Chen, M.-L. Tong, A. Mansikkamäki, R. A. Layfield, *Science* **2018**, *362*, 1400-1403.

[185] C. A. Gould, K. R. McClain, D. Reta, J. G. C. Kragskow, D. A. Marchiori, E. Lachman, E.-S. Choi, J. G. Analytis, R. D. Britt, N. F. Chilton, B. G. Harvey, J. R. Long, *Science* **2022**, *375*, 198-202.

[186] N. Mavragani, D. Errulat, D. A. Gálico, A. A. Kitos, A. Mansikkamäki, M. Murugesu, *Angew. Chem. Int. Ed.* **2021**, *60*, 24206-24213.

[187] P. Richardson, R. Marin, Y. Zhang, B. Gabidullin, J. Ovens, J. O. Moilanen, M. Murugesu, *Chem. Eur. J.* **2021**, *27*, 2361-2370.

[188] B. M. Day, F.-S. Guo, R. A. Layfield, *Acc. Chem. Res.* **2018**, *51*, 1880-1889.

[189] K. L. M. Harriman, J. L. Brosmer, L. Ungur, P. L. Diaconescu, M. Murugesu, *J. Am. Chem. Soc.* **2017**, *139*, 1420-1423.

[190] J. Flores Gonzalez, H. Douib, B. Le Guennic, F. Pointillart, O. Cador, *Inorg. Chem.* **2021**, *60*, 540-544.

[191] T. Pugh, V. Vieru, L. F. Chibotaru, R. A. Layfield, *Chem. Sci.* **2016**, *7*, 2128-2137.

[192] R. Grindell, B. M. Day, F.-S. Guo, T. Pugh, R. A. Layfield, *Chem. Commun.* **2017**, *53*, 9990-9993.

[193] J. Sieler, A. Simon, K. Peters, R. Taube, M. Geitner, *J. Organomet. Chem.* **1989**, *362*, 297-303.

[194] W. J. Evans, G. W. Rabe, M. A. Ansari, J. W. Ziller, *Angew. Chem. Int. Ed. Engl.* **1994**, *33*, 2110-2111.

[195] Z. Hou, Y. Zhang, O. Tardif, Y. Wakatsuki, *J. Am. Chem. Soc.* **2001**, *123*, 9216-9217.

[196] M. D. Walter, F. Weber, G. Wolmershäuser, H. Sitzmann, *Angew. Chem. Int. Ed.* **2006**, *45*, 1903-1905.

[197] V. Lorenz, A. Edelmann, S. Blaurock, F. Freise, F. T. Edelmann, *Organometallics* **2007**, *26*, 4708-4710.

[198] J. Cheng, K. Saliu, G. Y. Kiel, M. J. Ferguson, R. McDonald, J. Takats, *Angew. Chem. Int. Ed.* **2008**, *47*, 4910-4913.

[199] M. D. Morse, *Chem. Rev.* **1986**, *86*, 1049-1109.

[200] M. Moskovits, *Annu. Rev. Phys. Chem.* **1991**, *42*, 465-499.

[201] J. P. Wilcoxon, B. L. Abrams, *Chem. Soc. Rev.* **2006**, *35*, 1162-1194.

[202] J.-C. G. Bünzli, *Chem. Rev.* **2010**, *110*, 2729-2755.

[203] H. Yin, P. J. Carroll, J. M. Anna, E. J. Schelter, *J. Am. Chem. Soc.* **2015**, *137*, 9234-9237.

[204] H. Yin, P. J. Carroll, B. C. Manor, J. M. Anna, E. J. Schelter, *J. Am. Chem. Soc.* **2016**, *138*, 5984-5993.

[205] H. Yin, Y. Jin, J. E. Hertzog, K. C. Mullane, P. J. Carroll, B. C. Manor, J. M. Anna, E. J. Schelter, *J. Am. Chem. Soc.* **2016**, *138*, 16266-16273.

[206] Y. Qiao, E. J. Schelter, *Acc. Chem. Res.* **2018**, *51*, 2926-2936.

[207] Y. Qiao, T. Cheisson, B. C. Manor, P. J. Carroll, E. J. Schelter, *Chem. Commun.* **2019**, *55*, 4067-4070.

[208] P. L. Watson, J. F. Whitney, R. L. Harlow, *Inorg. Chem.* **1981**, *20*, 3271-3278.

[209] H.-S. Chan, Q. Yang, T. C. W. Mak, Z. Xie, *J. Organomet. Chem.* **2000**, *601*, 160-163.

[210] M. W. Bouwkamp, P. H. M. Budzelaar, J. Gercama, I. Del Hierro Morales, J. de Wolf, A. Meetsma, S. I. Troyanov, J. H. Teuben, B. Hessen, *J. Am. Chem. Soc.* **2005**, *127*, 14310-14319.

[211] M. D. Walter, D. Bentz, F. Weber, O. Schmitt, G. Wolmershäuser, H. Sitzmann, *New J. Chem.* **2007**, *31*, 305-318.

[212] M. E. Minyaev, A. A. Vinogradov, D. M. Roitershtein, R. S. Borisov, I. V. Ananyev, A. V. Churakov, I. E. Nifant'ev, *J. Organomet. Chem.* **2016**, *818*, 128-136.

[213] P. B. Hitchcock, A. G. Hulkes, M. F. Lappert, *Inorg. Chem.* **2004**, *43*, 1031-1038.

[214] L. Hirneise, C. Maichle-Mössmer, R. Anwander, *Inorg. Chem.* **2021**, *60*, 18211-18224.

E

Publications

Paper I

Nanoscale Organolanthanum Clusters: Nuclearity-Directing Role of Cyclopentadienyl and Halogenido Ligands

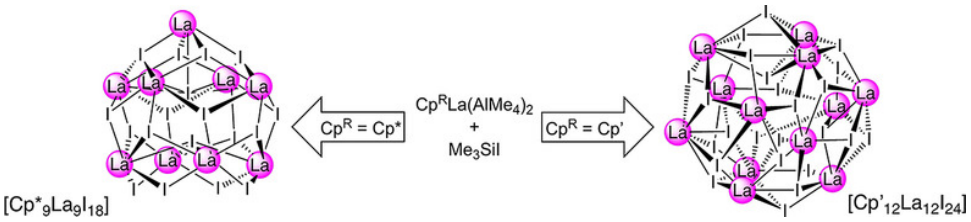

https://doi.org/10.1002/chem.202001482
Chem. Eur. J. ***2020****, 26, 10834 – 10840*

Chemistry Europe
European Chemical Societies Publishing

Organometallic Chemistry

Nanoscale Organolanthanum Clusters: Nuclearity-Directing Role of Cyclopentadienyl and Halogenido Ligands

Dennis A. Buschmann,[a] H. Martin Dietrich,[a] David Schneider,[a] Verena M. Birkelbach,[a] Christoph Stuhl,[a] Karl W. Törnroos,[b] Cäcilia Maichle-Mössmer,[a] and Reiner Anwander*[a]

Abstract: Tetramethylaluminato/halogenido(X) ligand exchange reactions in half-sandwich complexes $[Cp^RLa(AlMe_4)_2]$ are feasible in non-coordinating solvents and provide access to large coordination clusters of the type $[Cp^RLaX_2]_x$. Incomplete exchange reactions generate the hexalanthanum clusters $[Cp^R_6La_6X_8(AlMe_4)_4]$ ($Cp^R = Cp^* = C_5Me_5$, X = I; $Cp^R = Cp' = C_5H_4SiMe_3$, X = Br, I). Treatment of $[Cp^*La(AlMe_4)_2]$ with two equivalents Me_3SiI gave the nonalanthanum cluster $[Cp^*LaI_2]_9$, while the exhaustive reaction of $[Cp'La(AlMe_4)_2]$ with the halogenido transfer reagents Me_3GeX and Me_3SiX (X = I, Br, Cl) produced a series of monocyclopentadienyl rare-earth-metal clusters with distinct nuclearity. Depending on the halogenido ion size the homometallic clusters $[Cp'LaCl_2]_{10}$ and $[Cp'LaX_2]_{12}$ (X = Br, I) could be isolated, whereas different crystallization techniques led to the aggregation of clusters of distinct structural motifs, including the desilylated cyclopentadienyl-bridged cluster $[(\mu\text{-}Cp)_2\text{-}Cp'_8La_8I_{14}]$ and the heteroaluminato derivative $[Cp'_{10}La_{10}Br_{18}(AlBr_2Me_2)_2]$. The use of the Cp′ ancillary ligand facilitates cluster characterization by means of NMR spectroscopy.

Introduction

High-nuclearity rare-earth-metal (Ln) coordination clusters not only impress by sheer beauty but have gained increasingly in significance for magnetic and optical applications.[1,2] The so far largest Ln^{III} clusters have been achieved by self-assembly processes under hydrothermal or solvothermal conditions involving ligand ("carboxylato")- and pH-controlled, anion-templated hydrolyses.[3] The obtained nanoscale rare-earth-metal hydroxide clusters can be sub-divided into Ln-exclusive (e.g., $\{Gd_{140}\}$,[4] $\{Nd_{104}\}$,[5] $\{Dy_{76}\}$,[6] $\{Gd_{60}\}$[7]) and heterometallic 4f-3d derivatives (e.g., $\{Dy_{96}Ni_{64}\}$,[8] $\{La_{60}Ni_{76}\}$,[9] $\{Gd_{102}Ni_{36}\}$[10]), featuring overall complicated compositions such as $[Gd_{140}(\mu_3\text{-}OH)_{100}(CH_3COO)_{80}(LH_3)_{40}(H_2O)_{200}](NO_3)_{80}(H_2O)_x$ ($x \approx 80$; LH_6 = myo-inositol)[4] or $[Dy_{96}Ni_{64}(\mu_3\text{-}OH)_{156}(IDA)_{66}(DMPA)_{12}(CH_3COO)_{48}(NO_3)_{24}(H_2O)_{64}]Cl_{24}$ (IDA = iminodiacetate, DMPA = 2,2-dimethylol propionic acid).[8] Self-assembly processes in non-aqueous media as a rule produce significantly lower nuclearities as shown for, e.g., the selenide complexes $[(py)_{16}Ce_{17}NaSe_{18}(SePh)_{16}]$[11] and $[(py)_{24}Pr_{28}F_{68}(SePh)_{16}]$,[12] which display effective near-IR emitters. The syntheses of the latter fluorido-rich clusters from $Ln(SePh_3)$ and NH_4F in pyridine clearly emphasize the mandatory switch to distinct reaction protocols.[12]

In 1998, the highly symmetric chlorido-bridged $[Cp_{12}Sm_{12}Cl_{24}]$ emerged as a benchmark system in organolanthanide cluster chemistry.[13,14] This dodecanuclear cluster was obtained by desolvating $[CpSmCl_2(thf)_3]$ under reflux and repeatedly extracting it with toluene at 80 °C.[15] Ever since, the nuclearity of $\{Sm_{12}\}$ has remained unmatched for cyclopentadienyl-based derivatives (and organometallics in general), while the routinely observed nuclearity of the involved ring and cluster motifs seems stationary at $\{Ln_6\}$.[16] Crucially, while metallocene complexes of the general formula Cp_2LnX tend to form dimeric and higher-ring structures (highly polarized Ln–X bonding, X = small electron-withdrawing ligand),[17–19] donor-free half-sandwich complexes $CpLnX_2$ are prone to coordination cluster formation.[14,16] Beside $[Cp_{12}Sm_{12}Cl_{24}]$,[13] the only other reported donor-free $CpLnX_2$ derivatives comprise ring-like $[Cp^*_4Sc_4I_8]$[20] and $[Cp^*_3Dy_3I_6]$ ($Cp^* = C_5Me_5$).[21] Related mixed-valent $[Cp^*_6Yb_4I_4]$[22] and $[Cp^*_5Sm_5I_9]$,[23] Cp-enriched congeners $[Cp^*_6Yb_5F_9]$[24] and $[Cp^*_6Sm_5Cl_9]$,[21] as well as heterobimetallic $[Cp_7Dy_7I_{14}](\mu\text{-}I)[Cp_2V]$[25] form cluster motifs. Viable synthesis protocols for the half-sandwich coordination clusters include salt metathesis,[16b,e–g] hydrogenolysis,[16d,h] thermolysis/desolvation,[13,26] and Ln redox transformations.[21–25,27,28] In the realm of Ziegler–Natta catalysts and respective model compounds, we have embarked on alkylaluminato/halogenido ligand exchange and donor-promoted alkylaluminate cleavage

[a] D. A. Buschmann, Dr. H. M. Dietrich, Dr. D. Schneider, Dr. V. M. Birkelbach, Dr. C. Stuhl, Dr. C. Maichle-Mössmer, Prof. Dr. R. Anwander
Institut für Anorganische Chemie, Eberhard Karls Universität Tübingen
Auf der Morgenstelle 18, 72076 Tübingen (Germany)
E-mail: reiner.anwander@uni-tuebingen.de

[b] Prof. Dr. K. W. Törnroos
Department of Chemistry, University of Bergen
Allégaten 41, 5007 Bergen (Norway)

Supporting information and the ORCID identification number(s) for the author(s) of this article can be found under: https://doi.org/10.1002/chem.202001482.

of discrete half-sandwich complexes [Cp*Ln(AlMe$_4$)$_2$][29] and gained access to {La$_6$} and {Gd$_8$} entities of the type [Cp*$_6$La$_6$Cl$_8$(AlMe$_4$)$_4$][30] and [(Cp*$_8$Gd$_8$Me$_4$(AlMe$_4$)$_4$(CH$_2$O*t*Bu)$_8$].[31] Spurred by the ease and efficiency of the former partial alkyl-aluminato/halogenido ligand exchange and the dearth of data on higher-nuclearity organolanthanide clusters, we now targeted new types of donor-free CpLnX$_2$ derivatives via complete alkyl/halogenido exchange.

Results and Discussion

C$_5$Me$_5$ (Cp*)-supported half-sandwich La^{III} iodide clusters

To adequately assess any partial/complete alkyl/halogenido exchange in terms of structural implications, we initially selected the iodination reaction of known [Cp*La(AlMe$_4$)$_2$] (**1 a**)[29] with Me$_3$SiI. Thereby, the large La^{III} center and the large I$^-$ anion were anticipated to promote the formation of maximum-nuclearity clusters.

Accordingly, complex **1 a** was treated with various amounts of Me$_3$SiI. Already the equimolar reaction in unstirred *n*-hexane solutions led to the crystallization of the hexanuclear cluster [Cp*$_6$La$_6$I$_8$(AlMe$_4$)$_4$] (**2**) at ambient temperature within hours. Compound **2** incorporates one solvent molecule per cluster in the crystal lattice, which could not be removed in oil pump vacuum, and crystallized in the triclinic space group $P\bar{1}$. Complex **2** has the connectivity [La$_6$Cp*$_6${(μ-Me)$_3$AlMe}$_4$(μ$_3$-I)$_2$(μ$_2$-I)$_6$] (Figure S23) and is isostructural to the previously reported chloride complex [Cp*$_6$La$_6$Cl$_8$(AlMe$_4$)$_4$].[30] Thereby, two "Cp*$_3$La$_3$X$_4$" subunits are linked through the four tetramethyl-aluminato ligands in a μ$_2$-η^1:η^2 fashion. Each lanthanum atom is eight-coordinated by three iodido, two methyl, and one Cp* ligand. While the La–Cp* ancillary ligand distances as well as the aluminato coordination behavior are only marginally affected by the Cl$^-$/I$^-$ halogenido exchange, the La–Cl/I distances differ markedly by nature (La–Cl: 2.8049(9), 2.8439(9) Å (μ$_2$); 3.0060(7)–3.0708(8) Å (μ$_3$) versus La–I: 3.2096(4)–3.2323(5) Å (μ$_2$); 3.2327(4)–3.4366(4) Å (μ$_3$)).

Intriguingly, treatment of **1 a** with two equivalents of Me$_3$SiI afforded complete alkyl/halogenido exchange as envisaged (Scheme 1), and even more interestingly the hoped-for cluster enlargement. Nonametallic [Cp*$_9$La$_9$I$_{18}$] (**3**) is the first of its kind and its crystal structure is depicted in Figure 1. Crystalline **3** contains two independent clusters and 14 molecules of toluene in the unit cell. The large amount of solvent remained partly in the crystal lattice even when oil pump vacuum was applied. The nine lanthanum centers constitute a pseudo-tridecahedron with each metal center shielded by a Cp* ligand. The five lanthanum centers of the square pyramidal subunit are additionally coordinated by four μ$_3$-bridging iodido anions and one central μ$_5$-I. Eight out of a total of 12 μ$_3$-bridging iodido anions connect to the four lanthanum centers of the square planar subunit. These four lanthanum centers are μ$_2$-bridged with iodido anions to build a crown-like motif, and are further sharing a central μ$_4$-bridging iodido moiety. Complex **3** readily dissolves in THF to generate monomeric [Cp*LaI$_2$(thf)$_3$] (Figure S25).

The number of structurally characterized organometallic complexes containing iodido-bridged lanthanum atoms are limited. For comparison, the La–(μ$_2$-I) distances of 3.2050(7)–3.2561(7) Å are slightly shorter than those in [La(μ$_2$-I){N(SiMe$_3$)$_2$}$_2$(thf)]$_2$[32] (3.3096(11), 3.3051(11) Å) or [(COT)La(μ$_2$-I)(thf)$_2$]$_2$[33] (3.3832(2), 3.3157(2) Å). A series of salt-like mixed iodido/ethanido lanthanum-based solid-state materials including o-La$_5$I$_9$(C$_2$)[34a] and La$_{10}$I$_{15}$(C$_2$)$_2$[34b] were shown to feature La–(μ$_3$-I) (3.225(3)–3.544(2) Å) and La–(μ$_4$-I) moieties (3.1722(7)–3.3795(4) Å), which, however, appear considerably shorter than the distances of 3.1857(7)–3.6720(7) Å (μ$_3$) and 3.5187(7)–3.5447(7) Å (μ$_4$) in **3**. Surprisingly, organolanthanum complexes with μ$_5$-bridging iodido ligands seem even rarer. However, the

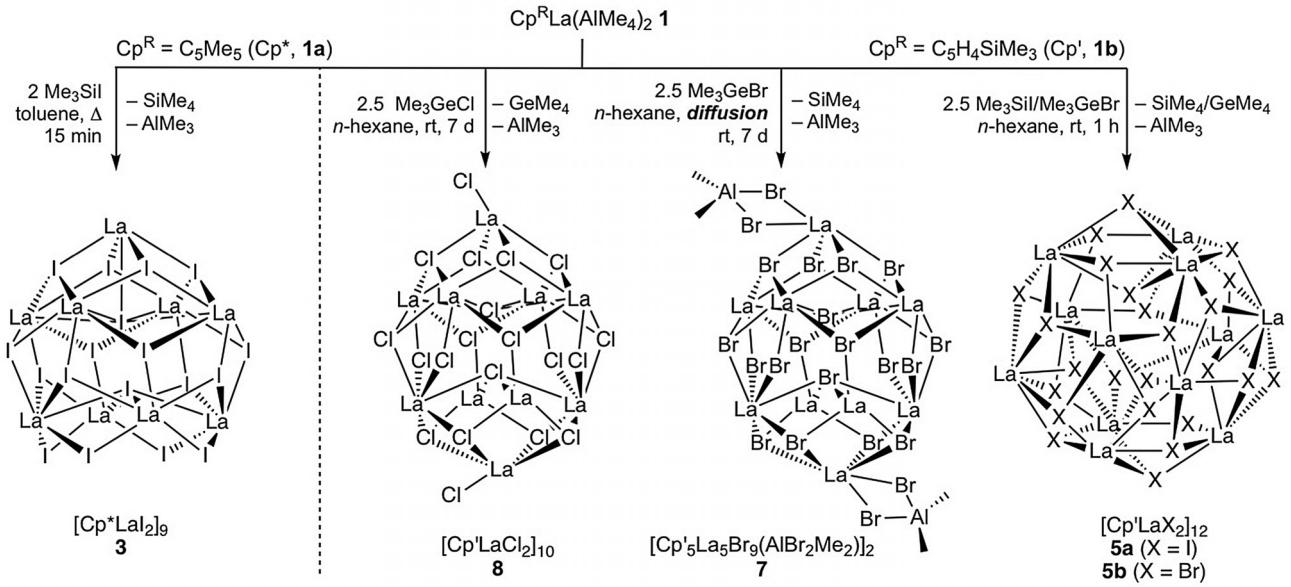

Scheme 1. Reactivity of half-sandwich complexes **1** toward halogenido transfer reagents applying different synthesis strategies (Cp′ and Cp* ligands are omitted for clarity).

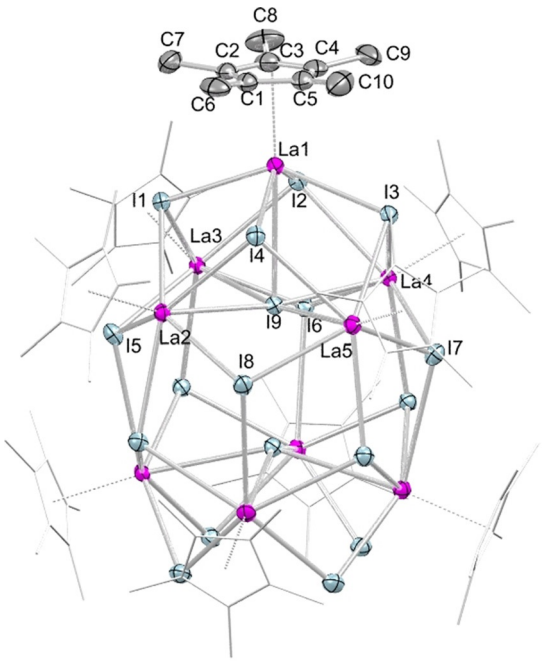

Figure 1. Crystal structure of **3** with atomic displacement parameters set at the 50% probability level. Hydrogen atoms are omitted for clarity. The Cp* ligands (except for one) are represented by a wireframe model for improved visualization. For selected interatomic distances and angles, see the Supporting Information.

La–(μ_5-I) distances of 3.5335(7)–3.6885(6) Å in **3** are comparable to the Sm–(μ_5-I) distances in octa- and pentametallic complexes $[\{[\mu\text{-}Ph_2C(C_4H_3N)_2]Sm\}_5(\mu_5\text{-}I)]^-$ $[\{[\mu\text{-}Ph_2C(C_4H_3N)_2]Sm(thf)\}_3(\mu_3\text{-}I)]^+$ and $[\{[\mu\text{-}MePhC(C_4H_3N)_2]Sm\}_5(\mu_5\text{-}I)]^-[K(thf)_6]^+$, respectively, where the samarium atoms are pentagonally arranged around a coplanar iodido ion (Sm–(μ_5-I), 3.434(1)–3.634(1); 3.517(1)–3.5566(6) Å).[35] For further comparison, a similar square pyramidal $\{Ln_5\}$ structural motif was also detected in donor-free mixed-valent complex $[Cp^*_5Sm_5(\mu_2\text{-}I)_4(\mu_3\text{-}I)_4(\mu_5\text{-}I)]$ (Sm–(μ_5-I): 3.281(1)–3.377(1) Å),[23] while the separated ion-pair $[Cp_6Yb_6Cl_{13}]^-[Cp_3Yb_3Cl_5(thf)_3]^+$ features another "nonametallic" half-sandwich arrangement.[13]

$C_5H_4SiMe_3$ (Cp′)-supported half-sandwich La^{III} iodide clusters

Having established the proof of concept for efficient cluster enlargement in Cp* derivatives $[Cp^*LnX_2]_x$, the next step was to investigate into the effect of the cyclopentadienyl ligand. Here, we decided upon the trimethylsilyl cyclopentadienyl (Cp′) ligand, offering two decisive advantages compared to Cp* derivatives: overall decreased steric demand (enforcing cluster enlargement) and mediation of better solubility (facilitating NMR-spectroscopic characterization). The half-sandwich lanthanum bis(tetramethylaluminato) precursor complex $[Cp'La(AlMe_4)_2]$ (**1b**) was straightforwardly synthesized from homoleptic $La(AlMe_4)_3$ and KCp′ following routine protocols.[36] Rather unexpectedly, the crystal structure of **1b** shows a symmetric tetramethylaluminato coordination with two planar $La(\mu\text{-}Me)_2Al$ units (in contrast to one planar and one bent one as routinely observed).[36] As a consequence, steric saturation of the La^{III} centers in **1b** is achieved by interaction with one aluminato methyl group of another molecule resulting in a μ_2-η^1:η^2 aluminato coordination mode. These weak intermolecular interactions (La···C 3.250 Å) imply a dimeric arrangement in the solid state (Figure S21).

Surprisingly, treatment of **1b** with two equivalents of Me_3SiI at ambient temperature in *n*-hexane did not result in the envisaged complete alkyl/halogenido exchange, but the tetramethylaluminato-bridged heterobimetallic hexalanthanum cluster $[Cp'_6La_6I_8(AlMe_4)_4]$ (**4a**). Again surprisingly, compound **4a** is isostructural to the Cp* derivatives $[Cp^*_6La_6Cl_8(AlMe_4)_4]$ and **2** (Figures 2 and S23).[30] Overall, the arrangement of the six lanthanum metal centers is reminiscent of two cuboid structures with cut-off corners. Complexes $[Cp^R_6La_6X_8(AlMe_4)_4]$ show similar metrical parameters concerning the lanthanum metal centers and the ancillary Cp^R moieties ($[Cp^*_6La_6Cl_8(AlMe_4)_4]$: 2.728(3)–2.819(4) Å; **2**: 2.748(4)–2.797(4); **4a**: 2.711(6)–2.793(5) Å). A striking difference of the La_3X_4 subunits is revealed by the bond angles. More precisely, the La–Cl–La angles of 100.55(2)–113.19(4)° are more obtuse than La–I–La angles in **2** (100.126(2)–108.169(2)°) and **4a** (99.962(2)–106.822(2)°), resulting in a maximum difference of 6.37°.

Crucially, complete $AlMe_4$/halogenido exchange could be accomplished by the addition of a slight excess of Me_3SiI (2.5 equiv.) to **1b** under vigorous stirring (Scheme 1), as confirmed by the isolation of the dodecalanthanum cluster $[Cp'LaI_2]_{12}$ (**5a**, 48% yield). XRD analysis of **5a** revealed a La_{12} icosahedron, with each of the 20 faces capped by one iodido

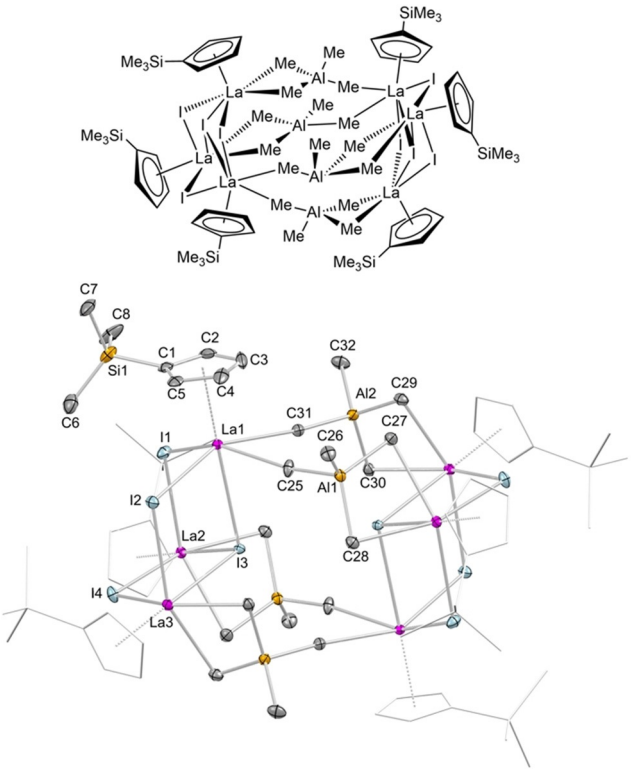

Figure 2. Molecular drawing (top) and crystal structure (bottom) of **4a** with atomic displacement parameters set at the 50% probability level. Hydrogen atoms are omitted for clarity. The Cp′ ligands (except for one) are represented by a wireframe model for improved visualization. For selected interatomic distances and angles, see the Supporting Information.

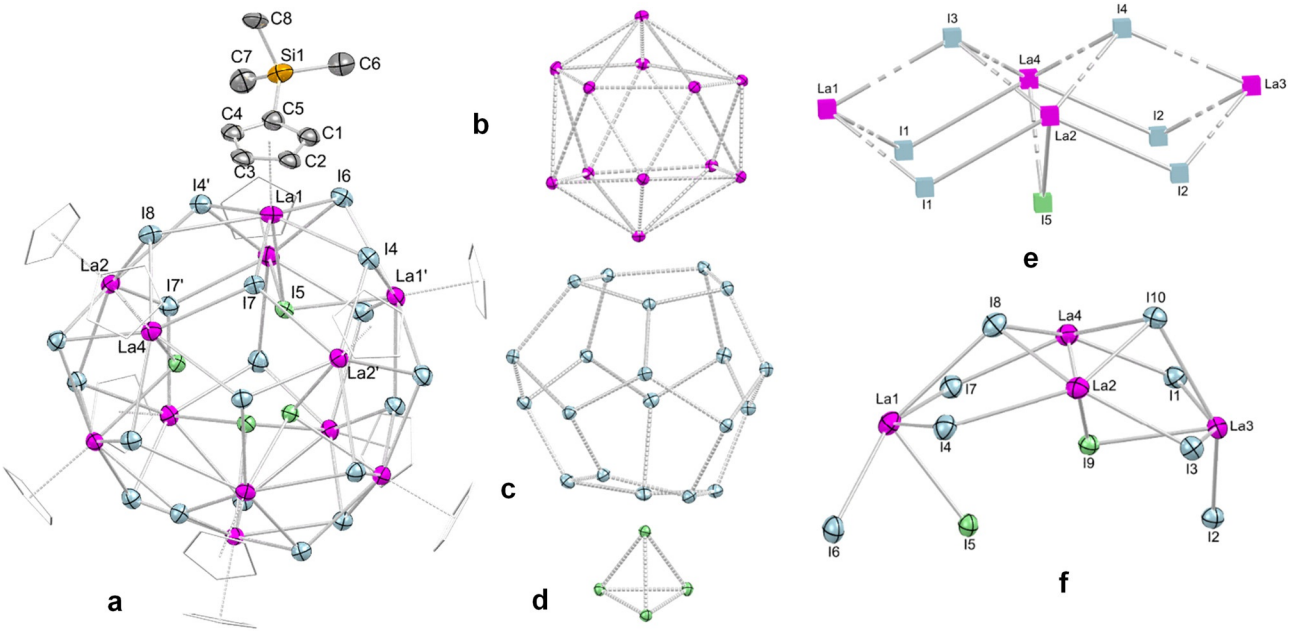

Figure 3. Crystal structure of **5a** with atomic displacement parameters set at the 50% probability level. a) The entire molecule with hydrogen atoms omitted for clarity and Cp′ ligands (except for one) represented by a wireframe model for improved visualization. (b), (c), and (d) represent the La_{12}, I_{20}, and I_4 polyhedra; comparison of the asymmetric unit (f) with the solid-state-structure of LaI_3 ((e), adapted from Zachariasen).[38] For selected interatomic distances and angles, see the Supporting Information.

ligand, as depicted in Figure 3 (space group *R*3*c*). The iodido ligands arrange in a dodecahedron with one additional I_4 tetrahedron located inside the cluster core. Complex **5a** is isostructural to the until-now unique dodecasamarium cluster $[CpSmCl_2]_{12}$, reported by Kretschmer et al. in 1998 (space group $I4_1/acd$).[13] For comparison, the Sm–Cl bond lengths at the cluster surface in $[CpSmCl_2]_{12}$ are in the range of 2.70(1) to 3.10(2) Å (av. 2.99 Å) and average 2.95 Å inside the cluster core. In contrast, the respective La–I bond lengths in the cluster periphery of **5a** average 3.3625 Å, being therefore considerably longer than inside the cluster core (av. La–I 3.2808 Å). Taking into account the ionic radii (Sm^{3+} + Cl^- = 2.77 Å; La^{3+} + I^- = 3.19 Å),[37] the average interatomic distances in $\{Sm_{12}\}$ and $\{La_{12}\}$ (**5a**) are noticeably larger. However, the overall bonding situation in these clusters is almost identical, differing marginally by only 0.021 Å. The asymmetric unit of **5a** shows a distinct La_4I_7 structural motif, which can be considered a distorted cutout of the LaI_3 solid-state structure,[38] indicating the general stability of the cluster (Figure S28).

The differences in the solid-state structures of **5a** (formally 9-coordinate La centers) and LaI_3 (8-coordinate La centers) are evidenced by the bent arrangement of the asymmetric unit in **5a**. More precisely, the La–I distances of 3.211(2), 3.267(2) and 3.287(2) Å (La1–I4/I7, La4–I7) in **5a** are slightly shorter than in LaI_3 (3.342 Å), while the La2–I1 bond length of 3.585(2) Å in **2** is considerably longer compared to LaI_3 (3.396 Å). The bending of the asymmetric unit of **5a** is further evidenced by marked differences in the interatomic distances of the central iodido ligands to La1 and La3 (La···I9: **5a**, 5.152(2), 3.303(2) Å), which is significantly shorter than in LaI_3 (5.638 Å). This results in a strongly bent arrangement of the La_4I_7 fragment in accord with the obtuse I–La–I angles in **5a** (I4–La1–I7 = 122.95(5)°, I1–La3–I3 = 146.00(5)°), while in lanthanum iodide the respective angle is 80.97°. This arrangement is clearly affected by the shielding and the steric effect of the ancillary Cp′ ligands. Comparison may be also drawn to the similarly sized metalloid aluminum cluster $[Al_{50}Cp^*_{12}]$ (diameter: 14.9 Å, **5a**: 14.6 Å), the topology of the 60 methyl groups of which bearing a close resemblance to that of fullerene C_{60}.[39] Indeed, Kretschmer et al. had also pointed out that the truncated icosahedron adopted by the 60 carbon atoms of 12 Cp ligand in $[CpSmCl_2]_{12}$ is "somewhat analogous" to fullerene C_{60}.[13]

In contrast to the hardly soluble (in non-donor solvents) Cp*-derived clusters **2** and **3**,[30] the new Cp′-supported clusters **4a** and **5a** dissolve readily in benzene. However, the ^{1}H NMR spectrum of methylaluminate/iodide cluster **4a** in [D$_6$]benzene at ambient temperature (Figure S5) revealed its fragmentation in solution, which is indicated by the appearance of additional resonances for **1b** and **5a**. Moreover, the triplet resonances at 6.78 and 6.66 ppm ($^3J_{H,H}$ = 2.5 Hz) and the multiplets at 6.74 and 6.63 ppm indicate non-equivalent Cp′ ligands, which is corroborated by signals at 0.41 and 0.37 ppm for the $SiMe_3$ groups. The singlet at −0.03 ppm can be assigned to the La-[$AlMe_4$] moieties of **4a**, indicating a rapid exchange of bridging and terminal methyl groups. The ^{1}H NMR spectrum of dodecalanthanum cluster $[Cp'La_2]_{12}$ (**5a**) in [D$_6$]benzene shows one signal set for the Cp′ ligands, indicating dynamic processes of **4a** in solution. The Cp′ hydrogen atoms at the positions 3/4 and 2/5 resonate at 7.20 ppm and 7.00 ppm, respectively, and the trimethylsilyl group at 0.61 ppm, significantly shifted to lower field in comparison to the corresponding signals of precursor **1b** (δ Cp′*H*, 6.40 ppm, 6.22 ppm, δ *CH*$_3$, 0.14 ppm). Moreover, a second set of signals with the same 6:1 integral ratio of singlet and triplets revealed the formation of another

similar species in solution. Therefore, a three-step process for the formation of cluster **5a** seems plausible: initial complete $[AlMe_4]$/I ligand exchange, followed by aggregation to $Cp'_4La_4I_8$ fragments, and subsequent self-assembly of three such La_4 units to afford the large $Cp'_{12}La_{12}I_{24}$ entity.

Supportive of such a mechanism of formation is the isolation and structural characterization of the mixed-Cp octalanthanum species $[(\mu\text{-Cp})_2Cp'_8La_8I_{14}]$ (**6**). Applying slow diffusion of Me_3SiI (2.5 equiv., dissolved in *n*-hexane) into an *n*-hexane solution of **1b** (instead of vigorous stirring) and subsequent crystallization at −40 °C afforded compound **6** in low yield (Figure 4 and Figure S29). An XRD analysis revealed that cluster **6** is composed of two $Cp'_4La_4I_7$ subunits with two eight- and nine-coordinate lanthanum centers each (4× μ_2-I, 2× μ_3-I, 1× μ_4-I), thus resembling the asymmetric unit of cluster **5a** (Figure 3). The nine-coordinate lanthanum centers at the vertices of the La1La2La1′ La2′ planar rectangular arrangement are μ_2:η^5,η^5-interconnected by unsubstituted cyclopentadienyl ligands in an inverse-sandwich-type fashion. The steric demand of the bridging Cp ligands effects the $Cp'_4La_4I_7$ subunits, resulting in an overall high symmetry in comparison to the asymmetric unit of **5a**.

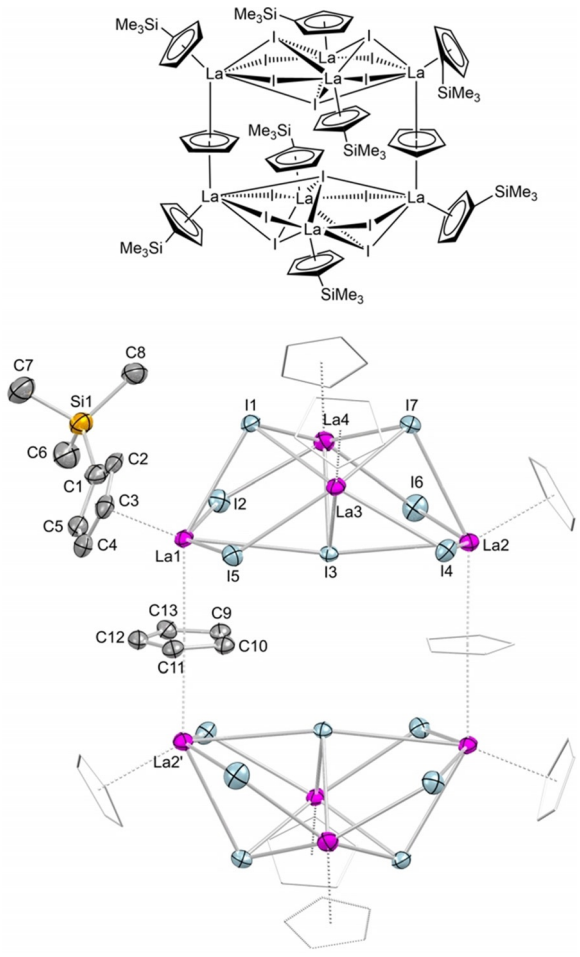

Figure 4. Molecular drawing (top) and crystal structure (bottom) of **6** with atomic displacement parameters set at the 50% probability level. Hydrogen atoms are omitted for clarity. The Cp′ ligands (except for one) are represented by a wireframe model and without $SiMe_3$ groups for improved visualization. For selected interatomic distances and angles, see the Supporting Information.

In complex **5a**, the outmost La–I bonds of the heavily distorted asymmetric unit are markedly elongated (La2–I4, 3.585(2) Å) to adapt to the stable La_{12} structure, while the respective bonds in **6** are in the range of 3.186(1) Å (La4–I6) to 3.292(2) Å (La2–I6). Moreover, the subunit of **6** shows a reduced interatomic distance between the outer lanthanum metal center and the central iodido ligand (La1–I3 = 3.734(1) Å; **5a**: La1···I9 = 5.152(2) Å), which might be due to the strain induced by the bridging Cp ligands.

^{1}H NMR spectroscopic studies corroborate the displacement of the trimethylsilyl groups from the respective Cp′ ligands in **6** (formation of Si_2Me_6 evidenced for three independent samples, Figure S11), subsequently enabling the bridging of the La_4I_7 fragments. It must be noted that the "Wanderlust" of trimethylsilyl groups has been recently emphasized in rare-earth metal triple-decker sandwich complexes of the type $Ln_2(COT'')_3$ (COT″ = bis(trimethylsilyl) cyclooctatetraenyl).[40] The ease of $SiMe_3$ dissociation in HCp′ is also reflected in the synthesis of the precursor of cluster $[CpSmCl_2]_{12}$ by dehalosilylation employing $SmCl_3$.[13] The ^{1}H NMR spectrum of **6** shows the presence of side products, while the protons at the 2/5 positions and 3/4 positions of the Cp′ ligand resonate at 7.19 and 7.00 ppm, respectively, and overlap with the respective signals of **5a** (minor product). The signals in the range of 1.64 to 0.92 ppm are likely generated by a solution side product, and the Me_3Si groups resonate at 0.61 ppm. It must be noted that the Cp′ resonances are shifted to higher field compared to precursor **1b**. Overall, the formation of the lanthanum iodide clusters **5a** and **6** is mainly depending on the crystallization technique, indicating a strong kinetic control of the alkylaluminato/halogenido ligand exchange reaction. Complex **5a** readily dissolves in THF to generate monomeric $[Cp'LaI_2(thf)_3]$ (Figure S22). Complexes **4a**, **5a** and **6** were further analyzed by SEM and EDX to check product purity via elemental ratios (Figures S41–S48, Tables S3–S14).

$C_5H_4SiMe_3$ (Cp′)-supported half-sandwich La^{III} bromide and chloride clusters

Changing the halogenido transfer reagent to Me_3GeBr while applying otherwise identical reaction protocols, the respective bromido-bridged clusters $[Cp'_6La_6Br_8(AlMe_4)_4]$ (**4b**) and $[Cp'LaBr_2]_{12}$ (**5b**) could be isolated. Accordingly, treatment of complex **1b** with 1.3 equiv. of Me_3GeBr afforded the heterobimetallic hexalanthanum cluster **4b** (Figure S30), which is isostructural to $[Cp^*_6La_6Cl_8(AlMe_4)_4]$,[30] **2**, and **4a**. Compound **4b** shows degradation behavior similar to **4a**, as indicated by NMR spectroscopy (Figures S12 and S13). The dodecalanthanum cluster **5b** could be selectively obtained by treatment of **1b** with 2.5 equiv. Me_3GeBr in a vigorously stirred *n*-hexane solution at ambient temperature (Scheme 1, 47% yield). The structural characterization of **5b** by XRD analysis (Figure S31) revealed the same structural motif as for the respective iodido-bridged cluster **5a**, with the La–Br distances following the same trend. The ^{1}H NMR spectrum of **5b** shows the expected set of signals for the Cp′ ligand, indicating a highly symmetric

coordination. In comparison to **5a** the signals are shifted to higher field.

Interestingly, a divergent reactivity was observed when applying the diffusion protocol. Thereby, the bromido transfer gave the decalanthanum cluster $[Cp'_{10}La_{10}Br_{18}(AlBr_2Me_2)_2]$ (**7**) featuring two heteroaluminato ligands (Scheme 1). The XRD analysis of **7** revealed an ellipsoidal structural motif involving eight lanthanum atoms, being terminated by two additional peripheral lanthanum metal centers (Figure 5 and Figure S32). The lanthanum centers at these apical positions coordinate to a η^5-Cp′ ligand, a $AlBr_2Me_2$ moiety, and cap a La_4Br_4 crown. The four lanthanum centers of the latter crown interact further with a central bromido ligand and another eight bromido ligands, which bridge to the other four lanthanum centers of the second La_4Br_4 crown. Overall, the eight inner lanthanum centers are connected to a total of $16\times\mu_3$-I and $2\times\mu_4$-I, as well as $8\times\eta^5$-Cp′. The terminal heteroaluminato ligands $[(\mu_2\text{-}Br)_2AlMe_2]$ in complex **7** coordinate symmetrically in a η^2 fashion to the lanthanum metal centers (La1–Br1 = 3.0945(4) Å, La1–Br2 = 3.0595(5) Å), involving La···Al distances of av. 4.0745 Å which are significantly longer than in complex **1b** (av. La···Al = 3.2678 Å). Similar alkyl/chlorido heteroaluminato moieties were previously reported for metallocene complexes of the type $[Cp^*_2Ln(\mu\text{-}Cl)_2AlR_2]$ (Ln = Y, Sm; R = Me, Et, *i*Bu).[41] The La–Br bond lengths of the apical 11-coordinate lanthanum to the La_4Br_4 crown are in the range of 3.1450(4) to 3.3167(4) Å, and hence longer than in lanthanum bromide $LaBr_3$ (9-coordinate La^{III}, 3.101 to 3.158 Å).[42]

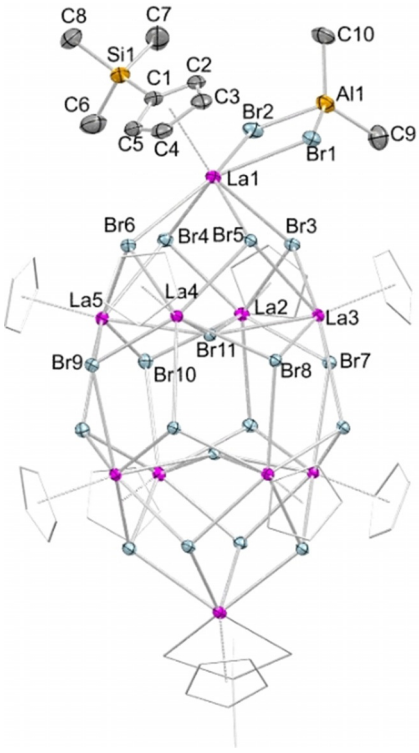

Figure 5. Crystal structure of **7** with atomic displacement parameters set at the 50% probability level. Hydrogen atoms are omitted for clarity. The Cp′ ligands (except for one) are represented by a wireframe model for improved visualization. For selected interatomic distances and angles, see the Supporting Information.

For further comparison, the La–(μ_4-Br) distances in **7** are similar, ranging from 3.2244(4) to 3.2758(4) Å. The ^{1}H NMR spectrum of compound **7** indicates the presence of dodecalanthanum cluster **5b** along with another minor co-product. The separation of **5b** and **7**, however, is hampered by similar crystal morphology and solubility (Figure S16). The trimethylsilyl groups of the Cp′ ligands of compound **7** resonate in the range of 0.64 to 0.42 ppm in accordance with non-equivalent positions. The heteroaluminato ligands $[AlMe_2Br_2]$ show one broad singlet at 0.33 ppm. EDX analyses for compounds **4b**, **5b**, and **7** were impeded by the overlap of the element signals of Al and Br, making a meaningful quantification of these elements difficult. Nevertheless, the atom ratios of lanthanum are within the expected range, further supporting the formation and purity of the respective clusters (Figures S49–S57, Tables S15–S26).

Using Me_3GeCl as the halogenido transfer reagent, the exclusive formation of one species was observed, regardless of the synthesis methods applied. Treatment of **1b** with Me_3GeCl resulted in the formation of the decalanthanum cluster $[Cp'LaCl_2]_{10}$ (**8**), featuring a similar structural motif as bromide cluster **7**. Instead of the terminal $AlMe_2Br_2$ ligands in complex **7**, the lanthanum metal centers in the apical positions of **8** bear terminal chlorido ligands. The connectivity of **8** was elucidated by XRD analysis (Figure S33). The ^{1}H NMR spectrum of **8** shows the expected set of signals for the Cp′ ligand as well as signals of a solution side product. In comparison to complexes **5a** and **5b**, the signals are shifted to lower field. The formation of **8** is further confirmed by an EDX analysis, which revealed the expected elemental ratios (Figures S58–S60, Tables S27–S30).

Conclusions

Half-sandwich complexes $[Cp^RLa(AlMe_4)_2]$ engage in selective alkyl/halogenido(X) ligand exchange reactions in non-coordinating solvents under mild conditions. The fully exchanged donor solvent-free $[Cp^RLaX_2]$ self-assemble to form distinct nanoscale coordination clusters. The size of the homometallic clusters depends on the steric demand of the cyclopentadienyl and halogenido ligands as revealed for $[Cp^*_9La_9I_{18}]$, $[Cp'_{10}La_{10}Cl_{20}]$, and $[Cp'_{12}La_{12}X_{24}]$ (X = Br, I). Moreover, the cluster formation/crystallization procedure is shown to affect the cluster composition, and more crucially, the use of the trimethylsilyl-substituted cyclopentadienyl ligand (Cp′) implies high cluster solubility and hence characterization by means of solution NMR spectroscopy. The isolation of such nanoscale clusters proves that the fascinating icosahedral arrangement of samarium centers detected ca. 20 years ago in $[Cp_{12}Sm_{12}Cl_{24}]$[13] is not a one-off occurrence in rare-earth metal chemistry. It can be anticipated that the present nanochemistry approach, which utilizes highly reactive organometallics and mild halogen-transfer reagents such as Me_3SiI or Me_3GeX (X = Br, Cl), will decisively promote the field of nanoscale rare-earth-metal cluster research. The findings might also stimulate similar research with paramagnetic rare-earth metals opening new avenues for the design of luminescent and magnetic clusters and materials.[2]

Experimental Section

Crystallographic data

Deposition Numbers 1992037, 1992038, 1992039, 1992040, 1992041, 1992042, 1992043, 1992044, 1992045, 1992046, 1992047, and 1992048 contain the supplementary crystallographic data for this paper. These data are provided free of charge by the joint Cambridge Crystallographic Data Centre and Fachinformationszentrum Karlsruhe Access Structures service.

Acknowledgements

We are grateful to the German Science Foundation for financial support (Grant AN 238/14-2).

Conflict of interest

The authors declare no conflict of interest.

Keywords: clusters · cyclopentadienyl · halogenido · lanthanum · self-assembly

[1] a) X.-Y. Zheng, X.-J. Kong, Z. Zheng, L.-S. Long, L.-S. Zheng, *Acc. Chem. Res.* **2018**, *51*, 517 – 525; b) X.-Y. Zheng, J. Xie, X.-J. Kong, L.-S. Long, L.-S. Zheng, *Coord. Chem. Rev.* **2019**, *378*, 222 – 236.
[2] a) F. Habib, M. Murugesu, *Chem. Soc. Rev.* **2013**, *42*, 3278 – 3288; b) D. N. Woodruff, R. E. P. Winpenny, R. A. Layfield, *Chem. Rev.* **2013**, *113*, 5110 – 5148; c) B. M. Day, F.-S. Guo, R. A. Layfield, *Acc. Chem. Res.* **2018**, *51*, 1880 – 1889.
[3] G. A. Kumar, R. E. Riman, J. G. Brennan, *Coord. Chem. Rev.* **2014**, *273 – 274*, 111 – 124.
[4] X.-Y. Zheng, J.-H. Jiang, G.-L. Zhuang, D.-P. Liu, H.-G. Liao, X.-J. Kong, L.-S. Long, L.-S. Zheng, *J. Am. Chem. Soc.* **2017**, *139*, 18178 – 18181.
[5] J.-B. Peng, X.-J. Kong, Q.-C. Zhang, M. Orendác, J. Prokleska, Y.-P. Ren, L.-S. Long, Z. Zheng, L.-S. Zheng, *J. Am. Chem. Soc.* **2014**, *136*, 17938 – 17941.
[6] X.-Y. Li, H.-F. Su, Q.-W. Li, R. Feng, H.-Y. Bai, H.-Y. Chen, J. Xu, X.-H. Bu, *Angew. Chem. Int. Ed.* **2019**, *58*, 10184 – 10188; *Angew. Chem.* **2019**, *131*, 10290 – 10294.
[7] L. Qin, G.-J. Zhuo, Y.-Z. Yu, H. Nojiri, C. Schöder, R. E. P. Winpenny, Y.-Z. Zheng, *J. Am. Chem. Soc.* **2017**, *139*, 16405 – 16411.
[8] W.-P. Chen, P.-Q. Liao, Y. Yu, Z. Zheng, X.-M. Chen, Y.-Z. Zheng, *Angew. Chem. Int. Ed.* **2016**, *55*, 9375 – 9379; *Angew. Chem.* **2016**, *128*, 9521 – 9525.
[9] X.-J. Kong, L.-S. Long, R.-B. Huang, L.-S. Zheng, T. D. Harris, Z. Zheng, *Chem. Commun.* **2009**, 4354 – 4356.
[10] W.-P. Chen, P.-Q. Liao, P.-B. Jin, L. Zhang, B.-K. Ling, S.-C. Wang, Y.-T. Chan, X.-M. Chen, Y.-Z. Zheng, *J. Am. Chem. Soc.* **2020**, *142*, 4663 – 4670.
[11] B. F. Moore, G. A. Kumar, M.-C. Tan, J. Kohl, R. E. Riman, M. G. Brik, T. J. Emge, J. G. Brennan, *J. Am. Chem. Soc.* **2011**, *133*, 373 – 378.
[12] M. Romanelli, G. A. Kumar, T. J. Emge, R. E. Riman, J. G. Brennan, *Angew. Chem. Int. Ed.* **2008**, *47*, 6049 – 6051; *Angew. Chem.* **2008**, *120*, 6138 – 6140.
[13] W. P. Kretschmer, J. H. Teuben, S. I. Troyanov, *Angew. Chem. Int. Ed.* **1998**, *37*, 88 – 90; *Angew. Chem.* **1998**, *110*, 92 – 94.
[14] R. Anwander, *Angew. Chem. Int. Ed.* **1998**, *37*, 599 – 602; *Angew. Chem.* **1998**, *110*, 619 – 622.
[15] $[Cp_{12}Sm_{12}Cl_{24}]$ was obtained in 35% yield and any analytical and spectroscopic data were not provided.
[16] For examples, see; a) J. Sieler, A. Simon, K. Peters, R. Taube, M. Geitner, *J. Organomet. Chem.* **1989**, *362*, 297 – 303; b) W. J. Evans, G. W. Rabe, M. A. Ansari, J. W. Ziller, *Angew. Chem. Int. Ed. Engl.* **1994**, *33*, 2110 – 2111; *Angew. Chem.* **1994**, *106*, 2200 – 2201; c) S. P. Constantine, G. M. De Lima, P. B. Hitchcock, J. M. Keates, G. A. Lawless, *Chem. Commun.* **1996**, 2421 – 2422; d) Z. Hou, Y. Zhang, O. Tardif, Y. Wakatsuki, *J. Am. Chem. Soc.* **2001**, *123*, 9216 – 9217; e) F. Bonnet, M. Visseaux, D. Barbier-Baudry, A. Hafid, E. Vigier, M. Kubicki, *Inorg. Chem.* **2004**, *43*, 3682 – 3690; f) M. D. Walter, F. Weber, G. Wolmershäuser, H. Sitzmann, *Angew. Chem. Int. Ed.* **2006**, *45*, 1903 – 1905; *Angew. Chem.* **2006**, *118*, 1937 – 1939; g) V. Lorenz, A. Edelmann, S. Blaurock, F. Freise, F. T. Edelmann, *Organometallics* **2007**, *26*, 4708 – 4710; h) J. Cheng, K. Saliu, G. Y. Kiel, M. J. Ferguson, R. McDonald, J. Takats, *Angew. Chem. Int. Ed.* **2008**, *47*, 4910 – 4913; *Angew. Chem.* **2008**, *120*, 4988 – 4991.
[17] W. J. Evans, S. E. Foster, *J. Organomet. Chem.* **1992**, *433*, 79 – 94.
[18] N. S. Radu, F. J. Hollander, T. D. Tilley, A. L. Rheingold, *Chem. Commun.* **1996**, 2459 – 2460.
[19] K. N. Raymond, C. W. Eigenbrot, Jr., *Acc. Chem. Res.* **1980**, *13*, 276 – 283.
[20] K. A. Tupper, T. D. Tilley, *J. Organomet. Chem.* **2005**, *690*, 1689 – 1698.
[21] W. J. Evans, T. M. Champagne, B. L. Davis, N. T. Allen, G. W. Nyce, M. A. Johnston, Y.-C. Lin, A. Khvostov, J. W. Ziller, *J. Coord. Chem.* **2006**, *59*, 1069 – 1087.
[22] C. J. Burns, D. J. Berg, R. A. Andersen, *J. Chem. Soc. Chem. Commun.* **1987**, 272 – 273.
[23] A. M. Bienfait, B. M. Wolf, K. W. Törnroos, R. Anwander, *Organometallics* **2016**, *35*, 3743 – 3750.
[24] P. L. Watson, T. H. Tulip, I. Williams, *Organometallics* **1990**, *9*, 1999 – 2009.
[25] M. E. Burin, M. V. Smirnova, G. K. Fukin, E. V. Baranov, M. N. Bochkarev, *Eur. J. Inorg. Chem.* **2006**, 351 – 356.
[26] C. O. Hollfelder, L. N. Jende, H. M. Dietrich, K. Eichele, C. Maichle-Mössmer, R. Anwander, *Chem. Eur. J.* **2019**, *25*, 7298 – 7302.
[27] M. T. Dumas, G. P. Chen, J. Y. Hu, M. A. Nascimento, J. M. Rawson, J. W. Ziller, F. Furche, W. J. Evans, *J. Organomet. Chem.* **2017**, *849*, 38 – 47.
[28] C. Schoo, S. Bestgen, A. Egeberg, J. Seibert, S. N. Konchenko, C. Feldmann, P. W. Roesky, *Angew. Chem. Int. Ed.* **2019**, *58*, 4386 – 4389; *Angew. Chem.* **2019**, *131*, 4430 – 4434.
[29] H. M. Dietrich, C. Zapilko, K. W. Törnroos, R. Anwander, *Organometallics* **2005**, *24*, 5767 – 5771.
[30] H. M. Dietrich, O. Schuster, K. W. Törnroos, R. Anwander, *Angew. Chem. Int. Ed.* **2006**, *45*, 4858 – 4863; *Angew. Chem.* **2006**, *118*, 4977 – 4982.
[31] C. O. Hollfelder, M. Meermann-Zimmermann, G. Spiridopoulos, D. Werner, K. W. Törnroos, C. Maichle-Mössmer, R. Anwander, *Molecules* **2019**, *24*, 3703.
[32] J. Collin, N. Giuseppone, N. Jaber, A. Domingos, L. Maria, I. Santos, *J. Organomet. Chem.* **2001**, *628*, 271 – 274.
[33] C. Meermann, K. Ohno, K. W. Törnroos, K. Mashima, R. Anwander, *Eur. J. Inorg. Chem.* **2009**, 76 – 85.
[34] a) H. Mattausch, C. Hoch, A. Simon, *Z. Anorg. Allg. Chem.* **2008**, *634*, 641 – 645; b) H. Mattausch, C. Hoch, A. Simon, *Z. Anorg. Allg. Chem.* **2005**, *631*, 1423 – 1429.
[35] a) T. Dubé, S. Conoci, S. Gambarotta, G. P. A. Yap, G. Vasapollo, *Angew. Chem. Int. Ed.* **1999**, *38*, 3657 – 3659; *Angew. Chem.* **1999**, *111*, 3890 – 3892; b) T. Dubé, S. Conoci, S. Gambarotta, G. P. A. Yap, *Organometallics* **2000**, *19*, 1182 – 1185.
[36] a) M. Zimmermann, N. Å. Frøystein, A. Fischbach, P. Sirsch, H. M. Dietrich, K. W. Törnroos, E. Herdtweck, R. Anwander, *Chem. Eur. J.* **2007**, *13*, 8784 – 8800; b) G. Occhipinti, C. Meermann, H. M. Dietrich, R. Litlabø, F. Auras, K. W. Törnroos, C. Maichle-Mössmer, V. R. Jensen, R. Anwander, *J. Am. Chem. Soc.* **2011**, *133*, 6323 – 6337.
[37] R. Shannon, *Acta Crystallogr. Sect. A* **1976**, *32*, 751 – 767.
[38] W. H. Zachariasen, *Acta Crystallogr.* **1948**, *1*, 265 – 268.
[39] J. Vollet, J. R. Hartig, H. Schnöckel, *Angew. Chem. Int. Ed.* **2004**, *43*, 3186 – 3189; *Angew. Chem.* **2004**, *116*, 3248 – 3252.
[40] V. Lorenz, P. Liebing, A. Bathelier, F. Engelhardt, L. Maron, L. Hilfert, S. Busse, F. T. Edelmann, *Chem. Commun.* **2018**, *54*, 10280 – 10283.
[41] W. J. Evans, T. M. Champagne, D. G. Giarikos, J. W. Ziller, *Organometallics* **2005**, *24*, 570 – 579.
[42] K. Krämer, T. Schleid, M. Schulze, W. Urland, G. Meyer, *Z. Anorg. Allg. Chem.* **1989**, *575*, 61 – 70.

Manuscript received: March 27, 2020
Accepted manuscript online: April 24, 2020
Version of record online: July 27, 2020

Chemistry–A European Journal

Supporting Information

Nanoscale Organolanthanum Clusters: Nuclearity-Directing Role of Cyclopentadienyl and Halogenido Ligands

Dennis A. Buschmann,[a] H. Martin Dietrich,[a] David Schneider,[a] Verena M. Birkelbach,[a] Christoph Stuhl,[a] Karl W. Törnroos,[b] Cäcilia Maichle-Mössmer,[a] and Reiner Anwander*[a]

Table of Contents

Experimental Section

General Considerations. All manipulations were performed under rigorous exclusion of air and moisture using standard Schlenk and glovebox techniques (MBraun MB200B; <0.1 ppm O_2, <0.1 ppm H_2O, argon atmosphere). The solvents *n*-hexane and toluene were purified using Grubbs-type columns (MBraun SPS, solvent purification system). [D_6]benzene (99.6%, Sigma-Aldrich) and [D_8]toluene (99.6%, Sigma-Aldrich) were dried over Na/K-alloy for at least 24 h and subsequently filtrated. All solvents were stored inside a glovebox. Pentamethylcyclopentadiene (98%) and trimethylsilyl cyclopentadiene (HCp', 97%) was obtained from abcr and used as received. Potassium trimethylsilyl cyclopentadienide was prepared according to standard procedures by treatment of the proligand with potassium.[2] Iodotrimethylsilane (97%, stabilized with copper), bromotrimethylsilane (98%), bromotrimethylgermane (98%), chlorotrimethylsilane (99%) and chlorotrimethylgermane (98%) were purchased from abcr and used without further purification. Homoleptic [$La(AlMe_4)_3$][2] and half-sandwich complex [$Cp^*La(AlMe_4)_2$] (**1a**)[3] were synthesized according to literature procedures. NMR spectra of air and moisture sensitive compounds were recorded by using J. Young valve NMR tubes at ambient temperature on a Bruker AVII+400 (^{1}H: 400.11 MHz; ^{13}C: 100.61 MHz) spectrometer. NMR chemical shifts are referenced to internal solvent resonances and reported in parts per million relative to tetramethylsilane. Coupling constants are given in Hertz. Elemental analyses were performed on an Elementar Vario Micro Cube. IR spectra were recorded on a NICOLET 6700 FTIR spectrometer with a DRIFT cell (KBr window, Kubelka-Munk conversion). EDX spectra were recorded on a HITACHI SU8030 scanning electron microscope.

Cp'La(AlMe$_4$)$_2$ (1b). To a suspension of potassium trimethylsilyl cyclopentadiene ($KC_5H_4SiMe_3$ = KCp') (89.95 mg, 0.51 mmol) in toluene (5 mL) a solution of [$La(AlMe_4)_3$] (200.14 mg, 0.5 mmol) in *n*-hexane (5 mL) was added under vigorous stirring. After stirring the reaction mixture for 4 h at ambient temperature, the suspension was centrifuged, the supernatant filtered, and the solvent was removed *in vacuo* to give **1b** as an off-white oil. Crystalline **1b** was obtained from a saturated *n*-hexane solution at -40 °C (216 mg, 0.48 mmol, 92%). ^{1}H NMR (400 MHz, [D_6]benzene, 26 °C): δ = 6.41 (t, $^3J_{H,H}$ = 2.5 Hz, 2H, 3/4 Cp*H*), 6.23 (t, $^3J_{H,H}$ = 2.5 Hz, 2H, 2/5 Cp*H*), 0.15 (s, 9H, Si*Me*$_3$), -0.27 (s, 24H, Al*Me*$_4$) ppm. ^{13}C{^{1}H} NMR (101 MHz, [D_6]benzene, 26 °C): δ = 129.4 (*Cp*), 124.8 (*Cp*), 121.5 (*Cp*), 2.2 (bs, Al*Me*$_4$), 0.3 (Si*Me*$_3$) ppm. IR (DRIFT): $\tilde{\upsilon}$ = 3080 (vw), 2950 (m), 2918 (s), 2890 (s), 2848 (m), 2817 (w), 2780 (w), 2021 (vw), 1763 (vw), 1705 (vw), 1671 (vw), 1610 (vw), 1442 (w), 1416 (w), 1365 (w), 1310 (vw), 1248 (s), 1200 (s), 1184 (s), 1171 (s), 1043 (vs), 901 (m), 838 (vs), 803 (vs), 755 (m), 706 (vs), 639 (m), 626

(m), 589 (m), 573 (m), 511 (m), 468 (vw), 419 (m), 405 (vw) cm^{-1}. Elemental analysis of **1b** calculated for $C_{16}H_{37}Al_2LaSi$ (450.41 g/mol): C 42.67%, H 8.28%; found: C 43.14%, 8.24%.

[Cp'LaI$_2$(thf)$_3$]. [Cp'La(AlMe$_4$)$_2$] (**1b**, 11.26 mg, 0.025 mmol) was dissolved in toluene (2 mL), Me$_3$SiI (10.01 mg, 0.05 mmol) was added, and the vial was shaken vigorously. After 5 min, 5 ml THF was added to the solution, and the vial was stored at -40 °C for 16 h. Afterwards, the solvent was removed *in vacuo*. Crystalline [Cp'LaI$_2$(thf)$_3$] was obtained from a saturated *n*-hexane/THF solution at -40 °C (15.37 mg, 0.021 mmol, 82%). Residual adduct AlMe$_3$(thf) was removed by trituating the crystalline material with *n*-hexane. ^{1}H NMR (400 MHz, [D$_8$]thf, 26 °C): δ = 6.64 (t, $^3J_{H,H}$ = 2.5 Hz, 2H, 3/4 Cp*H*), 6.42 (t, $^3J_{H,H}$ = 2.5 Hz, 2H, 2/5 Cp*H*), 3.61 (m, 6H, C$_4$*H*$_8$O), 1.77 (m, 6H, C$_4$*H*$_8$O), 0.29 (s, 9H, Si*Me*$_3$) ppm. ^{13}C{^{1}H} NMR (101 MHz, [D$_8$]thf, 26 °C): δ = 126.4 (*Cp*), 122.0 (*Cp*), 120.3 (*Cp*), 68.2 (*C*$_4$H$_8$O), 26.4 (*C*$_4$H$_8$O), 1.2 (Si*Me*$_3$) ppm. IR (DRIFT): $\tilde{\nu}$ = 3071 (vw), 2950 (w), 2925 (w), 2889 (w), 1683 (vw), 1651 (vw), 1594 (vw), 1456 (w), 1442 (w), 1404 (vw), 1364 (w), 1310 (vw), 1245 (m), 1173 (m), 1040 (m), 1012 (m), 901 (m), 835 (vs), 793 (vs), 759 (m), 752 (m), 704 (w), 693 (w), 638 (w), 627 (w), 419 (vs) cm^{-1}.

[Cp*$_6$La$_6$I$_8$(AlMe$_4$)$_4$] (2). A solution of SiMe$_3$I (116 mg, 0.58 mmol) in *n*-hexane (2 mL) was added to a solution of [Cp*La(AlMe$_4$)$_2$] (200 mg, 0.45 mmol) in *n*-hexane (2 mL). The reaction was stirred overnight at ambient temperatures. The precipitate was allowed to settle, washed with *n*-hexane (3 x 1 mL), and dried *in vacuo* to afford **2** as white powder (200 mg, 0.065 mmol, 87%). Crystals could be obtained by performing the reaction under the same conditions without stirring. ^{1}H NMR (500 MHz, [D$_6$]benzene, 26 °C): δ = 2.33 (broad irregular signal, 75 H, Cp*), -0.09 (s, 12H, *Me*Al) ppm; due to the poor solubility of **2** any meaningful NMR spectra could not be obtained. IR (DRIFT): $\tilde{\nu}$ = 2954 (s), 2915 (s), 2857 (m), 1487 (w), 1454 (m), 1436 (m), 1419 (w), 1388 (vw), 1378 (w), 1195 (m), 1037 (m), 1026 (m), 768 (w), 698 (vs), 616 (s), 583 (m), 555 (w), 523 (w) cm^{-1}. Elemental analysis of **2** calculated for $C_{76}H_{138}Al_4I_8La_6$ x C_6H_{14} (3094.71 g/mol): C 31.83, H 4.95; found: C 32.26, H 4.76.

[Cp*LaI$_2$]$_9$ (3). [Cp*La(AlMe$_4$)$_2$] (**1a**, 322 mg, 0.718 mmol) was dissolved in 5 ml toluene, and Me$_3$SiI (287 mg, 1.436 mmol) was added under pivoting and afterwards the solution was heated to the boiling point for 15 min. Upon storing at ambient temperature, crystallization occurred. After 8 h, 181 mg of **3** could be harvested as colorless crystals by decanting the mother liquor and drying in oil pump vacuum. After 36 h, another 54 mg of **3** were harvested, adding up to an overall yield of 58%. IR (DRIFT): 2972 (s), 2940 (s), 2898 (vs), 2855 (s), 1494 (m), 1451 (s), 1432 (s), 1377 (s), 1023 (s), 728 (s), 694 (m), 594 (w), 464 (w) cm^{-1}. Elemental analysis of **3** calculated for $C_{90}H_{135}I_{18}La_9 \cdot (C_7H_8)_3$ (5027.874 g/mol): C 26.52,

H 3.19; found C 26.37, H 2.87. The cluster is insufficiently soluble for proper NMR spectroscopy in [D_6]benzene and dissolves in [D_8]thf under formation of [Cp*$LaI_2(thf)_3$].

[Cp'$_6$La$_6$I$_8$(AlMe$_4$)$_4$] (4a). [Cp'La($AlMe_4$)$_2$] (**1b**, 56.3 mg, 0.125 mmol) was dissolved in *n*-hexane (3 mL), Me_3SiI (50.0 mg, 0.25 mmol) was added, and the vial was shaken vigorously. Within several days, **4a** formed as colorless crystals (23.1 mg, 0.008 mmol, 38%). ^{1}H NMR (400 MHz, [D_6]benzene, 26 °C): δ = 6.78 (t, $^3J_{H,H}$ = 2.5 Hz, 1H, 3/4 Cp*H*), 6.74 (m, 2H, Cp*H*), 6.66 (t, $^3J_{H,H}$ = 2.5 Hz, 1H, 2/5 Cp*H*), 6.63 (m, 2H, Cp*H*), 0.41 (s, 10H, Si*Me$_3$*), 0.37 (s, 5H, Si*Me$_3$*), -0.04 (s, 3H, Al*Me$_4$*) ppm. ^{13}C{^{1}H} NMR (101 MHz, [D_6]benzene, 26 °C): δ = 125.3 (*Cp*), 123.5 (*Cp*), 122.6 (*Cp*) 122.3 (*Cp*), 2.2 (Al*Me$_4$*), 1.0 (Si*Me$_3$*) ppm. IR (DRIFT): ῡ = 3077 (vw), 2952 (w), 2924 (w), 2913 (w), 2847 (vw), 1443 (w), 1403 (vw), 1365 (w), 1310 (vw), 1248 (s), 1201 (w), 1189 (w), 1171 (m), 1042 (s), 1028 (m), 901 (m), 837 (vs), 799 (vs), 756 (m), 699 (s), 637 (w), 626 (m), 590 (w), 586 (w), 553 (vw), 530 (vw), 420 (w), 416 (w) cm^{-1}. Elemental analysis of **4a** calculated for $C_{64}H_{126}I_8La_8Si_6Al_4$ (3020.76 g/mol): C 25.45%, H 4.20%; found: C 27.43%, H 4.47%. The significantly increased carbon content can be attributed to the presence of unreacted **1b**.

[Cp'$_6$La$_6$Br$_8$(AlMe$_4$)$_4$] (4b). [Cp'La($AlMe_4$)$_2$] (**1b**, 45.04 mg, 0.1 mmol) was dissolved in *n*-hexane (3 mL), Me_3SiBr (19.9 mg, 0.13 mmol) was added, and the reaction mixture was shaken vigorously. Within several days, **3b** formed as colorless crystals (43.5 mg, 0.016 mmol, 96%). ^{1}H NMR (400 MHz, [D_6]benzene, 26 °C): δ = 6.49 (t, $^3J_{H,H}$ = 2.5 Hz, 2H, 3/4 Cp*H*), 6.19 (t, $^3J_{H,H}$ = 2.5 Hz, 2H, 2/5 Cp*H*), 0.61 (s, 6H, Si*Me$_3$*), 0.57 (s, 9H, Si*Me$_3$*), 0.43 (s, 3H, Si*Me$_3$*), 0.17 (s, 9H, Si*Me$_3$*), -0.22 (bs, 6H, Al*Me$_4$*), -0.24 (bs, 3H, Al*Me$_4$*) ppm. ^{13}C{^{1}H} NMR (101 MHz, [D_6]benzene, 26 °C): δ = 123.2 (*Cp*), 119.7 (*Cp*), 2.2 (Al*Me$_4$*), 0.9 (Si*Me$_3$*), 0.2 (Si*Me$_3$*) ppm. IR (DRIFT): ῡ = 3071 (vw), 2951 (w), 2914 (w), 2894 (w), 2846 (vw), 1443 (vw), 1404 (vw), 1365 (vw), 1309 (vw), 1248 (m), 1188 (w), 1173 (m), 1042 (m), 902 (m), 839 (vs), 798 (vs), 756 (m), 701 (s), 638 (w), 626 (m), 591 (w), 550 (w), 528 (vw), 421 (m) cm^{-1}. Elemental analysis of **4b** calculated for $C_{70}H_{140}Br_8La_6Si_6$ (2730.99 g/mol): C 30.79%, H 5.17%; found: C 30.87%, H 5.06%.

[Cp'LaI$_2$]$_{12}$ (5a). [Cp'La($AlMe_4$)$_2$] (**1b**, 56.3 mg, 0.13 mmol) was dissolved in *n*-hexane (15 mL), and Me_3SiI (62.5 mg, 0.31 mmol) was added under vigorous stirring. After stirring the reaction mixture for 4 h at ambient temperature, the suspension was filtered. Within several hours at ambient temperature, **5** formed as colorless crystals (31.70 mg, 0.01 mmol, 48%). ^{1}H NMR (400 MHz, [D_6]benzene, 26 °C): δ = 7.20 (t, $^3J_{H,H}$ = 2.5 Hz, 2H, 3/4 Cp*H*), 7.00 (t, $^3J_{H,H}$ = 2.5 Hz, 2H, 2/5 Cp*H*), 0.61 (s, 9H, Si*Me$_3$*) ppm. ^{13}C{^{1}H} NMR (101 MHz, [D_6]benzene, 26 °C): δ = 131.7 (*Cp*), 125.5 (*Cp*), 123.8 (*Cp*), 1.8 (Si*Me$_3$*) ppm. IR (DRIFT): ῡ = 3079 (vw), 2950 (w), 2893 (vw), 2720 (vw), 1937 (vw), 1742 (vw), 1687 (vw), 1649

(vw), 1590 (vw), 1441 (w), 1405 (w), 1365 (w), 1309 (vw), 1248 (vs), 1170 (m), 1042 (s), 901 (s), 845 (vs), 837 (vs), 830 (vs), 802 (vs), 795 (vs), 755 (m), 692 (vw), 639 (w), 626 (m), 426 (vs), 420 (s) cm^{-1}. Elemental analysis of **5** calculated for $C_{96}H_{156}I_{24}La_{12}Si_{12}$ (6359.80 g/mol): C 18.13%, H 2.47%; found: C 18.26%, H 2.76%.

[Cp'LaBr$_2$]$_{12}$ (5b). [Cp'La(AlMe$_4$)$_2$] (**1b**, 56.3 mg, 0.13 mmol) was dissolved in *n*-hexane (15 mL), and Me$_3$GeBr (61.8 mg, 0.31 mmol) was added under vigorous stirring. After stirring the reaction mixture for 4 h at ambient temperature, the suspension was filtered. Within several days at ambient temperature, **5b** and **5b'** (*n*-hexane in crystal lattice) formed as colorless crystals (25.35 mg, 0.01 mmol, 47%). ^{1}H NMR (400 MHz, [D$_6$]benzene, 26 °C): δ = 7.08 (t, $^3J_{H,H}$ = 2.5 Hz, 2H, 3/4 Cp*H*), 6.97 (t, $^3J_{H,H}$ = 2.5 Hz, 2H, 2/5 Cp*H*), 0.63 (s, 9H, Si*Me$_3$*) ppm. ^{13}C{^{1}H} NMR (101 MHz, [D$_6$]benzene, 26 °C): δ = 131.0 (*Cp*), 125.2 (*Cp*), 123.7 (*Cp*), 1.2 (Si*Me$_3$*) ppm. IR (DRIFT): ῡ = 3092 (vw), 3079 (vw), 2951 (w), 2893 (w), 1743 (vw), 1689 (vw), 1650 (vw), 1593 (vw), 1443 (w), 1403 (w), 1365 (w), 1311 (w), 1246 (m), 1214 (vw), 1192 (vw), 1172 (m), 1061 (w), 1042 (m), 902 (w), 853 (m), 836 (m), 801 (m), 756 (w), 692 (w), 640 (w), 626 (w), 422 (m), 415 (vs) cm^{-1}. Elemental analysis of **5b** calculated for $C_{96}H_{156}Br_{24}La_{12}Si_{12}$ (5232.04 g/mol): C 22.04%, H 3.01%; found: C 22.92%, H 2.96%. The high carbon value can be attributed to residual *n*-hexane in the crystal lattice.

[(*μ*-Cp)$_2$Cp'$_8$La$_8$I$_{14}$] (6). In a 20-mL vial, [Cp'La(AlMe$_4$)$_2$] (**1b**, 56.43 mg, 0.13mmol) was dissolved in *n*-hexane (10 mL). In a 5-mL vial, Me$_3$SiI (62.53 mg, 0.31 mmol) was dissolved in *n*-hexane (1 mL). The smaller vial was placed inside the bigger one with the [Cp'La(AlMe$_4$)$_2$] solution, and the large vial was sealed afterwards. Diffusion of the Me$_3$SiI into the [Cp'La(AlMe$_4$)$_2$] solution and storing the vial at -40 °C for 1 h led to the formation of crystalline **6**. ^{1}H NMR (400 MHz, [D$_6$]benzene, 26 °C): δ = 7.19 (t, $^3J_{H,H}$ = 2.5 Hz, 3/4 Cp*H*), 7.00 (t, $^3J_{H,H}$ = 2.5 Hz, 2/5 Cp*H*), 6.92 (t, $^3J_{H,H}$ = 2.5 Hz, *μ*-Cp*H*), 6.88 (t, $^3J_{H,H}$ = 2.5 Hz, *μ*-Cp*H*), 6.68 (t, $^3J_{H,H}$ = 2.5 Hz, *μ*-Cp*H*), 6.62 (t, $^3J_{H,H}$ = 2.5 Hz, *μ*-Cp*H*), 0.61 (s, Si*Me$_3$*) ppm. ^{13}C{^{1}H} NMR (101 MHz, [D$_6$]benzene, 26 °C): δ = 120.4 (*Cp*), 116.9 (*μ-Cp*), 1.8 (Si*Me$_3$*) ppm. Any meaningful IR spectra and elemental analysis could not be performed due to the presence of co-products.

[Cp'$_5$La$_5$Br$_9$(AlBr$_2$Me$_2$)]$_2$ (7). In a 20-mL vial, [Cp'La(AlMe$_4$)$_2$] (56.43 mg, 0.13mmol) was dissolved in *n*-hexane (10 mL). In a 5-mL vial, Me$_3$GeBr (61.75 mg, 0.31 mmol) was dissolved in *n*-hexane (1 mL). The smaller vial was placed inside the larger one with the [Cp'La(AlMe$_4$)$_2$] solution, and the large vial was sealed afterwards. Storing the vial at ambient temperature led to the formation of crystalline **7** after several days. ^{1}H NMR (400 MHz, [D$_6$]benzene, 26 °C): δ = 7.20 (t, $^3J_{H,H}$ = 2.5 Hz, 2H, Cp*H*), 7.07 (t,

$^{3}J_{H,H}$ = 2.5 Hz, 5H, CpH), 6.94 (t, $^{3}J_{H,H}$ = 2.5 Hz, 3H, Cp*H*), 6.87 (t, $^{3}J_{H,H}$ = 2.5 Hz, 2H, Cp*H*), 6.84 (t, $^{3}J_{H,H}$ = 2.5 Hz, 2H, Cp*H*), 6.72 (t, $^{3}J_{H,H}$ = 2.5 Hz, 2H, Cp*H*), 6.64 (t, $^{3}J_{H,H}$ = 2.5 Hz, 2H, Cp*H*), 0.63 (s, 9H, Si*Me₃*), 0.59 (s, 9H, Si*Me₃*), 0.50 (s, 9H, Si*Me₃*), 0.42 (s, 9H, Si*Me₃*), 0.33 (bs, 6H, Al*Me₂*) ppm. $^{13}C\{^{1}H\}$ NMR (101 MHz, [D$_6$]benzene, 26 °C): δ = 132.0 (*Cp*), 125.9 (*Cp*), 123.9 (*Cp*), 122.8 (*Cp*), 120.4 (*Cp*), 118.9 (*Cp*), 118.3 (*Cp*), 1.1 (Si*Me₃*), 0.8 (Si*Me₃*), 0.5 (Si*Me₃*) ppm. IR spectroscopy and elemental analysis on **7** were not performed due to the presence of co-products.

[Cp'LaCl$_2$]$_{10}$ (8). [Cp'La(AlMe$_4$)$_2$] (**1b**, 44.3 mg, 0.1 mmol) was dissolved in *n*-hexane (15 mL) and Me$_3$GeCl (37.7 mg, 0.25 mmol) was added under vigorous stirring. After stirring the reaction mixture for 7 d at ambient temperature, the suspension was filtered, and the solvent was removed *in vacuo* to give **7** as a colorless solid. Crystalline **8** was obtained from a saturated toluene solution at -40 °C (11.58 mg, 0.003 mmol, 33%). ^{1}H NMR (400 MHz, [D$_6$]benzene, 26 °C): δ = 7.07 (t, $^{3}J_{H,H}$ = 2.5 Hz, 2H, 3/4 Cp*H*), 7.01 (t, $^{3}J_{H,H}$ = 2.5 Hz, 2H, 2/5 Cp*H*), 0.55 (s, 9H, Si*Me₃*) ppm. $^{13}C\{^{1}H\}$ NMR (101 MHz, [D$_6$]benzene, 26 °C): 131.8 (*Cp*), 125.7 (*Cp*), 123.6 (*Cp*), 120.4 (*Cp*), 0.9 (Si*Me₃*), 0.5 (Si*Me₃*) ppm. IR (DRIFT): ϑ̃ = 2953 (vw), 2894 (vw), 1444 (vw), 1406 (vw), 1365 (vw), 1312 (vw), 1249 (m), 1192 (vw), 1174 (w), 1044 (m), 1014 (vw), 904 (m), 848 (vs), 802 (s), 797 (s), 757 (w), 697 (w), 638 (vw), 628 (vw), 580 (vw), 422 (m), 417 (w) cm^{-1}. Elemental analysis of **8** calculated for $C_{80}H_{130}Cl_{20}La_{10}Si_{10}$ (3470.82 g/mol): C 27.68%, H 3.78%; found: C 27.59%, H 4.19%.

NMR Spectroscopy

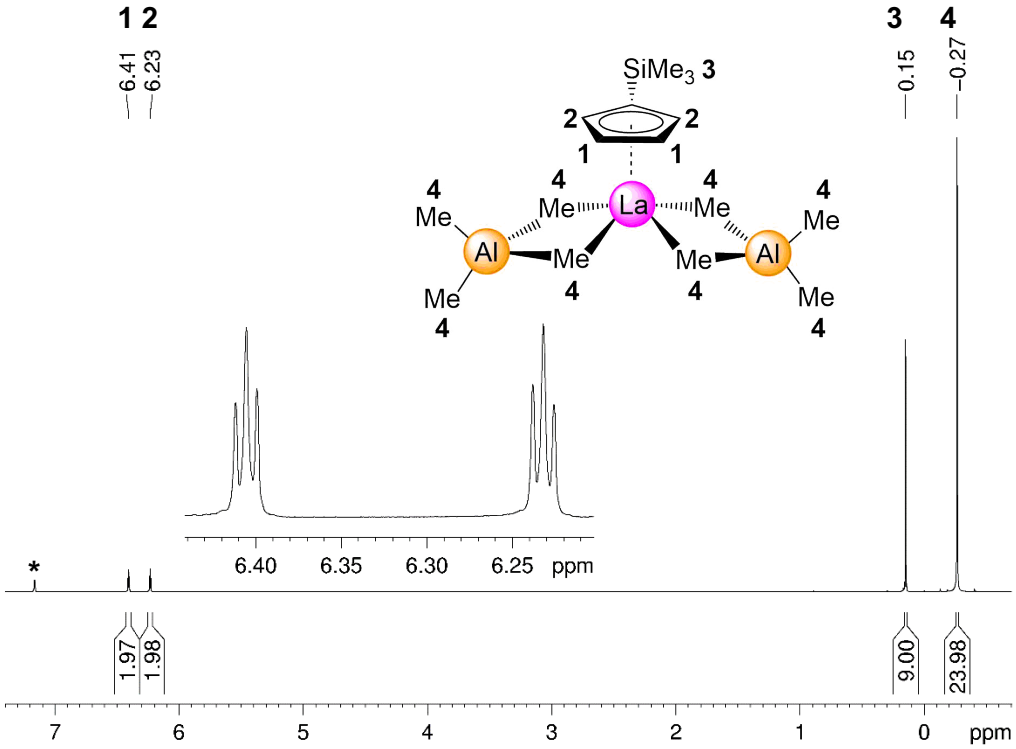

Figure S1. ^{1}H NMR spectrum (400 MHz) of **1b** in [D$_6$]benzene at 26 °C. The solvent residual signal is marked with an asterisk.

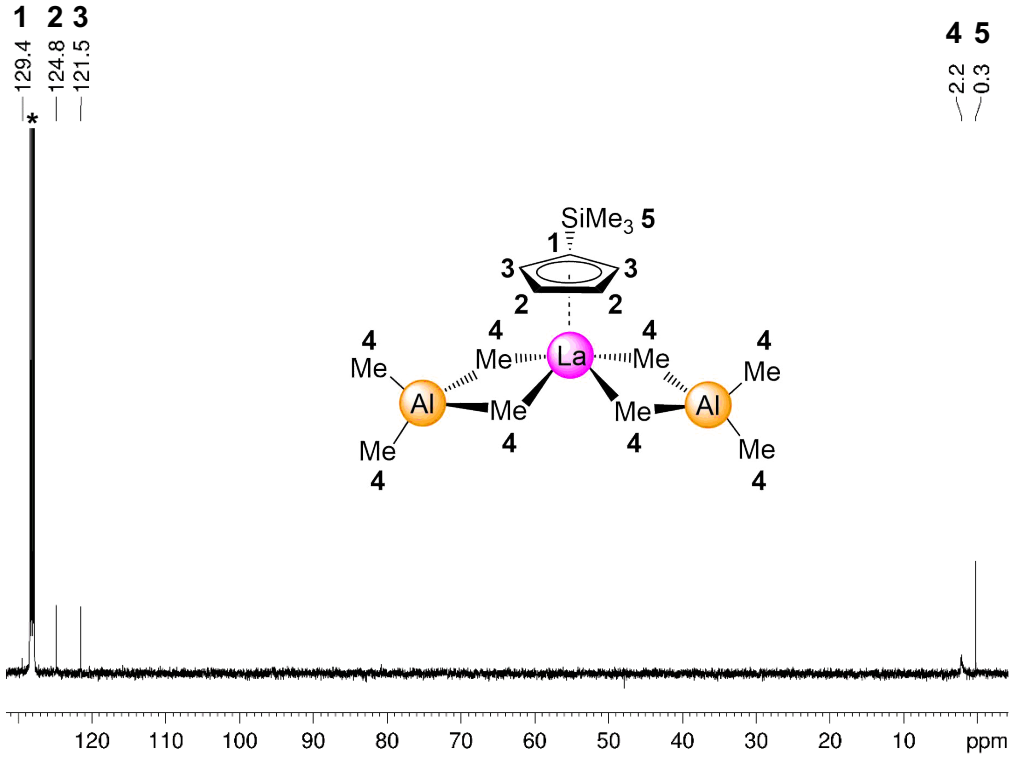

Figure S2. ^{13}C{^{1}H} NMR spectrum (101 MHz) of **1b** in [D$_6$]benzene at 26 °C. The solvent residual signal is marked with an asterisk.

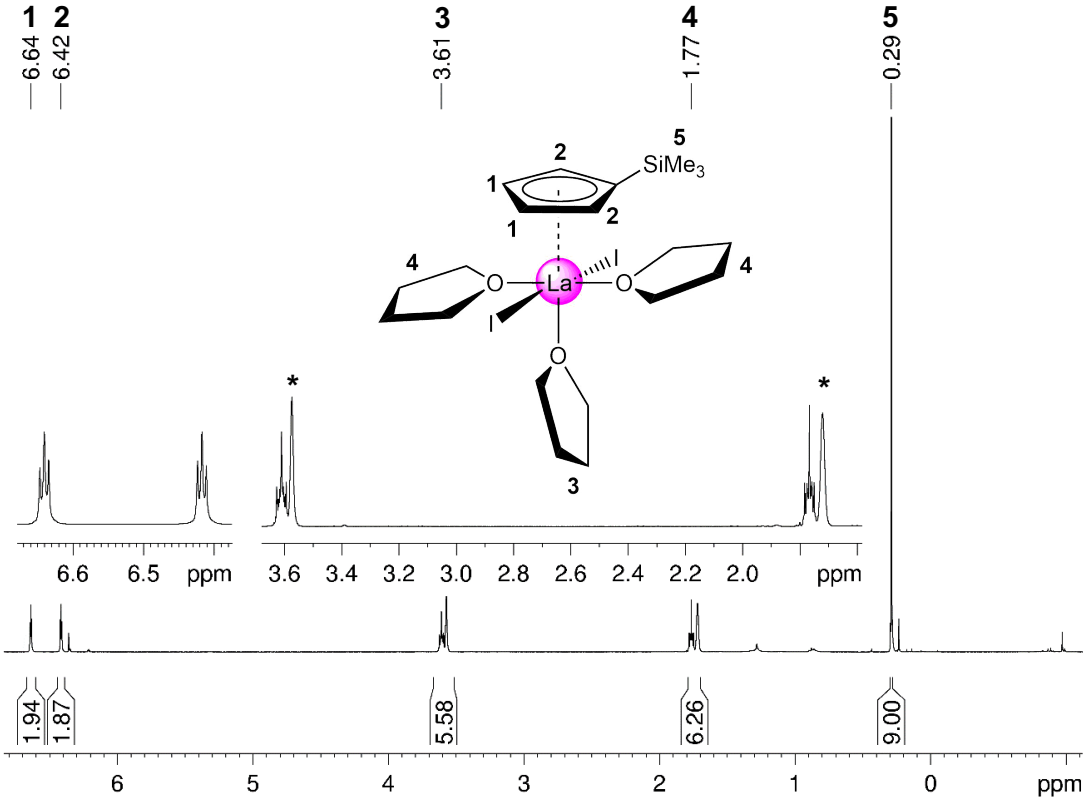

Figure S3. ^{1}H NMR spectrum (400 MHz) of [Cp'LaI$_2$(thf)$_3$] in [D$_8$]thf at 26 °C. The solvent residual signal is marked with an asterisk.

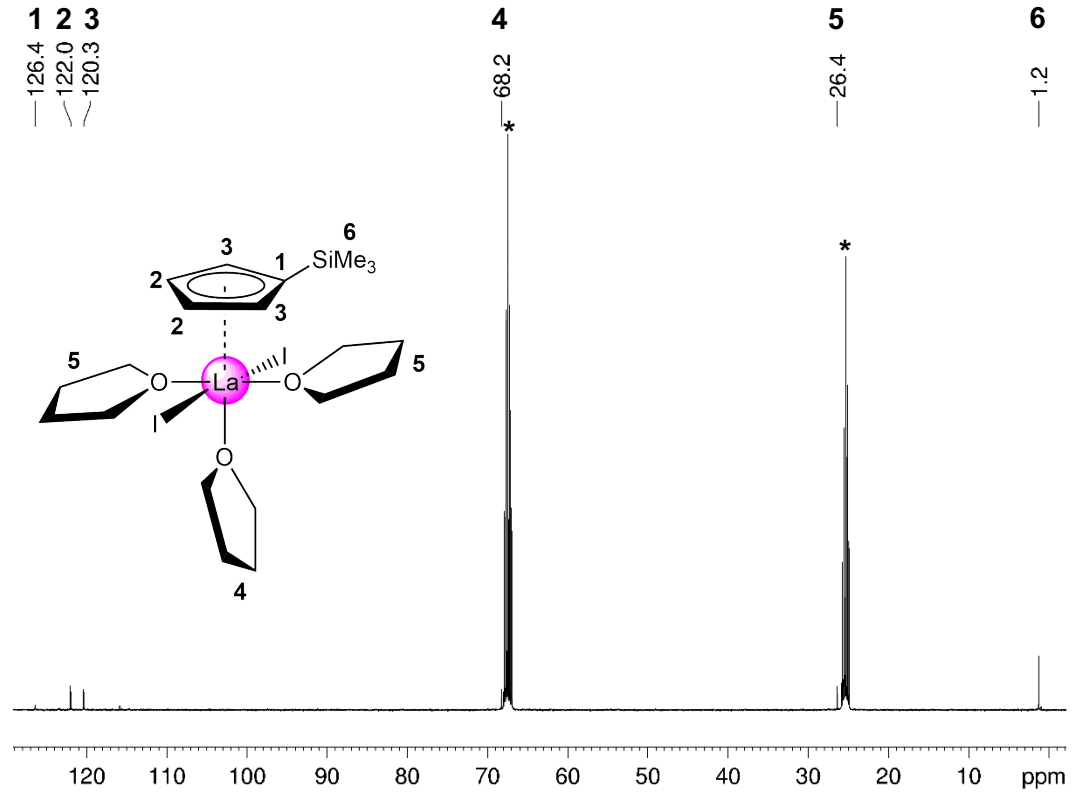

Figure S4. ^{13}C{^{1}H} NMR spectrum (101 MHz) of [Cp'LaI$_2$(thf)$_3$ in [D$_8$]thf at 26 °C. The solvent residual signal is marked with an asterisk.

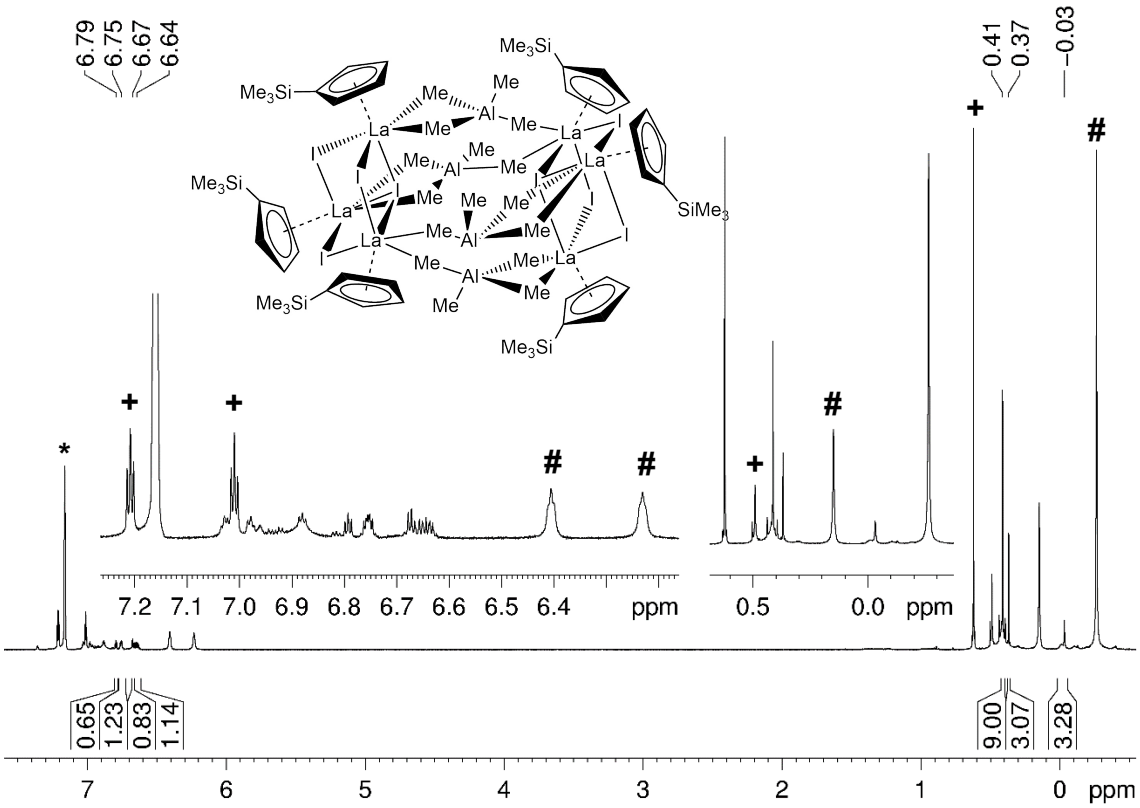

Figure S5. ^{1}H NMR spectrum (400 MHz) of **4a** in [D_6]benzene at 26 °C. The solvent residual signal is marked with an asterisk (+: **5a**; #: **1b**).

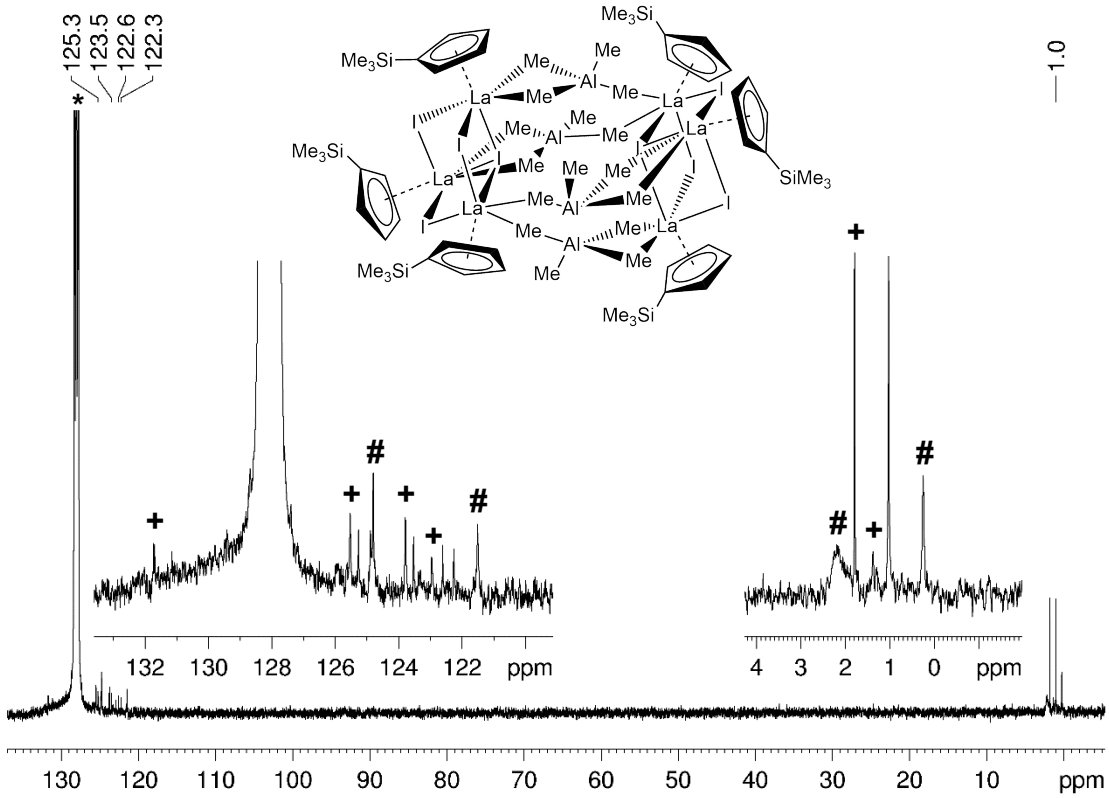

Figure S6. ^{13}C{^{1}H} NMR spectrum (101 MHz) of **4a** in [D_6]benzene at 26 °C. The solvent residual signal is marked with an asterisk (+: **5a**; #: **1b**).

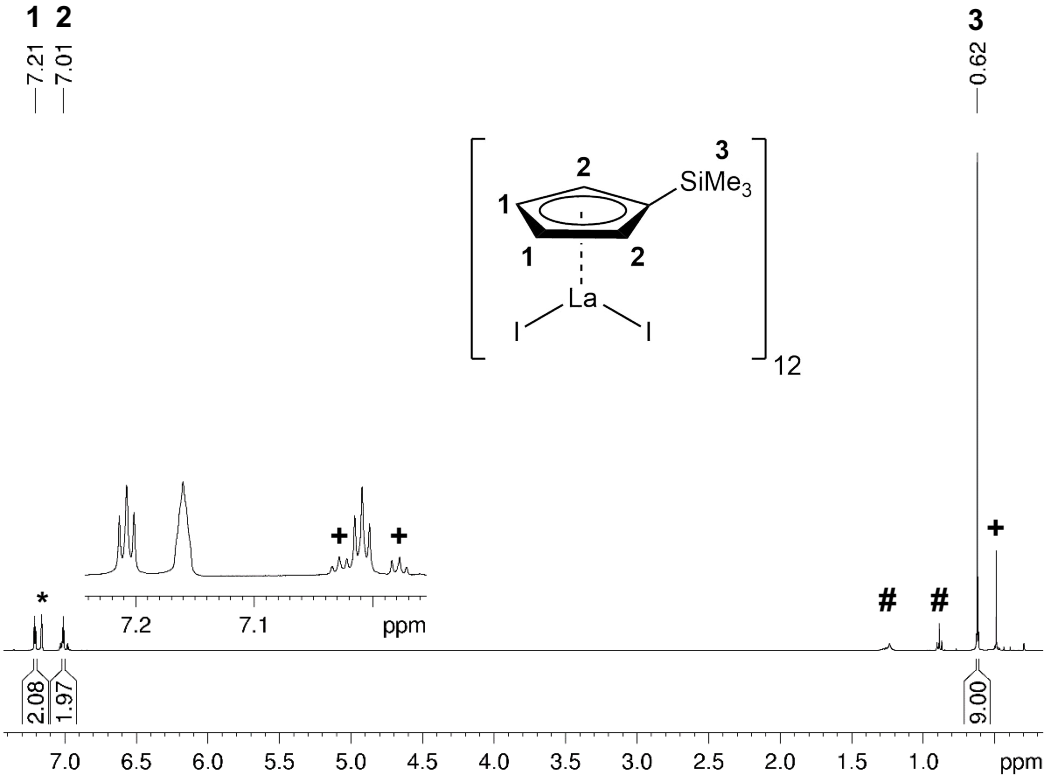

Figure S7. ^{1}H NMR spectrum (400 MHz) of **5a** in [D$_6$]benzene at 26 °C. The solvent residual signal is marked with an asterisk (+: side product; #: *n*-hexane).

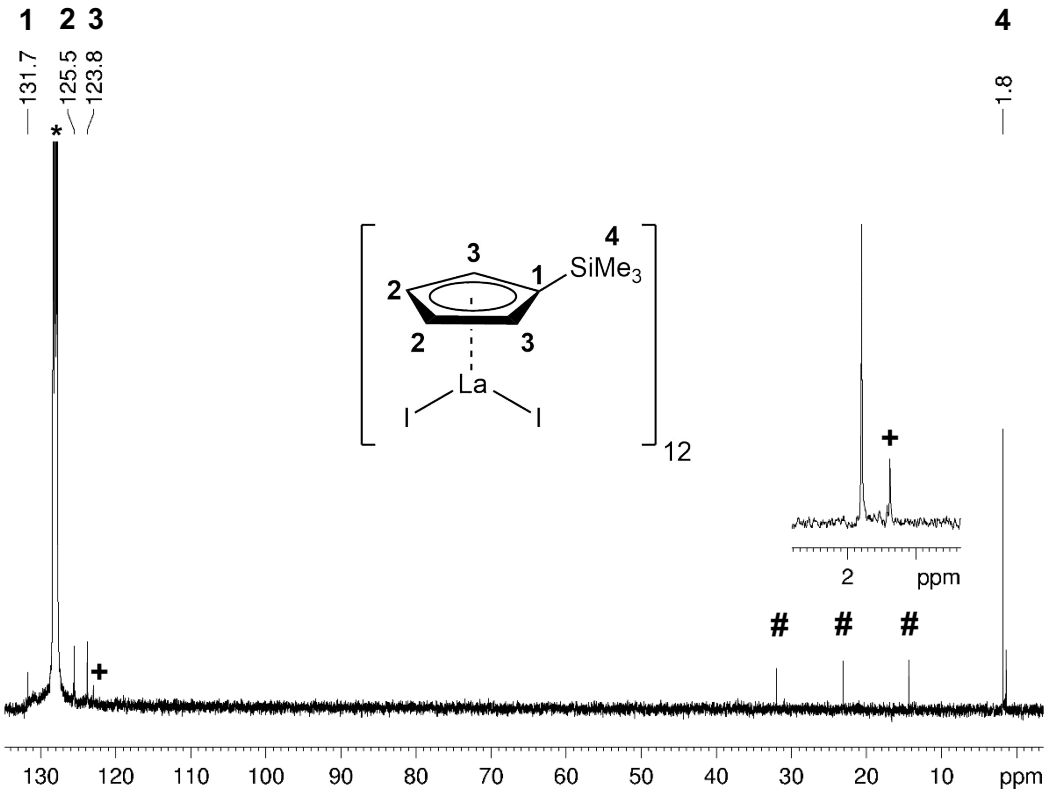

Figure S8. ^{13}C{^{1}H} NMR spectrum (101 MHz) of **5a** in [D$_6$]benzene at 26 °C. The solvent residual signal is marked with an asterisk (+: side product; #: *n*-hexane).

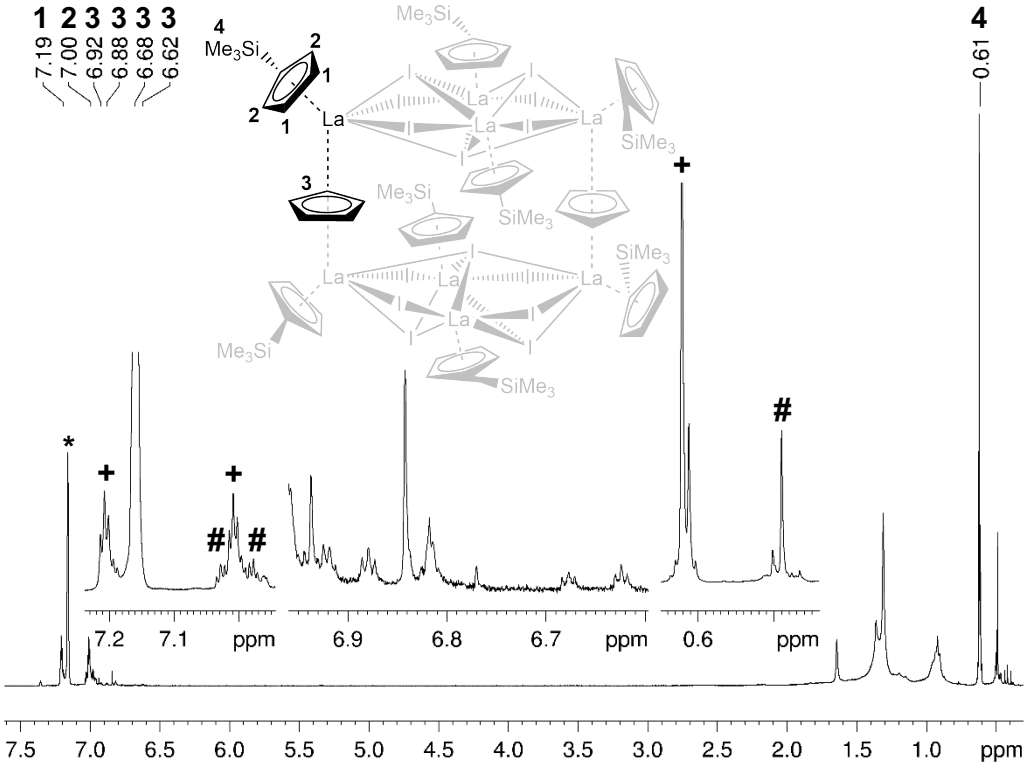

Figure S9. ^{1}H NMR spectrum (400 MHz) of **6** in [D$_6$]benzene at 26 °C. The solvent residual signal is marked with an asterisk (+: **5a**; #: side product).

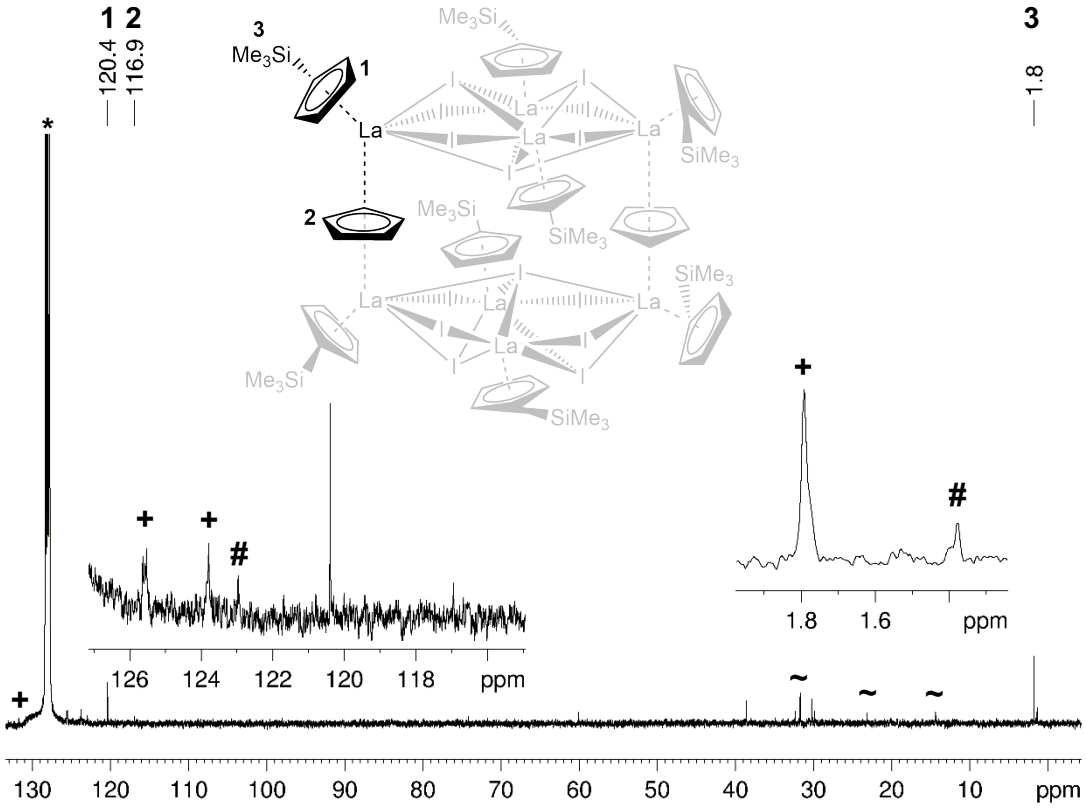

Figure S10. ^{13}C{^{1}H} NMR spectrum (101 MHz) of **6** in [D$_6$]benzene at 26 °C. The solvent residual signal is marked with an asterisk (+: **5a**; #: side product; ~: *n*-hexane).

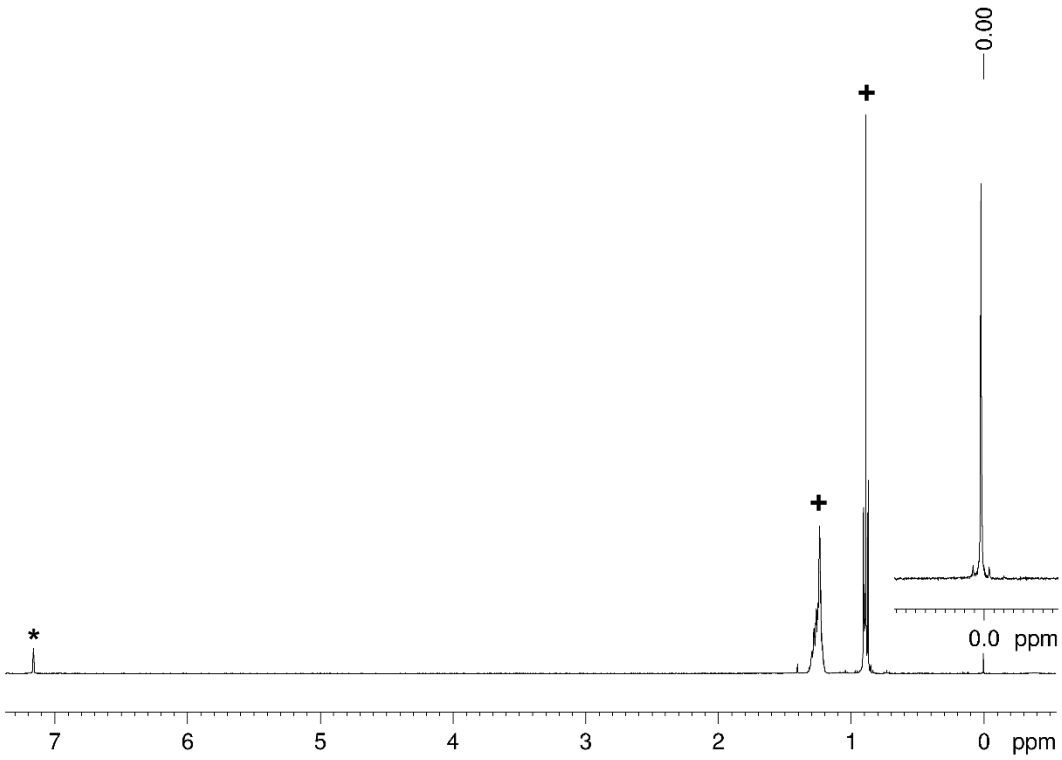

Figure S11. ^{1}H NMR spectrum (400 MHz) of the residual solution of **6** in [D_6]benzene at 26 °C, showing the presence of Me_6Si_2 (0.00 ppm) in solution. The solvent residual signal is marked with an asterisk (+: *n*-hexane).

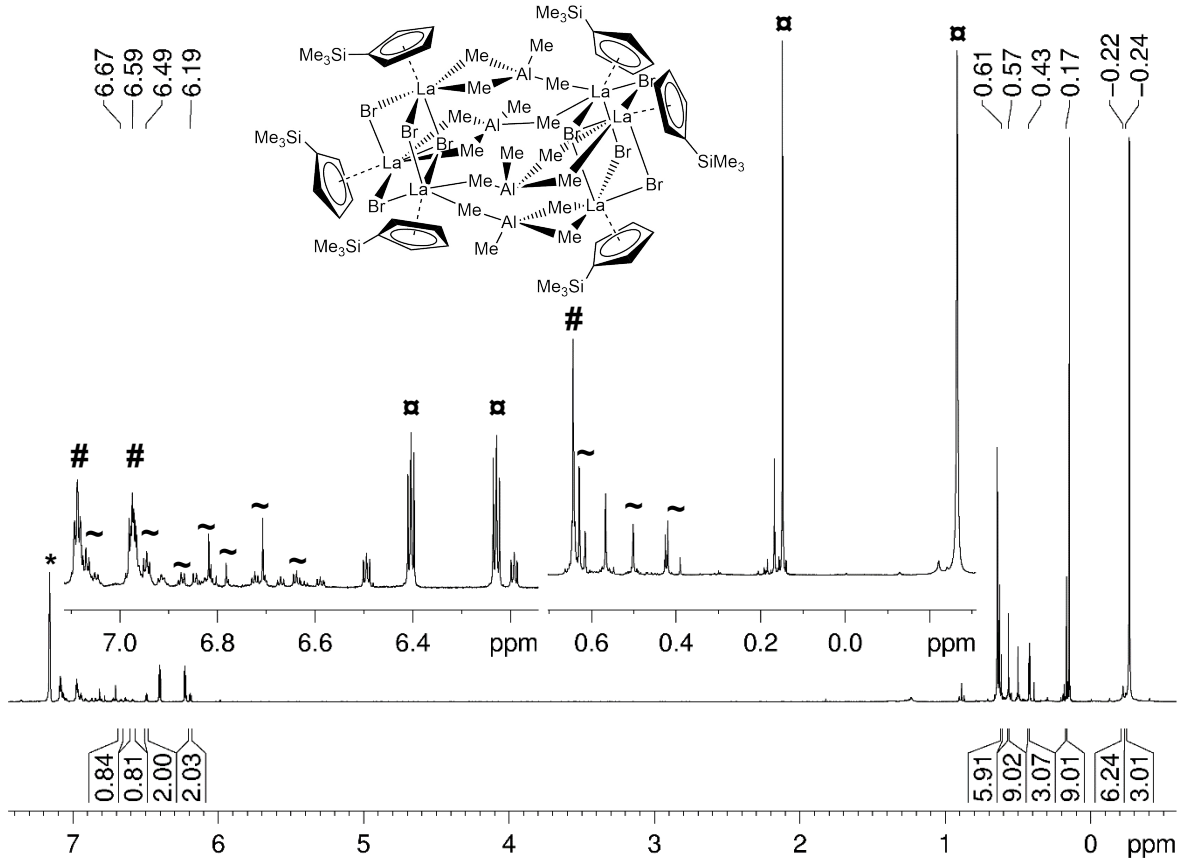

Figure S12. ^{1}H NMR spectrum (400 MHz) of **4b** in [D$_6$]benzene at 26 °C. The solvent residual signal is marked with an asterisk (+: *n*-hexane, #: **5b**, ~: **7**, ¤: **1b**).

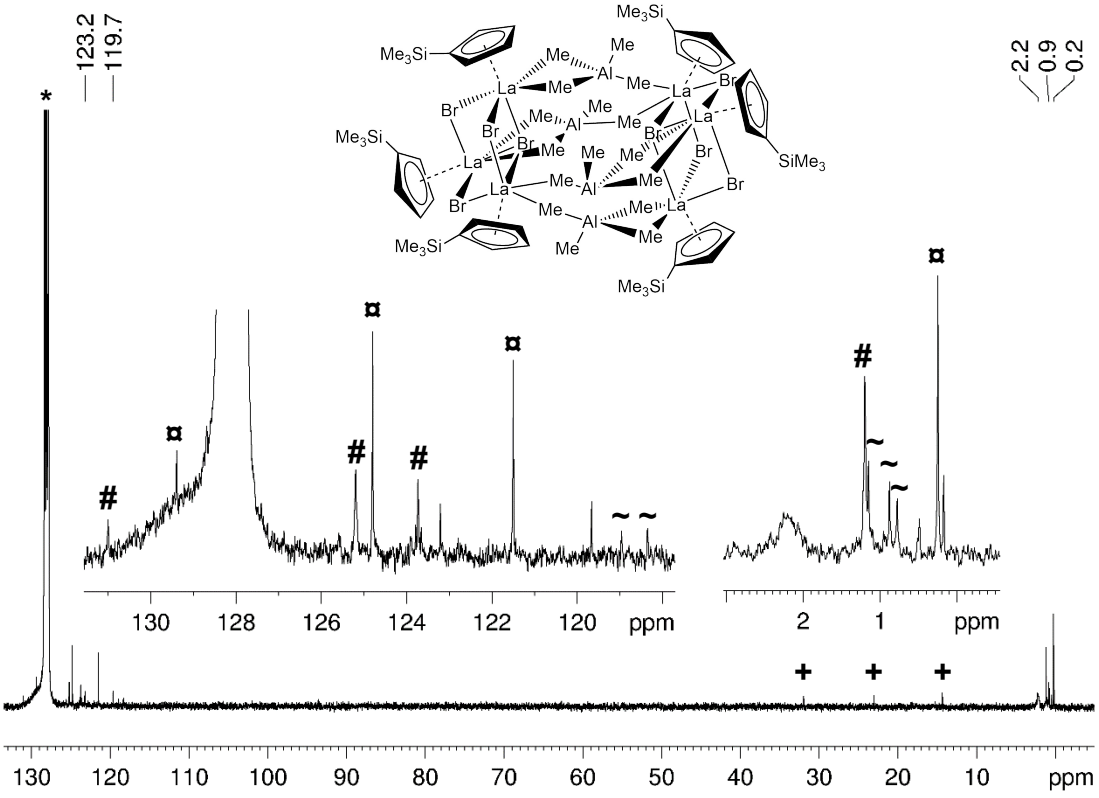

Figure S13. ^{13}C{^{1}H} NMR spectrum (101 MHz) of **4b** in [D$_6$]benzene at 26 °C. The solvent residual signal is marked with an asterisk (+: *n*-hexane, #: **5b**, ~: **7**, ¤: **1b**).

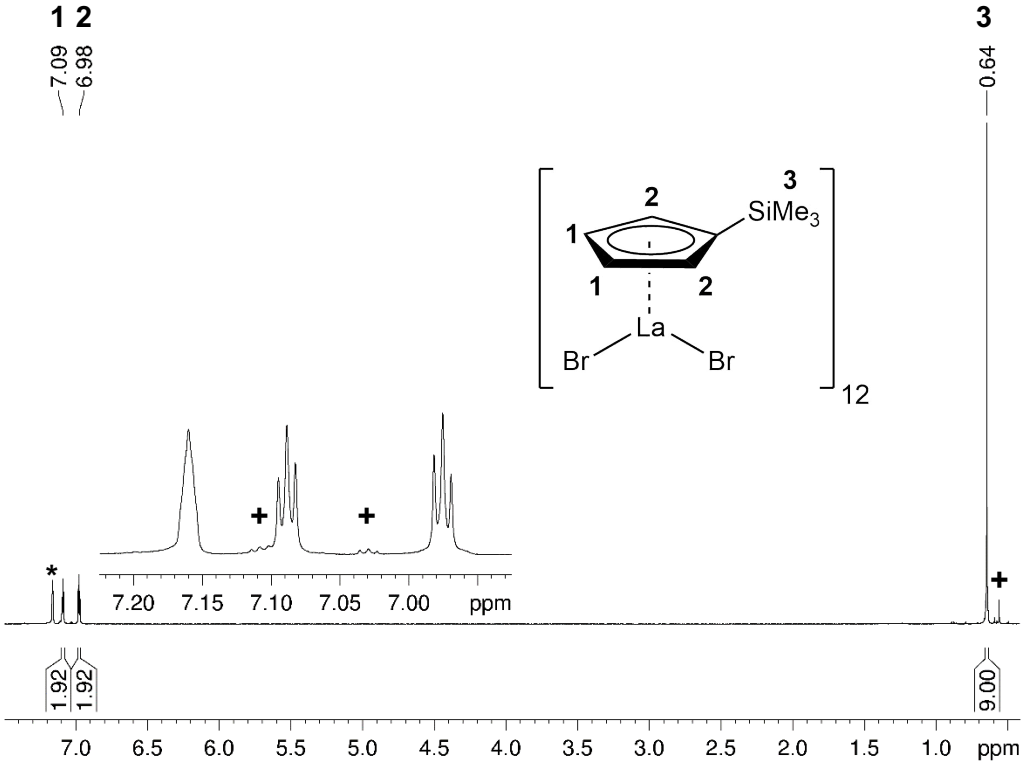

Figure S14. ^{1}H NMR spectrum (400 MHz) of **5b** in [D_6]benzene at 26 °C. The solvent residual signal is marked with an asterisk (+: side product).

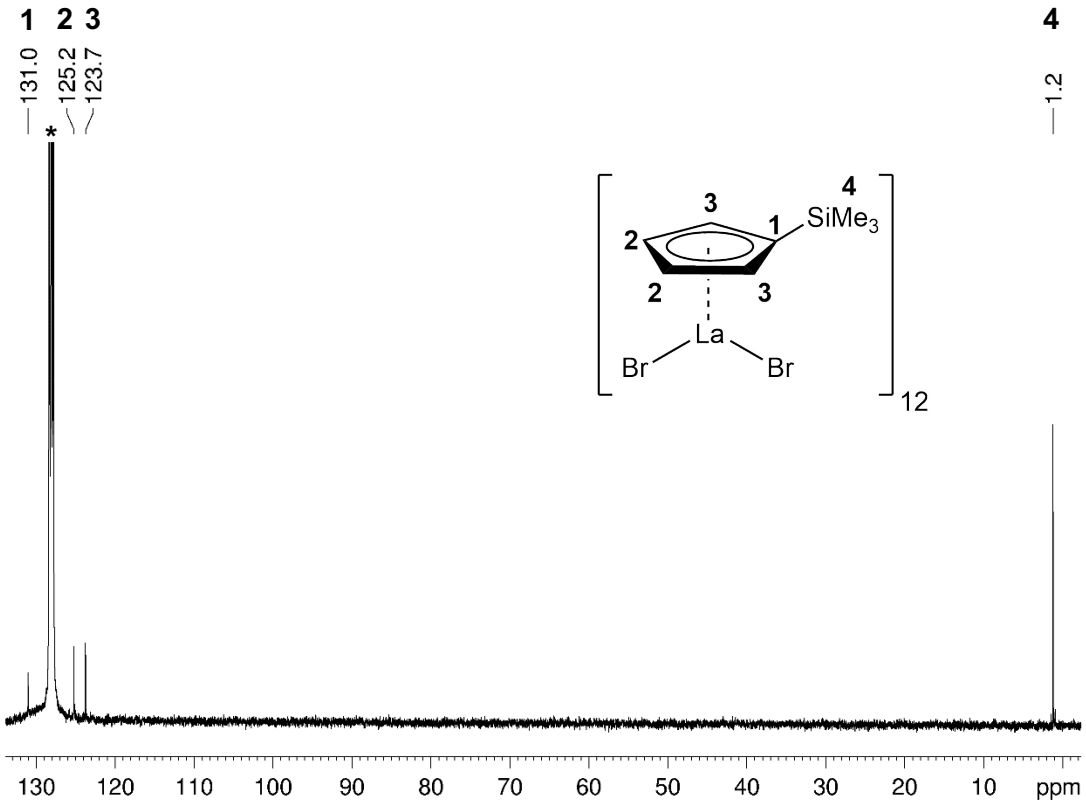

Figure S15. ^{13}C{^{1}H} NMR spectrum (101 MHz) of **5b** in [D_6]benzene at 26 °C. The solvent residual signal is marked with an asterisk.

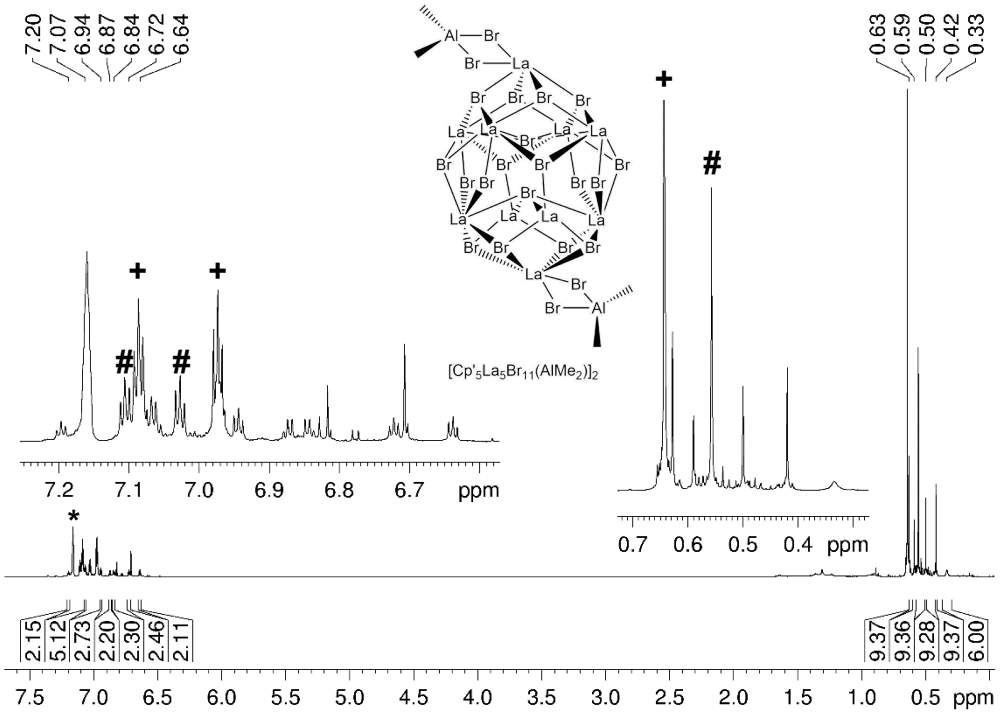

Figure S16. ^{1}H NMR spectrum (400 MHz) of **7** in [D_6]benzene at 26 °C. The solvent residual signal is marked with an asterisk (+: **5b**; #: side product).

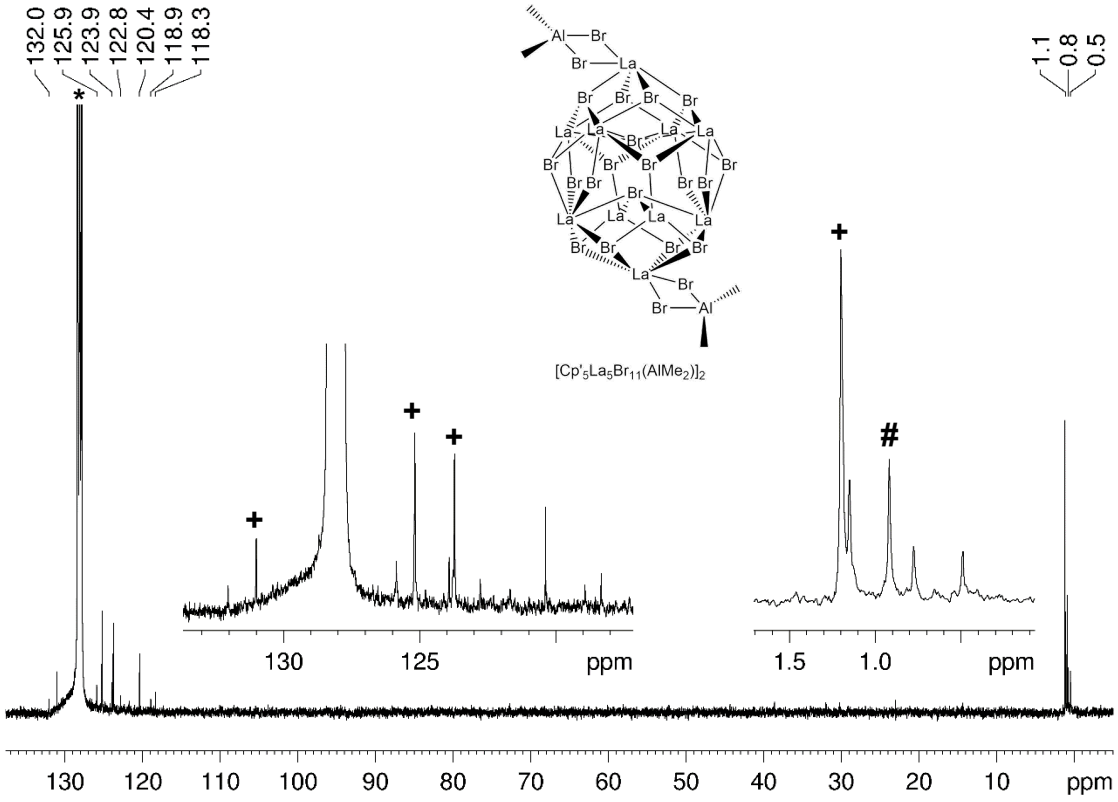

Figure S17. $^{13}C\{^{1}H\}$ NMR spectrum (101 MHz) of **7** in [D_6]benzene at 26 °C. The solvent residual signal is marked with an asterisk (+: **5b**; #: side product).

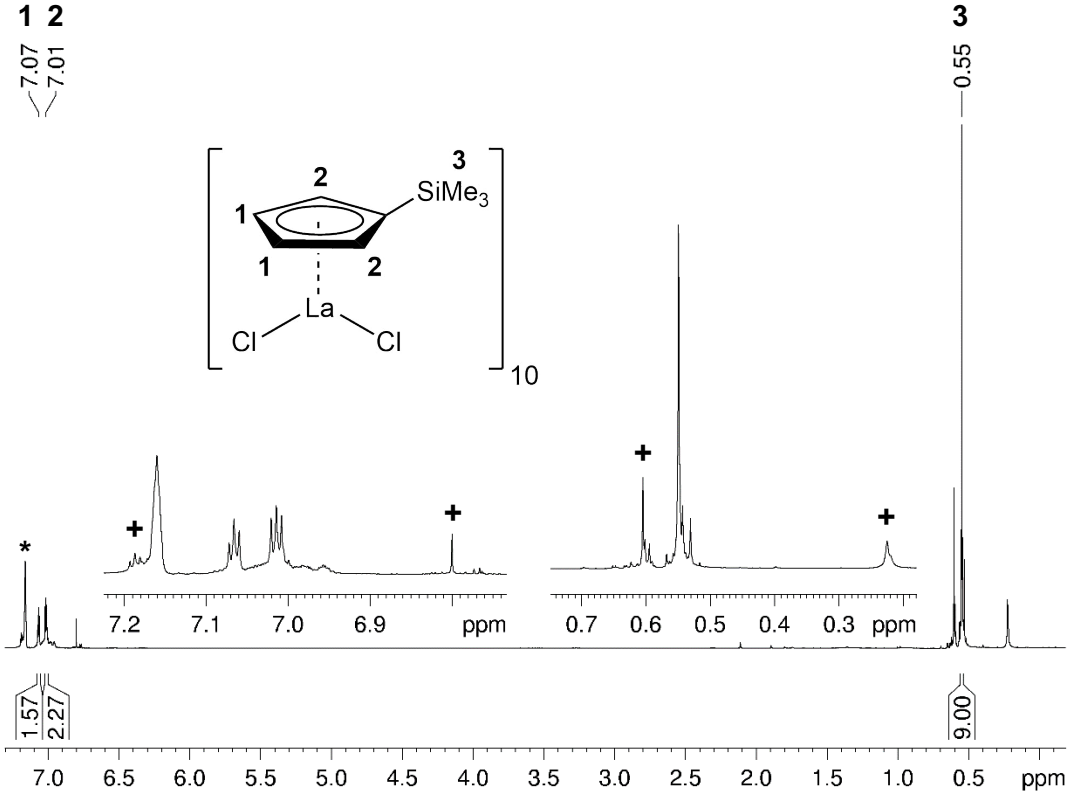

Figure S18. ^{1}H NMR spectrum (400 MHz) of **8** in [D_6]benzene at 26 °C. The solvent residual signal is marked with an asterisk (+: side product).

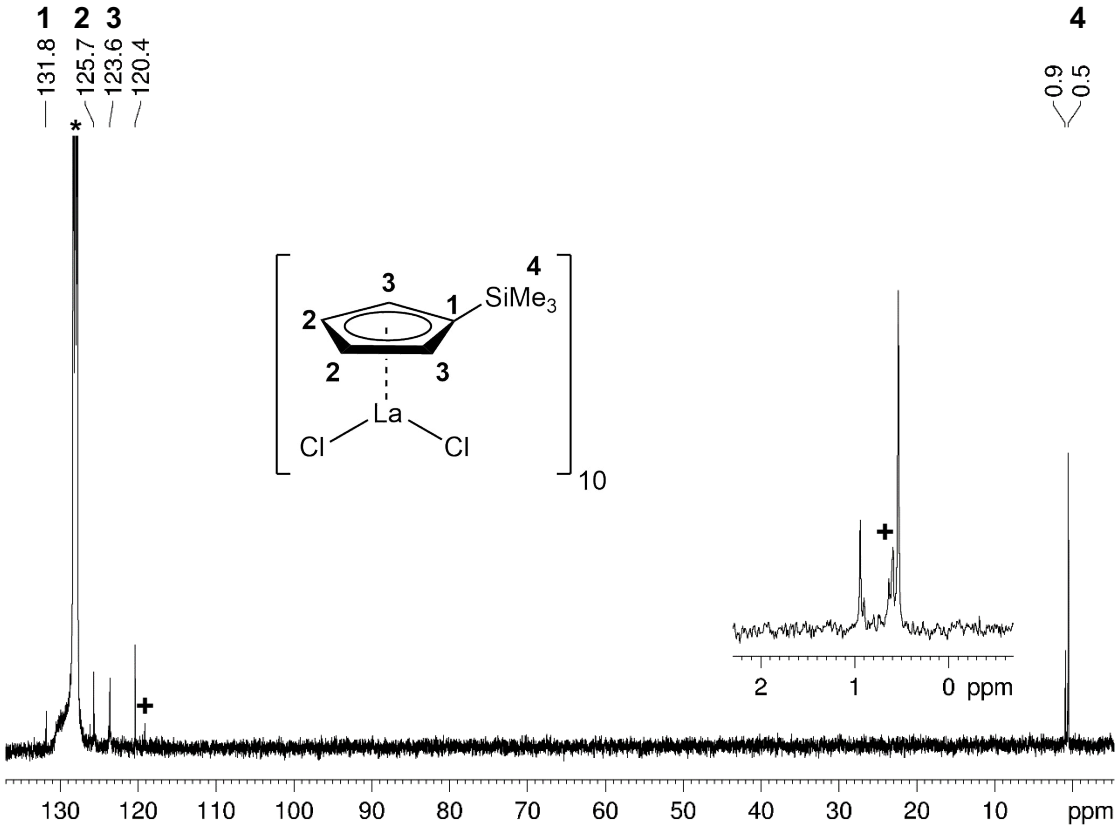

Figure S19. $^{13}C\{^{1}H\}$ NMR spectrum (101 MHz) of **8** in [D_6]benzene at 26 °C. The solvent residual signal is marked with an asterisk (+: side product).

Crystallography

X-Ray Crystallography and Crystal Structure Determinations. Single-crystals of **1b**, [Cp*$LaI_2(thf)_3$], [Cp'$LaI_2(thf)_3$], **4b**, and **8** were grown by standard techniques using saturated solutions of *n*-hexane (**1b**, **4b**), *n*-hexane/THF ([Cp*$LaI_2(thf)_3$], [Cp'$LaI_2(thf)_3$]) and toluene (**8**). Due to the insufficient crystal quality of **8**, data could be collected only to a resolution limit of 1.02 Å. Therefore, only a connectivity of **8** can be given. Crystals of **3**, **4a**, **5a**, and **5b** (**5b'**) were grown by aggregation from diluted *n*-hexane (**4a**, **5a**, **5b** (**5b'**)) and toluene (**3**) solutions. Crystals of **6** and **7** were grown by diffusion and subsequent aggregation. Suitable crystals for X-ray structure analyses were selected inside a glovebox, coated with Parabar 10312 (previously known as Paraton N, Hampton Research) and fixed on a nylon/loop glass fiber. All X-ray data except for compound **3** (STOE IPDS II) were collected on a Bruker APEX II DUO instrument equipped with an IμS microfocus sealed tube and QUAZAR optics for MoKα (λ = 0.71073 Å) radiation. The data collection was determined using COSMO[4] employing ω-scans. Raw data were processed using APEX[5] and SAINT,[6] corrections for absorption effects were applied by using SADABS.[7] The structures were solved by direct methods and refined against all data by full-matrix least-squares methods on F^2 using SHELXTL[8] and SHELXLE.[9] All graphics were generated employing CCDC Mercury 3.10.1.[10] Further details regarding the refinement and crystallographic data are listed in Table S1 and in the CIF files. CCDC depositions 1992037-1992048 contain all the supplementary crystallographic data for this paper. These data can be obtained free of charge from The Cambridge Crystallographic Data Centre via www.ccdc.cam.ac.uk/data_request/cif.

Table S1. Crystallographic data for compounds **1b**, [Cp'$LaI_2(thf)_3$], and **2**

	1b	[Cp'$LaI_2(thf)_3$]	**2**
CCDC	1992038	1992037	1992045
formula	$C_{16}H_{37}Al_2LaSi$	$C_{20}H_{37}I_2LaSiO_3$	$C_{88}H_{166}Al_4I_8La_6$
M_r [g/mol]	450.41	746.29	3180.78
color/shape	colorless/block	colorless/column	colorless/plate
crystal dimensions [mm]	0.305 x 0.250 x 0.194	0.150 x 0.118 x 0.065	0.181 x 0.125 x 0.086
crystal system	triclinic	orthorhombic	triclinic
space group	$P\bar{1}$	$P2_12_12_1$	$P\bar{1}$
a [Å]	9.7493(7)	8.219(3)	15.1879(2)
b [Å]	9.7900(8)	14.452(5)	15.4891(2)
c [Å]	27.449(2)	22.375(8)	15.6522(2)
α [°]	99.550(2)	90	103.083(3)
β [°]	90.686(2)	90	118.426(2)
γ [°]	119.474(2)	90	104.865(3)
V [Å³]	2235.8(3)	2657.7	2854.7(6)
Z	4	4	1
T [K]	101(2)	173(2)	100(2)
λ [Å]	0.71073	0.71073	0.71073
ρ_{calcd} [g/cm³]	1.338	1.865	1.850
μ [mm $^{-1}$]	2.035	3.992	4.423
F (000)	920	1432	1512
θ range [°]	2.271 – 29.189	2.302 – 30.578	1.491 – 30.077
unique reflections	12091	8124	16728
observed reflections (I > 2σ)	11532	7672	14086
R1/*w*R2 (I > 2σ)	0.0287/0.0661	0.0266/0.0620	0.0329/0.0798
R1/*w*R2 (all data)	0.0305/0.0667	0.0290/0.0632	0.0417/0.0861
GOF	1.116	0.965	1.064

Table S1 (continued). Crystallographic data for compounds **3**, [Cp*$LaI_2(thf)_3$], and **4a**

	3	[Cp*$LaI_2(thf)_3$]	**4a**
CCDC	1992039	1992043	1992044
formula	$C_{90}H_{135}I_{18}La_9 \cdot 2.5\ C_6H_6 \cdot 0.5\ C_7H_8$	$C_{22}H_{39}I_2LaO_3$	$C_{64}H_{126}Al_4I_8La_6Si_6$
M_r [g/mol]	4992.70	744.24	3020.76
color/shape	colorless/column	colorless/plate	colorless/needle
crystal dimensions [mm]	0.300 x 0.150 x 0.100	0.169 x 0.164 x 0.042	0.130 x 0.058 x 0.055
crystal system	monoclinic	trigonal	orthorhombic
space group	$P2_1$	$R\bar{3}$	*Pbca*
a [Å]	17.5518(3)	42.437(2)	24.1461(2)
b [Å]	32.3785(6)	42.437	11.8415(6)
c [Å]	27.0466(6)	9.155(3)	35.1341(2)
α [°]	90	90	90
β [°]	90.225(2)	90	90
γ [°]	90	120	90
V [Å³]	15370.5(5)	14278(1)	10045.8(9)
Z	4	18	4
T [K]	100(2)	160(2)	100(2)
λ [Å]	0.71073	0.71073	0.71073
ρ_{calcd} [g/cm³]	2.158	1.558	1.997
μ [mm $^{-1}$]	6.092	3.307	5.090
F (000)	9088	6444	5648
θ range [°]	2.586 – 29.573	0.960 – 26.661	2.001 – 28.126
unique reflections	68147	6688	12242
observed reflections (I > 2σ)	59962	3943	10216
R1/*w*R2 (I > 2σ)	0.0523/0.1196	0.0372/0.0664	0.0347/0.0653
R1/*w*R2 (all data)	0.0652/0.1266	0.0802/0.0766	0.0476/0.0696
GOF	1.038	0.763	1.147

Table S1 (continued). Crystallographic data for compounds **5a**, **6**, and **4b**

	5a	**6**	**4b**
CCDC	1992047	1992042	1992046
formula	$C_{96}H_{156}I_{24}La_{12}Si_{12}$	$C_{74}H_{114}I_{14}La_8Si_8$	$C_{70}H_{140}Br_8La_6Si_6$
M_r [g/mol]	6359.80	4116.25	2731.02
color/shape	colorless/block	colorless/block	colorless/block
crystal dimensions [mm]	0.150 x 0.149 x 0.109	0.323 x 0.264 x 0.224	0.418 x 0.141 x 0.115
crystal system	trigonal	triclinic	triclinic
space group	*R*3c	$P\bar{1}$	$P\bar{1}$
a [Å]	25.024(5)	13.287(5)	12.869(2)
b [Å]	25.024(5)	15.242(6)	17.812(3)
c [Å]	59.440(2)	16.924(7)	24.039(4)
α [°]	90	70.638(9)	87.062(3)
β [°]	90	78.664(13)	82.387(3)
γ [°]	120	69.889(9)	79.387(3)
V [Å³]	32234(14)	3023(2)	5366.1(14)
Z	6	1	2
T [K]	150(2)	273(2)	99(2)
λ [Å]	0.71073	0.71073	0.71073
ρ_{calcd} [g/cm³]	1.966	2.261	1.690
μ [mm $^{-1}$]	5.868	6.444	5.444
F (000)	17136	1868	2636
θ range [°]	4.113 – 28.280	1.281 – 28.282	1.425 – 27.103
unique reflections	17746	14955	23669
observed reflections (I > 2σ)	14444	12561	19976
R1/*w*R2 (I > 2σ)	0.0425/0.0955	0.0534/0.1384	0.0670/0.1534
R1/*w*R2 (all data)	0.0707/0.1191	0.0649/0.1522	0.0879/0.1690
GOF	1.142	1.032	1.046

Table S1 (continued). Crystallographic data for compounds **5b**, **5b'**, and **7**

	5b	**5b'**	**7**
CCDC	1992040	1992048	1992041
formula	$C_{96}H_{156}Br_{24}La_{12}Si_{12}$	$C_{108}H_{184}Br_{24}La_{12}Si_{12}$	$C_{90}H_{156}Al_2Br_{22}La_{10}Si_{10}$
M_r [g/mol]	5232.04	5404.38	4720.12
color/shape	colorless/cube	colorless/block	colorless/block
crystal dimensions [mm]	0.354 x 0.261 x 0.204	0.252 x 0.170 x 0.126	0.194 x 0.161 x 0.143
crystal system	monoclinic	monoclinic	triclinic
space group	*C*2/*c*	$P2_1/c$	$P\bar{1}$
a [Å]	29.5915(18)	22.9195(17)	18.6798(8)
b [Å]	18.9561(12)	29.214(2)	19.3010(8)
c [Å]	27.7599(17)	25.8590(19)	22.8183(10)
α [°]	90	90	82.0620(10)
β [°]	100.1190(10)	101.3160(10)	88.7740(10)
γ [°]	90	90	62.3840(10)
V [Å³]	15329.4(16)	16978(2)	7211.3(5)
Z	4	4	2
T [K]	100(2)	100(2)	173(2)
λ [Å]	0.71073	0.71073	0.71073
ρ_{calcd} [g/cm³]	2.267	2.114	2.174
μ [mm $^{-1}$]	9.647	8.714	9.116
F (000)	9696	10096	4404
θ range [°]	1.870 – 28.282	1.682 – 28.340	1.203 – 29.547
unique reflections	19039	42322	40138
observed reflections (I > 2σ)	17083	405987	33091
R1/*w*R2 (I > 2σ)	0.0260/0.0543	0.0282/0.0490	0.0284/0.0597
R1/*w*R2 (all data)	0.0320/0.0560	0.0478/0.0539	0.0415/0.0644
GOF	1.093	1.004	1.011

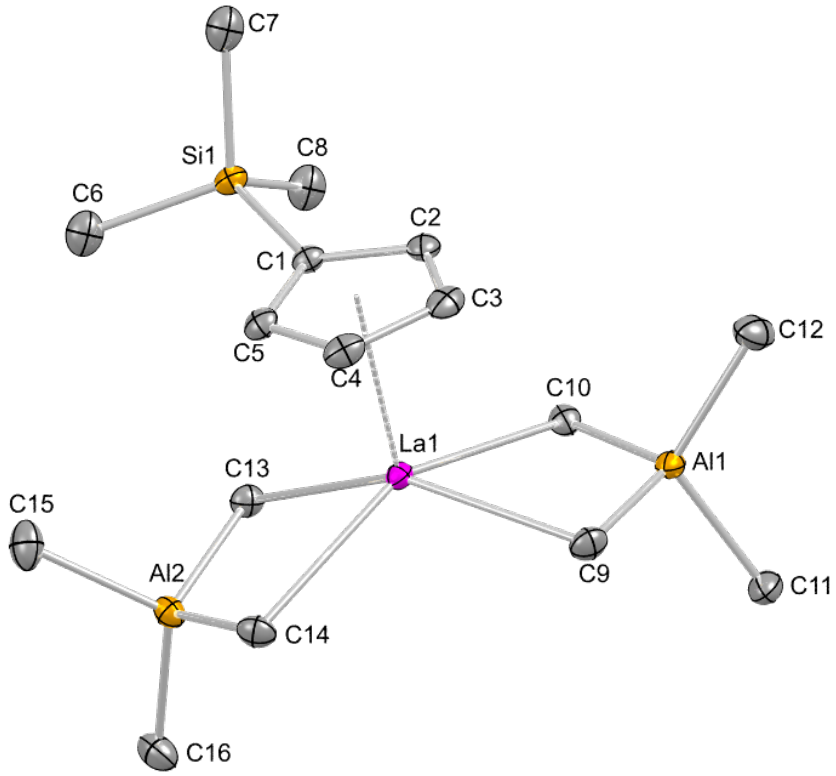

Figure S20. Crystal structure of Cp'La($AlMe_4$)$_2$ (**1b**) with atomic displacement parameters set at the 50% probability level. Hydrogen atoms are omitted for clarity. Selected interatomic distances [Å] and angles [°]: La1–C1 2.821(3); La1–C2 2.806(3); La1–C3 2.784(3); La1–C4 2.759(3); La1–C5 2.774(3); La1···Ct1 2.514; La1–C9 2.759(4); La1–C10 2.738(3); La1···Al1 3.258(1); La1–C13 2.710(3); La1–C14 2.752(4); La1···Al2 3.277(1); La1···C11' 3.267(4); C1–C2 1.428(4); C2–C3 1.410(4); C3–C4 1.418(5); C4–C5 1.409(4); C1–C5 1.426(4); C1–Si1 1.876(3); C1–C2–C3 109.3(3); C2–C3–C4 107.9(3); C3–C4–C5 107.4(3); C4–C5–C1 109.7(1); C5–C1–C2 105.6(2); Si1–C1–La1 126.58(2); C9–La1–C10 78.0(1); C13–La1–C14 78.1(1); C9–Al1–C10 113.10(2); C11–Al1–C12 114.51(2); C13–Al2–C14 112.16(2); C15–Al2–C16 115.64(2).

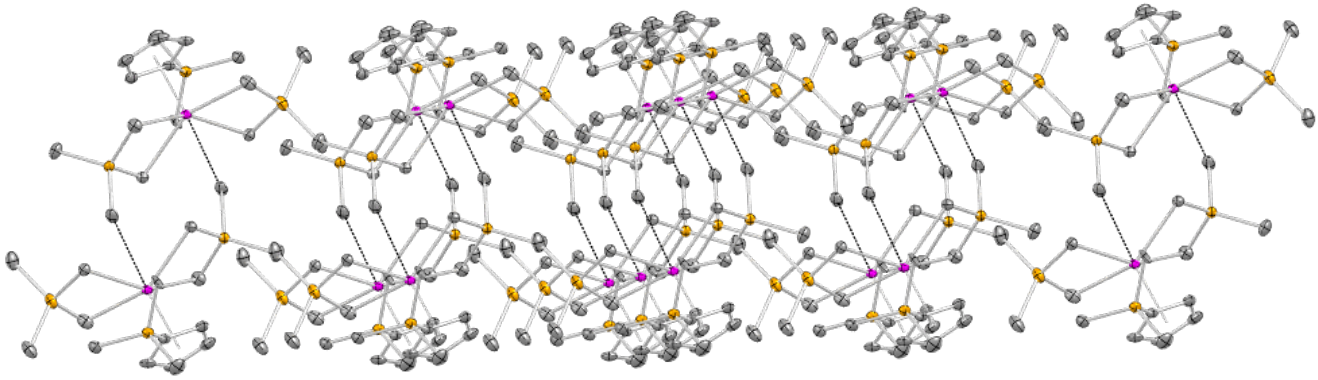

Figure S21. Crystal packing of **1b**. Each lanthanum metal center interacts with a methyl group of a neighboring molecule, resulting in a dimeric arrangement.

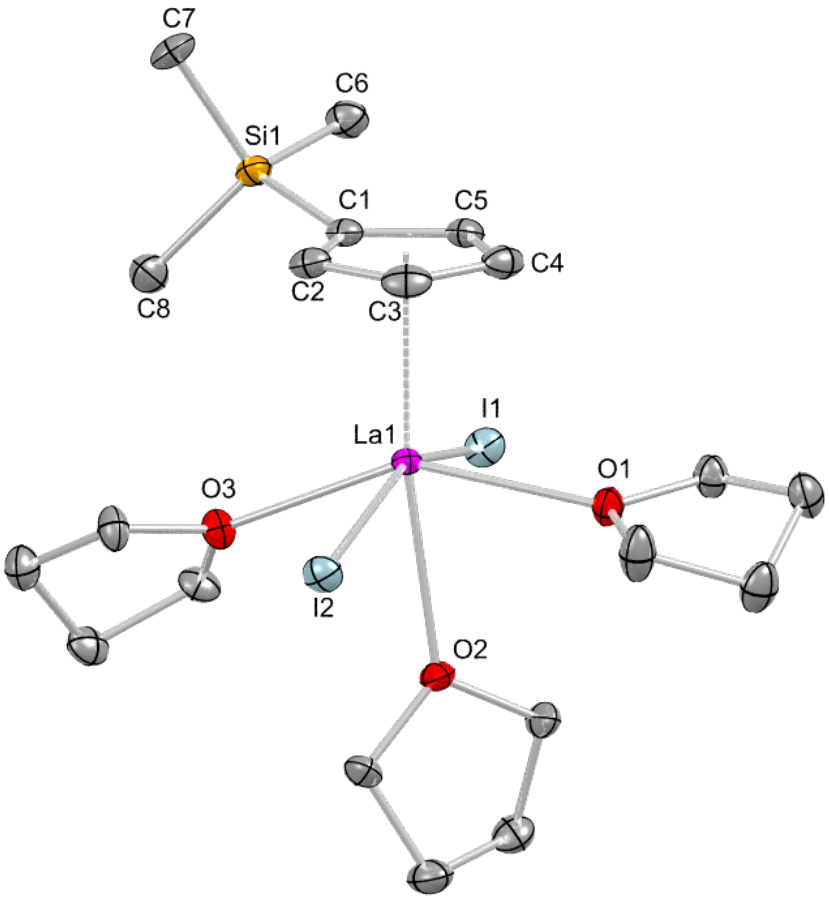

Figure S22. Crystal structure of [Cp'LaI$_2$(thf)$_3$] with atomic displacement parameters set at the 50% probability level. Hydrogen atoms are omitted for clarity. Selected interatomic distances [Å] and angles [°]: La1–C1 2.821(4); La1–C2 2.811(4); La1–C3 2.808(5); La1–C4 2.813(5); La1–C5 2.804(4); La1···Ct1 2.542; La1–I1 3.1909(8); La1–I2 3.2421(8); La1–O1 2.513(3); La1–O2 2.607(3); La1–O3 2.532(3); C1–C2 1.431(7); C2–C3 1.406(7); C3–C4 1.408(7); C4–C5 1.402(6); C1–C5 1.423(6); C1–Si1 1.867(5); C1–C2–C3 109.0(4); C2–C3–C4 108.1(4); C3–C4–C5 107.8(4); C4–C5–C1 109.6(4); C5–C1–C2 105.5(4); Si1–C1–La1 126.6(2); I1–La1–I2 158.590(2); I1–La1–O1 87.70(8); I1–La1–O2 80.93(8); I1–La1–O3 86.16(8); O1–La1–O2 72.65(2); O1–La1–O3 148.27(2); O2–La1–O3 75.65(2); Ct1···La1–I1 101.69; Ct1···La1–I2 99.70; Ct1···La1–O1 98.43; Ct1···La1–O2 170.70; Ct1···La1–O3 113.29.

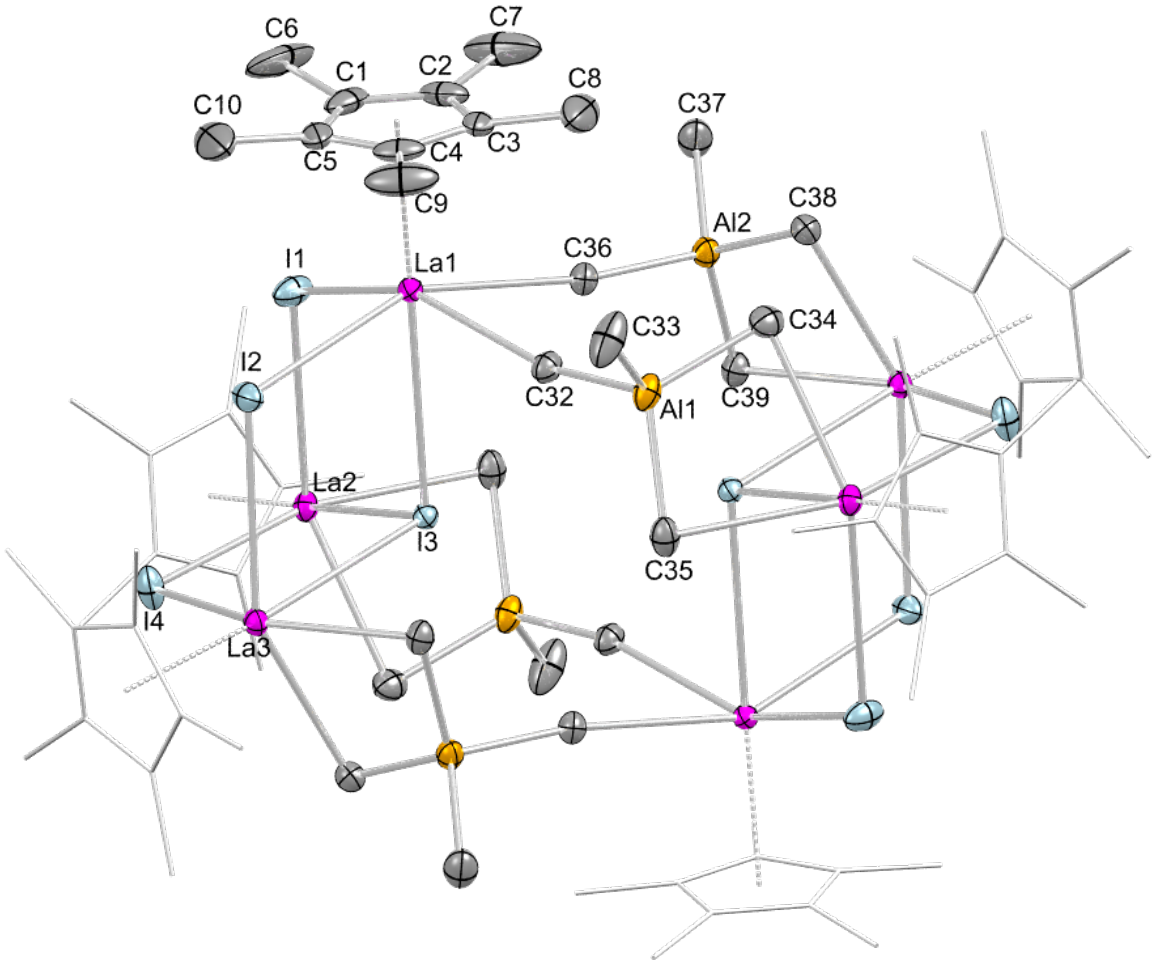

Figure S23. Crystal structure of $[Cp^*_6La_6I_8(AlMe_4)_4]$ (**2**) with atomic displacement parameters set at the 50% probability level. Hydrogen atoms are omitted for clarity. Selected interatomic distances [Å] and angles [°]: La1–C1 2.797(4); La1–C2 2.794(4); La1–C3 2.758(4); La1–C4 2.748(4); La1–C5 2.769(4); La1···Ct1 2.501; La1–C32 2.966(3); La1–C36 2.954(4); La1–I1 3.2096(4); La1–I2 3.2323(5); La1–I3 3.3455(4); La2–I1 3.2605(4); La2–I3 3.3981(4); La2–I4 3.2379(4); La2–C34 2.771(4); La2–C35 2.777(4); La2···Al1 3.3159(2); C1–C2 1.383(6); C2–C3 1.404(6); C3–C4 1.419(6); C4–C5 1.416(6); C1–C5 1.395(7); C1–C6 1.525(6); C1–C2–C3 108.3(4); C2–C3–C4 107.9(4); C3–C4–C5 106.8(4); C4–C5–C1 108.0(4); C5–C1–C2 109.0(4); C32–La1–C36 82.08(1); C34–La2–C35 76.06(2); C34–Al1–C35 112.94(2); C38–La3–C39 76.13(2); C38–Al2–C39 112.65(2); C32–La1–I2 86.05(7); C36–La1–I1 86.81(8); I1–La1–I2 94.909(2); I1–La1–I3 76.760(2); I2–La1–I3 76.072(2); La1–I1–La2 106.936(2); La1–I3–La2 100.876(2); La1–I2–La3 108.047(2); La1–I3–La3 101.265(2); La2–I3–La3 100.126(2); La2–I4–La3 108.169(2).

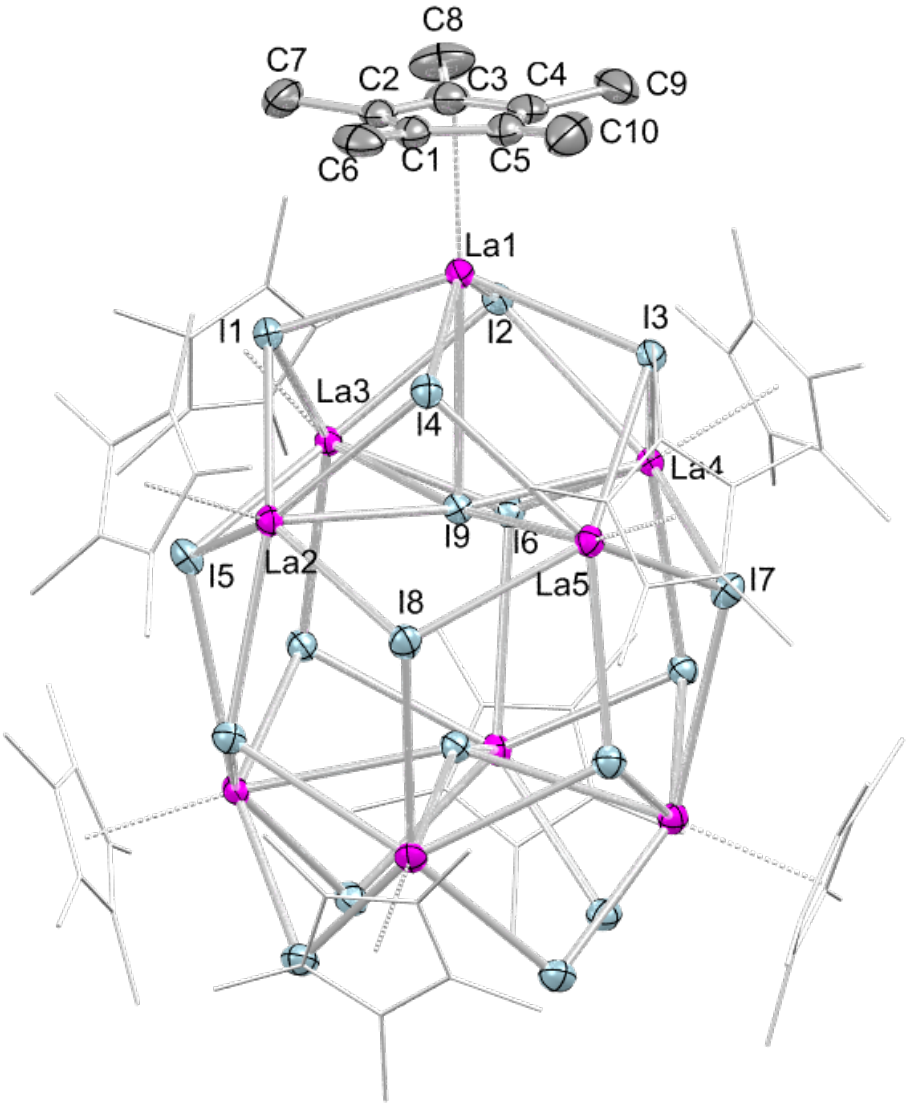

Figure S24. Crystal structure of $[Cp^*LaI_2]_9$ **(3)** with atomic displacement parameters set at the 50% probability level. Hydrogen atoms are omitted for clarity. The Cp* ligands (except for one) are represented by a wireframe model for improved visualization. Selected interatomic distances [Å] and angles [°]: La1–C1 2.76(2); La1–C2 2.76(2); La1–C3 2.76(2); La1–C4 2.73(2); La1–C5 2.74(2); La1···Ct1 2.456; La1–I1 3.1894(2); La1–I2 3.2012(2); La1–I3 3.2161(2); La1–I4 3.2170(2); La2–I1 3.4478(2); La2–I4 3.4631(2); La2–I5 3.3423(2); La2–I8 3.2991(2); La2–I9 3.5294(2); C1–C2 1.42(3); C2–C3 1.42(3); C3–C4 1.46(4); C4–C5 1.39(3); C1–C5 1.44(3); C1–C6 1.50(3); C1–C2–C3 109(2); C2–C3–C4 106(2); C3–C4–C5 109(2); C4–C5–C1 108(2); C5–C1–C2 108(2); I1–La1–I2 83.45(4); I1–La1–I3 138.90(5); I1–La1–I9 69.45; I1–La2–I4 76.50(4); I1–La2–I5 68.27(4); I1–La2–I8 140.17(4); I1–La2–I9 69.14(3); I5–La2–I8 129.16(5); I5–La2–I9 78.56(4); La1–I1–La2 95.66(4); La1–I4–La2 94.86(4); La1–I9–La2 85.49; La2–I1–La3 93.90(4); La2–I5–La3 98.57(4); La2–I9–La3 90.34(4); La2–I9–La4 171.11(4).

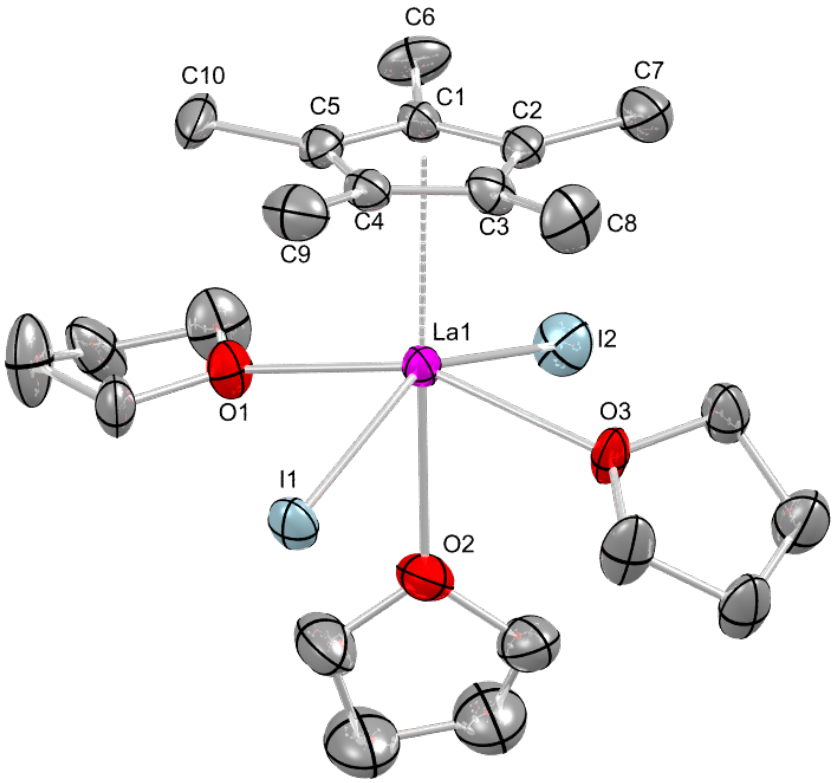

Figure S25. Crystal structure of [Cp*LaI$_2$(thf)$_3$] with atomic displacement parameters set at the 50% probability level. Hydrogen atoms are omitted for clarity. Selected interatomic distances [Å] and angles [°]: La1–C1 2.795(5); La1–C2 2.804(6); La1–C3 2.815(6); La1–C4 2.820(6); La1–C5 2.820(5); La1···Ct1 2.544; La1–I1 3.1974(9); La1–I2 3.2452(7); La1–O1 2.533(4); La1–O2 2.626(7); La1–O3 2.546(4); C1–C2 1.409(7); C2–C3 1.421(7); C3–C4 1.409(8); C4–C5 1.438(7); C1–C5 1.405(4); C1–C6 1.516(7); C1–C2–C3 108.7(5); C2–C3–C4 106.7(5); C3–C4–C5 109.2(5); C4–C5–C1 106.4(5); C5–C1–C2 109.0(5); I1–La1–I2 150.084(2); I1–La1–O1 86.76(9); I1–La1–O2 76.8(2); I1–La1–O3 85.15(9); O1–La1–O2 78.27(2); O1–La1–O3 154.54(2); O2–La1–O3 76.39(2); Ct1···La1–I1 105.64; Ct1···La1–I2 104.14; Ct1···La1–O1 102.14; Ct1···La1–O2 177.54; Ct1···La1–O3 103.28.

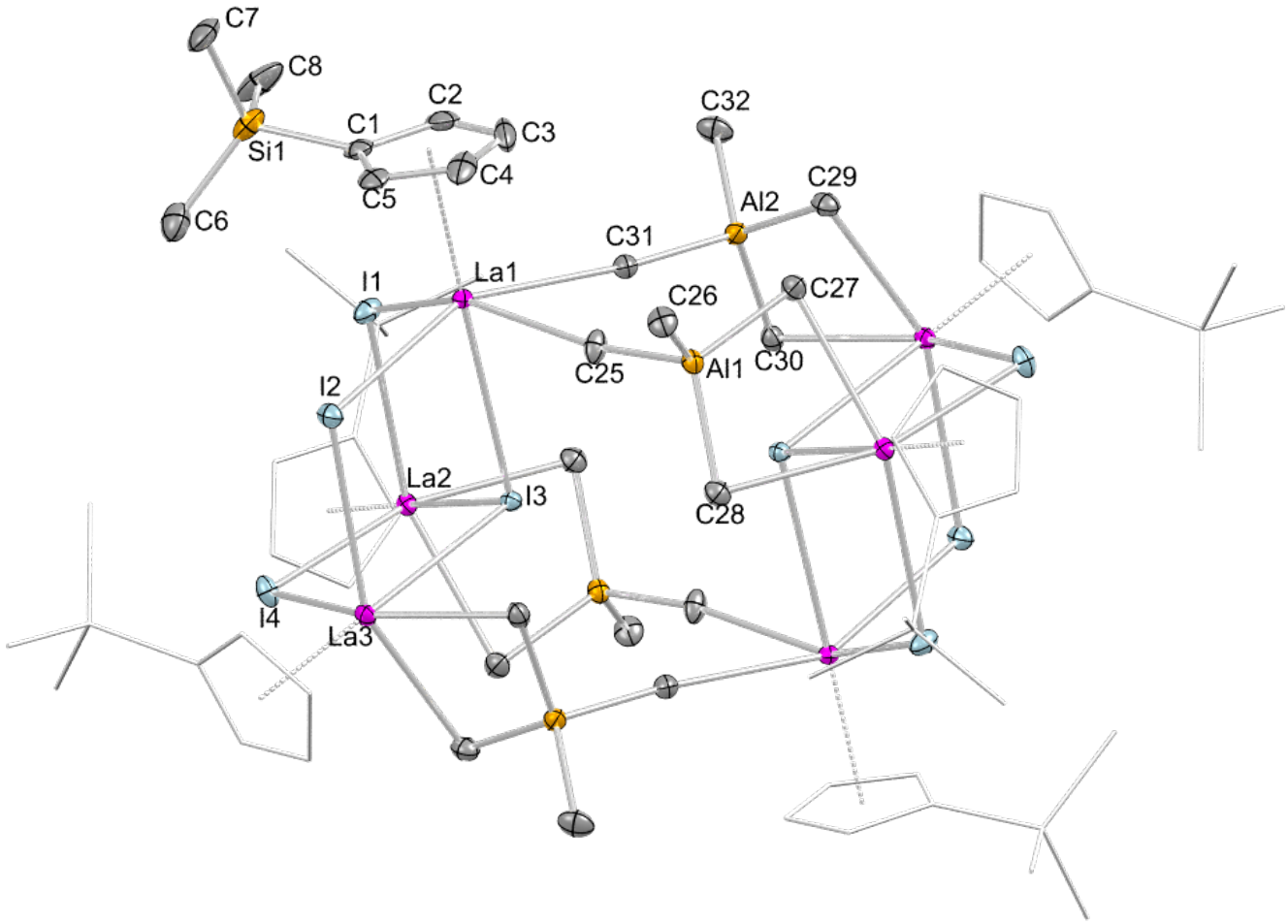

Figure S26. Crystal structure of $[Cp'_6La_6I_8(AlMe_4)_4]$ (**4a**) with atomic displacement parameters set at the 50% probability level. Hydrogen atoms are omitted for clarity. The Cp' ligands (except for one) are represented by a wireframe model for improved visualization. Selected interatomic distances [Å] and angles [°]: La1–C1 2.793(5); La1–C2 2.742(6); La1–C3 2.711(6); La1–C4 2.760(6); La1–C5 2.785(5); La1···Ct1 2.484; La1–C25 2.920(6); La1–C31 2.996(5); La1–I1 3.2163(5); La1–I2 3.1893(5); La1–I3 3.3435(4); La2–I1 3.2231(5); La2–I3 3.3685(5); La2–I4 3.2211(5); La2–C27 2.818(6); La2–C28 2.729(6); La2···Al1 3.2865(2); C1–C2 1.436(8); C2–C3 1.428(1); C3–C4 1.366(1); C4–C5 1.395(8); C1–C5 1.424(8); C1–Si1 1.869(6); C1–C2–C3 107.9(6); C2–C3–C4 108.0(5); C3–C4–C5 109.6(6); C4–C5–C1 108.9(6); C5–C1–C2 105.6(5); Si1–C1–La1 129.4(3); C25–La1–C31 79.8(2); C27–La2–C28 76.12(2); C27–Al1–C28 114.0(2); C29–La3–C30 76.09(2); C29–Al2–C30 113.1(2); C25–La1–I2 86.6(1); C31–La1–I1 84.7(1); I1–La1–I2 99.078(2); I1–La1–I3 76.899(2); I2–La1–I3 77.660(2); La1–I1–La2 106.326(2); La1–I3–La2 100.318(2); La1–I2–La3 106.670(2); La1–I3–La3 99.039(2); La2–I3–La3 99.962(2); La2–I4–La3 106.822(2).

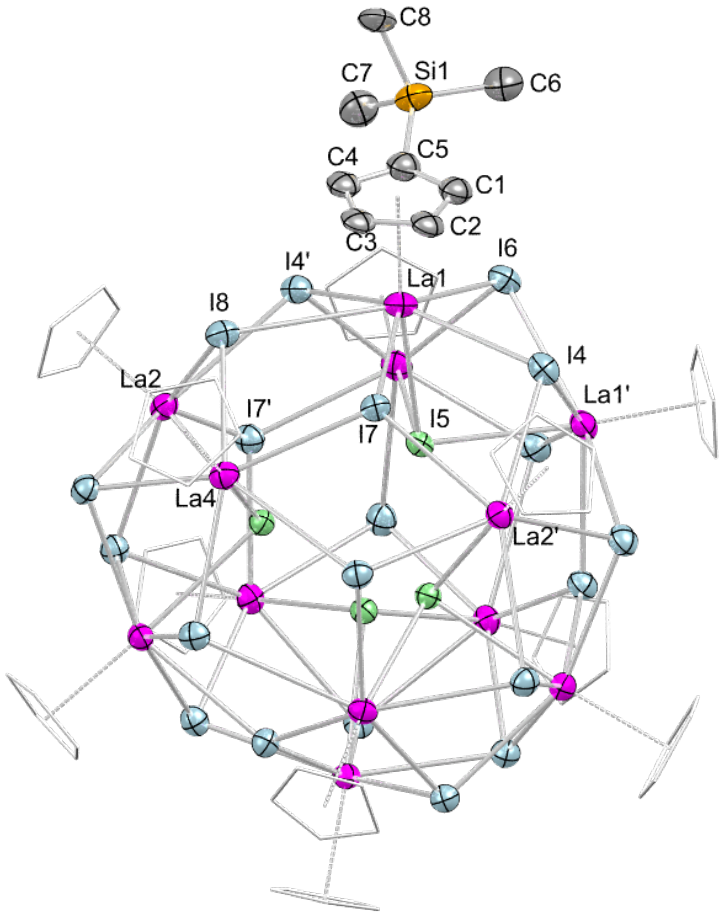

Figure S27. Crystal structure of $[Cp'LaI_2]_{12}$ (**5a**) with atomic displacement parameters set at the 50% probability level. Hydrogen atoms are omitted for clarity. The Cp' ligands (except for one) are represented by a wireframe model for improved visualization. Selected interatomic distances [Å] and angles [°]: La1–C1 2.71(4); La1–C2 2.67(5); La1–C3 2.70(4); La1–C4 2.76(3); La1–C5 2.75(4); La1···Ct1 2.453; La1–I4 3.2766(2); La1–I4' 3.2114(2); La1–I5 3.2811(2); La1–I6 3.3663(2); La1–I7 3.2669(2); La1–I8 3.6913(2); C1–C2 1.37(2); C2–C3 1.38(2); C3–C4 1.37(2); C4–C5 1.38(2); C1–C5 1.38(2); C5–Si1 1.90(3); C1–C2–C3 108.1(2); C2–C3–C4 107.9(2); C3–C4–C5 108.1(2); C4–C5–C1 107.9(2); C5–C1–C2 108.0(2); Si1–C5–La1 131.8(2); I4–La1–I6 76.70; I4'-La1–I6 77.57; I4–La1–I7 69.55(4); I4'–La1–I8 65.44(4); I7–La1–I8 64.59(4); La1–I4–La1' 93.78(5); La1–I5–La1' 92.41(4); La1–I6–La1' 89.43(4); La1–I4–La2' 105.17(4); La1–I8–La2 102.62(4); La1–I7–La4 114.70(4); La1–I8–La4 104.40(4).

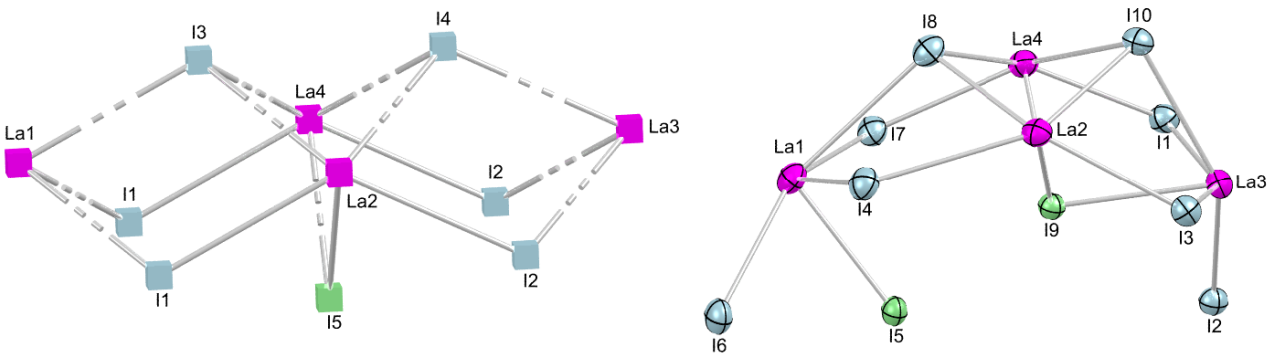

Figure S28. Comparison of the solid-state structure of LaI_3 (adapted from Zachariasen,[11] left) with the asymmetric unit of **5a** (right).

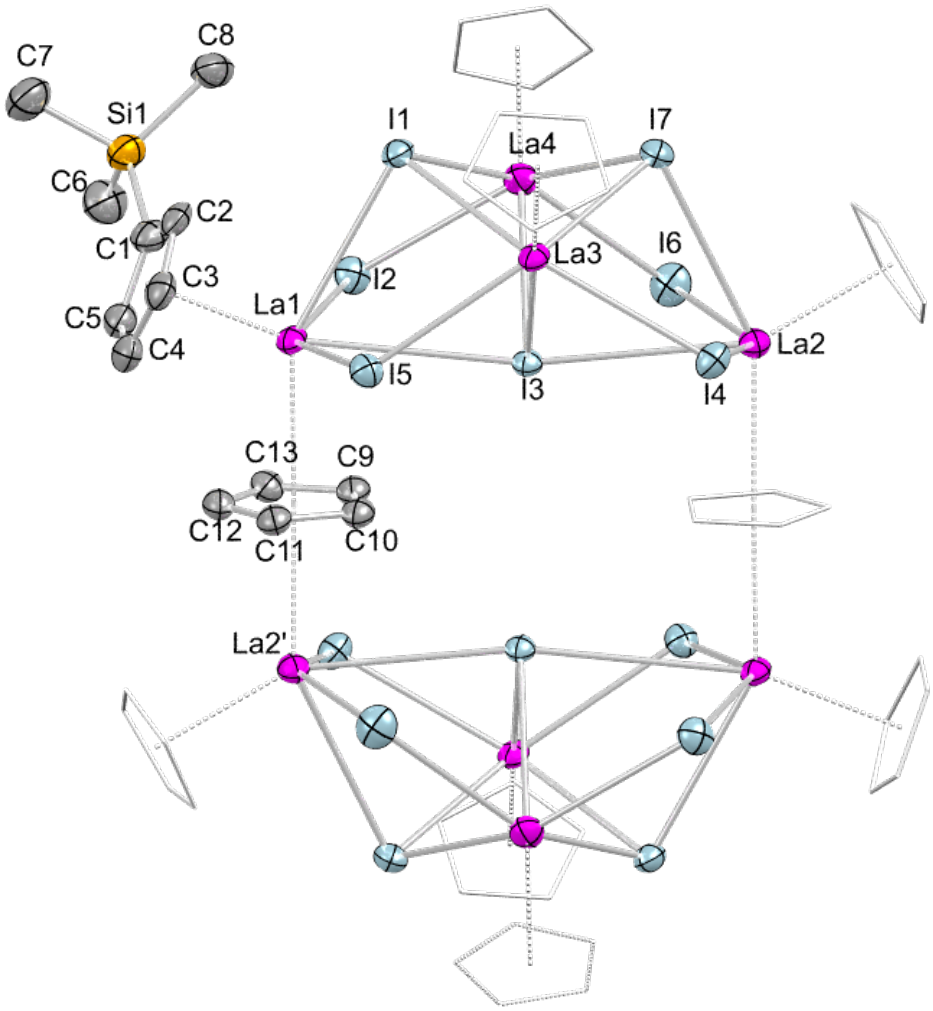

Figure S29. Crystal structure of $[(\mu\text{-Cp})_2\text{Cp'}_8\text{La}_8\text{I}_{14}]$ (**6**) with atomic displacement parameters set at the 50% probability level. Hydrogen atoms are omitted for clarity. The Cp' and Cp ligands (except for one) are represented by a wireframe model for improved visualization.

Table S2. Selected interatomic distances and angles for **6**.

Bond lengths [Å]		**Bond angles [°]**	
La1–C1	2.798(1)	C1–C2–C3	109.3(8)
La1–C2	2.780(8)	C2–C3–C4	107.7(9)
La1–C3	2.785(9)	C3–C4–C5	108.3(9)
La1–C4	2.746(9)	C4–C5–C1	108.5(8)
La1–C5	2.750(9)	C5–C1–C2	106.2(9)
La1···Ct(Cp')	2.509	Si1-C1-La1	132.1(5)
La1–C9	2.951(8)	C9–C10–C11	107.7(8)
La1–C10	2.915(8)	C10–C11–C12	107.8(8)
La1–C11	2.874(8)	C11–C12–C13	108.3(8)
La1–C12	2.912(8)	C12–C13–C9	108.6(8)
La1–C13	2.954(8)	C13–C9–C10	107.5(8)
La1···Ct(μ-Cp)	2.668	Ct(Cp')···La1···Ct(μ-Cp)	114.19

C1–C2	1.406(2)	La1···Ct(μ-Cp)···La2'	175.11
C2–C3	1.394(2)	La1–I1–La3	90.58(2)
C3–C4	1.384(2)	La1–I5–La3	95.60(2)
C4–C5	1.403(2)	La1–I1–La4	91.10(4)
C1–C5	1.406(2)	La1–I2–La4	95.80(4)
C1–Si1	1.865(1)	La2–I3–La3	88.08(2)
C9–C10	1.414(2)	La2–I4–La3	95.00(4)
C10–C11	1.414(2)	La2–I6–La4	94.03(3)
C11–C12	1.399(2)	La2–I7–La4	89.25(3)
C12–C13	1.396(2)	La3–I1–La4	91.17(2)
C9–C13	1.400(2)	La3–I3–La4	90.26(3)
La1–I1	3.4481(2)	I1–La1–I2	76.99(2)
La1–I2	3.2616(2)	I2–La1–I5	140.82(2)
La1–I3	3.734(1)	I3–La2–I4	75.22(3)
La1–I5	3.2727(2)	I3–La2–I6	70.79(3)
La2–I3	3.5895(2)	I1–La3–I3	74.14(3)
La2–I4	3.2485(2)	I1–La3–I4	146.42(2)
La2–I6	3.2924(2)	I1–La3–I5	79.27(2)
La2–I7	3.4739(2)	I1–La3–I7	76.35(2)
		I3–La3–I4	79.35(3)

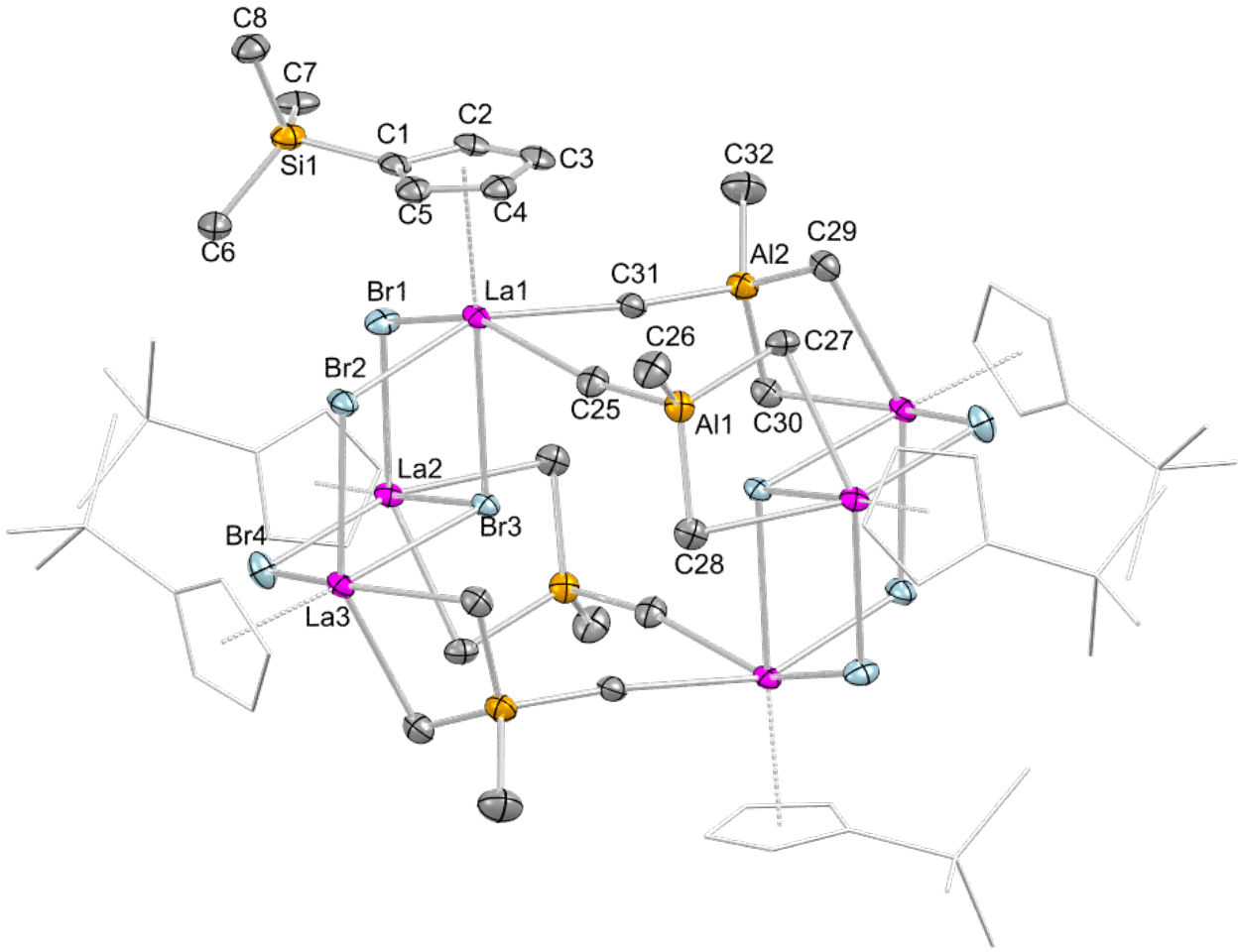

Figure S30. Crystal structure of $[Cp'_6La_6Br_8(AlMe_4)_4]$ (**4b**) with atomic displacement parameters set at the 50% probability level. Hydrogen atoms are omitted for clarity. The Cp' ligands (except for one) are represented by a wireframe model for improved visualization. Selected interatomic distances [Å] and angles [°]: La1–C1 2.780(2); La1–C2 2.775(2); La1–C3 2.794(2); La1–C4 2.772(2); La1–C5 2.777(2); La1···Ct1 2.505; La1–C25 2.961(2); La1–C31 2.961(5); La1–Br1 2.9740(2); La1–Br2 2.9681(2); La1–Br3 3.1473(2); La2–Br1 2.9953(2); La2–Br3 3.1917(2); La2–Br4 2.9967(2); La2–C27 2.763(2); La2–C28 2.773(2); La2···Al1 3.2865(2); C1–C2 1.383(2); C2–C3 1.398(2); C3–C4 1.444(2); C4–C5 1.385(2); C1–C5 1.445(2); C1–Si1 1.873(2); C1–C2–C3 113.0(2); C2–C3–C4 105.0(2); C3–C4–C5 107.8(2); C4–C5–C1 109.9(2); C5–C1–C2 104.2(2); Si1–C1–La1 127.4(5); C25–La1–C31 82.3(3); C27–La2–C28 76.8(4); C27–Al1–C28 114.5(5); C29–La3–C30 76.7(3); C29–Al2–C30 113.6(5); C25–La1–Br2 86.0(2); C31–La1–Br1 87.7(2); Br1–La1–Br2 94.10(4); Br1–La1–Br3 75.34(3); Br2–La1–Br3 75.11(3); La1–Br1–La2 109.59(4); La1–Br3–La2 100.60(4); La1–Br2–La3 109.91(4); La1–Br3–La3 100.89(3); La2–Br3–La3 98.79(3); La2–Br4–La3 107.77(4).

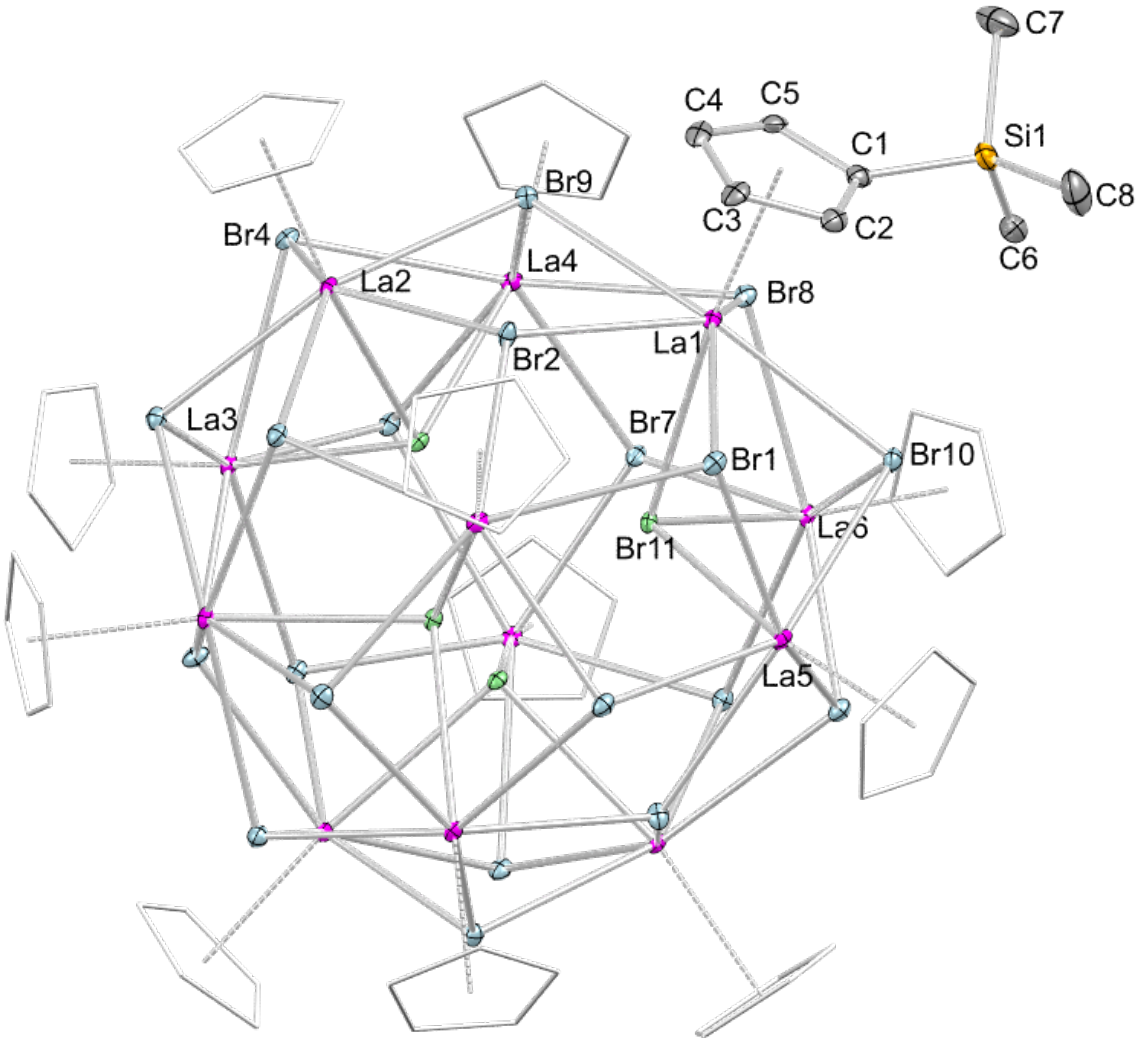

Figure S31. Crystal structure of $[Cp'LaBr_2]_{12}$ (**5b**) with atomic displacement parameters set at the 50% probability level. Hydrogen atoms are omitted for clarity. The Cp' ligands (except for one) are represented by a wireframe model for improved visualization. Selected interatomic distances [Å] and angles [°]: La1–C1 2.827(3); La1–C2 2.761(4); La1–C3 2.720(3); La1–C4 2.736(3); La1–C5 2.781(3); La1···Ct1 2.489; La1–Br1 3.1284(4); La1–Br2 3.1013(4); La1–Br8 3.0178 (4); La1–Br9 3.3451(4); La1–Br10 3.1461(4); La1–Br11 3.0972(4); C1–C2 1.425(5); C2–C3 1.424(5); C3–C4 1.405(5); C4–C5 1.411(6); C1–C5 1.425(5); C1–Si1 1.876(4); C1–C2–C3 109.1(3); C2–C3–C4 107.4(3); C3–C4–C5 108.4(3); C4–C5–C1 109.1(3); C5–C1–C2 106.0(3); Si1–C1–La1 133.00(2); Br1–La1–Br2 67.673(1); Br1–La1–Br10 75.057(1); Br2–La1–Br9 63.476(9); Br8–La1–Br9 68.432(1); Br8–La1–Br10 77.826(1); La1–Br2–La2 115.564(2); La1–Br8–La4 102.820(2); La1–Br9–La4 105.045(2); La1–Br1–La5 95.033(2); La1–Br10–La5 91.399(2); La1–Br11–La5 93.014(2); La1–Br8–La6 94.334(1); La1–Br10–La6 90.370(1); La1–Br11–La6 93.068(2).

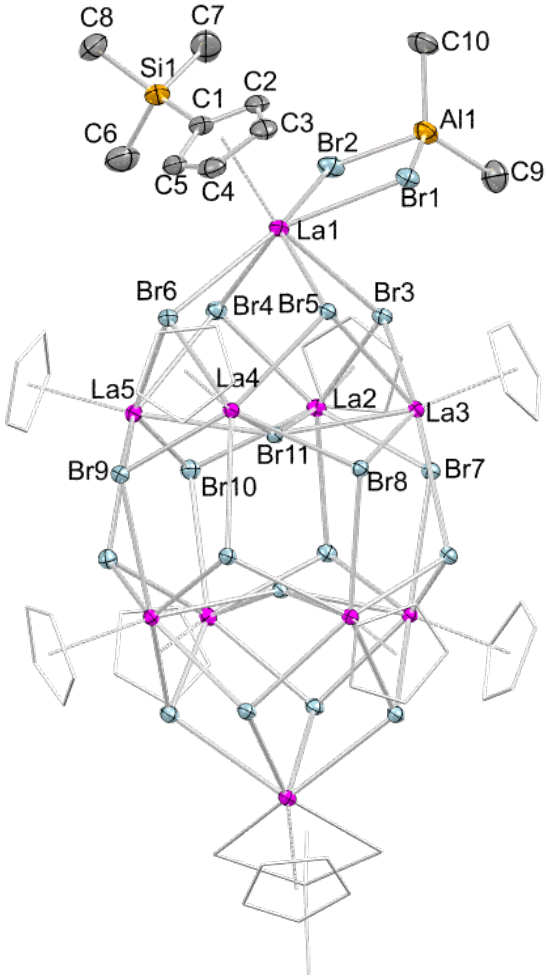

Figure S32. Crystal structure of $[Cp_5'La_5Br_{11}(AlMe_2]_2$ (**7**) with atomic displacement parameters set at the 50% probability level. Hydrogen atoms are omitted for clarity. The Cp' ligands (except for one) are represented by a wireframe model for improved visualization. Selected interatomic distances [Å] and angles [°]: La1–C1 2.803(4); La1–C2 2.764(4); La1–C3 2.757(4); La1–C4 2.753(4); La1–C5 2.766(4); La1···Ct1 2.494; La1–Br1 3.0945(4); La1–Br2 3.0595(5); La1···Al1 4.056; La1–Br3 3.2027(4); La1–Br4 3.1878(4); La1–Br5 3.1450(4); La1–Br6 3.3167(4); La2–Br3 3.0571(4); La2–Br4 3.1344(4); La2–Br7 3.1024(4); La2–Br10 3.0678(4); La2–Br11 3.2738(4); C1–C2 1.420(6); C2–C3 1.403(7); C3–C4 1.415(6); C4–C5 1.402(7); C1–C5 1.424(6); C1–Si1 1.877(5); Al1–Br1 2.4176(2); Al1–Br2 2.4494(2); Al1–C9 1.938(5); Al1–C10 1.936(5); C1–C2–C3 109.9(4); C2–C3–C4 107.6(4); C3–C4–C5 107.3(4); C4–C5–C1 110.1(4); C5–C1–C2 105.0(4); Si1–C1–La1 129.6(2); Br1–La1–Br2 73.474(2); Br1–Al1–Br2 98.28(5); La1–Br1–Al1 93.95(3); La1–Br2–Al1 94.18(3); Br1–La1–Br3 71.090(2); Br1–La1–Br4 139.239(2); Br1–La1–Br5 73.396(2); Br1–La1–Br6 140.703(2); Br3–La1–Br4 71.643(1); Br3–La1–Br5 73.381(1); Br3–La1–Br6 107.407(2)

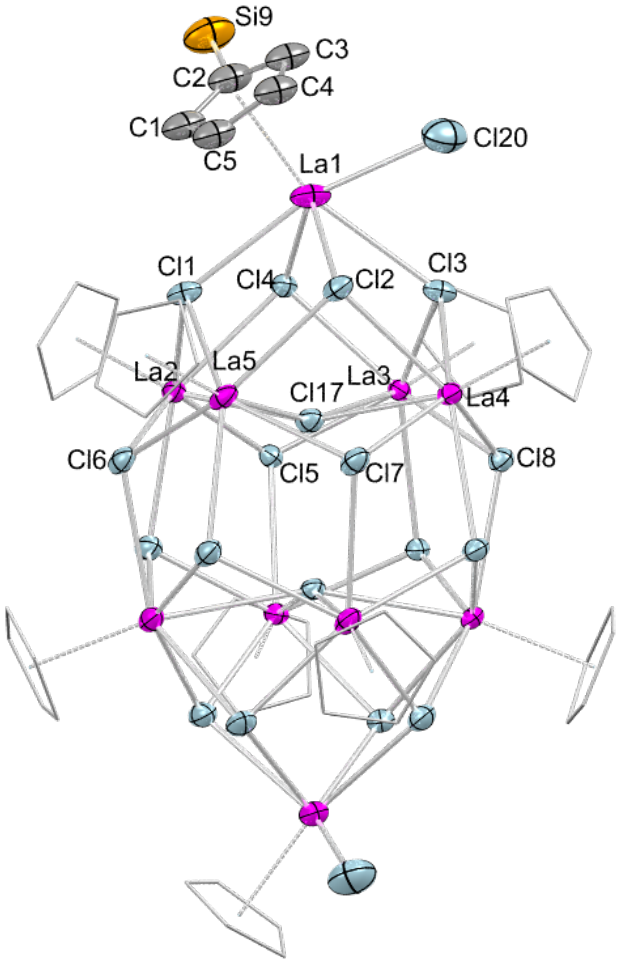

Figure S33. Connectivity of $[Cp'LaCl_2]_{10}$ (**8**) with atomic displacement parameters set at the 50% probability level. Hydrogen atoms are omitted for clarity. The Cp' ligands (except for one) are represented by a wireframe model for improved visualization. Due to disorder, the methyl groups of the Cp' ligands are omitted for clarity. Cell constants: a = 34.348(4), b = 16.020(2), 29.448(6), ß = 121.816(2), space group: *Cc*.

IR Spectroscopy

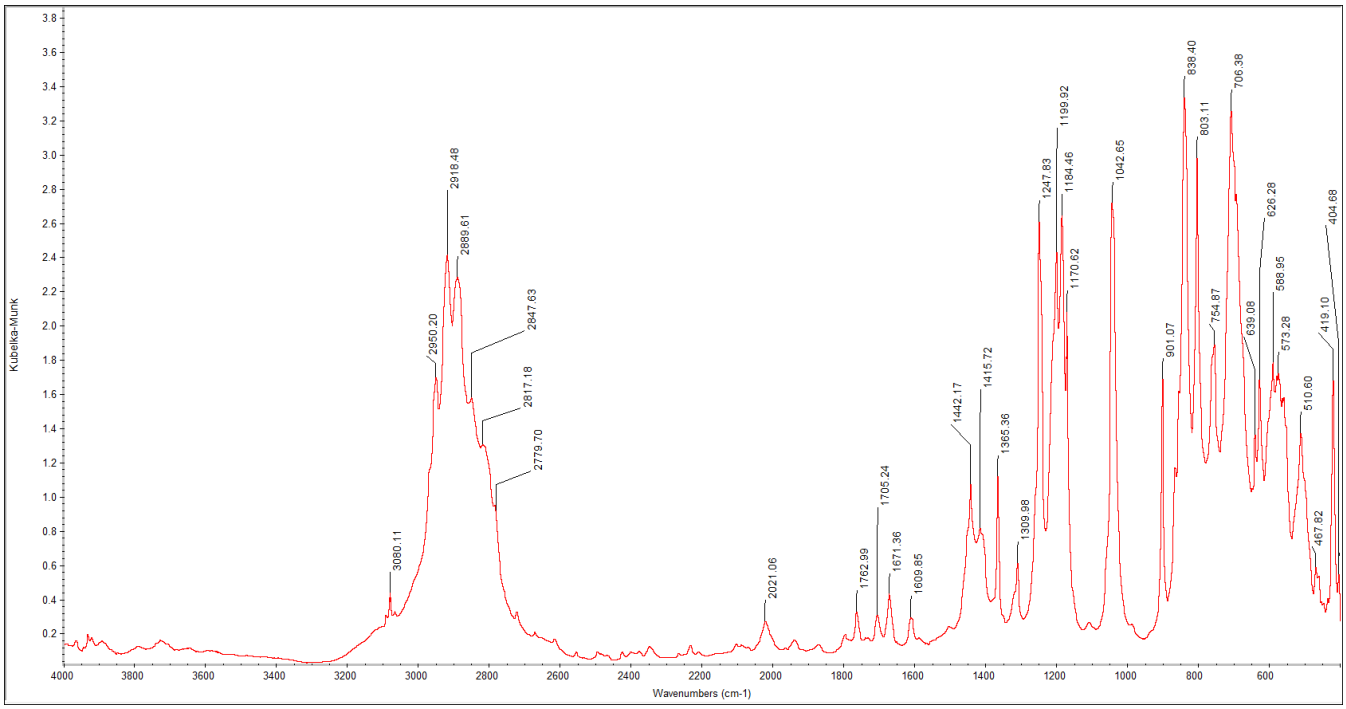

Figure S34. DRIFT spectrum of Cp'La($AlMe_4$)$_2$ (**1b**).

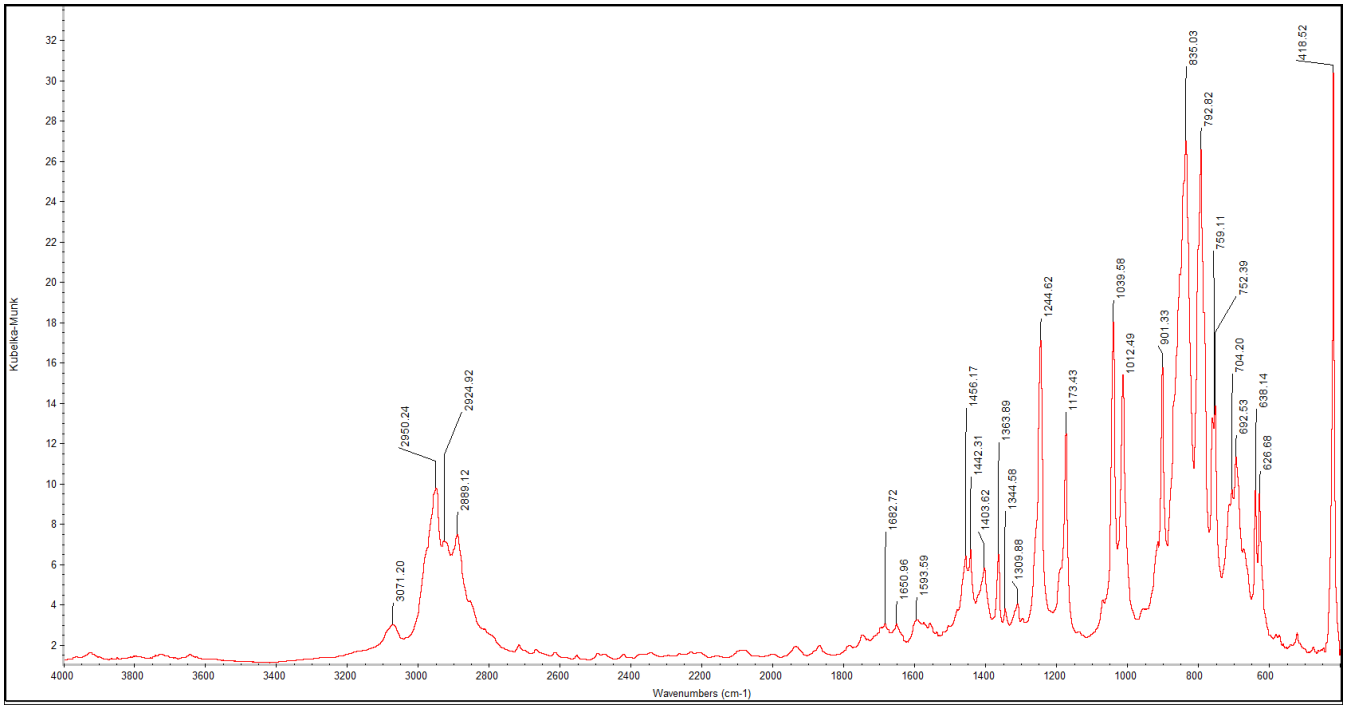

Figure S35. DRIFT spectrum of [Cp'$LaI_2(thf)_3$].

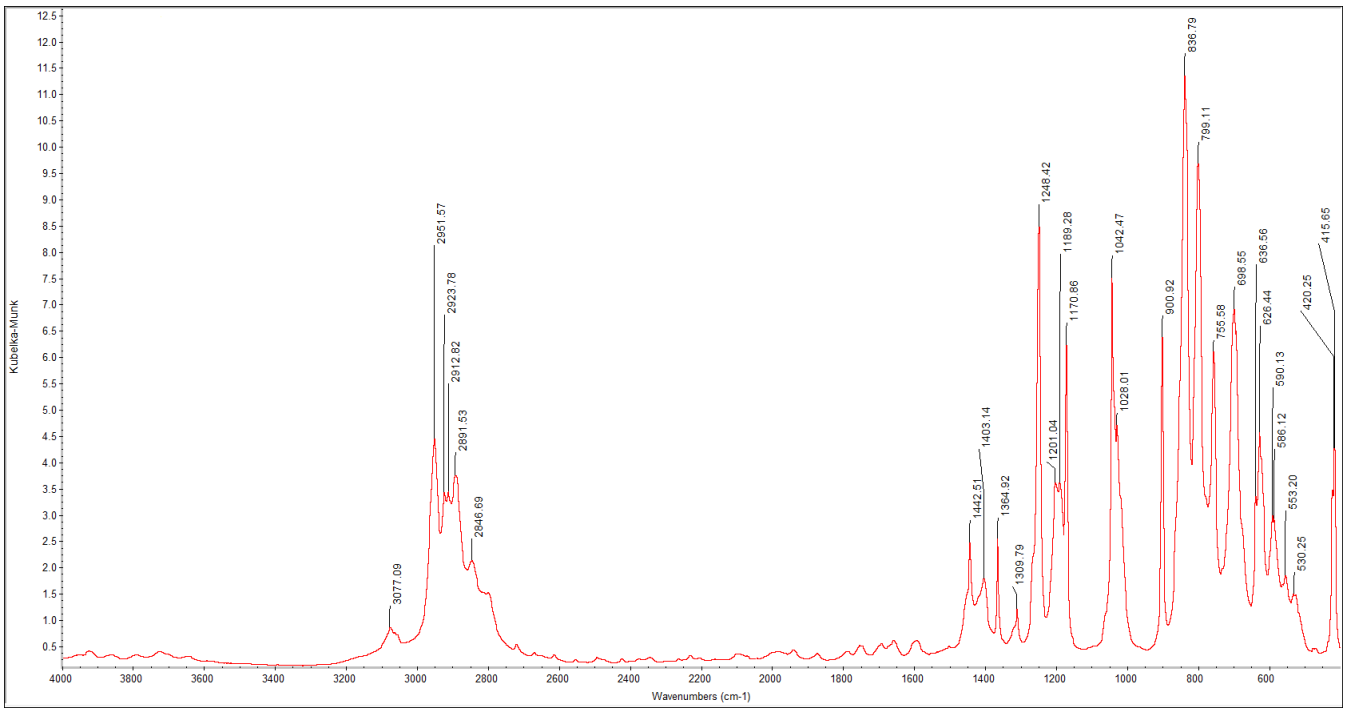

Figure S36. DRIFT spectrum of $[Cp'_6La_6I_8(AlMe_4)_4]$ (**4a**).

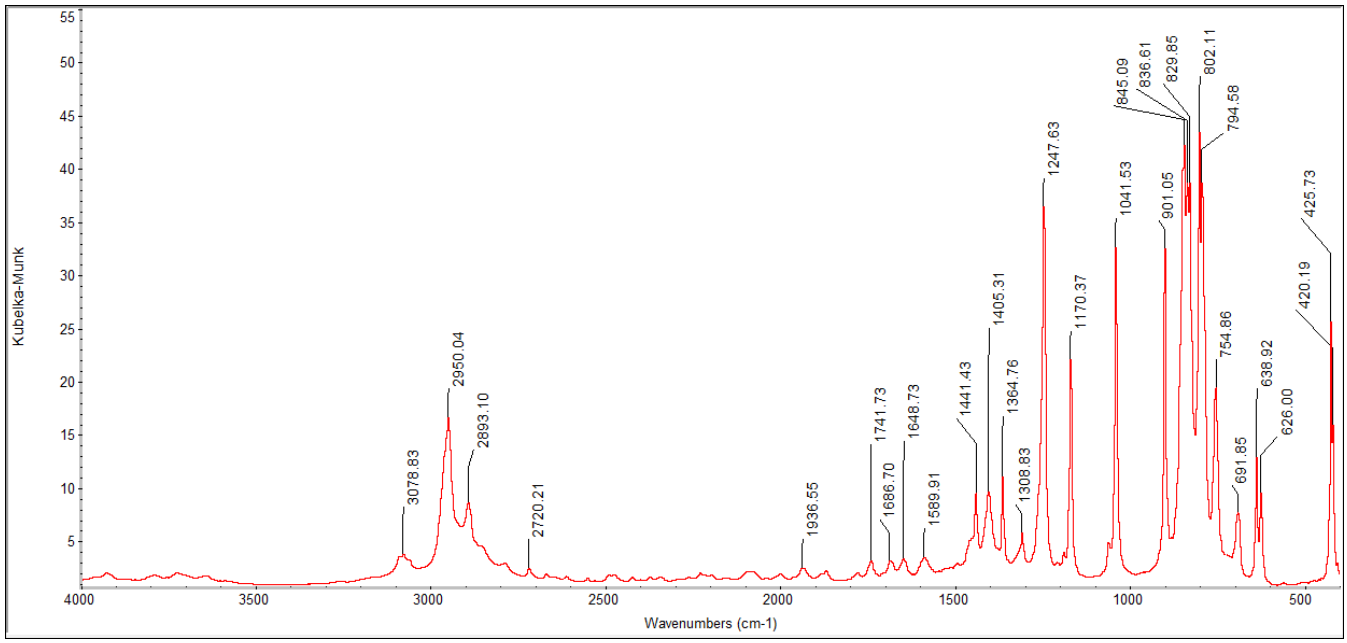

Figure S37. IR-DRIFT spectrum of $[Cp'LaI_2]_{12}$ (**5a**).

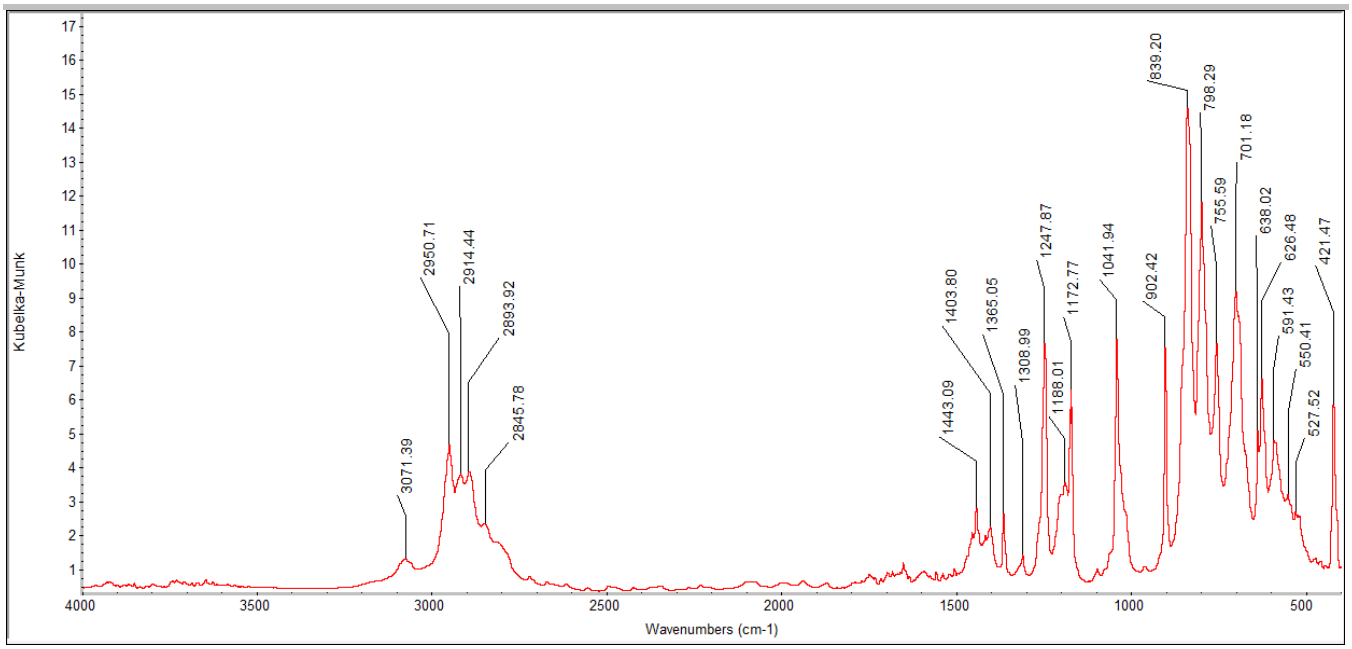

Figure S38. IR-DRIFT spectrum of $[Cp'_6La_6Br_8(AlMe_4)_4]$ (**4b**).

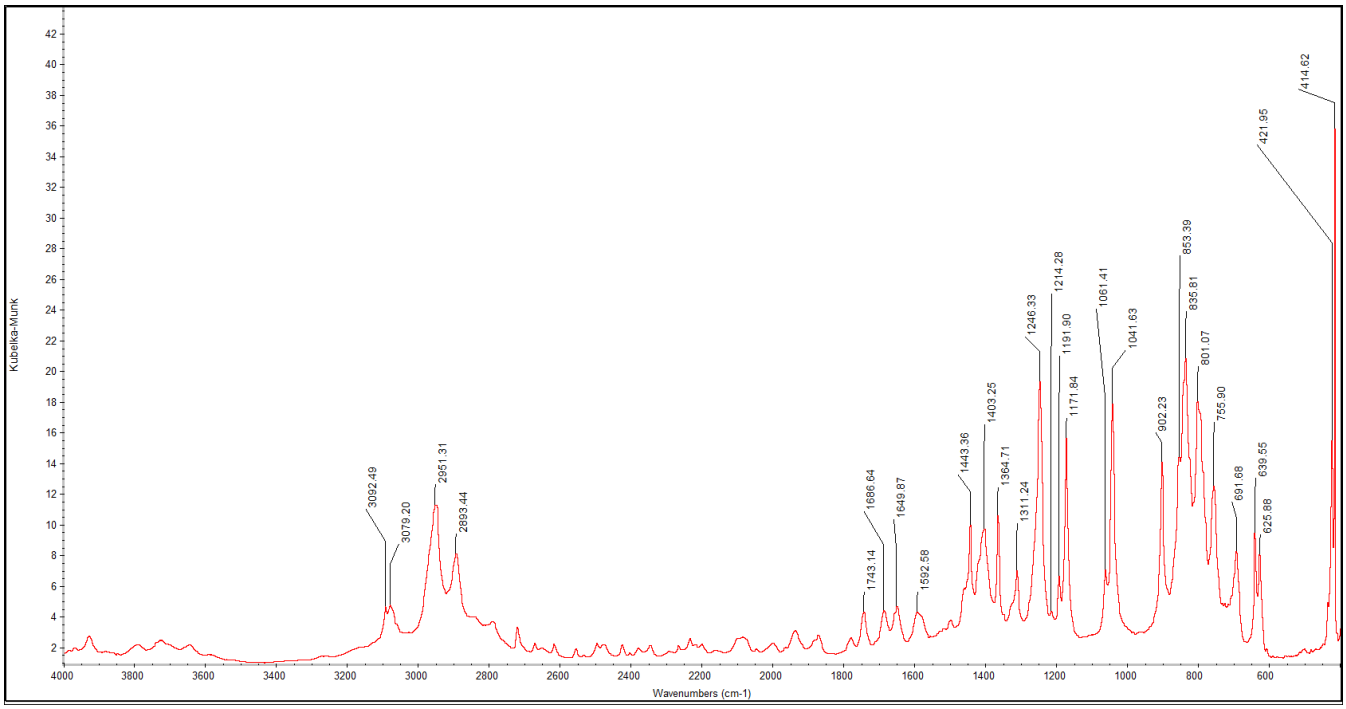

Figure S39. DRIFT spectrum of $[Cp'LaBr_2]_{12}$ (**5b**).

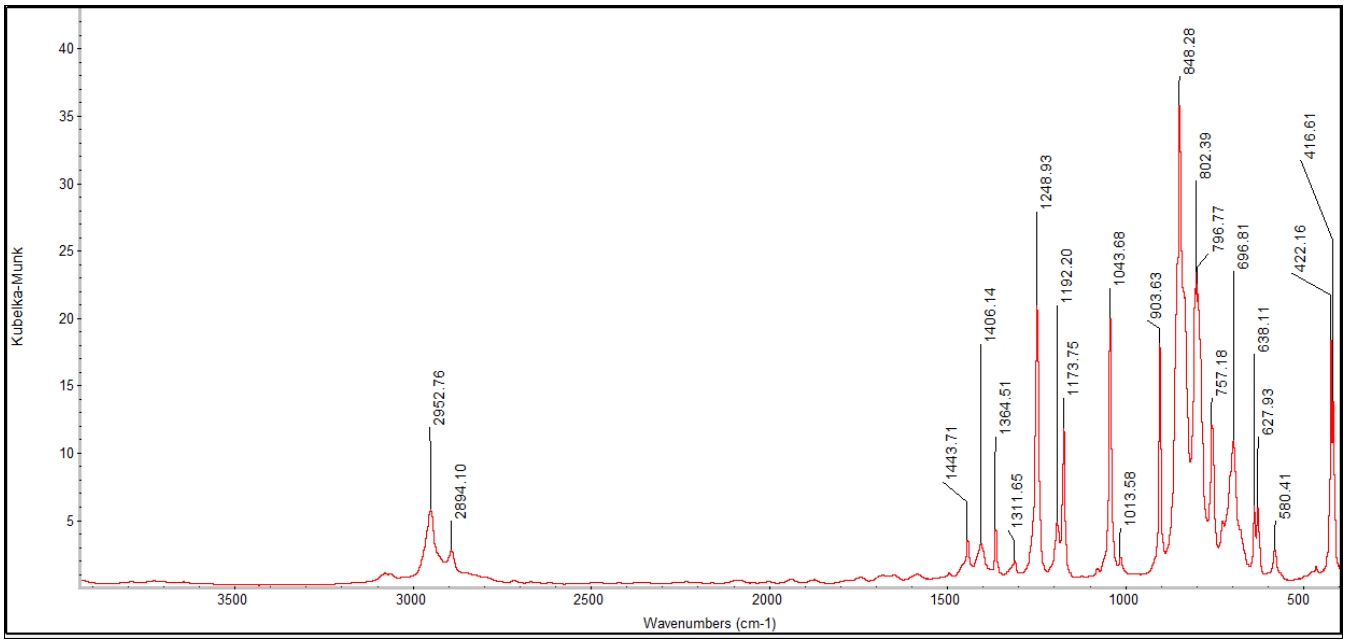

Figure S40. DRIFT spectrum of $[Cp'LaCl_2]_{10}$ (**8**).

EDX Measurements

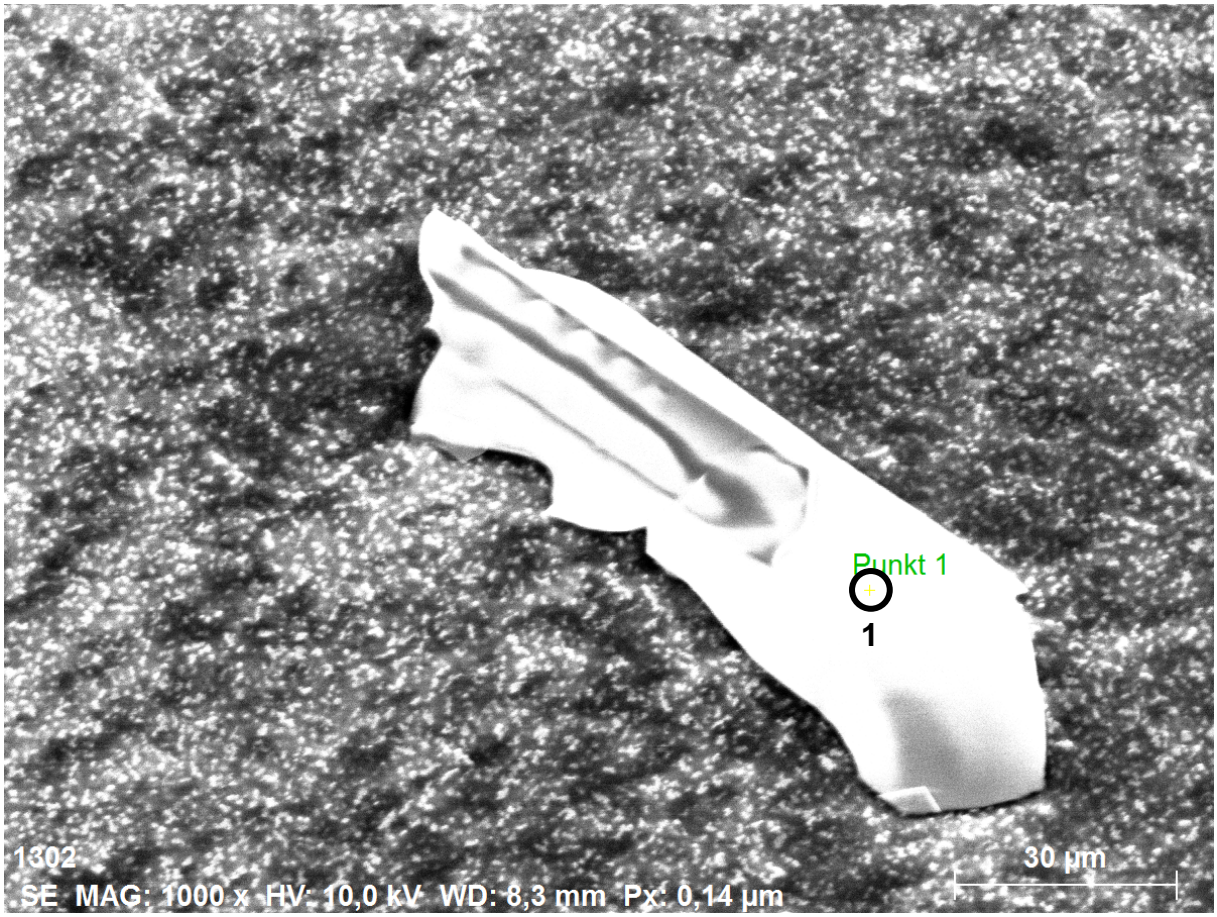

Figure S41. SEM image of crystalline $[Cp'_6La_6I_8(AlMe_4)_4]$ (**4a**) in position 1, where EDX measurement was performed.

Table S3. Results of EDX measurement at position 1 (Fig. S41)

Element	norm. wt. %	norm. atom %	3 σ	norm. wt. % calc.	norm. atom % calc.
Al	5.47	17.77	0.43	5.09	16.67
Si	8.01	24.99	0.56	7.93	25.00
La	40.75	25.68	2.16	39.22	25.00
I	45.75	31.56	2.29	47.77	33.33

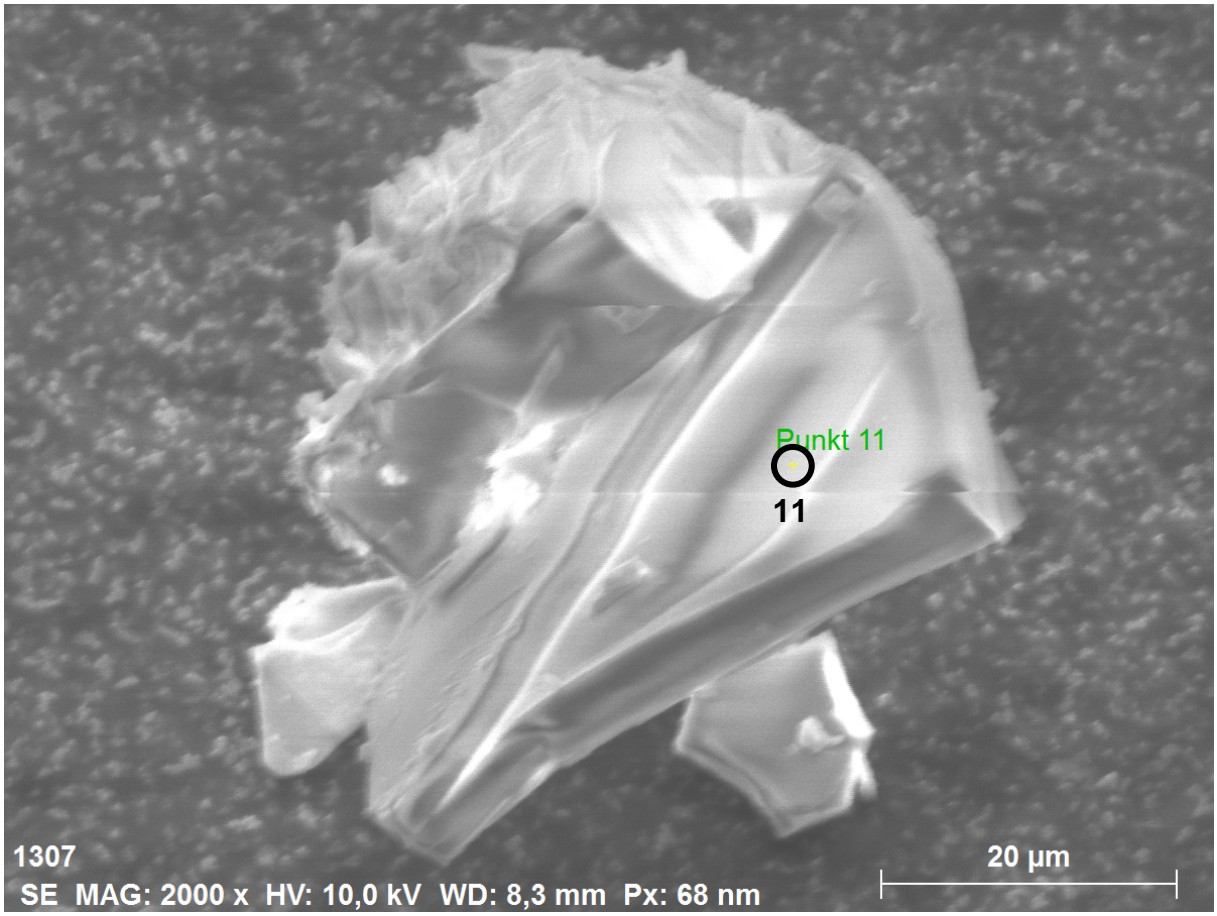

Figure S42. SEM image of crystalline $[Cp'_6La_6I_8(AlMe_4)_4]$ (**4a**) in position 11, where EDX measurement was performed.

Table S4. Results of EDX measurement at position 11 (Fig. S42)

Element	norm. wt. %	norm. atom %	3 σ	norm. wt. % calc.	norm. atom % calc.
Al	5.28	17.45	0.41	5.09	16.67
Si	7.45	23.65	0.52	7.93	25.00
La	39.86	25.59	2.07	39.22	25.00
I	47.39	33.30	2.31	47.77	33.33

Figure S43. SEM image of crystalline $[Cp'_6La_6I_8(AlMe_4)_4]$ (**4a**) in position 17, where EDX measurement was performed.

Table S5. Results of EDX measurement at position 17 (Fig. S43)

Element	norm. wt. %	norm. atom %	3 σ	norm. wt. % calc.	norm. atom % calc.
Al	5.33	17.38	0.43	5.09	16.67
Si	7.98	24.99	0.57	7.93	25.00
La	40.74	25.79	2.21	39.22	25.00
I	45.95	31.84	2.35	47.77	33.33

Table S6. Averaged results of all EDX measurements for **2a** (6 measurements)

Element	norm. wt. %	norm. atom %	3 σ	norm. wt. % calc.	norm. atom % calc.
Al	5.23	17.17	0.41	5.09	16.67
Si	7.77	24.52	0.54	7.93	25.00
La	40.77	26.02	2.16	39.22	25.00
I	46.24	32.30	2.31	47.77	33.33

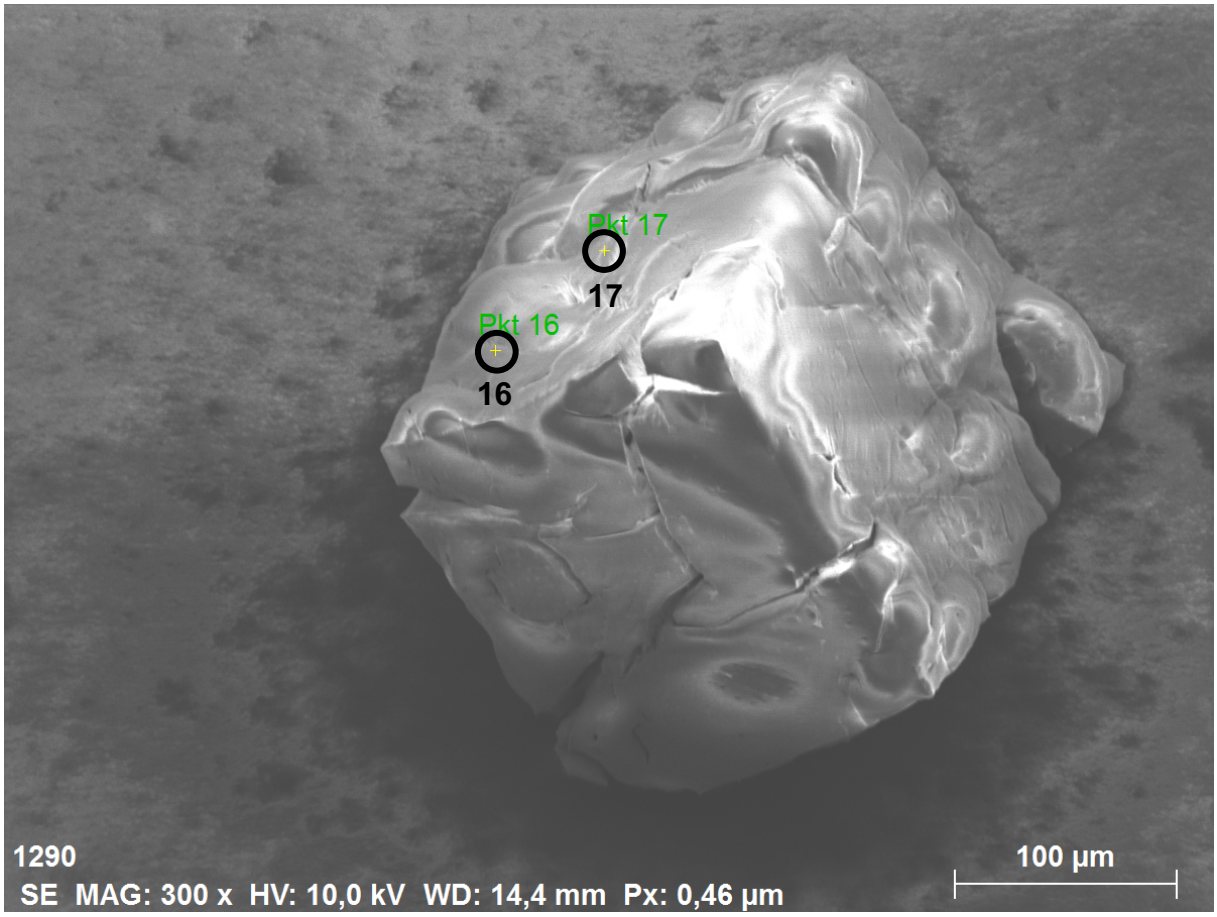

Figure S44. SEM image of crystalline $[Cp'LaI_2]_{12}$ (**5a**) in positions 16 and 17, where EDX measurements were performed.

Table S7. Results of EDX measurement at position 16 (Fig. S44)

Element	norm. wt. %	norm. atom %	3 σ	norm. wt. % calc.	norm. atom % calc.
Si	6.54	24.62	0.46	6.67	25.00
La	33.39	25.39	2.72	33.01	25.00
I	60.06	49.99	3.28	60.31	50.00

Table S8. Results of EDX measurement at position 17 (Fig. S44)

Element	norm. wt. %	norm. atom %	3 σ	norm. wt. % calc.	norm. atom % calc.
Si	6.59	24.74	0.48	6.67	25.00
La	32.59	24.73	2.68	33.01	25.00
I	60.82	50.52	3.12	60.31	50.00

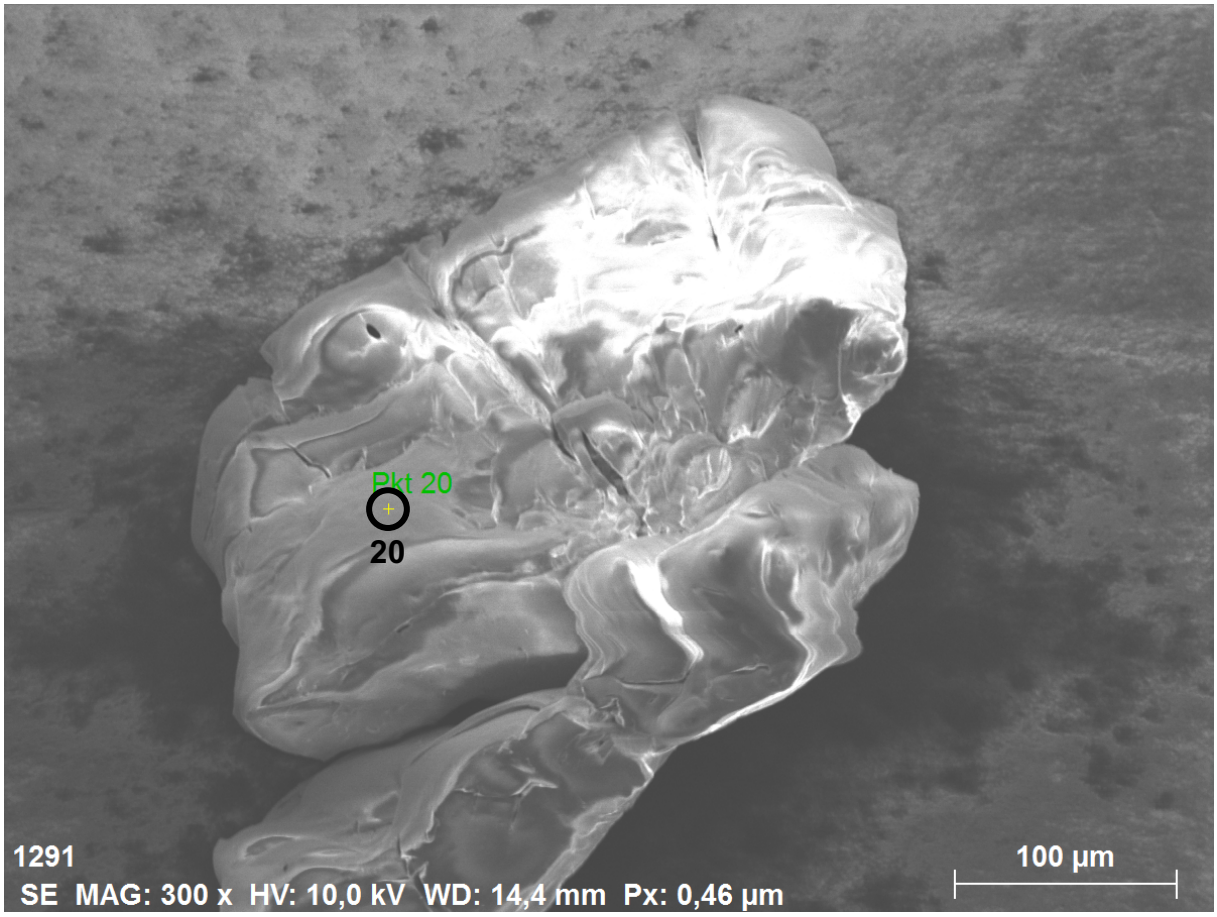

Figure S45. SEM image of crystalline $[Cp'LaI_2]_{12}$ (**5a**) in position 20, where EDX measurement was performed.

Table S9. Results of EDX measurement at position 20 (Fig. S45)

Element	norm. wt. %	norm. atom %	3 σ	norm. wt. % calc.	norm. atom % calc.
Si	6.74	25.19	0.45	6.67	25.00
La	32.51	24.57	3.61	33.01	25.00
I	60.74	50.24	4.04	60.31	50.00

Table S10. Averaged results of all EDX measurements for **2b** (12 measurements)

Element	norm. wt. %	norm. atom %	3 σ	norm. wt. % calc.	norm. atom % calc.
Si	6.41	24.19	0.41	6.67	25.00
La	33.27	25.41	2.65	33.01	25.00
I	60.32	50.40	2.98	60.31	50.00

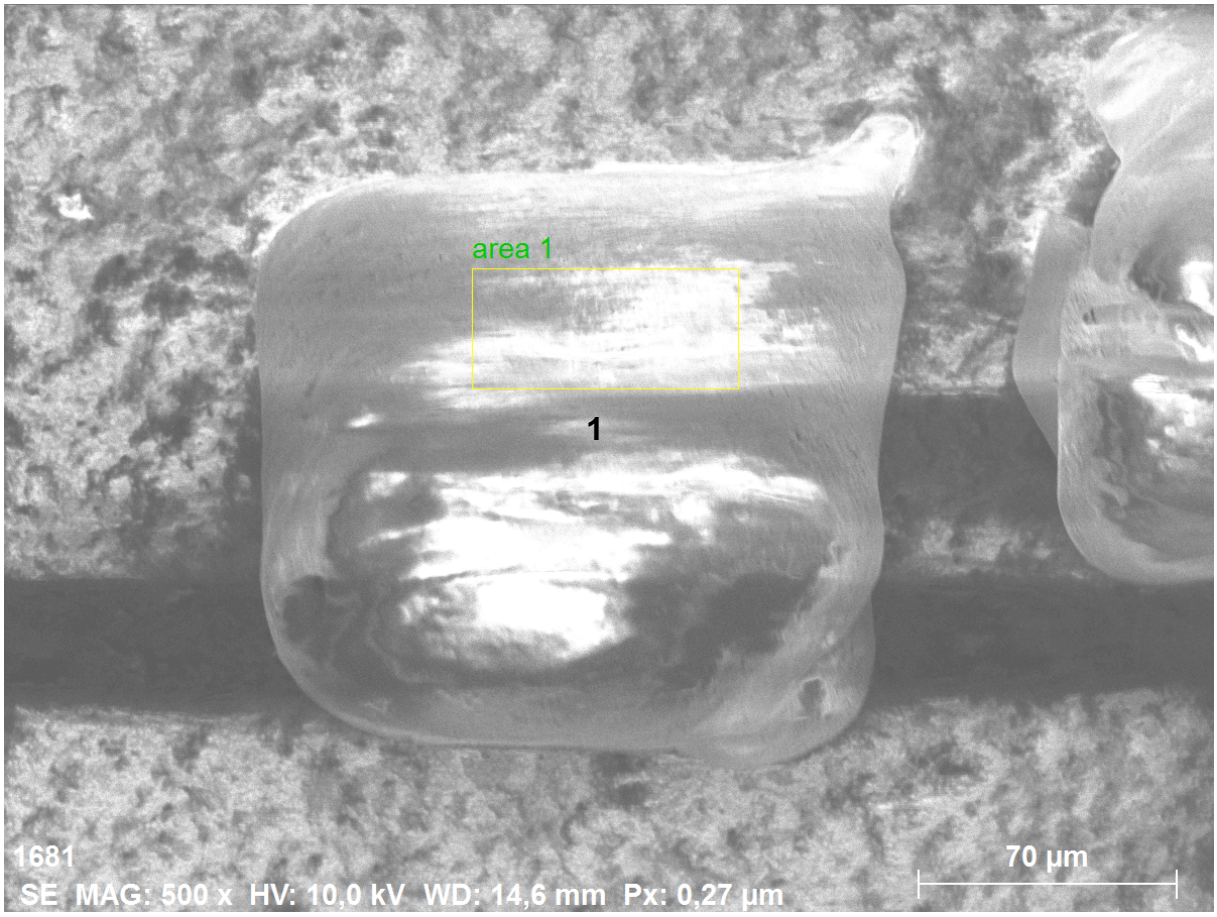

Figure S46. SEM image of crystalline [(μ-Cp)$_2$Cp'$_8$La$_8$I$_{14}$] (**6**) of area 1, where EDX measurement was performed.

Table S11. Results of EDX measurement of area 1 (Fig. S46)

Element	norm. wt. %	norm. atom %	3 σ	norm. wt. % calc.	norm. atom % calc.
Si	7.05	26.17	0.45	7.22	26.67
La	35.67	26.77	1.48	35.70	26.67
I	57.28	47.05	2.13	57.08	46.67

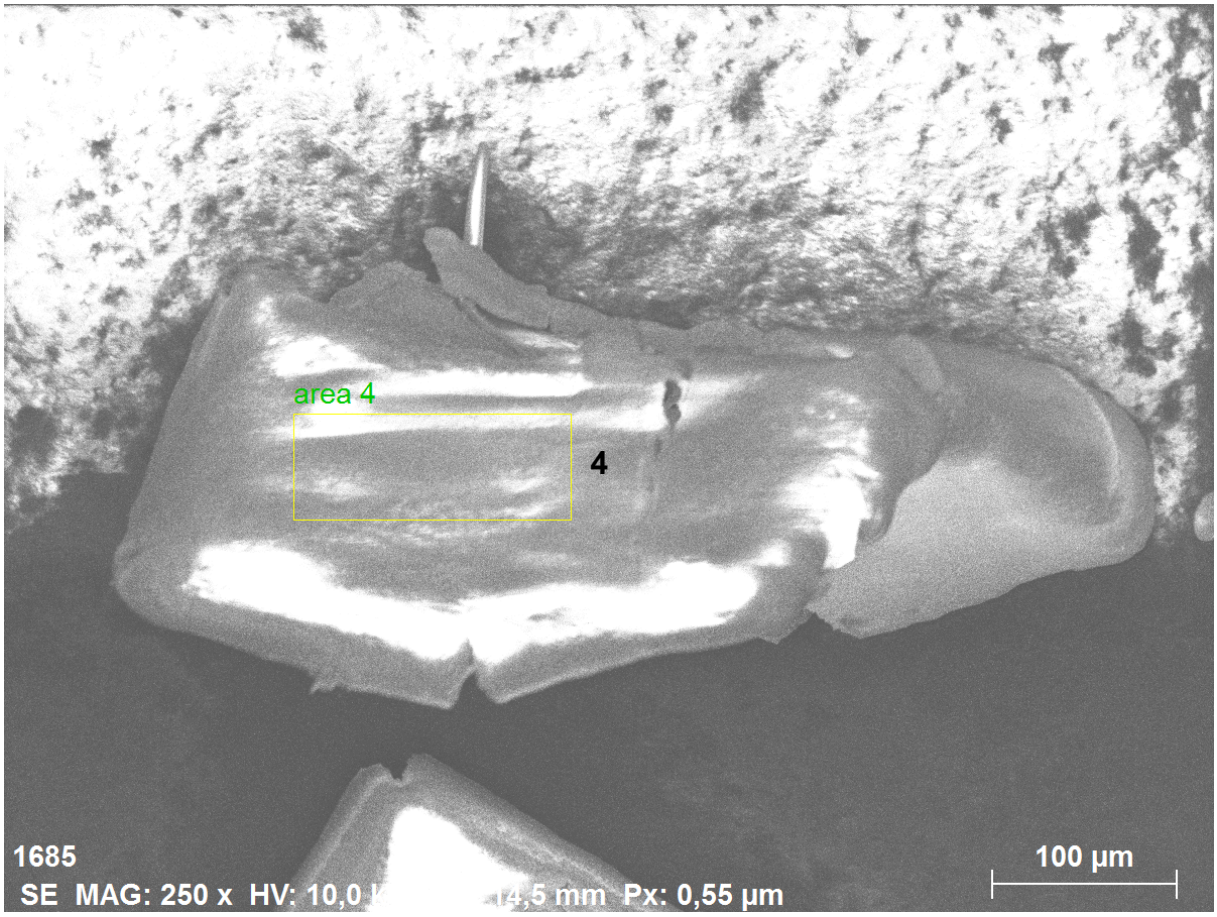

Figure S47. SEM image of crystalline [(μ-Cp)$_2$Cp'$_8$La$_8$I$_{14}$] (**6**) of area 4, where EDX measurement was performed.

Table S12. Results of EDX measurement of area 4 (Fig. S47)

Element	norm. wt. %	norm. atom %	3 σ	norm. wt. % calc.	norm. atom % calc.
Si	7.15	26.45	0.43	7.22	26.67
La	35.65	26.68	1.55	35.70	26.67
I	57.21	46.86	2.24	57.08	46.67

Figure S48. SEM image of crystalline [(μ-Cp)$_2$Cp'$_8$La$_8$I$_{14}$] (**6**) of area 5, where EDX measurement was performed.

Table S13. Results of EDX measurement of area 5 (Fig. S48).

Element	norm. wt. %	norm. atom %	3 σ	norm. wt. % calc.	norm. atom % calc.
Si	7.11	26.34	0.46	7.22	26.67
La	35.54	26.63	1.60	35.70	26.67
I	57.35	47.03	2.32	57.08	46.67

Table S14. Averaged results of all EDX measurements for **2c** (5 measurements)

Element	norm. wt. %	norm. atom %	3 σ	norm. wt. % calc.	norm. atom % calc.
Si	7.07	26.22	0.46	7.22	26.67
La	35.54	26.66	1.62	35.70	26.67
I	57.39	47.12	2.36	57.08	46.67

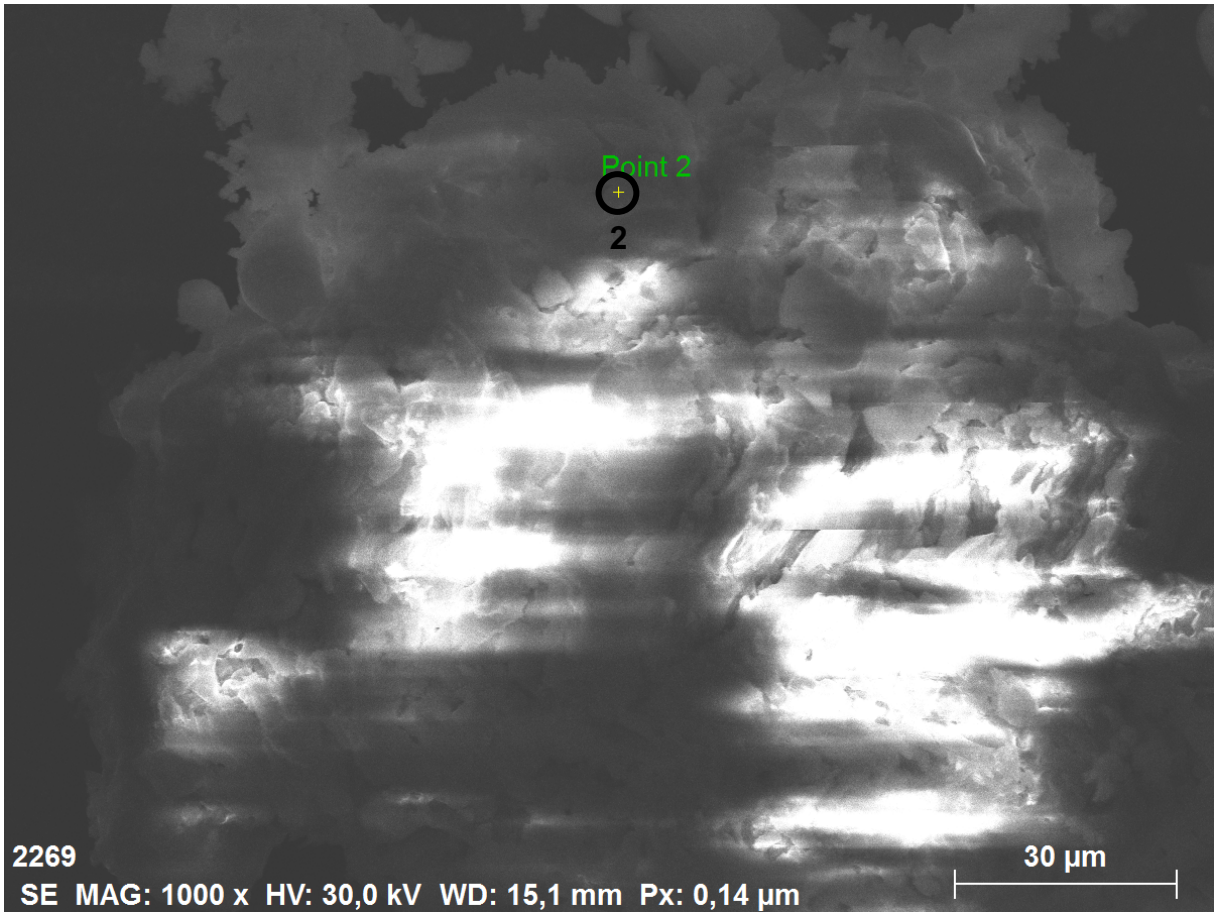

Figure S49. SEM image of crystalline $[Cp'_6La_6Br_8(AlMe_4)_4]$ (**4b**) in position 2, where EDX measurement was performed.

Table S15. Results of EDX measurement at position 2 (Fig. S49)

Element	norm. wt. %	norm. atom %	3 σ	norm. wt. % calc.	norm. atom % calc.
Si	8.40	25.58	1.04	9.63	25.00
La	54.29	33.42	3.74	47.65	25.00

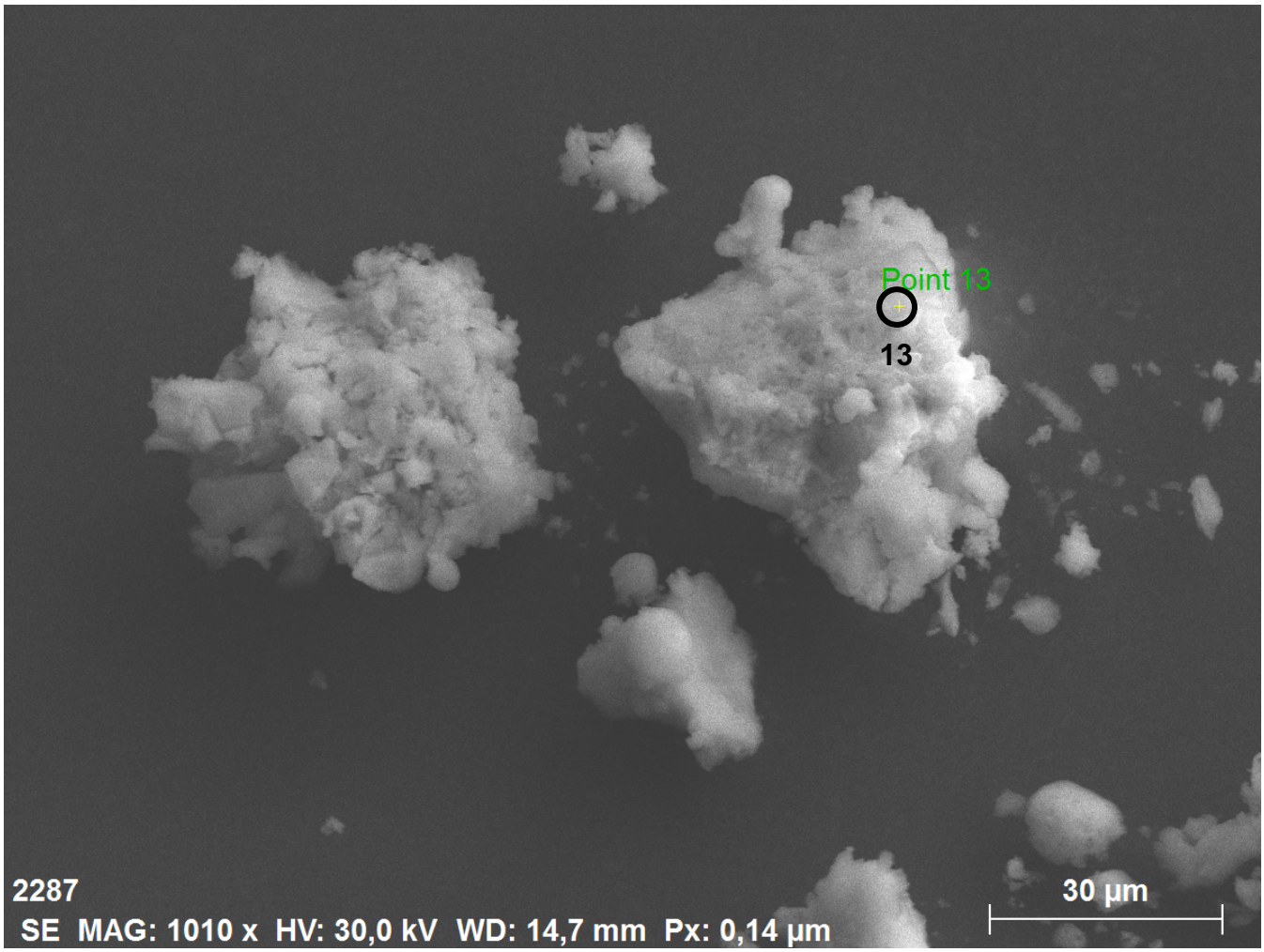

Figure S50. SEM image of crystalline $[Cp'_6La_6Br_8(AlMe_4)_4]$ (**4b**) in position 13, where EDX measurement was performed.

Table S16. Results of EDX measurement at position 13 (Fig. S50)

Element	norm. wt. %	norm. atom %	3 σ	norm. wt. % calc.	norm. atom % calc.
Si	7.89	24.03	1.04	9.63	25.00
La	49.85	30.71	3.74	47.65	25.00

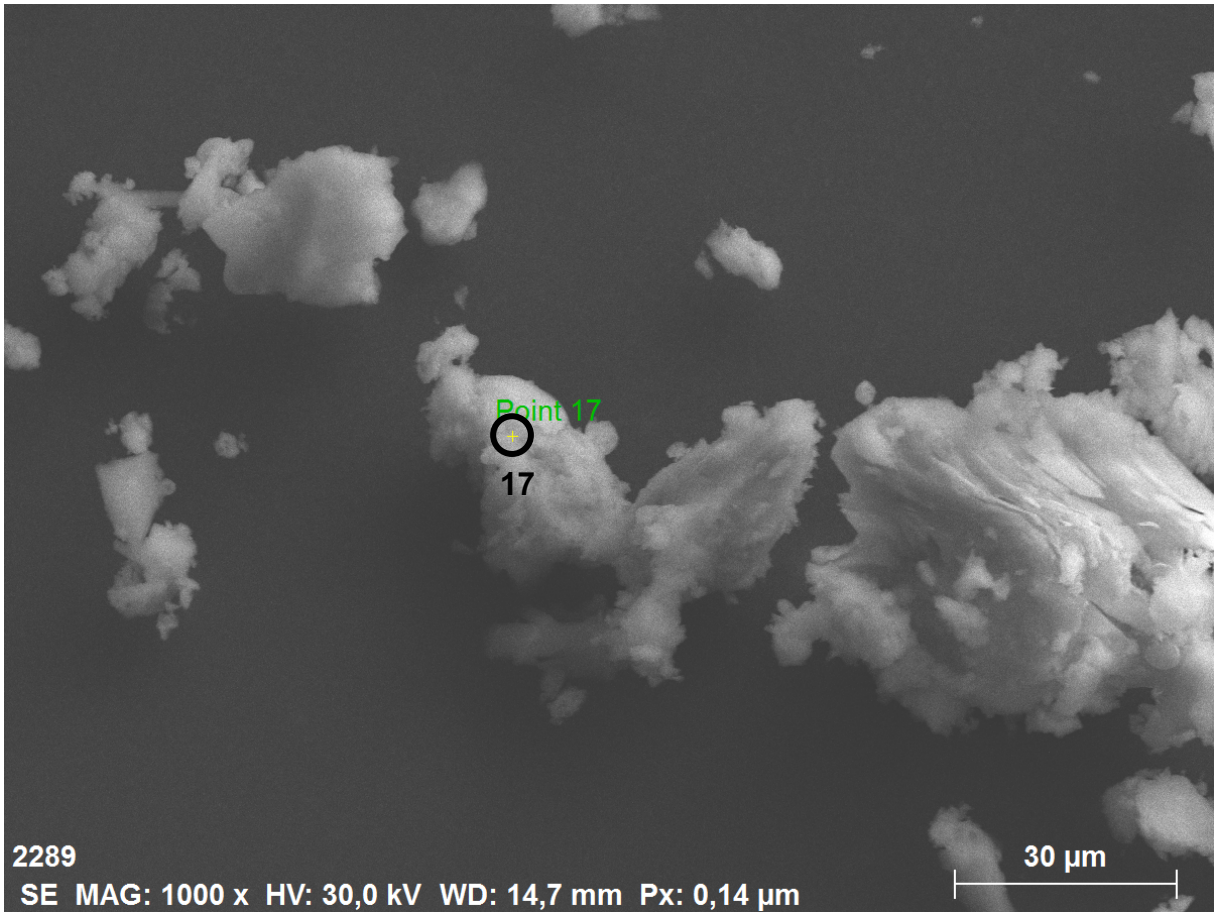

Figure S51. SEM image of crystalline $[Cp'_6La_6Br_8(AlMe_4)_4]$ (**4b**) in position 17, where EDX measurement was performed.

Table S17. Results of EDX measurement at position 17 (Fig. S51)

Element	norm. wt. %	norm. atom %	3 σ	norm. wt. % calc.	norm. atom % calc.
Si	7.56	22.86	1.04	9.63	25.00
La	46.70	30.71	3.56	47.65	25.00

Table S18. Averaged results of all EDX measurements for **3a** (18 measurements)

Element	norm. wt. %	norm. atom %	3 σ	norm. wt. % calc.	norm. atom % calc.
Si	6.99	21.85	0.90	9.63	25.00
La	48.76	32.64	3.62	47.65	25.00

The ratios for aluminum and bromine could not be determined reliably due to overlap of the respective signals.[11]

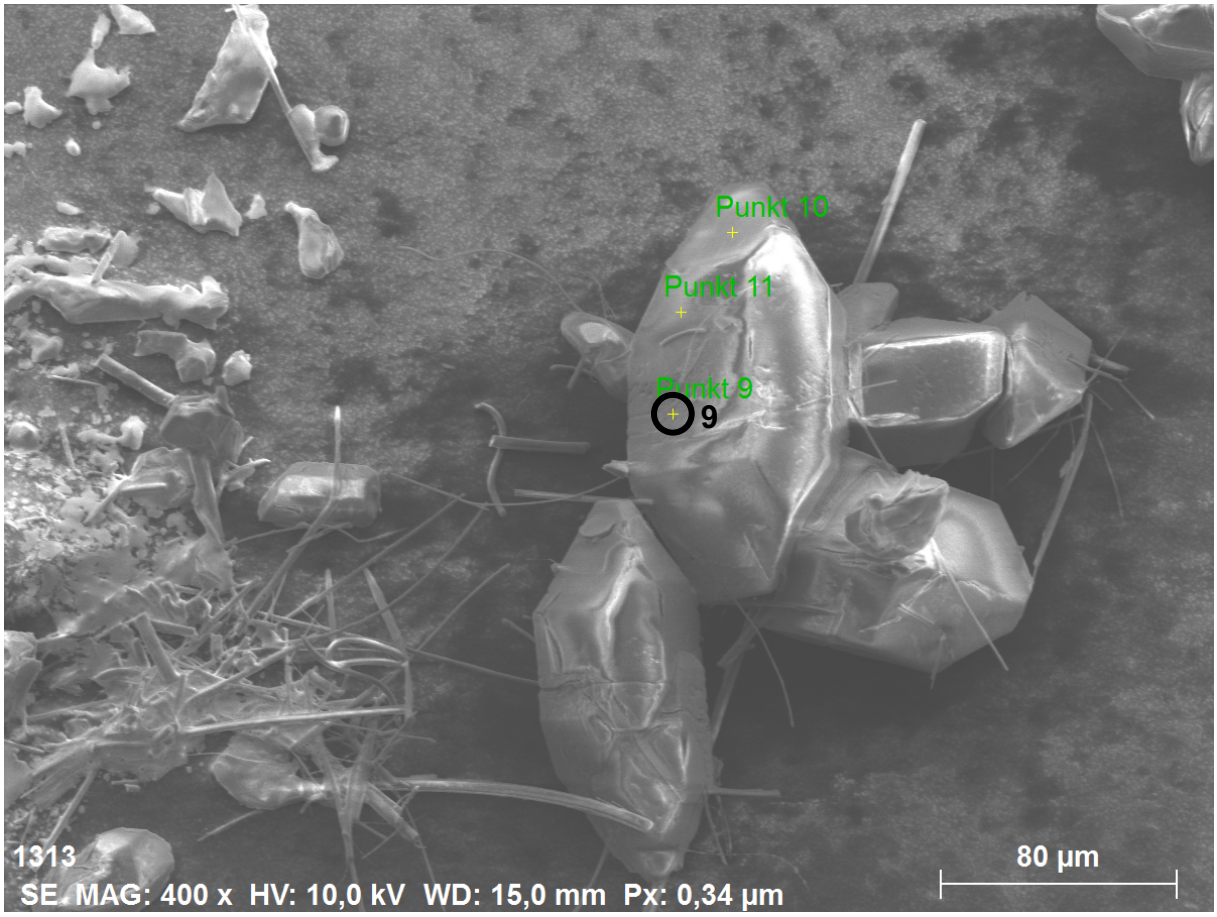

Figure S52. SEM image of crystalline $[Cp'LaBr_2]_{12}$ (**5b**) in position 9, where EDX measurement was performed.

Table S19. Results of EDX measurement at position 9 (Fig. S52)

Element	norm. wt. %	norm. atom %	3 σ	norm. wt. % calc.	norm. atom % calc.
Si	8.75	25.46	0.61	8.59	25.00
La	43.19	25.41	2.38	42.50	25.00
Br	48.05	49.14	3.16	48.90	50.00

Figure S53. SEM image of crystalline $[Cp'LaBr_2]_{12}$ (**5b**) in position 15, where EDX measurement was performed.

Table S20. Results of EDX measurement at position 15 (Fig. S53)

Element	norm. wt. %	norm. atom %	3 σ	norm. wt. % calc.	norm. atom % calc.
Si	8.24	24.07	0.73	8.59	25.00
La	41.91	24.75	2.36	42.50	25.00
Br	49.85	51.18	4.45	48.90	50.00

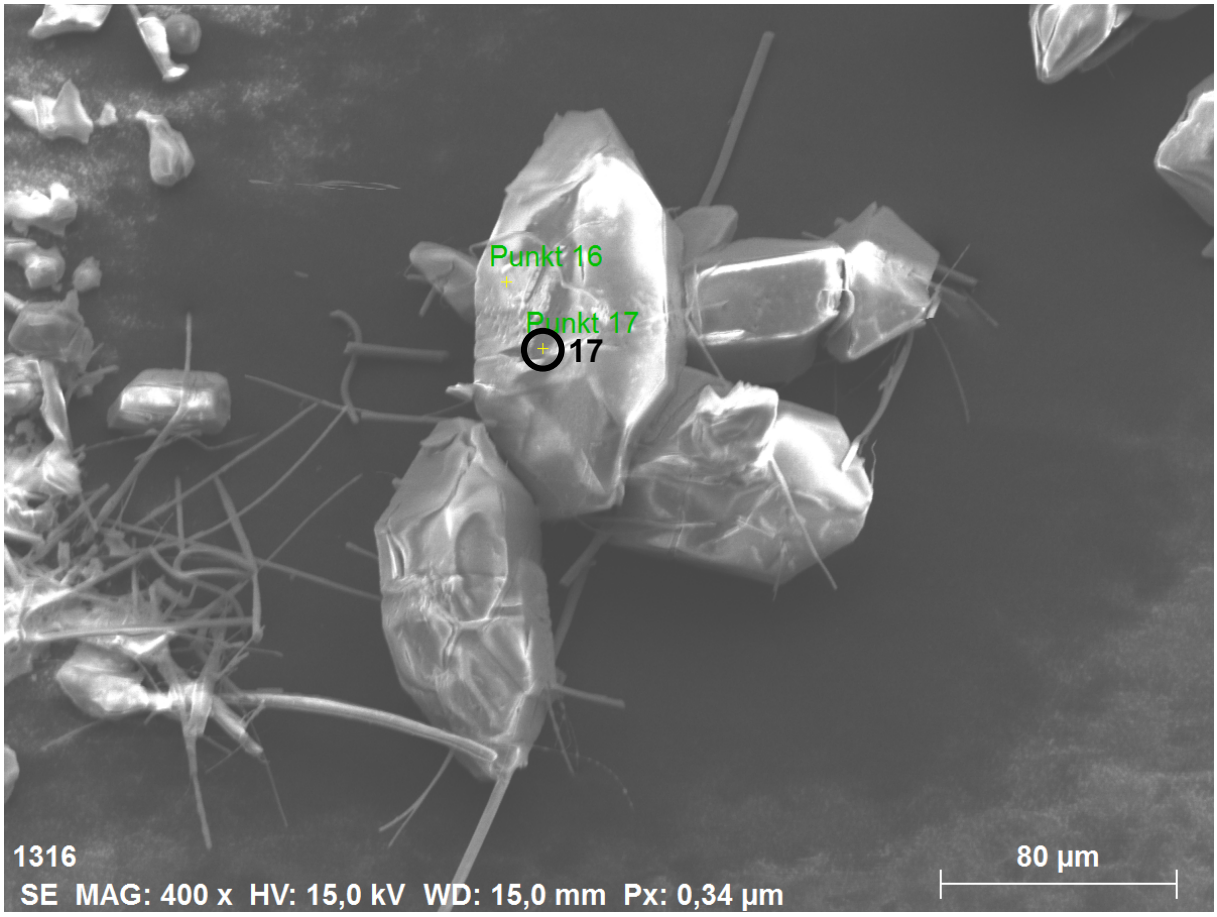

Figure S54. SEM image of crystalline $[Cp'LaBr_2]_{12}$ (**5b**) in position 17, where EDX measurement was performed.

Table S21. Results of EDX measurement at position 17 (Fig. S54)

Element	norm. wt. %	norm. atom %	3 σ	norm. wt. % calc.	norm. atom % calc.
Si	8.24	24.07	0.58	8.59	25.00
La	41.91	24.75	1.85	42.50	25.00
Br	49.85	51.18	3.35	48.90	50.00

Table S22. Averaged results of all EDX measurements for **3b** (11 measurements)

Element	norm. wt. %	norm. atom %	3 σ	norm. wt. % calc.	norm. atom % calc.
Si	8.27	24.24	0.57	8.59	25.00
La	42.78	25.35	2.13	42.50	25.00
Br	49.35	50.41	3.16	48.90	50.00

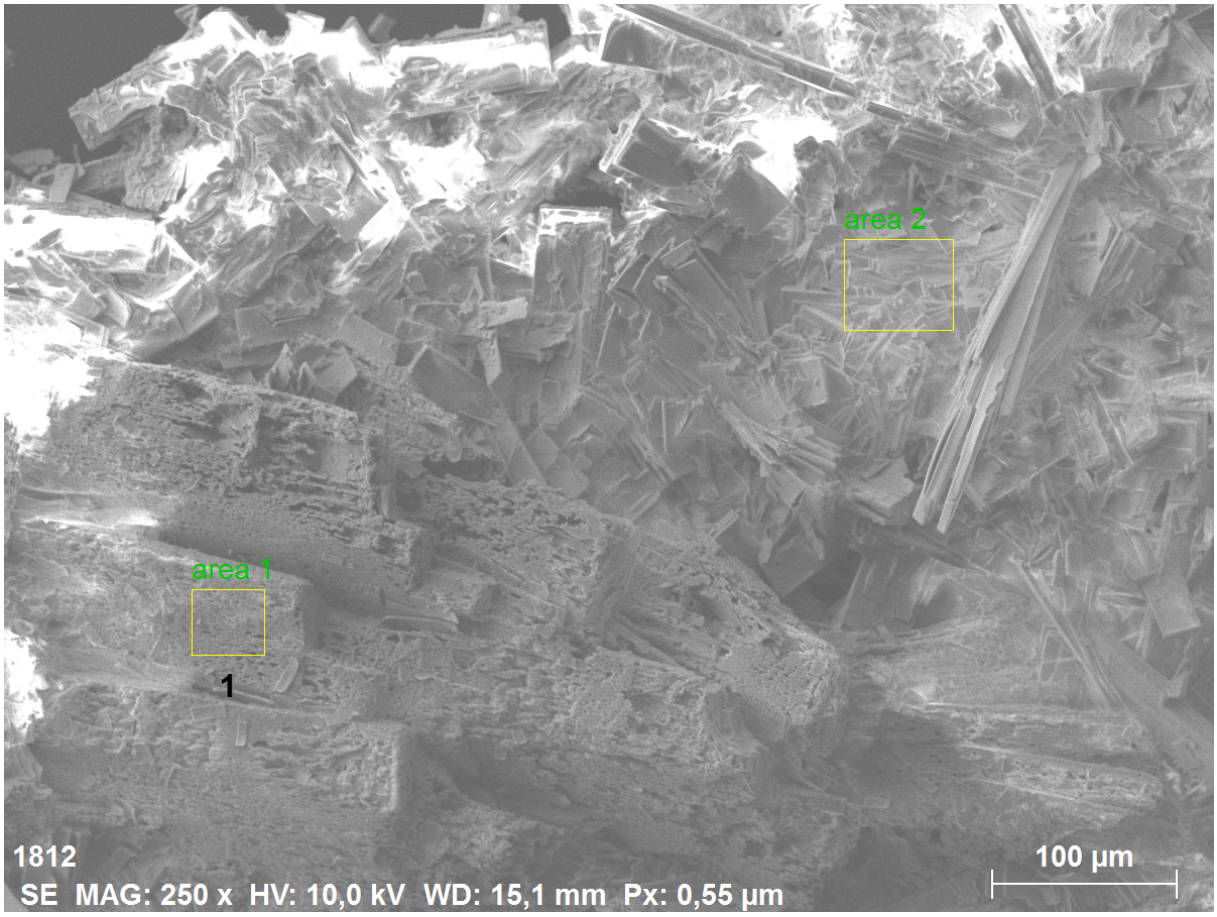

Figure S55. SEM image of crystalline [Cp'$_{10}$La$_{10}$Br$_{22}$(AlMe$_2$)$_2$] (**7**) of area 1, where EDX measurement was performed.

Table S23. Results of EDX measurement of area 1 (Fig. S55)

Element	norm. wt. %	norm. atom %	3 σ	norm. wt. % calc.	norm. atom % calc.
Si	7.59	22.23	0.74	8.07	22.73
La	39.64	23.47	3.17	39.90	22.73

The values for area 2 could not be determined due to shadowing effects caused by the morphology of the crystal.

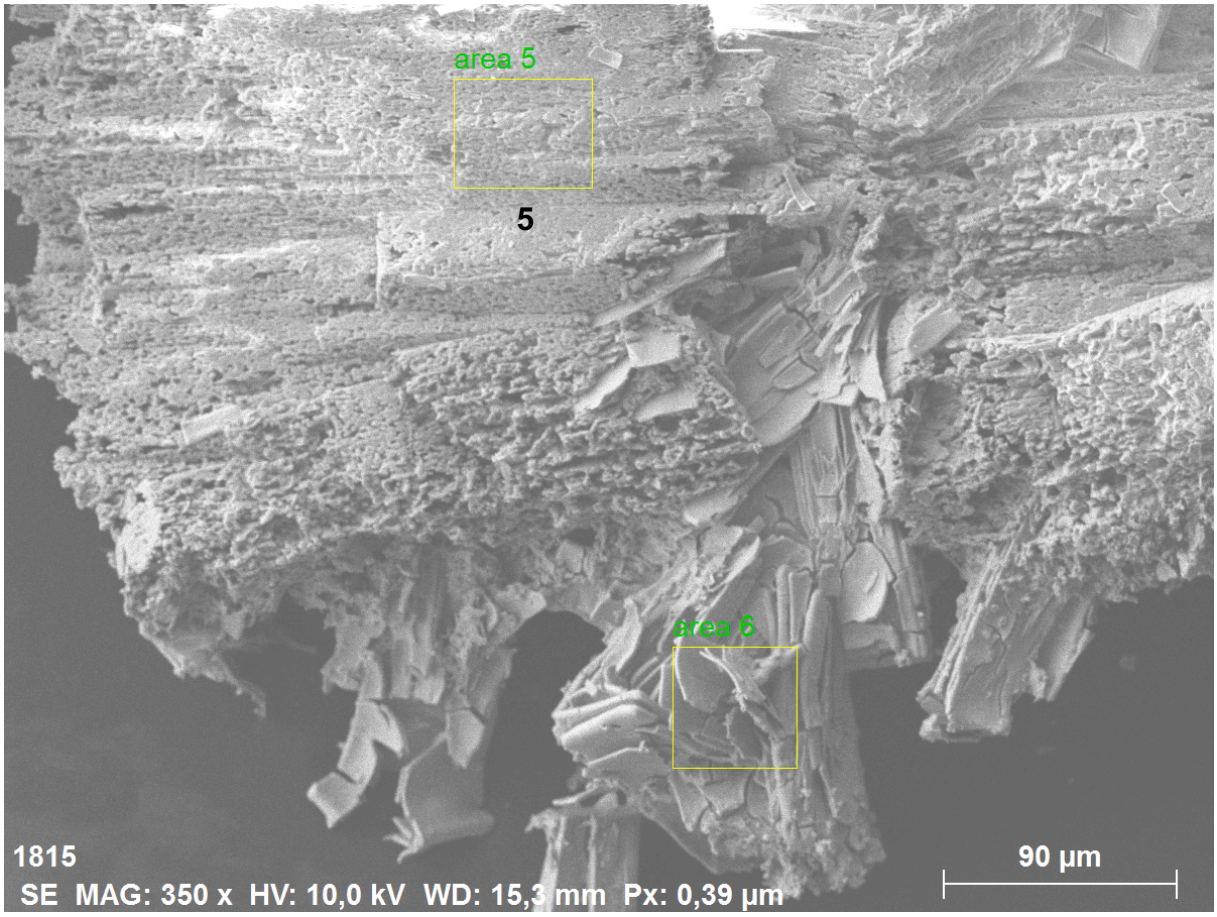

Figure S56. SEM image of crystalline [Cp'$_{10}$La$_{10}$Br$_{22}$(AlMe$_2$)$_2$] (**7**) of area 5, where EDX measurement was performed.

Table S24. Results of EDX measurement of area 5 (Fig. S56)

Element	norm. wt. %	norm. atom %	3 σ	norm. wt. % calc.	norm. atom % calc.
Si	7.76	22.62	0.75	8.07	22.73
La	39.40	23.23	3.13	39.90	22.73

The values for area 6 could not be determined due to shadowing effects caused by the morphology of the crystal.

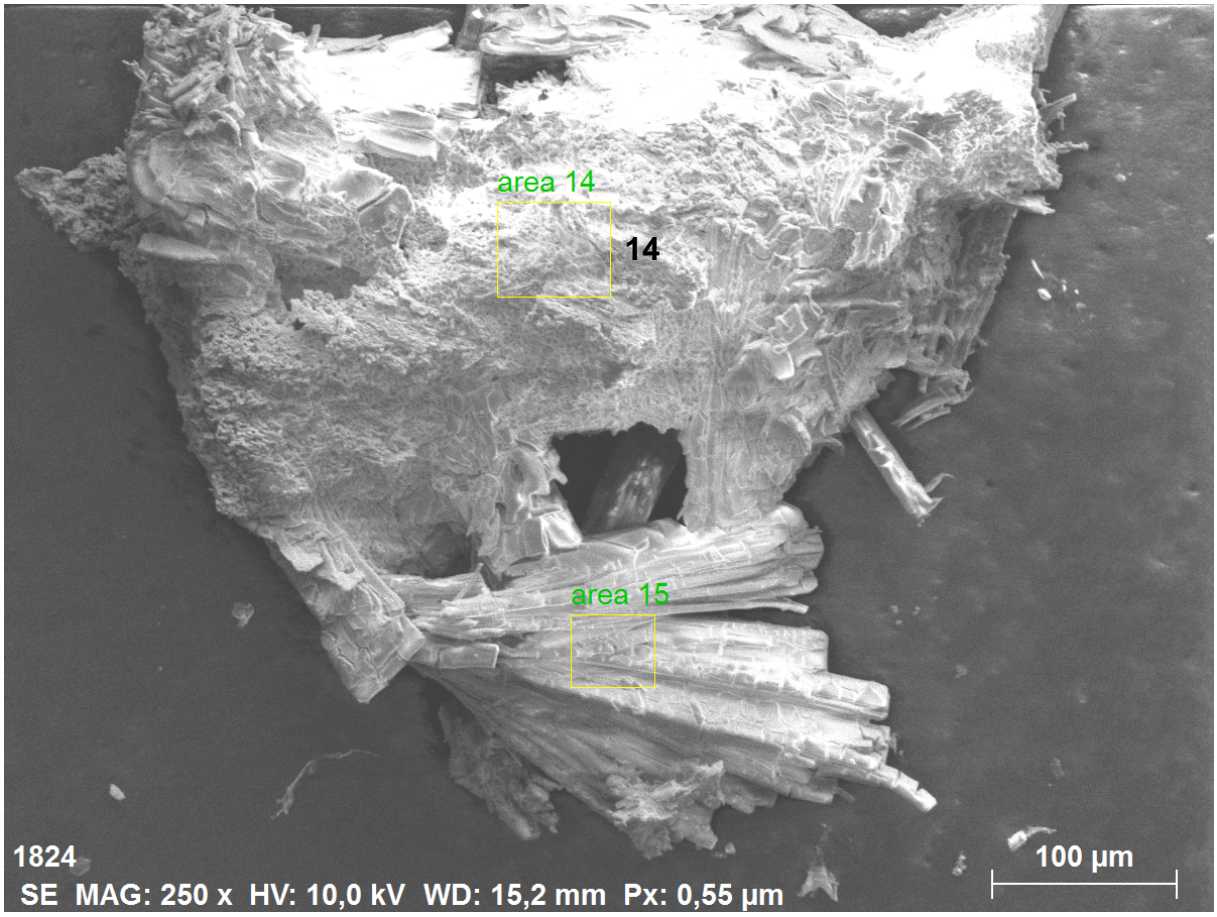

Figure S57. SEM image of crystalline [Cp'$_{10}$La$_{10}$Br$_{22}$(AlMe$_2$)$_2$] (**7**) of area 14, where EDX measurement was performed.

Table S25. Results of EDX measurement of area 14 (Fig. S57)

Element	norm. wt. %	norm. atom %	3 σ	norm. wt. % calc.	norm. atom % calc.
Si	8.09	23.39	0.89	8.07	22.73
La	38.96	22.78	3.49	39.90	22.73

The values for area 15 could not be determined due to shadowing effects caused by the morphology of the crystal.

Table S26. Averaged results of all EDX measurements for **3c** (5 measurements)

Element	norm. wt. %	norm. atom %	3 σ	norm. wt. % calc.	norm. atom % calc.
Si	7.64	22.26	0.83	8.07	22.73
La	38.84	22.89	3.40	39.90	22.73

The ratios for aluminum and bromine could not be determined reliably due to overlap of the respective signals.[11]

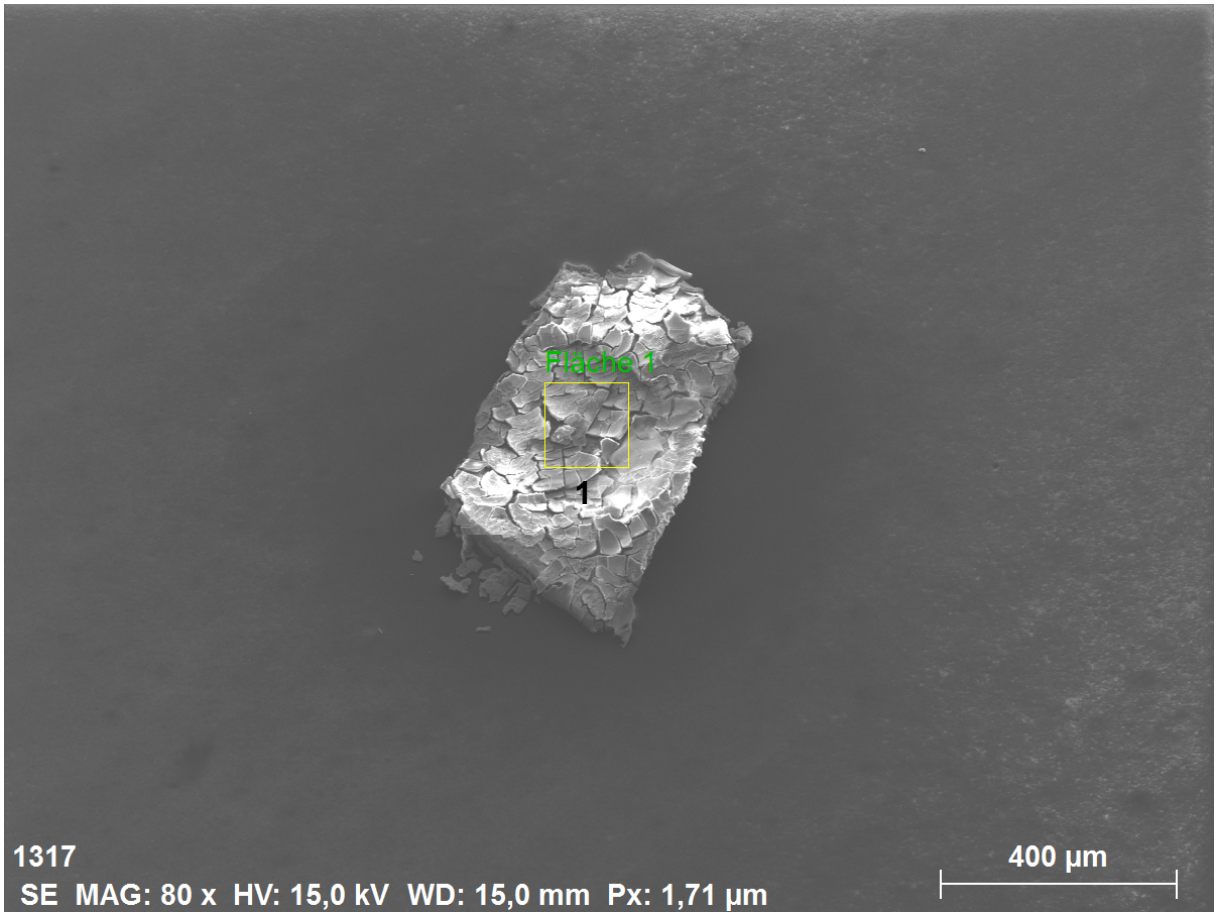

Figure S58. SEM image of crystalline $[Cp'La_2Cl_2]_{10}$ (**8**) of area 1, where EDX measurement was performed.

Table S27. Results of EDX measurement of area 1 (Fig. S58)

Element	norm. wt. %	norm. atom %	3 σ	norm. wt. % calc.	norm. atom % calc.
Si	11.33	24.06	0.72	11.81	25.00
La	58.47	25.11	2.34	58.39	25.00
Cl	30.20	50.82	1.43	29.80	50.00

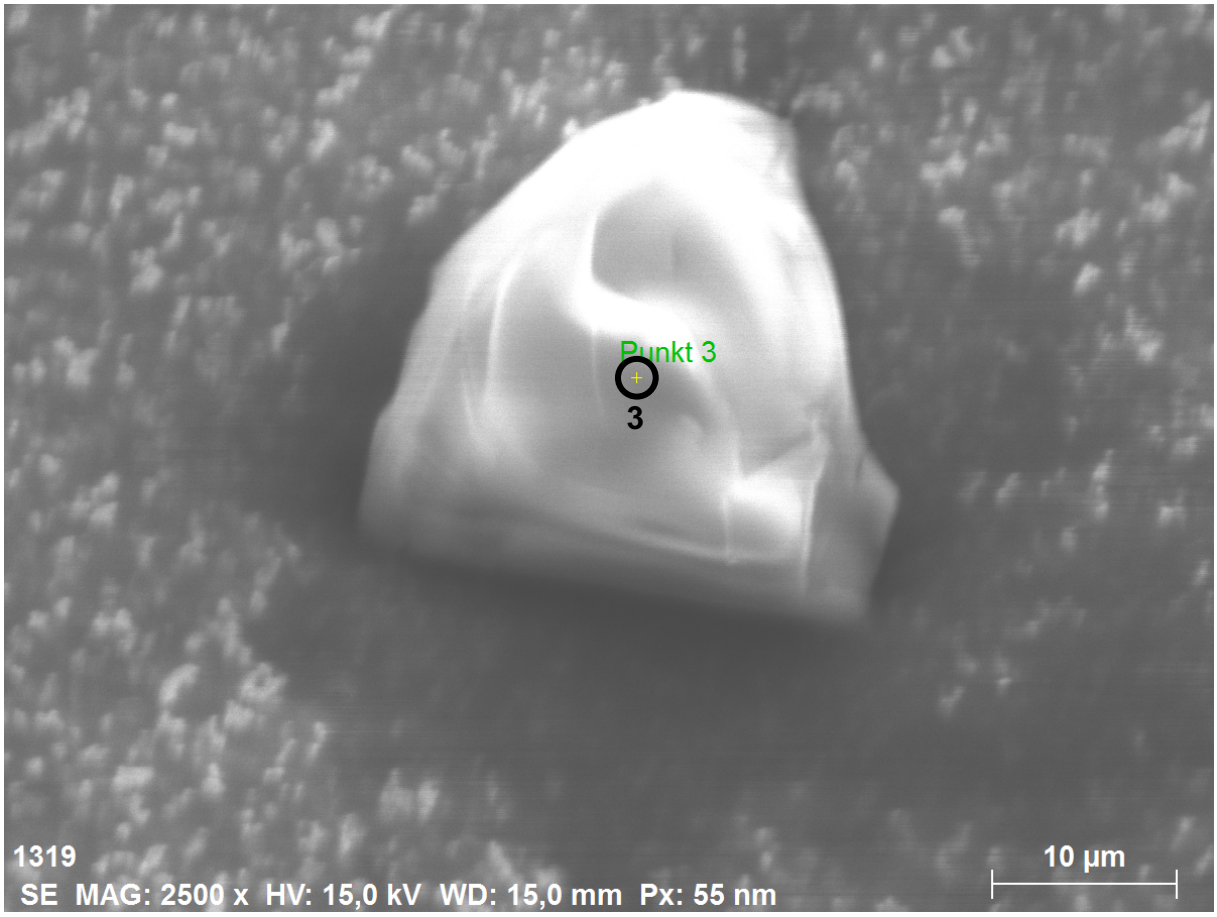

Figure S59. SEM image of crystalline $[Cp'La_2Cl_2]_{10}$ (**8**) in position 3, where EDX measurement was performed.

Table S28. Results of EDX measurement at position 3 (Fig. S59)

Element	norm. wt. %	norm. atom %	3 σ	norm. wt. % calc.	norm. atom % calc.
Si	11.60	24.37	1.10	11.81	25.00
La	57.68	24.50	3.61	58.39	25.00
Cl	30.72	51.13	2.25	29.80	50.00

Figure S60. SEM image of crystalline $[Cp'La_2Cl_2]_{10}$ (**8**) in position 4, where EDX measurement was performed.

Table S29. Results of EDX measurement at position 4 (Fig. S60)

Element	norm. wt. %	norm. atom %	3 σ	norm. wt. % calc.	norm. atom % calc.
Si	11.54	24.53	1.01	11.81	25.00
La	58.62	25.20	3.34	58.39	25.00
Cl	29.84	50.27	2.00	29.80	50.00

Table S30. Averaged results of all EDX measurements for **4** (3 measurements)

Element	norm. wt. %	norm. atom %	3 σ	norm. wt. % calc.	norm. atom % calc.
Si	11.49	24.32	0.94	11.81	25.00
La	58.26	24.94	3.13	58.39	25.00
Cl	30.25	50.74	1.89	29.80	50.00

References

[1] a) U. Behrens, R. E. Dinnebier, S. Neander, F. Olbrich, *Organometallics* **2008**, *27*, 5398-5400; b) P. Jutzi, W. Leffers, B. Hampel, S. Pohl, W. Saak, *Angew. Chem. Int. Ed.* **1987**, *26*, 583-584; *Angew. Chem.* **1987**, *99*, 563-564.

[2] M. Zimmermann, N. Å. Frøystein, A. Fischbach, P. Sirsch, H. M. Dietrich, K. W. Törnroos, E. Herdtweck, R. Anwander, *Chem. Eur. J.* **2007**, *13*, 8784-8800.

[3] H. M. Dietrich, C. Zapilko, K. W. Törnroos, R. Anwander, *Organometallics* **2005**, *24*, 5767-5771.

[4] COSMO, v. 1.61, Bruker AXS Inc., Madison, WI, 2012.

[5] APEX 3, v. 2016.5-0; Bruker AXS Inc., Madison, WI, 2012.

[6] SAINT, v. 8.34A; Bruker AXS Inc., Madison, WI, 2010.

[7] L. Krause, R. Herbst-Irmer, G. M. Sheldrick, D. Stalke, *J. Appl. Cryst.* **2015**, *48*, 3-10.

[8] G. Sheldrick, *Acta Crystallogr., Sect. A* **2015**, *71*, 3-8.

[9] C. B. Hübschle, G. M. Sheldrick, B. Dittrich, *J. Appl. Cryst.* **2011**, *44*, 1281-1284.

[10] C. F. Macrae, I. J. Bruno, J. A. Chisholm, P. R. Edgington, P. McCabe, E. Pidcock, L. Rodriguez-Monge, R. Taylor, J. van de Streek, P. A. Wood, *J. Appl. Cryst.* **2008**, *41*, 466-470.

[11] W. H. Zachariasen, *Acta Cryst.* **1948**, *1*, 265-268.

Paper II

Half-Sandwich Complexes $[Cp'_4Ln_4I_8]_4$ (Ln=Ce, Pr): Emergence of Donor-Free Organolanthanide Nanowheels

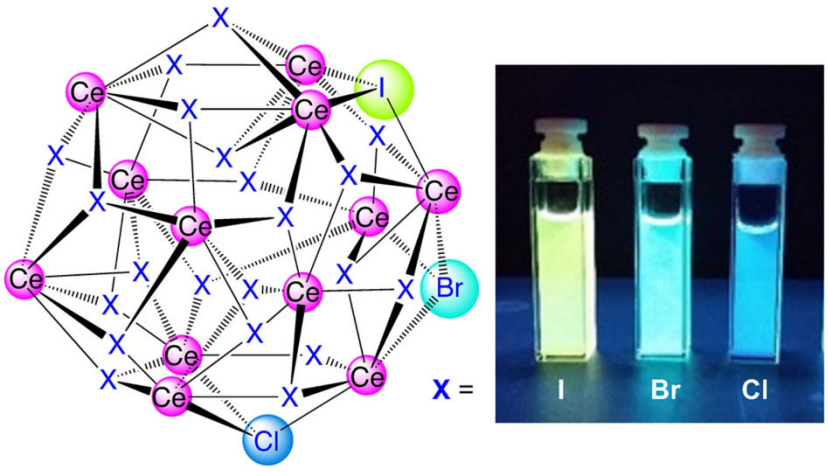

https://doi.org/10.1002/ejic.202100862
Eur. J. Inorg. Chem. **2022**, e202100862

EurJIC
European Journal of Inorganic Chemistry

Research Article
doi.org/10.1002/ejic.202100862

Chemistry Europe
European Chemical Societies Publishing

www.eurjic.org

Special Collection

Half-Sandwich Complexes $[Cp'_4Ln_4I_8]_4$ (Ln=Ce, Pr): Emergence of Donor-Free Organolanthanide Nanowheels

Dennis A. Buschmann,[a] David Schneider,[a] Cäcilia Maichle-Mössmer,[a] and Reiner Anwander*[a]

Dedicated to Professor Rinaldo Poli on the occasion of his 65th birthday.

Slow diffusion of Me_3SiI into an *n*-hexane solution of lanthanide half-sandwich complexes $[Cp'Ln(AlMe_4)_2]$ (Ln=Ce, Pr; Cp′=$C_5H_4SiMe_3$) gives access to the hexadecalanthanide ring-cluster hybrids $[Cp'_4Ln_4I_8]_4$, along with the cyclopentadienyl-bridged {Ce_8} cluster $[Cp'_4Ce_4I_7(\mu_2\text{-}Cp)]_2$. On the contrary, direct addition of the halogenating reagent to complex $[Cp'Ce(AlMe_4)_2]$ in solution affords the spherical dodecanuclear cluster $[Cp'CeI_2]_{12}$ in addition to $[Cp'_4Ln_4I_8]_4$. The isostructural bromide and chloride clusters $[Cp'LnX_2]_{12}$ (X=Cl, Br) were isolated via the same solution synthesis protocol, using the mild halogenido transfer reagents Me_3GeX (X=Cl, Br). The reaction $[Cp'Ce(AlMe_4)_2]$/Me_3GeCl yielded the decanuclear heteroaluminato derivative $[Cp'_5Ce_5Cl_9(AlCl_2Me_2)]_2$ as a coproduct. Attempts to isolate any intermediate species by performing the reaction at low temperature resulted in incomplete $AlMe_4$/iodido exchange, affording the hexanuclear homoaluminate cluster $[Cp'_6Pr_6I_8(AlMe_4)_4]$. All cerium clusters show bright photoluminescence under UV light. The luminescence properties of the dodecanuclear clusters $[Cp'CeX_2]_{12}$ (X=Cl, Br, I) were closer investigated.

Introduction

The main driving force behind rare-earth-metal (Ln) cluster research is marked by a wide range of potential applications.[1–13] While organolanthanide clusters assist in unravelling the active species of industrial 1,3-diene polymerization catalysis,[14] luminescent coordination clusters do impress with intriguing structural motifs and bright colors.[8,10,13,15–20] As for cerium(III) ($4f^1$), the photoluminescent properties are determined by dipole-allowed $5d\rightarrow4f$ transitions, which enables efficient tuning of the emission wavelength of complexes.[21–23] This effect can be further enhanced in terms of the luminescence intensity in combination with a variety of ligand systems, including cyclopentadienyl derivatives[24] or hydridotris(pyrazolyl)borato ligands,[25] given their stabilizing properties.[26] Super-large lanthanide cluster compounds such as $[Gd_{140}(CO_3)_{20}(\mu_3\text{-}OH)_{100}(CH_3COO)_{80}(LH_3)_{40}(H_2O)_{200}]$-$(NO_3)_{80}(H_2O)_x$ are generally synthesized via hydro- or solvothermal reaction pathways.[2,5,6,8,27] The switch to anhydrous, donor-free syntheses, which is mandatory for accessing organolanthanide clusters, goes hand in hand with a substantial decrease in cluster size.[28] Not surprisingly, it is the ubiquitous cyclopentadienyl ligand system which triggered the formation of single-crystalline clusters, as revealed for mono(cyclopentadienyl) derivatives.[29–33] Until now, the size of such half-sandwich-based clusters is restricted to Ln_{12} entities (dodecanuclear structures) of the general composition $[Cp^RLnX_2]_{12}$ (Cp^R=C_5H_5, Ln=Sm, X=Cl; Cp^R=$C_5H_4SiMe_3$, Ln=La, X=I, Br).[34,35] Herein, we report an extension of the previously discovered halogenation protocol applying half-sandwich lanthanide bis(tetramethylaluminato) complexes $[Cp'Ln(AlMe_4)_2]$ (Cp′=$C_5H_4SiMe_3$) as cluster precursors.[35] Special consideration is given to the Ln^{III} ion size and the type of halogenido ligand as well as the formation of nano-sized {Ln_{16}} ring-cluster hybrids.

Results and Discussion

Half-sandwich Ln^{III} Iodide Clusters Supported by $C_5H_4SiMe_3$ (Cp′)

Recently we found that the formation of half-sandwich organolanthanum clusters is crucially affected by the steric demand of the ancillary cyclopentadienyl ligand, the size of the bridging halogenido ligand, and the crystallization technique.[35] Consequently, we were interested in the effects of the Ln^{III} ion size using otherwise identical reaction conditions.

Since a strongly reduced Ln^{III} ionic radius is anticipated to markedly decrease cluster nuclearity,[36,37] we decided on the marginally smaller rare-earth elements cerium and praseodymium as metal centers to check for potential size effects (coordination number 6, Ln^{III} ionic radii [Å]: La=1.03, Ce=1.01, Pr=0.99).[38] By following established protocols,[39–41] the half-sandwich bis(tetramethylaluminato) precursors $Cp'Ln(AlMe_4)_2$

[a] D. A. Buschmann, D. Schneider, Dr. C. Maichle-Mössmer, Prof. Dr. R. Anwander
Institut für Anorganische Chemie, University of Tübingen, Auf der Morgenstelle 18, 72076 Tübingen, Germany
E-mail: reiner.anwander@uni-tuebingen.de
http://uni-tuebingen.de/syncat-anwander

Supporting information for this article is available on the WWW under https://doi.org/10.1002/ejic.202100862

Part of the "celebratory collection for Rinaldo Poli".

Research Article
doi.org/10.1002/ejic.202100862

(Ln=Ce (**1a**), Pr (**1b**)) were obtained as yellow and light green oils (>90% yield) from homoleptic $Ln(AlMe_4)_3$ and KCp′. The ^{1}H NMR spectrum of the cerium derivative **1a** in [D_6]benzene at ambient temperature shows four signals. Strikingly, the Cp′ hydrogen atoms at the 3/4 and 2/5 positions show strongly different chemical shifts, with resonances at 15.82 ppm and 0.17 ppm, respectively. The $AlMe_4$ hydrogen atoms resonate at 1.26 ppm, and the $SiMe_3$ hydrogen atoms at −3.60 ppm. Similarly, the praseodymium compound **1b** revealed paramagnetically shifted resonances at 26.31/8.49 ($C_5H_4SiMe_3$), −1.77 ($AlMe_4$), and −6.21 ($C_5H_4SiMe_3$) ppm. For the crystal structure of **1a**, see Figure S10 in the supporting information.

Aiming at the synthesis of coordination clusters, $AlMe_4$/iodido exchange was achieved by addition of a minor excess of Me_3SiI to a stirred *n*-hexane solution of **1a**. Keeping the reaction solution static at ambient temperature afforded the iodido-bridged dodecacerium cluster $[Cp'CeI_2]_{12}$ (**2**) along with the novel hexadecanuclear cluster $[Cp'_4Ce_4I_8]_4$ (**4a**) cluster in a total crystalline yield of 50% (Scheme 1). An X-ray diffraction (XRD) analysis revealed that **2** (Figure S12) is isostructural to the respective dodecalanthanum cluster $[Cp'LaI_2]_{12}$.[35] The ^{1}H NMR spectrum of both compounds shows a mixture of products, ruling out any conclusive signal assignment and further detailed characterization.

Slow diffusion (instead of direct addition) of Me_3SiI into an *n*-hexane/toluene solution of $[Cp'Ce(AlMe_4)_2]$ afforded different crystalline products. On the one hand, the cyclopentadienyl-bridged octanuclear cerium cluster $[Cp'_4Ce_4I_7(\mu_2\text{-Cp})]_2$ (**3**) could be identified (Scheme 1). Partly desilylated **3** is isostructural (Figure S13 and Figure S14) to the corresponding lanthanum cluster $[Cp'_4La_4(\mu_2\text{-I})_4(\mu_3\text{-I})_2(\mu_4\text{-I})(\mu_2\text{-Cp})]_2$[35] formed under the same synthesis conditions, using $[Cp'La(AlMe_4)_2]$/Me_3SiI. Surprisingly, the diffusion method resulted in a second batch of crystals, which were again identified as the hexadecanuclear cluster **4a** (Scheme 1). The obtained product mixture impeded complete characterization though. The new cerium cluster **4a** marks a record-breaking nuclearity of {Ln_{16}} for donor-free rare-earth-metal coordination clusters. The cluster-ring "nanowheel" arrangement is composed of a total of four $Cp'_4Ce_4I_7$ subunits, which are interlinked via four μ_2-bridging iodido ligands (Figure 1 and Figure S16). The same subunit structure of $Cp'_4Ln_4(\mu_2\text{-I})_4(\mu_3\text{-I})_2(\mu_4\text{-I})$ has been detected in $[Cp'_4Ln_4I_7(\mu_2\text{-Cp})]_2$ (Ln=La, Ce (**3**)), emphasizing the particular preference for/stability of this structural motif.

Comparing the {Ce_4} subunits of clusters **3** and **4a** revealed characteristic differences in the interatomic distances and angles, as a result of the distinct bridging moieties. While the outmost Ce–I distances in cluster **3** are within a range of 3.1853(6) Å (Ce3–I2) and 3.2825(6) Å (Ce4–I5) with an average distance of 3.2299 Å, the respective distances in complex **4a** are slightly but notably shortened (minimum: 3.1427(4) Å, Ce4–I3; maximum: 3.2297(4) Å, Ce3–I7; avg.: 3.1879 Å). Furthermore, the cerium centers in **3** show a distance of 4.5988 Å between the inner metal centers, and 7.3078 Å between the apical ones, whereas the subunit of cluster **4a** shows distances of 4.7257 Å (Ce2–C4) and 6.7251 Å (Ce1–Ce3), respectively. This can be explained by the higher degree of rotational and steric freedom for the subunit of cluster **4a**, which is bridged via μ_2-iodido ligands, compared to the subunit in compound **3**, where the bridging cyclopentadienyl ligands exert a high steric strain on the two subunits. Likewise, the distances between the apical cerium centers in complex **4a** and the μ_2-bridging iodido

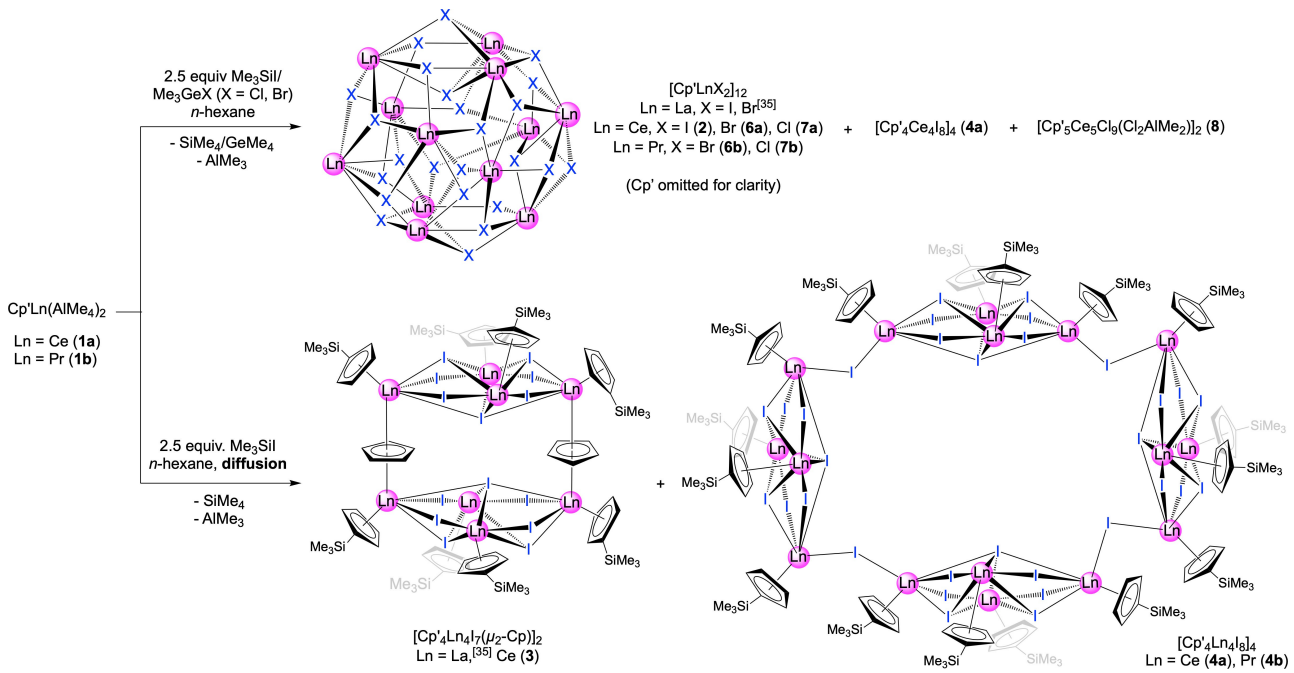

Scheme 1. Reactivity of half-sandwich complexes $[Cp'Ln(AlMe_4)_2]$ (Ln=La, Ce, Pr) toward Me_3SiI/Me_3GeX (X=Cl, Br) in solution (top) and toward Me_3SiI according to a diffusion synthesis protocol (bottom). Shown are complexes revealed by XRD analysis.

Research Article
doi.org/10.1002/ejic.202100862

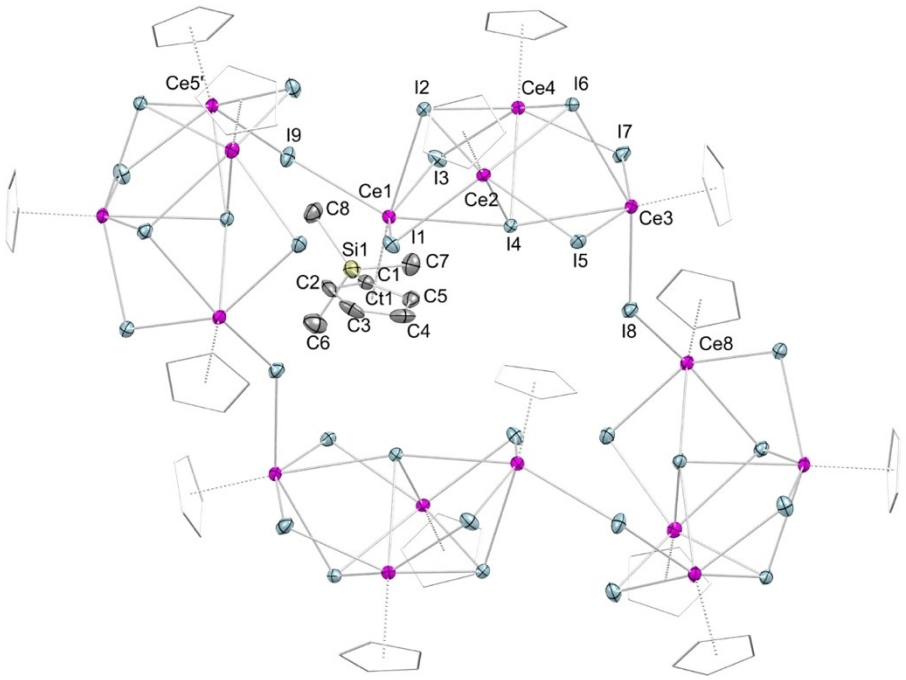

Figure 1. Crystal structure of $[Cp'_4Ce_4I_8]_4$ (**4a**) with atomic displacement parameters set at the 50% probability level. Hydrogen atoms are omitted for clarity. The Cp′ ligands (except for one) are represented by a wireframe model for improved visualization. For selected interatomic distances and angles, see the Supporting Information.

ligands range from 3.1451(4) Å (Ce8–I8) to 3.2061(4) Å (Ce1–I9), with bonding angles between the subunits of 134.777(11)° (Ce1–I9–Ce5′) and 138.802(11)° (Ce3–I8–Ce8). Striking are the distinct I–Ce–I angles featured by the μ_4-iodido ligand of the subunit. Whereas the three acute angles (I4–Ce3–I8, I9–Ce5–I11, I8–Ce8–I11) are within a range from 74.352(11)° to 81.913(9)°, the angle between I4–Ce1–I9, involving the subunit-bridging μ_2-iodido ligand, is drastically enlarged (153.61°). Consequently, the overall superstructure of the cluster resembles a distorted ellipse/ring-like motif, with relatively large axes lengths of 25.26 Å for the major axis and 18.56 Å for the minor axis (Cnt···Cnt distances, Cnt=cyclopentadienyl ring centroid). Complex **4a** shows distances of the cerium metals to the plane spanned by the interlinking μ_2-iodido ligands of 0.035 Å (Ce1) to a maximum distance of 5.243 Å (Ce6).

Whereas donor-free lanthanide clusters usually show spherical arrange-ments,[34,35,42–44] ring structural motifs are more common for lanthanide clusters bridged via donor ligands like, e.g., $\{Gd_{140}\}$ or $\{Yb_{42}\}$,[6,20,45,46] or smaller sandwich-type ring-cluster hybrids such as, e.g., $[(C_5Me_5)_2Sm(\mu_2\text{-}Cl)]_3$.[36,47–54] In sandwich-type ring structures, the metal centers display a more or less planar arrangement, while the deviation from planarity naturally increases with the steric demand of the ligand system or ligand complexity. The trinuclear fluorido-bridged samarium compound $[Cp_2Sm(\mu_2\text{-}F)]_3$[48] shows a diameter of 11.47 Å, as well as an almost planar 6-membered ring with alternating Sm and F atoms, with a maximum deviation from the mean plane spanned by the ring atoms of 0.018 Å. Changing to the cyanido-bridged decamethylsamarocene complex $[Cp^*_2Sm(CNC_6H_{11})(\mu_2\text{-}CN)]_3$[50] reduces the planarity of the 9-membered ring (max. distance 0.103 Å). Surprisingly, the ring diameter is only insignificantly affected (11.862 Å). These parameters are naturally further enhanced in the 18-membered ring-structure of $[Cp^*_2Sm(\mu_2\text{-}CN)]_6$. Therein, the maximum distance of the samarium metal center to the ring mean plane is 1.538 Å, while the ring diameter increases to 15.88 Å.[54] Other organolanthanide wheel-type structures comprise the aforementioned $\{Ln_3\}$ half-sandwich complexes,[36,37] as well as salt-included $\{Ce_4\}$ half-sandwich complex $[Cp^*Ce(C{\equiv}CPh)_2]_4(LiCl)$,[55] bimetallic $\{Ln_2K_4\}$ half-sandwich-type $[CpLn(NPh_2)_2\{N(PPh_2)_2\}_2K_2(THF)_4]_2$ (Ln=Er, Yb)[56] and the donor-free $\{Nd_6\}$ COT-sandwich $[(\mu\text{-}\eta^8{:}\eta^8\text{-}COT)\{Nd(c\text{-}C_3H_5{-}C{=}C{-}C)(NCy)_2\}(\mu\text{-}Cl)\}]_4$ bearing a cyclopropylethinylamidinato coligand.[57] Implementation of alkoxy or acetato bridging ligands often results in highly symmetric ring stuctures, as evidenced by the isolation of aforementioned $\{Y_{10}\}$,[45] $\{Yb_{42}\}$,[20] and $\{Gd_{140}\}$[6] clusters. Despite the increased complexity of the bridging ligand, the yttrium metal centers in $\{Y_{10}\}$ show a maximum distance of only 0.627 Å to their respective mean plane, with an overall ring diameter of 22.42 Å. The acetates $\{Yb_{42}\}$ and $\{Gd_{140}\}$ display metrical parameters of max. 1.960 Å/max. 5.398 Å and 36.58 Å/59.58 Å.

Since a ring-cluster hybrid similar to that of **4a** could not be identified for the larger rare-earth metal center lanthanum(III), we wondered about its existence of the smaller-sized praseodymium. And in fact, the diffusion method using $[Cp'Pr(AlMe_4)_2]$ (**1b**) and Me_3SiI also gave the hexadecanuclear ring-cluster hybrid $[Cp'_4Pr_4I_8]_4$ (**4b**) (Scheme 1, Figure S17), which is isostructural to the cerium complex **4a**. For further comparison, the values for the distances between the mean plane M1 spanned by the μ_2-bridging iodido ligands and the praseodymium metal

Research Article
doi.org/10.1002/ejic.202100862

Table 1. Selected interatomic distances and angles of dodecanuclear clusters $[Cp'LnBr_2]_{12}$ (Ln=La, Ce, Pr). Distances are given in [Å], angles in [°]. Br_s = surface bromido ligands, Br_c = core bromido ligands. Cnt = cyclopentadienyl ring centroid.

Bond/Angle	$[Cp'LaBr_2]_{12}$[35]	$[Cp'CeBr_2]_{12}$ (**6a**)	$[Cp'PrBr_2]_{12}$ (**6b**)
Ln–C(Cp')/Cnt	2.720(3)–2.827(3) / 2.489	2.714(2)–2.738(2) / 2.511	2.703(5)–2.746(5) / 2.446
Ln–Br_s	3.0178(4)–3.3451(1)	3.0003(2)–3.4302(2)	2.9870(5)–3.2972(5)
Ln–Br_c	3.0972(4)	3.0850(2)	3.0479(5)–3.0876(5); avg. 3.0647
Br_s–Ln–Br_s	63.476(9)–77.826(1)	65.13(3)–76.27(3)	66.058(2)–75.868(2)
Ln–Br_s–Ln	90.370(1)–115.564(2)	90.33(5)–115.34(3)	91.102(2)–114.615(2)

centers deviate only marginally (Pr8···M1 = 0.014 Å, Pr2···M1 = 5.139 Å; **4a**: 0.035–5.243 Å), reflecting the slightly smaller Pr^{III} ion size, as do the ellipsoid axes (**4a**: 25.26 Å, 18.56 Å; **4b**: 25.12 Å, 18.60 Å). Despite several attempts, a cyclopentadienyl-bridged praseodymium complex isostructural to $[Cp'_4Ce_4I_7(\mu_2\text{-}Cp)]_2$ (**3**) could not be isolated so far, possibly indicating a trend in size effect for the diffusion-controlled synthesis. While the diffusion reaction with $[Cp'La(AlMe_4)_2]$ exclusively afforded the cyclopentadienyl-bridged {La_8} complex $Cp'_4La_4I_7[(\mu_2\text{-}Cp)]_2$,[35] the reaction with $[Cp'Pr(AlMe_4)_2]$ resulted in the preferred formation of the larger {Pr_{16}} complex $[Cp'_4Pr_4I_8]_4$ (**4b**). For the similar reaction with $[Cp'Ce(AlMe_4)_2]$ both the {Ce_8} and {Ce_{16}} complexes **3** and **4a** could be isolated, clearly emphasizing the impact of Ln^{III} ion size on compound nuclearity.

Investigating the prospect of isolating any possible intermediate species, the diffusion reaction of Me_3SiI with the praseodymium half-sandwich precursor **1b** was repeated at 0 °C in order to slow down the diffusion process. Over the period of several weeks, light green crystals had deposited. An XRD analysis revealed the formation of the heterobimetallic, hexanuclear praseodymium cluster $[Cp'_6Pr_6I_8(AlMe_4)_4]$ (**5**) (Figure S18). Alternatively, cluster **5** was obtained according to standard synthesis routes pursuing a stoichiometry-controlled reaction pathway.[35,58,59] Unsurprisingly, the tetramethylaluminato-bridged compound **5** is isostructural to $[Cp'_6La_6I_8(AlMe_4)_4]$.[35] Apparently, low temperature hampers a complete alkyl/halogenido exchange.

Half-sandwich Ln^{III} Bromide and Chloride Clusters Supported by Cp′

To screen for further size effects, the "stirring" synthesis protocol was applied using the bromido transfer reagent Me_3GeBr. However, both reactions with the cerium (**1a**) and praseodymium half-sandwich precursor compound (**1b**) led to the crystallization of dodecanuclear clusters of the general composition $[Cp'LnBr_2]_{12}$ (Ln=Ce (**6a**), Pr (**6b**)) (Scheme 1) (Figure S19 and Figure S20), which is in accordance with the reaction employing the respective lanthanum precursor.[35] Moreover, both clusters are isostructural to $[Cp'LaBr_2]_{12}$, with marginally differing interatomic distances and bond angles, due to their slightly reduced ionic radii (see Table 1). The ^{1}H NMR spectrum of cerium bromide cluster **6a** in [D_6]benzene at ambient temperature (Figure S7) shows one signal set for the Cp′ ligands. The Cp′ hydrogen atoms resonate at 19.71 ppm and −0.31 ppm, respectively, and the trimethylsilyl group at −9.11 ppm. Compared to the half-sandwich precursor $[Cp'Ce(AlMe_4)_2]$, the signals are significantly shifted (**1a** δ Cp′*H*, 15.82 ppm, 0.17 ppm, δ *CH*$_3$, −3.60 ppm). In contrast, the ^{1}H NMR spectrum of cluster **6b** shows three signals, a broad singlet at 27.63 ppm (Cp′*H*), a doublet at 0.14 ppm (unidentified species), and a singlet at −6.20 ppm (*CH*$_3$).

Surprisingly, two different structural motifs were detected for the "stirring" reaction with the chlorido transfer reagent Me_3GeCl. Treatment of **1a** with 2.5 equivalents trimethylgermanium chloride led to the formation of the dodecanuclear cluster $[Cp'CeCl_2]_{12}$ (**7a**) as well as the heteroaluminato derivative $[Cp'_5Ce_5Cl_9(Cl_2AlMe_2)]_2$ (**8**). Both crystal structures were revealed by XRD analyses (Figure 2 and Figure S23). While **7a** is isostructural to the other {Ln_{12}} spherical clusters under study, the connectivity and structural motif of **8** has been found previously for $[Cp'_5La_5Br_9(Br_2AlMe_2)]_2$. However, the latter {$La_{10}Al_2$} cluster was obtained via the diffusion method employing $[Cp'La(AlMe_4)_2]$ and Me_3GeBr.[35] Cluster **8** features an ellipsoidal decanuclear cerium core structure, with the cerium

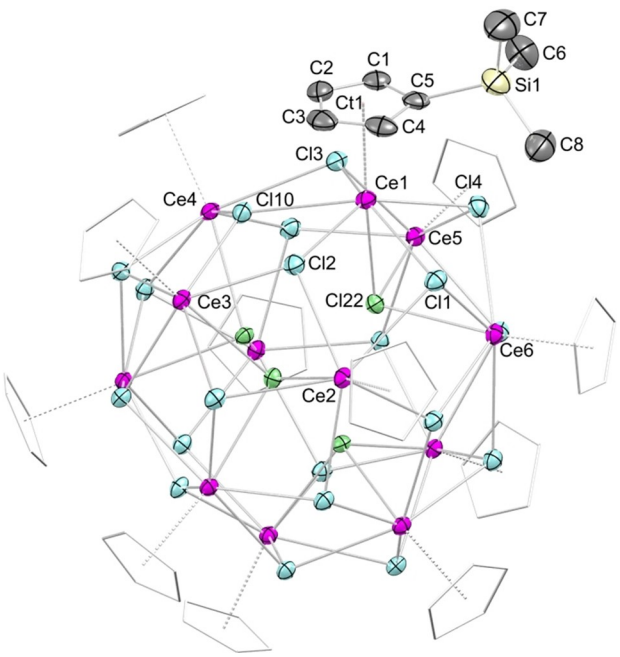

Figure 2. Crystal structure of $[Cp'CeCl_2]_{12}$ (**7a**) with atomic displacement parameters set at the 50% probability level. Hydrogen atoms are omitted for clarity. The Cp′ ligands (except for one) are represented by a wireframe model for improved visualization. For selected interatomic distances and angles, see the Supporting Information.

Research Article
doi.org/10.1002/ejic.202100862

centers at the apical positions bearing one heteroaluminato ligand each. The formation of a product mixture ruled out a full characterization.

Again surprisingly, applying the same synthesis protocol for the respective praseodymium precursor **1b** in turn afforded exclusively the dodecanuclear cluster $[Cp'PrCl_2]_{12}$ (**7b**) (Figure S22). Cluster **7b** crystallized in the monoclinic space group $P2_1/c$, and the XRD analysis revealed only negligible differences in interatomic distances or bond angles in comparison to $[Cp'PrBr_2]_{12}$ (**6b**) in accordance with the smaller ionic radii of the chlorido ligands. Once again, the effect of the rare-earth-metal ion size is displayed in the isolated clusters. While the reaction of $[Cp'La(AlMe_4)_2]$ with Me_3GeCl solely afforded the decalanthanum cluster $[Cp'LaCl_2]_{10}$ with two terminal chlorido ligands,[35] the reaction for cerium produced a mixture of the decanuclear cluster $[Cp'_5Ce_5Cl_9(Cl_2AlMe_2)]_2$ (**8**) and the dodecanuclear cluster $[Cp'CeCl_2]_{12}$ (**7a**), whereas on the other hand the reaction with the praseodymium precursor complex $[Cp'Pr(AlMe_4)_2]$ exclusively resulted in the formation of the dodecanuclear cluster $[Cp'PrCl_2]_{12}$ (**7b**).

Luminescence Properties of the Cerium Clusters

Given the electron-dipole allowed $5d^1 \rightarrow 4f^1$ emission and associated ligand effects (nephelauxetic effects), the photoluminescence properties of a series of cerium(III) organometallics has been investigated. In particular, the cyclopentadienyl-sandwich complexes $[Cp^*_2Ce(\mu\text{-}Cl)]_2$[60] and $[Cp^{tBu}_2Ce(\mu\text{-}Cl)]_2$ ($Cp^{tBu} = C_5H_3tBu_2$-1,3)[24] were shown to exhibit intense bright-yellow photoluminescence and high quantum yields. Other studied cerium(III) cyclopentadienyl derivatives include Cp_3Ce/$Cp_3Ce(THF)$, ate complexes of the type $[M(Do)_2][Cp^*_2CeX_2]$ (M=Li, K; Do=OEt_2, THF; X=Ce, I, Me), as well as donor adducts $[Cp^*_2CeX(THF)]$ and half-sandwich complexes $[Cp^*CeX_2(THF)_x]$ (X=Cl, I).[61,62] The photoluminescent properties of cerium(III) can be effectively used in cerium photosensitizers for photoredox catalysis.[22,63–65] We have also recently reported on distinct color changes of donor-free cerium(III) sandwich complexes $[Cp^*_2CeL]$ in solution, being highly affected by the monoanionic ligand L (L=N*i*Pr_2, blue; $N(SiHMe_2)_2$, red; CH_2–C_6H_4-*o*-NMe_2, purple).[55]

Naturally, we were interested in color/luminescence effects of the half-sandwich-type clusters under study. Under ambient light, the addition of the halogenido transfer reagent to the bis(tetramethylaluminato) complex **1a** did not cause any spectacular color change (pale yellow to colorless). In contrast, a pronounced color change of the photoluminescence is observable upon irradiation with UV-light (302 nm). Depending on the halogenido ligand, a striking transition from light green ($[Cp'CeI_2]_{12}$ (**2**) and $[Cp'_4Ce_4I_8]_4$ (**4a**)) over turquoise ($[Cp'CeBr_2]_{12}$, **6a**) to a blue luminescence ($[Cp'CeCl_2]_{12}$ (**7a**) and $[Cp'_5Ce_5Cl_9(Cl_2AlMe_2)]_2$ (**8**)) was found, while the initial solution of **1a** in toluene displayed a green-blue luminescence under UV-light. Consequently, we decided to scrutinize the luminescence properties of the respective clusters. The following measurements were performed with a [1 mM] toluene solution of the respective cluster in a J.Young-valved NMR tube.

The iodide clusters **2** and **4a** revealed two excitation maxima (see Figure 3 and Figure S33), a global maximum at 286 nm with a relatively steady asymmetric decrease, and a smaller local maximum at 420 nm. This local maximum is notably shifted in comparison to the maximum in the absorption spectrum (428 nm, Figure S30). In contrast, bromide cluster **6a** displays a broadened excitation peak, with a global excitation maximum at 291 nm along with a small shoulder at 328 nm (Figure 3). The second, local excitation maximum is significantly shifted toward lower wavelengths (370 nm) in comparison with the iodide clusters. Compared with the absorption spectrum (Figure S31), the absorption and excitation maxima show nearly identical values (371 and 370 nm). The chloride clusters **7a** and **8** exhibit very similar excitation behavior, with a global excitation maximum at 287 nm and a shoulder as well (Figure 3). The local maximum (350 nm) is further shifted toward lower wavelengths compared to the other clusters, but shows only a small shift compared to the maximum of the absorption spectrum (349 nm, Figure S32). Unlike the iodido- and bromido-bridged clusters, the chlorido-bridged clusters display a second local excitation maximum at 396 nm. This is reflected in the absorption spectrum as well, which shows an asymmetric decrease.

For all absorption spectra, the absorbance did not exceed a value of 0.15. Strikingly, the emission spectra exhibit a distinct shift toward smaller wavelengths with decreasing halogenido ion size. The iodido-bridged clusters **2** and **4a** show a global emission maximum at 489 nm, as well as a pronounced shoulder at 533 nm (Figure 4 and Figure S33).

Overall, compounds **2** and **4a** exhibit a relatively broad emission ranging from ~430 nm to 700 nm. Bromide cluster **6a** displays a similar emission behavior (Figure 4 and Figure S34), though the emission maximum as well as the shoulder are slightly shifted toward lower wavelengths (473 nm, 514 nm). Likewise, further decreasing the halogenido ion size (increasing the hardness) again shifts the maxima to lower wavelengths (**7a**, **8**: 459 nm, 500 nm, Figure 4 and Figure S35). Interestingly, the emission maxima of the donor-solvated monomeric half-sandwich complexes $[Cp^*CeX_2(THF)_x]$ (X=Cl, I) appear to follow

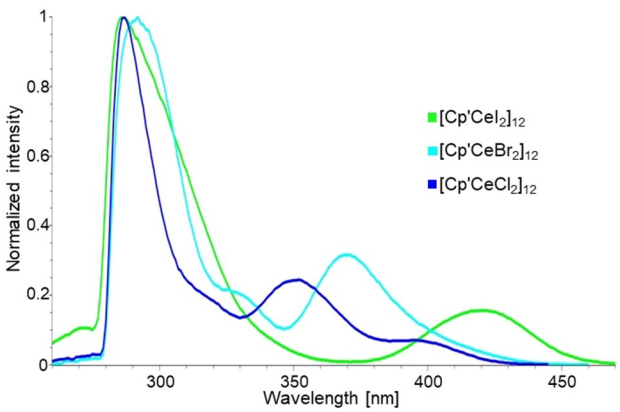

Figure 3. Excitation spectra of dodecanuclear clusters $[Cp'CeX_2]_{12}$ (X=I (**2**), Br (**6a**), Cl (**7a**)).

Research Article
doi.org/10.1002/ejic.202100862

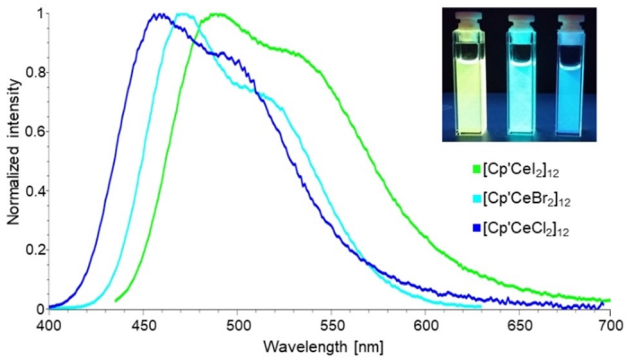

Figure 4. Emission spectra of dodecanuclear clusters $[Cp'CeX_2]_{12}$ (X=I (**2**), Br (**6a**), Cl (**7a**)) and under UV-light (302 nm).

an opposite trend, with the iodide derivative emitting at comparatively higher energy than the chloride compound (465 versus 490 nm).[60,62] Moreover, a qualitatively similar color switch from yellowish to blue luminescence was observed for mixed silylamido/guanidinato complexes $Ce[N(SiMe_3)_2]_x$-$[(Me_3Si)_2NC(N{i}Pr)_2]_{3-x}$.[66] All clusters under study show similar luminescence lifetimes, which are in the range of reported molecular Ce(III) emitters.[62] The luminescence decay curves were fitted by a single exponential or a bi-exponential model. In case of the iodido-bridged clusters $[Cp'CeI_2]_{12}$ (**2**) and $[Cp'_4Ce_4I_8]_4$ (**4a**) the bi-exponential model yielded 92.8 ns (71%) and 147 ns (29%). The bromido-bridged cluster **6a** could be analyzed using a single exponential, with a luminescence lifetime of 115 ns. For the chlorido-bridged clusters **7a** and **8** lifetimes of 77.3 ns (18%) and 111 ns (82%) were obtained with the bi-exponential model, though the longer lifetime dominates the decay in this case.

Conclusion

The seemingly small difference in ionic radii between lanthanum, cerium, and praseodymium has a significant impact on the formation of half-sandwich halogenido clusters. In addition to the previously reported spherical dodecanulcear clusters of the type $[Cp'LnX_2]_{12}$ (X=Cl, Br, I), the $AlMe_4$/I exchange reaction protocol favors the even larger donor-free rare-earth-metal ring-cluster hybrids $[Cp'_4Ln_4I_8]_4$. Furthermore, the rare-earth-metal center ion size in combination with the crystallization technique greatly affects the self-assembly process of the clusters, as evidenced by the isolation of coordination clusters with different structural motifs for the same bridging halogenido ligands ($[Cp'_4Ce_4I_7(\mu_2\text{-}Cp)]_2$ and $[Cp'_4Ce_4I_8]_4$ versus $[Cp'_4Pr_4I_8]_4$, $[Cp'CeCl_2]_{12}$ and $[Cp'_5Ce_5Cl_9(Cl_2AlMe_2)]_2$) versus $[Cp'PrCl_2]_{12}$. The cerium(III) half-sandwich clusters exhibit interesting luminescence behavior, with the emission wavelengths being halogenido-dependent. The newly gained insights into the formation process of organorare-earth-metal clusters open new perspectives for designing luminescent or magnetic clusters or materials.

Experimental Section

General considerations

All manipulations were performed under rigorous exclusion of air and moisture, using standard Schlenk and glovebox techniques (MBraun MB200B; <0.1 ppm O_2, <0.1 ppm H_2O, argon atmosphere). The solvents *n*-hexane and toluene were purified using Grubbs-type columns (MBraun SPS, solvent purification system). [D_6]benzene (99.6%, Sigma-Aldrich) was dried over Na/K-alloy for at least 24 h prior to filtration. All solvents were stored inside a glovebox. Trimethylsilyl cyclopentadiene (HCp′, 97%) was obtained from abcr and used as received. Potassium trimethylsilyl cyclopentadienide was prepared according to standard procedures by treatment of the proligand with potassium.[39] Iodotrimethylsilane (97%, stabilized with copper), bromotrimethylgermane (98%), and chlorotrimethylgermane (98%) were purchased from abcr and used without further purification. Homoleptic $[Ln(AlMe_4)_3]$ (Ln=Ce, Pr)[39,40] was synthesized according to literature procedures. NMR spectra of air and moisture sensitive compounds were recorded using J.Young valve NMR tubes at ambient temperature on a Bruker AVII+400 (^{1}H: 400.11 MHz; ^{13}C: 100.61 MHz) spectrometer. NMR chemical shifts are referenced to internal solvent resonances and reported in parts per million relative to tetramethylsilane. Coupling constants are given in Hertz. Elemental analyses were performed on an Elementar Vario Micro Cube. IR spectra were recorded on a Vertex70 IR spectrometer (Nujol, CsI window). Steady-state spectra were measured on a Horiba Fluorolog-3 spectrofluorimeter equipped with a 450 W xenon lamp for steady-state measurements. Emitted light was detected by a Hamamatsu R2658P PMT (UV/vis/NIR, 200 nm $<\lambda_{em}<$ 1000 nm) detector. A double grating monochromator 320DFX (1200 grooves/nm, blazed at 330 nm) was used for spectral selection in the excitation path, while in the visible emission path the single grating monochromator iHR550 (1200 grooves/nm, blazed at 500 nm) was used. To avoid higher order excitation light, long pass filter glass plates (3 mm thickness from Schott) were used when needed. For fluorescence lifetime determination, a pulsed UV-LED (DeltaDiode-310, $\lambda_{exc}=308\pm$ 10 nm, pulse width ca. 1 ns FWHM, $P_{avg}=5$ µW) without further spectral selection was used for excitation. Lifetime data analysis (deconvolution, statistical parameters, etc.) was performed using the software package FeliX32 from PTI or DAS analysis from Horiba. The decay data were analyzed by tail-fitting (exclusion of the lamp-puls region).

$[Cp'Ce(AlMe_4)_2]$ (1a). To a suspension of potassium trimethylsilyl cyclopentadienide ($KC_5H_4SiMe_3$=KCp′) (45.86 mg, 0.26 mmol) in *n*-hexane (3 mL) a solution of $[Ce(AlMe_4)_3]$ (100.37 mg, 0.25 mmol) in *n*-hexane (3 mL) was added under vigorous stirring. After stirring the reaction mixture for 16 h at ambient temperature, the suspension was centrifuged, the supernatant filtered, and the solvent was removed under vacuum to give **1a** as a yellow oil (101.9 mg, 0.23 mmol, 90%). Crystals suitable for XRD analysis were obtained from a saturated *n*-hexane solution at −40 °C. ^{1}H NMR (400 MHz, [D_6]benzene, 26 °C): $\delta=15.82$ (2H, $C_5H_4SiMe_3$), 1.26 (24H, $AlMe_4$), 0.17 (2H, $C_5H_4SiMe_3$), −3.60 (9H, $C_5H_4SiMe_3$) ppm. IR (Nujol): $\tilde{\nu}=2954$ (Cp, Nujol), 2924 (Cp, Nujol), 2855 (Cp, Nujol), 2789 (Cp, Nujol), 1456 (Nujol), 1445 (Nujol), 1365 (Nujol), 1251 (w), 1218 (vw), 1191 (w), 1174 (w), 1043 (w), 902 (vw), 837 (s), 801 (w), 755 (w), 697 (vs), 639 (vw), 627 (vw), 577 (w), 538 (vw), 517 (vw), 477 (vw), 418 (vw) cm^{-1}. Elemental analysis of **1a** calculated for $C_{16}H_{37}Al_2CeSi$ (451.64 g/mol): C 42.55%, H 8.26%; found: C 42.60%, H 7.98%.

$[Cp'Pr(AlMe_4)_2]$ (1b). To a suspension of KCp′ (45.86 mg, 0.26 mmol) in *n*-hexane (3 mL) a solution of $[Pr(AlMe_4)_3]$ (100.58 mg, 0.25 mmol) in *n*-hexane (3 ml) was added under vigorous stirring. After stirring the reaction mixture for 16 h at ambient temperature,

the suspension was centrifuged, the supernatant filtered, and the solvent was removed under vacuum to give **1 b** as a light green oil (105.2 mg, 0.23 mmol, 93 %). Attempts to crystallize **1 b** from a saturated *n*-hexane solution at −40 °C were unsuccessful. ^{1}H NMR (400 MHz, [D$_6$]benzene, 26 °C): $\delta = 26.31$ (2H, $C_5H_4SiMe_3$), 8.49 (2H, $C_5H_4SiMe_3$), −1.77 (24H, Al*Me*$_4$), −6.21 (9H, C_5H_4Si*Me*$_3$) ppm. IR (Nujol): $\tilde{\nu} = 2954$ (Cp, Nujol), 2925 (Cp, Nujol), 2853 (Cp, Nujol), 2792 (Cp, Nujol), 1661 (vw) 1459 (Nujol), 1412 (Nujol), 1377 (Nujol), 1366 (Nujol), 1311 (vw), 1251 (vs), 1192 (s), 1043 (s), 985 (vw), 968 (vw), 903 (w), 839 (vs), 805 (w), 755 (w), 694 (vs), 639 (vw), 627 (vw), 582 (w), 515 (vw), 478 (vw), 418 (vw) cm^{-1}. Elemental analysis of **1 b** calculated for $C_{16}H_{37}Al_2PrSi$ (452.43 g/mol): C 42.48 %, H 8.24 %; found: C 39.62 %, H 7.39 %. The deviation between theoretical and experimental values are likely caused by incomplete combustion of the compound.

[Cp′CeI$_2$]$_{12}$ (2) and [Cp′$_4$Ce$_4$I$_8$]$_4$ (4 a). [Cp′Ce(AlMe$_4$)$_2$] (**1 a**, 45.2 mg, 0.1 mmol), was dissolved in *n*-hexane (15 mL), and Me$_3$SiI (50.02 mg, 0.25 mmol) was added under vigorous stirring. After stirring the reaction mixture for 4 h, the suspension was filtered, and the vial was stored at ambient temperature. Within several hours, **2** and **4 a** formed as light yellow crystals (27.1 mg, 50 % total yield). No signal assignment in the ^{1}H NMR spectrum was possible due to the presence of a product mixture. Any meaningful IR spectra could not be recorded due to the presence of a product mixture. Elemental analysis of **2**/**4 a** calculated for $C_{96}H_{156}Ce_{12}I_{24}Si_{12}$ (6374.42 g/mol) and $C_{128}H_{208}Ce_{16}I_{32}Si_{16}$ (8499.23 g/mol): C 18.09 %, H 2.47 %; found: C 19.99 %, H 3.29 %. The deviation between theoretical and experimental values can be explained by residual lattice *n*-hexane in the crystalline material.

[Cp′$_4$Ce$_4$I$_7$(μ$_2$-Cp)]$_2$ (3) and [Cp′$_4$Ce$_4$I$_8$]$_4$ (4 a). In a 20-mL vial, [Cp′Ce(AlMe$_4$)$_2$] (**1 a**, 45.2 mg, 0.1 mmol) was dissolved in a toluene/*n*-hexane mixture (5 mL). In a 5-mL vial, Me$_3$SiI (50.02 mg, 0.25 mmol) was dissolved in *n*-hexane (1 mL). The smaller vial was placed inside the bigger one with the [Cp′Ce(AlMe$_4$)$_2$] solution, and the large vial was sealed afterwards. Diffusion of the Me$_3$SiI into the [Cp′Ce(AlMe$_4$)$_2$] solution and storing the vial at ambient temperature led to the formation of crystalline **3** and **4 a** in low yields after several days. No signal assignment in the ^{1}H NMR spectrum was possible due to the presence of a product mixture. Any meaningful IR spectra and elemental analysis could not be performed due to the presence of a product mixture.

[Cp′$_4$Pr$_4$I$_8$]$_4$ (4 b). In a 20-mL, [Cp′Pr(AlMe$_4$)$_2$] (**1 b**, 45.2 mg, 0.1 mmol) was dissolved in *n*-hexane (5 mL). In a 5-mL vial, Me$_3$SiI (50.02 mg, 0.25 mmol) was dissolved in *n*-hexane (1 mL). The smaller vial was placed inside the bigger one with the [Cp′Pr(AlMe$_4$)$_2$] solution, and the large vial was sealed afterwards. Diffusion of the Me$_3$SiI into the [Cp′Pr(AlMe$_4$)$_2$] solution and storing the vial at ambient temperature led to the formation of crystalline **4 b** in low yields after several days. The ^{1}H NMR spectrum of the non-crystalline residue was inconclusive. Any meaningful IR spectra and elemental analysis could not be performed due to the presence of co-products.

[Cp′$_6$Pr$_6$I$_8$(AlMe$_4$)$_4$] (**5**). a) In a 20-mL vial, [Cp′Pr(AlMe$_4$)$_2$] (**1 b**, 45.2 mg, 0.1 mmol) was dissolved in *n*-hexane (5 mL). In a 5-mL vial, Me$_3$SiI (50.02 mg, 0.25 mmol) was dissolved in *n*-hexane (1 mL). The smaller vial was placed inside the bigger one with the [Cp′Pr(AlMe$_4$)$_2$] solution, and the large vial was sealed afterwards. Diffusion of the Me$_3$SiI into the [Cp′Pr(AlMe$_4$)$_2$] solution and storing the vial at 0 °C led to the formation of crystalline **5** in low yield after several weeks.

b) [Cp′Pr(AlMe$_4$)$_2$] (**1 b**, 45.2 mg, 0.1 mmol) was dissolved in *n*-hexane (2.5 mL), Me$_3$SiI (26.00 mg, 0.13 mmol) was dissolved in *n*-hexane (0.5 mL) and added, and the vial was shaken vigorously. Storing the vial at −40 °C led to the formation of crystalline **5** (23.4 mg, 7.5 μmol, 45 %) overnight. ^{1}H NMR (400 MHz, [D$_6$]benzene, 26 °C): $\delta = 26.32$ (2H, $C_5H_4SiMe_3$), 8.51 (2H, $C_5H_4SiMe_3$), 8.36 (2H, $C_5H_4SiMe_3$), −1.79 (24H, Al*Me*$_4$), −6.20 (9H, C_5H_4Si*Me*$_3$) ppm. IR (Nujol): $\tilde{\nu} = 2954$ (Cp, Nujol), 2924 (Cp, Nujol), 2855 (Cp, Nujol), 2726 (w), 2670 (w), 2620 (w), 2092 (w), 1461 (Nujol), 1401 (Nujol), 1377 (Nujol), 1310 (w), 1248 (s), 1206 (w), 1192 (w), 1171 (m), 1042 (m), 1019 (m), 902 (m), 838 (vs), 801 (vs), 755 (s), 722 (vs), 697 (s), 625 (m), 585 (m), 547 (w), 530 (w), 418 (w) cm^{-1}. Elemental analysis of **5** calculated for $C_{64}H_{126}Al_4Pr_6I_8Si_6$ (3032.83 g/mol): C 25.35 %, H 4.19 %; found: C 28.20 %, H 4.86 %. The deviation between theoretical and experimental values can be explained by residual lattice *n*-hexane in the crystalline material.

[Cp′CeBr$_2$]$_{12}$ (6 a). [Cp′Ce(AlMe$_4$)$_2$] (**1 a**, 45.2 mg, 0.1 mmol), was dissolved in *n*-hexane (2 mL), and Me$_3$GeBr (49.41 mg, 0.25 mmol) was added under vigorous stirring, resulting in a gradual color change of the solution from light yellow to colorless. After stirring the reaction mixture for 4 h, the suspension was filtered, and the vial was stored at ambient temperature. Within several days at ambient temperature, **6 a** formed as colorless crystals (28.0 mg, 5.33 μmol, 64 %). ^{1}H NMR (400 MHz, [D$_6$]benzene, 26 °C): $\delta = 19.71$ (2H, $C_5H_4SiMe_3$), −0.31 (2H, $C_5H_4SiMe_3$), −9.11 (9H, C_5H_4Si*Me*$_3$) ppm. IR (Nujol): $\tilde{\nu} = 2954$ (Cp, Nujol), 2924 (Cp, Nujol), 2854 (Cp, Nujol), 1460 (vs, Nujol), 1377 (s, Nujol), 1246 (w), 1172 (w), 1042 (w), 903 (w), 837 (w), 798 (w), 753 (w), 722 (w), 693 (w), 639 (w), 627 (w), 421 (w) cm^{-1}. Elemental analysis of **6 a** calculated for $C_{96}H_{156}Ce_{12}Br_{24}Si_{12}$ (5246.41 g/mol): C 21.98 %, H 3.00 %; found: C 23.71 %, H 3.25 %. The high carbon value can be attributed to residual lattice *n*-hexane in the crystalline material.

[Cp′PrBr$_2$]$_{12}$ (6 b). [Cp′Pr(AlMe$_4$)$_2$] (**1 a**, 45.2 mg, 0.1 mmol), was dissolved in *n*-hexane (2 mL), and Me$_3$GeBr (49.41 mg, 0.25 mmol) was added, and the vial was shaken vigorously, resulting in a gradual color change of the solution from light green to colorless. Storing the reaction solution at −40 °C led to the formation of **6 b** as colorless crystals (28.8 mg, 5.39 μmol, 65 %). ^{1}H NMR (400 MHz, [D$_6$]benzene, 26 °C): $\delta = 27.63$ (bs), 0.14 (d), −6.20 (s) ppm. IR (Nujol): $\tilde{\nu} = 2953$ (Cp, Nujol), 2923 (Cp, Nujol), 2854 (Cp, Nujol), 2726 (w), 2670 (w), 2620 (w), 2092 (w), 1461 (Nujol), 1405 (Nujol), 1377 (Nujol), 1311 (m), 1247 (s), 1173 (m), 1042 (s), 1015 (w), 903 (s), 839 (vs), 800 (vs), 754 (m), 724 (vs), 693 (w), 638 (m), 626 (w), 422 (m) cm^{-1}. Elemental analysis of **6 b** calculated for $C_{102}H_{170}Pr_{12}Br_{24}Si_{12}$ (5342.09 g/mol): C 22.93 %, H 3.21 %; found: C 23.15 %, H 3.46 %.

[Cp′CeCl$_2$]$_{12}$ (7 a) and [Cp′$_5$Ce$_5$Cl$_9$(Cl$_2$AlMe$_2$)]$_2$ (8). [Cp′Ce(AlMe$_4$)$_2$] (**1 a**, 45.2 mg, 0.1 mmol), was dissolved in *n*-hexane (2 mL), and Me$_3$GeCl (38.3 mg, 0.25 mmol) was added under vigorous stirring, resulting in a gradual color change of the solution from light yellow to colorless. After stirring the reaction mixture for 4 h, the suspension was filtered, and the vial was stored at ambient temperature. Within several days at ambient temperature, **7 a** and **8** formed as colorless crystals (28.2 mg, 78 % total yield). The ^{1}H NMR spectrum shows a mixture of products. Any meaningful IR spectra and elemental analysis could not be performed due to the presence of a product mixture.

[Cp′PrCl$_2$]$_{12}$ (7 b). [Cp′Pr(AlMe$_4$)$_2$] (**1 a**, 45.2 mg, 0.1 mmol), was dissolved in *n*-hexane (2 mL), and Me$_3$GeCl (38.3 mg, 0.25 mmol) was added, and the vial was shaken vigorously, resulting in a gradual color change of the solution from light green to colorless. Storing the reaction solution at −40 °C led to the formation of **7 b** as colorless crystals (3.2 mg, 0.76 μmol, 9 %). The ^{1}H NMR spectrum of the crystalline product was inconclusive. IR (Nujol): $\tilde{\nu} = 3173$ (vw), 2954 (Cp, Nujol), 2924 (Cp, Nujol), 2854 (Cp, Nujol), 2724 (w), 2669 (w), 1461 (Nujol), 1377 (Nujol), 1305 (m), 1248 (w), 1169 (w), 1156 (w), 1043 (vw), 1018 (vw), 996 (vw), 935 (vw), 904 (vw), 892 (vw), 843 (w), 769 (w), 724 (vs), 638 (vw), 626 (vw), 564 (vw) 424 (vw)

cm^{-1}. Elemental analysis of **7b** calculated for $C_{96}H_{156}Pr_{12}Cl_{24}Si_{12}$ (4189.00 g/mol): C 27.53 %, H 3.75 %; found: C 28.09 %, H 4.15 %.

X-Ray Crystallography and Crystal Structure Determinations. Single-crystals of **1a** were grown from a saturated *n*-hexane solution. Single-crystals of **2**, **4a**, **5**, **6a**, **6b**, **7a**, **7b**, and **8** were grown from diluted *n*-hexane solutions. Crystals of **3** and **4b** were grown by the diffusion technique. Due to insufficient crystal quality of **2**, only a connectivity structure could be obtained. Suitable crystals for X-ray structure analyses were selected inside a glovebox, coated with Parabar 10312 (previously known as Paraton N, Hampton Research) and fixed on a nylon/loop glass fiber. X-ray data were collected on a Bruker APEX III DUO instrument equipped with an IμS microfocus sealed tube and QUAZAR optics for MoK_α ($\lambda = 0.71073$ Å) and CuK_α ($\lambda = 1.54184$ Å) radiation. The data collection was determined using COSMO[67] employing ω-scans. Raw data were processed using APEX[68] and SAINT,[69] corrections for absorption effects were applied by using SADABS.[70] For compounds **3**, **4b**, and **5a** numerical absorption correction was performed, for all other compounds multi-scans were applied. The structures were solved by direct methods and refined against all data by full-matrix least-squares methods on F^2 using SHELXTL[71] and SHELXLE.[72] Disorder models are calculated using DSR, a program for refining disordered structures in SHELXLE.[73] All graphics were generated employing CCDC Mercury 3.10.1.[74] Further details regarding the refinement and crystallographic data are listed in Table S1 and in the CIF files.

Deposition Numbers 2114125 (for **1a**), 2114126 (for **6a**), 2114127 (for **4b**), 2114128 (for **4a**), 2114129 (for **5**), 2114130 (for **7a**), 2114131 (for **6b**), 2114132 (for **8**), 2114133 (for **3**), and 2114134 (for **7b**) contain the supplementary crystallographic data for this paper. These data are provided free of charge by the joint Cambridge Crystallographic Data Centre and Fachinformationszentrum Karlsruhe Access Structures service www.ccdc.cam.ac.uk/structures.

Acknowledgements

We are grateful to the German Science Foundation for financial support (Grant: AN 238/14-2). We thank Prof. Dr. Michael Seitz for providing the equipment for the luminescence measurements and Dr. Wolfgang Leis for conducting the measurements as well as assistance in the discussion of the luminescence part. Open Access funding enabled and organized by Projekt DEAL.

Conflict of Interest

The authors declare no conflict of interest.

Keywords: Cluster compounds · Cyclopentadienyl ligands · Halides · Lanthanides · Luminescence

[1] J.-B. Peng, Q.-C. Zhang, X.-J. Kong, Y.-Z. Zheng, Y.-P. Ren, L.-S. Long, R.-B. Huang, L.-S. Zheng, Z. Zheng, *J. Am. Chem. Soc.* **2012**, *134*, 3314–3317.
[2] J.-B. Peng, X.-J. Kong, Q.-C. Zhang, M. Orendáč, J. Prokleška, Y.-P. Ren, L.-S. Long, Z. Zheng, L.-S. Zheng, *J. Am. Chem. Soc.* **2014**, *136*, 17938–17941.
[3] L. Qin, Y.-Z. Yu, P.-Q. Liao, W. Xue, Z. Zheng, X.-M. Chen, Y.-Z. Zheng, *Adv. Mater.* **2016**, *28*, 10772–10779.
[4] X.-Y. Zheng, J.-B. Peng, X.-J. Kong, L.-S. Long, L.-S. Zheng, *Inorg. Chem. Front.* **2016**, *3*, 320–325.
[5] L. Qin, G.-J. Zhou, Y.-Z. Yu, H. Nojiri, C. Schröder, R. E. P. Winpenny, Y.-Z. Zheng, *J. Am. Chem. Soc.* **2017**, *139*, 16405–16411.
[6] X.-Y. Zheng, Y.-H. Jiang, G.-L. Zhuang, D.-P. Liu, H.-G. Liao, X.-J. Kong, L.-S. Long, L.-S. Zheng, *J. Am. Chem. Soc.* **2017**, *139*, 18178–18181.
[7] X.-Y. Zheng, X.-J. Kong, Z. Zheng, L.-S. Long, L.-S. Zheng, *Acc. Chem. Res.* **2018**, *51*, 517–525.
[8] D. Shi, X. Yang, H. Chen, Y. Ma, D. Schipper, R. A. Jones, *J. Mater. Chem. C* **2019**, *7*, 13425–13431.
[9] X.-Y. Zheng, J. Xie, X.-J. Kong, L.-S. Long, L.-S. Zheng, *Coord. Chem. Rev.* **2019**, *378*, 222–236.
[10] D. A. Gálico, J. S. Ovens, M. Murugesu, *Nanoscale* **2020**, *12*, 11435–11439.
[11] X.-Y. Li, Y. Jing, J. Zheng, H. Ding, Q. Li, M.-H. Yu, X.-H. Bu, *Cryst. Growth Des.* **2020**, *20*, 5294–5301.
[12] J. Wu, S. Demeshko, S. Dechert, F. Meyer, *Chem. Commun.* **2020**, *56*, 3887–3890.
[13] D. A. Gálico, A. A. Kitos, J. S. Ovens, F. A. Sigoli, M. Murugesu, *Angew. Chem. Int. Ed.* **2021**, *60*, 6130–6136; *Angew. Chem.* **2021**, *133*, 6195–6201.
[14] C. O. Hollfelder, L. N. Jende, H.-M. Dietrich, K. Eichele, C. Maichle-Mössmer, R. Anwander, *Chem. Eur. J.* **2019**, *25*, 7298–7302.
[15] D. T. Thielemann, A. T. Wagner, E. Rösch, D. K. Kölmel, J. G. Heck, B. Rudat, M. Neumaier, C. Feldmann, U. Schepers, S. Bräse, P. W. Roesky, *J. Am. Chem. Soc.* **2013**, *135*, 7454–7457.
[16] F. Le Natur, G. Calvez, J.-P. Guégan, L. Le Pollès, X. Trivelli, K. Bernot, C. Daiguebonne, C. Neaime, K. Costuas, F. Grasset, O. Guillou, *Inorg. Chem.* **2015**, *54*, 6043–6054.
[17] I. Mylonas-Margaritis, A. A. Kitos, C. C. Panteli, K. Skordi, A. J. Tasiopoulos, V. Bekiari, A. Escuer, S. P. Perlepes, *Inorg. Chem. Commun.* **2017**, *83*, 118–122.
[18] H. Yao, G. Calvez, C. Daiguebonne, K. Bernot, Y. Suffren, M. Puget, C. Lescop, O. Guillou, *Inorg. Chem.* **2017**, *56*, 14632–14642.
[19] D. Shi, X. Yang, H. Chen, D. Jiang, J. Liu, Y. Ma, D. Schipper, R. A. Jones, *Chem. Commun.* **2019**, *55*, 13116–13119.
[20] D. Shi, X. Yang, Z. Xiao, X. Liu, H. Chen, Y. Ma, D. Schipper, R. A. Jones, *Nanoscale* **2020**, *12*, 1384–1388.
[21] S. V. Eliseeva, J.-C. G. Bünzli, *Chem. Soc. Rev.* **2010**, *39*, 189–227.
[22] H. Yin, P. J. Carroll, B. C. Manor, J. M. Anna, E. J. Schelter, *J. Am. Chem. Soc.* **2016**, *138*, 5984–5993.
[23] Z. Xia, A. Meijerink, *Chem. Soc. Rev.* **2017**, *46*, 275–299.
[24] M. Suta, N. Harmgarth, M. Kühling, P. Liebing, F. T. Edelmann, C. Wickleder, *Chem. Asian J.* **2018**, *13*, 1038–1044.
[25] M. Kühling, C. Wickleder, M. J. Ferguson, C. G. Hrib, R. McDonald, M. Suta, L. Hilfert, J. Takats, F. T. Edelmann, *New J. Chem.* **2015**, *39*, 7617–7625.
[26] S. Harder, D. Naglav, C. Ruspic, C. Wickleder, M. Adlung, W. Hermes, M. Eul, R. Pöttgen, D. B. Rego, F. Poineau, *Chem. Eur. J.* **2013**, *19*, 12272–12280.
[27] X. Y. Li, H. F. Su, Q. W. Li, R. Feng, H. Y. Bai, H. Y. Chen, J. Xu, X. H. Bu, *Angew. Chem. Int. Ed.* **2019**, *58*, 10184–10188; *Angew. Chem.* **2019**, *131*, 10290–10294.
[28] R. Anwander, *Angew. Chem. Int. Ed.* **1998**, *37*, 599–602; *Angew. Chem.* **1998**, *110*, 619–622.
[29] W. J. Evans, G. W. Rabe, M. A. Ansari, J. W. Ziller, *Angew. Chem. Int. Ed. Engl.* **1994**, *33*, 2110–2111.
[30] S. P. Constantine, G. M. De Lima, P. B. Hitchcock, J. M. Keates, G. A. Lawless, *Chem. Commun.* **1996**, 2421–2422.
[31] Z. Hou, Y. Zhang, O. Tardif, Y. Wakatsuki, *J. Am. Chem. Soc.* **2001**, *123*, 9216–9217.
[32] F. Bonnet, M. Visseaux, D. Barbier-Baudry, A. Hafid, E. Vigier, M. M. Kubicki, *Inorg. Chem.* **2004**, *43*, 3682–3690.
[33] M. D. Walter, F. Weber, G. Wolmershäuser, H. Sitzmann, *Angew. Chem. Int. Ed.* **2006**, *45*, 1903–1905; *Angew. Chem.* **2006**, *118*, 1937–1939.
[34] W. P. Kretschmer, J. H. Teuben, S. I. Troyanov, *Angew. Chem. Int. Ed.* **1998**, *37*, 88–90; *Angew. Chem.* **1998**, *110*, 92–94.
[35] D. A. Buschmann, H. M. Dietrich, D. Schneider, V. M. Birkelbach, C. Stuhl, K. W. Törnroos, C. Maichle-Mössmer, R. Anwander, *Chem. Eur. J.* **2020**, *26*, 10834–10840.
[36] W. J. Evans, D. K. Drummond, J. W. Grate, H. Zhang, J. L. Atwood, *J. Am. Chem. Soc.* **1987**, *109*, 3928–3936.
[37] N. S. Radu, F. J. Hollander, T. D. Tilley, A. L. Rheingold, *Chem. Commun.* **1996**, 2459–2460.
[38] R. D. Shannon, *Acta Crystallogr. Sect. A* **1976**, *32*, 751–767.

[39] M. Zimmermann, N. Å Frøystein, A. Fischbach, P. Sirsch, H. M. Dietrich, K. W. Törnroos, E. Herdtweck, R. Anwander, *Chem. Eur. J.* **2007**, *13*, 8784–8800.
[40] G. Occhipinti, C. Meermann, H. M. Dietrich, R. Litlabø, F. Auras, K. W. Törnroos, C. Maichle-Mössmer, V. R. Jensen, R. Anwander, *J. Am. Chem. Soc.* **2011**, *133*, 6323–6337.
[41] D. Schneider, N. Harmgarth, F. T. Edelmann, R. Anwander, *Chem. Eur. J.* **2017**, *23*, 12243–12252.
[42] O. Tardif, M. Nishiura, Z. Hou, *Organometallics* **2003**, *22*, 1171–1173.
[43] M. Nishiura, J. Baldamus, T. Shima, K. Mori, Z. Hou, *Chem. Eur. J.* **2011**, *17*, 5033–5044.
[44] D. Diether, K. Tyulyunov, C. Maichle-Mössmer, R. Anwander, *Organometallics* **2017**, *36*, 4649–4659.
[45] O. Poncelet, L. G. Hubert-Pfalzgraf, J.-C. Daran, R. Astier, *J. Chem. Soc. Chem. Commun.* **1989**, 1846–1848.
[46] D. M. Barnhart, D. L. Clark, J. C. Gorden, J. C. Huffman, J. G. Watkin, B. D. Zwick, *J. Am. Chem. Soc.* **1993**, *115*, 8461–8462.
[47] W. J. Evans, J. H. Meadows, A. L. Wayda, W. E. Hunter, J. L. Atwood, *J. Am. Chem. Soc.* **1982**, *104*, 2015–2017.
[48] F. Bottomley, D. E. Paez, P. S. White, *J. Organomet. Chem.* **1985**, *291*, 35–41.
[49] C. J. Burns, D. J. Berg, R. A. Andersen, *J. Chem. Soc. Chem. Commun.* **1987**, 272–273.
[50] W. J. Evans, D. K. Drummond, *Organometallics* **1988**, *7*, 797–802.
[51] W. J. Evans, M. S. Sollberger, S. I. Khan, R. Bau, *J. Am. Chem. Soc.* **1988**, *110*, 439–446.
[52] S. Y. Knjazhanskij, B. M. Bulychev, O. K. Kireeva, V. K. Belsky, G. L. Soloveichik, *J. Organomet. Chem.* **1991**, *414*, 11–22.
[53] H. Schumann, M. R. Keitsch, J. Winterfeld, J. Demtschuk, *J. Organomet. Chem.* **1996**, *525*, 279–281.
[54] Y. Obora, T. Ohta, C. L. Stern, T. J. Marks, *J. Am. Chem. Soc.* **1997**, *119*, 3745–3755.
[55] D. Schneider, R. Anwander, *Eur. J. Inorg. Chem.* **2017**, *2017*, 1180–1188.
[56] M. T. Gamer, P. W. Roesky, *Inorg. Chem.* **2005**, *44*, 5963–5965.
[57] F. M. Sroor, C. G. Hrib, P. Liebing, L. Hilfert, S. Busse, F. T. Edelmann, *Dalton Trans.* **2016**, *45*, 13332–13346.
[58] H. M. Dietrich, O. Schuster, K. W. Törnroos, R. Anwander, *Angew. Chem. Int. Ed.* **2006**, *45*, 4858–4863; *Angew. Chem.* **2006**, *118*, 4977–4982.
[59] V. M. Birkelbach, F. Kracht, H. M. Dietrich, C. Stuhl, C. Maichle-Mössmer, R. Anwander, *Organometallics* **2020**, *39*, 3490–3504.
[60] P. N. Hazin, J. W. Bruno, H. G. Brittain, *Organometallics* **1987**, *6*, 913–918.
[61] M. D. Rausch, K. J. Moriarty, J. L. Atwood, J. A. Weeks, W. E. Hunter, H. G. Brittain, *Organometallics* **1986**, *5*, 1281–1283.
[62] P. N. Hazin, C. Lakshminarayan, L. S. Brinen, J. L. Knee, J. W. Bruno, W. E. Streib, K. Folting, *Inorg. Chem.* **1988**, *27*, 1393–1400.
[63] H. Yin, P. J. Carroll, J. M. Anna, E. J. Schelter, *J. Am. Chem. Soc.* **2015**, *137*, 9234–9237.
[64] H. Yin, Y. Jin, J. E. Hertzog, K. C. Mullane, P. J. Carroll, B. C. Manor, J. M. Anna, E. J. Schelter, *J. Am. Chem. Soc.* **2016**, *138*, 16266–16273.
[65] Y. Qiao, E. J. Schelter, *Acc. Chem. Res.* **2018**, *51*, 2926–2936.
[66] Y. Qiao, D.-C. Sergentu, H. Yin, A. V. Zabula, T. Cheisson, A. McSkimming, B. C. Manor, P. J. Carroll, J. M. Anna, J. Autschbach, *J. Am. Chem. Soc.* **2018**, *140*, 4588–4595.
[67] COSMO, v. 1.61, Bruker AXS Inc., Madison, WI **2012**.
[68] APEX 3, v. 2016.2015-2010; Bruker AXS Inc., Madison, WI **2012**.
[69] SAINT, v. 8.34 A; Bruker AXS Inc., Madison, WI **2010**.
[70] L. Krause, R. Herbst-Irmer, G. M. Sheldrick, D. Stalke, *J. Appl. Crystallogr.* **2015**, *48*, 3–10.
[71] G. M. Sheldrick, *Acta Crystallogr. Sect. A* **2015**, *71*, 3–8.
[72] C. B. Hübschle, G. M. Sheldrick, B. Dittrich, *J. Appl. Crystallogr.* **2011**, *44*, 1281–1284.
[73] D. Kratzert, J. J. Holstein, I. Krossing, *J. Appl. Crystallogr.* **2015**, *48*, 933–938.
[74] C. F. Macrae, P. R. Edgington, P. McCabe, E. Pidcock, G. P. Shields, R. Taylor, M. Towler, J. Streek, *J. Appl. Crystallogr.* **2006**, *39*, 453–457.

Manuscript received: October 7, 2021
Revised manuscript received: October 21, 2021
Accepted manuscript online: October 24, 2021

European Journal of Inorganic Chemistry

Supporting Information

Half-Sandwich Complexes $[Cp'_4Ln_4I_8]_4$ (Ln=Ce, Pr): Emergence of Donor-Free Organolanthanide Nanowheels

Dennis A. Buschmann, David Schneider, Cäcilia Maichle-Mössmer, and Reiner Anwander*

Supporting Information

Table of Contents

NMR Spectroscopy

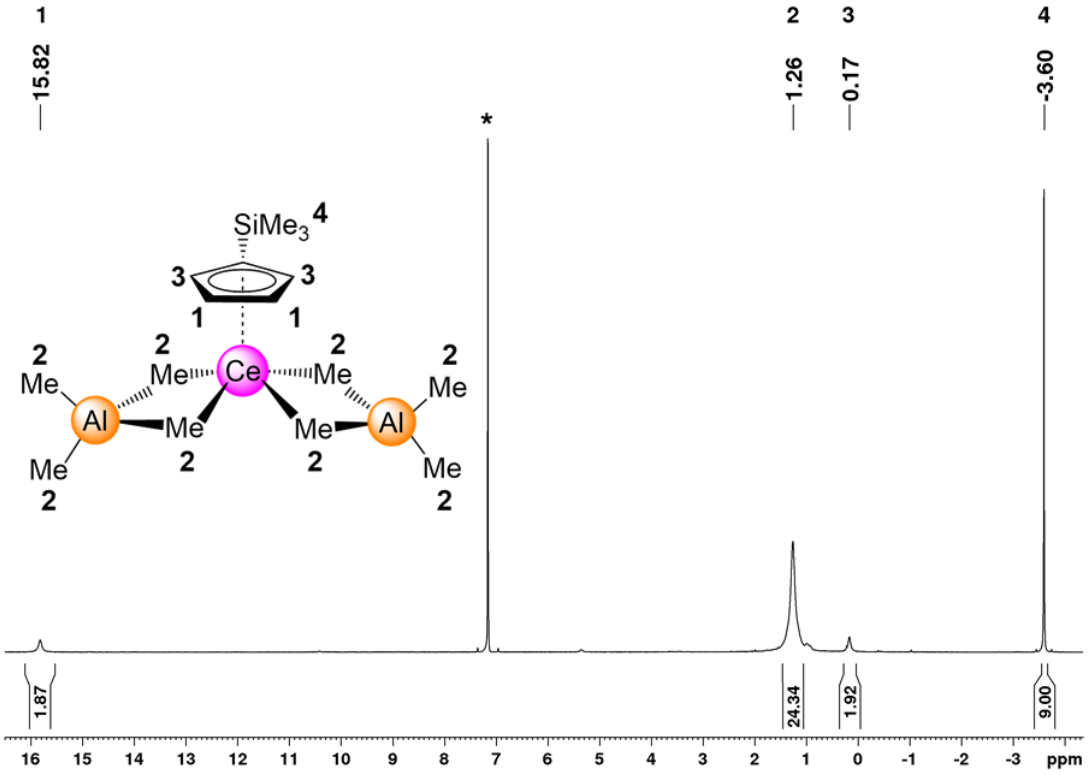

Figure S1. ^{1}H NMR spectrum (400 MHz) of Cp'Ce(AlMe$_4$)$_2$ (**1a**) in [D$_6$]benzene at 26 °C. The solvent residual signal is marked with an asterisk.

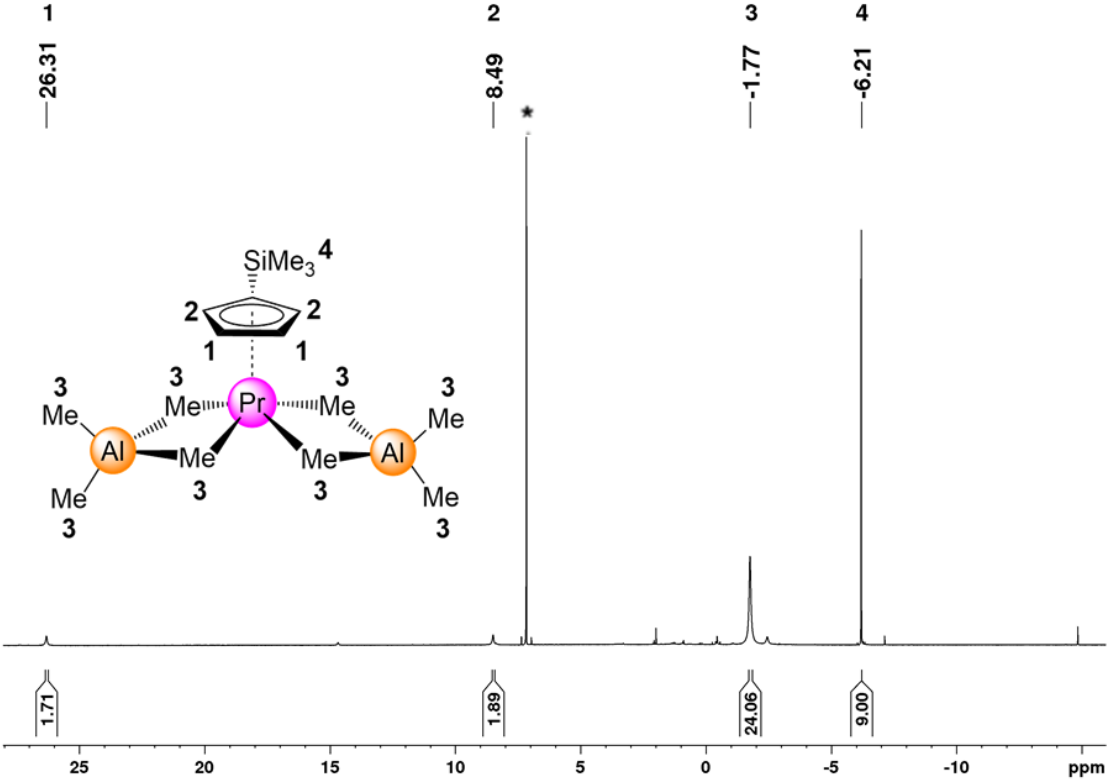

Figure S2. ^{1}H NMR spectrum (400 MHz) of [Cp'Pr(AlMe$_4$)$_2$] (**1b**) in [D$_6$]benzene at 26 °C. The solvent residual signal is marked with an asterisk.

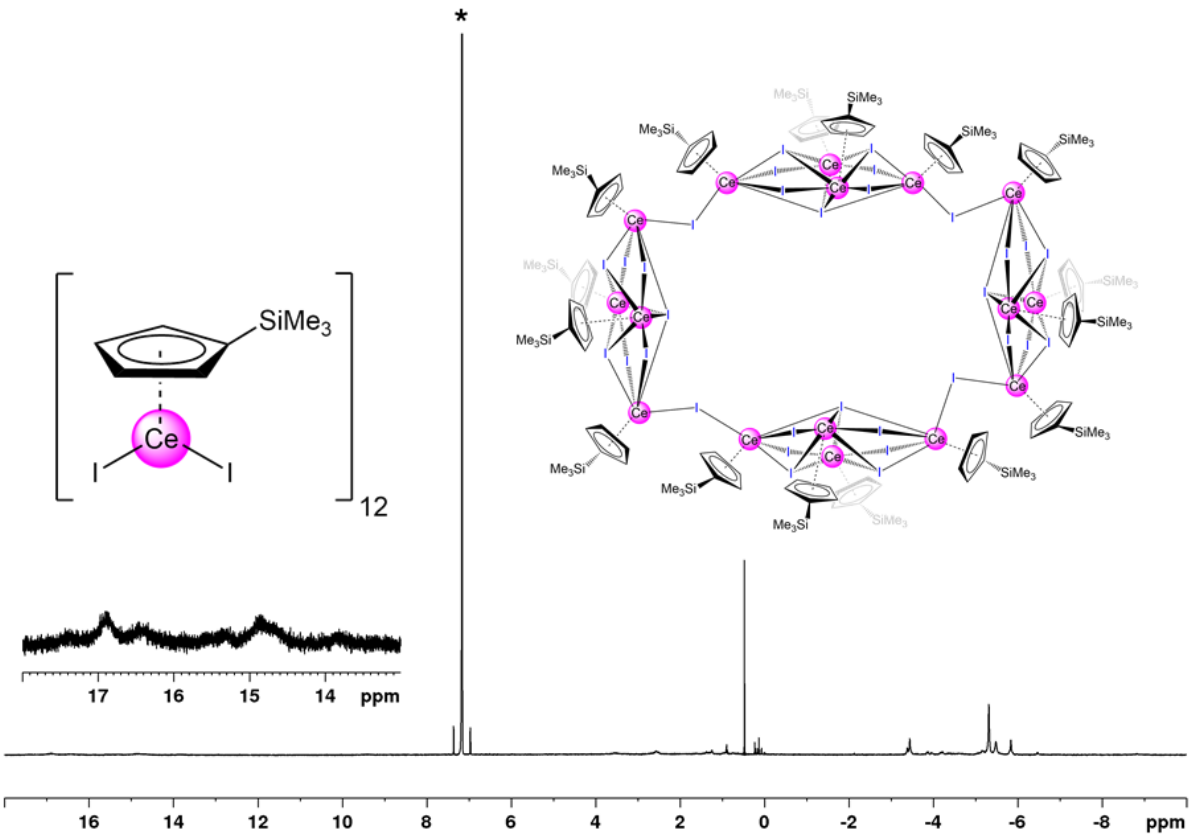

Figure S3. ^{1}H NMR spectrum (400 MHz) of $[Cp'CeI_2]_{12}$ (**2**) and $[Cp'_4Ce_4I_8]_4$ (**4a**) in $[D_6]$benzene at 26 °C. The solvent residual signal is marked with an asterisk.

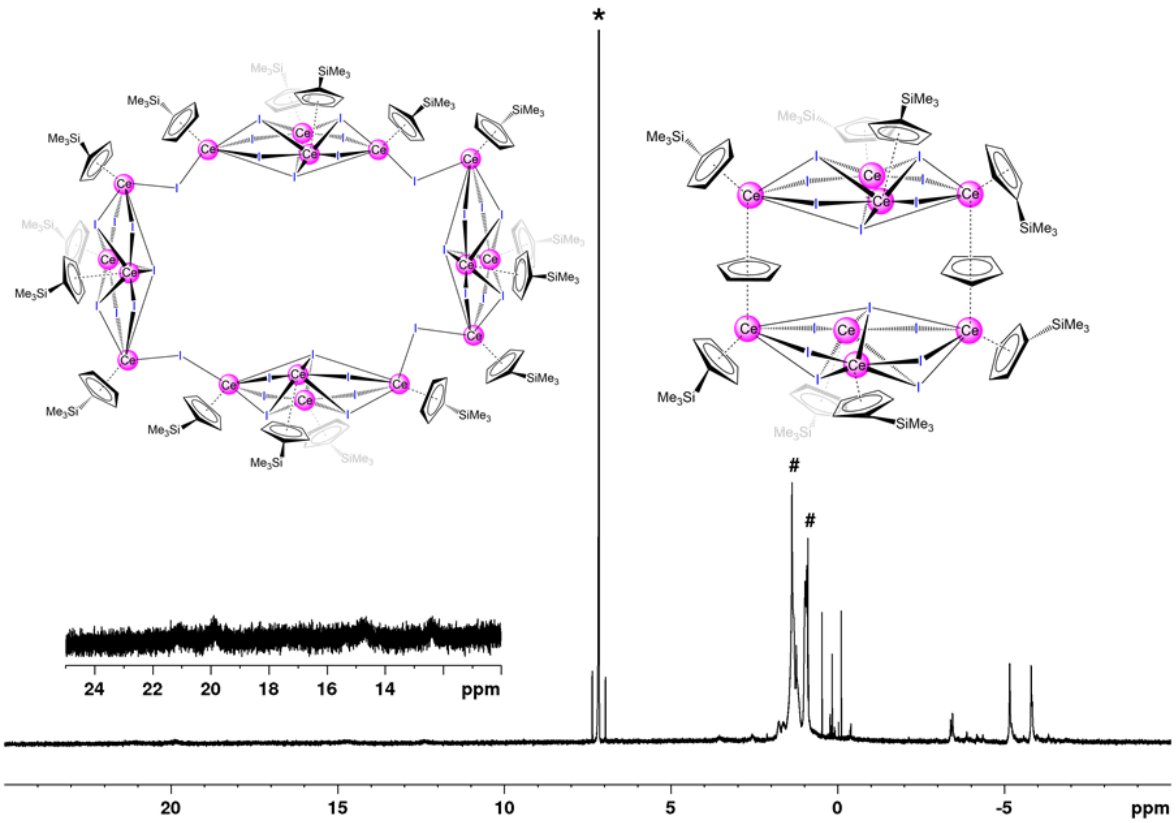

Figure S4. ^{1}H NMR spectrum (400 MHz) of $[Cp'_4Ce_4I_7(\mu_2\text{-}Cp)]_2$ (**3**) and $[Cp'_4Ce_4I_8]_4$ (**4a**) in $[D_6]$benzene at 26 °C. The solvent residual signal is marked with an asterisk (#: *n*-hexane).

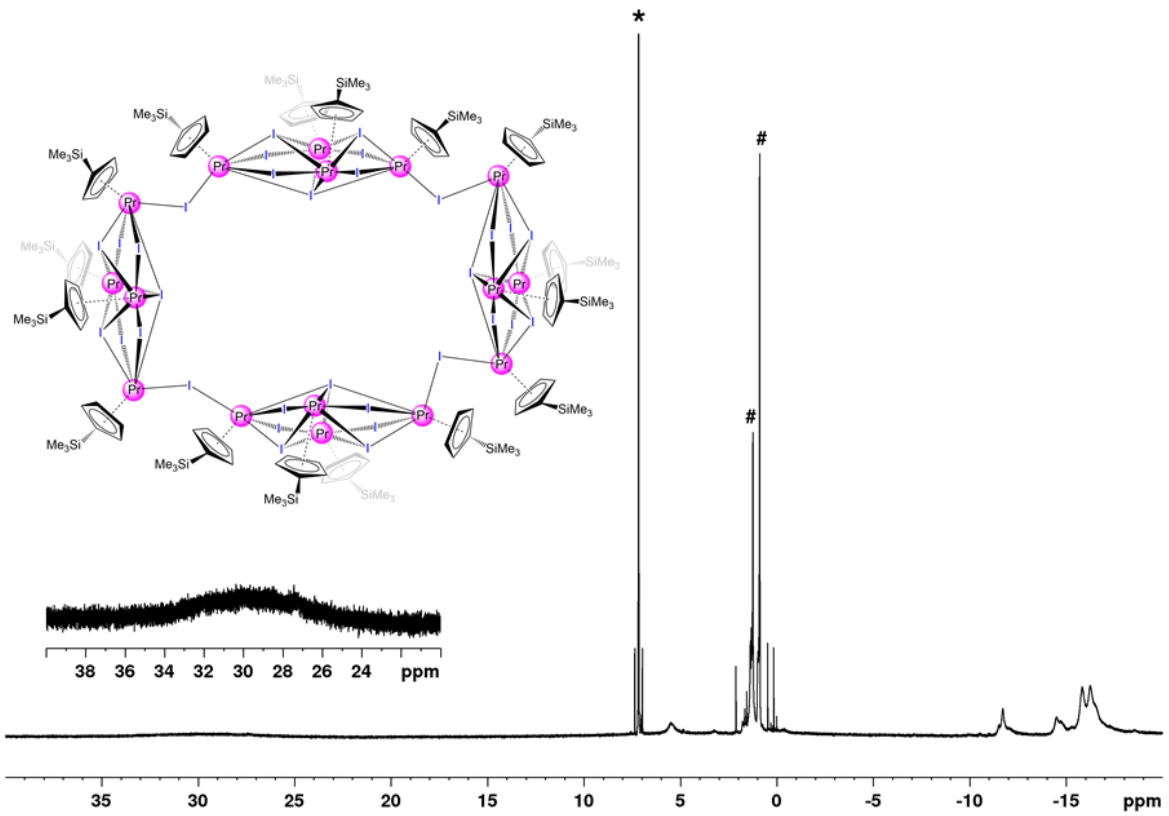

Figure S5. ^{1}H NMR spectrum (400 MHz) of $[Cp'_4Pr_4I_8]_4$ (**4b**) in $[D_6]$benzene at 26 °C. The solvent residual signal is marked with an asterisk (#: *n*-hexane).

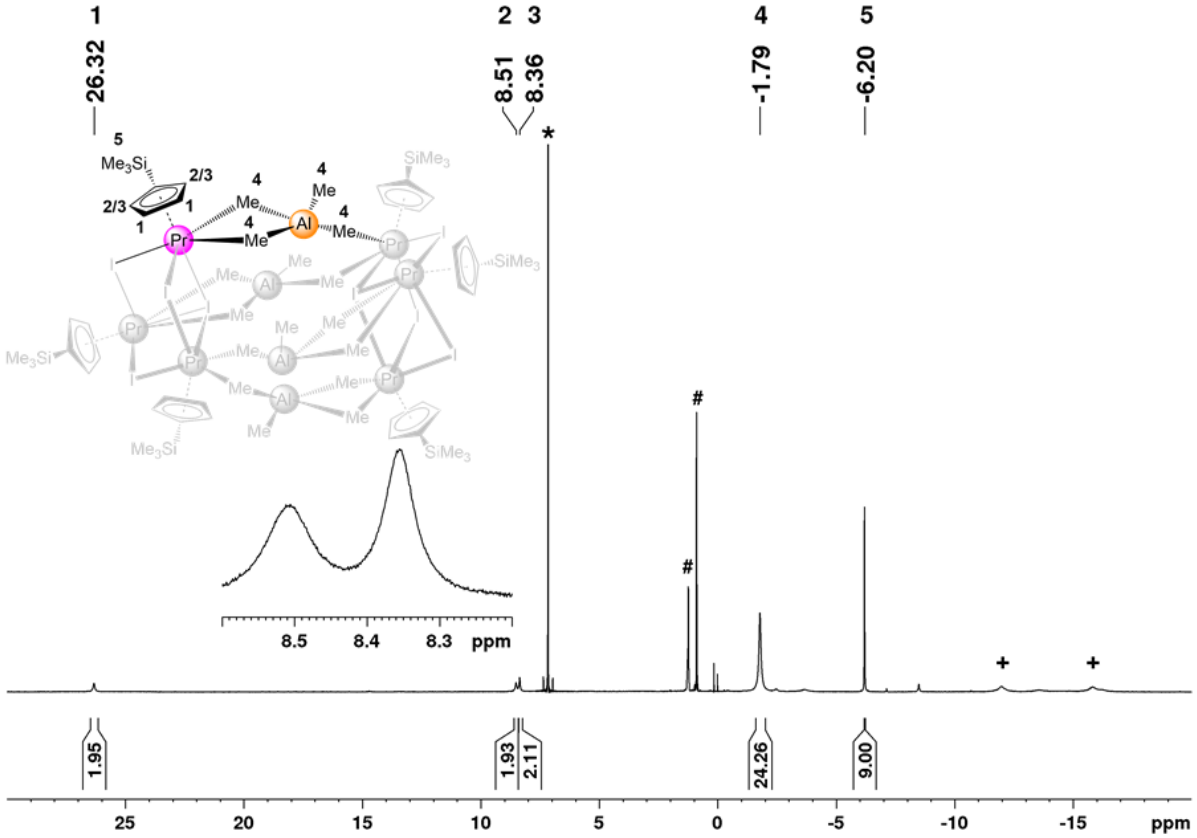

Figure S6. ^{1}H NMR spectrum (400 MHz) of $[Cp'_6Pr_6I_8(AlMe_4)_4]$ (**5**) in $[D_6]$benzene at 26 °C. The solvent residual signal is marked with an asterisk (#: *n*-hexane, +: praseodymium-containing side product).

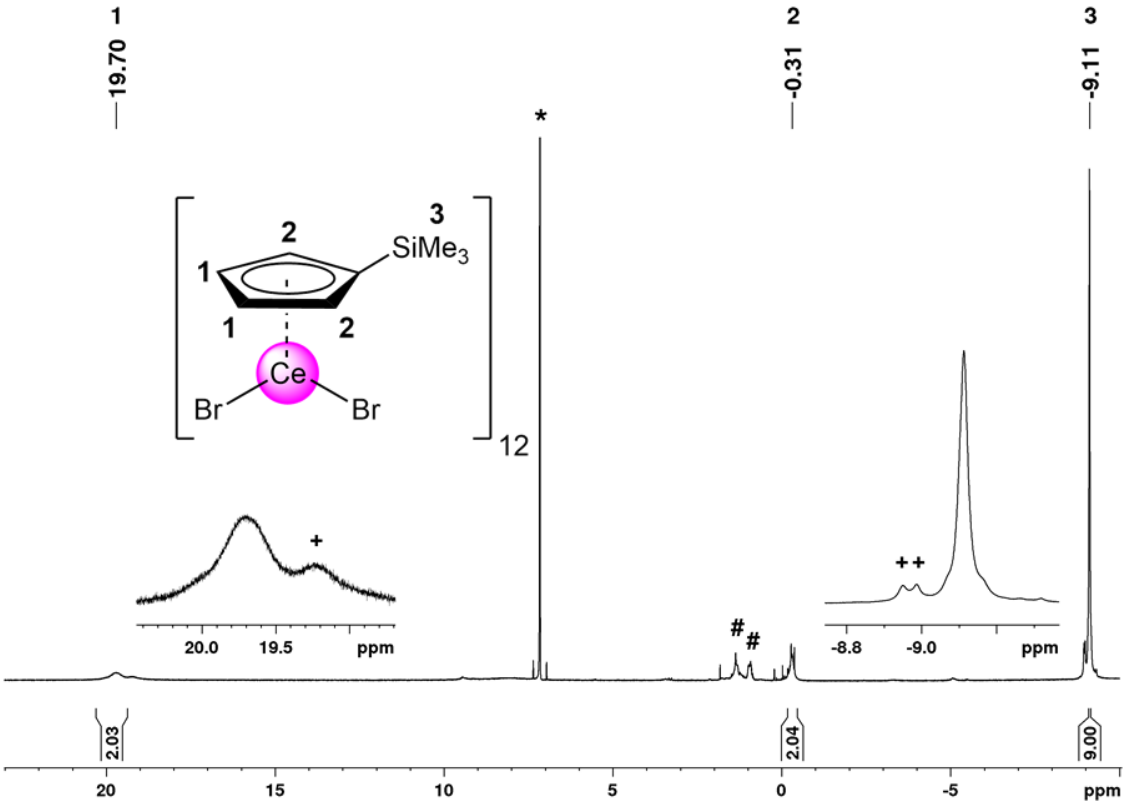

Figure S7. ^{1}H NMR spectrum (400 MHz) of $[Cp'CeBr_2]_{12}$ (**6a**) in $[D_6]$benzene at 26 °C. The solvent residual signal is marked with an asterisk (#: *n*-hexane, +: cerium-containing side product).

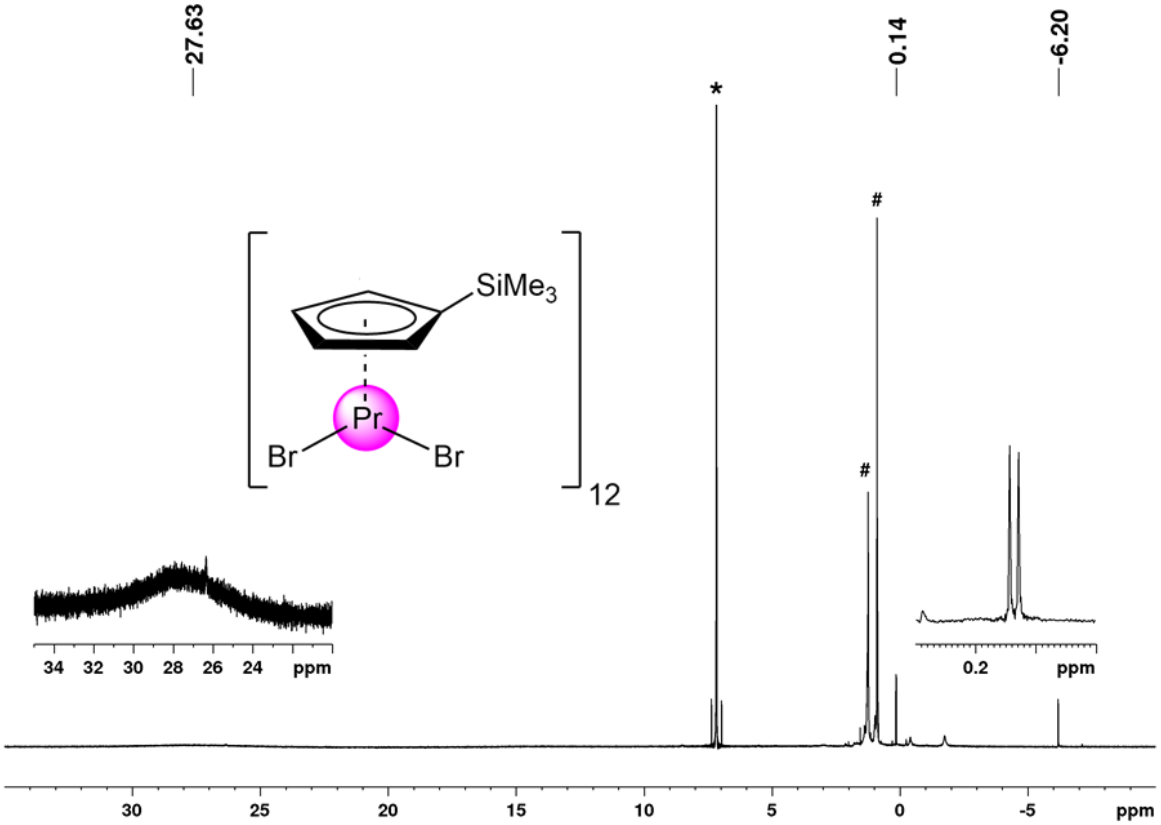

Figure S8. ^{1}H NMR spectrum (400 MHz) of $[Cp'PrBr_2]_{12}$ (**6b**) in $[D_6]$benzene at 26 °C. The solvent residual signal is marked with an asterisk (#: *n*-hexane).

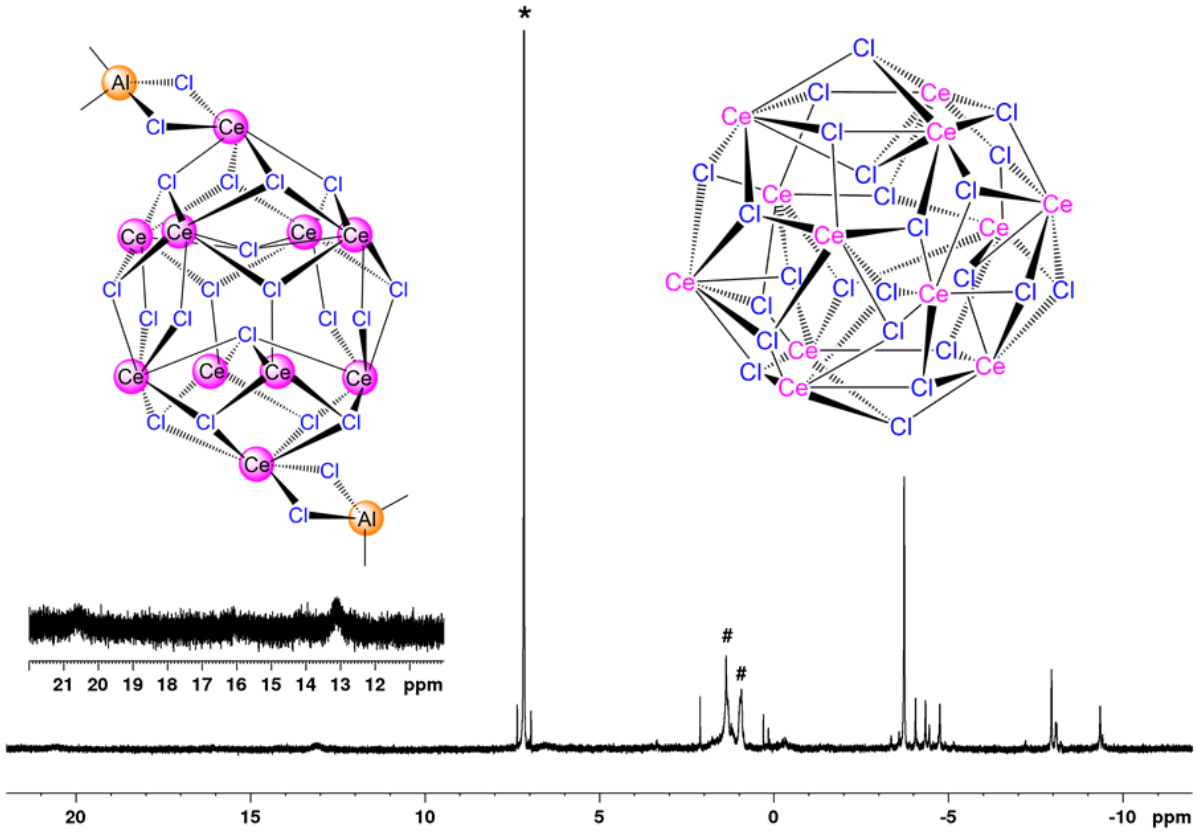

Figure S9. ^{1}H NMR spectrum (400 MHz) of $[Cp'CeCl_2]_{12}$ (**7a**) and $[Cp_5'Ce_5Cl_9(Cl_2AlMe_2)]_2$ (**8**) in $[D_6]$benzene at 26 °C. The solvent residual signal is marked with an asterisk (#: *n*-hexane).

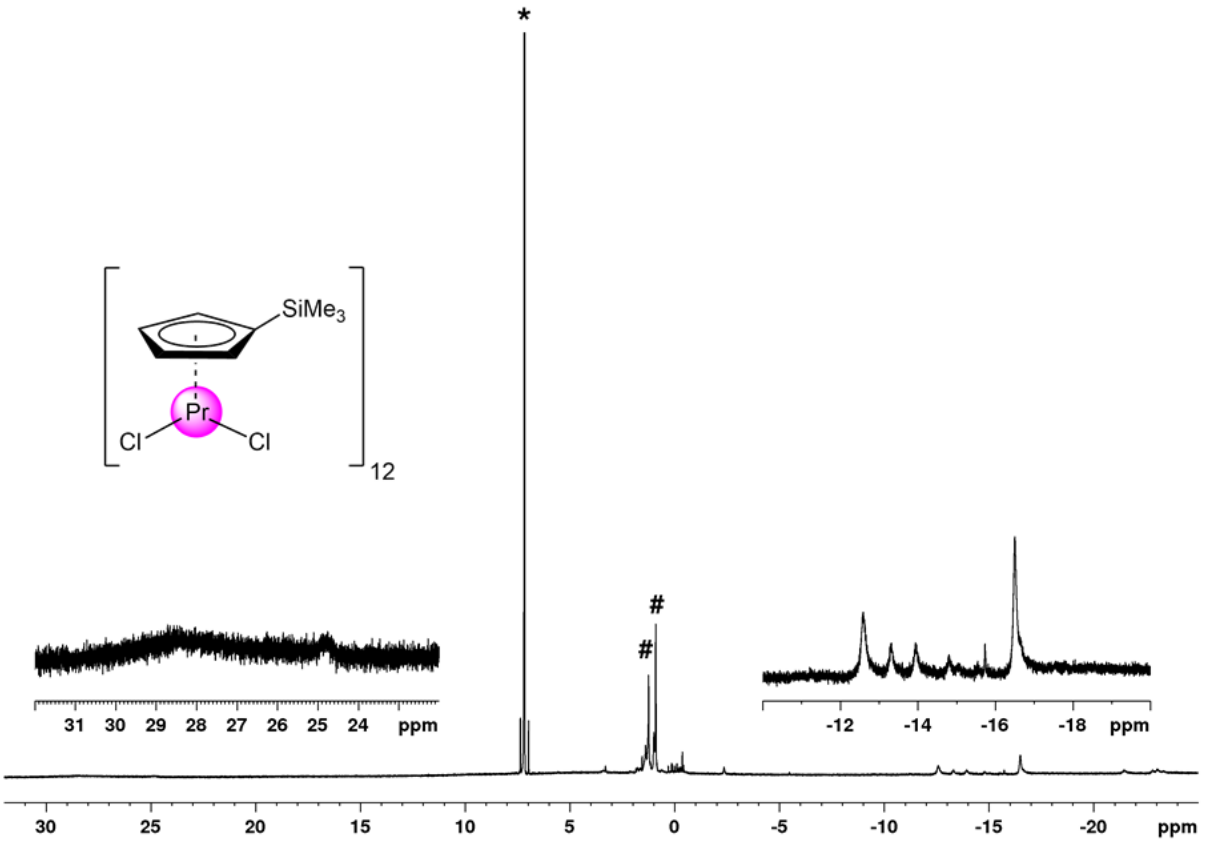

Figure S10. ^{1}H NMR spectrum (400 MHz) of $[Cp'PrCl_2]_{12}$ (**7b**) in $[D_6]$benzene at 26 °C. The solvent residual signal is marked with an asterisk (#: *n*-hexane).

Crystallography

Table S1. Crystallographic data for compounds **1a**, **3**, and **4a**

	1a	**3**	**4a**
CCDC	2114125	2114133	2114128
formula	$C_{16}H_{37}Al_2CeSi$	$C_{80}H_{128}I_{14}Ce_8Si_8$	$C_{142}H_{224}I_{32}Ce_{16}Si_{16}$
M_r [g/mol]	451.62	4212.10	8683.36
color/shape	yellow/plate	yellow/plate	yellow/block
crystal dimensions [mm]	0.701 x 0.200 x 0.189	0.110 x 0.088 x 0.061	0.300 x 0.079 x 0.038
crystal system	monoclinic	triclinic	triclinic
space group	*Cc*	$P\bar{1}$	$P\bar{1}$
a [Å]	16.811(3)	12.5067(4)	17.1355(10)
b [Å]	9.8456(14)	16.7089(5)	17.2062(10)
c [Å]	26.908(4)	16.7606(5)	22.4322(13)
α [°]	90	112.7410(10)	96.0430(10)
β [°]	95.138(4)	105.1710(10)	100.566(11)
γ [°]	90	96.4470(10)	113.1350(10)
V [Å³]	4435.7(12)	3026.69(16)	5862.7(6)
Z	8	1	1
T [K]	100(2)	100(2)	173(2)
λ [Å]	0.71073	0.71073	0.71073
ρ_{calcd} [g/cm³]	1.353	2.311	2.459
μ [mm $^{-1}$]	2.178	6.624	7.363
F (000)	1848	1926	3924
θ range [°]	2.400 – 32.649	1.361 – 26.409	2.023 – 29.494
absorption correction	multi-scan	numerical	multi-scan
independent reflections	14835	12416	32457
reflections collected (I > 2σ)	35626	72415	298052
R1/*w*R2 (I > 2σ)	0.0187/0.0384	0.0342/0.0736	0.0281/0.0653
R1/*w*R2 (all data)	0.0199/0.0388	0.0484/0.0809	0.0347/0.0695
GOF	1053	1.037	1.049

Table S1 (continued). Crystallographic data for compounds **4b**, **5**, and **6a**

	4b	**5**	**6a**
CCDC	2114127	2114129	2114126
formula	$C_{134}H_{222}I_{32}Pr_{16}Si_{16}$	$C_{64}H_{126}Al_4I_8Pr_6Si_6$ $2 \cdot C_6H_{14}$	$C_{96}H_{156}Br_{24}Ce_{12}Si_{12}$
M_r [g/mol]	8597.90	3205.10	5246.56
color/shape	colorless/plate	colorless/plate	colorless/block
crystal dimensions [mm]	0.266 x 0.128 x 0.093	0.139 x 0.083 x 0.053	0.305 x 0.170 x 0.154
crystal system	triclinic	triclinic	cubic
space group	$P\bar{1}$	$P\bar{1}$	$F\bar{4}3c$
a [Å]	17.2257(9)	12.9604(11)	34.313(3)
b [Å]	17.3404(9)	15.7349(13)	34.313(3)
c [Å]	22.0530(12)	15.7795(12)	34.313(3)
α [°]	101.801(2)	104.655(2)	90
β [°]	94.808(2)	96.882(2)	90
γ [°]	113.271(2)	111.671(2)	90
V [Å³]	5823.3(5)	2810.6(4)	40398(11)
Z	1	2	8
T [K]	100(2)	100(2)	173(2)
λ [Å]	0.71073	0.71073	0.71073
ρ_{calcd} [g/cm³]	2.452	1.894	1.725
μ [mm $^{-1}$]	7.631	4.874	7.488
F (000)	3890	1524	19488
θ range [°]	1.309 – 25.681	1.373 – 28.356	1.187 – 24.113
absorption correction	numerical	numerical	multi-scan
independent reflections	22104	14008	2696
reflections collected (I > 2σ)	131258	109142	25908
R1/*w*R2 (I > 2σ)	0.0510/0.1243	0.0338/0.0805	0.0334/0.0808
R1/*w*R2 (all data)	0.0753/0.1489	0.0450/0.0870	0.0477/0.0914
GOF	1.069	1.056	1.126

Table S1 (continued). Crystallographic data for compounds **6b**, **7a** and **7b**

	6b	**7a**	**7b**
CCDC	2114131	2114130	2114134
formula	$C_{102}H_{170}Br_{24}Pr_{12}Si_{12}$	$C_{103.50}H_{174}Cl_{24}Ce_{12}Si_{12}$	$C_{96}H_{156}Cl_{24}Pr_{12}Si_{12}$
M_r [g/mol]	5342.21	4287.74	4189.00
color/shape	colorless/block	colorless/block	colorless/needle
crystal dimensions [mm]	0.210 x 0.208 x 0.162	0.100 x 0.080 x 0.050	0.151 x 0.084 x 0.048
crystal system	monoclinic	monoclinic	monoclinic
space group	$P2_1/c$	$P2_1/c$	$P2_1/c$
a [Å]	22.8057(8)	22.835(6)	23.0379(17)
b [Å]	29.0703(10)	28.506(8)	28.379(2)
c [Å]	25.6943(9)	25.286(7)	25.2369(19)
α [°]	90	90	90
β [°]	101.5050(10)	101.552(4)	101.8870(10)
γ [°]	90	90	90
V [Å³]	16692.2(10)	16126(8)	16146(2)
Z	4	4	4
T [K]	173(2)	100(2)	173(2)
λ [Å]	0.71073	0.71073	0.71073
ρ_{calcd} [g/cm³]	2.126	1.766	1.723
μ [mm $^{-1}$]	9.293	3.832	4.063
F (000)	9992	8268	8064
θ range [°]	1.149 – 28.762	1.694 – 25.681	1.696 – 25.731
absorption correction	multi-scan	multi-scan	multi-scan
independent reflections	43256	30626	30743
reflections collected (I > 2σ)	436873	151330	199662
R1/*w*R2 (I > 2σ)	0.0319/0.0675	0.0502/0.0996	0.0487/0.1083
R1/*w*R2 (all data)	0.0518/0.0760	0.1044/0.1223	0.0894/0.1286
GOF	1.033	1.015	1.020

Table S1 (continued). Crystallographic data for compound **8**

	8
CCDC	2114132
formula	$C_{90}H_{156}Al_2Cl_{22}Ce_{10}Si_{10}$
M_r [g/mol]	3754.10
color/shape	colorless/needle
crystal dimensions [mm]	0.251 x 0.067 x 0.050
crystal system	monoclinic
space group	$P2_1/n$
a [Å]	18.318(3)
b [Å]	33.485(5)
c [Å]	22.740(3)
α [°]	90
β [°]	90.239(2)
γ [°]	90
V [Å³]	13948(4)
Z	4
T [K]	100(2)
λ [Å]	0.71073
ρ_{calcd} [g/cm³]	1.788
μ [mm $^{-1}$]	3.745
F (000)	7264
θ range [°]	1.648 – 25.019
absorption correction	multi-scan
independent reflections	24425
reflections collected (I > 2σ)	202444
R1/*w*R2 (I > 2σ)	0.0795/0.1804
R1/*w*R2 (all data)	0.1230/0.2037
GOF	1.078

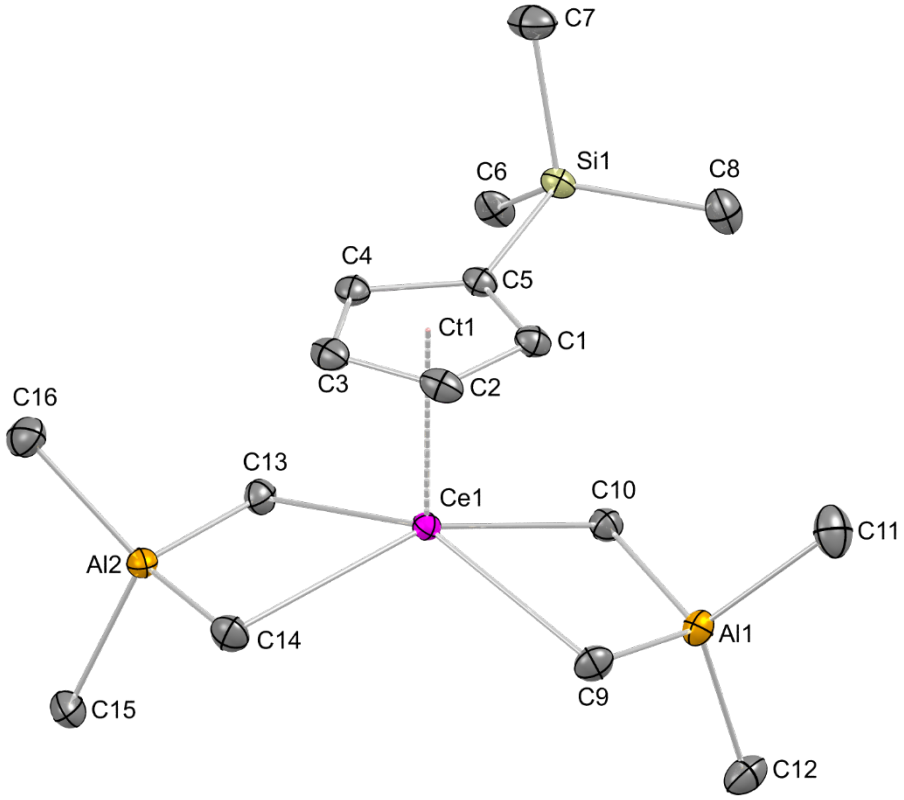

Figure S11. Crystal structure of [Cp'Ce(AlMe$_4$)$_2$] (**1a**) with atomic displacement parameters set at the 50% probability level. Hydrogen atoms are omitted for clarity. Selected interatomic distances [Å] and angles [°]: Ce1–C1 2.752(3); Ce1–C2 2.741(4); Ce1–C3 2.762(3); Ce1–C4 2.790(3); Ce1–C5 2.798(3); Ce1···Ct1 2.4997; Ce1–C9 2.720(3); Ce1–C10 2.680(3); Ce1···Al1 3.2519(11); Ce1–C13 2.705(3); Ce1–C14 2.735(3); Ce1···Al2 3.2328(10); Ce1–C31 3.237(3); Ce2–C15 3.289 (3) ; Si1–C5–Ce1 126.81(13); C9–Ce1–C10 78.81(9); Ce1–C9–Al1 84.21(10); Ce1–C10–Al1 85.42(10); C9–Al1–C10 111.53(12); C11–Al1–C12 115.33(15); C13–Ce1–C14 78.69(9); Ce1–C13–Al2 84.13(10); Ce1–C14–Al2 83.17(10); C13–Al2–C14 112.51(13); C15–Al2–C16 114.42(15).

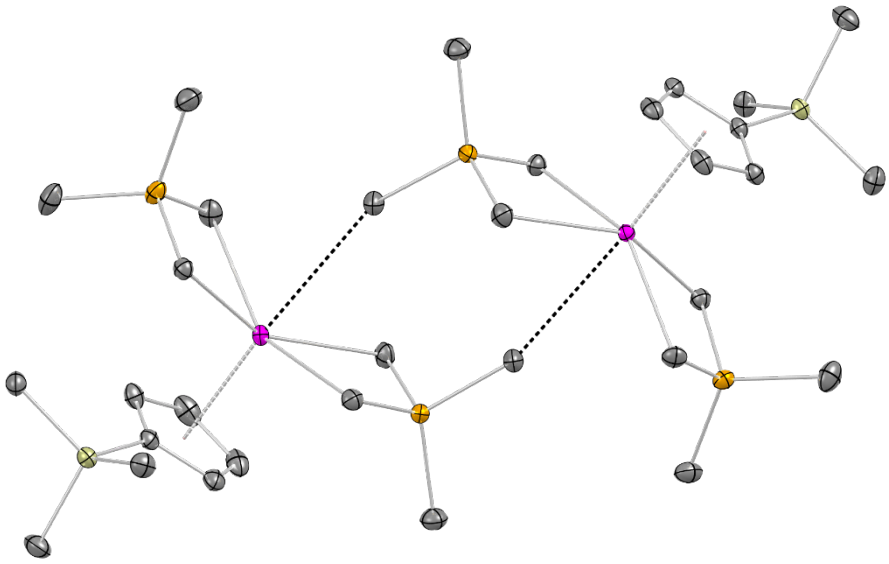

Figure S12. Unit cell of **1a**. Each cerium metal center interacts with a methyl group of a neighboring molecule, resulting in a dimeric arrangement.

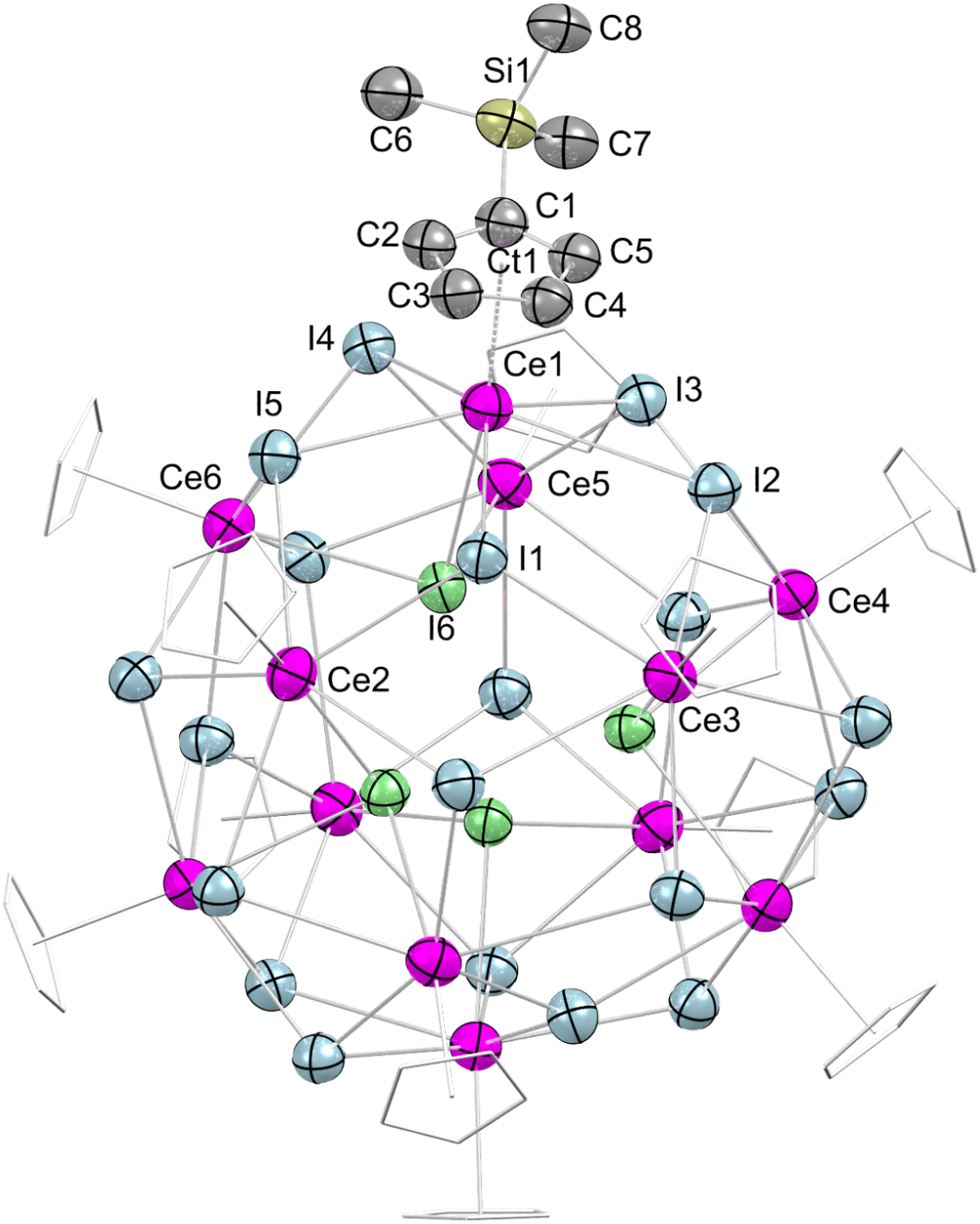

Figure S13. Connectivity of $[Cp'CeI_2]_{12}$ (**2**) with atomic displacement parameters set at the 50% probability level. Hydrogen atoms are omitted for clarity. The Cp' ligands (except for one) are represented by a wireframe model for improved visualization.

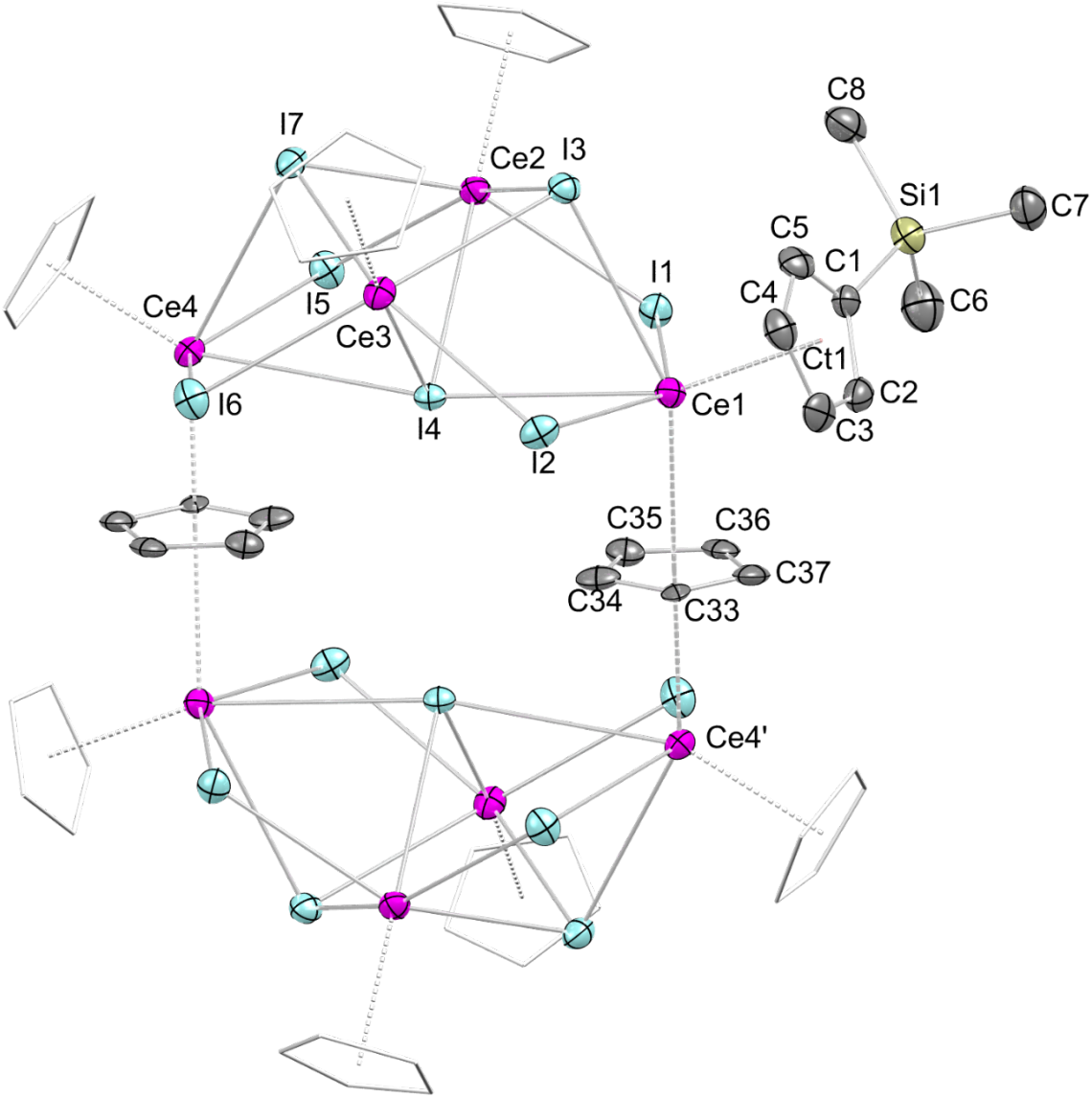

Figure S14. Crystal structure of $[Cp'_4Ce_4I_7(\mu_2\text{-}Cp)]_2$ (**3**) with atomic displacement parameters set at the 50% probability level. Hydrogen atoms and lattice *n*-hexane are omitted for clarity. The Cp' ligands (except for one) are represented by a wireframe model for improved visualization. Selected interatomic distances [Å] and angles [°]: Ce1–C1 2.864(6); Ce1–C2 2.738(7); Ce1–C3 2.679(6); Ce1–C4 2.731(7); Ce1–C5 2.819(6); Ce1···Ct1 2.4990; Ce1–C33 2.909(6); Ce1–C34 2.889(7); Ce1–C35 2.878(6); Ce1–C36 2.869(6); Ce1–C37 2.901(6); Ce1···Ct(μ_2-Cp) 2.6452; Ce1–I1 3.2375(5); Ce1–I2 3.2747(6); Ce1–I3 3.3783(6); Ce1–I4 3.6487(6); Ce2–I1 3.1868(6); Ce2–I3 3.2521(6); Ce2–I4 3.3074(5); Ce2–I5 3.2177(6); Ce2–I7 3.2205(6); Ct1···Ce1···Ct(μ_2-Cp) 112.18; Ce1···Ct(μ_2-Cp)···Ce4' 179.28; I1–Ce1–I2 140.050(16); I1–Ce1–I3 78.90(2); I1–Ce1–I4 70.00(1); I1–Ce2–I3 81.541(14); I1–Ce2–I4 75.212(13); I1–Ce2–I5 103.409(16); I1–Ce2–I7 147.698(16); Ce1–I1–Ce2 94.633(14); Ce1–I3–Ce2 90.821(14); Ce1–I4–Ce2 85.371(13); Ce1–I4–Ce4 169.01(2); Ce2–I3–Ce3 89.679(14); Ce2–I4–Ce3 88.476(13).

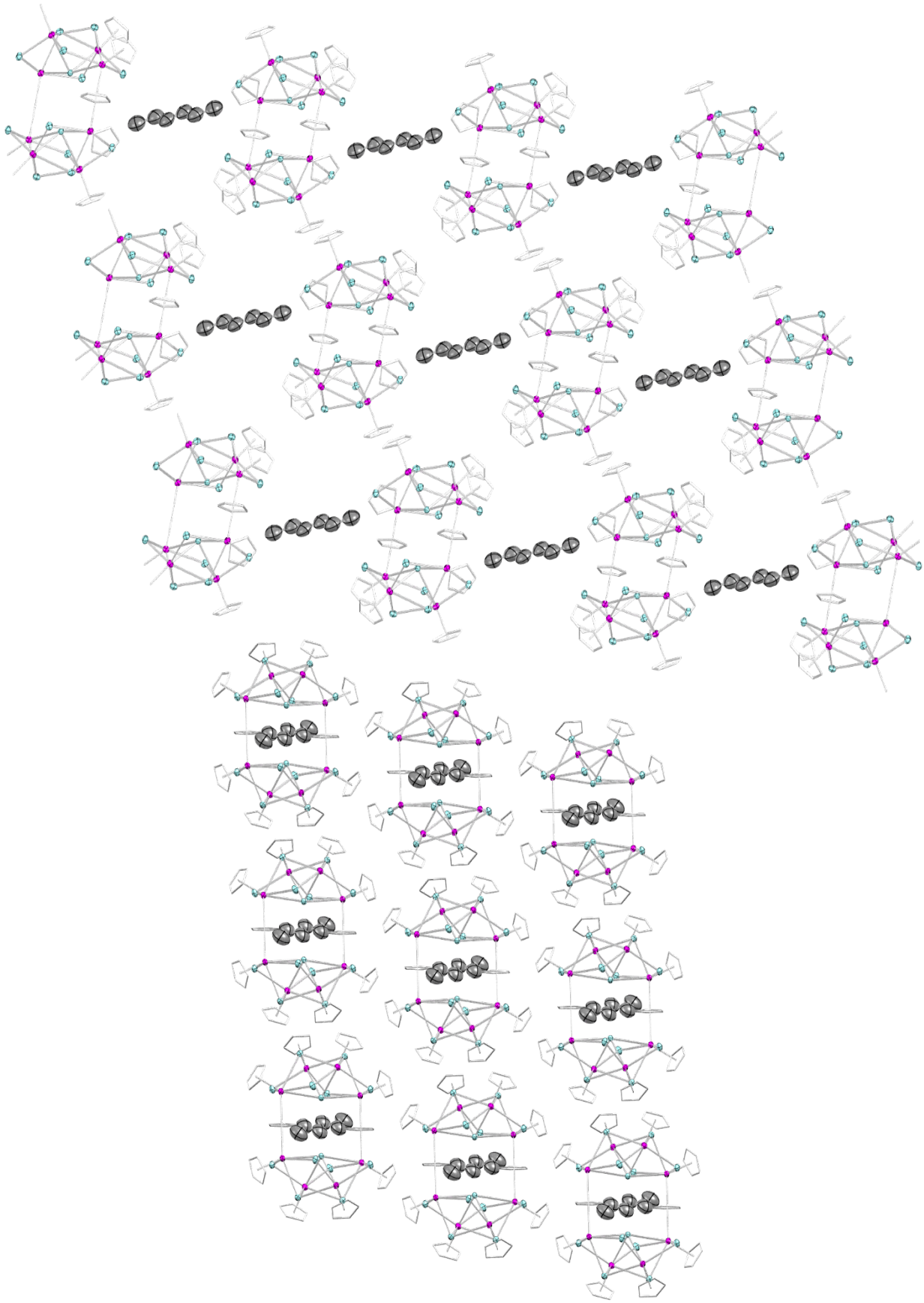

Figure S15. Crystal packing of **3**, view along a axis (top) and b axis (bottom).

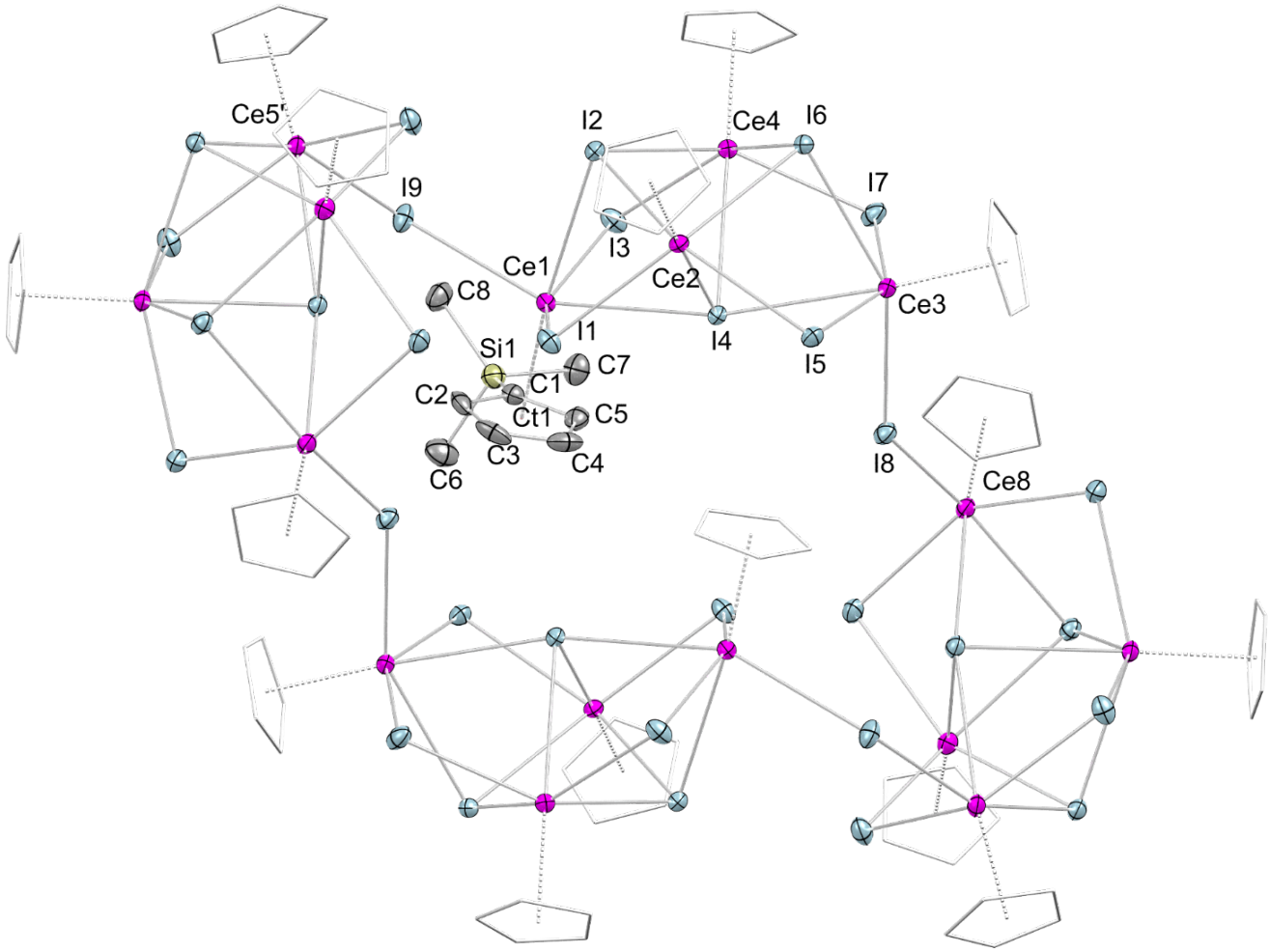

Figure S16. Crystal structure of $[Cp'_4Ce_4I_8]_4$ (**4a**) with atomic displacement parameters set at the 50% probability level. Hydrogen atoms and lattice toluene are omitted for clarity. The Cp' ligands (except for one) are represented by a wireframe model for improved visualization. Selected interatomic distances [Å] and angles [°]: Ce1–C1 2.748(4); Ce1–C2 2.711(4); Ce1–C3 2.695(4); Ce1–C4 2.708(4); Ce1–C5 2.727(4); Ce1···Ct1 2.437; Ce1–I1 3.2225(4); Ce1–I2 3.3678(4); Ce1–I3 3.1845(4); Ce1–I4 3.3529(4); Ce1–I9' 3.2061(4); Ce2–I1 3.1571(5); Ce2–I2 3.2614(4); Ce2–I4 3.3805(4); Ce3–I8 3.1927(4); Ce5–I9 3.1684(4); Ce8–I8 3.1451(4); I1–Ce1–I2 77.921(9); I1–Ce1–I3 148.566(11); I1–Ce1–I4 77.869(9); I1–Ce1–I9 104.042(11); I2–Ce1–I9 81.187(12); I4–Ce1–I9 153.609(10); I1–Ce2–I2 80.441(8); I1–Ce2–I4 78.352(9); I1–Ce2–I5 109.149(11); I1–Ce2–I6 148.346(11); I4–Ce3–I8 74.352(11); I5–Ce3–I8 98.379(13); I6–Ce3–I8 147.934(11); Ce1–I1–Ce2 91.211(9); Ce1–I2–Ce2 86.876(8); Ce1–I4–Ce2 85.224(10); Ce1–I4–Ce3 166.187(9); Ce1'–I9–Ce 134.777(11); Ce2–I2–Ce4 92.528(8); Ce2–I4–Ce4 87.719(8); Ce3–I8–Ce8 138.802(13).

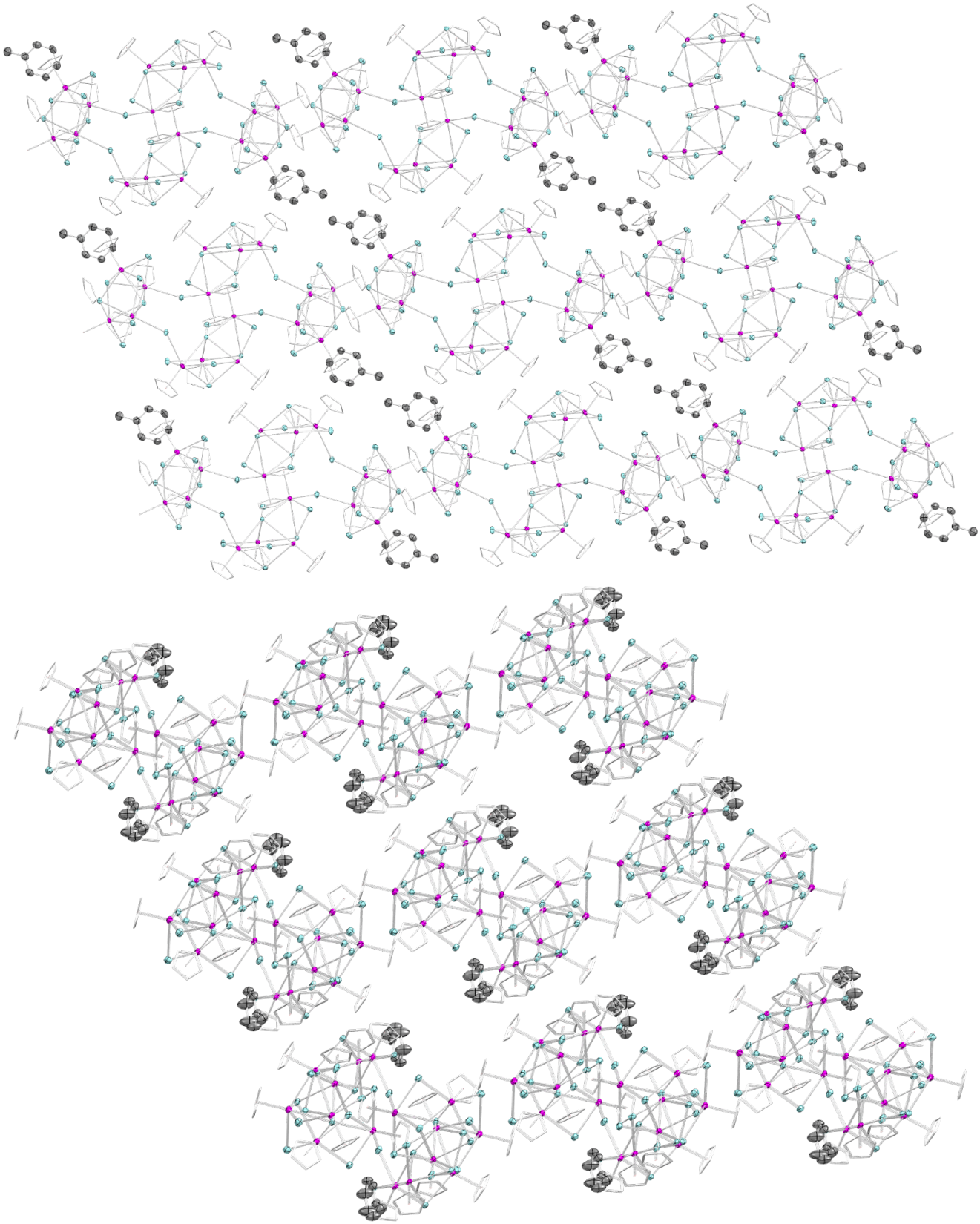

Figure S17. Crystal packing of **4a**, view along b axis (top) and c axis (bottom).

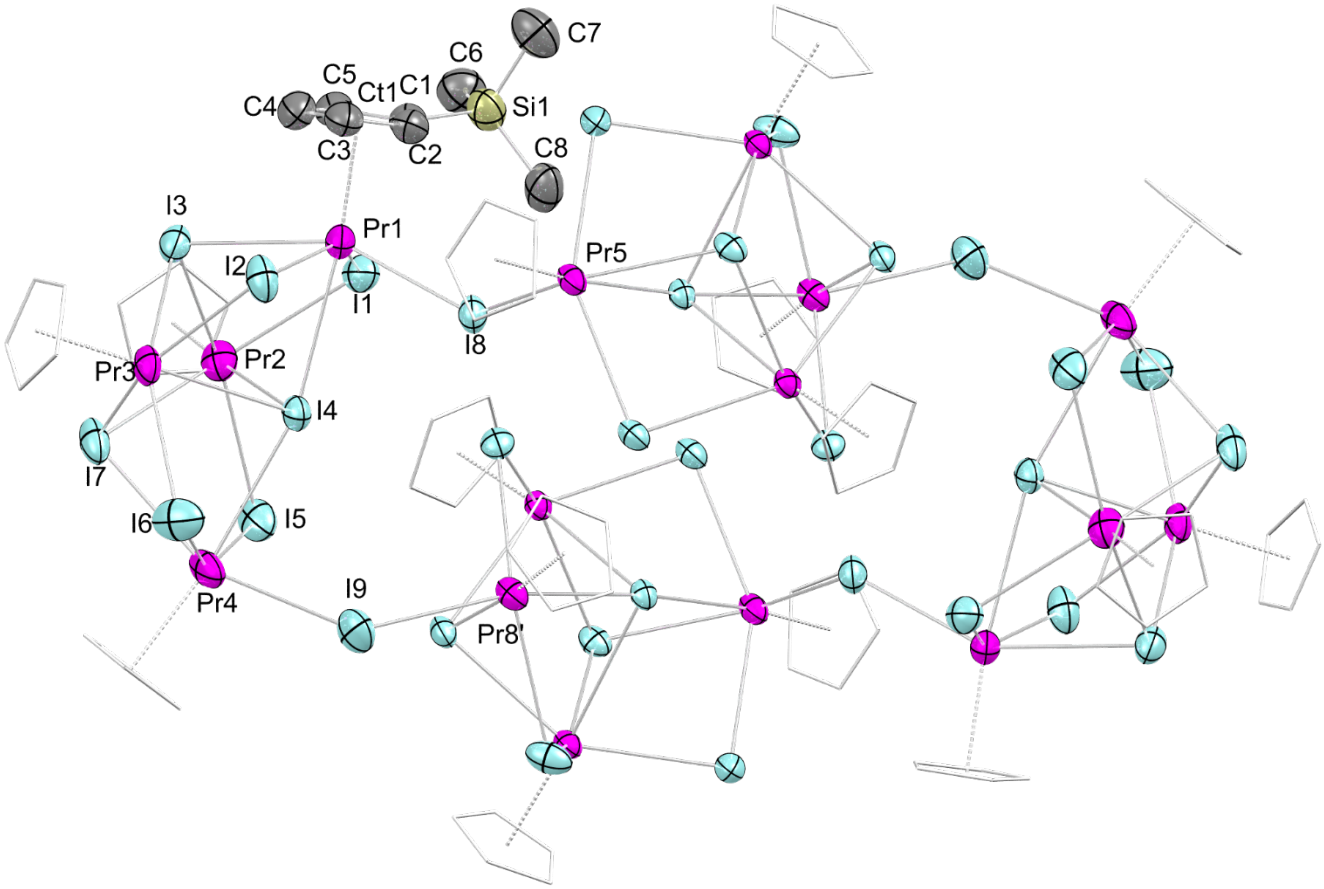

Figure S18. Crystal structure of $[Cp'_4Pr_4I_8]_4$ (**4b**) with atomic displacement parameters set at the 50% probability level. Hydrogen atoms and lattice *n*-hexane are omitted for clarity. The Cp' ligands (except for one) are represented by a wireframe model for improved visualization. . Pr1–C1 2.700(14); Pr1–C2 2.696(14); Pr1–C3 2.715(14); Pr1–C4 2.652(15); Pr1–C5 2.680(14); Pr1···Ct1 2.4097; Pr1–I1 3.1803(12); Pr1–I2 3.1941(12); Pr1–I3 3.3022(11); Pr1–I4 3.3928(11); Pr1–I8 3.1378(11); Pr2–I1 3.1654(12); Pr2–I3 3.2277(12); Pr2–I4 3.3257(12); Pr4–I9 3.1142(15); Pr5–I8 3.1691(11); Pr8–I9' 3.1593(12); I1–Pr1–I2 148.06(3); I1–Pr1–I3 79.59(3); I1–Pr1–I4 74.90(3); I1–Pr1–I8 101.73(3); I3–Pr1–I8 151.83(3); I4–Pr1–I8 79.37(3); I1–Pr2–I3 80.95(3); I1–Pr2–I4 76.04(3); I1–Pr2–I5 108.20(3); I1–Pr2–I7 148.51(4); I4–Pr4–I9 81.50(3); I5–Pr4–I9 89.34(3); I7–Pr4–I9 154.49(4); Pr1–I1–Pr2 91.24(3); Pr1–I3–Pr2 87.97(3); Pr1–I4–Pr2 84.91(3); Pr1–I4–Pr4 164.39(3); Pr1–I8–Pr5 134.09(3); Pr2–I3–Pr3 90.55(3); Pr2–I4–Pr3 86.81(3); Pr4–I9–Pr8' 136.79(4).

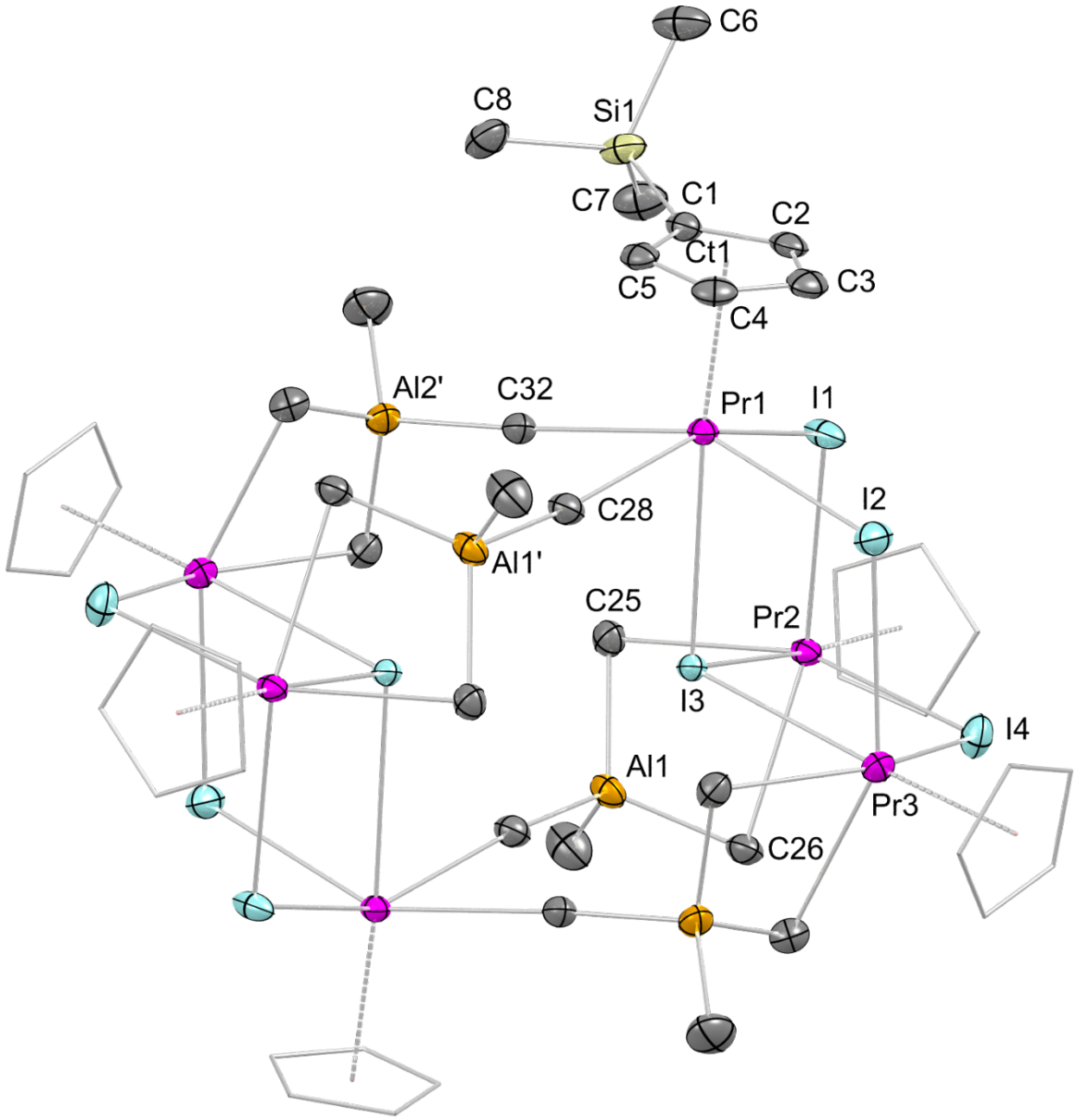

Figure S19. Crystal structure of $[Cp'_6Pr_6I_8(AlMe_4)_4]$ (**5**) with atomic displacement parameters set at the 50% probability level. Hydrogen atoms are omitted for clarity. The Cp' ligands (except for one) are represented by a wireframe model for improved visualization. Selected interatomic distances [Å] and angles [°]: Pr1–C1 2.753(4); Pr1–C2 2.741(4); Pr1–C3 2.720(4); Pr1–C4 2.680(4); Pr1–C5 2.703(4); Pr1···Ct1 2.4538; Pr1–I1 3.1582(4); Pr1–I2 3.1795(5); Pr1–I3 3.3133(4); Pr1–C28 2.930(5); Pr1–C32 2.910(5); Pr2–I1 3.1880(4); Pr2–I3 3.3446(4); Pr2–I4 3.1765(4); Pr2–C25 2.730(5); Pr2–C26 2.763(4); Pr2···Al1 3.284; C25–Al1 2.045(5); C26–Al1 2.036(5); C27–Al1 1.970(5); C31–Al2 1.969(5); I1–Pr1–I2 94.857(11); I1–Pr1–I3 75.630(11); I1–Pr1–C28' 85.11(9); I1–Pr1–C32' 153.79(9); I1–Pr1···Ct1 100.43; I3–Pr1···Ct1 176.04; I1–Pr2–I3 74.800(10); I1–Pr2–I4 91.497(12); I3–Pr2–I4 76.796(9); Pr1–I2–Pr3 107.031(11); Pr1–I1–Pr2 108.141(11); Pr1–I3–Pr2 101.036(11); Pr1'–C28–Al1 174.7(2); Pr1'–C32–Al2 172.9(2); Pr2–I3–Pr3 99.501(10); Pr2–I4–Pr3 106.910(11); C25–Pr2–C26 76.52(14); C25–Al1–C26 112.93(19); C28–Pr1–C32 81.50(13).

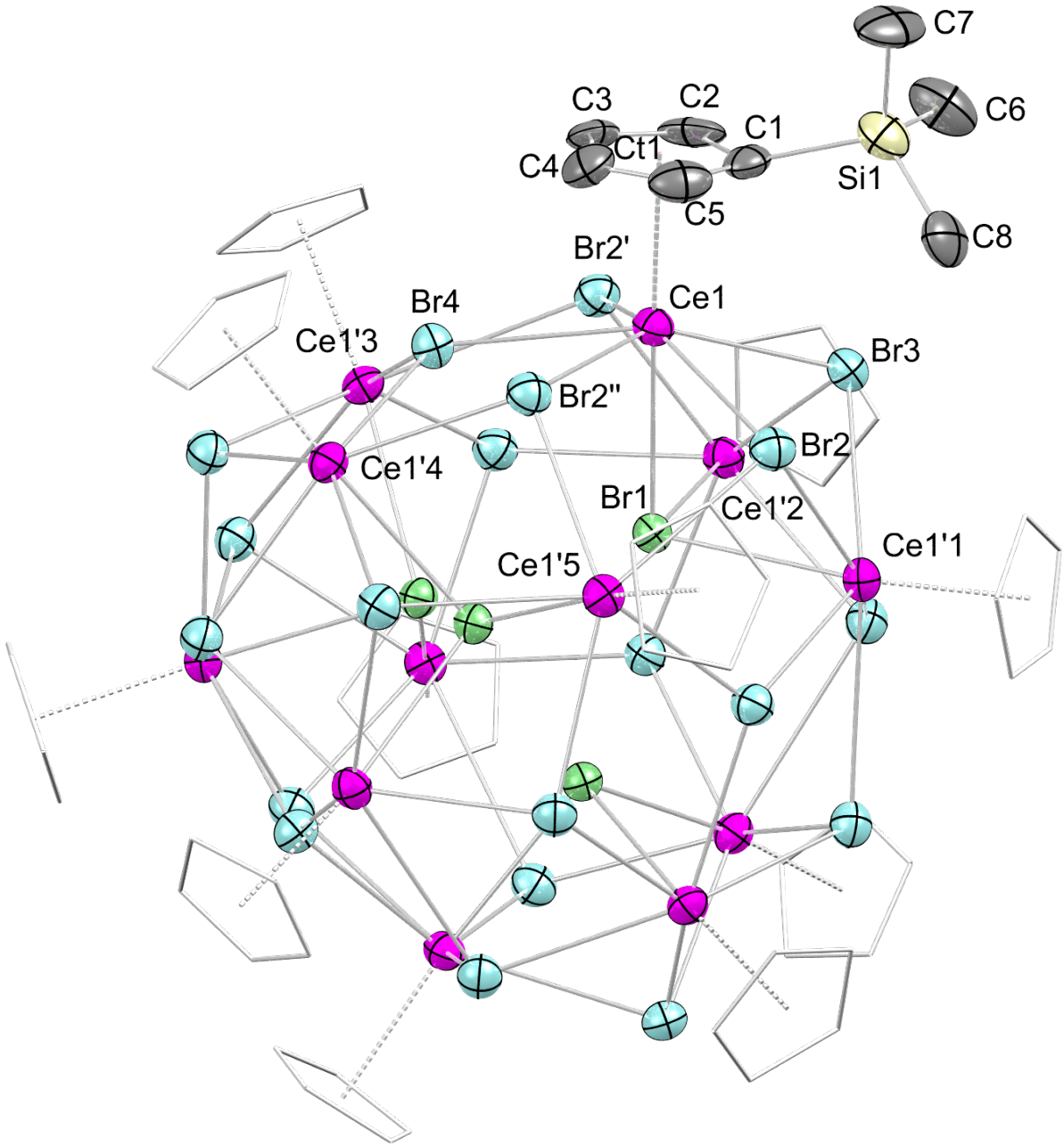

Figure S20. Crystal structure of $[Cp'CeBr_2]_{12}$ (**6a**) with atomic displacement parameters set at the 50% probability level. Hydrogen atoms are omitted for clarity. The Cp' ligands (except for one) are represented by a wireframe model for improved visualization. Selected interatomic distances [Å] and angles [°]: Ce1–C1 2.731(14); Ce1–C2 2.722(13); Ce1–C3 2.738(13); Ce1–C4 2.714(16); Ce1–C5 2.734(14); Ce1···Ct1 2.4740; Ce1–Br1 3.0850(14); Ce1–Br2 3.0003(16); Ce1–Br2' 3.0636(16); Ce1–Br2" 3.4302(17); Ce1–Br3 3.1584(15); Ce1–Br4 3.0439(9); Br2–Ce1–Br3 76.27(3); Br3–Ce1–Br2' 75.39(3); Br2'–Ce1–Br4 69.93(3); Br4–Ce1–Br2" 65.13(3); Br2"–Ce1–Br2 66.33(5); Br1–Ce1–Br2 75.57(3); Ce1–Br2–Ce1'1 95.24(5); Ce1–Br3–Ce1'1 90.33(5); Ce1–Br2–Ce1'2 95.24(5); Ce1–Br2–Ce1'3 104.64(5); Ce1–Br4–Ce1'3 115.34(3); Ce1–Br2–Ce1'4 104.36(4); Ce1–Br1–Ce1'1 93.11(5).

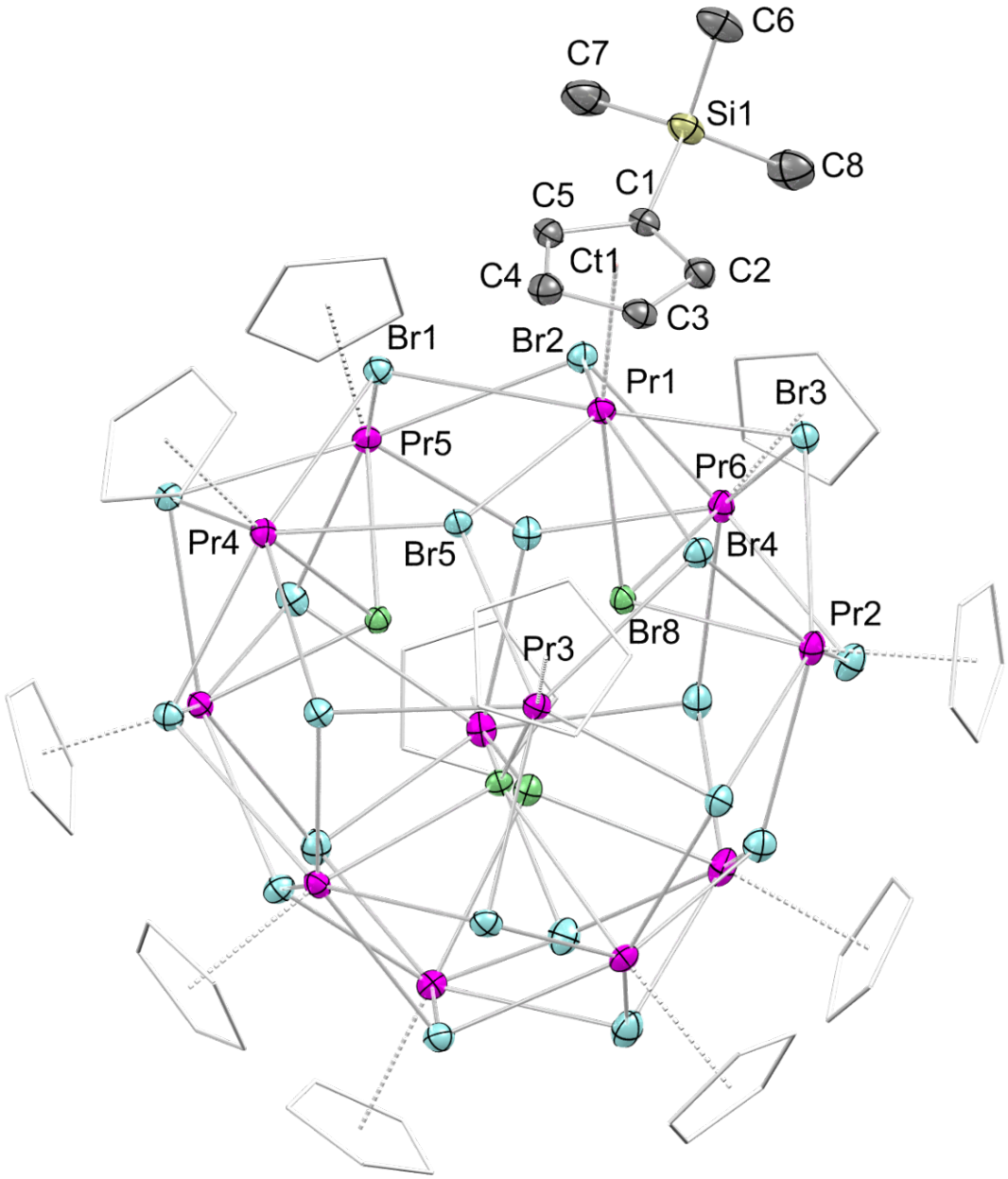

Figure S21. Crystal structure of $[Cp'PrBr_2]_{12}$ (**6b**) with atomic displacement parameters set at the 50% probability level. Hydrogen atoms and lattice *n*-hexane are omitted for clarity. The Cp' ligands (except for one) are represented by a wireframe model for improved visualization. Selected interatomic distances [Å] and angles [°]: Pr1–C1 2.746(5); Pr1–C2 2.715(5); Pr1–C3 2.703(5); Pr1–C4 2.704(5); Pr1–C5 2.721(5); Pr1···Ct1 2.4455; Pr1–Br1 3.2972(5); Pr1–Br2 2.9870(5); Pr1–Br3 3.1108(5); Pr1–Br4 3.0829(5); Pr1–Br5 3.0524(5); Pr1–Br8 3.0876(5); Br1–Pr1–Br2 68.259(13); Br2–Pr1–Br3 75.868(14); Br3–Pr1–Br4 75.322(13); Br4–Pr1–Br5 67.621(3); Br1–Pr1–Br5 66.058(12); Br1–Pr1–Br8 96.725(13); Pr1–Br1–Pr4 105.977(14); Pr1–Br1–Pr5 103.365(15); Pr1–Br2–Pr5 102.218(14); Pr1–Br2–Pr6 95.446(14); Pr1–Br3–Pr2 91.572(14); Pr1–Br3–Pr6 91.102(14); Pr1–Br4–Pr2 95.524(14); Pr1–Br4–Pr3 107.677(15); Pr1–Br5–Pr3 114.615(15); Pr1–Br5–Pr4 113.675(15); Pr1–Br8–Pr2 93.137(14); Pr1–Br8–Pr6 93.497(14).

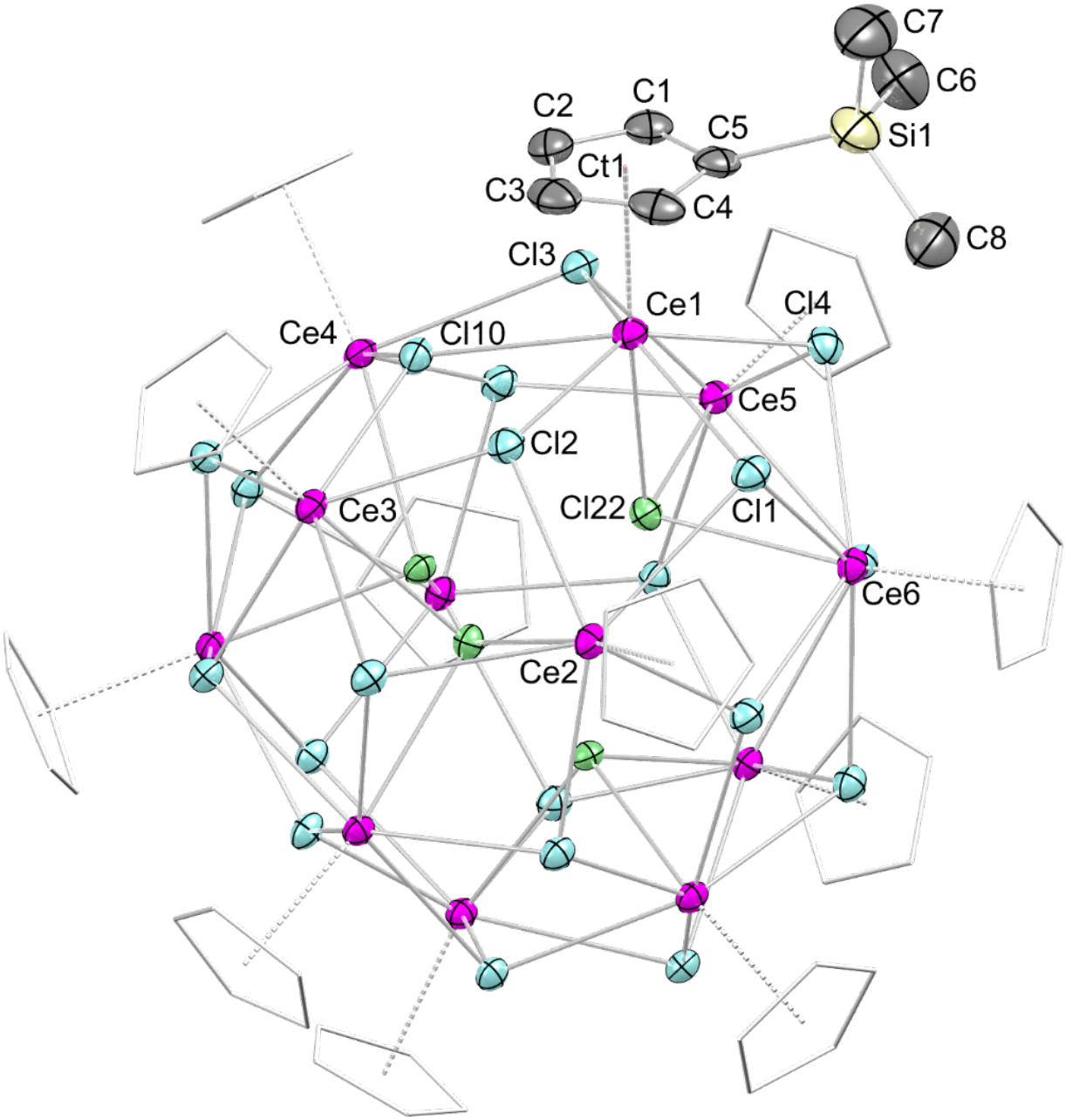

Figure S22. Crystal structure of $[Cp'CeCl_2]_{12}$ (**7a**) with atomic displacement parameters set at the 50% probability level. Hydrogen atoms and lattice solvent molecules are omitted for clarity. The Cp' ligands (except for one) are represented by a wireframe model for improved visualization. Selected interatomic distances [Å] and angles [°]: Ce1–C1 2.732(10); Ce1–C2 2.730(10); Ce1–C3 2.723(10); Ce1–C4 2.729(10); Ce1–C5 2.764(10); Ce1···Ct1 2.4697; Ce1–Cl1 2.845(2); Ce1–Cl2 3.164(3); Ce1–Cl3 2.909(2); Ce1–Cl4 2.998(3); Ce1–Cl10 2.882(2); Ce1–Cl22 2.944(2); Cl1–Ce1–Cl2 67.28(7); Cl2–Ce1–Cl10 64.65(7); Cl10–Ce1–Cl3 69.25(7); Cl3–Ce1–Cl4 74.76(7); Cl1–Ce1–Cl4 75.69(7); Cl1–Ce1–Cl22 75.12(7); Ce1–Cl1–Ce2 103.81(7); Ce1–Cl2–Ce2 105.98(8); Ce1–Cl2–Ce3 106.82(8); Ce1–Cl10–Ce3 116.18(8); Ce1–Cl10–Ce4 114.52(8); Ce1–Cl3–Ce4 105.90(8); Ce1–Cl3–Ce5 97.27(7); Ce1–Cl4–Ce5 92.15(7); Ce1–Cl4–Ce6 92.07(7); Ce1–Cl1–Ce6 96.64(7); Ce1–Cl22–Ce5 94.17(7); Ce1–Cl22–Ce6 94.42(7).

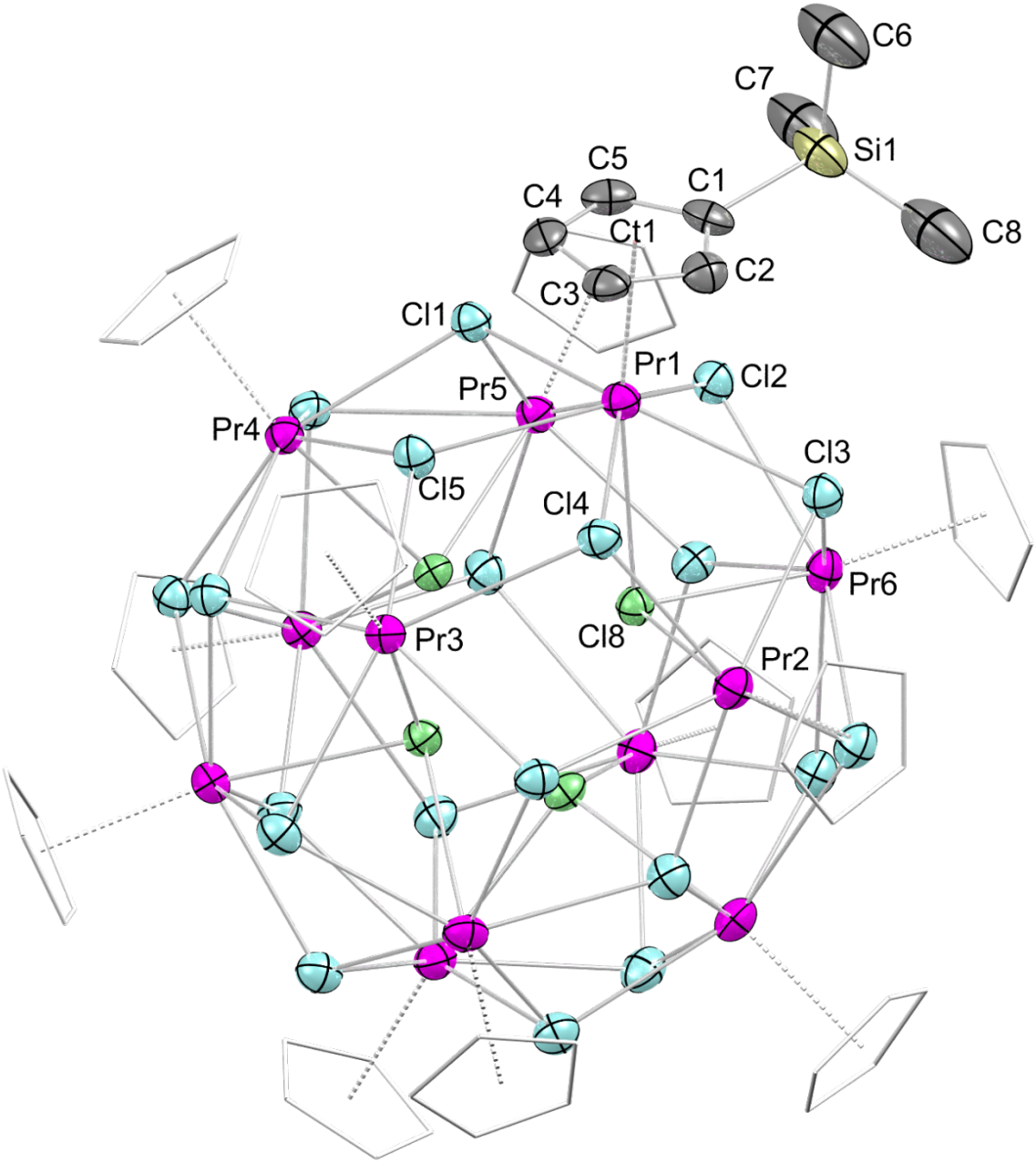

Figure S23. Crystal structure of $[Cp'PrCl_2]_{12}$ (**7b**) with atomic displacement parameters set at the 50% probability level. Hydrogen atoms and lattice *n*-hexane are omitted for clarity. The Cp' ligands (except for one) are represented by a wireframe model for improved visualization. Selected interatomic distances [Å] and angles [°]: Pr1–C1 2.752(9); Pr1–C2 2.695(9); Pr1–C3 2.691(8); Pr1–C4 2.696(8); Pr1–C5 2.716(9); Pr1···Ct1 2.4257; Pr1–Cl1 3.104(2); Pr1–Cl2 2.823(2); Pr1–Cl3 2.972(2); Pr1–Cl4 2.911(2); Pr1–Cl5 2.877(2); Pr1–Cl8 2.924(2); Cl1–Pr1–Cl2 68.12(6); Cl2–Pr1–Cl3 75.46(6); Cl3–Pr1–Cl4 74.63(6); Cl4–Pr1–Cl5 67.82(6); Cl1–Pr1–Cl5 65.60(6); Cl1–Pr1–Cl8 95.89(6); Pr1–Cl1–Pr4 106.75(6); Pr1–Cl1–Pr5 104.23(6); Pr1–Cl2–Pr5 103.70(7); Pr1–Cl2–Pr6 97.03(6); Pr1–Cl3–Pr2 92.25(6); Pr1–Cl3–Pr6 92.26(6); Pr1–Cl4–Pr2 97.43(6); Pr1–Cl4–Pr3 107.29(7); Pr1–Cl5–Pr3 115.16(7); Pr1–Cl5–Pr4 115.03(7); Pr1–Cl8–Pr2 94.37(6); Pr1–Cl8–Pr6 94.36(6).

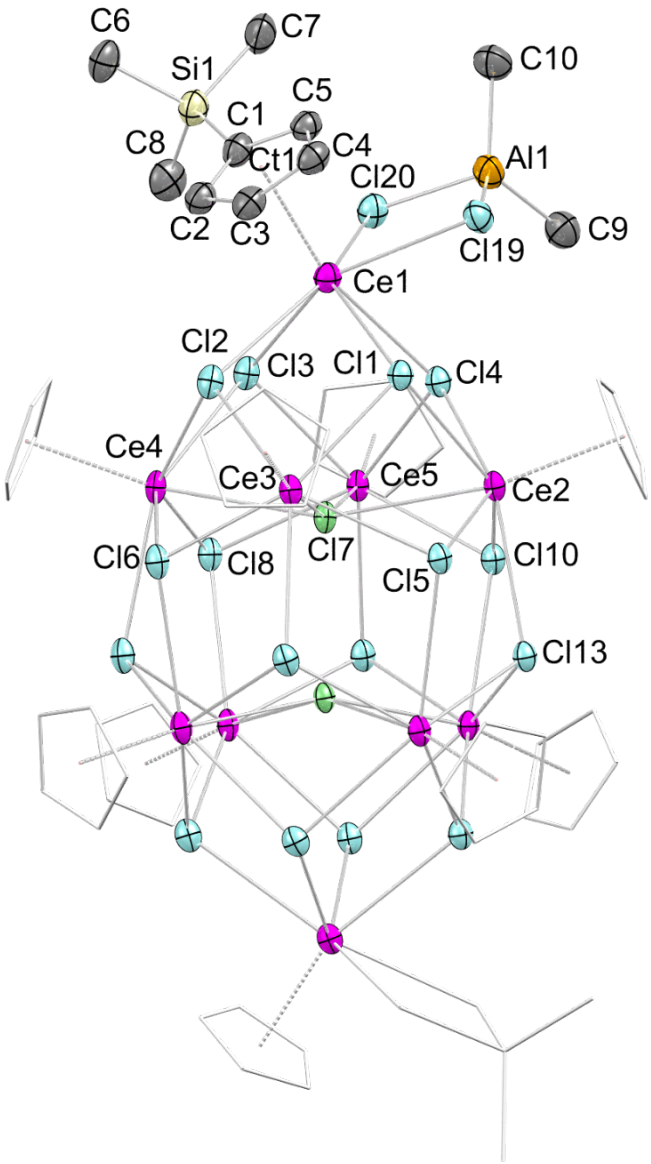

Figure S24. Crystal structure of $[Cp_5'Ce_5Cl_9(Cl_2AlMe_2)]_2$ (**8**) with atomic displacement parameters set at the 50% probability level. Hydrogen atoms are omitted for clarity. The Cp' and (Cl_2AlMe_2) ligands (except for one each) are represented by a wireframe model for improved visualization. Selected interatomic distances [Å] and angles [°]: Ce1–C1 2.769(17); Ce1–C2 2.770(18); Ce1–C3 2.734(18); Ce1–C4 2.749(18); Ce1–C5 2.745(17); Ce1···Ct1 2.4708; Ce1–Cl1 2.994(4); Ce1–Cl2 3.102(4); Ce1–Cl3 2.972(4); Ce1–Cl4 3.014(4); Ce1–Cl19 2.896(4); Ce1–Cl20 2.903(4); Ce1···Al1 3.8686; Ce2–Cl1 2.962(4); Ce2–Cl4 2.882(4); Ce2–Cl5 2.894(4); Ce2–Cl7 3.117(4); Ce2–Cl10 2.926(4); Ce2–Cl13 3.063(4); Al1–Cl19 2.271(7); Al1–Cl20 2.278(7); Al1–C9 1.93(2); Al1–C10 1.93(2); Cl1–Ce1–Cl2 68.66(10); Cl2–Ce1–Cl3 68.53(10); Cl3–Ce1–Cl4 70.53(10); Cl1–Ce1–Cl4 71.32(11); Cl1–Ce1–Cl3 109.94(11); Cl1–Ce2–Cl4 73.65(11); Cl1–Ce2–Cl5 72.05(11); Cl1–Ce2–Cl7 70.97(10); Cl1–Ce2–Cl10 136.86(11); Cl1–Ce2–Cl13 137.57(11); Cl19–Ce1–Cl20 71.56(12); Cl19–Al1–Cl20 96.4(3); Ce1–Cl19–Al1 96.2(2); Ce1–Cl20–Al1 95.9(2); C9–Al1–C10 121.2(9); Ce1–Cl1–Ce2 106.40(12); Ce1–Cl1–Ce3 108.88(12); Ce2–Cl1–Ce3 93.54(11); Ce2–Cl5–Ce3 96.15(11); Ce2–Cl7–Ce3 88.23(9); Ce2–Cl7–Ce4 159.89(14).

IR Spectroscopy

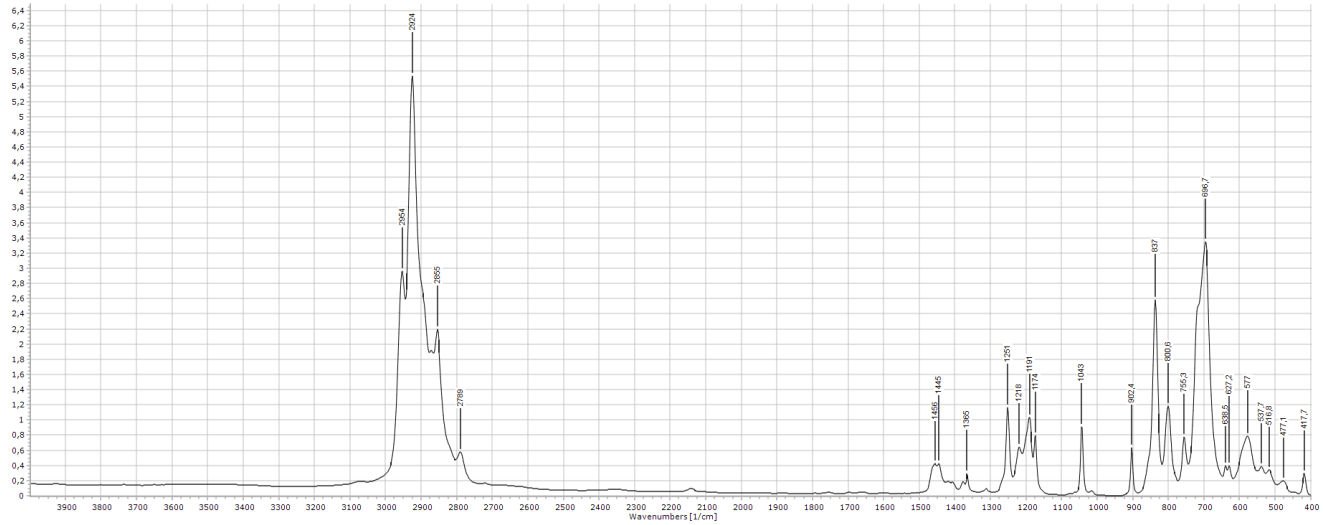

Figure S25. IR spectrum of [Cp'Ce($AlMe_4$)$_2$] (**1a**).

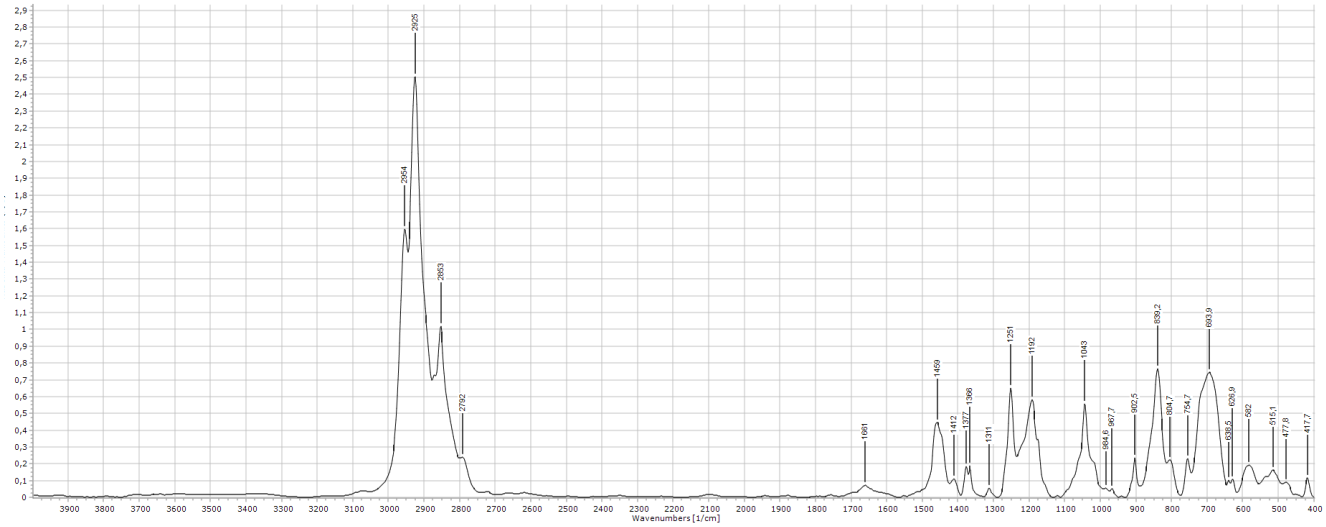

Figure S26. IR spectrum of [Cp'Pr($AlMe_4$)$_2$] (**1b**).

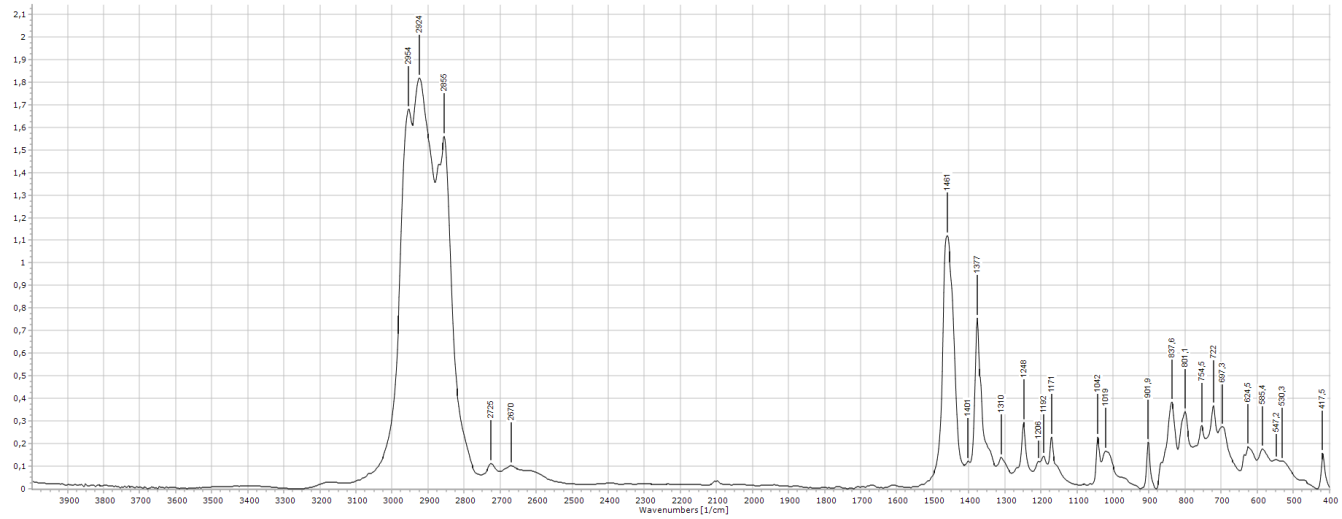

Figure S27. IR spectrum of [Cp'$_6$Pr$_6$I$_8$($AlMe_4$)$_4$] (**5**).

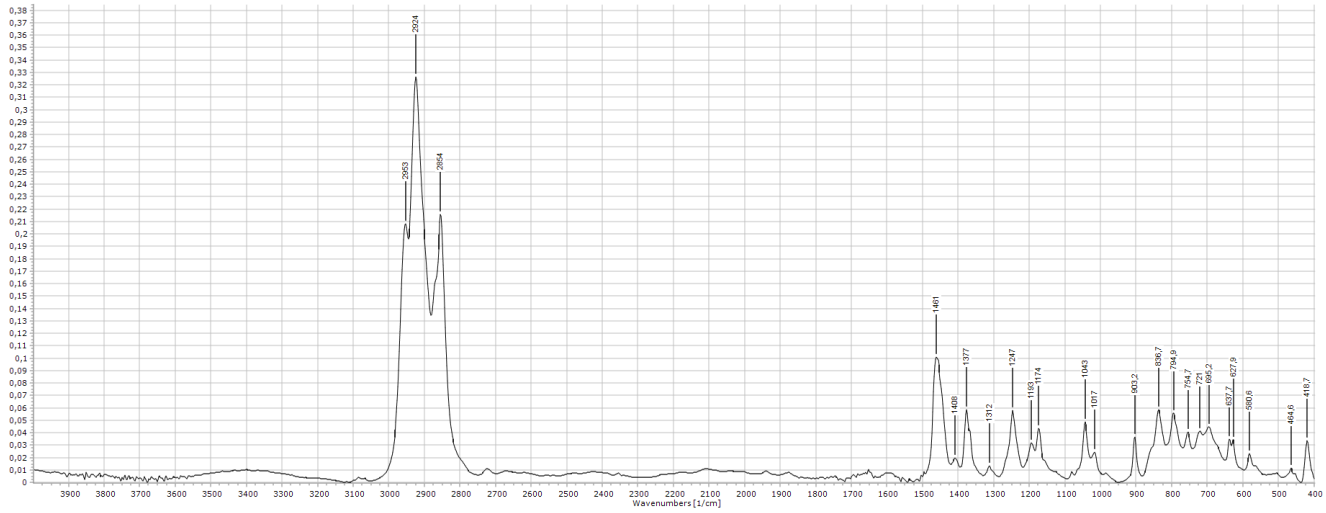

Figure S28. IR spectrum of $[Cp'CeBr_2]_{12}$ (**6a**).

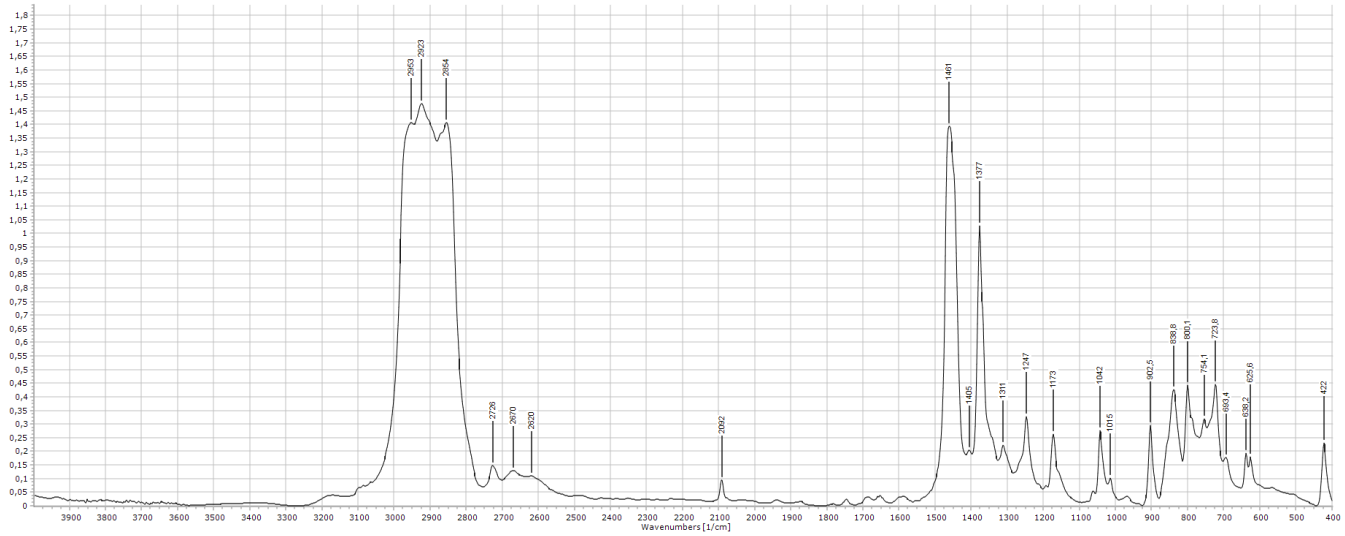

Figure S29. IR spectrum of $[Cp'PrBr_2]_{12}$ (**6b**).

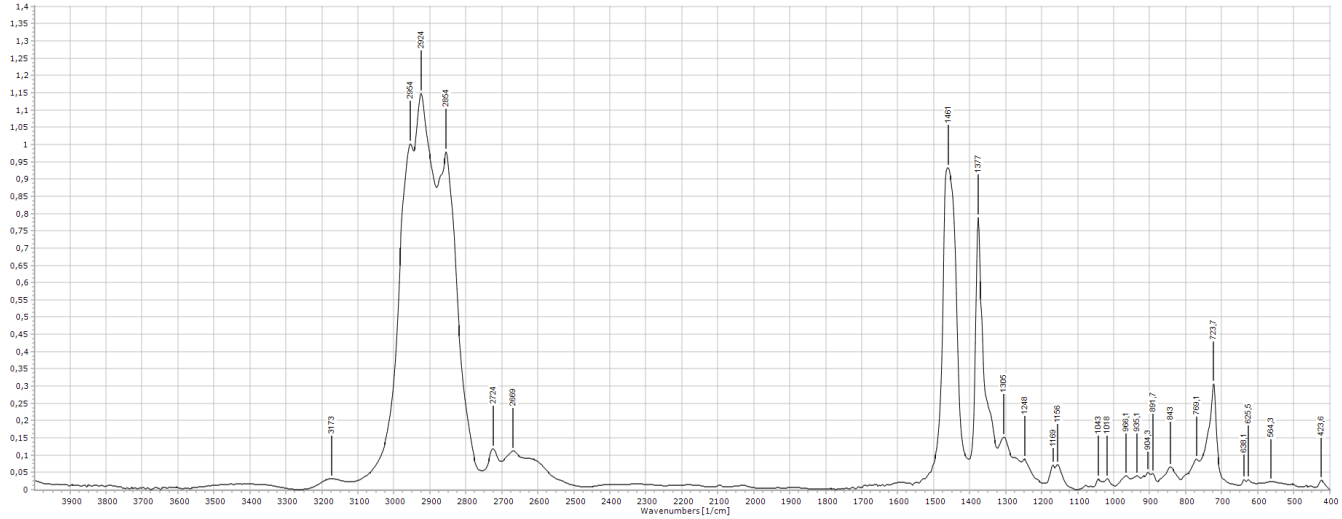

Figure S30. IR spectrum of $[Cp'PrCl_2]_{12}$ (**7b**).

Luminescence

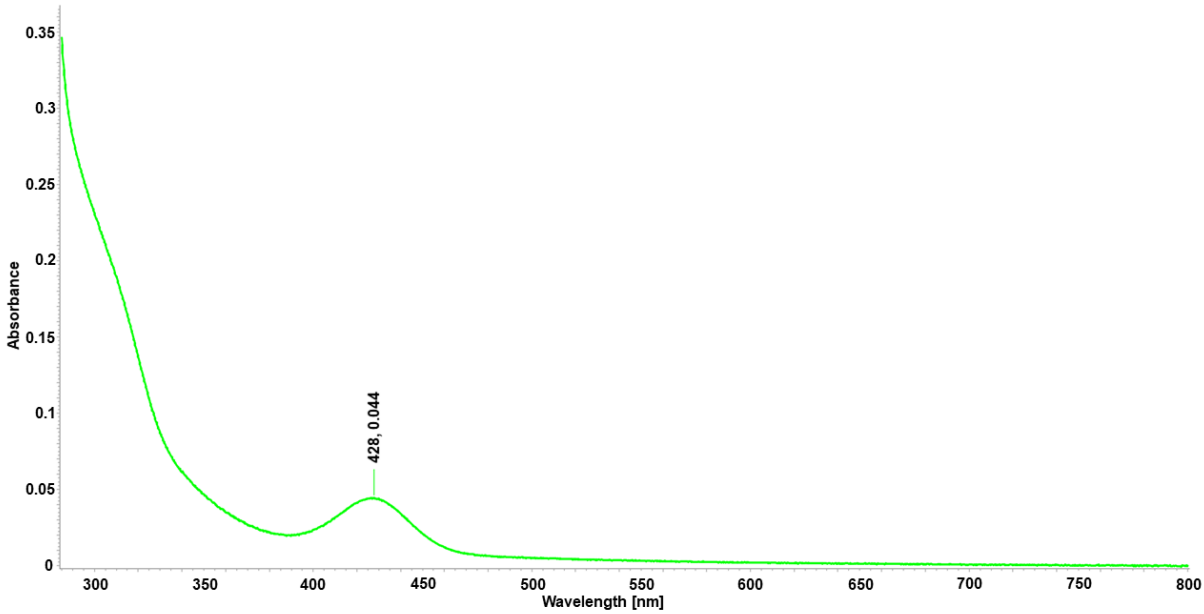

Figure S31. Absorption spectrum of a 1 [mM] solution of $[Cp'CeI_2]_{12}$ (**2**) and $[Cp'_4Ce_4I_8]_4$ (**4a**) in toluene.

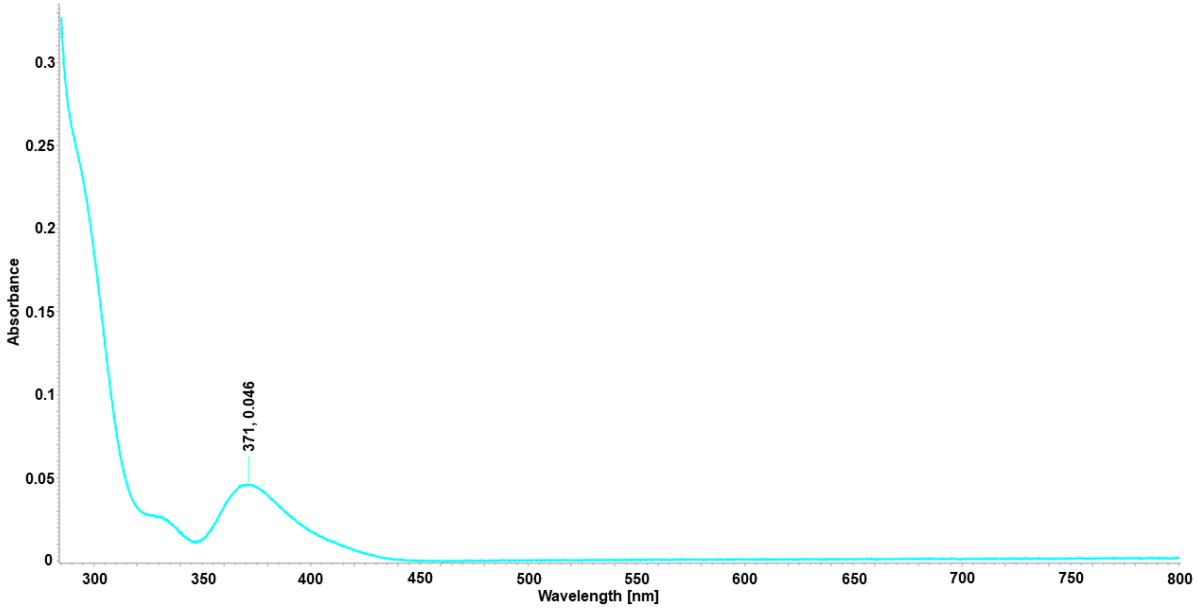

Figure S32. Absorption spectrum of a 1 [mM] solution of $[Cp'CeBr_2]_{12}$ (**6a**) in toluene.

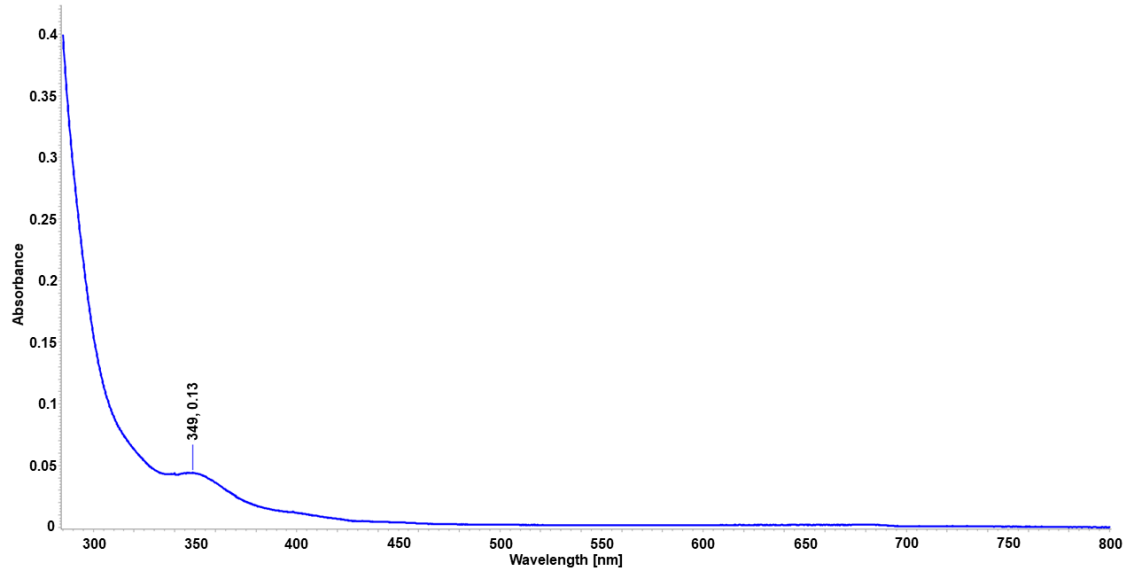

Figure S33. Absorption spectrum of a 1 [mM] solution of $[Cp'CeCl_2]_{12}$ (**7a**) and $[Cp_5'Ce_5Cl_9(Cl_2AlMe_2)]_2$ (**8**) in toluene.

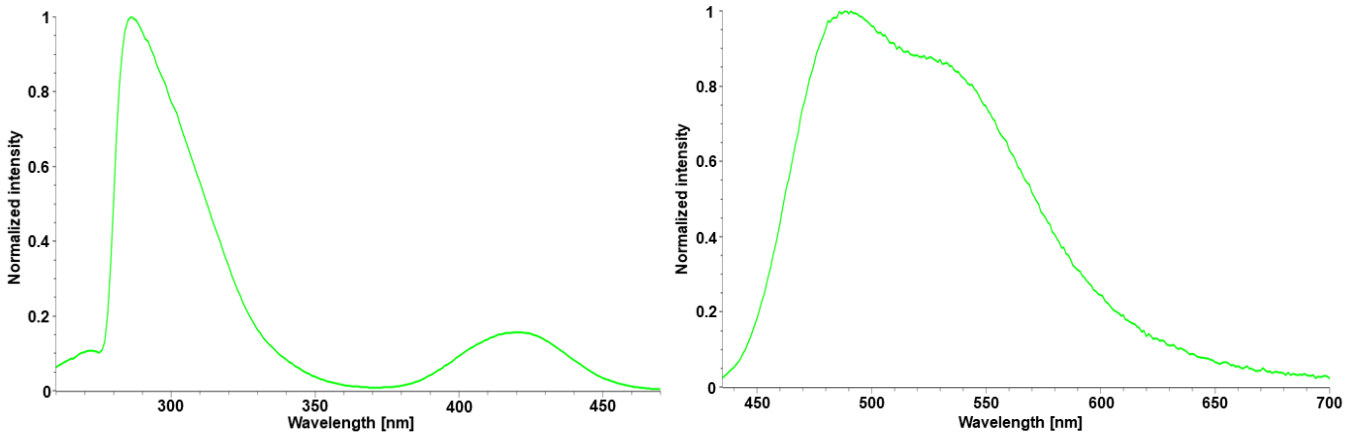

Figure S34. Excitation spectrum (left, emission wavelength 490 nm) and emission spectrum (right, excitation wavelength 420 nm) of $[Cp'CeI_2]_{12}$ (**2**) and $[Cp'_4Ce_4I_8]_4$ (**4a**) in toluene.

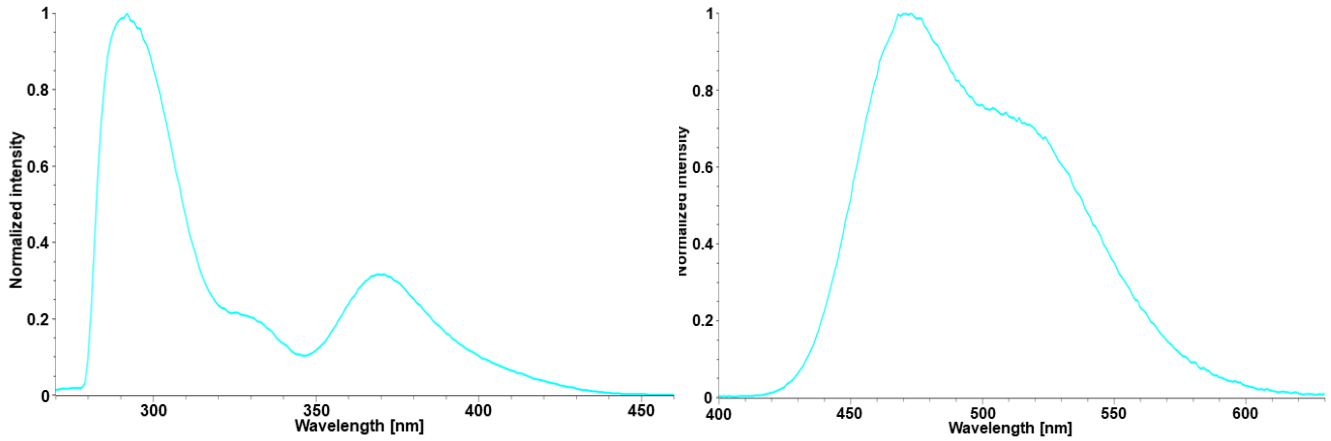

Figure S35. Excitation spectrum (left, emission wavelength 470 nm) and emission spectrum (right, excitation wavelength 320 nm) of $[Cp'CeBr_2]_{12}$ (**6a**).

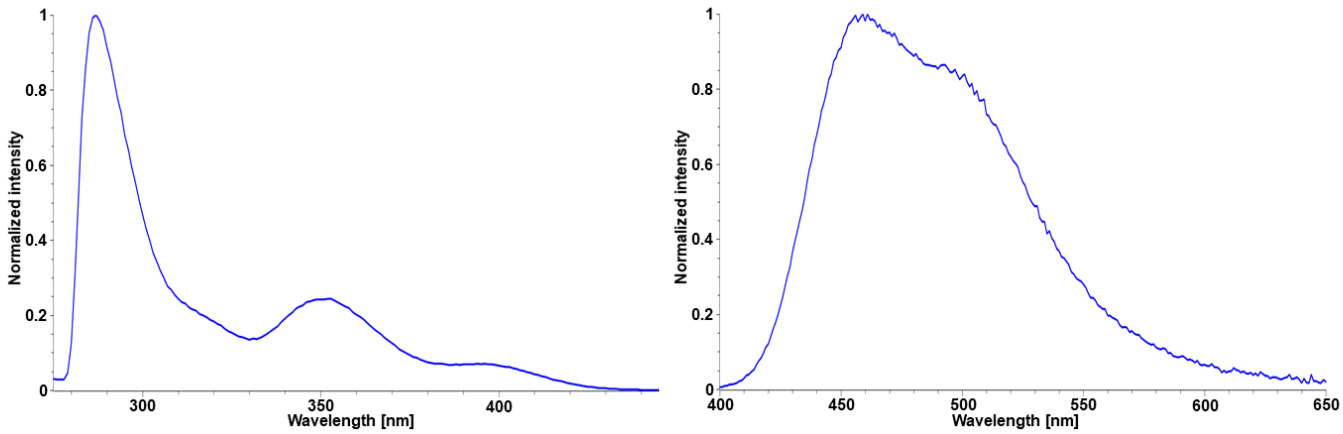

Figure S36. Excitation spectrum (left, emission wavelength 450 nm) and emission spectrum (right, excitation wavelength 352 nm) of $[Cp'CeCl_2]_{12}$ (**7a**) and $[Cp_5'Ce_5Cl_9(Cl_2AlMe_2)]_2$ (**8**).

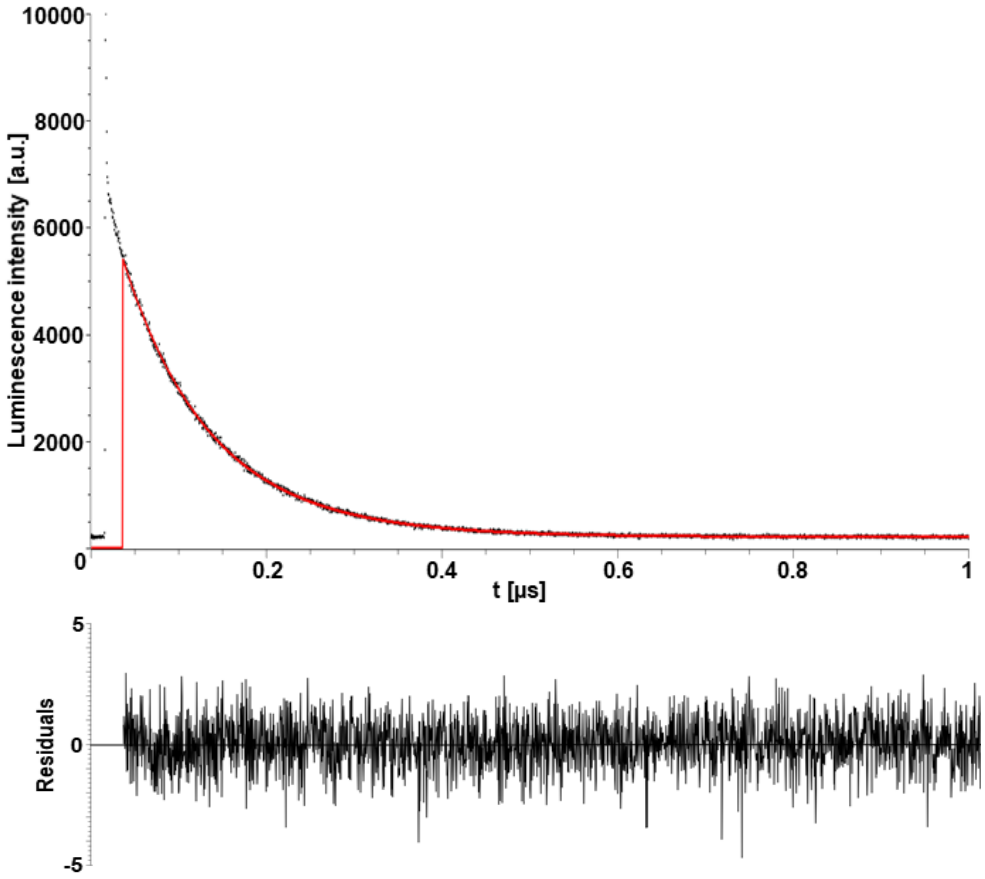

Figure S37. Luminescence decay profile (black scatter plot) of $[Cp'CeI_2]_{12}$ (**2**) and $[Cp'_4Ce_4I_8]_4$ (**4a**) and biexponential fit (red solid line). The residual shown below underlines the suitability of the fit.

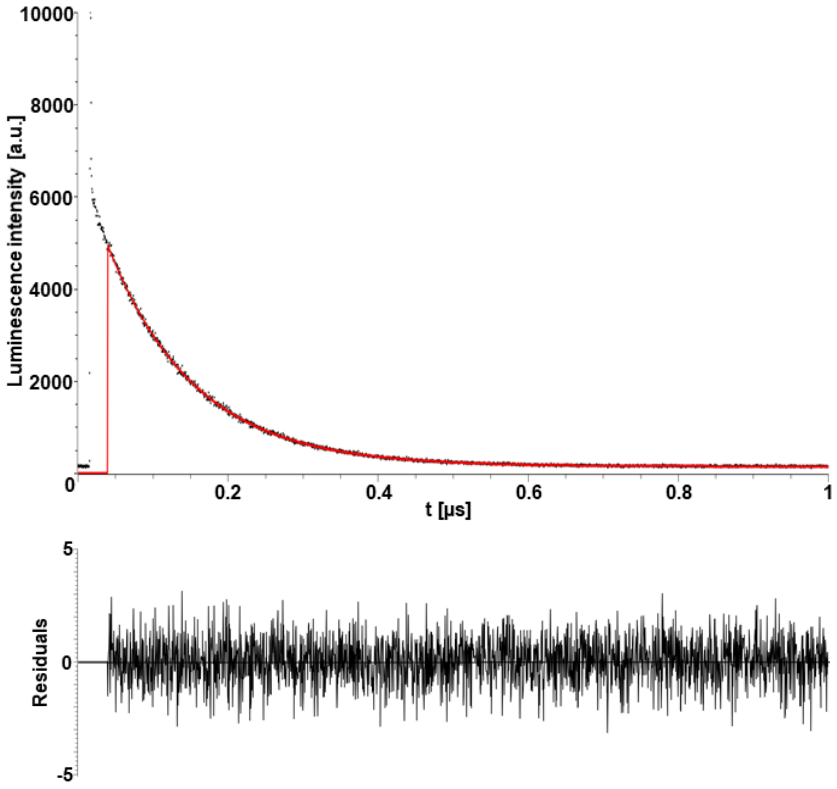

Figure S38. Luminescence decay profile (black scatter plot) of $[Cp'CeBr_2]_{12}$ (**6a**) and single exponential fit (red solid line). The residual shown below underlines the suitability of the fit.

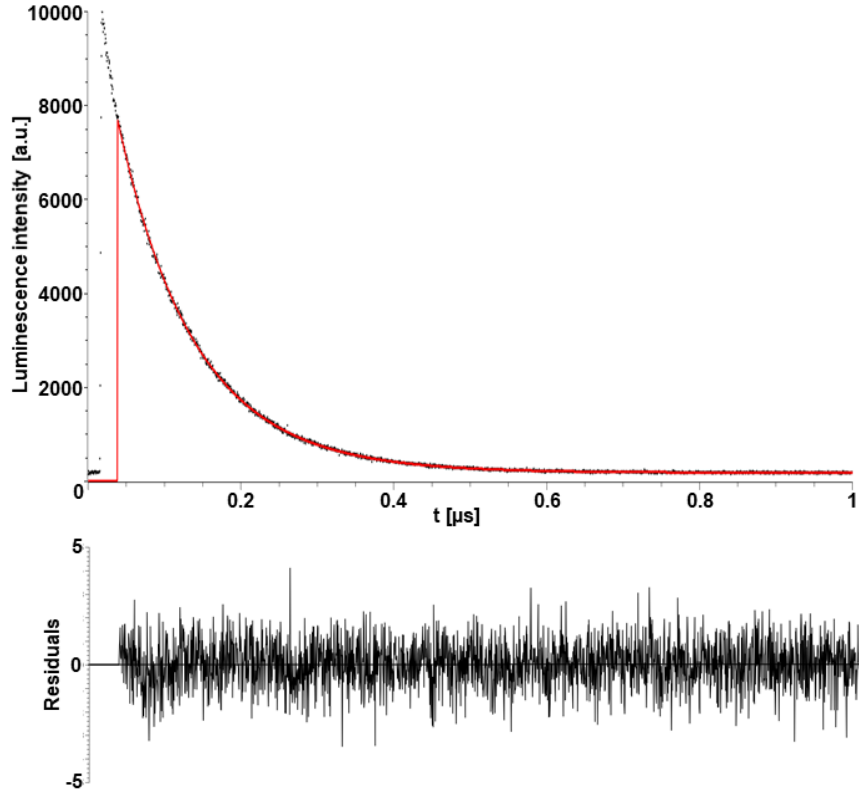

Figure S39. Luminescence decay profile (black scatter plot) of $[Cp'CeCl_2]_{12}$ (**7a**) and $[Cp_5'Ce_5Cl_9(Cl_2AlMe_2)]_2$ (**8**) and biexponential fit (red solid line). The residual shown below underlines the suitability of the fit.

Paper III

Cerium Fluorenyl Complexes Including CC-Coupling Reactions

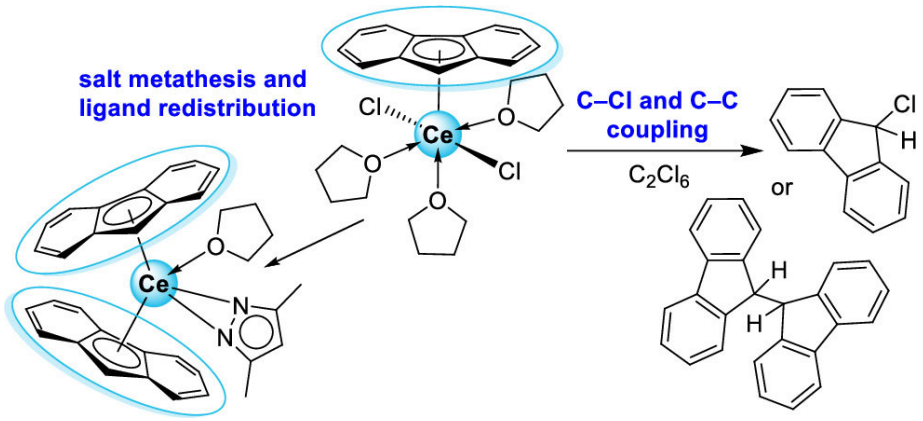

https://doi.org/10.1021/acs.organomet.2c00029
Organometallics **2022**, *41*, 962-976

ORGANOMETALLICS

pubs.acs.org/Organometallics Article

Cerium Fluorenyl Complexes Including CC Coupling Reactions

Lars Hirneise,[†] Dennis A. Buschmann,[†] Cäcilia Maichle-Mössmer, and Reiner Anwander*

Cite This: *Organometallics* 2022, 41, 962−976 Read Online

ACCESS | Metrics & More | Article Recommendations | Supporting Information

ABSTRACT: The first structurally characterized fluorenyl (Flu) complexes of cerium are reported, bearing one, two, and three fluorenyl ligands. The reaction of $CeX_3(THF)_x$ (X = Cl and I) with KFlu led to the half-sandwich complexes $FluCeX_2(THF)_3$. The chloride derivative was utilized in salt metathesis reactions, affording complexes $FluCeR_2(THF)_x$ with R = O*t*Bu, $OSiMe_3$, $OC_6H_3iPr_2$-2,6, Me_2Pz, and Cp (x = 1 or 2; Me_2Pz = 3,5-dimethylpyrazolato, Cp = C_5H_5). The mono(fluorenyl) complexes $FluCeR_2(THF)_x$ are prone to ligand redistribution at ambient temperature, leading to the respective sandwich complexes $Flu_2CeR(THF)$. Utilization of K(2,10-tBu$_2$Flu) (KFlu^{tBu}) afforded tris(fluorenyl) complex Flu$^{tBu}{}_3$Ce(THF) instead, showcasing two η^5- and one η^1-bound fluorenyl ligands. Treatment of $FluCeCl_2(THF)_3$ with halogenating oxidants such as C_2Cl_6, I_2, or $TeBr_4$ did not afford stable cerium(IV) species but mixtures of 9-halogenidofluorene and 1,1′-bifluorene. Selective fluorenyl coupling reactions could be achieved for C_2Cl_6. Respective investigations with lanthanum and neodymium complexes support σ-bond metathesis as the main reaction path for C−C-bond formation.

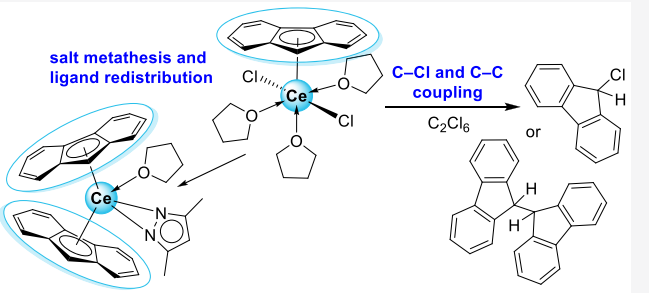

INTRODUCTION

Cerium fluorenyl complexes were first mentioned in a paper from 1971 by Kalsotra et al., claiming the synthesis of "tetra(fluorenyl) cerium(IV)".[1] This organoceric compound was stated to display a light yellow color, thermal stability up to 104 °C, and solubility in protic solvents such as ethanol.[1] The formation of "tetra(fluorenyl) cerium(IV)" $Ce(C_{13}H_9)_4$ (as was that of "tetra(cyclopentadienyl) cerium(IV)" $CeCp_4$) according to the original protocol (employing $(pyH)_2CeCl_6$ as a precursor) was later refuted by Deacon et al.[2] Few rare-earth-metal (Ln) complexes bearing a nonfunctionalized "free-standing" fluorenyl (Flu) ligand were reported before 2000, the most notable being bis(fluorenyl) samarium, obtained from SmI_2.[3] Further research on Ln-Flu chemistry has mainly focused on the design of *ansa*-lanthanidocene complexes[4] and Flu-tethered/linked constrained geometry complexes[5] and their use in polymerization catalysis. The X-ray crystal structures of the first neutral mono(fluorenyl) complexes, $FluLnI_2(pyridine)_3$ (Ln = La and Nd), were reported by Giesbrecht et al. in 2005.[6] Our recent studies on fluorenyl-supported tetramethylaluminate complexes also emphasized the particular stability of half-sandwich complexes of the larger rare-earth metals.[7] On the other hand, sterically demanding fluorenyl ligands also stabilize half-sandwich derivatives of the smaller rare-earth metals as shown for, for example, (Flu^R)Ln-$(CH_2SiMe_3)_2(THF)$ (Ln = Sc, Y, and Lu)[8] and (Tbf)Y-$(CH_2SiMe_3)_2(THF)$ (Tbf = tetrabenzo[a,c,g,i]fluorenyl).[9]

To this day, neither tris(fluorenyl) rare-earth metal complexes nor any cerium-fluorenyl derivatives have been fully characterized. Since cerium provides ready access to the oxidation state +IV, we were tempted to investigate into the redox chemistry of cerium-fluorenyl complexes. The redox potential of cerium strongly depends on its ligand environment,[10] but organocerium(IV) compounds such as Cp_3CeCl are isolable and have been fully characterized.[11−13] The electron-donating capability of the ligands was ascribed an important role in stabilizing the cerium(IV) oxidation state.[10,14,15] In the case of unsymmetrical ruthenocene complexes, the relative electron-donating power of Cp-type ligands was shown to increase in the order pentachlorocyclopentadienyl, acetylcyclopentadienyl, cyclopentadienyl, indenyl, pentamethylcyclopentadienyl, and fluorenyl by X-ray photoelectron spectroscopy and electrochemical measurements.[16] This is consistent with our findings regarding the redox potentials of cyclopentadienyl and methylcyclopentadienyl complexes of cerium(IV).[14] Thus, albeit having in mind that the type of metal and its oxidation state greatly affect the donor capability of these ligands,[17] the fluorenyl ligand should in theory provide a good stabilization of cerium(IV) in terms of electron donation capability. However, in contrast to their cyclopentadienyl congeners, fluorenyl ligands engage in distinct coordination chemistry, as revealed by the ease of haptotropic coordination switches ranging from η^1 to η^6

Received: January 17, 2022
Published: April 8, 2022

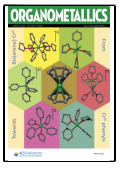

(Figure 1).[18] Such ring-slippage has been shown to be increasingly involved in the reactivity, via an extension of the

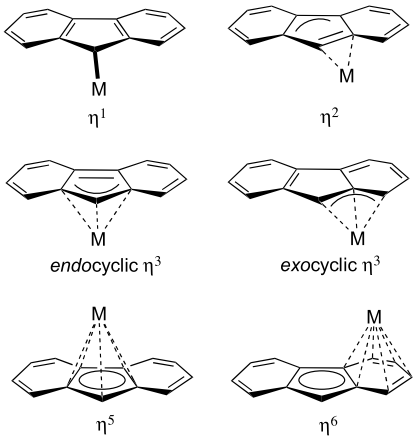

Figure 1. Different coordination modes of fluorenyl ligands available through haptotropic shifts.[18]

π system.[18−22] The most common coordination mode observed in rare-earth-metal complexes is the η^5 mode as revealed in the case of, for example, $Flu_2Sm(THF)_2$[3] or $FluLnI_2(pyridine)_3$ (Ln = La and Nd).[6] Interestingly, the reaction of $(FluSiMe_3\text{-}1)Ln(THF)_2$ (Ln = Sm and Yb) with AlR_3 (R = Me and Et) led to a reversible η^1 to η^6 switch at the divalent rare-earth-metal center.[19] The switch to η^3-allylic bonding or σ bonds (η^1 coordination) involving C1 is in most cases triggered by steric encumbrance or formation of polymer chain structures as evidenced for $[NaFlu(TMEDA)]_n$.[18,23] In particular, alkali-metal-fluorenide salts, supported by different donor ligands, provide a good overview of the possible coordination modes. In the case of the binuclear structure of $(KFlu)_2(DIGLYME)$, the relatively rare η^6 coordination to the phenyl rings was detected, while the analogous lithium compound formed a separated ion pair.[33] Moreover, the polymeric structures of the DIGYLME adducts of sodium and rubidium fluorenide revealed multiple alternating coordination modes between η^1 and η^5.[24] The use of crown ethers afforded complete fluorenyl anion separation for [K(18-crown-6)][Flu].[25] Although the formation of such "metals-in-a-box" is also known for alkaline-earth-metal fluorenyl complexes[26] and other cyclopentadienyl derivatives, extensive haptotropic shifts seem to be exclusive for indenyl and fluorenyl ligands.[25] This additional feature of the fluorenyl ligands might trigger further reactivity and reaction pathways for cerium complexes. Note that while cerium(IV) alkyl or allyl complexes have not yet been isolated, the Schelter group has recently reported on the isolation and full characterization of a covalent cerium(IV) aryl complex.[27]

RESULTS AND DISCUSSION

Dihalogenido Cerium(III) Half-Sandwiches Including an Unprecedented Tris(fluorenyl) Complex. Cyclopentadienyl (Cp^R) ligands (Cp^R = C_5H_5, C_5H_4Me, $C_5H_4SiMe_3$, $C_5H_3(SiMe_3)_2$, and C_5Me_5) were shown to be capable of stabilizing the +IV oxidation state of cerium. Since these Cp^R ligands also support chemically and often electrochemically reversible cerium-centered redox properties, it stirred up the question of the feasibility of a similar ceric fluorenyl (Flu) chemistry.[14,15] As aforementioned, in contrast to the strictly η^5-bound cyclopentadienyl ligands, fluorenyl is prone to $\eta^5 \rightarrow \eta^3 \rightarrow \eta^1$ coordination switches, thus tailoring metal centers to enhanced reactivity and alternative reaction pathways.[20,28,29]

When treating $CeCl_3(THF)_{1.04}$ with 1−5 equiv. of lithium, sodium or potassium fluorenide,[30] we were surprised to learn that only one species could be isolated. Regardless of how much excess of fluorenyl salt was used, crystallization always led to the half-sandwich complex $FluCeCl_2(THF)_3$ ($\mathbf{1}^{Ce,Cl}$). Performing an equimolar reaction, $\mathbf{1}^{Ce,Cl}$ could be obtained in 90% crystalline yield (Scheme 1). Usage of commercially

Scheme 1. Synthesis of $FluLnCl_2(THF)_3$ ($\mathbf{1}^{Ln,Cl}$) and $FluCeI_2(THF)_3$ ($\mathbf{1}^{Ce,I}$)

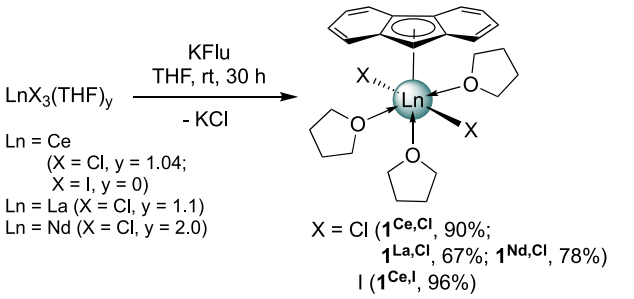

available CeI_3 under the same conditions led to the respective iodide complex $FluCeI_2(THF)_3$ ($\mathbf{1}^{Ce,I}$), both of which could be analyzed via X-ray diffraction (XRD).

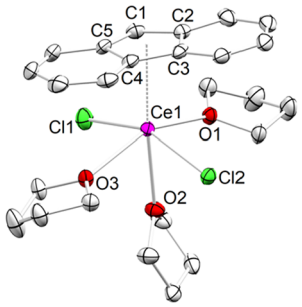

Figure 2. Crystal structure of $FluCeCl_2(THF)_3$ ($\mathbf{1}^{Ce,Cl}$). Hydrogen atoms are omitted for clarity. Atomic displacement ellipsoids are set at the 30% probability level. Complexes $\mathbf{1}^{La,Cl}$ and $\mathbf{1}^{Nd,Cl}$ are isostructural. Selected interatomic distances and angles are listed in Table 1 ($\mathbf{1}^{Ce,Cl}$) and the Supporting Information ($\mathbf{1}^{La,Cl}$ and $\mathbf{1}^{Nd,Cl}$). Due to low crystal quality, the metrical parameters of $\mathbf{1}^{Nd,Cl}$ should be carefully evaluated.

The solid-state structure of $\mathbf{1}^{Ce,Cl}$ is depicted in Figure 2, showing (like $\mathbf{1}^{Ce,I}$, Figure S40) a pseudo-octahedral coordination geometry (Figure 2). The *trans*-positioned chlorido (iodido) ligands and the three-coordinated THF molecules are bent slightly away from the sterically more demanding fluorenyl. The Ce−Cnt (centroid) distance accounts for similar 2.595 Å ($\mathbf{1}^{Ce,Cl}$) and 2.590 Å ($\mathbf{1}^{Ce,I}$), which is significantly longer than the distances found in $Cp_3Ce(THF)$ (avg. 2.480 Å)[31] or the pentamethylcyclopentadienyl-supported half-sandwich and metallocene complexes $Cp^*CeI_2(THF)_3$ (2.523 Å)[32] and $[Cp^*_2CeCl_2K(THF)]_n$ (2.523 and 2.524 Å), respectively.[33] For reasons of steric oversaturation, homoleptic Cp^*_3Ce features an extremely large Ce−Cnt distance of 2.619 Å.[34] As expected, the Ce−halogen

https://doi.org/10.1021/acs.organomet.2c00029
Organometallics 2022, 41, 962−976

Table 1. Overview of Selected Interatomic Distances (Å) and Angles (deg) of the Compounds $1^{Ce,Cl}$, $1^{Ce,I}$, 2, 3^{Cp}, 3^{OAr}, 3^{Pz}, $3^{Pz,THF}$, 4^{Pz}, 4^{OtBu}, 4^{OSiMe3}, and 6 (Cnt = Flu/Cp Ring Centroid)

	Ce−C(Flu)$_{range}$	Ce−C(Flu) avg.	Ce−Cnt (Flu)	Ce−X	X−R	Cnt−Ce−Cnt	Cnt−Ce−X	Ce−X−R
FluCeCl$_2$(THF)$_3$ ($1^{Ce,Cl}$) (X = Cl)	2.756(3) (C1)−2.965(3) (C7)	2.860	2.595	2.7360(9)			102.3	
				2.7379(8)			100.8	
FluCeI$_2$(THF)$_3$ ($1^{Ce,I}$) (X = I)	2.752(3) (C1)−2.967(3) (C7)	2.856	2.590	3.1323(3)			101.58	
				3.1836(3)				
Flu$^{tBu}_3$Ce(THF) (2) (X = C55, R = C)	2.653(3) (C13)−3.083(3) (C6)	2.870	2.578	2.648(3)	1.441(4)	123.1	99.2	92.5(2)
			2.613 (3.212)	4.030(3) (C49)	1.448(4)	119.0	112.8	110.3(2)
						104.4		
FluCeCp$_2$(THF) (3^{Cp}) (X/R = C(Cp))* X = Cnt(Cp)	2.797(2) (C23)−2.984(2) (C17)	2.905	2.637	2.535*	1.396(3)	118.7		
				2.560*		116.6		
					1.414(3)	117.3		
FluCe(OAr)$_2$(THF)$_2$ (3^{OAr}) (X = O, R = C)	2.806(2) (C12)−2.961(2) (C1)	2.886	2.625	2.226(1)	1.342(2)		116.5	174.5(1)
				2.212(1)	1.344(2)		112.3	177.5(1)
FluCe(Me$_2$Pz)$_2$(THF)$_2$ (3^{Pz}) (X/R = N)	2.819(4) (C13)−3.014(4) (C7)	2.914	2.646	2.516(4)	1.387(5)		102.8	75.4(2)
				2.476(4)				72.3(2)
				2.443(4)				75.2(2)
				2.486(4)				71.8(2)
FluCe(Me$_2$Pz)$_2$(THF)$_5$ ($3^{Pz,THF}$) (X/R = N)	6.498 (C36)−7.219 (37)	6.910	6.822	2.48(2)	1.40(3)		75.3	73.6(13)
				2.48(2)			103.3	73.6(13)
				2.48(2)			100.0	73.4(13)
				2.47(2)			81.3	73.4(13)
Flu$_2$Ce(Me$_2$Pz) (THF) (4^{Pz}) (X/R = N)	2.714(3) (C1)−2.946(3) (C7)	2.849	2.574	2.406(3)	1.397(4)	125.6	105.0	72.7(2)
				2.419(3)			107.1	73.7(2)
							101.8	
							128.6	
Flu$_2$Ce(OtBu) (THF) (4^{OtBu}) (X = O, R = C)	2.765(6) (C26)−2.927(C6)	2.863	2.588	2.096(4)	1.424(8)	125.1	113.4	172.7(4)
			2.581				109.0	
Flu$_2$Ce(OSiMe$_3$) (THF) (4^{OSiMe3}) (X = O, R = Si)	2.737(5) (C13)−2.944(5) (C6)	2.845	2.587	2.133(4)	1.619(4)	126.3	110.1	173.2(2)
			2.579				111.0	
Ce(dipp)$_3$ (6)	2.718(3) (C14)−2.866(13) (C1A)	2.818	2.401			120.4		
			2.392			120.5		
			2.391			119.1		

distances elongate from $1^{Ce,Cl}$ (avg. 2.737 Å) to $1^{Ce,I}$ (avg. 3.158 Å), whereas the Ce−O(THF) distances barely vary. Compared to FluLaI$_2$(pyridine)$_3$ with a La−Cnt distance of 2.593 Å and La−I distances of 3.240 and 3.174 Å, the distance to the fluorenyl ligand in $1^{Ce,I}$ is almost identical, while the M−I bonds are elongated for the lanthanum complex.[6]

For comparison reasons, especially concerning the reactivity behavior (vide infra), the lanthanum and neodymium derivatives $1^{La,Cl}$ and $1^{Nd,Cl}$ were synthesized analogously (Scheme 1). In the solid state, these complexes are isotypical with the cerium congener (Figures S41 and S42) and display Ln−Cl average distances of 2.763 and 2.703 Å, respectively. The ^{1}H NMR spectra of complexes $1^{Ln,Cl}$ show the expected 1:2:2:2:2 peak pattern for the fluorenyl ligand. Striking is the pronounced paramagnetic shift of the C1 proton for complexes $1^{Ce,Cl}$ (26 °C: 33.7 ppm) and $1^{Nd,Cl}$ (26 °C: 27.5 ppm), which is strongly emphasized at low temperature as shown for the cerium complex (−80 °C: 55.6 ppm).

When performing an equimolar reaction of CeCl$_3$(THF)$_{1.04}$ with the *tert*-butyl-substituted fluorenyl salt K(2,10-*t*Bu$_2$Flu) (KFlu^{tBu}), fully exchanged Flu$^{tBu}_3$Ce(THF) (2) formed (Scheme 2). Amazingly, despite the higher steric demand (Flu^{tBu} vs Flu), the formation of a half-sandwich complex along

Scheme 2. Synthesis of Flu$^{tBu}_3$Ce(THF) (2)

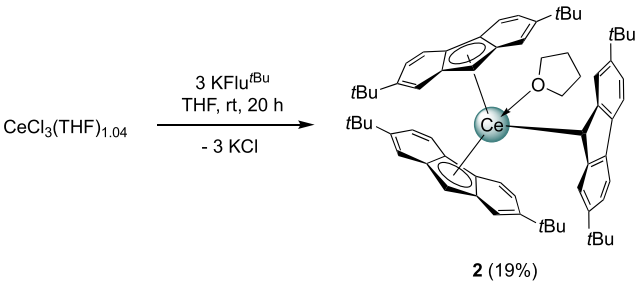

2 (19%)

https://doi.org/10.1021/acs.organomet.2c00029
Organometallics 2022, 41, 962−976

the lines of $\mathbf{1}^{Ce,Cl}$ was not observed. To our knowledge, **2** represents the first tris(fluorenyl) rare-earth-metal complex. In stark contrast, tris(indenyl) derivatives $(Ind)_3Ln$ and $(Ind)_3Ln(Do)$ have been extensively investigated (Do = neutral donor molecules),[35] including the crystal structures of $Ind_3Ce(py)$[36] and $Ind_3Ce(THF)$.[13] Moreover, the existence of **2** definitely rules out sterics to be the crucial factor for the formation of $\mathbf{1}^{Ce,Cl}$. At ambient temperature, the $CeCl_3(THF)_{1.04}/KFlu^{tBu}$ reaction required a large excess of cerium chloride and afforded only a crystalline yield of 19%, after a stirring period of 2 days. Applying the same conditions with a 1:3 mixture of $CeCl_3(THF)_{1.04}$ and $KFlu^{tBu}$, the reaction was incomplete with large amounts of the fluorenyl salt left.

The solid-state structure of **2** bears two η^5- and one η^1-coordinated fluorenyl ligand, showcasing distinct coordination modes in the same molecule for direct comparison (Figure 3).

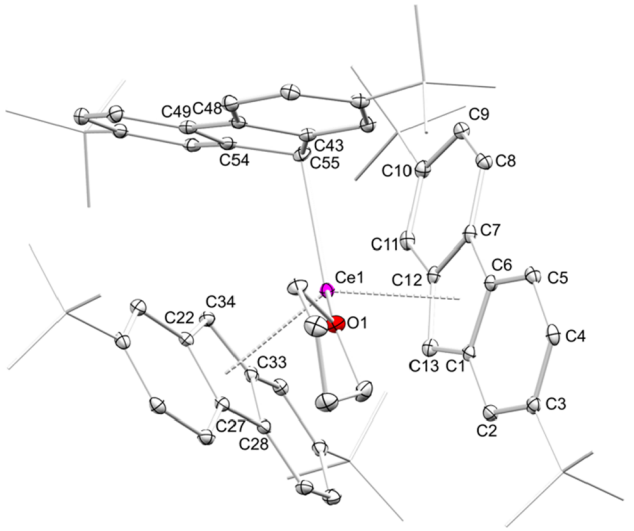

Figure 3. Crystal structure of $Flu^{tBu}{}_3Ce(THF)$ (**2**). Hydrogen atoms are omitted for clarity. Atomic displacement ellipsoids are set at the 30% probability level. Selected interatomic distances and angles are listed in Table 1.

The η^5 coordination involves Ce−C(Flu) distances ranging from 2.653(3) to 3.083(3) Å and Ce−Cnt distances of 2.578 and 2.613 Å, while the η^1 coordination to C55 is indicated by a shorter Ce−C(Flu) distance of 2.648(3) Å and a wide Ce1−C55−Cnt angle of 105.71°. The latter angle is even wider than the respective Li−C1−Cnt angle of $LiFlu(THF)_3$ (Figure S45). Moreover, the changed hapticity of the fluorenyl ligand is also indicated by the relatively obtuse Ce1−C55−C54 angle of 110.31(18)°. The other Ce−C(Flu) distances are as long as 4.030(3) Å (C49), accounting for a Ce−Cnt distance of 3.212 Å. For comparison, the Ce−C(silylalkyl) distance in the donor-free (and hence formally lower coordinated) alkyl complex $Cp^*{}_2Ce[CH(SiMe_3)_2]$ was reported as 2.546(5) Å.[37] Furthermore, the Ce−C(ring) distances in $Ind_3Ce(py)$ range from 2.748(5) to 3.009(5) Å, and the Ce−Cnt distance in $Ind_3Ce(THF)$ averages 2.584 Å.[13]

The distinct fluorenyl coordination in **2** is not preserved in solution since there is only one set of signals for the fluorenyl ligands. Thus, all the three fluorenyl ligands are chemically equivalent, and the coordination switch appears too fast on the NMR timescale. Instead, the corresponding ^1H NMR spectrum displays seven signals for the fluorenyl protons and one singlet for all *t*Bu groups. As observed for $\mathbf{1}^{Ce,Cl}$, at low temperatures, the paramagnetic shifting gets more pronounced and splitting of the *t*Bu groups in a 1:1 integral ratio in accordance with the seven distinct ring protons of the Flu ligand occurred. This indicates some magnetic inequality of the ring and *t*Bu protons, which has also been detected for substituted indenyl ligands due to prochiral effects. Considering the steric constraints of the fluorenyl ligands, which clearly hinder rotation, similar effects might apply for **2**.[38]

Salt Metathesis Reactions Promoted by Flu-$CeCl_2(THF)_3$ ($\mathbf{1}^{Ce,Cl}$). Given the preferred formation and stability toward ligand redistribution of compound Flu-$CeCl_2(THF)_3$ ($\mathbf{1}^{Ce,Cl}$), we next aimed at salt metathesis ligand exchange. Targeted Cl/R exchange should further improve the thermodynamic and electrochemical stabilization of any envisioned/putative Ce(IV) fluorenyl complexes, particularly in the case of R = alkoxy or siloxy.[14,15,39] Accordingly, the following ligand types could be implemented in complexes $\mathbf{3}^{R}$: cyclopentadienyl (using NaCp), aryloxy ($NaOC_5H_3iPr_2$-2,6 = NaOAr), alkoxy (NaO*t*Bu), siloxy ($NaOSiMe_3$), and pyrazo-

Scheme 3. Overview of Salt Metathesis Reactions of $\mathbf{1}^{Ce,Cl}$ Affording Cerous Half-Sandwich Complexes with Alkoxy, Siloxy, Aryloxy, Pyrazolato, and Cyclopentadienyl Ligands

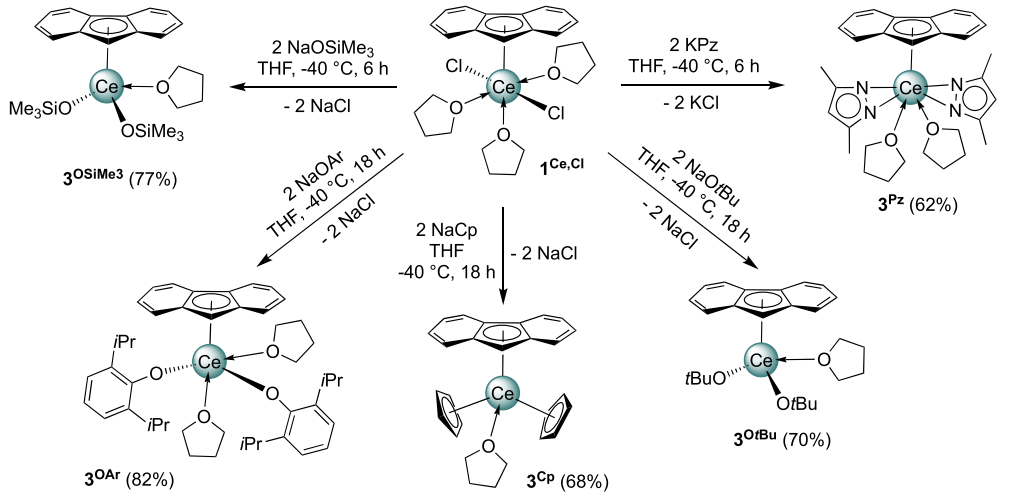

https://doi.org/10.1021/acs.organomet.2c00029
Organometallics 2022, 41, 962−976

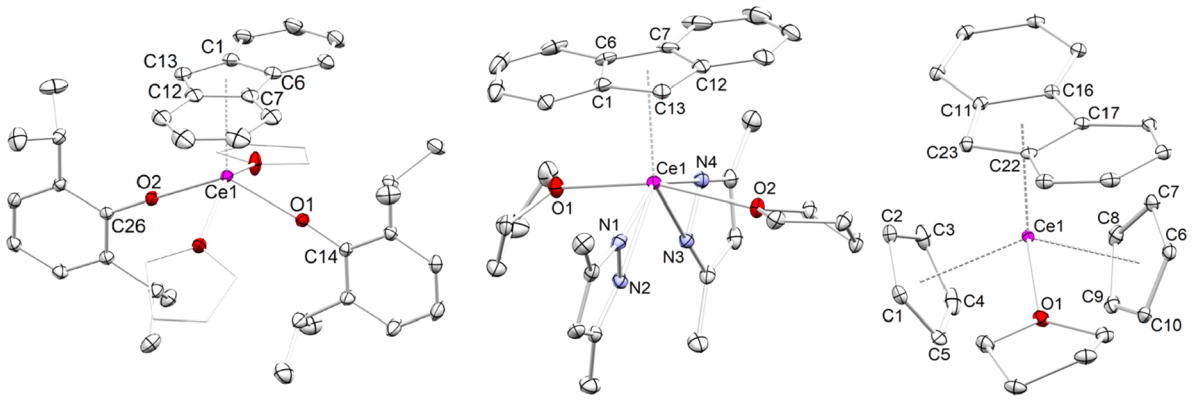

Figure 4. Crystal structures of FluCe($OC_5H_3iPr_2$-2,6)$_2$(THF)$_2$ ($\mathbf{3}^{OAr}$, left), $Flu_2Ce(Me_2Pz)$(THF) ($\mathbf{3}^{Pz}$, middle), and $FluCeCp_2$(THF) ($\mathbf{3}^{Cp}$, right). Hydrogen atoms and lattice toluene ($\mathbf{3}^{OAr}$) are omitted for clarity. Atomic displacement ellipsoids are set at the 30% probability level. Selected interatomic distances and angles are listed in Table 1.

Scheme 4. Solvent- and Temperature-Dependent Cerium Fluorenyl Pyrazolato Chemistry

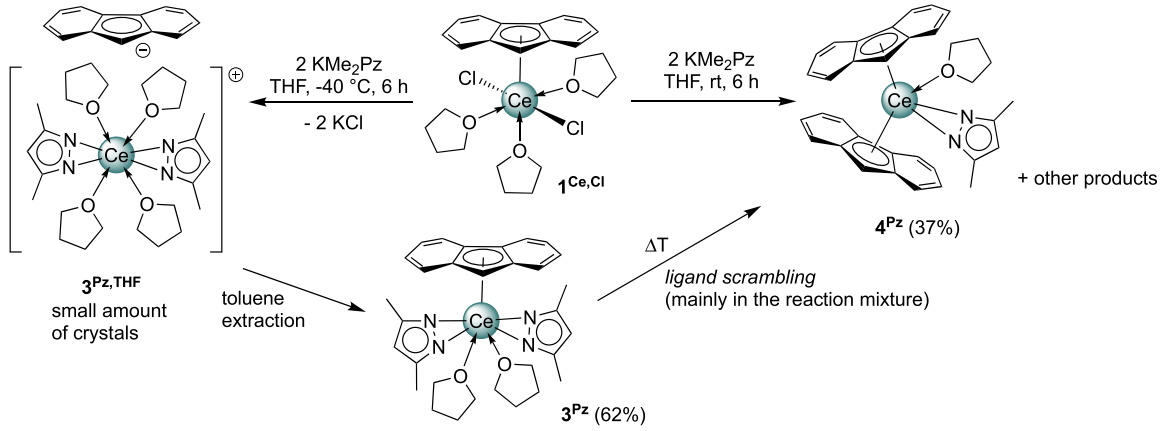

lato (potassium 3,5-dimethylpyrazolate = KMe_2Pz) (Scheme 3). These reactions were carried out at −40 °C in THF for 6–18 h and the reaction residues subsequently extracted with toluene. At ambient temperature, the toluene extracts suffered ligand rearrangement processes in all cases with the exception of the aryloxy derivative $\mathbf{3}^{OAr}$. The ligand rearrangement reactions were even more rapid in THF solution. Although ligand rearrangement can be sufficiently suppressed at lower temperature (−40 °C), it took place as a side reaction to produce the sandwich complexes $\mathbf{4}^{R}$. The sandwich compound $Flu_2Ce(Me_2Pz)$(THF) ($\mathbf{4}^{Pz}$) could be synthesized independently and purified, while single-crystalline material was obtained also for $Flu_2Ce(OtBu)$(THF) ($\mathbf{4}^{OtBu}$) and $Flu_2Ce(OSiMe_3)$(THF) ($\mathbf{4}^{OSiMe3}$) (vide infra).

The crystal structures of mono(fluorenyl) complexes FluCe($OC_5H_3iPr_2$-2,6)$_2$(THF)$_2$ ($\mathbf{3}^{OAr}$), FluCe(Me_2Pz)$_2$(THF)$_2$ ($\mathbf{3}^{Pz}$), and $FluCeCp_2$(THF) ($\mathbf{3}^{Cp}$) are depicted in Figure 4. The cerium centers in complexes $\mathbf{3}^{OAr}$ and $\mathbf{3}^{Pz}$ both adopt a slightly bent pseudo-square pyramidal coordination geometry, clearly dictated by the flat spread of the fluorenyl ligand. The Ce–centroid (Cnt) distances amount 2.625 Å ($\mathbf{3}^{OAr}$) and 2.646 Å ($\mathbf{3}^{Pz}$). It appears that the latter represents the longest distance for a cerium to a cyclopentadienyl-type ligand detected so far and stresses the fact that such fluorenyl half-sandwich complexes **3** show generally longer Ce–Cnt distances than the respective sandwich complexes **4**. The Ce–O(aryloxy) distances (avg. 2.219 Å) in $\mathbf{3}^{OAr}$ match those reported for six-coordinate Ce($OC_5H_3iPr_2$-2,6)$_3$(THF)$_3$ (avg. 2.12 Å).

The η^5-fluorenyl ligand is sterically more demanding than the aryloxy ligand, giving space to the additional coordination of only two THF molecules.[40] For further comparison, the half-sandwich complex Cp*Ce($OC_5H_3tBu_2$-2,6)$_2$ synthesized by Heeres et al., bearing a slightly bulkier aryloxy ligand, shows significantly longer Ce–O distances (avg. 2.253 Å) but an average Ce–C distance of 2.76 Å in comparison with 2.886 Å for $\mathbf{3}^{OAr}$.[41]

The pyrazolato derivative $\mathbf{3}^{Pz}$ is isostructural to $\mathbf{3}^{OAr}$ with *trans*-positioned η^2-pyrazolatos instead of the aryloxys. The Ce–N distances average 2.480 Å matching those of the four terminal ones in adducts [Ce(Me_2Pz)$_3$(Do)]$_2$ (avg. 2.478 Å (Do = THF) and avg. 2.475 Å (Do = HMe_2Pz)).[42]

The mono(fluorenyl) compound $FluCeCp_2$(THF) ($\mathbf{3}^{Cp}$) represents a rare example of a rare-earth-metal complex bearing different (non-linked) η^5-coordinated cyclopentadienyl-type ligands. The other examples include trivalent Cp*$_2$LnCp (Ln = Nd and Sm)[43] or divalent FluYbCp*(DME).[44] The isolation of such complexes with sterically less demanding ligands is counteracted by ligand rearrangement and formation of the respective homoleptic complexes. This is also the case for heteroleptic $\mathbf{3}^{Cp}$. Treating $\mathbf{1}^{Ce,Cl}$ with NaCp at ambient temperature afforded Cp_3Ce(THF) as the major side product, but after toluene extraction of $\mathbf{3}^{Cp}$ to remove Cp_3Ce(THF) and other impurities, no further scrambling has been observed at −40 °C.[31,45] Also for $\mathbf{3}^{Cp}$, the Ce–

https://doi.org/10.1021/acs.organomet.2c00029
Organometallics 2022, 41, 962–976

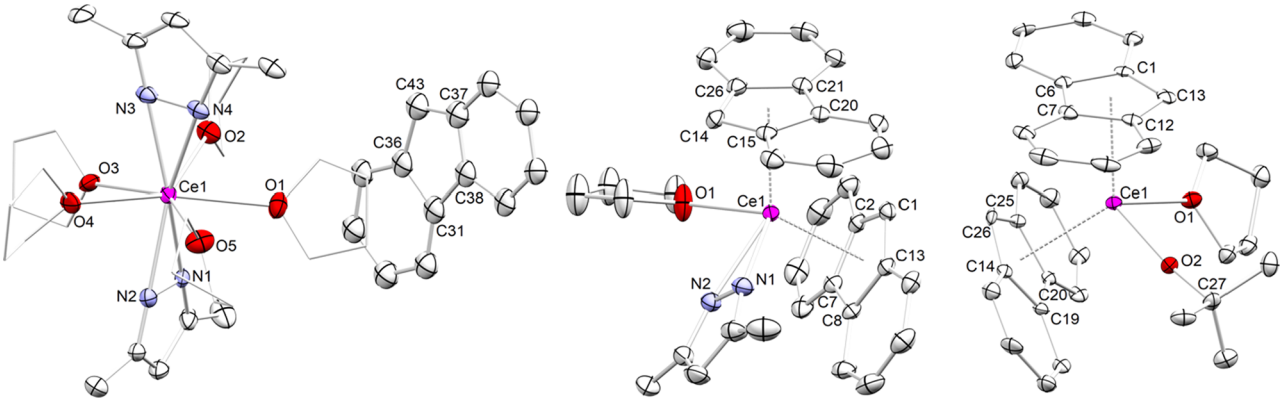

Figure 5. Crystal structures of $FluCe(Me_2Pz)_2(THF)_4$ ($\mathbf{3}^{Pz,THF}$, left), $Flu_2Ce(Me_2Pz)(THF)$ ($\mathbf{4}^{Pz}$, middle), and $Flu_2Ce(OtBu)(THF)$ ($\mathbf{4}^{OtBu}$, right). Hydrogen atoms have been omitted for clarity. Atomic displacement ellipsoids are set at the 30% probability level. Selected interatomic distances and angles are listed in Table 1.

Cnt(Flu) distance of 2.637 Å appears rather long. Even the comparatively shorter Ce−Cnt(Cp) distances of avg. 2.548 Å are considerably longer than those in $Cp_3Ce(THF)$ (avg. 2.480 Å),[31] indicating significant steric hindrance. Well-examined unsymmetrical metallocenes relate to the metals Fe, Ru, and Os, for example, FluFeCp or FluRuCp*, where haptotropic rearrangements of the fluorenyl ligands are known.[16,28,46]

The ligand rearrangement processes involving the pyrazolato ligand have been elucidated in more detail, as not only the half-sandwich complex $\mathbf{3}^{Pz}$ (vide supra) could be isolated (Scheme 4). Additionally, the sandwich complex $Flu_2Ce(Me_2Pz)(THF)$ ($\mathbf{4}^{Pz}$) could be obtained in 37% yield upon warming to ambient temperature. Assuming ligand rearrangement to tris(pyrazolyl) $[Ce(Me_2Pz)_3(THF)]_2$ as the dominant reaction path, which could be detected among other unidentified products in the NMR spectrum, a maximum yield of 50% of $\mathbf{4}^{Pz}$ should be possible.[42]

Furthermore, crystallization of the chilled reaction mixture (in THF) before toluene extraction did not only yield half-sandwich $\mathbf{3}^{Pz}$ but also crystals of $[Flu]^-[Ce(Me_2Pz)_2(THF)_5]^+$ ($\mathbf{3}^{Pz,THF}$). The latter complex $\mathbf{3}^{Pz,THF}$ features a solvent-separated ion pair, reaffirming easily separable/abstractable fluorenyl anions (Figure 5).[7] Indeed, $\mathbf{3}^{Pz,THF}$ is the first rare-earth-metal complex bearing a solvent-only separated fluorenyl anion (Ce−Cnt distance = 6.822 Å). It has been revealed previously that such solvent-separated fluorenyl anions are favorably observed in the presence of crown ethers or other multidentate O-donors as for $[BaFlu(18\text{-crown-}6)(pyridine)]^+$ $[Flu]^-$ and $[M(diethyleneglycol\text{-}dimethylether)_2]^+$ $[Flu]^-$ (M = Li and Na).[24,47] The Ce−N distances of the seven-coordinate cation of $\mathbf{3}^{Pz,THF}$ (avg. 2.475 Å) are slightly shorter than in the seven-coordinate charge-balanced $\mathbf{3}^{Pz}$. The cerium center in $\mathbf{3}^{Pz,THF}$ adopts a rare pseudo-pentagonal bipyramidal coordination geometry, with the THF ligands in the equatorial positions. The *trans*-positioned pyrazolato ligands feature a torsion angle of 93.3° (N2N1−N3N4) to minimize steric hindrance of the methyl groups.

The sandwich complex $Flu_2Ce(Me_2Pz)(THF)$ ($\mathbf{4}^{Pz}$) shows a pseudo-tetrahedral geometry and a staggered conformation of the fluorenyl ligands, which has also been found for other lanthanide sandwich fluorenyl complexes (e.g., $Flu_2La(AlMe_4)$).[7] The two fluorenyl ligands bear an angle of 125.6° and display Ce−Cnt distances of 2.574 Å, which are way shorter than that in the half-sandwich complex $\mathbf{3}^{Pz}$ (2.646 Å). The Ce−N distance amounts 2.413 Å in average and is thus also shorter than those in $\mathbf{3}^{Pz}$ and $\mathbf{3}^{Pz,THF}$. In fact, it is to our knowledge the shortest distance known in the literature for this particular ligand at cerium(III). For further comparison, the donor-free complex $[Ce(Me_2Pz)_3]_4$ shows a roughly similar average Ce−N distance of 2.436 Å for the terminal η^2-bound pyrazolato ligands.[48]

Similar to the chlorido/pyrazolato ligand exchange, alkoxy and siloxy implementation led to the formation of the sandwich complexes as the major ligand rearrangement products (Scheme 5).

Scheme 5. Ligand Scrambling Reaction of Half-Sandwich Complexes $\mathbf{3}^{OtBu}$ and $\mathbf{3}^{OSiMe3}$ toward Sandwich Complexes $\mathbf{4}^{OtBu}$ and $\mathbf{4}^{OSiMe3}$ at Ambient Temperature or upon Crystallization

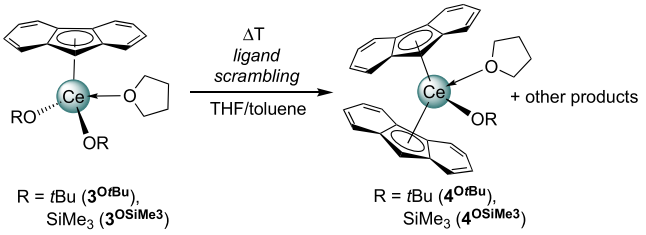

As shown in Scheme 3, the exchange reactions at a low temperature of −40 °C led to the half-sandwich complexes $FluCe(OR)_2(THF)$ in yields of 70% ($\mathbf{3}^{OtBu}$, R = O*t*Bu) and 77% ($\mathbf{3}^{OSiMe3}$, R = $OSiMe_3$). The sandwich complexes $Flu_2Ce(OtBu)(THF)$ ($\mathbf{4}^{OtBu}$) and $Flu_2Ce(OSiMe_3)(THF)$ ($\mathbf{4}^{OSiMe3}$) could be isolated and crystallized only as side products from equimolar ambient-temperature reactions. There, the bulk of the product was still $\mathbf{3}^{R}$, but the comparatively lower solubility of the sandwich complexes favored crystallization. Correspondingly, the respective alkoxy, siloxy, aryloxy, or pyrazolato ligands impart higher solubility than the fluorenyl ligand. The cerous metallocenes $\mathbf{4}^{OtBu}$ and $\mathbf{4}^{OSiMe3}$ are isostructural to $\mathbf{4}^{Pz}$. Similarly, the Ce−Cnt distances are rather short (avg. 2.584 and 2.583 Å), and the Cnt−Ce−Cnt angles are 125.1° ($\mathbf{4}^{OtBu}$) and 126.3° ($\mathbf{4}^{OSiMe3}$). As expected, the Ce−O distance is slightly shorter for $\mathbf{4}^{OtBu}$ (2.096(4) Å) in comparison to $\mathbf{4}^{OSiMe3}$ (2.113(4) Å). The terminal *tert*-butoxy ligands in the homoleptic trivalent complex $[Ce(OtBu)_3]_4$[40] display slightly shortened Ce−O distances of avg. 2.08 Å (five-coordinate cerium), and

https://doi.org/10.1021/acs.organomet.2c00029
Organometallics 2022, 41, 962−976

$[Cp^*Ce(OtBu)_2]_2$ shows slightly elongated terminal Ce−O distances of avg. 2.120 Å.[49] For further comparison, the Ce−O(siloxy) distance of $\mathbf{4}^{\mathbf{OSiMe3}}$ appears to be short in comparison to those detected in the few known trivalent cerium siloxide complexes, such as $[Ce(OSiPh_3)_3(THF)_3]$-(THF) (avg. 2.222 Å).[50]

Unlike the chlorido/OAr exchange reaction, treatment of $\mathbf{1}^{\mathbf{Ce,Cl}}$ with lithium thiomesitolate $Li(SC_6H_2Me_3$-2,4,6) (=LiSMes) at ambient temperature proved less effective. The complicated mixture did only produce the partly exchanged $\{Ce_3Li\}$-bimetallic cluster $Flu_3Ce_3(SC_6H_2Me_3$-2,4,6$)_4Cl_3Li$-$(THF)_2$ (**5**) (Scheme 6). The small crystalline yield of 22% could not be improved by starting out with proper stoichiometry, which failed to afford the desired product.

Scheme 6. Salt Metathesis Reactions of $\mathbf{1}^{\mathbf{Ce,Cl}}$ Showing Incomplete Chlorido/Thiolato Exchange Forming the $\{Ce_3Li\}$-Bimetallic Cluster 5 and Rapid Ligand Rearrangement toward Homoleptic $Ce(dipp)_3$ (6)

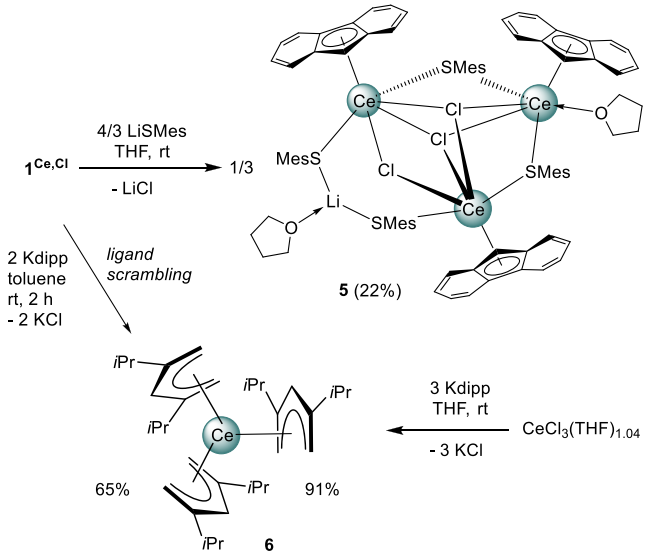

Due to bad crystal quality, the XRD analysis only provided the connectivity of **5** (Figure S44), ruling out a detailed discussion of the metrical parameters. In complex **5**, the half-sandwich motif retained, but both the thiolato and non-exchanged chlorido ligands are located in bridging positions. Two μ_2-thiolato ligands, one μ_2-chlorido, and the cerium centers form a distorted six-membered ring, with μ_3-chloridos above and below this metallacycle. Additionally, the two cerium centers which are linked via the μ_2-chlorido ligand are bridged by a $[Li(SMes)_2(THF)]$ unit. Interestingly, all the three cerium centers are six-coordinated with distorted pseudo-octahedral coordination geometries but exhibit two distinct ligand spheres. The structurally related non-ate complex $[Cp^*_2Ce(SPh)]_2$ could be accessed by the reaction of Cp^*_3Ce with PhSSPh, affording Cp*−Cp* as a coupling byproduct.[51]

Examination of increasingly basic ligands in exchange reactions according to Scheme 3 led to decomposition or follow-up reactivity such as ligand scrambling. This was the case for amides $LiNH_2$, $LiNMe_2$, $LiNiPr_2$, and silylamides $LiN(SiHMe_2)_2$ and $LiN(SiMe_3)_2$, where complicated product mixtures were observed via NMR spectroscopy. Products identified from these reactions are $LiFlu(THF)_3$ (Figure S45) and $Ce[N(SiMe_3)_2]_3$. The rapid formation of non-targeted decomposition products was also observed for alkyls MeLi, KBn, $LiCH_2SiMe_3$, and *n*BuLi. In contrast, treatment of $\mathbf{1}^{\mathbf{Ce,Cl}}$ with potassium 2,4-diisopropylpentadienide (Kdipp) led to a rather directed ligand rearrangement, affording bright orange donor-free $Ce(dipp)_3$ (**6**) in 65% yield. This corresponds to a nearly complete conversion of Kdipp. The ligand rearrangement to **6** seems similar to that occurring along the cyclopentadienyl derivative $\mathbf{3}^{\mathbf{Cp}}$, but more pronounced and faster, possibly due to the haptotropic coordination switches accessible to "open" pentadienyls. The respective half-sandwich complex could not be obtained, even when the reaction was conducted at −40 °C. The direct synthesis using a 1:3 mixture of $CeCl_3(THF)_{1.04}$ and Kdipp afforded **6** in a crystalline yield of 91%. The solid-state structure of complex **6** (Figure 6) is isostructural to $Ce(dtbp)_3$ (dtbp = 2,4-

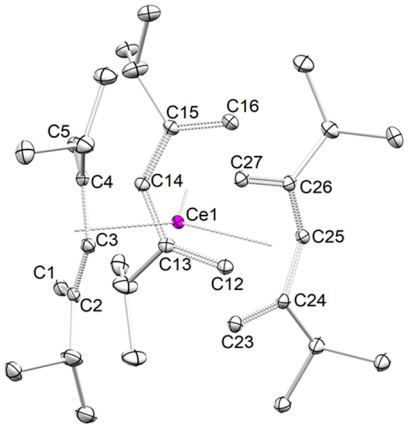

Figure 6. Crystal structure of $Ce(dipp)_3$ (**6**). Hydrogen atoms are omitted for clarity. Atomic displacement ellipsoids are set at the 30% probability level. Selected interatomic distances and angles are listed in Table 1.

$tBu_2C_5H_5$),[52] showing a typical short−long−short−long pattern across the pentadienyl ligand indicative of ionic bonding. The Ce−Cnt distance averages 2.395 Å, thus being slightly longer than the respective one in $Ce(dtbp)_3$ (avg. 2.373 Å).[52]

Reactivity toward Halogenating Reagents: CC Coupling. Aiming at cerium(IV) complexes, the reactivity of halogenating reagents such as C_2Cl_6, $TeBr_4$, I_2, and 1,4-benzoquinone was examined. The reactions of $\mathbf{1}^{\mathbf{Ln,Cl}}$ with hexachloroethane were investigated more closely (Table 2). Addition of approximately 0.5 equiv. of C_2Cl_6 to an orange solution of half-sandwich complex $\mathbf{1}^{\mathbf{Ce,Cl}}$ afforded instantly a colorless reaction mixture. Its ^{1}H NMR spectrum revealed the presence of only diamagnetic products, with the proton positioned at the five-membered ring (C1) acting as a useful probe. Instead of a diamagnetic cerium(IV) species, such as putative "$FluCeCl_3(THF)_x$" (Scheme 7), the formation of a mixture of 1,1′-bifluorene **A** (4.80 ppm in $CDCl_3$) 9-chlorofluorene **B** (ClFlu, 5.92 ppm in THF-d_8) and 9-*H*-fluorene **C** (HFlu, 3.49 ppm in THF-d_8, 3.89 ppm in C_6D_6) was observed (Table 2). Apart from 1,1′-bifluorene, discrete $CeCl_3(THF)_4$ could be analyzed by XRD analysis (Figure S46). Crystalline $CeCl_3(THF)_4$ could be obtained after separation of the organic components by toluene extraction. A THF adduct of cerous chloride was previously characterized as polymeric $[CeCl_3(THF)_4]_n$.[53] The formation of an arbitrary

https://doi.org/10.1021/acs.organomet.2c00029
Organometallics 2022, 41, 962−976

Table 2. Reactivity of Fluorenyl Complexes with C_2Cl_6

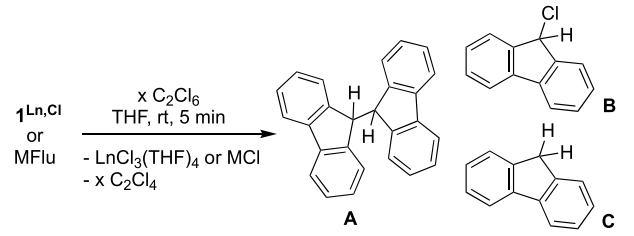

entry	fluorenyl compound	ratio Ln/C_2Cl_6	A/%	B/%	C/%
1	$\mathbf{1}^{Ce,Cl}$	1.0:0.48 (2.0:0.48)[a]	38 (69)	34 (-)	28 (31)
2	$\mathbf{1}^{Ce,Cl}$	1.0:0.24	74		26
3	$\mathbf{1}^{Ce,Cl}$	1.0:1.21 (3.0:1.21)[b]	- (72)	75 (-)	25 (28)
4	$\mathbf{1}^{La,Cl}$	1.0:0.47	58	21	21
5	$\mathbf{1}^{La,Cl}$	1.0:1.21	2	70	28
6	$\mathbf{1}^{Nd,Cl}$	1.0:0.47	16	41	43
7	$\mathbf{1}^{Nd,Cl}$	1.0:1.21	<1	60	40
8	LiFlu	1.0:0.48	70		30
9	LiFlu	1.0:1.21	81	10	9
10	KFlu	1.0:0.48	7	9	84
11	KFlu	1.0:1.21	4	17	79

[a]Addition of another equiv. of $\mathbf{1}^{Ce,Cl}$ to a THF solution of the toluene extract after work. [b]Addition of another 2 equiv. of $\mathbf{1}^{Ce,Cl}$ to a THF solution of the toluene extract after work.

mixture of **A** (38%, Table 2, entry 1), **B** (34%), and **C** (28%) suggested a radical-driven transformation. We initially hypothesized that transient fluorenyl radicals might possibly emerge from a short-lived cerium(IV) species via homolysis (Scheme 7, upper trace). This redox behavior is a favored reaction path in organocerium chemistry[11,13,54] and was recently observed along the formation of metallocene $Cp^*_2CeR_2$, yielding 1,1′-bis(pentamethylcyclopentadiene) as a side product.[15,34] Interestingly, when the **A**/**B**/**C** mixture (after work-up and separation of $CeCl_3(THF)_4$) was treated with another equivalent of $\mathbf{1}^{Ce,Cl}$, 9-chlorofluorene **B** got fully converted into 1,1′-bifluorene **A** (Table 2, entry 1). Similarly, the reaction of $\mathbf{1}^{Ce,Cl}$ and C_2Cl_6 in a 4:1 ratio afforded predominantly **A** (74%), no **B**, but a significant amount of **C** (26%) (Table 2, entry 2). Moreover, when treating $\mathbf{1}^{Ce,Cl}$ with excess of C_2Cl_6, the formation of a mixture of **B** (75%) and **C** (25%) was observed (Table 2, entry 3). On the other hand, addition of another 2 equiv. of $\mathbf{1}^{Ce,Cl}$ to the latter reaction mixture again converted all **B** into **A** (Table 2, entry 3).

This behavior strongly favors a classic CC coupling reaction or a σ-bond metathesis as shown for the lower trace of Scheme 7. Similar reactivity was described by Kagan in 1987, when generating the respective dibenzyl derivative from $Cp_2Sm(CH_2C_6H_4tBu\text{-}4)$ and benzyl bromide.[55] Closely related is also the σ-bond metathesis observed in the reaction of sterically crowded complexes $Ln(C_5Me_5)_3$ with PhSSPh.[51] Interestingly, the reaction of divalent complex $Yb(Flu)_2(THF)$ with diazadiene $[(2,6\text{-}iPr_2C_6H_3)-N{=}CH-CH{=}N-(2,6\text{-}iPr_2C_6H_3)]$ led to a CC coupling product involving the fluorenyl ligand.[56] Accordingly, a "cross-coupling" reaction could be achieved, when complex $FluCeCl_2(THF)_3$ ($\mathbf{1}^{Ce,Cl}$) was reacted with an equimolar amount of benzyl chloride, affording 9-benzylfluorene (preliminary investigation, Figure S35).

Speaking against the hypothesis of a transient tetravalent species (upper trace, Scheme 7) is also the absence of intensely colored reaction mixtures and the occurrence of a similar chemistry when the redox-inactive isostructural half-sandwich complexes $FluLnCl_2(THF)_3$ (Ln = La, $\mathbf{1}^{La,Cl}$; Nd $\mathbf{1}^{Nd,Cl}$, Scheme 1) were employed as the fluorenyl source (Table 2, entries 4−7). Overall, the reaction of the neodymium half-sandwich complex is more selective toward the generation of ClFlu, even when treated with <0.5 equiv. of C_2Cl_6 (Table 2, entries 6 and 7). The formation of significant amounts of *H*-fluorene (**C**) points out to σ-bond metathesis and radical reactions as competing pathways, although the reaction mixture $\mathbf{1}^{La,Cl}/C_2Cl_6$ applied for entry 4 did not show any EPR signal.

The scope of metal complexes was extended to the fluorenide salts $LiFlu(THF)_3$ and KFlu, displaying distinct fluorenyl derivatization reactions with C_2Cl_6. The lithium-promoted reactions produced mainly 1,1′-bifluorene **A**, independent of the molar ratio of C_2Cl_6, while the <0.5 equiv. reaction did not afford **B** at all (Table 2, entries 8 and 9). In stark contrast, treatment of KFlu with C_2Cl_6 resulted predominantly in the formation of **C** (Table 2, entries 10 and 11).

The reaction of $\mathbf{1}^{Ce,Cl}$ with other halogenating agents such as I_2 or $TeBr_4$ afforded 1,1′-bifluorene as well (72 and 22%, respectively), along with the respective 9-halogenidofluorenes as side products. Additionally, the formation of minor amounts of HFlu was observed. C_2Cl_6 was tested on the other fluorenyl complexes as well, resulting similarly in mixtures of fluorenyl species with no isolable cerium(IV) species. The possibility of C−C coupling using C_2Cl_6 as a reagent was tested on $CeBn_3$ (Bn = benzyl), resulting quantitatively in the formation of

Scheme 7. Possible Reaction Pathways for the Formation of the C−C Coupling Product A

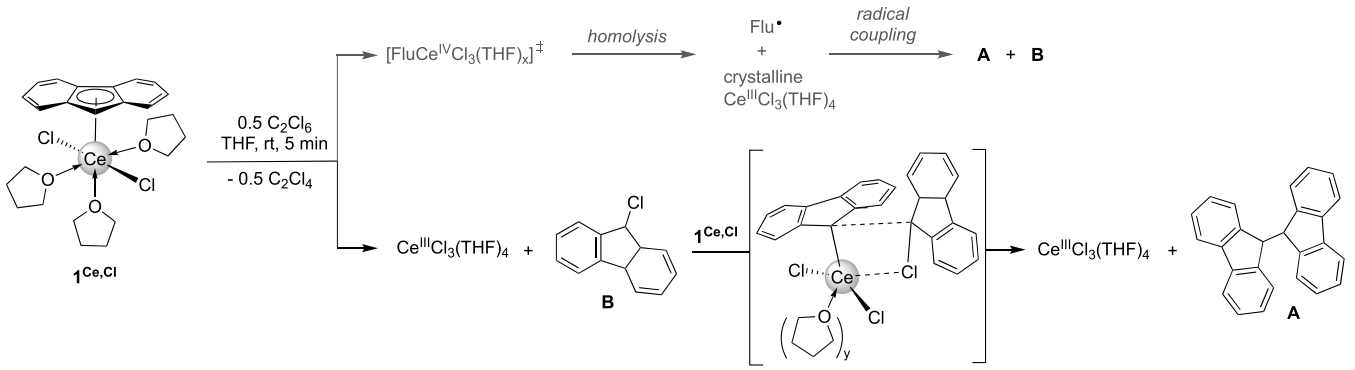

https://doi.org/10.1021/acs.organomet.2c00029
Organometallics 2022, 41, 962−976

benzyl chloride. Similarly, the reaction of $Ind_3Ce(THF)$ with C_2Cl_6 produced 1-chloroindene and $CeCl_3$ as a side product. In contrast, $Ce(dipp)_3$ (**6**) was inert toward the halogenating agents under study.

Clearly, the reactivity of cerium(III) fluorenyl complexes toward halogenating oxidants follows a reaction path different from that of cyclopentadienyl derivatives. For example, the transformation of cerous $Cp^{Me}{}_3Ce(THF)$ to ceric $Cp^{Me}{}_3CeX$ (X = Cl, Br, and I) proceeds smoothly. The feasibility of $\eta^5 \rightarrow \eta^3 \rightarrow \eta^1$ fluorenyl coordination switches, even of charge-separated fluorenyl anions in donor solvents such as THF, should trigger decomposition pathways, characteristic of cerium(IV) complexes.[11,13,14] η^3 and η^1 coordination would involve highly elusive Ce(IV) allyl and alkyl species, respectively. The distinct reactivity of Ce(III)−Flu versus Ce(III)−Cp with halogenating reagents was also evident when examining a mixture of $(C_5Me_5)CeCl_2(THF)_3/C_2Cl_6$, which did not indicate a reaction at all. In contrast to $Ce(C_5Me_5)_3$,[34] the half-sandwich complex $(C_5Me_5)CeCl_2(THF)_3$ cannot engage in σ-bond metathesis. On the other hand, the CC coupling pathway observed in this study might be exploited for carbon−carbon bond formation reactions otherwise difficult to achieve. The coupling of fluorene to 1,1′-bifluorene by radical pathways is common in d-block metal chemistry, as revealed for, for example, iron(III)−isoporphyrin complexes or, even in a catalytic manner, for $Ru_3(CO)_{12}$ or $CoCl_2$.[57−59]

In order to expand the scope of potential cerium redox chemistry, 1,4-benzoquinone was probed as a non-halogenating oxidant.[39] Correspondingly, treatment of a solution of $\mathbf{1}^{Ce,Cl}$ with 1,4-benzoquinone led to an immediate color change to dark blue and subsequently the formation of a suspension. The suspension consisted of a colorless solution, with HFlu and 1,1′-bifluorene as the major diamagnetic components, as well as of a deep blue solid, insoluble in any organic solvent. Although we did not attempt to identify the intensely colored residues, it can be hypothesized that the redox chemistry will involve the formation of cerous semiquinolate derivatives.[45]

CONCLUSIONS

The synthesis and derivatization of $FluCeX_2(THF)_3$ (X = Cl and I) showcase the feasibility of fluorenyl-based cerium half-sandwich complexes. Respective salt metathesis reactions give easy access to monomeric alkoxy, siloxy, aryloxy, pyrazolato, and cyclopentadienyl derivatives $FluCeR_2(THF)_x$. With the exception of the aryloxide complex $FluCe(OC_5H_3iPr_2\text{-}2,6)_2(THF)$, all compounds readily engage in ligand rearrangement processes to form sandwich complexes $Flu_2CeR(THF)$. The routine sandwich-type structural motif with staggered η^5-coordinated fluorenyl ligands has been elucidated for R = O*t*Bu, $OSiMe_3$, and Me_2Pz. The potential $\eta^5 \rightarrow \eta^3 \rightarrow \eta^1$ coordination switch has been detected in the solid-state structure of tris(fluorenyl) $Flu^{tBu}{}_3Ce(THF)$, which features two fluorenyl rings in η^5 and one in η^1 coordination mode. This coordinative flexibility most likely bears on the cerium(III/IV) redox chemistry, so far counteracting the isolation of a cerium(IV) fluorenyl compound. However, the reaction of complex $FluCeCl_2(THF)_3$ with halogenating oxidants such as C_2Cl_6 can be tuned to selectively form 1,1′-bifluorene or 9-chlorofluorene, involving σ-bond metathesis pathways. Such CC couplings can be potentially expanded and advanced to cross-coupling reactions.

EXPERIMENTAL SECTION

All operations were performed under rigorous exclusion of oxygen and moisture in an argon atmosphere using standard Schlenk, high-vacuum, and glovebox techniques (MB Braun MB150B-G-I; <0.1 ppm of O_2, <0.1 ppm of H_2O). The solvents were dried and degassed prior to use and provided by an MBraun SPS800. Benzene-d_6 (99.5%) was received from Deutero GmbH and THF-d_8 from Eurisotop. The deuterated solvents were dried over the NaK alloy for a minimum of 48 h and filtered through a filter pipette (Whatman) before use. Anhydrous $CeCl_3$ (99.99%) (Sigma-Aldrich) was converted into $CeCl_3(THF)_{1.04}$ via Soxhlet extraction. Hexachloroethane, benzyl choride, iodine (99.99%), NaO*t*Bu, $NaOSiMe_3$, and CeI_3 were purchased from Sigma-Aldrich and used as received. Chlorotrimethylgermane (abcr) and $TeBr_4$ (Alfa Aesar, 99.999%) were also employed without further purification. NaCp,[60] NaOAr,[61] KFlu,[62] LiSMes,[63] KMe_2Pz,[64] Kdipp,[65] $Ce(CH_2Ph)_3$,[66] $Ind_3Ce(THF)$,[13] and $(C_5Me_5)Ce(AlMe_4)_2$ (ref 67) were prepared according to literature procedures. NMR spectra were recorded on a Bruker AVII+400 (^{1}H: 400.13 MHz; ^{13}C: 100.61 MHz), AVI+300 (^{29}Si: 79.5 MHz), or AVII +500 (^{1}H: 500.13 MHz; ^{13}C: 125.76 MHz) spectrometer in dried and deuterated solvents. EPR spectra were recorded on a continuous wave X-band Bruker ESP 300E using 5 mm O.D. Wilmad quartz (CFQ) EPR tubes. DRIFT spectra were recorded on a Thermo Fisher Scientific NICOLET 6700 FTIR spectrometer using dried KBr and KBr windows. The collected data were converted using the Kubelka−Munk refinement. Alternatively, Nujol oil was used as a carrier material sandwiched in between CsI windows. CHN elemental analyses were performed on an Elementar Vario MICRO cube.

$FluCeCl_2(THF)_3$ ($\mathbf{1}^{Ce,Cl}$). $CeCl_3(THF)_{1.04}$ (824.5 mg, 2.564 mmol) and KFlu (524.0 mg, 2.564 mmol) were suspended in THF (18 mL) and stirred for 7 d at ambient temperature. The mixture was filtered, and the filtrate was concentrated multiple times to yield the crystals of $\mathbf{1}^{Ce,Cl}$ (1.369 g, 2.310 mmol, 90%) at −40 °C suitable for XRD analysis. ^{1}H NMR (500.1 MHz, THF-d_8, 26 °C): δ 33.73 (s, 1H, Flu), 8.58 (s, 2H, Flu), 3.77 (s, 2H, Flu), 3.59 (m, 12H, THF), 3.15 (s, 2H, Flu), 2.15 (s, 2H, Flu), 1.77 (m, 12H, THF) ppm. DRIFT: $\tilde{\nu}$ 3041 (w), 2981 (m), 2883 (m), 1594 (w), 1475 (m), 1444 (m), 1328 (s), 1223 (m), 1198 (w), 1118 (vw), 1019 (s), 986 (vw), 915 (w), 863 (s), 753 (vs), 726 (s), 436 (m), 423 (w) cm^{-1}. Elemental analysis (%) calcd for $C_{25}H_{33}CeCl_2O_3$, (592.55 g mol^{-1}): C, 50.67; H, 5.31. Found: C, 49.84; H, 5.37. The deviation between theoretical and experimental values can be attributed to the loss of coordinated THF under vacuum. Calcd for $FluCeCl_2(THF)_2$: C 48.46. H 4.84. Although the results are still outside the range viewed as establishing analytical purity (C: +1.32%, H: +0.53%), they are provided to illustrate the best values obtained to date.

$FluLaCl_2(THF)_3$ ($\mathbf{1}^{La,Cl}$). $LaCl_3(THF)_{1.1}$ (100 mg, 0.31 mmol) and KFlu (62.95 mg, 0.31 mmol) were suspended in THF (5 mL) and stirred for 3 d at ambient temperature. The mixture was filtered and washed with *n*-hexane, and the solvent was removed under vacuum to yield $\mathbf{1}^{La,Cl}$ as an orange powder (113.0 mg, 0.21 mmol, 67%). Single crystals of $\mathbf{1}^{La,Cl}$ (64.5 mg, 0.11 mmol, 35%) were obtained from a saturated THF solution at −40 °C. ^{1}H NMR (400.1 MHz, THF-d_8, 26 °C): δ 8.14 (s, 2H, Flu), 7.56 (s, 2H, Flu), 7.14 (s, 2H, Flu), 6.96 (s, 2H, Flu), 3.61 (m, 2H, coord. THF), 2.30 (s, 1H, Flu), 1.77 (m, 2H, coord. THF) ppm. ^{13}C{^{1}H} NMR (100.6 MHz, THF-d_8, 26 °C): δ 128.9 (Flu), 127.4 (Flu), 126.0 (Flu), 124.9 (Flu), 124.1 (Flu), 121.7 (Flu), 120.9 (Flu), 117.8 (Flu), 68.2 (coord. THF), 67.5 (coord. THF), 26.4 (coord. THF), 25.4 (coord. THF), 21.5 (Flu) ppm. IR: $\tilde{\nu}$ 2954 (Flu, Nujol), 2924 (Flu, Nujol), 2855 (Flu, Nujol), 2361 (w) 2338 (w), 1558 (w), 1541 (w), 1507 (w), 1459 (Nujol), 1377 (Nujol), 1328 (w), 1221 (w), 1197 (vw), 1152 (vw), 1011 (w), 986 (w), 933 (w), 917 (w), 853 (w), 751 (s), 724 (vs), 695 (m), 668 (m), 613 (w), 564 (w), 434 (m), 421 (m) cm^{-1}. Elemental analysis (%) calcd for $C_{25}H_{33}LaCl_2O_3$, (591.34 g mol^{-1}): C, 50.78; H, 5.63. Found: C, 47.97; H, 4.09. The deviation between theoretical and experimental values can be attributed to the loss of coordinated THF under vacuum: calcd for $FluLaCl_2(THF)_2$: C 48.58. H 4.85. Although the results are still outside the range viewed as establishing analytical

https://doi.org/10.1021/acs.organomet.2c00029
Organometallics 2022, 41, 962−976

purity (C: −0.61%, H: −0.76%), they are provided to illustrate the best values obtained to date.

FluNdCl$_2$(THF)$_3$ (1^{Nd,Cl}). $NdCl_3(THF)_2$ (100 mg, 0.25 mmol) and KFlu (51.75 mg, 0.25 mmol) were suspended in THF (5 mL) and stirred for 3 d at ambient temperature. The mixture was filtered and washed with *n*-hexane, and the solvent was removed under vacuum to yield **1^{Nd,Cl}** as a yellow powder (115.8 mg, 0.19 mmol, 78%). Single crystals of **1^{Nd,Cl}** (42.9 mg, 0.11 mmol, 35%) were obtained from a saturated THF solution at −40 °C. ^{1}H NMR (400.1 MHz, THF-d_8, 26 °C): δ 27.49 (br s), 9.87 (br s), 8.69 (br s), 7.82 (br s), 5.07 (br s), 4.82 (br s), 3.60 (s), 1.77 (s), −0.99 (br s), −1.08 (br s), −1.33 (br s) ppm. IR: $\tilde{\nu}$ 3064 (w), 2954 (Flu, Nujol), 2924 (Flu, Nujol), 2854 (Flu, Nujol), 2724 (vw), 2669 (vw), 1595 (w) 1564 (w), 1461 (Nujol), 1377 (Nujol), 1330 (s), 1296 (w), 1222 (m), 1198 (w), 1152 (w), 1119 (vw), 1016 (m), 986 (w), 973 (w), 917 (vw), 862 (m), 754 (vs), 725 (vs), 671 (vw), 564 (vw), 435 (w), 422 (w) cm^{-1}. Elemental analysis (%) calcd for $C_{25}H_{33}NdCl_2O_3$, (596.68 g mol^{-1}): C, 50.32; H, 5.57. Found: C, 38.84; H, 4.69. The deviation between theoretical and experimental values can be attributed in part to removal of coordinated THF under vacuum: calcd. $FluNdCl_2(THF)_0$: C 41.05, H 2.39. Although these results are still outside the range viewed as establishing analytical purity (C: −2.21%, H: +2.30%), they are provided to illustrate the best values obtained to date.

FluCeI$_2$(THF)$_3$ (1^{Ce,I}). CeI_3 (200.4 mg, 0.3848 mmol) and KFlu (78.6 mg, 0.3848 mmol) were suspended in THF (15 mL) and stirred for 3 d at ambient temperature. The mixture was filtered, and the filtrate was concentrated to yield yellow crystals of **1^{Ce,I}** (259.0 mg, 0.3682 mmol, 96%) at −40 °C suitable for XRD analysis. ^{1}H NMR (400.1 MHz, THF-d_8, 26 °C): δ 38.00 (s, 1H, Flu), 11.42 (s, 2H, Flu), 5.00 (s, 2H, Flu), 3.62 (m, 12H, THF), 2.51 (s, 2H, Flu), 2.32 (s, 2H, Flu), 1.77 (m, 12H, THF) ppm. DRIFT: $\tilde{\nu}$ 3028 (w), 2980 (s), 2885 (m), 1594 (w), 1475 (m), 1444 (m), 1346 (vw), 1326 (m), 1221 (w), 1198 (w), 1037 (vw), 1013 (vs), 924 (w), 880 (vs), 851 (vs), 830 (s), 757 (vs), 745 (s), 727 (s), 709 (w), 668 (w), 439 (w) cm^{-1}. Elemental analysis (%) calcd for $C_{21}H_{25}CeI_2O_2$, (703.35 g mol^{-1}): C, 35.86; H, 3.58. Found: C, 36.33; H, 4.29. Although these results are outside the range viewed as establishing analytical purity (C: +0.47%, H: +0.71%), they are provided to illustrate the best values obtained to date.

(Flu^{tBu})$_3$Ce(THF) (2). $CeCl_3(THF)_{1.04}$ (103.7 mg, 0.3276 mmol) and KFlu^{tBu} (105.3 mg, 0.3276 mmol) were suspended in THF (18 mL) and stirred for 2 d at ambient temperature. The mixture was filtered, and the filtrate was concentrated to yield yellow crystals of **2** (64.9 mg, 0.0621 mmol, 19%) at −40 °C suitable for XRD analysis. ^{1}H NMR (400.1 MHz, THF-d_8, 26 °C): δ 10.47 (s, 3H, Flu), 8.68 (s, 3H, Flu), 8.32 (s, 3H, Flu), 7.37 (s, 3H, Flu), 5.28 (s, 3H, Flu), 3.65 (m, 4H, THF), 2.82 (s, 3H, Flu), 1.81 (m, 4H, THF), 1.67 (s, 3H, Flu), 1.05 (s, 54H, *t*Bu) ppm. DRIFT: $\tilde{\nu}$ 2960 (vs), 2902 (m), 2866 (m), 1590 (s), 1479 (w), 1460 (w), 1392 (vw), 1361 (m), 1338 (m), 1305 (vw), 1260 (s), 1207 (w), 1086 (w), 908 (w), 864 (w), 802 (s), 745 (m), 729 (vs), 694 (vw), 671 (s), 653 (w) cm^{-1}. Elemental analysis (%) calcd for $C_{67}H_{83}CeO$, (1044.52 g mol^{-1}): C, 77.04; H, 8.01. Found: C, 76.82; H, 7.79.

FluCe(OC$_6$H$_3$*i*Pr$_2$-2,6)$_2$(THF)$_2$ (3^{OAr}). Compound **1^{Ce,Cl}** (53.7 mg, 0.0906 mmol) was dissolved in THF (10 mL), and Na(OC$_6$H$_3$*i*Pr$_2$-2,6) (36.3 mg, 0.181 mmol) was added at ambient temperature. The mixture was stirred for 18 h at ambient temperature. Then, the mixture was filtrated, the solution evaporated to dryness, and the residue extracted with toluene (10 mL). Upon concentration and storage at −40 °C, **3^{OAr}** was obtained as bright red crystals (59.5 mg, 0.0740 mmol, 82%). ^{1}H NMR (400.1 MHz, THF-d_8, 26 °C): δ 27.45 (s, 1H, FluH), 15.71 (s, 3H), 12.97 (d, J_{HH} = 5.9 Hz; 4H, *m*-Ar), 11.01 (s, 2H), 6.67 (s, 2H), 3.84 (s, 2H), 3.65 (m, 8H, THF), 3.48 (s, 12H, CH(CH_3)$_2$), 2.03 (s, 2H), 1.81 (m, 8H, THF), 0.74 (s, 2H), −0.07 (s, 2H) ppm. DRIFT: $\tilde{\nu}$ 2957 (s), 2863 (w), 1589 (w), 1460 (m), 1431 (vs), 1357 (w), 1324 (s), 1261 (vs), 1222 (w), 1203 (s), 1103 (vw), 1025 (m), 884 (m), 866 (m), 850 (s), 762 (m), 750 (s), 733 (w), 722 (w), 703 (vw), 691 (w), 565 (m) cm^{-1}. Elemental analysis (%) calcd for $C_{45}H_{59}CeO_4$, (804.08 g mol^{-1}): C, 67.22; H, 7.40. Found: C, 66.77; H, 6.89. Although these results are outside the range viewed as establishing analytical purity (C: −0.55%, H: −0.51%), they are provided to illustrate the best values obtained to date.

FluCeCp$_2$(THF) (3^{Cp}). Compound **1^{Ce,Cl}** (70.7 mg, 0.119 mmol) was dissolved in THF (12 mL), and NaCp (21.0 mg, 0.239 mmol) was added at −40 °C. The mixture was stirred for 18 h at −40 °C. The mixture was then filtrated at −40 °C, the solution was evaporated to dryness, and the residue was extracted with toluene (10 mL). Upon concentration and storage at −40 °C, **3^{Cp}** was obtained as orange crystals (41.3 mg, 0.0814 mmol, 68%) suitable for XRD analysis. ^{1}H NMR (400.1 MHz, THF-d_8, 26 °C): δ 26.41 (s, 1H, FluH), 10.05 (s, 10H, CpH), 8.35 (s, 2H, Flu), 4.27 (s, 2H, Flu), 3.85 (s, 2H, Flu), 2.94 (s, 2H, Flu), −3.77 (s, 4H, THF), −7.82 (s, 4H, THF) ppm. DRIFT: $\tilde{\nu}$ 3039 (m), 2956 (m), 1590 (w), 1558 (vw), 1471 (w), 1444 (w), 1328 (m), 1224 (w), 1199 (w), 1016 (m), 985 (vw), 560 (w), 783 (s), 765 (s), 754 (vs), 728 (m), 567 (vw), 496 (vw), 443 (m), 421 (w) cm^{-1}. Elemental analysis (%) calcd for $C_{27}H_{27}CeO$, (507.63 g mol^{-1}): C, 63.88; H, 5.36. Found: C, 63.49; H, 5.21.

FluCe(OSiMe$_3$)$_2$(THF) (3^{OSiMe3}) and (Flu)$_2$Ce(OSiMe$_3$)(THF) (4^{OSiMe3}). Compound **1^{Ce,Cl}** (63.5 mg, 0.107 mmol) was dissolved in THF (10 mL), and $NaOSiMe_3$ (24.0 mg, 0.214 mmol) was added at ambient temperature. The mixture was stirred for 6 h while turning pale orange and evaporated to dryness, and subsequently, the residue was extracted with toluene (10 mL). Concentration and storage at −40 °C afforded orange crystals of **3^{OSiMe3}** (46.0 mg, 0.0828, 77%). The crystals proved not suitable for XRD analysis (amorphous or intergrown), but dark orange crystals of **4^{OSiMe3}** could be hand-picked among the bulk of **3^{OSiMe3}**. ^{1}H NMR (400.1 MHz, THF-d_8, 26 °C): δ 31.18 (s, 1H, Flu*H*), 12.14 (s, 1H), 11.91 (s, 6H), 10.84 (s, 18H, $SiMe_3$), 4.73 (s, 2H, Flu), 3.61 (m, THF), 1.77 (m, THF), −0.90 (s, 2H, Flu), −4.67 (s, 2H, Flu) ppm. Additional signals and integral mismatch is likely caused by the half-sandwich/sandwich complex equilibrium in solution. DRIFT: $\tilde{\nu}$ 3060 (w), 3038 (w), 2950 (s), 1590 (vw), 1473 (vw), 1446 (m), 1402 (w), 1325 (w), 1298 (vw), 1245 (s), 1019 (w), 1000 (w), 942 (vs), 889 (s), 836 (s), 737 (vs), 697 (vs), 673 (vs), 423 (m) cm^{-1}. Elemental analysis (%) calcd for $C_{23}H_{35}CeO_3Si_2$, (555.82 g mol^{-1}; **3^{OSiMe3}**): C, 49.70; H, 6.35. Found: C, 50.53; H, 6.38. Although these results are outside the range viewed as establishing analytical purity (C: +0.83%), they are provided to illustrate the best values obtained to date.

FluCe(O*t*Bu)$_2$(THF) (3^{OtBu}) and Flu$_2$Ce(O*t*Bu)(THF) (4^{OtBu}). Compound **1^{Ce,Cl}** (90.5 mg, 0.153 mmol) was dissolved in THF (12 mL), and NaO*t*Bu (29.4 mg, 0.306 mmol) was added at −40 °C. The mixture was stirred for 18 h at −40 °C, while the solution turned from orange to yellow. The mixture was then filtrated −40 °C, the solution was evaporated to dryness, and the residue was extracted with toluene (10 mL). Upon concentration and storage at −40 °C, **3^{OtBu}** was obtained as yellow crystals (55.8 mg, 0.107 mmol, 70%). The crystals proved not suitable for XRD (amorphous), but orange crystals of **4^{OtBu}** could be hand-picked among the bulk of **3^{OtBu}**. ^{1}H NMR (400.1 MHz, THF-d_8, 26 °C): δ 20.34 (s, 4H), 14.13 (s, 3H), 9.47 (s, 2H), 7.15 (s, 6H), 5.79 (s, 3H), 4.98 (s, 7H), −3.61 (s, 8H), −12.09 (s, 2H) ppm. DRIFT: $\tilde{\nu}$ 3039 (vw), 2962 (vs), 1589 (vs), 1469 (w), 1445 (w), 1355 (m), 1325 (m), 1222 (s), 1194 (vs), 1021 (vw), 980 (vs), 932 (s), 893 (w), 752 (s), 740 (m), 725 (m), 516 (m), 478 (m), 434 (w) cm^{-1}. Elemental analysis (%) calcd for $C_{25}H_{35}CeO_3$, (523.67 g mol^{-1}, **3^{OtBu}**): C, 57.34; H, 6.74. Found: C, 56.27; H, 7.59. Although these results are outside the range viewed as establishing analytical purity (C: −1.07%, H: +0.83%), they are provided to illustrate the best values obtained to date.

FluCe(Me$_2$Pz)$_2$(THF)$_2$ (3^{Pz}). Compound **1^{Ce,Cl}** (82.4 mg, 0.139 mmol) was dissolved in THF (10 mL), and KMe_2Pz (37.3 mg, 0.278 mmol) was added at −40 °C. The mixture was stirred for 6 h at −40 °C. The mixture was then filtrated at −40 °C, toluene (15 mL) was added, and the solution was concentrated. Storage at −40 °C yielded **3^{Pz}** as orange crystals (54.8 mg, 0.0857 mmol, 62%). ^{1}H NMR (400.1 MHz, THF-d_8, 26 °C): δ 12.54 (s, 2H), 11.77 (s, 1H), 7.86 (s, 2H), 6.21 (s, 4H), 5.83 (s, 12H, Pz(CH_3)$_2$), 3.65 (m, 12H, THF), 1.81 (m, 12H, THF) ppm. DRIFT: $\tilde{\nu}$ 3036 (m), 2980 (m), 2917 (m), 1591 (w), 1515 (vs), 1473 (m), 1429 (s), 1366 (vw), 1325 (s), 1222 (m),

https://doi.org/10.1021/acs.organomet.2c00029
Organometallics 2022, 41, 962−976

1198 (w), 1029 (s), 1007 (s), 986 (w), 959 (w), 920 (vw), 874 (s), 770 (m), 752 (vs), 731 (s), 724 (s), 693 (m), 433 (m) cm^{-1}. Elemental analysis (%) calcd for $C_{31}H_{39}CeN_4O_2$, (639.80 g mol^{-1}): C, 58.20; H, 6.14; N, 8.76. Found: C, 55.52; H, 6.09; N, 8.50. Although these results are outside the range viewed as establishing analytical purity (C: −2.68%), they are provided to illustrate the best values obtained to date.

$Flu_2Ce(Me_2Pz)$ (THF) (4^{Pz}). Compound $\mathbf{1}^{Ce,Cl}$ (109.3 mg, 0.1845 mmol) was dissolved in THF (12 mL), and KMe_2Pz (49.5 mg, 0.3689 mmol) was added at ambient temperature. The mixture was stirred for 6 h and filtrated, and the filtrate was evaporated to dryness. Upon extraction with toluene (12 mL), concentration, and storage at −40 °C, $\mathbf{4}^{Pz}$ was obtained as orange crystals (43.5 mg, 0.0682 mmol, 37%). ^{1}H NMR (400.1 MHz, THF-d_8, 26 °C): δ 12.60 (s, 1H, PzH), 7.82 (s, 4H, Flu), 7.32 (s, 6H, Flu), 5.85 (s, 6H, Flu), 5.37 (s, 2H, Flu), 3.91 (s, 6H, $Pz(CH_3)_2$), 3.65 (m, 4H, THF), 1.81 (m, 4H, THF) ppm. DRIFT: $\tilde{\nu}$ 3030 (m), 2919 (w), 1591 (m), 1516 (m), 1473 (m), 1443 (m), 1431 (s), 1326 (s), 1222 (m), 1199 (m), 1023 (w), 1003 (w), 986 (vw), 871 (w), 773 (w), 750 (vs), 729 (s), 692 (w), 432 (m), 422 (m) cm^{-1}. Elemental analysis (%) calcd for $C_{35}H_{33}CeN_2O$, (637.78 g mol^{-1}): C, 65.91; H, 5.22; N, 4.39. Found: C, 65.26; H, 5.72; N, 5.00. Although these results are outside the range viewed as establishing analytical purity (C: −0.65%, H: +0.50%, N: +0.61%), they are provided to illustrate the best values obtained to date.

$Flu_3Ce_3(SC_6H_2Me_3$-2,4,6)$_4Cl_3Li(THF)_2$ (5). Compound $\mathbf{1}^{Ce,Cl}$ (47.5 mg, 0.0802 mmol) was dissolved in THF (12 mL), and $Li(SC_6H_2Me_3$-2,4,6) (30.2 mg, 0.159 mmol) was added at ambient temperature. The mixture was stirred for 6 h and filtrated, and the filtrate was evaporated to dryness. Upon extraction with toluene (12 mL), concentration, and storage at −40 °C, **5** was obtained as yellow crystals (10.6 mg, 0.00596 mmol, 22%). Elemental analysis (%) calcd for $C_{83}H_{87}Ce_3Cl_3LiO_2S_4$, (1778.53 g mol^{-1}): C, 56.05; H, 4.93; S, 7.21. Found: C, 55.85; H, 5.27; S, 6.73.

$Ce(dipp)_3$ (6). $CeCl_3(THF)_{1.04}$ (81.4 mg, 0.253 mmol) and Kdipp (144.7 mg, 0.761 mmol) were suspended in THF (15 mL) and stirred for 20 h at ambient temperature. The red mixture was filtrated and evaporated to dryness, and the residue was extracted with toluene (15 mL). Upon concentration and storage at −40 °C, bright orange crystals of **6** (137.1 mg, 0.2308 mmol, 91%) suitable for XRD analysis had formed. ^{1}H NMR (400.1 MHz, THF-d_8, 26 °C): δ 17.94 (s, 6H, $CH(CH_3)_2$), 15.39 (s, 3H, *CH*-3), 3.17 (s, 18H, $CH(CH_3)_2$), 2.81 (s, 6H, $CH_{terminal}$), −6.79 (s, 18H, $CH(CH_3)_2$), −7.39 (s, 6H, $CH_{terminal}$) ppm. DRIFT: $\tilde{\nu}$ 3088 (w), 2962 (vs), 2924 (m), 2866 (m), 1556 (w), 1528 (w), 1453 (s), 1375 (m), 1358 (s), 1326 (w), 1228 (vw), 1163 (w), 1148 (w), 1087 (m), 906 (vw), 798 (s), 769 (s), 652 (w), 596 (w) cm^{-1}. Elemental analysis (%) calcd for $C_{33}H_{57}Ce$, (593.94 g mol^{-1}): C, 66.74; H. 9.67. Found: C, 66.29; H, 9.57. Alternative route to **6**: compound $\mathbf{1}^{Ce,Cl}$ (47.0 mg, 0.0793 mmol) was dissolved in THF (12 mL), and Kdipp (30.2 mg, 0.159 mmol) was added at ambient temperature. The mixture was stirred for 6 h and filtrated, and the filtrate was evaporated to dryness. Upon extraction of the residue with toluene (12 mL), concentration, and storage at −40 °C, **6** was obtained as bright orange crystals (30.5 mg, 0.0514 mmol, 65%).

$(C_5Me_5)CeCl_2(THF)_3$. $Cp^*Ce(AlMe_4)_2$ (100 mg, 0.22 mmol) was dissolved in *n*-hexane (5 mL), and Me_3GeCl (85.2 mg, 0.56 mmol) was added under vigorous stirring. A color change from intense to pale yellow was observed. After stirring the reaction mixture for 30 min, 2 mL of THF was added. After stirring the reaction mixture for another 10 min, the solvent was removed under vacuum, and the crude product was washed extensively with *n*-hexane to remove residual $AlMe_3$/THF adduct. The product was obtained as a light yellow powder (94.5 mg, 76%). ^{1}H NMR (400.1 MHz, THF-d_8, 26 °C): δ 3.60 (m, coord. THF), 3.38 (br s, 15H, C_5Me_5), 1.77 (m, coord. THF) ppm. IR: $\tilde{\nu}$ 2954 (Cp, Nujol), 2924 (Cp, Nujol), 2853 (Cp, Nujol), 2725 (w), 2669 (w), 2168 (vw), 1712 (vw), 1626 (vw), 1461 (Nujol), 1377 (Nujol), 1297 (w), 1243 (w), 1194 (w), 1069 (w), 1018 (vs), 913 (w), 865 (vs), 722 (vs), 692 (s), 671 (m), 580 (vw) cm^{-1}. Elemental analysis (%) calcd for $C_{22}H_{39}CeCl_2O_3$, (562.57 g mol^{-1}) C, 46.97; H, 6.99. Found: C, 40.91; H, 5.98. The deviation between theoretical and experimental values can be attributed to the removal of coordinated THF under vacuum. The loss of two THF molecules per cerium would afford calcd C 40.19, H 5.54. Although these results are then outside the range viewed as establishing analytical purity (C: +0.72%, H: +0.544%), they are provided to illustrate the best values obtained to date.

Reactivity toward Halogenating Reagents (cf., Table 2): Hexachloroethane. Compound $\mathbf{1}^{Ce,Cl}$ (20 mg, 0.034 mmol) was dissolved in THF (3 mL), and a solution of C_2Cl_6 (3.84 mg, 0.016 mmol) in THF (1 mL) was added under stirring at ambient temperature. Upon addition of C_2Cl_6, the solution showed a slow color change from yellow to light yellow over 5 min. After stirring the reaction mixture for 5 min, the solvent was removed under vacuum, and upon toluene extraction, 4.1 mg of an off-white solid was obtained. The ^{1}H NMR spectrum in C_6D_6 showed a mixture of 1,1′-bifluorene (38%), 9-chlorofluorene (34%), and fluorene (28%). The toluene extract was redissolved in THF and added to a THF solution of $\mathbf{1}^{Ce,Cl}$ (1 equiv). After stirring the reaction mixture for 5 min, the solvent was removed under vacuum, and upon toluene extraction, 7.8 mg of an off-white solid was obtained. The ^{1}H NMR spectrum in C_6D_6 showed a mixture of 1,1′-bifluorene (69%) and fluorene (31%).

Compound $\mathbf{1}^{Ce,Cl}$ (20 mg, 0.034 mmol) was dissolved in THF (3 mL), and a solution of C_2Cl_6 (1.92 mg, 0.008 mmol) in THF (1 mL) was added under stirring at ambient temperature. Upon addition of C_2Cl_6, the yellow solution showed no color change over 5 min. After stirring the reaction mixture for 5 min, the solvent was removed under vacuum, and upon toluene extraction, 3.4 mg of an off-white solid was obtained. The ^{1}H NMR spectrum in C_6D_6 showed a mixture of 1,1′-bifluorene (74%) and fluorene (26%).

Compound $\mathbf{1}^{Ce,Cl}$ (20 mg, 0.034 mmol) was dissolved in THF (3 mL), and a solution of C_2Cl_6 (9.75 mg, 0.041 mmol) in THF (1 mL) was added under stirring at ambient temperature. Upon addition of C_2Cl_6, the yellow solution turned colorless immediately. After stirring the reaction mixture for 5 min, the solvent was removed under vacuum, and upon toluene extraction, 5.3 mg of an off-white solid was obtained. The ^{1}H NMR spectrum in C_6D_6 showed a mixture of 9-chlorofluorene (75%) and fluorene (25%). The toluene extract was redissolved in THF and added to a THF solution of $\mathbf{1}^{Ce,Cl}$ (2 equiv). After stirring the reaction mixture for 5 min, the solvent was removed under vacuum, and upon toluene extraction, 6.5 mg of a light yellow solid was obtained. The ^{1}H NMR spectrum in C_6D_6 showed a mixture of 1,1′-bifluorene (72%) and fluorene (28%).

Compound $\mathbf{1}^{La,Cl}$ (20 mg, 0.034 mmol) was dissolved in THF (3 mL), and a solution of C_2Cl_6 (3.84 mg, 0.016 mmol) in THF (1 mL) was added under stirring at ambient temperature. No color change of the orange solution was observed upon addition of C_2Cl_6. After stirring the reaction mixture for 5 min, the solvent was removed under vacuum. Upon toluene extraction, 3.9 mg of a colorless solid was obtained. The ^{1}H NMR spectrum in C_6D_6 showed a mixture of 1,1′-bifluorene (58%), 9-chlorofluorene (21%), and fluorene (21%).

Compound $\mathbf{1}^{La,Cl}$ (20 mg, 0.034 mmol) was dissolved in THF (3 mL), and a solution of C_2Cl_6 (9.77 mg, 0.041 mmol) in THF (1 mL) was added under stirring at ambient temperature. The orange reaction solution turned pink instantly and adopted a pale yellow color after stirring for 5 min. Then, the solvent was removed under vacuum, and upon toluene extraction, 7.2 mg of a colorless solid was obtained. The ^{1}H NMR spectrum in C_6D_6 showed a mixture of 9-chlorofluorene (70%), fluorene (28%), and 1,1′-bifluorene (2%). A solution of $\mathbf{1}^{La,Cl}$ (5 mg, 85 μmol, 0.4 mL) and C_2Cl_6 (0.96 mg, 41 μmol, 0.1 mL) in THF-d_8 precooled to −40 °C was prepared in an equally cold J.Young-valved NMR tube. After sealing the NMR tube and cooling to −78 °C, within 10 min, an EPR measurement was performed. At the start of the measurement, the solution displayed a bright pink color, but a signal assignable to the fluorenyl radical was not observed.

Compound $\mathbf{1}^{Nd,Cl}$ (20 mg, 0.034 mmol) was dissolved in THF (3 mL), and a solution of C_2Cl_6 (3.84 mg, 0.016 mmol) in THF (1 mL) was added under stirring at ambient temperature. The orange reaction solution turned pink instantly and adopted a pale yellow color after stirring for 5 min. Then, the solvent was removed under vacuum, and upon toluene extraction, 5.4 mg of a colorless solid was obtained. The

https://doi.org/10.1021/acs.organomet.2c00029
Organometallics 2022, 41, 962−976

^{1}H NMR spectrum in C_6D_6 showed a mixture of fluorene (43%), 9-chlorofluorene (41%), and 1,1′-bifluorene (16%).

Compound $\mathbf{1}^{Nd,Cl}$ (20 mg, 0.034 mmol) was dissolved in THF (3 mL), and a solution of C_2Cl_6 (9.68 mg, 0.041 mmol) in THF (1 mL) was added under stirring at ambient temperature. The reaction solution showed a color transition from orange over pink to bright yellow within 30 s and adopted a pale yellow color after stirring for 5 min. Then, the solvent was removed under vacuum, and upon toluene extraction, 6.1 mg of a colorless solid was obtained. The ^{1}H NMR spectrum in C_6D_6 showed a mixture of 9-chlorofluorene (60%), fluorene (40%), and 1,1′-bifluorene (<1%).

Compound **LiFlu(THF)$_3$** (20 mg, 0.052 mmol) was dissolved in THF (3 mL), and a solution of C_2Cl_6 (5.85 mg, 0.025 mmol) in THF (1 mL) was added under stirring at ambient temperature. Upon addition of C_2Cl_6, the solution showed a slow color change from orange to a dark green-brown. After stirring the reaction mixture for 5 min, the solvent was removed under vacuum, and upon toluene extraction, 26.4 mg of a dark red-brown solid was obtained. The ^{1}H NMR spectrum in C_6D_6 showed a mixture of 1,1′-bifluorene (70%) and fluorene (30%).

Compound **LiFlu(THF)$_3$** (20 mg, 0.052 mmol) was dissolved in THF (3 mL), and a solution of C_2Cl_6 (14.87 mg, 0.063 mmol) in THF (1 mL) was added under stirring at ambient temperature. Upon addition of C_2Cl_6, the reaction turned yellow instantly. After stirring the reaction mixture for 5 min, the solvent was removed under vacuum, and upon toluene extraction, 20.4 mg of an off-white solid was obtained. The ^{1}H NMR spectrum in C_6D_6 showed a mixture of 1,1′-bifluorene (81%), 9-chlorofluorene (10%), and fluorene (9%).

Compound **KFlu** (20 mg, 0.098 mmol) was dissolved in THF (3 mL), and a solution of C_2Cl_6 (11.12 mg, 0.047 mmol) in THF (1 mL) was added under stirring at ambient temperature. Upon addition of C_2Cl_6, the solution showed a slow color change from orange over dark red to a dark yellow-brown. After stirring the reaction mixture for 5 min, the solvent was removed under vacuum, and upon toluene extraction, 10.4 mg of a bright orange solid was obtained. The ^{1}H NMR spectrum in C_6D_6 showed a mixture of fluorene (84%), 9-chlorofluorene (9%), and 1,1′-bifluorene (7%).

Compound **KFlu** (20 mg, 0.098 mmol) was dissolved in THF (3 mL), and a solution of C_2Cl_6 (28.27 mg, 0.12 mmol) in THF (1 mL) was added under stirring at ambient temperature. Upon addition of C_2Cl_6, the solution turned yellow instantly and adopted a dark yellow color after stirring for 5 min. Then, the solvent was removed under vacuum, and upon toluene extraction, 18.0 mg of a brown solid was obtained. The ^{1}H NMR spectrum in C_6D_6 showed a mixture of fluorene (79%), 9-chlorofluorene (17%), and 1,1′-bifluorene (4%).

Reactivity toward Halogenating Reagents: Benzyl Chloride. Compound $\mathbf{1}^{Ce,Cl}$ (17.4 mg, 0.0294 mmol) was dissolved in THF (2 mL), and a solution of benzyl chloride (3.7 mg, 0.0294 mmol) in THF (1 mL) was added at ambient temperature. The reaction turned pale yellow instantly. The solvent was removed under reduced pressure, and the ^{1}H NMR spectrum revealed 9-benzylfluorene as the only product in quantitative yield after toluene extraction.

Reactivity toward Halogenating Reagents: Iodine. Compound $\mathbf{1}^{Ce,Cl}$ (34.8 mg, 0.0587 mmol) was dissolved in THF (3 mL), and a solution of I_2 (7.5 mg, 0.0294 mmol) in THF (1 mL) was added at ambient temperature. The reaction turned pale yellow instantly, and a colorless precipitation occurred ($CeCl_3(THF)_x$). Upon solvent removal and toluene extraction, a pale yellow solid was obtained in quantitative yield, which was analyzed as 1,1′-bifluorene.

Reactivity toward Halogenating Reagents: Tellurium(IV) Bromide. Compound $\mathbf{1}^{Ce,Cl}$ (29.9 mg, 0.0505 mmol) was dissolved in THF (3 mL), and a solution of $TeBr_4$ (5.6 mg, 0.0126 mmol) in THF (2 mL) was added at ambient temperature. The reaction turned yellow instantly, and a black precipitation (Te(0)) occurred. The ^{1}H NMR spectrum revealed a mixture of 1,1′-bifluorene, 9-bromofluorene, and fluorene. The obtained crystals were analyzed by XRD as $CeBr_3(THF)_3$.

■ ASSOCIATED CONTENT

Supporting Information

The Supporting Information is available free of charge at https://pubs.acs.org/doi/10.1021/acs.organomet.2c00029.

NMR and IR spectra of compounds **1**−**6**, ^{1}H NMR spectra of reactions with oxidants, collection of crystallographic data, crystal structures (PDF)

Accession Codes

CCDC 2141911−2141924 and 2156077 contain the supplementary crystallographic data for this paper. These data can be obtained free of charge via www.ccdc.cam.ac.uk/data_request/cif, or by emailing data_request@ccdc.cam.ac.uk, or by contacting The Cambridge Crystallographic Data Centre, 12 Union Road, Cambridge CB2 1EZ, UK; fax: +44 1223 336033.

■ AUTHOR INFORMATION

Corresponding Author

Reiner Anwander − *Institut für Anorganische Chemie, Eberhard Karls Universität Tübingen, 72076 Tübingen, Germany;* orcid.org/0000-0002-1543-3787; Email: reiner.anwander@uni-tuebingen.de

Authors

Lars Hirneise − *Institut für Anorganische Chemie, Eberhard Karls Universität Tübingen, 72076 Tübingen, Germany;* orcid.org/0000-0003-2715-9882

Dennis A. Buschmann − *Institut für Anorganische Chemie, Eberhard Karls Universität Tübingen, 72076 Tübingen, Germany*

Cäcilia Maichle-Mössmer − *Institut für Anorganische Chemie, Eberhard Karls Universität Tübingen, 72076 Tübingen, Germany;* orcid.org/0000-0001-7638-1610

Complete contact information is available at: https://pubs.acs.org/10.1021/acs.organomet.2c00029

Author Contributions

†L.H. and D.A.B. contributed equally.

Notes

The authors declare no competing financial interest.

■ ACKNOWLEDGMENTS

We thank the NMR section of the Institute of Organic Chemistry at EKUT for the EPR measurements.

■ REFERENCES

(1) Kalsotra, B. L.; Multani, R. K.; Jain, B. D. Studies on tetrafluorenyl cerium(IV). *J. Inorg. Nucl. Chem.* **1972**, *34*, 2679−2680.

(2) Deacon, G. B.; Tuong, T. D.; Vince, D. G. Refutation of the synthesis of tetrakis(cyclopentadienyl)cerium(IV). *Polyhedron* **1983**, *2*, 969−970.

(3) Evans, W. J.; Gummersheimer, T. S.; Boyle, T. J.; Ziller, J. W. Synthesis and Structure of New Soluble Organosamarium(II) Reagents: $(Indenyl)_2Sm(THF)$ and $(Fluorenyl)_2Sm(THF)_2$. *Organometallics* **1994**, *13*, 1281−1284.

(4) (a) Lee, M. H.; Hwang, J.-W.; Kim, Y.; Kim, J.; Han, Y.; Do, Y. The First Fluorenyl ansa-Yttrocene Complexes: Synthesis, Structures, and Polymerization of Methyl Methacrylat. *Organometallics* **1999**, *18*, 5124−5129. (b) Eppinger, J.; Spiegler, M.; Hieringer, W.; Herrmann, W. A.; Anwander, R. C_2-Symmetric ansa-Lanthanidocene Complexes. Synthesis via Silylamine Elimination and β-SiH Agostic Rigidity. *J. Am. Chem. Soc.* **2000**, *122*, 3080−3096. (c) Qian, C.; Nie, W.; Sun, J. C_s-Symmetric ansa-Lanthanocenes Designed for Stereospecific Polymerization of Methyl Methacrylate. Synthesis and Structural

Characterization of Silylene-Bridged Fluorenyl Cyclopentadienyl Lanthanide Halides, Amides, and Hydrocarbyls. *Organometallics* **2000**, *19*, 4134−4140. (d) Qian, C.; Nie, W.; Chen, Y.; Sun, J. Synthesis and crystal structure of one carbon-atom bridged lutetium complex $[Ph_2C(Flu)(Cp)]LuN(TMS)_2$ and catalytic activity for polymerization of polar monomers. *J. Organomet. Chem.* **2002**, *645*, 82−86. (e) Dash, A. K.; Razavi, A.; Mortreux, A.; Lehmann, C. W.; Carpentier, J.-F. Amine Elimination Reactions between Homoleptic Silylamide Lanthanide Complexes and an Isopropylidene-Bridged Cyclopentadiene−Fluorene System. *Organometallics* **2002**, *21*, 3238−3249. (f) Kirillov, E.; Toupet, L.; Lehmann, C. W.; Razavi, A.; Kahlal, S.; Saillard, J.-Y.; Carpentier, J.-F. $[(Cp\text{-}CMe_2\text{-}Flu)_2]^-[Li(ether)_n]^+$ (Ln = Y, La): Complexes with Unusual Coordination Modes of the Fluorenyl Ligand and the First Examples of Bis-Ansa Lanthanidocenes. *Organometallics* **2003**, *22*, 4038−4046. (g) Kirillov, E.; Lehmann, C. W.; Razavi, A.; Carpentier, J.-F. Synthesis, Structure, and Polymerization Activity of Neutral Halide, Alkyl, and Hydrido Yttrium Complexes of Isopropylidene-Bridged Cyclopentadienyl-Fluorenyl Ligands. *Organometallics* **2004**, *23*, 2768−2777. (h) Kirillov, E.; Lehmann, C. W.; Razavi, A.; Carpentier, J.-F. Highly Syndiospecific Polymerization of Styrene Catalyzed by Allyl Lanthanide Complexes. *J. Am. Chem. Soc.* **2004**, *126*, 12240−12241. (i) Rodrigues, A.-S.; Kirillov, E.; Lehmann, C. W.; Roisnel, T.; Vuillemin, B.; Razavi, A.; Carpentier, J.-F. Allyl ansa-Lanthanidocenes: Single-Component, Single-Site Catalysts for Controlled Syndiospecific Styrene and Styrene−Ethylene (Co)Polymerization. *Chem.—Eur. J.* **2007**, *13*, 5548−5565. (j) Cortial, G.; Le Goff, X.-F.; Bousquié, M.; Boisson, C.; Le Floch, P.; Nief, F.; Thuilliez, J. Neutral ansa-bis(fluorenyl)silane neodymium borohydrides: synthesis, structural study and behaviour as catalysts in butadiene−ethylene copolymerisation. *New J. Chem.* **2010**, *34*, 2290−2297. (k) Wang, C.; Xiang, L.; Leng, X.; Chen, Y. Synthesis and Structure of Silicon-Bridged Boratabenzene Fluorenyl Rare-Earth Metal Complexes. *Organometallics* **2016**, *35*, 1995−2002. (l) Wang, C.; Xiang, L.; Leng, X.; Chen, Y. Rare-earth metal hydrides supported by silicon-bridged boratabenzene fluorenyl ligands: synthesis, structure and reactivity. *Dalton Trans.* **2017**, *46*, 1218−1227. (m) Laur, E.; Louyriac, E.; Dorcet, V.; Welle, A.; Vantomme, A.; Miserque, O.; Brusson, J.-M.; Maron, L.; Carpentier, J.-F.; Kirillov, E. Substitution Effects in Highly Syndioselective Styrene Polymerization Catalysts Based on Single-Component Allyl ansa-Lanthanidocenes: An Experimental and Theoretical Study. *Macromolecules* **2017**, *50*, 6539−6551.

(5) (a) Kirillov, E.; Toupet, L.; Lehmann, C. W.; Razavi, A.; Carpentier, J.-F. Constrained Geometry Group 3 Metal Complexes of the Fluorenyl-Based Ligands $[(3,6\text{-}tBu_2Flu)SiR_2NtBu]$: Synthesis, Structural Characterization, and Polymerization Activity. *Organometallics* **2003**, *22*, 4467−4479. (b) Downing, S. P.; Guadaño, S. C.; Pugh, D.; Danopoulos, A. A.; Bellabarba, R. M.; Hanton, M.; Smith, D.; Tooze, R. P. Indenyl- and Fluorenyl-Functionalized N-Heterocyclic Carbene Complexes of Titanium, Zirconium, Vanadium, Chromium, and Yttrium. *Organometallics* **2007**, *26*, 3762−3770. (c) Wang, B.; Cui, D.; Lv, K. Highly 3,4-Selective Living Polymerization of Isoprene with Rare Earth Metal Fluorenyl N-Heterocyclic Carbene Precursors. *Macromolecules* **2008**, *41*, 1983−1988. (d) Jian, Z.; Cui, D.; Hou, Z. Rare-Earth-Metal−Hydrocarbyl Complexes Bearing Linked Cyclopentadienyl or Fluorenyl Ligands: Synthesis, Catalyzed Styrene Polymerization, and Structure−Reactivity Relationship. *Chem.—Eur. J.* **2012**, *18*, 2674−2684. (e) Jian, Z.; Petrov, A. R.; Hangaly, N. K.; Li, S.; Rong, W.; Mou, Z.; Rufanov, K. A.; Harms, K.; Sundermeyer, J.; Cui, D. Phosphazene-Functionalized Cyclopentadienyl and Its Derivatives Ligated Rare-Earth Metal Alkyl Complexes: Synthesis, Structures, and Catalysis on Ethylene Polymerization. *Organometallics* **2012**, *31*, 4267−4282. (f) Yao, C.; Wu, C.; Wang, B.; Cui, D. Copolymerization of Ethylene with 1-Hexene and 1-Octene Catalyzed by Fluorenyl N-Heterocyclic Carbene Ligated Rare-Earth Metal Precursors. *Organometallics* **2013**, *32*, 2204−2209. (g) Deng, M.; Chi, S.; Luo, Y. Rare-earth metal bis(alkyl) complexes bearing pyrrolidinyl-functionalized cyclopentadienyl, indenyl and fluorenyl ligands: synthesis, characterization and the ligand effect on isoprene polymerization. *New J. Chem.* **2015**, *39*, 7575−7581. (h) Lin, F.; Wang, X.; Pan, Y.; Wang, M.; Liu, B.; Luo, Y.; Cui, D. Nature of the Entire Range of Rare Earth Metal-Based Cationic Catalysts for Highly Active and Syndioselective Styrene Polymerization. *ACS Catal.* **2016**, *6*, 176−185.

(6) Giesbrecht, G. R.; Gordon, J. C.; Clark, D. L.; Scott, B. L. Crystallographic report: (η^5-Fluorenyl)-tris-pyridine-di-iodo-lanthanum(III) and -neodymium(III). *Appl. Organomet. Chem.* **2005**, *19*, 98−99.

(7) Diether, D.; Tyulyunov, K.; Maichle-Mössmer, C.; Anwander, R. Fluorenyl Half-Sandwich Bis(tetramethylaluminate) Complexes of the Rare-Earth Metals: Synthesis, Structure, and Isoprene Polymerization. *Organometallics* **2017**, *36*, 4649−4659.

(8) (a) Li, X.; Wang, X.; Tong, X.; Zhang, H.; Chen, Y.; Liu, Y.; Liu, H.; Wang, X.; Nishiura, M.; He, H.; Lin, Z.; Zhang, S.; Hou, Z. Aluminum Effects in die Syndiospecific Copolymerization of Styrene with Ethylene by Cationic Fluorenyl Scandium Alkyl Catalysts. *Organometallics* **2013**, *32*, 1445−1458. (b) Du, G.; Long, Y.; Xue, J.; Zhang, S.; Dong, Y.; Li, X. 1,4-Selective Polymerization of 1,3-Cyclohexadiene and Copolymerization with Styrene by Cationic Half-Sandwich Fluorenyl Rare Earth Metal Alkyl Catalysts. *Macromolecules* **2015**, *48*, 1627−1635.

(9) Sun, J.; Berg, D. J.; Twamley, B. Supersize Cp! Tetrabenzo-[a,c,g,i]fluorenyl complexes of yttrium. *Can. J. Chem.* **2017**, *95*, 363−370.

(10) Piro, N. A.; Robinson, J. R.; Walsh, P. J.; Schelter, E. J. The electrochemical behavior of cerium(III/IV) complexes: Thermodynamics, kinetics and applications in synthesis. *Coord. Chem. Rev.* **2014**, *260*, 21−36.

(11) Anwander, R.; Dolg, M.; Edelmann, F. T. The difficult search for organocerium(IV) compounds. *Chem. Soc. Rev.* **2017**, *46*, 6697−6709.

(12) Dröse, P.; Crozier, A. R.; Lashkari, S.; Gottfriedsen, J.; Blaurock, S.; Hrib, C. G.; Maichle-Mössmer, C.; Schädle, C.; Anwander, R.; Edelmann, F. T. Facile Access to Tetravalent Cerium Compounds: One-Electron Oxidation Using Iodine(III) Reagents. *J. Am. Chem. Soc.* **2010**, *132*, 14046.

(13) Schneider, D.; Harmgarth, N.; Edelmann, F. T.; Anwander, R. Ceric Cyclopentadienides Bearing Alkoxy, Aryloxy, Chlorido, or Iodido Co-Ligands. *Chem.—Eur. J.* **2017**, *23*, 12243−12252.

(14) Hirneise, L.; Langmann, J.; Zitzer, G.; Ude, L.; Maichle-Mössmer, C.; Scherer, W.; Speiser, B.; Anwander, R. Tuning Organocerium Electrochemical Potentials by Extending Tris(cyclopentadienyl) Scaffolds with Terminal Halogenido, Siloxy, and Alkoxy Ligands. *Organometallics* **2021**, *40*, 1786−1800.

(15) Hirneise, L.; Maichle-Mössmer, C.; Anwander, R. Pentamethylcyclopentadienyl Complexes of Cerium(IV): Synthesis, Reactivity, and Electrochemistry. *Inorg. Chem.* **2021**, *60*, 18211−18224.

(16) Gassman, P. G.; Winter, C. H. Preparation, electrochemical oxidation, and XPS studies of unsymmetrical ruthenocenes bearing the pentamethylcyclopentadienyl ligand. *J. Am. Chem. Soc.* **1988**, *110*, 6130−6135.

(17) Tellers, D. M.; Skoog, S. J.; Bergman, R. G.; Gunnoe, T. B.; Harman, W. D. Comparison of the Relative Electron-Donating Abilities of Hydridotris(pyrazol)borate and Cyclopentadienyl Ligands: Different Interactions with Different Transition Metals. *Organometallics* **2000**, *19*, 2428−2432.

(18) Veiros, L. F. Haptotropic shifts in organometallic complexes with η^5-coordinated π ligands. *J. Organomet. Chem.* **1999**, *587*, 221−232.

(19) Nakamura, H.; Nakayama, Y.; Yasuda, H.; Maruo, T.; Kanehisa, N.; Kai, Y. Alternative η^5- and η^6-Bonding Modes for Bis(fluorenyl)-lanthanide Complexes by Reactions with AlR_3 and Succesive Addition of THF. *Organometallics* **2000**, *19*, 5392−5399.

(20) Veiros, L. F. Haptotropic Shifts in Cyclopentadienyl Organometallic Complexes: Ring Folding vs Ring Slippage. *Organometallics* **2000**, *19*, 5549−5558.

(21) Albright, T. A.; Hofmann, P.; Hoffmann, R.; Lillya, C. P.; Dobosh, P. A. Haptotropic rearrangements of polyene-MLn

https://doi.org/10.1021/acs.organomet.2c00029
Organometallics 2022, 41, 962−976

complexes. 2. Bicyclic polyene-MCp, $M(CO)_3$ systems. *J. Am. Chem. Soc.* **1983**, *105*, 3396−3411.
(22) Razavi, A.; Bellia, V.; De Brauwer, Y.; Hortmann, K.; Lambrecht, M.; Miserque, O.; Peters, L.; Van Belle, S. Syndiotactic and Isotactic Specific Metallocene Catalysts with Hapto-flexible Cyclopentadienyl-Fluorenyl Ligand. *Metalorganic Catalysts for Synthesis and Polymerization*; Springer: Berlin, Heidelberg, 1999; pp 236−247.
(23) Corbelin, S.; Kopf, J.; Weiss, E. Über Metallalkyl- und -arylverbindungen, 48 Monomeres, tetrameres und polymeres Natriumfluorenid S [S = $Me_2N(CH_2)_2N(Me)(CH_2)_2NMe_2$, $Me_2N(CH_2)_nNMe_2$ (n = 2, 3)]. *Chem. Ber.* **1991**, *124*, 2417−2422.
(24) Neander, S.; Körnich, J.; Olbrich, F. Novel fluorenyl alkali metal DIGLYME complexes: synthesis and solid state structures. *J. Organomet. Chem.* **2002**, *656*, 89−96.
(25) Neander, S.; Tio, F. E.; Buschmann, R.; Behrens, U.; Olbrich, F. Cyclopentadienyl, indenyl, fluorenyl, and pentamethylcyclopentadienyl complexes of potassium with 18-crown-6. *J. Organomet. Chem.* **1999**, *582*, 58−65.
(26) Harder, S.; Feil, F.; Repo, T. Alkaline-Earth Metals in a Box: Structures of Solvent-Separated Ion Pairs. *Chem.—Eur. J.* **2002**, *8*, 1991−1999.
(27) Panetti, G. B.; Sergentu, D.-C.; Gau, M. R.; Carroll, P. J.; Autschbach, J.; Walsh, P. J.; Schelter, E. J. Isolation and characterization of a covalent Ce^{IV}-Aryl complex with an anomalous ^{13}C chemical shift. *Nat. Commun.* **2021**, *12*, 1713.
(28) Kirillov, E.; Kahlal, S.; Roisnel, T.; Georgelin, T.; Saillard, J.-Y.; Carpentier, J.-F. Haptotropic Rearrangements in Sandwich (Fluorenyl)(Cyclopentadienyl) Iron and Ruthenium Complexes. *Organometallics* **2008**, *27*, 387−393.
(29) Brydges, S.; Reginato, N.; Cuffe, L. P.; Seward, C. M.; McGlinchey, M. J. High and low barriers to haptotropic shifts across polycyclic surfaces: the relevance of aromatic character during the migration process. *C. R. Chim.* **2005**, *8*, 1497−1505.
(30) Schlenk, W.; Bergmann, E. Forschungen auf dem Gebiete der alkaliorganischen Verbindungen. I. Über Produkte der Addition von Alkalimetal an mehrfache Kohlenstoff-Kohlenstoff-Bindungen. *Liebigs Ann.* **1928**, *463*, 1−97.
(31) Wenqi, C.; Guanyang, L.; Jusong, X.; Gecheng, W.; Yin, Z.; Zhongsheng, J. *J. Organomet. Chem.* **1994**, *467*, 75−78.
(32) Hazin, P. N.; Huffman, J. C.; Bruno, J. W. Synthetic and structural studies of pentamethylcyclopentadienyl complexes of lanthanum and cerium. *Organometallics* **1987**, *6*, 23−27.
(33) Evans, W. J.; Olofson, J. M.; Zhang, H.; Atwood, J. L. Synthesis and X-ray crystal structure of an unusual oligomeric bis(pentamethylcyclopentadienyl) halide complex of cerium: $[(C_5Me_5)_2CeCl_2K(THF)]_n$. *Organometallics* **1988**, *7*, 629−633.
(34) Evans, W. J.; Perotti, J. M.; Kozimor, S. A.; Champagne, T. M.; Davis, B. L.; Nyce, G. W.; Fujimoto, C. H.; Clark, R. D.; Johnston, M. A.; Ziller, J. W. Synthesis and Comparative η^1-Alkyl and Sterically Induced Reduction Reactivity of $(C_5Me_5)_3Ln$ Complexes of La, Ce, Pr, Nd, and Sm. *Organometallics* **2005**, *24*, 3916−3931.
(35) Guana, J.; Fischer, R. D. Tris(indenyl)lanthanoid Complexes (Ln = La, Pr, Nd) Containing either (S)-(−)-Nicotine or Two Simpler Pyridine Bases. *Eur. J. Inorg. Chem.* **2001**, 2497−2508. and references therein.
(36) Zazzetta, A.; Greco, A. The structure of triindenylcerium pyridinate. *Acta Crystallogr., Sect. B: Struct. Crystallogr. Cryst. Chem.* **1979**, *35*, 457−460.
(37) Heeres, H. J.; Renkema, J.; Booij, M.; Meetsma, A.; Teuben, J. H. Bis(pentamethylcyclopentadienyl) complexes of cerium(III). Crystal structure of $(C_5Me_5)_2CeCH(SiMe_3)_2$. *Organometallics* **1988**, *7*, 2495−2502.
(38) Diether, D.; Maichle-Mössmer, C.; Anwander, R. Implications of Indenyl Substitution for the Structural Chemistry of Rare-Earth Metal (Half-)Sandwich Complexes and Performance in Living Isoprene Polymerization. *Organometallics* **2019**, *38*, 3007−3017.
(39) Bayer, U.; Werner, D.; Berkefeld, A.; Maichle-Mössmer, C.; Anwander, R. Cerium−quinone redox couples put under scrutiny. *Chem. Sci.* **2021**, *12*, 1343−1351.
(40) Boyle, T. J.; Tribby, L. J.; Bunge, S. D. Synthesis and Structural Characterization of a Series of Carboxylic Acid Modified Cerium(III) Alkoxides. *Eur. J. Inorg. Chem.* **2006**, 4553−4563.
(41) Heeres, H. J.; Meetsma, A.; Teuben, J. H.; Rogers, R. D. Mono(pentamethylcyclopentadienyl) complexes of cerium(III). Synthesis, molecular structure, thermal stability, and reactivity of $(C_5Me_5)CeX_2$ (X = 2,6-di-tert-butylphenoxo, $CH(SiMe_3)_2$, and $N(SiMe_3)_2$) complexes. *Organometallics* **1989**, *8*, 2637−2646.
(42) Deacon, G. B.; Harika, R.; Junk, P. C.; Skelton, B. W.; Werner, D.; White, A. H. The Synthesis, Structures and Polymorphism of the Dimeric Trivalent Rare-Earth 3,5-Dimethylpyrazolate Complexes $[Ln(Me_2pz)_3(thf)]_2$. *Eur. J. Inorg. Chem.* **2014**, 2412−2419.
(43) Evans, W. J.; Ulibarri, T. A. Reactivity of $(C_5Me_5)_2Sm$ with cyclopentadiene and cyclopentadienide: isolation of the mixed-valence complex $(C_5Me_5)_2Sm(III)(\mu\text{-}C_5H_5)Sm(II)(C_5Me_5)_2$. *J. Am. Chem. Soc.* **1987**, *109*, 4292−4297.
(44) Trifonov, A. A.; Kirillov, E. N.; Dechert, S.; Schumann, H.; Bochkarev, M. N. Fluorenyl and ansa-Dimethylsilylbis(fluorenyl) Derivatives of Divalent Ytterbium and Samarium − Synthesis and Structure of the First Mixed-Ligand LnII Classic Sandwich Complex $(C_{13}H_9)(C_5Me_5)Yb(DME)$. *Eur. J. Inorg. Chem.* **2001**, 2509−2514.
(45) Gradeff, P. S.; Yunlu, K.; Deming, T. J.; Olofson, J. M.; Ziller, J. W.; Evans, W. J. Reactivity of ceric ammonium nitrate with sodium cyclopentadienide. The x-ray crystal structure of bis (dimethoxyethane) trinitratocerium. *Inorg. Chem.* **1989**, *28*, 2600−2604.
(46) Arachchige, S. M.; Heeg, M. J.; Winter, C. H. Synthesis and structural characterization of unsymmetrical osmocenes containing the pentamethylcyclopentadienyl ligand. *J. Organomet. Chem.* **2005**, *690*, 4356−4365.
(47) Fichtel, K.; Höxter, S.; Behrens, U. Strukturen von polaren Bariumorganylen: Synthese und Struktur von Ether-, Pyridin- und Kronenether-Addukten des Bis(fluorenyl)bariums. *Z. Anorg. Allg. Chem.* **2006**, *632*, 2003−2009.
(48) Werner, D.; Bayer, U.; Rad, N. E.; Junk, P. C.; Deacon, G. B.; Anwander, R. Unique and contrasting structures of homoleptic lanthanum(III) and cerium(III) 3,5-dimethylpyrazolates. *Dalton Trans.* **2018**, *47*, 5952−5955.
(49) Heeres, H. J.; Teuben, J. H.; Rogers, R. D. Novel monopentamethylcyclopentadienyl alkoxides of La and Ce; X-ray crystal structure of $(C_5Me_5Ce(OCMe_3)_2)_2$. *J. Organomet. Chem.* **1989**, *364*, 87−96.
(50) Gradeff, P. S.; Yunlu, K.; Deming, T. J.; Olofson, J. M.; Doedens, R. J.; Evans, W. J. Synthesis of Yttrium and Lanthanide Silyloxy Complexes from Anhydrous Nitrate and Oxo Alkoxide Precursors and the X-Ray Structure of $[Ce(OSiPh_3)_3(THF)_3](THF)$. *Inorg. Chem.* **1990**, *29*, 420−424.
(51) Mueller, T. J.; Ziller, J. W.; Evans, W. J. Sigma bond metathesis with pentamethylcyclopentadienyl ligands in sterically crowded $(C_5Me_5)_3M$ complexes. *Dalton Trans.* **2010**, *39*, 6767−6773.
(52) Raeder, J.; Reiners, M.; Baumgarten, R.; Münster, K.; Baabe, D.; Freytag, M.; Jones, P. G.; Walter, M. D. Synthesis and molecular structure of pentadienyl complexes of the rare-earth metals. *Dalton Trans.* **2018**, *47*, 14468−14482.
(53) (a) Evans, W. J.; Shreeve, J. L.; Ziller, J. W.; Doedens, R. J. Structural Diveristy in Solvated Lanthanide Halide Complexes. *Inorg. Chem.* **1995**, *34*, 576−585. (b) Deacon, G. B.; Feng, T.; Junk, P. C.; Skelton, B. W.; Sobolev, A. N.; White, A. H. Preparation and X-Ray Crystal Structures of Tetrahydrofuran-Complexed Rare Earth Chlorides − a Structurally Rich Series. *Aust. J. Chem.* **1998**, *51*, 75−89.
(54) Yin, H.; Carroll, P. J.; Manor, B. C.; Anna, J. M.; Schelter, E. J. Cerium Photosensitizers: Structure−Function Relationships and Applications in Photocatalytic Aryl Coupling Reactions. *J. Am. Chem. Soc.* **2016**, *138*, 5984−5993.
(55) Collin, J.; Namy, J. L.; Bied, C.; Kagan, H. B. Benzylsamarium Complexes and their Reactivity. *Inorg. Chim. Acta* **1987**, *140*, 29−30.

https://doi.org/10.1021/acs.organomet.2c00029
Organometallics 2022, 41, 962−976

(56) Trifonov, A. A.; Fedorova, E. A.; Fukin, G. K.; Druzhkov, N. O.; Bochkarev, M. N. C−C Coupling and C−H Bond Activation—Unexpected Pathways in the Reactions of $[Yb(\eta^5\text{-}C_{13}H_9)_2(thf)_2]$ with Diazadienes. *Angew. Chem., Int. Ed.* **2004**, *43*, 5045−5048.
(57) Gericke, R.; Doyle, L. M.; Farquhar, E. R.; McDonald, A. R. Oxo-Free Hydrocarbon Oxidation by an Iron(III)-Isoporphyrin Complex. *Inorg. Chem.* **2020**, *59*, 13952−13961.
(58) Sridevi, V. S.; Leong, W. K.; Zhu, Y. Catalytic Reductive Coupling of 9-Bromofluorene. *Organometallics* **2006**, *25*, 283−288.
(59) Al-Afyouni, M. H.; Huang, T. A.; Hung-Low, F.; Bradley, C. A. Synthesis of bifluorenes via cobalt halide radical coupling. *Tetrahedron Lett.* **2011**, *52*, 3261−3265.
(60) Panda, T. K.; Gamer, M. T.; Roesky, P. W. An Improved Synthesis of Sodium and Potassium Cyclopentadienide. *Organometallics* **2003**, *22*, 877−878.
(61) See, X. Y.; Beaumier, E. P.; Davis-Gilbert, Z. W.; Dunn, P. L.; Larsen, J. A.; Pearce, A. J.; Wheeler, T. A.; Tonks, I. A. Generation of TiII Alkyne Trimerization Catalysts in the Absence of Strong Metal Reductants. *Organometallics* **2017**, *36*, 1383−1390.
(62) Gawley, R. E.; Zhang, X.; Wang, Q. *Potassium Hydride*; John Wiley & Sons, Ltd., 2007; pp 1−5.
(63) Leis, C.; Zybill, C.; Lachmann, J.; Müller, G. Silylene complexes stabilized by sulphur substituents; a structure and reactivity study. *Polyhedron* **1991**, *10*, 1163−1171.
(64) Kozimor, S. A.; Bartlett, B. M.; Rinehart, J. D.; Long, J. R. Magnetic Exchange Coupling in Chloride-Bridged 5f−3d Heterometallic Complexes Generated via Insertion into a Uranium(IV) Dimethylpyrazolate Dimer. *J. Am. Chem. Soc.* **2007**, *129*, 10672−10674.
(65) Barisic, D.; Buschmann, D. A.; Schneider, D.; Maichle-Mössmer, C.; Anwander, R. Rare-Earth-Metal Pentadienyl Half-Sandwich and Sandwich Tetramethylaluminates−Synthesis, Structure, Reactivity, and Performance in Isoprene Polymerization. *Chem.—Eur. J.* **2019**, *25*, 4821−4832.
(66) Wooles, A. J.; Mills, D. P.; Lewis, W.; Blake, A. J.; Liddle, S. T. Lanthanide tri-benzyl complexes: structural variations and useful precursors to phosphorus-stabilised lanthanide carbenes. *Dalton Trans.* **2010**, *39*, 500−510.
(67) Dietrich, H. M.; Zapilko, C.; Herdtweck, E.; Anwander, R. $Ln(AlMe_4)_3$ as New Synthetic Precursors in Organolanthanide Chemistry: Efficient Access to Half-Sandwich Hydrocarbyl Complexes. *Organometallics* **2005**, *24*, 5767−5771.

https://doi.org/10.1021/acs.organomet.2c00029
Organometallics 2022, 41, 962−976

Supporting Information

Cerium Fluorenyl Complexes Including CC-Coupling Reactions

Lars Hirneise,[§] Dennis A. Buschmann,[§] Cäcilia Maichle-Mössmer, and Reiner Anwander*

*Institut für Anorganische Chemie, Eberhard Karls Universität Tübingen, Auf der Morgenstelle 18, 72076 Tübingen, Germany

Email: reiner.anwander@uni-tuebingen.de

Table of Contents

NMR spectra

* → solvent, # → small impurities

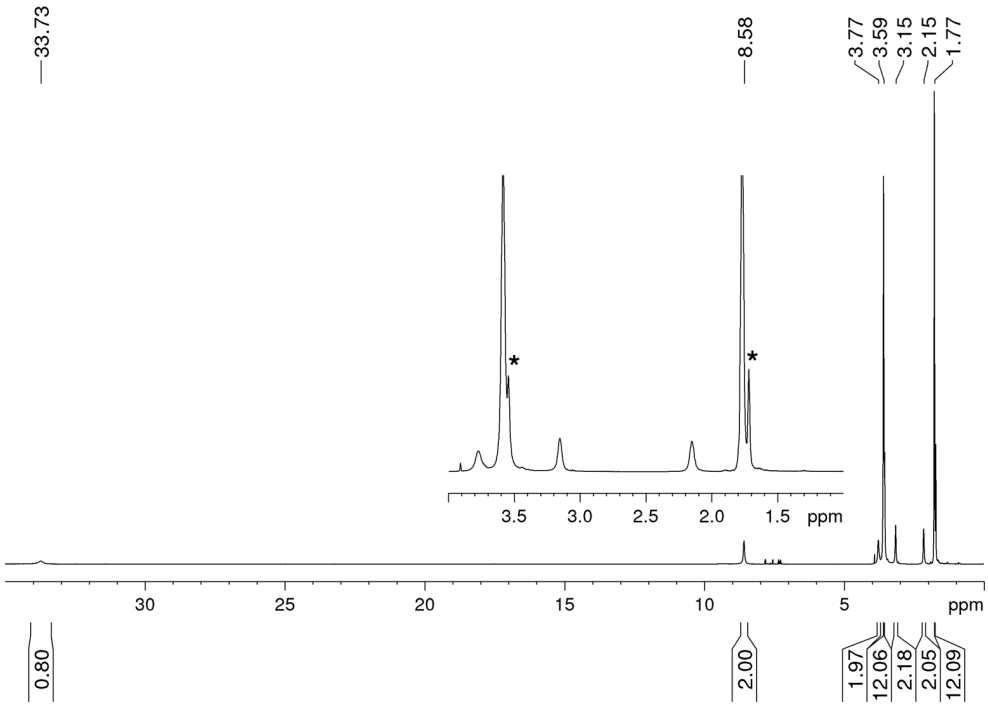

Figure S1. ^{1}H NMR spectrum (500.1 MHz, THF-d_8, 26 °C) of $FluCeCl_2(THF)_3$ (**1**^{Ce,Cl}).

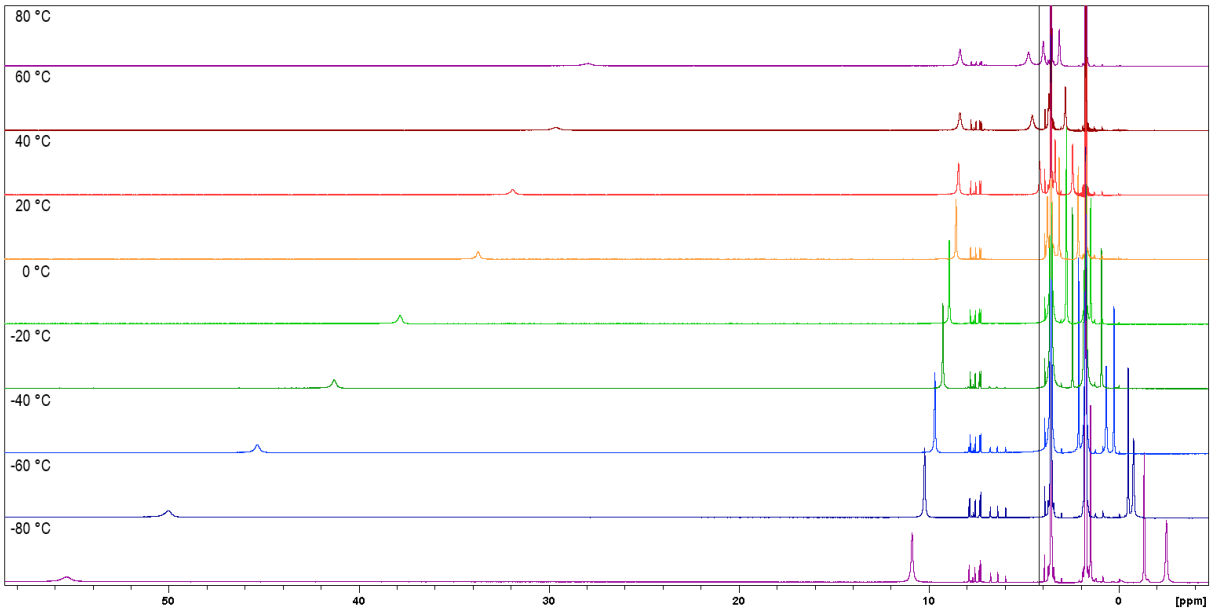

Figure S2. ^{1}H VT NMR spectrum (500.1 MHz, THF-d_8) from -80 °C to 80 °C of $FluCeCl_2(THF)_3$ (**1**^{Ce,Cl}).

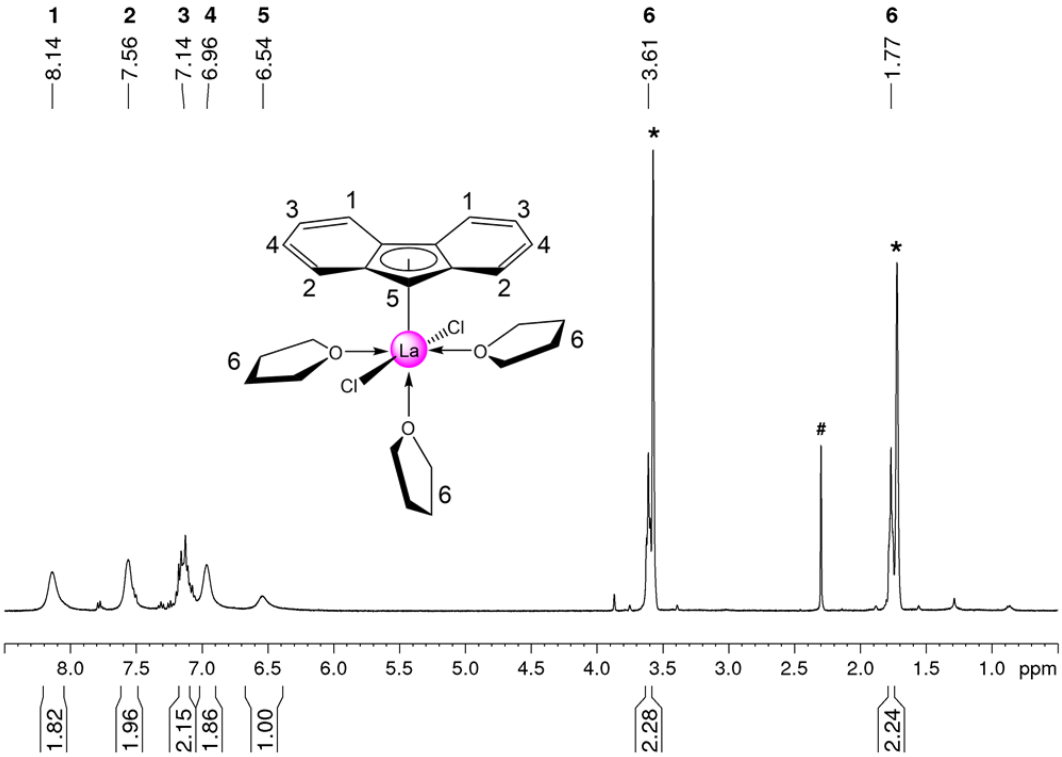

Figure S3. ^{1}H NMR spectrum (400.1 MHz, THF-d_8, 26 °C) of $FluLaCl_2(THF)_3$ (**1**^{La,Cl}). Solvent residual signals are marked with an asterisk (# toluene).

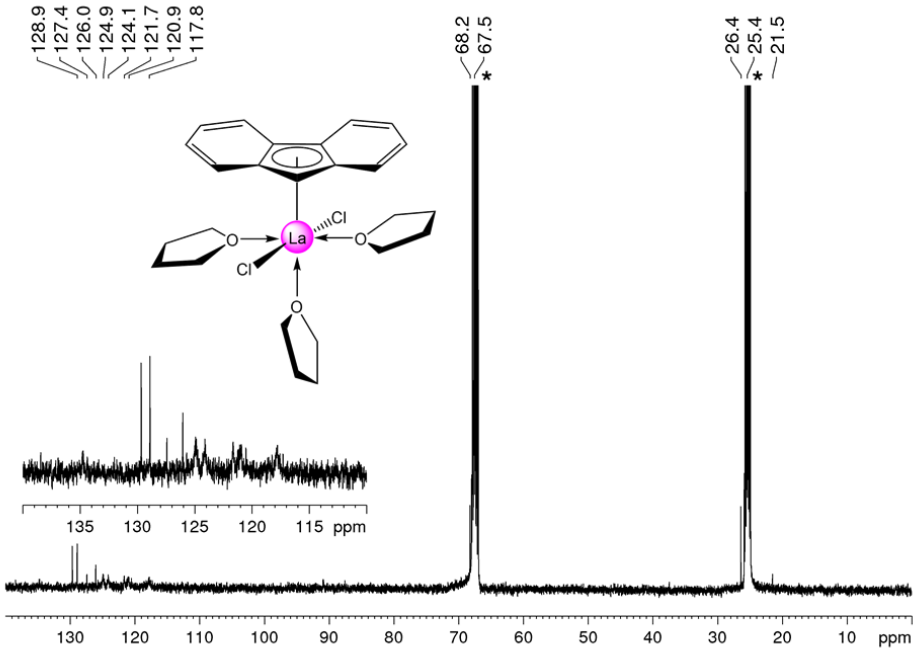

Figure S4. ^{13}C NMR spectrum (100.6 MHz, THF-d_8, 26 °C) of $FluLaCl_2(THF)_3$ (**1**^{La,Cl}). Solvent residual signals are marked with an asterisk.

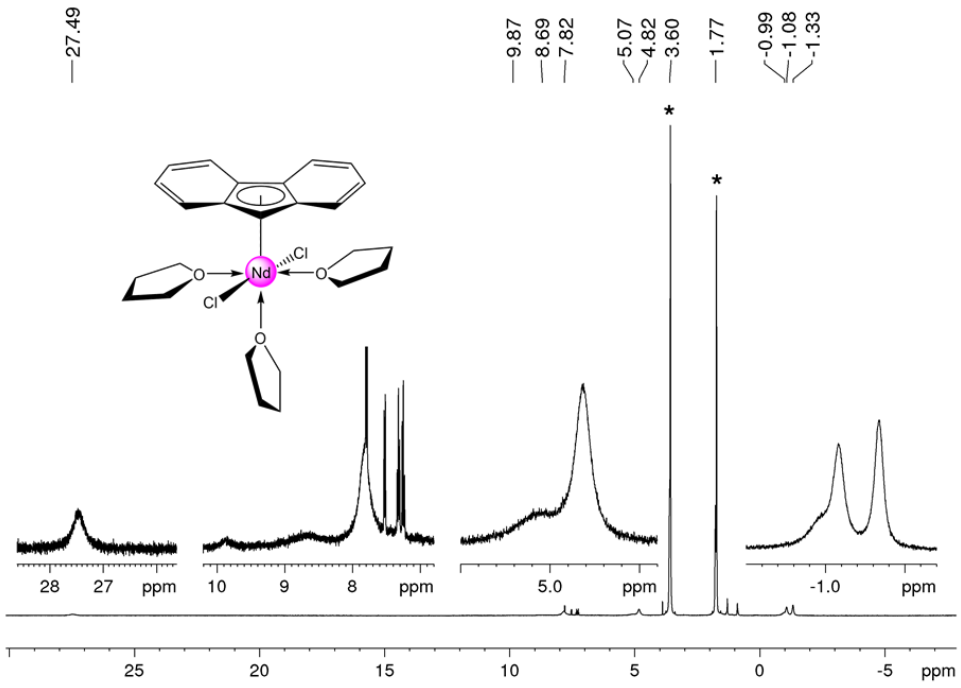

Figure S5. ^{1}H NMR spectrum (400.1 MHz, THF-d_8, 26 °C) of $FluNdCl_2(THF)_3$ (**1**^{Nd,Cl}). Solvent residual signals are marked with an asterisk.

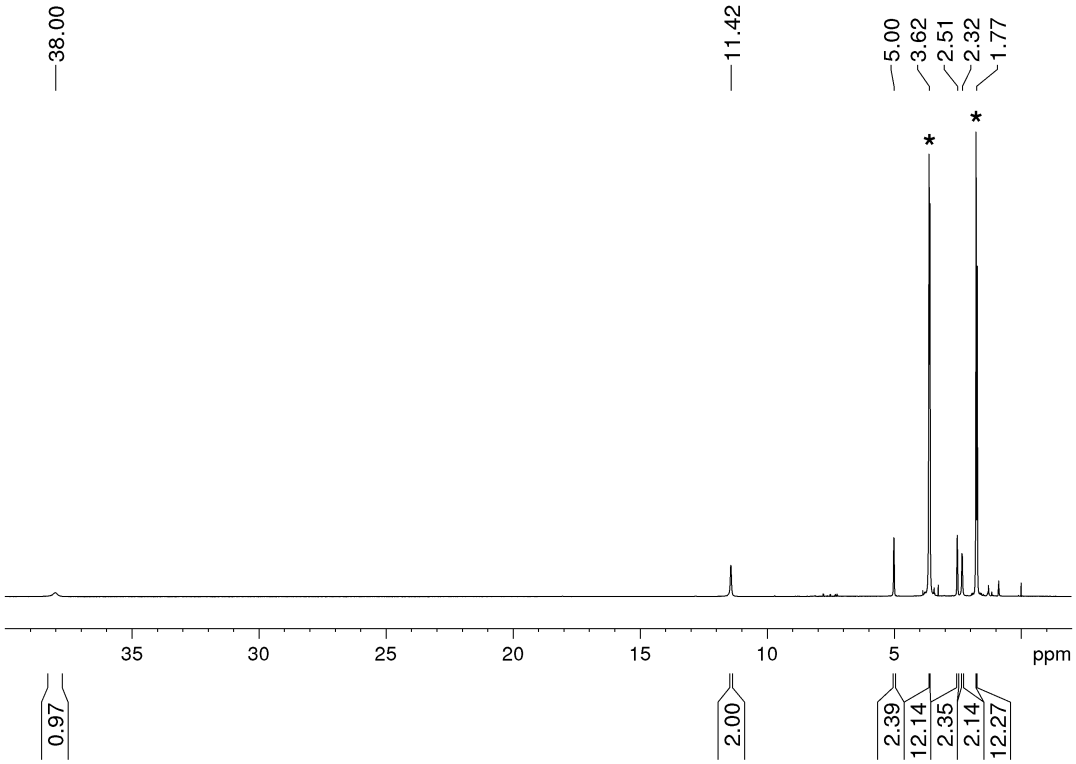

Figure S6. ^{1}H NMR spectrum (400.1 MHz, THF-d_8, 26 °C) of $FluCeI_2(THF)_3$ (**1**^{Ce,I}).

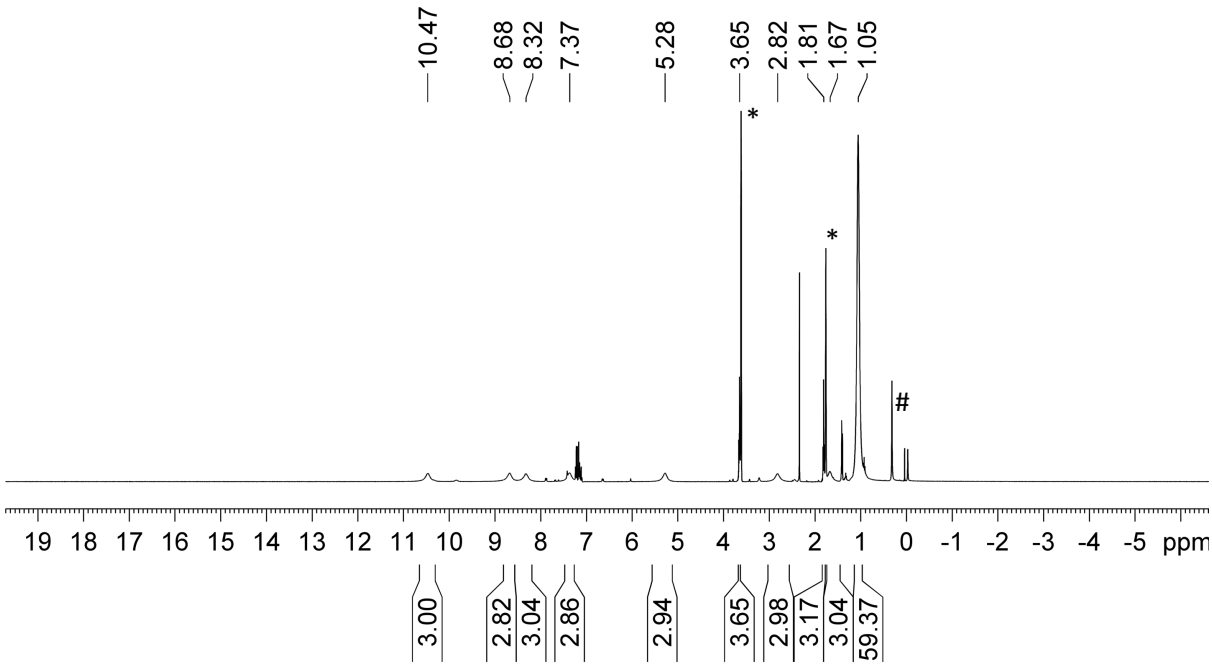

Figure S7. ^{1}H NMR spectrum (400.1 MHz, THF-d_8, 26 °C) of Flu$^{t\mathrm{Bu}}{}_3$Ce(THF) (**2**).

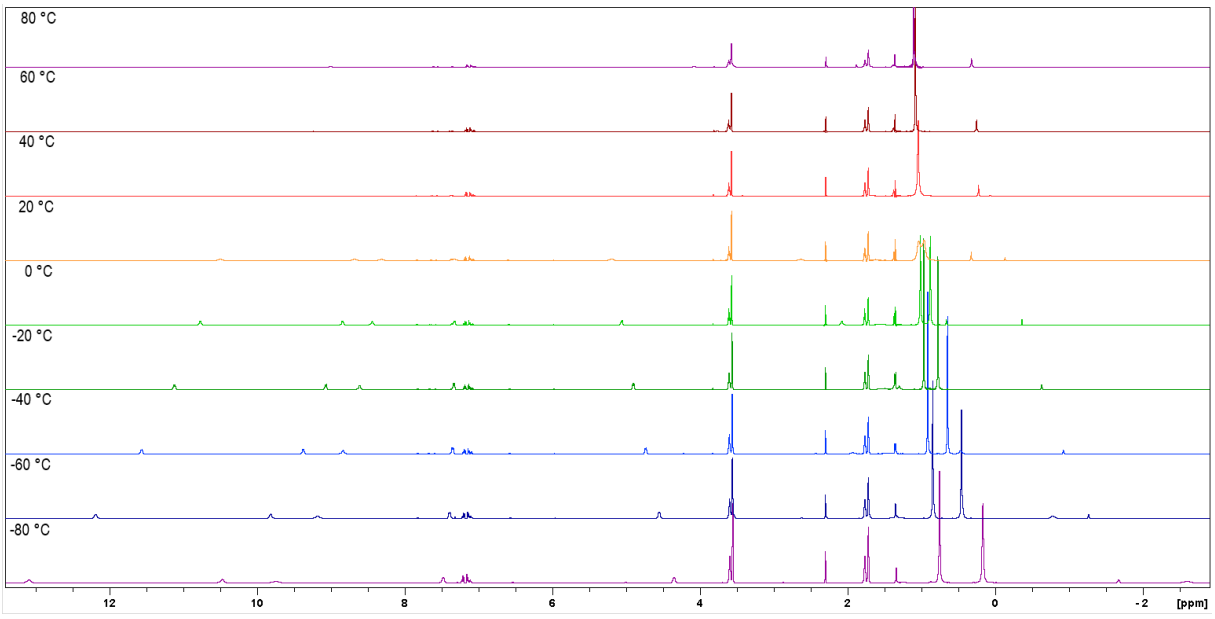

Figure S8. VT ^{1}H NMR spectrum (500.1 MHz, THF-d_8) from -80 °C to 80 °C of Flu$^{t\mathrm{Bu}}{}_3$Ce(THF) (**2**).

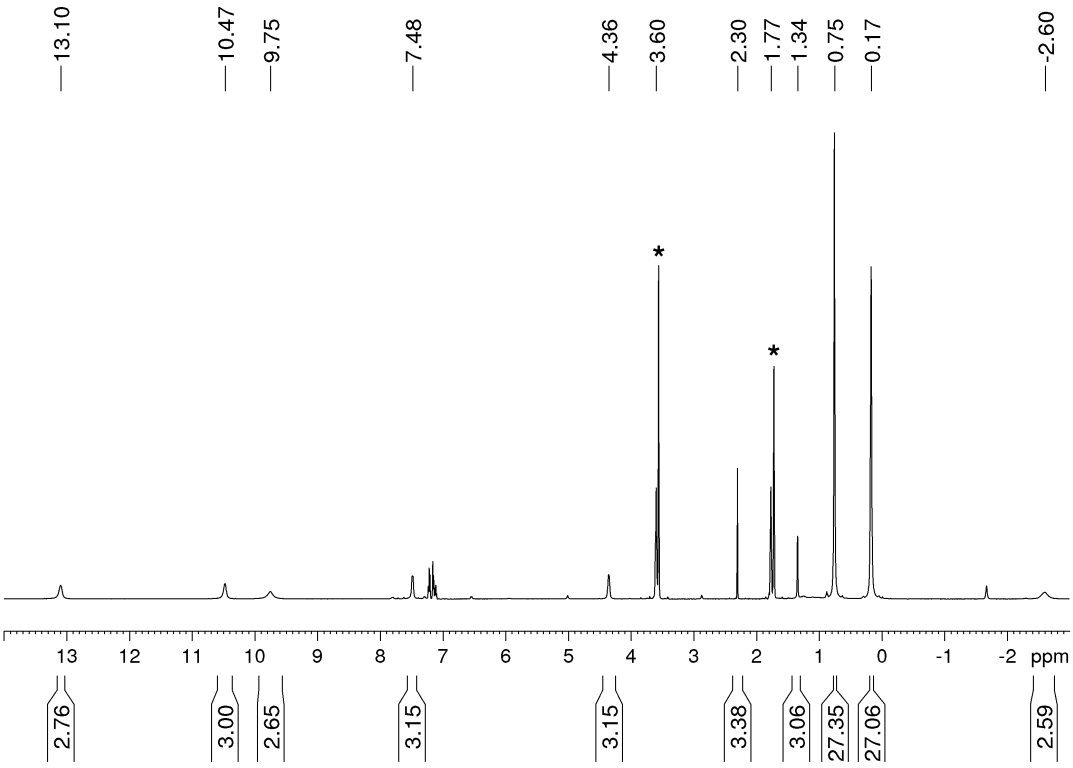

Figure S9. ^{1}H NMR spectrum (400.1 MHz, THF-d_8, -80 °C) of Flu$^{t\mathrm{Bu}}{}_3$Ce(THF) (**2**).

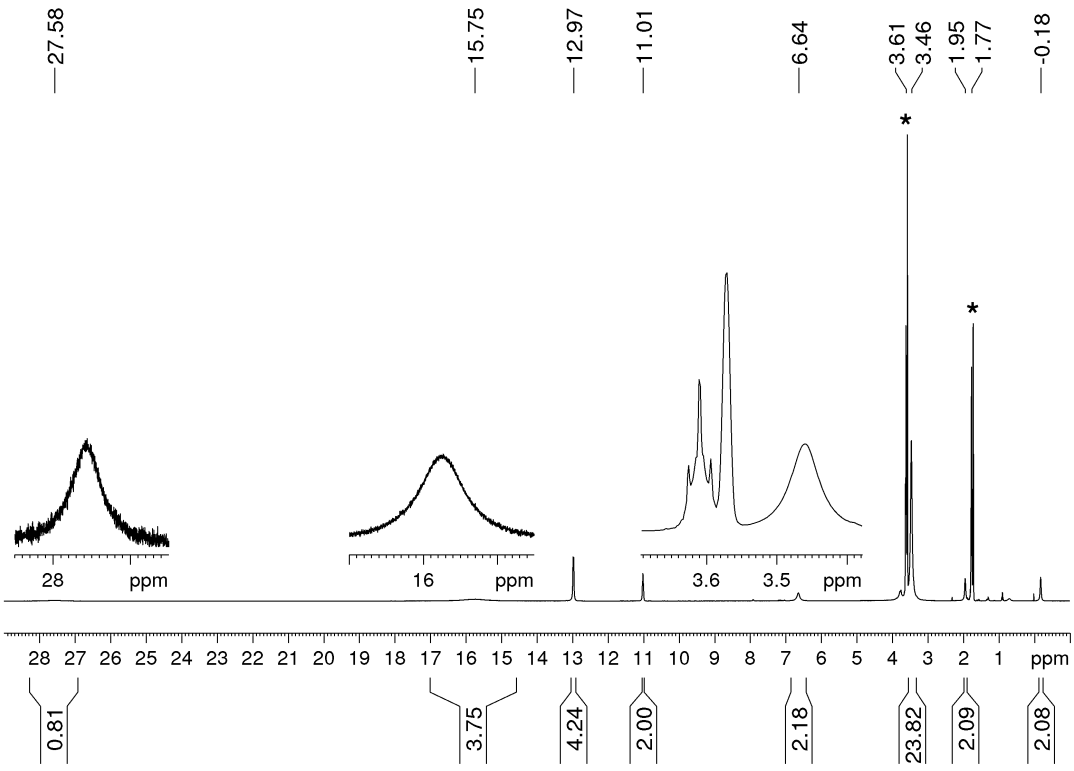

Figure S10. ^{1}H NMR spectrum (400.1 MHz, THF-d_8, 26 °C) of FluCe(OC$_6$H$_3$*i*Pr$_2$-2,6)$_2$(THF)$_2$ (**3$^{\mathrm{OAr}}$**).

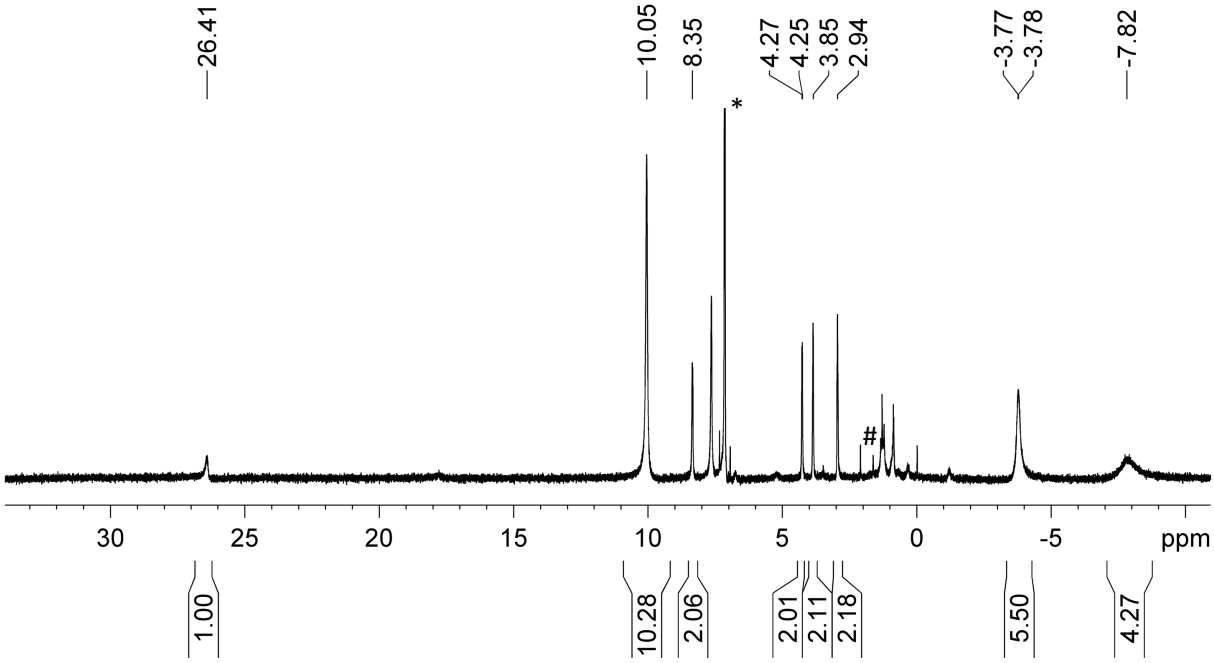

Figure S11. ^{1}H NMR spectrum (400.1 MHz, C_6D_6, 26 °C) of FluCeCp$_2$(THF) (**3^{Cp}**).

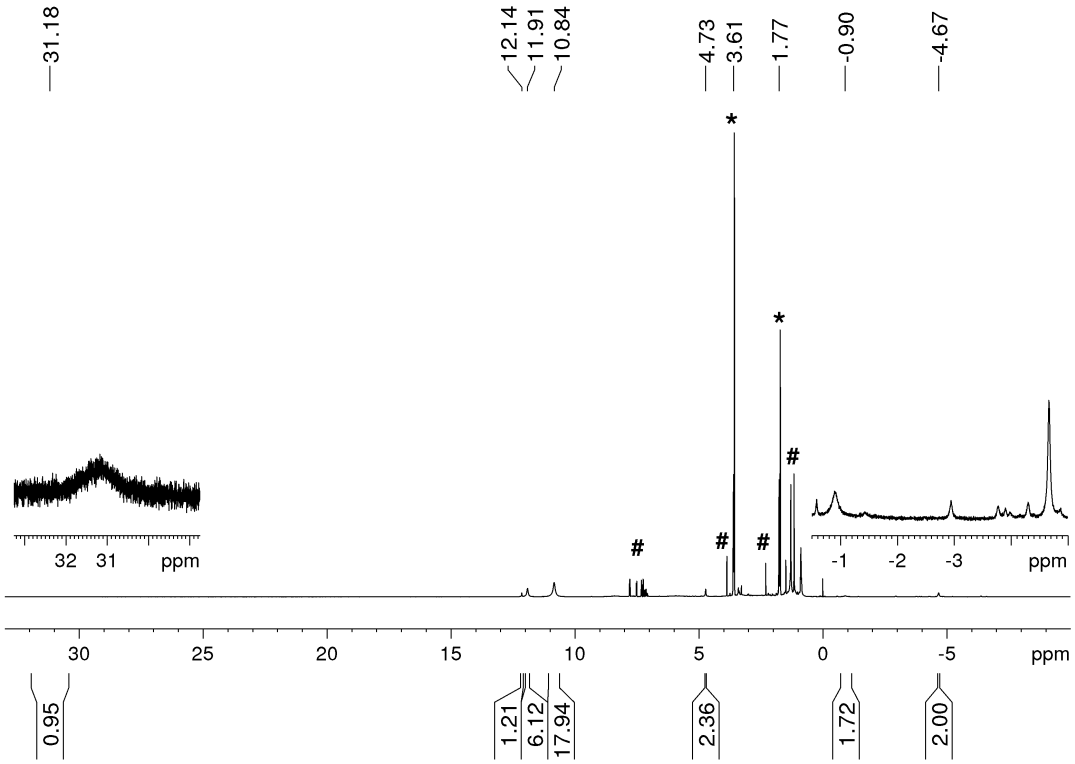

Figure S12. ^{1}H NMR spectrum (400.1 MHz, THF-d_8, 26 °C) of FluCe(OSiMe$_3$)$_2$(THF) (**3^{OSiMe3}**).

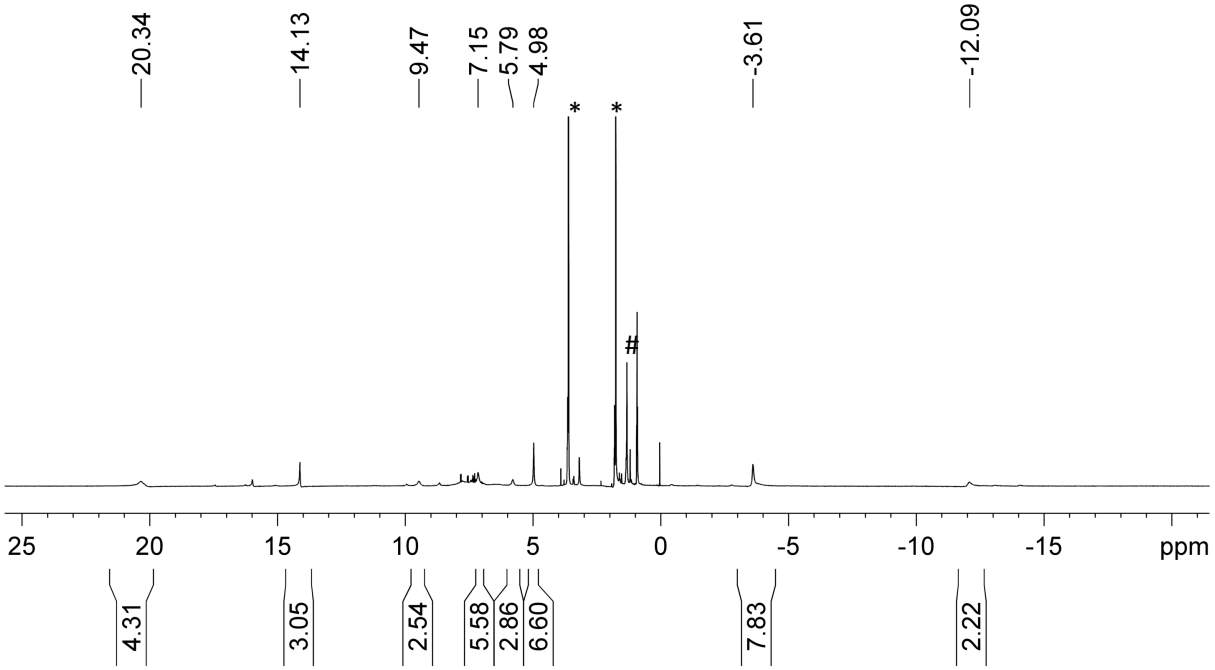

Figure S13. ^{1}H NMR spectrum (400.1 MHz, THF-d_8, 26 °C) of FluCe(O*t*Bu)$_2$(THF) (**3^{OtBu}**).

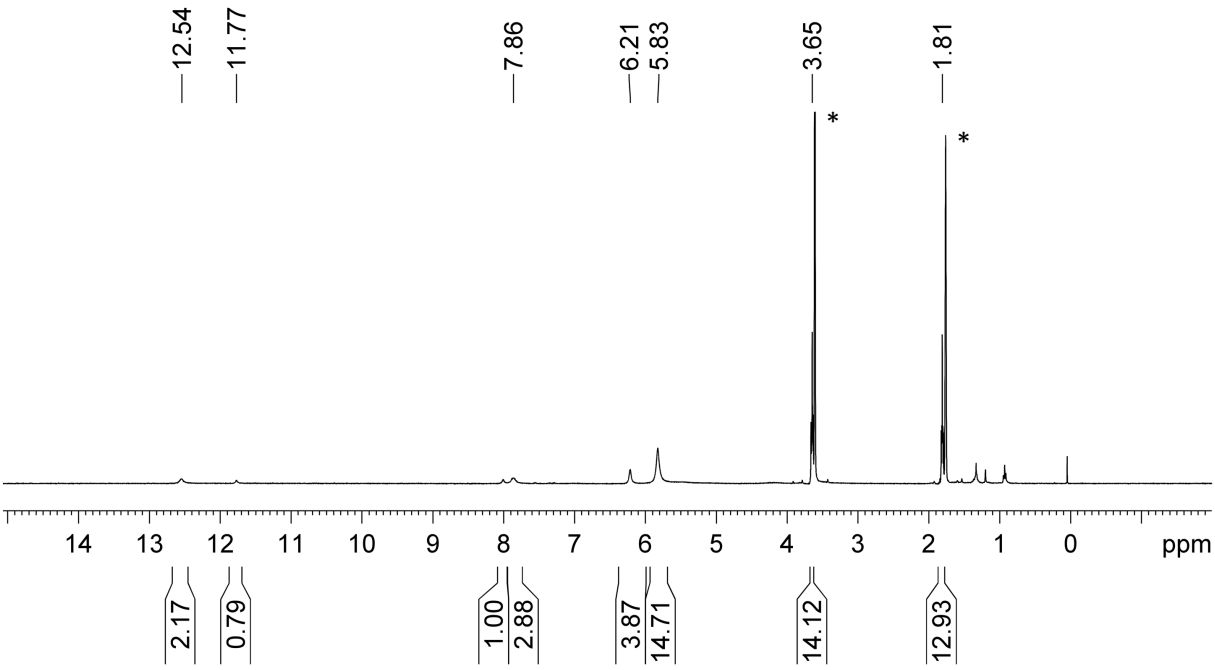

Figure S14. ^{1}H NMR spectrum (400.1 MHz, THF-d_8, 26 °C) of FluCe(Pz)$_2$(THF)$_2$ (**3^{Pz}**).

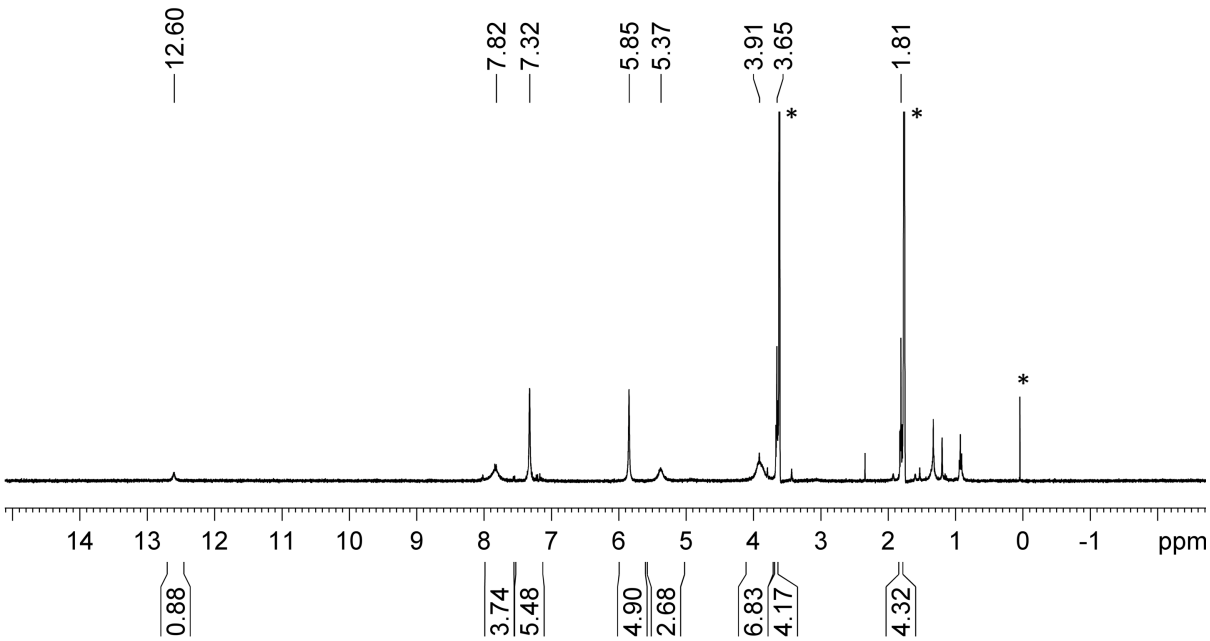

Figure S15. ^{1}H NMR spectrum (400.1 MHz, THF-d_8, 26 °C) of $Flu_2Ce(Pz)(THF)$ (**4^{Pz}**).

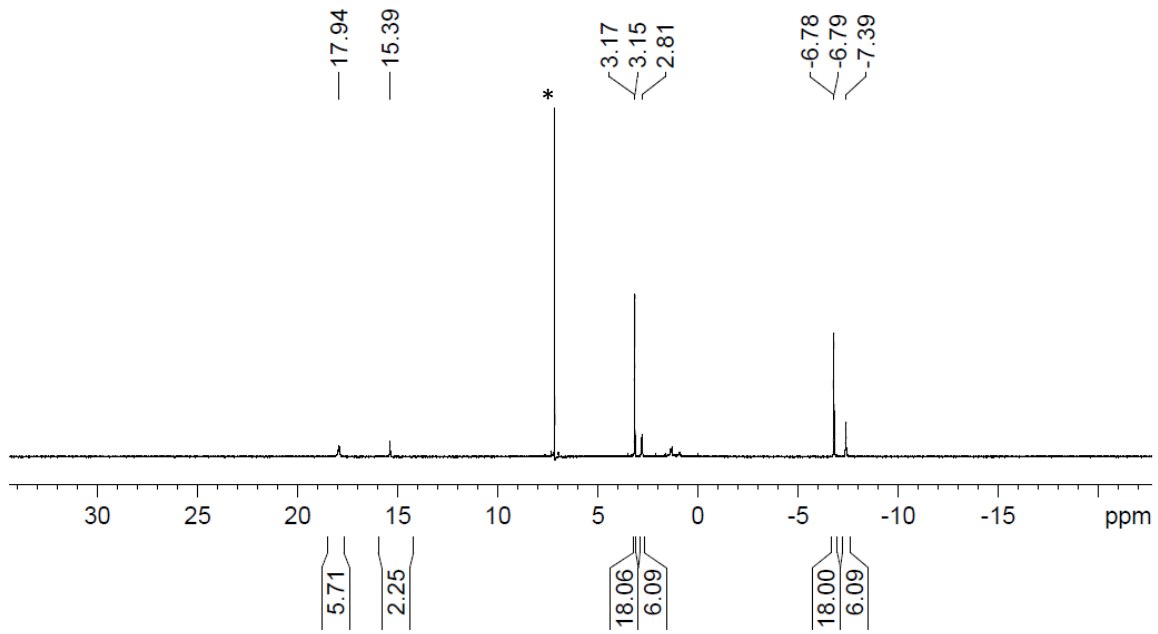

Figure S16. ^{1}H NMR spectrum (400.1 MHz, C_6D_6, 26 °C) of $Ce(dipp)_3$ (**6**).

NMR Spectra of Reactions with Oxidants

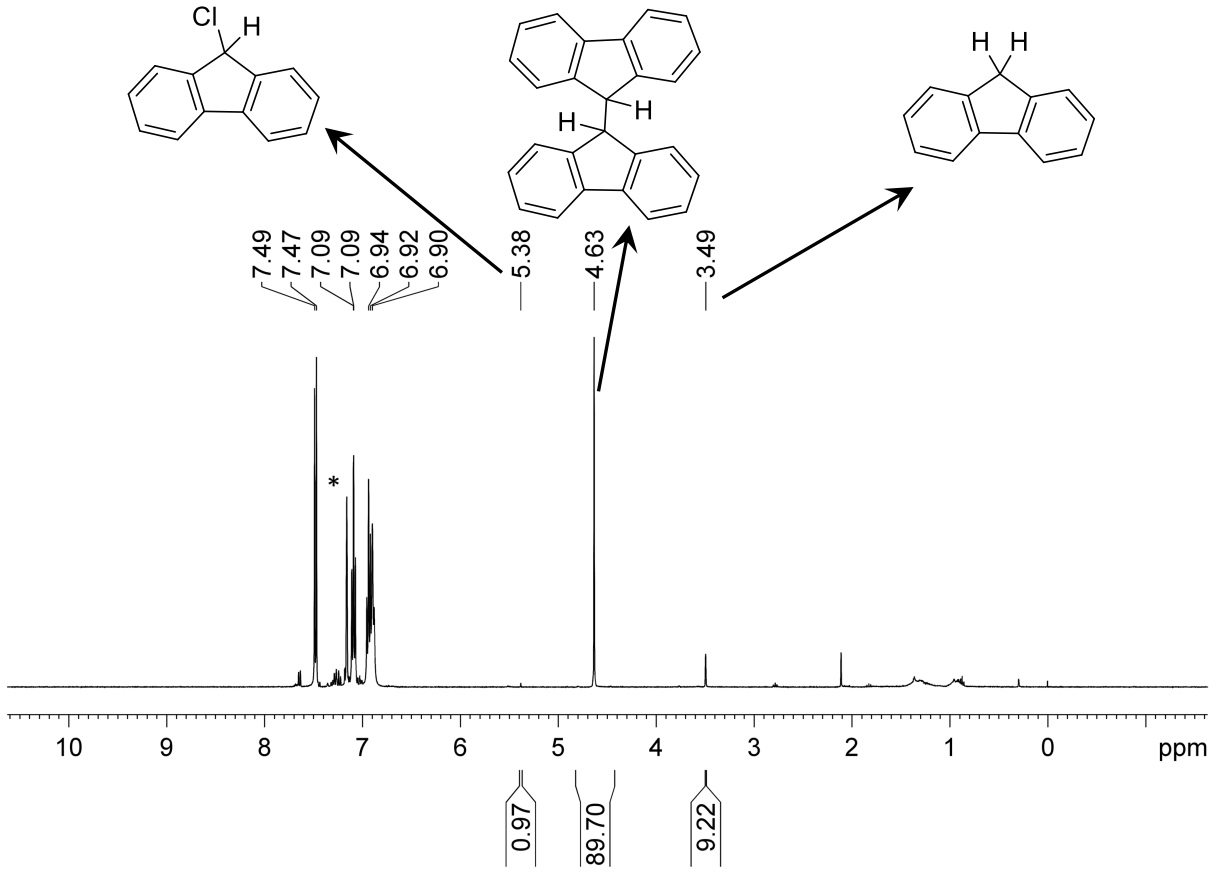

Figure S17. ^{1}H NMR spectrum (400.1 MHz, C_6D_6, 26 °C) of the reaction of $FluCeCl_2(THF)_3$ (**1**^{Ce,Cl}) with <0.5 equiv. C_2Cl_6 affording mainly 1,1'-bifluorene (screening experiment, not listed in Table 2).

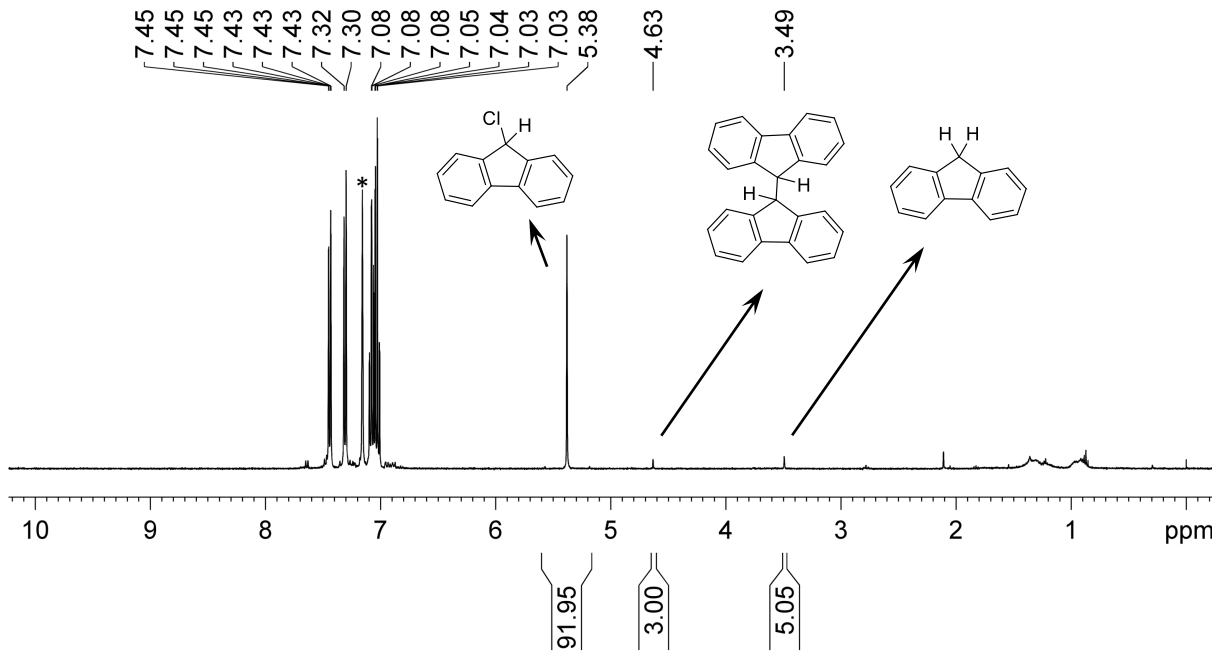

Figure S18. ^{1}H NMR spectrum (400.1 MHz, C_6D_6, 26 °C) of the reaction of $FluCeCl_2(THF)_3$ (**1**^{Ce,Cl}) with >1 equiv. C_2Cl_6 affording mainly 9-chlorofluorene (screening experiment, not listed in Table 2).

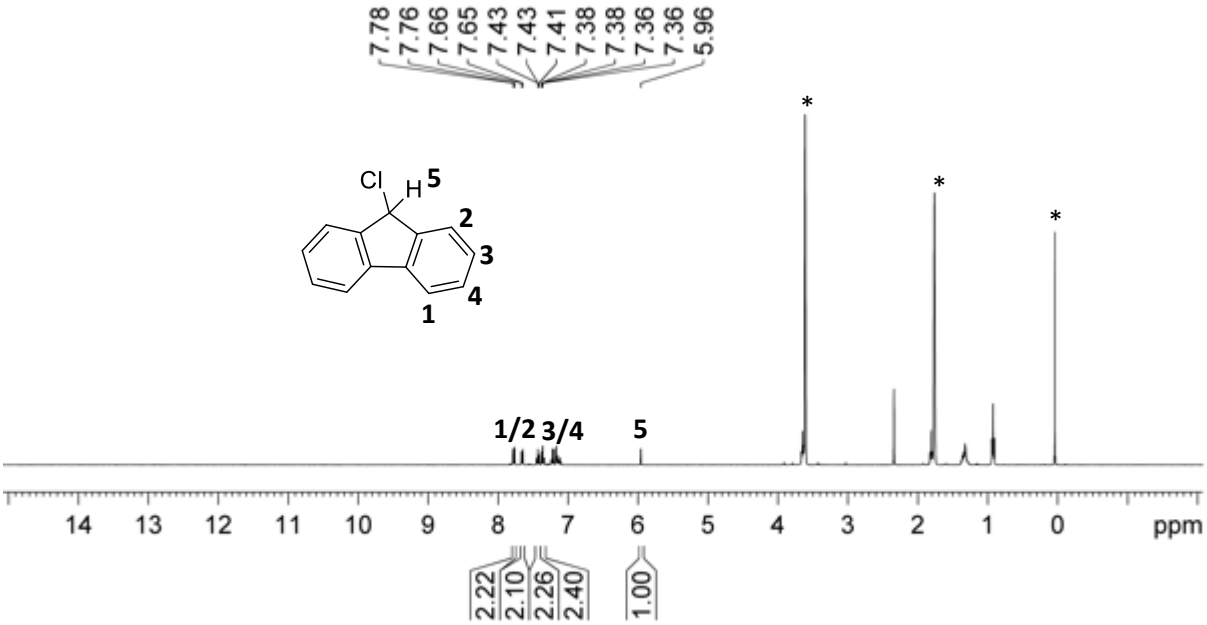

Figure S19. ^{1}H NMR spectrum (400.1 MHz, THF-d_8, 26 °C) of the reaction of $FluCeCl_2(THF)_3$ (**1**^{Ce,Cl}) with excess C_2Cl_6 affording 9-chlorofluorene (screening experiment, not listed in Table 2).

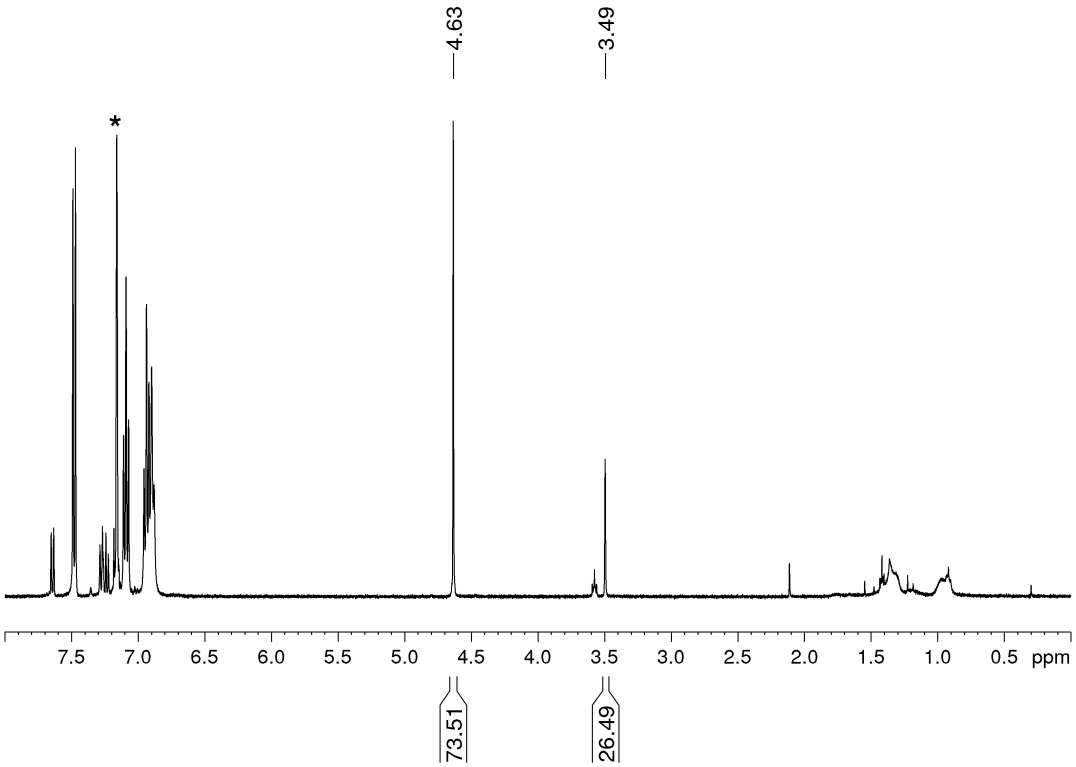

Figure S20. ^{1}H NMR spectrum (400.1 MHz, THF-d_8, 26 °C) of the reaction of $FluCeCl_2(THF)_3$ (**1**^{Ce,Cl}) with C_2Cl_6 in the ratio 1.0:0.24 affording mainly 1,1'-bifluorene (Table 2, entry 2).

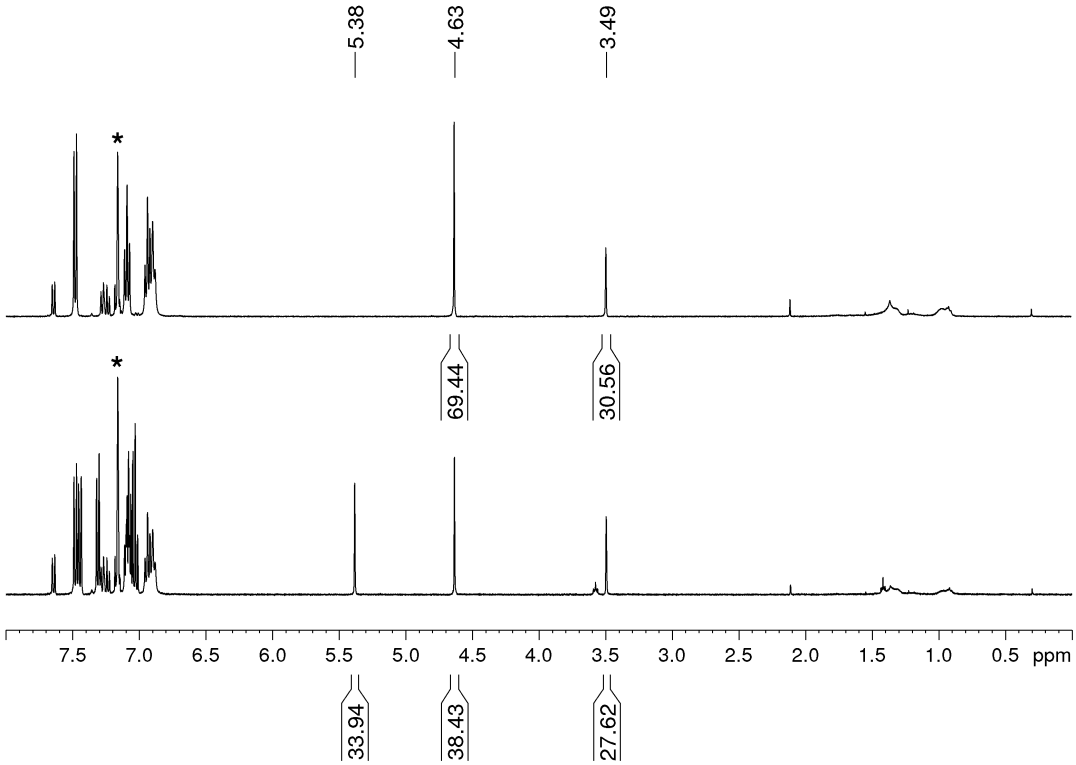

Figure S21. Stacked ^{1}H NMR spectra (400.1 MHz, THF-d_8, 26 °C) of the reaction of $FluCeCl_2(THF)_3$ (**1**^{Ce,Cl}) with C_2Cl_6: bottom, ratio 1.0:0.48 affording a mixture of mainly 1,1'-bifluorene and 9-chlorofluorene; top, after addition of another equiv. of **1**^{Ce,Cl} (ratio 2.0:0.48) full conversion of 9-chlorofluorene into 1,1'-bifluorene (Table 2, entry 1).

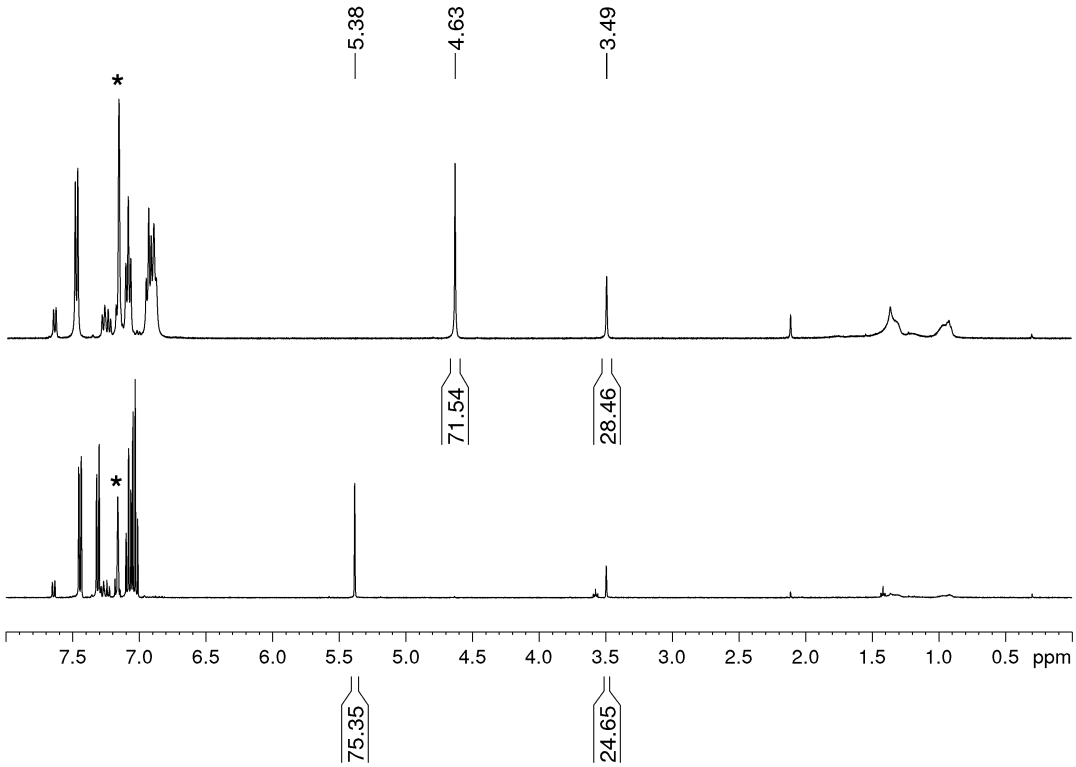

Figure S22. Stacked ^{1}H NMR spectra (400.1 MHz, THF-d_8, 26 °C) of the reaction of $FluCeCl_2(THF)_3$ (**1**^{Ce,Cl}) with C_2Cl_6: bottom, ratio 1.0:1.21 affording mainly 9-chlorofluorene; top, after addition of another 2 equiv. of **1**^{Ce,Cl} (ratio 3.0:1.21) full conversion of 9-chlorofluorene into 1,1'-bifluorene (Table 2, entry 3).

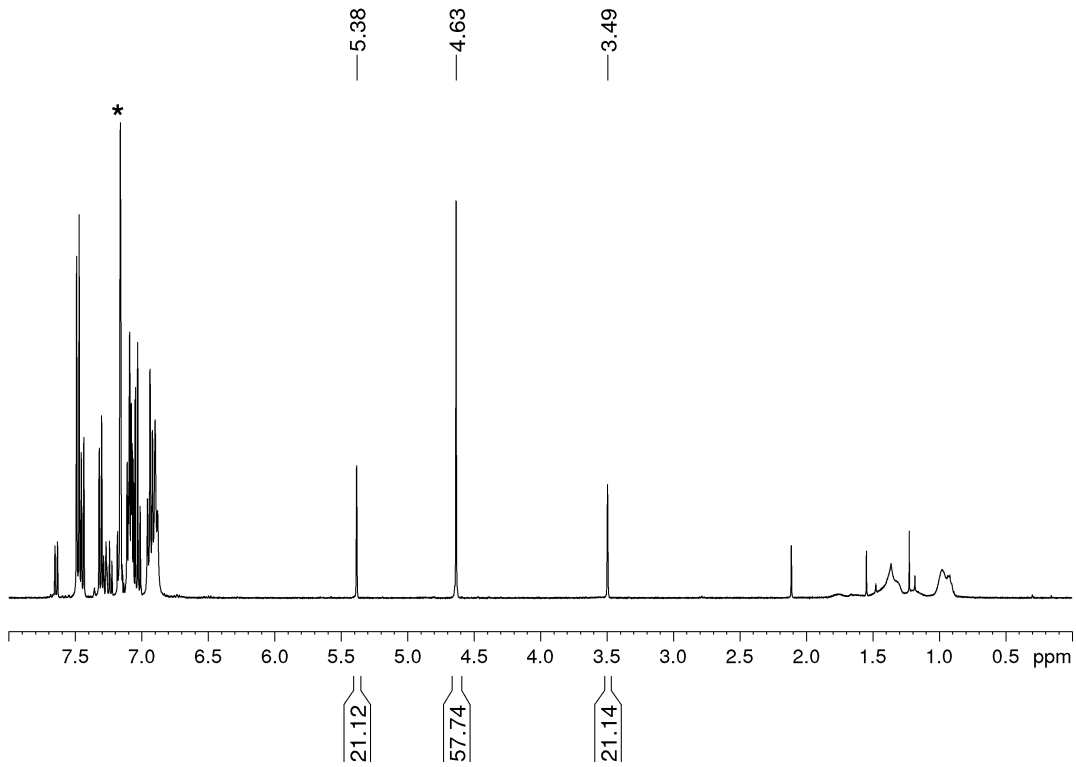

Figure S23. ^{1}H NMR spectrum (400.1 MHz, C_6D_6, 26 °C) of the reaction of $FluLaCl_2(THF)_3$ (**1**^{La,Cl}) with <0.5 equiv. C_2Cl_6 affording a mixture of 9-chlorofluorene and 1,1'-bifluorene (Table 2, entry 4).

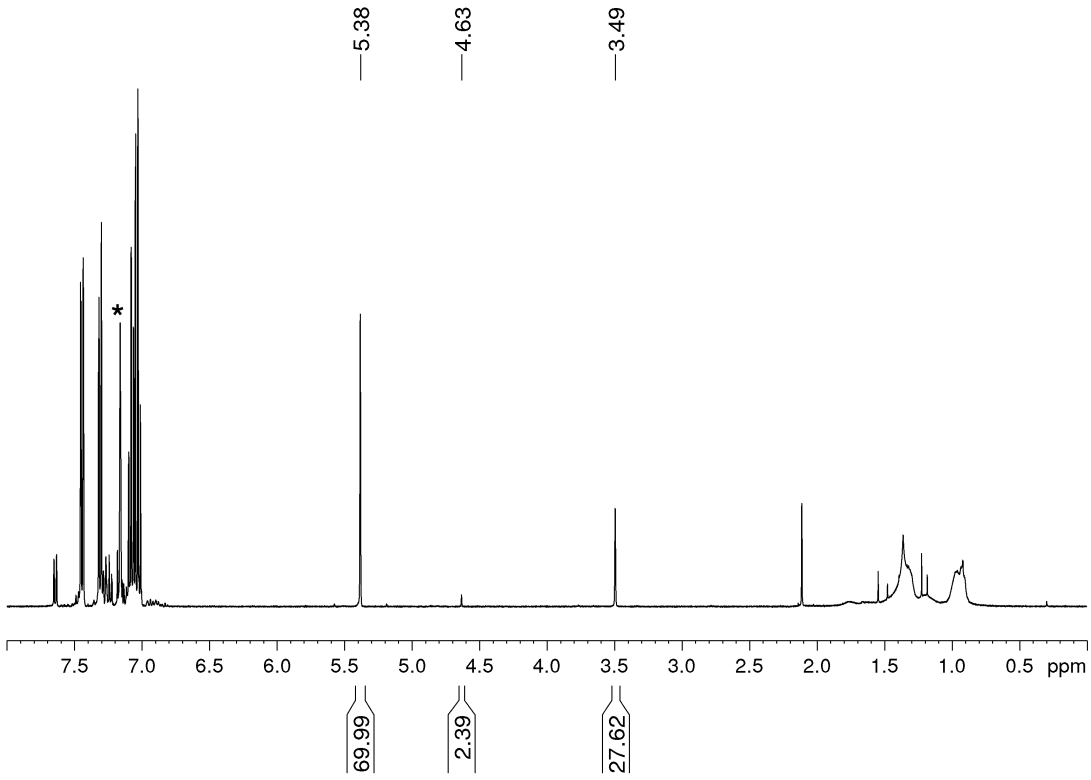

Figure S24. ^{1}H NMR spectrum (400.1 MHz,C_6D_6, 26 °C) of the reaction of $FluLaCl_2(THF)_3$ (**1**^{La,Cl}) with >1 equiv. C_2Cl_6 affording mainly 9-chlorofluorene (Table 2, entry 5).

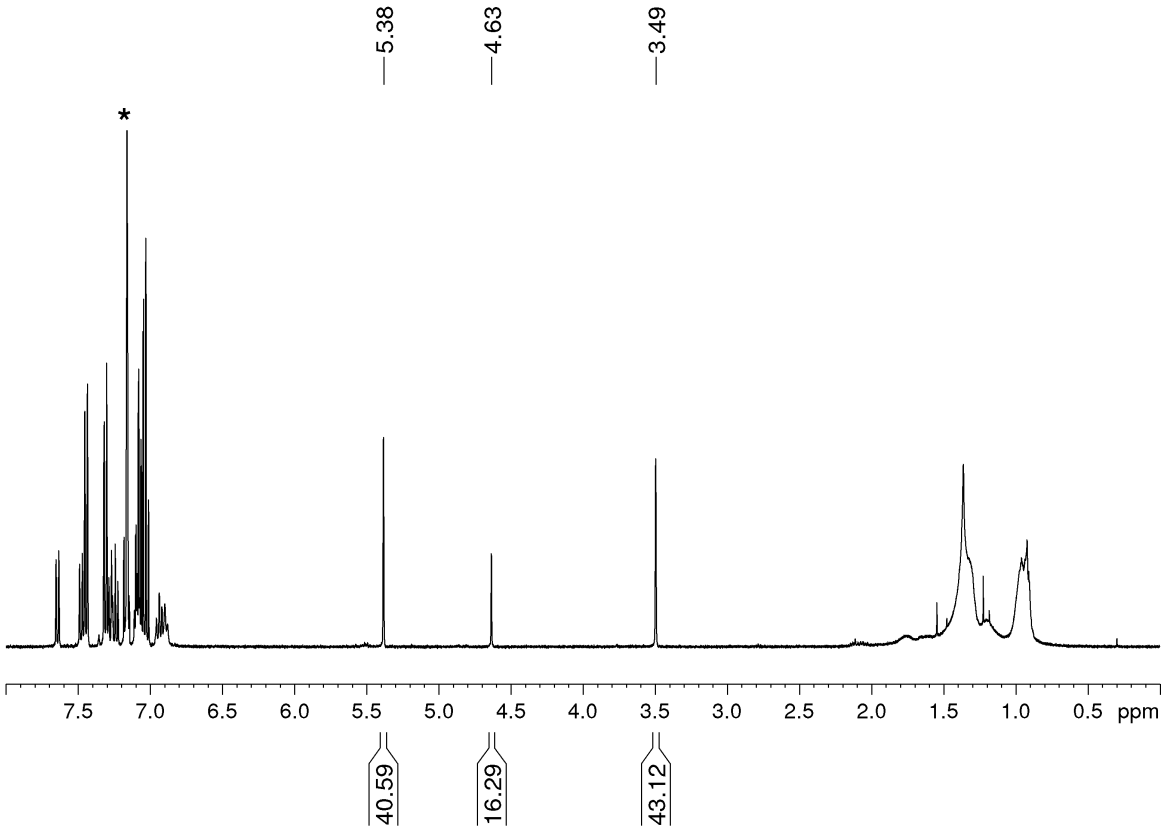

Figure S25. ^{1}H NMR spectrum (400.1 MHz, C_6D_6, 26 °C) of the reaction of $FluNdCl_2(THF)_3$ (**1**^{Nd,Cl}) with <0.5 equiv. C_2Cl_6 affording a mixture of mainly 9-chlorofluorene and 1,1'-bifluorene (Table 2, entry 6).

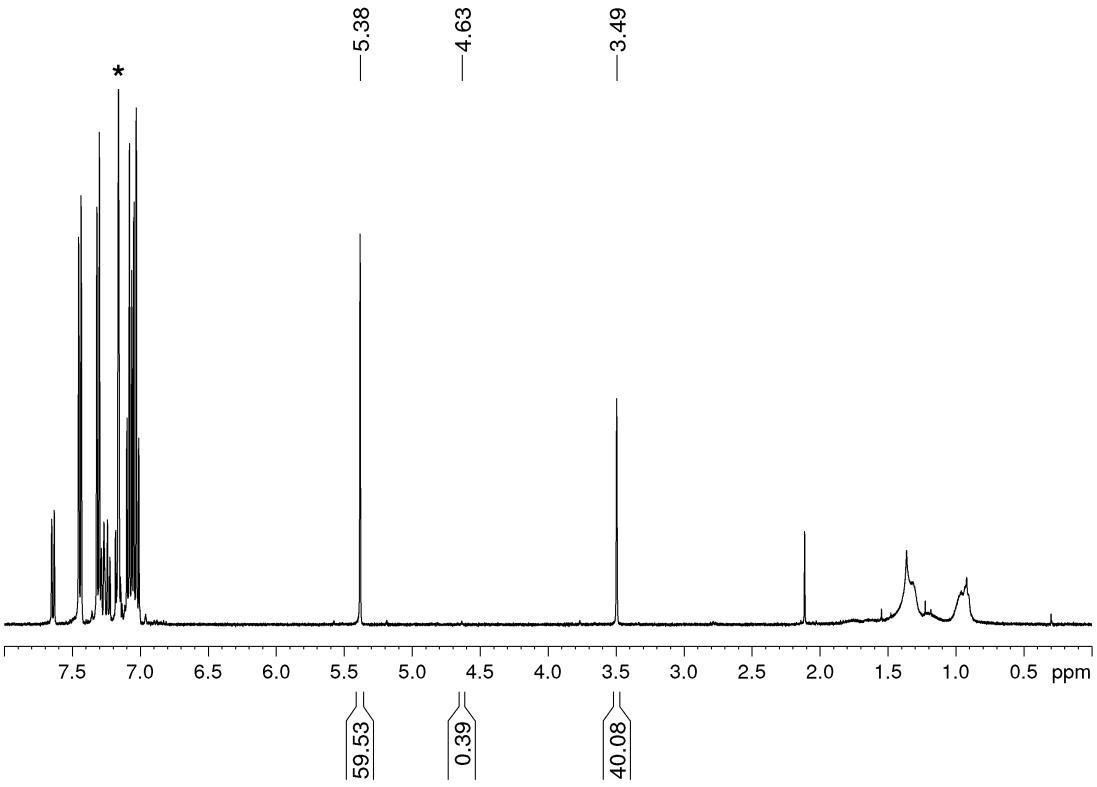

Figure S26. ^{1}H NMR spectrum (400.1 MHz,C_6D_6, 26 °C) of the reaction of $FluNdCl_2(THF)_3$ (**1**^{Nd,Cl}) with >1 equiv. C_2Cl_6 affording mainly 9-chlorofluorene (Table 2, entry 7).

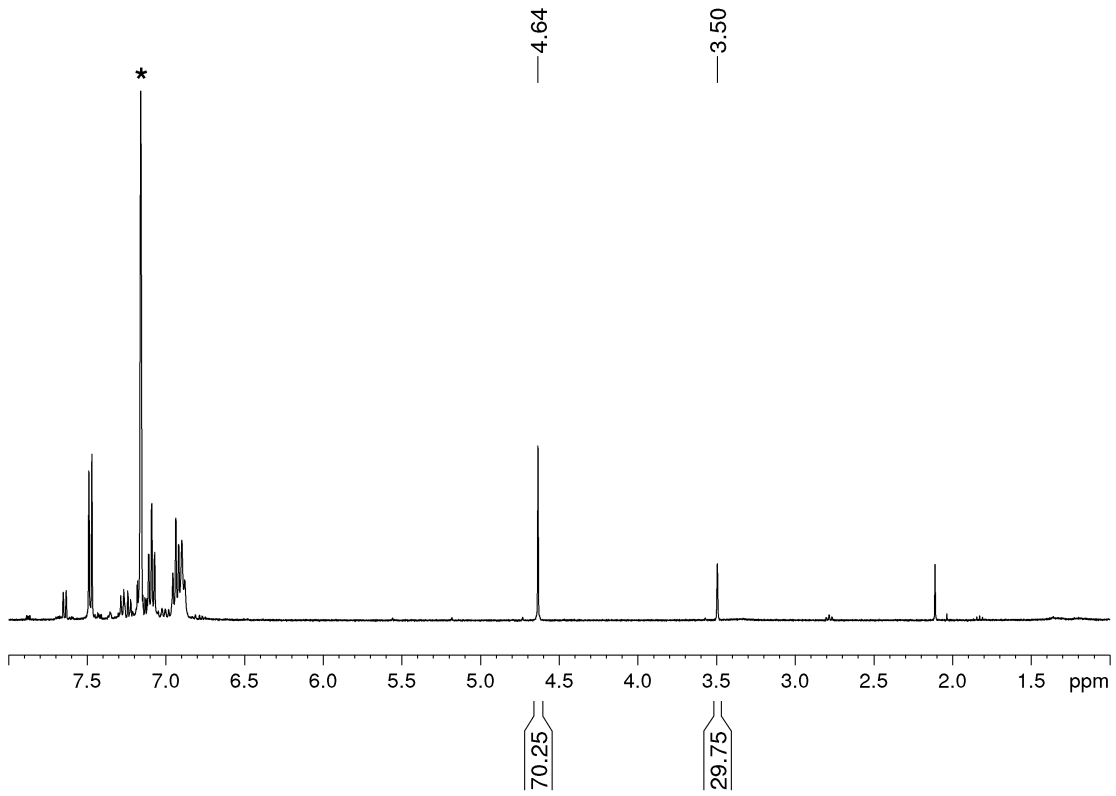

Figure S27. ^{1}H NMR spectrum (400.1 MHz, C_6D_6, 26 °C) of the reaction of LiFlu(THF)$_3$ with <0.5 equiv. C_2Cl_6 affording mainly 1,1'-bifluorene (Table 2, entry 8).

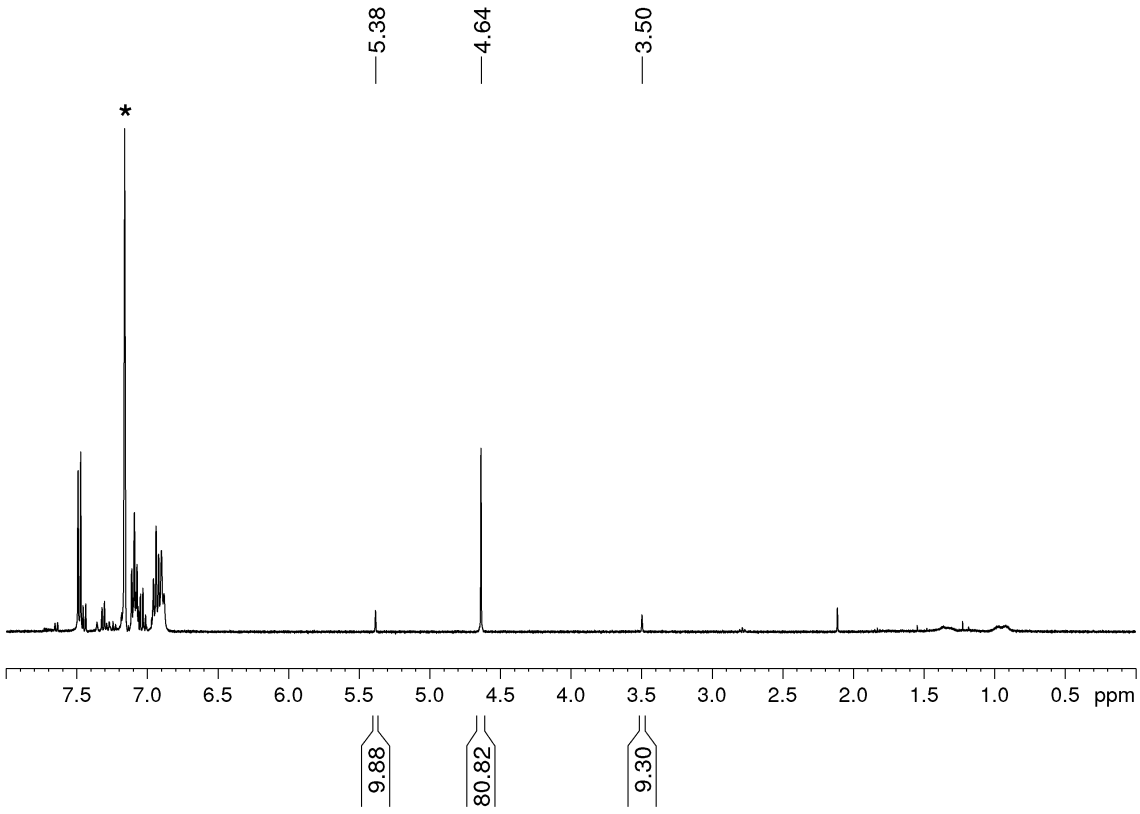

Figure S28. ^{1}H NMR spectrum (400.1 MHz, C_6D_6, 26 °C) of the reaction of LiFlu(THF)$_3$ with >1 equiv. C_2Cl_6 affording mainly 1,1'-bifluorene (Table 2, entry 9).

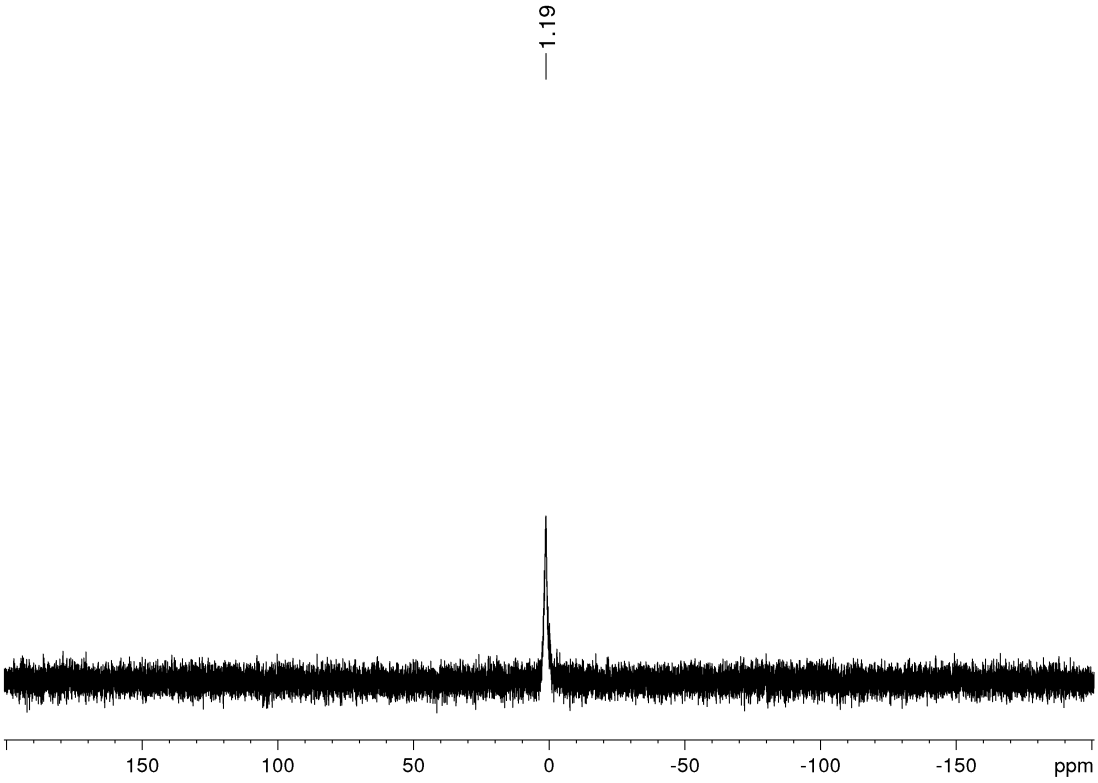

Figure S29. ^{7}Li NMR spectrum (116.6 MHz, C_6D_6, 26 °C) of the reaction of LiFlu(THF)$_3$ with <0.5 equiv. C_2Cl_6.

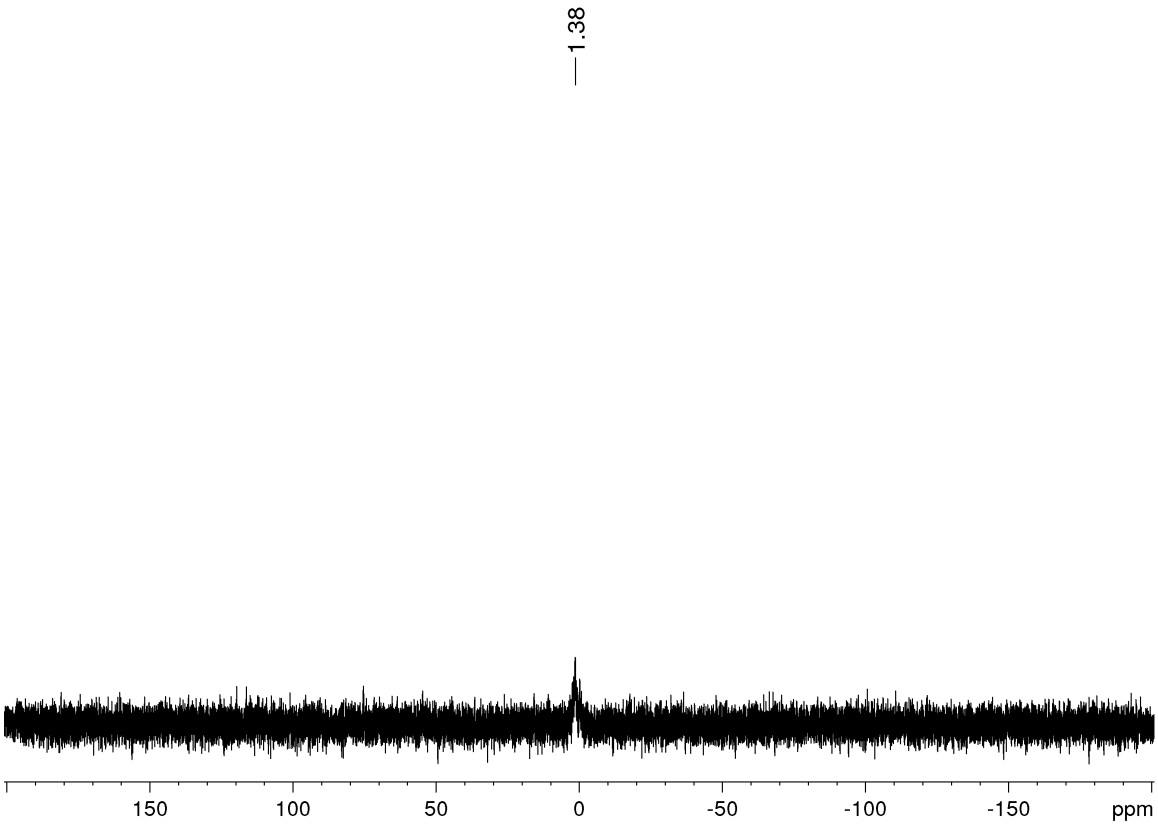

Figure S30. ^{7}Li NMR spectrum (116.6 MHz, C_6D_6, 26 °C) of the reaction of LiFlu(THF)$_3$ with >1 equiv. C_2Cl_6.

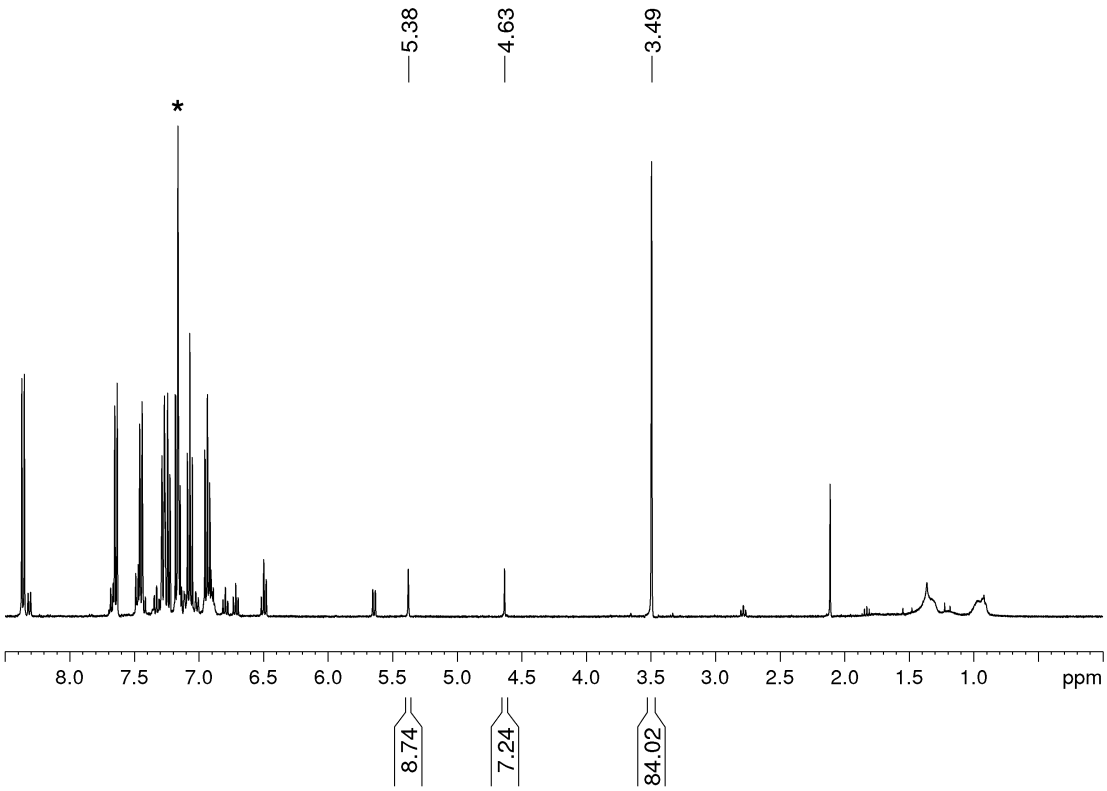

Figure S31. ^{1}H NMR spectrum (400.1 MHz, C_6D_6, 26 °C) of the reaction of KFlu with <0.5 equiv. C_2Cl_6 affording mainly 9-*H*-bifluorene (Table 2, entry 10).

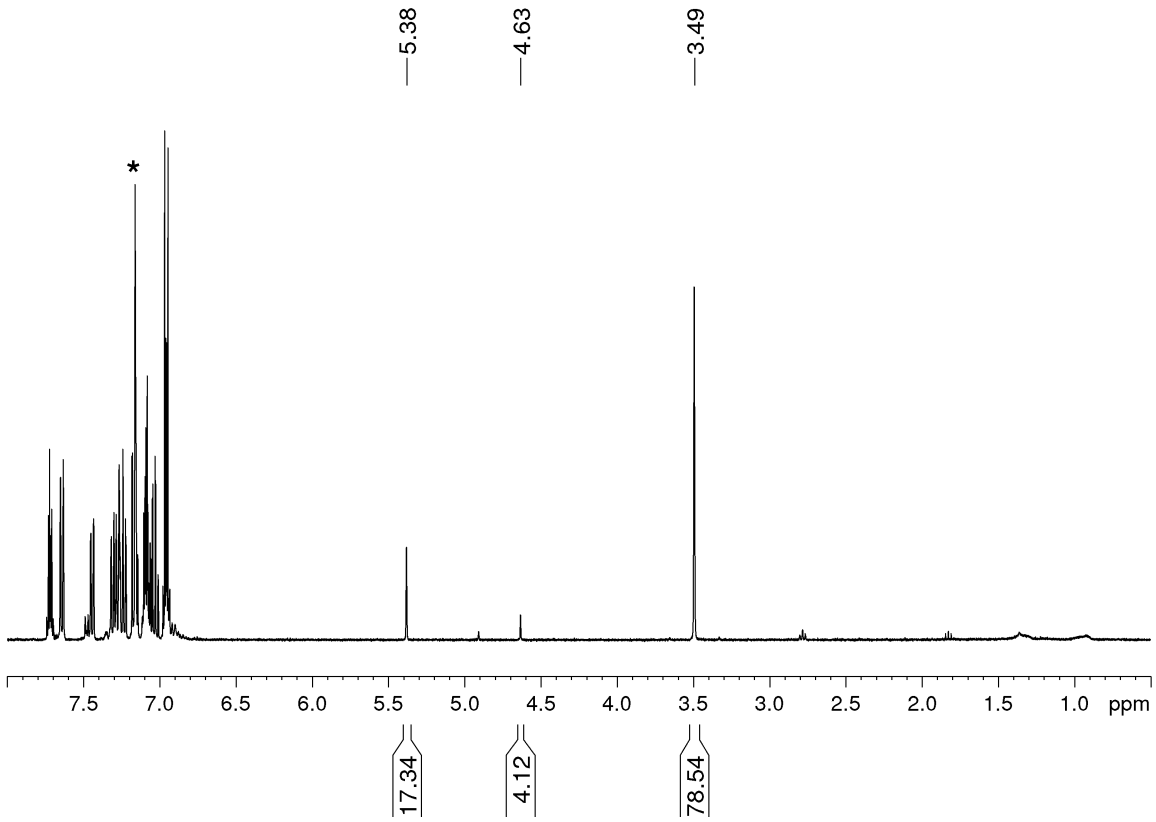

Figure S32. ^{1}H NMR spectrum (400.1 MHz, C_6D_6, 26 °C) of the reaction of KFlu with >1 equiv. C_2Cl_6 affording mainly 9-*H*-bifluorene (Table 2, entry 11).

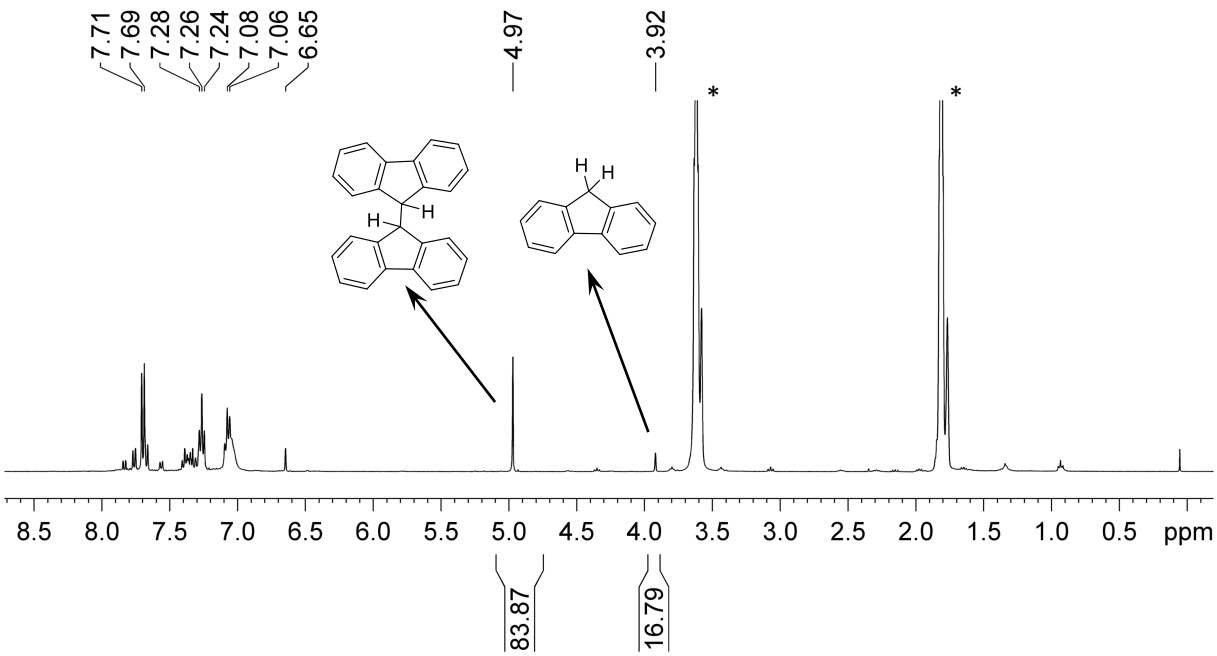

Figure S33. ^{1}H NMR spectrum (400.1 MHz, THF-d_8, 26 °C) of the reaction of $FluCeCl_2(THF)_3$ (**1**^{Ce,Cl}) with 0.5 equiv. I_2 affording mainly 1,1'-bifluorene and fluorene.

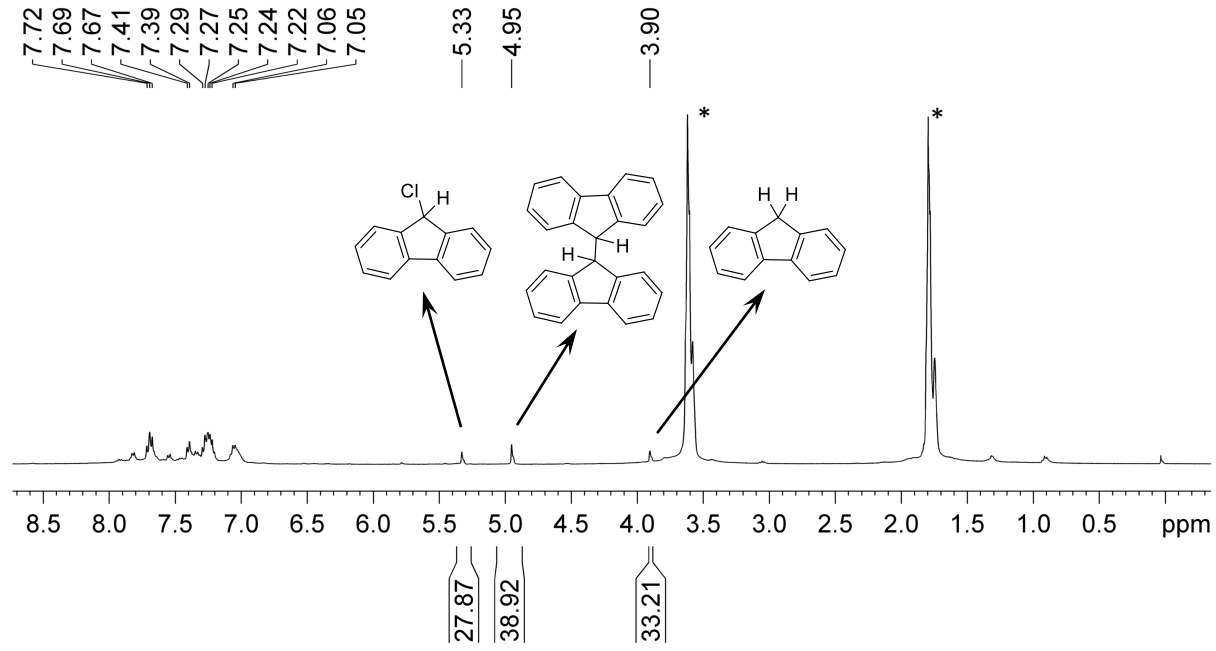

Figure S34. ^{1}H NMR spectrum (400.1 MHz, THF-d_8, 26 °C) of the reaction of $FluCeCl_2(THF)_3$ (**1**^{Ce,Cl}) with 0.25 equiv. $TeBr_4$ affording a mixture of 9-chlorofluorene, 1,1'-bifluorene, and 9-*H*-bifluorene.

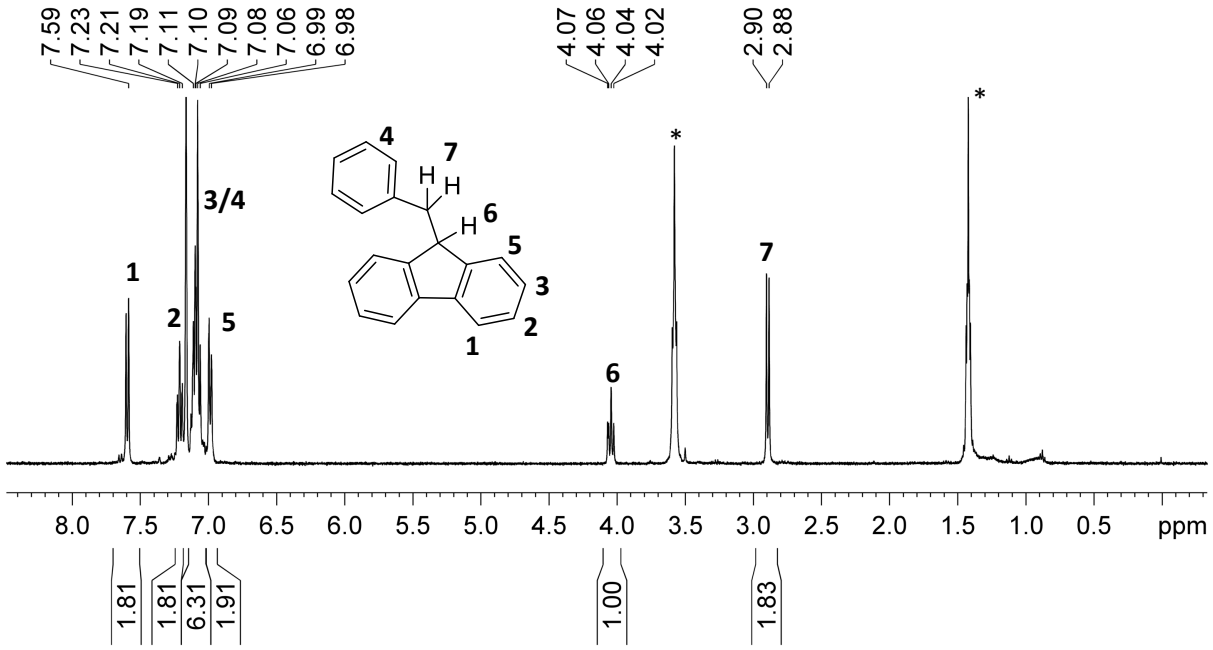

Figure S35. ^{1}H NMR spectrum (400.1 MHz, THF-d_8, 26 °C) of the reaction of $FluCeCl_2(THF)_3$ (**1**^{Ce,Cl}) with 1 equiv. benzyl chloride affording mainly 9-benzylfluorene.

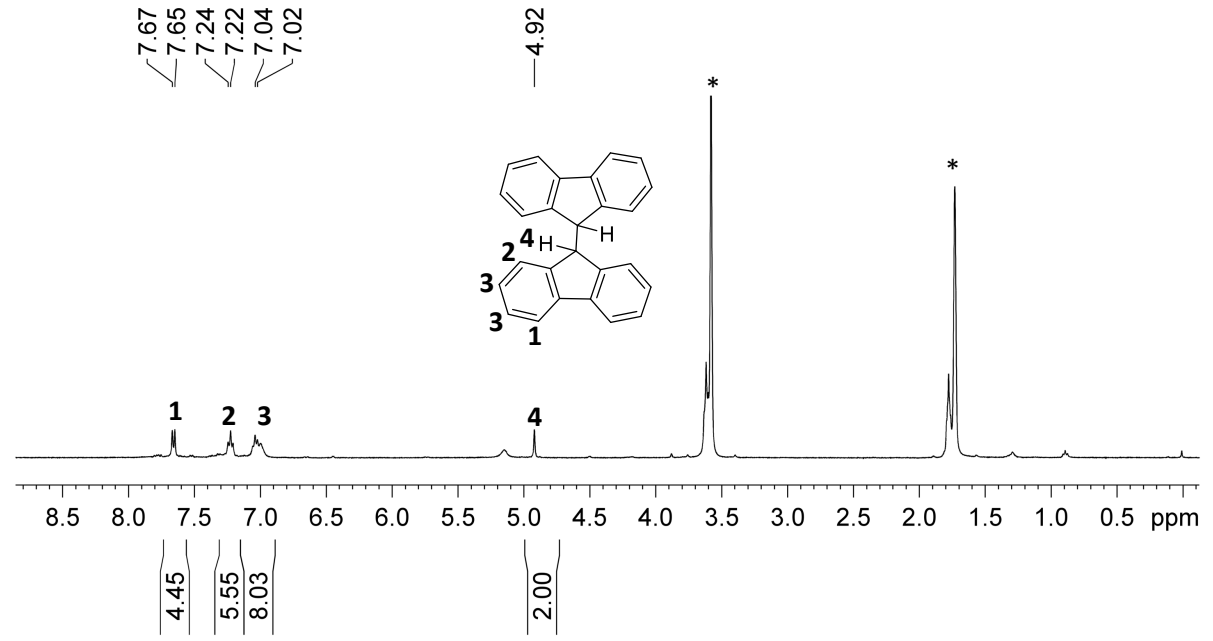

Figure S36. ^{1}H NMR spectrum (400.1 MHz, THFd_8, 26 °C) of the reaction of $FluCeCl_2(THF)_3$ (**1**^{Cl}) with 1 equiv. 1,4-benzoquinone affording mainly 1,1'-bifluorene.

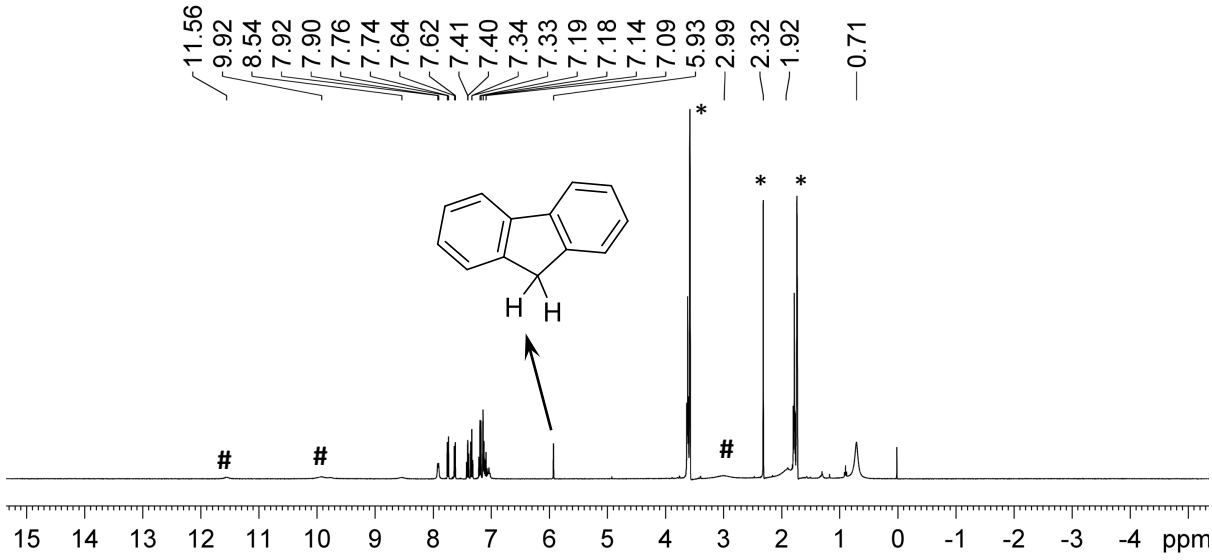

Figure S37. ^{1}H NMR spectrum (400.1 MHz, thf-d_8, 26 °C) of the reaction of FluCe(OAr)$_2$(THF)$_2$ (**3^{OAr}**) with C_2Cl_6 affording 9-*H*-bifluorene; minor paramagnetic signals as marked with #.

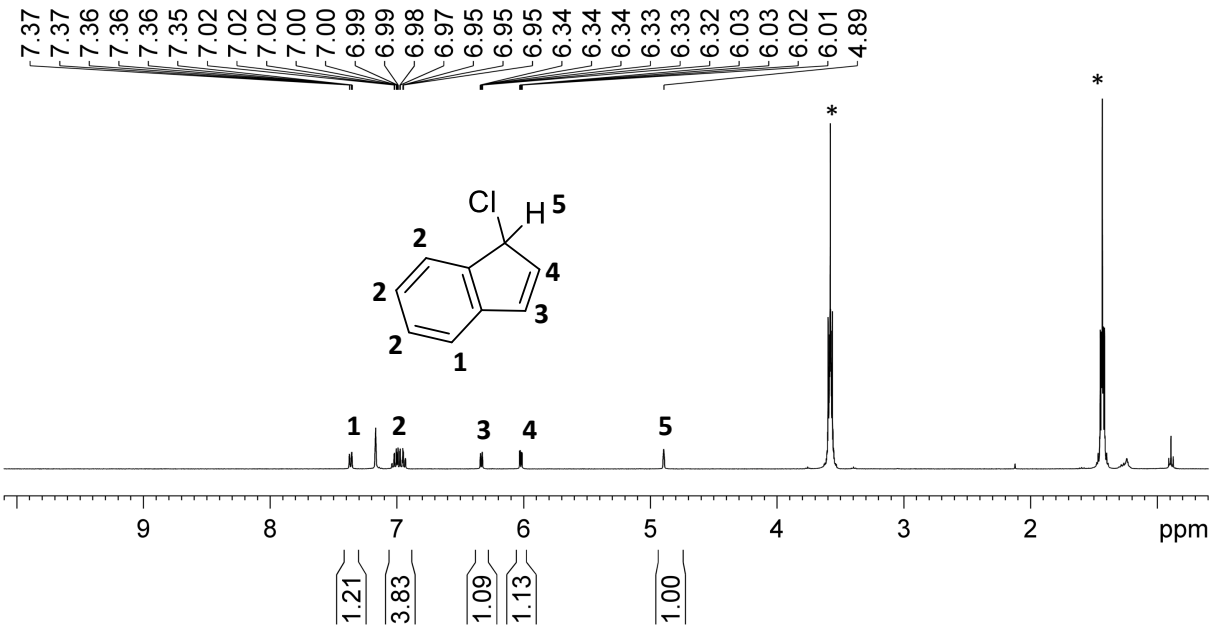

Figure S38. ^{1}H NMR spectrum (400.1 MHz, thf-d_8, 26 °C) of the reaction of Ind$_3$Ce(THF) with 1.5 equiv. C_2Cl_6 affording 1-chloroindene.

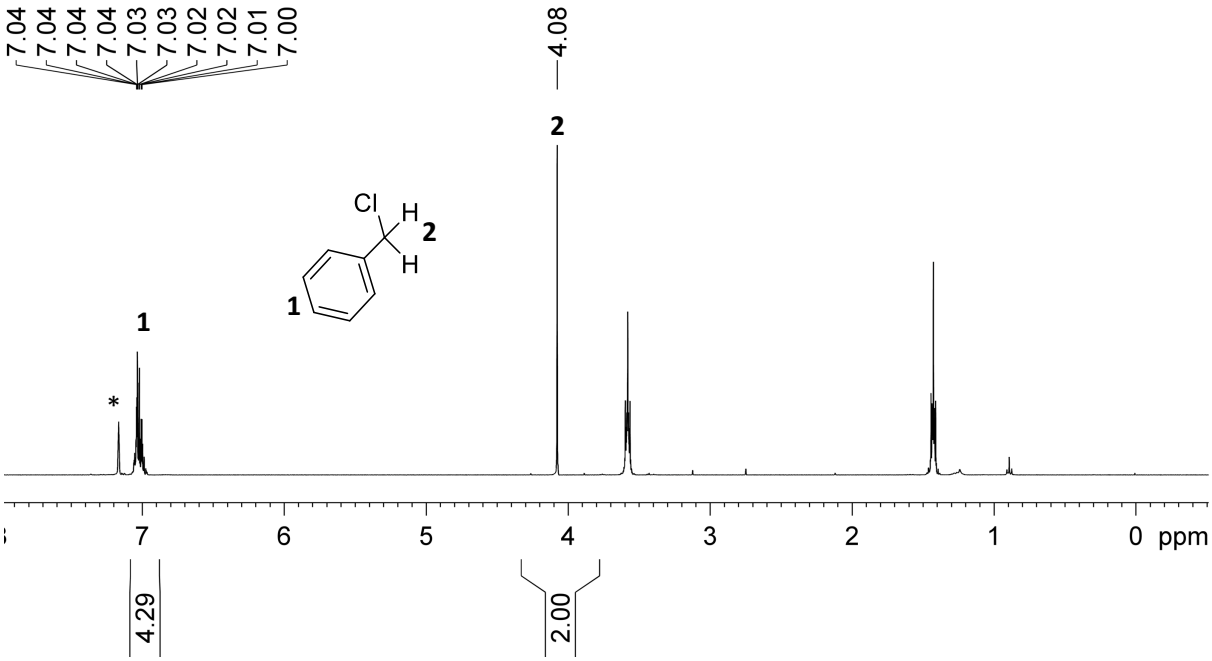

Figure S39. ^{1}H NMR spectrum (400.1 MHz, C_6D_6, 26 °C) of the reaction of $Ce(CH_2Ph)_3$ with 1.5 equiv. C_2Cl_6 affording benzyl chloride.

Solid-State Structures

Single crystals for X-ray crystallography were grown using saturated solutions of toluene (**3**^{Cp}, **3**^{OAr}, **4**^{OfBu}, **4**^{OSiMe3}, **4**^{Pz}, **5**, and **6**) or THF (**1**^{CeCl}, **1**^{Ce,I}, **1**^{La,Cl}, **1**^{Nd,Cl}, **2**, **3**^{Pz}, **3**^{Pz,THF}, **LiFlu(THF)$_3$**, and **CeCl$_3$(THF)$_4$**). Suitable crystals for X-ray diffraction analysis were handpicked in a glovebox, coated with Parabar 10312 and stored on microscope slides. Data collection was done on a Bruker APEX II Duo diffractometer by using QUAZAR optics and Mo K_α radiation (λ = 0.71073 Å) and Cu K_α (λ = 1.54178 Å). The data collection strategy was determined using COSMO[1] employing ω scans. Raw data were processed by APEX[2] and SAINT,[3] corrections for absorption effects were applied using SADABS.[4] The structures were solved by direct methods and refined against all data by full-matrix least-squares methods on F^2 using SHELXTL[5] and SHELXLE.[6] Disorder models are calculated using DSR, a program included in ShelXle[7] , for refining disorder. Plots were generated by using CCDC Mercury 3.19.1.[8] Further details regarding the refinement and crystallographic data are listed in Table S1 and in the CIF files.

[1] COSMO, v. 1.61; Bruker AXS Inc., Madison, WI, 2012.

[2] APEX 3, v. 2017.3-0; Bruker AXS Inc., Madison, WI, 2017.

[3] SAINT, v. 8.34A; Bruker AXS Inc., Madison, WI, 2017.

[4] Krause, L.; Herbst-Irmer, R.; Sheldrick, G. M.; Stalke, D., SADABS – Comparison of silver and molybdenum microfocus X-ray sources for single-crystal structure determination. *J. Appl. Cryst.* **2015**, *48*, 3-10.

[5] Sheldrick, G. M., SHELXTL – Integrated space-group and crystal-structure determination. *Acta Cryst.* **2015**, *A71*, 3–8.

[6] Hübschle, C. B.; Sheldrick, G. M.; Dittrich, B., ShelXle: a Qt graphical user interface for ShelXle. *J. Appl. Cryst.* **2011**, *44*, 1281-1284..

[7] Kratzert, D.; Holstein, J. J.; Krossing, I., DSR: enhanced modelling and refinement of disordered structures with SHELXL. *J. Appl. Cryst.* **2015,** *48*, 933-938.

[8] Macrae, C. F.; Bruno, I. J.; Chisholm, J. A.; Edgington, P. R.; McCabe, P.; Pidcock, E.; Rodriguez-Monge, L.; Taylor, R.; van de Streek, J.; Wood, P. A., Mercury CSD 2.0 - New Features for the Visualization and Investigation of Crystal Structures. *J. Appl. Cryst.* **2008**, *41*, 466-470.

Table S1. Collection of crystallographic data of $\mathbf{1}^{Ce,Cl}$, $\mathbf{1}^{Ce,I}$, $\mathbf{1}^{La,Cl}$, $\mathbf{1}^{Nd,Cl}$, **2**, $\mathbf{3}^{Cp}$, $\mathbf{3}^{Pz}$, $\mathbf{3}^{Pz,THF}$, $\mathbf{3}^{OAr}$, $\mathbf{4}^{OtBu}$, $\mathbf{4}^{OSiMe3}$, $\mathbf{4}^{Pz}$, **5**, **6**, **LiFlu(THF)$_3$**, and **CeCl$_3$(THF)$_4$**

	$\mathbf{1}^{Ce,Cl}$	$\mathbf{1}^{Ce,I}$	$\mathbf{1}^{La,Cl}$	$\mathbf{1}^{Nd,Cl}$	**2**
CCDC	2141923	2141912	2141911	2141916	2141915
formula	$C_{25}H_{33}CeCl_2O_3$	$C_{25}H_{33}CeI_2O_3$	$C_{25}H_{33}LaCl_2O_3$	$C_{25}H_{33}NdCl_2O_3$	$C_{74}H_{91}CeO$
M [$g \cdot mol^{-1}$]	592.53	775.43	591.32	596.65	1136.58
λ [Å]	0.71073	0.71073	0.71073	1.54178	0.71073
cell	monoclinic	monoclinic	monoclinic	monoclinic	monoclinic
space group	$P2_1/c$	$P2_1/c$	$P2_1/c$	$P2_1/c$	$P2_1/c$
a [Å]	15.7295(9)	17.7588(12)	15.6924(15)	15.6132(8)	13.3994(7)
b [Å]	19.0754(11)	18.7839(13)	18.9899(18)	18.9973(9)	18.7291(10)
c [Å]	16.9069(10)	15.9243(11)	16.9123(15)	16.8230(8)	24.6500(13)
α [°]	90	90	90	90	90
β [°]	93.2310(10)	93.7160(10)	92.940(2)	93.195(3)	100.894(2)
γ [°]	90	90	90	90	90
V [$Å^3$]	5064.8(5)	5300.9(6)	5033.2(8)	4982.1(4)	6074.6(6)
Z	8	8	8	8	4
F(000)	2392	2968	2384	2408	2404
T [K]	100(2)	100(2)	100(2)	100(2)	100(2)
ρ_{calcd} [$g \cdot mol^3$]	1.554	1.943	1.561	1.591	1.243
μ [mm^{-1}]	2.032	4.070	1.933	18.058	0.793
R_1 ($I>2\sigma(I)$)	0.0378	0.0288	0.0389	0.0589	0.0439
ωR_2 (all data)	0.0850	0.0710	0.0802	0.1425	0.0997
Goodness of fit	1.064	1.062	1.022	1.024	1.017

Table S1. Collection of crystallographic data of $\mathbf{1}^{Ce,Cl}$, $\mathbf{1}^{Ce,I}$, $\mathbf{1}^{La,Cl}$, $\mathbf{1}^{Nd,Cl}$, **2**, $\mathbf{3}^{Cp}$, $\mathbf{3}^{Pz}$, $\mathbf{3}^{Pz,THF}$, $\mathbf{3}^{OAr}$, $\mathbf{4}^{OtBu}$, $\mathbf{4}^{OSiMe3}$, $\mathbf{4}^{Pz}$, **5**, **6**, **LiFlu(THF)$_3$**, and **CeCl$_3$(THF)$_4$** (continued)

	$\mathbf{3}^{Cp}$	$\mathbf{3}^{Pz}$	$\mathbf{3}^{Pz,THF}$	$\mathbf{3}^{OAr}$	$\mathbf{4}^{OtBu}$
CCDC	2141914	2141917	2141913	2141920	2141918
formula	$C_{27}H_{27}CeO$	$C_{31}H_{39}CeN_4O_2$	$C_{43}H_{63}CeN_4O_5$	$C_{59}H_{75}CeO_4$	$C_{34}H_{35}CeO_2$
M [g · mol^{-1}]	507.60	639.78	856.09	988.31	615.74
λ [Å]	0.71073	0.71073	0.71073	0.71073	0.71073
cell	monoclinic	monoclinic	monoclinic	monoclinic	monoclinic
space group	$P2_1/c$	$P2_1/c$	Cc	$P2_1/c$	$P2_1/c$
a [Å]	12.3611(14)	24.742(3)	19.380(17)	18.1532(12)	12.089(2)
b [Å]	9.2882(11)	9.5613(12)	15.573(14)	13.3312(9)	14.929(3)
c [Å]	18.301(2)	25.071(3)	14.649(14)	21.5653(15)	15.165(2)
α [°]	90	90	90	90	90
β [°]	94.103(2)	99.538(3)	107.50(3)	97.5890(10)	95.445(4)
γ [°]	90	90	90	90	90
V [Å^3]	2095.8(4)	5849.0(13)	4217(7)	5173.2(6)	2724.7(8)
Z	4	8	4	4	4
F(000)	1020	2616	1788	2076	1252
T [K]	100(2)	100(2)	100(2)	100(2)	100(2)
ρ_{calcd} [g · mol^3]	1.609	1.453	1.349	1.269	1.501
μ [mm^{-1}]	2.187	1.590	1.126	0.924	1.700
R_1 (I>2σ(I))	0.0226	0.0399	0.0575	0.0301	0.0498
ωR_2 (all data)	0.0558	0.0945	0.1341	0.0731	0.1083
Goodness of fit	1.077	1.027	1.013	1.027	0.980

Table S1. Collection of crystallographic data of $\mathbf{1}^{Ce,Cl}$, $\mathbf{1}^{Ce,I}$, $\mathbf{1}^{La,Cl}$, $\mathbf{1}^{Nd,Cl}$, **2**, $\mathbf{3}^{Cp}$, $\mathbf{3}^{Pz}$, $\mathbf{3}^{Pz,THF}$, $\mathbf{3}^{OAr}$, $\mathbf{4}^{OtBu}$, $\mathbf{4}^{OSiMe3}$, $\mathbf{4}^{Pz}$, **5**, **6**, **LiFlu(THF)$_3$**, and **CeCl$_3$(THF)$_4$** (continued)

	$\mathbf{4}^{OSiMe3}$	$\mathbf{4}^{Pz}$	**5**[a]	**6**	**FluLi (THF)$_3$**[b]	**CeCl$_3$(THF)$_4$**
CCDC	2141921	2141924		2141922	2141919	2156077
formula	$C_{33}H_{35}CeO_2Si$ • ½ C_7H_8	$C_{35}H_{33}CeN_2O$	$C_{97}H_{103}Ce_3Cl_3LiO_2S_4$	$C_{33}H_{57}Ce$	$C_{25}H_{33}LiO_3$	$C_{16}H_{32}CeCl_3O_4$
M [g · mol^{-1}]	677.88	637.75	1962.68	593.90	388.45	534.88
λ [Å]	0.71073	0.71073	0.71073	0.71073	0.71073	0.71073
cell	monoclinic	monoclinic	monoclinic	monoclinic	monoclinic	orthorhombic
space group	$P2_1/c$	$P2_1/c$	$P2_1/n$	$P2_1/n$	$P2_1/c$	Fdd2
a [Å]	16.683(2)	15.8625(18)	19.990(2)	11.1289(8)	7.3630(5)	16.3321(10)
b [Å]	9.4666(13)	9.7332(12)	31.191(3)	11.9637(8)	14.4664(9)	29.5093(18)
c [Å]	19.889(3)	19.971(3)	31.945(3)	23.7661(16)	20.6822(13)	9.0527(6)
α [°]	90	90	90	90	90	90
β [°]	92.109(2)	112.598(2)	96.918(3)	93.3260(10)	92.7720(10)	90
γ [°]	90	90	90	90	90	90
V [Å^3]	3138.9(7)	2846.6(6)	19772(3)	3159.0(4)	2200.4(2)	4362.9(5)
Z	4	4	8	4	4	8
F(000)	1384	1292	–	1252	840	2152
T [K]	100(2)	173(2)	100(2)	100(2)	100(2)	100
ρ_{calcd} [g · mol^3]	1.434	1.488	–	1.249	1.173	1.629
μ [mm^{-1}]	1.519	1.629	–	1.458	0.074	2.470
R_1 (I>2σ(I))	0.0416	0.0373	–	0.0368	0.0421	0.0260
ωR_2 (all data)	0.1023	0.0954	–	0.0899	0.1156	0.0730
Goodness of fit	1.013	1.035	–	1.022	1.044	1.103

[a]Connectivity structure. [b] The solid-state structure of LiFlu(THF)$_3$ has been determined previously by F. Olbrich in 2002 (CSD Communication (Private Communication), CCDC 114095) with different cell parameters, but in the same space group $P2_1/c$ (a 13.4096(4) Å, b 10.1105(2) Å, c 16.5364(7) Å, b 91.516(1)°). Likely occurrence of a phase transition as a result of different data collection temperatures (T = 100 K versus 173 K).

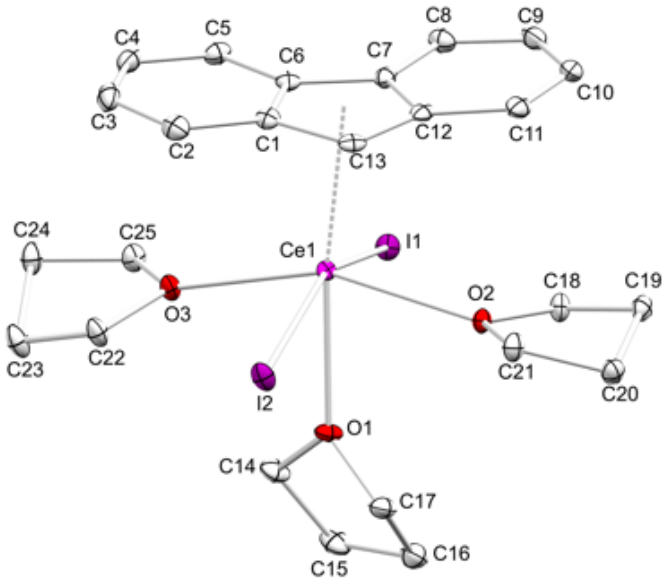

Figure S40. Crystal structure of $\mathbf{1}^{Ce,I}$. Hydrogen atoms are omitted for clarity. Atomic displacement ellipsoids are set at the 30% probability level. Selected interatomic distances and angles are listed in Table 1.

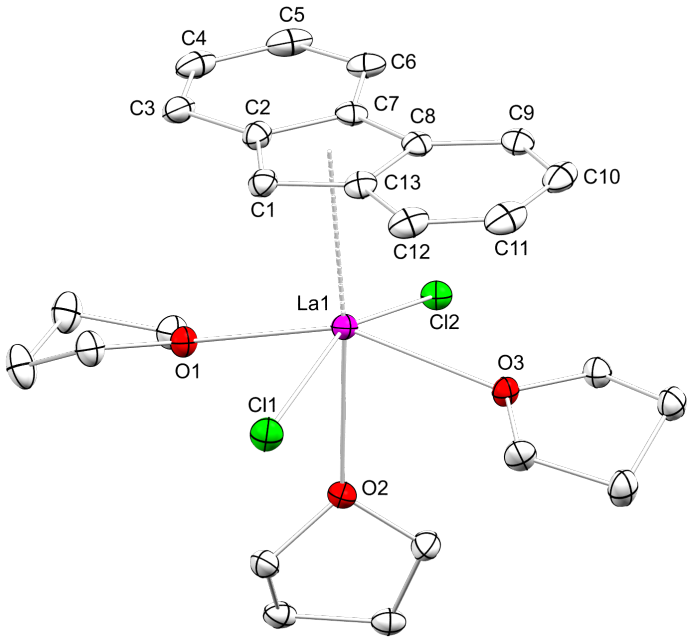

Figure S41. Crystal structure of $\mathbf{1}^{La,Cl}$. Hydrogen atoms are omitted for clarity. Atomic displacement ellipsoids set at the 30% probability level. Selected interatomic distances [Å] and angles [°]: La1–C1 2.792(4), La1–C2 2.955(4), La1–C7 2.979(4), La1–C8 2.893(4), La1–C13 2.795(4), La1···Cnt1 2.6242, La1–Cl1 2.7632(11), La1–Cl2 2.7685(11), La1–O1 2.484(2), La1–O2 2.549(3), La1–O3 2.516(2Cnt1···La1–Cl1 102.12, Cnt1···La1–O1 98.94, Cnt1···La1–O2 174.28, Cl1–La1–Cl2 156.27(3), Cl1–La1–O1 84.88(7), Cl1–La1–O2 77.74(7), O1–La1–O2 75.35(9), O1–La1–O3 152.83(8).

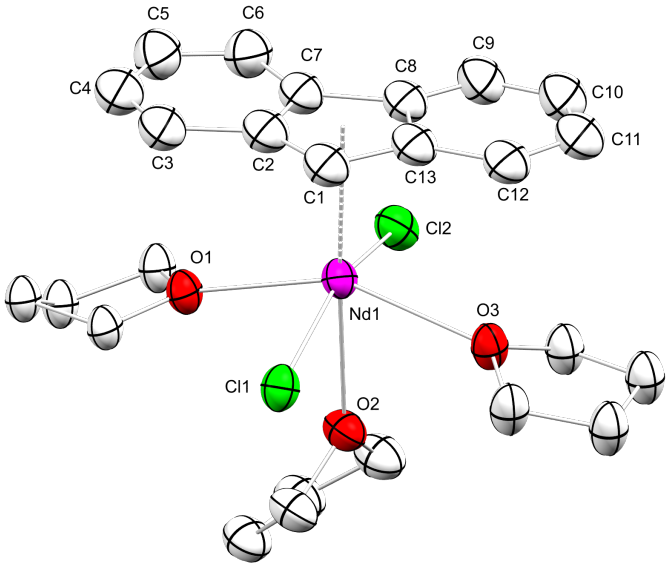

Figure S42. Crystal structure of $\mathbf{1}^{Nd,Cl}$. Hydrogen atoms are omitted for clarity. Atomic displacement ellipsoids set at the 30% probability level. Selected interatomic distances [Å] and angles [°]: Nd1–C1 2.832(18), Nd1–C2 2.870(18), Nd1–C7 2.791(17), Nd1–C8 2.807(17), Nd1–C13 2.872(17), Nd1···Cnt1 2.5583, Nd1–Cl1 2.698(4), Nd1–Cl2 2.699(5), Nd1–O1 2.451(10), Nd1–O2 2.544(10), Nd1–O3 2.458(10), Cnt1···Nd1–Cl1 98.87, Cnt1···Nd1–O1 105.66, Cnt1···Nd1–O2 177.10, Cl1–Nd1–Cl2 159.14(13), Cl1–Nd1–O1 85.8 (3), Cl1–Nd1–O2 81.3(3), O1–Nd1–O2 77.2(3), O1–Nd1–O3 150.2(3).

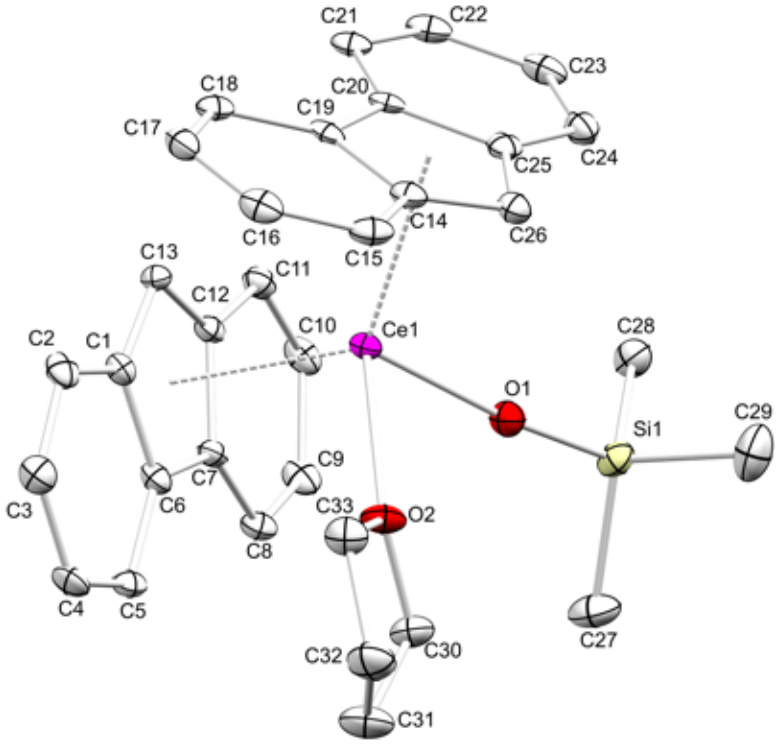

Figure S43. Crystal structure of $\mathbf{4}^{OSiMe3}$. Hydrogen atoms and lattice toluene are omitted for clarity. Atomic displacement ellipsoids are set at the 30% probability level. Selected interatomic distances and angles are listed in Table 1.

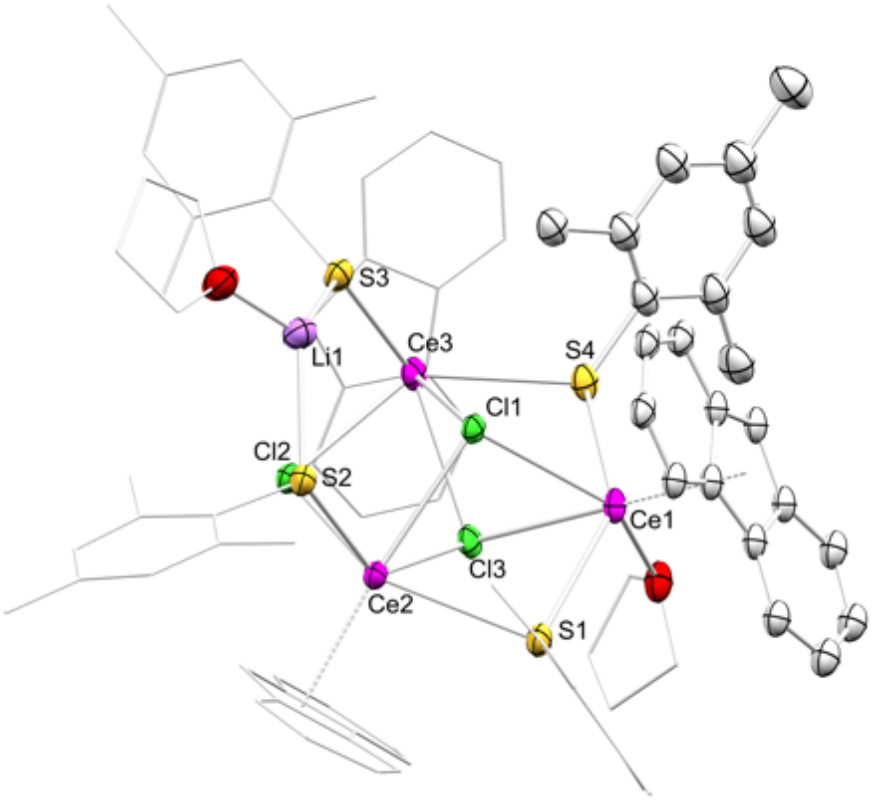

Figure S44. Connectivity of **5**. Hydrogen atoms are omitted for clarity. Atomic displacement ellipsoids are set at the 30% probability level.

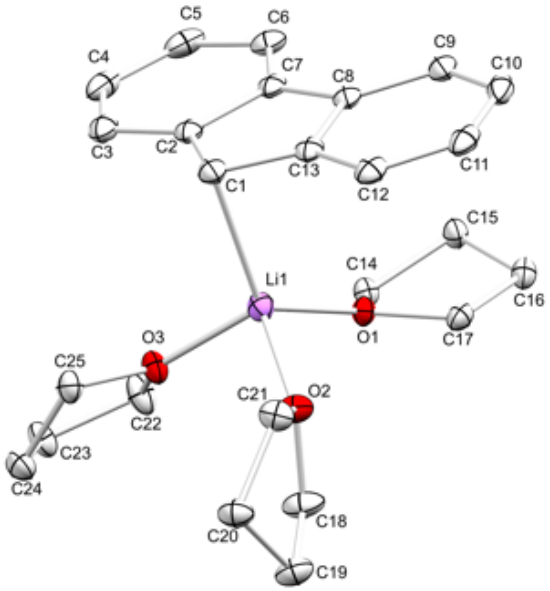

Figure S45. Crystal structure of **LiFlu(THF)$_3$**. Hydrogen atoms have been omitted for clarity. Atomic displacement ellipsoids are set at the 30% probability level. Selected interatomic distances and angles: Li-C1 2.294(2) Å, Li1-C2/C13 2.674(2) Å, Li1-O 1.879(2) (O1) – 1.973(2) (O2), Li1-C1-C2 88.71(8)°, Li1-C1-Cnt(Flu) 87.50°. The solid-state structure of **LiFlu(THF)$_3$**. Has been determined previously by F. Olbrich in 2002 (CSD Communication (Private Communication), CCDC 114095) with different cell parameters, but in the same space group $P2_1/c$ (a 13.4096(4) Å, b 10.1105(2) Å, c 16.5364(7) Å, β 91.516(1)°; T = 173 K).

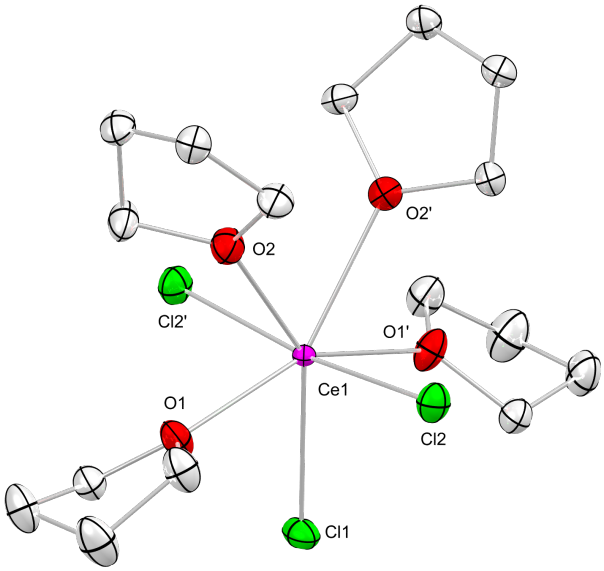

Figure S46. Crystal structure of **$CeCl_3(THF)_4$**. Hydrogen atoms have been omitted for clarity. Atomic displacement ellipsoids are set at the 30% probability level. Selected interatomic distances [Å] and angles [°]: Ce1-Cl1 2.6415(19), Ce1-Cl2/Cl2' 2.6181(11), Ce-O1/O1' 2.406(3), Ce1-O2/O2' 2.463(3), O1/O1'-Ce1-Cl1 76.06(11), O1/O1'-Ce1-O2/O2' 139.16(14), O2-Ce1-O2' 70.46(17), Cl2-Ce1-Cl2' 172.58(7).

IR Spectra

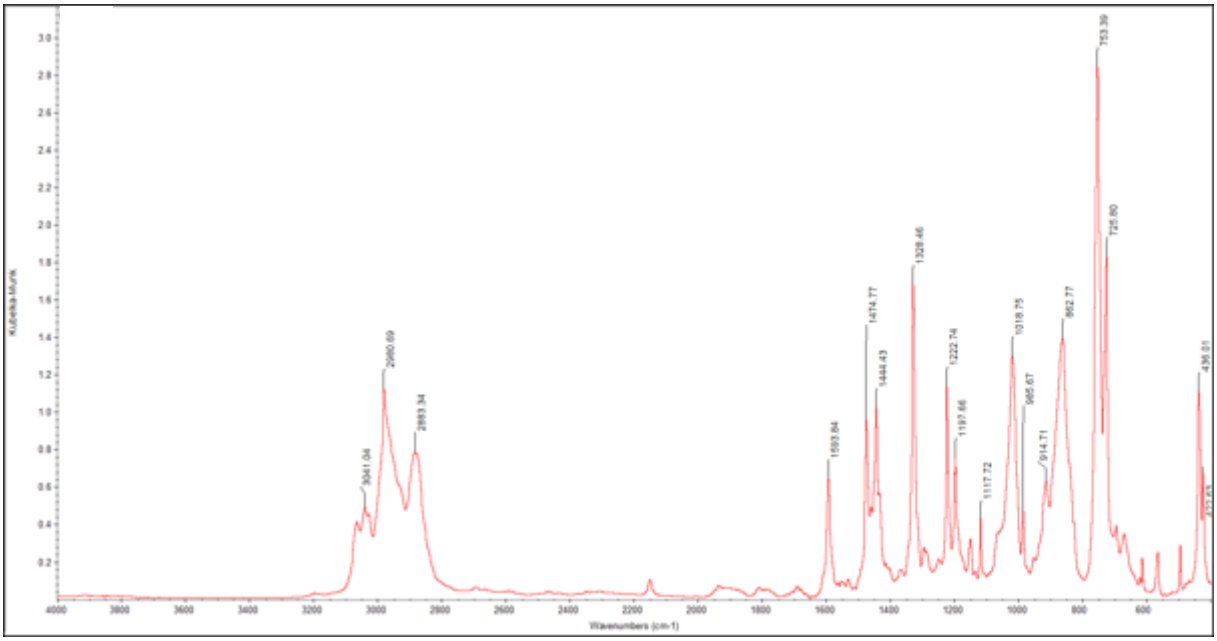

Figure S47. DRIFT spectrum of $FluCeCl_2(THF)_3$ ($\mathbf{1}^{Ce,Cl}$).

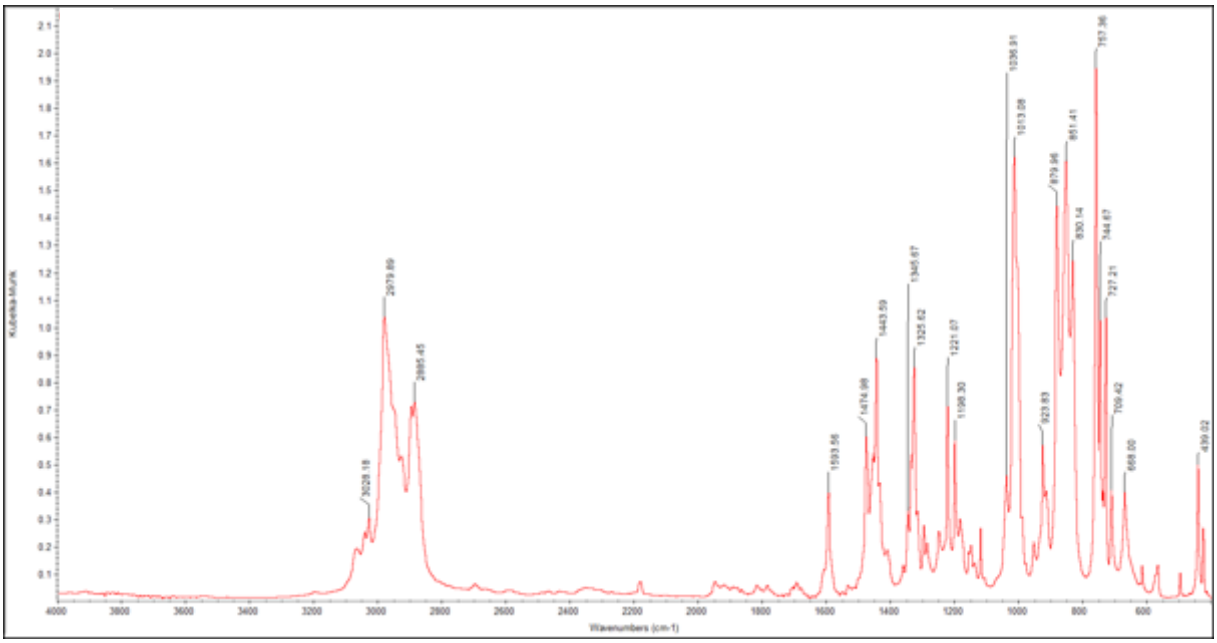

Figure S48. DRIFT spectrum of $FluCeI_2(THF)_3$ ($\mathbf{1}^{Ce,I}$).

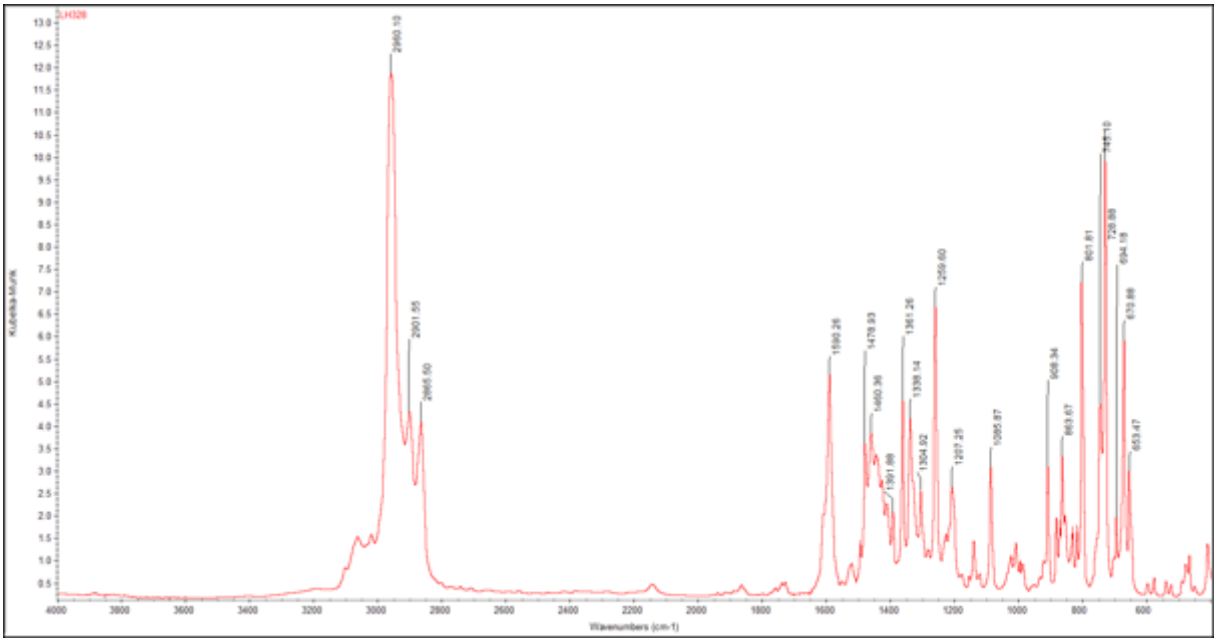

Figure S49. DRIFT spectrum of Flu$^{t\text{Bu}}{}_3$Ce(THF) (**2**).

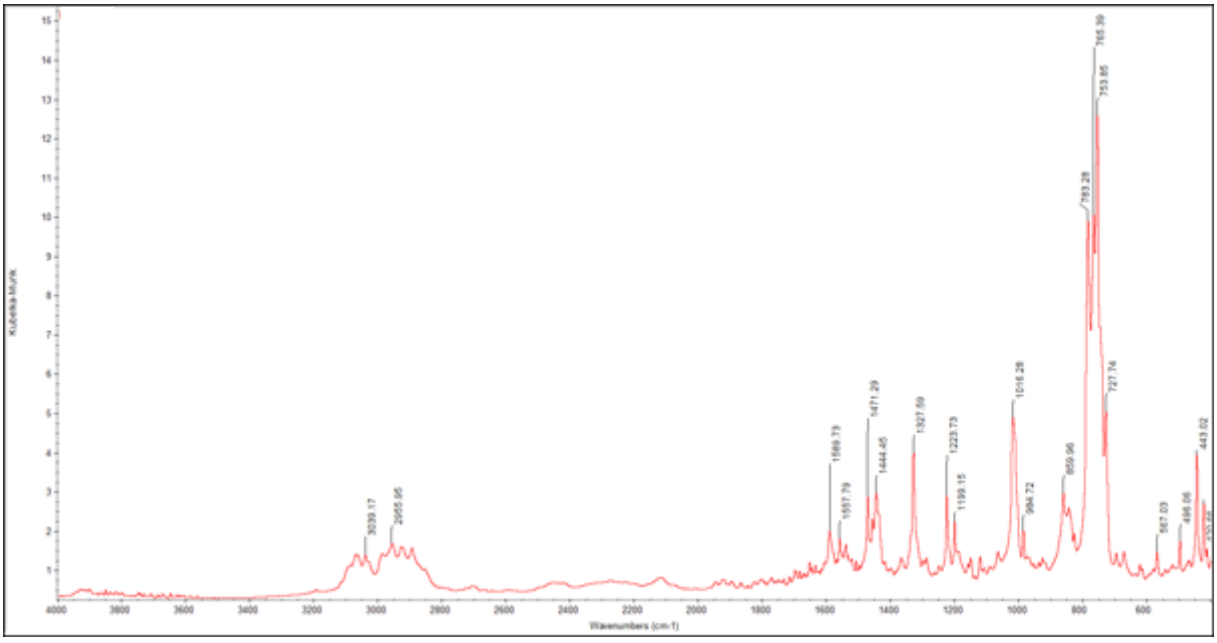

Figure S50. DRIFT spectrum of FluCeCp$_2$(THF) (**3$^{\text{Cp}}$**).

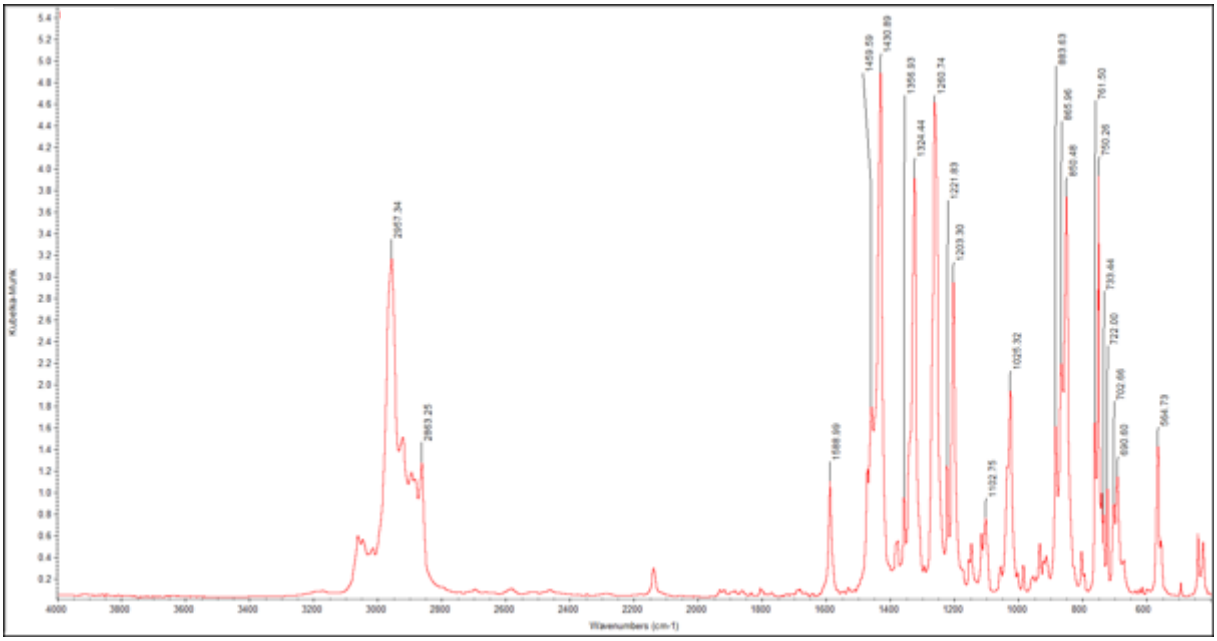

Figure S51. DRIFT spectrum of FluCe(OAr)$_2$(THF)$_2$ (**3^{OAr}**).

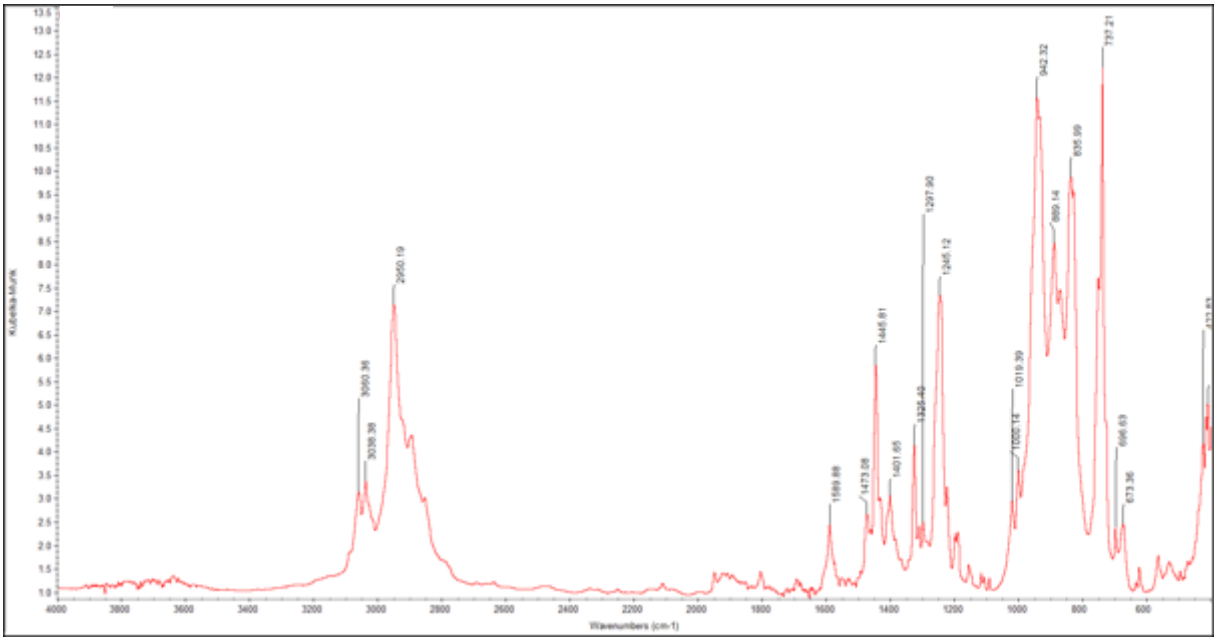

Figure S52. DRIFT spectrum of FluCe(OSiMe$_3$)$_2$(THF) (**3^{OSiMe3}**).

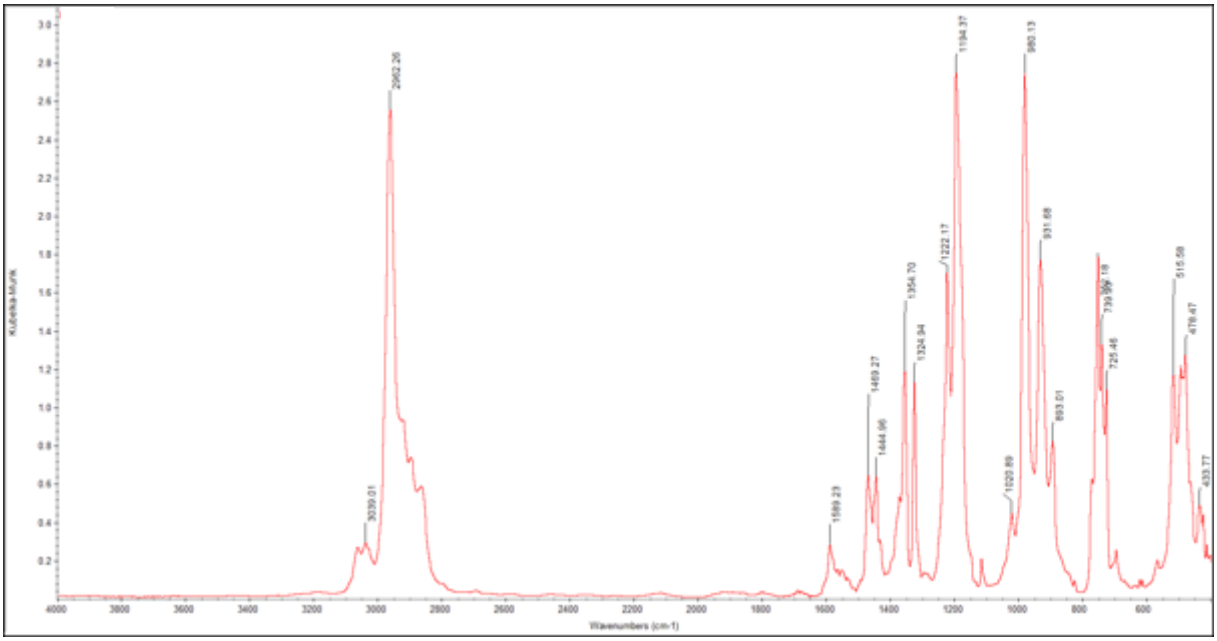

Figure S53. DRIFT spectrum of FluCe(O*t*Bu)$_2$(THF) (**3$^{O\mathit{t}Bu}$**).

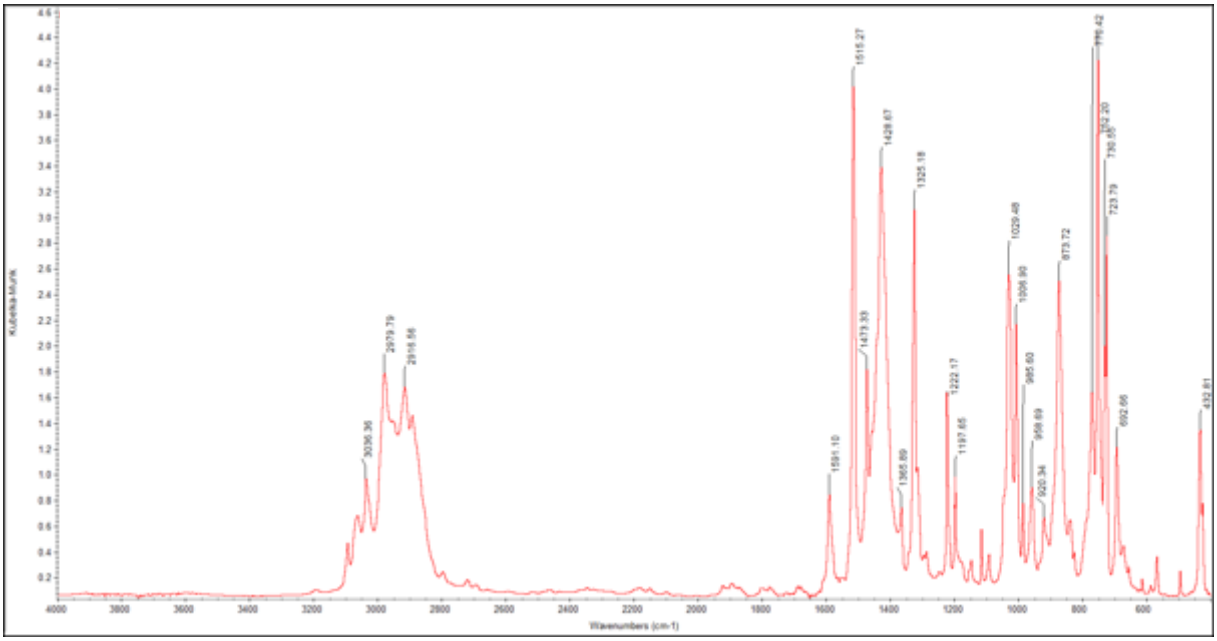

Figure S54. DRIFT spectrum of FluCe(Pz)$_2$(THF)$_2$ (**3^{Pz}**).

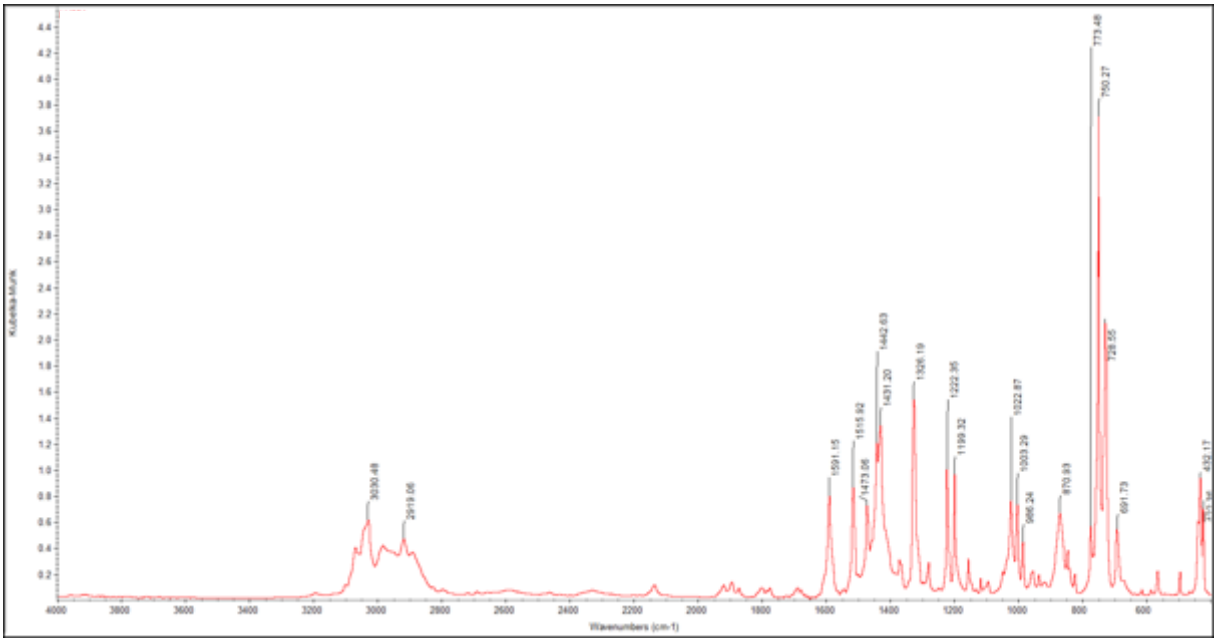

Figure S55. DRIFT spectrum of $Flu_2Ce(Pz)(THF)$ (**4**^{Pz}).

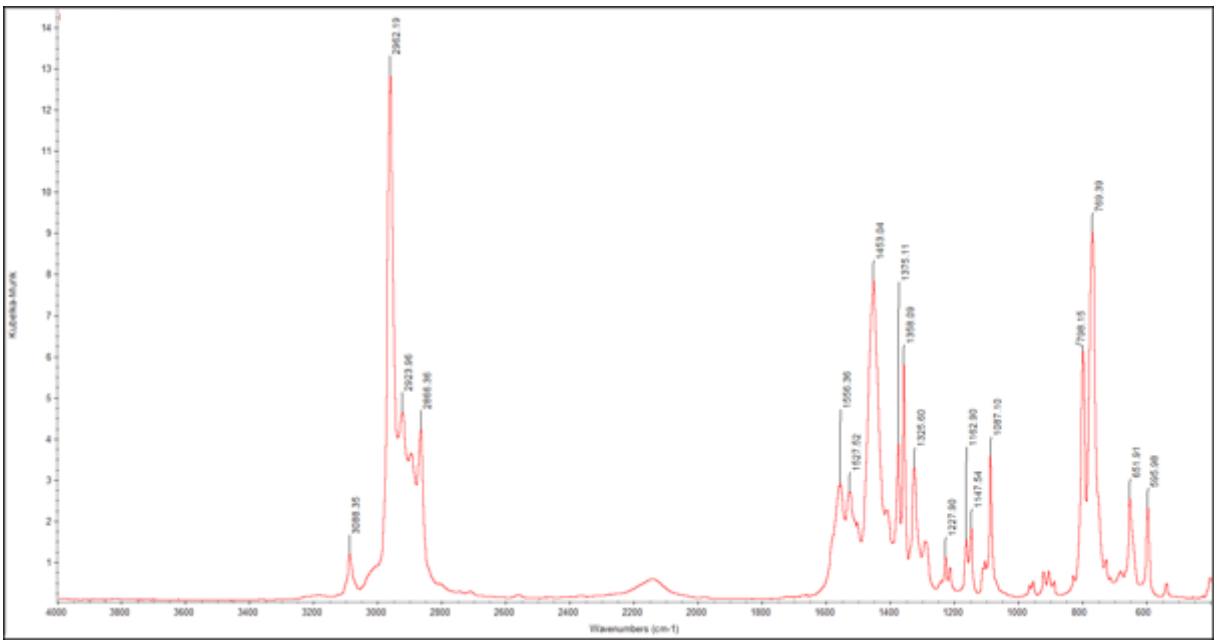

Figure S56. DRIFT spectrum of $Ce(dipp)_3$ (**6**).

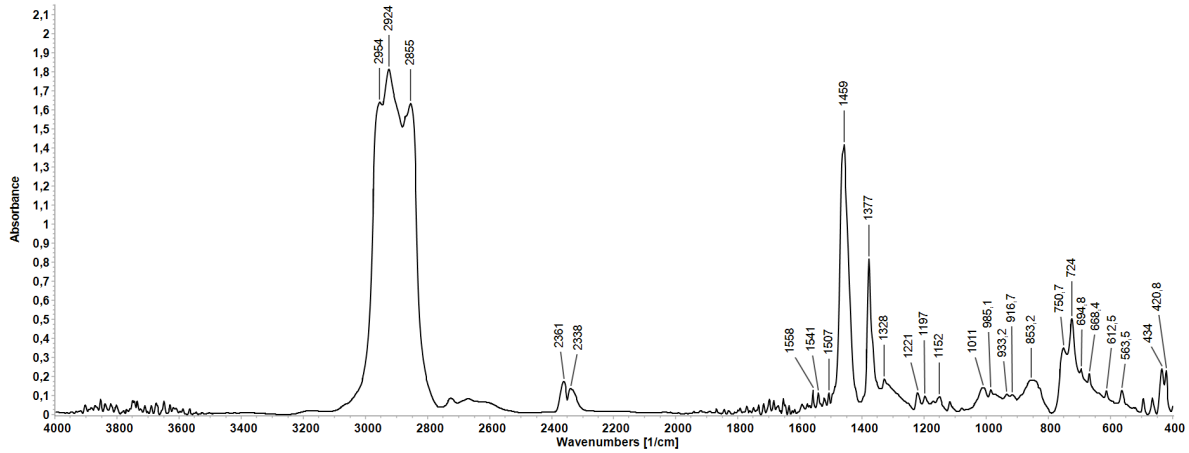

Figure S57. IR spectrum (Nujol mull) of $FluLaCl_2(THF)_3$ ($\mathbf{1}^{La,Cl}$).

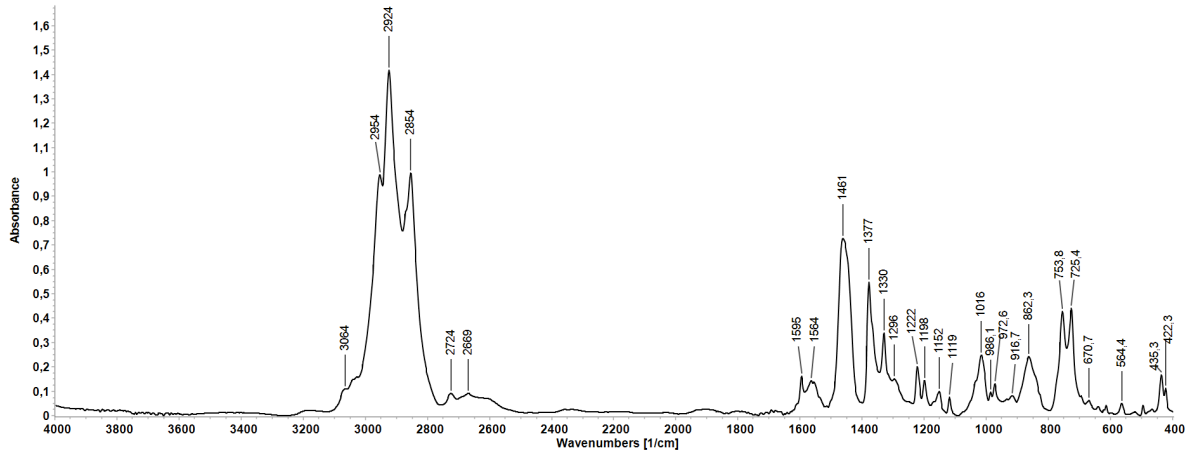

Figure S58. IR spectrum (Nujol mull) of $FluNdCl_2(THF)_3$ ($\mathbf{1}^{Nd,Cl}$).

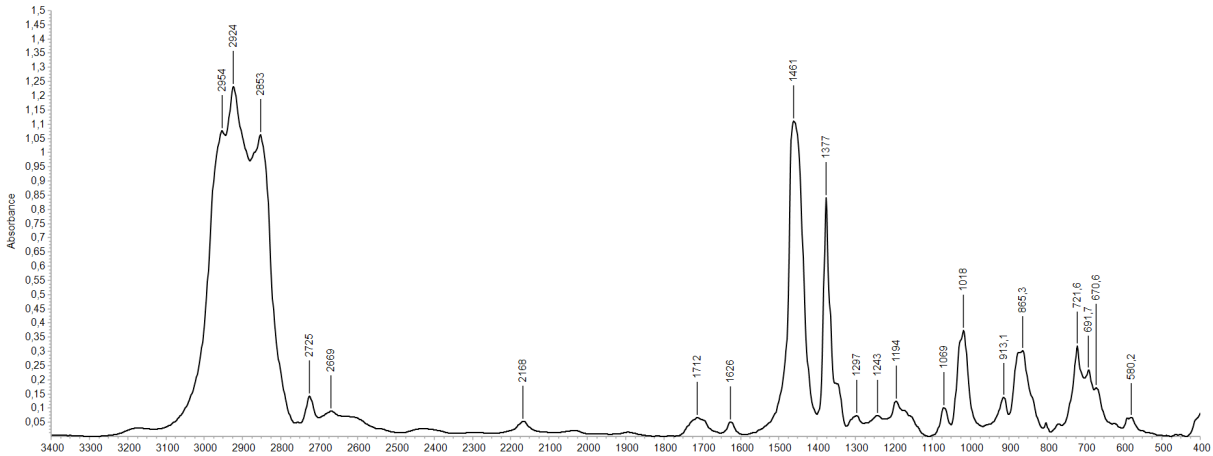

Figure S59. IR spectrum (Nujol mull) of $(C_5Me_5)CeCl_2(THF)_3$.

Paper IV

Rare-earth-metal half-sandwich complexes incorporating methyl, methylidene, and hydrido ligands

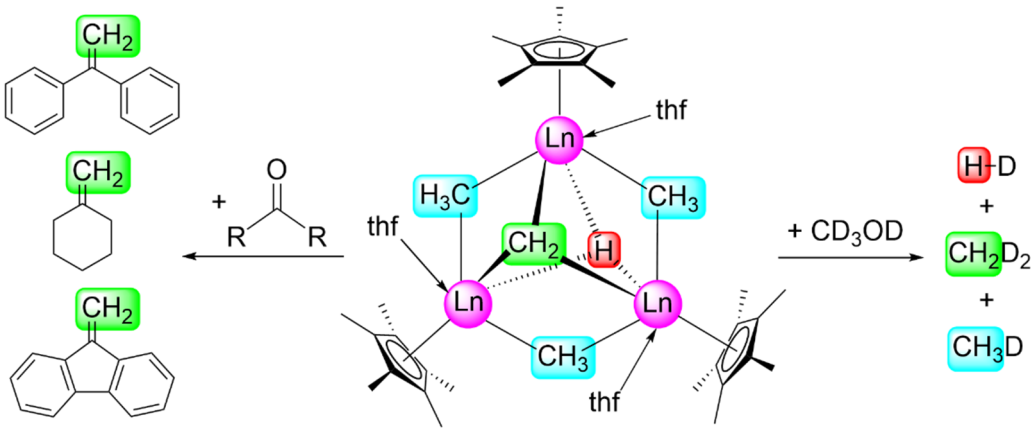

https://doi.org/10.1039/d2cc03532d
Chem. Commun. **2022**, *58*, 9132-9135

ChemComm

COMMUNICATION

View Article Online
View Journal | View Issue

Cite this: *Chem. Commun.*, 2022, **58**, 9132

Received 24th June 2022,
Accepted 17th July 2022

DOI: 10.1039/d2cc03532d

rsc.li/chemcomm

Rare-earth-metal half-sandwich complexes incorporating methyl, methylidene, and hydrido ligands†

Dennis A. Buschmann, Lion Schumacher and Reiner Anwander *

Complexes $Cp^*_3Ln_3(\mu_2\text{-}CH_3)_3(\mu_3\text{-}CH_2)(\mu_3\text{-}H)(thf)_3$ (Ln = Y, Dy; Cp* = C_5Me_5) are formed *via* elimination of CH_4 and C_2H_4 from the respective trinuclear polymethyl complexes $[Cp^*Ln(\mu_2\text{-}CH_3)_2]_3$, involving the methyl/methylidene complex $Cp^*_3Ln_3(\mu_2\text{-}CH_3)_3(\mu_3\text{-}CH_2)(\mu_3\text{-}CH_3)(thf)_2$ as an intermediate. Compound $Cp^*_3Y_3(\mu_2\text{-}CH_3)_3(\mu_3\text{-}CH_2)(\mu_3\text{-}H)(thf)_3$ displays "Schrock-type" nucleophilic carbene reactivity, converting ketones into the corresponding terminal alkenes. Treatment of $Cp^*_3Y_3(\mu_2\text{-}CH_3)_3(\mu_3\text{-}CH_2)(\mu_3\text{-}H)(thf)_3$ with [D4]methanol proved accessibility of all small-group functionalities as indicated by the simultaneous formation of deuterated HD and deuterated methanes CH_3D and CH_2D_2.

Rare-earth-metal hydride [Ln–H][1] and methylidene [Ln–CH_2] moieties[2] display unique reaction behavior. This is impressively documented for small molecule activation as well as for catalytic processes such as olefin polymerization or hydroelementation.[1,2] Although such compounds feature stabilizing ancillary ligands, the reactive hydrido and methylidene ligands routinely adopt bridging positions of high-nuclearity complexes.[1,2] Reactions of the half-sandwich clusters $[(C_5Me_4SiMe_3)Ln(\mu\text{-}H)_2]_4(thf)$ (Ln = Y, Lu) with carbon monoxide have been applied as mechanistic Fischer–Tropsch models and revealed the non-catalytic selective formation of ethylene *via* oxymethylene and enolate intermediates.[3] The yttrium complex $[(C_5Me_4SiMe_3)Y(\mu\text{-}H)_2]_4(thf)$ was also shown to exhibit distinct reactivity toward half-sandwich transition metal carbonyls such as $Cp^*Re(CO)_3$ and $Cp^*M(CO)_2$ (M = Rh, Ir).[4] Interestingly, the Y/Ir metal combination gave a bimetallic, pentanuclear complex $(C_5Me_4SiMe_3)_4Y_4(\mu\text{-}O)_2(\mu\text{-}H)_3(\mu\text{-}CH_2)(\mu\text{-}CH_3)Ir(C_5Me_5)$ featuring bridging hydrido, methyl, and methylidene ligands.[4] Here, we report on the first homolanthanide complexes featuring methylidene, methyl, and hydrido ligands. Special consideration has been given to the reactivity of such multi-functional complexes towards ketones and methanol.

Dissolving the well-defined trinuclear polymethyl yttrium complex $[Cp^*Y(\mu_2\text{-}CH_3)_2]_3$ (ref. 2*a*) in THF at ambient temperature led to the formation and crystallization of complex $[Cp^*_3Y_3(\mu_2\text{-}CH_3)_3(\mu_3\text{-}CH_2)(\mu_3\text{-}H)(thf)_3]$ ($\mathbf{1^Y}$). Complex $\mathbf{1^Y}$ is formed over a period of several days, with the reaction solution showing a gradual color change from colorless over yellow and orange to a deep red. The red THF solution produced colorless crystals of $\mathbf{1^Y}$ (26%), while the overall yield could be increased to 76% by the addition of *n*-hexane, which led to extensive precipitation of amorphous $\mathbf{1^Y}$.

Complex $\mathbf{1^Y}$ can be readily dissolved in [D_8]THF, with the ^{1}H NMR spectrum (Fig. S1, ESI†) revealing six signals. A μ_3-bridging hydrido ligand was indicated by a quartet at 4.61 ppm, showing a chemical shift and coupling constant ($^1J_{Y,H}$ = 12.2 Hz) in accordance with previously reported similar yttrium hydride complexes (*e.g.* $[(C_5Me_4SiMe_3)Y(\mu\text{-}H)_2]_4(thf)$, $[(Ap^*Y)_3(\mu_2\text{-}H)_3(\mu_3\text{-}H)_2(thf)_3]^+[B(C_6F_5)_4]^-$, Ap* = (2,6-diisopropylphenyl)[6-(2,4,6-triisopropylphenyl)pyridin-2-yl]amide).[5] The Cp* hydrogen atoms appeared as a singlet at 1.90 ppm, indicating an unhindered rotation about the yttrium–Cnt(Cp*) axes.[2a,6a,b] The quartet at −0.28 ppm is assigned to the μ_3-bridging CH_2 group, and shows a similar chemical shift as related half-sandwich methylidene complexes,[6] but slightly shifted toward lower field. The μ_2-bridging methyl ligands resonate at −1.03 ppm. The ^{13}C NMR spectrum (Fig. S2, ESI†) revealed three signals beside the solvent resonances. The signal at 115.0 ppm can be attributed to the Cp* ring carbon atoms, whereas the Cp*–CH_3 carbon atoms resonate at 12.0 ppm. The carbon resonance of the μ_2-bridging methyl groups was detected at 21.3 ppm and could be unambiguously identified by the ^{13}C–^{89}Y scalar coupling ($^1J_{YC}$ = 22.8 Hz). The μ_3-CH_2 carbon atom could be assigned by a cross peak in the HSQC-NMR spectrum at 95.3 ppm (Fig. S3, ESI†). For comparison, the respective μ_2-CH_3 and μ_3-CH_2 signals of complex $[Cp^*_3Y_3(\mu_2\text{-}CH_3)_3(\mu_3\text{-}CH_2)(\mu_3\text{-}CH_3)(thf)_2]$ (**I**) were reported at 24.7 and 95.6 ppm, respectively.[6]

Compound $\mathbf{1^Y}$ crystallized in the monoclinic space group $P2_1/n$ and is the first homometallic rare-earth-metal complex

Institut für Anorganische Chemie, Eberhard Karls Universität Tübingen, Auf der Morgenstelle 18, 72076, Tübingen, Germany. E-mail: reiner.anwander@uni-tuebingen.de

† Electronic supplementary information (ESI) available. CCDC 2181381 and 2181382. For ESI and crystallographic data in CIF or other electronic format see DOI: https://doi.org/10.1039/d2cc03532d

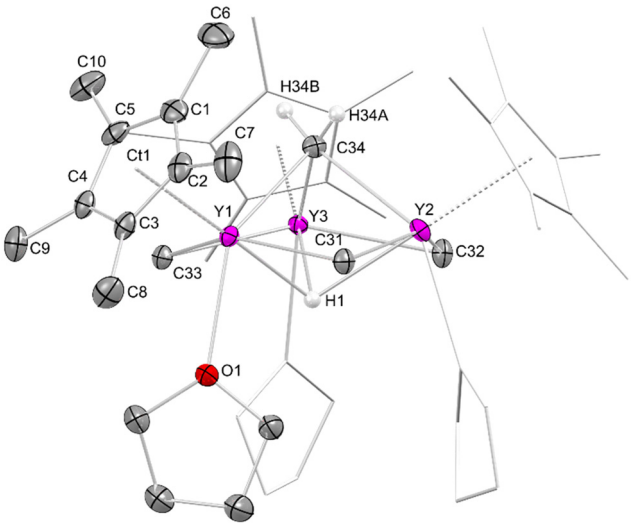

Fig. 1 Crystal structure of $\mathbf{1^Y}$ with atomic displacement parameters set at the 50% probability level. Hydrogen atoms (except for methylidene hydridos and μ_3-H) are omitted for clarity. The Cp* ligands and coordinated THF (except for one each) are represented by a wireframe model for improved visualization. For selected interatomic distances and angles, see the ESI.†

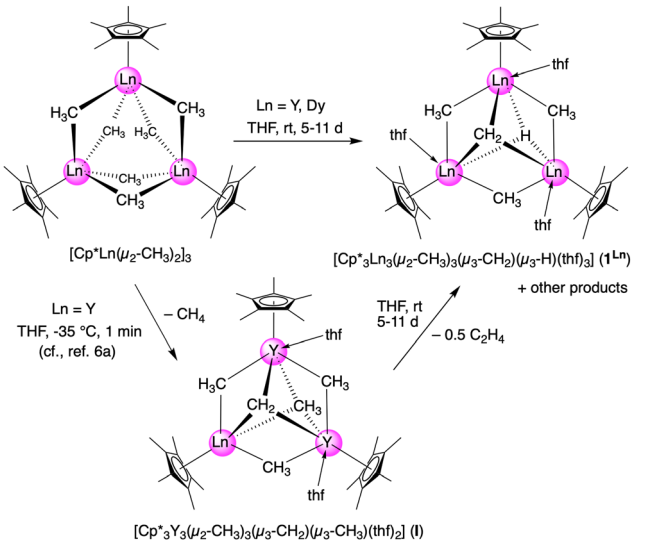

Scheme 1 Conversion of compound $[Cp^*Ln(\mu_2\text{-}CH_3)_2]_3$ into $[Cp^*_3Y_3(\mu_2\text{-}CH_3)_3(\mu_3\text{-}CH_2)(\mu_3\text{-}CH_3)(thf)_2]$ (**I**)[6] and $[Cp^*_3Ln_3(\mu_2\text{-}CH_3)_3(\mu_3\text{-}CH_2)(\mu_3\text{-}H)(thf)_3]$ (Ln = Y: $\mathbf{1^Y}$, Ln = Dy: $\mathbf{1^{Dy}}$).

bearing μ_3-bridging hydrido and methylidene ligands (Fig. 1). The XRD analysis further revealed that the μ_3-bridging moieties cap the faces of a six-membered metallacycle with alternating μ_2-bridging methyl groups and metal centers. By nature, compound $\mathbf{1^Y}$ displays metrics similar to the respective methyl/methylidene-bridged complex $[Cp^*_3Y_3(\mu_2\text{-}CH_3)_3(\mu_3\text{-}CH_2)(\mu_3\text{-}CH_3)(thf)_2]$ (**I**),[6] as evidenced by the Y1–C(Cp*) ($\mathbf{1^Y}$: 2.700(2)–2.728(2) Å; **I**: 2.703(3)–2.711(3) Å) and Y1–C(μ_2-Me) distances ($\mathbf{1^Y}$: 2.572(2) Å; **I**: 2.591(4) and 2.548(4) Å). However, the Y1–C(μ_3-CH_2) distances deviate notably between the two complexes. While the yttrium-methylene distances are similar in complex $\mathbf{1^Y}$ (Y–(μ_3-CH_2) = 2.416(2)–2.448(2) Å), the respective ones in complex **I** range between 2.283(4) Å and 2.477(3) Å. The same short–long–long pattern can be found for the μ_3-bridging CH_3 groups in **I** (Y1–(μ_3-CH_3) = 2.597(4), Y2–(μ_3-CH_3) = 2.744(4), Y3–(μ_3-CH_3) = 2.777(4) Å), while in $\mathbf{1^Y}$ the Y–(μ_3-H) distances deviate only slightly (Y–(μ_3-H) = 2.22(2)–2.34(2) Å). These notably distinct distances in complex **I** can be attributed to the asymmetric coordination of two yttrium centers by one THF molecule each. Not surprisingly, such distinct coordination chemistry bears also on the interatomic angles. For example, the Cnt(Cp*)···Y1-μ_2-CH_2 angle is more obtuse in complex **I** (122.93°) compared to the values involving the other two metal centers (Cnt2···Y2–(μ_2-CH_2) = 109.18°; Cnt3···Y3–(μ_2-CH_2) = 108.11°), which are comparable to those in complex $\mathbf{1^Y}$ (111.28–111.52°). Overall, complex $\mathbf{1^Y}$ shows a more symmetric arrangement than **I**, certainly due to all yttrium metal centers bearing additional coordinated THF molecules.

The synthesis shown in Scheme 1 also applies for other mid-sized rare-earth metals, as demonstrated for paramagnetic dysprosium. Keeping the corresponding dysprosium polymethyl complex $[Cp^*Dy(\mu_2\text{-}CH_3)_2]_3$ (ref. 6*b*) for several days in THF solution afforded the respective mixed methylidene/hydride complex $[Cp^*_3Dy_3(\mu_2\text{-}CH_3)_3(\mu_3\text{-}CH_2)(\mu_3\text{-}H)(thf)_3]$ ($\mathbf{1^{Dy}}$, 74%). Complex $\mathbf{1^{Dy}}$ is isostructural to complex $\mathbf{1^Y}$, revealing marginally longer interatomic distances as expected for the slightly increased ionic radius of the dysprosium metal centers compared to yttrium.

As the methyl complex $[Cp^*Y(\mu_2\text{-}CH_3)_2]_3$ (ref. 2*a*) converts rapidly to the methyl/methylidene-bridged complex $[Cp^*_3Y_3(\mu_2\text{-}CH_3)_3(\mu_3\text{-}CH_2)(\mu_3\text{-}CH_3)(thf)_2]$ (**I**), even at −35 °C,[6] we reasoned that **I** might display an intermediate along the slow formation of $\mathbf{1^Y}$. For clarification, a ^{1}H NMR spectrum in [D$_8$]THF was recorded for the previously reported methyl/methylidene-bridged complex $[Cp^*_3Y_3(\mu_2\text{-}CH_3)_3(\mu_3\text{-}CH_2)(\mu_3\text{-}CH_3)(thf)_2]$ (**I**).[6] The respective signals resonate at 1.91 ppm (C_5Me_5), −0.33 ppm (μ_3-CH_2), −0.54 ppm (μ_2-CH_3) and −0.90 ppm (μ_3-CH_3) (Fig. S4, ESI†). In order to more closely examine such thermodynamically controlled formation of $\mathbf{1^{Ln}}$, a solution of $[Cp^*Y(\mu_2\text{-}Me)_2]_3$ (ref. 2*a*) in [D$_8$]THF was examined by ^{1}H NMR spectroscopy (Fig. S8–S14, ESI†). The reaction progress was monitored by repeatedly taking samples from a solution placed in a 20 mL vial. The ^{1}H NMR spectrum recorded immediately after the addition of [D$_8$]THF, shows the expected signal set of $[Cp^*Y(\mu_2\text{-}CH_3)_2]_3$,[2a] with resonances from the C_5Me_5 groups (1.95 ppm) and the μ_2-bridging methyl groups (−1.38 ppm) (Fig. S8, ESI†). After 2 days, the spectrum revealed a significant decrease in intensity of both resonances, as well as new resonances for C_5Me_5 moieties (1.91, 1.87, 1.85 ppm) assignable to complexes **I** and **1Y** (Fig. S9, ESI†), and the persistence of the signal at 0.18 ppm ascribed to methane (formation of ethene not yet observable). In addition to the resonances of the μ_2-bridging methyl groups of **I** and $\mathbf{1^Y}$ located at −0.90 ppm (**I**) and −1.03 ppm ($\mathbf{1^Y}$), two other doublets resonate at −0.77 ppm and −1.21 ppm, respectively, which represent other unidentified yttrium methyl species generated during the decomposition process. Together with the emergence of the aforementioned two new C_5Me_5 resonances, the spectrum alludes to the coexistence of **I** and $\mathbf{1^Y}$ in solution. Ten days after the start of the

experiment, the initial resonance of the C_5Me_5 methyl groups of $[Cp^*Y(\mu_2\text{-}CH_3)_2]_3$ was no longer visible, indicating the complete conversion into either one species (Fig. S10, ESI†). After 17 days, the detection of the resonance of the μ_3-bridging hydrido ligand (4.61 ppm) unequivocally confirmed the formation of $\mathbf{1^Y}$. Surprisingly, an emerging signal at 5.33 ppm pointed to the formation of ethene while the methane signal had disappeared *via* gas diffusion (Fig. S12, ESI†). The ethene resonance (5.33 ppm) became only prominent 24 days after the start of the reaction (Fig. S13, ESI†). In combination with the gradually receding μ_2-CH_3 signals of **I** (δ_{Me} = −0.77 ppm) and the simultaneous growth of the respective resonance of $\mathbf{1^Y}$ (δ_{Me} = −1.02 ppm), the presence of ethene in solution corroborates the proposed stepwise mechanism of a fast formation of **I** *via* the elimination of methane, followed by a slow transformation into $\mathbf{1^Y}$ *via* the elimination of ethene. After 30 days of reaction time, no further changes in the ^{1}H NMR spectrum were observed (Fig. S14, ESI†). In conclusion, the ^{1}H NMR data suggest a bimolecular mechanism *via* an elimination of CH_2 fragments from complex **I** and subsequent coupling to ethene.

Due to the appearance of several unknown species during the formation process of $\mathbf{1^Y}$, we wondered whether its generation indeed involves complex **I** as an intermediate species. Alternatively, both compounds might display decomposition products of $[Cp^*Y(\mu_2\text{-}CH_3)_2]_3$. Therefore, complex **I** was synthesized and isolated according to literature procedures.[6] Subsequently, the complex was redissolved in THF (Scheme 1), and its decomposition monitored *via* ^{1}H NMR spectroscopy. The respective spectra after 7 days (Fig. S6, ESI†) and 14 days (Fig. S7, ESI†) show the expected signals of both complexes **I** and $\mathbf{1^Y}$, as well as resonances for methane and ethene. In particular, the steadily increasing signal intensity for $\mathbf{1^Y}$ and the gradual disappearance of the μ_3-bridging methyl group (−0.54 ppm) support the initial hypothesis of a transformation of **I** into $\mathbf{1^Y}$, according to Scheme 1.

In order to assess the accessibility of the various functional groups in compound $\mathbf{1^Y}$, reactions with ketones and methanol were examined (Scheme 2). Rare-earth-metal methylidene complexes are considered as Schrock-type nucleophilic carbenes, engaging in efficient methylenation of carbonylic substrates.[2a,d,q] Hence, complex $\mathbf{1^Y}$ was treated with various ketones (benzophenone, cyclohexanone, 9-fluorenone) in a 2 : 1 ratio in $[D_8]$THF at ambient temperature, and the reaction progress monitored by ^{1}H NMR spectroscopy. Complete consumption of the methylidene resonance of $\mathbf{1^Y}$ (−0.28 ppm) was revealed for all tested ketones, already after 15 minutes. This indicated a methylenation performance similar to the Tebbe reagent $Cp_2Ti(\mu\text{-}CH_2)(\mu\text{-}Cl)AlMe_2$.[7] The methylene signals were detected as singlets at 5.42 ppm (1,1-diphenyl ethylene, Fig. S15, ESI†), 4.54 ppm (methylene cyclohexane, S15, ESI†), and 6.11 ppm (9-methylene fluorene, S16, ESI†).

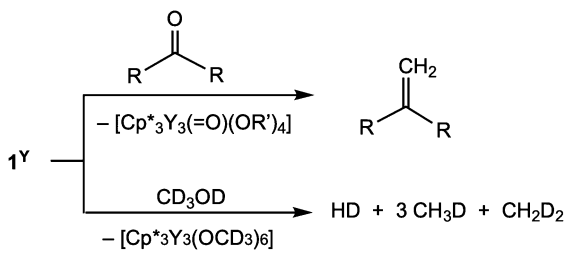

Scheme 2 Reactivity of $[Cp^*_3Y_3(\mu_2\text{-}CH_3)_3(\mu_3\text{-}CH_2)(\mu_3\text{-}H)(thf)_3]$ ($\mathbf{1^Y}$) towards benzophenone, cyclohexanone and 9-fluorenone as well as $[D_4]$methanol.

The use of two equivalents of ketone entailed competitive ketone-to-alkoxy transformations, as indicated by NMR spectroscopy (further signals in the range between 1.5 and 2.5 ppm). In particular, the disappearance of the hydrido resonance at 4.61 ppm and a significantly reduced intensity and low-field shift of the a μ_2-methyl resonance (−0.93 ppm *vs.* −1.03 ppm) support the occurrence of competitive reactions.

To assess any preference/selectivity for methylenation, an equimolar reaction of $\mathbf{1^Y}$ with 9-fluorenone was performed under otherwise identical conditions (Fig. S18, ESI†). Surprisingly, the signals of the methylenated product 9-methylene fluorene (7.76 ppm, 7.71 ppm, 6.11 ppm) were much more prominent in contrast to the 2 : 1 reaction. Seemingly, after 15 minutes, 9-fluorenone had been converted selectively into the methylenated product (76% yield). Moreover, the ^{1}H NMR spectrum indicated the preservation of the trinuclear structure, proposing a composition of $[Cp^*_3Y_3(\mu_2\text{-}CH_3)_3(\mu_3\text{-}O)(\mu_3\text{-}H)(thf)_3]$. Apparently, competitive reactions of 9-fluorenone with the hydrido or methyl ligands of $\mathbf{1^Y}$ only occur in the presence of excess amount of ketone.

Next, we reasoned that a small protic substrate $[D_4]$methanol should be able to track all sufficiently basic ligands in $\mathbf{1^Y}$. For comparison, previous studies by Evans *et al.* on complex $[\{Cp_2Y(\mu_2\text{-}H)\}_3(\mu_3\text{-}H)][Li(thf)_4]$ revealed the inertness of the μ_3-bridging hydrido ligand toward methanol, even at elevated temperatures.[8] The exclusive conversion of the μ_2-bridging hydridos to methoxy ligands in compound $[\{Cp_2Y(\mu_2\text{-}OCH_3)\}_3(\mu_3\text{-}H)][Li(thf)_4]$ pointed to a steric inaccessibility of the μ_3-bridging hydrido ligand. In contrast, complex $\mathbf{1^Y}$ has a much lower steric saturation around the μ_3-bridging hydrido ligand, caused by fluxional THF ligands. Extensive protonolysis of $\mathbf{1^Y}$ by $[D_4]$methanol could be easily detected by ^{1}H NMR spectroscopy (Scheme 2). The ^{1}H NMR spectrum recorded after 5 minutes (Fig. S18, ESI†) revealed the disappearance of the signals assigned to the bridging methyl, methylidene and hydrido ligands. Instead, resonances of the deuterated ligands, HD (triplet at 4.50 ppm, $^1J_{HD}$ = 42.6 Hz),[9] as well as CH_3D (triplet at 0.16 ppm, $^2J_{HD}$ = 1.9 Hz) and CH_2D_2 (quintet at 0.14 ppm, $^2J_{HD}$ = 1.9 Hz) could be detected.[10] The slight deviation of the expected integral ratio of 9 : 2 of the deuterated methanes' triplet and quintet is attributed to signal overlap. For comparison, non-deuterated methane resonates at 0.18 ppm. Overall, treatment of $\mathbf{1^Y}$ with $[D_4]$methanol revealed complete deuteration of the bridging ligands. Unlike the aforementioned $[\{Cp_2Y(\mu_2\text{-}OCH_3)\}_3(\mu_3\text{-}H)][Li(thf)_4]$, the bridging μ_3-hydrido ligand of complex $\mathbf{1^Y}$ engages in a deuterolysis reaction as well, likely due to the reduced steric shielding by only three ancillary Cp* ligands.

To conclude, treatment of half-sandwich complexes $[Cp^*Ln(\mu_2\text{-}CH_3)_2]_3$ (Ln = Y, Dy) with THF revealed a new reaction path to the methyl–methylidene–hydrido-bridged trinuclear species

$Cp^*_3Ln_3(\mu_2\text{-}CH_3)_3(\mu_3\text{-}CH_2)(\mu_3\text{-}H)(thf)_3$. The methyl/methylidene-bridged complex $[Cp^*_3Y_3(\mu_2\text{-}CH_3)_3(\mu_3\text{-}CH_2)(\mu_3\text{-}CH_3)(thf)_2]$ was identified as a reaction intermediate. Complex $Cp^*_3Ln_3(\mu_2\text{-}CH_3)_3(\mu_3\text{-}CH_2)(\mu_3\text{-}H)(thf)_3$ readily engages in the olefination of ketones and extensive protonolysis with methanol.

Conflicts of interest

There are no conflicts to declare.

Notes and references

1 For reviews on rare-earth-metal hydride chemistry, see: (*a*) M. Ephritikhine, *Chem. Rev.*, 1997, **97**, 2193–2242; (*b*) Z. Hou, M. Nishiura and T. Shima, *Eur. J. Inorg. Chem.*, 2007, 2535–2545; (*c*) M. Konkol and J. Okuda, *Coord. Chem. Rev.*, 2008, **252**, 1577–1991; (*d*) M. Nishiura and Z. Hou, *Nat. Chem.*, 2010, **2**, 257–268; (*e*) A. A. Trifonov, *Coord. Chem. Rev.*, 2010, **254**, 1327–1347; (*f*) J. Cheng, K. Saliu, M. J. Ferguson, R. McDonald and J. Takats, *J. Organomet. Chem.*, 2010, **695**, 2696–2702; (*g*) W. Fegler, A. Venugopal, M. Kramer and J. Okuda, *Angew. Chem., Int. Ed.*, 2015, **54**, 1724–1736; (*h*) T. Shima and Z. Hou, Molecular Rare Earth Hydride Clusters, in *Recent Development in Clusters of Rare Earths and Actinides: Chemistry and Materials*, ed. Z. Zheng, Springer, Berlin, Heidelberg, 2016, pp. 315–335; (*i*) J. Okuda, *Coord. Chem. Rev.*, 2017, **340**, 2–9.

2 (*a*) H. M. Dietrich, K. W. Törnroos and R. Anwander, *J. Am. Chem. Soc.*, 2006, **128**, 9298–9299; (*b*) J. Scott, H. Fan, B. F. Wicker, A. R. Fout, M.-H. Baik and D. J. Mindiola, *J. Am. Chem. Soc.*, 2008, **130**, 14438–14439; (*c*) R. Litlabø, M. Zimmermann, K. Saliu, J. Takats, K. W. Törnroos and R. Anwander, *Angew. Chem., Int. Ed.*, 2008, **47**, 9560–9564; (*d*) M. Zimmermann, D. Rauschmaier, K. Eichele, K. W. Törnroos and R. Anwander, *Chem. Commun.*, 2010, **46**, 5346–5348; (*e*) W.-X. Zhang, Z. Wang, M. Nishiura, Z. Xi and Z. Hou, *J. Am. Chem. Soc.*, 2011, **133**, 5712–5715; (*f*) J. Hong, L. Zhang, X. Yu, M. Li, Z. Zhang, P. Zheng, M. Nishiura, Z. Hou and X. Zhou, *Chem. – Eur. J.*, 2011, **17**, 2130–2137; (*g*) T. Li, M. Nishiura, J. Cheng, Y. Li and Z. Hou, *Chem. – Eur. J.*, 2012, **18**, 15079–15085; (*h*) T. Li, M. Nishiura, J. Cheng, W. Zhang, Y. Li and Z. Hou, *Organometallics*, 2013, **32**, 4142–4148; (*i*) J. Hong, L. Zhang, K. Wang, Y. Zhang, L. Weng and X. Zhou, *Chem. – Eur. J.*, 2013, **19**, 7865–7873; (*j*) K. Wang, G. Luo, J. Hong, X. Zhou, L. Weng, Y. Luo and L. Zhang, *Angew. Chem., Int. Ed.*, 2014, **53**, 1053–1056; (*k*) J. Kratsch and P. W. Roesky, *Angew. Chem., Int. Ed.*, 2014, **53**, 376–383; (*l*) J. Zhou, T. Li, L. Maron, X. Leng and Y. Chen, *Organometallics*, 2015, **34**, 470–476; (*m*) D. Schädle, M. Meermann-Zimmermann, C. Maichle-Mössmer, C. Schädle, K. W. Törnroos and R. Anwander, *Dalton Trans.*, 2015, **44**, 18101–18110; (*n*) M. Zhang, J. Zhang, X. Ni and Z. Shen, *RSC Adv.*, 2015, **5**, 83295–83303; (*o*) J. Hong, Z. Li, Z. Chen, L. Weng, X. Zhou and L. Zhang, *Dalton Trans.*, 2016, **45**, 6641–6649; (*p*) J. Hong, H. Tian, L. Zhang, X. Zhou, I. del Rosal, L. Weng and L. Maron, *Angew. Chem., Int. Ed.*, 2018, **57**, 1062–1067; (*q*) V. M. Birkelbach, F. Kracht, H. M. Dietrich, C. Stuhl, C. Maichle-Mössmer and R. Anwander, *Organometallics*, 2020, **39**, 3490–3504; (*r*) P. Zatsepin, E. Lee, J. Gu, M. R. Gau, P. J. Carroll, M.-H. Baik and D. J. Mindiola, *J. Am. Chem. Soc.*, 2020, **142**, 10143–10152.

3 T. Shima and Z. Hou, *J. Am. Chem. Soc.*, 2006, **128**, 8124–8125.

4 Y. Takenaka, T. Shima, J. Baldamus and Z. Hou, *Angew. Chem., Int. Ed.*, 2009, **48**, 7888–7891.

5 (*a*) K. C. Hultzsch, P. Voth, T. P. Spaniol and J. Okuda, *Z. Anorg. Allg. Chem.*, 2003, **629**, 1272–1276; (*b*) D. Cui, O. Tardif and Z. Hou, *J. Am. Chem. Soc.*, 2004, **126**, 1312–1313; (*c*) D. M. Lyubov, C. Döring, S. Y. Ketkov, R. Kempe and A. A. Trifonov, *Chem. – Eur. J.*, 2011, **17**, 3824–3826; (*d*) T. Shima and Z. Hou, *Chem. – Eur. J.*, 2013, **19**, 3458–3466.

6 (*a*) C. O. Hollfelder, L. N. Jende, H. M. Dietrich, K. Eichele, C. Maichle-Mössmer and R. Anwander, *Chem. – Eur. J.*, 2019, **25**, 7298–7302; (*b*) C. O. Hollfelder, M. Zimmermann-Meermann, G. Spiridopoulos, D. Werner, K. W. Törnroos, C. Maichle-Mössmer and R. Anwander, *Molecules*, 2019, **24**, 3703.

7 F. N. Tebbe, G. W. Parshall and G. S. Reddy, *J. Am. Chem. Soc.*, 1978, **100**, 3611–3613.

8 (*a*) W. J. Evans, M. S. Sollberger, S. I. Khan and R. Bau, *J. Am. Chem. Soc.*, 1988, **110**, 439–446; (*b*) P. Garbacz, *Chem. Phys.*, 2014, **443**, 1–7.

9 X. L. Wang, W. Liu, Y.-Y. Yu, Y. Song, W. Q. Fang, D. Wei, X.-Q. Gong, Y.-F. Yao and H. G. Yang, *Nat. Commun.*, 2016, **7**, 1–7.

10 R. Bernheim and B. Lavery, *J. Chem. Phys.*, 1965, **42**, 1464.

Electronic Supplementary Material (ESI) for Chemical Communications.

Supporting Information

Rare-earth-metal half-sandwich complexes incorporating methyl, methylidene, and hydrido ligands

Dennis A. Buschmann,[a] Lion Schumacher[a] and Reiner Anwander*[a]

[a] Eberhard Karls Universität Tübingen, Institut für Anorganische Chemie, Auf der Morgenstelle 18, 72076 Tübingen, Germany

Correspondence: reiner.anwander@uni-tuebingen.de

Table of Contents

Experimental Procedures

General considerations.

All manipulations were performed under rigorous exclusion of air and moisture using standard Schlenk and glovebox techniques (MBraun MB200B; <0.1 ppm O_2, <0.1 ppm H_2O, argon atmosphere). The solvents *n*-hexane, toluene, THF and Et_2O were purified using Grubbs-type columns (MBraun SPS, solvent purification system). [D_8]THF (99.5%, Sigma-Aldrich) was dried over Na/K-alloy for 24 h, vacuum transferred prior to use and stored inside a glovebox. [D_4]methanol (≥ 99.8%, Sigma-Aldrich) was stored over molecular sieve inside a glovebox. Benzophenone (99%, Fluka) was used without further purification. Cyclohexanone (>99%, Acros Organics) was destilled prior to use. 9-fluorenone (98%, Sigma-Aldrich) was sublimed prior to use. 1,2,3,4,5-pentamethyl cyclopentadiene (HCp*) (98%, abcr) was used as received. Homoleptic $Ln(AlMe_4)_3$ (Ln = Y, Dy),[1] half-sandwich complexes $Cp^*Ln(AlMe_4)_2$ (Ln = Y, Dy)[2,3] and trinuclear complex $[Cp^*_3Y_3(\mu_2\text{-}CH_3)_3(\mu_3\text{-}CH_3)(\mu_3\text{-}CH_2)(thf)_2]$ (**I**)[4] were synthesized according to literature procedures. NMR spectra of air and moisture sensitive compounds were recorded by using J. Young valve NMR tubes on a Bruker AVII+400 spectrometer (^{1}H: 400.11 MHz; ^{13}C: 100.61 MHz) and on a Bruker AVII+500 spectrometer (^{1}H: 500.13 MHz, ^{13}C: 125.76 MHz). NMR chemical shifts are referenced to internal solvent resonances and reported in parts per million relative to tetramethyl silane. Coupling constants are given in Hertz. Elemental analyses were performed on an Elementar Vario Micro Cube. IR spectra were recorded on a NICOLET 6700 FTIR spectrometer with a DRIFT cell (KBr window, Kubelka-Munk conversion).

$[Cp^*_3Y_3(\mu_2\text{-}CH_3)(\mu_3\text{-}CH_2)(\mu_3\text{-}H)(thf)_3]$ ($\mathbf{1^Y}$). $Cp^*Y(AlMe_4)_2$ (49.7 mg, 0.125 mmol) was dissolved in *n*-hexane (2 mL) and diethyl ether (37.1 mg, 0.5 mmol) was added, which led to immediate precipitation of amorphous $[Cp^*YMe_2]_3$. After stirring the suspension for 30 min at ambient temperature, the product was separated by centrifugation. The precipitate was washed with *n*-hexane (3 x 2 mL) and then $[Cp^*YMe_2]_3$ was dried under vacuum (yield: 23.4 mg, 0.092 mmol, 74%) for 30 min. Afterwards, $[Cp^*YMe_2]_3$ was dissolved in THF (1 mL), the formation of gas (CH_4) could be observed, and the solution was stored at ambient temperature. Over a period of five days, a color was observed (colorless, yellow (1 d), orange (3 d), red (5 d)). After five days, light yellow crystals formed. The red supernatant was removed, and the crystalline product was washed with *n*-hexane (3 x 2 mL) and with *n*-pentane (1 x 2 mL). The crystalline product was dried under vacuum (yield: 7.5 mg, 7.9 μmol, 26%). The overall yield was increased to 76% (22.1 mg, 0.023 mmol) by treating the red supernatant with the same workup procedure as described before. ^{1}H NMR (400 MHz, [D_8]THF, 26 °C): δ = 4.61 (q, $^1J_{YH}$ = 12.2 Hz, 1H, μ_3-*H*), 3.61 (m, coord. C_4H_8O), 1.90 (s, 45H, $CpCH_3$), 1.77 (m, coord. C_4H_8O), -0.28 (q, $^2J_{YH}$ = 3.8 Hz, 2H, μ_3-CH_2), -1.03 (s, 9H, μ_2-CH_3) ppm. $^{13}C\{^1H\}$ NMR (126 MHz, [D_8]THF, 26 °C): δ = 115.0 (C_5Me_5), 95.3 (μ_3-CH_2, HSQC), 21.3 (μ_2-CH_3, $^1J_{YC}$ = 22.8 Hz), 12.2 ($Cp(CH_3)_5$) ppm. IR(DRIFT): $\tilde{\nu}$ = 2958 (m), 2901 (m), 2857 (m), 2715 (vw), 1445 (w), 1373 (vw), 1342 (vw), 1294 (vw), 1249 (vw), 1154 (w), 1034 (s), 955 (s), 923 (m), 878 (vs), 665 (w), 593 (m), 559 (m), 540 (m), 515 (vs), 502 (vs), 492 (s), 478 (s), 455 (s), 444 (s), 432 (m), 425 (s), 413 (vs) cm^{-1}. Elemental analysis of $\mathbf{1^Y}$ calculated for $C_{46}H_{81}Y_3O_3$ (948.87 g/mol): C 58.23%, H 8.60%; found: C 57.10%, H 8.33%. The low carbon value can be attributed to a loss of coordinated THF upon drying the product under vacuum.

[Cp*$_3$Dy$_3$(μ_2-Me)(μ_3-CH$_2$)(μ_3-H)(thf)$_3$] ($\mathbf{1^{Dy}}$). Cp*Dy(AlMe$_4$)$_2$ (118.0 mg, 0.25 mmol) was dissolved in *n*-hexane (2 mL) and diethyl ether (74.1 mg, 1.0 mmol) was added, which lead to immediate precipitation of amorphous [Cp*DyMe$_2$]$_3$. After stirring the suspension for 30 min at ambient temperature, the product was separated by centrifugation. The precipitate was washed with *n*-hexane (3 x 2 mL) and then [Cp*DyMe$_2$]$_3$ was dried under vacuum (yield: 65.1 mg, 0.2 mmol, 79%) for 30 min. Afterwards, 10 mg (0.03 mmol) of [Cp*DyMe$_2$]$_3$ were dissolved in THF (0.5 mL), the formation of gas (CH$_4$) was observed, and the solution was stored at ambient temperature. Over a period of five days, a color change was observed (colorless, yellow (1 d), orange (3 d)). After eight days, the solution was stored at -40 °C, followed by partial removal of the solvent under vacuum until colorless crystals formed. The orange supernatant was removed, and the crystalline product was washed with *n*-hexane (3 x 2 mL) and with *n*-pentane (1 x 2 mL). The crystalline product was dried under vacuum (yield: 2.5 mg, 2.1 μmol, 21%). The overall yield was increased to 74% (9.0 mg, 7.7 µmol) by treating the orange supernatant with the same workup procedure as described before. IR(DRIFT): $\tilde{\nu}$ = 2961 (s), 2910 (vs), 2901 (vs), 2856 (vs), 2721 (vw), 1487 (vw), 1436 (m), 1375 (w), 1340 (vw), 1299 (vw), 1244 (vw), 1179 (w), 1086 (w), 1057 (w), 1020 (s), 912 (m), 868 (s), 800 (w), 740 (w), 671 (s), 619 (m), 598 (m), 587 (m), 565 (m), 549 (m), 539 (m), 529 (m), 515 (m), 502 (s), 488 (m), 469 (m), 457 (m), 451 (m), 445 (m), 434 (s), 427 (s), 419 (s) cm^{-1}. Elemental analysis of $\mathbf{1^{Dy}}$ calculated for C$_{46}$H$_{81}$Dy$_3$O$_3$ (1169.65 g/mol): C 47.24%, H 6.98%; found: C 47.46%, H 6.35%.

Reaction of Cp*$_3$Y$_3$(μ_2-CH$_3$)$_3$(μ_3-CH$_3$)(μ_3-CH$_2$)(thf)$_2$ (I) with THF. Compound **I** was synthesized according to literature procedures.[4] Afterwards, **I** was redissolved in THF and stirred at ambient temperature. Samples were repeatedly taken from the reaction mixture, the solvent was removed completely under vacuum, the residual solid was redissolved in [D$_8$]THF, and a ^{1}H NMR spectrum was recorded to monitor the reaction progress.

General procedure for methylidene transfer reactions. All reactions were monitored via ^{1}H NMR spectroscopy. In a *J. Young* valve NMR tube, 5 mg of $\mathbf{1^{Y}}$ were dissolved in [D$_8$]THF (0.3 mL). Two equivalents of the respective ketone (benzophenone, cyclohexanone, 9-fluorenone) or an equimolar amount of 9-fluorenone were dissolved in [D$_8$]THF (0.2 mL) and added, and the tube was sealed immediately. After 15 minutes, during which the tube was shaken repeatedly, a ^{1}H NMR spectrum was recorded. The yields of all reactions were calculated from the integral ratio olefinic functionality/Y-CH$_2$.

Reaction with [D$_4$]methanol. In a *J. Young* NMR-tube, complex $\mathbf{1^{Y}}$ (5 mg, 0.005 mmol) was dissolved in [D$_8$]THF, [D$_4$]methanol was added (0.05 mL), and the tube was sealed immediately. Gas evolution was observed for approximately 3 min. After 5 min, a ^{1}H NMR spectrum was recorded.

NMR Spectroscopy

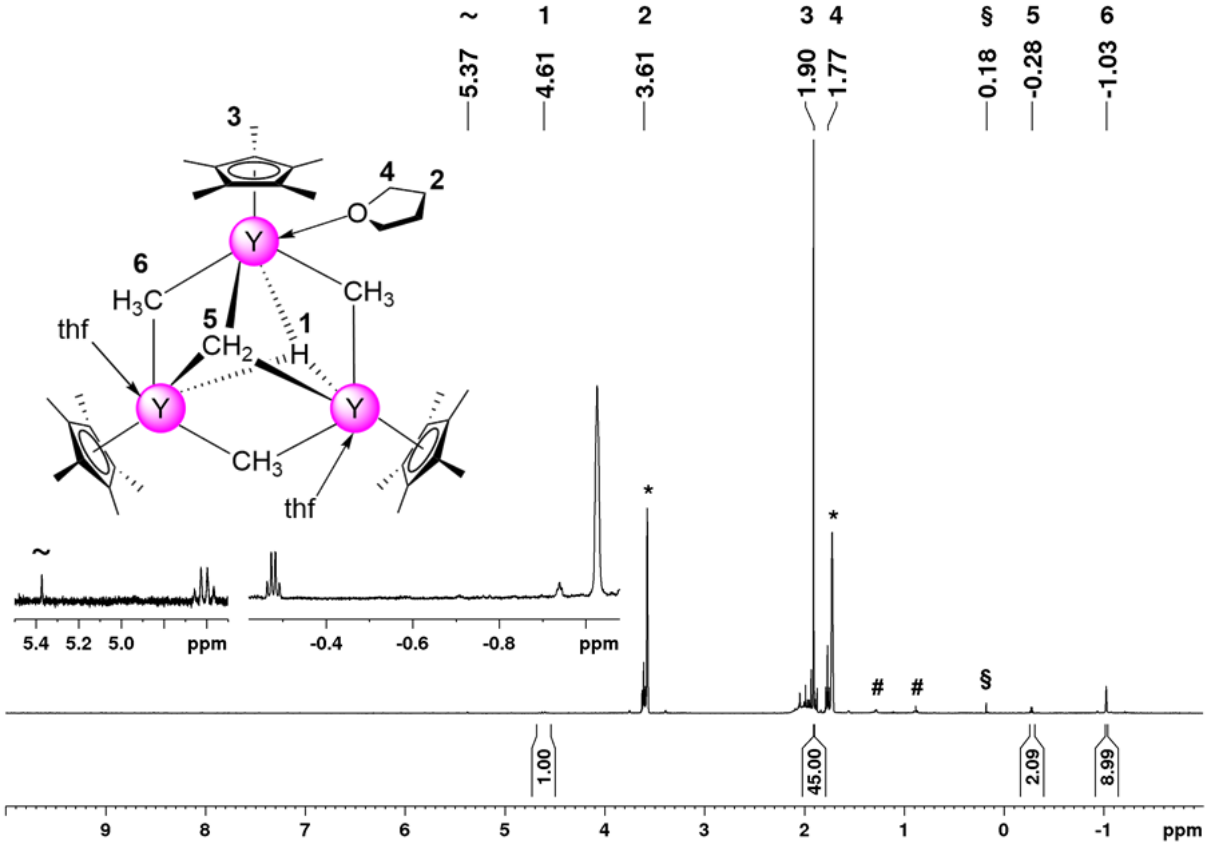

Figure S2. ^{1}H NMR spectrum (400 MHz) of **1^{Y}** in [D$_8$]THF at 26 °C. The solvent residual signals are marked with an asterisk (#: *n*-hexane, §: methane, ~: ethene).

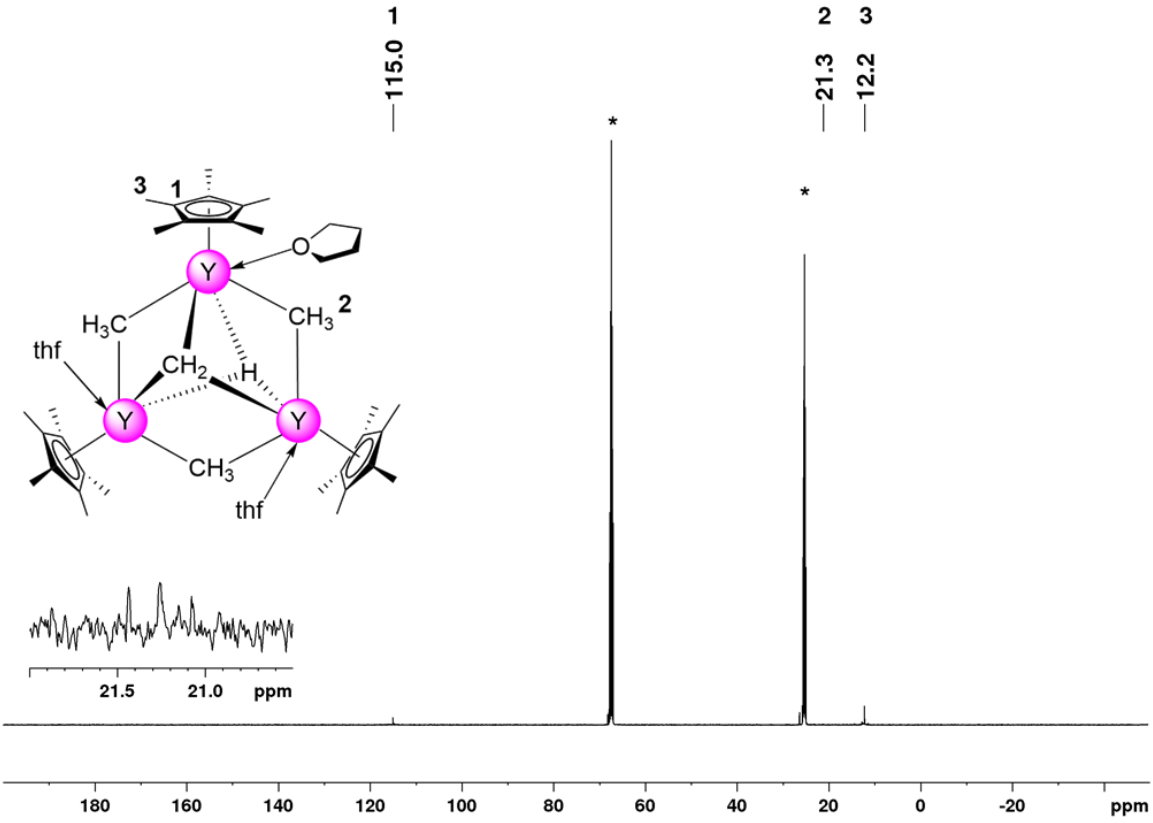

Figure S1. ^{13}C{^{1}H} NMR spectrum (126 MHz) of **1^{Y}** in [D$_8$]THF at 26 °C. The solvent residual signals are marked with an asterisk.

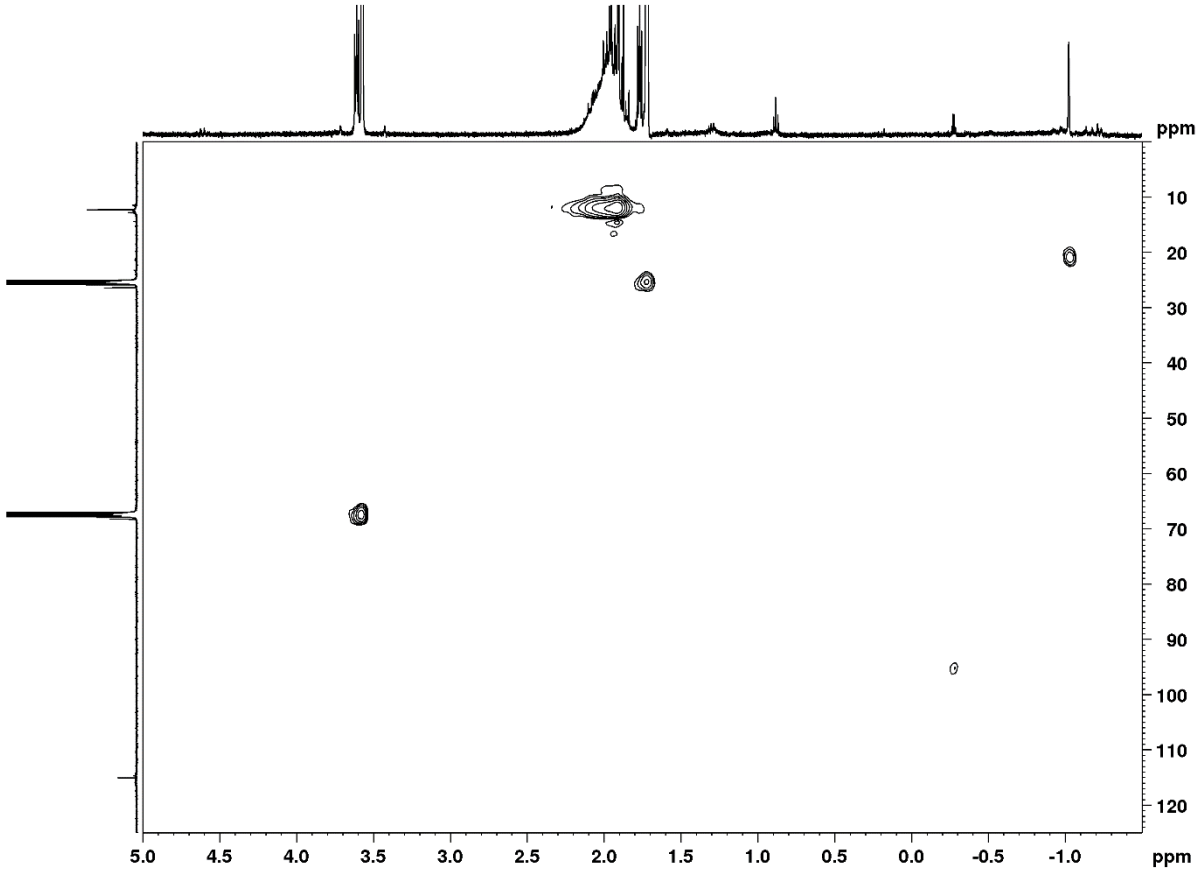

Figure S3. HSQC NMR spectrum of **1**^{Y} in [D_8]THF at 26 °C.

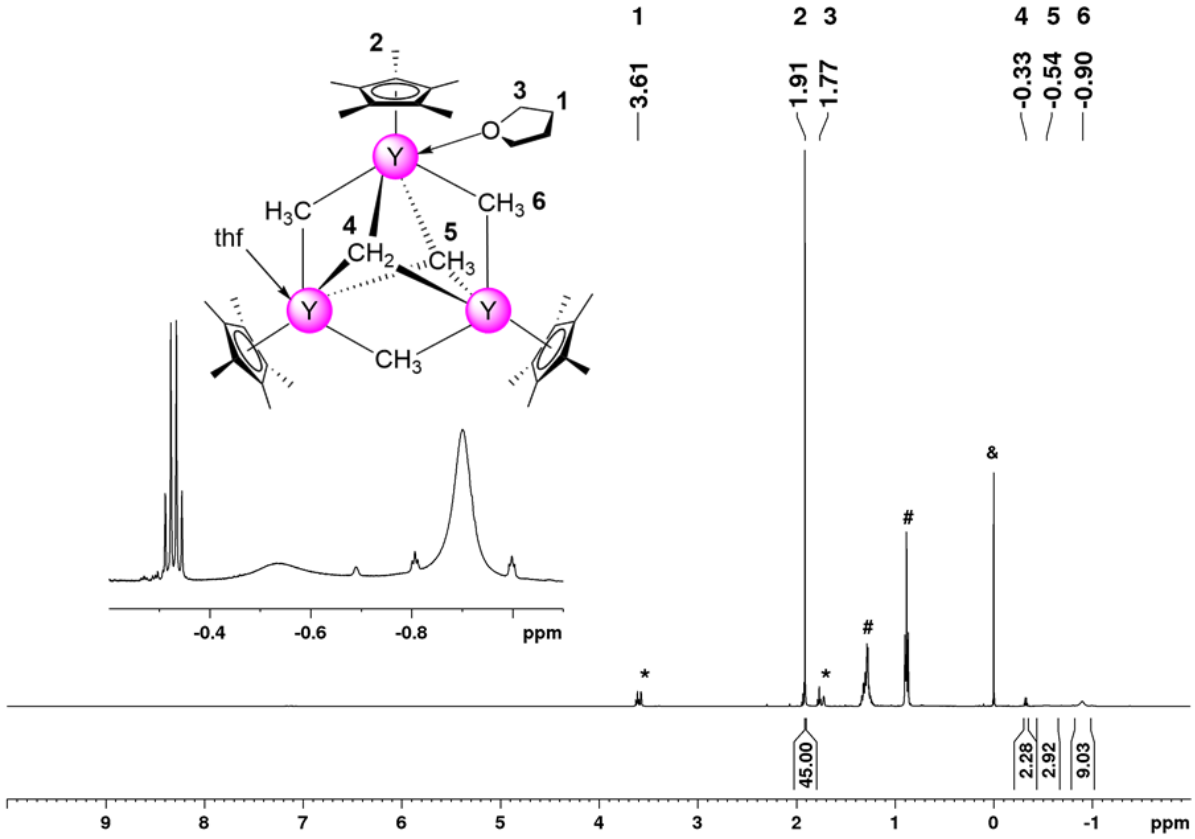

Figure S4. ^{1}H NMR spectrum (400 MHz) of [Cp*$_3$Y$_3$(μ_2-CH$_3$)$_3$(μ_3-CH$_3$)(μ_3-CH$_2$)(thf)$_2$] (**I**) in [D$_8$]THF at 26 °C. The solvent residual signals are marked with an asterisk (#: *n*-hexane, &: SiMe$_4$).

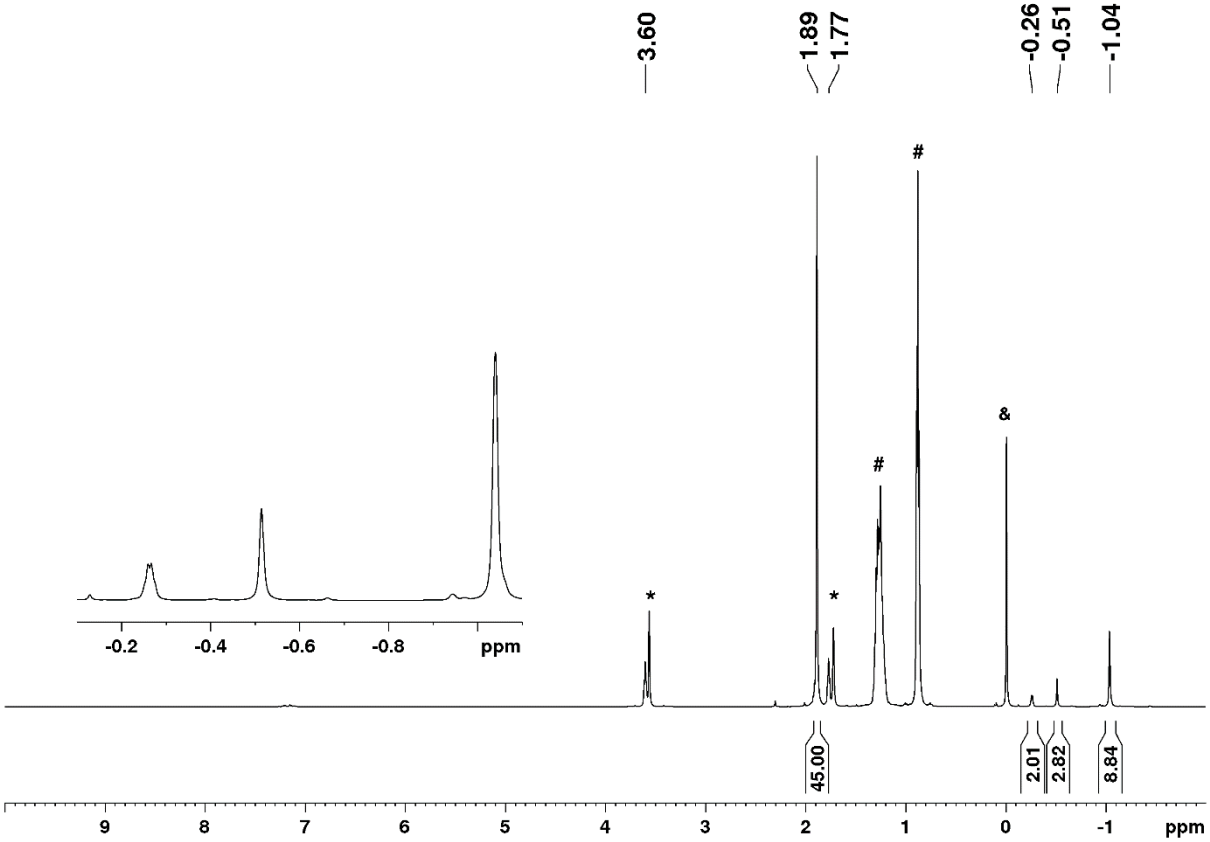

Figure S5. ^{1}H NMR spectrum (500 MHz) of [Cp*$_3$Y$_3$(μ_2-CH$_3$)$_3$(μ_3-CH$_3$)(μ_3-CH$_2$)(thf)$_2$] (**I**) in [D$_8$]THF at -60 °C. The solvent residual signals are marked with an asterisk (#: *n*-hexane, &: SiMe$_4$).

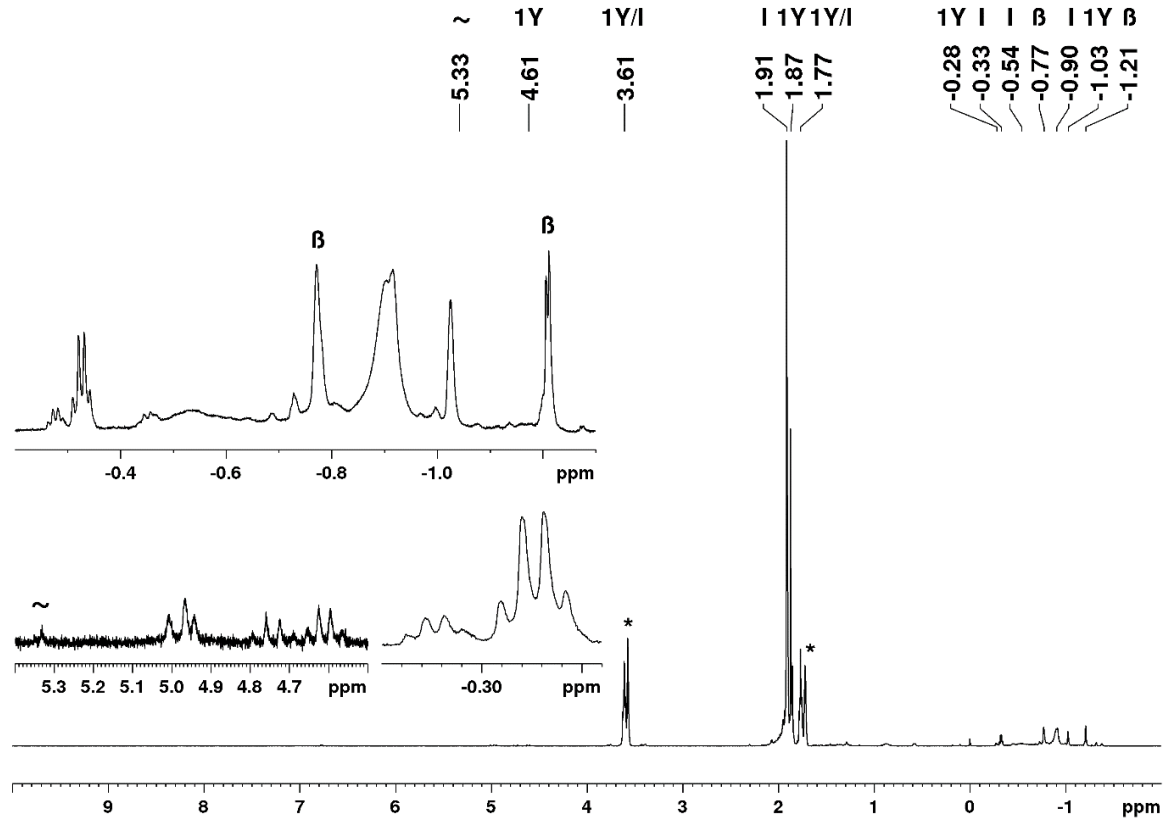

Figure S6. ^{1}H NMR spectrum (400 MHz) of [Cp*$_3$Y$_3$(μ_2-CH$_3$)$_3$(μ_3-CH$_3$)(μ_3-CH$_2$)(thf)$_2$] (**I**) in [D$_8$]THF at 26 °C after 7 days. The solvent residual signals are marked with an asterisk (~: ethene, ß: unknown yttrium species).

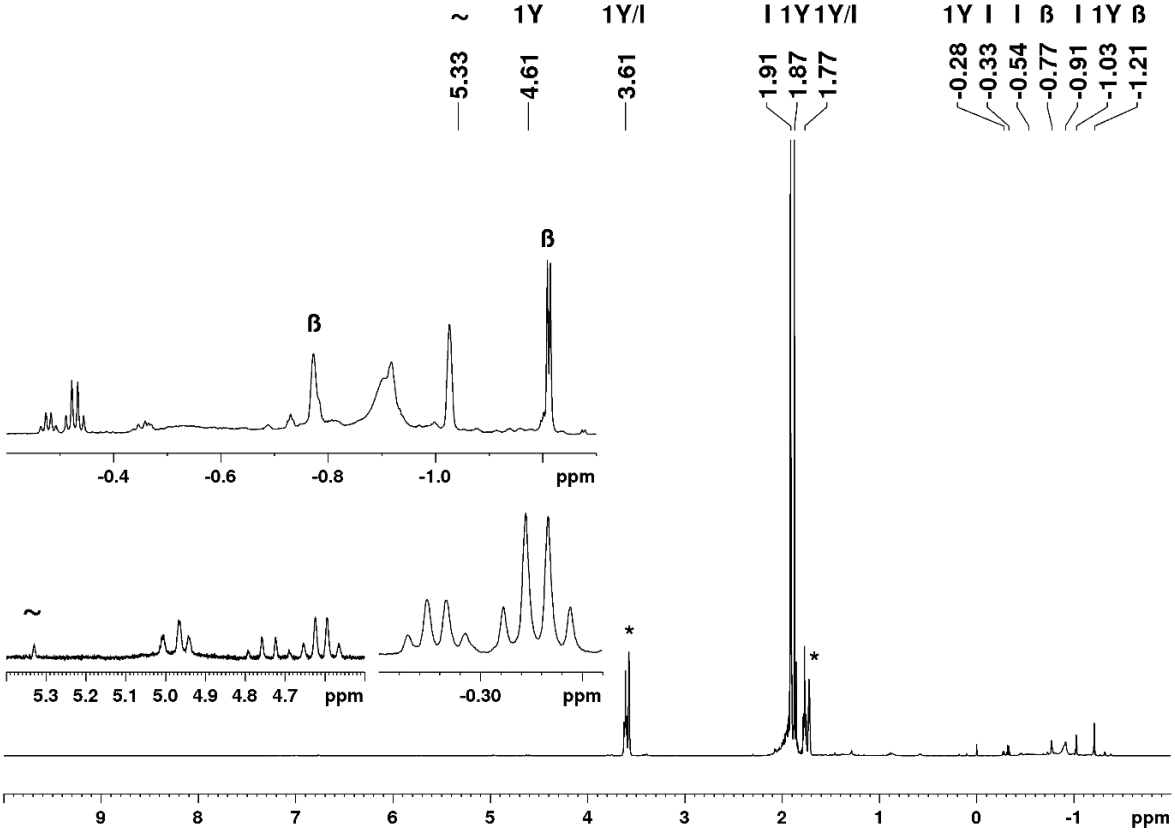

Figure S7. ^{1}H NMR spectrum (400 MHz) of [Cp*$_3$Y$_3$(μ_2-CH$_3$)$_3$(μ_3-CH$_3$)(μ_3-CH$_2$)(thf)$_2$] (**I**) in [D$_8$]THF at 26 °C after 14 days. The solvent residual signals are marked with an asterisk (~: ethene, ß: unknown yttrium species).

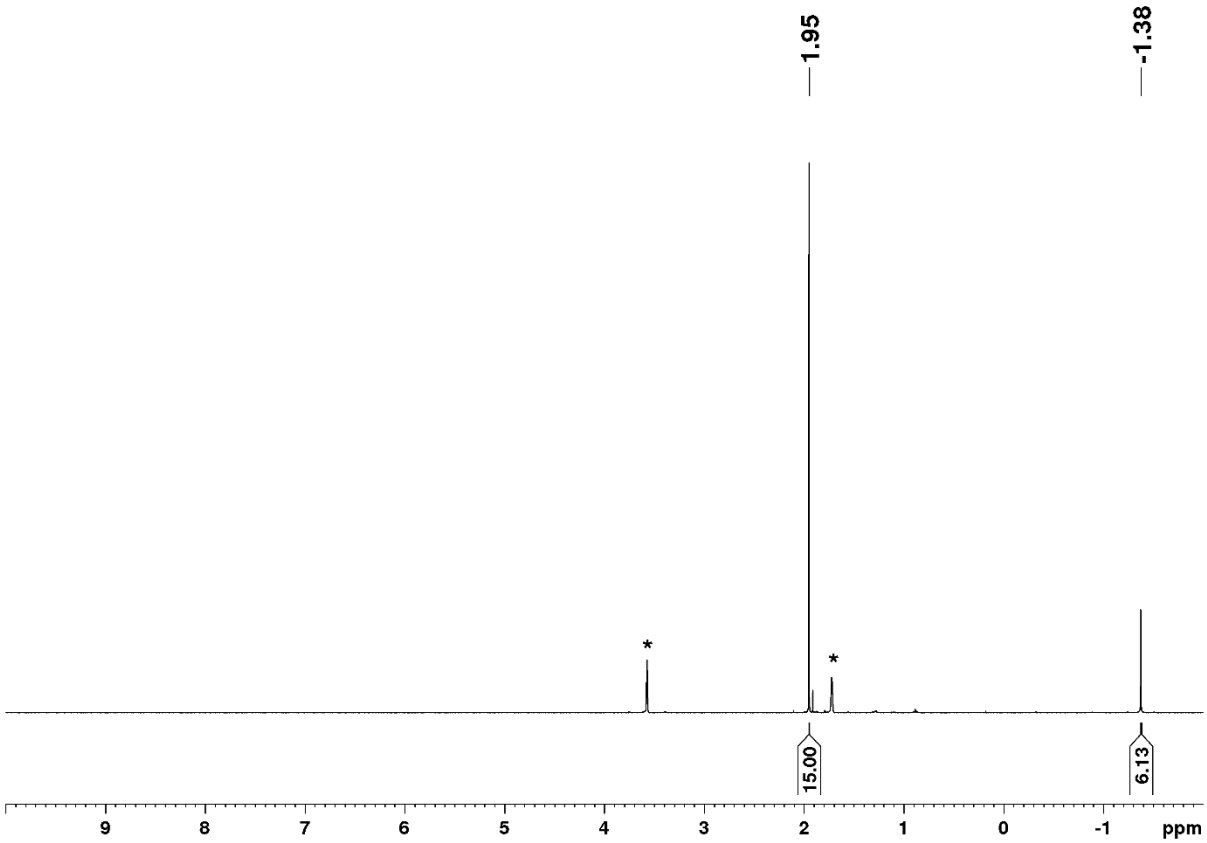

Figure S8. ^{1}H NMR spectrum (400 MHz) of $[Cp^*YMe_2]_3$ in $[D_8]$THF at 26 °C immediately after the addition of $[D_8]$THF. The solvent residual signals are marked with an asterisk.

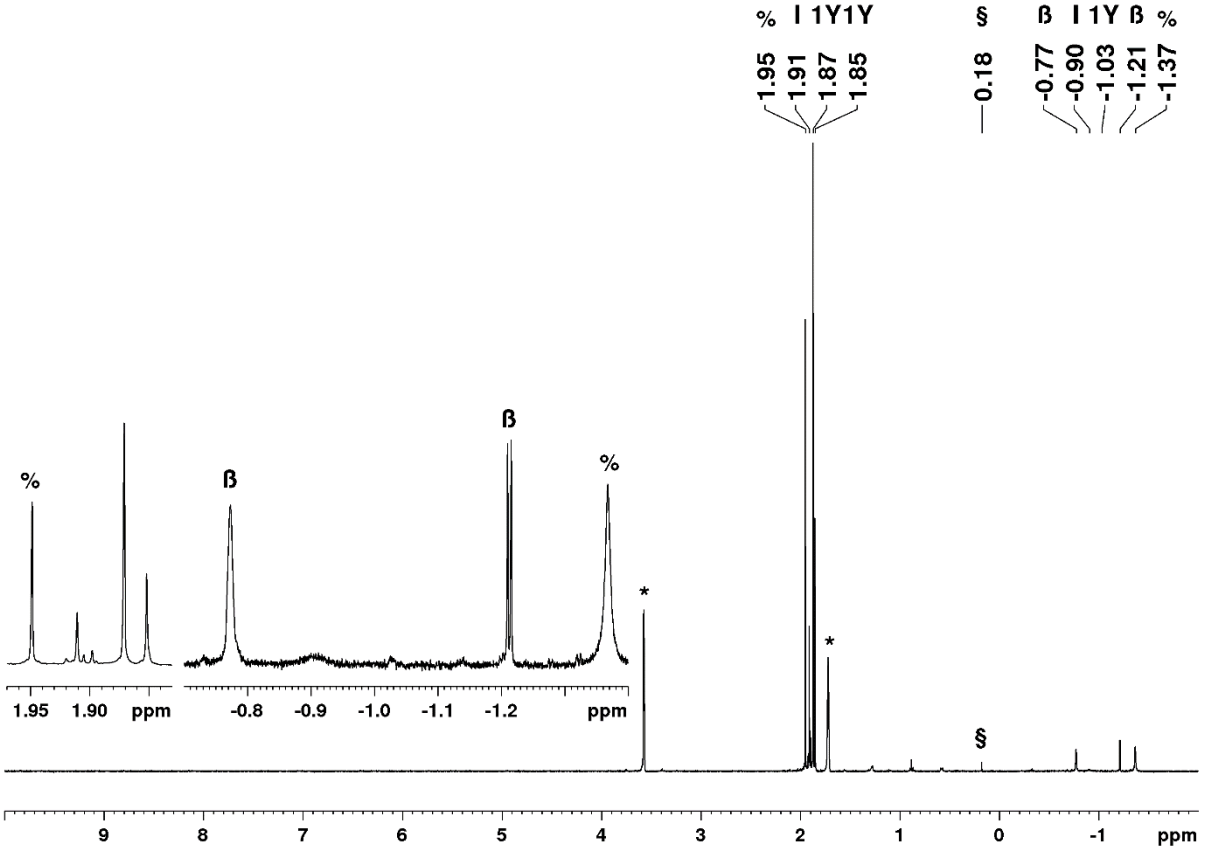

Figure S9. ^{1}H NMR spectrum (400 MHz) of $[Cp^*YMe_2]_3$ in $[D_8]$THF at 26 °C after two days. The solvent residual signals are marked with an asterisk (%: $[Cp^*YMe_2]_3$, §: methane, ß: unknown yttrium species).

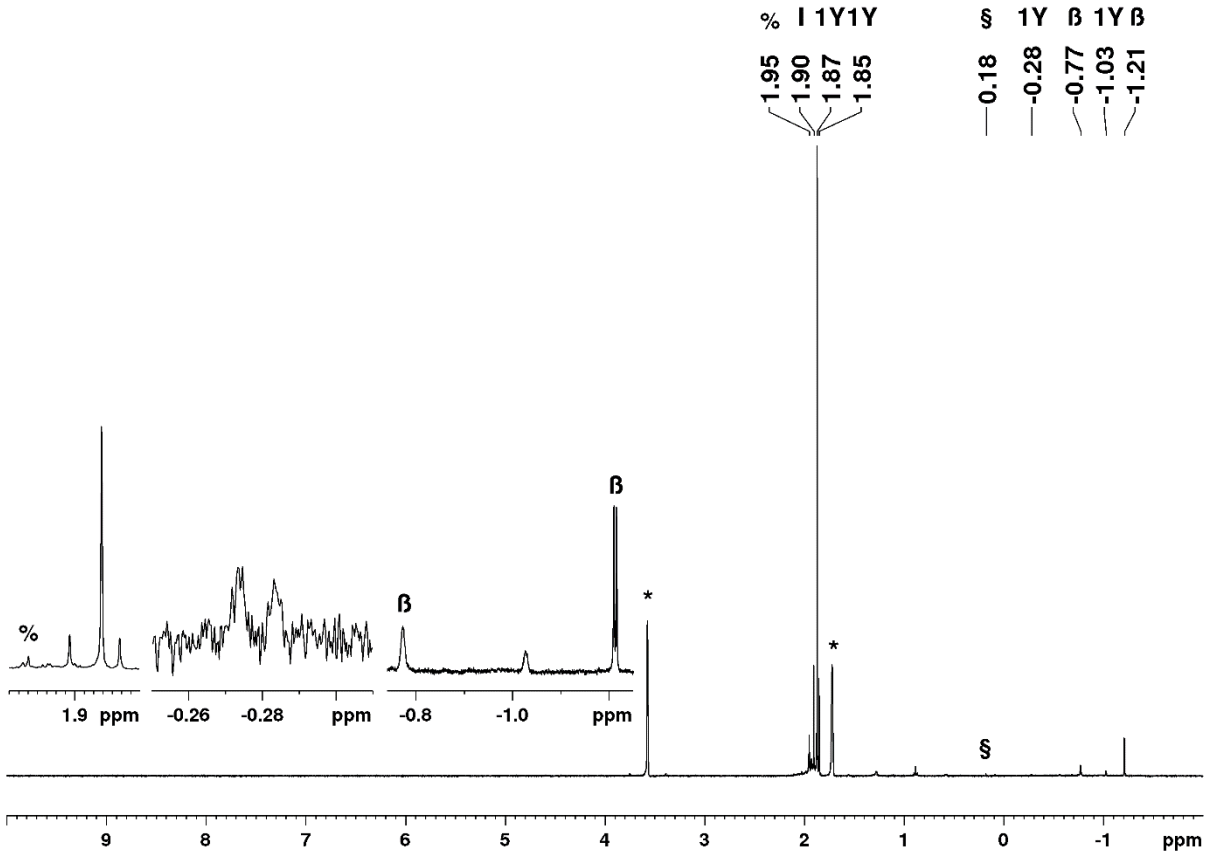

Figure S10. ^{1}H NMR spectrum (400 MHz) of $[Cp^{*}YMe_2]_3$ in $[D_8]$THF at 26 °C after 10 days. The solvent residual signals are marked with an asterisk (%: $[Cp^{*}YMe_2]_3$, §: methane, ß: unknown yttrium species).

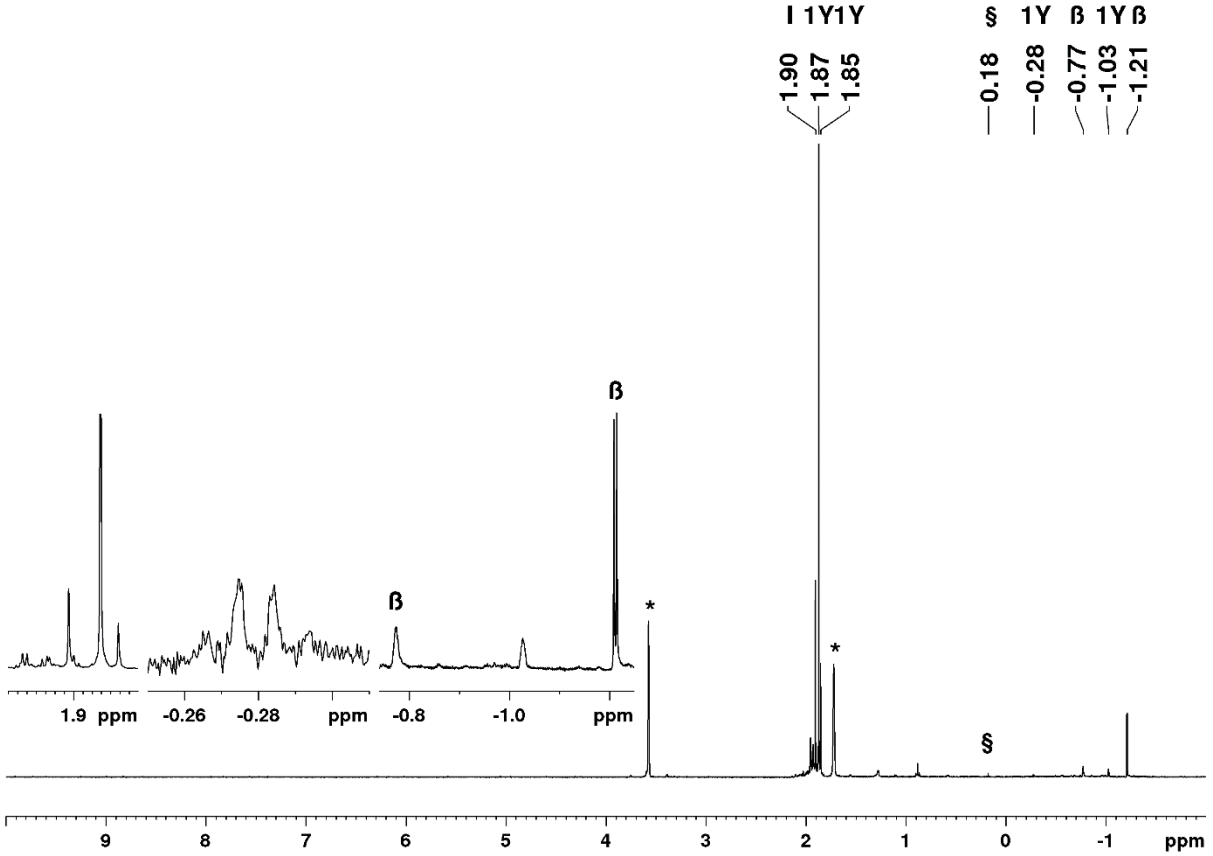

Figure S11. ^{1}H NMR spectrum (400 MHz) of $[Cp^{*}YMe_2]_3$ in $[D_8]$THF at 26 °C after 14 days. The solvent residual signals are marked with an asterisk (§: methane, ß: unknown yttrium species).

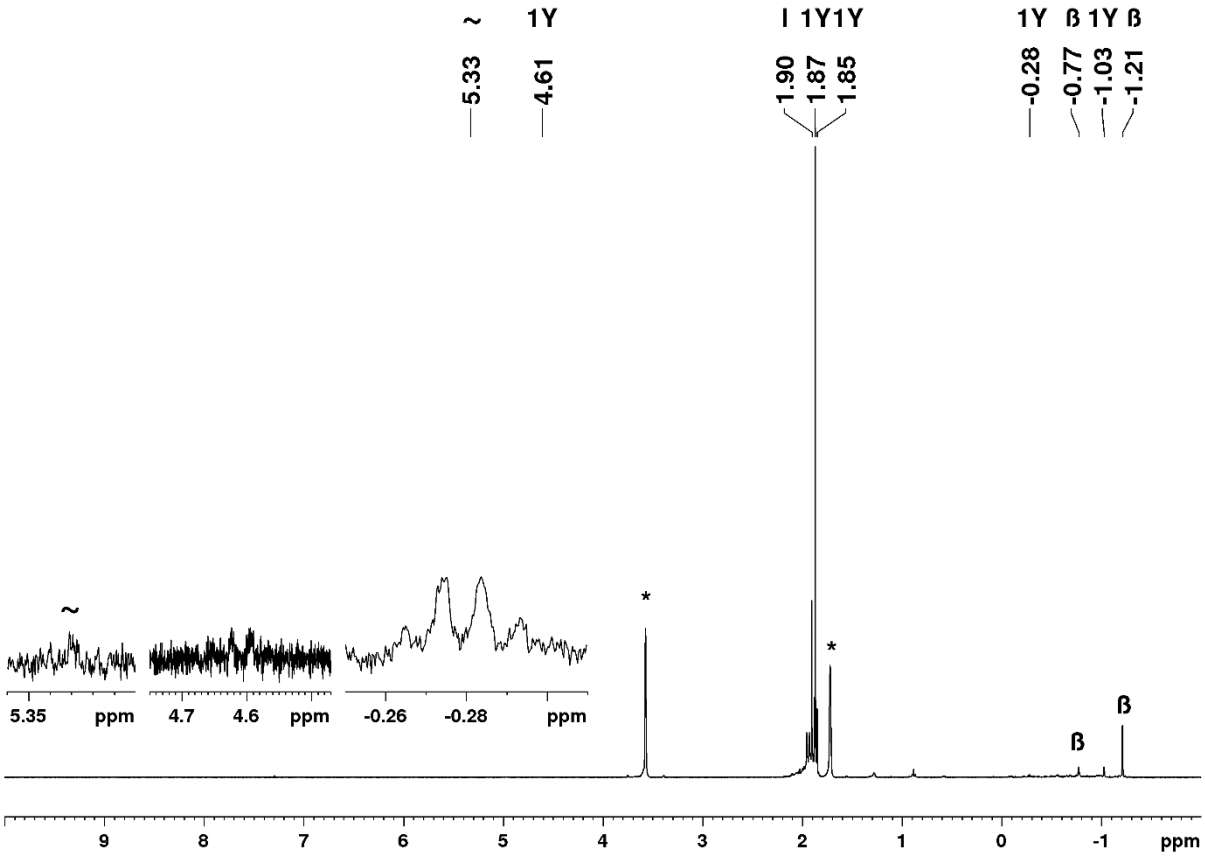

Figure S12. ^{1}H NMR spectrum (400 MHz) of $[Cp^{*}YMe_2]_3$ in $[D_8]$THF at 26 °C after 17 days. The solvent residual signals are marked with an asterisk (~: ethene, ß: unknown yttrium species).

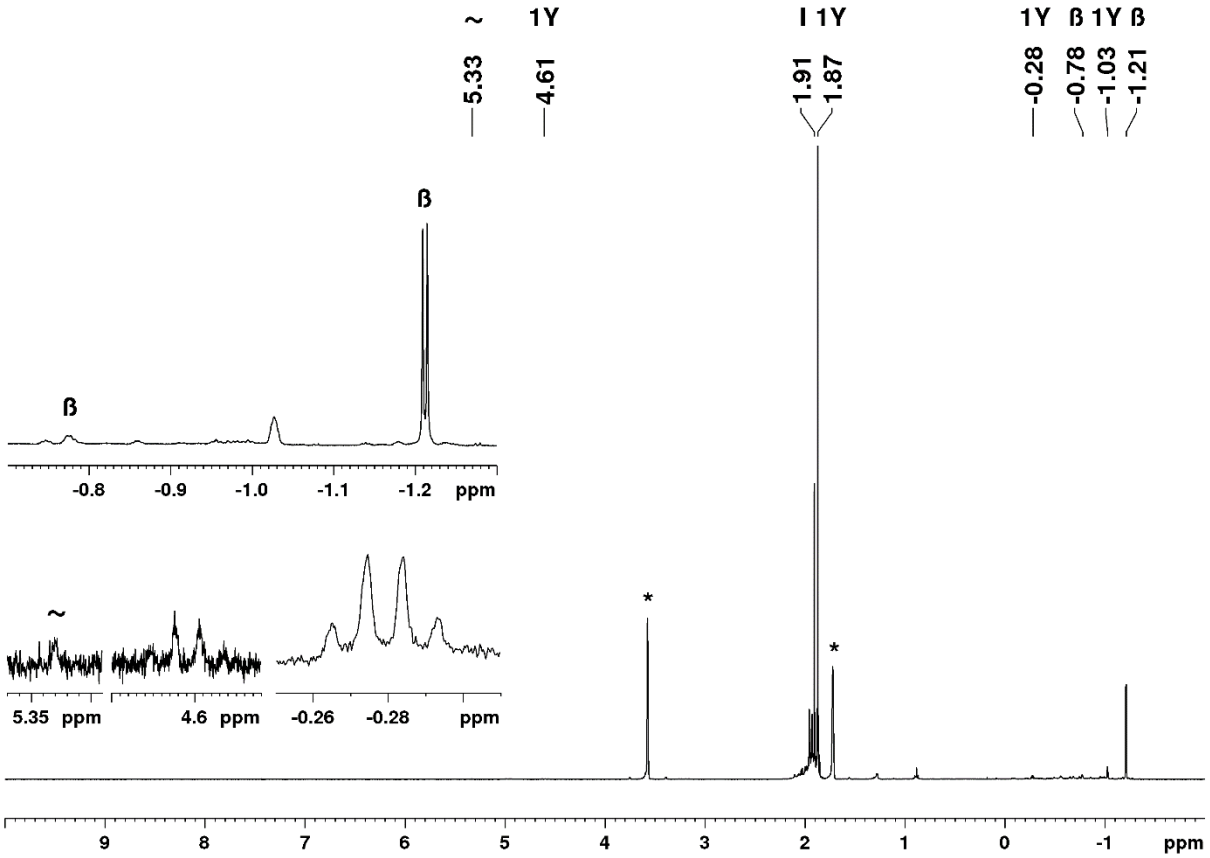

Figure S13. ^{1}H NMR spectrum (400 MHz) of $[Cp^{*}YMe_2]_3$ in $[D_8]$THF at 26 °C after 24 days. The solvent residual signals are marked with an asterisk (~: ethene, ß: unknown yttrium species).

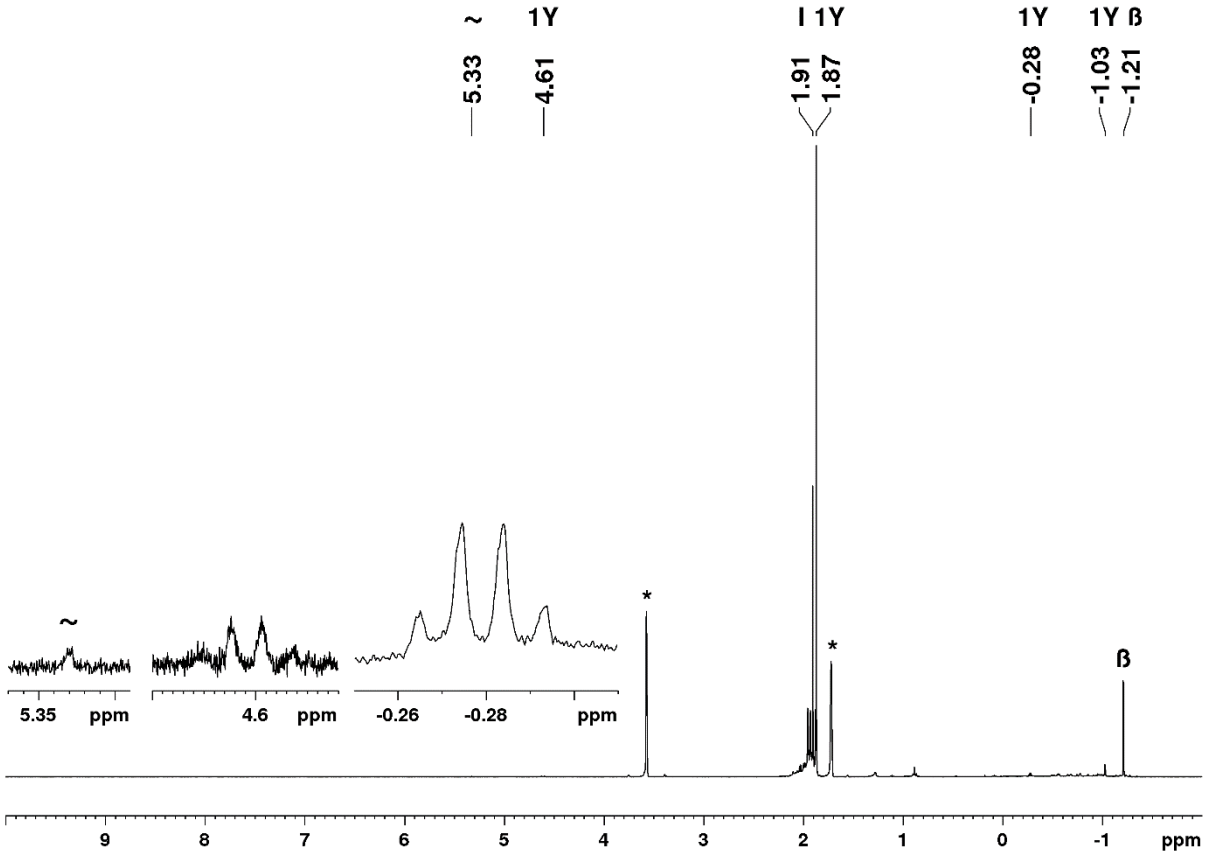

Figure S14. ^{1}H NMR spectrum (400 MHz) of $[Cp^*YMe_2]_3$ in $[D_8]$THF at 26 °C after 30 days. The solvent residual signals are marked with an asterisk (~: ethene, ß: unknown yttrium species).

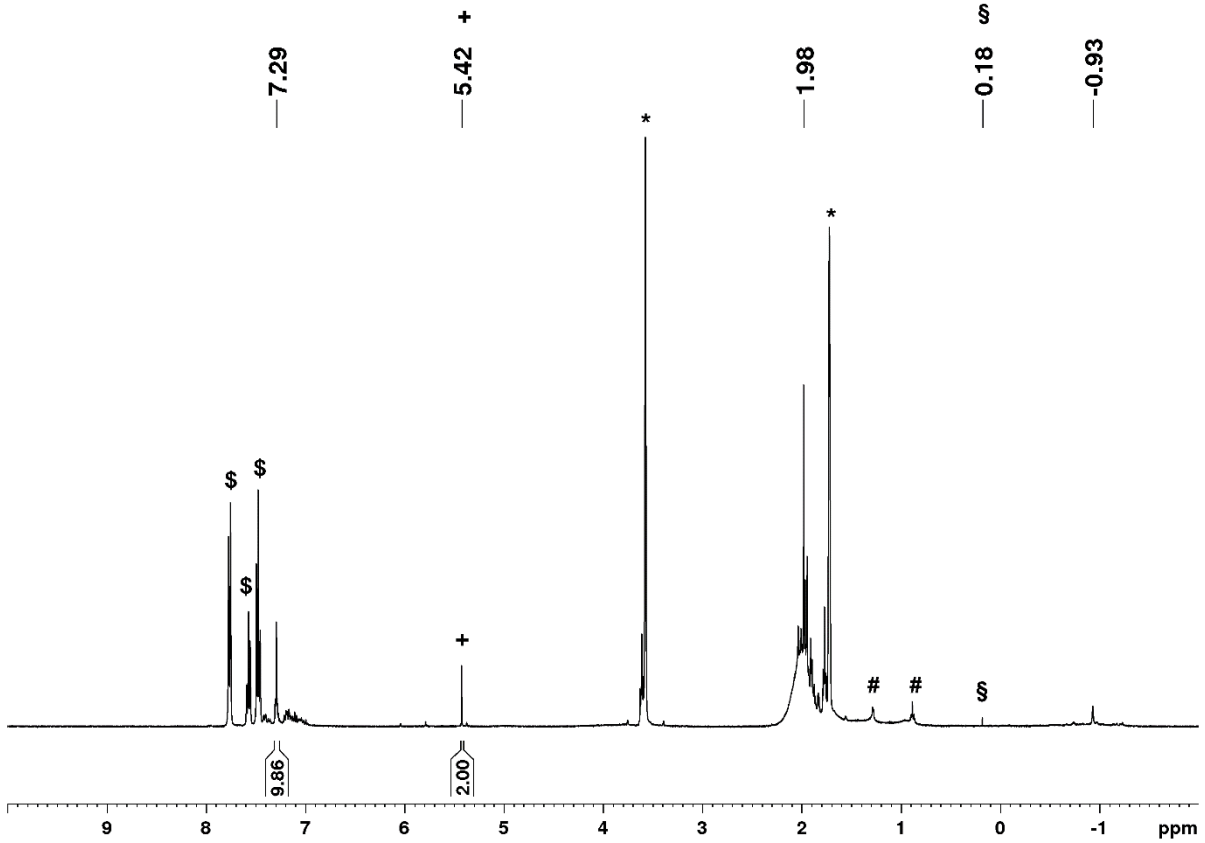

Figure S15. ^{1}H NMR spectrum (400 MHz) of $\mathbf{1^Y}$ in $[D_8]$THF at 26 °C, 15 minutes after addition of benzophenone. The solvent residual signals are marked with an asterisk (+: methylene, #: *n*-hexane, §: methane, $: benzophenone).

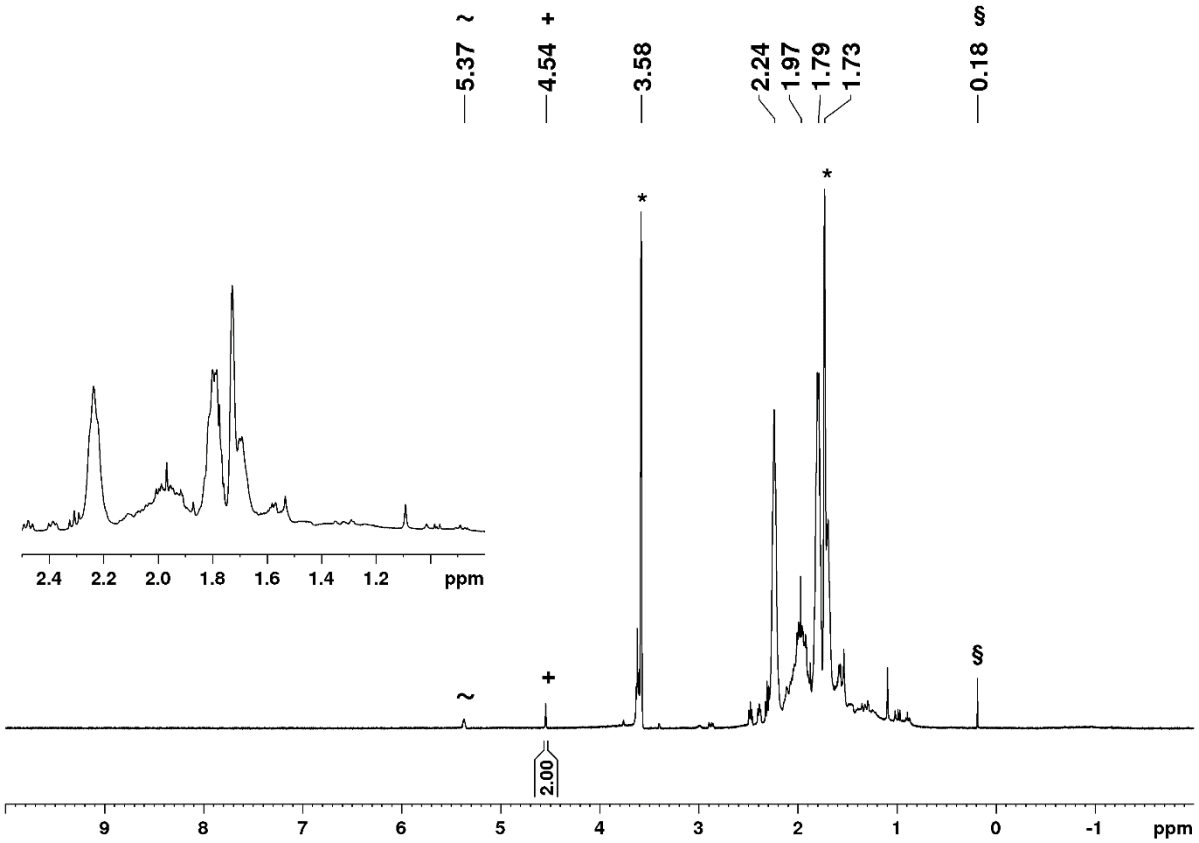

Figure S16. ^{1}H NMR spectrum (400 MHz) of $\mathbf{1^{Y}}$ in [D_8]THF at 26 °C, 15 minutes after addition of cyclohexanone. The solvent residual signals are marked with an asterisk (+: methylene, §: methane, ~: ethene).

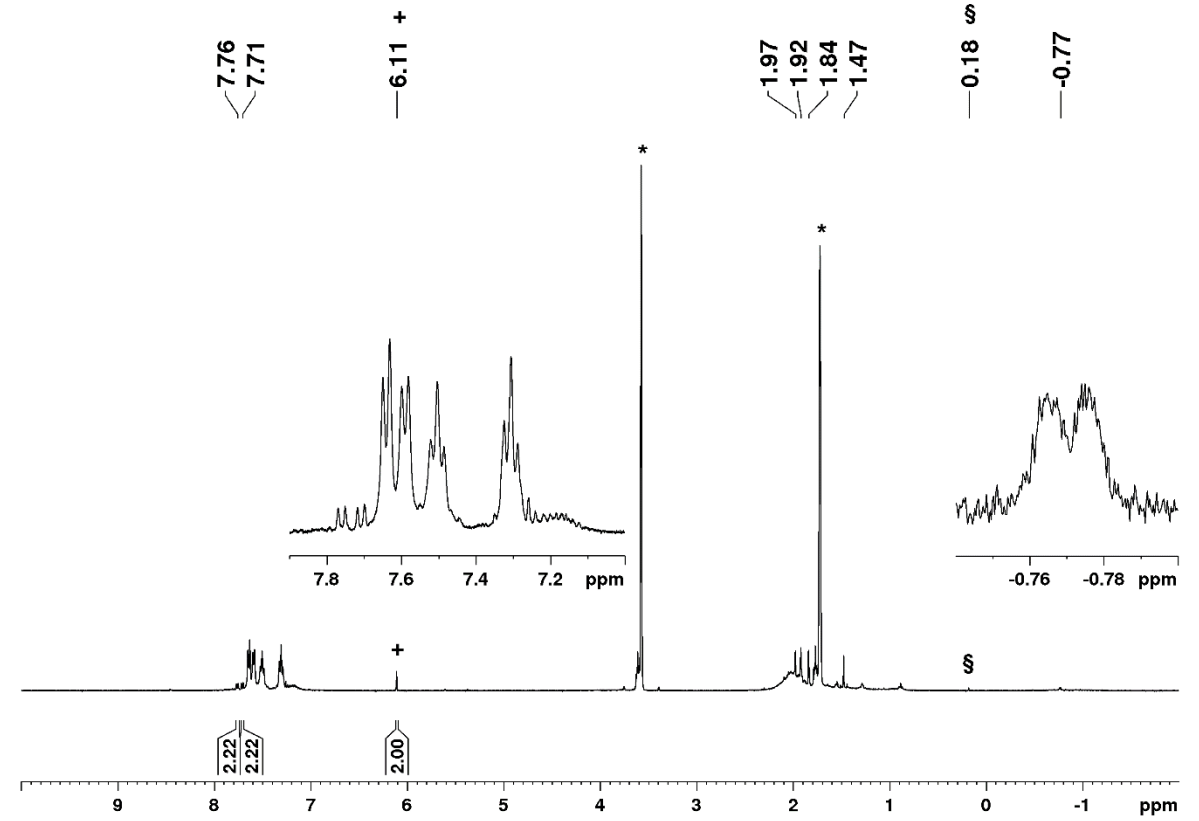

Figure S17. ^{1}H NMR spectrum (400 MHz) of $\mathbf{1^{Y}}$ in [D_8]THF at 26 °C, 15 minutes after addition of 9-fluorenone. The solvent residual signals are marked with an asterisk (+: methylene, §: methane).

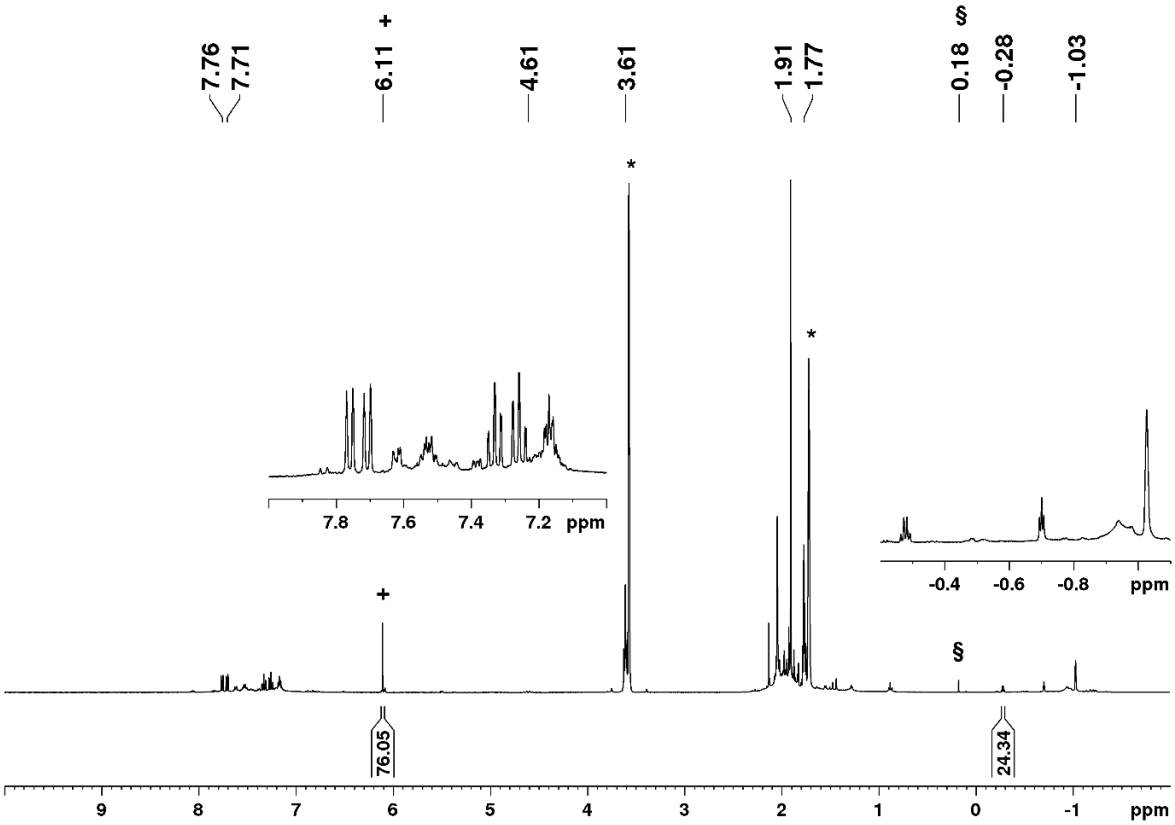

Figure S18. ^{1}H NMR spectrum (400 MHz) of $\mathbf{1}^{Y}$ in [D_8]THF at 26 °C, 15 minutes after addition of an equimolar amount of 9-fluorenone. The solvent residual signals are marked with an asterisk (+: methylene, §: methane).

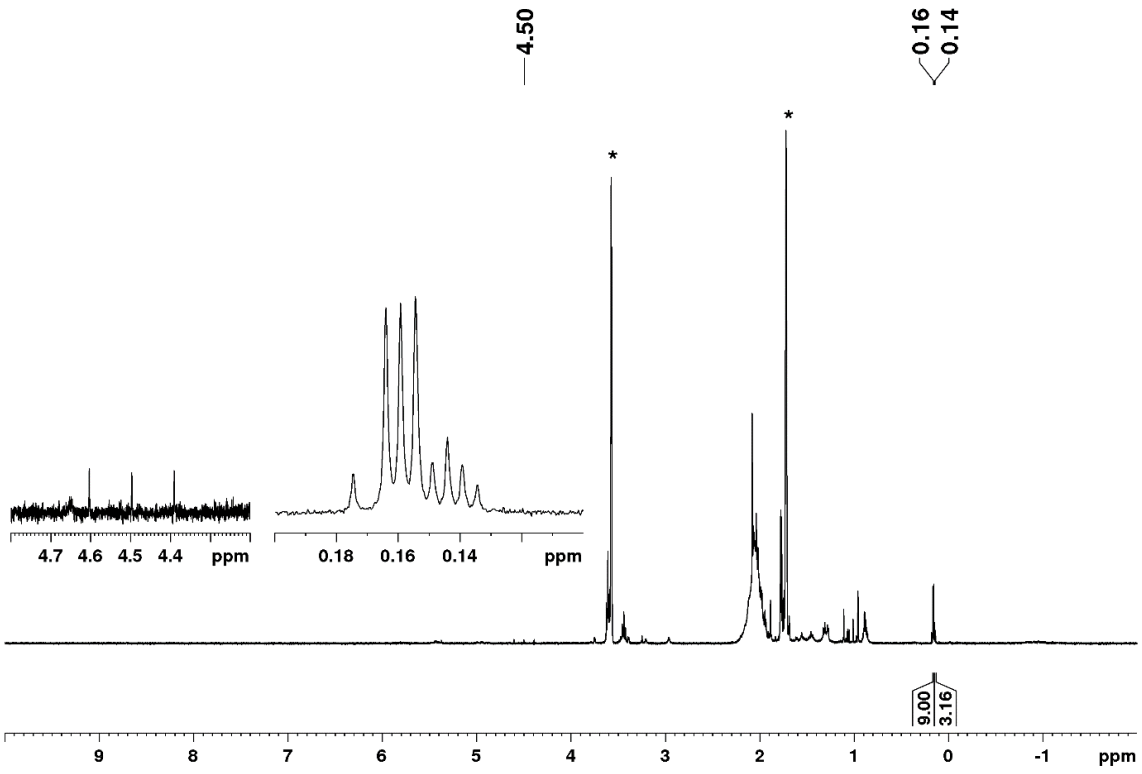

Figure S19. ^{1}H NMR spectrum (400 MHz) of $\mathbf{1}^{Y}$ in [D_8]THF at 26 °C, 5 minutes after addition of [D_4]methanol. The solvent residual signals are marked with an asterisk.

Crystallography

X-Ray Crystallography and Crystal Structure Determinations.

Single-crystals of $\mathbf{1}^{Y}$ and $\mathbf{1}^{Dy}$ were grown by aggregation from diluted THF solutions. Suitable crystals for X-ray structure analyses were selected inside a glovebox, coated with Parabar 10312, and fixed on a nylon/loop glass fiber. All X-ray data were collected on a Bruker APEX II DUO instrument equipped with an IμS microfocus sealed tube and QUAZAR optics for MoK_{α} (λ = 0.71073 Å) radiation. The data collection was determined using COSMO[5] employing ω-scans. Raw data were processed using APEX[6] and SAINT,[7] corrections for absorption effects were applied by using SADABS.[8] The structures were solved by direct methods and refined against all data by full-matrix least-squares methods on F^2 using SHELXTL[9] and SHELXLE.[10] All non-hydrogen atoms were refined anisotropic. Hydrogen atoms for the CH_2 group, the hydrido, and most of the hydrogen atoms of the CH_3 groups were found in the difference Fourier map. All graphics were generated employing CCDC Mercury 4.3.1.[11] Further details regarding the refinement and crystallographic data are listed in Table S1 and in the CIF files. CCDC depositions 2181381 and 2181382 contain all the supplementary crystallographic data for this paper. These data can be obtained free of charge from The Cambridge Crystallographic Data Centre via www.ccdc.cam.ac.uk/data_request/cif.

Table S1. Crystallographic data for compounds $\mathbf{1^{Y}}$ and $\mathbf{1^{Dy}}$

	$\mathbf{1^{Y}}$	$\mathbf{1^{Dy}}$
CCDC	2181381	2181382
Formula	$C_{46}H_{81}Y_3O_3$	$C_{46}H_{81}Dy_3O_3$
M_r [g/mol]	948.83	1169.60
Color/shape	plate/yellow	plate/colorless
Crystal dimensions [mm]	0.287 x 0.255 x 0.099	0.098 x 0.096 x 0.045
Crystal system	monoclinic	triclinic
Space group	$P2_1/n$	$P\bar{1}$
a [Å]	12.5260(9)	11.3103(7)
b [Å]	19.1070(14)	11.9001(7)
c [Å]	18.9963(14)	21.1333(12)
α [°]	90	97.942(2)
β [°]	92.1920(10)	91.931(2)
γ [°]	90	114.983(2)
V [Å³]	4543.1(6)	2540.1(3)
Z	4	2
T [K]	100(2)	100(2)
λ [Å]	0.71073	0.71073
ρ_{calcd} [g/cm³]	1.387	1.529
μ [mm^{-1}]	3.837	4.400
F (000)	1992	1158
θ range [°]	1.945 – 30.536	1.915 – 24.634
independent reflections	13876	8536
reflections collected (I > 2σ)	103801	51818
R1/*w*R2 (I > 2σ)	0.0343/0.0707	0.0332/0.0697
R1/*w*R2 (all data)	0.0592/0.0789	0.0491/0.0763
GOF	1.008	1.019

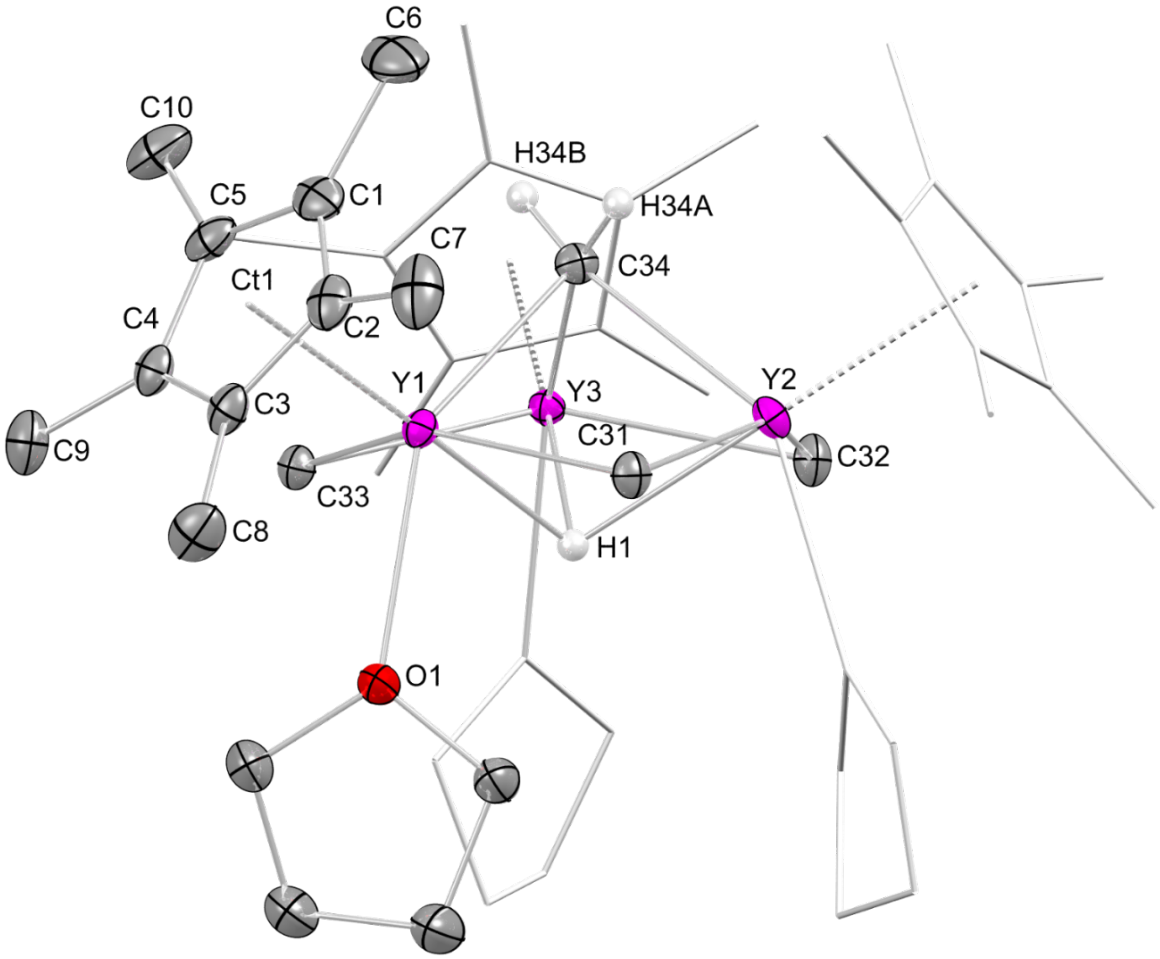

Figure S20. Crystal structure of $[Cp^*_3Y_3(\mu_2\text{-}CH_3)_3(\mu_3\text{-}CH_2)(\mu_3\text{-}H)(thf)_3]$ (**1**^{Y}) with atomic displacement parameters set at the 50% probability level. Hydrogen atoms, except for methylidene hydrides and the μ_3-bridging hydride, are omitted for clarity. Ancillary Cp* ligands and coordinated THF (except for one each) are represented by a wireframe model for improved visualization. Selected interatomic distances [Å] and angles [°]: Y1–C1 2.705(2), Y1–C2 2.723(2), Y1–C3 2.782(2), Y1–C4 2.711(2), Y1–C5 2.700(2), Y1···Ct1 2.427, Y1–H1 2.22(2), Y2–H1 2.34(2), Y3–H1 2.29(2), Y1–C34 2.448(2), Y2–C34 2.422(2), Y3–C34 2.416(2), Y1–C31 2.572(2), Y1–C33 2.572(2), Y1–O1 2.4816(15), C34–H34A 0.921(19), C34–H34B 0.922(19), C1–C2 1.406(3), C2–C3 1.417(3), C3–C4 1.423(3), C4–C5 1.426(3), C5–C1 1.406(3), C1–C6 1.507(3), C1–C2–C3 108.2(2), C2–C3–C4 107.78(19), C3–C4–C5 107.42(19), C4–C5–C1 108.07(19), C5–C1–C2 108.5(2), Ct1···Y1–H1 178.62, Ct1···Y1–C31 104.87, Ct1···Y1–C33 105.24, Ct1···Y1–C34 111.46, Ct1···Y1–O1 105.69, Y1–C31–Y2 81.83(6), Y2–C32–Y3 81.01(6), Y1–C33–Y3 81.68(6), Y1–C34–Y2 87.74(7), Y1–C34–Y3 87.83(7), Y2–C34–Y3 87.08(7), Y1–H1–Y2 95.53, Y1–H1–Y3 96.71, Y2–H1–Y3 92.00, C31–Y1–H1 76.2(6), C33–Y1–H1 73.7(6), C34–Y1–H1 69.4(6), C34–Y1–O1 142.72(6), H1–Y1–O1 73.5(6).

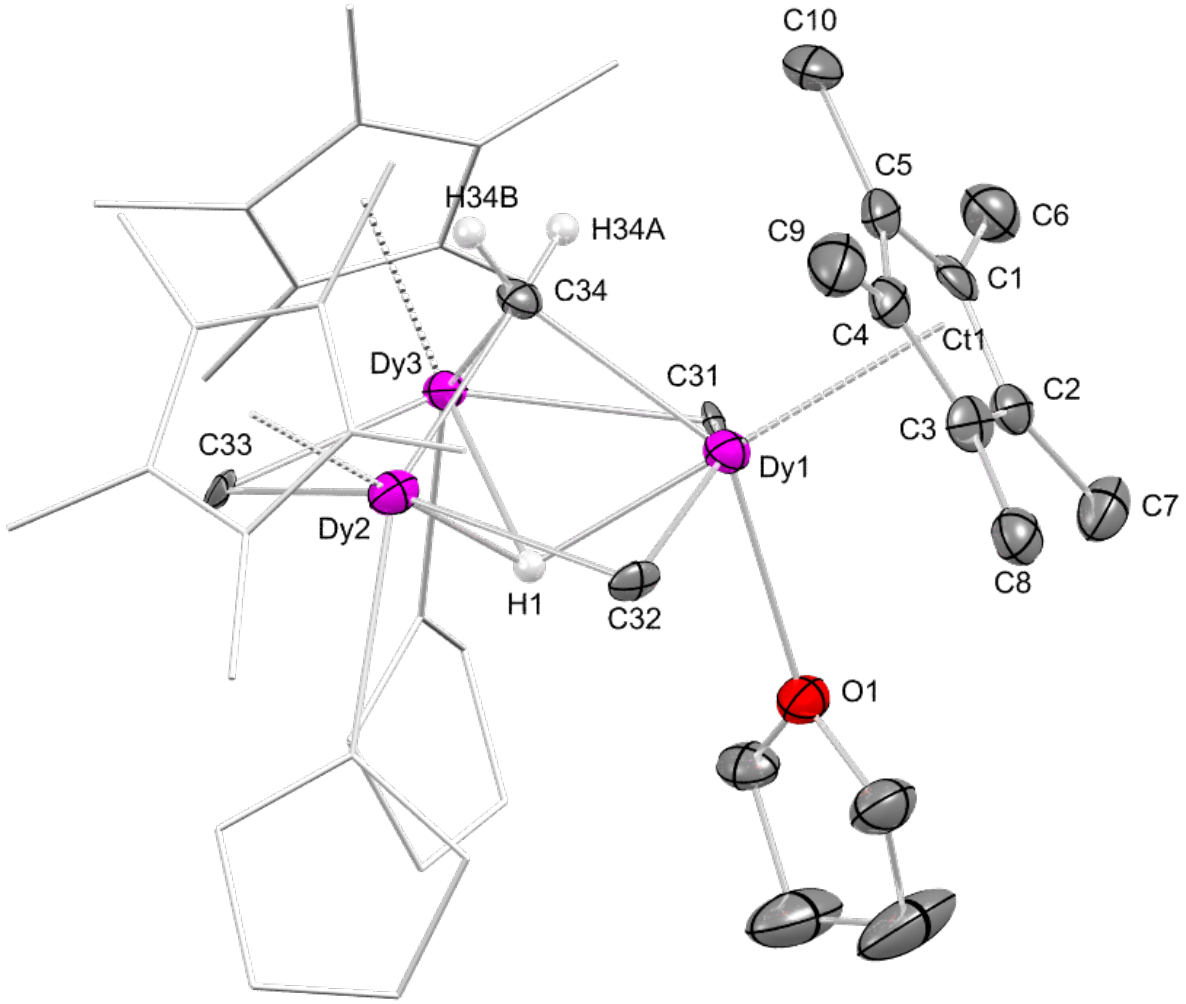

Figure S21. Crystal structure of $[Cp^*_3Dy_3(\mu_2\text{-}Me)_3(\mu_3\text{-}CH_2)(\mu_3\text{-}H)(thf)_3]$ (**1**^{Dy}) with atomic displacement parameters set at the 50% probability level. Hydrogen atoms, except for methylidene hydrides and the μ_3-bridging hydride, are omitted for clarity. Ancillary Cp* ligands and coordinated THF (except for one each) are represented by a wireframe model for improved visualization. Selected interatomic distances [Å] and angles [°]: Dy1–C1 2.733(6), Dy1–C2 2.707(6), Dy1–C3 2.694(5), Dy1–C4 2.716(6), Dy1–C5 2.731(6), Dy1···Ct1 2.436, Dy1–H1 2.26(6), Dy2–H1 2.31(5), Dy3–H1 2.29(5), Dy1–C34 2.420(6), Dy2–C34 2.384(6), Dy3–C34 2.445(6), Dy1–C31 2.584(5), Dy1–C32 2.568(6), Dy1–O1 2.532(4), C34–H34A 0.91(9), C34–H34B 1.02(8), C1–C2 1.421(8), C2–C3 1.419(9), C3–C4 1.416(8), C4–C5 1.398(9), C5–C1 1.402(9), C1–C6 1.494(9), C1–C2–C3 107.3(5), C2–C3–C4 108.1(5), C3–C4–C5 107.8(6), C4–C5–C1 108.9(5), C5–C1–C2 107.9(6), Ct1···Dy1–H1 177.82, Ct1···Dy1–C31 105.43, Ct1···Dy1–C32 106.30, Ct1···Dy1–C34 111.63, Ct1···Dy1–O1 106.73, Dy1–C32–Dy2 80.18(14), Dy2–C33–Dy3 80.52(16), Dy1–C31–Dy3 82.76(16), Dy1–C34–Dy2 87.97(19), Dy1–C34–Dy3 89.3(2), Dy2–C34–Dy3 87.63(19), Dy1–H1–Dy2 93.60, Dy1–H1–Dy3 97.47, Dy2–H1–Dy3 93.28, C31–Dy1–H1 72.4(14), C32–Dy1–H1 75.8(14), C34–Dy1–H1 68.6(14), C34–Dy1–O1 141.55(16), H1–Dy1–O1 73.0(14).

IR Spectroscopy

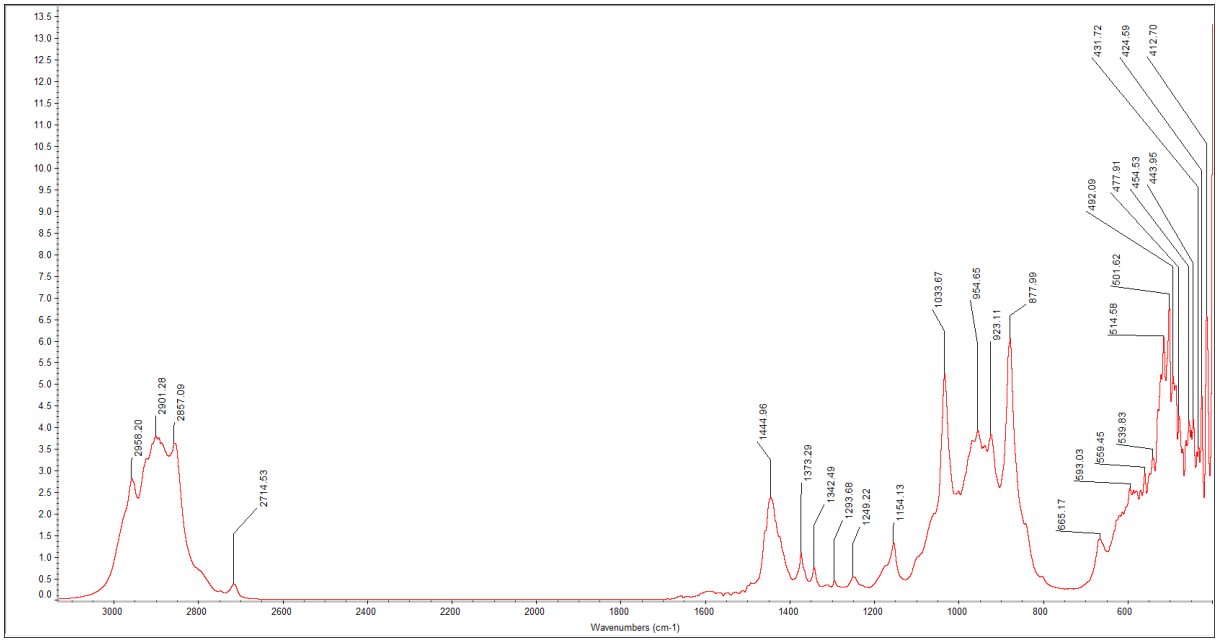

Figure S22. DRIFT spectrum of $[Cp^*_3Y_3(\mu_2\text{-}CH_3)_3(\mu_3\text{-}CH_2)(\mu_3\text{-}H)(thf)_3]$ ($\mathbf{1^Y}$).

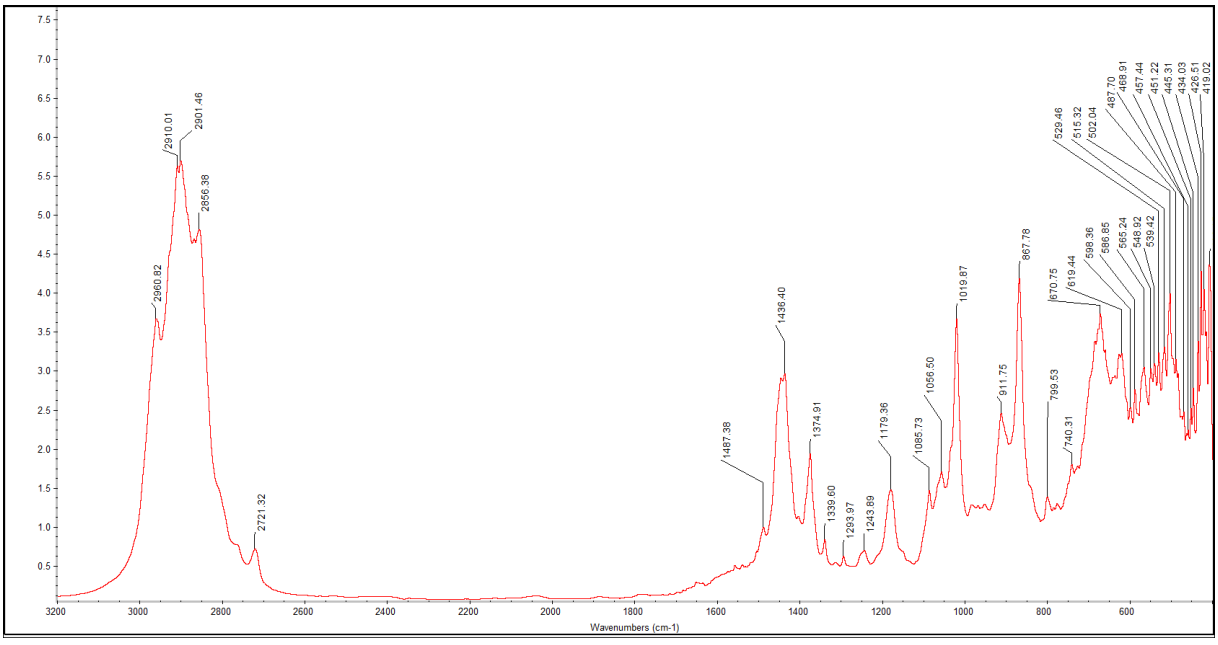

Figure S23. DRIFT spectrum of $[Cp^*_3Dy_3(\mu_2\text{-}CH_3)_3(\mu_3\text{-}CH_2)(\mu_3\text{-}H)(thf)_3]$ ($\mathbf{1^{Dy}}$).

References

1 G. Occhipinti, C. Meermann, H. M. Dietrich, R. Litlabø, F. Auras, K. W. Törnroos, C. c. Maichle-Mössmer, V. R. Jensen and R. Anwander, *J. Am. Chem. Soc.* 2011, **133**, 6323-6337.

2 H. M. Dietrich, K. W. Törnroos, E. Herdtweck and R. Anwander, *Organometallics* 2009, **28**, 6739-6749.

3 C. O. Hollfelder, M. Meermann-Zimmermann, G. Spiridopoulos, D. Werner, K. W. Törnroos, C. Maichle-Mössmer and R. Anwander, *Molecules* 2019, **24**, 3703.

4 C. O. Hollfelder, L. N. Jende, H. M. Dietrich, K. Eichele, C. Maichle-Mössmer and R. Anwander, *Chem. Eur. J.* 2019, **25**, 7298-7302.

5 COSMO, v. 1.61, Bruker AXS Inc., Madison, WI, 2012.

6 APEX 3, v. 2016.2015-2010; Bruker AXS Inc., Madison, WI, 2012.

7 SAINT, v. 8.34A; Bruker AXS Inc., Madison, WI, 2010.

8 L. Krause, R. Herbst-Irmer, G. M. Sheldrick and D. Stalke, *J. Appl. Crystallogr.* 2015, **48**, 3-10.

9 G. M. Sheldrick, *Acta Crystallogr. Sect. A* 2015, **71**, 3-8.

10 C. B. Hübschle, G. M. Sheldrick and B. Dittrich, *J. Appl. Crystallogr.* 2011, **44**, 1281-1284.

11 C. F. Macrae, P. R. Edgington, P. McCabe, E. Pidcock, G. P. Shields, R. Taylor, M. Towler and J. Streek, *J. Appl. Crystallogr.* 2006, **39**, 453-457.

Paper V

Half-Sandwich Rare-Earth-Metal Clusters – Synthesis, Characterization, and Magnetic Properties

Manuscript

Rare-earth metal clusters – Synthesis, characterization, and magnetic properties

Dennis A. Buschmann,[a] James Durrant,[b] Cäcilia Maichle-Mössmer,[a] Richard A. Layfield,*[b] and Reiner Anwander*[a]

* Corresponding authors

[a] Institut für Anorganische Chemie, Eberhard Karls Universität Tübingen, Auf der Morgenstelle 18, 72076 Tübingen, Germany

[b] Department of Chemistry, School of Life Sciences, University of Sussex, Falmer, Brighton, BN1 9QJ, United Kingdom

cyclopentadienyl ligands, halogenido ligands, rare-earth metals, cluster compounds, single-molecule magnetism

ABSTRACT: Cluster compounds for the ferromagnetic lanthanides Ln = Gd, Tb, Dy, Ho, Er as well as for the diamagnetic yttrium are readily accessible via $AlMe_4$/halogenido exchange reactions with the mild halogenido transfer reagents Me_3SiI and Me_3GeX (X = Br, Cl). Depending on the rare-earth metal center and halogenido ion size, clusters of distinct structural motifs and nuclearities are obtained, including dimeric compounds $[Cp^*Ln(AlMe_4)Cl]_2$ for the smaller metal centers Ln = Ho, Er, iodido-bridged tetranuclear ring-shaped clusters $[Cp^*LnI_2]_4$ (Ln = Y, Tb, Dy, Ho, Er) and a heterobimetallic tetramethylaluminato-bridged gadolinium cluster $[Cp^*_4Gd_4I_7(AlMe_4)]_2$. The tetranuclear dysprosium cluster $[Cp^*DyI_2]_4$ shows single-molecule magnet (SMM) behavior in zero applied field with an effective energy barrier of 164(10) cm^{-1}.

INTRODUCTION

The ubiquitous cyclopentadienyl (Cp) ligand has played a vital role in the advancement of rare-earth-organometallic chemistry ever since the first isolation of homoleptic complexes $LnCp_3$.[1-3] Highly reactive half-sandwich hydrocarbyl complexes of the general formula $Cp^RLn(AlMe_4)_2$ are easily accessible via protonolysis, salt metathesis, or redox synthesis protocols for the entire Ln(III) size range.[4-10] The incorporation of the $AlMe_4$ ligand facilitates further derivatization reactions, including methyl formation via donor-promoted cleavage of $AlMe_3$(THF), halogenido transfer, or C–H bond activation reactions.[6, 11-17] Organometallic complexes of the rare-earth metals have gained significant interest with respect to optical or magnetic applications.[18-22] Several rare-earth metals (Gd, Tb, Dy, Ho, Er) show ferromagnetic behavior and slow magnetic relaxation at lower temperatures. In combination with the stabilizing properties of Cp derivatives,[2-3, 23] organometallic compounds of those rare-earth metal centers represent attractive precursors for the synthesis of single-molecule magnets (SMMs). Ever since the mentioning of the anionic phthalocyanine double-decker complexes $[Pc_2Ln][N(C_4H_9)_4]$ (Ln = Dy, Tb) as the first lanthanide-based SMMs in 2003,[24] especially dysprosium compounds have emerged as potent SMMs.[25-28] Crucial factors for the design of effective lanthanide-based SMMs are large effective barriers to magnetization reversal (U_{eff}) as well as high hysteresis temperatures,[29] which can be readily achieved by the usage of ancillary Cp derivatives.[25, 28] Recent advances in SMM design mainly focus on the design of the ligand field surrounding the metal center, aiming at maximizing U_{eff}.[30-34] We have recently reported on the synthesis of large halogenido-bridged half-sandwich clusters, feasible via a $AlMe_4$/halogenido ligand exchange reaction protocol involving large rare-earth metals (Ln = La, Ce, Pr).[35-36] Following this established synthesis route, we targeted the synthesis of clusters using the smaller paramagnetic rare-earth metals Ln = Gd, Tb, Dy, Ho, Er, with possible prospects of single-molecular magnet behavior.

RESULTS AND DISCUSSION

Preparation of iodido-bridged clusters $[Cp^*LnI_2]_4$ (Ln = Y, Tb, Dy, Ho, Er) and $[(Cp^*_4Gd_4I_7\{AlMe_4\})_2]$. As previously mentioned, half-sandwich complexes are commonly used as precursors for the synthesis of rare-earth metal cluster compounds, mainly due to their favorable reactivity and enhanced thermal stability.[2, 23, 37] Pentamethylcyclopentadienyl ($Cp^* = C_5Me_5$) was chosen as an ancillary ligand, given its symmetry and stabilizing effects. The synthesis of cluster compounds was attempted via the previously established $AlMe_4$/X (X = Cl, Br, I) exchange reaction using Me_3SiI as the halogenating reagent.[13, 35] Whereas the $Cp^*Gd(AlMe_4)_2/Me_3SiI$ reaction afforded the heterobimetallic octanuclear Gd cluster **3**, all other Ln (Ln = Y, Tb, Dy, Ho, Er) form isostructural tetrameric ring clusters of the general composition $[Cp^*LnI_2]_4$.(**2^{Ln}**), crystallizing in the monoclinic space group $P2_1/n$. Although no obvious steric hindrance restricts the cluster formation, the distance between the metal centers is notably different, despite adopting a ring-like geometry. In complex **2^{Y}**,

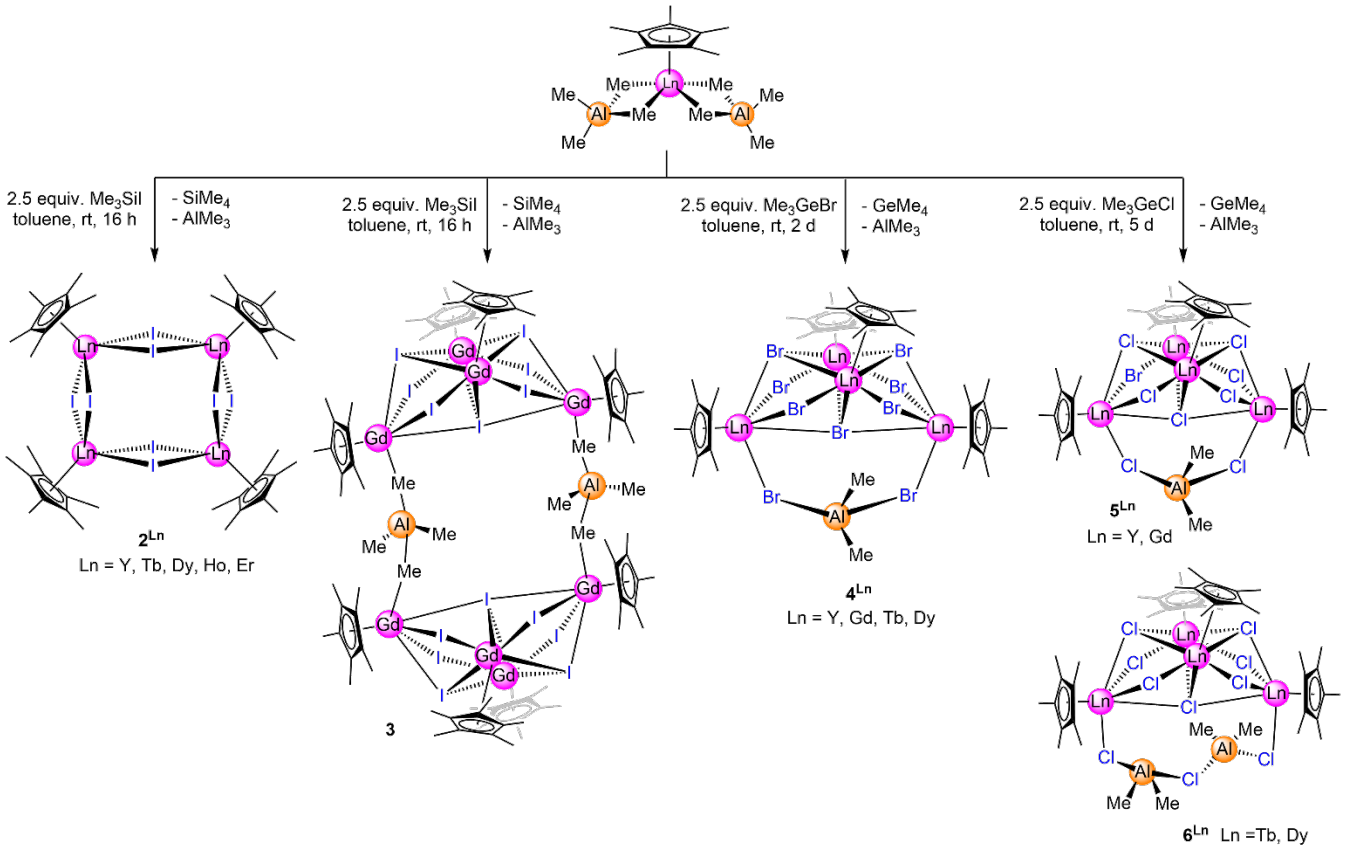

Scheme 1. Synthesis of tetranuclear clusters $\mathbf{2^{Ln}}$ (Ln = Y, Tb, Dy, Ho, Er) and dimeric octanuclear gadolinium cluster **3** via an alkyl/halogenido exchange reaction protocol.

the interatomic Y···Y distances range from 4.3263(8) Å (Y1···Y4) to 4.5790(9) Å (Y1···Y2) (Δ = 0.25 Å). This difference is due to the coordination mode of the bridging iodido ligands. Whereas the Y1–I1 distance of 3.0557(6) Å, connecting to Y2, is only slightly shorter than the Y1–I7 distance (3.0917(6) Å) bridging to Y4, the bond angles deviate by almost 8° (Y1–I1–Y2 = 96.962(2)°, Y1–I7–Y4 = 89.220(2)°), resulting in the large difference in the Y···Y interatomic distances. The other ring-like clusters show a similar difference in the distances between the metal centers, only deviating by the respective difference in the ionic radii.[38-39] Beside these ring-like clusters, the only previously reported molecular, donor-free rare-earth-metal diiodides are $[Cp^*Sc(\mu\text{-}I)_2]_4$ and $[Cp^*Dy(\mu\text{-}I)_2]_3$.[40-41]

Despite the marginal difference in ionic radii of 0.01 Å between 6-coordinate Gd(III) and Tb(III),[39] applying the same synthesis protocol for the half-sandwich complex $Cp^*Gd(AlMe_4)_2$ led to the isolation of a heterobimetallic gadolinium cluster **3**. The cluster crystallized in the monoclinic space group *C*2/*c* and consists of two $Cp^*_4Gd_4I_7$ subunits, exhibiting the characteristic Ln_4X_7 (X = Hal) structural motif established in other rare-earth-metal halide complexes.[13, 35-36, 41-43] The two gadolinium subunits are bridged via two $AlMe_4$ ligands. Unlike other tetramethylaluminato-bridged clusters,[13, 35] the different subunits are connected by two μ_2-bridging methyl groups instead of three, rendering bent Gd–Al–Gd linkages (e.g., Gd1–Al1–Gd4 = 107.42(2)°). In comparison to the cluster $[Cp^*_4Sm_4I(\mu_2\text{–}I)_4(\mu_3\text{–}I)_2(\mu_4\text{–}I)(thf)(toluene)_2]$ (**I**),[43] the interatomic distances deviate notably, taking the difference in ionic radii into consideration. Complex **I**, representing one half of complex **3**, shows a higher overall strain, resulting in generally shorter interatomic distances. Whereas the two outer gadolinium metal centers Gd1 and Gd4 in complex **3** show a distance of 6.792(1) Å, the respective distance in complex **I** is significantly shorter (Sm1···Sm3 = 6.2674(8) Å). For further

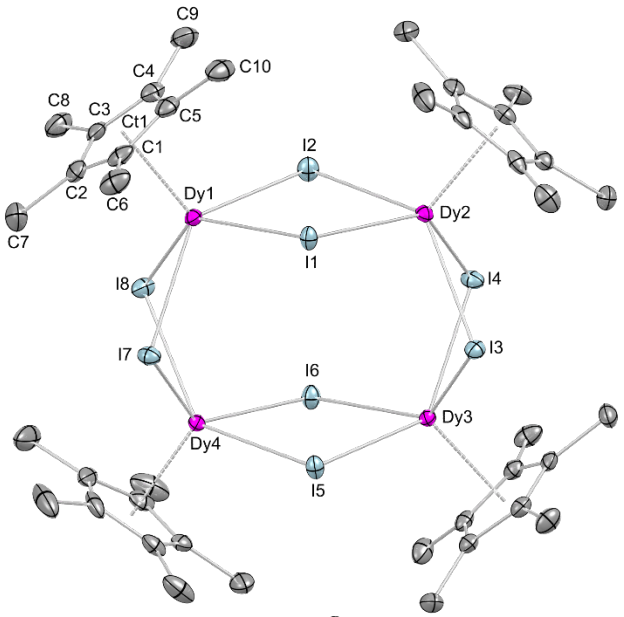

Figure 1. Crystal structure of $\mathbf{2^{Dy}}$ with atomic displacement parameters set at the 50% probability level. Hydrogen atoms have been omitted for improved visualization. For selected interatomic distances and angles, see the Supporting Information.

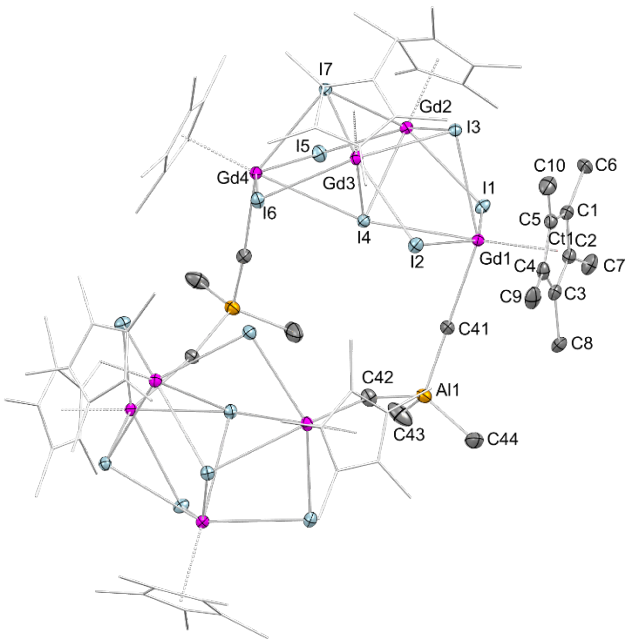

Figure 2. Crystal structure of **3** with atomic displacement parameters set at the 50% probability level. Hydrogen atoms and lattice toluene have been omitted for improved visualization. Ancillary Cp* ligands (except for one) are represented by a wireframe model. For selected interatomic distances and angles, see the Supporting Information.

comparison, the interatomic distances of the two central rare-earth metal centers (**3**: Gd2···Gd3 = 4.5987(7) Å; **I**: Sm2···Sm4 = 4.4968 (6) Å) as well as the outer bridging iodido ligands (**3**: I1···I5 = 5.030(1) Å; **I**: I3···I4 = 4.5376(9) Å). Only the distance between the capping μ_3-bridging iodido ligands is larger in complex **I** (I5···I6 = 4.2279(7) Å) compared to the respective distance in **3** (I3···I7 = 3.980(1) Å). The geometry in cluster **3** derives likely from the bridging of the two subunits in the apical positions. The EDX spectra are in accordance with the calculated atom and weight ratios, further corroborating the uniformity of the product formation.

Preparation of bromido-bridged clusters [Cp*$_4$Ln$_4$Br$_7$(Br$_2$AlMe$_2$)] (Ln = Y, Gd, Tb, Dy).

Using a similar synthesis protocol, the reaction of half-sandwich complexes Cp*Ln(AlMe$_4$)$_2$ with the bromido transfer reagent Me$_3$GeBr led to the isolation of bromido-bridged clusters of the general formula [Cp*$_4$Ln$_4$Br$_7$(Br$_2$AlMe$_2$)] (Ln = Y, Gd, Tb, Dy; Scheme 1). Even though excess of Me$_3$GeBr was used (2.5 equiv.), a complete AlMe$_4$/Br exchange could not be detected. Instead, complexes **4^{Ln}** display the common Ln$_4$Br$_7$ subunit, now being "terminated" by a AlMe$_2$Br$_2$ heteroaluminato moiety. Monoanionic AlMe$_2$Br$_2$ bridges two rare-earth-metal centers of the Ln$_4$Br$_7$ core via the bromidos (Figure 3). Such heteroaluminato moieties have been found previously in metallocene complexes of the type Cp*$_2$Ln(μ-Cl)$_2$AlR$_2$ (Ln = Y, Sm; R = Me, Et, *i*Bu)[44] and rare-earth-metal half-sandwich clusters (C$_5$H$_4$SiMe$_3$)$_{10}$La$_{10}$Br$_{18}$(AlBr$_2$Me$_2$)$_2$ and (C$_5$H$_4$SiMe$_3$)$_{10}$Ce$_{10}$Cl$_{18}$ (AlCl$_2$Me$_2$)$_2$,[35-36] but coordinated to one rare-earth-metal center exclusively. Structurally similar lanthanide clusters like [Cp*$_5$Nd{(μ-Me)$_3$AlMe}(μ_4-Cl)(μ_3-Cl)$_2$(μ_2-Cl)$_6$], [{Cp*$_2$Sm}(μ-Cl)$_6$(μ_3-Cl)$_2$(μ_4-Cl){SmCp*}$_4$], and [Cp*$_6$Yb$_5$(μ_4-F)(μ_3-F)$_2$(μ_2-F)$_6$][13, 41, 45] feature rare-earth-metal centers with Cp ancillaries instead of the "AlMe$_2$" group observed in **4^{Ln}**. The AlMe$_2$ moiety is tilted out of the mean plane spanned by two lanthanide metal centers and the bridging bromido ligands (Ln1, Ln4, Br8, Br9) for all complexes **4^{Ln}**.

The diamagnetic complex **4^{Y}** readily dissolves in [D$_8$]toluene, hence the complex was investigated by ^{1}H NMR spectroscopy. The resonance at 2.17 ppm can be attributed to the methyl groups of the ancillary Cp* ligands. A set of resonances appear in the range from 2.25 – 1.95 ppm, likely generated by a species formed in solution. Further resonances appear in the region from 1.0 – -0.5 ppm that are generated by the dimethyl aluminum group, although no precise assignment of the AlMe$_2$ group of **4^{Y}** was possible.

Unlike the iodido-bridged congeners **2^{Ln}** and **3**, the bromido-bridged clusters **4^{Ln}** crystallize with either one or two lattice solvent molecules. For example, compound **4^{Y}** crystallized in the triclinic space group $P\bar{1}$ with two molecules of lattice toluene. The Y1–Ct1 (ring centroid) and the Y1–C(Cp*) distances of 2.295 Å and 2.575(7) Å to 2.629(9) Å, respectively, are in the expected range. Overall, the Cp*$_4$Y$_4$Br$_7$ subunit exhibits a highly symmetrical arrangement. While the distances of the yttrium centers Y2 and Y3 to the central bridging bromido ligand differ slightly (Y2–Br4 = 2.9881(1) Å, Y3–Br4 = 2.9611(2) Å), the respective distances of the metal centers Y1 and Y4 are very close (Y1–Br4 = 2.9324(1) Å, Y4–Br4 = 2.9270(1) Å). Those three atoms show an almost linear arrangement of Y1–Br4–Y4 = 178.24(3)°. The Y–Br distances involving the bridging Br2AlMe2 moiety are very long (Y1–Br8 = 2.8842(2) Å, Y4–Br9 = 2.8936(2) Å), while the Al–Br distances differ marginally (Br8–Al1 = 2.440(2) Å, Br9–Al1 = 2.480(2) Å). The dimethyl aluminum group is bent out of the mean plane span by the yttrium metal centers Y1 and Y4, and the bridging bromido ligands Br8 and Br9, by 51.87°, and shows a bond angle C41–Al1–C42 of 126.5(4)°.

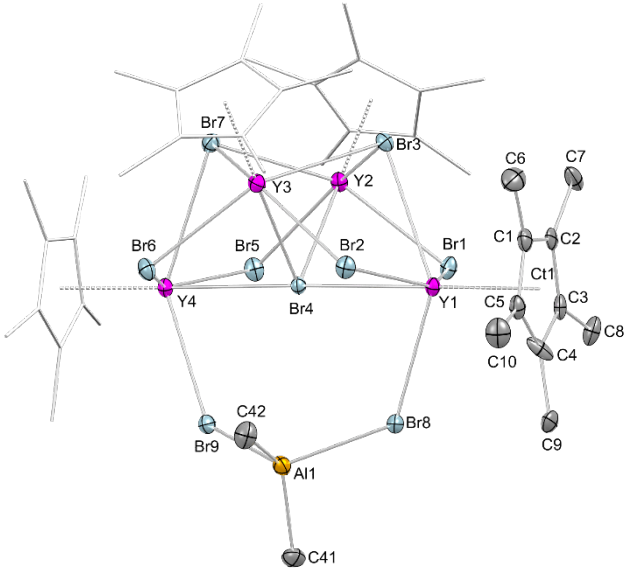

Figure 3. Crystal structure of **4^{Y}** with atomic displacement parameters set at the 50% probability level. Hydrogen atoms and lattice toluene have been omitted for improved visualization. Ancillary Cp* ligands (except for one) are represented by a wireframe model. For selected interatomic distances and angles, see the Supporting Information.

Preparation of chlorido-bridged clusters [Cp*$_4$Ln$_4$Cl$_7$(Cl$_2$AlMe$_2$)] (Ln = Tb, Dy), [Cp*$_4$Ln$_4$Cl$_7$(Cl$_3${AlMe2}2)] (Ln = Y, Gd) and [Cp*Ln(AlMe$_4$)Cl]$_2$ (Ln = Ho, Er).

Treatment of half-sandwich complexes Cp*Ln(AlMe4)2 with the chlorido transfer reagent Me_3GeCl (ratio 1:2.5, Scheme 1) afforded the chlorido-bridged clusters of the general formula [Cp*$_4$Ln$_4$Cl$_7$(Cl$_2$AlMe$_2$)] (**6^{Ln}**, Ln = Tb, Dy), isostructural to the bromido-bridged clusters, with the interatomic distances only deviating by the reduced ionic radius of the chlorido ligands. The reaction with the respective yttrium and gadolinium precursors resulted in a slightly different structural motif, where bridging between the yttrium metal centers Ln1 and Ln4 is achieved by three chlorido and two $AlMe_2$ ligands (Figures 4 and S22). In contrast to **4Y**, the resonances of **5Y** in the ^{1}H NMR spectrum are shifted slightly towards higher field, with the resonance of the Cp* methyl groups located at 2.14 ppm. A broad multiplet, generated by the bridging $AlMe_2$ unit, resonates at -0.2 ppm The Cp*$_4$Y$_4$Cl$_7$ subunit can be compared with the respective Sm subunit in the cluster [(C$_5$Me$_5$)$_2$Sm](μ-Cl)$_6$(μ_3-Cl)$_2$(μ_4-Cl)[Sm(C$_5$Me$_5$)]$_4$ (**II**) by Evans *et al.* from 2006.[41] Due to the larger ionic radius (CN = 6) of samarium (Sm(III): 96 Å) compared to yttrium (Y(III): 90 Å),[46] the interatomic distances in **II** are slightly larger than in complex **5^Y**. In complex **5^Y**, the Cp* and the yttrium metal center Y1 show distance of Y1–Ct1 = 2.307 Å , the respective distance in **II** is approximately 7 Å larger (Sm2–Ct2 = 2.378 Å). A similar difference is found in the distances between the Cp* ring carbon atoms and the respective metal centers. The Cp* carbon-yttrium distances in **5^Y** are within a range of 2.586(3) Å to 2.622(3) Å, whereas the bond distances in **II** only vary from 2.66(1) Å to 2.677(9) Å. Due to the incorporation of the bridging (AlMe$_2$)$_2$Cl$_3$ unit, a reduced strain is exerted on the Y$_4$Cl$_7$ subunit of the cluster. This is reflected in the bond lengths and bond angles in the subunit. While the interatomic distance in **5^Y** between the yttrium center Y1 and the central bridging chlorido ligand Cl3 is 2.8867(4) Å, the respective distance in **II** is larger by only 1 Å (Sm2–Cl3 = 2.897(2) Å). Furthermore, the bond angle between Y1–Cl3–Y1' is smaller by almost 5° compared to complex **II** (Y1–Cl3–Y1' = 173.59(3)°, Sm2–Cl3–Sm3 = 178.38(7)°). This leads to an enlarged distance between the metal centers Y1···Y1' (5.7645 Å) compared to the samarium metal centers in **II** (5.7750(6) Å). Additionally, the reduced strain in **5^Y** is reflected in the distance and angle of the μ_2-bridging chlorido ligand. Compared to the Sm–Cl distance in **II** (Sm2–Cl1 = 2.714(2) Å), the respective distance in **5^Y** is larger overall (Y1–Cl5 = 2.7158(8) Å). Similar to that, the angle between the central bridging chlorido ligand, the metal center and the μ2-bridging chlorido ligand is slightly wider in **5^Y** (Cl3–Y1–Cl5 = 76.80(2)°) compared to **II** (Cl1–Sm2–Cl3 = 74.55(6)°).

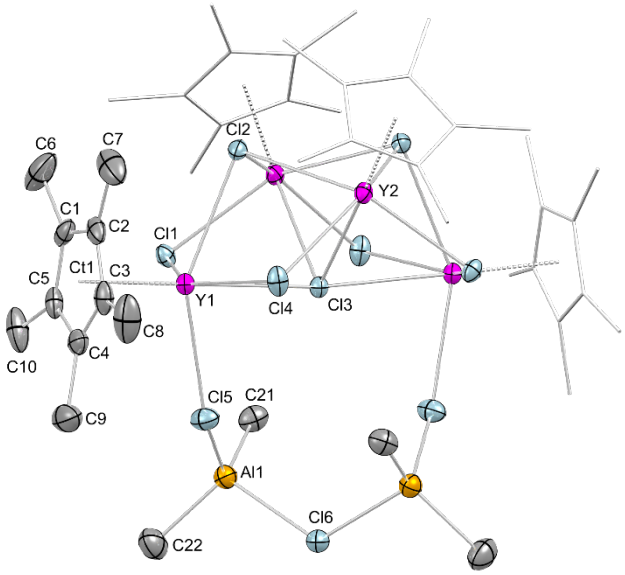

Figure 4. Crystal structure of **5^Y** with atomic displacement parameters set at the 50% probability level. Hydrogen atoms and lattice toluene have been omitted for improved visualization. Ancillary Cp* ligands (except for one) are represented by a wireframe model. For selected bond lengths and angles, see the Supporting Information.

Like for the bromido-bridged complexes, the chlorido-bridged compounds always crystallize with either one or two molecules of lattice solvent. Furthermore, two dimeric compounds of the general formula [Cp*Ln(AlMe$_4$)Cl]$_2$ (Ln = Ho, Er) could be isolated, which can be attributed to the smaller ionic radii of those two lanthanides, preventing the aggregation of larger cluster compounds.

Ether cleavage with Et$_2$O.

In contrast to the larger lanthanide metal centers, the donor-free reaction of Cp*Ln(AlMe$_4$)$_2$ (Ln = Ho, Er) with the bromido transfer reagent Me_3GeBr afforded an insoluble precipitate for the synthesis in toluene. Hence, diethyl ether was added dropwise to the reaction mixture until the precipitate was redissolved. Storing the reaction mixture at ambient temperature led to the formation of light red crystals after several days, which were analyzed via single-crystal X-ray diffractometry. Surprisingly, the respective reactions with holmium and erbium did not yield isostructural complexes. For holmium, the dimeric hexanuclear holmium cluster [(μ-Br)Cp*$_3$Ho$_3$Br$_5$(Et$_2$O)]$_2$ (**8**) could be isolated. This cluster crystallizes in the triclinic space group $P\bar{1}$, and consists of two Cp*$_3$Ho$_3$Br$_5$ subunits, with two holmium metal centers bridging to the opposite metal centers via two μ_2-Br ligands. The other holmium metal center has an additional coordinating diethyl ether ligand. Whereas the structural motif of the trinuclear subunit is quite common in rare-earth-metal chemistry for halogenido[5, 43, 47-54] and mixed halogenido-methylidene compounds,[55-56] the dimeric arrangement of two trinuclear subunits is rarer, and involves halogenido and borohydride-bridged species.[57-61] Complex **8** is isostructural to the chlorido-bridged holmium cluster [{(Me$_4$CpNMe$_2$AlEt$_3$)$_2$(Me$_4$CpNMe$_2$)Ho$_3$Cl$_5$}(μ-Cl)]$_2$ (**III**)by ANWANDER *et al.* from the year 2015.[58] Like cluster **8**, this complex crystallizes in the triclinic space group $P\bar{1}$. Both clusters show a similar arrangement of the trinuclear subunits. The distances of the respective holmium metal centers and the μ_2-bridging halogenido ligands to their mean plane are comparable (**8**: min. 0.006 Å, max. 0.113 Å; **III**: min. 0.018 Å, max. 0.092 Å). In both clusters, the most protruding atom outward of the mean plane is the holmium metal center with the coordinating donor ligand attached to it. While the interatomic distance between the respective holmium metal center Ho3 and the diethyl ether oxygen atom O1 is slightly longer (2.364(4) Å) than the sum of the ionic radii (2.30 Å), this distance is noticeably enlarged in **IV** (Ho3–N3 = 2.516(1) Å; $Ho^{+3} + N^{-3}$ = 2.36 Å), which can be attributed to the strain of the chelating

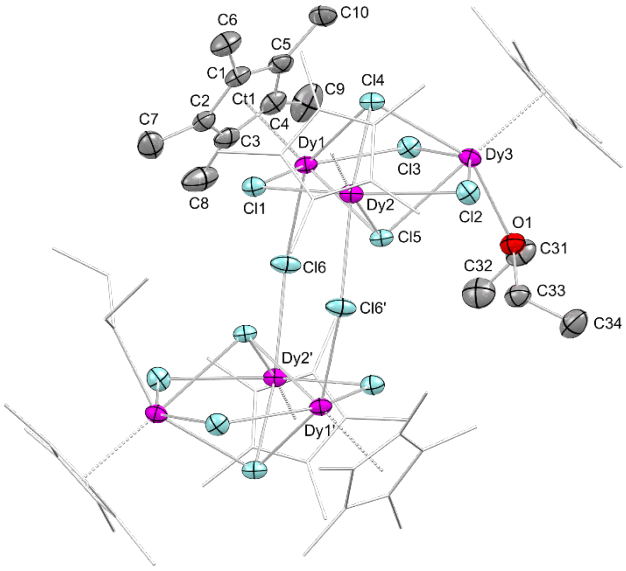

Figure 5. Crystal structure of $\mathbf{6^{Dy}Et_2O}$ with atomic displacement parameters set at the 50% probability level. Hydrogen atoms and lattice toluene have been omitted for improved visualization. Ancillary Cp* ligands and diethyl ether (except for one each) are represented by a wireframe model. For selected interatomic distances and angles, see the Supporting Information.

η^5/κ^1 coordination mode of the Me_4CpNMe_2 ligand. Cluster **8** shows a more planar arrangement of the μ_2-bridging bromido ligands and the metal centers Ho1 and Ho2, with a maximum distance of the atoms to their mean plane of 0.013 Å (**III**: max. 0.049 Å). The overall bonding situation in the trinuclear subunit is similar in both clusters, with comparable ranges for the respective interatomic distances between the holmium metal centers and the μ_2-bridging halogenido ligands (**8**: 2.8335(6) – 2.8824(6) Å; **III**: 2.6673(6) – 2.7049(6) Å). Likewise, the metal centers and the μ_3-bridging halogenido ligands display only minor deviations in the interatomic distances as well, whereas the distances to the lower halogenido ligand are slightly shorter on average in both clusters (**8**: Ho–Br^{top} = 3.0033 Å, Ho–Br^{btm} = 2.9387 Å; **III**: Ho–Cl^{top} = 2.8299 Å, Ho–Cl^{btm} = 2.7848 Å). The reaction with the respective erbium precursor afforded a separated ion pair. Single-crystal X-ray diffraction revealed a tetranuclear arrangement of the erbium metal centers, similar to the previously described tetranuclear iodido-bridged clusters, but with an additional μ_4-bridging bromido/methyl ligand (50/50 occupancy) in the center of the monoanionic complex. The diethyl ether adduct of dimethyl aluminum serves as counterion. So far, only two other related anionic complexes are known, exclusively centered by the respective halogenido ligand though.[59, 62] Complex **9** shows the same structural features as the anionic chlorido-bridged neodymium compound $[(Cp^*NdCl_2)_4(\mu_4\text{-}Cl)]_2[LiO_2][LiO_2{\cdot}Li_2O{\cdot}O_2]$ (**IV**) by EISEN *et al.* from 2007.[59] While **9** crystallizes in the triclinic space group $P\bar{1}$, **IV** crystallizes in the monoclinic space group $C2/m$. The interatomic distances in **9** between the erbium metal center Er1 and the outer bridging bromido ligands are within a range from 2.8603(4) Å (Er1–Br1) to 2.8794(4) Å (Er1–Br2), whereas **IV** shows a slightly higher range in the interatomic distances, ranging from 2.824 Å (Nd1–Cl1) to 2.878 Å (Nd1–Cl2). Both clusters show only minor deviations in the distances between the metal centers opposing each other (Er1–Er1' = 5.7047 Å, Er2–Er2' = 5.6993 Å; Nd1–Nd3 = 5.782 Å, Nd2–Nd2' = 5.749 Å), resulting in an overall symmetric ring structure of the respective compounds. This is further reflected in the inner angles of the two complexes, between the metal centers and the centroid between the two bridging halogenido ligands. These angles are in a range from 132.93° to 136.51° (average: 134.96°) for cluster **9**, and 133.88° to 135.75° (average: 134.94°) for **IV**, and resulting in a sum of the inner angles close to the expected 1080° for a symmetric octagon (9: 1079.68°; IV: 1079.49°).

Spurred by these findings, we targeted ether cleavage reactions for the larger clusters **3**, $\mathbf{4^Y}$, $\mathbf{4^{Dy}}$, $\mathbf{5^Y}$ and $\mathbf{5^{Dy}}$. For the yttrium and dysprosium clusters, compounds with the general formula $[(\mu_2\text{-}X)Cp^*_3Ln_3X_5(Et_2O)]_2$ (Ln = Y, Dy; X = Br, Cl) – isostructural to **8** – could be isolated. Complexes $\mathbf{4^YEt_2O}$ and $\mathbf{5^YEt_2O}$ were further investigated NMR spectroscopically. The ^{1}H NMR spectrum reveals a dynamic equilibrium in solution, likely between the monomeric and dimeric species of the respective cluster. Two triplets, generated by the diethyl ether CH_2 hydrogen atoms, resonate at 3.56 ppm and 3.26 ppm, respectively. Additionally, the spectrum shows four singlets from the Cp* methyl group hydrogen atoms at 2.31 ppm, 2.18 ppm, 2.17 ppm and 1.98 ppm. The diethyl ether CH_3 hydrogen atoms resonate as two triplets at 1.08 ppm and 0.85 ppm. Similar to the ^{1}H NMR spectrum, a splitting of the signals can be observed in the $^{13}C\{^1H\}$ NMR spectrum as well, although no resonances can be attributed to the diethyl ether carbon atoms. Two signals can be assigned to the Cp* ring carbon atoms, resonating at 124.0 ppm and 123.9 ppm. The other three resonances at 13.4, 13.3 and 13.2 ppm are generated by the Cp* methyl carbon atoms. Unlike complex $\mathbf{4^YEt_2O}$, the chlorido-bridged cluster $\mathbf{5^YEt_2O}$ does not show a splitting of the signals in solution, hinting at a higher stability of the chlorido-bridged cluster compared with the bromido-bridged one. The respective ^{1}H NMR spectrum in [D_8]toluene at ambient temperature shows three signals that can be attributed to $\mathbf{5^YEt_2O}$. The quartet at 3.26 ppm is generated by the diethyl ether CH_2 hydrogen atoms, the methyl groups of the Cp* ligand resonate at 2.14 ppm, and the diethyl ether CH_3 hydrogen atoms show a triplet at 1.09 ppm. Furthermore, the respective integrals give the expected 2 : 15 : 3 ratio. In the $^{13}C\{^1H\}$ NMR spectrum, only two signals generated by the complex are visible. The resonance at 122.9 ppm is generated by the Cp* ring carbon atoms, whereas the Cp* methyl carbon atoms resonate at 12.4 ppm. As previously seen for $\mathbf{4^YEt_2O}$, no signals from the coordinated diethyl ether are visible in the spectrum. Exemplary applying the same reaction protocol for $\mathbf{4^{Dy}}$, but using tetrahydrofuran instead of diethyl ether, resulted in decomposition of the cluster and afforded the half-sandwich dibromide tetrahydrofuran adduct $Cp^*DyBr_2(thf)_3$ ($\mathbf{4^{Dy}THF}$). In contrast to the formation of dimeric clusters for the ether cleavage reaction with the respective yttrium and dysprosium clusters, a different reaction behavior was observed when **3** was treated with diethyl ether accordingly. Immediately after addition of diethyl ether, the colorless solution turned yellow. Crystalline product was obtained by storing the reaction solution at -40 °C for several days. The crystalline material was identified as $[Cp^*_2Gd(AlMe_4)]_2$ via single-crystal X-ray diffraction,[7] indicating a decomposition of the cluster substructure.

Magnetic property measurements.

Lanthanide complexes supported by cyclopentadienyl derivatives display impressive single-molecule magnet properties like high blocking temperatures and effective energy barriers, as prominent examples show.[22, 28, 31, 63-65] Naturally, we were interested in possible single-molecular magnet behavior of clusters $\mathbf{2^{Ln}}$ as well. Due to the electronic properties of the dysprosium metal center,[66] dysprosium cluster $\mathbf{2^{Dy}}$ seemed the most promising candidate for SMM behavior. Hence, SQUID measurements were performed for cluster $\mathbf{2^{Dy}}$ as well as the magnetically diluted congener $\mathbf{2^{Y/Dy}}$ (10% dilution level; for details on the magnetic measurements, see the Supporting Information).

Whereas $\mathbf{2^{Dy}}$ did in fact display SMM behavior, its properties are rather complex. In the 6-9 K region, multiple relaxation processes have been observed that could be explained by crystallographic disorder of both the four dysprosium metal centers and the eight iodido ligands, leading to a superimposition of the respective unique relaxation processes. Outside of this region, $\mathbf{2^{Dy}}$ shows regular relaxation behavior, with an effective energy barrier to reversal of the magnetization (U_{eff}) of 164(10) cm^{-1}.

Table 1. Selected Cp^R-based single-molecule magnets with U_{eff} (effective energy barrier to reversal of the magnetization) and T_B (100s blocking temperature).

Compound	U_{eff} [cm^{-1}]	T_B [K]
$[Cp_2Dy(\mu\text{-Cl})]_2$ [67]	37.9	
$[Cp_2Dy(\mu\text{-Cl})]_n$ [67]	97.6	
$[Cp_2Dy(thf)(\mu\text{-Cl})]_2$ [67]	48.7	
$[Cp^*_2DyI(thf)]$ [68]	419	
$[Cp^*_2DyBr(thf)]$ [68]	163	
$[Cp^*_2DyCl(thf)]$ [68]	112	
$[Dy(C_5H_2{}^tBu_3\text{-}1,2,4)_2][B(C_6F_5)_4]$ [63-64]	1223/1277	53
$[(C^{iPr5})Dy(Cp^*)][B(C_6F_5)_4]$ [28]	1541	80
$[Dy(Cp^{iPr4H})_2][B(C_6F_5)_4]$ [65]	1285	17
$[Dy(Cp^{iPr4Me})_2][B(C_6F_5)_4]$ [65]	1468	62
$[Dy(Cp^{iPr4}Et)_2][B(C_6F_5)_4]$ [65]	1380	59
$[Dy(Cp^{iPr5})_2][B(C_6F_5)_4]$ [65]	1334	56
$Tb^{II}(Cp^{iPr5})_2$ [69]	1205	52
$Dy^{II}(Cp^{iPr5})_2$ [69]	37.4	5
$[(Cp^*Dy)_6K_4Cl_{16}(thf)_6]$ [70]	561	4.5

In order to scrutinize the magnetic properties of $\mathbf{2^{Dy}}$, AC susceptibility measurements were conducted for the respective magnetically dilute complex $\mathbf{2^{Y/Dy}}$ as well, which allows investigating the properties for single Dy^{3+} ions. Dilution leads to a more uniform frequency dependence of the out-of-phase susceptibility X'', supporting the hypothesis of superimposition-related properties for $\mathbf{2^{Dy}}$. Furthermore, a notable increase in U_{eff} for $\mathbf{2^{Y/Dy}}$ to 204(25) cm^{-1} was observed in case of magnetic dilution.

CONCLUSION

Rare-earth-metal complexes of distinct nuclearities and structural motifs are readily accessible via an alkyl/halogenido exchange reaction. The versatile synthesis protocol, using the highly reactive half-sandwich complexes $Cp^*Ln(AlMe_4)_2$ as precursors in combination with the mild halogenido transfer reagents Me_3SiI and Me_3GeX (X = Br, Cl), enables the isolation of coordination clusters, whereas the steric demand of the halogenido ligand strongly influences both cluster size and coordination mode. SQUID measurements for $[Cp^*DyI_2]_4$ as well as the magnetically diluted version $Dy@[Cp^*YI_2]_4$ revealed single-molecule magnet behavior for the respective complex, with a moderate U_{eff} of 164 cm^{-1}. The established synthesis protocol will likely contribute to advancement in the field of high-nuclearity single-molecule magnets, given that the modular exchangeable synthesis protocol facilitates variation of both organometallic precursor and ligand system.

EXPERIMENTAL SECTION

General Considerations.

All manipulations were performed under rigorous exclusion of air and moisture using standard Schlenk and glovebox techniques (MBraun MB200B; <0.1 ppm of O_2, <0.1 ppm of H_2O, argon atmosphere). Toluene, tetrahydrofuran and diethyl ether were purified using Grubbs-type columns (MBraun SPS, solvent purification system). Benzene (≥ 99%, Honeywell) was dried over CaH_2 and subsequently destilled. [D_6]benzene (99.6%, Sigma-Aldrich) and [D_8]toluene (99.6%, Sigma-Aldrich) were dried by letting the solvents stand over Na/K alloy for at least 24 h and subsequent filtration. All solvents were stored inside a glovebox. $Ln(AlMe_4)_3$ (Ln = Y, Gd, Tb, Dy, Ho, Er),[71-74] and $Cp^*Ln(AlMe_4)_2$ (Ln = Y, Gd, Tb, Dy, Ho)[7, 75] were prepared according to literature procedures. Iodotrimethylsilane (97%), bromotrimethylgermane (98%) and chlorotrimethylgermane (98%) were purchased from abcr and used without further purification. NMR spectra of air- and moisture-sensitive compounds were recorded by using J. Young valve NMR tubes at ambient temperature on a Bruker AVII+400 (^1H, ^{13}C) NMR spectrometer. NMR chemical shifts are reported in parts per million relative to tetramethylsilane. Coupling constants are given in Hertz. Elemental analyses were performed on an Elementar Vario Micro Cube. IR spectra were recorded on a Nicolet 6700 FTIR spectrometer with a DRIFT cell (KBr window, Kubelka-Munk conversion), and the samples were prepared in a glovebox and mixed with KBr powder. EDX spectra were recorded on a HITACHI SU8030 scanning electron microscope. Magnetic measurements were recorded on a Quantum Design MPMS-XL7 SQUID magnetometer equipped with a 7 T magnet.

$Cp^*Er(AlMe_4)_2$ (1). In a vial, $Er(AlMe_4)_3$ (250 mg, 0.58 mmol) was dissolved in toluene (5 ml). HCp* (79.46 mg, 0.58 mmol) was dissolved in toluene (1 ml), added, and the reaction mixture was stirred for 16 h at ambient temperature. Afterward, the solvent was removed under vacuum. The light red solid obtained this way was dissolved in toluene and stored at -40 °C. After 16 h, light red crystals of **1** could be harvested. Crystalline yield: 249 mg, 0.52 mmol, 90%. DRIFT (KBr, cm^{-1}): 2925 (s), 2888 (m), 2820 (w), 2794 (w), 2735 (vw), 1487 (vw), 1435 (w), 1381 (w), 1234 (w), 1212 (m), 1192 (m), 1023 (vw), 890 (vw), 798 (vw), 717 (vs), 699 (vs), 665 (m), 639 (m), 627 (m), 609 (m), 588 (s), 569 (s), 557 (vs), 548 (s), 529 (m), 508 (m), 496 (m), 489 (m), 470 (m), 454 (m). Anal. (%) Calcd for $C_{18}H_{39}ErAl_2$ (476.73 g/mol) C 45.35, H 8.25; found C 43.26, H 8.27. Although these values are outside the range of analytical

purity, no better values could be obtained despite several attempts.

[Cp*Y(I$_2$)]$_4$ (2^{Y}). In a vial, Cp*Y(AlMe$_4$)$_2$ (7.97 mg, 0.02 mmol) was dissolved in toluene (1.5 ml). Me$_3$SiI (10.02 mg, 0.05 mmol) was dissolved in toluene (0.5 ml) and added. The vial was shaken vigorously and stored at ambient temperature. After 16 h, colorless crystals of **2^{Y}** could be harvested. Crystalline yield: 5.4 mg, 0.003 mmol, 57%. Due to the low solubility of **2^{Y}**, no meaningful NMR data could be provided. DRIFT (KBr, cm^{-1}): 2971 (m), 2942 (s), 2904 (vs), 2856 (m), 2759 (vw), 2728 (vw), 1485 (w), 1450 (m), 1431 (m), 1377 (s), 1063 (vw), 1025 (m), 802 (vw), 593 (vw). Anal. (%) Calcd for C$_{40}$H$_{60}$Y$_4$I$_8$ (1911.78 g/mol) C 25.13, H 3.16; found C 25.42, H 3.06.

[Cp*Tb(I$_2$)]$_4$ (2^{Tb}). In a vial, Cp*Tb(AlMe$_4$)$_2$ (9.37 mg, 0.02 mmol) was dissolved in toluene (1.5 ml). Me$_3$SiI (10.02 mg, 0.05 mmol) was dissolved in toluene (0.5 ml) and added. The vial was shaken vigorously and stored at ambient temperature. After 16 h, colorless crystals of **2^{Tb}** could be harvested. Crystalline yield: 9.5 mg, 0.004 mmol, 86%. DRIFT (KBr, cm^{-1}): 2919 (m), 2889 (m), 2793 (w), 2732 (vw), 1435 (w), 1416 (w), 1381 (w), 1232 (m), 1206 (m), 1191 (m), 1060 (vw), 1023 (w), 801 (vw), 723 (vs), 717 (vs), 701 (vs), 683 (vs), 647 (m), 635 (m), 589 (vs), 580 (vs), 561 (s), 515 (s), 509 (s), 470 (m), 454 (w). Anal. (%) Calcd for C$_{40}$H$_{60}$Tb$_4$I$_8$ (2191.86 g/mol) C 21.92, H 2.76; found C 22.28, H 3.03.

[Cp*Dy(I$_2$)]$_4$ (2^{Dy}). In a vial, Cp*Dy(AlMe$_4$)$_2$ (9.44 mg, 0.02 mmol) was dissolved in toluene (1.5 ml). Me$_3$SiI (10.02 mg, 0.05 mmol) was dissolved in toluene (0.5 ml) and added. The vial was shaken vigorously and stored at ambient temperature. After 16 h, yellow crystals of **2^{Dy}** could be harvested. Crystalline yield: 6.5 mg, 0.003 mmol, 59%. DRIFT (KBr, cm^{-1}): 3599 (w), 3547 (w), 3019 (w), 2972 (s), 2943 (vs), 2904 (vs), 2855 (s), 2727 (w), 1645 (vw), 1602 (w), 1487 (m), 1452 (vs), 1432 (vs), 1420 (s), 1377 (vs), 1268 (vw), 1179 (w), 1063 (vw), 1023 (m), 857 (w), 802 (m), 730 (s), 694 (s), 682 (s), 631 (m), 595 (m), 570 (m), 558 (w), 524 (m), 465 (w). Anal. (%) Calcd for C$_{40}$H$_{60}$Dy$_4$I$_8$ (2206.16 g/mol) C 21.78, H 2.74; found C 22.58, H 3.04.

[Cp*Ho(I$_2$)]$_4$ (2^{Ho}). In a vial, Cp*Ho(AlMe$_4$)$_2$ (9.49 mg, 0.02 mmol) was dissolved in toluene (1.5 ml). Me$_3$SiI (10.02 mg, 0.05 mmol) was dissolved in toluene (0.5 ml) and added. The vial was shaken vigorously and stored at ambient temperature. After 2 d, orange crystals of **2^{Ho}** could be harvested. Crystalline yield: 9,1 mg, 0.004 mmol, 82%. DRIFT (KBr, cm^{-1}): 2971 (s), 2943 (s), 2904 (vs), 2855 (s), 2756 (vw), 2728 (w), 1646 (vw), 1556 (vw), 1538 (vw), 1486 (m), 1449 (s), 1431 (s), 1421 (s), 1377 (vs), 1240 (vw), 1025 (w), 952 (vw), 802 (vw), 727 (vw), 706 (vw), 694 (vw) 593 (w), 551 (vw). Anal. (%) Calcd for C$_{40}$H$_{60}$Ho$_4$I$_8$ (2215.88 g/mol) C 21.68, H 2.73; found C 21.72, H 3.06.

[Cp*Er(I$_2$)]$_4$ (2Er). In a vial, Cp*Er(AlMe$_4$)$_2$ (9.53 mg, 0.02 mmol) was dissolved in toluene (1.5 ml). Me$_3$SiI (10.02 mg, 0.05 mmol) was dissolved in toluene (0.5 ml) and added. The vial was shaken vigorously and stored at ambient temperature. After 16 h, light red crystals of **2Er** could be harvested. Crystalline yield: 9.5 mg, 0.004 mmol, 75%. DRIFT (KBr, cm^{-1}): 2922 (m), 2885 (m), 2794 (vw), 2733 (vw), 1484 (vw), 1439 (w), 1381 (w), 1235 (w), 1211 (w), 1193 (w), 1023 (vw), 801 (vw), 719 (vs), 712 (vs), 681 (vs), 632 (m), 607 (m), 594 (m), 578 (s), 561 (m), 500 (m), 472 (w), 455 (m). Anal. (%) Calcd for C$_{40}$H$_{60}$Er$_4$I$_8$ (2191.86 g/mol) C 21.59, H 2.72; found C 21.69, H 2.93.

[Cp*Y/Dy(I$_2$)]$_4$ (2$^{Y/Dy}$). In a vial, a toluene solution (1.5 ml) of Cp*Y(AlMe$_4$)$_2$ (35.85 mg, 0.09 mmol) and a toluene solution (0.5 ml) of Cp*Dy(AlMe$_4$)$_2$ (4.69 mg, 0.01 mmol) were mixed. Me$_3$SiI (50.03 mg, 0.25 mmol) was dissolved in toluene (0.5 ml) and added. The vial was shaken vigorously and stored at ambient temperature. After 16 h, light yellow crystals of **2$^{Y/Dy}$** could be harvested. Crystalline yield: 45.8 mg, 0.024 mmol, 94%. DRIFT (KBr, cm^{-1}): 3544 (vw), 2971 (m), 2943 (m), 2904 (s), 2855 (m), 2757 (vw), 2729 (vw), 1644 (vw), 1485 (m), 1450 (s), 1431 (s), 1420 (s), 1377 (vs), 1245 (vw), 1189 (vw), 1064 (w), 1025 (s), 953 (vw), 802 (w), 728 (w), 694 (w), 593 (m), 551 (vw), 464 (w). Anal. (%) Calcd for C$_{40}$H$_{60}$Y$_{3.52}$Dy$_{0.48}$I$_8$ (1947.22 g/mol) C 24.67, H 3.11; found C 25.11, H 3.11.

[(Cp*$_4$Gd$_4$I$_7${AlMe$_4$})$_2$](C$_7$H$_8$)$_2$ (3). In a vial, Cp*Gd(AlMe$_4$)$_2$ (9.33 mg, 0.02 mmol) was dissolved in toluene (1.5 ml). Me$_3$SiI (10.02 mg, 0.05 mmol) was dissolved in toluene (0.5 ml) and added. The vial was shaken vigorously and stored at ambient temperature. After 16 h, colorless crystals of **3** could be harvested. Crystalline yield: 6.6 mg, 0.001 mmol, 56%. DRIFT (KBr, cm^{-1}): 2915 (m), 2883 (m), 2791 (w), 2733 (vw), 1487 (vw), 1435 (m), 1417 (w), 1381 (w), 1231 (w), 1204 (m), 1191 (m), 1061 (vw), 1022 (w), 801 (vw), 733 (vs), 720 (vs), 710 (vs), 652 (m), 643 (m), 609 (m), 597 (s), 584 (s), 556 (m), 525 (w), 515 (m), 505 (m), 482 (w), 450 (w), 433 (vw). Anal. (%) Calcd for C$_{109}$H$_{168}$Gd$_8$I$_{14}$ (4567.17 g/mol) C 28.67, H 3.71; found C 26.89, H 3.37. The deviation between theoretical and experimental microanalytical data derives likely from the removal of lattice toluene under vacuum.

[Cp*$_4$Y$_4$Br$_7$(Br$_2$AlMe$_2$)](C$_7$H$_8$)$_2$ (4^{Y}). In a vial, Cp*Y(AlMe$_4$)$_2$ (7.97 mg, 0.02 mmol) was dissolved in toluene (1.5 ml). Me$_3$GeBr (9.88 mg, 0.05 mmol) was dissolved in toluene (0.5 ml) and added. The vial was shaken vigorously and stored at -40 °C. After 2 d, colorless crystals of **4^{Y}** could be harvested. Crystalline yield: 5.3 mg, 0.003 mmol, 59%. ^{1} H NMR (400 MHz, [D$_8$]toluene, 26 °C): δ 2.17 (s, 15 H, CC*H$_3$*) ppm. DRIFT (KBr, cm^{-1}): 2972 (w), 2947 (m), 2902 (m), 2857 (w), 2729 (vw), 1488(w), 1454 (m), 1433 (m), 1192 (w), 1064 (vw), 1024 (w), 802 (vw), 728 (m), 706 (vs), 686 (s), 593 (w), 580 (w), 464 (vw). Anal. (%) Calcd for C$_{56}$H$_{82}$AlY$_4$Br$_9$ (1857.01 g/mol) C 36.22, H 4.45; found C 34.56, H 4.50. The deviation between theoretical and experimental microanalytical data derives likely from the removal of lattice toluene under vacuum.

[(μ$_2$-Br)Cp*$_3$Y$_3$Br$_5$(Et$_2$O)]$_2$(C$_7$H$_8$) (4^{Y}Et$_2$O). In a vial, Cp*Y(AlMe$_4$)$_2$ (15.94 mg, 0.04 mmol) was dissolved in toluene (1.5 ml). Me$_3$GeBr (19.76 mg, 0.1 mmol) was dissolved in toluene (0.5 ml) and added. The vial was shaken vigorously and stored at ambient temperature for 24 h. Afterwards, the solvent was removed under vacuum. The remaining precipitate was resuspended in toluene (1 ml), 10 drops of diethylether were added, and the reaction mixture was stored at ambient temperature. After 16 h, colorless crystals of **4^{Y}Et$_2$O** could be harvested Crystalline yield: 14.1 mg, 0.005 mmol, 81%. ^{1}H NMR (400 MHz, [D$_8$]toluene, 26 °C): δ = 3.56 (q, $^{2}J_{H,H}$ = 6.99 Hz, 2H, OC*H$_2$*CH$_3$), 3.26 (q, $^{2}J_{H,H}$ = 6.99 Hz, 2H, OC*H$_2$*CH$_3$), 2.30 (s, 6H, CC*H$_3$*), 2.18 (s, 11H, CC*H$_3$*), 2.17 (s, 9H, CC*H$_3$*), 1.98 (s, 4H, CC*H$_3$*), 1.08 (t, $^{2}J_{H,H}$ = 7.00 Hz, 3H, OCH$_2$C*H$_3$*), 0.85 (t, $^{2}J_{H,H}$ = 7.00 Hz, 2H, OCH$_2$C*H$_3$*) ppm. ^{13}C{^{1}H} NMR (101 MHz, [D$_8$]toluene, 26 °C): δ = 124.0 (*Cp*), 123.9 (*Cp*), 13.4 (Cp*C*H$_3$), 13.3 (Cp*C*H$_3$), 13.2 (Cp*C*H$_3$) ppm. DRIFT (KBr, cm^{-1}): 3079 (vw), 3018 (vw), 2974 (m), 2946 (m), 2902 (s),

2857 (m), 2807 (vw), 2726 (vw), 1944 (vw), 1857 (vw), 1805 (vw), 1644 (vw), 1602 (w), 1494 (m), 1452 (vs), 1433 (s), 1390 (s), 1377 (vs), 1321 (vw), 1290 (vw), 1242 (vw), 1187 (w), 1146 (w), 1092 (m), 1063 (w), 1029 (vs), 996 (m), 889 (m), 860 (vw), 831 (w), 802 (w), 792 (w), 773 (s), 731 (vs), 695 (m), 621 (vw), 596 (m), 550 (vw), 508 (w), 465 (s), 455 (w). Anal. (%) Calcd for $C_{82}H_{126}Y_6Br_{12}O_2$ (2636.19 g/mol) C 37.36 H 4.82; found C 37.04 H 5.32.

[Cp*$_4$Gd$_4$Br$_7$(Br$_2$AlMe$_2$)](C$_7$H$_8$)$_2$ (4^{Gd}). In a vial, Cp*Gd(AlMe$_4$)$_2$ (9.33 mg, 0.02 mmol) was dissolved in toluene (1.5 ml). Me$_3$GeBr (9.88 mg, 0.05 mmol) was dissolved in toluene (0.5 ml) and added. The vial was shaken vigorously and stored at -40 °C. After 7 d, colorless crystals of **4^{Gd}** could be harvested. Crystalline yield: 3.3 mg, 0.002 mmol, 31%. DRIFT (KBr, cm^{-1}): 3081 (vw), 3022 (w), 2971 (m), 2946 (s), 2901 (vs), 2858 (s), 2759 (vw), 2728 (w), 1644 (vw), 1603 (vw), 1493 (m), 1452 (s), 1432 (s), 1423 (s), 1378 (s), 1241 (vw), 1185 (w), 1080 (vw), 1063 (w), 1024 (m), 954 (vw), 893 (vw), 802 (w), 728 (vs), 701 (vs), 679 (s), 620 (vw), 591 (w), 577 (w), 464 (w). Anal. (%) Calcd for $C_{56}H_{82}AlGd_4Br_9$ (2130.39 g/mol) C 31.57, H 3.88; found C 27.45, H 3.48. The deviation between theoretical and experimental microanalytical data derives likely from the removal of lattice toluene under vacuum.

[Cp*$_4$Tb$_4$Br$_7$(Br$_2$AlMe$_2$)](C$_7$H$_8$) (4^{Tb}). In a vial, Cp*Tb(AlMe$_4$)$_2$ (9.37 mg, 0.02 mmol) was dissolved in toluene (1.5 ml). Me$_3$GeBr (9.88 mg, 0.05 mmol) was dissolved in toluene (0.5 ml) and added. The vial was shaken vigorously and stored at ambient temperature. After 3 d, colorless crystals of **4^{Tb}** could be harvested. Crystalline yield: 6.9 mg, 0.003 mmol, 68%. DRIFT (KBr, cm^{-1}): 3084 (vw), 3058 (vw), 3027 (vw), 2970 (m), 2944 (m), 2904 (s), 2858 (m), 2727 (vw), 2178 (vw), 2159 (vw), 2048 (vw), 1604 (vw), 1558 (vw), 1539 (vw), 1494 (w), 1455 (m), 1434 (m), 1421 (m), 1378 (m), 1239 (vw), 1191 (w), 1080 (vw), 1064 (vw), 1024 (w), 890 (vw), 802 (vw), 729 (vs), 704 (vs), 694 (vs), 686 (s), 592 (w), 574 (w), 464 (w). Anal. (%) Calcd for $C_{47}H_{68}AlTb_4Br_9$ (2014.88 g/mol) C 28.02, H 3.40; found C 27.93, H 3.16.

[Cp*$_4$Dy$_4$Br$_7$(Br$_2$AlMe$_2$)](C$_6$D$_6$)$_2$ (4^{Dy}). In a vial, Cp*Dy(AlMe$_4$)$_2$ (4.72 mg, 0.01 mmol) was dissolved in [D$_6$]benzene (0.5 ml). Me$_3$GeBr (4.94 mg, 0.025 mmol) was dissolved in [D$_6$]benzene (0.5 ml) and added. The vial was shaken vigorously and stored at ambient temperature. After 4 d, yellow crystals of **4^{Dy}** could be harvested. Crystalline yield: 3.9 mg, 0.002 mmol, 37%. DRIFT (KBr, cm^{-1}): 3590 (w), 3084 (vw), 3058 (vw), 3027 (w), 2969 (m), 2944 (s), 2905 (s), 2857 (m), 2727 (vw), 1604 (vw), 1557 (vw), 1538 (vw), 1494 (m), 1455 (s), 1431 (m), 1420 (m), 1378 (m), 1241 (vw), 1191 (w), 1080 (vw), 1064 (vw), 1024 (m), 891 (vw), 802 (vw), 728 (vs), 704 (vs), 695 (vs), 593 (w), 575 (w), 464 (m). Anal. (%) Calcd for $C_{54}H_{66}D_{12}AlDy_4Br_9$ (2135.41 g/mol) C 30.37, H 4.25; found C 30.30, H 3.84.

[{(μ_2-Br)(Cp*$_3$Dy$_3$Br$_5$)(Et$_2$O)}$_3$]$_2$(C$_7$H$_8$) (4^{Dy}Et$_2$O). In a vial, Cp*Dy(AlMe$_4$)$_2$ (9.44 mg, 0.02 mmol) was dissolved in toluene (1.5 ml). Me$_3$GeBr (9.88 mg, 0.05 mmol) was dissolved in toluene (0.5 ml) and added. The vial was shaken vigorously and stored at ambient temperature for 24 h. Afterwards, the solvent was removed under vacuum. The remaining precipitate was resuspended in toluene (1 ml), 10 drops of diethylether were added, and the reaction mixture was stored at ambient temperature. After 16 h, yellow crystals of **4^{Dy}Et$_2$O** could be harvested. Crystalline yield: 9.6 mg, 0.003 mmol, 94%. DRIFT (KBr, cm^{-1}): 3612 (vw), 2974 (s), 2947 (s), 2901 (vs), 2857 (s), 2726 (vw), 1642 (vw), 1602 (vw), 1493 (m), 1452 (vs), 1433 (vs), 1390 (s), 1376 (vs), 1290 (vw), 1241 (vw), 1187 (w), 1146 (w), 1092 (m), 1083 (m), 1064 (w), 1034 (vs), 997 (m), 890 (m), 862 (w), 830 (w), 802 (w), 791 (w), 772 (s), 731 (s), 695 (m), 621 (vw), 594 (m), 550 (vw), 502 (w), 465 (m), 455 (w). Anal. (%) Calcd for $C_{82}H_{126}Dy_6Br_{12}O_2$ (3077.74 g/mol) C 32.00 H 4.13; found C 30.21 H 4.30. The deviation between theoretical and experimental microanalytical data can be attributed to removal of lattice toluene under vacuum.

[Cp*DyBr$_2$(thf)$_3$] (4^{Dy}THF). In a vial, Cp*Dy(AlMe$_4$)$_2$ (18.76 mg, 0.04 mmol) was dissolved in toluene (1.5 ml). Me$_3$GeBr (19.77 mg, 0.1 mmol) was dissolved in toluene (0.5 ml) and added. The vial was shaken vigorously and stored at ambient temperature for 5 min. Afterwards, 10 drops of tetrahydrofuran were added, and the reaction mixture was stored at -40 °C. Crystalline **4^{Dy}THF** was obtained from a saturated toluene/THF solution. Crystalline yield: 18.5 mg, 0.025 mmol, 62%. DRIFT (KBr, cm^{-1}): 3584 (vw), 2972 (w), 2899 (m), 2854 (w), 2723 (vw), 1485 (vw), 1453 (w), 1431 (w), 1377 (w), 1345 (vw), 1297 (vw), 1247 (vw), 1191 (w), 1137 (vw), 1062 (vw), 1036 (w), 1009 (vs), 954 (vw), 919 (w), 857 (vs), 804 (vw), 694 (m), 621 (vw), 593 (vw), 576 (vw), 522 (vw), 465 (vw). Anal. (%) Calcd for $C_{26}H_{47}DyBr_2O_4$ (745.95 g/mol) C 41.86, H 6.35; found C 31.25, H 4.61. The deviation between theoretical and experimental microanalytical data can be attributed to removal of coordinated and lattice tetrahydrofuran under vacuum.

[Cp*$_4$Y$_4$Cl$_7${Cl$_3$(AlMe$_2$)$_2$}](C$_7$H$_8$) (5^{Y}). In a vial, Cp*Y(AlMe$_4$)$_2$ (7.97 mg, 0.02 mmol) was dissolved in toluene (1.5 ml). Me$_3$GeCl (7.66 mg, 0.05 mmol) was dissolved in toluene (0.5 ml) and added. The vial was shaken vigorously and stored at -40 °C. After 5 d, colorless crystals of **5^{Y}** could be harvested. Crystalline yield: 5.3 mg, 0.003 mmol, 69%. ^{1}H NMR (400 MHz, [D$_8$]toluene, 26 °C): δ 2.14 (s, 15 H, CC*H$_3$*), -0.20 m, 12H, Al*Me$_2$*) ppm. ^{13}C{^{1}H} NMR (101 MHz, [D$_8$]toluene, 26 °C): δ = 123.8 (*Cp*), 122.9 (*Cp*), 12.4 (Cp*C*H$_3$), 12.1 (Cp*C*H$_3$), 12.0 (Al*Me$_2$*) ppm.DRIFT (KBr, cm^{-1}): 2970 (m), 2942 (m), 2908 (s), 2861 (m), 2730 (vw), 1651 (vw), 1604 (vw), 1494 (m), 1455 (s), 1434 (m), 1423 (m), 1379 (m), 1249 (vw), 1194 (w), 1065 (w), 1024 (m), 891 (vw), 802 (vw), 729 (vs), 718 (s), 707 (vs), 699 (vs), 583 (m), 464 (w). Anal. (%) Calcd for $C_{51}H_{80}Al_2Y_4Cl_{10}$ (1457.29 g/mol) C 42.03, H 5.53; found C 42.71, H 5.43.

[(μ_2-Cl)Cp*$_3$Y$_3$Cl$_5$(Et$_2$O)]$_2$(C$_7$H$_8$) (5^{Y}Et$_2$O). In a vial, Cp*Y(AlMe$_4$)$_2$ (15.94 mg, 0.04 mmol) was dissolved in toluene (1.5 ml). Me$_3$GeCl (15.32 mg, 0.1 mmol) was dissolved in toluene (0.5 ml) and added. The vial was shaken vigorously and stored at ambient temperature for 24 h. Afterwards, the solvent was removed under vacuum. The remaining precipitate was resuspended in toluene (1 ml), 10 drops of diethylether were added, and the reaction mixture was stored at ambient temperature. After 16 h, colorless crystals of **5^{Y}Et$_2$O** could be harvested Crystalline yield: 13.9 mg, 0.007 mmol, 99%. ^{1}H NMR (400 MHz, [D$_8$]toluene, 26 °C): δ = 3.26 (q, $^2J_{H,H}$ = 6.98 Hz, 2H, OC*H$_2$*CH$_3$), 2.14 (s, 15H, CC*H$_3$*), 1.09 (t, $^2J_{H,H}$ = 6.98 Hz, 3H, OCH$_2$C*H$_3$*) ppm. ^{13}C{^{1}H} NMR (101 MHz, [D$_8$]toluene, 26 °C): δ = 122.9 (*Cp*), 12.4 (Cp*C*H$_3$) ppm. DRIFT (KBr, cm^{-1}): 2974 (s), 2945 (s), 2904 (vs), 2858 (s), 2725 (w), 1651 (w), 1602 (w), 1494 (m), 1454 (vs), 1435 (vs), 1392 (s), 1376 (s), 1292 (w), 1246 (w), 1183 (w), 1147 (w), 1086 (m), 1063 (m), 1035 (vs), 1000 (m), 891 (m), 868 (w), 830 (w), 791 (w), 773 (m), 730 (m), 694 (w), 623 (vw), 595 (m), 514 (w), 464 (w). Anal. (%) Calcd for $C_{82}H_{126}Y_6Cl_{12}O_2$ (2102.68 g/mol)

C 46.84, H 6.04; found C 45.45, H 5.91. The deviation between theoretical and experimental microanalytical data can be attributed to removal of lattice toluene under vacuum.

[Cp*$_4$Gd$_4$Cl$_7${Cl$_3$(AlMe$_2$)$_2$}](C$_7$H$_8$) (5^{Gd}). In a vial, Cp*Gd(AlMe$_4$)$_2$ (18.67 mg, 0.04 mmol) was dissolved in toluene (2 ml). Me$_3$GeCl (15.32 mg, 0.1 mmol) was dissolved in toluene (0.5 ml) and added. The vial was shaken vigorously and stored at -40 °C. After 5 d, colorless crystals of **5^{Gd}** could be harvested. Crystalline yield: 11.3 mg, 0.006 mmol, 62%. DRIFT (KBr, cm^{-1}): 2969 (m), 2944 (s), 2910 (s), 2860 (m), 2730 (vw), 1648 (vw), 1604 (vw), 1494 (w), 1454 (s), 1434 (m), 1421 (m), 1379 (m), 1246 (vw), 1194 (w), 1064 (vw), 1025 (m), 952 (vw), 802 (vw), 728 (s), 706 (vs), 693 (vs), 623 (vw), 582 (w), 464 (w). Anal. (%) Calcd for C$_{49}$H$_{74}$Al$_2$Gd$_4$Cl$_{10}$ (1822.81 g/mol) C 35.17, H 4.46; found C 35.07, H 4.20.

[Cp*$_4$Tb$_4$Cl$_7$(Cl$_2$AlMe$_2$)](C$_7$H$_8$) (6^{Tb}). In a vial, Cp*Tb(AlMe$_4$)$_2$ (9.37 mg, 0.02 mmol) was dissolved in toluene (1.5 ml). Me$_3$GeCl (7.66 mg, 0.05 mmol) was dissolved in toluene (0.5 ml) and added. The vial was shaken vigorously and stored at ambient temperature. After 7 d, colorless crystals of **6^{Tb}** could be harvested. Crystalline yield: 7.4 mg, 0.004 mmol, 90%. DRIFT (KBr, cm^{-1}): 3086 (vw), 3026 (w), 2971 (m), 2945 (m), 2907 (s), 2860 (m), 2729 (vw), 2163 (vw), 2135 (vw), 2048 (vw), 1652 (vw), 1604 (vw), 1558 (vw), 1539 (vw), 1520 (vw), 1505 (w), 1495 (m), 1456 (m), 1435 (m), 1423 (m), 1378 (m), 1245 (vw), 1194 (w), 1079 (vw), 1065 (vw), 1025 (w), 889 (vw), 802 (vw), 729 (vs), 702 (vs), 695 (vs), 577 (w), 464 (w). Anal. (%) Calcd for C$_{49}$H$_{74}$AlTb$_4$Cl$_9$ (1644.86 g/mol) C 35.78, H 4.53; found C 36.30, H 4.28.

[Cp*$_4$Dy$_4$Cl$_7$(Cl$_2$AlMe$_2$)](C$_6$D$_6$)$_2$ (6^{Dy}). In a vial, Cp*Dy(AlMe$_4$)$_2$ (9.44 mg, 0.02 mmol) was dissolved in [D6]benzene (0.5 ml). Me$_3$GeCl (7.66 mg, 0.05 mmol) was dissolved in [D$_6$]benzene (0.5 ml) and added. The vial was shaken vigorously and stored at ambient temperature. The solvent was removed under vacuum to obtain **6^{Dy}** as yellow powder (6.3 mg, 0.004 mmol, 74%). Single crystals 0f **6^{Dy}** were grown inside a *J.Young* NMR tube by storing the reaction mixture for seven days. DRIFT (KBr, cm^{-1}): 3591 (vw), 2969 (w), 2941 (m), 2909 (m), 2859 (w), 2728 (vw), 1487 (vw), 1452 (w), 1433 (w), 1424 (w), 1379 (w), 1196 (w), 1024 (vw), 803 (vw), 772 (vw), 708 (vs), 674 (m), 580 (vw). Anal. (%) Calcd for C$_{54}$H$_{66}$D$_{12}$AlDy$_4$Cl$_9$ (1735.32 g/mol) C 37.38, H 5.23; found C 35.41, H 4.44. The deviation between theoretical and experimental microanalytical data derives likely from removal of lattice C$_6$D$_6$ under vacuum.

[(μ_2-Cl)Cp*$_3$Dy$_3$Cl$_5$(Et$_2$O)]$_2$(C$_7$H$_8$) (6^{Dy}Et$_2$O). In a vial, Cp*Dy(AlMe$_4$)$_2$ (18.76 mg, 0.04 mmol) was dissolved in toluene (1.5 ml). Me$_3$GeCl (15.32 mg, 0.1 mmol) was dissolved in toluene (0.5 ml) and added. The vial was shaken vigorously and stored at ambient temperature for 24 h. Afterwards, the solvent was removed under vacuum. The remaining precipitate was resuspended in toluene (1 ml), 10 drops of diethylether were added, and the reaction mixture was stored at ambient temperature. After 16 h, yellow crystals of **6^{Dy}Et$_2$O** could be harvested Crystalline yield: 14.9 mg, 0.006 mmol, 88%. DRIFT (KBr, cm^{-1}): 3612 (vw), 2975 (m), 2946 (m), 2904 (vs), 2858 (m), 2726 (vw), 1493 (w), 1452 (s), 1431 (s), 1392 (m), 1376 (m), 1245 (vw), 1183 (w), 1148 (w), 1086 (m), 1064 (w), 1037 (vs), 1002 (m), 892 (m), 824 (vw), 802 (w), 792 (w), 773 (m), 729 (m), 694 (w), 594 (w), 508 (w), 464 (w). Anal. (%) Calcd for C$_{82}$H$_{126}$Dy$_6$Cl$_{12}$O$_2$ (2544.31 g/mol) C 38.71, H 4.99; found C 35.60, H 4.32. The deviation between theoretical and experimental microanalytical data can be attributed to removal of lattice toluene and coordinated diethyl ether under vacuum.

[(μ_2-Cl)Cp*Ho(AlMe$_4$)]$_2$ (7^{Ho}). In a vial, Cp*Ho(AlMe$_4$)$_2$ (9.49 mg, 0.02 mmol) was dissolved in toluene (1.5 ml). Me$_3$GeCl (7.66 mg, 0.05 mmol) was dissolved in toluene (0.5 ml) and added. The vial was shaken vigorously and stored at ambient temperature for 24 h. Subsequently the solvent was removed under vacuum to obtain **7^{Ho}** as light red powder (7.4 mg, 0.009 mmol, 87%). DRIFT (KBr, cm^{-1}): 2973 (s), 2945 (s), 2907 (vs), 2862 (s), 2761 (vw), 2732 (w), 1698 (w), 1683 (w), 1652 (w), 1635 (vw), 1601 (w), 1558 (w), 1539 (w), 1520 (w), 1506 (w), 1488 (m), 1456 (s), 1435 (s), 1379 (m), 1025 (vw), 801 (vw), 728 (w), 694 (w), 590 (vw). Anal. (%) Calcd for C$_{28}$H$_{54}$Al$_2$Ho$_2$Cl$_2$ (845.46 g/mol) C 39.78, H 6.44; found C 25.64, H 3.84. The large difference between theoretical and experimental values was found for all measurements and adumbrates the formation of a different species, contrary to previously reported syntheses. However, crystalline material could not be obtained, preventing a determination of the exact substructure.

[(μ_2-Cl)Cp*Er(AlMe$_4$)]$_2$ (7Er). In a vial, Cp*Er(AlMe$_4$)$_2$ (9.53 mg, 0.02 mmol) was dissolved in toluene (1.5 ml). Me$_3$GeCl (7.7 mg, 0.05 mmol) was dissolved in toluene (0.5 ml) and added. The vial was shaken vigorously and stored at ambient temperature for 7 d. Afterwards, the vial was stored at -40 °C. After 2 d, light red crystals of **7** could be harvested. Crystalline yield: 1.3 mg, 0.002 mmol, 15%. DRIFT (KBr, cm^{-1}): 2971 (s), 2943 (s), 2907 (vs), 2860 (s), 2731 (w), 1702 (vw), 1683 (vw), 1652 (w), 1602 (w), 1558 (w), 1539 (w), 1506 (w), 1488 (m), 1455 (vs), 1435 (s), 1379 (s), 1196 (vw), 1024 (vw), 900 (vw), 867 (w), 801 (w), 727 (s), 703 (vs), 591 (w), 464 (vw). Anal. (%) Calcd for C$_{28}$H$_{54}$Al$_2$Er$_2$Cl$_2$ (850.12 g/mol) C 39.56, H 6.40; found C 42.22, H 6.40. The difference between the theoretical and experimental values is likely due to contamination with an unknown side product.

[(μ_2-Br)Cp*$_3$Ho$_3$Br$_5$(Et$_2$O)]$_2$ (8). In a vial, Cp*Ho(AlMe4)2 (19.00 mg, 0.04 mmol) was dissolved in toluene (1.5 ml) Me$_3$GeBr (19.76 mg, 0.1 mmol) was dissolved in toluene (0.5 ml) and added. The vial was shaken vigorously and stored at ambient temperature. After a few minutes, the solution became turbid. After letting the suspension stand for 1 h, diethyl ether was added dropwise until the suspension became a clear solution again. After several days, light red crystals formed. Crystalline yield: 12.6 mg, 0.004 mmol, 61%. DRIFT (KBr, cm^{-1}): 3019 (vw), 2975 (m), 2946 (m), 2901 (s), 2856 (m), 2725 (vw), 1602 (vw), 1493 (m), 1451 (s), 1433 (s), 1390 (m), 1376 (s), 1289 (vw), 1240 (vw), 1187 (w), 1146 (w), 1087 (s), 1064 (m), 1030 (vs), 996 (m), 889 (m), 831 (w), 802 (w), 791 (w), 774 (s), 731 (vs), 695 (m), 621 (vw), 595 (m), 508 (w), 465 (s), 455 (m). Anal. (%) Calcd for C$_{82}$H$_{126}$Ho$_6$Br$_{12}$O$_2$ (3092.34 g/mol) C 31.85, H 4.11; found C 31.31, H 4.23.

[{Cp*$_4$Er$_4$(μ_4-Br/CH$_3$)Br$_8$}$^-${(Et$_2$O)$_2$AlMe$_2$}$^+$] (9). In a vial, Cp*Er(AlMe$_4$)$_2$ (9.53 mg, 0.02 mmol) was dissolved in toluene (1.5 ml). Me$_3$GeBr (9.88 mg, 0.05 mmol)was dissolved in toluene (0.5 ml) and added. The vial was shaken vigorously and stored at ambient temperature. After a few minutes, the solution became turbid. After letting the suspension stand for 1 h, diethyl ether was added dropwise until the suspension became a clear solution again. After several days, light red crystals formed in low yield.

AUTHOR INFORMATION

Corresponding Authors

*reiner.anwander@uni-tuebingen.de
*r.layfield@sussex.ac.uk

Notes

The authors declare no competing financial interest.

ACKNOWLEDGMENT

We are grateful to the German Science Foundation for financial support (Grant: AN 238/14-2). Furthermore, we would like to thank Prof. Marcus Scheele for providing the equipment for EDX measurements as well as Elke Nadler for conducting the measurements.

REFERENCES

1. Birmingham, J. M.; Wilkinson, G., The Cyclopentadienides of Scandium, Yttrium and Some Rare Earth Elements. *J. Am. Chem. Soc.* **1956**, *78* (1), 42-44.
2. Schumann, H.; Meese-Marktscheffel, J. A.; Esser, L., Synthesis, structure, and reactivity of organometallic. pi.-complexes of the rare earths in the oxidation state Ln3+ with aromatic ligands. *Chem. Rev.* **1995**, *95* (4), 865-986.
3. Arndt, S.; Okuda, J., Mono(cyclopentadienyl) Complexes of the Rare-Earth Metals. *Chem. Rev.* **2002**, *102* (6), 1953-1976.
4. Anwander, R.; Klimpel, M. G.; Dietrich, H. M.; Shorokhov, D. J.; Scherer, W., High tetraalkylaluminate fluxionality in half-sandwich complexes of the trivalent rare-earth metals. *Chem. Commun.* **2003** (8), 1008-1009.
5. Bienfait, A. M.; Wolf, B. M.; Törnroos, K. W.; Anwander, R., Ln(II)/Pb(II)–Ln(III)/Pb(0) Redox Approach toward Rare-Earth-Metal Half-Sandwich Complexes. *Organometallics* **2015**, *34* (24), 5734-5744.
6. Dietrich, H. M.; Zapilko, C.; Herdtweck, E.; Anwander, R., Ln(AlMe4)3 as New Synthetic Precursors in Organolanthanide Chemistry: Efficient Access to Half-Sandwich Hydrocarbyl Complexes. *Organometallics* **2005**, *24* (23), 5767-5771.
7. Hollfelder, C. O.; Meermann-Zimmermann, M.; Spiridopoulos, G.; Werner, D.; Törnroos, K. W.; Maichle-Mössmer, C.; Anwander, R., C–H-Bond Activation and Isoprene Polymerization Studies Applying Pentamethylcyclopentadienyl-Supported Rare-Earth-Metal Bis(Tetramethylaluminate) and Dimethyl Complexes. *Molecules* **2019**, *24* (20), 3703.
8. Robert, D.; Spaniol, T. P.; Okuda, J., Neutral and Monocationic Half-Sandwich Methyl Rare-Earth Metal Complexes: Synthesis, Structure, and 1,3-Butadiene Polymerization Catalysis. *Eur. J. Inorg. Chem.* **2008**, *2008* (18), 2801-2809.
9. Zimmermann, M.; Törnroos, K. W.; Sitzmann, H.; Anwander, R., Half-Sandwich Bis(tetramethyl-aluminate) Complexes of the Rare-Earth Metals: Synthesis, Structural Chemistry, and Performance in Isoprene Polymerization. *Chem. Eur. J.* **2008**, *14* (24), 7266-7277.
10. Zimmermann, M.; Volbeda, J.; Törnroos, K. W.; Anwander, R., Tetramethylcyclopentadienyl-supported rare-earth metal bis(tetramethyl)aluminate complexes: Synthesis, structural chemistry, cation formation, and isoprene polymerization. *C. R. Chim.* 2010, 13 (6-7), 651-660.
11. Dietrich, H. M.; Raudaschl-Sieber, G.; Anwander, R., Trimethylyttrium and Trimethyllutetium. *Angew. Chem. Int. Ed.* **2005**, *44* (33), 5303-5306.
12. Dietrich, H. M.; Grove, H.; Törnroos, K. W.; Anwander, R., Multiple C−H Bond Activation in Group 3 Chemistry: Synthesis and Structural Characterization of an Yttrium−Aluminum−Methine Cluster. *J. Am. Chem. Soc.* **2006**, *128* (5), 1458-1459.
13. Dietrich, H. M.; Schuster, O.; Törnroos, K. W.; Anwander, R., Heterobimetallic Half-Lanthanidocene Clusters: Novel Mixed Tetramethylaluminato/Chloro Coordination. *Angew. Chem. Int. Ed.* **2006**, *45* (29), 4858-4863.
14. Hamidi, S.; Jende, L. N.; Martin Dietrich, H.; Maichle-Mössmer, C.; Törnroos, K. W.; Deacon, G. B.; Junk, P. C.; Anwander, R., C–H Bond Activation and Isoprene Polymerization by Rare-Earth-Metal Tetramethylaluminate Complexes Bearing Formamidinato N-Ancillary Ligands. *Organometallics* **2013**, *32* (5), 1209-1223.
15. Jende, L. N.; Maichle-Mössmer, C.; Anwander, R., Rare-Earth-Metal Alkylaluminates Supported by N-Donor-Functionalized Cyclopentadienyl Ligands: C–H Bond Activation and Performance in Isoprene Polymerization. *Chem. Eur. J.* **2013**, *19* (48), 16321-16333.
16. Bonath, M.; Hollfelder, C. O.; Schädle, D.; Maichle-Mössmer, C.; Sirsch, P.; Anwander, R., C–H Bond Activation and Isoprene Polymerization by Lutetium Alkylaluminate/gallate Complexes Bearing a Peripheral Boryl and a Bulky Hydrotris(pyrazolyl)borate Ligand. *Eur. J. Inorg. Chem.* **2017**, *2017* (38-39), 4683-4692.
17. Barisic, D.; Diether, D.; Maichle-Mössmer, C.; Anwander, R., Trimethylscandium. *J. Am. Chem. Soc.* **2019**, *141* (35), 13931-13940.
18. Woodruff, D. N.; Winpenny, R. E. P.; Layfield, R. A., Lanthanide single-molecule magnets. *Chem. Rev.* **2013**, *113* (7), 5110-5148.
19. Habib, F.; Murugesu, M., Lessons learned from dinuclear lanthanide nano-magnets. *Chem. Soc. Rev.* **2013**, *42* (8), 3278-3288.
20. Zheng, X.-Y.; Xie, J.; Kong, X.-J.; Long, L.-S.; Zheng, L.-S., Recent advances in the assembly of high-nuclearity lanthanide clusters. *Coord. Chem. Rev.* **2019**, *378*, 222-236.
21. Zheng, X.-Y.; Kong, X.-J.; Zheng, Z.; Long, L.-S.; Zheng, L.-S., High-Nuclearity Lanthanide-Containing Clusters as Potential Molecular Magnetic Coolers. *Acc. Chem. Res.* **2018**, *51* (2), 517-525.
22. Day, B. M.; Guo, F.-S.; Layfield, R. A., Cyclopentadienyl Ligands in Lanthanide Single-Molecule Magnets: One Ring To Rule Them All? *Acc. Chem. Res.* **2018**, *51* (8), 1880-1889.
23. Poli, R., Monocyclopentadienyl Halide Complexes of the d-and f-Block Elements. *Chem. Rev.* **1991**, *91* (4), 509-551.

24. Ishikawa, N.; Sugita, M.; Ishikawa, T.; Koshihara, S.-Y.; Kaizu, Y., Lanthanide double-decker complexes functioning as magnets at the single-molecular level. *J. Am. Chem. Soc.* **2003**, *125* (29), 8694-8695.
25. Ding, Y.-S.; Chilton, N. F.; Winpenny, R. E. P.; Zheng, Y.-Z., On Approaching the Limit of Molecular Magnetic Anisotropy: A Near-Perfect Pentagonal Bipyramidal Dysprosium(III) Single-Molecule Magnet. *Angew. Chem. Int. Ed.* **2016**, *55* (52), 16071-16074.
26. Wu, J.; Demeshko, S.; Dechert, S.; Meyer, F., Hexanuclear [Cp*Dy]6 single-molecule magnet. *Chem. Commun.* **2020**, *56* (27), 3887-3890.
27. Evans, P.; Reta, D.; Goodwin, C. A. P.; Ortu, F.; Chilton, N. F.; Mills, D. P., A double-dysprosocenium single-molecule magnet bound together with neutral ligands. *Chem. Commun.* **2020**, *56* (27), 5677-5680.
28. Guo, F.-S.; Day, B. M.; Chen, Y.-C.; Tong, M.-L.; Mansikkamäki, A.; Layfield, R. A., Magnetic hysteresis up to 80 kelvin in a dysprosium metallocene single-molecule magnet. *Science* **2018**, *362* (6421), 1400.
29. Rinehart, J. D.; Long, J. R., Exploiting single-ion anisotropy in the design of f-element single-molecule magnets. *Chem. Sci.* **2011**, *2* (11), 2078-2085.
30. Collins, R.; Heras Ojea, M. a. J.; Mansikkamäki, A.; Tang, J.; Layfield, R. A., Carbonyl Back-Bonding Influencing the Rate of Quantum Tunnelling in a Dysprosium Metallocene Single-Molecule Magnet. *Inorg. Chem.* **2020**, *59* (27), 642-647.
31. Demir, S.; Boshart, M. D.; Corbey, J. F.; Woen, D. H.; Gonzalez, M. I.; Ziller, J. W.; Meihaus, K. R.; Long, J. R.; Evans, W. J., Slow magnetic relaxation in a dysprosium ammonia metallocene complex. *Inorg. Chem.* **2017**, *56* (24), 15049-15056.
32. Pugh, T.; Chilton, N. F.; Layfield, R. A., A Low-Symmetry Dysprosium Metallocene Single-Molecule Magnet with a High Anisotropy Barrier. *Angew. Chem. Int. Ed.* **2016**, *55* (37), 11082-11085.
33. Demir, S.; Zadrozny, J. M.; Long, J. R., Large Spin-Relaxation Barriers for the Low-Symmetry Organolanthanide Complexes [Cp*2Ln(BPh4)](Cp* = pentamethylcyclopentadienyl; Ln= Tb, Dy). *Chem. Eur. J.* **2014**, *20* (31), 9524-9529.
34. Münzfeld, L.; Schoo, C.; Bestgen, S.; Moreno-Pineda, E.; Köppe, R.; Ruben, M.; Roesky, P. W., Synthesis, structures and magnetic properties of [(η9-C9H9)Ln(η8-C8H8)] super sandwich complexes. *Nat. Commun.* **2019**, *10* (1), 3135.
35. Buschmann, D. A.; Dietrich, H. M.; Schneider, D.; Birkelbach, V. M.; Stuhl, C.; Törnroos, K. W.; Maichle-Mössmer, C.; Anwander, R., Nanoscale Organolanthanum Clusters: Nuclearity-Directing Role of Cyclopentadienyl and Halogenido Ligands. *Chem. Eur. J.* **2020**, *26* (47), 10834-10840.
36. Buschmann, D. A.; Schneider, D.; Maichle-Mössmer, C.; Anwander, R., Half-Sandwich Complexes [Cp′4Ln4I8]4 (Ln=Ce, Pr):Emergence of Donor-Free Organolanthanide Nanowheels. *Eur. J. Inorg. Chem.* **2022**, *2022* (1), e202100862.
37. Arndt, S.; Okuda, J., Mono (cyclopentadienyl) complexes of the rare-earth metals. *Chem. Rev.* **2002**, *102* (6), 1953-1976.
38. Shannon, R. D., Revised effective ionic radii and systematic studies of interatomic distances in halides and chalcogenides. *Acta Crystallogr. Sect. A* **1976**, *32* (5), 751-767.
39. Müller, U., Anorganische Strukturchemie. Vieweg + Teubner: Wiesbaden, **2008**; *Vol. 6*.
40. Tupper, K. A.; Tilley, T. D., Synthesis and characterization of scandium complexes with reduced ligands: Crystal structures of Cp∗ScI2, [Cp∗ScI(bpy)]2, and [Cp∗ScCl(bpy)]2. *J. Organomet. Chem.* **2005**, *690* (7), 1689-1698.
41. Evans, W. J.; Champagne, T. M.; Davis, B. L.; Allen, N. T.; Nyce, G. W.; Johnston, M. A.; Lin, Y.-C.; Khvostov, A.; Ziller, J. W., Structural studies of mono(pentamethylcyclopentadienyl) lanthanide complexes. *J. Coord. Chem.* **2006**, *59* (10), 1069-1087.
42. Burin, M. E.; Smirnova, M. V.; Fukin, G. K.; Baranov, E. V.; Bochkarev, M. N., Neodymium (ii) and Dysprosium (ii) Iodides in the Reactions with Metallocenes of d-Transition Metals. *Eur. J. Inorg. Chem.* **2006**, *2006* (2), 351-356.
43. Bienfait, A. M.; Wolf, B. M.; Törnroos, K. W.; Anwander, R., Donor-Solvent-Dependent Cluster Formation of (C5Me5)SmI2(THF) x-Type Half-Sandwich Complexes. *Organometallics* **2016**, *35* (21), 3743-3750.
44. Evans, W. J.; Champagne, T. M.; Giarikos, D. G.; Ziller, J. W., Lanthanide Metallocene Reactivity with Dialkyl Aluminum Chlorides: Modeling Reactions Used to Generate Isoprene Polymerization Catalysts. *Organometallics* **2005**, *24* (4), 570-579.
45. Watson, P. L.; Tulip, T. H.; Williams, I., Defluorination of perfluoroolefins by divalent lanthanoid reagents: activating carbon-fluorine bonds. *Organometallics* **1990**, *9* (7), 1999-2009.
46. Shannon, R., Revised effective ionic radii and systematic studies of interatomic distances in halides and chalcogenides. *Acta Crystallorg. Sect. A* **1976**, *32* (5), 751-767.
47. Rufanov, K. A.; Pruß, N. K.; Sundermeyer, J., Simple entry into N-tert-butyl-iminophosphonamide rare-earth metal alkyl and chlorido complexes. *Dalton Trans.* **2016**, *45* (4), 1525-1538.
48. Wang, C.; Xiang, L.; Leng, X.; Chen, Y., Synthesis and Structure of Silicon-Bridged Boratabenzene Fluorenyl Rare-Earth Metal Complexes. *Organometallics* **2016**, *35* (11), 1995-2002.
49. Corbey, J. F.; Woen, D. H.; Palumbo, C. T.; Fieser, M. E.; Ziller, J. W.; Furche, F.; Evans, W. J., Ligand Effects in the Synthesis of Ln2+ Complexes by Reduction of Tris(cyclopentadienyl) Precursors Including C–H Bond Activation of an Indenyl Anion. *Organometallics* **2015**, *34* (15), 3909-3921.
50. Werner, D.; Deacon, G. B.; Junk, P. C.; Anwander, R., Cerium (III/IV) formamidinate chemistry, and a stable cerium(IV) diolate. *Chem. Eur. J.* **2014**, *20* (15), 4426-4438.
51. Li, D.; Li, S.; Cui, D.; Zhang, X., β-Diketiminato Rare-Earth Metal Complexes. Structures, Catalysis, and Active Species for Highly cis-1,4-Selective Polymerization of Isoprene. *Organometallics* **2010**, *29* (9), 2186-2193.

52. Evans, W. J.; Walensky, J. R.; Champagne, T. M.; Ziller, J. W.; DiPasquale, A. G.; Rheingold, A. L., Displacement, reduction, and ligand redistribution reactivity of the cationic mono-C5Me5 Ln2+ complexes (C5Me5)Ln(BPh4) (Ln=Sm, Yb). *J. Organomet. Chem.* **2009**, *694* (7), 1238-1243.
53. Kretschmer, W. P.; Teuben, J. H.; Troyanov, S. I., Novel, Highly Symmetrical Halogen-Centered Polynuclear Lanthanide Complexes: [Cp6Yb6Cl13]$^-$ and [Cp12Sm12Cl24]. *Angew. Chem. Int. Ed.* **1998**, *37* (1-2), 88-90.
54. Deacon, G. B.; Fallon, G. D.; Forsyth, C. M.; Harris, S. C.; Junk, P. C.; Skelton, B. W.; White, A. H., Manipulation of reaction pathways in redox transmetallation–ligand exchange syntheses of lanthanoid(ii)/(iii) aryloxide complexes. *Dalton Trans.* **2006** (6), 802-812.
55. Dietrich, H. M.; Törnroos, K. W.; Anwander, R., "Ionic Carbenes": Synthesis, Structural Characterization, and Reactivity of Rare-Earth Metal Methylidene Complexes. *J. Am. Chem. Soc.* **2006**, *128* (29), 9298-9299.
56. Birkelbach, V. M.; Kracht, F.; Dietrich, H. M.; Stuhl, C.; Maichle-Mössmer, C.; Anwander, R., A Rare-Earth-Metal Ensemble of the Tebbe Reagent: Scope of Coligands and Carbonyl Olefination. *Organometallics* **2020**, *39* (19), 3490-3504.
57. Diether, D.; Tyulyunov, K.; Maichle-Mössmer, C. c.; Anwander, R., Fluorenyl Half-Sandwich Bis (tetramethylaluminate) Complexes of the Rare-Earth Metals: Synthesis, Structure, and Isoprene Polymerization. *Organometallics* **2017**, *36* (23), 4649-4659.
58. Jende, L. N.; Hollfelder, C. O.; Maichle-Mössmer, C.; Anwander, R., Rare-earth-metal allyl complexes supported by the [2-(N,N-dimethylamino)ethyl] tetramethylcyclopentadienyl ligand: structural characterization, reactivity, and isoprene polymerization. *Organometallics* **2015**, *34* (1), 32-41.
59. Barnea, E.; Averbuj, C.; Kapon, M.; Botoshansky, M.; Eisen, M. S., Synthesis and Crystal Structure of New Early-Lanthanide Organometallic Clusters. *Eur. J. Inorg. Chem.* **2007**, *2007* (28), 4535-4540.
60. Bonnet, F.; Visseaux, M.; Barbier-Baudry, D.; Hafid, A.; Vigier, E.; Kubicki, M. M., Organometallic early lanthanide clusters: Syntheses and X-ray structures of new monocyclopentadienyl complexes. *Inorg. Chem.* **2004**, *43* (12), 3682-3690.
61. Sieler, J.; Simon, A.; Peters, K.; Taube, R.; Geitner, M., Komplexkatalyse: XXXI. Kristallstruktur des hexameren Mono-2,4-dimethyl-pentadienyldichloro-neodymium(III)·0.33 Tetrahydrofuran. [Nd6(2,4-C7H11)6Cl12(THF)2] eines Präkatalysators für die 1,4-cis-Polymerisation des Butadiens. *J. Organomet. Chem.* **1989**, *362* (3), 297-303.
62. Fridrichová, A.; Varga, V.; Pinkas, J.; Lamač, M.; Růžička, A.; Horáček, M., Yttrocene Chloride and Methyl Complexes with Variously Substituted Cyclopentadienyl Ligands: Synthesis, Characterization, and Reactivity toward Ethylene. *Eur. J. Inorg. Chem.* **2016**, *2016* (23), 3713-3721.
63. Goodwin, C. A. P.; Ortu, F.; Reta, D.; Chilton, N. F.; Mills, D. P., Molecular magnetic hysteresis at 60 kelvin in dysprosocenium. *Nature* **2017**, *548* (7668), 439-442.
64. Guo, F.-S.; Day, B. M.; Chen, Y.-C.; Tong, M.-L.; Mansikkamäki, A.; Layfield, R. A., A Dysprosium Metallocene Single-Molecule Magnet Functioning at the Axial Limit. *Angew. Chem. Int. Ed.* **2017**, *56* (38), 11445-11449.
65. McClain, K. R.; Gould, C. A.; Chakarawet, K.; Teat, S. J.; Groshens, T. J.; Long, J. R.; Harvey, B. G., High-temperature magnetic blocking and magneto-structural correlations in a series of dysprosium (III) metallocenium single-molecule magnets. *Chem. Sci.* **2018**, *9* (45), 8492-8503.
66. Gatteschi, D., Anisotropic dysprosium. *Nature Chemistry* **2011**, *3* (10), 830-830.
67. Sulway, S. A.; Layfield, R. A.; Tuna, F.; Wernsdorfer, W.; Winpenny, R. E. P., Single-molecule magnetism in cyclopentadienyl-dysprosium chlorides. *Chem. Commun.* **2012**, *48* (10), 1508-1510.
68. Meng, Y.-S.; Zhang, Y.-Q.; Wang, Z.-M.; Wang, B.-W.; Gao, S., Weak Ligand-Field Effect from Ancillary Ligands on Enhancing Single-Ion Magnet Performance. *Chem. Eur. J.* **2016**, *22* (36), 12724-12731.
69. Gould, C. A.; McClain, K. R.; Yu, J. M.; Groshens, T. J.; Furche, F.; Harvey, B. G.; Long, J. R., Synthesis and Magnetism of Neutral, Linear Metallocene Complexes of Terbium(II) and Dysprosium(II). *J. Am. Chem. Soc.* **2019**, *141* (33), 12967-12973.
70. Wu, J.; Demeshko, S.; Dechert, S.; Meyer, F., Hexanuclear [Cp* Dy] 6 single-molecule magnet. *Chem. Commun.* **2020**, *56* (27), 3887-3890.
71. Evans, W. J.; Anwander, R.; Ziller, J. W., Inclusion of Al2Me6 in the Crystalline Lattice of the Organometallic Complexes LnAl3Me12. *Organometallics* **1995**, *14* (3), 1107-1109.
72. Hollfelder, C.; Jende, L.; Diether, D.; Zelger, T.; Stauder, R.; Maichle-Mössmer, C.; Anwander, R., 1, 3-Diene Polymerization Mediated by Homoleptic Tetramethylaluminates of the Rare-Earth Metals. *Catalysts* **2018**, *8* (2), 61.
73. König, S. N.; Chilton, N. F.; Maichle-Mössmer, C.; Pineda, E. M.; Pugh, T.; Anwander, R.; Layfield, R. A., Fast magnetic relaxation in an octahedral dysprosium tetramethyl-aluminate complex. *Dalton Trans.* **2014**, *43* (8), 3035-3038.
74. Nieland, A.; Mix, A.; Neumann, B.; Stammler, H.-G.; Mitzel, N. W., Lanthanoid Tetramethylaluminates and Their Paramagnetic NMR Parameters. *Eur. J. Inorg. Chem.* **2014**, *2014* (1), 51-57.
75. Dietrich, H. M.; Törnroos, K. W.; Herdtweck, E.; Anwander, R., Tetramethylaluminate and Tetramethylgallate Coordination in Rare-Earth Metal Half-Sandwich and Metallocene Complexes. *Organometallics* **2009**, *28* (23), 6739-6749.

Supporting Information

Half-Sandwich Rare-Earth-Metal Clusters – Synthesis, Characterization, and Magnetic Properties

Dennis A. Buschmann, James Durrant, Cäcilia Maichle-Mössmer, Richard A. Layfield,* and Reiner Anwander*

Table of Contents

NMR Spectra

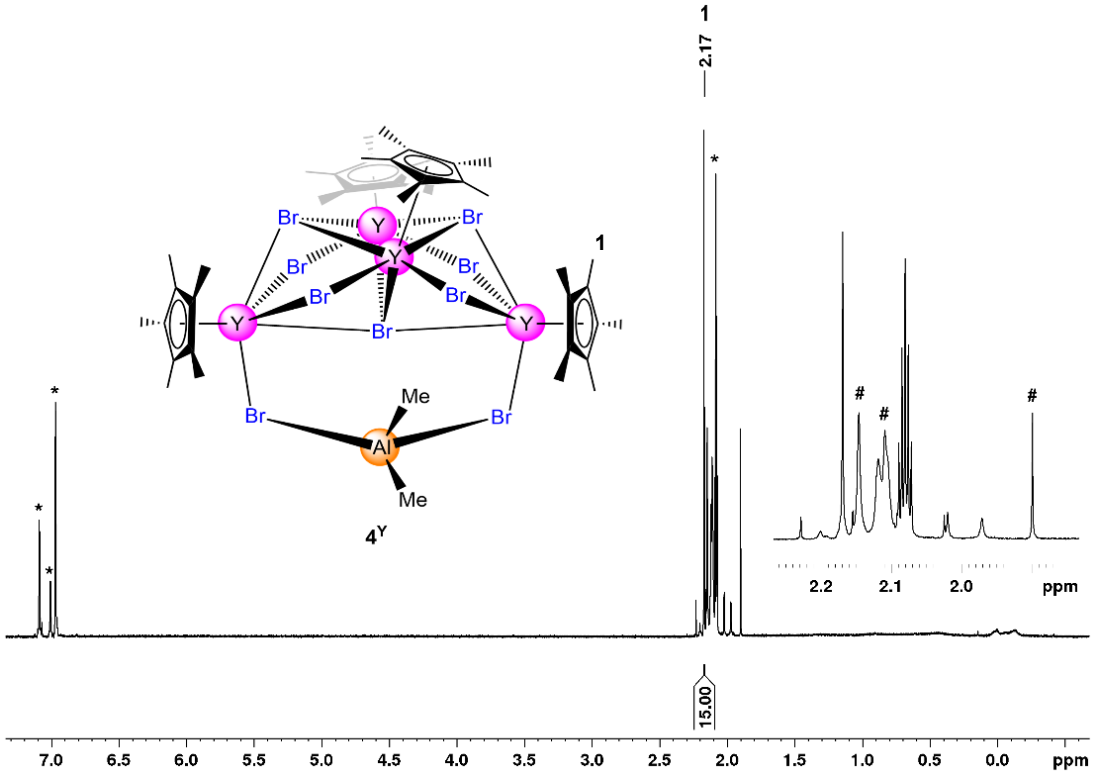

Figure S1. ^{1}H NMR spectrum (400 MHz) of [Cp*$_4$Y$_4$Br$_7$(Br$_2$AlMe$_2$)] (**4^{Y}**) in [D$_8$]toluene at 26 °C (Solvent residual signals: *, solution species: #).

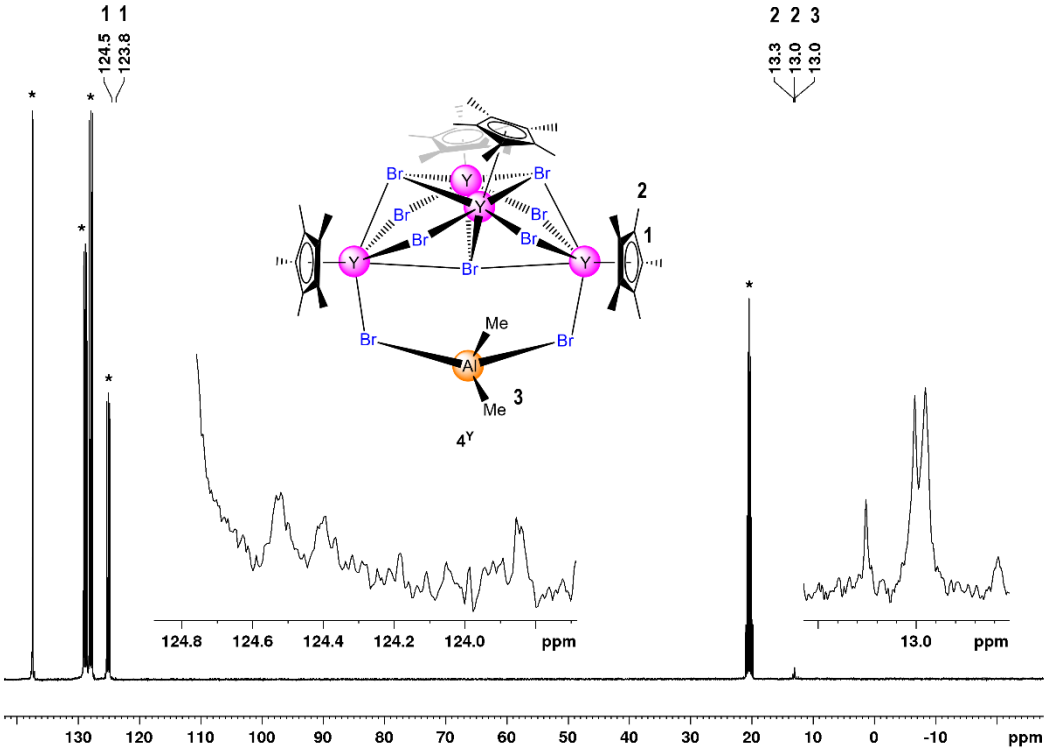

Figure S2. ^{13}C{^{1}H} NMR spectrum (101 MHz) of [Cp*$_4$Y$_4$Br$_7$(Br$_2$AlMe$_2$)] (**4^{Y}**) in [D$_8$]toluene at 26 °C (Solvent residual signals: *).

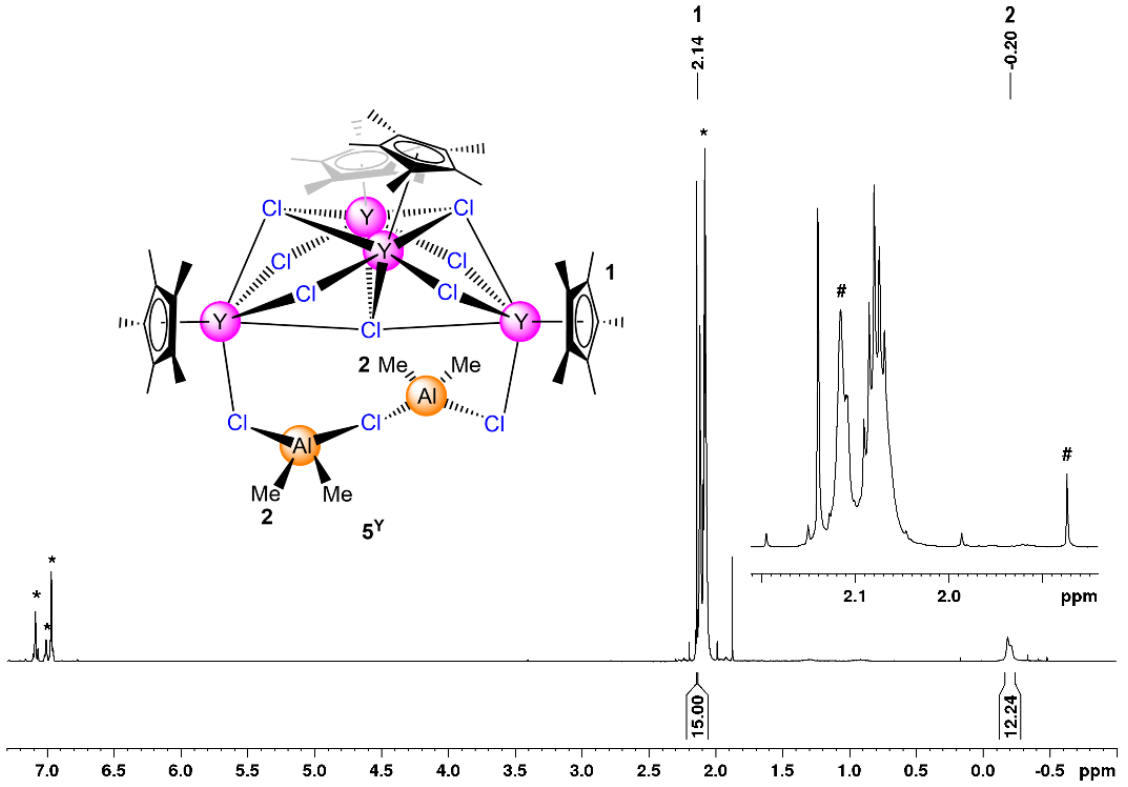

Figure S3. ^{1}H NMR spectrum (400 MHz) of [Cp*$_4$Y$_4$Cl$_7$(Cl$_3${AlMe$_2$}$_2$)] (**5^{Y}**) in [D$_8$]toluene at 26 °C (Solvent residual signals: *, solution species: #).

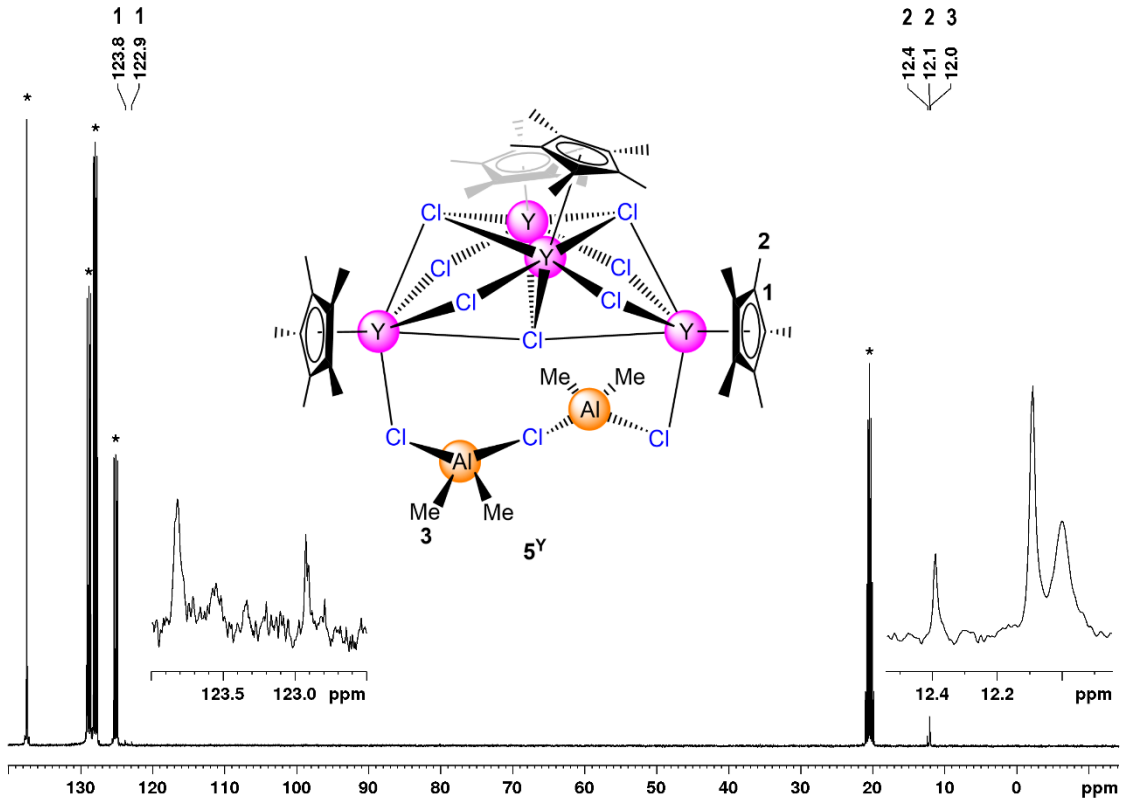

Figure S4. ^{13}C{^{1}H} NMR spectrum (101 MHz) of [Cp*$_4$Y$_4$Cl$_7$(Cl$_3${AlMe$_2$}$_2$)] (**5^{Y}**) in [D$_8$]toluene at 26 °C (Solvent residual signals: *).

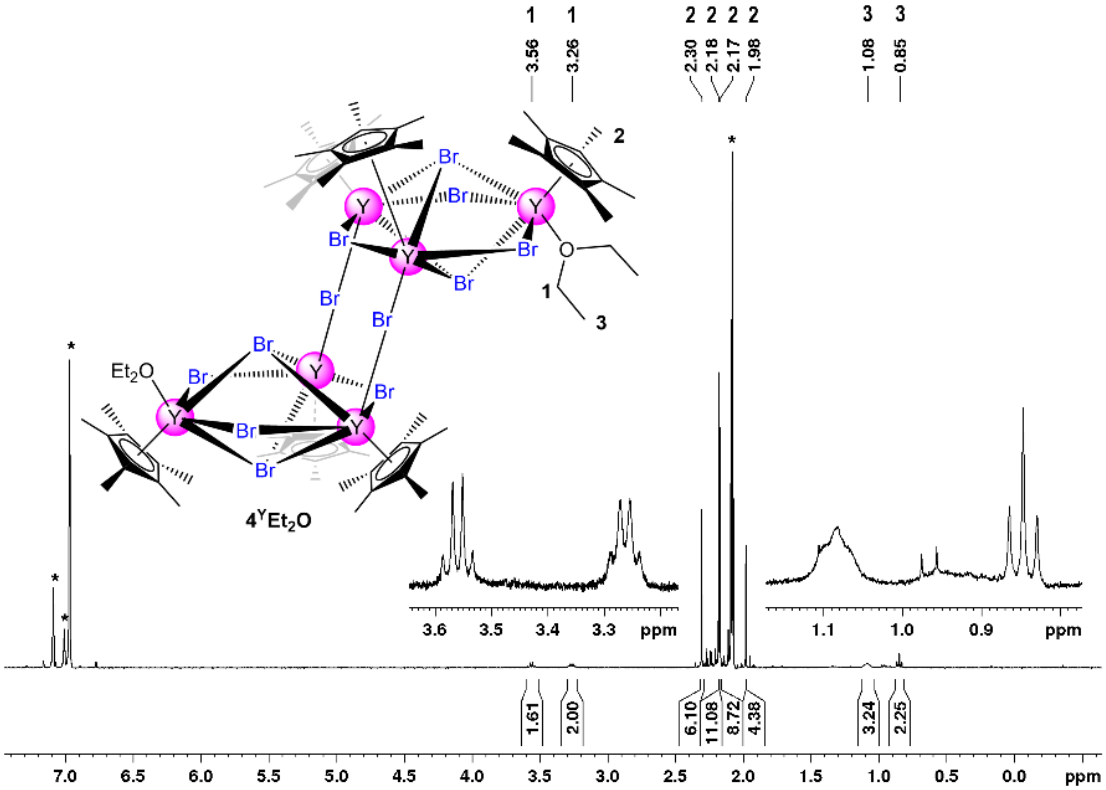

Figure S5. ^{1}H NMR spectrum (400 MHz) of [(μ_2-Br)Cp*$_3$Y$_3$Br$_5$(Et$_2$O)]$_2$ (**4^{Y}Et$_2$O**) in [D$_8$]toluene at 26 °C (Solvent residual signals:*).

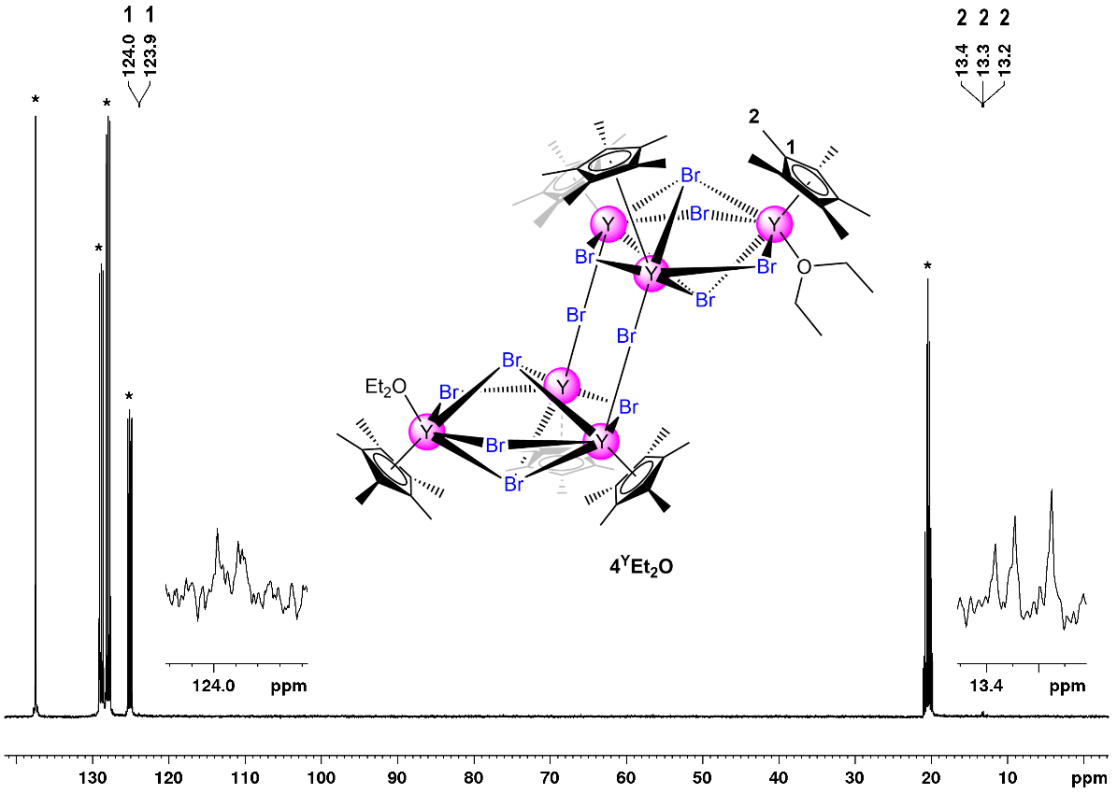

Figure S6. ^{13}C{^{1}H} NMR spectrum (101 MHz) of [(μ_2-Br)Cp*$_3$Y$_3$Br$_5$(Et$_2$O)]$_2$ (**4^{Y}Et$_2$O**) in [D$_8$]toluene at 26 °C (Solvent residual signals:*).

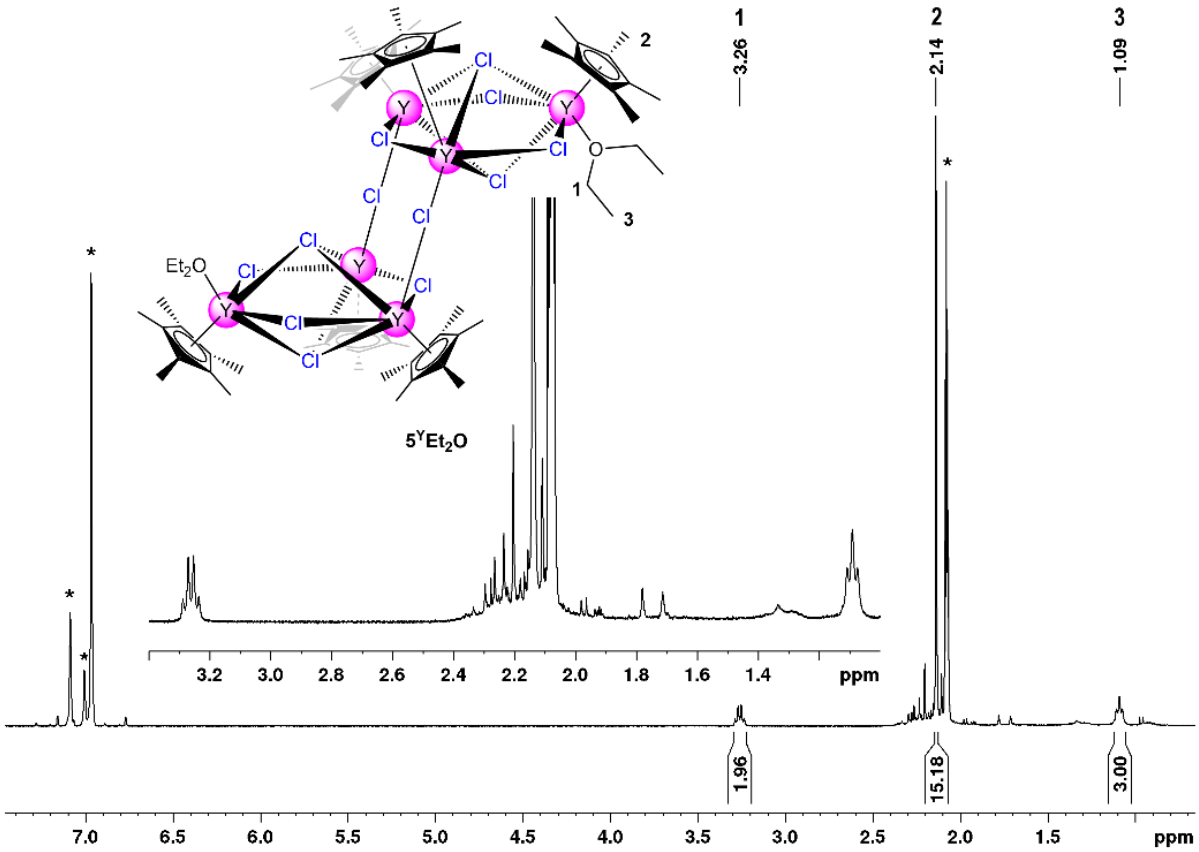

Figure S7. ^{1}H NMR spectrum (400 MHz) of $[(\mu_2\text{-Cl})Cp^*_3Y_3Cl_5(Et_2O)]_2$ (**$5^{Y}Et_2O$**) in $[D_8]$toluene at 26 °C (Solvent residual signals: *).

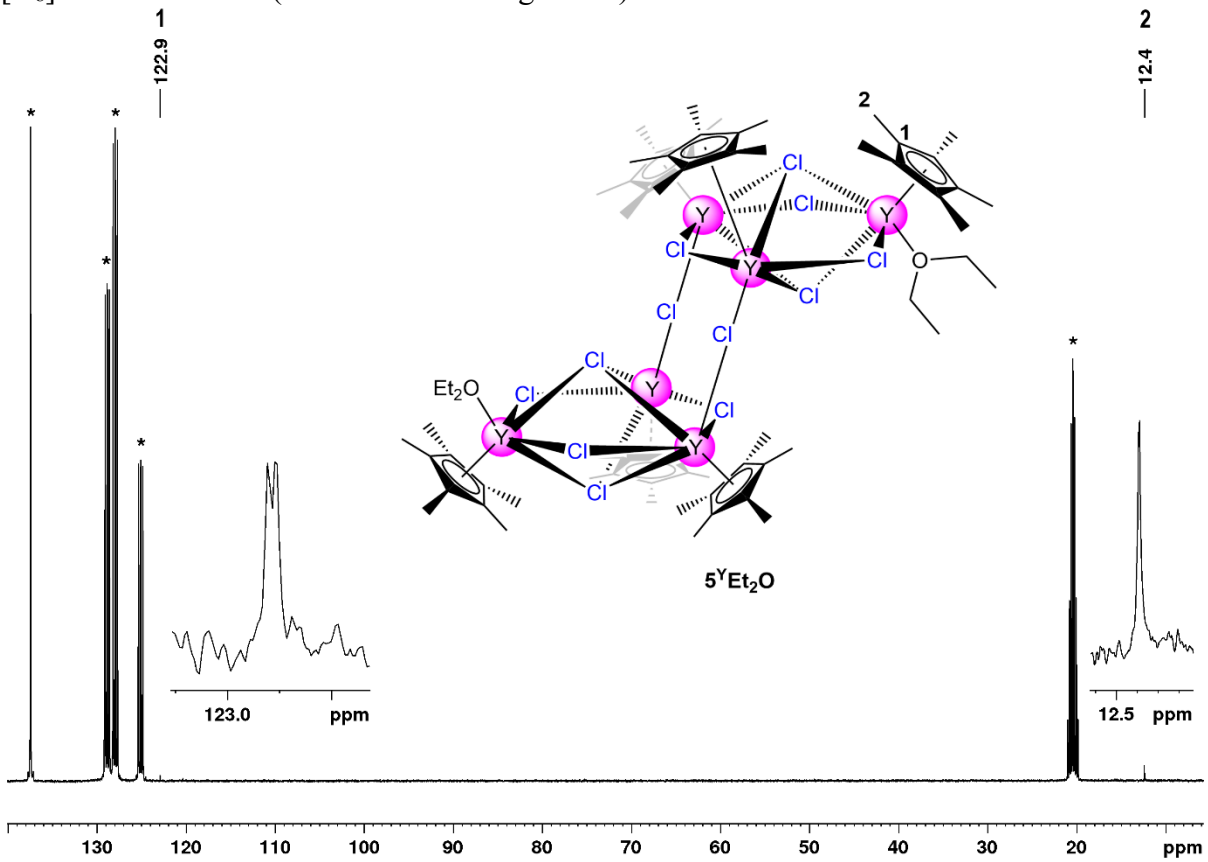

Figure S8. $^{13}C\{^{1}H\}$ NMR spectrum (101 MHz) of $[(\mu_2\text{-Cl})Cp^*_3Y_3Cl_5(Et_2O)]_2$ (**$5^{Y}Et_2O$**) in $[D_8]$toluene at 26 °C (Solvent residual signals: *).

X-ray Crystallography

X-Ray Crystallography and Crystal Structure Determinations. Crystals of **1** and **4^{Dy}THF** were grown by standard techniques using saturated solutions of toluene or toluene/THF, respectively. Crystals of **2^{Y}**, **2^{Tb}**, **2^{Dy}**, **2^{Ho}**, **2Er**, **3**, **4^{Y}**, **4^{Y}Et$_2$O**, **4^{Gd}**, **4^{Tb}**, **4^{Dy}**, **4^{Dy}Et$_2$O**, **5^{Y}**, **5^{Y}Et$_2$O**, **5^{Gd}**, **6^{Tb}**, **6^{Dy}**, **6^{Dy}Et$_2$O**, **7Er**, **8** and **9** were grown from diluted solutions of [D$_6$]benzene or toluene. Suitable crystals for X-ray structure analyses were selected in a glovebox and coated with Parabar 10312 (previously known as Paratone N, Hampton Research) and fixed on a nylon/loop. X-ray data for compounds **1**, **2^{Y}**, **2^{Tb}**, **2^{Dy}**, **2^{Ho}**, **2Er**, **3**, **4^{Y}**, **4^{Y}Et$_2$O**, **4^{Gd}**, **4^{Tb}**, **4^{Dy}**, **4^{Dy}Et$_2$O**, **4^{Dy}THF**, **5^{Y}**, **5^{Y}Et$_2$O**, **5^{Gd}**, **6^{Tb}**, **6^{Dy}**, **6^{Dy}Et$_2$O**, **7Er**, **8** and **9** were collected on a Bruker APEX III DUO instrument equipped with an IμS microfocus sealed tube and QUAZAR optics for MoK$_\alpha$ (λ = 0.71073 Å) radiation. The data collection strategy was determined using COSMO[1] employing ω-scans. Raw data were processed using APEX[2] and SAINT[3], corrections for absorption effects were applied using SADABS[4]. The structures were solved by direct methods and refined against all data by full-matrix least-squares methods of F^2 using SHELXTL[5] and SHELXLE[6]. All graphics were produced employing CSD Mercury 4.1.0[7]. Further details regarding the refinement and crystallographic data are listed in Table S1 and in the CIF files. CCDC depositions Nr contain all the supplementary crystallographic data for this paper. These data can be obtained free of charge from The Cambridge Crystallographic Data Centre via www.ccdc.cam.ac.uk/data_request/cif.

Table S1. Crystallographic data for compounds **1**, $\mathbf{2^{Y}}$, and $\mathbf{2^{Tb}}$.

	1	$\mathbf{2^{Y}}$	$\mathbf{2^{Tb}}$
CCDC	Nr	Nr	Nr
formula	$C_{18}H_{39}Al_2Er$	$C_{40}H_{60}Y_4I_8$	$C_{40}H_{60}Tb_4I_8$
M_r [g/mol]	476.73	1911.78	2191.86
color/shape	pink/block	colorless/block	colorless/block
crystal dimensions [mm]	0.397 x 0.366 x 0.262	0.302 x 0.292 x 0.281	0.309 x 0.230 x 0.152
crystal system	orthorhombic	monoclinic	monoclinic
space group	*Pbca*	$P2_1/n$	$P2_1/n$
a [Å]	17.0944(7)	16.540(3)	16.521(4)
b [Å]	14.2733(6)	21.893(5)	21.956(6)
c [Å]	17.9200(8)	16.708(3)	16.765(5)
α [°]	90	90	90
β [°]	90	118.033(3)	117.947(6)
γ [°]	90	90	90
V [Å^3]	4372.4(3)	5340.6(19)	5372(2)
Z	8	4	4
T [K]	100(2)	100(2)	100(2)
λ [Å]	0.71073	0.71073	0.71073
ρ_{calcd} [g/cm^3]	1.448	2.378	2.710
μ [mm $^{-1}$]	3.914	8.953	9.825
F (000)	1928	3520	3936
θ range [°]	2.179 – 30.548	1.705 – 28.282	1.675 – 33.182
unique reflections	6693	13235	20517
observed reflections (I > 2σ)	76931	138450	189438
R1/*w*R2 (I > 2σ)	0.0154/0.0366	0.0257/0.0597	0.0269/0.0619
R1/*w*R2 (all data)	0.0165/0.0371	0.0309/0.0622	0.0321/0.0652
GOF	1.075	1.168	1.110

Table S1 (continued). Crystallographic data for compounds $\mathbf{2^{Dy}}$, $\mathbf{2^{Ho}}$, and $\mathbf{2^{Er}}$.

	$\mathbf{2^{Dy}}$	$\mathbf{2^{Ho}}$	$\mathbf{2^{Er}}$
CCDC	Nr	Nr	Nr
formula	$C_{40}H_{60}Dy_4I_8$	$C_{40}H_{60}Ho_4I_8$	$C_{40}H_{60}Er_4I_8$
M_r [g/mol]	2206.16	2215.88	2225.19
color/shape	yellow/column	orange/plate	pink/plate
crystal dimensions [mm]	0.313 x 0.141 x 0.092	0.186 x 0.166 x 108	0.170 x 0.148 x 0.099
crystal system	monoclinic	monoclinic	monoclinic
space group	$P2_1/n$	$P2_1/n$	$P2_1/n$
a [Å]	16.5329(2)	16.538(2)	16.558(5)
b [Å]	21.878(2)	21.878(3)	21.858(7)
c [Å]	16.7304(2)	16.697(2)	16.694(5)
α [°]	90	90	90
β [°]	117.999(4)	118.004(5)	118.017(5)
γ [°]	90	90	90
V [Å^3]	5343.2(9)	5333.9(2)	5334(3)
Z	4	4	4
T [K]	100(2)	100(2)	100(2)
λ [Å]	0.71073	0.71073	0.71073
ρ_{calcd} [g/cm^3]	2.742	2.759	2.771
μ [mm $^{-1}$]	10.176	10.524	10.884
F (000)	3952	3968	3984
θ range [°]	1.677 – 28.282	1.430 – 29.575	2.320 – 36.373
unique reflections	13226	14950	25894
observed reflections (I > 2σ)	116437	181311	234839
R1/*w*R2 (I > 2σ)	0.0208/0.0459	0.0191/0.0420	0.0278/0.0633
R1/*w*R2 (all data)	0.0242/0.0482	0.0218/0.0433	0.0373/0.0685
GOF	1.084	1.097	1.043

Table S1 (continued). Crystallographic data for compounds **3**, $\mathbf{4^{Y}}$, and $\mathbf{4^{Tb}}$.

	$\mathbf{2^{Y/Dy}}$	**3**	$\mathbf{4^{Y}}$
CCDC	Nr	Nr	Nr
formula	$C_{40}H_{60}Y_{3.52}Dy_{0.48}I_8$	$C_{116}H_{176}Al_2Gd_8I_{14}$	$C_{52.5}H_{78}AlY_4Br_9$
M_r [g/mol]	1947.22	4659.31	1810.94
color/shape	yellow/needle	colorless/needle	colorless/cube
crystal dimensions [mm]	0.176 x 0.082 x 0.061	0.126 x 0.096 x 0.070	0.138 x 0.138 x 0.134
crystal system	monoclinic	monoclinic	triclinic
space group	$P2_1/n$	$C2/c$	$P\bar{1}$
a [Å]	16.5415(2)	40.547(4)	12.5041(2)
b [Å]	21.901(2)	11.5341(2)	14.359(2)
c [Å]	16.7179(2)	30.103(3)	17.885(3)
α [°]	90	90	98.302(4)
β [°]	118.0450(1)	99.457(2)	93.459(4)
γ [°]	90	90	99.096(4)
V [Å^3]	5345.3(9)	13887(2)	3126.2(8)
Z	4	4	2
T [K]	100(2)	100(2)	100(2)
λ [Å]	0.71073	0.71073	0.71073
ρ_{calcd} [g/cm^3]	2.420	2.228	1.924
μ [mm $^{-1}$]	9.093	6.928	9.474
F (000)	3572	8608	1754
θ range [°]	2.316 – 30.525	2.037 – 30.560	1.710 – 28.484
unique reflections	16326	21288	15615
observed reflections (I > 2σ)	122636	157602	80097
R1/*w*R2 (I > 2σ)	0.0260/0.0569	0.0232/0.0526	0.0612/0.1437
R1/*w*R2 (all data)	0.0392/0.0618	0.0282/0.0550	0.0857/0.1554
GOF	1.022	1.055	1.033

Table S1 (continued). Crystallographic data for compounds $\mathbf{4}^{Tb}$, $\mathbf{4}^{Dy}$, and $\mathbf{5}^{Y}$.

	$\mathbf{4}^{Gd}$	$\mathbf{4}^{Tb}$	$\mathbf{4}^{Dy}$
CCDC	Nr	Nr	Nr
formula	$C_{52.5}H_{78}AlGd_4Br_9$	$C_{52.5}H_{78}AlTb_4Br_9$	$C_{51}H_{66}D_9AlDy_4Br_9$
M_r [g/mol]	2084.31	2090.99	2093.33
color/shape	colorless/needle	colorless/needle	yellow/plate
crystal dimensions [mm]	0.122 x 0.085 x 0.051	0.119 x 0.080 x 0.042	0.134 x 0.111 x 0.039
crystal system	triclinic	triclinic	triclinic
space group	$P\bar{1}$	$P\bar{1}$	$P\bar{1}$
a [Å]	12.5625(2)	12.5308(2)	12.590(9)
b [Å]	14.4228(2)	14.417(2)	14.405(1)
c [Å]	16.694(5)	17.830(3)	17.369(2)
α [°]	98.088(3)	98.176(3)	97.804(1)
β [°]	93.438(3)	93.535(3)	92.32(2)
γ [°]	98.756(3)	99.106(3)	99.052(1)
V [Å^3]	3133.6(7)	3136.6(8)	3076(4)
Z	2	2	2
T [K]	100(2)	100(2)	100(2)
λ [Å]	0.71073	0.71073	0.71073
ρ_{calcd} [g/cm^3]	2.209	2.214	2.260
μ [mm $^{-1}$]	9.962	10.233	10.694
F (000)	1954	1962	1946
θ range [°]	1.164 – 26.480	1.158 – 28.550	2.085 – 28.427
unique reflections	12906	15777	15275
observed reflections (I > 2σ)	65097	123126	129412
R1/*w*R2 (I > 2σ)	0.0458/0.1020	0.0337/0.0759	0.0382/0.0752
R1/*w*R2 (all data)	0.0750/0.1166	0.0502/0.0838	0.0640/0.0847
GOF	1.026	1.032	1.093

Table S1 (continued). Crystallographic data for compounds $\mathbf{5}^{Gd}$, $\mathbf{6}^{Tb}$, and $\mathbf{6}^{Dy}$.

	$\mathbf{5}^{Y}$	$\mathbf{5}^{Gd}$	$\mathbf{6}^{Tb}$
CCDC	Nr	Nr	Nr
formula	$C_{58}H_{88}Al_2Y_4Cl_{10}$	$C_{58}H_{88}Al_2Gd_4Cl_{10}$	$C_{49}H_{74}AlTb_4Cl_9$
M_r [g/mol]	1549.43	1822.74	1644.86
color/shape	colorless/block	colorless/block	colorless/column
crystal dimensions [mm]	0.165 x 0.159 x 0.149	0.521 x 0.382 x 0.295	0.338 x 0.172 x 0.098
crystal system	monoclinic	monoclinic	triclinic
space group	*C*2/*c*	*C*2/*c*	$P\bar{1}$
a [Å]	17.295(3)	17.3782(1)	12.434(4)
b [Å]	17.104(3)	17.1784(1)	14.100(4)
c [Å]	23.023(4)	23.0945(2)	17.714(5)
α [°]	90	90	97.990(3)
β [°]	92.103(3)	91.848(2)	92.832(3)
γ [°]	90	90	98.280(3)
V [Å^3]	6806(2)	6890.8(7)	3035.7(2)
Z	4	4	2
T [K]	100(2)	100(2)	100(2)
λ [Å]	0.71073	0.71073	0.71073
ρ_{calcd} [g/cm^3]	1.512	1.757	1.779
μ [mm $^{-1}$]	3.829	4.247	5.043
F (000)	3152	3552	1588
θ range [°]	1.675 – 28.392	1.869 – 30.507	2.093 – 25.106
unique reflections	8535	10536	10778
observed reflections (I > 2σ)	66615	200522	78973
R1/*w*R2 (I > 2σ)	0.0335/0.0728	0.0243/0.0569	0.0633/0.1597
R1/*w*R2 (all data)	0.0490/0.0790	0.0248/0.0572	0.0768/0.1690
GOF	1.022	1.264	1.049

	6^{Dy}	**7Er**	**8**
CCDC	Nr	Nr	Nr
formula	$C_{51}H_{66}D_9AlDy_4Cl_9$	$C_{28}H_{54}Al_2Er_2Cl_2$	$C_{82}H_{126}Ho_6Br_{12}O_2$
M_r [g/mol]	1693.25	850.12	3092.32
color/shape	yellow/plate	pink/cube	pink/block
crystal dimensions [mm]	0.206 x 0.132 x 0.072	0.083 x 0.077 x 0.068	0.109 x 0.066 x 0.046
crystal system	triclinic	triclinic	triclinic
space group	$P\bar{1}$	$P\bar{1}$	$P\bar{1}$
a [Å]	12.3023(2)	8.6376(6)	13.4095(9)
b [Å]	14.0595(2)	10.2098(6)	13.9928(9)
c [Å]	17.4711(2)	10.2702(7)	14.8556(9)
α [°]	82.367(2)	69.5760(1)	112.001(2)
β [°]	89.617(2)	86.6190(1)	113.403(2)
γ [°]	84.362(2)	84.1170(1)	90.159(2)
V [Å^3]	2980.5(4)	844.04(1)	2333.9(3)
Z	2	1	1
T [K]	100(2)	100(2)	100(2)
λ [Å]	0.71073	0.71073	0.71073
ρ_{calcd} [g/cm^3]	1.887	1.672	2.200
μ [mm $^{-1}$]	5.406	5.162	10.201
F (000)	1622	418	1456
θ range [°]	1.755 – 28.282	2.137 – 28.377	1.595 – 26.475
unique reflections	14775	4228	9616
observed reflections (I > 2σ)	149864	34829	55568
R1/*w*R2 (I > 2σ)	0.0308/0.0700	0.0202/0.0429	0.0288/0.0626
R1/*w*R2 (all data)	0.0386/0.0762	0.0228/0.0443	0.0399/0.0673
GOF	1.136	1.075	1.043

	9	**$4^{Y}Et_2O$**	**$4^{Dy}Et_2O$**
CCDC	Nr	Nr	Nr
formula	$C_{50.5}H_{87.5}AlEr_4Br_{8.5}O_2$	$C_{82.33}H_{126.99}Y_6Br_{11.67}O_2$	$C_{82}H_{126}Dy_6Br_{12}O_2$
M_r [g/mol]	2101.95	2614.79	3077.74
color/shape	light pink/plate	colorless/block	yellow/needle
crystal dimensions [mm]	0.228 x 0.227 x 0.092	0.154 x 0.086 x 0.046	0.153 x 0.096 x 0.061
crystal system	triclinic	triclinic	triclinic
space group	$P\bar{1}$	$P\bar{1}$	$P\bar{1}$
a [Å]	12.4970(7)	13.3379(2)	13.408(2)
b [Å]	14.3576(9)	14.0656(2)	13.995(2)
c [Å]	20.4363(2)	14.9091(2)	14.897(2)
α [°]	85.451(2)	112.406(2)	112.078(3)
β [°]	73.2930(1)	113.053(2)	113.215(3)
γ [°]	65.5400(1)	90.162(2)	90.073(3)
V [$Å^3$]	3193.5(3)	2341.0(3)	2343.7(7)
Z	2	1	1
T [K]	100(2)	173(2)	100(2)
λ [Å]	0.71073	0.71073	0.71073
ρ_{calcd} [g/cm^3]	2.186	1.855	2.181
μ [mm^{-1}]	10.567	8.697	9.877
F (000)	1978	1279	1450
θ range [°]	1.560 – 30.521	1.592 – 26.422	1.595 – 26.432
unique reflections	19433	9616	9642
observed reflections (I > 2σ)	139007	49002	48896
R1/*w*R2 (I > 2σ)	0.0261/0.0570	0.0445/0.0948	0.0284/0.0608
R1/*w*R2 (all data)	0.0358/0.0616	0.0759/0.1071	0.0398/0.0654
GOF	1.028	1.020	1.027

	4^{Dy}THF	**$5^{Y}Et_2O$**	**$6^{Dy}Et_2O$**
CCDC	Nr	Nr	Nr
formula	$C_{26}H_{47}DyBr_2O_4$	$C_{82}H_{126}Y_6Cl_{12}O_2$	$C_{82}H_{126}Br_{12}Dy_6O_2$
M_r [g/mol]	745.95	2102.68	3077.74
color/shape	colorless/block	colorless/needle	colorless/prism
crystal dimensions [mm]	0.353 x 0.282 x 0.112	0.165 x 0.112 x 0.056	0.153 x 0.096 x 0.061
crystal system	monoclinic	triclinic	triclinic
space group	$P2_1/c$	$P\bar{1}$	$P\bar{1}$
a [Å]	12.3392(2)	13.1586(6)	13.408(2)
b [Å]	11.8911(2)	13.9660(7)	13.995(2)
c [Å]	20.227(2)	14.7092(7)	14.897(2)
α [°]	90	112.113(2)	112.078(3)
β [°]	104.169(3)	112.827(2)	113.215(3)
γ [°]	90	90.299(2)	90.073(3)
V [Å^3]	2877.6(6)	2271.68(2)	2343.7(7)
Z	4	1	1
T [K]	100(2)	100(2)	100(2)
λ [Å]	0.71073	0.71073	0.71073
ρ_{calcd} [g/cm^3]	1.722	1.537	2.181
μ [mm $^{-1}$]	5.402	4.183	9.877
F (000)	1484	1072	1450
θ range [°]	1.702 – 30.538	1.599 – 27.157	1.595 – 26.432
unique reflections	8778	10058	9642
observed reflections (I > 2σ)	132775	56613	48896
R1/*w*R2 (I > 2σ)	0.0247/0.0563	0.0354/0.0691	0.0284/0.0608
R1/*w*R2 (all data)	0.0362/0.0628	0.0547/0.0749	0.0398/0.0654
GOF	1.075	1.023	1.026

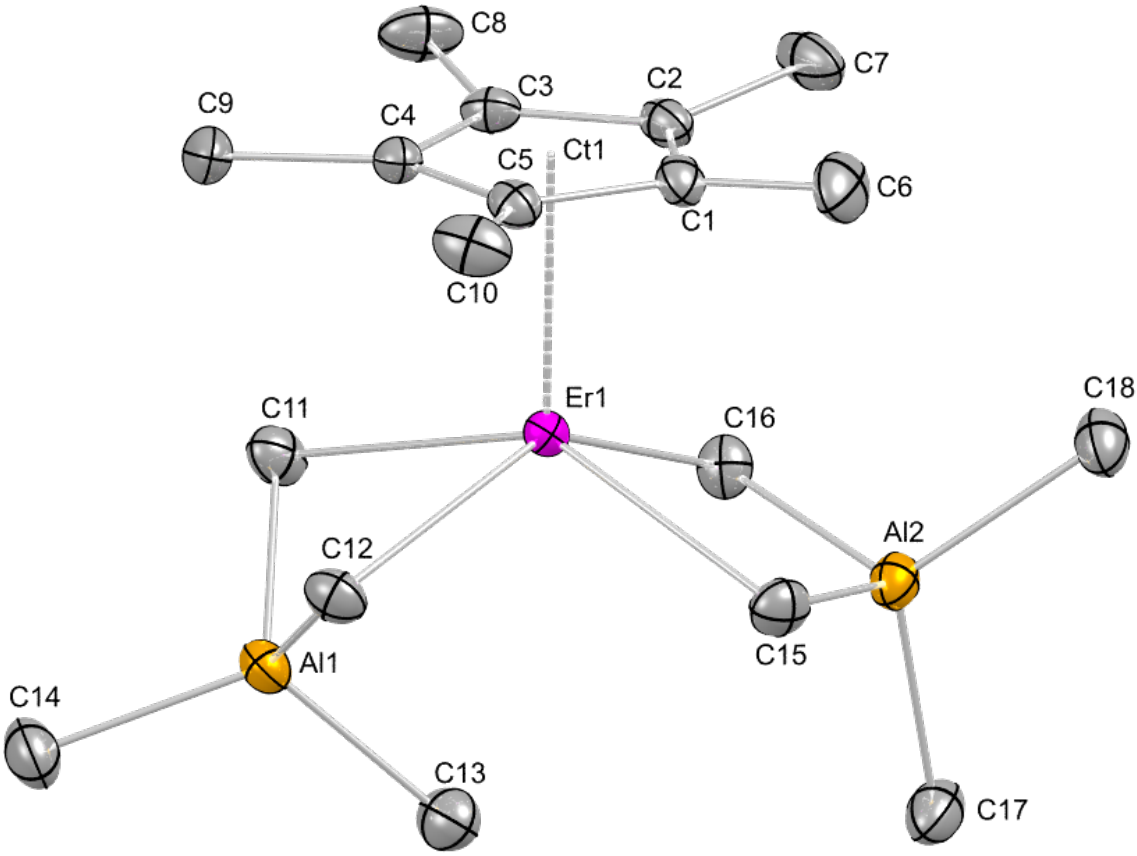

Figure S9. Crystal structure of **1**. Hydrogen atoms are omitted for clarity. Atomic displacement ellipsoids are set at the 50% probability level. Selected interatomic distances [Å] and angles [°]: Er1–C1 2.6321(2), Er1–C2 2.6247(2), Er1–C3 2.6030(2), Er1–C4 2.5990(2), Er1–C5 2.6107(2), Er1···Ct1 2.3261, Er1–C11 2.6373(2), Er1–C12 2.6256(2), Er1–C15 2.5330(2), Er1–C16 2.5369(2), Er1···Al1 2.8978(4), Er1···Al2 3.0870(4), C1–C2 1.418(2), C2–C3 1.4253(2), C3–C4 1.4187(2), C4–C5 1.4171(2), C1–C5 1.4191(2), C1–C6 1.503(2), Al1–C11 2.0647(2), Al1–C12 2.0601(2), Al1–C13 1.9772(2), Al1–C14 1.9638(2), C1–C2–C3 107.68(2), C2–C3–C4 108.01(2), C3–C4–C5 108.06(2), C4–C5–C1 108.00(2), C5–C1–C2 108.25(2), C11–Er1–C12 79.02(5), C11–Al1–C12 108.54(6), C13–Al1–C14 118.85(7), Er1–C11–Al1 74.99(5), Er1–C12–Al1 75.32(5).

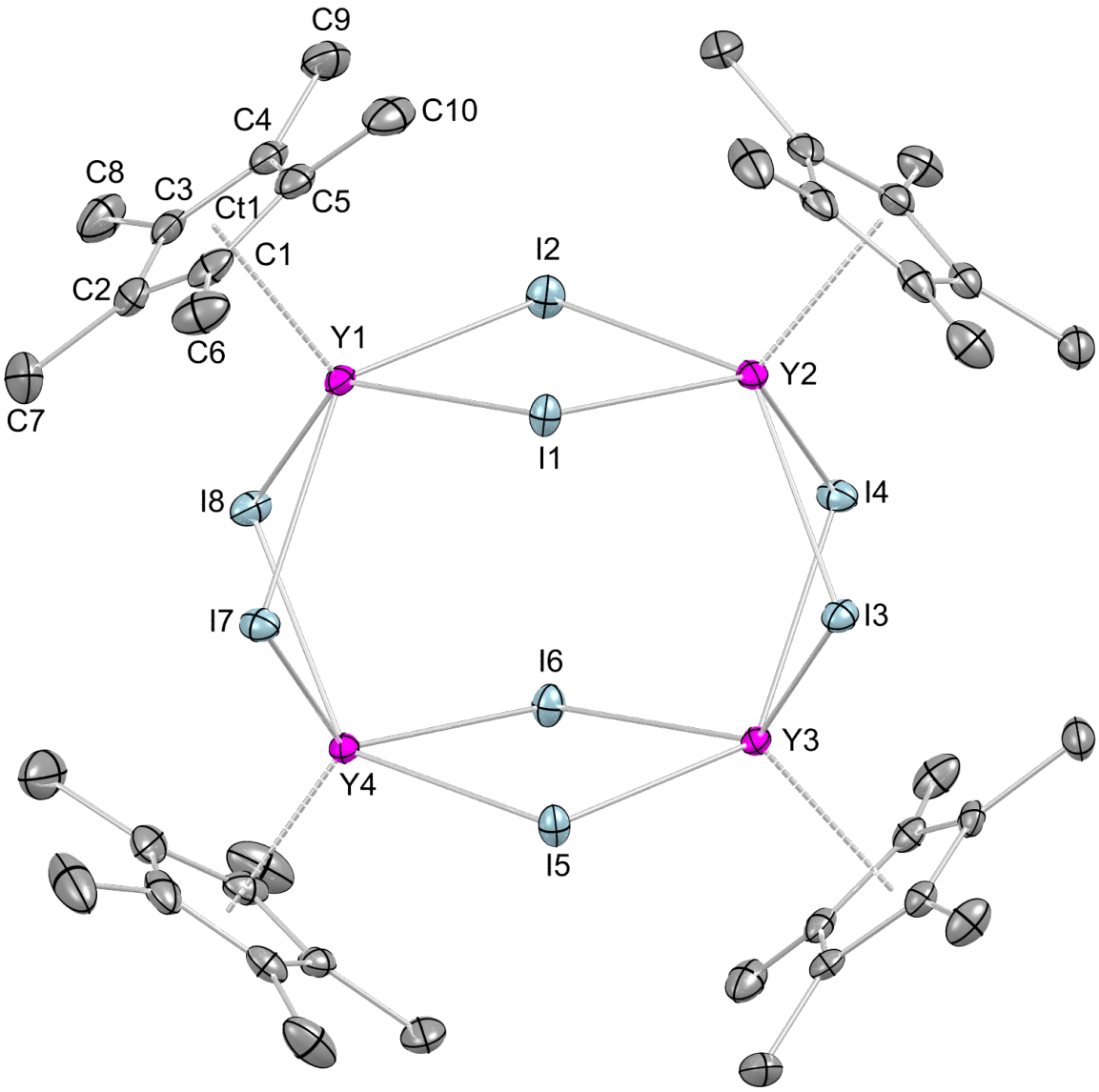

Figure S10. Crystal structure of $\mathbf{2^{Y}}$. Hydrogen atoms are omitted for clarity. Atomic displacement ellipsoids are set at the 50% probability level. Selected interatomic distances [Å] and angles [°]: Y1–C1 2.582(3), Y1–C2 2.580(3), Y1–C3 2.599(3), Y1–C4 2.602(4), Y1–C5 2.594(3), Y1···Ct1 2.2948, Y1–I1 3.0557(6), Y1–I2 3.0600(6), Y1–I7 3.0917(6), Y1–I8 3.0734(6), C1–C2 1.439(5), C2–C3 1.417(5), C3–C4 1.407(5), C4–C5 1.401(5), C1–C5, 1.432(5), C1–C6 1.486(5), C1–C2–C3 107.6(3), C2–C3–C4 108.4(3), C3–C4–C5 108.8(3), C4–C5–C1 108.3(3), C5–C1–C2 106.9(3), I1–Y1–I2 82.228(2), I7–Y1–I8 79.146(2), I1–Y1–I7 81.670(2), I2–Y1–I8 84.174(2), Y1–I1–Y2 96.962(2), Y1–I2–Y2 97.181(2).

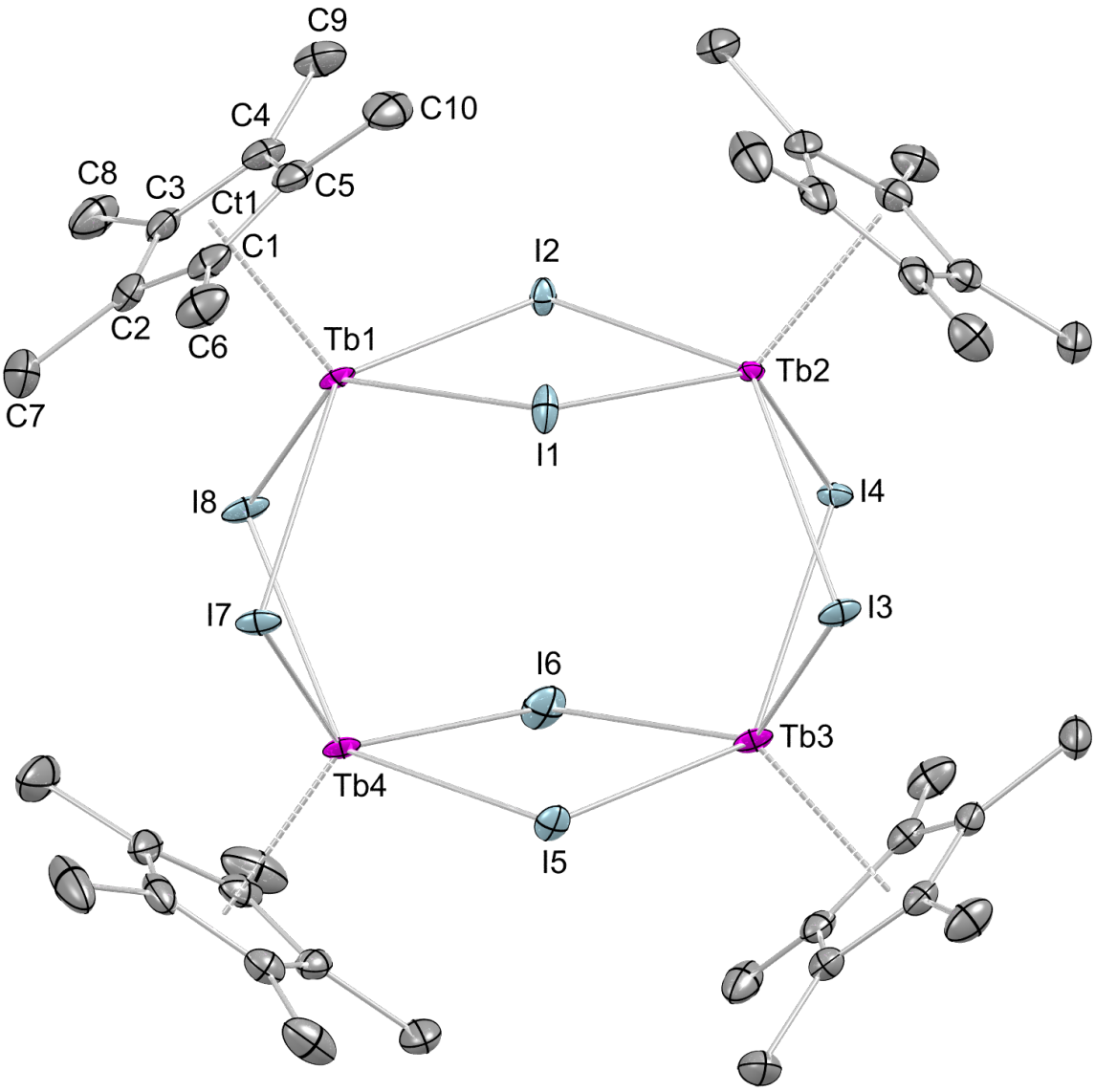

Figure S11. Crystal structure of $\mathbf{2}^{\mathbf{Tb}}$. Hydrogen atoms are omitted for clarity. Atomic displacement ellipsoids are set at the 50% probability level. Selected interatomic distances [Å] and angles [°]: Tb1–C1 2.619(3), Tb1–C2 2.612(3), Tb1–C3 2.621(3), Tb1–C4 2.630(3), Tb1–C5 2.629(3), Tb1···Ct1 2.3312, Tb1–I1 3.092(3), Tb1–I2 3.071(2), Tb1–I7 3.109(2), Tb1–I8 3.100(3), C1–C2 1.441(5), C2–C3 1.419(5), C3–C4 1.410(5), C4–C5 1.413(5), C1–C5, 1.425(5), C1–C6 1.498(5), C1–C2–C3 107.5(3), C2–C3–C4 108.4(3), C3–C4–C5 108.6(3), C4–C5–C1 108.1(3), C5–C1–C2 107.4(3), I1–Tb1–I2 82.14(7), I7–Tb1–I8 79.34(6), I1–Tb1–I7 81.80(7), I2–Tb1–I8 84.25(7), Tb1–I1–Tb2 96.70(8), Tb1–I2–Tb2 97.21(7).

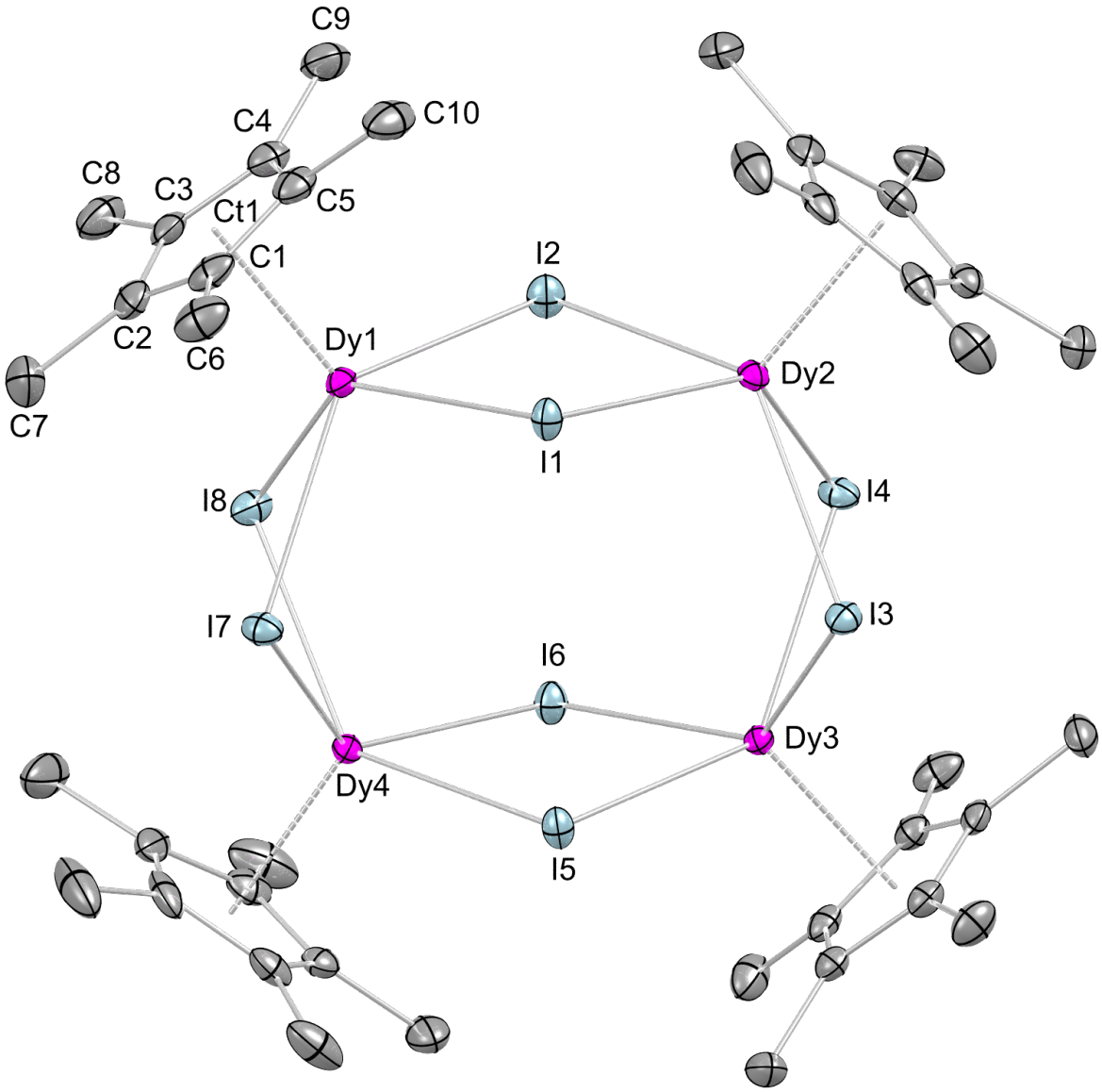

Figure S12. Crystal structure of $\mathbf{2^{Dy}}$. Hydrogen atoms are omitted for clarity. Atomic displacement ellipsoids are set at the 50% probability level. Selected interatomic distances [Å] and angles [°]: Dy1–C1 2.589(3), Dy1–C2 2.587(3), Dy1–C3 2.604(3), Dy1–C4 2.611(3), Dy1–C5 2.599(3), Dy1···Ct1 2.2981, Dy1–I1 3.0587(4), Dy1–I2 3.0500(4), Dy1–I7 3.0936(3), Dy1–I8 3.0752(4), C1–C2 1.439(6), C2–C3 1.415(5), C3–C4 1.408(5), C4–C5 1.415(5), C1–C5, 1.416(6), C1–C6 1.498(5), C1–C2–C3 107.5(3), C2–C3–C4 108.8(3), C3–C4–C5 107.8(3), C4–C5–C1 108.8(3), C5–C1–C2 107.0(3), I1–Dy1–I2 82.343(1), I7–Dy1–I8 79.222(9), I1–Dy1–I7 81.596(1), I2–Dy1–I8 84.052(1), Dy1–I1–Dy2 96.877(1), Dy1–I2–Dy2 97.088(1).

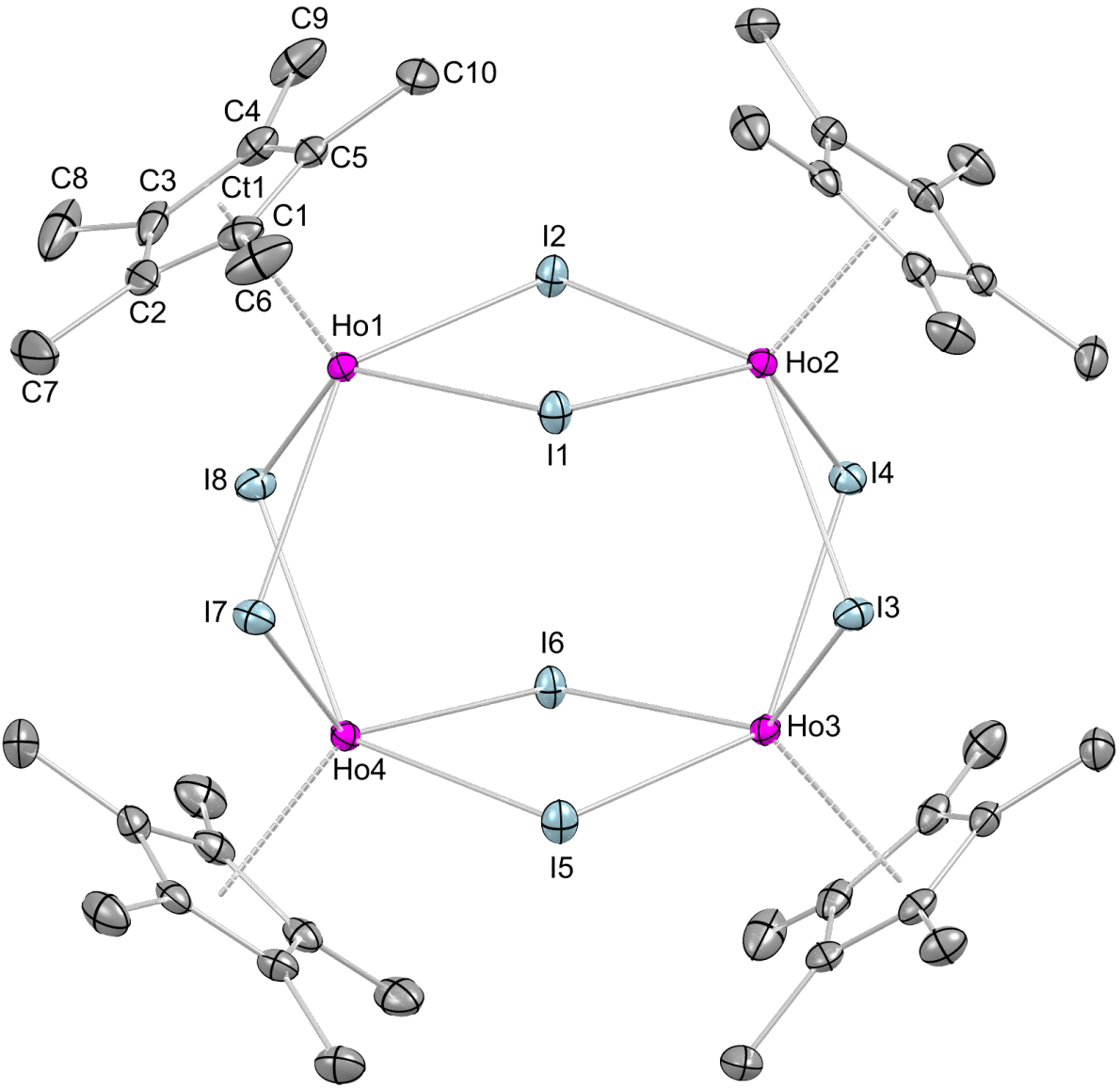

Figure S13. Crystal structure of $\mathbf{2}^{\mathbf{Ho}}$. Hydrogen atoms are omitted for clarity. Atomic displacement ellipsoids are set at the 50% probability level. Selected interatomic distances [Å] and angles [°]: Ho1–C1 2.585(3), Ho1–C2 2.596(3), Ho1–C3 2.601(3), Ho1–C4 2.586(3), Ho1–C5 2.578(3), Ho1···Ct1 2.3027, Ho1–I1 3.0662(4), Ho1–I2 3.0530(3), Ho1–I7 3.0695(4), Ho1–I8 3.0606(4), C1–C2 1.419(5), C2–C3 1.419(5), C3–C4 1.416(4), C4–C5 1.414(4), C1–C5, 1.418(4), C1–C6 1.511(4), C1–C2–C3 108.3(3), C2–C3–C4 107.9(3), C3–C4–C5 107.9(3), C4–C5–C1 108.6(3), C5–C1–C2 107.4(3), I1–Ho1–I2 82.031(2), I7–Ho1–I8 79.562(2), I1–Ho1–I7 82.960(2), I2–Ho1–I8 82.569(2), Ho1–I1–Ho2 96.377(2), Ho1–I2–Ho2 97.375(2).

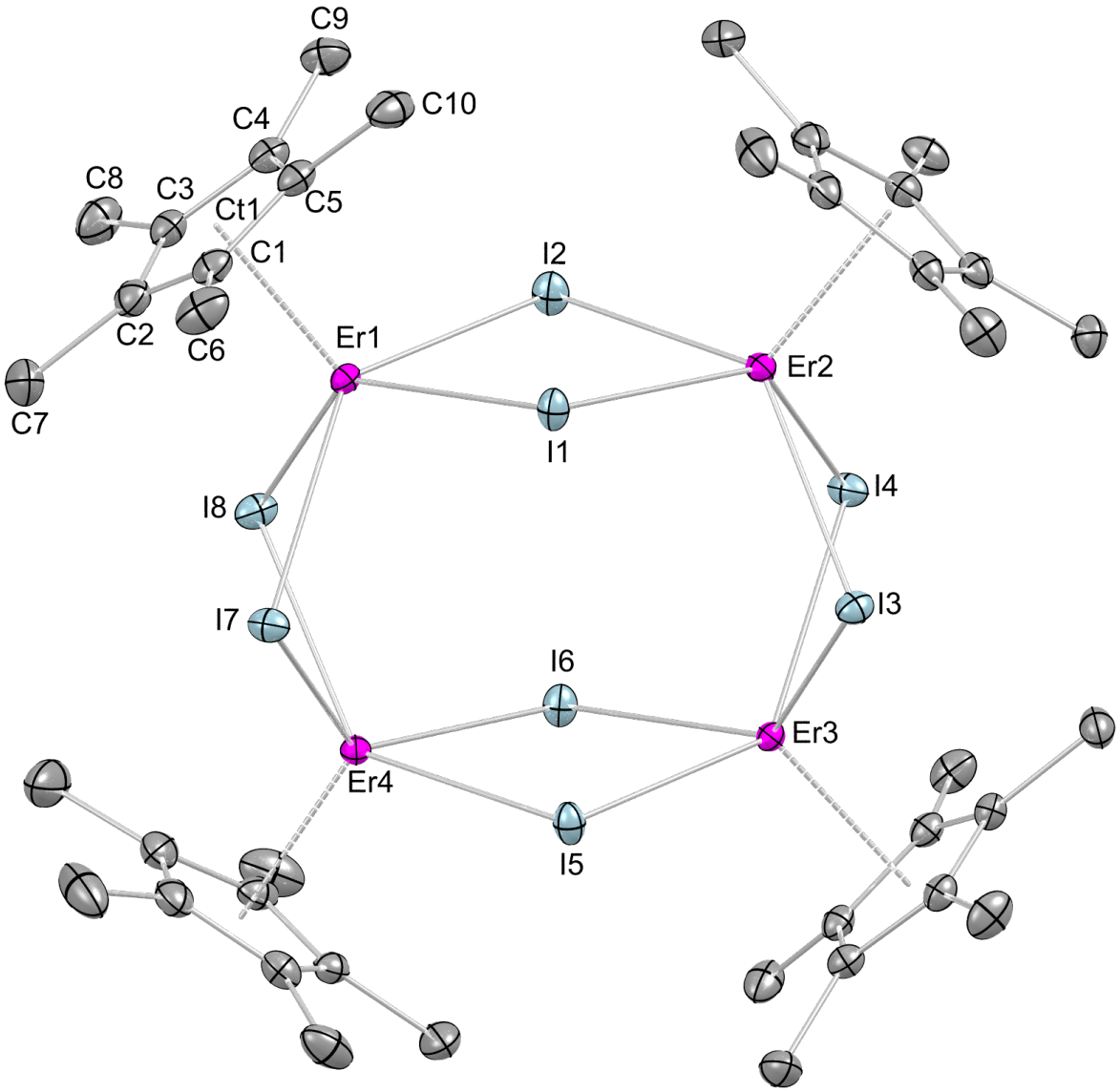

Figure S14. Crystal structure of $\mathbf{2}^{\mathbf{Er}}$. Hydrogen atoms are omitted for clarity. Atomic displacement ellipsoids are set at the 50% probability level. Selected interatomic distances [Å] and angles [°]: Er1–C1 2.576(3), Er1–C2 2.575(3), Er1–C3 2.594(3), Er1–C4 2.594(3), Er1–C5 2.586(3), Er1···Ct1 2.2772, Er1–I1 3.0399(7), Er1–I2 3.0317(8), Er1–I7 3.0745(7), Er1–I8 3.0578(8), C1–C2 1.438(4), C2–C3 1.419(4), C3–C4 1.418(4), C4–C5 1.413(4), C1–C5, 1.428(4), C1–C6 1.502(4), C1–C2–C3 108.0(3), C2–C3–C4 108.1(3), C3–C4–C5 108.4(3), C4–C5–C1 108.4(3), C5–C1–C2 107.1(3), I1–Er1–I2 82.30(2), I7–Er1–I8 79.27(2), I1–Er1–I7 81.56(2), I2–Er1–I8 84.09(2), Er1–I1–Er2 96.96(2), Er1–I2–Er2 97.14(2).

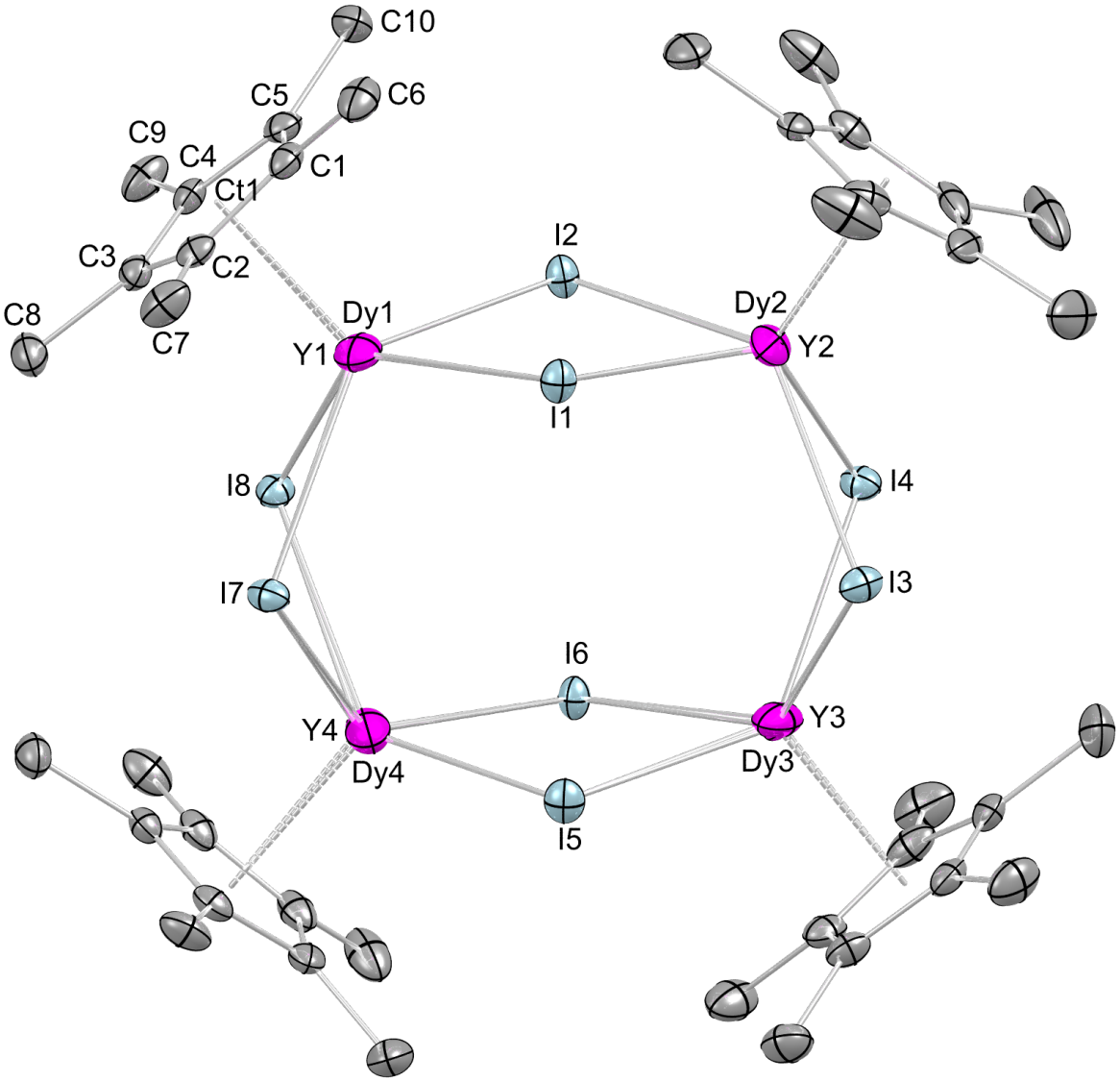

Figure S15. Crystal structure of $\mathbf{2}^{\mathbf{Y/Dy}}$. Hydrogen atoms are omitted for clarity. Atomic displacement ellipsoids are set at the 50% probability level. Selected interatomic distances [Å] and angles [°]: Y1–C1 2.608(4), Y1–C2 2.579(3), Y1–C3 2.579(4), Y1–C4 2.596(4), Y1–C5 2.614(4), Y1···Ct1 2.2977, Y1–I1 3.077(2), Y1–I2 3.0332(2), Y1–I7 3.0793(2), Y1–I8 3.064(2), Dy1–C1 2.579(9), Dy1–C2 2.570(8), Dy1–C3 2.613(9), Dy1–C4 2.636(9), Dy1–C5 2.615(9), Dy1···Ct1 2.3063, Dy1–I1 3.003(9), Dy1–I2 3.083(6), Dy1–I7 3.086(7), Dy1–I8 3.136(9), C1–C2 1.422(4), C2–C3 1.428(4), C3–C4 1.421(4), C4–C5 1.426(4), C1–C5, 1.420(4), C1–C6 1.505(4), C1–C2–C3 108.1(3), C2–C3–C4 107.7(3), C3–C4–C5 108.2(3), C4–C5–C1 107.9(3), C5–C1–C2 108.1(3), I1–Y1–I2 82.40(5), I7–Y1–I8 79.75(5), I1–Y1–I7 82.37(4), I2–Y1–I8 82.35(4), Y1–I1–Y2 96.36(4), Y1–I2–Y2 97.53(4), I1–Dy1–I2 83.8(2), I7–Dy1–I8 78.5(2), I1–Dy1–I7 83.5 (2), I2–Dy1–I8 81.26(2), Dy1–I1–Dy2 96.49(2), Dy1–I2–Dy2 96.49(2).

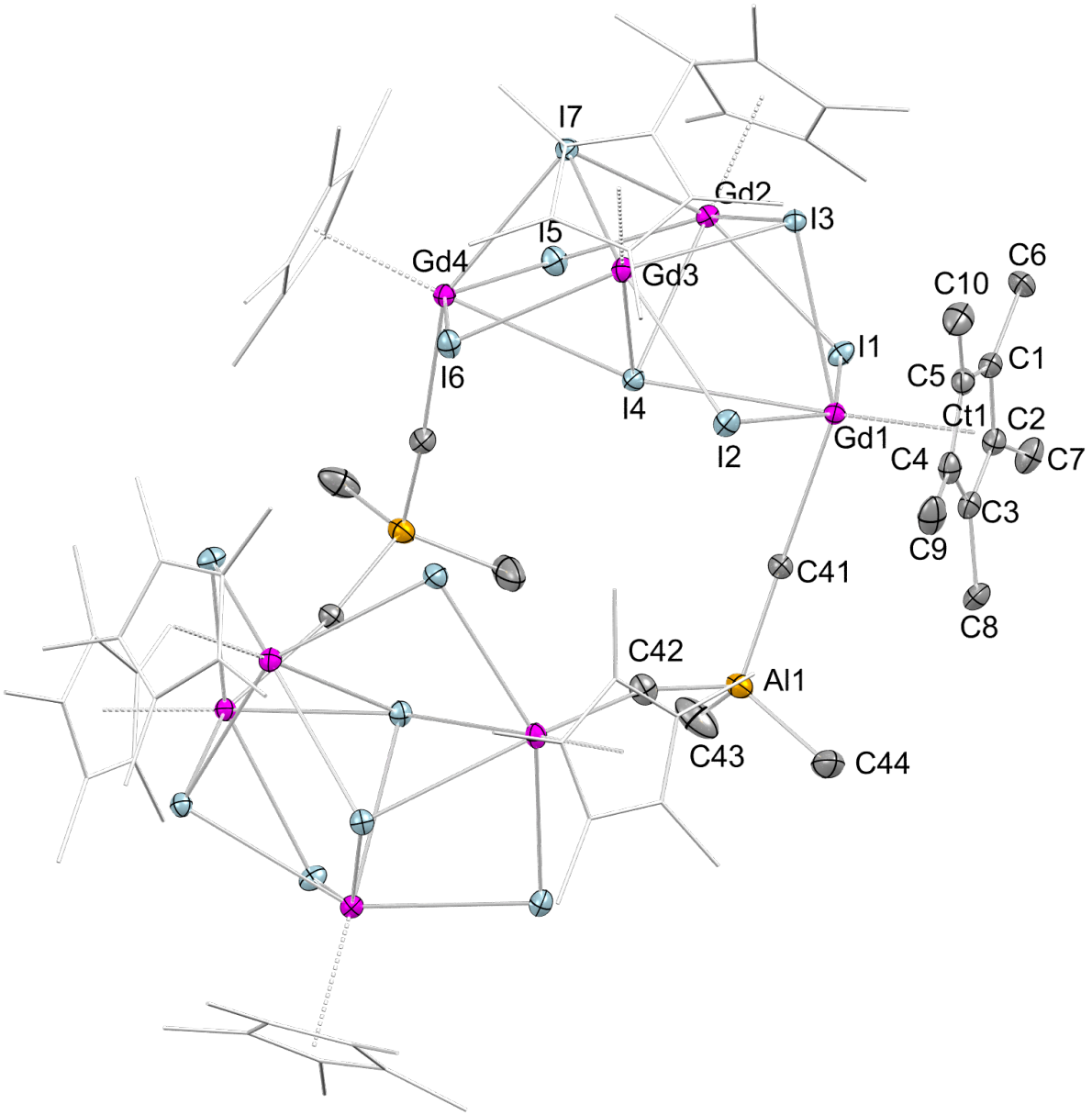

Figure S16. Crystal structure of **3**. Hydrogen atoms and lattice toluene are omitted for clarity. Ancillary Cp* (Cp* = C_5Me_5) ligands (except for one) are represented by a wireframe model for improved visualization. Atomic displacement ellipsoids are set at the 50% probability level.

Table S2. Selected interatomic distances and angles for **3**.

Bond lengths [Å]		**Bond angles [°]**	
Gd1–C1	2.650(3)	C1–C2–C3	108.1(3)
Gd1–C2	2.656(3)	C2–C3–C4	108.1(3)
Gd1–C3	2.676(3)	C3–C4–C5	107.8(3)
Gd1–C4	2.670(3)	C4–C5–C1	108.0(3)
Gd1–C5	2.656(3)	C5–C1–C2	107.9(3)
Gd1···Ct1	2.3627	I1–Gd1–I2	145.036(7)
Gd1–C41	2.677(3)	I1–Gd1–I3	79.549(1)
Gd1–I1	3.1187(3)	I1–Gd1–I4	72.749(7)
Gd1–I2	3.1151(3)	I3–Gd2–I4	74.215(9)

Gd1–I3	3.2060(3)	I3–Gd2–I5	146.615(7)
Gd1–I4	3.4524(3)	I3–Gd2–I7	76.765(8)
Gd2–I1	3.1367(3)	Gd1–I1–Gd2	93.506(2)
Gd2–I3	3.2218(3)	Gd1–I3–Gd2	90.284(9)
Gd2–I4	3.2703(3)	Gd1–I4–Gd2	85.294(1)
Gd2–I5	3.0802(3)	Gd2–I3–Gd3	91.112(8)
Gd2–I7	3.1888(3)	Gd2–I4–Gd3	88.453(6)
Al1–C41	2.047(3)	Gd2–I7–Gd3	92.379(7)
Al1–C42	2.064(3)	Gd1–I4–Gd4	164.320(7)
Al1–C43	1.961(4)	Gd1–C41–Al1	171.48(2)
Al1–C44	1.995(4)	Gd4–C42–Al1	164.03(2)
C1–C2	1.419(4)	Ct1···Gd1–C41	104.40
C2–C3	1.419(4)	I4–Gd1–C41	77.41(7)
C3–C4	1.420(4)	C41–Al1–C42	103.90(2)
C4–C5	1.423(4)	C41–Al1–C43	113.88(2)
C1–C5	1.421(4)	C41–Al1–C44	110.81(2)
C1–C6	1.504(4)	C43–Al1–C44	110.2(2)

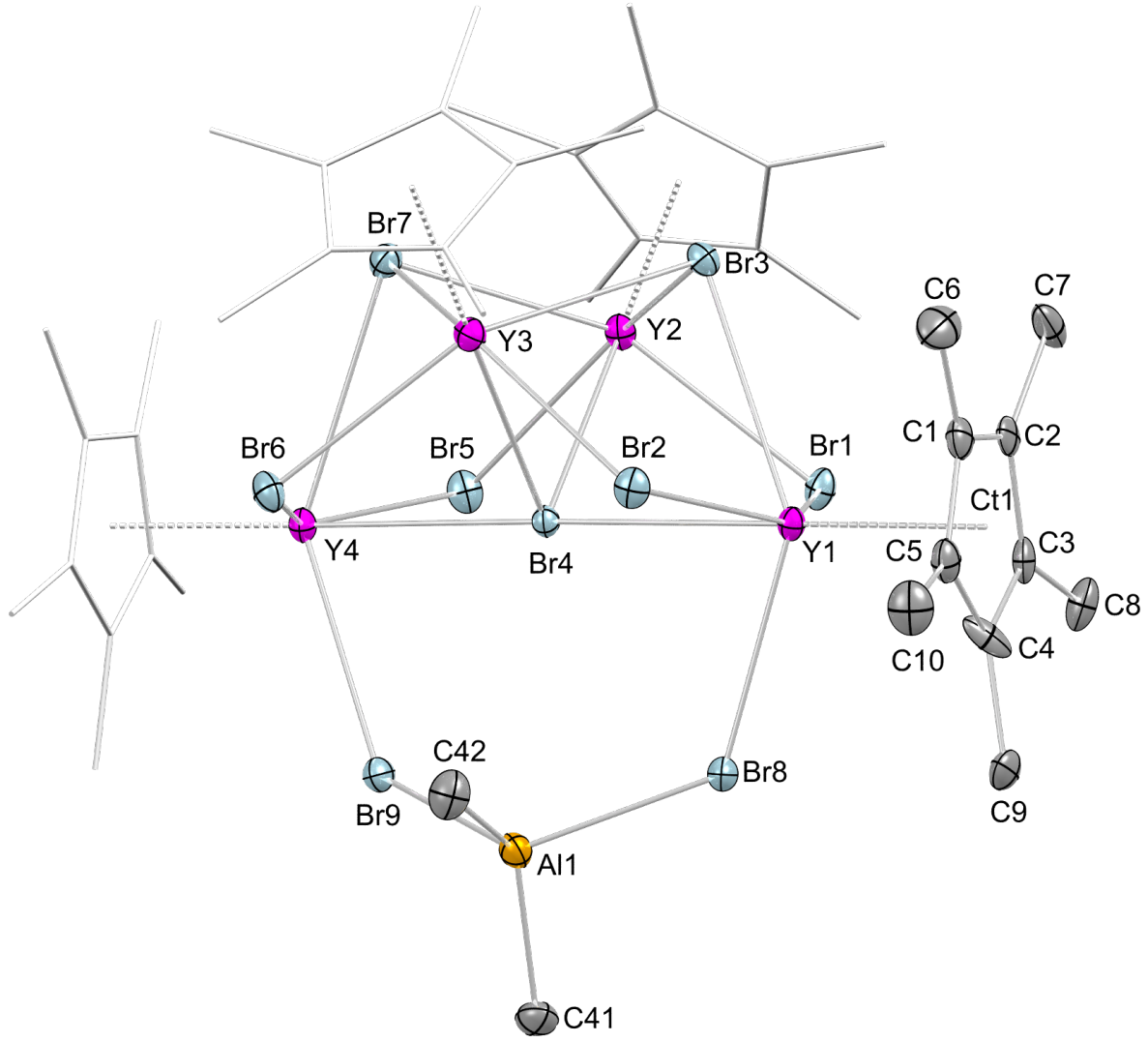

Figure S17. Crystal structure of $\mathbf{4^{Y}}$. Hydrogen atoms and lattice toluene are omitted for clarity. Ancillary Cp* ligands (except for one) are represented by a wireframe model for improved visualization. Atomic displacement ellipsoids are set at the 50% probability level. Selected interatomic distances [Å] and angles [°]: Y1–C1 2.575(7), Y1–C2 2.586(7), Y1–C3 2.605(7), Y1–C4 2.629(9), Y1–C5 2.589(8), Y1···Ct1 2.2949, Y1–Br1 2.8591(2), Y1–Br2 2.8702(1), Y1–Br3 3.0982(2), Y1–Br4 2.9324(1), Y1–Br8 2.8842(2), Y2–Br1 2.8160(2), Y2–Br3 2.9679(1), Y2–Br4 2.9881(1), Y2–Br5 2.8346(2), Y2–Br7 2.9655(1), Al1–Br8 2.440(2), Al1–Br9 2.480(2), Al1–C41 1.954(9), Al1–C42 1.945(9), C1–C2 1.427(2), C2–C3 1.440(2), C3–C4 1.416(2), C4–C5 1.430(2), C1–C5 1.415(2), C1–C6 1.509(2), C1–C2–C3 107.2(7), C2–C3–C4 108.4(7), C3–C4–C5 107.5(7), C4–C5–C1 108.6(7), C5–C1–C2 108.2(7), Br1–Y1–Br2 144.71(3), Br1–Y1–Br3 77.65(3), Br1–Y1–Br4 74.00(3), Br1–Y2–Br5 98.03(3), Br1–Y2–Br7 143.63(3), Br3–Y2–Br4 70.83(3), Br3–Y2–Br5 143.82(3), Br3–Y2–Br7 79.81(3), Y1–Br1–Y2 95.33(3), Y1–Br3–Y2 87.49(3), Y1–Br4–Y2 90.24(3), Y1–Br4–Y4 178.24(3), Y2–Br3–Y3 91.84(3), Y2–Br4–Y3 91.52(3), Y2–Br7–Y3 91.63(3), Y1–Br8–Al1 124.68(7), Y4–Br9–Al1 124.84(6), Br8–Al1–Br9 114.37(9), C41–Al1–C42 126.5(4).

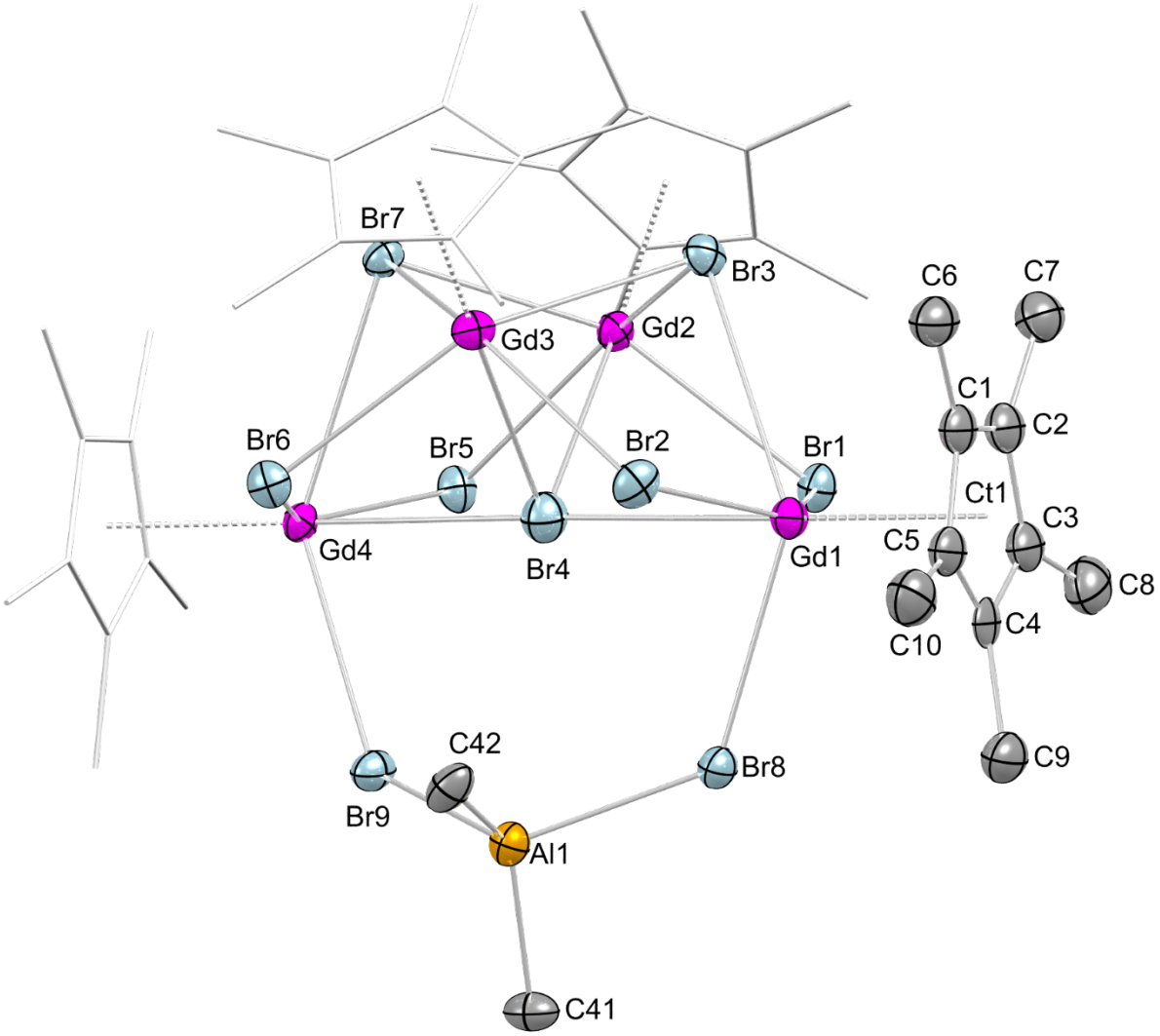

Figure S18. Crystal structure of $\mathbf{4}^{\mathbf{Gd}}$. Hydrogen atoms and lattice toluene are omitted for clarity. Ancillary Cp* ligands (except for one) are represented by a wireframe model for improved visualization. Atomic displacement ellipsoids are set at the 50% probability level. Selected interatomic distances [Å] and angles [°]: Gd1–C1 2.607(9), Gd1–C2 2.614(9), Gd1–C3 2.659(9), Gd1–C4 2.636(9), Gd1–C5 2.637(9), Gd1···Ct1 2.3470, Gd1–Br1 2.8923(2), Gd1–Br2 2.8909(2), Gd1–Br3 3.1053(1), Gd1–Br4 2.9276(2), Gd1–Br8 2.9135(1), Gd2–Br1 2.8559(1), Gd2–Br3 2.9930(1), Gd2–Br4 3.0055(2), Gd2–Br5 2.8404(1), Gd2–Br7 2.9970(1), Al1–Br8 2.481(3), Al1–Br9 2.444(3), Al1–C41 1.954(9), Al1–C42 1.933(9), C1–C2 1.386(2), C2–C3 1.410(2), C3–C4 1.434(2), C4–C5 1.392(2), C1–C5 1.428(2), C1–C6 1.508(2), C1–C2–C3 109.2(9), C2–C3–C4 106.3(9), C3–C4–C5 108.9(9), C4–C5–C1 107.1(9), C5–C1–C2 108.4(9), Br1–Gd1–Br2 146.39(3), Br1–Gd1–Br3 78.42(3), Br1–Gd1–Br4 75.14(3), Br1–Gd2–Br5 98.54(3), Br1–Gd2–Br7 144.36(3), Br3–Gd2–Br4 71.14(3), Br3–Gd2–Br5 144.12(3), Br3–Gd2–Br7 80.06(3), Gd1–Br1–Gd2 93.72(3), Gd1–Br3–Gd2 86.89(3), Gd1–Br4–Gd2 89.96(3), Gd1–Br4–Gd4 178.40(4), Gd2–Br3–Gd3 91.33(3), Gd2–Br4–Gd3 91.69(3), Gd2–Br7–Gd3 91.31(3), Gd1–Br8–Al1 124.97(7), Gd4–Br9–Al1 125.01(7), Br8–Al1–Br9 113.55(2), C41–Al1–C42 126.0(4).

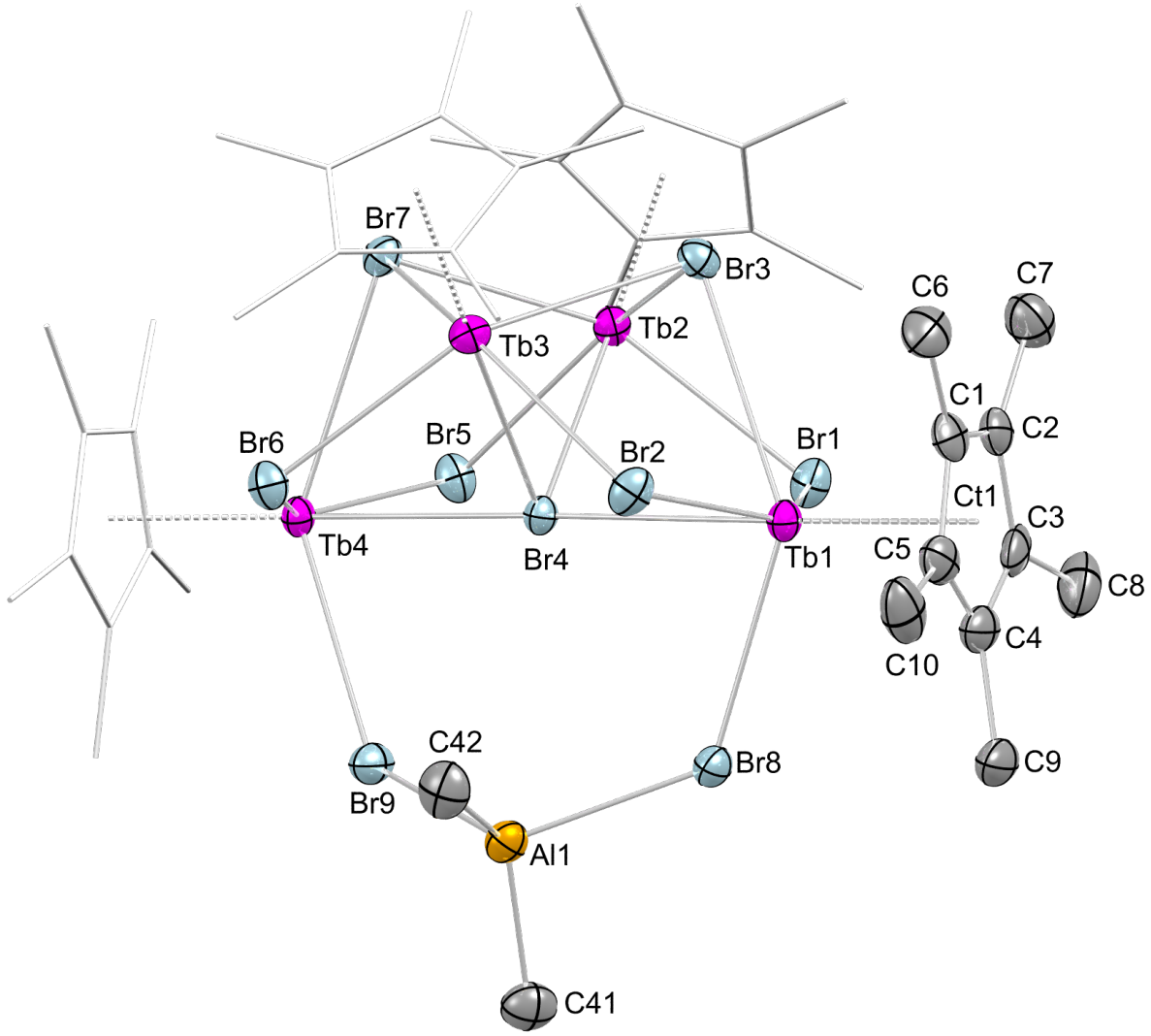

Figure S19. Crystal structure of $\mathbf{4}^{\mathbf{Tb}}$. Hydrogen atoms and lattice toluene are omitted for clarity. Ancillary Cp* ligands (except for one) are represented by a wireframe model for improved visualization. Atomic displacement ellipsoids are set at the 50% probability level. Selected interatomic distances [Å] and angles [°]: Tb1–C1 2.602(5), Tb1–C2 2.587(5), Tb1–C3 2.620(5), Tb1–C4 2.633(5), Tb1–C5 2.620(5), Tb1···Ct1 2.3175, Tb1–Br1 2.8798(7), Tb1–Br2 2.8719(7), Tb1–Br3 3.0999(7), Tb1–Br4 2.9356(7), Tb1–Br8 2.8987(7), Tb2–Br1 2.8444(6), Tb2–Br3 2.9903(6), Tb2–Br4 2.9897(7), Tb2–Br5 2.8248(6), Tb2–Br7 2.9778(6), Al1–Br8 2.4667(2), Al1–Br9 2.4417(2), Al1–C41 1.949(6), Al1–C42 1.939(6), C1–C2 1.410(8), C2–C3 1.426(8), C3–C4 1.414(9), C4–C5 1.407(8), C1–C5 1.428(8), C1–C6 1.503(8), C1–C2–C3 108.4(5), C2–C3–C4 107.7(5), C3–C4–C5 108.1(5), C4–C5–C1 108.5(5), C5–C1–C2 107.3(5), Br1–Tb1–Br2 145.520(2), Br1–Tb1–Br3 78.273(2), Br1–Tb1–Br4 74.318(2), Br1–Tb2–Br5 98.43(2), Br1–Tb2–Br7 143.899(2), Br3–Tb2–Br4 70.771(2), Br3–Gd2–Br5 143.907(2), Br3–Gd2–Br7 79.779(2), Tb1–Br1–Tb2 94.505(2), Tb1–Br3–Tb2 87.277(2), Tb1–Br4–Tb2 90.373(2), Tb1–Br4–Tb4 178.19(2), Tb2–Br3–Tb3 91.715(2), Tb2–Br4–Tb3 91.782(2), Tb2–Br7–Tb3 91.628(2), Tb1–Br8–Al1 125.06(4), Tb4–Br9–Al1 125.11(4), Br8–Al1–Br9 114.08(7), C41–Al1–C42 126.4(3).

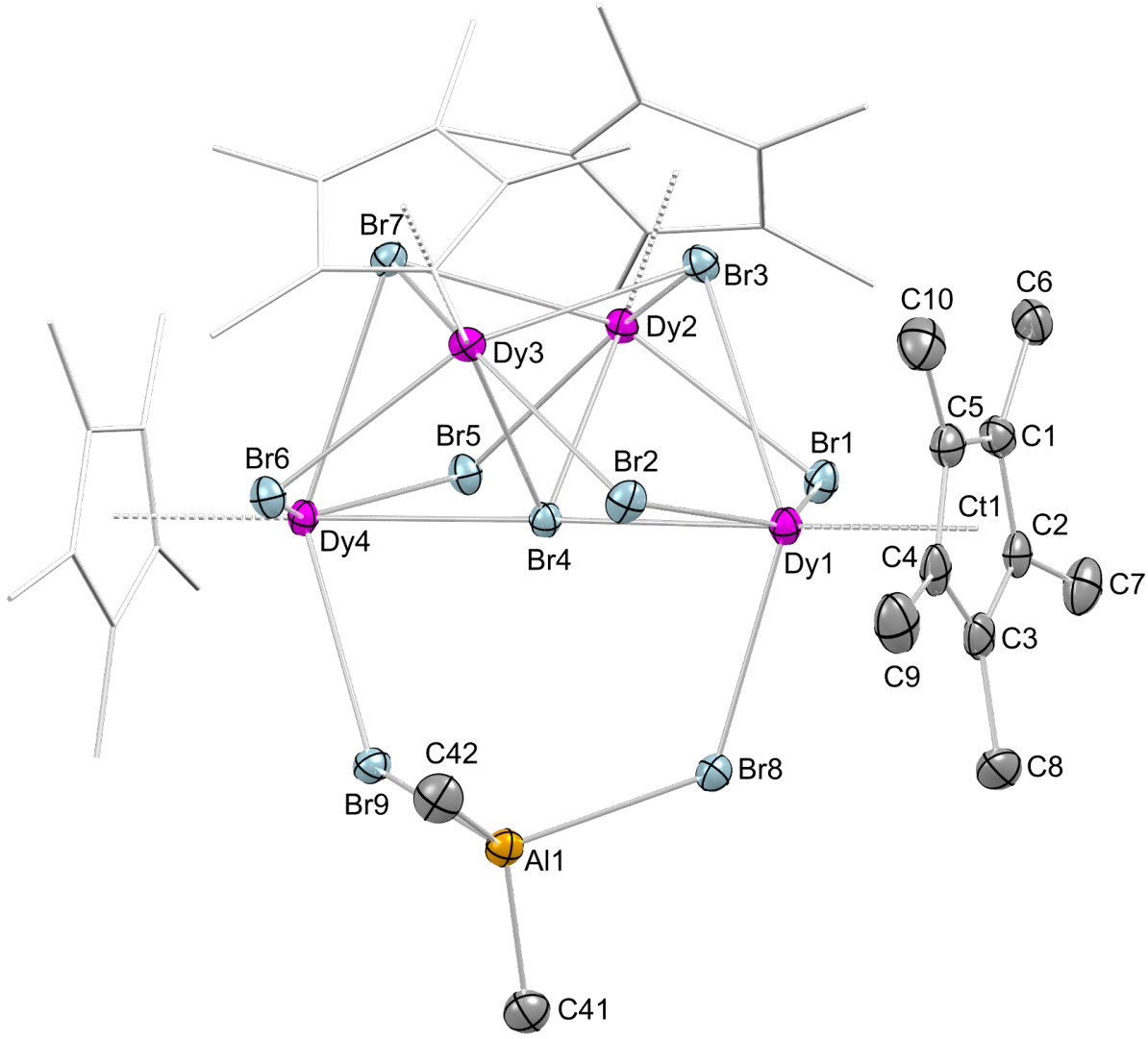

Figure S20. Crystal structure of $\mathbf{4}^{\mathbf{Dy}}$. Hydrogen atoms and lattice [D_6]benzene are omitted for clarity. Ancillary Cp* ligands (except for one) are represented by a wireframe model for improved visualization. Atomic displacement ellipsoids are set at the 50% probability level. Selected interatomic distances [Å] and angles [°]: Dy1–C1 2.592(7), Dy1–C2 2.615(6), Dy1–C3 2.623(6), Dy1–C4 2.596(6), Dy1–C5 2.601(7), Dy1···Ct1 2.309, Dy1–Br1 2.881(2), Dy1–Br2 2.8753(2), Dy1–Br3 3.092(2), Dy1–Br4 2.925(2), Dy1–Br8 2.908(2), Dy2–Br1 2.8377(2), Dy2–Br3 2.9850(2), Dy2–Br4 2.991(2), Dy2–Br5 2.8271(2), Dy2–Br7 2.9814(2), Al1–Br8 2.488(2), Al1–Br9 2.451(2), Al1–C41 1.946(7), Al1–C42 1.938(7), C1–C2 1.419(1), C2–C3 1.412(9), C3–C4 1.411(1), C4–C5 1.426(1), C1–C5 1.430(9), C1–C6 1.500(9), C1–C2–C3 108.3(6), C2–C3–C4 108.0(6), C3–C4–C5 108.7(6), C4–C5–C1 106.9(6), C5–C1–C2 108.0(6), Br1–Dy1–Br2 145.97(4), Br1–Dy1–Br3 78.11(4), Br1–Dy1–Br4 74.69(2), Br1–Dy2–Br5 99.54(6), Br1–Dy2–Br7 143.72(3), Br3–Dy2–Br4 70.86(5), Br3–Dy2–Br5 143.28(3), Br3–Dy2–Br7 79.28(5), Dy1–Br1–Dy2 94.27(3), Dy1–Br3–Dy2 87.20(5), Dy1–Br4–Dy2 90.23(2), Dy1–Br4–Dy4 178.98(3), Dy2–Br3–Dy3 91.77(6), Dy2–Br4–Dy3 92.24(5), Dy2–Br7–Dy3 92.23(6), Dy1–Br8–Al1 124.85(5), Dy4–Br9–Al1 125.76(6), Br8–Al1–Br9 114.30(9), C41–Al1–C42 126.3(3).

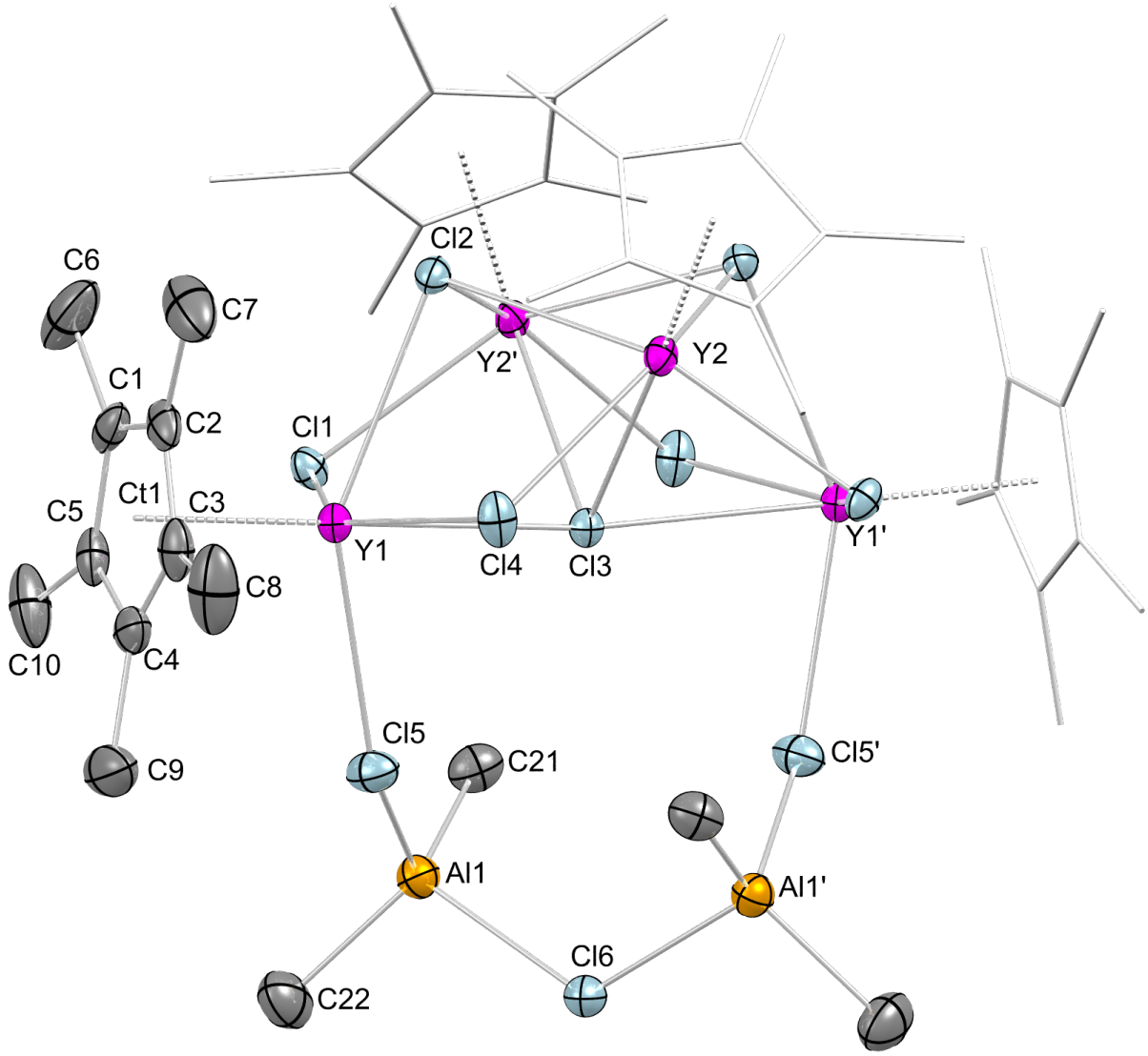

Figure S21. Crystal structure of $\mathbf{5^{Y}}$. Hydrogen atoms and lattice toluene are omitted for clarity. Ancillary Cp* ligands (except for one) are represented by a wireframe model for improved visualization. Atomic displacement ellipsoids are set at the 50% probability level. Selected interatomic distances [Å] and angles [°]: Y1–C1 2.586(3), Y1–C2 2.593(2), Y1–C3 2.618(3), Y1–C4 2.622(3), Y1–C5 2.589(3), Y1···Ct1 2.3071, Y1–Cl1 2.6936(7), Y1–Cl2 2.8282(8), Y1–Cl3 2.8867(4), Y1–Cl4 2.6910(8), Y1–Cl5 2.7158(8), Y2–Cl1 2.6731(7), Y2–Cl2 2.7930(8), Y2–Cl3 2.8769(7), Y2–Cl4 2.6835(7), Al1–Cl5 2.2479(2), Al1–Cl6 2.3116(1), Al1–C21 1.925(3), Al1–C22 1.940(3), C1–C2 1.413(4), C2–C3 1.397(4), C3–C4 1.393(4), C4–C5 1.406(4), C1–C5 1.427(4), C1–C6 1.498(4), C1–C2–C3 108.2(2), C2–C3–C4 108.7(2), C3–C4–C5 108.5(3), C4–C5–C1 107.5(2), C5–C1–C2 107.2(2), Cl1–Y1–Cl2 77.450(2), Cl1–Y1–Cl3 73.814(2), Cl1–Y1–Cl4 143.88(2), Cl2–Y1–Cl3 69.91(2), Cl2–Y1–Cl4 78.18(2), Cl3–Y1–Cl4 72.97(2), Cl1–Y2–Cl2 78.40(2), Cl1–Y2–Cl3 74.27, Cl1–Y2–Cl2' 142.47(2), Cl1–Y2–Cl4 103.00(2), Cl2–Y2–Cl2' 78.21(2), Cl2–Y2–Cl3 70.53, Cl2–Y2–Cl4 141.84(2), Cl3–Y2–Cl4 73.24, Y1–Cl1–Y2 96.09(2), Y1–Cl2–Y2 90.46(2), Y1–Cl3–Y2 87.644(2), Y1–Cl3–Y1' 173.59(3), Y1–Cl5–Al1 132.43(4), Cl5–Al1–Cl6 98.59(4), C21–Al1–C22 121.80(2), Cl5–Al1–C21 113.01(1), Cl5–Al1–C22 107.33(2), Cl6–Al1–C21 109.59(1), Cl6–Al1–C22 103.66(2).

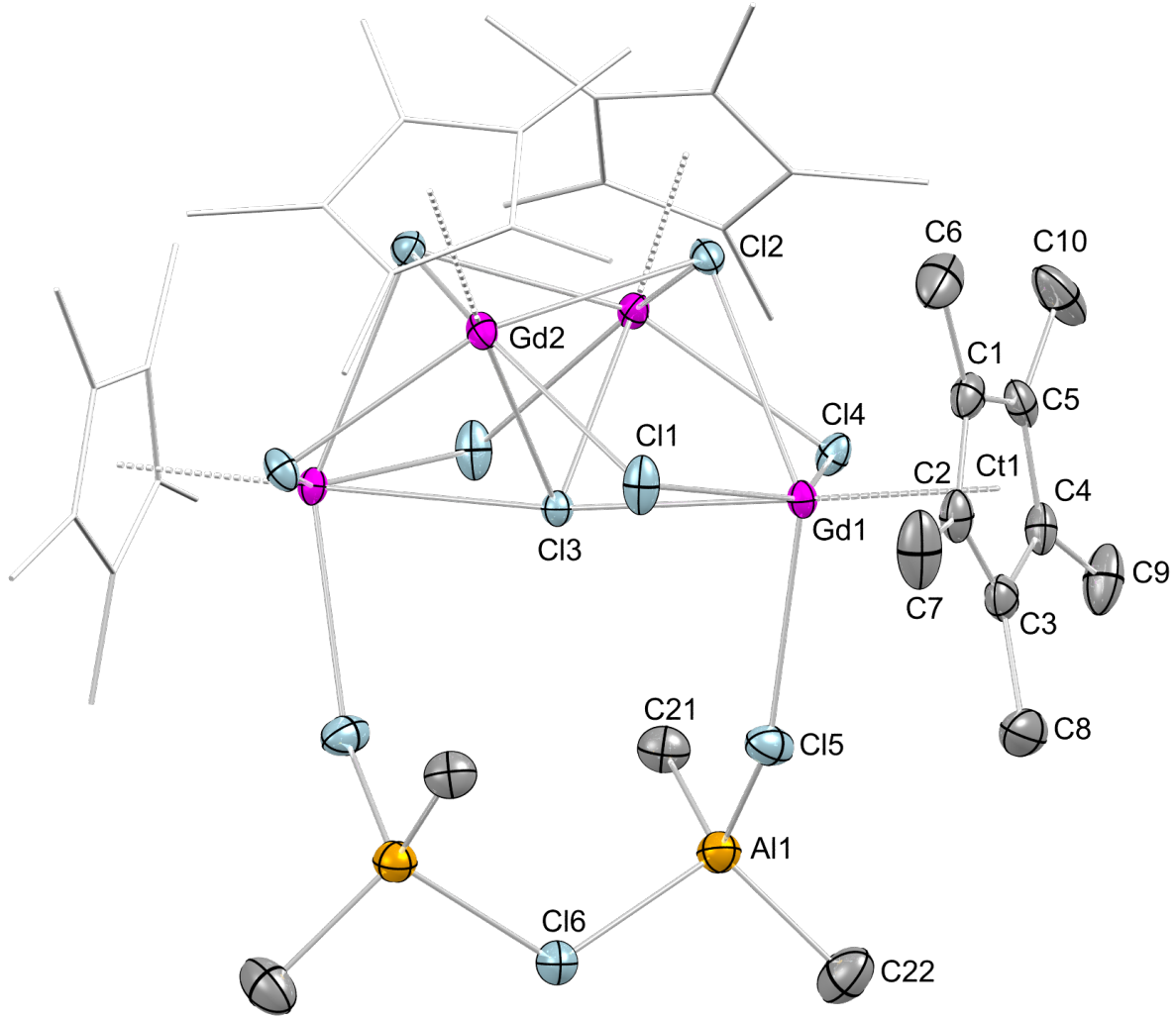

Figure S22. Crystal structure of $\mathbf{5}^{Gd}$. Hydrogen atoms and lattice toluene are omitted for clarity. Ancillary Cp* ligands (except for one) are represented by a wireframe model for improved visualization. Atomic displacement ellipsoids are set at the 50% probability level. Selected interatomic distances [Å] and angles [°]: Gd1–C1 2.635(3), Gd1–C2 2.657(3), Gd1–C3 2.658(3), Gd1–C4 2.632(3), Gd1–C5 2.625(3), Gd1···Ct1 2.3468, Gd1–Cl1 2.7296(6), Gd1–Cl2 2.8651(6), Gd1–Cl3 2.92204(2), Gd1–Cl4 2.7304(6), Gd1–Cl5 2.7532(7), Gd2–Cl1 2.7196(7), Gd2–Cl2 2.8359(6), Gd2–Cl3 2.9188(6), Gd2–Cl4 2.7056(6), Al1–Cl5 2.2491(2), Al1–Cl6 2.3010(1), Al1–C21 1.931(3), Al1–C22 1.948(4), C1–C2 1.407(4), C2–C3 1.409(4), C3–C4 1.415(4), C4–C5 1.423(4), C1–C5 1.421(4), C1–C6 1.503(4), C1–C2–C3 108.5(2), C2–C3–C4 108.2(3), C3–C4–C5 107.6(2), C4–C5–C1 107.8(2), C5–C1–C2 107.9(3), Cl1–Gd1–Cl2 77.94(2), Cl1–Gd1–Cl3 73.469(2), Cl1–Gd1–Cl4 144.470(2), Cl2–Gd1–Cl3 70.07(2), Cl2–Gd1–Cl4 77.183(2), Cl3–Gd1–Cl4 74.415(2), Cl1–Gd2–Cl2 78.61, Cl1–Gd2–Cl3 73.66, Cl1–Gd2–Cl4 104.35, Cl2–Gd2–Cl3 70.51, Cl2–Gd2–Cl4 142.80, Cl3–Gd2–Cl4 74.83, Gd1–Cl1–Gd2 95.96(2), Gd1–Cl2–Gd2 90.487(2), Gd1–Cl3–Gd2 87.752(2), Gd1–Cl3–Gd1' 173.23(3), Gd1–Cl5–Al1 132.32(4), Cl5–Al1–Cl6 99.53(4), C21–Al1–C22 121.89(2), Cl5–Al1–C21 112.80(2), Cl5–Al1–C22 106.93(2), Cl6–Al1–C21 109.67(2), Cl6–Al1–C22 103.36(2).

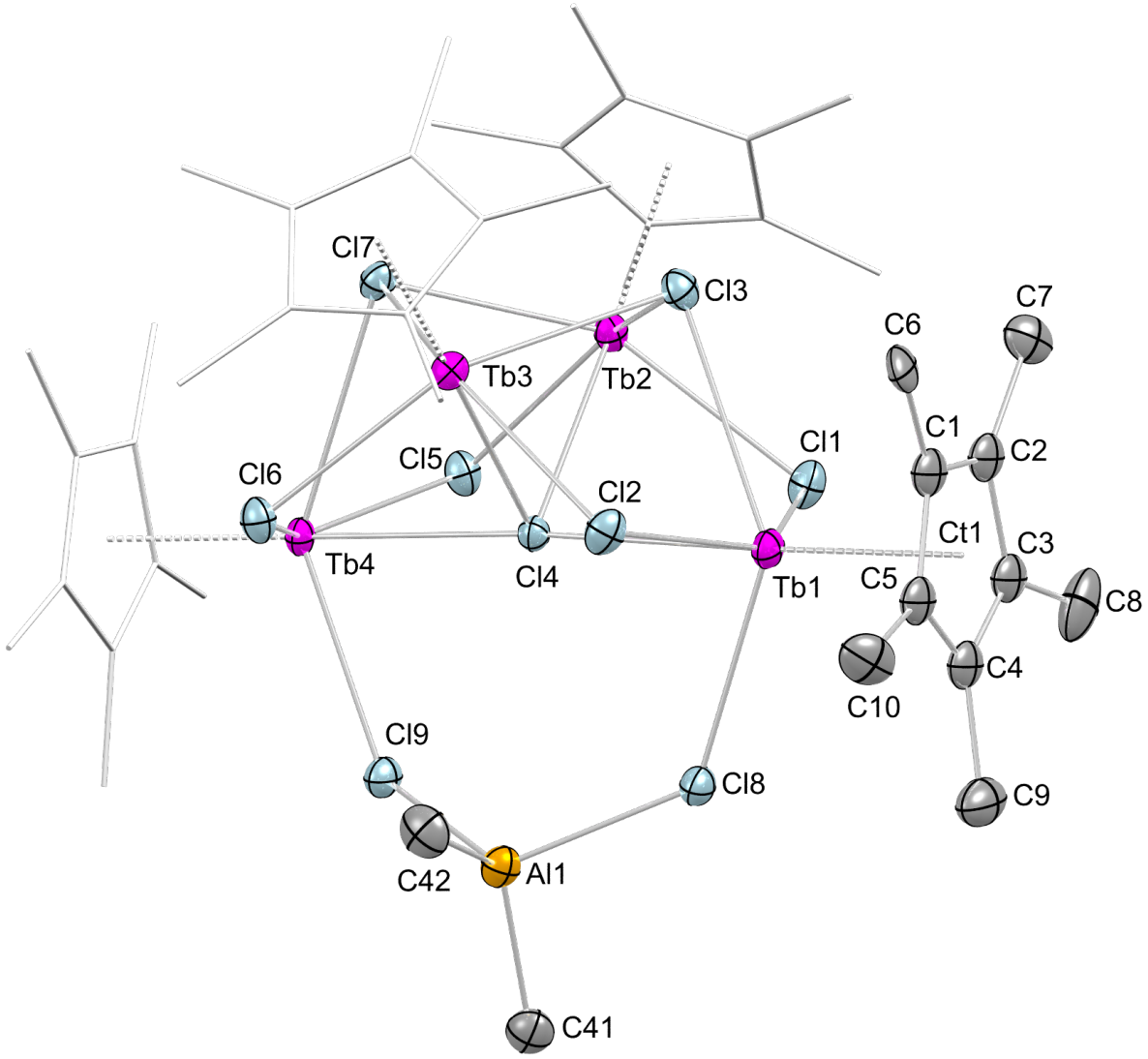

Figure S23. Crystal structure of $\mathbf{6}^{\mathbf{Tb}}$. Hydrogen atoms and lattice toluene are omitted for clarity. Ancillary Cp* ligands (except for one) are represented by a wireframe model for improved visualization. Atomic displacement ellipsoids are set at the 50% probability level. Selected interatomic distances [Å] and angles [°]: Tb1–C1 2.585(2), Tb1–C2 2.601(2), Tb1–C3 2.631(2), Tb1–C4 2.629(2), Tb1–C5 2.607(2), Tb1···Ct1 2.3126, Tb1–Cl1 2.726(3), Tb1–Cl2 2.722(3), Tb1–Cl3 2.907(3), Tb1–Cl4 2.800(3), Tb1–Cl8 2.759(3), Tb2–Cl1 2.698(3), Tb2–Cl3 2.835(3), Tb2–Cl4 2.864(3), Tb2–Cl5 2.685(3), Tb2–Cl7 2.838(3), Al1–Cl8 2.310(5), Al1–Cl9 2.274(5), Al1–C41 1.936(2), Al1–C42 1.939(2), C1–C2 1.427(2), C2–C3 1.429(2), C3–C4 1.412(2), C4–C5 1.394(2), C1–C5 1.416(2), C1–C6 1.502(2), C1–C2–C3 106.9(2), C2–C3–C4 108.2(2), C3–C4–C5 108.3(2), C4–C5–C1 108.9(2), C5–C1–C2 107.7(2), Cl1–Tb1–Cl2 143.79(9), Cl1–Tb1–Cl3 76.50(8), Cl1–Tb1–Cl4 74.18(8), Cl1–Tb2–Cl5 99.81(9), Cl1–Tb2–Cl7 141.95(9), Cl3–Tb2–Cl4 69.68(8), Cl3–Tb2–Cl5 141.85(9), Cl3–Tb2–Cl7 79.20(8), Tb1–Cl1–Tb2 96.48(9), Tb1–Cl3–Tb2 88.34(8), Tb1–Cl4–Tb2 91.16(8), Tb1–Cl4–Tb4 175.93(2), Tb2–Cl3–Tb3 93.16(8), Tb2–Cl4–Tb3 92.15(8), Tb2–Cl7–Tb3 93.22(8), Tb1–Cl8–Al1 128.01(2), Tb4–Cl9–Al1 126.64(2), Cl8–Al1–Cl9 112.10(2), C41–Al1–C42 124.2(6).

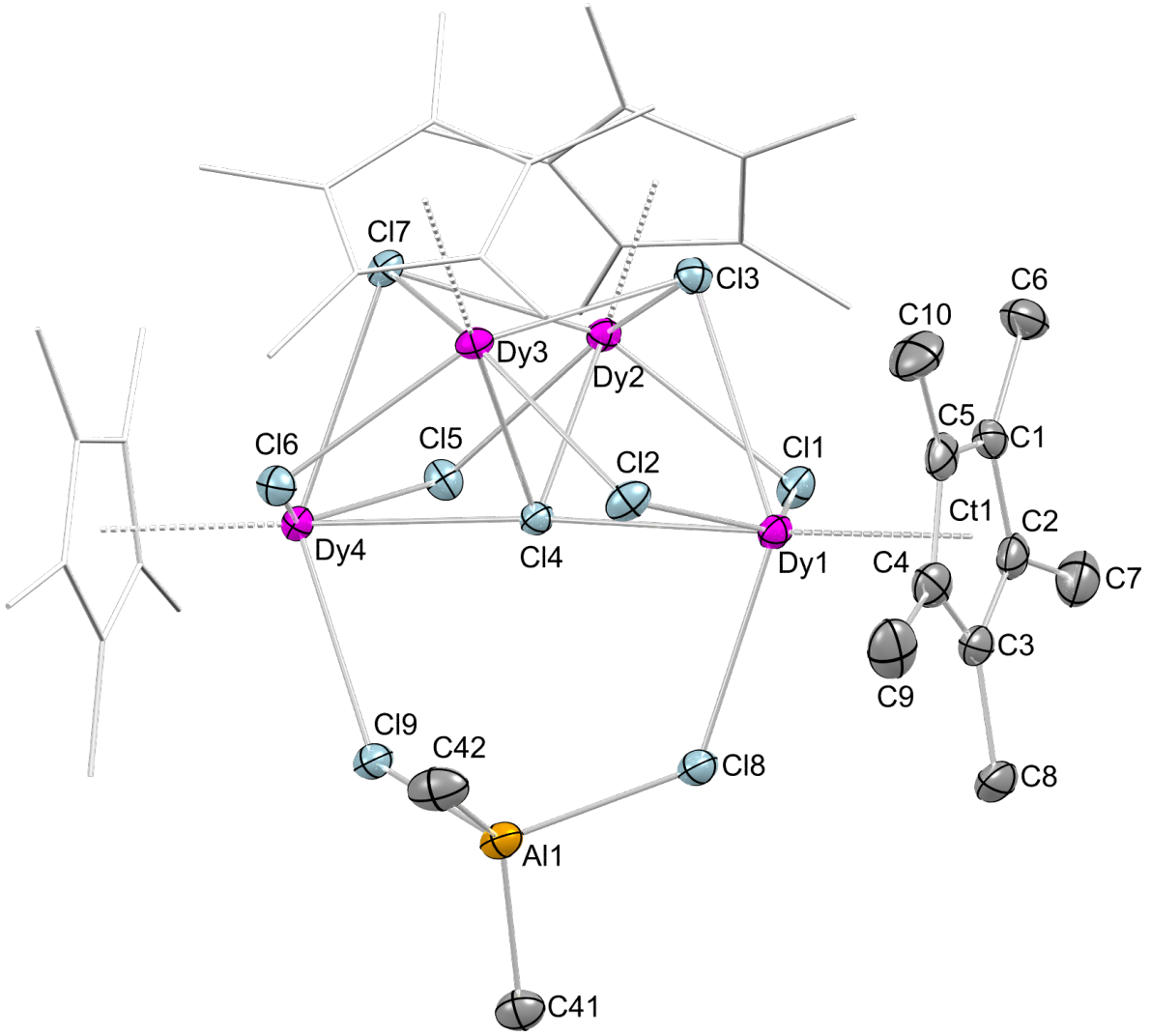

Figure S24. Crystal structure of $\mathbf{6}^{\mathbf{Dy}}$. Hydrogen atoms and lattice [D_6]benzene are omitted for clarity. Ancillary Cp* ligands (except for one) are represented by a wireframe model for improved visualization. Atomic displacement ellipsoids are set at the 50% probability level. Selected interatomic distances [Å] and angles [°]: Dy1–C1 2.582(4), Dy1–C2 2.627(4), Dy1–C3 2.625(4), Dy1–C4 2.589(4), Dy1–C5 2.579(4), Dy1···Ct1 2.3003, Dy1–Cl1 2.7172(1), Dy1–Cl2 2.7113(2), Dy1–Cl3 2.9511(1), Dy1–Cl4 2.7869(1), Dy1–Cl8 2.7414(2), Dy2–Cl1 2.6890(1), Dy2–Cl3 2.8288(1), Dy2–Cl4 2.8429(1), Dy2–Cl5 2.6716(1), Dy2–Cl7 2.8229(1), Al1–Cl8 2.2996(2), Al1–Cl9 2.2840(2), Al1–C41 1.952(5), Al1–C42 1.929(5), C1–C2 1.421(6), C2–C3 1.415(7), C3–C4 1.413(7), C4–C5 1.425(7), C1–C5 1.420(7), C1–C6 1.494(6), C1–C2–C3 108.0(4), C2–C3–C4 108.3(4), C3–C4–C5 108.1(4), C4–C5–C1 107.6(4), C5–C1–C2 108.0(4), Cl1–Dy1–Cl2 143.93(3), Cl1–Dy1–Cl3 76.53(3), Cl1–Dy1–Cl4 74.23(3), Cl1–Dy2–Cl5 100.12(3), Cl1–Dy2–Cl7 142.07(3), Cl3–Dy2–Cl4 69.59(3), Cl3–Dy2–Cl5 141.79(3), Cl3–Dy2–Cl7 78.88(3), Dy1–Cl1–Dy2 96.33(3), Dy1–Cl3–Dy2 88.33(3), Dy1–Cl4–Dy2 91.36(3), Dy1–Cl4–Dy4 175.85(4), Dy2–Cl3–Dy3 93.39(3), Dy2–Cl4–Dy3 92.49(3), Dy2–Cl7–Dy3 93.10(3), Dy1–Cl8–Al1 126.95(5), Dy4–Cl9–Al1 126.60(5), Cl8–Al1–Cl9 112.12(7), C41–Al1–C42 124.8(2).

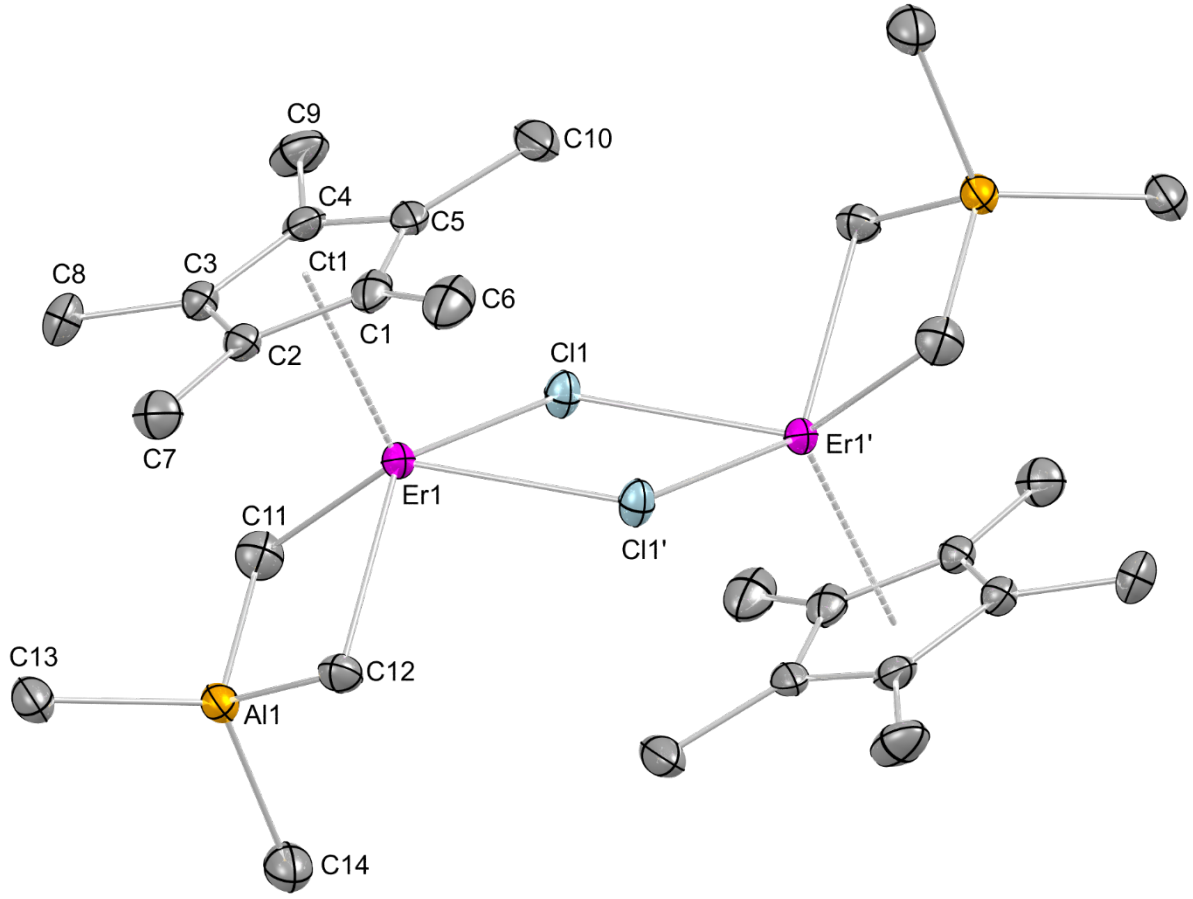

Figure S25. Crystal structure of $\mathbf{7^{Er}}$. Hydrogen atoms are omitted for clarity. Atomic displacement ellipsoids are set at the 50% probability level. Selected interatomic distances [Å] and angles [°]: Er1–C1 2.583(3), Er1–C2 2.601(3), Er1–C3 2.596(3), Er1–C4 2.571(3), Er1–C5 2.565(3), Er1···Ct1 2.2896, Er1–C11 2.526(3), Er1–C12 2.509(3), Er1···Al1 3.0659(8), Er1–Cl1 2.6628(6), Er1–Cl1' 2.6801(7), Er1···Er1' 4.1492, C1–C2 1.420(4), C2–C3 1.416(4), C3–C4 1.422(4), C4–C5 1.412(4), C1–C5 1.422(4), C1–C6 1.501(4), Al1–C11 2.073(3), Al1–C12 2.070(3), Al1–C13 1.966(3), Al1–C14 1.969(3), C1–C2–C3 108.2(2), C2–C3–C4 107.9(2), C3–C4–C5 108.1(2), C4–C5–C1 108.2(2), C5–C1–C2 107.7(2), C11–Er1–C12 83.94(1), C11–Al1–C12 108.73(2), C13–Al1–C14 117.93(2), Er1–C11–Al1 82.99(2), Er1–C12–Al1 83.46(1), Cl1–Er1–C11 83.55(7), Cl1'–Er1–C12 82.93(7), Cl1–Er1–Cl1' 78.10(2), Er1–Cl1–Er1' 101.90.

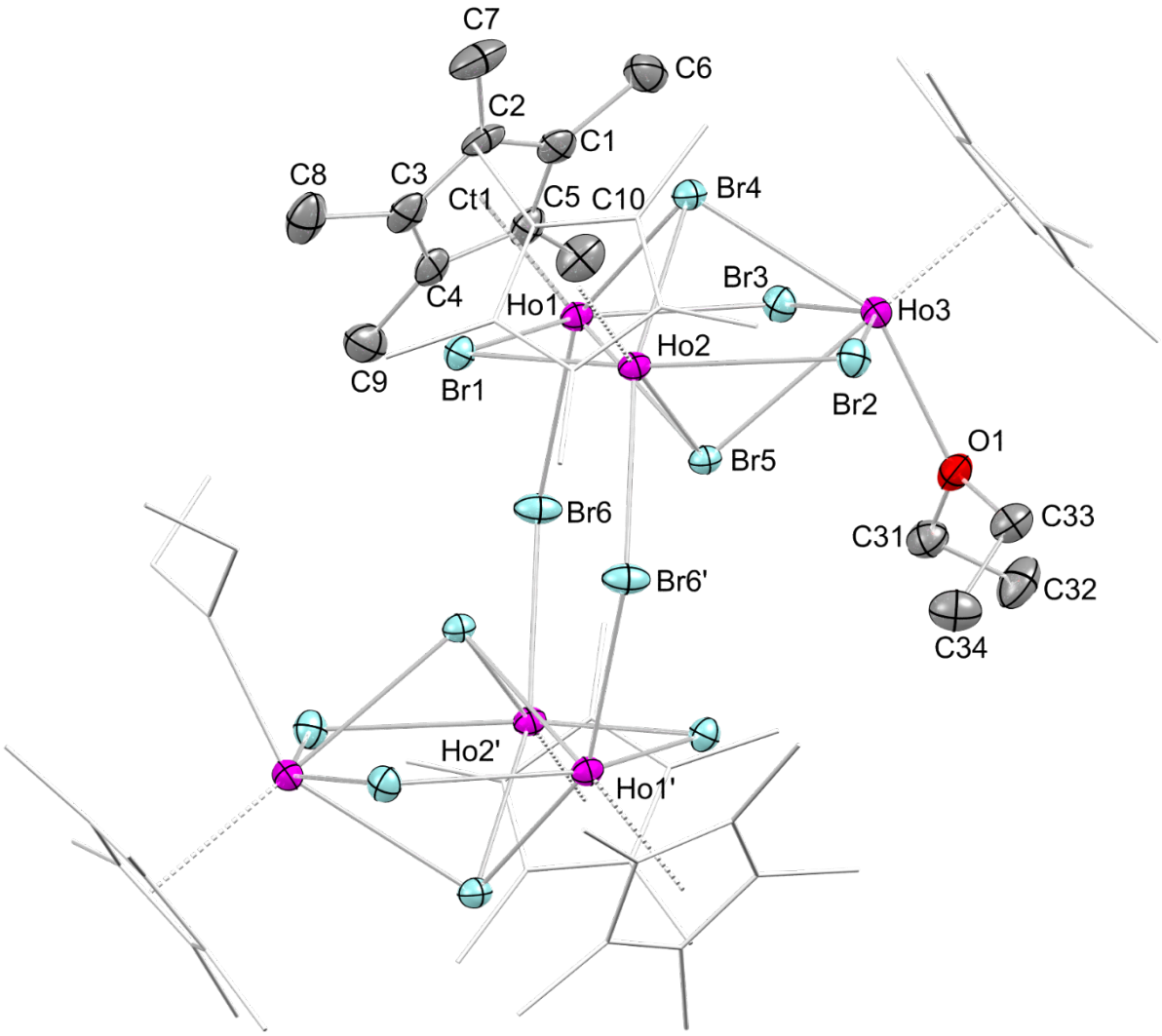

Figure S26. Crystal structure of **8**. Hydrogen atoms and one lattice toluene molecule are omitted for clarity. Ancillary Cp* ligands and coordinated diethyl ether (except for one each) are represented by a wireframe model for improved visualization. Atomic displacement ellipsoids are set at the 50% probability level. Selected interatomic distances [Å] and angles [°]: Ho1–C1 2.607(5), Ho1–C2 2.622(5), Ho1–C3 2.657(5), Ho1–C4 2.646(5), Ho1–C5 2.605(5), Ho1···Ct1 2.3373, Ho1–Br1 2.8335(6), Ho1–Br3 2.8824(6), Ho1–Br4 2.9971(6), Ho1–Br5 2.9492(5), Ho1–Br6 2.8407(6), Ho3–O1 2.364(4), C1–C2 1.397(8), C2–C3 1.397(8), C3–C4 1.394(7), C4–C5 1.442(7), C1–C5 1.423(7), C1–C6 1.512(7), C1–C2–C3 108.5(5), C2–C3–C4 109.0(5), C3–C4–C5 107.6(5), C4–C5–C1 106.5(5), C5–C1–C2 108.3(5), Br1–Ho1–Br3 145.970(2), Br1–Ho1–Br4 77.268(2), Br1–Ho1–Br5 76.311(2), Br1–Ho1–Br6 96.662(2), Br4–Ho1–Br5 72.066(2), Br4–Ho1–Br6 148.918(2), Br5–Ho1–Br6 76.872(2), Br2–Ho3–O1 92.67(9), Br4–Ho3–O1 149.00(9), Br5–Ho3–O1 76.24(9), Ho1–Br1–Ho2 94.260(2), Ho1–Br4–Ho2 86.867(2), Ho1–Br5–Ho2 90.399(2), Ho1–Br6–Ho2' 140.99(2).

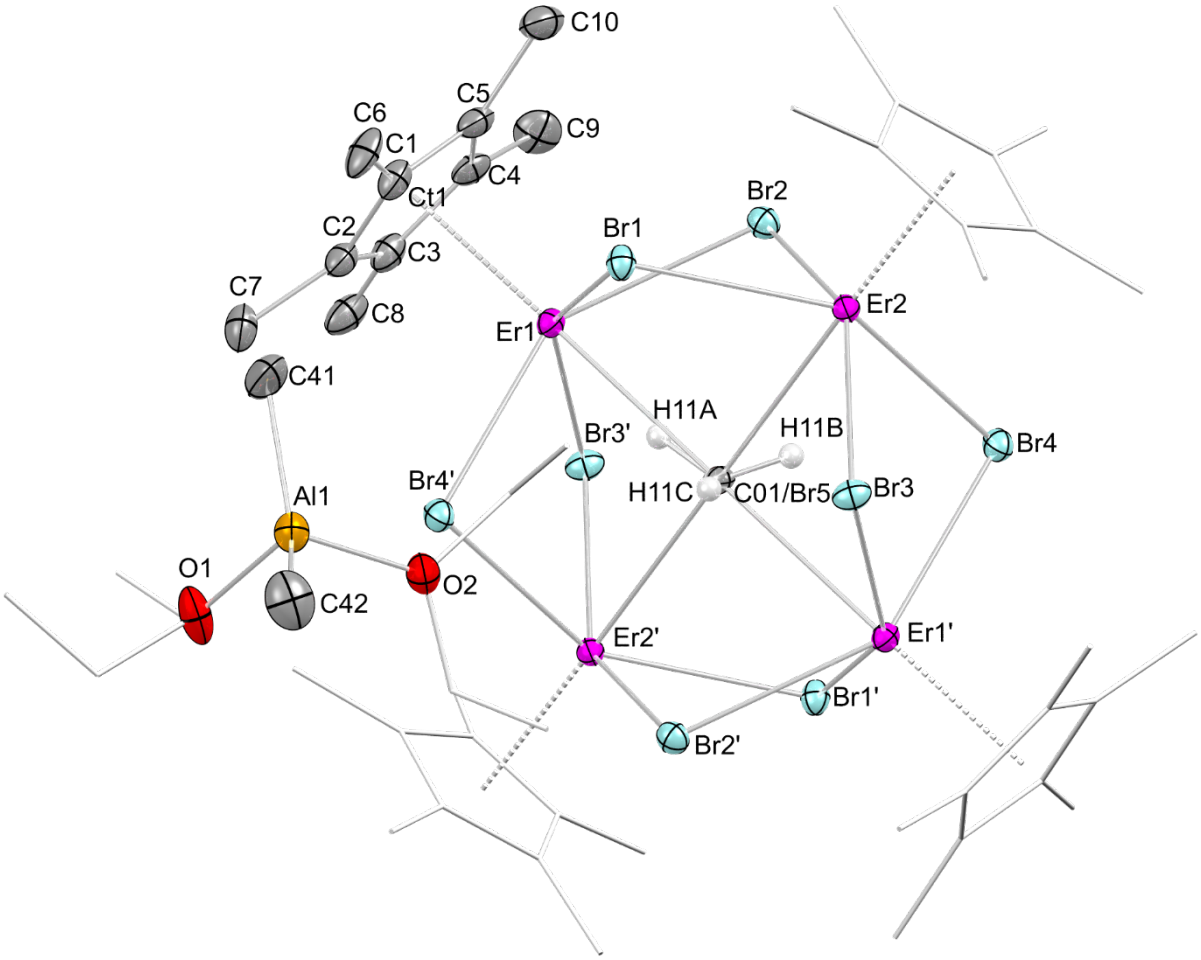

Figure S27. Crystal structure of **9**. Hydrogen atoms are omitted for clarity. Ancillary Cp* ligands (except for one) and ethyl groups of the bis(diethyl ether) dimethyl aluminum cation are represented by a wireframe model for improved visualization. Atomic displacement ellipsoids are set at the 50% probability level. Selected interatomic distances [Å] and angles [°]: Er1–C1 2.612(3), Er1–C2 2.638(3), Er1–C3 2.621(3), Er1–C4 2.579(3), Er1–C5 2.580(3), Er1···Ct1 2.3085, Er1–Br1 2.8603(4), Er1–Br2 2.8794(4), Er1–Br3' 2.8616(4), Er1–Br4' 2.8604(4), Er1–C01/Br5 2.85237(2), Al1–C41 1.932(5), Al1–O1 1.871(3), C1–C2 1.414(5), C2–C3 1.419(5), C3–C4 1.415(5), C4–C5 1.430(5), C1–C5, 1.429(5), C1–C6 1.514(5), C1–C2–C3 107.9(3), C2–C3–C4 108.6(3), C3–C4–C5 107.8(3), C4–C5–C1 107.4(3), C5–C1–C2 108.3(3), Br1–Er1–Br2 79.181(1), Br3'–Er1–Br4' 82.210(1), Br1–Er1–Br3' 146.788(2), Br1–Er1–Br4' 90.922(2), Er1–Br1–Er2 90.693(2), Er1–Br2–Er2 89.104(2), Er1–C01/Br5–Er2 90.620(6), Er1–C01/Br5–Er1' 180.0, Ct1···Er1–C01/Br5 179.47, C41–Al1–C42 125.6(3), O1–Al1–O2 96.18(2), C41–Al1–O1 107.7(2).

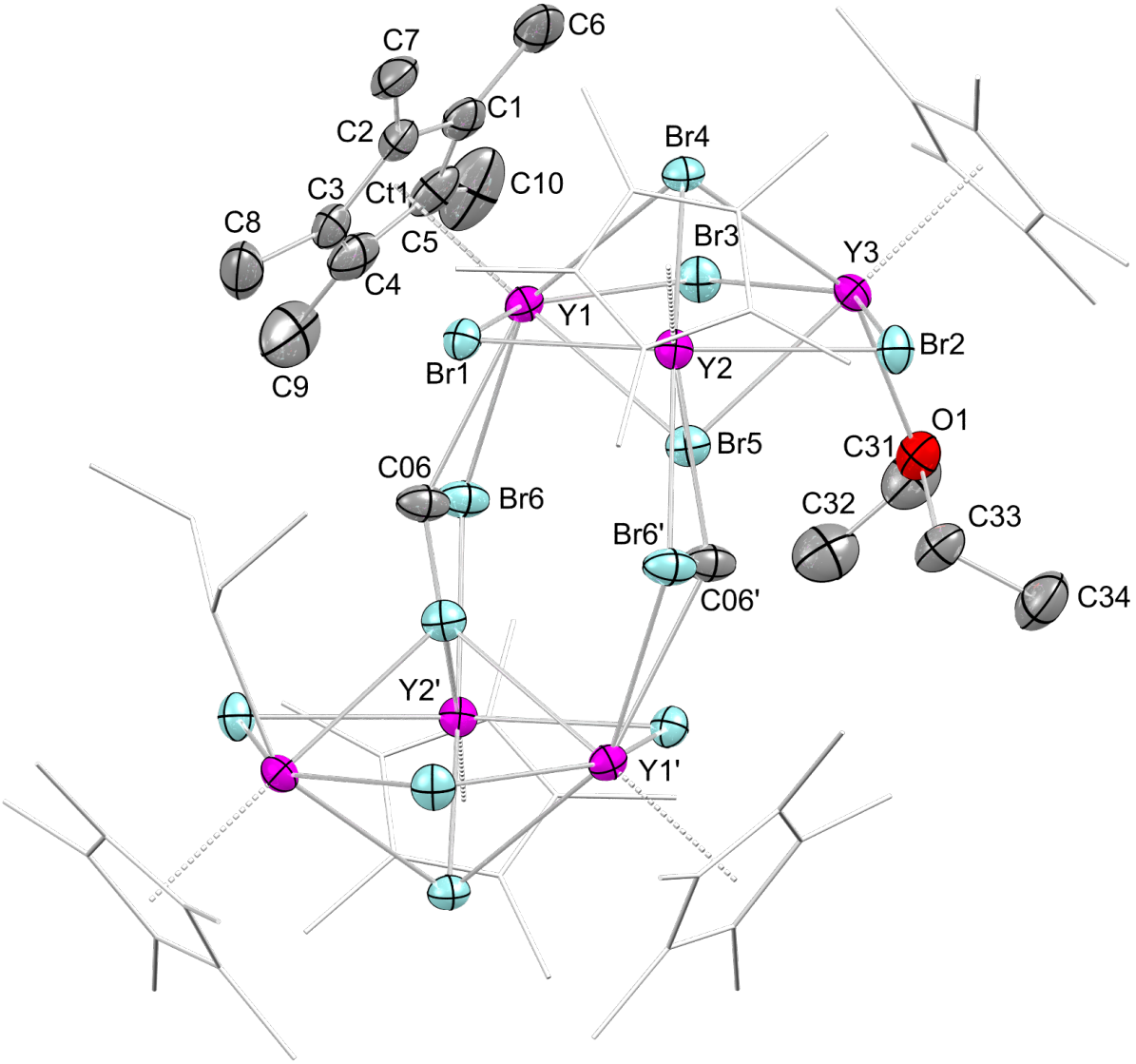

Figure S28. Crystal structure of $\mathbf{4^{Y}Et_2O}$. Hydrogen atoms and one lattice toluene molecule are omitted for clarity. Ancillary Cp* ligands and coordinated diethyl ether (except for one each) are represented by a wireframe model for improved visualization. Atomic displacement ellipsoids are set at the 50% probability level. Selected interatomic distances [Å] and angles [°]: Y1–C1 2.607(6), Y1–C2 2.620(6), Y1–C3 2.629(6), Y1–C4 2.647(7), Y1–C5 2.621(6), Y1···Ct1 2.3339, Y1–Br1 2.8534(8), Y1–Br3 2.8718(8), Y1–Br4 3.0717(9), Y1–Br5 2.9170(9), Y1–Br6 2.8135(1), Y1–C06 2.86(4), Y3–O1 2.366(4), C1–C2 1.411(9), C2–C3 1.427(9), C3–C4 1.391(1), C4–C5 1.396(2), C1–C5 1.417(1), C1–C6 1.491(1), C1–C2–C3 107.4(6), C2–C3–C4 108.7(6), C3–C4–C5 107.8(7), C4–C5–C1 109.2(6), C5–C1–C2 107.0(6), Br1–Y1–Br3 145.72(3), Br1–Y1–Br4 75.81(2), Br1–Y1–Br5 76.75(2), Br1–Y1–Br6 99.14(3), Br4–Y1–Br5 71.31(2), Br4–Y1–Br6 149.29(3), Br5–Y1–Br6 78.03(3), Br2–Y3–O1 92.42(2), Br4–Y3–O1 149.14(2), Br5–Y3–O1 76.32(2), Y1–Br1–Y2 94.20(2), Y1–Br4–Y2 86.67(2), Y1–Br5–Y2 90.85(2), Y1–Br6–Y2' 141.60(4), Y1–C06–Y2' 143.3(2).

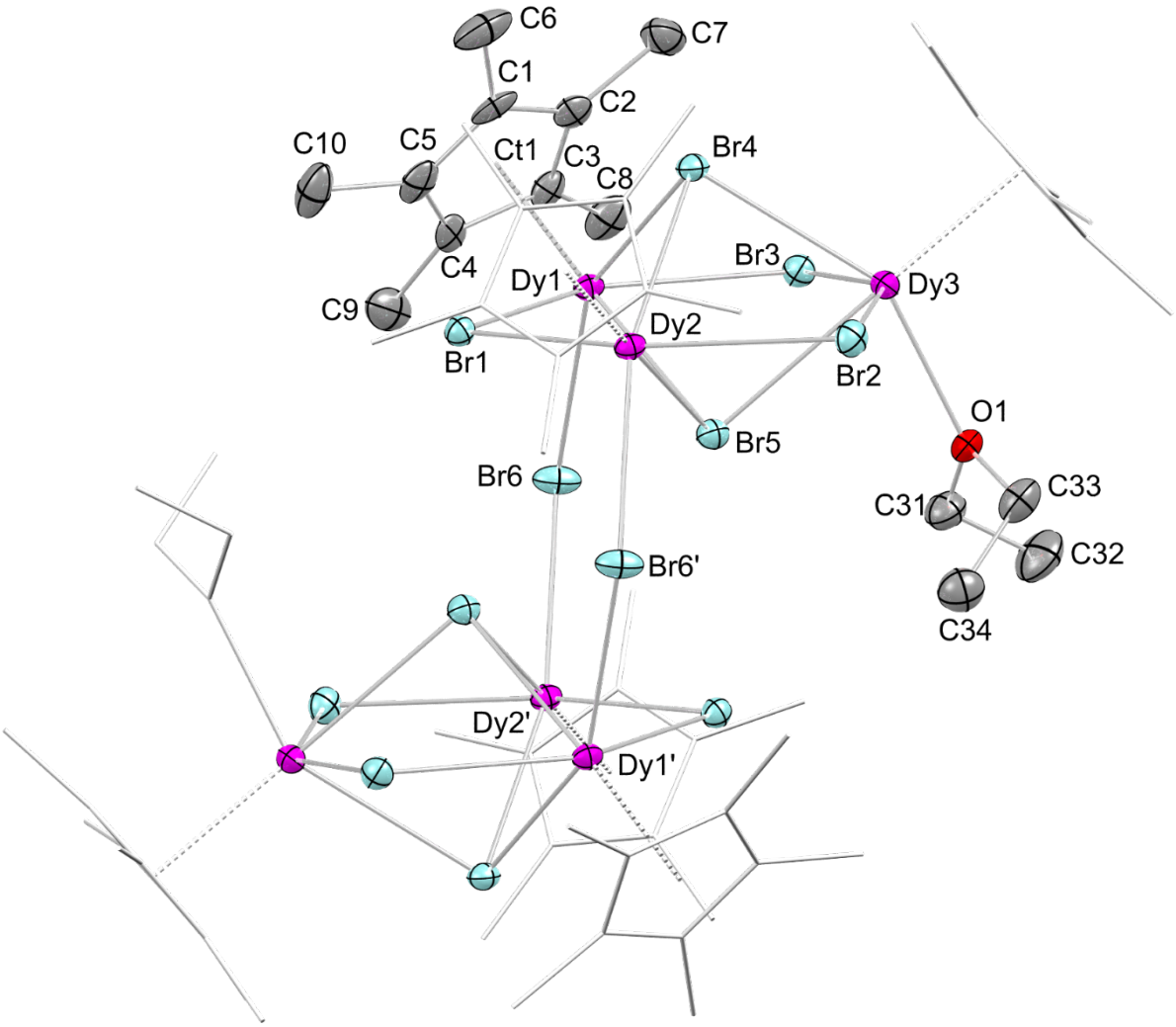

Figure S29. Crystal structure of $\mathbf{4^{Dy}Et_2O}$. Hydrogen atoms and one lattice toluene molecule are omitted for clarity. Ancillary Cp* ligands and coordinated diethyl ether (except for one each) are represented by a wireframe model for improved visualization. Atomic displacement ellipsoids are set at the 50% probability level. Selected interatomic distances [Å] and angles [°]: Dy1–C1 2.637(5), Dy1–C2 2.610(5), Dy1–C3 2.622(5), Dy1–C4 2.651(5), Dy1–C5 2.666(5), Dy1···Ct1 2.3572, Dy1–Br1 2.8487(7), Dy1–Br3 2.8925(7), Dy1–Br4 3.0088(7), Dy1–Br5 2.9451(7), Dy1–Br6 2.8528(6), Dy3–O1 2.371(3), C1–C2 1.389(8), C2–C3 1.417(7), C3–C4 1.432(7), C4–C5 1.402(8), C1–C5 1.404(8), C1–C6 1.512(8), C1–C2–C3 108.8(5), C2–C3–C4 106.8(5), C3–C4–C5 107.6(5), C4–C5–C1 108.5(5), C5–C1–C2 108.4(5), Br1–Dy1–Br3 146.234(2), Br1–Dy1–Br4 77.462(2), Br1–Dy1–Br5 76.257(2), Br1–Dy1–Br6 96.550(2), Br4–Dy1–Br5 72.062(2), Br4–Dy1–Br6 148.974(2), Br5–Dy1–Br6 76.94(2), Br2–Dy3–O1 92.48(9), Br4–Dy3–O1 148.89(8), Br5–Dy3–O1 76.08(8), Dy1–Br1–Dy2 93.925(2), Dy1–Br4–Dy2 86.729(2), Dy1–Br5–Dy2 90.686(2), Dy1–Br6–Dy2' 141.24(2).

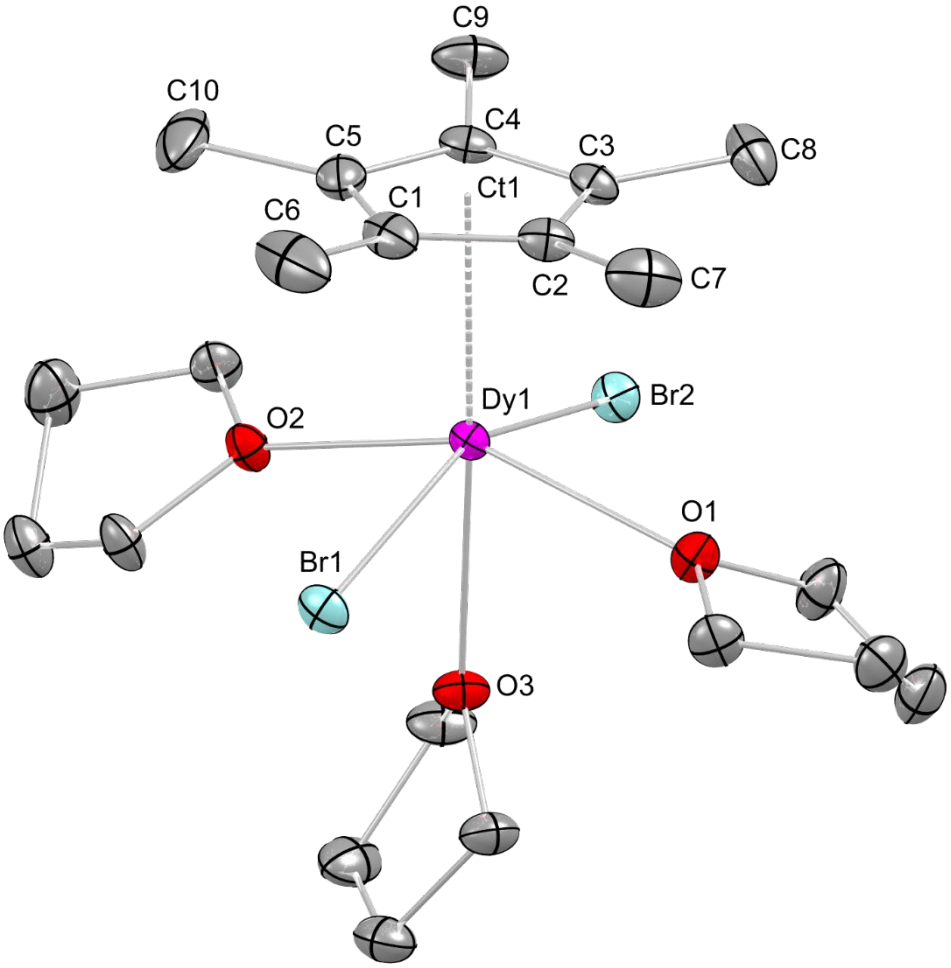

Figure S30. Crystal structure of **4^{Dy}THF**. Hydrogen atoms are omitted for clarity. Atomic displacement ellipsoids are set at the 50% probability level. Selected interatomic distances [Å] and angles [°]: Dy1–C1 2.716(3), Dy1–C2 2.668(2), Dy1–C3 2.649(2), Dy1–C4 2.691(2), Dy1–C5 2.724(3), Dy1···Ct1 2.4043, Dy1–Br1 2.8282(4) , Dy1–Br2 2.8301(4) , Dy1–O1 2.4243(2) , Dy1–O2 2.3834(2) , Dy1–O3 2.4866(2), C1–C2 1.410(4) , C2–C3 1.412(3) , C3–C4 1.419(4), C4–C5 1.421(4), C1–C5 1.419(4), C1–C6 1.504(4), C1–C2–C3 108.3(2), C2–C3–C4 108.0(2), C3–C4–C5 107.8(2), C4–C5–C1 107.8(2), C5–C1–C2 108.1(2), Br1–Dy1–Br2 154.587(9), Br1–Dy1–O1 86.52(4), Br1–Dy1–O2 88.09(4), Br1–Dy1–O3 76.89(4), O1–Dy1–O2 150.05(6), O1–Dy1–O3 75.65(6), O2–Dy1–O3 74.43(6), Ct1···Dy1–Br1 103.00, Ct1···Dy1–Br2 102.41, Ct1···Dy1–O1 106.75, Ct1···Dy1–O2 103.17, Ct1···Dy1–O3 177.60.

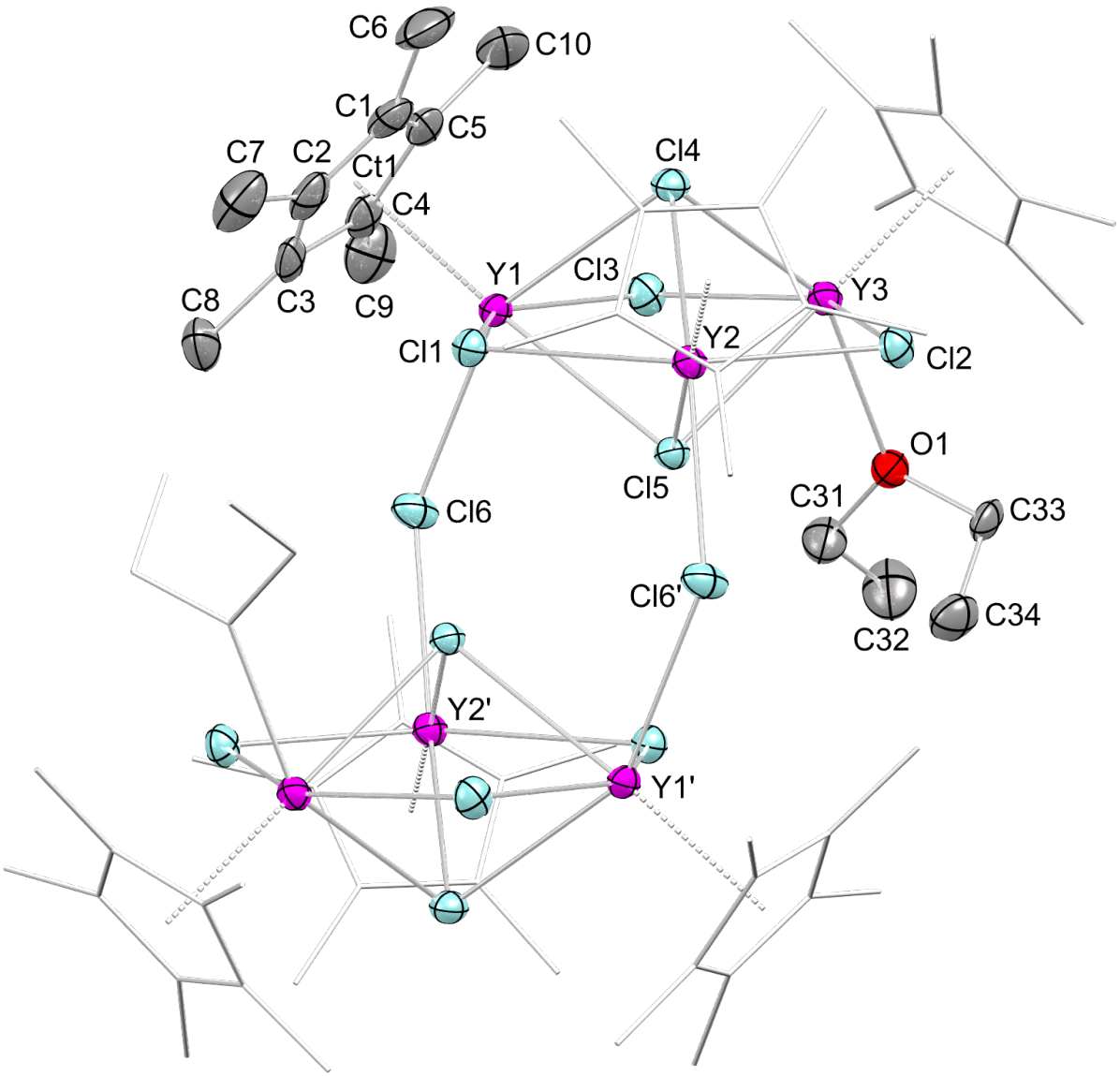

Figure S31. Crystal structure of **5^{Y}Et$_2$O**. Hydrogen atoms and one lattice toluene molecule are omitted for clarity. Ancillary Cp* ligands and coordinated diethyl ether (except for one each) are represented by a wireframe model for improved visualization. Atomic displacement ellipsoids are set at the 50% probability level. Selected interatomic distances [Å] and angles [°]: Y1–C1 2.640(5), Y1–C2 2.660(5), Y1–C3 2.647(5), Y1–C4 2.610(4), Y1–C5 2.630(5), Y1···Ct1 2.3456, Y1–Cl1 2.6926(8), Y1–Cl3 2.7305(8), Y1–Cl4 2.8495(8), Y1–Cl5 2.8032(8), Y1–Cl6 2.6861(8), Y3–O1 2.349(2), C1–C2 1.376(8), C2–C3 1.430(8), C3–C4 1.427(7), C4–C5 1.430(7), C1–C5 1.393(8), C1–C6 1.507(7), C1–C2–C3 108.4(5), C2–C3–C4 106.7(4), C3–C4–C5 107.4(5), C4–C5–C1 107.5(4), C5–C1–C2 109.9(5), Cl1–Y1–Cl3 144.70(1), Cl1–Y1–Cl4 76.18(1), Cl1–Y1–Cl5 76.20(1), Cl1–Y1–Cl6 93.01(3), Cl4–Y1–Cl5 70.80(1), Cl4–Y1–Cl6 147.76(1), Cl5–Y1–Cl6 77.16(1), Cl2–Y3–O1 92.26(6), Cl4–Y3–O1 148.24(6), Cl5–Y3–O1 76.72(6), Y1–Cl1–Y2 95.55(3), Y1–Cl4–Y2 87.52(2), Y1–Cl5–Y2 91.37(2), Y1–Cl6–Y2' 144.10(3).

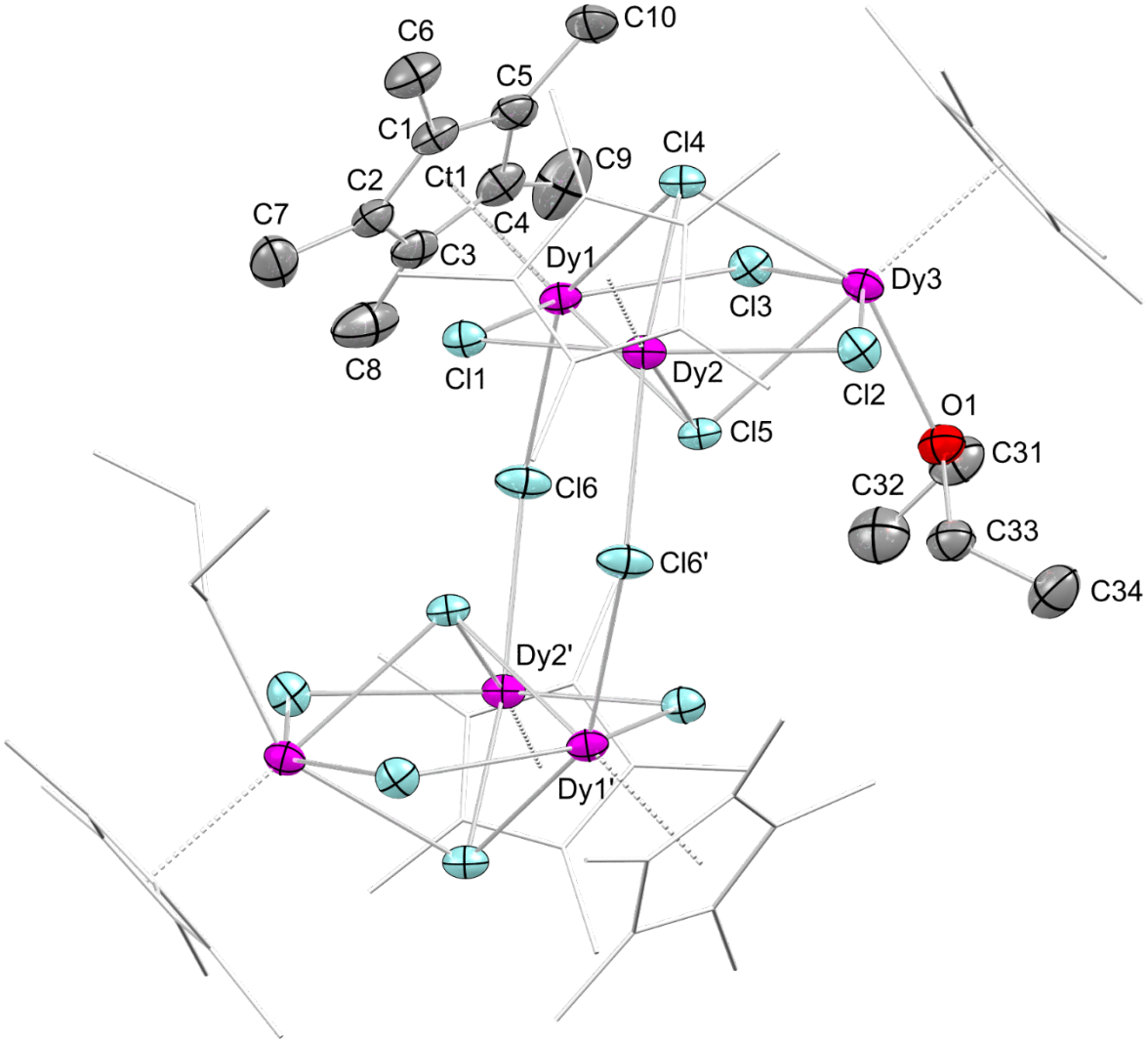

Figure S32. Crystal structure of **5^{Dy}Et$_2$O**. Hydrogen atoms and one lattice toluene molecule are omitted for clarity. Ancillary Cp* ligands and coordinated diethyl ether (except for one each) are represented by a wireframe model for improved visualization. Atomic displacement ellipsoids are set at the 50% probability level. Selected interatomic distances [Å] and angles [°]: Dy1–C1 2.605(6), Dy1–C2 2.644(6), Dy1–C3 2.646(6), Dy1–C4 2.633(6), Dy1–C5 2.623(6), Dy1···Ct1 2.3358, Dy1–Cl1 2.7057(2), Dy1–Cl3 2.7261(2), Dy1–Cl4 2.9216(2), Dy1–Cl5 2.7764(2), Dy1–Cl6 2.6801(2), Dy3–O1 2.363(4), C1–C2 1.405(9), C2–C3 1.413(9), C3–C4 1.398(1), C4–C5 1.429(9), C1–C5 1.422(9), C1–C6 1.503(9), C1–C2–C3 108.5(6), C2–C3–C4 108.1(6), C3–C4–C5 108.4(6), C4–C5–C1 107.0(6), C5–C1–C2 108.0(6), Cl1–Dy1–Cl3 144.24(5), Cl1–Dy1–Cl4 74.87(4), Cl1–Dy1–Cl5 76.42(4), Cl1–Dy1–Cl6 99.26(5), Cl4–Dy1–Cl5 70.18(4), Cl4–Dy1–Cl6 148.10(5), Cl5–Dy1–Cl6 77.95(5), Cl2–Dy3–O1 92.50(2), Cl4–Dy3–O1 147.96(2), Cl5–Dy3–O1 76.36(2), Dy1–Cl1–Dy2 95.43(5), Dy1–Cl4–Dy2 87.54(2), Dy1–Cl5–Dy2 91.57(4), Dy1–Cl6–Dy2' 144.17(6).

IR-Spectra

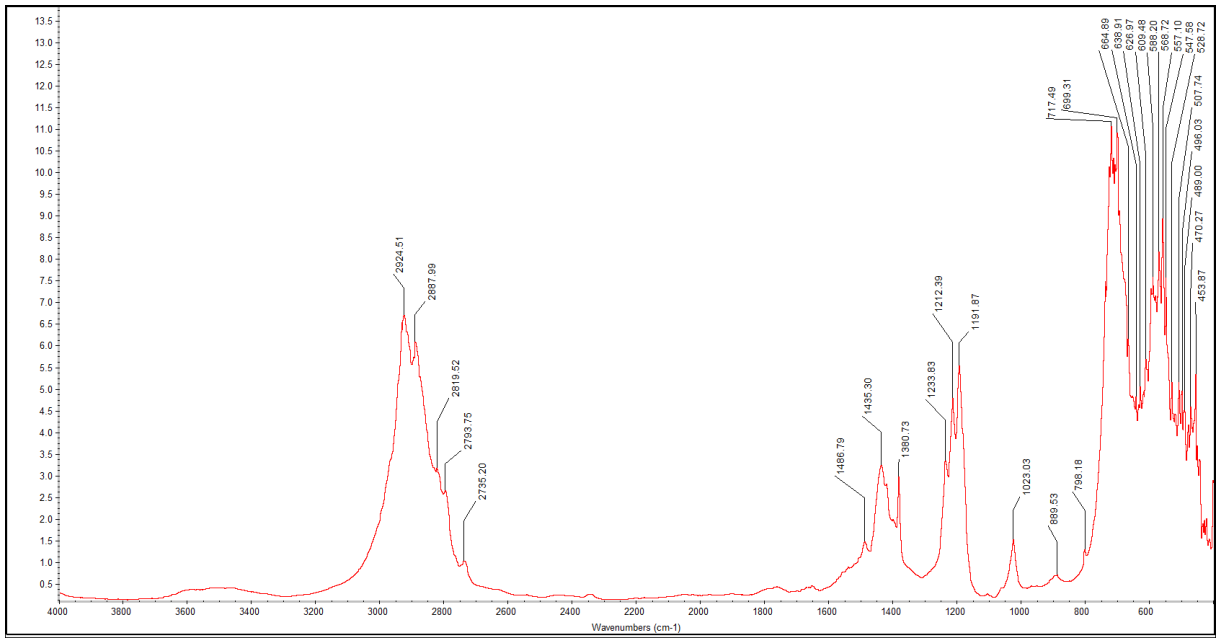

Figure S33. DRIFT spectrum of $Cp^*Er(AlMe_4)_2$ (**1**).

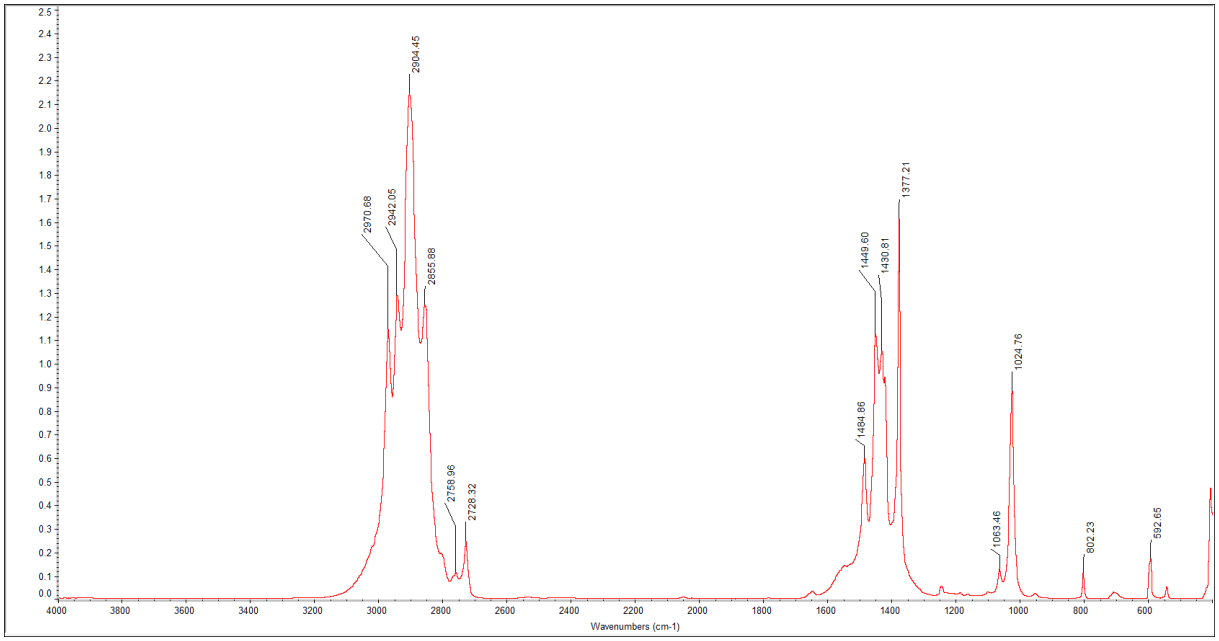

Figure S34. DRIFT spectrum of $[Cp^*YI_2]_4$ (**2^Y**).

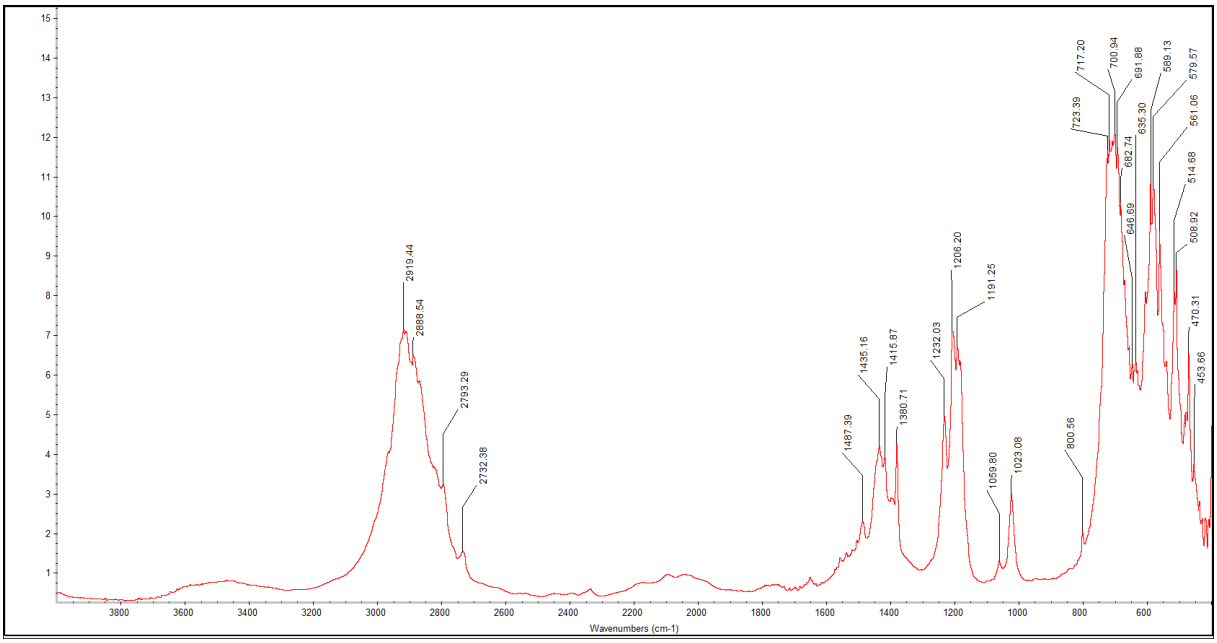

Figure S35. DRIFT spectrum of $[Cp^*TbI_2]_4$ ($\mathbf{2^{Tb}}$).

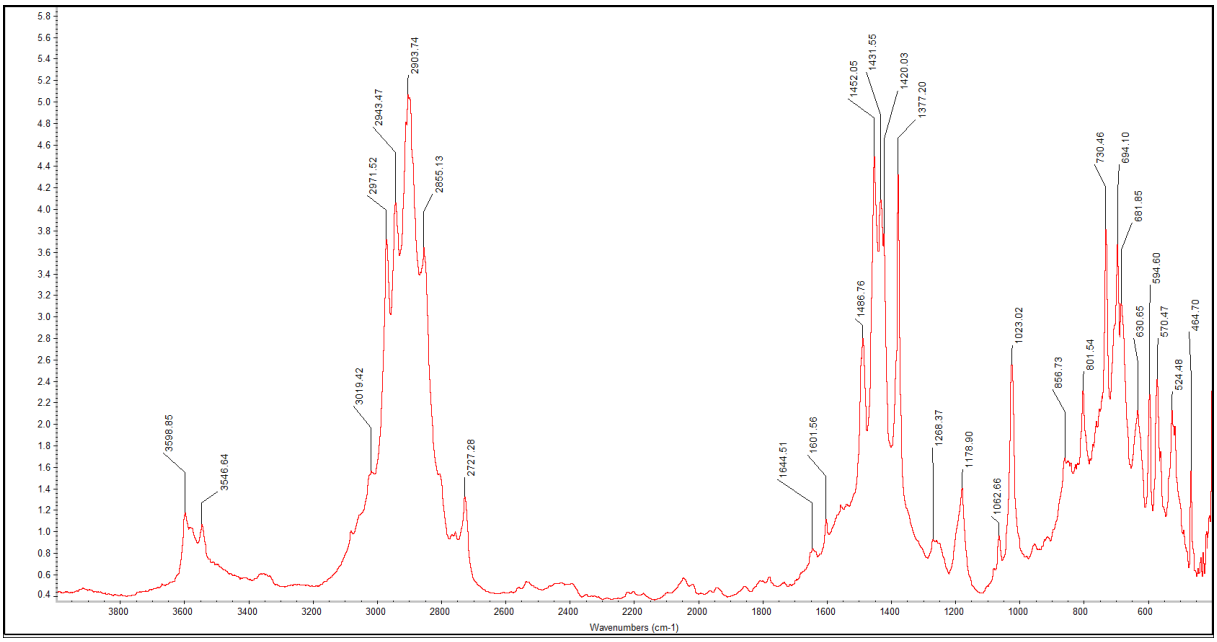

Figure S36. DRIFT spectrum of $[Cp^*DyI_2]_4$ ($\mathbf{2^{Dy}}$).

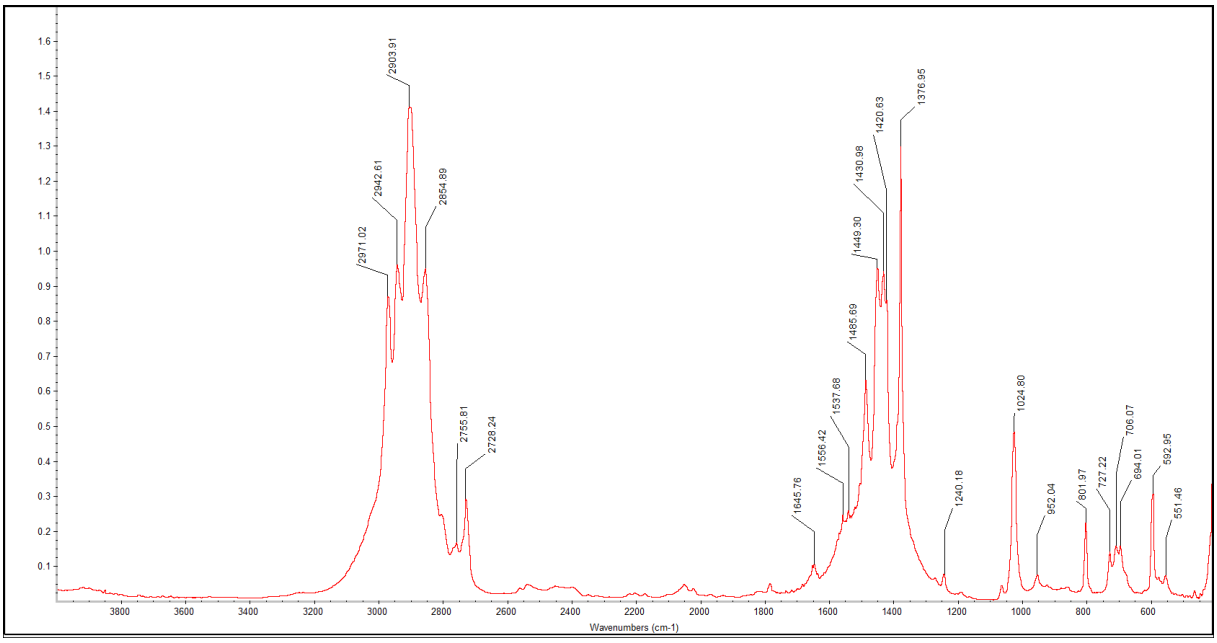

Figure S37. DRIFT spectrum of $[Cp^*HoI_2]_4$ ($\mathbf{2^{Ho}}$).

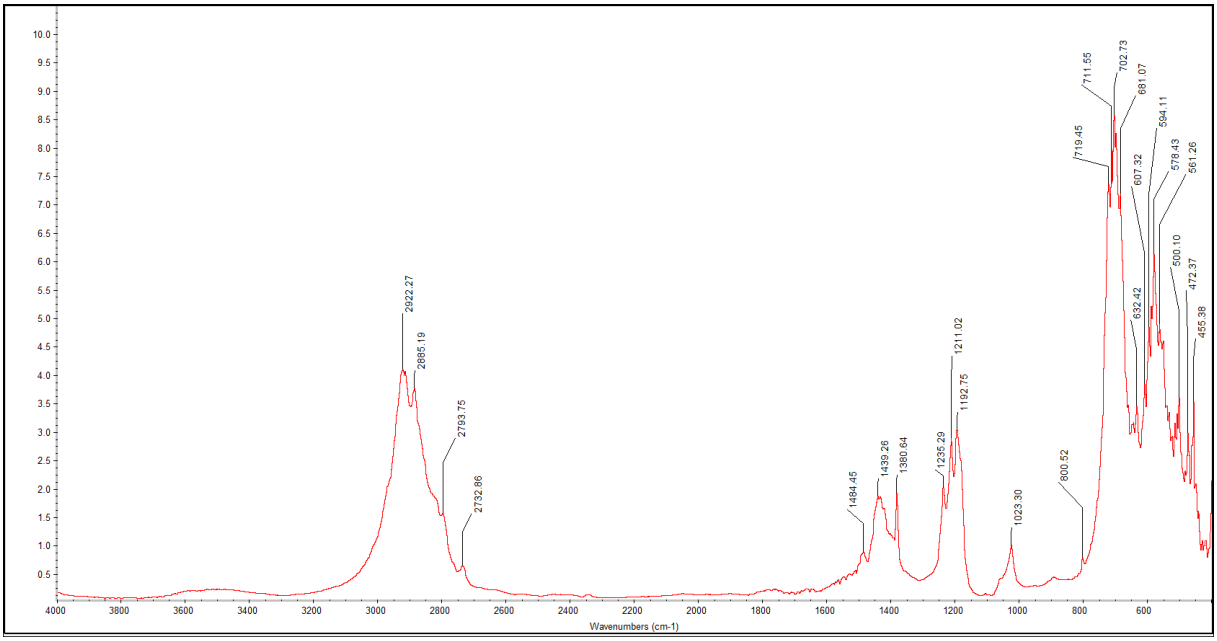

Figure S38. DRIFT spectrum of $[Cp^*ErI_2]_4$ ($\mathbf{2^{Er}}$).

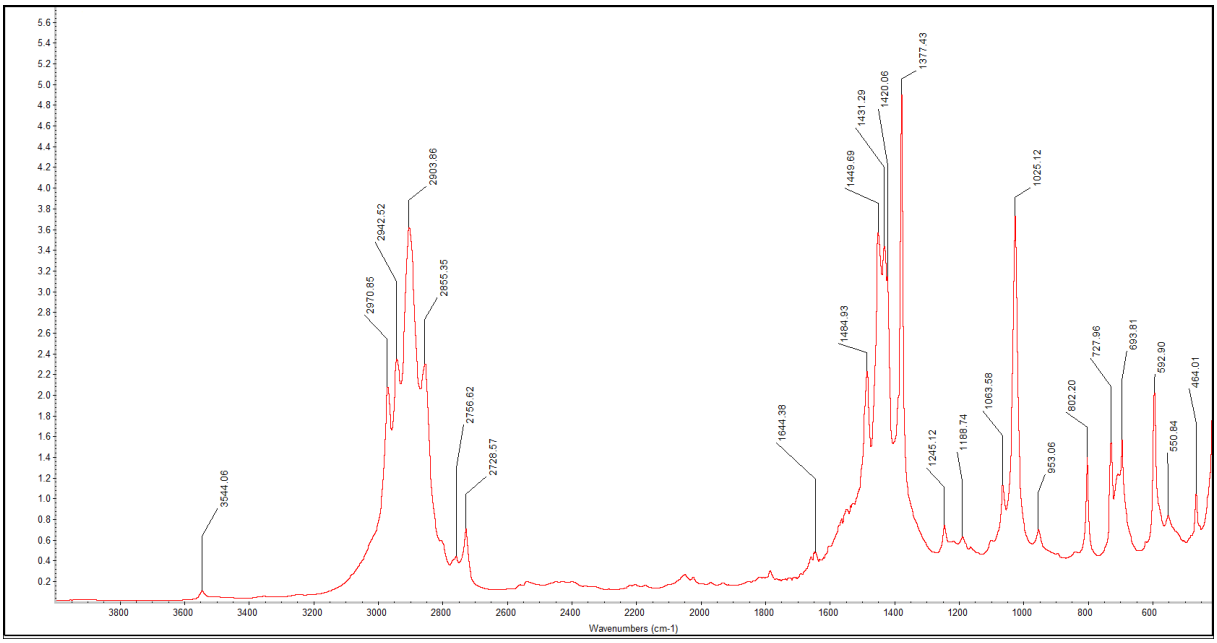

Figure S39. DRIFT spectrum of $[Cp^*Y/DyI_2]_4$ (**2**$^{Y/Dy}$).

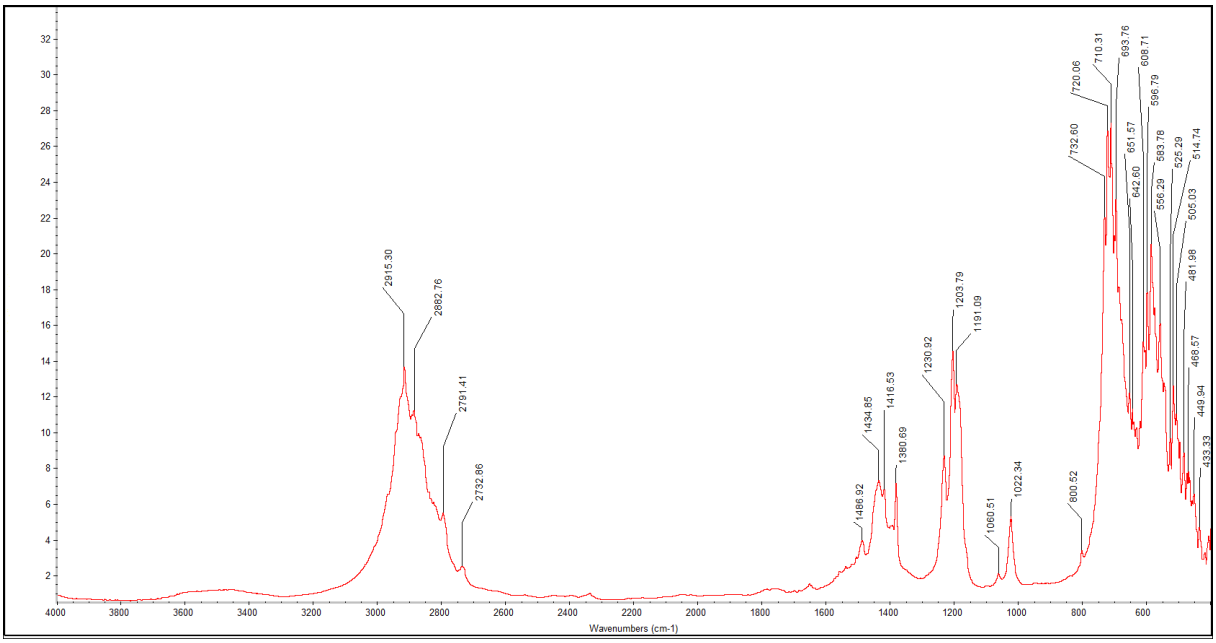

Figure S40. DRIFT spectrum of $[(Cp^*_4Gd_4I_7\{AlMe_4\}_2)_2]$ (**3**).

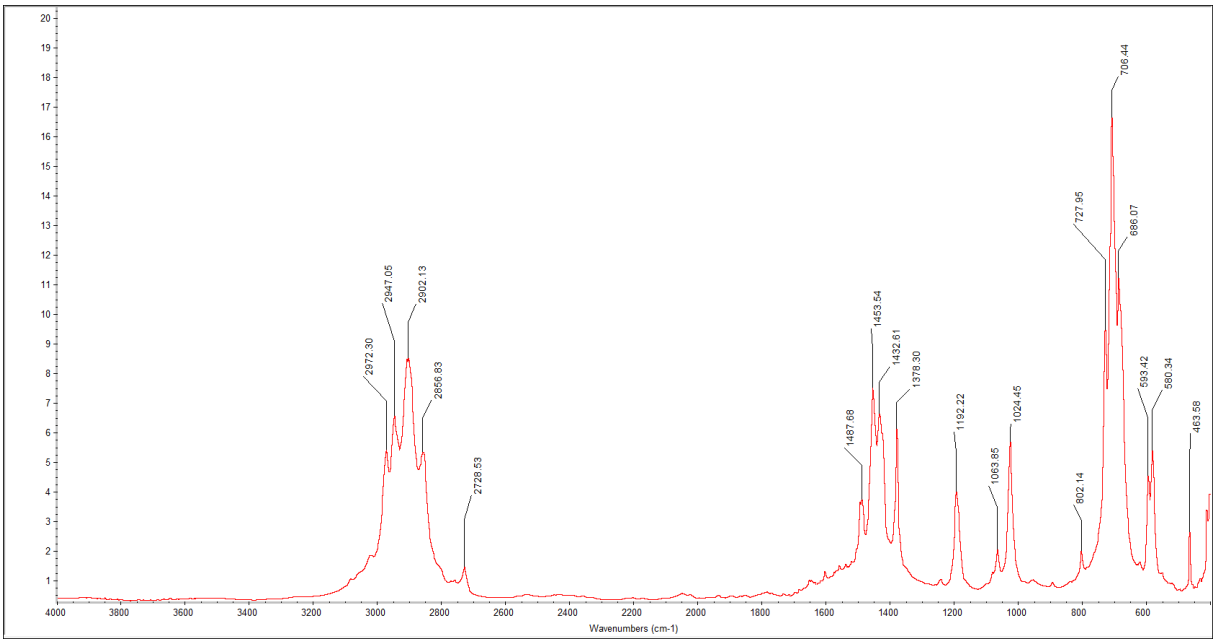

Figure S41. DRIFT spectrum of [Cp*$_4$Y$_4$Br$_9$(AlMe$_2$)] (**4^{Y}**).

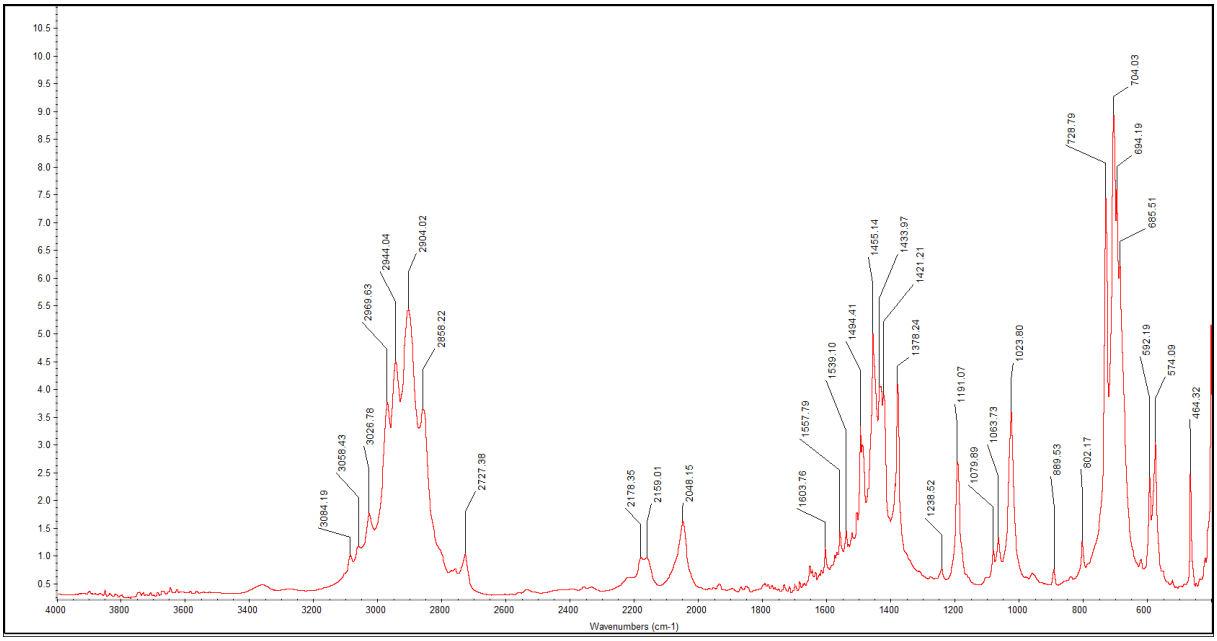

Figure S42. DRIFT spectrum of [Cp*$_4$Gd$_4$Br$_9$(AlMe$_2$)] (**4^{Gd}**).

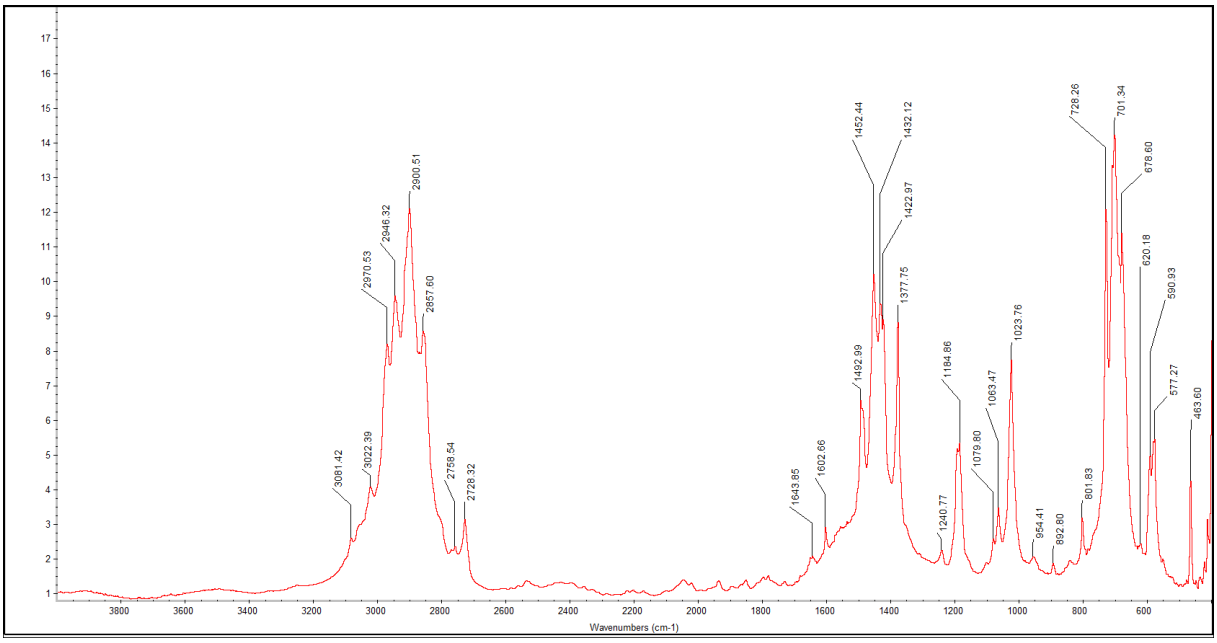

Figure S43. DRIFT spectrum of [Cp*$_4$Tb$_4$Br$_9$(AlMe$_2$)] (**4^{Tb}**).

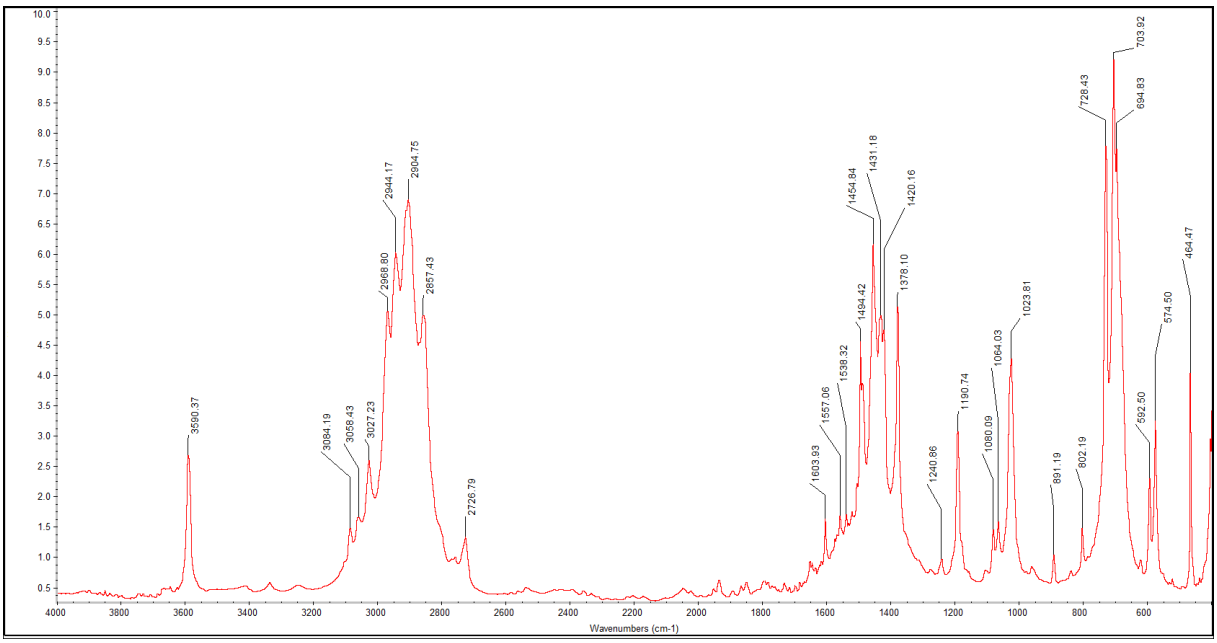

Figure S44. DRIFT spectrum of [Cp*$_4$Dy$_4$Br$_9$(AlMe$_2$)] (**4^{Dy}**).

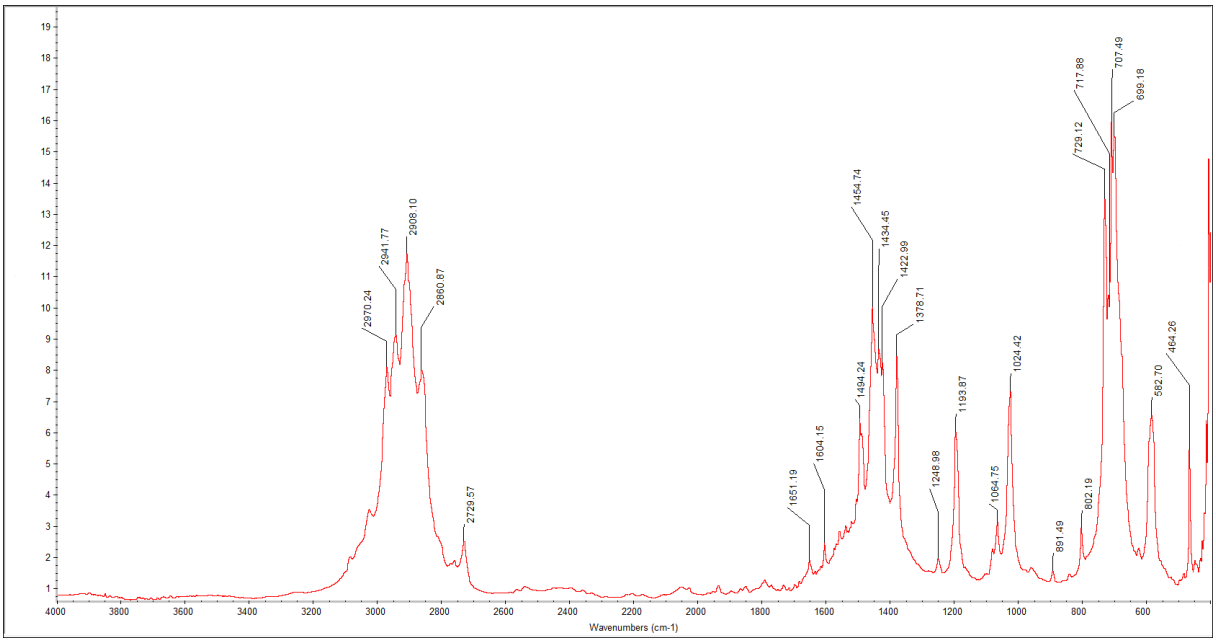

Figure S45. DRIFT spectrum of $[Cp^*_4Y_4Cl_{10}(AlMe_2)_2]$ (**5^{Y}**).

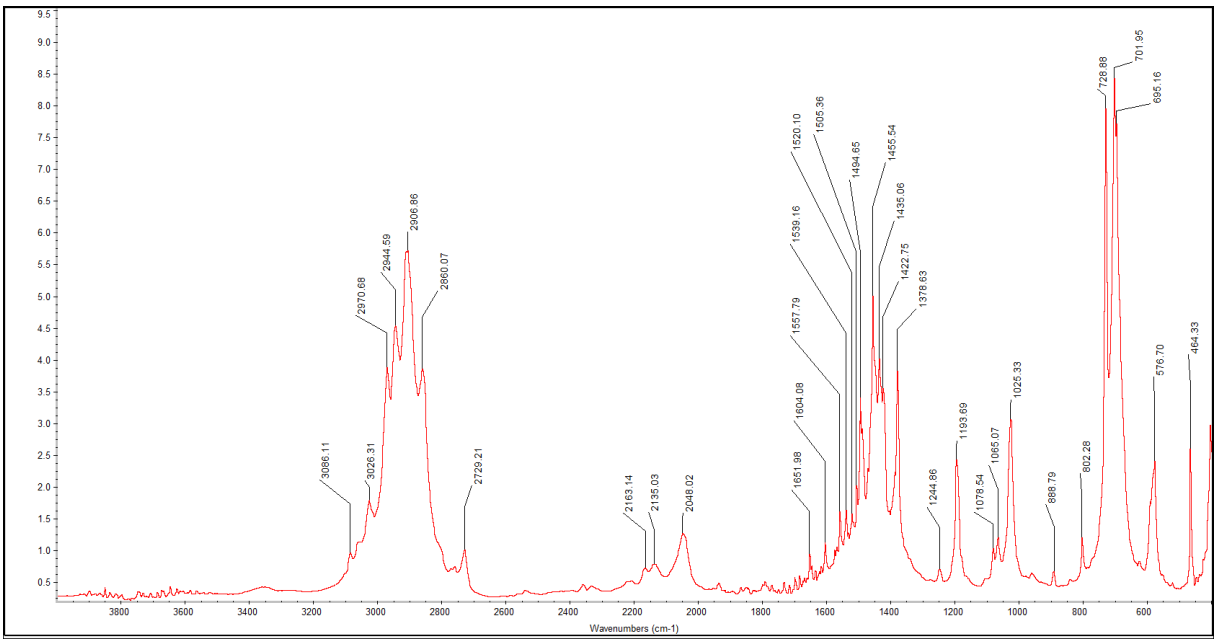

Figure S46. DRIFT spectrum of $[Cp^*_4Gd_4Cl_{10}(AlMe_2)_2]$ (**5^{Gd}**).

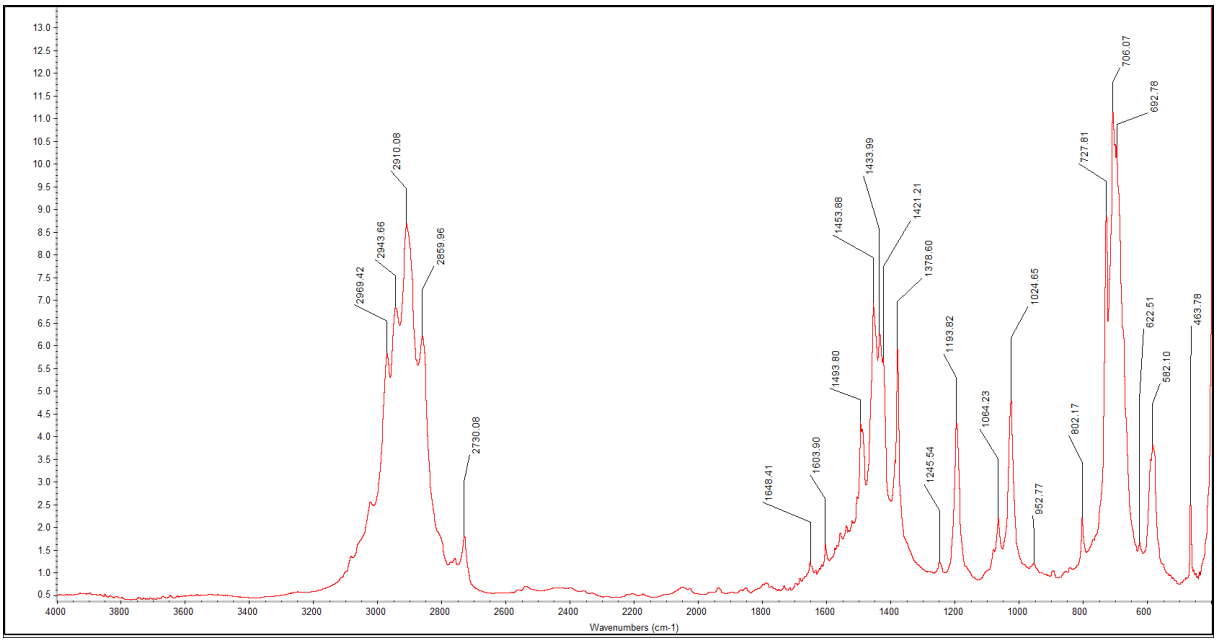

Figure S47. DRIFT spectrum of [Cp*$_4$Tb$_4$Cl$_9$(AlMe$_2$)] (**6^{Tb}**).

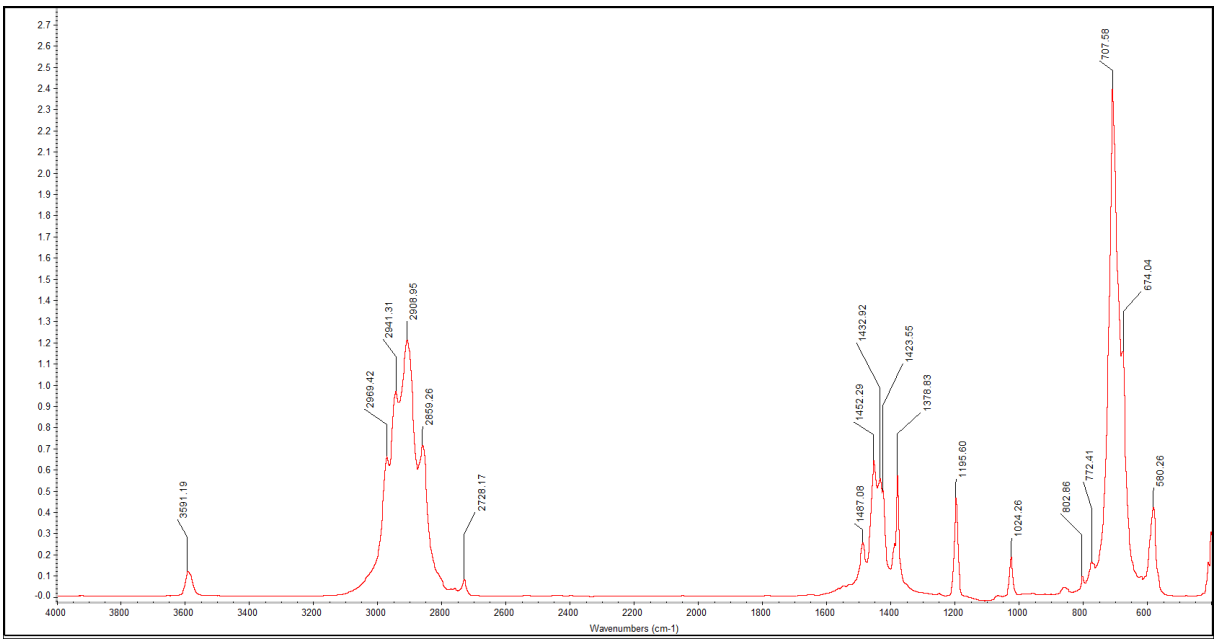

Figure S48. DRIFT spectrum of [Cp*$_4$Dy$_4$Cl$_9$(AlMe$_2$)] (**6^{Dy}**).

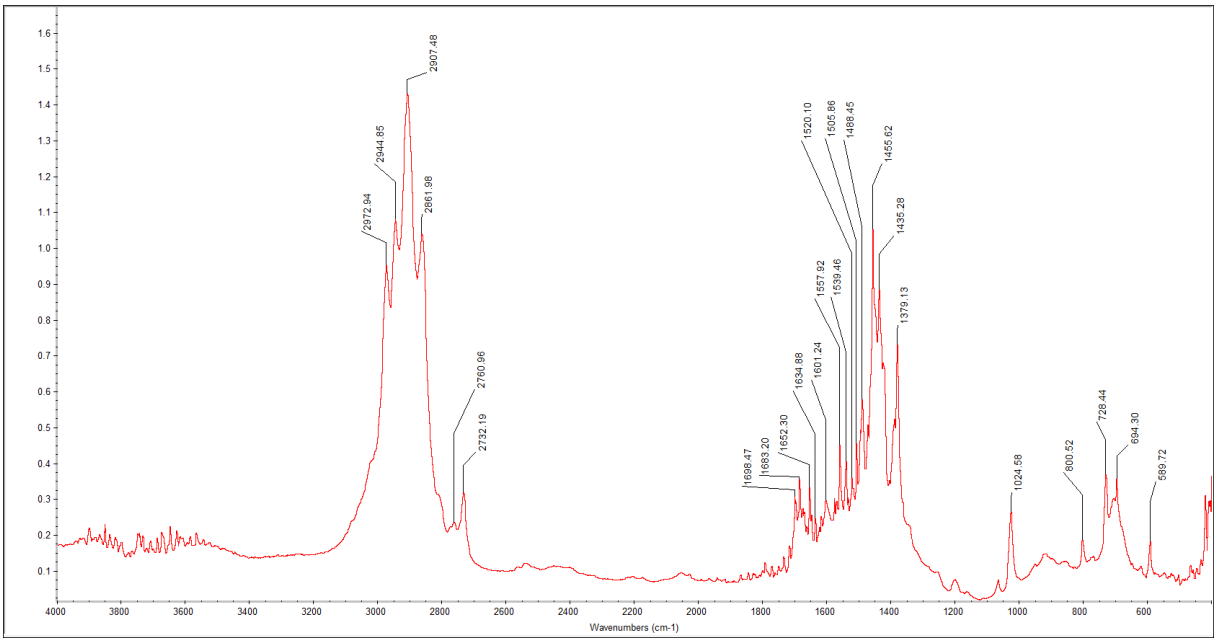

Figure S49. DRIFT spectrum of $[Cp^*Ho(AlMe_4)Cl]_2$ ($\mathbf{7^{Ho}}$).

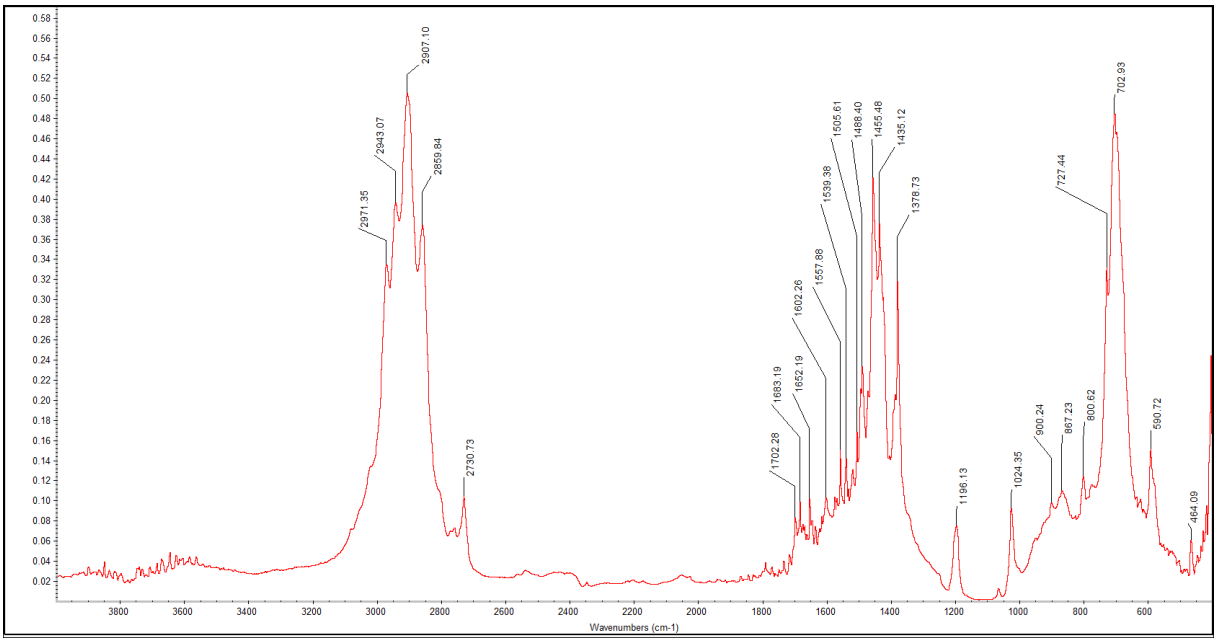

Figure S50. DRIFT spectrum of $[Cp^*Er(AlMe_4)Cl]_2$ ($\mathbf{7^{Er}}$).

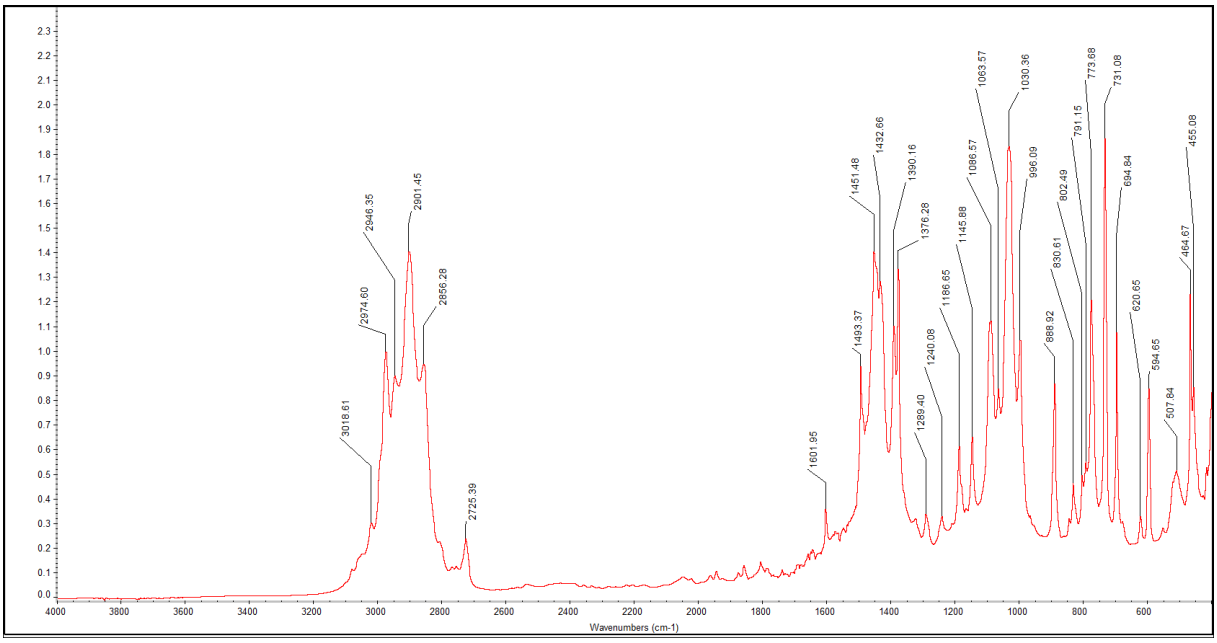

Figure S51. DRIFT spectrum of $[(\mu_2\text{-Br})Cp^*_3Ho_3Br_5(Et_2O)]_2$ (**8**).

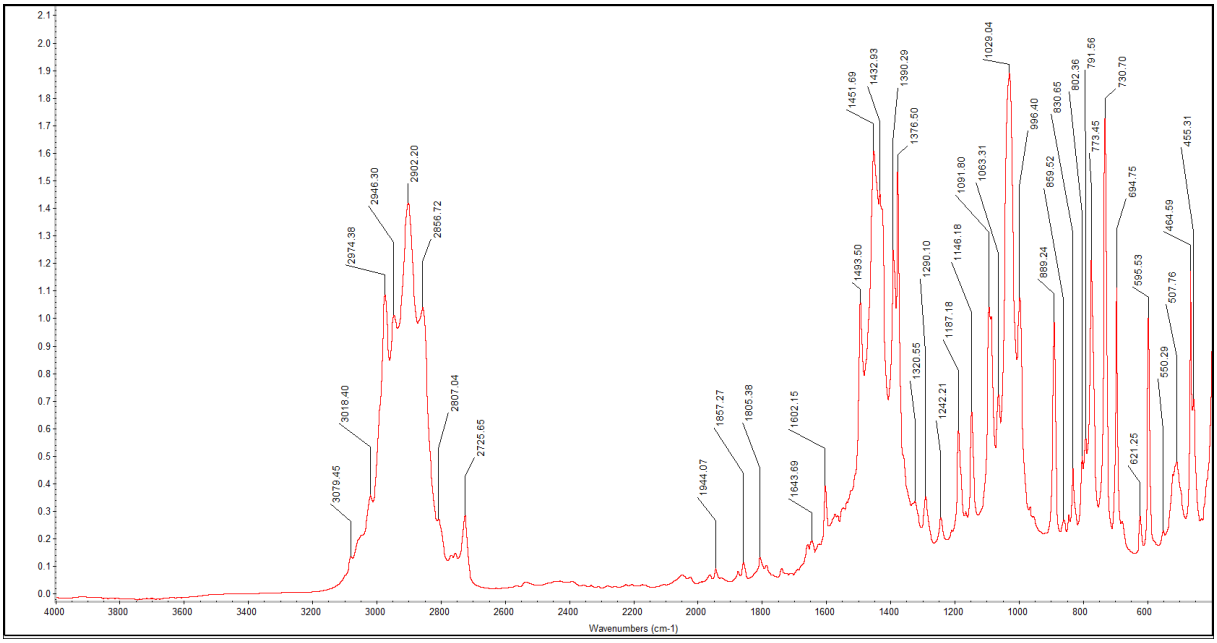

Figure S52. DRIFT spectrum of $[(\mu_2\text{-Br})Cp^*_3Y_3Br_5(Et_2O)]_2$ (**4^YEt₂O**).

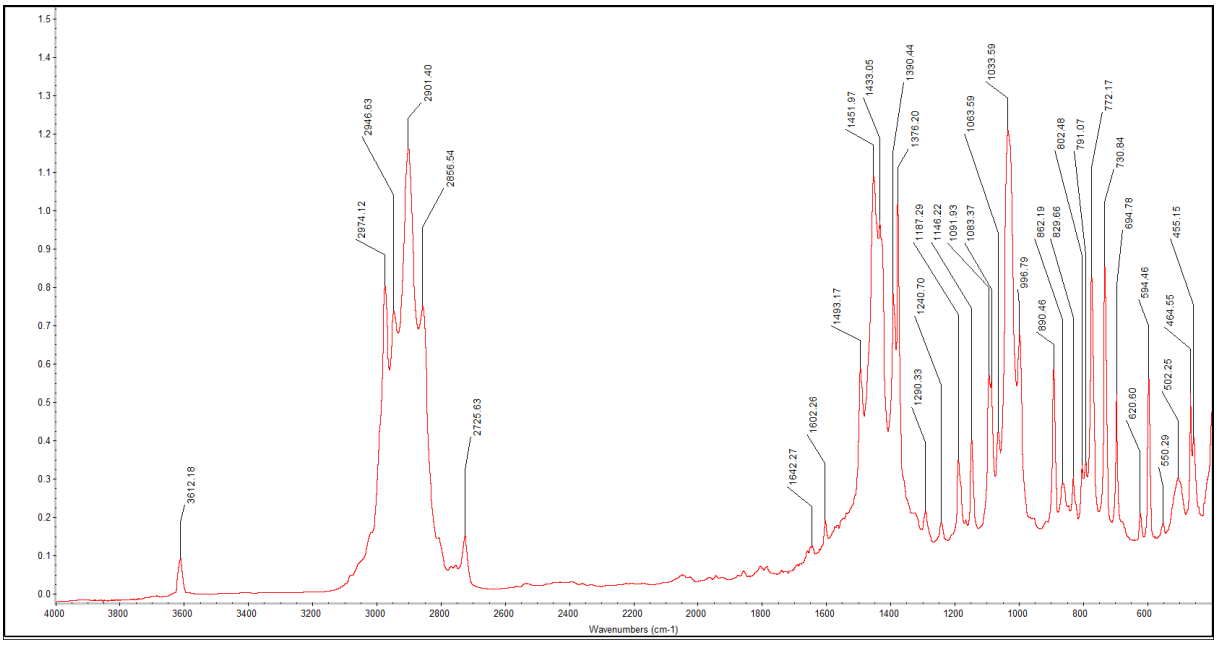

Figure S53. DRIFT spectrum of [(μ_2-Br)Cp*$_3$Dy$_3$Br$_5$(Et$_2$O)]$_2$ (**4^{Dy}Et$_2$O**).

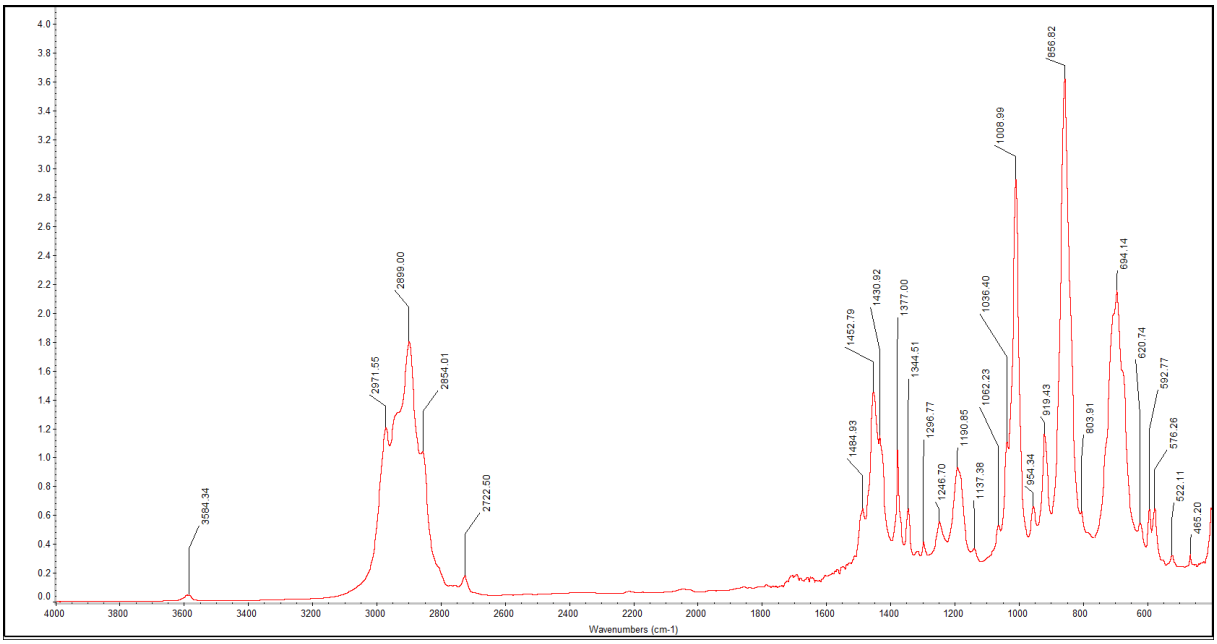

Figure S54. DRIFT spectrum of [Cp*DyBr$_2$(thf)$_3$] (**4^{Dy}THF**).

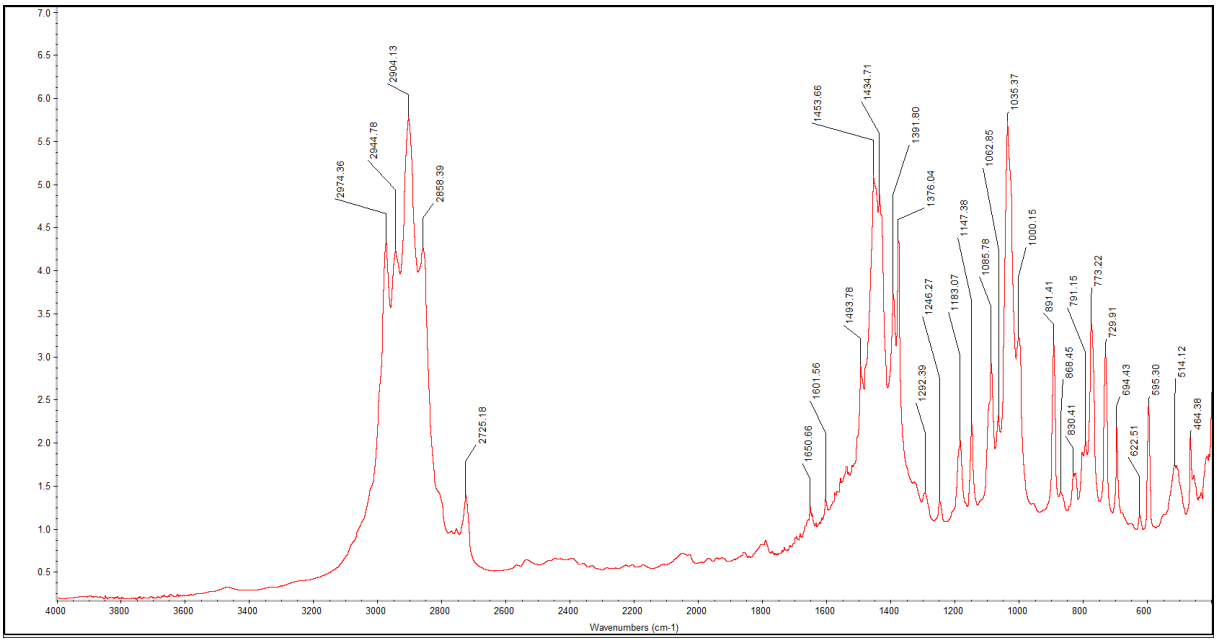

Figure S55. DRIFT spectrum of $[(\mu_2\text{-Cl})Cp^*_3Y_3Cl_5(Et_2O)]_2$ (**5^{Y}Et$_2$O**).

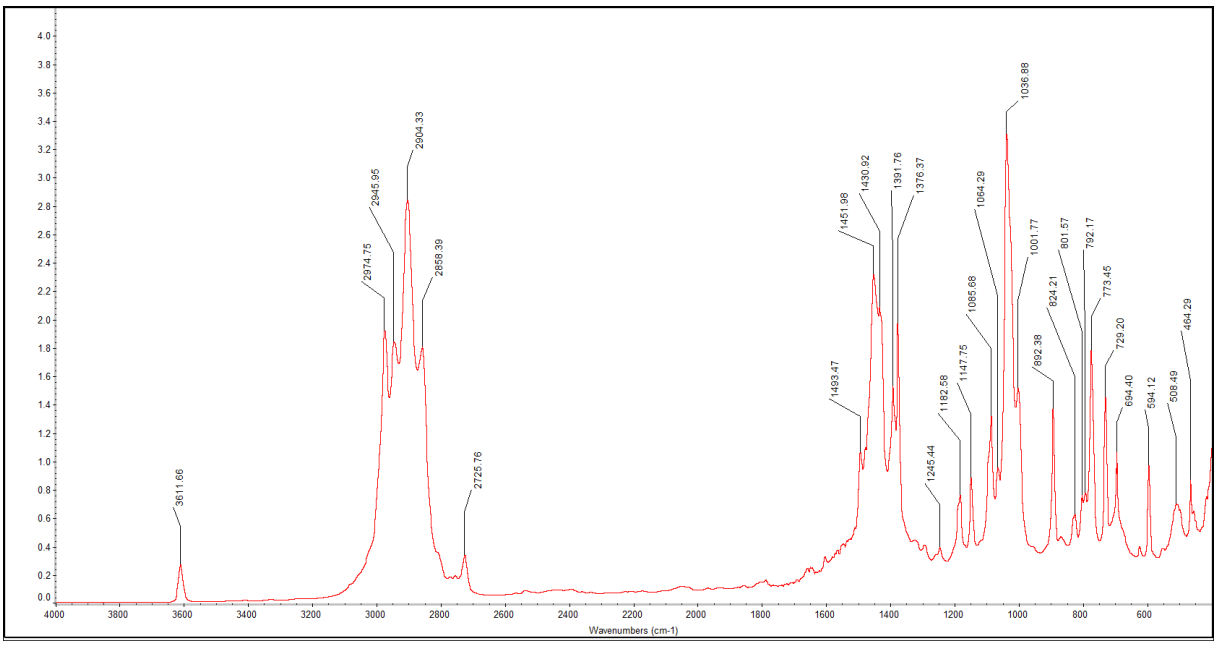

Figure S56. DRIFT spectrum of $[(\mu_2\text{-Cl})Cp^*_3Dy_3Cl_5(Et_2O)]_2$ (**6^{Dy}Et$_2$O**).

EDX Spectroscopy

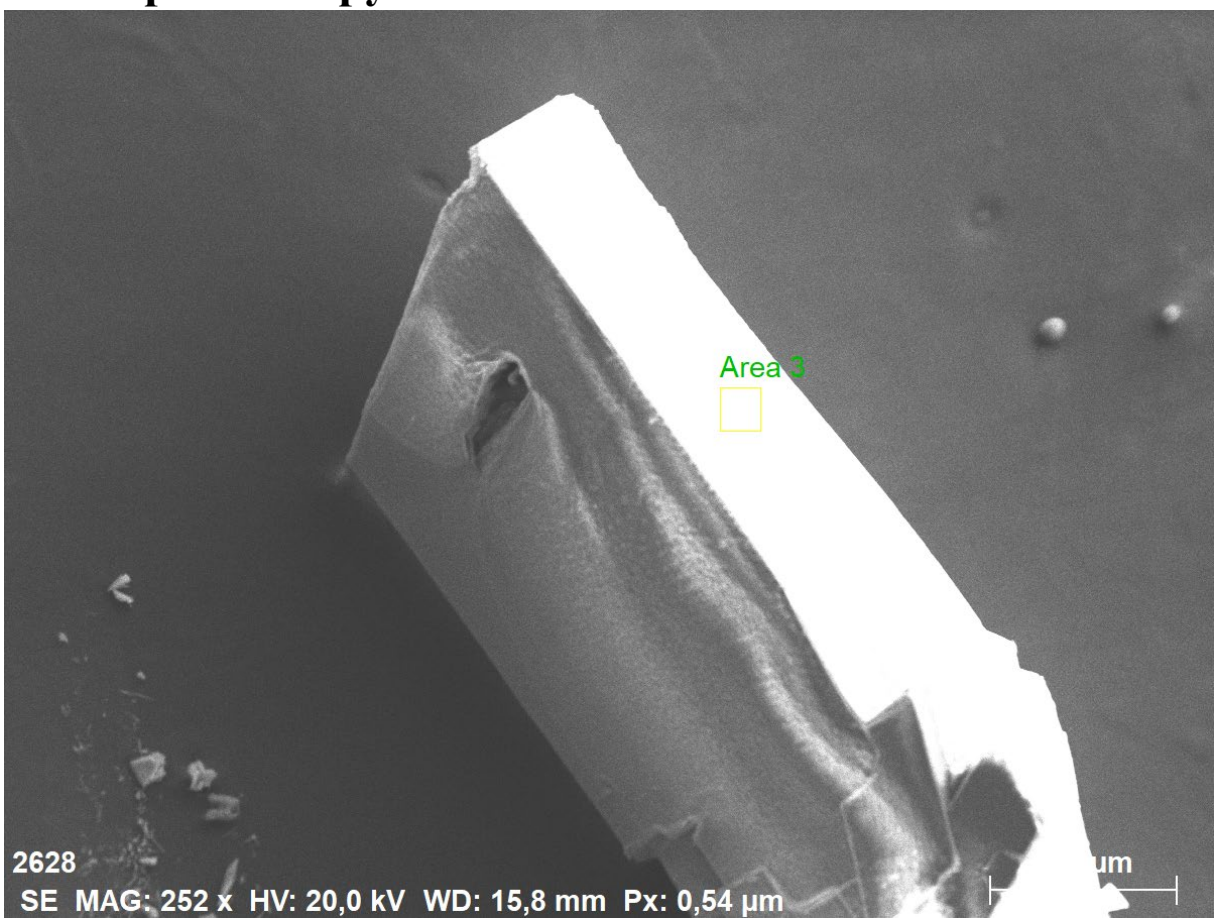

Figure S57. SEM image of crystalline $[Cp^*YI_2]_4$ (**2**^{Y}) of area 3, where EDX spectroscopy was performed.

Table S3. Results of EDX spectroscopy of area 3 (Fig. S57).

Element	norm. wt. %	norm. atom %	3 σ	norm. wt. % calc.	norm. atom % calc.
Y	26.03	33.43	2.36	25.94	33.33
I	73.97	66.57	4.70	74.06	66.67

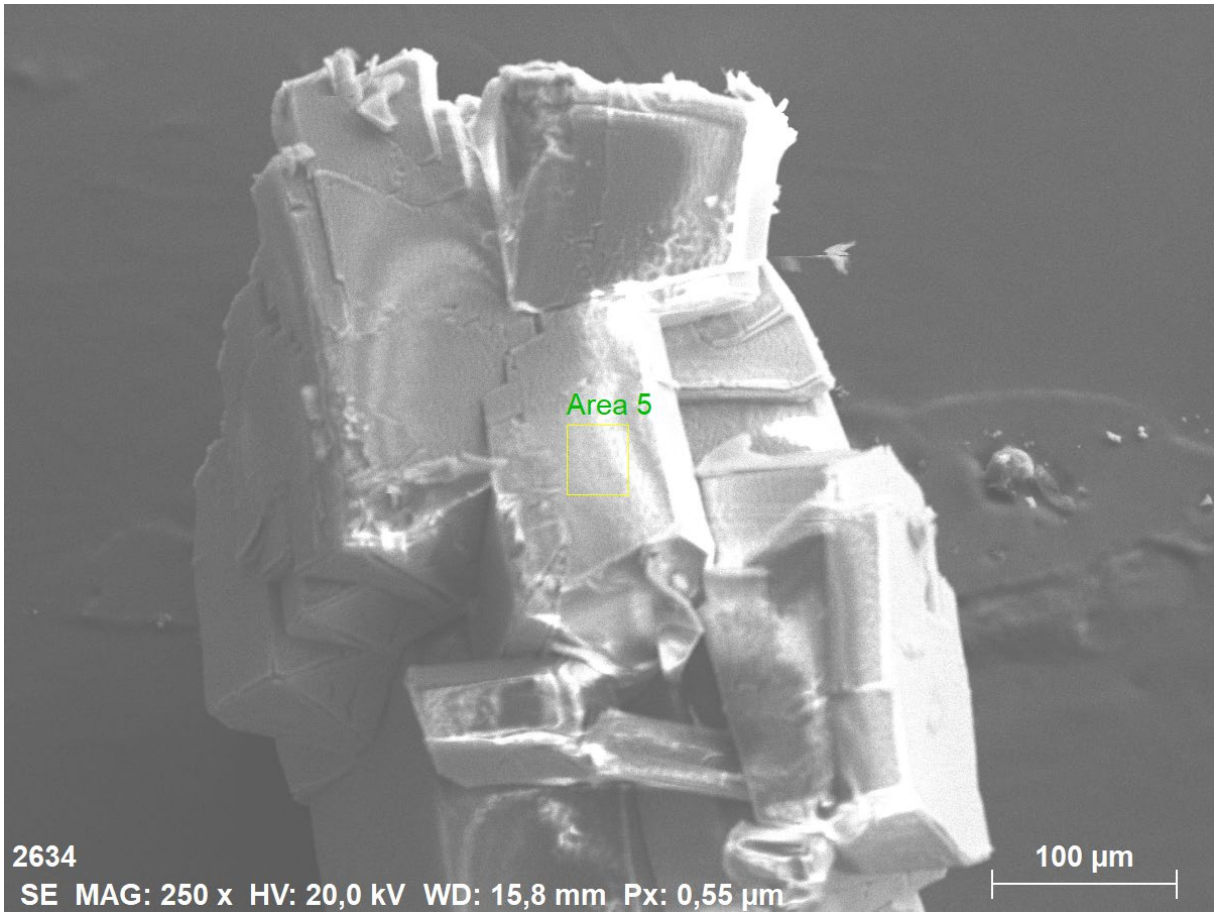

Figure S58. SEM image of crystalline $[Cp^*YI_2]_4$ (**2**^{Y}) of area 5, where EDX spectroscopy was performed.

Table S4. Results of EDX spectroscopy of area 5 (Fig. S58).

Element	norm. wt. %	norm. atom %	3 σ	norm. wt. % calc.	norm. atom % calc.
Y	26.11	33.53	2.54	25.94	33.33
I	73.89	66.47	5.06	74.06	66.67

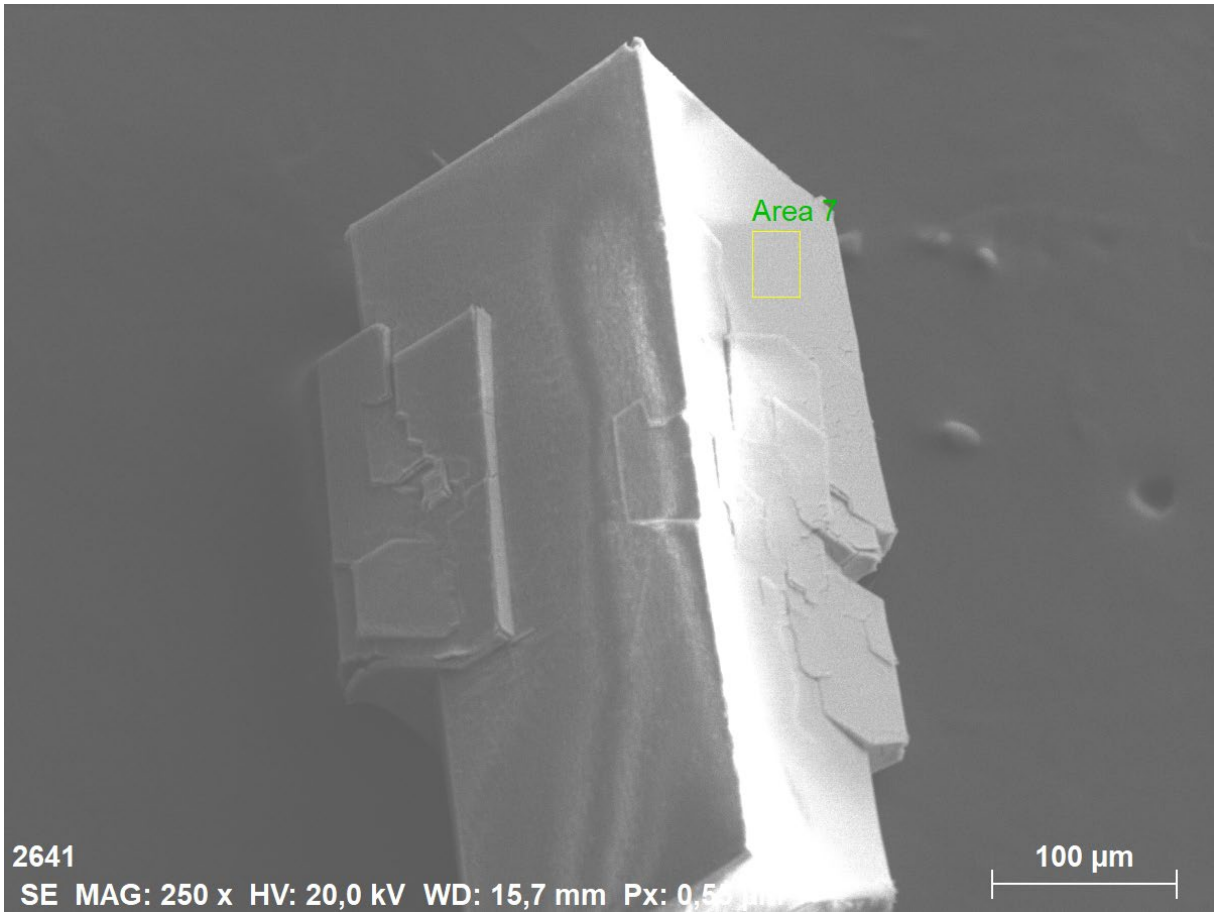

Figure S59. SEM image of crystalline $[Cp^*YI_2]_4$ ($\mathbf{2^Y}$) of area 7, where EDX spectroscopy was performed.

Table S5. Results of EDX spectroscopy of area 7 (Fig. S59).

Element	norm. wt. %	norm. atom %	3 σ	norm. wt. % calc.	norm. atom % calc.
Y	26.24	33.68	2.64	25.94	33.33
I	73.76	66.32	5.23	74.06	66.67

Table S6. Averaged results of all EDX analyses for $\mathbf{2^Y}$ (10 measurements).

Element	norm. wt. %	norm. atom %	3 σ	norm. wt. % calc.	norm. atom % calc.
Y	26.20	33.63	2.49	25.94	33.33
I	73.80	66.37	4.94	74.06	66.67

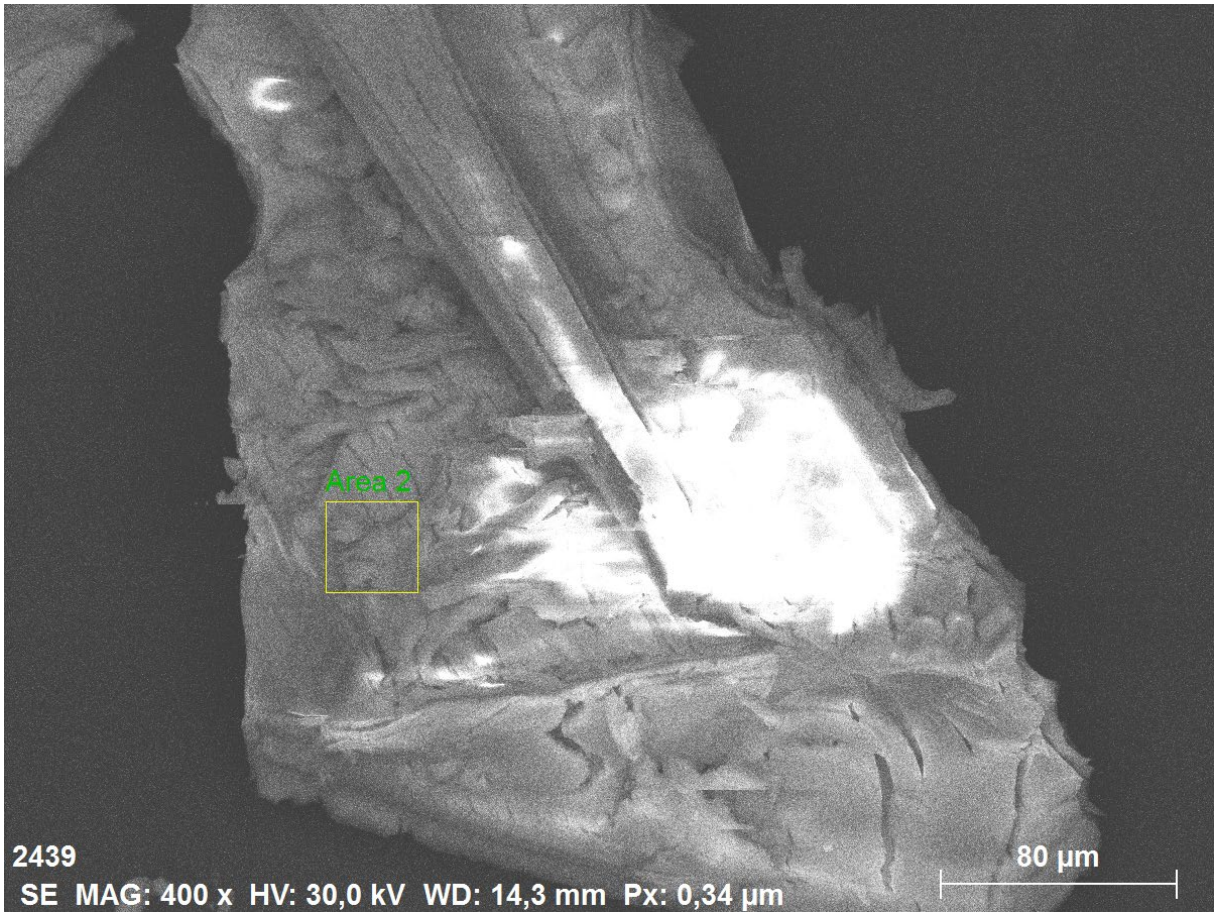

Figure S60. SEM image of crystalline $[Cp^*TbI_2]_4$ (**2**^{Tb}) of area 2, where EDX spectroscopy was performed.

Table S7. Results of EDX spectroscopy of area 2 (Fig. S60).

Element	norm. wt. %	norm. atom %	3 σ	norm. wt. % calc.	norm. atom % calc.
Tb	38.18	33.02	2.34	38.51	33.33
I	61.82	66.97	4.17	61.49	66.67

Figure S61. SEM image of crystalline $[Cp^*TbI_2]_4$ (**2**^{Tb}) of area 5, where EDX spectroscopy was performed.

Table S8. Results of EDX spectroscopy of area 5 (Fig. S61).

Element	norm. wt. %	norm. atom %	3 σ	norm. wt. % calc.	norm. atom % calc.
Tb	38.68	33.49	2.82	38.51	33.33
I	61.32	66.51	4.94	61.49	66.67

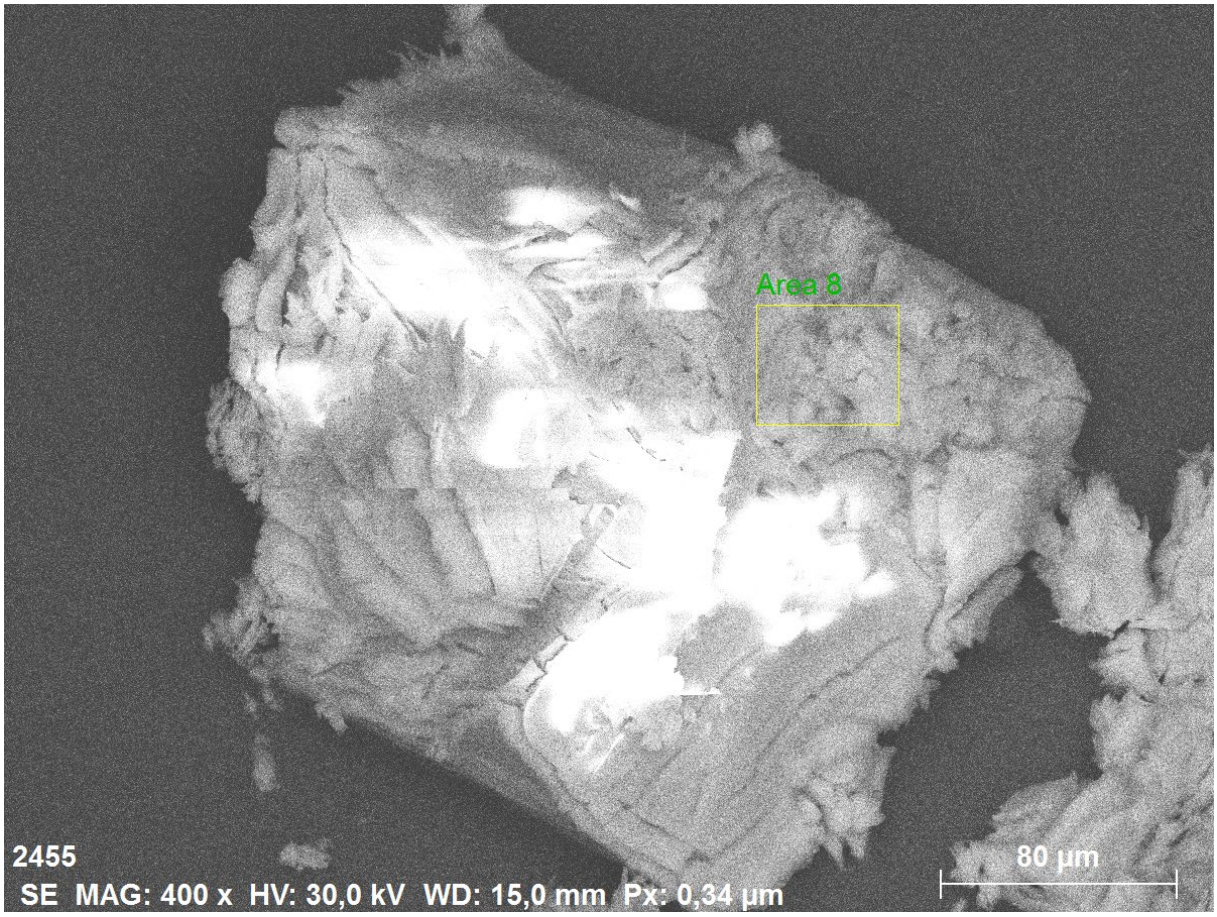

Figure S62. SEM image of crystalline $[Cp^*TbI_2]_4$ (**2**^{Tb}) of area 8, where EDX spectroscopy was performed.

Table S9. Results of EDX spectroscopy of area 8 (Fig. S62).

Element	norm. wt. %	norm. atom %	3 σ	norm. wt. % calc.	norm. atom % calc.
Tb	38.25	33.10	2.84	38.51	33.33
I	61.75	66.90	5.08	61.49	66.67

Table S10. Averaged results of all EDX analyses for **2**^{Tb} (12 measurements).

Element	norm. wt. %	norm. atom %	3 σ	norm. wt. % calc.	norm. atom % calc.
Tb	38.33	33.17	2.61	38.51	33.33
I	61.67	66.84	4.64	61.49	66.67

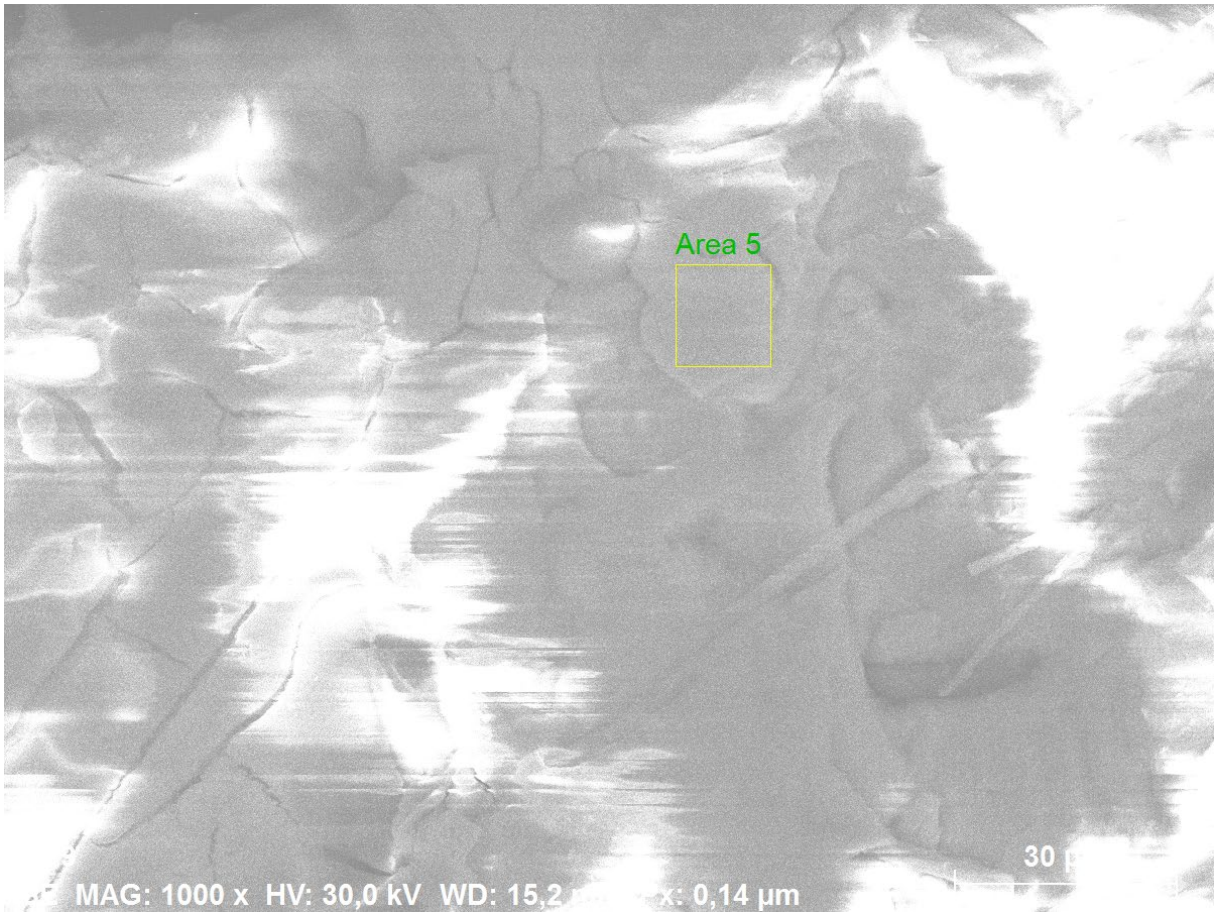

Figure S63. SEM image of crystalline $[Cp^*DyI_2]_4$ ($\mathbf{2^{Dy}}$) of area 5, where EDX spectroscopy was performed.

Table S11. Results of EDX spectroscopy of area 5 (Fig. S63).

Element	norm. wt. %	norm. atom %	3 σ	norm. wt. % calc.	norm. atom % calc.
Dy	39.94	34.18	2.36	39.03	33.33
I	60.06	65.82	3.93	60.97	66.67

Figure S64. SEM image of crystalline $[Cp^*DyI_2]_4$ (**2**^{Dy}) of area 6, where EDX spectroscopy was performed.

Table S12. Results of EDX spectroscopy of area 6 (Fig. S64).

Element	norm. wt. %	norm. atom %	3 σ	norm. wt. % calc.	norm. atom % calc.
Dy	39.67	33.93	2.13	39.03	33.33
I	60.33	66.07	3.60	60.97	66.67

Figure S65. SEM image of crystalline $[Cp^*DyI_2]_4$ ($\mathbf{2^{Dy}}$) of area 7, where EDX spectroscopy was performed.

Table S13. Results of EDX spectroscopy of area 7 (Fig. S65).

Element	norm. wt. %	norm. atom %	3 σ	norm. wt. % calc.	norm. atom % calc.
Dy	39.76	34.01	2.04	39.03	33.33
I	60.24	65.99	3.42	60.97	66.67

Table S14. Averaged results of all EDX analyses for $\mathbf{2^{Dy}}$ (9 measurements).

Element	norm. wt. %	norm. atom %	3 σ	norm. wt. % calc.	norm. atom % calc.
Dy	39.95	34.20	2.23	39.03	33.33
I	60.05	65.80	3.71	60.97	66.67

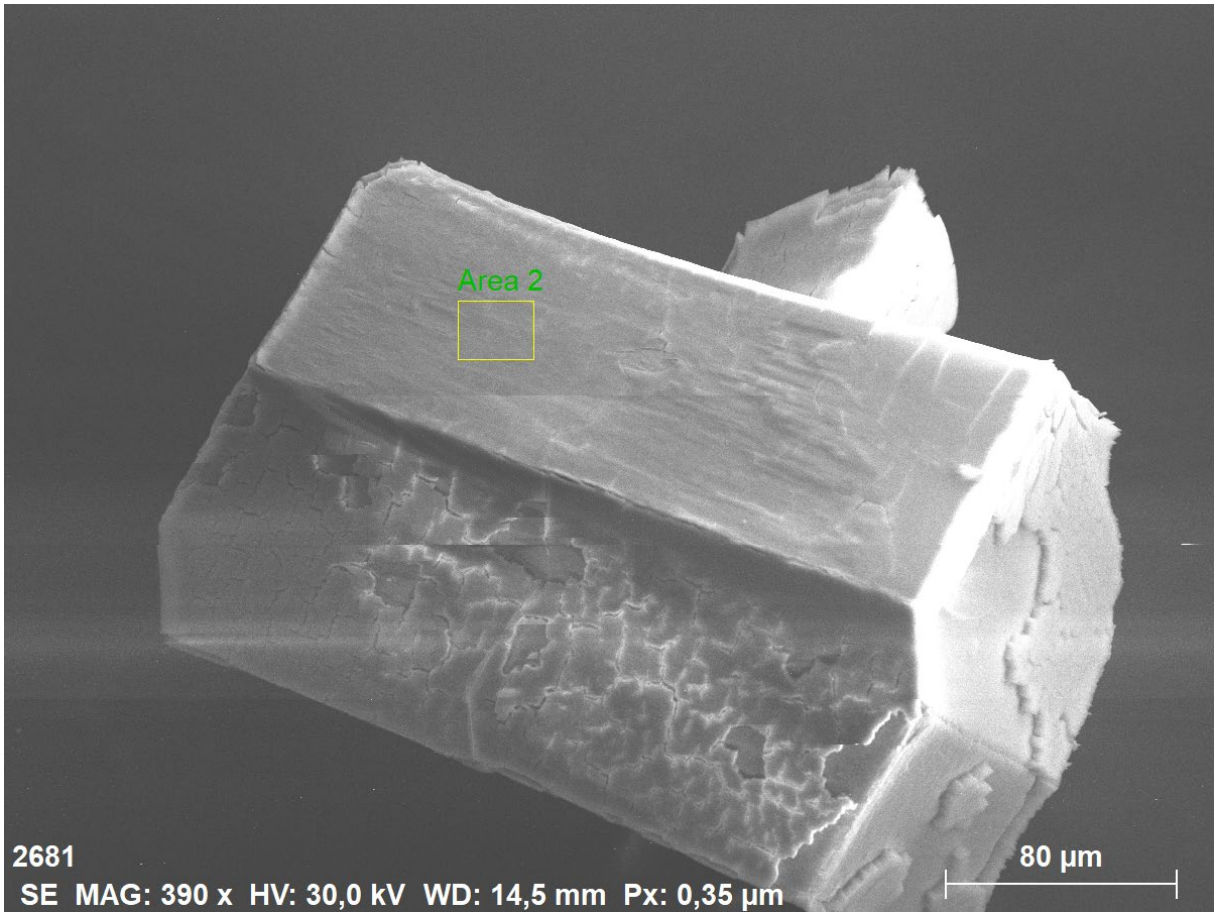

Figure S66. SEM image of crystalline $[Cp^*HoI_2]_4$ (**2^{Ho}**) of area 2, where EDX spectroscopy was performed.

Table S15. Results of EDX spectroscopy of area 2 (Fig. S66).

Element	norm. wt. %	norm. atom %	3 σ	norm. wt. % calc.	norm. atom % calc.
Ho	39.09	33.05	1.65	39.39	33.33
I	60.91	66.95	2.81	60.61	66.67

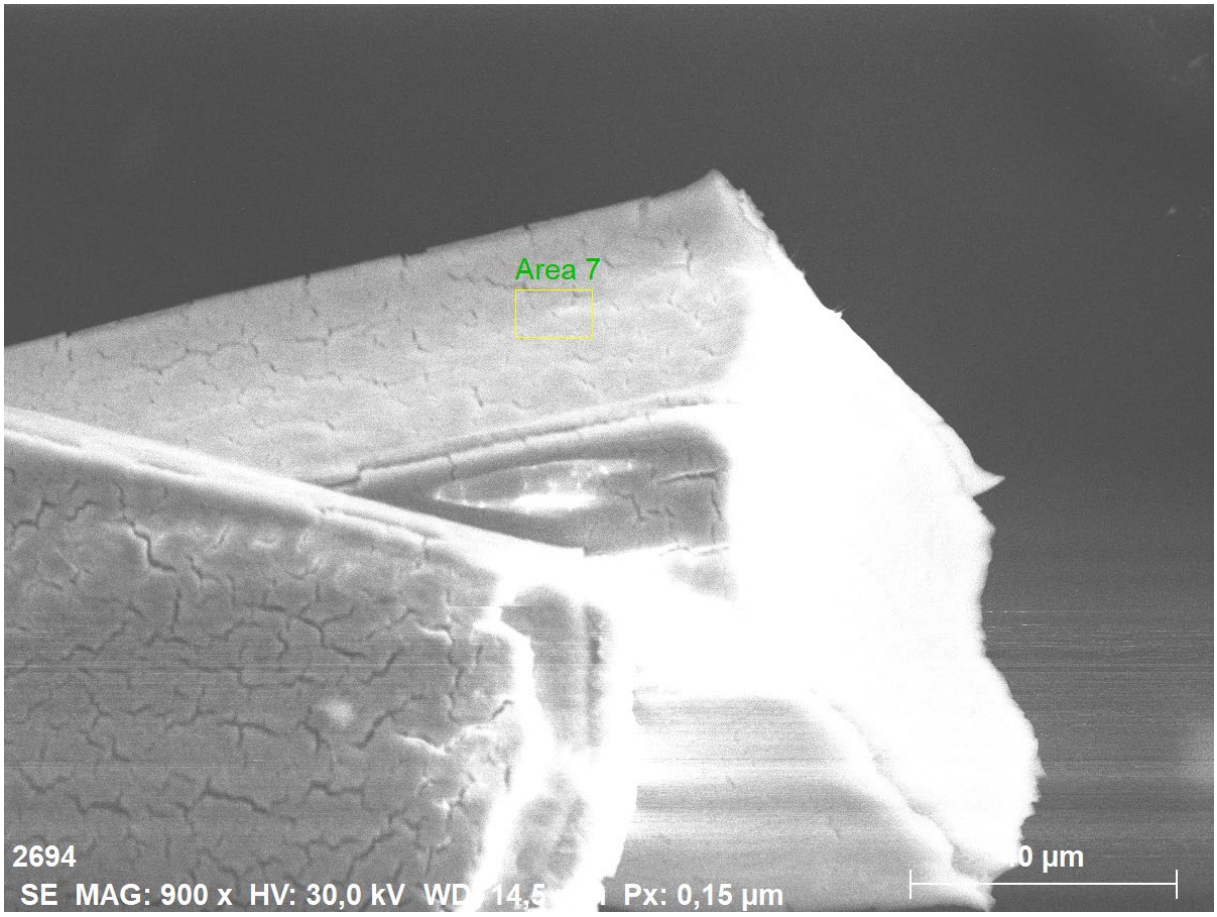

Figure S67. SEM image of crystalline $[Cp^*HoI_2]_4$ (**2^{Ho}**) of area 7, where EDX spectroscopy was performed.

Table S16. Results of EDX spectroscopy of area 7 (Fig. S67).

Element	norm. wt. %	norm. atom %	3 σ	norm. wt. % calc.	norm. atom % calc.
Ho	39.32	33.27	2.53	39.39	33.33
I	60.68	66.73	4.19	60.61	66.67

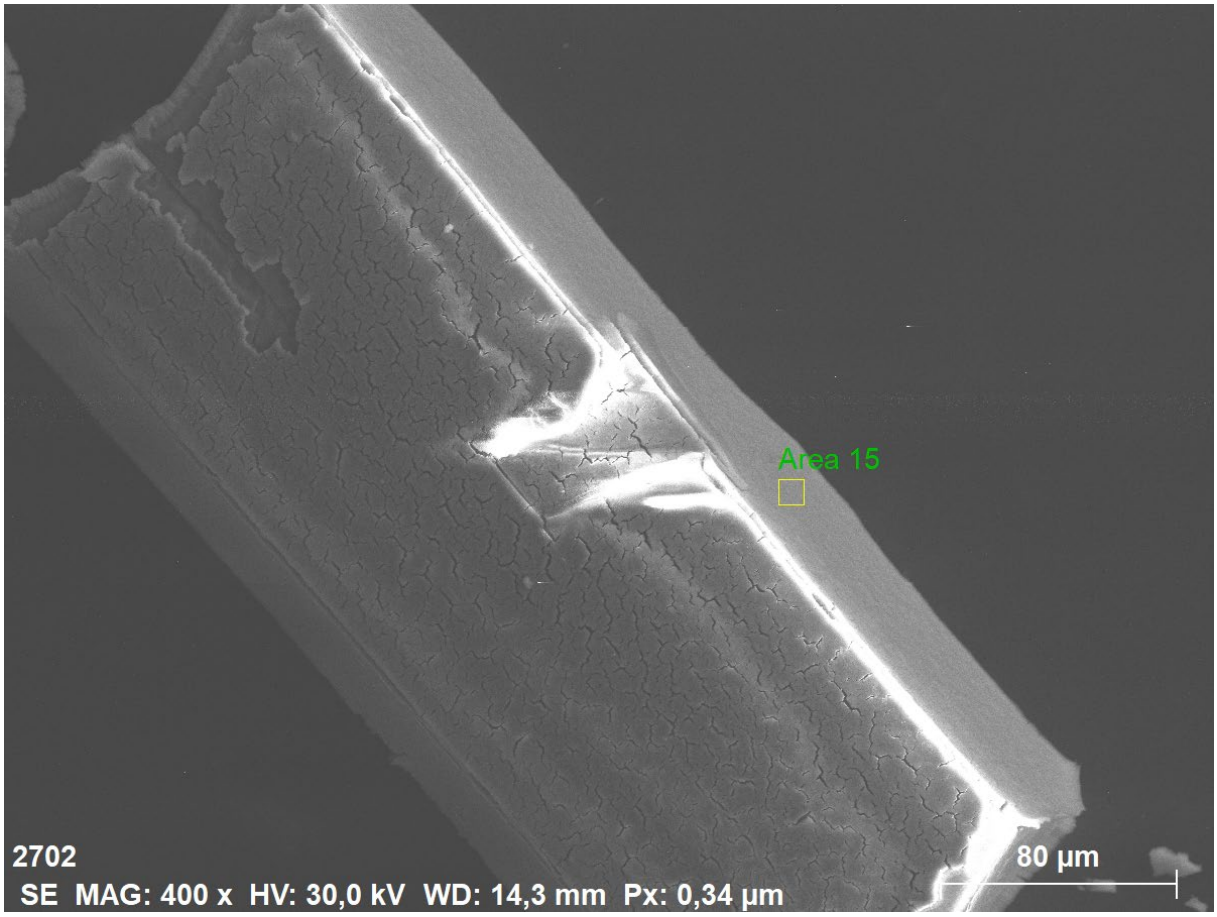

Figure S68. SEM image of crystalline $[Cp^*HoI_2]_4$ (**2^{Ho}**) of area 2, where EDX spectroscopy was performed.

Table S17. Results of EDX spectroscopy of area 2 (Fig. S68).

Element	norm. wt. %	norm. atom %	3 σ	norm. wt. % calc.	norm. atom % calc.
Ho	39.09	33.05	2.04	39.39	33.33
I	60.91	66.95	3.42	60.61	66.67

Table S18. Averaged results of all EDX analyses for **2^{Ho}** (15 measurements).

Element	norm. wt. %	norm. atom %	3 σ	norm. wt. % calc.	norm. atom % calc.
Ho	38.94	32.92	2.56	39.39	33.33
I	61.06	67.08	4.31	60.61	66.67

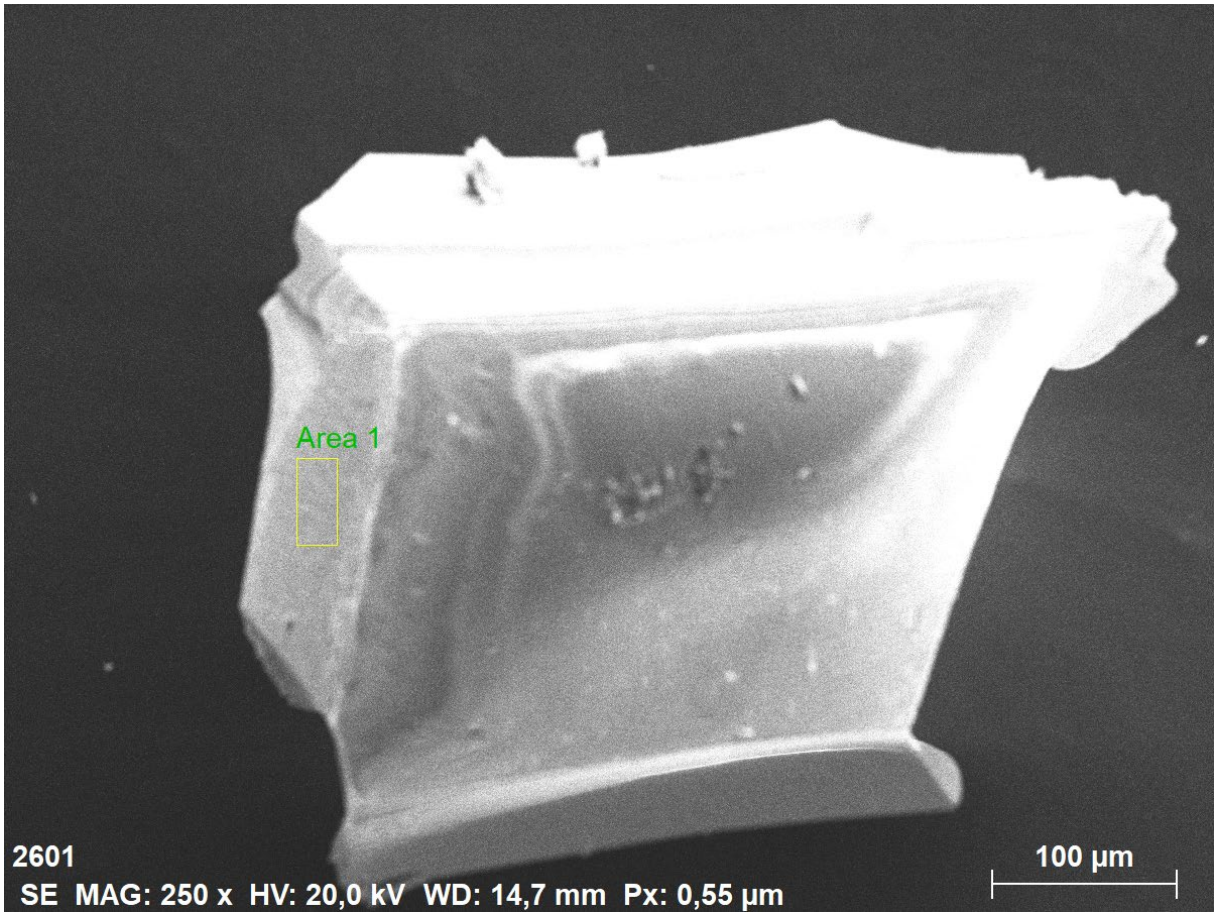

Figure S69. SEM image of crystalline $[Cp^*ErI_2]_4$ (**2**^{Er}) of area 1, where EDX spectroscopy was performed.

Table S19. Results of EDX spectroscopy of area 1 (Fig. S69).

Element	norm. wt. %	norm. atom %	3 σ	norm. wt. % calc.	norm. atom % calc.
Er	39.40	33.03	2.87	39.72	33.33
I	60.60	66.97	3.58	60.28	66.67

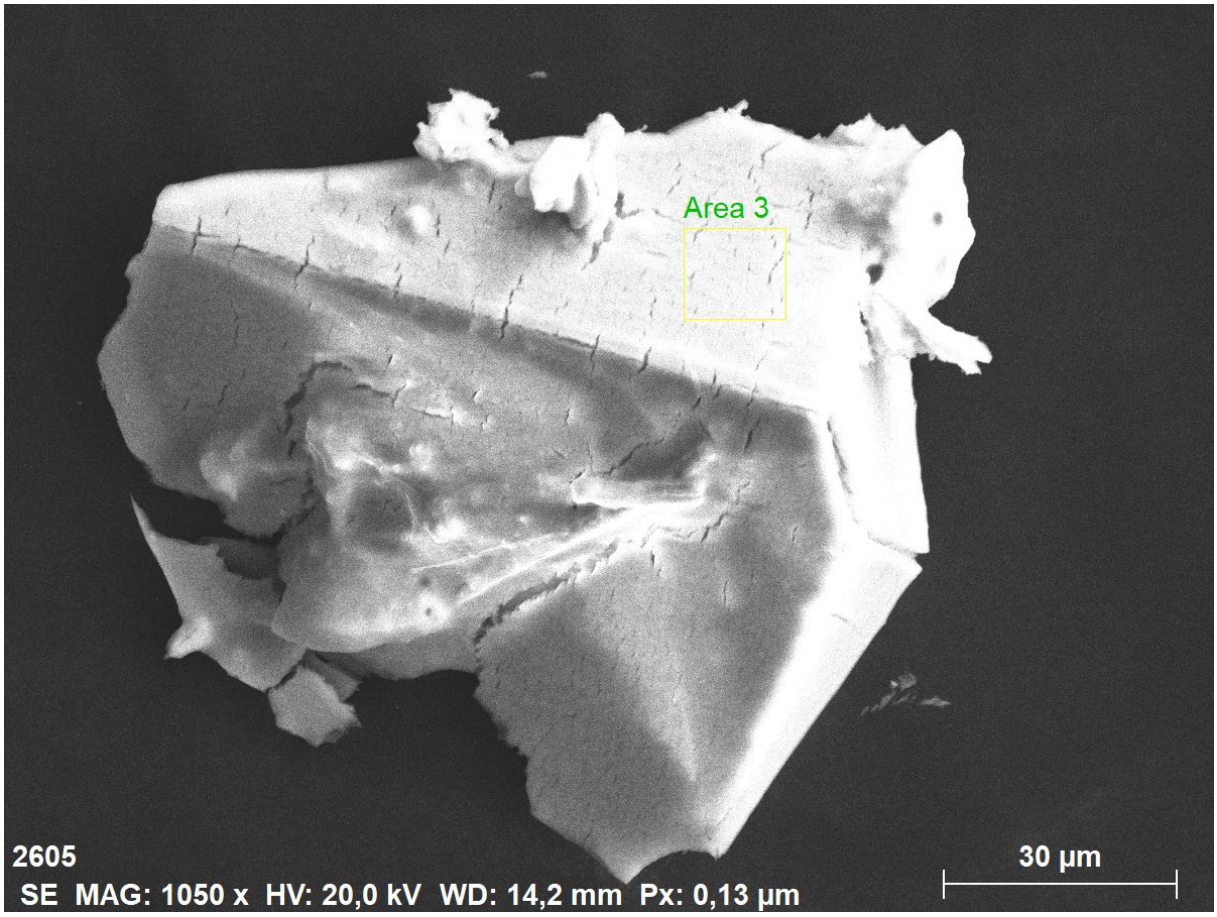

Figure S70. SEM image of crystalline $[Cp^*ErI_2]_4$ (**2**^{Er}) of area 3, where EDX spectroscopy was performed.

Table S20. Results of EDX spectroscopy of area 3 (Fig. S70).

Element	norm. wt. %	norm. atom %	3 σ	norm. wt. % calc.	norm. atom % calc.
Er	39.52	33.15	2.82	39.72	33.33
I	60.48	66.85	4.47	60.28	66.67

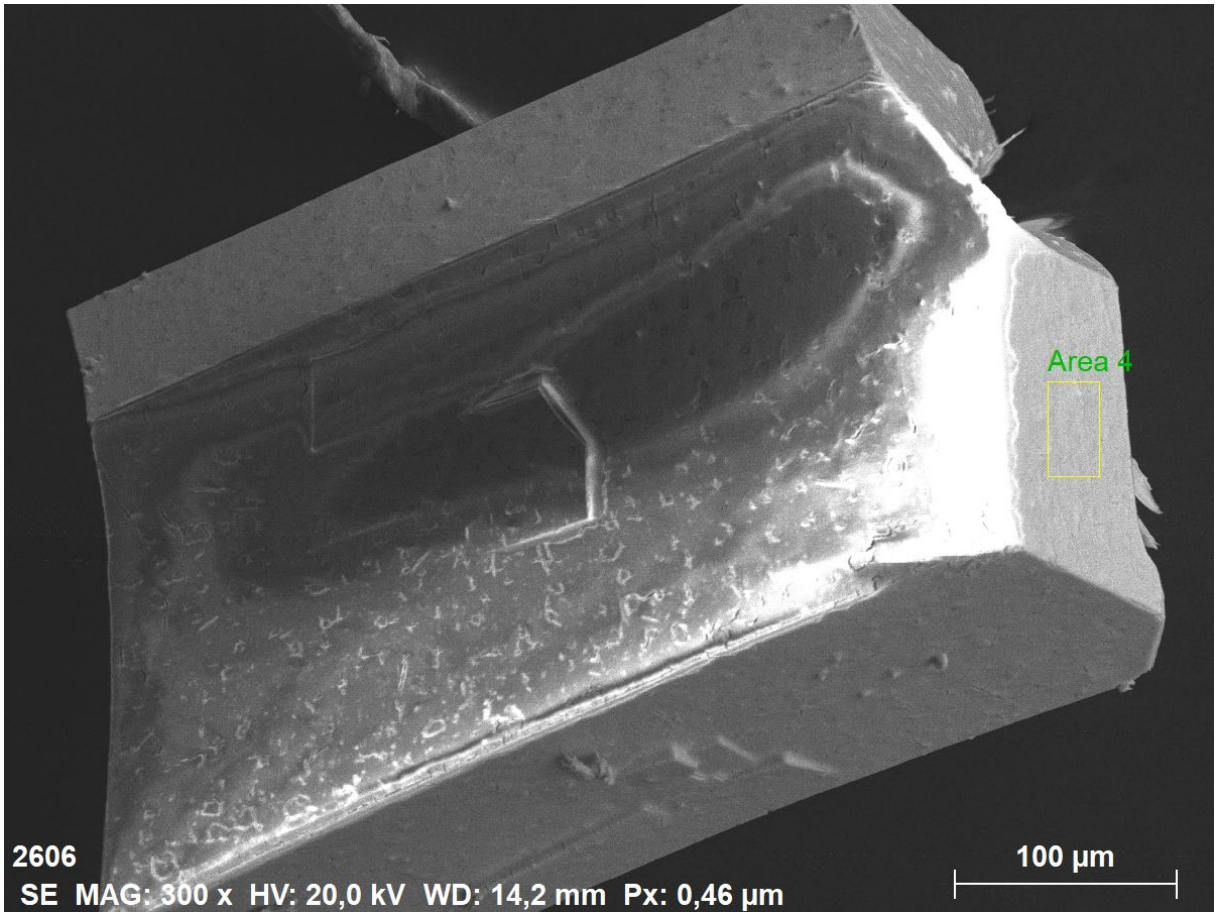

Figure S71. SEM image of crystalline $[Cp^*ErI_2]_4$ ($\mathbf{2^{Er}}$) of area 4, where EDX spectroscopy was performed.

Table S21. Results of EDX spectroscopy of area 4 (Fig. S71).

Element	norm. wt. %	norm. atom %	3 σ	norm. wt. % calc.	norm. atom % calc.
Er	39.40	33.04	3.01	39.72	33.33
I	60.60	66.96	4.80	60.28	66.67

Table S22. Averaged results of all EDX spectroscopy for $\mathbf{2^{Er}}$ (11 measurements).

Element	norm. wt. %	norm. atom %	3 σ	norm. wt. % calc.	norm. atom % calc.
Er	39.47	33.10	2.77	39.72	33.33
I	60.53	66.90	4.39	60.28	66.67

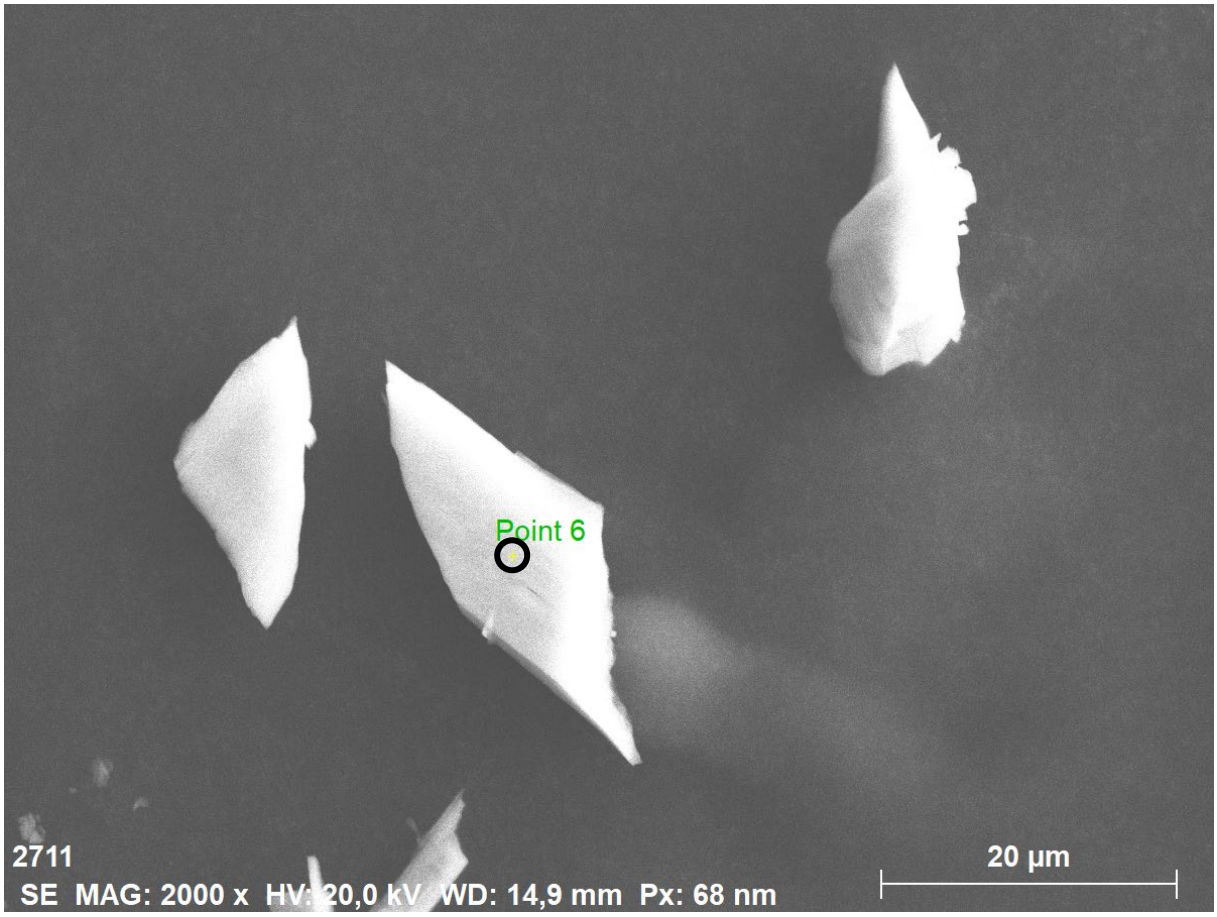

Figure S72. SEM image of crystalline [(Cp*$_4$Gd$_4$I$_7${AlMe$_4$}$)_2$] (**3**) of point 6, where EDX spectroscopy was performed.

Table S23. Results of EDX spectroscopy of point 6 (Fig. S72).

Element	norm. wt. %	norm. atom %	3 σ	norm. wt. % calc.	norm. atom % calc.
Gd	40.01	32.97	2.89	40.73	33.33
I	58.45	59.68	4.40	57.52	58.33
Al	1.53	7.36	0.29	1.75	8.33

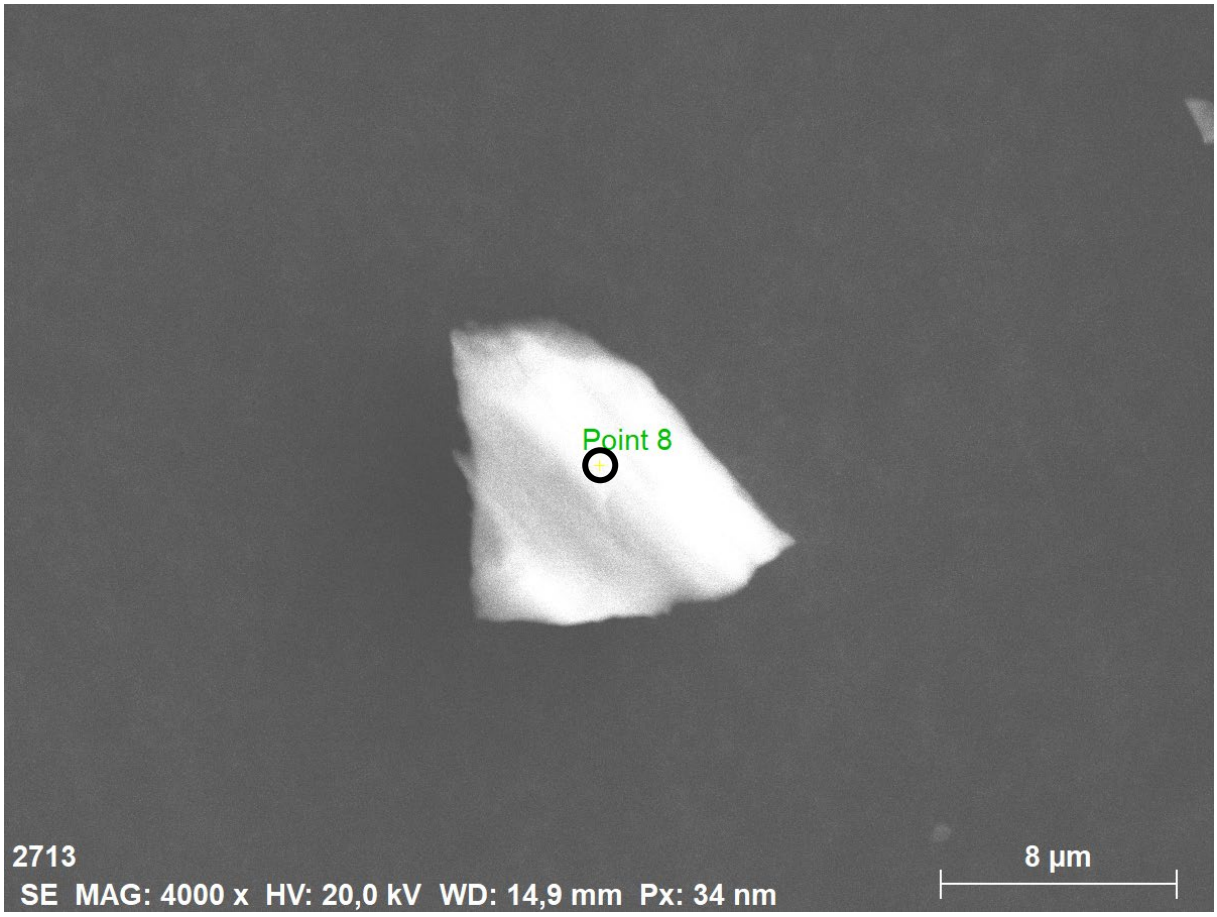

Figure S73. SEM image of crystalline [(Cp*$_4$Gd$_4$I$_7${AlMe$_4$}$)_2$] (**3**) of point 8, where EDX spectroscopy was performed.

Table S24. Results of EDX spectroscopy of point 8 (Fig. S73).

Element	norm. wt. %	norm. atom %	3 σ	norm. wt. % calc.	norm. atom % calc.
Gd	40.66	33.42	3.12	40.73	33.33
I	57.71	58.77	4.62	57.52	58.33
Al	1.63	7.80	0.32	1.75	8.33

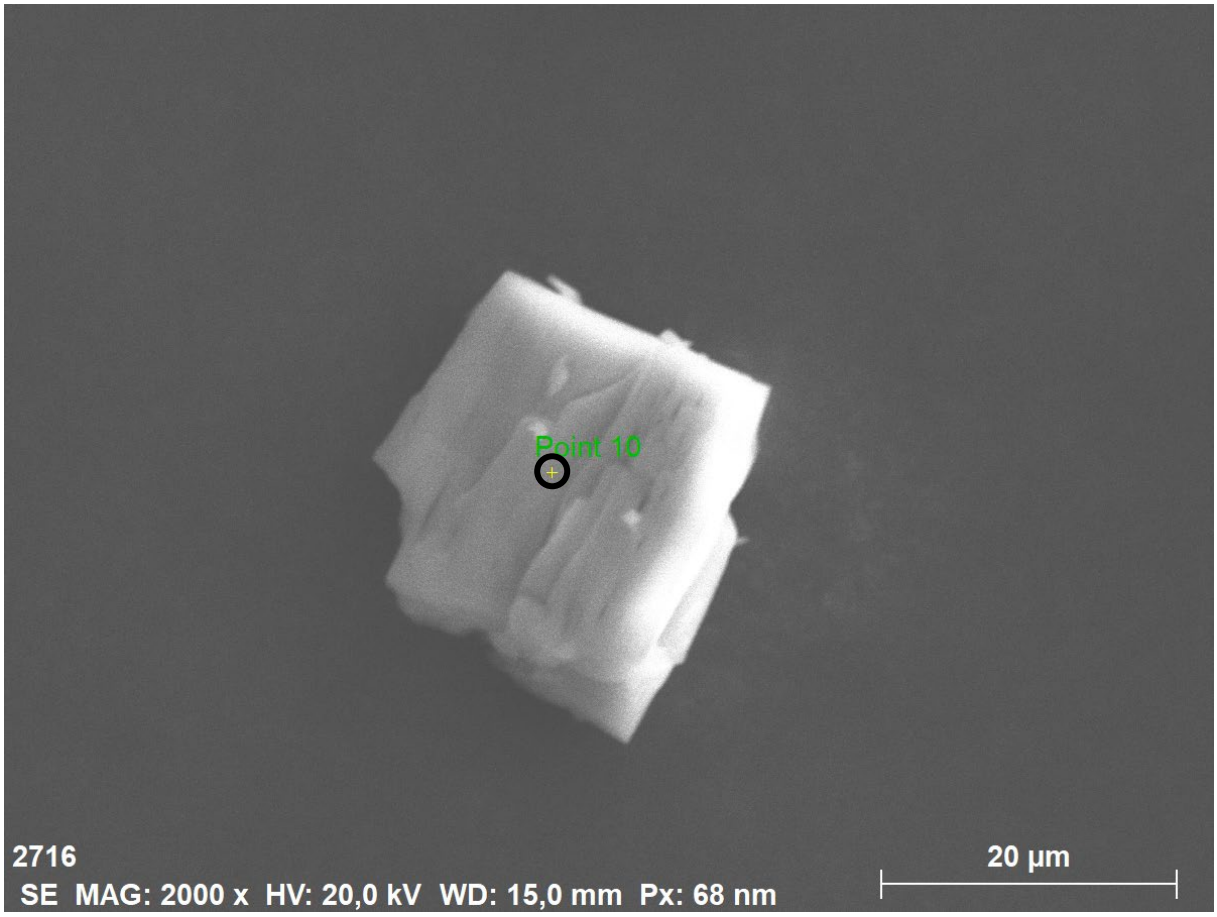

Figure S74. SEM image of crystalline [(Cp*$_4$Gd$_4$I$_7${AlMe$_4$}$_2$] (**3**) of point 10, where EDX spectroscopy was performed.

Table S25. Results of EDX spectroscopy of point 10 (Fig. S74).

Element	norm. wt. %	norm. atom %	3 σ	norm. wt. % calc.	norm. atom % calc.
Gd	40.01	32.97	2.89	40.73	33.33
I	58.45	59.68	4.40	57.52	58.33
Al	1.53	7.36	0.29	1.75	8.33

Table S26. Averaged results of all EDX analyses for **3** (12 measurements).

Element	norm. wt. %	norm. atom %	3 σ	norm. wt. % calc.	norm. atom % calc.
Gd	41.47	33.92	3.11	40.73	33.33
I	56.72	57.48	4.41	57.52	58.33
Al	1.81	8.61	0.34	1.75	8.33

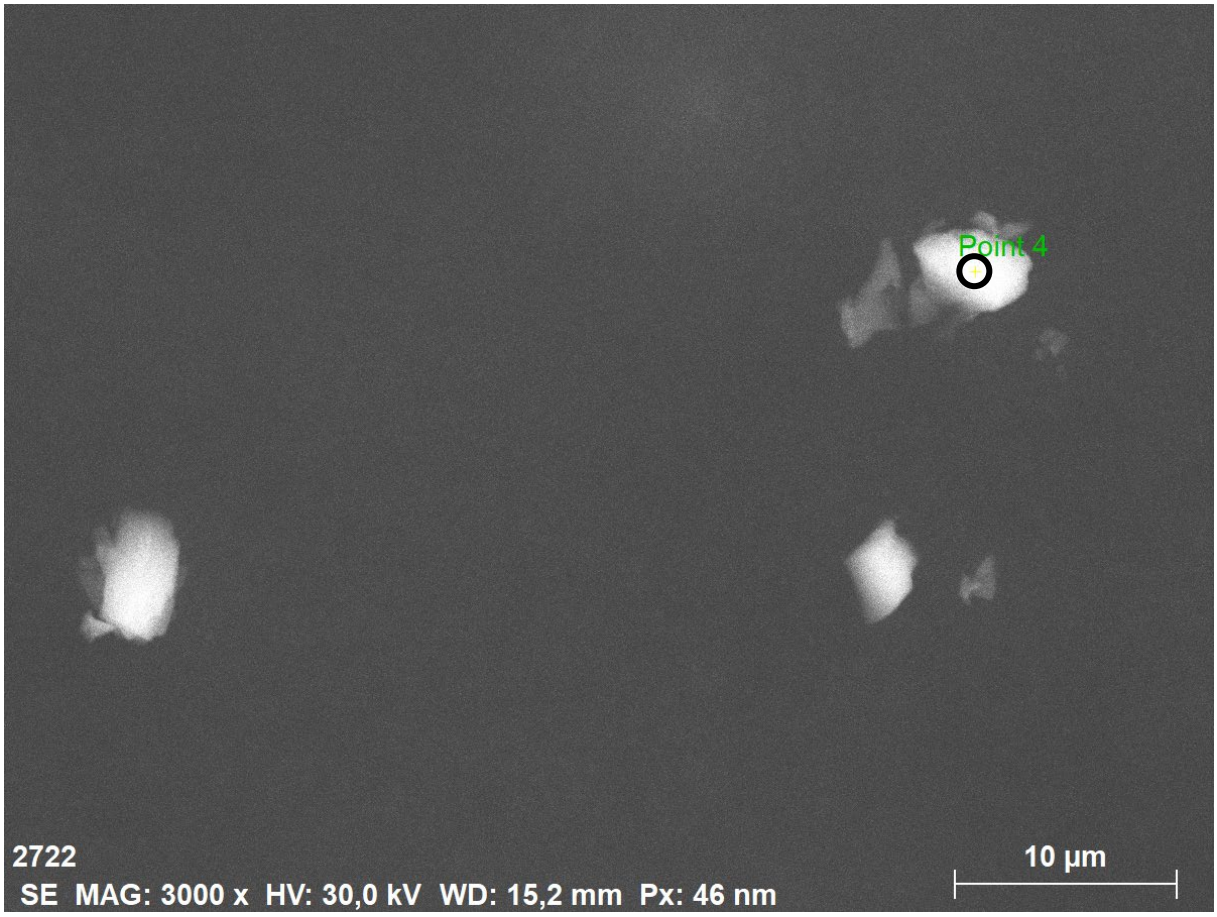

Figure S75. SEM image of crystalline [Cp*$_4$Y$_4$Br$_9$(AlMe$_2$)] (**4^{Y}**) of point 4, where EDX spectroscopy was performed.

Table S27. Results of EDX spectroscopy of point 4 (Fig. S75).

Element	norm. wt. %	norm. atom %	3 σ	norm. wt. % calc.	norm. atom % calc.
Y	31.93	28.33	2.11	32.28	28.57
Br	65.77	64.94	3.78	65.27	64.29
Al	2.30	6.73	4.00	2.45	7.14

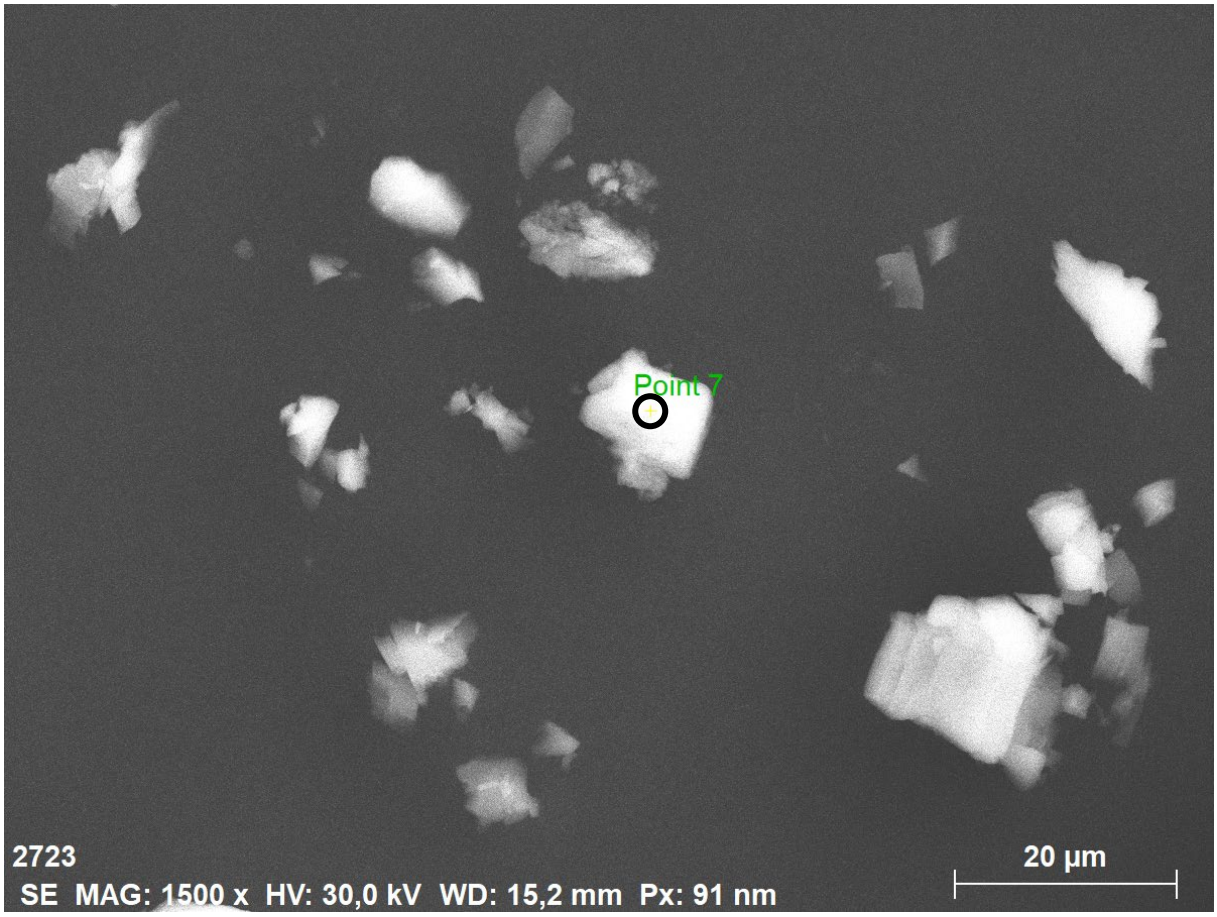

Figure S76. SEM image of crystalline [Cp*$_4$Y$_4$Br$_9$(AlMe$_2$)] (**4^{Y}**) of point 7, where EDX spectroscopy was performed.

Table S28. Results of EDX spectroscopy of point 7 (Fig. S76).

Element	norm. wt. %	norm. atom %	3 σ	norm. wt. % calc.	norm. atom % calc.
Y	31.28	27.49	2.44	32.28	28.57
Br	65.96	64.51	4.58	65.27	64.29
Al	2.76	7.99	5.86	2.45	7.14

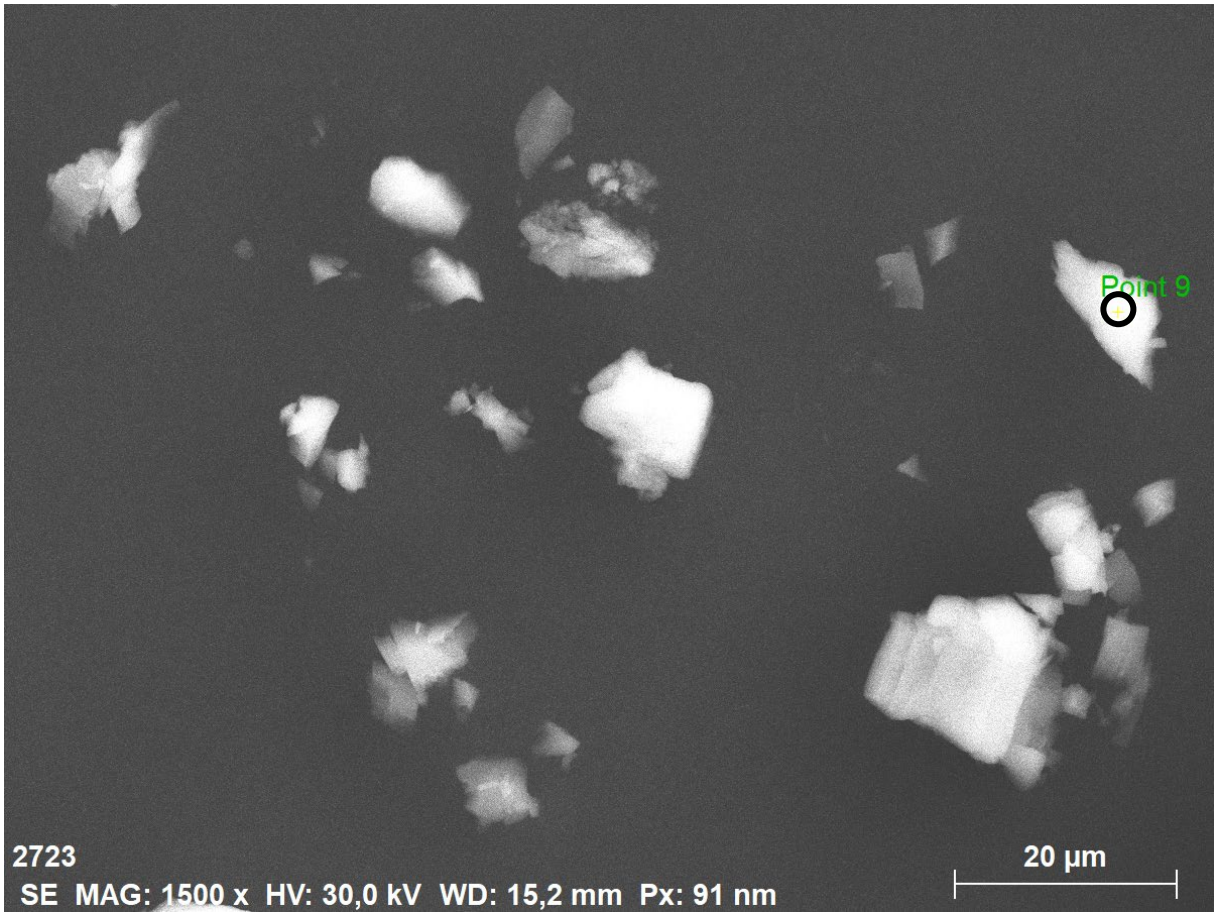

Figure S77. SEM image of crystalline [Cp*$_4$Y$_4$Br$_9$(AlMe$_2$)] (**4^{Y}**) of point 9, where EDX spectroscopy was performed.

Table S29. Results of EDX spectroscopy of point 9 (Fig. S77).

Element	norm. wt. %	norm. atom %	3 σ	norm. wt. % calc.	norm. atom % calc.
Y	31.80	27.98	2.43	32.28	28.57
Br	65.47	64.10	4.45	65.27	64.29
Al	2.73	7.92	5.67	2.45	7.14

Table S30. Averaged results of all EDX analyses for **4^{Y}** (11 measurements).

Element	norm. wt. %	norm. atom %	3 σ	norm. wt. % calc.	norm. atom % calc.
Y	31.81	27.89	2.33	32.28	28.57
Br	65.26	63.66	4.23	65.27	64.29
Al	2.93	8.45	5.79	2.45	7.14

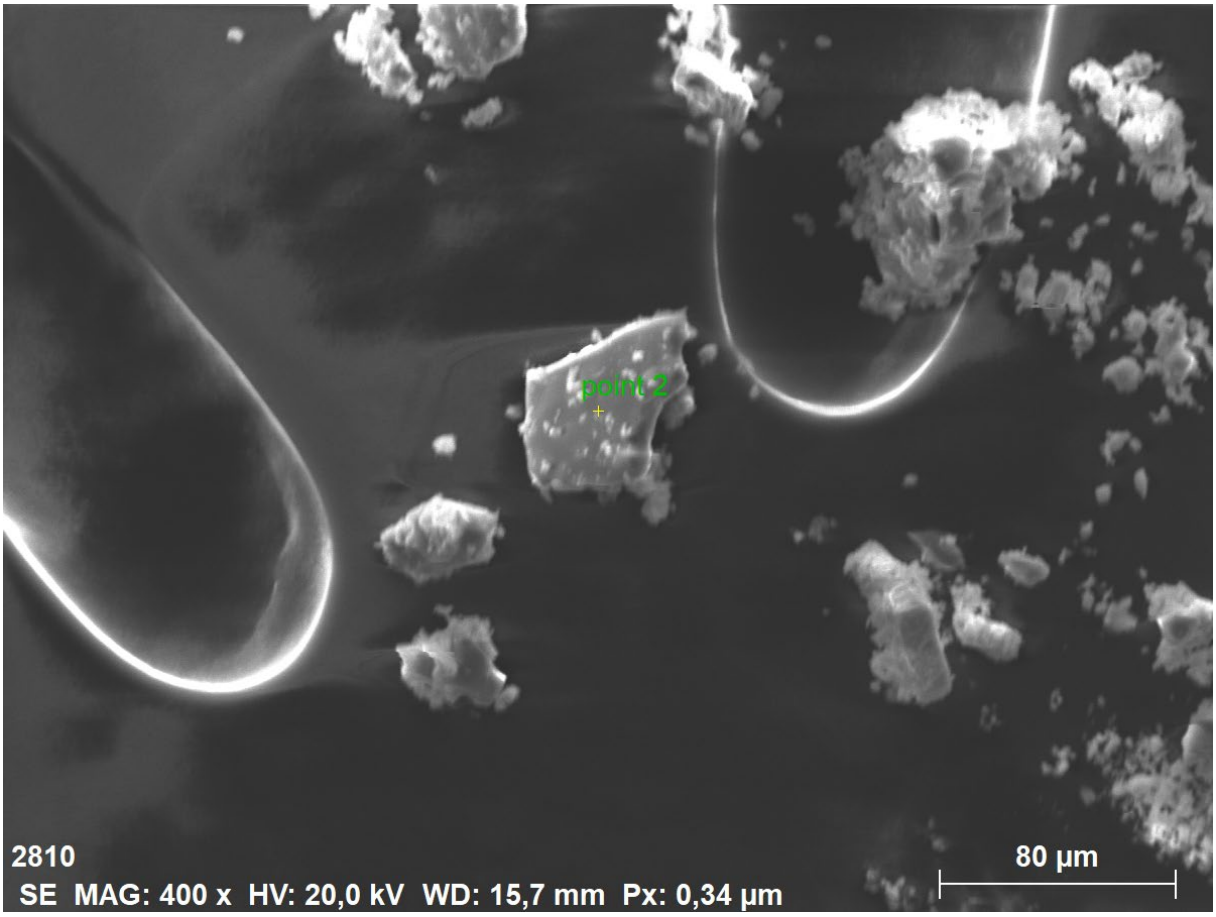

Figure S78. SEM image of crystalline [Cp*$_4$Gd$_4$Br$_9$(AlMe$_2$)] (**4^{Gd}**) of point 2, where EDX spectroscopy was performed.

Table S31. Results of EDX spectroscopy of point 2 (Fig. S78).

Element	norm. wt. %	norm. atom %	3 σ	norm. wt. % calc.	norm. atom % calc.
Gd	47.28	29.55	2.20	45.74	28.57
Br	50.36	61.87	2.78	52.30	64.29
Al	2.36	8.58	3.12	1.96	7.14

Figure S79. SEM image of crystalline [Cp*$_4$Gd$_4$Br$_9$(AlMe$_2$)] (**4^{Gd}**) of point 7, where EDX spectroscopy was performed.

Table S32. Results of EDX spectroscopy of point 7 (Fig. S79).

Element	norm. wt. %	norm. atom %	3 σ	norm. wt. % calc.	norm. atom % calc.
Gd	45.79	28.44	3.08	45.74	28.57
Br	52.00	63.57	4.11	52.30	64.29
Al	2.21	7.99	4.23	1.96	7.14

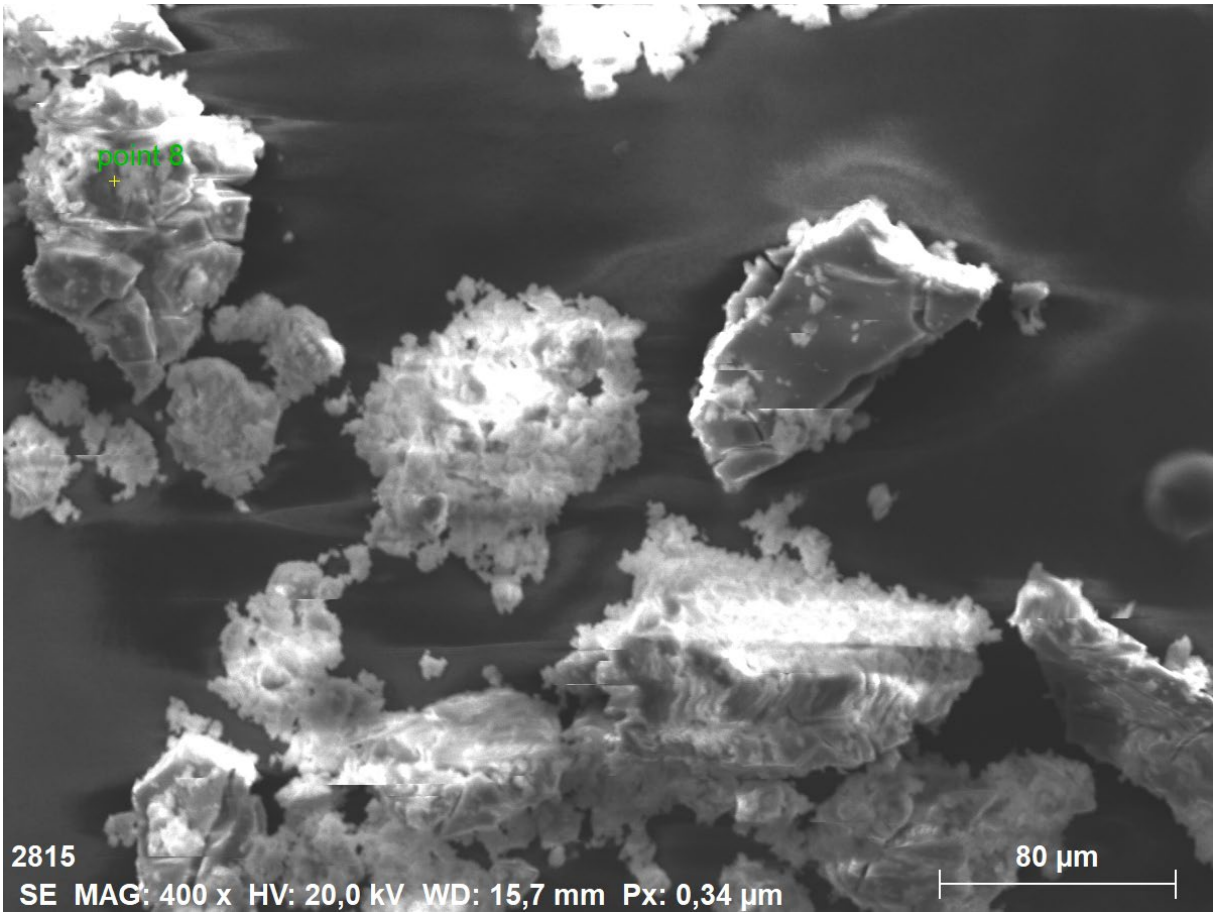

Figure S80. SEM image of crystalline [Cp*$_4$Gd$_4$Br$_9$(AlMe$_2$)] (**4^{Gd}**) of point 8, where EDX spectroscopy was performed.

Table S33. Results of EDX spectroscopy of point 8 (Fig. S80).

Element	norm. wt. %	norm. atom %	3 σ	norm. wt. % calc.	norm. atom % calc.
Gd	44.66	27.66	2.02	45.74	28.57
Br	53.29	64.96	2.81	52.30	64.29
Al	2.04	7.38	2.63	1.96	7.14

Table S34. Averaged results of all EDX analyses for **4^{Gd}** (14 measurements).

Element	norm. wt. %	norm. atom %	3 σ	norm. wt. % calc.	norm. atom % calc.
Gd	31.81	27.89	2.33	45.74	28.57
Br	65.26	63.66	4.23	52.30	64.29
Al	2.93	8.45	5.79	1.96	7.14

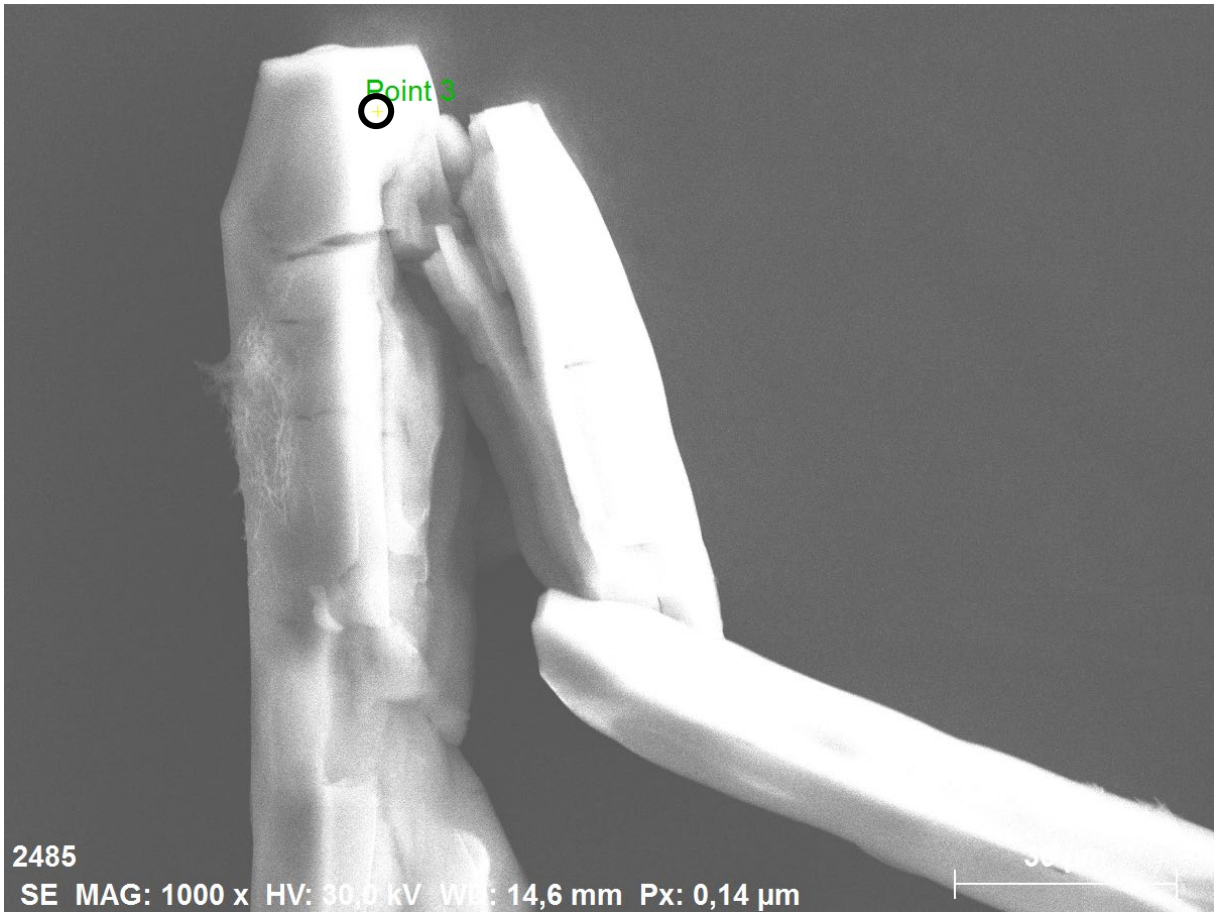

Figure S81. SEM image of crystalline [Cp*$_4$Tb$_4$Br$_9$(AlMe$_2$)] (**4^{Tb}**) of point 3, where EDX spectroscopy was performed.

Table S35. Results of EDX spectroscopy of point 3 (Fig. S81).

Element	norm. wt. %	norm. atom %	3 σ	norm. wt. % calc.	norm. atom % calc.
Tb	45.58	28.05	3.06	46.00	28.57
Br	52.21	63.92	3.45	52.04	64.29
Al	2.22	8.03	4.50	1.95	7.14

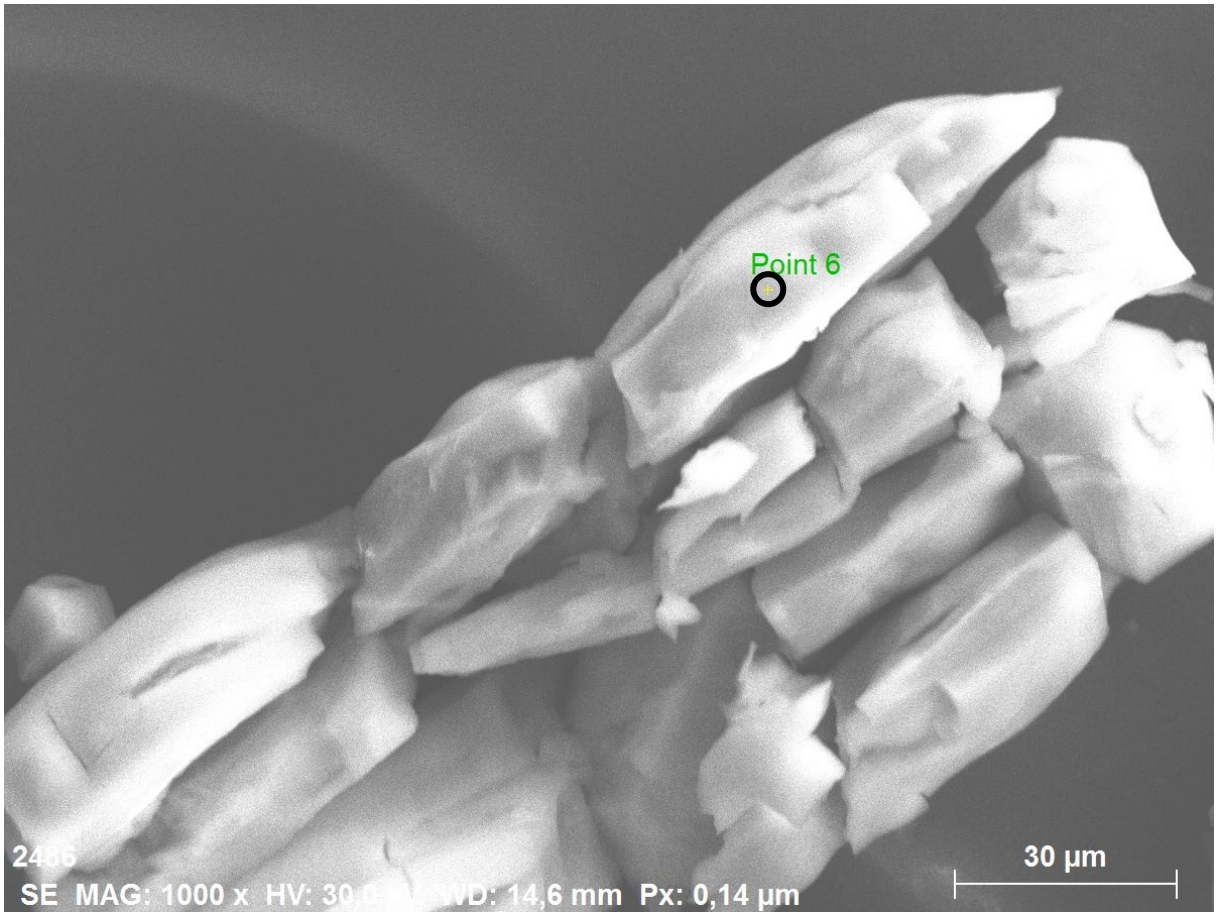

Figure S82. SEM image of crystalline [Cp*$_4$Tb$_4$Br$_9$(AlMe$_2$)] (**4^{Tb}**) of point 6, where EDX spectroscopy was performed.

Table S36. Results of EDX spectroscopy of point 6 (Fig. S82).

Element	norm. wt. %	norm. atom %	3 σ	norm. wt. % calc.	norm. atom % calc.
Tb	46.76	29.21	2.89	46.00	28.57
Br	51.34	63.79	3.13	52.04	64.29
Al	1.90	7.00	2.51	1.95	7.14

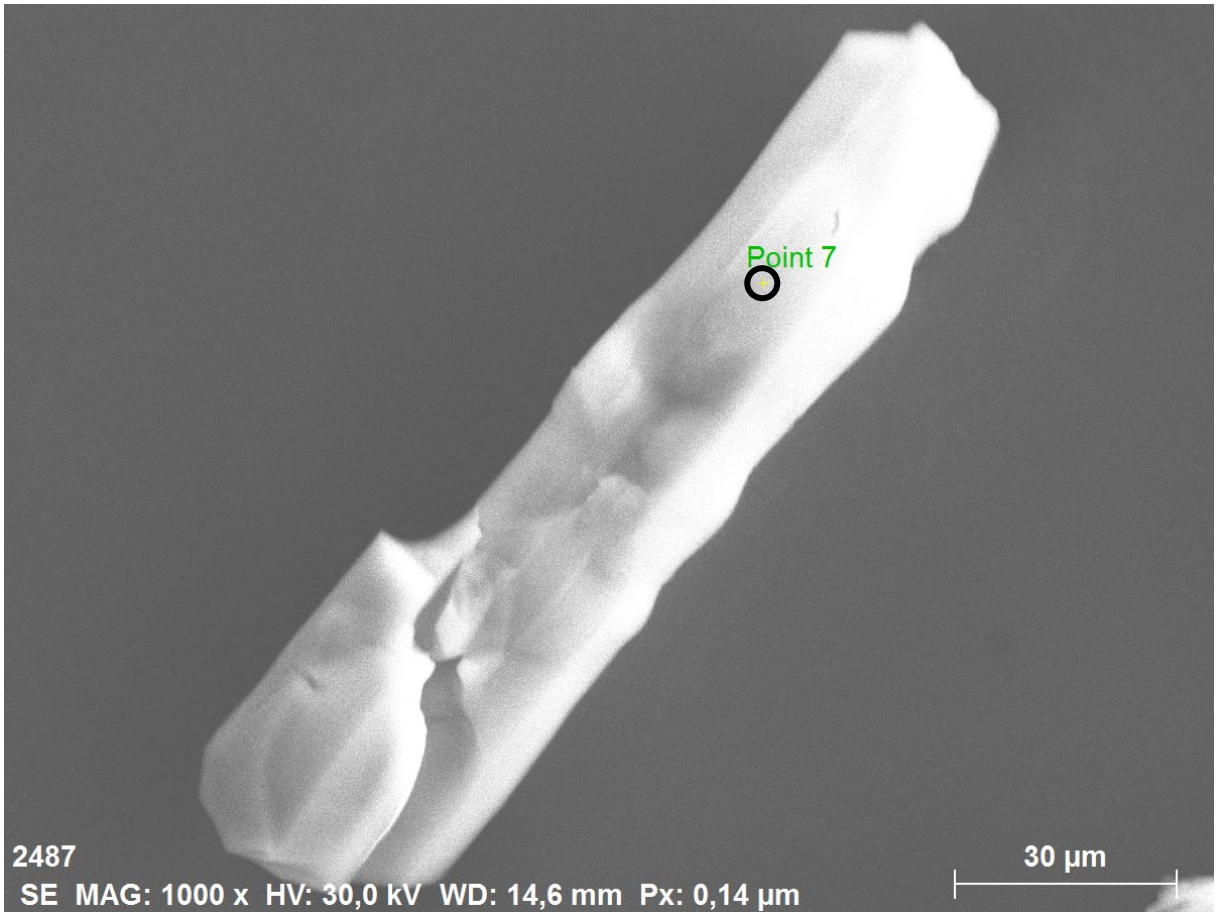

Figure S83. SEM image of crystalline [Cp*$_4$Tb$_4$Br$_9$(AlMe$_2$)] (**4^{Tb}**) of point 7, where EDX spectroscopy was performed.

Table S37. Results of EDX spectroscopy of point 7 (Fig. S83).

Element	norm. wt. %	norm. atom %	3 σ	norm. wt. % calc.	norm. atom % calc.
Tb	45.90	28.40	3.19	46.00	28.57
Br	52.03	64.04	3.56	52.04	64.29
Al	2.07	7.56	3.24	1.95	7.14

Table S38. Averaged results of all EDX analyses for **4^{Tb}** (12 measurements).

Element	norm. wt. %	norm. atom %	3 σ	norm. wt. % calc.	norm. atom % calc.
Tb	45.65	28.24	3.08	46.00	28.57
Br	52.32	64.37	3.48	52.04	64.29
Al	2.03	7.39	3.61	1.95	7.14

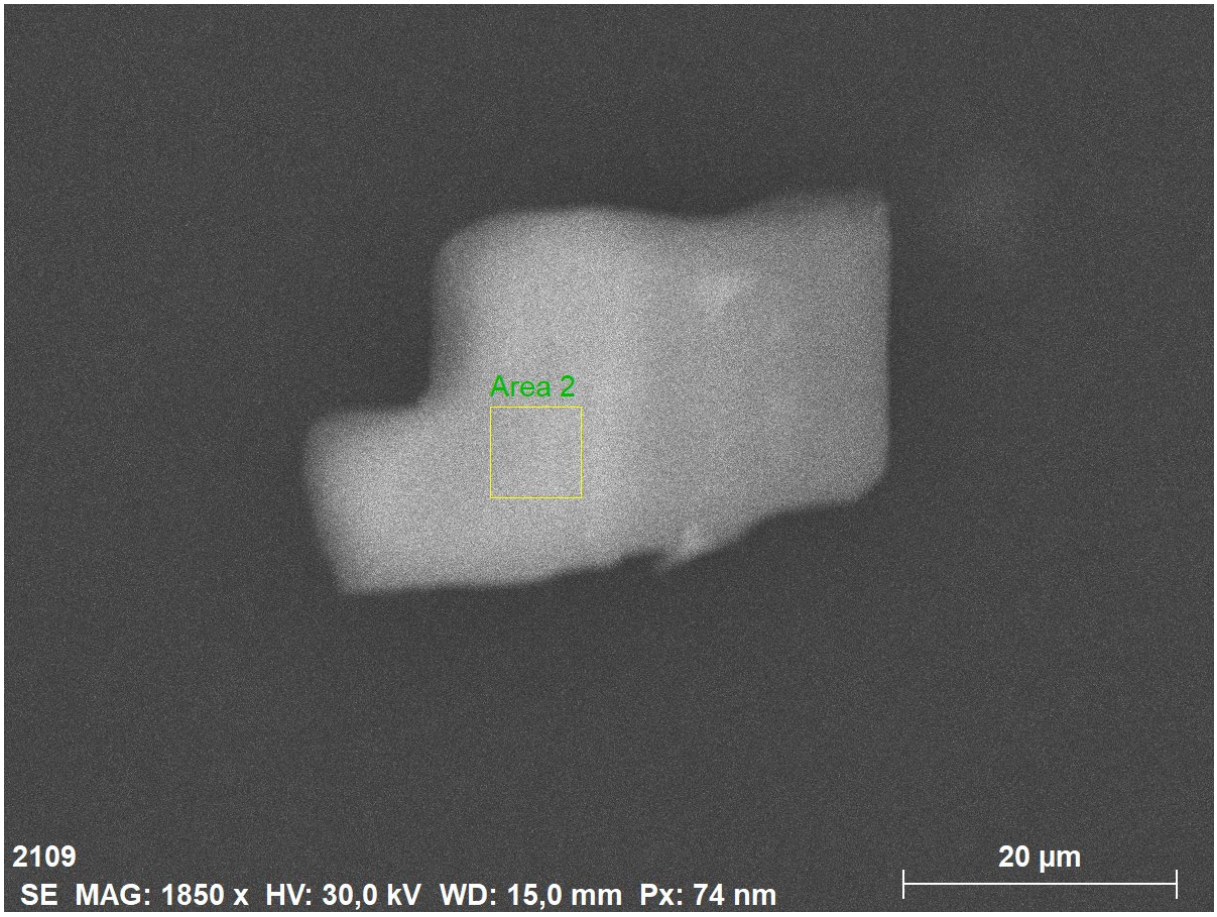

Figure S84. SEM image of crystalline [Cp*$_4$Dy$_4$Br$_9$(AlMe$_2$)] (**4^{Dy}**) of area 2, where EDX spectroscopy was performed.

Table S39. Results of EDX spectroscopy of area 2 (Fig. S84).

Element	norm. wt. %	norm. atom %	3 σ	norm. wt. % calc.	norm. atom % calc.
Dy	46.30	28.47	3.17	46.56	28.57
Br	51.92	64.94	3.50	51.51	64.29
Al	1.78	6.58	2.82	1.93	7.14

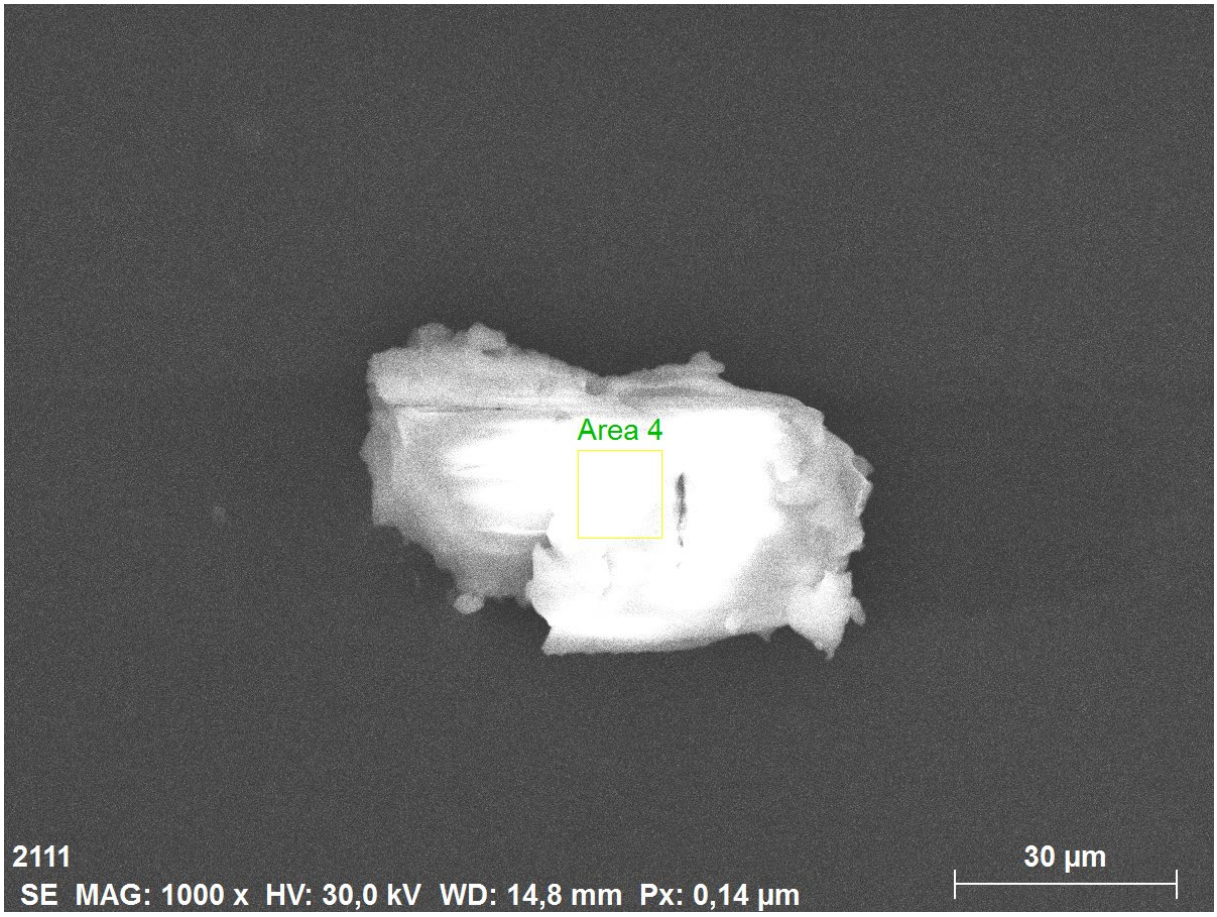

Figure S85. SEM image of crystalline [Cp*$_4$Dy$_4$Br$_9$(AlMe$_2$)] (**4^{Dy}**) of area 4, where EDX spectroscopy was performed.

Table S40. Results of EDX spectroscopy of area 4 (Fig. S85).

Element	norm. wt. %	norm. atom %	3 σ	norm. wt. % calc.	norm. atom % calc.
Dy	47.16	29.03	3.22	46.56	28.57
Br	50.87	63.68	3.43	51.51	64.29
Al	1.97	7.29	2.86	1.93	7.14

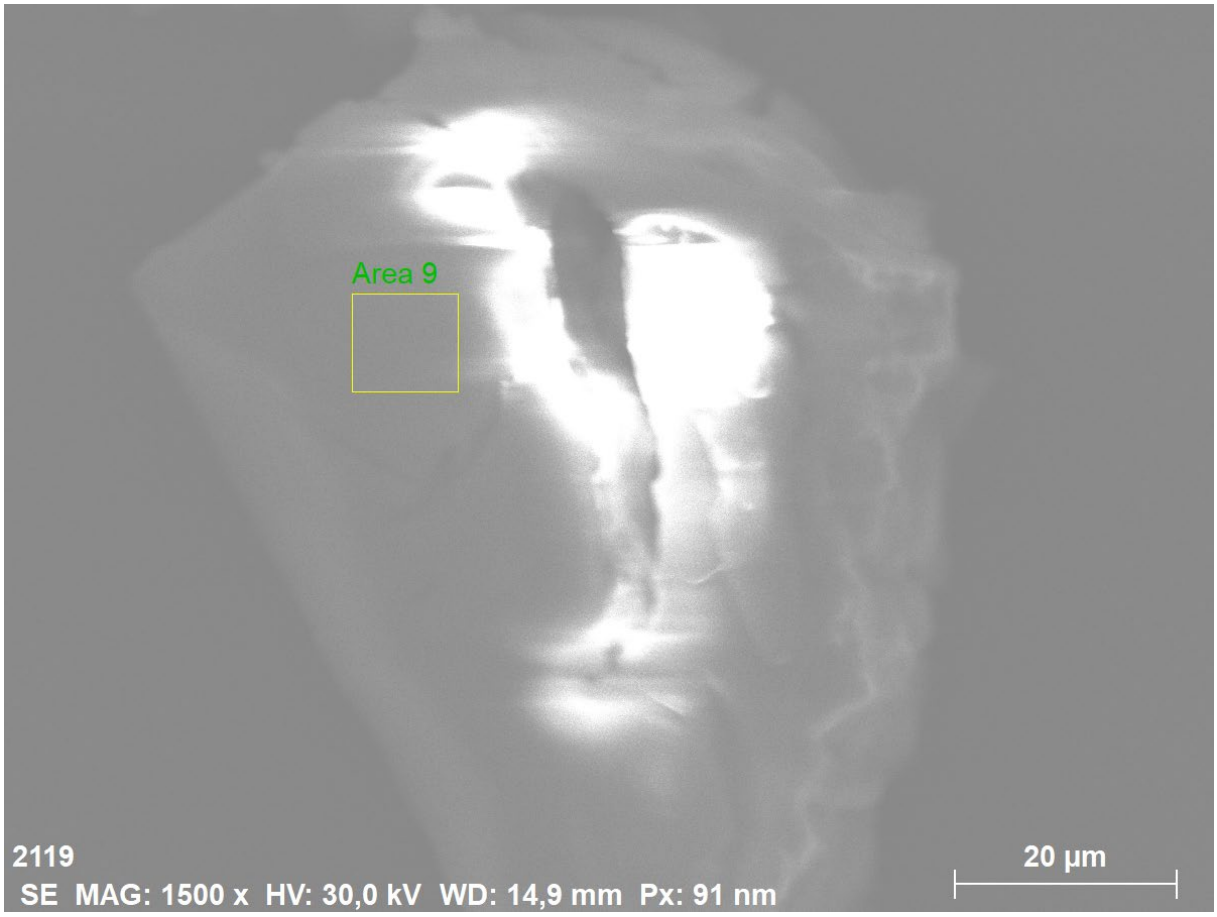

Figure S86. SEM image of crystalline [Cp*$_4$Dy$_4$Br$_9$(AlMe$_2$)] (**4^{Dy}**) of area 9, where EDX spectroscopy was performed.

Table S41. Results of EDX spectroscopy of area 9 (Fig. S86).

Element	norm. wt. %	norm. atom %	3 σ	norm. wt. % calc.	norm. atom % calc.
Dy	47.05	28.93	2.97	46.56	28.57
Br	50.97	63.74	3.18	51.51	64.29
Al	1.98	7.33	2.99	1.93	7.14

Table S42. Averaged results of all EDX analyses for **4^{Dy}** (11 measurements).

Element	norm. wt. %	norm. atom %	3 σ	norm. wt. % calc.	norm. atom % calc.
Dy	46.23	28.25	3.12	46.56	28.57
Br	51.64	64.10	3.51	51.51	64.29
Al	2.08	7.65	2.84	1.93	7.14

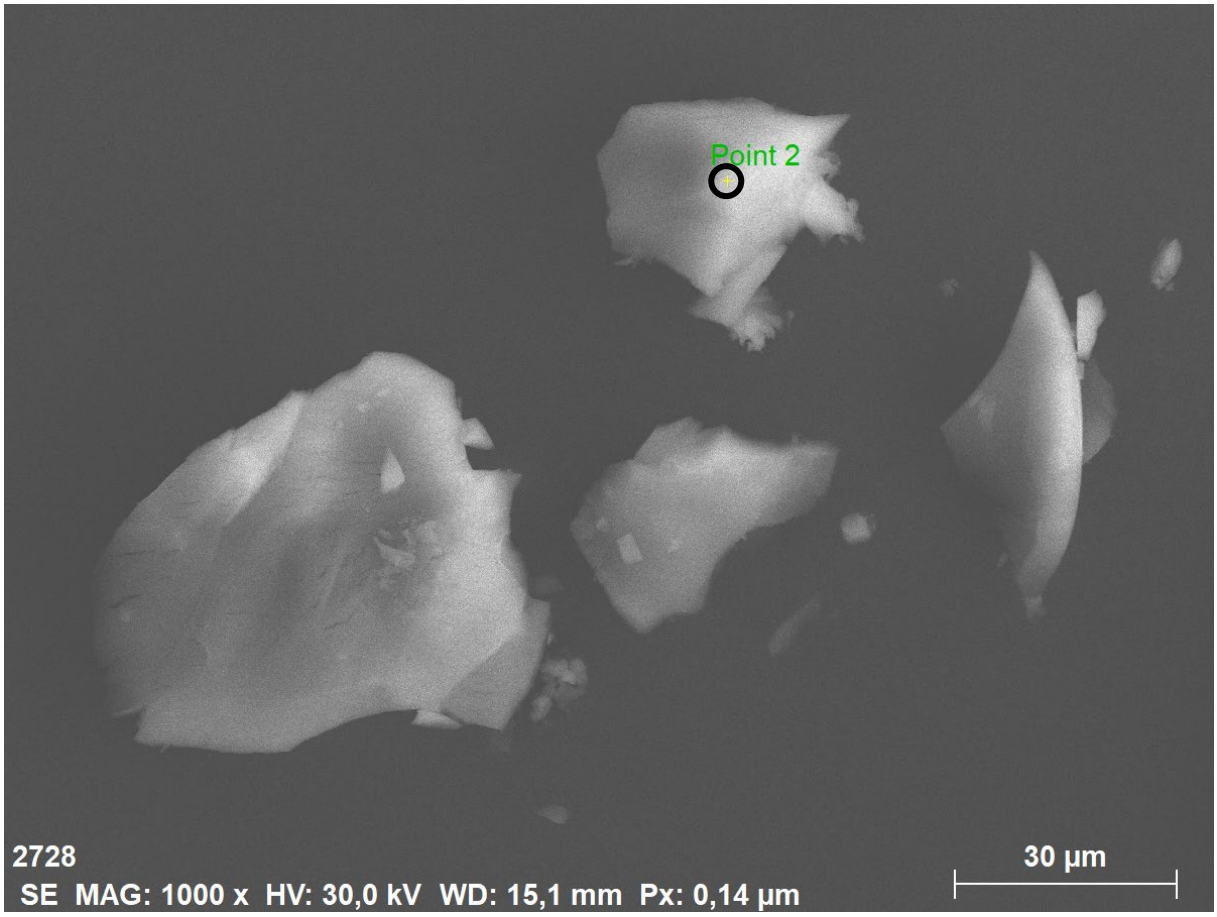

Figure S87. SEM image of crystalline $[Cp^*_4Y_4Cl_{10}(AlMe_2)_2]$ (**5**$^{\mathbf{Y}}$) of point 2, where EDX spectroscopy was performed.

Table S43. Results of EDX spectroscopy of point 2 (Fig. S87).

Element	norm. wt. %	norm. atom %	3 σ	norm. wt. % calc.	norm. atom % calc.
Y	46.40	24.88	3.19	46.54	25.00
Cl	46.33	62.28	3.84	46.40	62.50
Al	7.27	12.84	0.95	7.06	12.50

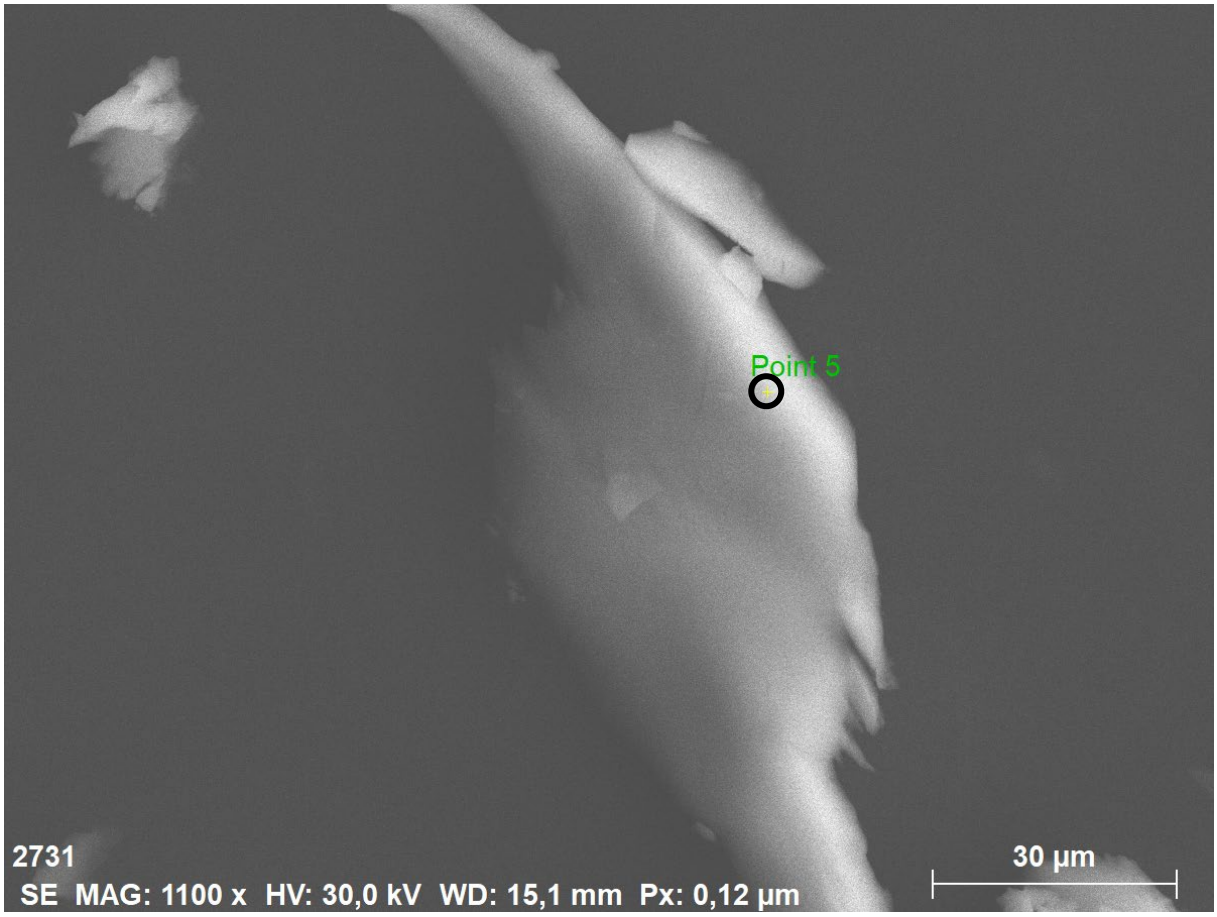

Figure S88. SEM image of crystalline $[Cp^*_4Y_4Cl_{10}(AlMe_2)_2]$ ($\mathbf{5^Y}$) of point 5, where EDX spectroscopy was performed.

Table S44. Results of EDX spectroscopy of point 5 (Fig. S88).

Element	norm. wt. %	norm. atom %	3 σ	norm. wt. % calc.	norm. atom % calc.
Y	46.28	24.83	3.09	46.54	25.00
Cl	46.95	63.19	3.82	46.40	62.50
Al	6.77	11.97	0.87	7.06	12.50

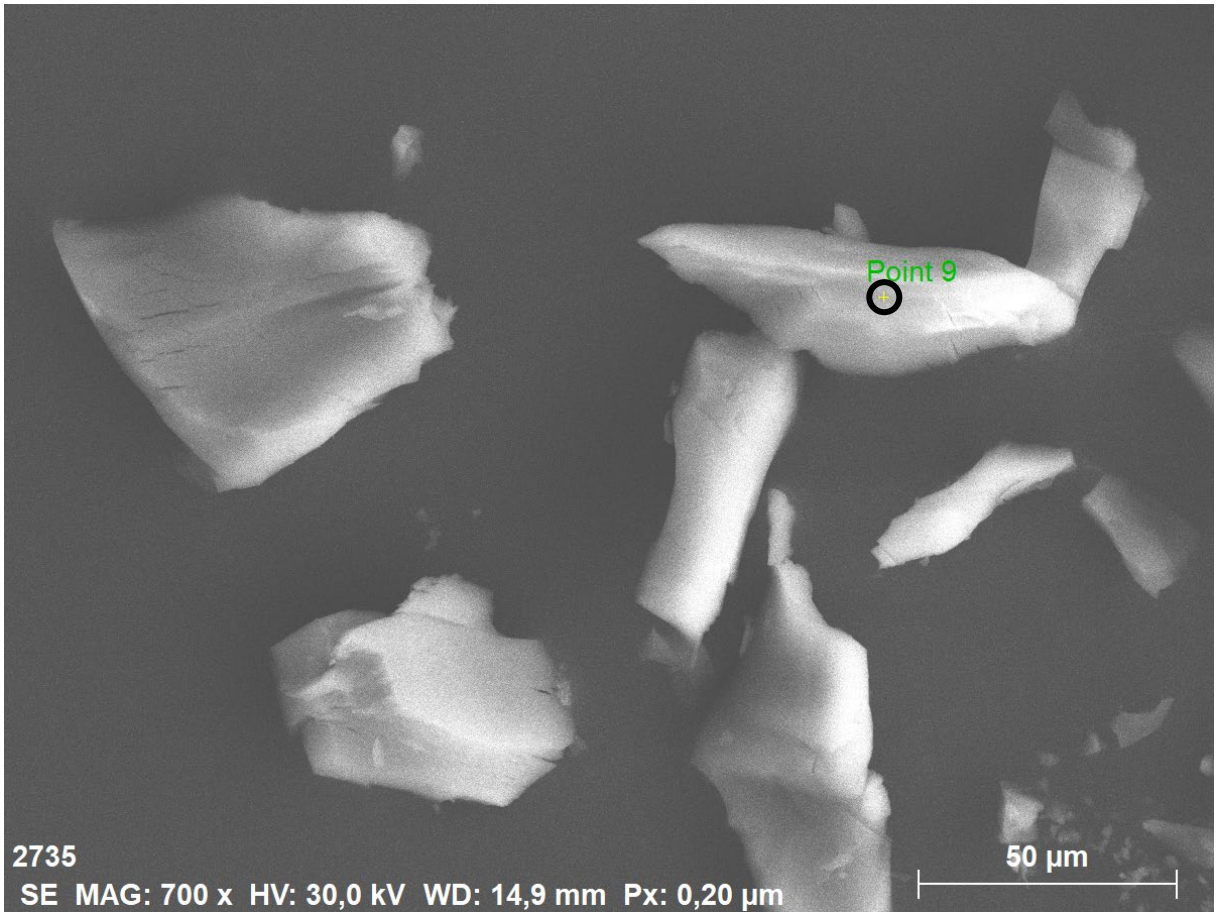

Figure S89. SEM image of crystalline $[Cp^*_4Y_4Cl_{10}(AlMe_2)_2]$ (**5^Y**) of point 9, where EDX spectroscopy was performed.

Table S45. Results of EDX spectroscopy of point 9 (Fig. S89).

Element	norm. wt. %	norm. atom %	3 σ	norm. wt. % calc.	norm. atom % calc.
Y	46.13	24.65	2.77	46.54	25.00
Cl	46.30	62.03	3.36	46.40	62.50
Al	7.57	13.32	0.88	7.06	12.50

Table S46. Averaged results of all EDX analyses for **5^Y** (11 measurements).

Element	norm. wt. %	norm. atom %	3 σ	norm. wt. % calc.	norm. atom % calc.
Y	46.51	24.99	3.08	46.54	25.00
Cl	46.45	62.56	3.75	46.40	62.50
Al	7.04	12.46	0.90	7.06	12.50

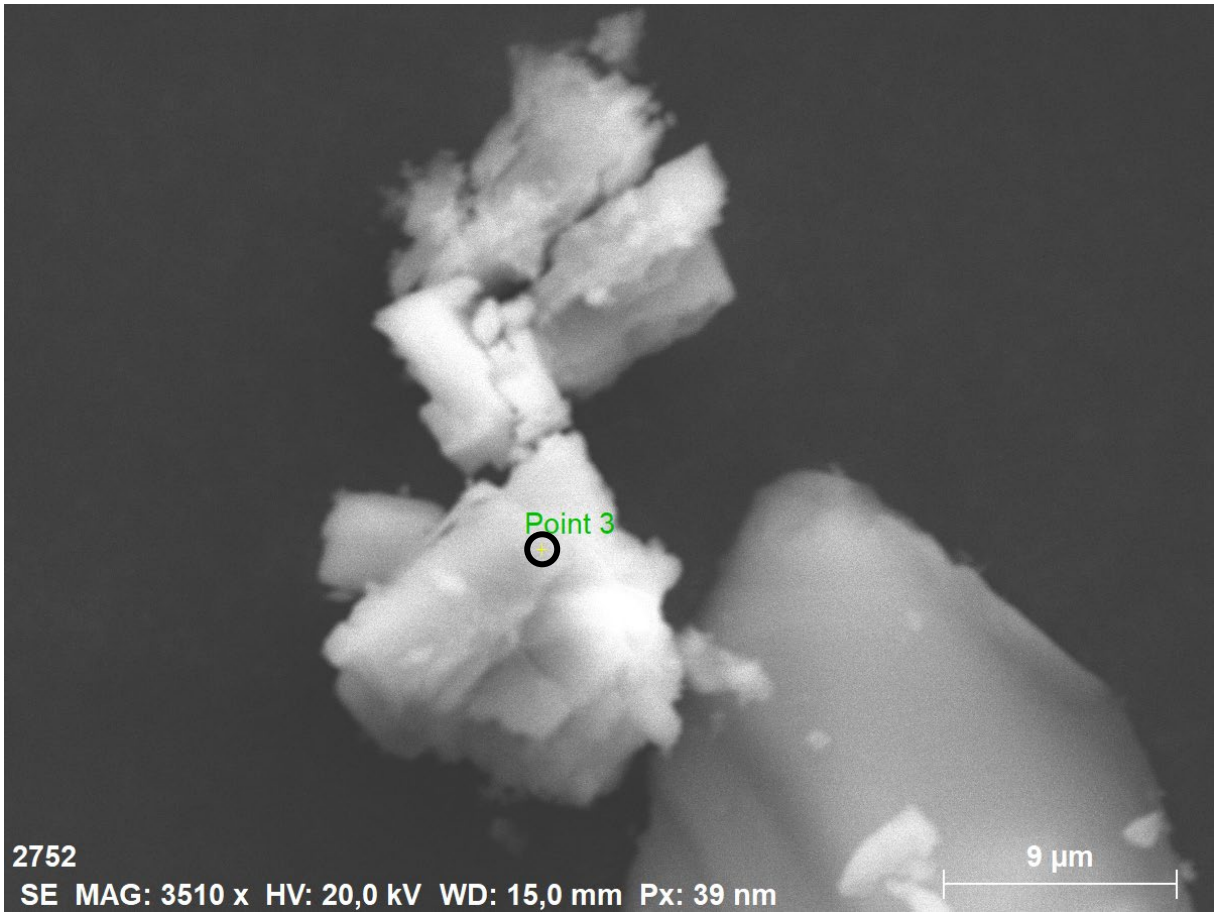

Figure S90. SEM image of crystalline $[Cp^*_4Gd_4Cl_{10}(AlMe_2)_2]$ (**5**^{Gd}) of point 3, where EDX spectroscopy was performed.

Table S47. Results of EDX spectroscopy of point 3 (Fig. S90).

Element	norm. wt. %	norm. atom %	3 σ	norm. wt. % calc.	norm. atom % calc.
Gd	61.01	25.33	3.66	60.63	25.00
Cl	34.03	62.66	2.58	34.17	62.50
Al	4.96	12.01	0.61	5.20	12.50

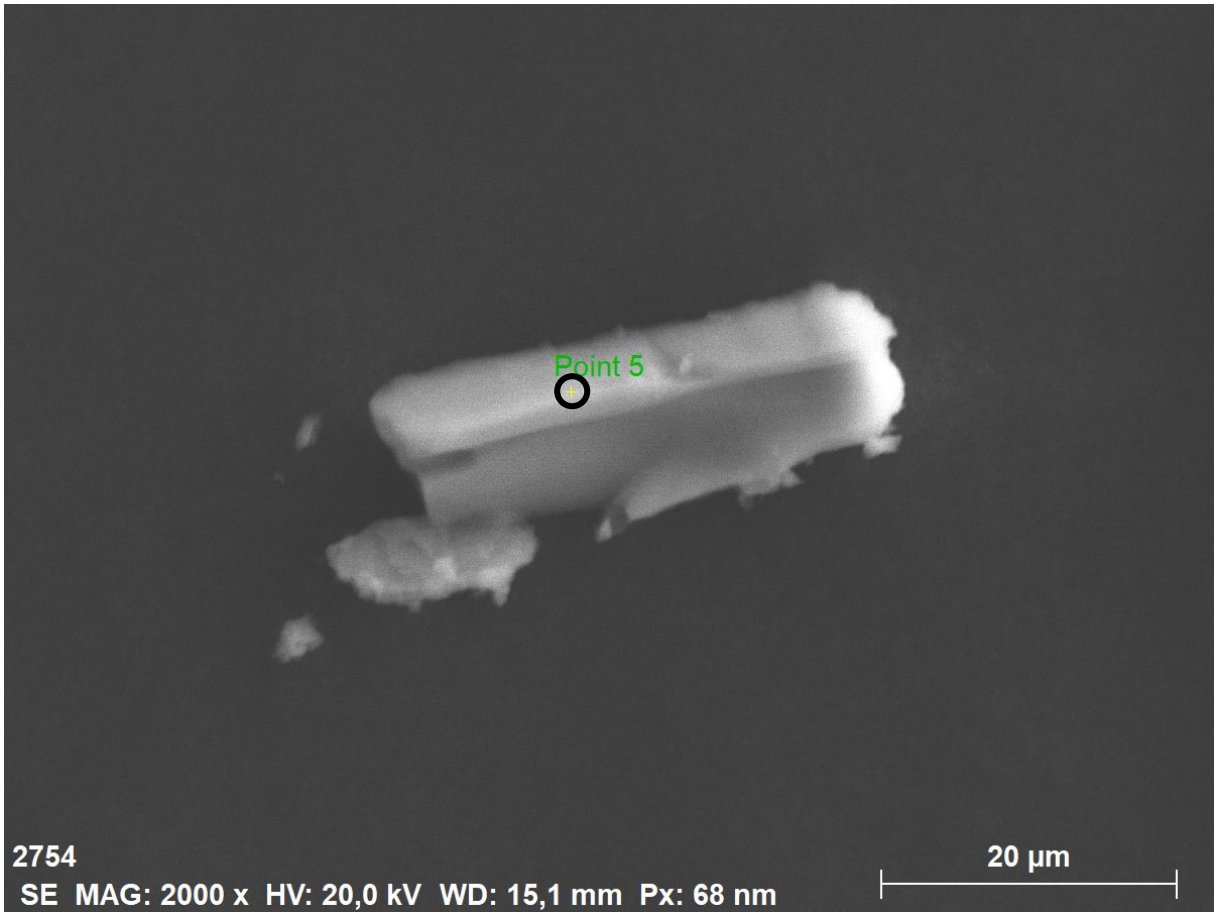

Figure S91. SEM image of crystalline $[Cp^*_4Gd_4Cl_{10}(AlMe_2)_2]$ (**5**^{Gd}) of point 5, where EDX spectroscopy was performed.

Table S48. Results of EDX spectroscopy of point 5 (Fig. S91).

Element	norm. wt. %	norm. atom %	3 σ	norm. wt. % calc.	norm. atom % calc.
Gd	61.14	25.44	3.90	60.63	25.00
Cl	33.92	62.59	2.74	34.17	62.50
Al	4.94	11.97	0.64	5.20	12.50

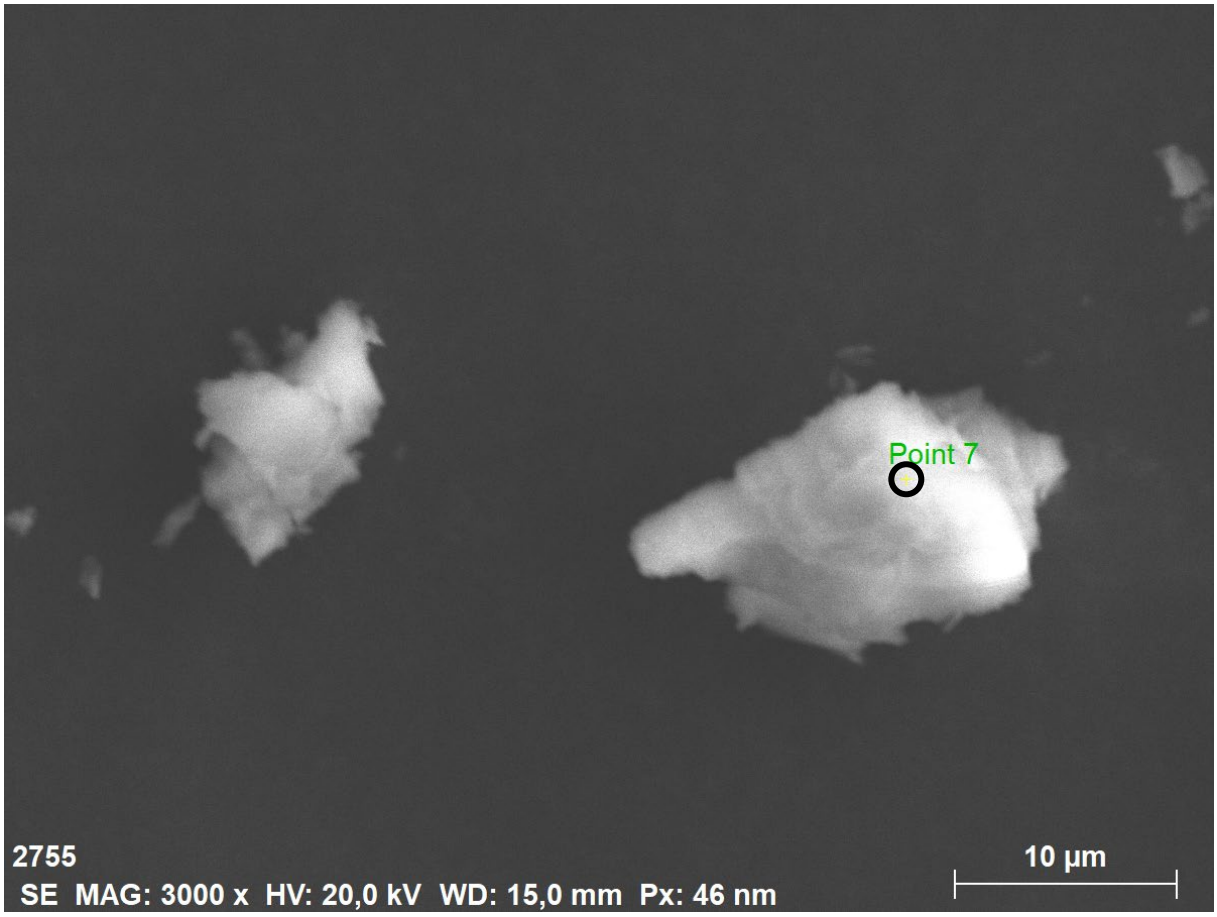

Figure S92. SEM image of crystalline $[Cp^*_4Gd_4Cl_{10}(AlMe_2)_2]$ (**5**^{Gd}) of point 3, where EDX spectroscopy was performed.

Table S49. Results of EDX spectroscopy of point 3 (Fig. S92).

Element	norm. wt. %	norm. atom %	3 σ	norm. wt. % calc.	norm. atom % calc.
Gd	61.60	25.78	4.08	60.63	25.00
Cl	33.36	61.92	2.80	34.17	62.50
Al	5.04	12.30	0.67	5.20	12.50

Table S50. Averaged results of all EDX analyses for **5**^{Gd} (12 measurements).

Element	norm. wt. %	norm. atom %	3 σ	norm. wt. % calc.	norm. atom % calc.
Gd	60.56	24.97	3.78	60.63	25.00
Cl	34.30	62.70	2.71	34.17	62.50
Al	5.13	12.33	0.65	5.20	12.50

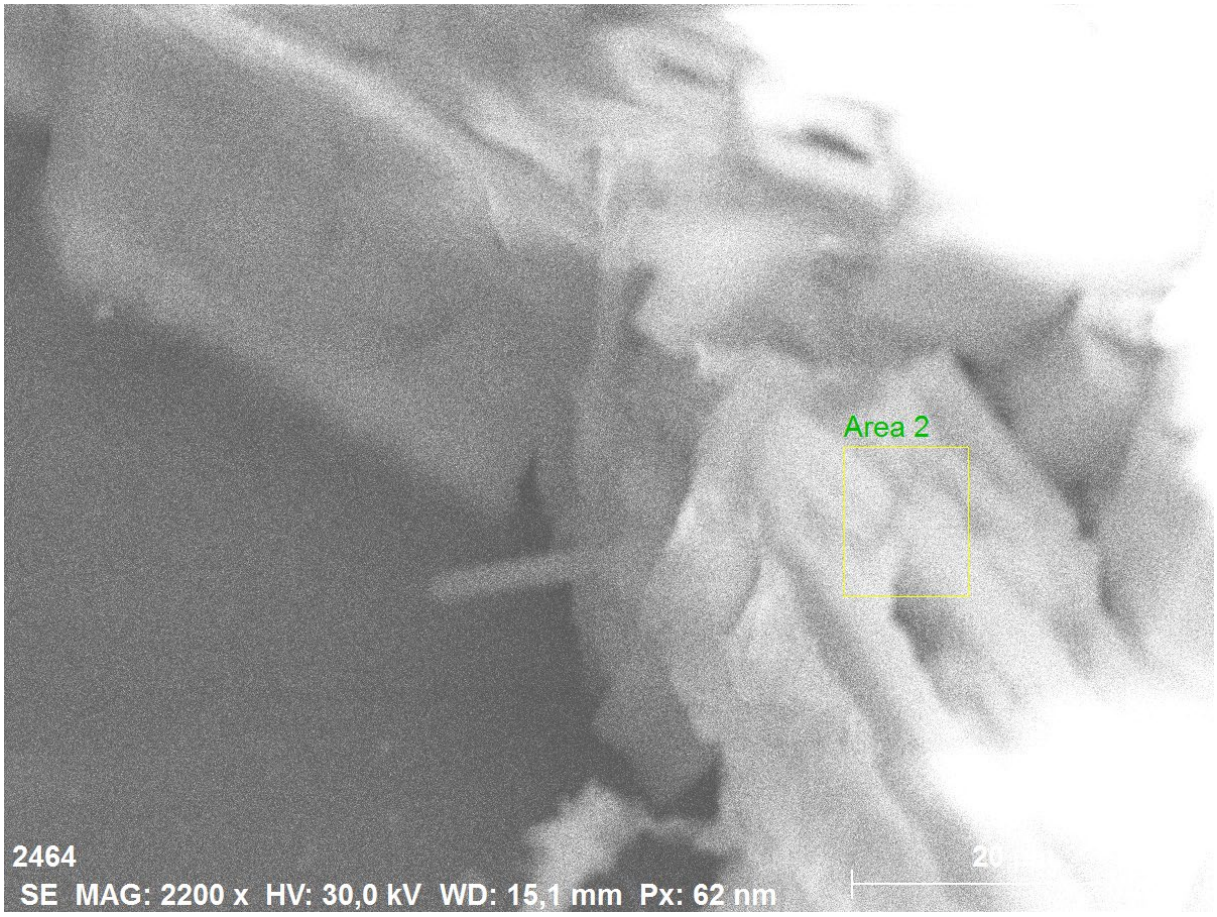

Figure S93. SEM image of crystalline [Cp*$_4$Tb$_4$Cl$_9$(AlMe$_2$)] (**6^{Tb}**) of area 2, where EDX spectroscopy was performed.

Table S51. Results of EDX spectroscopy of area 2 (Fig. S93).

Element	norm. wt. %	norm. atom %	3 σ	norm. wt. % calc.	norm. atom % calc.
Tb	64.38	28.24	4.55	64.75	28.57
Cl	32.86	64.61	3.22	32.50	64.29
Al	2.77	7.14	0.48	2.75	7.14

Figure S94. SEM image of crystalline [Cp*$_4$Tb$_4$Cl$_9$(AlMe$_2$)] (**6^{Tb}**) of area 4, where EDX spectroscopy was performed.

Table S52. Results of EDX spectroscopy of area 4 (Fig. S94).

Element	norm. wt. %	norm. atom %	3 σ	norm. wt. % calc.	norm. atom % calc.
Tb	65.04	28.86	3.82	64.75	28.57
Cl	32.41	64.46	2.64	32.50	64.29
Al	2.56	6.68	0.38	2.75	7.14

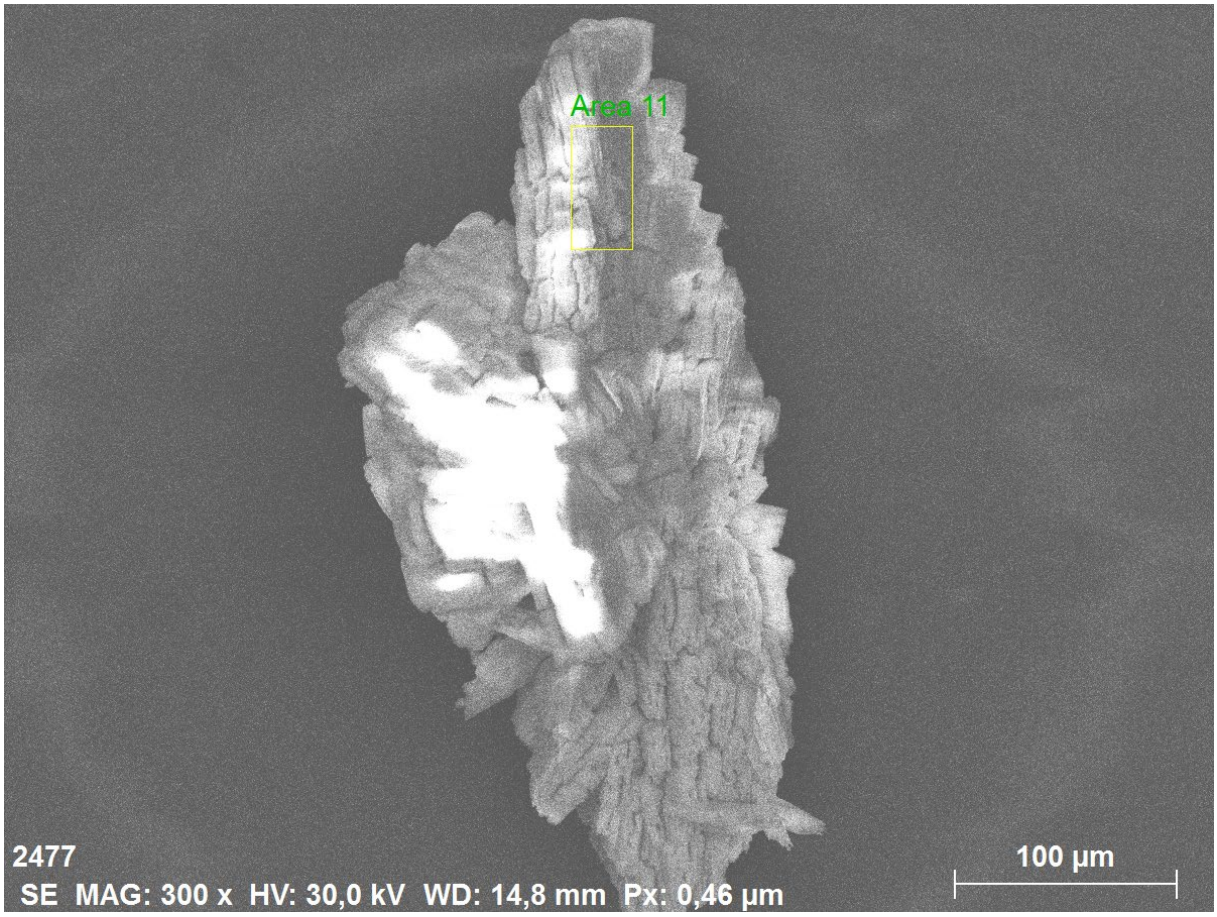

Figure S95. SEM image of crystalline [Cp*$_4$Tb$_4$Cl$_9$(AlMe$_2$)] (**6^{Tb}**) of area 11, where EDX spectroscopy was performed.

Table S53. Results of EDX spectroscopy of area 11 (Fig. S95).

Element	norm. wt. %	norm. atom %	3 σ	norm. wt. % calc.	norm. atom % calc.
Tb	65.14	28.96	4.40	64.75	28.57
Cl	32.37	64.52	3.03	32.50	64.29
Al	2.49	6.52	0.42	2.75	7.14

Table S54. Averaged results of all EDX analyses for **6^{Tb}** (12 measurements).

Element	norm. wt. %	norm. atom %	3 σ	norm. wt. % calc.	norm. atom % calc.
Tb	64.18	28.07	3.98	64.75	28.57
Cl	33.00	64.68	2.83	32.50	64.29
Al	2.82	7.25	0.43	2.75	7.14

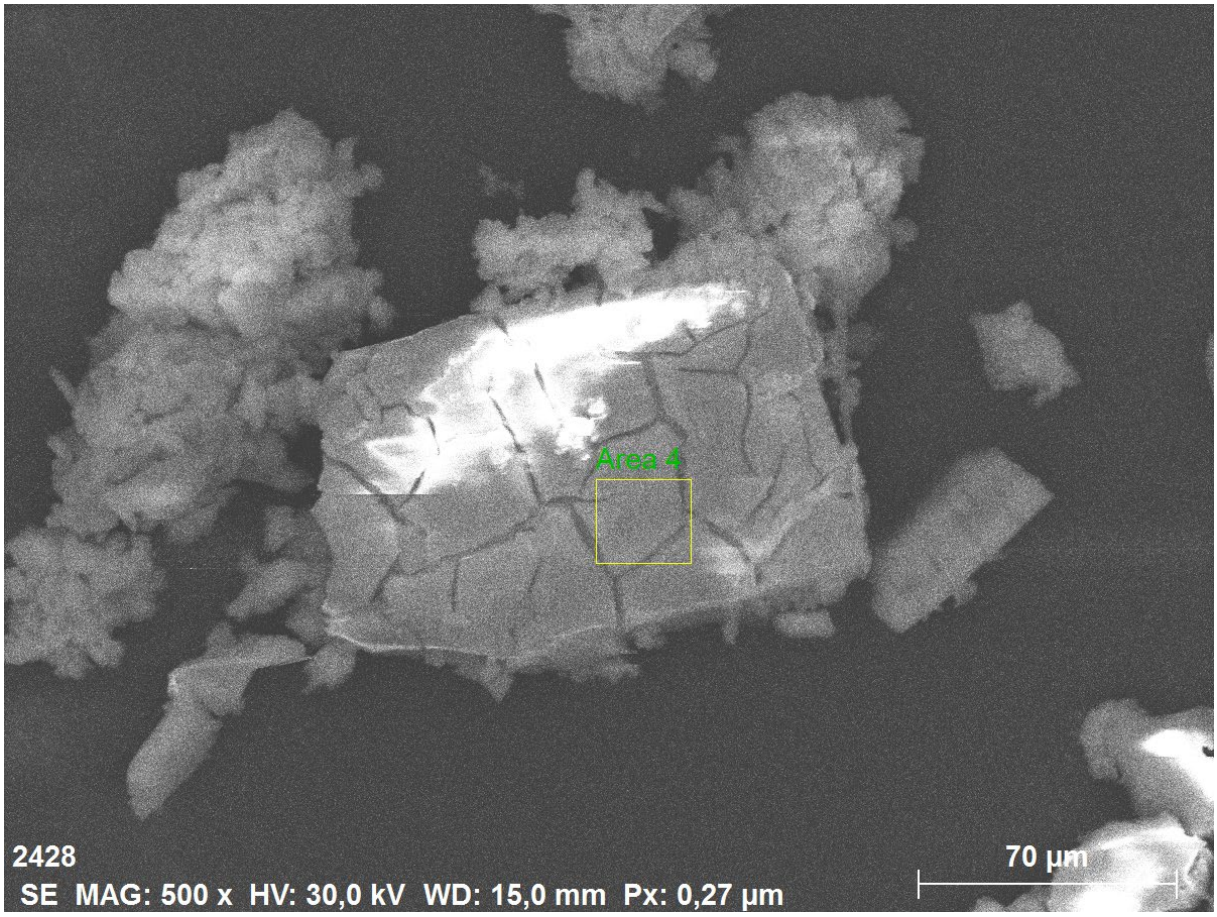

Figure S96. SEM image of crystalline [Cp*$_4$Dy$_4$Cl$_9$(AlMe$_2$)] (**6^{Dy}**) of area 4, where EDX spectroscopy was performed.

Table S55. Results of EDX spectroscopy of area 4 (Fig. S96).

Element	norm. wt. %	norm. atom %	3 σ	norm. wt. % calc.	norm. atom % calc.
Dy	65.22	28.52	3.51	65.26	28.57
Cl	32.00	64.14	2.40	32.03	64.29
Al	2.78	7.33	0.38	2.71	7.14

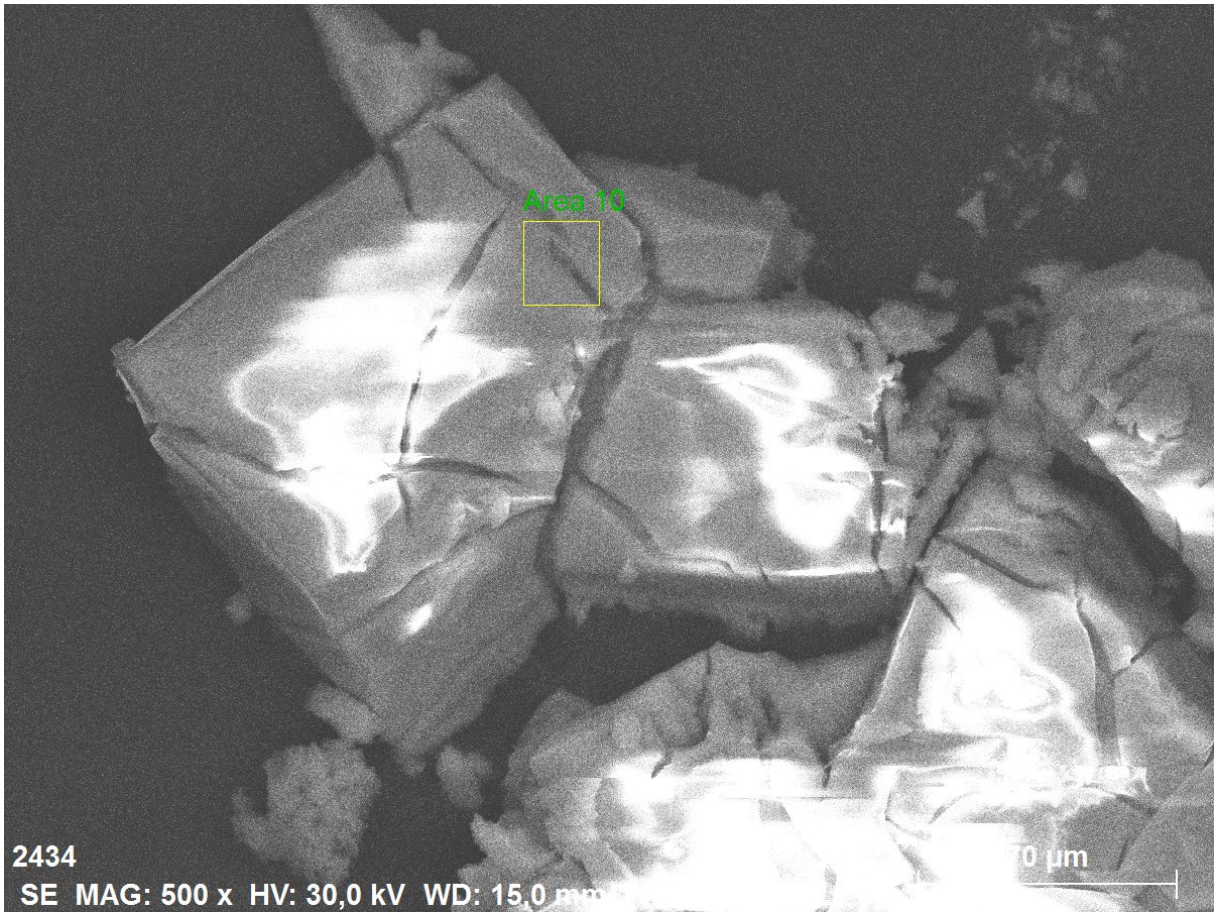

Figure S97. SEM image of crystalline [Cp*$_4$Dy$_4$Cl$_9$(AlMe$_2$)] (**6^{Dy}**) of area 10, where EDX spectroscopy was performed.

Table S56. Results of EDX spectroscopy of area 10 (Fig. S97).

Element	norm. wt. %	norm. atom %	3 σ	norm. wt. % calc.	norm. atom % calc.
Dy	65.32	28.64	3.70	65.26	28.57
Cl	32.00	64.31	2.52	32.03	64.29
Al	2.67	7.05	0.38	2.71	7.14

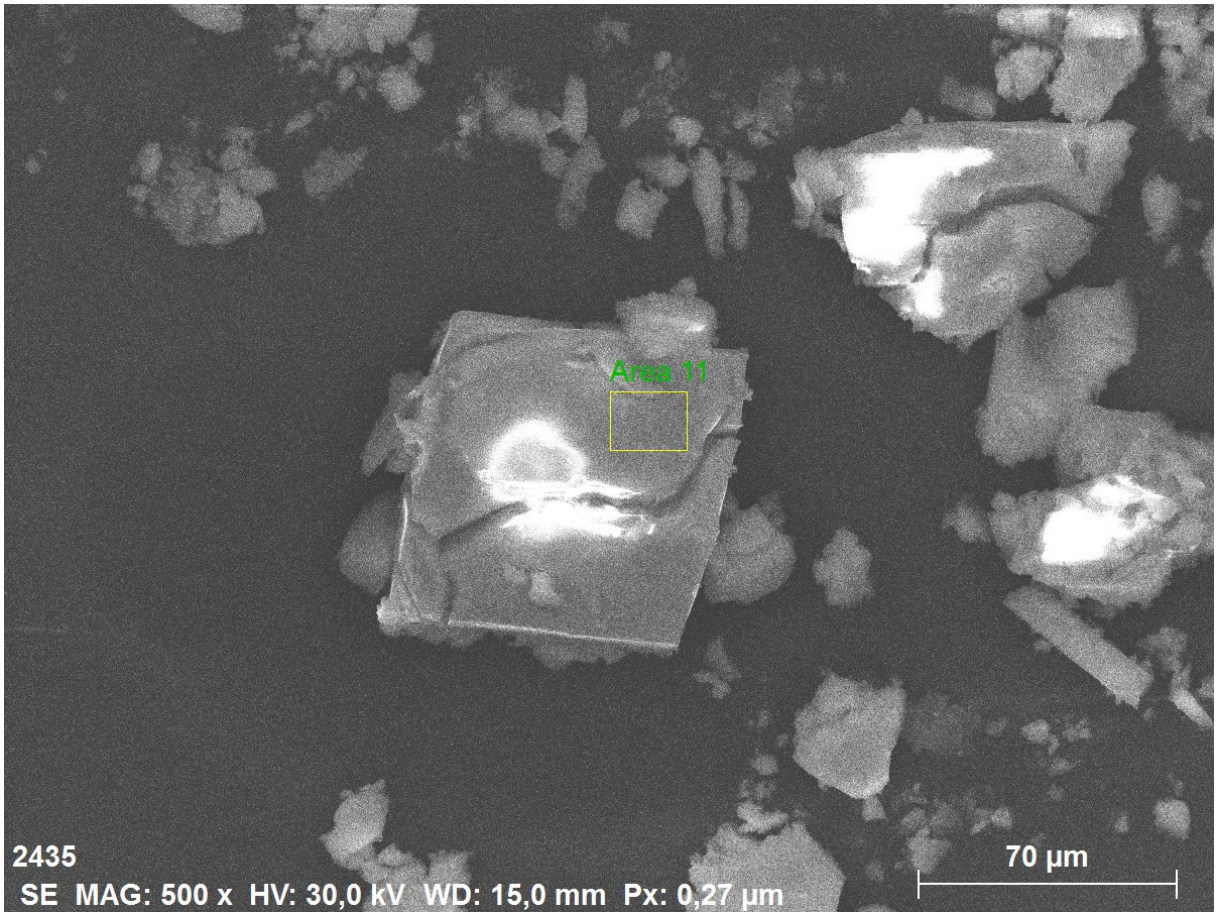

Figure S98. SEM image of crystalline [Cp*$_4$Dy$_4$Cl$_9$(AlMe$_2$)] (**6^{Dy}**) of area 11, where EDX spectroscopy was performed.

Table S57. Results of EDX spectroscopy of area 11 (Fig. S98).

Element	norm. wt. %	norm. atom %	3 σ	norm. wt. % calc.	norm. atom % calc.
Dy	65.25	28.60	3.63	65.26	28.57
Cl	32.23	64.75	2.50	32.03	64.29
Al	2.52	6.65	0.36	2.71	7.14

Table S58. Averaged results of all EDX analyses for **6^{Dy}** (11 measurements).

Element	norm. wt. %	norm. atom %	3 σ	norm. wt. % calc.	norm. atom % calc.
Dy	65.46	28.76	3.85	65.26	28.57
Cl	31.86	64.15	2.61	32.03	64.29
Al	2.68	7.09	0.40	2.71	7.14

Magnetic Measurements

Sample Preparation and Measurement Details

Magnetic measurements were recorded on a Quantum Design MPMS-XL7 SQUID magnetometer equipped with a 7 T magnet. Crystals of $[Cp^*DyI_2]_4$ were gently crushed (not ground into a powder) and added to a 7 mm NMR tube. A small amount of eicosane was melted onto the crystals to prevent the crystals from experiencing torque effects. The samples were then flame-sealed under a slight negative pressure. Samples masses were 32.8 mg for $[Cp^*DyI_2]_4$ and 59.2 mg for the magnetically dilute version $Dy@[Cp^*YI_2]_4$.

Direct current (DC) magnetic susceptibility measurements were performed in the temperature range 1.9-300 K with an applied field of 1000 Oe. AC susceptibility measurements were performed using an AC field of 3 Oe in zero DC field for $[Cp^*DyI_2]_4$ and for the 10% magnetically dilute sample $Dy@[Cp^*YI_2]_4$. Diamagnetic corrections were made using Pascal's constants.

$$\chi'(\nu_{ac}) = \chi_\infty + \frac{(\chi_s - \chi_\infty)[1 + (2\pi\nu_{ac}\tau)^{1-\alpha}\sin(\alpha\pi/2)]}{1 + 2(2\pi\nu_{ac}\tau)^{1-\alpha}\sin(\alpha\pi/2) + (2\pi\nu_{ac}\tau)^{2(1-\alpha)}} \qquad \text{Equation 1}$$

$$\chi''(\nu_{ac}) = \frac{(\chi_s - \chi_\infty)(2\pi\nu_{ac}\tau)^{1-\alpha}\cos(\alpha\pi/2)}{1 + 2(2\pi\nu_{ac}\tau)^{1-\alpha}\sin(\alpha\pi/2) + (2\pi\nu_{ac}\tau)^{2(1-\alpha)}} \qquad \text{Equation 2}$$

$$\tau^{-1} = \tau_0^{-1} e^{-U_{\text{eff}}/k_B T} + CT^n + \tau_{QTM}^{-1} \qquad \text{Equation 3}$$

U_{eff} is the effective energy barrier to reversal of the magnetization (the anisotropy barrier).
τ_0 is the pre-exponential factor (or attempt time).
C is the Raman coefficient.
n is the Raman exponent.
τ_{QTM} is the QTM time and τ_{QTM}^{-1} is the QTM rate.

Magnetic property measurements.

Static Field (DC) Magnetic Susceptibility and Isothermal Magnetization Measurements.

The temperature-dependence of the $X_M T$ product, where X_M is the molar magnetic susceptibility, is shown in Figure S99. The measurements were made at 1 K intervals in the region 2-30 K, 5 K intervals in the region 30-50 K, and 10 K intervals in the region 90-300 K. The value of $X_M T$ at 300 K is 52.82 cm^3 K mol^{-1} or 13.21 cm^3 K mol^{-1} per Dy^{3+} ion ($4f^9$, $^6H_{15/2}$). These data are typical of a molecule consisting of four weakly coupled Dy^{3+} ions, which should produce a theoretical maximum $X_M T$ value of 56.4 cm^3 K mol^{-1}. The discrepancy between the measured and predicted susceptibility is about 7%, which is normal for a compound of this type. The steady decrease in the susceptibility with decreasing temperature is also typical of a polymetallic dysprosium compound, reflecting progressive depopulation of the excited crystal field levels and, probably, weak antiferromagnetic exchange interactions. At 2 K, the value of $X_M T$ is 31.31 cm^3 K mol^{-1}. The field-dependence of the magnetization was measured at temperatures of 1.9, 3.0 and 5.0 K (Figure S100). The results are also typical, showing a steep

increase in magnetization in fields up to about 1.5 T, before increasing more slowly at higher field. The data at 1.9 K come close to saturation but do not fully saturate, reaching M = 18.89 Nβ in a field of 7 T. The magnetization of 4.72 Nβ per Dy^{3+} is slightly (7%) well below the theoretical value of 10 Nβ, but this again has been observed previously in many compounds of this nature and is the signature of magnetic anisotropy. The magnetic hysteresis curve is typical of a dysprosium SMM in which there is extensive mixing of the M_J wavefunctions within the magnetic ground state of the $^6H_{15/2}$ multiplet, *i.e.* narrow or waist-restricted loops.

Dynamic Field (AC) Magnetic Susceptibility Measurements.

The in-phase (real component, X') and out-of-phase (imaginary component, X'') AC magnetic susceptibility as functions of the AC frequency (ν) were measured at various temperatures in the range 1.9-22 K. Zero DC field was used. The data are shown in Figures S101 and S102, respectively.

The observation of well-defined maxima in zero DC field indicate SMM properties. However, relatively complex behavior is apparent, indicated by the observation of two groups of curves in green and red/yellow, respectively. The data point towards the occurrence of multiple thermally activated relaxation processes, although with the low-temperature set of curves (in green) quantum tunnelling of the magnetization (QTM) is apparent from the weak temperature-independence of the peak maxima. The Cole-Cole plots of X' versus X'' in Figure S103 further suggest the occurrence of multiple relaxation process in the region T = 6-9 K, since for a single relaxation process these curves would be semi-circular. From the Cole-Cole plot in Figure S103, it is possible to determine the relaxation time (τ) for each temperature. A plot of ln (τ/s) against T^{-1} allows the magnetic relaxation to be modelled using equation 3.

The relaxation time data for $[Cp^*DyI_2]_4$ are normal outside the temperature range 6-9 K, but very unusual if these temperatures are also considered. For the entire data set, a good fit using equation 3 is not possible. A rough estimate of anisotropy barrier can be obtained by considering the region in which ln t has a linear dependence on T^{-1}. In the region T = 12-19 K, a linear fit using the Orbach term $\tau^{-1} = \tau_0^{-1} e^{-U_{\text{eff}}/k_B T}$ yields $U_{\text{eff}} \approx 142(3)$ cm^{-1} with $\tau_0 \approx 1.6(2) \times 10^{-10}$ s. Alternatively, if the data points at 6-9 K are omitted, a good fit (R^2 = 0.99930) of the data from high to low temperature can be obtained using: U_{eff} = 164(10) cm^{-1}, τ_0 = 2(2) x 10^{-11} s, C = 3(26) x 10^{-8} s^{-1} K^{-n}, n = 9(3), τ_{QTM}^{-1} = 9.3(4) s^{-1} or τ_{QTM} = 0.107(4) s. Given the significant differences in the key bond lengths and angles, all parameters represent an average for the four dysprosium sites in each disordered molecule. Note that the region in which the data points have been omitted from the fit corresponds to the crossover region in which dominant thermal activation typically gives way to dominant Raman relaxation, before entering the QTM regime. The result is a significant error on the Raman coefficient C, which in this case is not physically meaningful.

The anisotropy barrier is reasonable for a molecule containing dysprosium in the geometry found in the crystal structure. That is, the $[Cp^*]^-$ ligand will provide a dominant axial crystal field; however, the iodide ligands provide a competing equatorial crystal field that allows significant mixing of the various M_J wavefunctions within the ground $^6H_{15/2}$ multiplet of Dy^{3+}. This scenario should facilitate relaxation predominantly via the first-excited Kramers doublet.

The proposed explanation is also consistent with the prominent QTM at low temperatures, which is common in dysprosium SMMs with non-negligible equatorial components to the crystal field (*i.e.* almost all dysprosium SMMs).

In terms of the molecular structure, a possible explanation for the observed multiple relaxation processes and unusual data points in the 6-9 K region could be crystallographic disorder, which is observed at the four distinct dysprosium positions and the eight iodide positions (Figure S105). The differences in the bond lengths and angles associated with dysprosium and the atoms bound to it are chemically very significant. Depending on the relative occupancies of the various disordered sites, each environment would have its own SMM signature, but this scenario would be impossible to resolve with AC susceptibility measurements. Experimentally, all possible dysprosium sites giving rise to a unique relaxation process would be superimposed.

In addition, it is reasonable to expect non-negligible exchange interactions between the various dysprosium centers, which complicate matters considerably. The total exchange is the sum of the dipolar and ligand-mediated super-exchange. The dipolar part would involve one dysprosium interacting with two adjacent dysprosium centers and with the diagonally opposite dysprosium, with each of the six possible interactions being of a different magnitude because of the asymmetry in the structure. Although likely to be weak, the super-exchange would further complicate the picture. In an effort to resolve the complex properties of $[Cp^*DyI_2]_4$, AC susceptibility measurements on the magnetically dilute sample $Dy@[Cp^*YI_2]_4$ (10% dilution level) were performed. These experiments effectively switch off all the available intra- and inter-molecular exchange pathways, allowing the properties to be studied at the level of single Dy^{3+} ions. The AC susceptibility and relaxation time data are shown in Figures S106-109. The results show that the dynamic magnetism in the dilute version is qualitatively similar to that of the pure dysprosium sample but quantitatively different. In particular, the variation of $X''(\nu)$ with temperature is more uniform, resulting a more normal dependence of ln (τ/s) on T^{-1}.
For the dilute sample, a very good fit (R^2 = 0.99274) of the relaxation time data was possible with the following parameters: U_{eff} = 204(25) cm^{-1}, τ_0 = 6.6(1) x 10^{-13} s, C = 1(3) x 10^{-8} s^{-1} K^{-n}, n = 9(1), τ_{QTM}^{-1} = 0.13(3) s^{-1} or τ_{QTM} = 7.88(4) s. Thus, a slight increase in the anisotropy barrier occurs upon dilution, as is often observed for lanthanide SMMs. The rate of QTM is slower and the QTM time is longer in the dilute sample, consistent with the elimination of exchange pathways in the dilute sample.

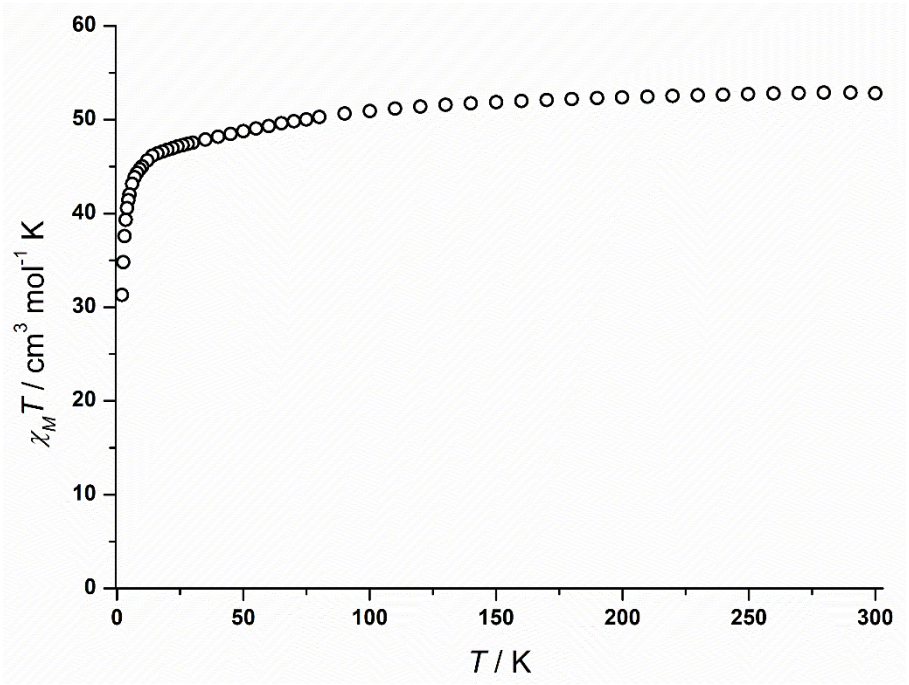

Figure S99. Temperature-dependence of $c_M T$ in the range 2-300 K for $[Cp^*DyI_2]_4$.

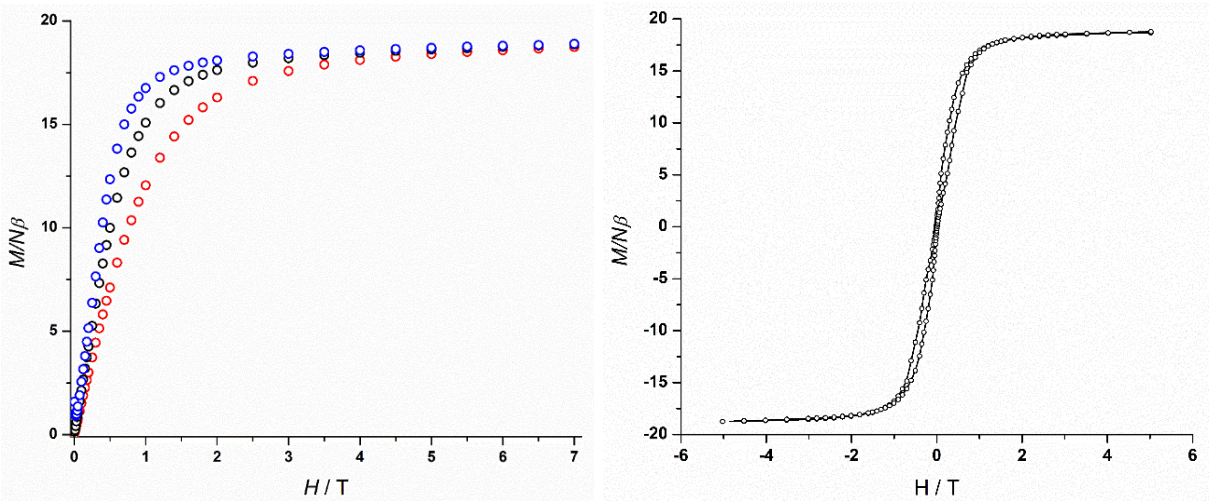

Figure S100. *Left:* Field (H) dependence of the magnetization (M) at 1.9 K (blue circles), 3.0 K (black circles) and 5.0 K (red circles) for $[Cp^*DyI_2]_4$. *Right:* Magnetic hysteresis collected at 1.9 K under a varying field sweep rate (1.1 mT s^{-1} │0-1│ T, 3.0 mT s^{-1} │1-2│ T, 4.5 mT s^{-1} │2-3│ T and 8.5 mT s^{-1} │3-5│ T).

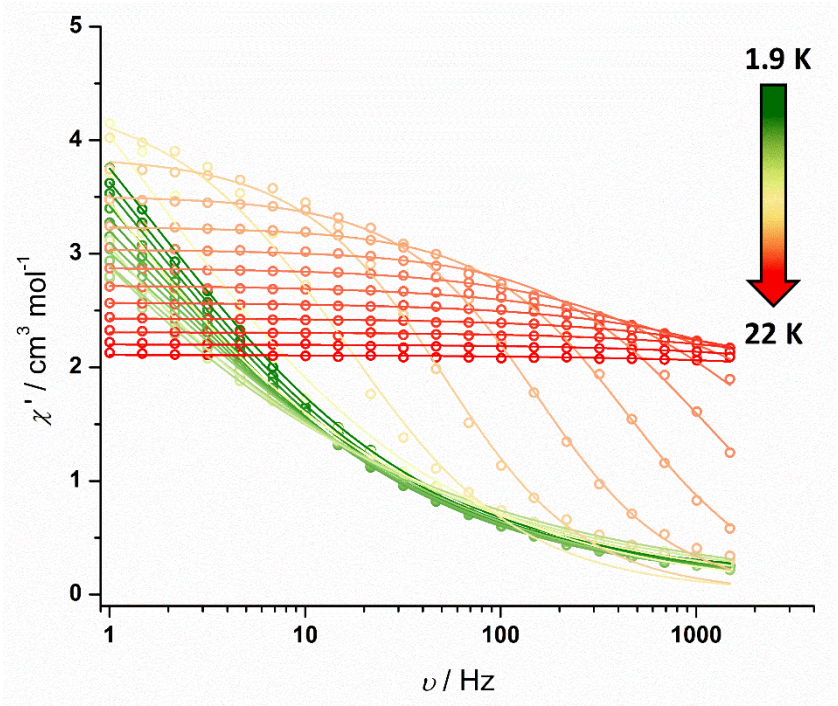

Figure S101. Frequency dependence of the in-phase susceptibility (χ') for $[Cp^*DyI_2]_4$ in zero DC field at ν = 1-1488 Hz and temperatures of 1.9-22 K. Solid lines represent fits to the data using equation 1.

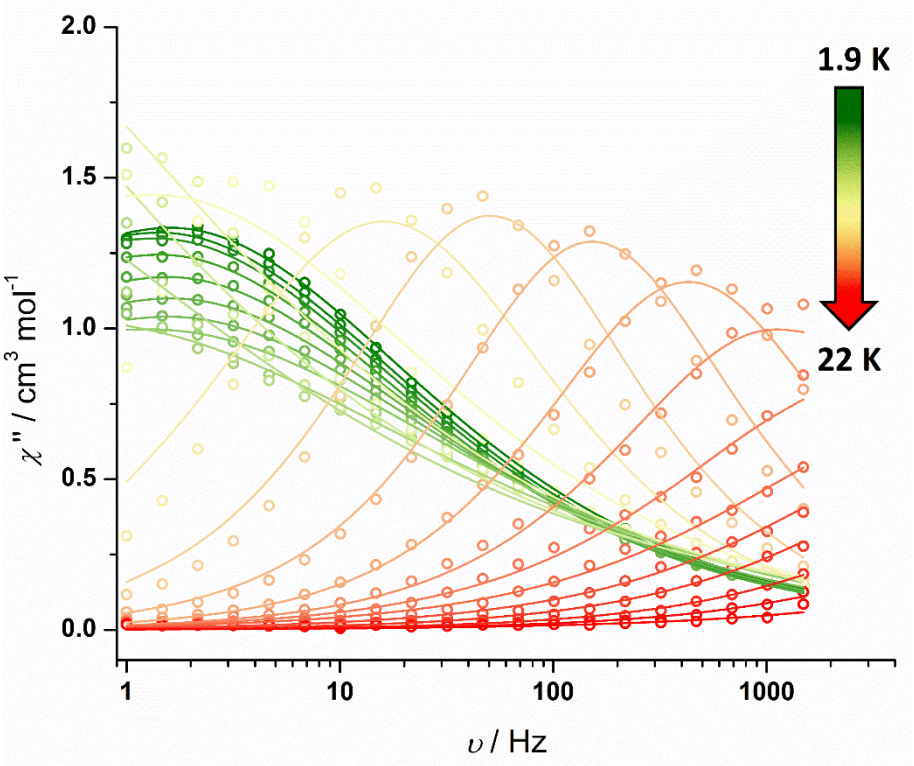

Figure S102. Frequency dependence of the out-of-phase susceptibility (χ'') for $[Cp^*DyI_2]_4$ in zero DC field at ν = 1-1488 Hz and temperatures of 1.9-22 K. Solid lines represent fits to the data using equation 2.

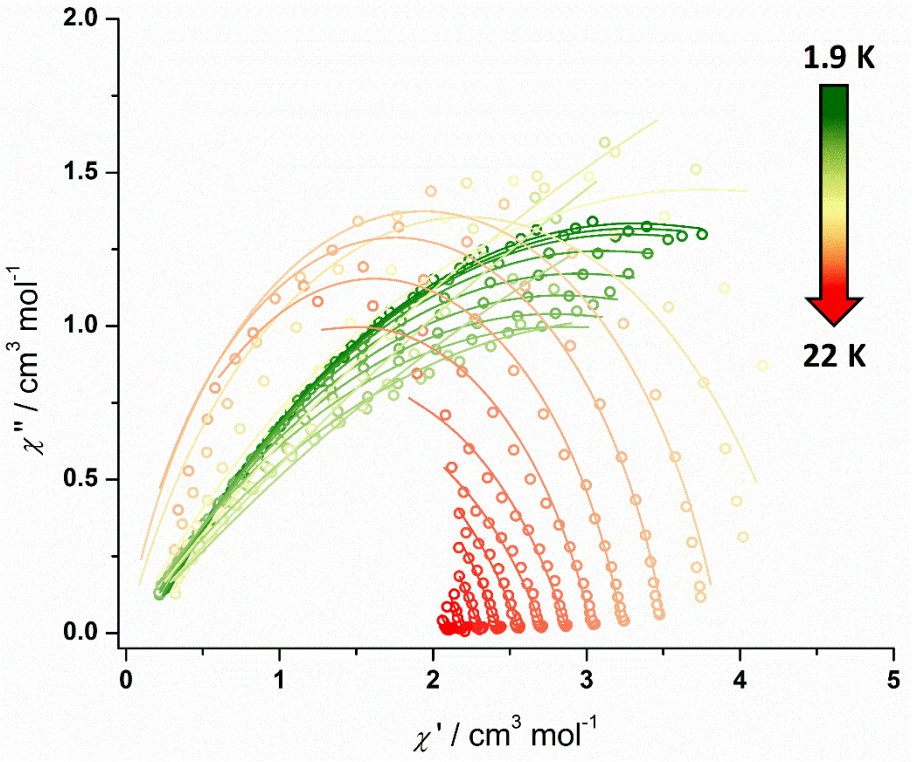

Figure S103. Cole-Cole plots for the AC susceptibilities in zero DC field for $[Cp^*DyI_2]_4$ from 1.9-22 K. Solid lines represent fits to the data using equations 1 and 2.

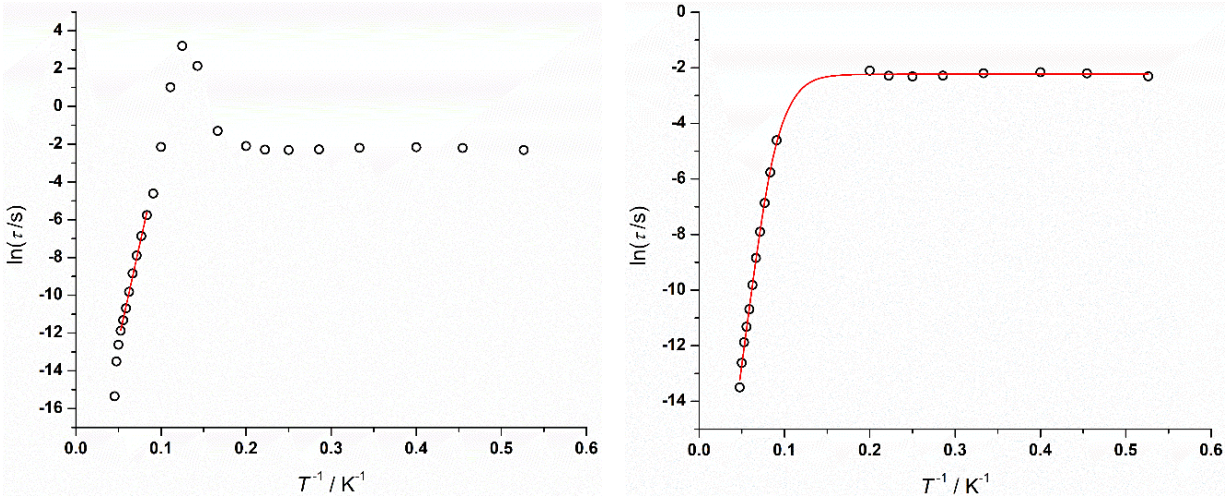

Figure S104. *Left:* plot of natural log of the relaxation time (t) *vs.* inverse temperature for $[Cp^*DyI_2]_4$. The solid red line indicates a fit of the data from 12-19 K using only the Orbach term $\tau^{-1} = \tau_0^{-1} e^{-U_{\mathrm{eff}}/k_B T}$. *Right*: the same data with a fit ($R^2 = 0.99930$) according to equation 3 and the parameters stated in the text, with the data points from 6-9 K omitted.

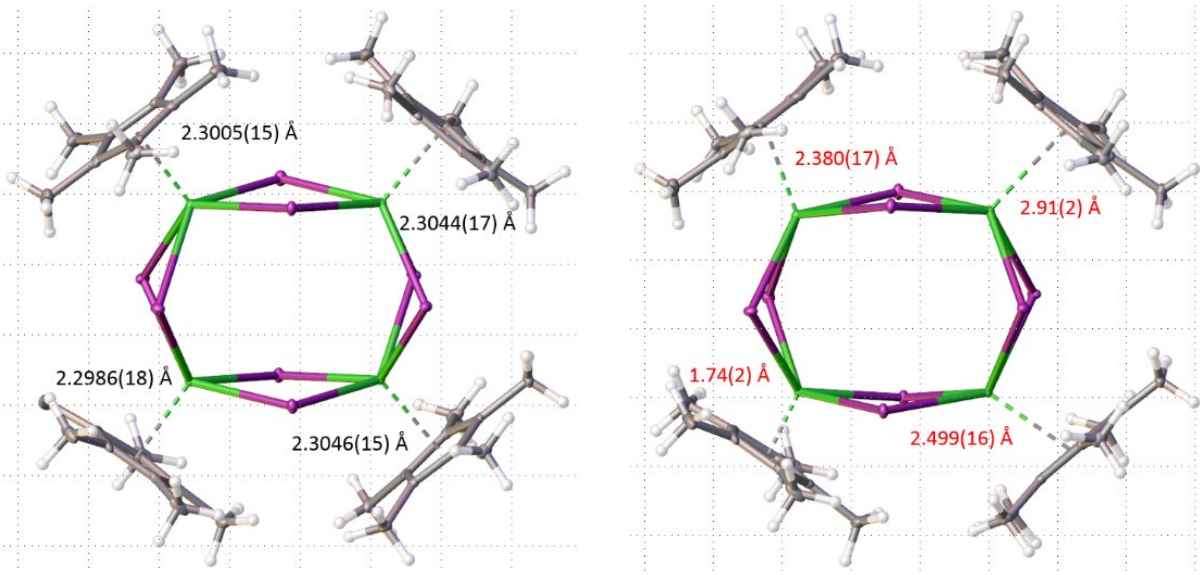

Figure S105. The two disordered components of $[Cp^*DyI_2]_4$. The Dy–Ct distances are shown.

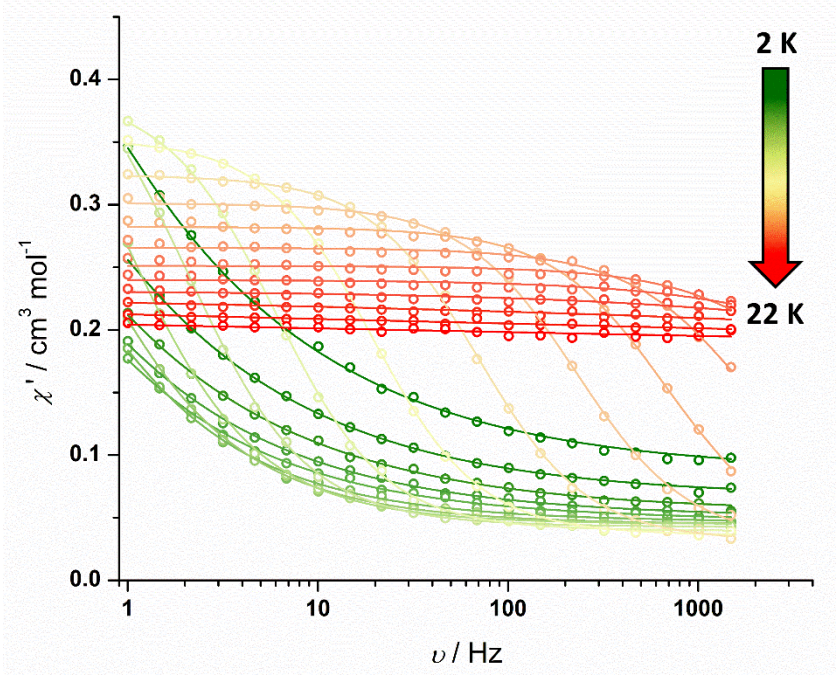

Figure S106. Frequency dependence of the in-phase susceptibility (χ') for $Dy@[Cp^*YI_2]_4$ in zero DC field at ν = 1-1488 Hz and temperatures of 2-22 K. Solid lines represent fits to the data using equation 1.

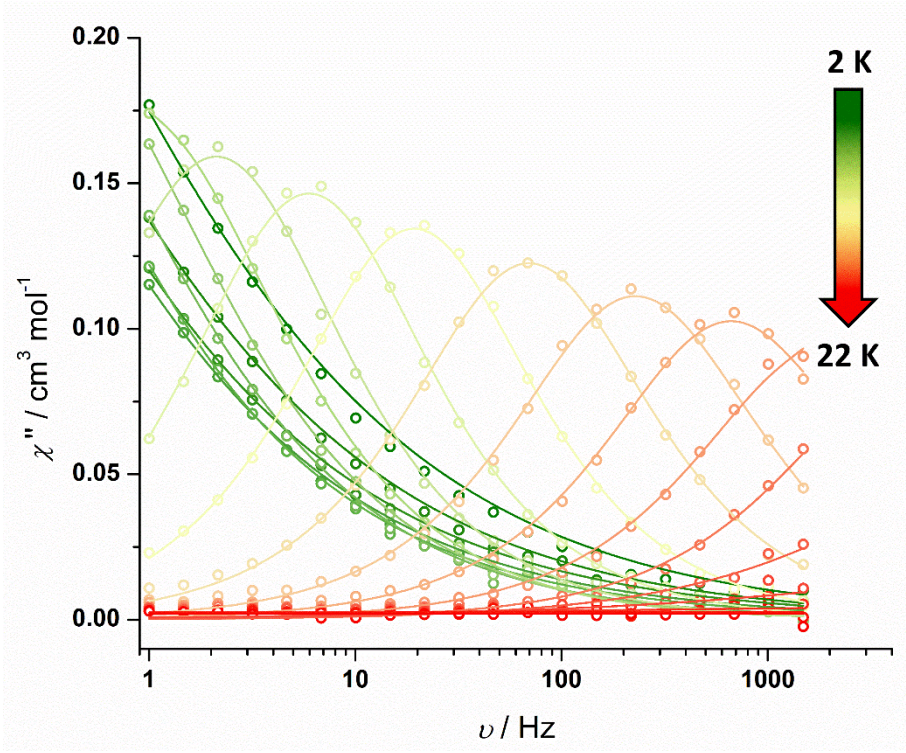

Figure S107. Frequency dependence of the out-of-phase susceptibility (χ'') for $[Cp^*DyI_2]_4$ in zero DC field at ν = 1-1488 Hz and temperatures of 1.9-22 K. Solid lines represent fits to the data using equation 2.

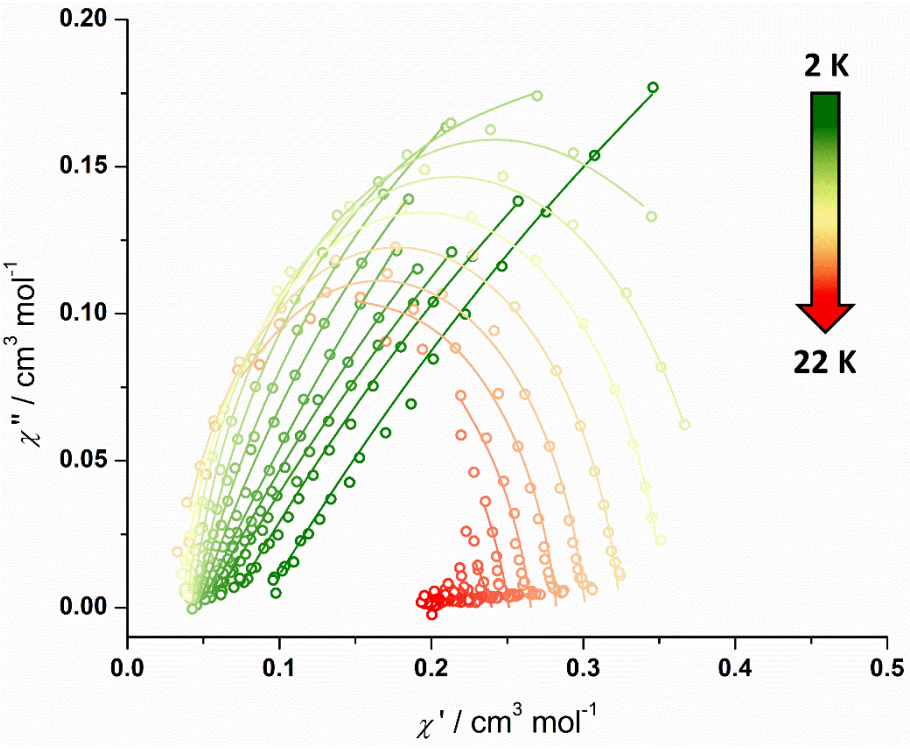

Figure S108. Cole-Cole plots for the AC susceptibilities in zero DC field for $[Cp^*DyI_2]_4$ from 1.9-22 K. Solid lines represent fits to the data using equations 1 and 2.

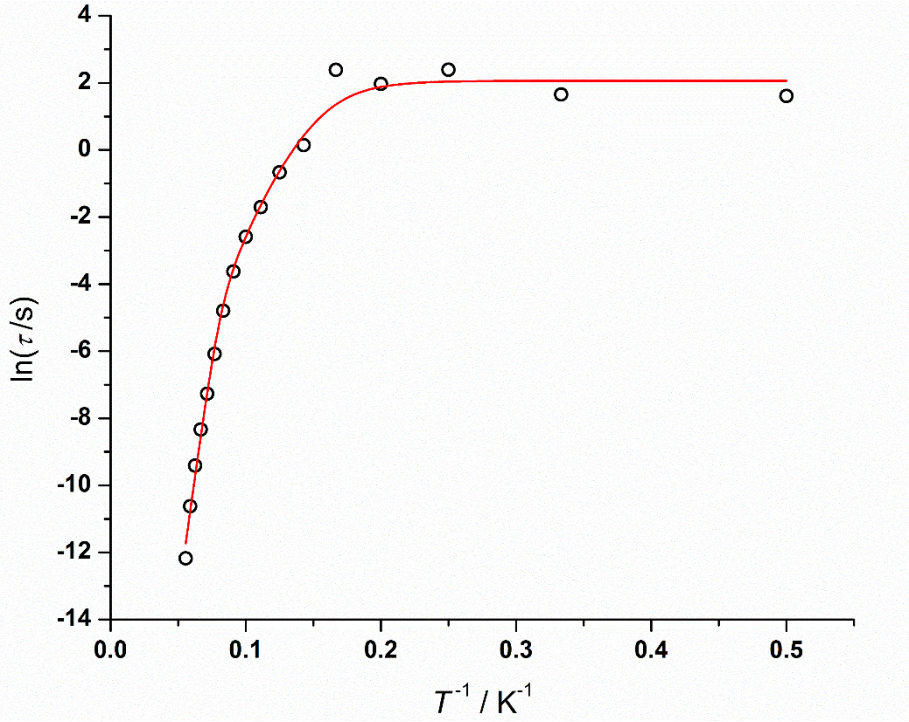

Figure S109. Plot of natural log of the relaxation time (t) *vs.* inverse temperature for Dy@[Cp*YI_2]$_4$. The solid red line indicates a fit (R^2 = 0.99274) according to equation 3 and the parameters stated in the text.

References

[1] COSMO, v. 1.61, Bruker AXS Inc., Madison, WI, **2012**.
[2] APEX 3, v. 2016.5-0, Bruker AXS Inc., Madison, WI, **2012**.
[3] SAINT, v. 8.34A, Bruker AXS Inc., Madison, WI, **2010.**
[4] L. Krause, R. Herbst-Irmer, G. M. Sheldrick, D. Stalke, *J. Appl. Cryst.* **2015**, *48*, 3-10.
[5] G. M. Sheldrick, *Acta Crystallogr. Sect. A* **2015**, *71*, 3-8.
[6] C. B. Hübschle, G. M. Sheldrick, B. Dittrich, *J. Appl. Cryst.* **2011**, *44*, 1281-1284.
[7] C. F. Macrae, I. J. Bruno, J. A. Chisholm, P. R. Edgington, P. McCabe, E. Pidcock, L. Rodriguez-Monge, R. Taylor, J. Streek, P. A. Wood, *J. Appl. Cryst.* **2008**, *41*, 466-470.

F

Appendix

Appendix

Analytical data of compounds not included in the main results or manuscripts

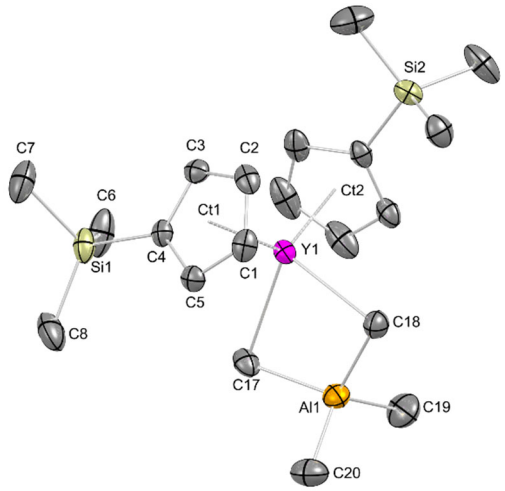

[Cp'$_2$Ce(AlMe$_4$)] DAB40
R_1[I>2σ(I)] 3.09%, *w*R_2 (all data) 7.77%
a = 13.554(5) Å α = 90°
b = 13.447(5) Å β = 96.835(6)°
c = 13.812(4) Å γ = 90°

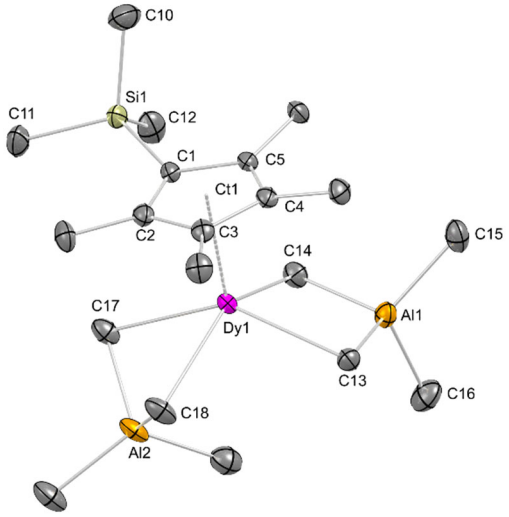

[Cp*'Dy(AlMe$_4$)$_2$] DAB69
R_1[I>2σ(I)] 1.59%, *w*R_2 (all data) 3.99%
a = 11.7994(3) Å α = 90°
b = 15.5598(4) Å β = 91.5020(10)°
c = 13.9552(4) Å γ = 90°

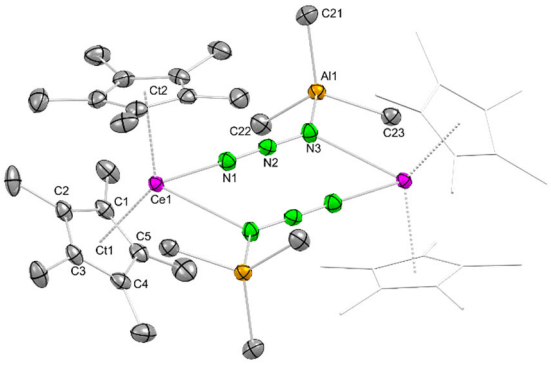

[Cp*$_2$CeN$_3$(AlMe$_3$)]$_2$ JB26_2
R_1[I>2σ(I)] 2.65%, *w*R_2 (all data) 6.80%
a = 10.8795(11) Å α = 90°
b = 12.8273(13) Å β = 103.091(2)°
c = 18.2181(19) Å γ = 90°
Additional analyses: ^{1}H NMR, ^{13}C{^{1}H}NMR, EA, IR

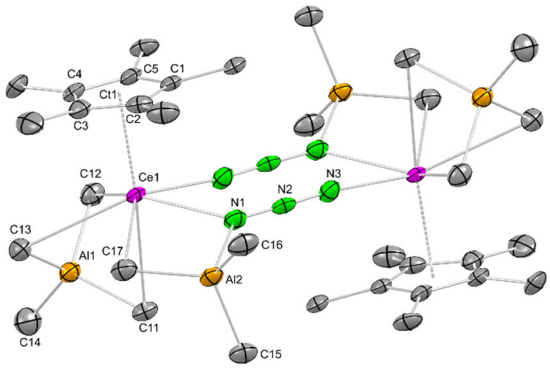

[Cp*Ce(AlMe$_4$)(AlMe$_3$)N$_3$]$_2$ JB27_2
R_1[I>2σ(I)] 5.60%, *w*R_2 (all data) 15.24%
a = 9.6465(13) Å α = 97.843(3)°
b = 10.1182(14) Å β = 93.530(3)°
c = 12.8953(18) Å γ = 110.852(3)°
Additional analyses: ^{1}H NMR, ^{13}C{^{1}H}NMR, EA, IR